Proceedings of the Symposium on Particle Identification at High Luminosity Hadron Colliders

April 5-7, 1989

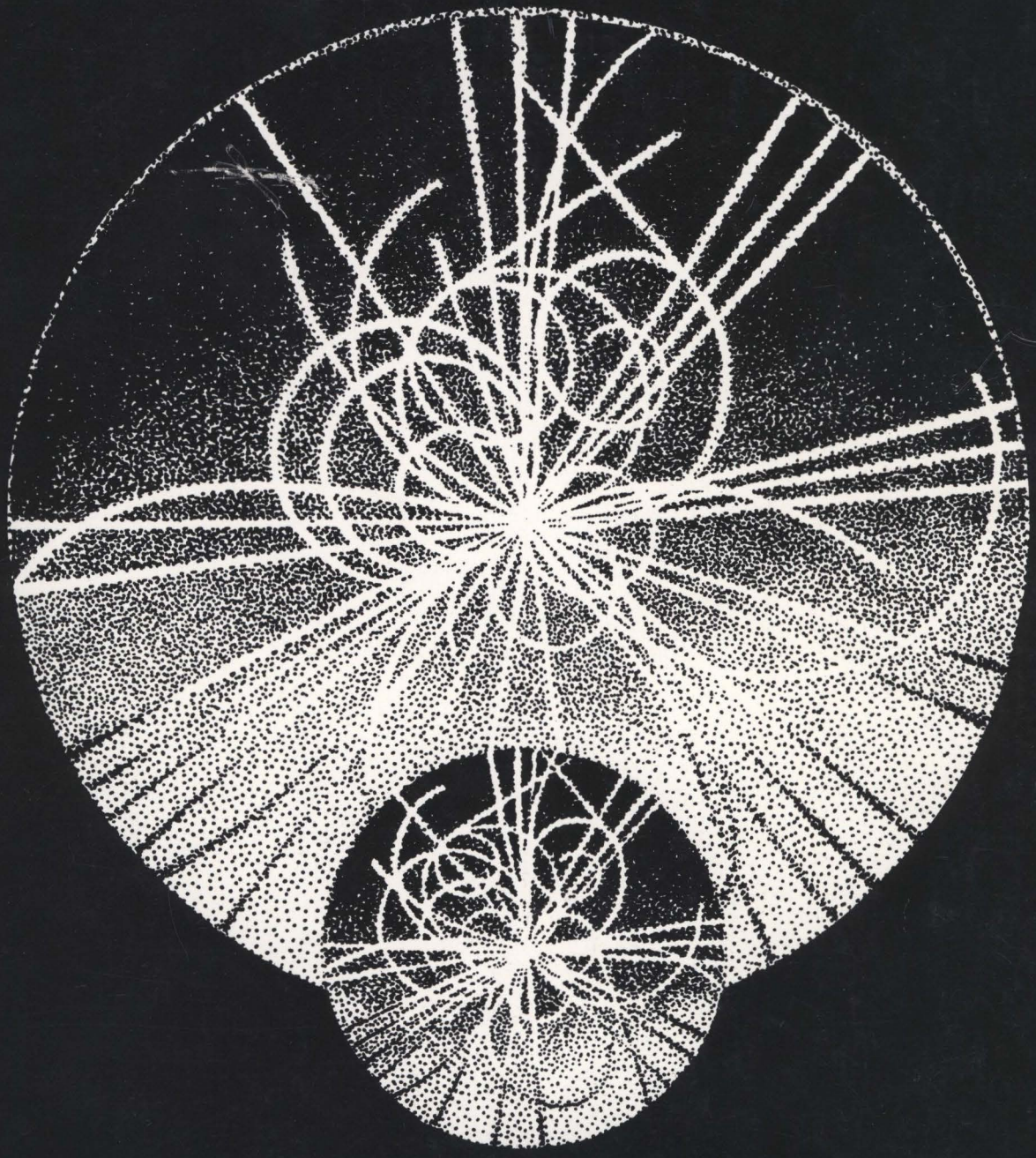

Fermi National Accelerator Laboratory
Batavia, Illinois

•

Editors
Treva J. Gourlay and Jorge G. Morfín

Proceedings of the Symposium on Particle Identification at High Luminosity Hadron Colliders

April 5-7, 1989

Editors: Treva J. Gourlay and Jorge G. Morfín

Fermi National Accelerator Laboratory
Batavia, Illinois

Operated by Universities Research Association, Inc.
Under Contract with the United States Department of Energy

Proceedings of the Symposium on Particle Identification at High Luminosity Hadron Colliders

held at

Fermi National Accelerator Laboratory
Batavia, Illinois
April 5-7, 1989

Editors: Treva J. Gourlay *and* Jorge G. Morfín

Operated by Universities Research Association, Inc., under contract with the United States Department of Energy

Proceedings of the Symposium on Particle Identification at High Luminosity Hadron Colliders

held at

Fermi National Accelerator Laboratory
Batavia, Illinois
April 5-7, 1989

Preface

Experimental particle physics has been preoccupied with the task of identifying particles from the very beginnings of the field. With the onset of each new and higher energy regime, new problems in identification were faced and overcome. We are once again at a transition point where the era of fixed-target experiments is slowly giving way to the era of large collider experiments. It is true that this new era does not bring a great change in the energy scale of the particles that must be identified. However, the amount of solid-angle that must be covered and, most importantly, the speed in which the various signals must be acquired has increased dramatically.

This Symposium is the first to concentrate the community's efforts on solving the problems of Particle Identification at High Luminosity Hadron Colliders. Over 130 participants from Europe, North America, South America, and the Soviet Union gathered at Fermilab to share their ideas with their colleagues. They heard 32 talks covering every aspect of particle identification and the physics which would be influenced by knowledge of the particle's mass. We gratefully acknowledge the contributions and enthusiasm of all the participants with special thanks to the speakers for the high quality of their presentations.

We greatly appreciate the efforts of everyone that contributed to making this Symposium a success. Both the CDG/SSC and the Fermilab Directorate were most generous with their financial support. The excellent choice of speakers and topics was due to the hard work of the organizing committee: **D. Anderson** (co-chair), **S. Dhawan**, **J. Bjorken**, **P. Garbincius**, **M. Gilchriese**, **T. Gourlay**, **D. Green**, **D. Leith**, **N. Lockyer**, **J. Morfín** (co-chair), **M. Sheaff**, **R. Stefanski**, **S. Whitaker**, and **T. Ypsilantis**. We wish to thank our co-editors D. Anderson, P. Garbincius, D. Green, N. Lockyer, M. Sheaff, and R. Stefanski who helped "molest and terrorize" the speakers until their written contributions were in-hand. We extend our sincere thanks to **Richard Fenner** and **Stephanie Novack** from the Fermilab Publications Office for their help in getting these Proceedings to print; to **Angela Gonzales** for the poster and proceedings artwork; and to the secretariat, **Corrine Harris**, **Pat Hatcher**, **Barb Kristen**, and **Florence Sherter**, for their assistance. Finally we wish to thank the **Fermilab Cafeteria** for catering the very enjoyable Reception and the Symposium dinner.

Treva J. Gourlay
Jorge G. Morfín

I. Physics Issues at Hadron Colliders: The Role of Particle Identification

USES OF PARTICLE IDENTIFICATION FOR SUPERCOLLIDER PHYSICS

CHRIS QUIGG

SSC CENTRAL DESIGN GROUP
LAWRENCE BERKELEY LABORATORY
BERKELEY, CA 94720 USA

Abstract

I summarize the basic characteristics of the Superconducting Super Collider and describe the experimental environment of its high-luminosity interaction regions. I then review some of the discovery possibilities opened by the SSC, with special attention to the advantages conferred by particle identification.

1. The Importance of Particle Identification

In this talk, I will try to remind you of the benefits that experimentation with the SSC can derive from efficient identification of particle species and of the battle conditions under which particle identification will have to be carried out. My presentation will be schematic, in that I will not show simulations of events or comment in detail on event topologies and the complexity of events.[1] Nor will I comment on practical experimental techniques for identifying particles; I shall leave practical matters to the professionals and concentrate on potential benefits. In view of the generality of my remarks, it may be helpful to begin with a statement of my conclusions:

(i) A use will be found for anything you can do: identification of light and heavy quarks, gauge bosons, and leptons will all aid the search for new phenomena and the detailed measurement of familiar processes.

(ii) The requirements for particle identification, measured by the desires of those who conceive experiments, will always exceed what is practical. If one isolated particle can be identified efficiently, we will next want to identify several particles, including those in jets of light hadrons.

(iii) Ideally, we will want to measure the momenta of short-lived particles, not simply to tag them. Generally speaking, the requirements for momentum measurement will be set by the need to identify narrow states that decay into heavy flavors of quarks and leptons.

Although such statements will not come as a surprise to aficionados of particle identification, I will attempt to show you some of the reasons for their correctness—and importance—in the SSC setting.

The parameters of the SSC have been set by considering the demands of hard-scattering processes and by our conviction that it is essential for the next machine to make possible a thorough exploration of the 1-TeV scale. This has been a sensible way to proceed, because the scientific goals are of high importance and because these are the reactions that make the most severe demands on energy and luminosity (both instantaneous and average), the parameters that drive accelerator design. However, the experimental program of the SSC will be broader than the set of experiments we have used to define the capabilities of the machine. It is very important that our vision of experiments or of detector components not be narrowed by what QCD predicts or by what theorists find most interesting today. Similarly, we must not assume that every experiment for the SSC will take the form of a 4π, general-purpose device.

In most of my remarks, I will ignore the virtues of identifying the light quarks and hadrons composed of them. However, it is hard to imagine an initial program of exploration with the SSC that does not include measurements expected to be prosaic, but with the capacity to surprise, such as particle surveys of the kind carried out in the past with highly instrumented single-arm spectrometers. Though the SSC does not seem to be the most favorable environment for producing a quark-gluon plasma, it would be a mistake to deny ourselves the opportunity to look for signs of changes of phase: copious production of strange particles, or of photons, as well as changes in the kinematical characteristics of events. Similar remarks apply to every kind of "zoo" event hinted in cosmic-ray experiments. For many of these studies, which in any case will help give us a general awareness of the characteristics of a typical event, particle identification is an important—perhaps decisive—element.

2. Main Parameters of the SSC

The chief attributes of the SSC's superconducting collider rings and of the cascade of accelerators providing intense proton beams to them are set forth in the 1986 Conceptual Design Report.[2] The SSC is planned as a proton-proton collider with 20 TeV per beam and a peak luminosity of $\mathcal{L} = 10^{33}$ cm^{-2}sec^{-1}. To achieve this luminosity while keeping the number of inelastic events per beam crossing within reason, the Conceptual Design calls for 1.3×10^{14} protons per ring, divided among 1.7×10^{4} bunches, each containing about 7×10^{9} protons. The bunch length will be about 6 cm; bunches will be spaced by 4.8 m or, in terms more meaningful for the

design of experiments, about 15 ns. The counter-rotating proton beams will be confined by two separate rings of 6.6-T dipoles, one atop the other, with the beam centers separated by about 70 cm. The dipoles will be 17 m long; about 3840 will be needed for each ring.

The collider rings will be fed by a cascade of accelerators. The Conceptual Design Report calls for a 600-MeV linac followed by two rapid-cycling synchrotrons built of conventional (nonsuperconducting) magnets. These will boost the proton momentum to 8 and then to 100 GeV/c. A superconducting High-Energy Booster synchrotron will take the particles up to 1 TeV/c and inject them into the collider rings. The acceleration cycle will take about 1000 sec, and colliding beams will be stored for about a day at a time.

A possible layout[3] of the Supercollider is shown in Figure 1. Four long straight sections are clustered on the two gently curved sides of the collider ring. In this schematic diagram, the near cluster incorporates the injector complex, the radio-frequency accelerating system, beam absorbers, and two of the six interaction halls. The far cluster adds four more interaction halls, two of which will be reserved for development after research begins, according to the Conceptual Design Report. The space between interaction points is gently curved, so muons produced in beam-beam collisions at one interaction region are offset by 94 meters from the next collision point. Current concepts for the interaction regions will leave ±20 m of free space for detectors in the high-luminosity ($\mathcal{L} = 0.06$–10^{33} cm^{-2}sec^{-1}) areas and ±120 m of free space in the intermediate-luminosity ($\mathcal{L} = 0.8$–5.0×10^{31} cm^{-2}sec^{-1}) areas. This work provides a firm foundation for the creation of a site-specific conceptual design; the configuration of the experimental areas will be determined by the scientific program the SSC Laboratory develops in consultation with the user community.

3. Experimental Environment of the SSC

Signals and backgrounds for specific phenomena at the SSC have been studied extensively over the past four years.[4–10] To design experiments, it is also important to be aware of the general environment in which SSC detectors must function and events must be selected and recorded. At the design luminosity of 10^{33} cm^{-2}sec^{-1}, we expect about 10^8 inelastic collisions per second and an average of 1.7 events per crossing. A general-purpose detector will have about 10^6 electronic channels.

A good way to gain respect for the conditions that will prevail at the SSC is to examine the trigger rate for events with transverse energy E_T greater than some threshold $E_T^{\min}$. This is shown in Figure 2 for the nominal operating conditions of the SSC: $\sqrt{s} = 40$ TeV and $\mathcal{L} = 10^{33}$ cm^{-2} sec^{-1}, as well as at 10 and 100 TeV. At 40 TeV, a high-E_T trigger with threshold set at 2 TeV will count at 1 Hz from two-jet QCD events. This is of interest in planning triggers to efficiently select interesting events.

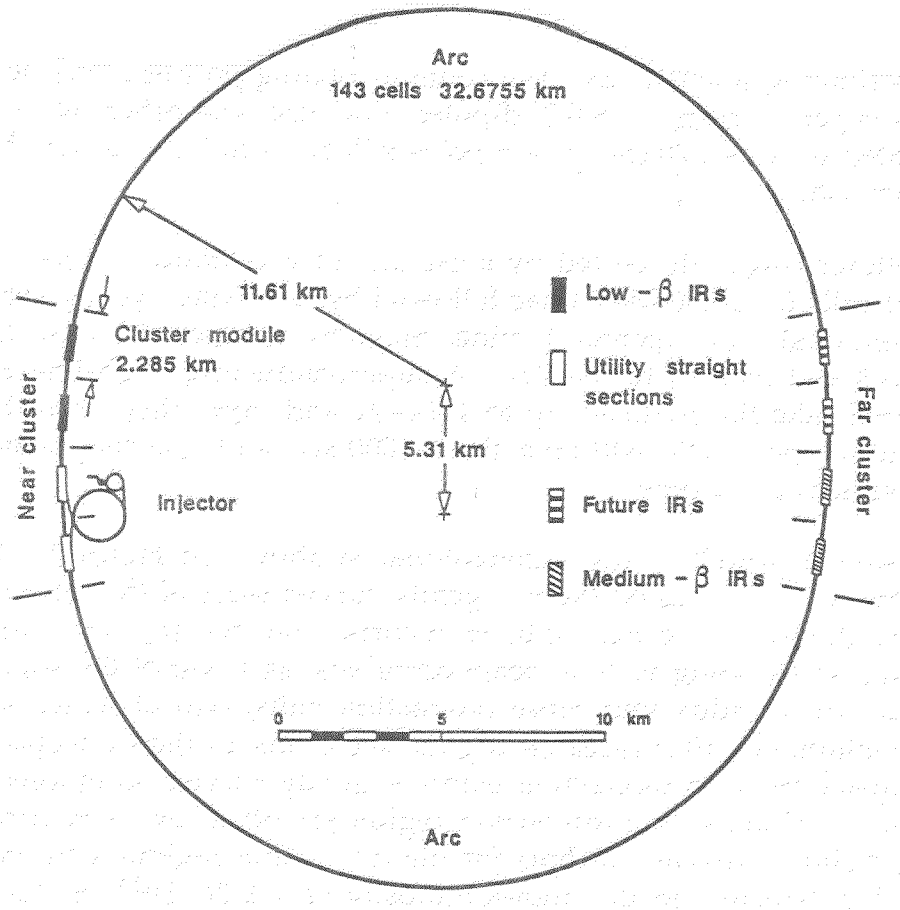

Figure 1: Collider ring layout envisaged in the 90° (September 1987) Lattice of the SSC [from Ref. 3].

The SSC experimental environment is complex and presents a challenge to technology for many aspects of detector components. This does not mean that we do not know how to build experiments for the SSC, but simply that we can profit from improvements in many areas of detector technology. There is time to carry out detector R&D that can yield rich rewards before designs of first-round experiments must be frozen.[13]

I have listed in Table 1 particles that we wish to identify. I shall have nothing further to say about the first group of light particles. For the examples I will discuss, they play no role except as possible impediments to electron identification. However, it is easy to find processes that make identification of these particles interesting in its own right. The study of prompt photon production and signatures for quark-gluon plasma come immediately to mind. Particles in the second group—the leptons and the quarks with picosecond lifetimes—are those that we should insist on identifying well in SSC experiments. Efficient identification of particles in the final group would make our experimental life much richer and would greatly enhance our ability to explore the new terrain opened up by the SSC.

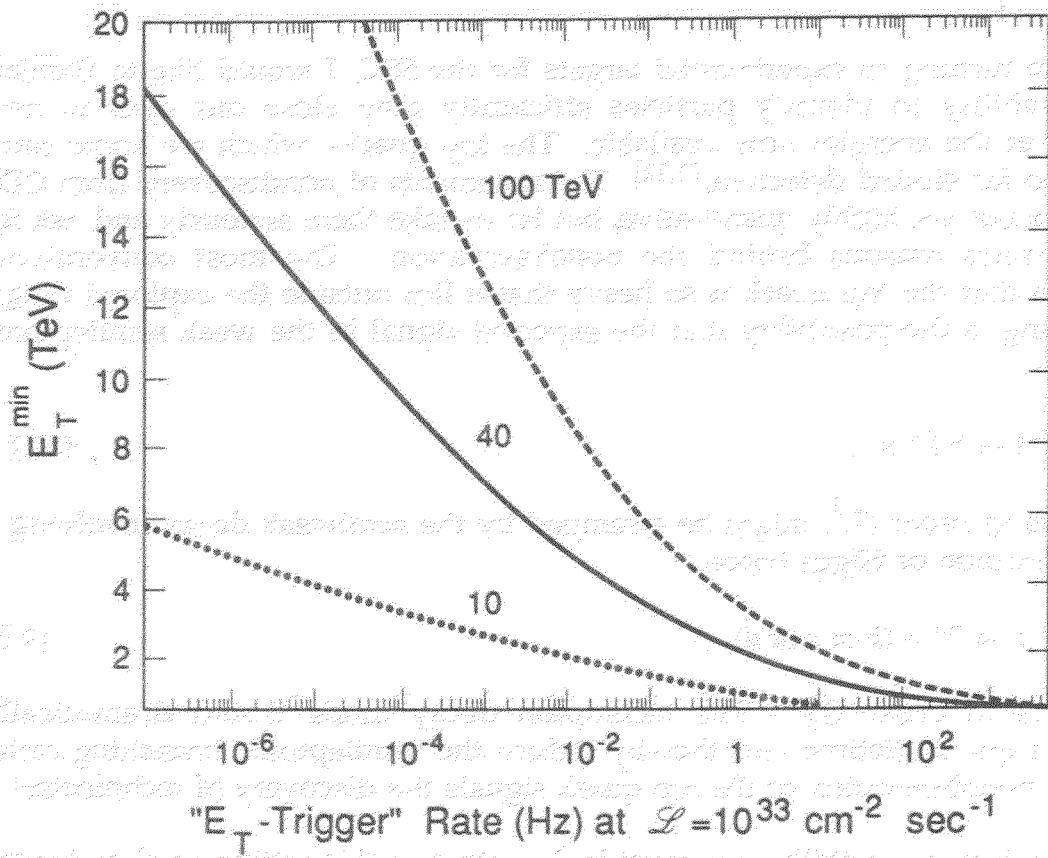

Figure 2: Counting rate for an E_T-trigger in pp collisions at an instantaneous luminosity of $\mathcal{L} = 10^{33}\text{cm}^{-2}\text{sec}^{-1}$. The threshold is defined for transverse energy deposited in the central region of rapidity, defined by $|y_i| < 2.5$ for jets 1 and 2.

Table 1. Candidates for Particle Identification

$\pi^{\pm}, K^{\pm}, K^0, p^{\pm}, n, \ldots$
γ, π^0
c, b
e
μ
τ
$W^{\pm}$
Z^0
t
g

Before turning to experimental targets for the SSC, I would like to indicate how the inability to identify particles efficiently may close our eyes to new phenomena at the energies now available. The top quark—which we know must exist—has so far eluded detection.[11,12] The statements of nondiscovery from CDF and UA2 are not yet highly quantitative, but let us take them seriously and ask for possible physics reasons behind the nonobservation. The most conventional possibility is that the top quark is so heavy that it lies outside the explored range. More amusing is the possibility that the expected signal in the weak semileptonic decay

$$t \to b\, \ell^+ \nu \quad , \tag{3.1}$$

which occurs in order G_F^2, might be swamped by the semiweak decay involving a charged technipion or Higgs boson,

$$t \to P^+ + (b \text{ or } s \text{ or } d) \quad , \tag{3.2}$$

which occurs in order G_F. The technipion decay mode would dramatically shorten the t-quark lifetime and thereby reduce the semileptonic branching ratio. Perhaps the nonobservation of the top quark signals the discovery of technicolor!

To check this possibility, we must look—either in this setting or elsewhere—for the light technipions. This can be done in experiments at SLC or LEP, once the study of rare decays of the Z^0 becomes possible. The branching ratio expected for the decay $Z^0 \to P^+ P^-$ exceeds 10^{-3} for technipion masses up to about 40 GeV/c^2. The technipion pairs are to be reconstructed in final states such as $(c\,\bar{b})(\bar{c}\,b)$, etc., for which efficient particle identification is indispensable.

4. Some Hadron Collider Discovery Possibilities

The standard model hints that the frontier of our ignorance lies at about 1 TeV for collisions among the fundamental constituents. This conclusion is specific to electroweak symmetry breaking, but that is not the only interesting issue we face. More generally, the success of our theoretical framework suggests that a significant step is needed to see breakdowns of the standard model. Hadron colliders opening unexplored territory offer a broad range of discovery possibilities. Let us consider a few examples.

4.1 New Gauge Bosons

There are many reasons to be open to the possibility of new gauge bosons. These include the idea of high-energy parity restoration in an electroweak gauge theory based on the symmetry group $SU(2)_L \otimes SU(2)_R \otimes U(1)_Y$ and the occurrence of extra $U(1)$ gauge symmetries in unification groups larger than $SU(5)$, such as the low-energy gauge groups emerging from superstring models.

In a specific theory, the calculation of $W^{\pm}$ and Z^0 production rates is easily modified to yield an estimate of the cross section for the production of new gauge bosons. I show in Figure 3 the cross section for the production of a new W-boson with standard gauge couplings to the light quarks. The discovery signal is an isolated electron or muon—which must be identified—plus missing energy, which is to say an identified neutrino. For the 40-TeV energy projected for the SSC, we may anticipate sensitive searches out to a mass of about 6 TeV/c^2. Once we get over the excitement attending the discovery of a new force, we should also ask about the decay products of the new gauge boson, for they may contain new species of fermions. In an $SU(2)_L \otimes SU(2)_R \otimes U(1)_Y$ electroweak theory, the right-handed W may decay into a neutral heavy lepton

$$W^+ \rightarrow e^+ N_e \qquad \hookrightarrow e^+\mu^- \nu_\mu \text{ or } e^-\mu^+\bar{\nu}_\mu \tag{4.1}$$

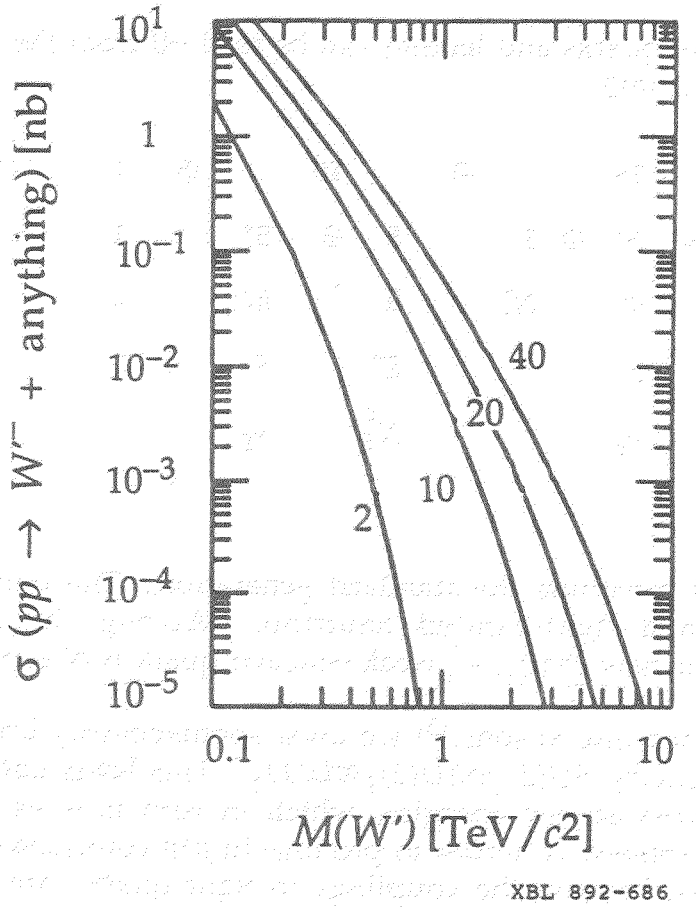

Figure 3: Cross section for the production of a heavy W-boson with rapidity $|y| < 1.5$ in pp collisions at 2, 10, 20, and 40 TeV (after EHLQ).

(In some models, this may be the signature for discovery of the new gauge bosons.) The ability to detect both electrons and muons increases the number of decay channels useful for identifying a heavy W-boson and is essential for examining the decay products of the new W.

The exceptional group E_6 has a long history as a candidate group for the unification of the strong, weak, and electromagnetic interactions. Historically, the motivation for considering E_6 derived mainly from the observation that E_6 is the group beyond $SO(10)$, which is in turn the group beyond $SU(5)$:

$$E_6 \supset SO(10) \supset SU(5)\,. \tag{4.2}$$

The current revival is owed to the possibility that E_6 may be the surviving symmetry of the $E_8 \otimes E_8'$ internal symmetry group of the heterotic string.[14] Like all applications of superstring ideas to phenomenology, the "derivation" of E_6 is very vague and tentative. Nevertheless, it provides us with a reason to look again at some possible consequences of an E_6 gauge symmetry.

The spectrum of quarks and leptons can be read off from the fundamental **27** representation of the group:

E_6:	**27**	=		**16**			$\oplus$		**10**		$\oplus$	**1**	: $SO(10)$	
	$SU(5)$:	**10**	$\oplus$	**5***	$\oplus$	**1**		**5**	$\oplus$	**5***		**1**		
		u		d^c		N_e^c		h		h^c		n		
		d		e				E^+		E^-				
		u^c		ν_e				N_E^c		ν_E				
		e^c												(4.3)

The **10** $\oplus$ **5*** of $SU(5)$ constitute the standard generation. The remaining member of the $SO(10)$ **16** is a right-handed neutrino. Among the novel particles characteristic of E_6, the new charge $-\frac{1}{3}$ weak isoscalar quark is of especial interest.

To determine the interactions,[15] we must spontaneously break E_6 down to the low-energy symmetry $SU(3)_c \otimes SU(2)_L \otimes U(1)_Y$. This leads naturally to one or more extra $U(1)$ factors at low energies, which in turn implies an extra gauge boson, Z'. The Z' is somewhat harder to produce in $p^{\pm}p$ collisions than a standard Z^0 of the same mass, because the couplings to light quarks are inhibited. The branching ratio for the decay into charged leptons, for example, is

$$\Gamma(Z' \to e^+ e^-) \approx 3\%/n_g\,, \tag{4.4}$$

where n_g is the number of generations, which is somewhat smaller (by about $1/n_g$) than that of the conventional Z^0. The production cross sections for the new Z' are shown in Figure 4. We expect to be sensitive to this new object in the e^+e^- or $\mu^+\mu^-$ channel for masses as large as about 3–4 TeV/c^2 at the SSC.

Discovery of the Z' would open the prospect of finding the new fermions that inhabit the fundamental representation of E_6. Table 2 shows that the branching ratio is especially favorable for the charge $-\frac{1}{3}$ quark h. It cannot be absolutely stable, for we have no evidence of it in relics from the big bang. We expect it to decay by mixing with the weak-isodoublet charge $-\frac{1}{3}$ quarks,

$$h \leftrightarrow \left\{ \begin{array}{c} d \\ s \\ b \end{array} \right\} \leftrightarrow \left(\begin{array}{c} u \\ c \end{array} \right) \ell \nu \,, \tag{4.5}$$

or through flavor-changing neutral-current interactions into dilepton channels. Direct detection is hopeless without effective particle identification.

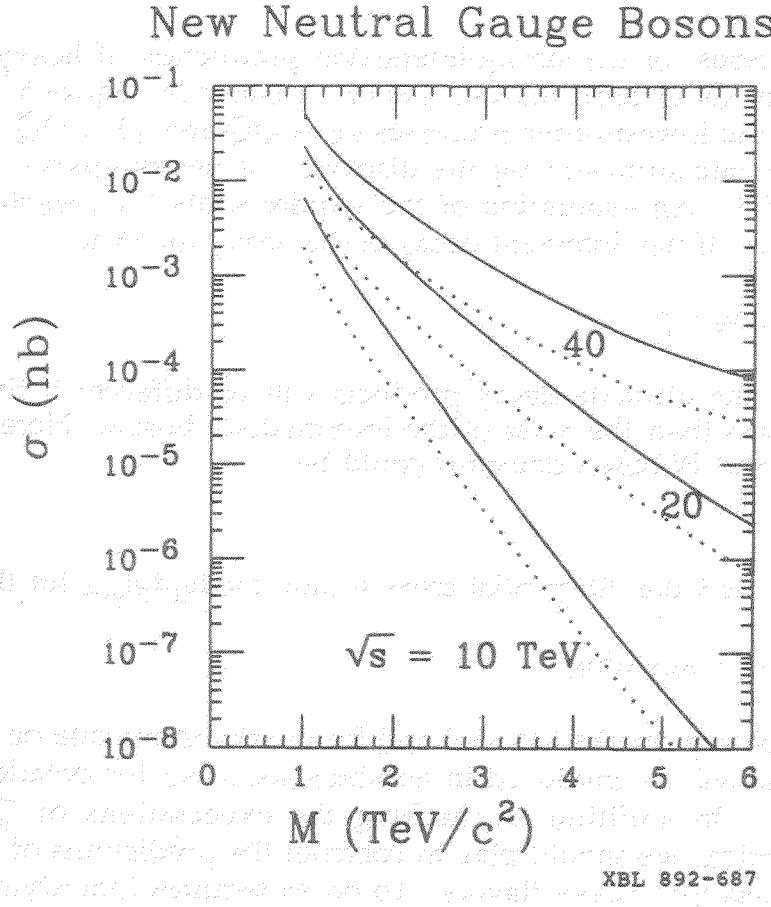

Figure 4: Cross section for the production of a heavy $Z^{0\prime}$-boson with rapidity $|y| < 1.5$ in pp collisions at 10, 20, and 40 TeV. Solid lines: Weinberg-Salam couplings; dotted lines: E_6 couplings.

Table 2. $Z^{0'}$ Branching Fractions per Generation

$u\bar{u}$	24/180
$d\bar{d}$	15/180
e^+e^-	5/180
$h\bar{h}$	51/180
E^+E^-	17/180
$\nu_e\bar{\nu}_e$	1/180
$\nu_E\bar{\nu}_E$	1/180
$N_e\overline{N_e}$	25/180
$N_E\overline{N_E}$	16/180
$n\bar{n}$	25/180

4.2 Heavy Quarks

The cross sections for the strong-interaction production of heavy quarks are readily calculated in QCD perturbation theory. I show in Figure 5 the yield of heavy quarks from the lowest-order processes $gg \to Q\bar{Q}$ and $q\bar{q} \to Q\bar{Q}$ at the SSC. We expect an event rate sufficient for the discovery of heavy quarks with masses up to about 2 TeV/c^2. An evaluation of the requirements for detection depends upon the decay chain. If the dominant decay of the heavy quark is

$$Q \to t + W^- \ , \tag{4.6}$$

as it is likely to be, the ultimate decay products will be different if the top-quark mass is greater or less than the mass of the intermediate boson. Here we see just how useful t-quark and W-boson detectors could be!

4.3 Two-Jet Events

I show in Figure 6 the differential cross section $d\sigma/dp_\perp dy|_{y=0}$ for the reaction

$$p\,p \to \text{jet} + \text{anything} \tag{4.7}$$

at 40 TeV, for elementary quarks ($\Lambda^* = \infty$) and for quarks composite on scales of 10, 15, and 20 TeV. Jets will be produced in numbers sufficient for detailed study out to $p_\perp$ = 6–7 TeV/c. In addition to checking the expectations of QCD for the differential cross section, we should plan to confront the predictions of QCD for the evolution of gluon jets into heavy flavors. To do so requires identifying gluon jets and the heavy quarks.

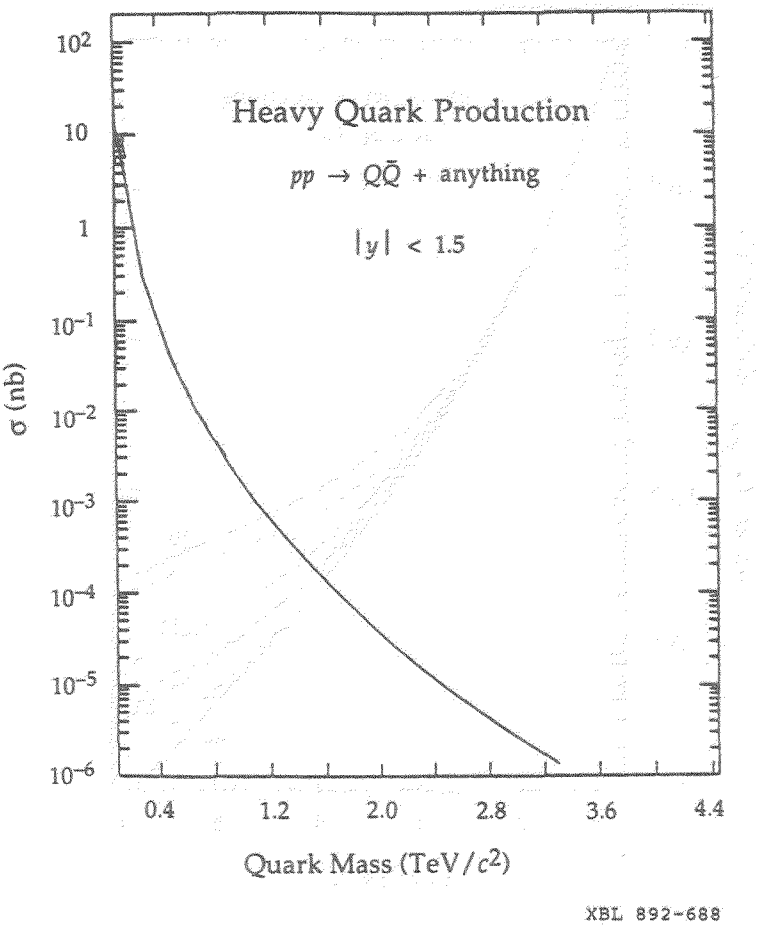

Figure 5: Integrated cross section for pair production of heavy quarks satisfying $|y_Q|$, $|y_{\bar{Q}}| < 1.5$ in pp collisions at 40 TeV.

4.4 Pairs of Gauge Bosons

Incisive tests of the structure of the electroweak interactions may be achieved in detailed measurements of the cross sections for the production of W^+W^-, $W^\pm Z^0$, Z^0Z^0, $W^\pm\gamma$, and $Z^0\gamma$ pairs. The rate for $W^\pm\gamma$ production is sensitive to the magnetic moment of the intermediate boson. In the standard model there are important cancellations in the amplitudes for W^+W^- and $W^\pm Z^0$ production that rely on the gauge structure of the WWZ trilinear coupling. The Z^0Z^0 and $Z^0\gamma$ reactions do not probe trilinear gauge couplings in the standard model, but they are sensitive to nonstandard interactions such as might arise if the gauge bosons were composite. In addition, the W^+W^- and Z^0Z^0 final states may be significant backgrounds to the detection of heavy Higgs bosons and possible new degrees of freedom.

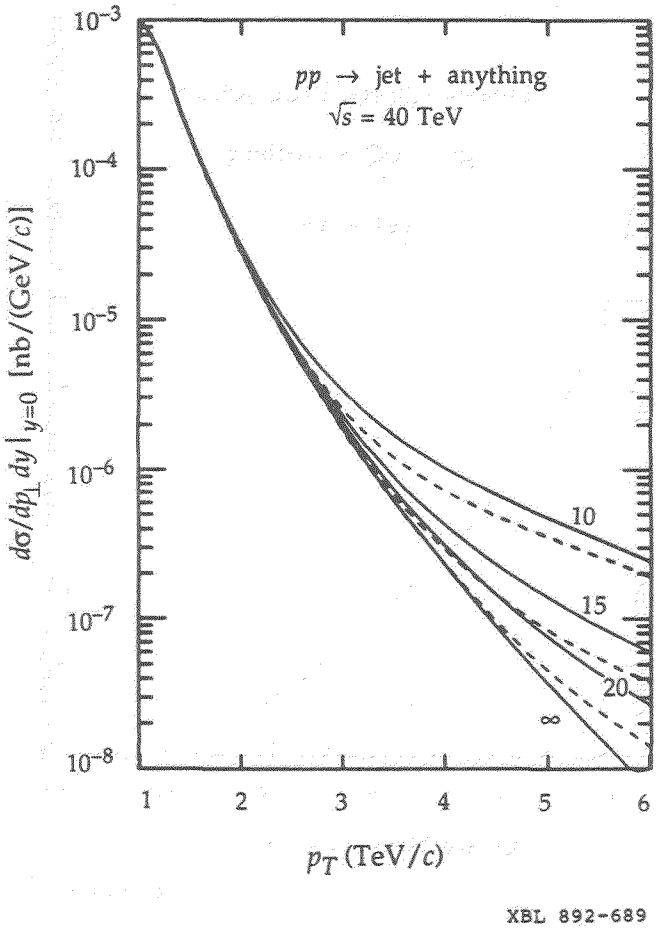

Figure 6: Differential cross section $d\sigma/dp_\perp dy|_{y=0}$ for the reaction $pp \rightarrow$ jet + anything at 40 TeV. The curves are labeled by the compositeness scale Λ^* (in TeV). Solid (dashed) lines indicate constructive (destructive) interference between the QCD amplitude for (anti)quark-(anti)quark scattering and the contact term.

The mass spectrum of W^+W^- pairs is of interest both for the verification of gauge cancellations and for the assessment of backgrounds to heavy Higgs boson decays. The calculated spectrum is shown for intermediate bosons satisfying $|y| < 2.5$ in Figure 7. At an energy of 40 TeV and integrated luminosity of $10^{40}\,\mathrm{cm}^{-2} = 10^4\,\mathrm{pb}^{-1}$, we can look forward to 2×10^6 W^+W^- pairs per year. This seems adequate for a test of the gauge cancellations, provided that the intermediate bosons can be detected with high efficiency.

4.5 The Higgs Boson

A heavy Higgs boson (by which we mean one with $M_H > 2M_Z$) will have the characteristic signature of decay into a pair of gauge bosons, with branching fraction roughly 2/3 into the W^+W^- channel and 1/3 into the Z^0Z^0 channel. Event rate permitting, the simplest mode in which to detect a heavy Higgs boson is the four–charged-lepton final state arising from the decay chain

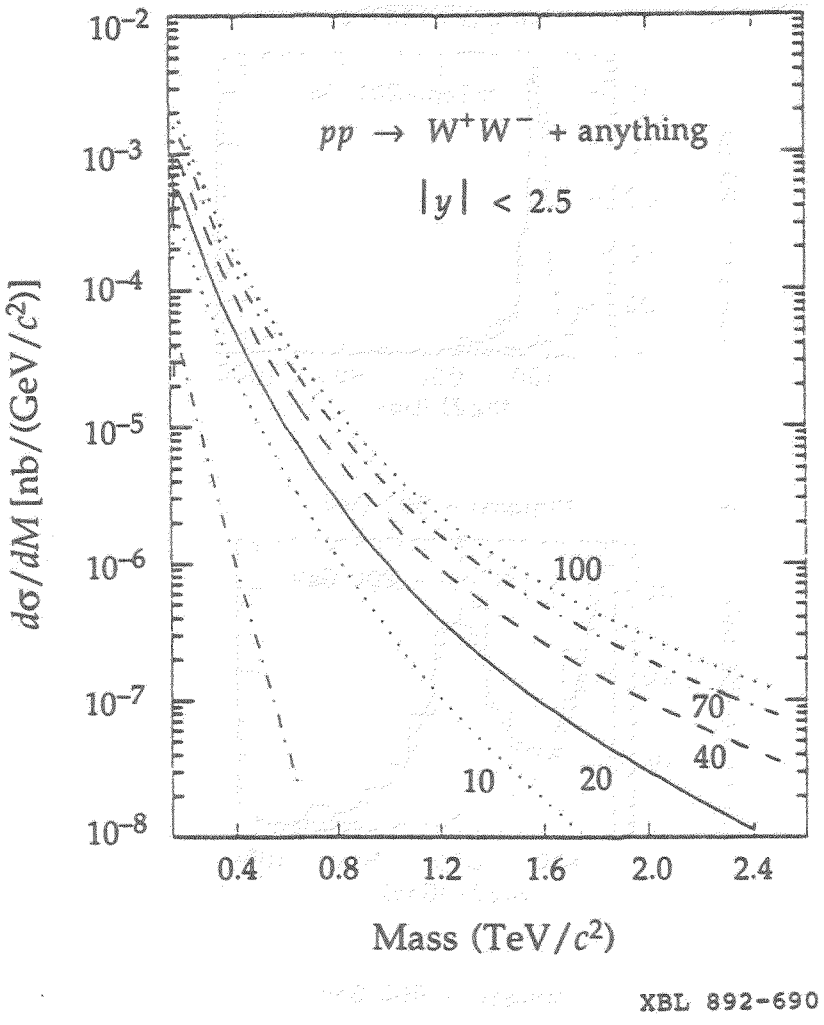

Figure 7: Mass spectrum of W^+W^- pairs produced in pp collisions at 40 TeV, according to the standard model and Set 2 of the EHLQ parton distributions. Both the W^+ and the W^- must satisfy $|y| < 2.5$.

$$H^0 \rightarrow Z^0 \quad Z^0 \qquad (4.8)$$
$$\hookrightarrow \ell^+\ell^- \ \hookrightarrow \ell^+\ell^- \ .$$

The most promising mechanisms for Higgs-boson production are the gluon fusion process and the intermediate-boson fusion process. The rate for gluon fusion is sensitive to the masses of the quarks circulating in the loop, particularly to the top-quark mass. I show in Figure 8 for various Higgs-boson masses the yield of Z^0Z^0 events detected through the cascade (4.8) in the reaction $pp \rightarrow H^0$ + anything. The signal becomes less distinct at high masses, both because the number of events decreases and because the Higgs-boson width is proportional to $G_F M_H^3$. The SSC should nevertheless allow us to carry out a thorough search for a heavy Higgs boson for masses up to 1 TeV/c^2, if both electrons and muons can be identified efficiently and measured with good precision.

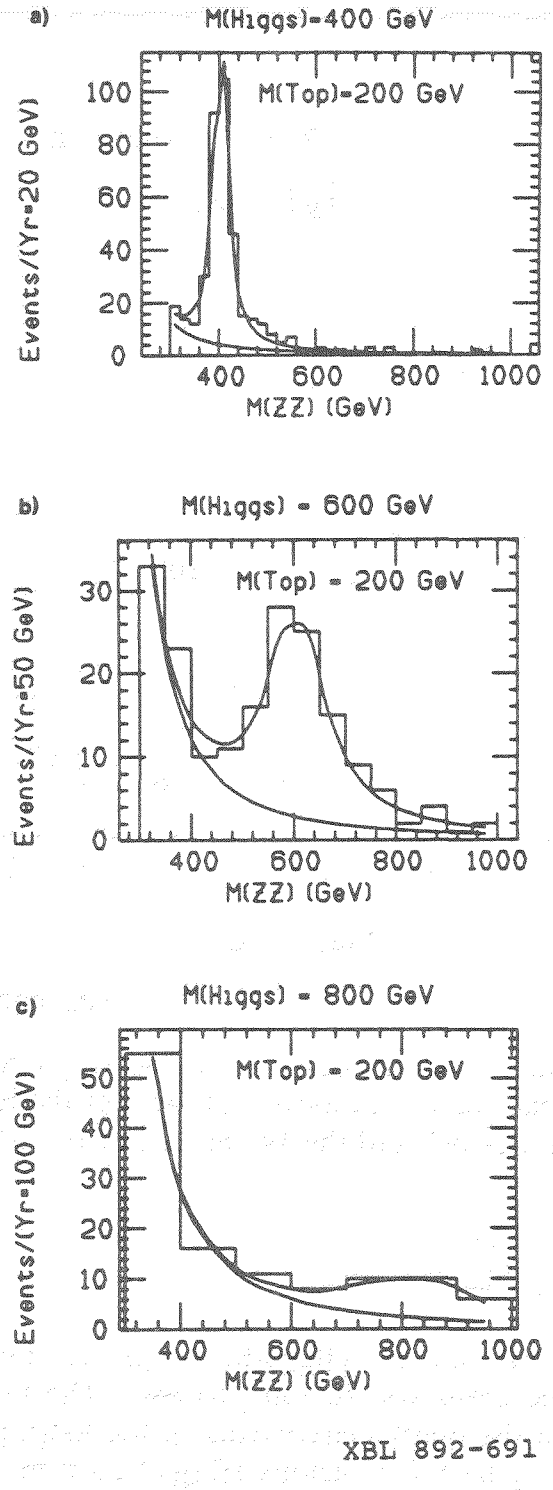

Figure 8: The ZZ invariant mass distribution arising from the production and decay of a Higgs boson in the reaction $pp \rightarrow H$ + anything, and from the background process $q\bar{q} \rightarrow ZZ$ at $\sqrt{s} = 40$ TeV with an integrated luminosity of 10^{40} cm^{-2}. Both gauge bosons must satisfy the cut $|y_i| < 1.5$. The top-quark mass is taken to be 200 GeV/c^2, and perfect resolution and detection efficiency is assumed for both electrons and muons (from Ref. 16).

5. Concluding Remarks

The initial goals of experimentation at the SSC help define detector issues that we should address vigorously. In the realm of particle identification, more is better. The examples we have considered highlight areas of special interest beyond the standard goals of identifying light hadrons, photons, and leptons. High-efficiency W and Z detectors will have great utility. The discovery physics we have considered in assessing the prospects of the SSC can all be done by relying upon the leptonic decays of the gauge bosons, but we can move to a deeper level of experimentation by learning to use the nonleptonic decays as well. Examples from technicolor and the Higgs sector of the standard model indicate that good-efficiency τ, b, ... tags will be of considerable value in enhancing signals over background. Full utilization of the heavy-flavor tag requires measuring the four-momenta of the short-lived particles as well.

Acknowledgments

It is a pleasure to thank Jorge Morfín and his colleagues for their efficient organization of this Symposium. I am grateful to Kate Metropolis for helpful comments on the manuscript.

Footnotes and References

1. Frank Paige has more to say about the structure of events in his presentation in these Proceedings, p.

2. *Superconducting Super Collider Conceptual Design*, Central Design Group Report SSC-SR-2020 (March, 1986).

3. A. A. Garren and D. E. Johnson, "The 90° (September 1987) SSC Lattice," SSC-146.

4. E. Eichten, I. Hinchliffe, K. D. Lane, and C. Quigg, *Rev. Mod. Phys.* **56**, 579 (1984); ibid. **58**, 1065E (1986).

5. *Large Hadron Collider in the LEP Tunnel*, edited by G. Brianti, et al., CERN 84-10.

6. *Proceedings of the 1984 Summer Study on Design and Utilization of the Superconducting Super Collider*, edited by R. Donaldson and J. G. Morfín (Fermilab, Batavia, Illinois, 1984); *$\bar{p}p$ Options for the Supercollider*, edited by J. E. Pilcher and A. R. White (University of Chicago, 1984); *Physics at the Superconducting Super Collider Summary Report*, edited by P. Hale and B. Winstein (Fermilab, 1984).

7. *Supercollider Physics*, edited by D. E. Soper (World Scientific, Singapore, 1986).

8. *Proceedings of the Summer Study on the Physics of the Superconducting Super Collider, Snowmass, 1986,* edited by R. Donaldson and J. Marx (Division of Particles and Fields of the American Physical Society, New York, 1987).

9. *Les Rencontres de Physique de la Vallée d'Aoste, Results and Perspectives in Particle Physics,* edited by M. Greco (Editions Frontières, Gif-sur-Yvette, France, 1987).

10. *Proceedings of the Workshop on Experiments, Detectors, and Experimental Areas for the Supercollider,* Berkeley, 1987, edited by R. Donaldson and M. G. D. Gilchriese (World Scientific, Singapore, 1988).

11. Preliminary results of the CDF and UA2 collaborations, presented at the XXIV Rencontre de Moriond, Les Arcs, France, March 12-18, 1989, by D. Baden (CDF) and S. Grunendahl (UA2).

12. Recent reports from TRISTAN experiments include T. Mori, et al. (AMY collaboration), KEK-Preprint-88-109; K. Abe, et al. (VENUS Collaboration), KEK-Preprint-88-111.

13. See the report on SSC Detector R&D by M. Gilchriese, in these Proceedings, p.

14. M. Green and J. Schwarz, *Phys. Lett.* **149B,** 117 (1984); ibid. **151B,** 21 (1985); D. J. Gross, J. A. Harvey, E. Martinec, and R. Rolm, *Phys. Rev. Lett.* **54,** 502 (1985); idem, *Nucl. Phys.* **B256,** 253 (1985); E. Witten, *Nucl. Phys.* **B258,** 75 (1985); M. Dine, V. Kaplunovsky, M. Mangano, C. Nappi, and N. Seiberg, *Nucl. Phys.* **B259,** 519 (1985).

15. For more details, see §5.1 of C. Quigg, "Hadron Colliders Beyond the Z^0," SSC-154, in *Looking Beyond the Z,* Proceedings of the Fifteenth SLAC Summer Institute on Particle Physics, SLAC Report No. 328, edited by Eileen C. Brennan (SLAC, Stanford, California, 1988), p. 179.

16. R. N. Cahn, et al., in *Proceedings of the Workshop on Experiments, Detectors, and Experimental Areas for the Supercollider,* Berkeley, 1987, edited by R. Donaldson and M. G. D. Gilchriese (World Scientific, Singapore, 1988), p. 20.

CERN $p\bar{p}$ Collider Physics – a Short Review

W.J. Stirling
Department of Physics, University of Durham,
Durham DH1 3LE, England

Abstract

Some of the most important physics results from the CERN Sp$\bar{p}$S collider are reviewed. Topics discussed include hard parton-parton scattering, W and Z physics, heavy quark production and limits on new physics beyond the standard model.

1 Introduction

In recent years, the CERN Sp$\bar{p}$S collider has provided some of the most compelling evidence in support of the 'standard model' of strong, weak and electromagnetic interactions [1]. Apart from the discovery of the $W^{\pm}$ and Z^0 bosons, there have been many other highlights: unambiguous evidence for the hard scattering of quarks and gluons as manifest in the production of large transverse momentum jets and direct photons, the accumulation of a large sample of b quark events which allows a study of $B - \overline{B}$ mixing, and stringent limits on a wide variety of new particles and interactions.

It is not the purpose of this short review to discuss the details of the machine and the detectors – there are several excellent accounts in the literature [2,3,4]. Rather, the focus here is on the *physics* that has resulted. Even so it is impossible in a short review to cover all aspects of $p\bar{p}$ collider physics. The topics selected here come under the general heading of 'hard' or 'large momentum transfer' processes. These are the processes that lead to precision tests of the standard model, free from most of the uncertainties of less well-understood soft hadronic physics. Thus, there will unfortunately be no discussion of topics which come under the general heading of 'soft physics', including the total and elastic cross sections, minimum bias and diffractive physics etc. Again, the reader is referred to more complete discussions in the literature [2,3,4,5].

With this in mind, the attention focusses on the two large experiments UA1 and UA2. Each of these received just less than 1 pb^{-1} of integrated luminosity in the period up to 1985, originally at a centre of mass energy of 540 GeV and latterly at an energy of 630 GeV. Most of the physics topics discussed here have been studied by both collaborations, and it is worth emphasising that the overall agreement and consistency between the two sets of results is striking.

At time of writing, the CERN $p\bar{p}$ collider is again running, but at a higher luminosity. Detailed physics analyses of these new data are in progress and published results are

expected soon. At the same time, of course, the FNAL Tevatron $p\bar{p}$ collider has come into operation at the higher energy of $1.8\ TeV$, and preliminary results are beginning to emerge. Thus, the results described in this review will soon be superseded. However, unless some dramatic new physics emerges, the task will be one of consolidating and improving the existing collider results, and the relevant underlying theory – as described in this review – will be the same.

There are four basic topics reviewed here. In the next section, the physics of large transverse momentum jet and direct photon production is studied in the context of hard quark and gluon scattering. Section 3 covers W and Z physics, showing not only how detailed information can be extracted on the basic structure of the electroweak interaction, but also how tests of perturbative QCD and limits on physics beyond the standard model can be obtained. Section 4 discusses heavy quark production, in particular bottom quark production and the search for the top quark. Finally, in section 5, a brief summary of limits on new particles and interactions is presented.

2 Hard Parton – Parton Scattering

High energy $p\bar{p}$ collisions can be used to study the short distance interactions between quarks and gluons. Examples are the fusion of quarks and antiquarks to produce virtual photons, W and Z bosons (the Drell-Yan process), and the wide-angle scattering of quarks and gluons to produce large transverse momentum jets of hadrons.

There is a fundamental theorem of QCD which states that if there is a large momentum transfer in a parton scattering process, the hadronic cross section can be expressed as a convolution of universal parton distributions and a subprocess scattering cross section, calculable in principle to arbitrary order in perturbation theory:

$$d\sigma^{p\bar{p}\to X+\cdots} = \sum_{a,b=q,g} \int_0^1 dx_a dx_b G_{a/p}(x_a,\mu) G_{b/\bar{p}}(x_b,\mu) d\hat{\sigma}^{ab\to X} \qquad (1)$$

Two examples of such hard-scattering cross sections will be discussed in this section – the production of large p_T jets and the production of large p_T direct photons.

2.1 Large p_T jet production

The hard scattering of quarks and gluons, $qq \to qq$, $qg \to qg$, $gg \to gg$, etc., can be studied in high energy hadron-hadron collisions. The final state partons appear as *jets* of closely collimated hadrons, which can be identified by segmented calorimetric detectors [2,3]. Although large p_T jet production has been studied at different accelerators over a period of many years, the definitive data so far are from the UA1 and UA2 experiments at CERN. It appears that only at the high collision energies of the $p\bar{p}$ colliders does the the identification and measurement of large p_T jets become relatively unambiguous. At lower energies it is difficult to separate the jets from the other 'underlying' hadrons in the event.

The leading order QCD cross section for large p_T jet production is obtained from the $2 \to 2$ scattering processes shown in Fig.1. By combining the corresponding matrix ele-

ments with parton distributions and a value for $\Lambda_{\overline{MS}}$ one obtains, in principle, an absolute prediction for the jet inclusive cross section. In particular, there are three distinct tests:

(i) *normalisation*: the cross section is proportional to α_s^2.

(ii) *scale invariance*: the inclusive cross section scales, up to logarithms, like p_T^{-4}:

$$\frac{d\sigma}{dp_T^2} \sim \frac{\alpha_s^2(\mu)}{p_T^4} F\Big(x_T = \frac{2p_T}{\sqrt{s}}, ln(\frac{\mu}{p_T})\Big) \tag{2}$$

(iii) *scattering dynamics*: the variation of the cross section with the jet scattering angle θ^* directly probes the $\hat{s}, \hat{t}, \hat{u}$ dependence of the scattering amplitudes:

$$\frac{d\sigma}{d\cos\theta^*} \sim |M|^2 \tag{3}$$

with $\hat{t} = -\hat{s}(1 - \cos\theta^*)/2$ and $\hat{u} = -\hat{s}(1 + \cos\theta^*)/2$.

As always, in practice things are not so straightforward. Theoretically, there is inevitably some uncertainty arising from the parton distributions, especially the gluon distribution. The gluon distribution is known to be strongly peaked at small x and therefore contributes significantly to the jet cross section at small and medium p_T values. In addition, although all the relevant next-to-leading order diagrams have been calculated [6], the complete set of higher order corrections to the jet cross section have not yet been evaluated. Calculations are, however, in progress [7]. Until all the next-to-leading corrections are known, there is still a freedom in the choice of scale μ in the leading order cross section which is not compensated by the higher order corrections. (Recall that the more higher order corrections are included, the less the cross section depends on the arbitrary renormalisation/factorisation scale μ, so that ultimately the all-orders cross section is scale (strictly renormalisation-scheme) invariant.) Experimentally, the problems are just as severe. In order to make a precise measurement, the energy of the jet must be known accurately. In practice there is a finite energy resolution which translates into a normalisation uncertainty of the cross section. There is also some ambiguity as to exactly which particles, especially soft hadrons, are part of the jet and which are part of the 'underlying event'.

Despite these caveats, the agreement between theory and jet data from UA1 and UA2 is very satisfactory. Data from the UA2 collaboration [8] on the quantity $\frac{d^2\sigma}{dp_T d\eta}$ at $\eta = 0$ and $\sqrt{s} = 630\ GeV$ are shown in Fig.2. The curve is the leading order QCD prediction, using the MRS1 parton distributions [9] and with the scale set (arbitrarily) at $\mu = p_T/2$. The agreement is excellent over the complete p_T range. Different scales μ and different parton distributions change the cross section by up to 50% [9], but this is comparable to the overall experimental normalisation uncertainty. It is interesting to note that the contribution from quark-gluon scattering is roughly half of the total across the whole p_T range. The other half is dominantly gluon-gluon scattering at small p_T, changing to quark-(anti-)quark scattering at large p_T (Fig.3) [10].

The level of agreement between theory and experiment can be used to put limits on possible additional 'contact interactions' between the partons, which would arise, for example, in composite models. A non-zero value for the inverse of the compositeness scale Λ_c

would lead to a flattening of the inclusive cross section at large p_T. There is no evidence for such behaviour in the data and the corresponding lower limits on Λ_c from UA1 [11], UA2 [8] (and the recent stronger limit from CDF [12]) are shown in Table 3.

The jet angular distribution also yields interesting information. The UA1 collaboration [13] have measured the jet angular distribution (in the jet-jet centre-of-mass) in a sample of events with two jets of large invariant mass. Numerically the most important subprocesses are $gg \to gg$, $gq \to gq$ and $q\bar{q} \to q\bar{q}$. For each of these, the θ^* distributions have the familiar Rutherford scattering behaviour at small angle, characteristic of the exchange of a vector boson in the t-channel:

$$\frac{d\hat{\sigma}}{d\cos\theta^*} \sim \frac{1}{\sin^4(\frac{\theta^*}{2})} \tag{4}$$

The UA1 data are shown in Fig.4, with the QCD prediction (solid curve). Again, there is excellent agreement. Note that these data automatically rule out certain other quark scattering mechanisms. For example, a model in which quarks scatter by exchanging a *scalar* gluon would give a less singular behaviour ($\sin^{-2}(\theta^*/2)$) at small angle.

In the naive parton model, all the θ^* dependence of the cross section comes from the scattering matrix elements. In QCD this will only be true if the scale μ in the parton distributions and in the coupling constant is independent of the angle, e.g. $\mu = M_{JJ}$. Interestingly, the data indicate that this is *not* the case. In Fig.4, the dashed line is the 'parton model' prediction in which the only angular dependence comes from the matrix elements. The data clearly have a steeper dependence. This implies that the effective scale μ *decreases* with decreasing angle. This is incorporated in the complete QCD prediction (solid line) where the scale choice is $\mu = p_T$. One can say, therefore, that the angular dependence of the jet cross section provides additional evidence of scaling violations consistent with perturbative QCD.

It is evidently difficult to measure α_s from the normalisation of the jet inclusive cross section. A more accurate method, with potentially fewer uncertainties, is to measure the relative number of 2,3,... jet events. In perturbative QCD, multijet events are generated by higher order diagrams involving multiple quark and gluon bremsstrahlung. Examples of diagrams for two, three and four jet production are shown in Fig.5. The matrix elements for all the $2 \to 2, 3, 4$ QCD processes are known exactly. Since each n-jet cross section is proportional to α_s^n, the cross sections fall roughly geometrically with increasing n. The simplest way of determining α_s, therefore, is to fit the ratio

$$\frac{\#(3 \text{ jet events})}{\#(2 \text{ jet events})} = \left(\frac{\sigma^3}{\sigma^2}\right)_{QCD} \tag{5}$$

Further, if the two and three jet systems are required to have the same invariant mass, $M_{JJ} = M_{JJJ}$, then the dependence of this ratio on the parton distributions is weak. Luminosity uncertainties, energy scale uncertainties, etc. also tend to cancel in the ratio. The main problem in practice is that the higher order perturbative corrections to σ^2 and σ^3 are completely unknown. What is determined, therefore, is not α_s but rather $\alpha_s K_3/K_2$, where the K_i are the theoretical K-factors for the lowest order cross sections:

$K_i = 1 + O(\alpha_s)$. The experimental results are [14,15]

$$\alpha_s \frac{K_3}{K_2} = 0.24 \pm 0.01 \pm 0.04 \quad \text{(UA2)}$$
$$= 0.23 \pm 0.02 \pm 0.04 \quad \text{(UA1)} \tag{6}$$

The results from the two experiments are consistent. Although the value for α_s appears slightly high, there is no obvious disagreement with other, more precise determinations.

Qualitatively, the measured rate of four jet production is also consistent with QCD expectations [16]. In fact detailed studies of four jet events – in particular the pairwise transverse momentum imbalance of the jets – lead to an upper limit on the contribution of 'double parton scattering', i.e. two simultaneous $2 \rightarrow 2$ hard parton scatterings [17]. The double scattering cross section can be written schematically as

$$\sigma^{4J} \simeq \frac{\sigma^{2J} * \sigma^{2J}}{\sigma_{\text{eff}}} \tag{7}$$

and the UA2 lower limit [17] of $\sigma_{\text{eff}} > 10\ mb$ is not inconsistent with earlier ISR results [18].

2.2 Large p_T direct photons

Direct photon production at large transverse momentum is one of the few 'precision' QCD tests in hadron-hadron collisions. There is a large amount of high-statistics data, principally from fixed target experiments [19], and the theoretical cross sections are known to next-to-leading order in perturbation theory.

The leading order subprocesses are (i) the annihilation process $q\bar{q} \rightarrow \gamma g$ and (ii) the Compton process $qg \rightarrow \gamma q$. Depending on the nature of the colliding hadrons and on the collision energy either of these two processes can dominate. At the CERN $p\bar{p}$ collider, the annihilation process dominates at large transverse momentum, $p_T^\gamma > O(50\ GeV/c)$ (Fig.3). Apart from poorer statistics, compared with fixed target experiments, there is also the problem of photon isolation. Large p_T photons can only be unambiguously identified and measured if they are *isolated* from hadronic jets. This isolation requirement affects the next-to-leading order QCD corrections, since there are higher order diagrams in which the photon is radiated off a final state large p_T quark produced in a $2 \rightarrow 2$ scattering. Isolation removes, in effect, part of the contribution from these diagrams, and there is a problem in matching the experimental and theoretical isolation criteria.

Despite this small uncertainty, there is very good agreement between theory and experiment. Fig.6 shows data from the UA2 collaboration [20], together with the next-to-leading order QCD predictions from Aurenche et al. [21]. The solid curve is the complete theoretical prediction, while the dashed curve shows the effect of imposing a theoretical isolation requirement, designed to mimic the experimental situation. Evidently, the effects of isolation are negligible at large p_T^γ.

Since both the leading order $2 \rightarrow 2$ processes for direct photon production involve *fermion* exchange in the $t-$ and $s-$channels, the angular distribution is less singular at

small angles than the corresponding jet distribution, eqn.(4). In fact it is straightforwa to show that

$$\frac{d\sigma^{\gamma}}{d\sigma^{\rm jet}} \sim 1 - \cos\theta^{*} \qquad (4$$

The effect is clearly seen in Fig.7, which shows the ratio of the angular dstributions for and 'π' production as measured by UA2 [20]. (Here 'π' refers to a multiphoton jet, rathe than a standard hadronic jet, but the above argument should still be valid.)

3 W and Z Physics

The W and Z bosons were discovered at the CERN $p\bar{p}$ collider in 1983-4, with precisely the properties predicted by the Glashow-Salam-Weinberg electroweak model:

$$\begin{aligned} \mathcal{L}_{GSW} &= \bar{\psi}\gamma^{\mu}\Big[eQA_{\mu} + \frac{e(1-\gamma_5)}{2\sqrt{2}\sin\theta_W}(T^{+}W_{\mu}^{+} + T^{-}W_{\mu}^{-}) \\ &\quad + \frac{e}{\sin\theta_W\cos\theta_W}(\frac{1}{2}(1-\gamma_5)T^{3} - Q\sin^{2}\theta_W)Z_{\mu}\Big]\psi \end{aligned} \qquad (9)$$

with the W and Z masses given in terms of the fine structure constant α, the Fermi constant G_F and the weak mixing angle $\sin^2\theta_W$:

$$\begin{aligned} M_W &= \frac{\sqrt{\pi\alpha/(\sqrt{2}G_F)}}{\sin\theta_W} \\ M_Z &= \frac{M_W}{\cos\theta_W} \end{aligned} \qquad (10)$$

The numerical predictions of $M_W = 81\ GeV/c^2$ and $M_Z = 92\ GeV/c^2$ are obtained by substituting the most recent values for the three parameters [22]:

$$\begin{aligned} \alpha_{em}^{-1} &= 137.03604(11) \\ G_F &= 1.16637(2)\times 10^{-5}\ GeV^{-2} \\ \sin^2\theta_W &= 0.230 \pm 0.005 \end{aligned} \qquad (11)$$

A large sample of W and Z events have been collected by the UA1 and UA2 collaborations, and many important standard model tests have been performed. These can be grouped into three classes:

(i) precision electroweak tests

(ii) tests of perturbative QCD

(iii) limits on 'new physics'

So far, all the detailed studies use the leptonic decay modes. The published results from UA1 and UA2 correspond to a total sample of order 600 $W \to l\nu_l$ events and of order 100 $Z \to l^{+}l^{-}$ events. The UA2 collaboration have also performed a careful analysis [23] of the

jet-jet invariant mass distribution and found an excess of events in the $70 - 100\ GeV/c^2$ mass range (Fig.8). The obvious interpretation is that the extra events are due to the $q\bar{q}$ *hadronic* decays of W and Z bosons, and indeed the observed rate is consistent, within large errors, with the expected rate.

3.1 Precision standard model tests

A high energy $p\bar{p}$ collider provides a copious source of valence $\bar{u}$, $\bar{d}$ and u, d quarks. Hence the dominant W and Z production mechanisms are

$$\begin{aligned} u\,\bar{d} &\rightarrow W^+ \\ d\,\bar{u} &\rightarrow W^- \\ u\,\bar{u} &\rightarrow Z^0 \\ d\,\bar{d} &\rightarrow Z^0 \end{aligned} \tag{12}$$

and the production cross-sections have the general structure of eqn.(1). Since the masses and couplings can be determined from other processes – using the standard model relations such as those of eqn.(10) – absolute predictions for the production cross sections can be made.

The measured values of $\sigma \cdot B$ for the various leptonic final states are in excellent agreement with the theoretical predictions. Fig.9 shows the results from UA1 [24] and UA2 [25] for W and Z production at $\sqrt{s} = 630\ GeV$ [26]. The dependence of the theoretical predictions on the top quark mass arises because the *total* W and Z decay widths – and hence the branching ratios – depend on m_t for $m_t < (M_W - m_b)$, $m_t < M_Z/2$ respectively. The Z decay width also depends on the number of light neutrinos (see below). The predictions in Fig.9 correspond to $N_\nu = 3$. Perturbative QCD $O(\alpha_s)$ corrections give an $O(30\%)$ increase in the lowest order cross section and are included in the predictions. Unfortunately it is not possible to extract any information on m_t from Fig.9, principally because of several additional theoretical uncertainties in the predictions. The two lines in each figure correspond to different sets of parton distributions (the MRSE and MRSB distributions of reference [26]), and indicate the level of uncertainty from this source. Also shown as error bars on the theoretical curves are the effects of a $\pm 1 GeV/c^2$ variation in the W and Z masses, and an (unknown) $\pm 10\%$ $O(\alpha_s^2)$ QCD correction. Note that the experimental data from UA1 in Fig.9 also provide a beautiful confirmation of the $e - \mu - \tau$ universality of the standard model.

The mass of the Z can be measured directly from the lepton pair mass spectrum. For example, the UA1 candidate events in the $Z \rightarrow e^+e^-$ channel are shown in Fig.10 [24]. For W events, the signature is a single charged lepton balanced by missing transverse energy from the undetected neutrino. Although the mass cannot in this case be reconstructed directly (the *longitudinal* component of p_ν^μ is completely unknown), the charged lepton transverse momentum distribution shows a sharp Jacobian peak near $M_W/2$. The distributions for the electron and muon W candidate events from UA1 are shown in Fig.11. The distributions are fitted to determine the W mass, adding several refinements such as the

channel	experiment	mass (GeV/c^2)
$Z \to e^+e^-$	UA1	$93.1 \pm 1.0 \pm 3.0$
$Z \to e^+e^-$	UA2	$91.5 \pm 1.2 \pm 1.7$
$Z \to \mu^+\mu^-$	UA1	$90.7\ ^{+5.2}_{-4.8} \pm 3.2$
$W \to e\nu$	UA1	$82.7 \pm 1.0 \pm 2.7$
$W \to e\nu$	UA2	$80.2 \pm 1.2 \pm 0.6 \pm 0.5 \pm 1.3$
$W \to \mu\nu$	UA1	$81.8\ ^{+6.0}_{-5.3} \pm 2.6$
$W \to \tau\nu$	UA1	$89.0 \pm 3.0 \pm 6.0$

Table 1. W and Z masses from UA1 [24] and UA2 [25].

finite width of the W and a simulation of the W transverse momentum. In this connection a better variable for fitting is the 'transverse mass', defined as

$$M_T^2 = 2p_T^e p_T^\nu (1 - \cos\Delta\phi_{e\nu}) \tag{13}$$

which is less sensitive to p_T^W. The results for M_W and M_Z from UA1 [24] and UA2 [25] are given in Table 1.

In principle, one can also determine the total width of the Z from the shape of the lepton pair mass spectrum, but in practice the measurement errors (coming mainly from the resolution on the lepton energy) are of the same order as the width. One may summarise the results on the weak boson masses by combining the results from UA1 and UA2 (adding the statistical and systematic errors linearly for each experiment):

$$\begin{aligned} M_W &= 81.0 \pm 2.0\ GeV/c^2 \\ M_Z &= 92.0 \pm 2.4\ GeV/c^2 \end{aligned} \tag{14}$$

These results are in excellent agreement with the predictions given above. In fact, the level of agreement leads to constraints on new physics beyond the standard model [27].

Another interesting test of the theory concerns the $V-A$ structure of the weak charged current, eqn.(10). It follows from this that the matrix element for the process $d\bar{u} \to W^- \to e^-\bar{\nu}_e$ is maximal when the outgoing electron is collinear with the incoming d quark, and vanishes when the electron is collinear with the incoming $\bar{u}$ quark. More precisely, the normalised distribution of the electron scattering angle in the W centre-of-mass frame is predicted to be

$$\frac{dN}{d\cos\theta^*} = \frac{3}{8}(1 - \cos\theta^*)^2 \tag{15}$$

Here the direction $\theta^* = 0$ is defined by the incoming $\bar{u}$ quark direction, which may, to a good approximation, be identified with the incoming $\bar{p}$ direction. The theory therefore predicts that the outgoing electron prefers the direction of the incoming proton. A similar calculation leads to an outgoing positron preferring the incoming antiproton direction. There is in fact a simple angular momentum argument for this. In the standard model the W couples to negative helicity fermions and positive helicity antifermions. Angular

momentum conservation therefore requires the outgoing fermion (electron) to follow the direction of the incoming fermion (quark), which is usually the direction of the incoming proton.

This lepton asymmetry is clearly visible in the data. Fig.12(a) shows the results from the UA1 collaboration [24]. Note that electron and positron data have been combined with an appropriate redefinition of the angle for the latter. The data are consistent with the $V-A$ hypothesis. However, since there are *two* W-fermion-fermion vertices in the scattering amplitude, the arguments are unchanged if the $(1-\gamma_5)$ coupling is replaced by $(1+\gamma_5)$. The corresponding $Z \to l^+l^-$ asymmetry – which follows from the generic $(v-a\gamma_5)$ couplings, eqn.(9)– is a function of $\sin^2\theta_W$. As shown in Fig.12(b), the data are consistent with the standard values.

3.2 Tests of perturbative QCD

It has already been mentioned that the total W and Z cross sections receive a large next-to-leading order perturbative QCD correction:

$$\sigma_W \;=\; \sigma_0[1+O(\alpha_s)] \tag{16}$$

At $p\bar{p}$ collider energies the correction is large and of order 30%, and is certainly needed to give a good description of the experimental measurements (Fig.9). However because of the various uncertainties discussed above, there is no possibility at present of using this correction to obtain a precision measurement of $\Lambda_{\overline{MS}}$.

More dramatic evidence of perturbative QCD effects is the production of W and Z with large transverse momentum. The lowest order subprocesses are $q\bar{q} \to Wg$ and $qg \to Wq$, and the complete next-to-leading $O(\alpha_s^2)$ corrections have recently been computed [28,29]. Since the leading order cross sections are proportional to α_s, large p_T W and Z production offers, at least in principle, a measurement of the strong coupling constant.

Data on the W p_T distribution from the UA1 [30] and UA2 [31] experiments are shown in Fig.13. The curves are QCD predictions from Reno and Arnold [28], incorporating the full next-to-leading order corrections. The lines correspond to two different sets of parton distributions. Evidently the agreement is very reasonable over the complete p_T range. However, because of the large experimental errors, it is clearly not yet possible to use such data for a *precision* $\Lambda_{\overline{MS}}$ measurement. The UA2 collaboration have, however, derived a value of α_s to leading order by comparing the relative rates of $W+1$ jet and $W+0$ jet events [32]:

$$\alpha_s(\overline{MS}, Q=M_W) \;=\; 0.13 \;\pm\; 0.03\;(stat) \;\pm\; 0.03\;(exp.sys) \;\pm\; 0.02\;(th.sys) \tag{17}$$

This result is consistent with measurements from other processes [33], and is in fact the only 'precision' measurement of α_s at $p\bar{p}$ colliders so far. There are also a small number of large p_T Z events, at a rate consistent with QCD expectations [28].

A further comment concerns the tail of the UA1 p_T^W distribution. The highest bin contains two events – one electron, one muon, and each with two large p_T hadronic jets – with W transverse momenta substantially larger than the rest of the sample. The expected

rate of such events in QCD is roughly an order of magnitude smaller than that observed [34]. The origin of this discrepancy is unclear at present, but the most likely explanations are that the two events result either from non-gaussian fluctuations in the response of the UA1 calorimetry or from a statistical fluctuation [30]. With the expected large increase in statistics in the very near future the issue will presumably be resolved.

The average transverse momentum of the W and Z bosons at the CERN collider energy is of order 10 GeV/c, in line with theoretical expectations. As the collider energy increases, more phase space is available for hard gluon emission and the average weak boson p_T grows. This is illustrated in Fig.14, which shows $< p_T^W >$ and $< p_T^Z >$ as functions of $\sqrt{s}$, together with data from UA1 [30] and UA2 [31]. The next-to-leading order theoretical calculation [35] does not include any 'intrinsic' or 'primordial' transverse momentum smearing, and this *may* account for the slight underestimate of the experimental measurements.

Higher order QCD processes, for example $q\bar{q} \rightarrow W(Z) + ng$ give rise to multijet production with W and Z, at a rate determined by the strong coupling:

$$f_n(W) = \frac{\sigma(W + n\,\text{jets})}{\sigma_{tot}(W)} \sim \alpha_s^n \tag{18}$$

The parton-level cross sections for the production of W and Z with up to 3 jets have recently been calculated [36,37]. Although there are significant uncertainties in comparing leading-order parton cross sections with the experimental data, a simple comparison of the theoretical predictions with the experimental measurements gives very reasonable agreement. This is illustrated in Fig.15, which shows the theoretical predictions for the jet multiplicity $f_n(W)$ from reference [37] compared with data from UA1 [24]. Since W, Z + jets production is an important background for many 'new physics' processes it is reassuring that perturbative QCD provides a good quantitative explanation of the data.

3.3 Limits on new physics

With large enough samples, one can look for rare decays of W and Z bosons which might signal physics beyond the standard model. Various limits of this type have been set by the UA1 and UA2 collaborations. A discussion of these will be postponed to section 5. The remainder of this section discusses one of the most important techniques for obtaining limits on the number of light neutrinos and on the top quark mass.

It has already been mentioned that the branching ratios for $W, Z \rightarrow$ *leptons* depend on the top quark mass and, for the Z branching ratio, on the number of light neutrinos. Unfortunately, theoretical and systematic errors preclude any limits from data on the cross sections $\sigma(p\bar{p} \rightarrow W)B(W \rightarrow l\nu)$ and $\sigma(p\bar{p} \rightarrow Z)B(Z \rightarrow l^+l^-)$ themselves (Fig.9). Most of the uncertainties cancel, however, in the *ratio* of these quantities [38]. Denoting this ratio by R one has

$$\begin{aligned} R &= R_\sigma\, R_B \\ R_B &= \frac{B(W \rightarrow l\nu)}{B(Z \rightarrow l^+l^-)} \\ R_\sigma &= \frac{\sigma(p\bar{p} \rightarrow W)}{\sigma(p\bar{p} \rightarrow Z)} \end{aligned} \tag{19}$$

i.e. the ratio of the observed number of $W \to l\nu$ and $Z \to l^+l^-$ events is (after correcting for lepton acceptance) given by the ratio of the total production cross sections (R_σ) times the ratio of the relevant branching ratios (R_B).

If one assumes that (i) there are N_ν (≥ 3) light neutrinos which contribute to Z decay, (ii) apart from $Z \to \nu_L\bar{\nu}_L$ the fourth (L, ν_L, U, D) and higher generations do not contribute to W or Z decay, (iii) there are no other non-standard (e.g. supersymmetric) decay modes, then the ratio R_B is, to a very good approximation, a function only of m_t and N_ν.

The dominant theoretical uncertainty on R comes from the ratio of production cross sections R_σ, and this can be traced back to uncertainties in the parton distributions (in particular the ratio of the u to d distributions) at the relevant values of x for W and Z production [39]. The most complete analysis to date is by Martin et al. [40]. Fig.16 shows the resulting theoretical predictions for R at 630 GeV and 1.8 TeV as a function of N_ν and m_t. The edges of the shaded bands correspond to different parton distributions and give a rough estimate of the net theoretical error on R. The combined UA1 and UA2 data point and 90% confidence level upper limit are also shown. Given the uncertainty in R_σ, the only definite conclusion is that there are almost certainly no more than five species of light neutrinos. Notice that the corresponding theoretical uncertainty from parton distributions is much reduced at the higher FNAL Tevatron energy. This is because the higher collider energy probes smaller x values of the quarks, where the sea distributions become important and the up and down quark distributions become more alike. A precision measurement of R at $\sqrt{s} = 1.8\ TeV$ will therefore be one of the most important measurements in the near future.

The weakness of this method for setting an upper limit on m_t is that there is no sensitivity at all to m_t if $m_t > M_W - m_b$. While it is tempting to extract an upper limit on m_t from Fig.16, for example by noting that the lower edge of the theoretical band for $N_\nu = 3$ exceeds the 90% c.l. upper limit for $m_t = O(70\ GeV/c^2)$, this mass limit is too close to the critical value – given the overall uncertainties – for the result to have any meaning.

4 Heavy Quark Production

The two most important aspects of heavy quark production at the CERN $p\bar{p}$ collider are the production of bottom quarks and the search for the top quark. The two are quite closely related, since the production mechanisms are the same and the former provides a significant background for the latter. Bottom production can also provide important information on $B^0 - \overline{B^0}$ mixing which, when combined with data from e^+e^- annihilation, gives constraints on the Kobayashi-Maskawa mixing angles [1].

The lowest-order processes for $b\bar{b}$ production in hadronic collisions are $q\bar{q}, gg \to b\bar{b}$ (Fig.17). In the UA1 experiment b quarks are tagged by their semi-leptonic muon decay: $b \to \mu\nu X$. Because the scale of the transverse momentum of the b quark is set by the quark mass, this production and decay process gives events with low and medium p_T muons, in contrast to the high p_T muons from W and Z decay. Low p_T muons are also copiously produced in charm decay. Fig.18 shows the inclusive p_T^μ spectrum from UA1 [41], showing

parton distr.	$\mu^2 = m_b^2/2$	$\mu^2 = m_b^2$	$\mu^2 = 2m_b^2$
MRSE	10.0	8.5	7.4
MRSB	15.3	12.3	10.3

Table 2. Next-to-leading order $b\bar{b}$ cross sections (in μb) calculated using different sets of parton distributions and different scales.

the contributions – as simulated in the ISAJET Monte Carlo – from the various processes. The $b\bar{b}$ contribution is readily identified in the distribution of the momentum of the muon perpendicular to the jet axis in the decay $b \to \mu\nu\, jet$. The larger Q-value in the b decay gives a hard tail to the distribution, and the bottom and charm contributions are easily distinguished (Fig.19). With a Monte Carlo to estimate the acceptance corrections, the total $b\bar{b}$ cross section can therefore be extracted from the inclusive muon spectrum [41]. Measurements of the cross section can also be made from a sample of *dimuon* events. These are produced in several distinct processes. Low mass opposite-sign dimuons come from the cascade semi-leptonic decay process

$$p + \bar{p} \to b\,(\to c\,(\to s + \mu^+ + \nu_\mu) + \mu^- + \bar{\nu}_\mu) + X \tag{20}$$

while higher mass dimuons are produced in double semi-leptonic $b\bar{b}$ decay

$$p + \bar{p} \to b\,(\to c + \mu^- + \bar{\nu}_\mu) + \bar{b}\,(\to \bar{c} + \mu^+ + \nu_\mu) + X \tag{21}$$

Finally, dimuons are also produced via the J/ψ decay of B mesons

$$p + \bar{p} \to b \to B \to J/\psi \to \mu^+\mu^- \tag{22}$$

Combining all these channels, and using ISAJET to correct for acceptance, the UA1 collaboration find [42]

$$\sigma(p\bar{p} \to b\bar{b}X) \;=\; 10.2 \;\pm\; 3.3\ \mu b \tag{23}$$

How does this cross section compare with theoretical expectations? The theoretical cross section is obtained in the usual way by convoluting the subprocess cross sections calculated from the diagrams of Fig.17 with quark and gluon distributions. The $O(\alpha_s^3)$ corrections to the $O(\alpha_s^2)$ leading order cross sections have also recently been calculated [43,44]. Including these corrections reduces the dependence of the cross section on the undetermined QCD renormalisation/factorisation scale μ. Table 2 shows the theoretical predictions for the total $b\bar{b}$ cross section for three different choices of scale μ^2 and two sets of parton distributions (the latest MRSE and MRSB sets from Martin et al. [26], with $\Lambda_{\overline{MS}} = 100\ MeV$ and 200 MeV respectively). Note that, in addition to the variation shown, there is also some dependence on the b quark mass – a value of 5 GeV/c^2 is used in Table 2.

Evidently the agreement is very satisfactory. The UA1 collaboration have also measured [42] the b quark transverse momentum distribution, again from the different samples of single muon and dimuon events. Fig.20 shows the data compared with the theoretical

predictions calculated by Ellis et al. [43]. The dashed lines indicate the typical theoretical uncertainty from varying the scale and parton distributions. The data are reasonably well-reproduced, except perhaps at the largest transverse momentum values. In this region however there are potentially important additional contributions from higher order QCD corrections containing large logarithms of p_T^b/m_b [43].

Since b quark production is quantitatively well-understood, it is possible to make reliable predictions for top quark production cross sections, with m_t as an unknown parameter. Top cross sections at the CERN (630 GeV) and FNAL (1.8 TeV) $p\bar{p}$ colliders are shown as functions of m_t in Fig.21 [45]. The solid lines correspond to the QCD production mechanisms $q\bar{q}, gg \rightarrow t\bar{t}$ of Fig.17 while the dashed lines are the contributions from W decay. At the CERN collider the W decay mechanism is dominant over almost all of the mass range allowed for the decay, while at the higher FNAL energy – where smaller parton x-values are probed – the strong production mechanism is dominant for all top quark masses.

A heavy top quark will decay weakly by emitting a real or virtual W boson, i.e the decay process is

$$t \rightarrow b + W^{(*)} \rightarrow b + f + \bar{f}' \tag{24}$$

Because of the enormous QCD background from multiple light quark and gluon production, the only viable detection scenario at a $p\bar{p}$ collider is from the semi-leptonic decays $t \rightarrow b\mu\nu_\mu$ or $t \rightarrow be\nu_e$ with the b quark manifest as a hadronic jet. The characteristic signature is thus *charged lepton + jets + missing transverse energy*. However this channel is also afflicted with backgrounds, principally from the production of b and c quarks and of W and Z bosons with additional light quark and gluon jets.

The UA1 collaboration have performed an extensive search for the top quark in this channel [46]. They find that even after selection cuts which would favour a top signal there is no evidence for an excess of events over the expectation from standard processes. This is illustrated in Fig.22, which shows the inclusive muon transverse momentum distribution together with the Monte Carlo prediction including all other (i.e. non-top processes). Fig.23 shows the corresponding top quark cross-section upper limit from UA1, as a function of m_t, compared to the theoretical prediction. The intersection of the theoretical curve with the experimental upper limit gives a 95% confidence level *lower* limit of 56 GeV/c^2 on m_t.

This limit was derived by UA1 before the $O(\alpha_s^3)$ corrections to the theoretical cross section [43,44] were available. The results of a more recent analysis by Altarelli et al. [47] – incorporating these corrections – are shown in Fig.24. From this figure, the 95% confidence level lower limit on m_t becomes 41 GeV/c^2.

Note that the same analysis can be repeated with the hypothesis that the next heaviest quark is the $-1/3$-charged fourth generation b' quark. Since there is presumably no longer any contribution from W decay, the expected cross section, and hence the lower mass limit, is smaller. From Fig.24 Altarelli et al. derive a 95% confidence level lower mass limit of $m_{b'} > 34\ GeV/c^2$ [47].

Evidently, then, the CERN $p\bar{p}$ collider mass limits do not contradict (i) the more rigorous lower mass limits of order 27 GeV/c^2 for *any* new quark from the TRISTAN e^+e^- collider [48], and (ii) the upper limit of order 200 GeV/c^2 on m_t from analyses of electroweak

radiative corrections [27]. With the detailed analysis of the new higher luminosity data from CERN and the higher energy data from FNAL, these $p\bar{p}$ collider limits will improve significantly in the very near future.

5 Limits on New Physics

All of the $p\bar{p}$ collider data is in beautiful agreement with the standard model, i.e. the $SU(3) \times SU(2) \times U(1)$ gauge theory of the strong and electroweak interactions with a minimal Higgs (doublet) structure and three generations of fermions. There are, however, strong theoretical reasons (see for example reference [1]) why the model is most likely only a low-energy manifestation of a more complete, unified theory. It follows that additional structure, in the form of new particles or interactions, should emerge as higher energies are probed.

Both CERN experiments have performed extensive searches for this 'new physics' beyond the standard model [49,50]. Some examples of processes looked for are:

(i) *fourth generation heavy lepton production:*

$$p\bar{p} \rightarrow W\,(\rightarrow L\bar{\nu}_L) + X \tag{25}$$

with the heavy lepton detected via its hadronic (jet) decay: $L \rightarrow \nu_L +$ hadrons. The signature is therefore an excess of 'missing transverse energy + jets' events.

(ii) *supersymmetric particle production.* In conventional SUSY extensions of the standard model, quarks and gluons have heavy supersymmetric partners (squarks and gluinos) and there is a light supersymmetric particle (usually the photino) which is stable and therefore escapes detection. The dominant lowest order strong production processes are

$$\left.\begin{array}{l} q\bar{q} \\ gg \end{array}\right\} \rightarrow \left\{\begin{array}{l} \tilde{q}\bar{\tilde{q}} \\ \tilde{g}\tilde{g} \end{array}\right. \tag{26}$$

Several decay modes are possible depending on the relative masses of the squarks and gluinos. For example if $m_{\tilde{q}} > m_{\tilde{g}}$ then

$$\begin{array}{lll} \tilde{g} & \rightarrow q\bar{q}\tilde{\gamma} & \\ \tilde{q} & \rightarrow q\tilde{g} & \rightarrow qq\bar{q}\tilde{\gamma} \end{array} \tag{27}$$

whereas if $m_{\tilde{g}} > m_{\tilde{q}}$ then

$$\begin{array}{lll} \tilde{g} & \rightarrow \bar{q}\tilde{q} & \rightarrow \bar{q}q\tilde{\gamma} \\ \tilde{q} & \rightarrow q\tilde{\gamma} & \end{array} \tag{28}$$

In either case the experimental signature is '$\geq$ 2 jets + missing transverse energy'. The region in the two-dimensional $m_{\tilde{q}}$, $m_{\tilde{g}}$ plane which is excluded at the 90% confidence limit by the UA1 experiment is shown in Fig.25.

Object	Limit	Confidence Level (%)
new quarks and leptons:		
top quark	$m_t > 41\ GeV/c^2$ (UA1)	95
b' quark	$m_{b'} > 34\ GeV/c^2$ (UA1)	95
heavy charged lepton	$m_L > 41\ GeV/c^2$ (UA1)	90
light neutrinos	$N_\nu \leq 6$ (UA1 + UA2)	90
compositeness:		
quarks	$\Lambda_c > 415\ GeV$ (UA1)	95
	$\Lambda_c > 370\ GeV$ (UA2)	95
	$\Lambda_c > 700\ GeV$ (CDF)	95
leptoquark	$m_{lq} > 33\ GeV/c^2$ (UA1)	90
heavy bosons:		
W'	$m_{W'} > 232\ GeV/c^2$ (UA1)	90
	$m_{W'} > 209\ GeV/c^2$ (UA2)	90
Z'	$m_{Z'} > 188\ GeV/c^2$ (UA1)	90
	$m_{Z'} > 180\ GeV/c^2$ (UA2)	90
supersymmetry:		
squark	$m_{\tilde{q}} > 45\ GeV/c^2$ (UA1)	90
gluino	$m_{\tilde{g}} > 53\ GeV/c^2$ (UA1)	90
selectron, sneutrino	$m_{\tilde{e},\tilde{\nu}} > 30\ GeV/c^2$ (UA1)	90
miscellaneous:		
axigluon ($\Gamma_A < 0.4 m_A$)	$m_A > 310\ GeV/c^2$	
	or $m_A < 150\ GeV/c^2$ (UA1)	95

Table 3. Limits on particles and processes in and beyond the standard model.

(iii) *new heavy gauge bosons.* In some string-theory inspired models additional $U(1)$ symmetries survive to relatively low energy, and new heavy Z' bosons result. These can be looked for in the usual $Z' \rightarrow f\bar{f}$ decay channel and, for sufficiently heavy new bosons, $Z' \rightarrow W^+W^-$. Fig.26 shows mass limits on W' and Z' bosons decaying leptonically, from the UA2 experiment. The limits are functions of (a) the coupling strengths of the heavy bosons to the annihilating quarks and (b) the branching ratios for the $e\nu_e$ and e^+e^- final states. In Fig.26 these are normalised to the corresponding values for the standard W and Z.

The result of extensive searches by both UA1 and UA2 is that there is no evidence for new processes of these or any other type. The situation is summarised in Table 3 which is an updated version of a similar table in reference [49]. An improved compositeness limit from the CDF experiment at the FNAL Tevatron [12] is also included.

It is a pleasure to congratulate and thank the organisers, and in particular Professor Jorge Morfin, for such an interesting and stimulating meeting.

References

[1] See for example: P.D.B. Collins, A.D. Martin and E.J. Squires, *Particle Physics and Cosmology*, Wiley (1989).

[2] L. DiLella, *Proton-Antiproton Collider Physics: Experimental Aspects*, Lectures given at the Cargese Summer School, Cargese, France (1987), preprint CERN-EP/88-02 (1988).

[3] P. Jenni, *Collider Experiments*, Lectures given at the 1988 CERN Summer School, Corfu, Greece, preprint CERN-EP/89-51 (1989).

[4] P. Bagnaia and S.D. Ellis, *CERN Collider Results and the Standard Model*, Ann. Rev. Nucl. Part. Phys. **38** (1988) 659.

[5] V.D. Barger and R.J.N. Phillips, *Collider Physics*, Addison Wesley (1987).

[6] R.K. Ellis and J.C. Sexton, Nucl. Phys. **B269** (1986) 445.

[7] S.D. Ellis, Z. Kunszt and D.E. Soper, Phys. Rev. Lett. **62** (1989) 726.

[8] UA2 collaboration: J.A. Appel et al., Phys. Lett. **160B** (1985) 349.

[9] A.D. Martin, R.G. Roberts and W.J. Stirling, Phys. Rev. **D37** (1988) 1161.

[10] A.D. Martin, R.G. Roberts and W.J. Stirling, Z. Phys. **C42** (1989) 277.

[11] UA1 collaboration: G. Arnison et al., Phys. Lett. **172B** (1986) 461.

[12] CDF collaboration: F. Abe et al., Phys. Rev. Lett. **62** (1989) 613.

[13] UA1 collaboration: G. Arnison et al., Phys. Lett. **177B** (1986) 244.

[14] UA1 collaboration: G. Arnison et al., Phys Lett. **158B** (1985) 494.

[15] UA2 collaboration: J.A. Appel et al., Z. Phys. **C30** (1985) 341.

[16] Z. Kunszt and W.J. Stirling, Phys. Lett. **171B** (1986) 307.

[17] M. Valdata-Nappi, Proc. XXIV Int. Conf. on High Energy Physics, Munich 1988, eds. R. Kotthaus and J.H. Kuhn, Springer-Verlag (1989), page 705.

[18] T. Akesson et al., Z. Phys. **C34** (1987) 163.

[19] See for example: R. Turnbull, J. Phys. G: Nucl. Phys. **14** (1988) 135.

[20] UA1 collaboration: C. Albajar et al., Phys. Lett. **209B** (1988) 385.
UA2 collaboration: R. Ansari et al., preprint CERN-EP/88-102 (1988).

[21] P. Aurenche, R. Baier, M. Fontannaz and D. Schiff, Phys. Lett. **140B** (1984) 87.

[22] Review of Particle Properties, Phys. Lett. **204B** (1988).

[23] UA2 collaboration: R. Ansari et al., Phys. Lett. **186B** (1987) 452.

[24] UA1 collaboration: C. Albajar et al., preprint CERN-EP/88-168 (1988).

[25] UA2 collaboration: R. Ansari et al., Phys. Lett. **186B** (1987) 440; **194B** (1987) 158.

[26] A.D. Martin, R.G. Roberts and W.J. Stirling, RAL preprint RAL-88-113 (1989).

[27] U. Amaldi, A. Bohm, L.S. Durkin, P. Langacker, A.K. Mann, W.J. Marciano, A. Sirlin and H.H. Williams, Phys. Rev. **D36** (1987) 1385.
G. Costa et al., Nucl. Phys. **B297** (1988) 244.

[28] P.B. Arnold and M.H. Reno, Fermilab preprint FERMILAB-PUB-88/168-T (1988).

[29] R. Gonsalves, J. Pawlowski and C.-F. Wai, SUNY Buffalo preprint UB-HET-89/2 (1989).

[30] UA1 collaboration: C. Albajar et al., Phys. Lett. **193B** (1987) 289.

[31] P. Jenni, Proc. Int. Symposium on Lepton and Photon Interactions at High Energies, Hamburg (1987), page 341.

[32] UA2 collaboration: R. Ansari et al., Phys. Lett. **194B** (1987) 158.

[33] M. Barnett, I. Hinchliffe and W.J. Stirling in Review of Particle Properties, Phys. Lett. **204B** (1988).

[34] R. Kleiss and W.J. Stirling, Phys. Lett. **180B** (1986) 171.

[35] A.C. Bawa and W.J. Stirling, unpublished.

[36] V. Barger, T. Han, J. Ohnemus and D. Zeppenfeld, Madison preprint MAD/PH/455 (1988).

[37] F.A. Berends, W.T. Giele, R. Kleiss, H. Kuijf and W.J. Stirling, Phys. Lett. **224B** (1989) 237.

[38] F. Halzen and K. Mursula, Phys. Rev. Lett. **51** (1983) 857.

[39] A.D. Martin, R.G. Roberts and W.J. Stirling, Phys. Lett. **189B** (1987) 220.

[40] A.D. Martin, R.G. Roberts and W.J. Stirling, Phys. Lett. **207B** (1988) 205.

[41] UA1 collaboration: C. Albajar et al., Z. Phys. **C37** (1988) 489.

[42] UA1 collaboration: C. Albajar et al., Phys. Lett. **213B** (1988) 405.

[43] P. Nason , S. Dawson and R.K. Ellis, Nucl. Phys. **B303** (1988) 607.

[44] W. Beenakker, H. Kuijf, W.L. Van Neerven and J. Smith, University of Leiden preprint 88-0717 (1988).

[45] R. Kleiss, A.D. Martin and W.J. Stirling, Z. Phys. **C39** (1988) 393.

[46] UA1 collaboration: C. Albajar et al., Z. Phys. **C37** 505 (1988).

[47] G. Altarelli, M. Diemoz, G. Martinelli and P. Nason, Nucl. Phys. **B308** (1988) 724.

[48] T. Kamae, Proc. XXIV Int. Conf. on High Energy Physics, Munich 1988, eds. R. Kotthaus and J.H. Kuhn, Springer-Verlag (1989), page 156.

[49] S. Geer, Proc. Int. Europhysics Conf. on High Energy Physics, Uppsala, Sweden (1987), and references therein.

[50] UA2 collaboration: R. Ansari et al., Phys. Lett. **195B** (1987) 613.

[51] CDF collaboration: F. Abe et al., Phys. Rev. Lett. **62** (1989) 1005.

Figure Captions

[1] QCD $2 \rightarrow 2$ quark and gluon subprocess scattering diagrams, from [4].

[2] The jet p_T distribution in $p\bar{p} \rightarrow jet + X$ at $\eta = 0$ for $\sqrt{s} = 630\ GeV$. The data are from the UA2 collaboration [8]. The curve is a QCD prediction from reference [9] as described in the text.

[3] Relative contributions of the different leading order subprocesses for large p_T jet, W and γ production in $p\bar{p}$ collisions at $\sqrt{s} = 630\ GeV$ and $1.8\ TeV$, from reference [10].

[4] Jet centre-of-mass angular distribution measured by the UA1 collaboration [13]. The curves are described in the text.

[5] Examples of QCD Feynman diagrams which contribute to two, three and four jet production.

[6] Inclusive direct photon production cross section from UA2 [20]. The QCD curves show the effect of including photon isolation, as described in the text.

[7] Ratio of the scattering angle distributions of $\gamma + jet$ and $\pi + jet$ systems – where the 'π' is a multiphoton jet – from UA2 [20]. The curve is the theoretical expectation from the leading $2 \rightarrow 2$ QCD subprocesses.

[8] Dijet invariant mass distribution from UA2 [23]. Curve (a) is the fitted background while curve (b) includes the W and Z resonances.

[9] The W and Z cross sections measured by the UA1 [24], UA2 [25] and CDF [51] collaborations. The theoretical predictions [26] are shown as a function of m_t for $N_\nu = 3$. The dashed error bar on the theoretical predictions indicates the effect of a $\pm 20\%$ $O(\alpha_s^2)$ correction and the solid error bar indicates the effect of varying the W and Z masses by $\pm 1\ GeV$ about their central values of 81 and 92 GeV respectively.

[10] $Z \rightarrow e^+e^-$ events from UA1 [24].

[11] Electron and muon candidate W events from UA1 [24].

[12] (a) W decay angular distribution from the UA1 collaboration [24], together with the standard model expectation including higher order effects.
(b) Z decay angular distribution from UA1 [24] showing the standard model curves for different values of $\sin^2\theta_W$.

[13] Next-to-leading order QCD predictions from reference [28] for the W transverse momentum distribution, compared with data from the UA1 [30] and UA2 [31] collaborations.

[14] Average W transverse momentum in $p\bar{p}$ collisions, as a function of energy, in next-to-leading order QCD (solid curve) [35]. Data from UA1 [30] and UA2 [31] are shown. The dashed curve is the theoretical prediction for $< p_T^Z >$.

[15] Multiplicity of jets $f_n(W)$ as a function of n. Data from the UA1 collaboration [24] on $p\bar{p} \to W(\to l\nu)+$jets are compared with the theoretical predictions from reference [37]. The upper edge of the bands corresponds to the MRSB parton distributions [26] with $\mu = M_W$ and the lower edge to the MRSE distributions with $\mu = \sqrt{\hat{s}}$. In accordance with [24] there are no lepton cuts. The jet minimum transverse momentum, rapidity and separation cuts are 5 GeV, 2.5 and 1.0 respectively.

[16] The average value (solid data point) and combined 90% c.l. upper limit (hatched line) of the ratio R of the W and Z cross sections measured by the UA1 and UA2 collaborations [30,31], together with theoretical expectations using different parton distributions [26], as explained in the text. Predictions for $\sqrt{s} = 1.8\ TeV$ are also shown.

[17] Leading order QCD Feynman diagrams for heavy quark pair production in hadron hadron collisions.

[18] Inclusive muon transverse momentum distribution from UA1 [41], including the distribution from events with an identified large p_T hadronic jet. The curves are predictions from the ISAJET Monte Carlo.

[19] The distribution of muon transverse momentum relative to the nearby jet, from UA1 [41], showing the fitted contributions from bottom (dashed curve), charm (dash-dot curve) and decay background (dotted curve).

[20] Bottom quark cross sections at $\sqrt{s} = 630\ GeV$ as a function of the b quark transverse momentum threshold. The data are from UA1 [42] and the QCD curves are the next-to-leading order predictions of Ellis et al. [43].

[21] Theoretical top quark production cross sections at the CERN (630 GeV) and Fermilab (1.8 TeV) $p\bar{p}$ colliders as functions of m_t, from reference [45].

[22] The inclusive muon transverse momentum distribution as measured by the UA1 collaboration [46], together with Monte Carlo predictions for various values of the top quark mass.

[23] The UA1 top quark production cross section 95% upper limit (hatched line), together with theoretical predictions, as a function of m_t [46].

[24] Top quark and b' production cross sections as functions of the quark masses together with the UA1 cross section upper limits [46], from Altarelli et al. [47].

[25] UA1 90% *cl* limits on squark and gluino masses derived from the large missing transverse energy multijet sample [49]. The arrows indicate the asymptotic values of the limits.

[26] UA2 limits on additional (a) W' and (b) Z' bosons obtained from an analysis of single electron and electron pair candidates respectively, as a function of the couplings and branching ratio [50].

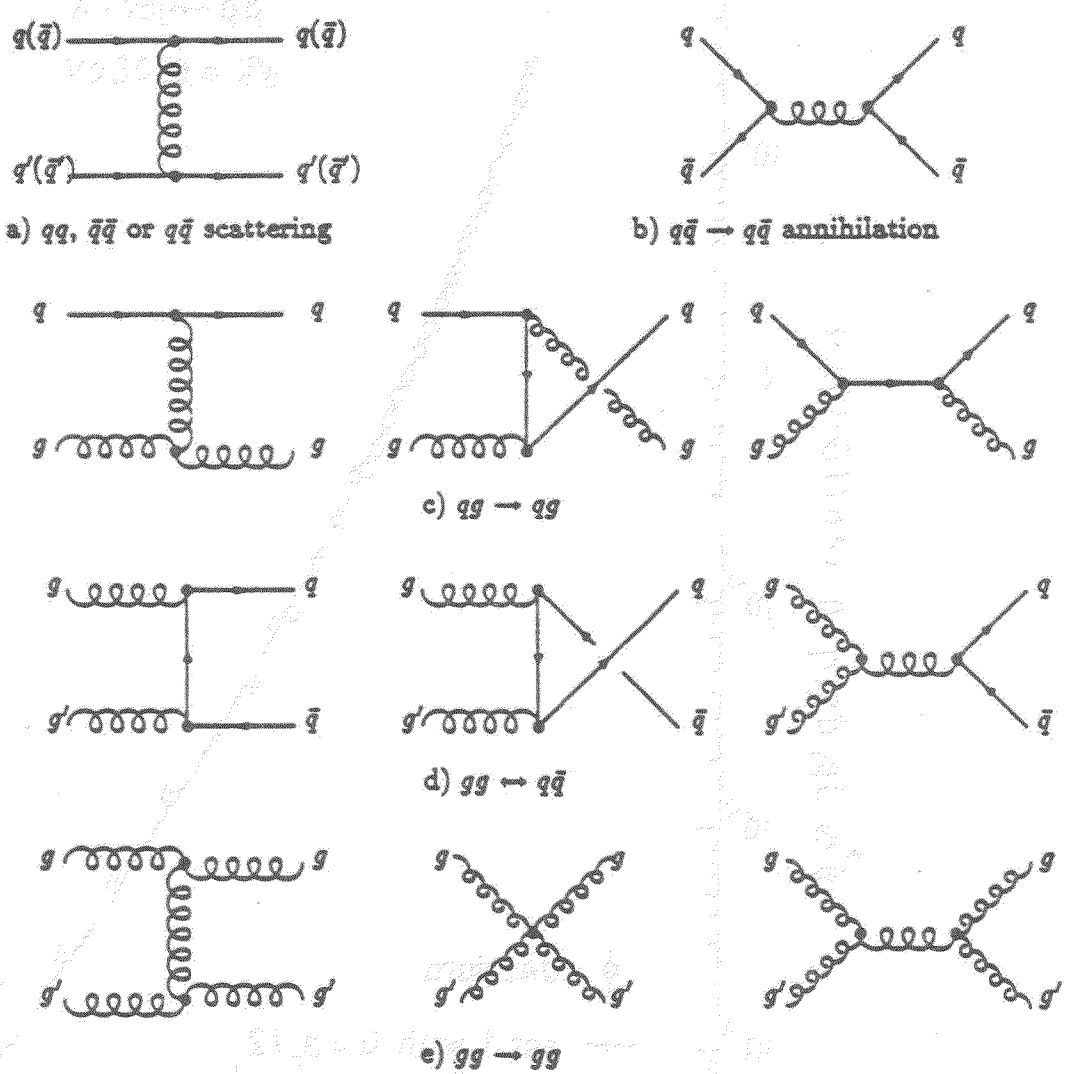
q(q̄)
q(q̄)
q′(q̄′)
q′(q̄′)
a) qq, q̄q̄ or qq̄ scattering
q
q
q̄
q̄
b) qq̄ → qq̄ annihilation
q
q
g
g
q
q
g
g
q
q
g
g
c) qg → qg
g
q
g′
q̄
g
q
g′
q̄
g
q
g′
q̄
d) gg ↔ qq̄
g
g
g′
g′
g
g
g′
g′
g
g
g′
g′
e) gg → gg

Figure 1

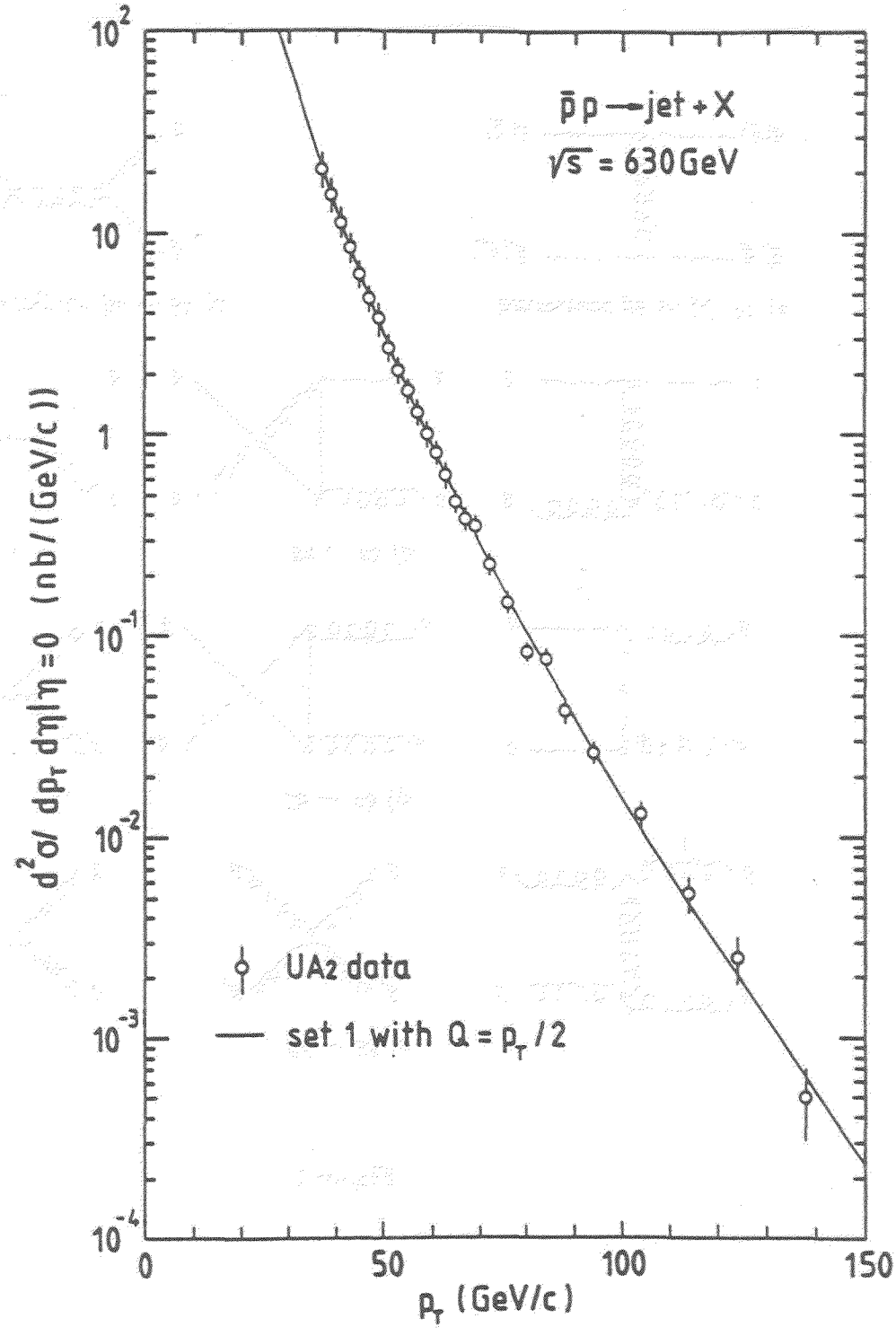
$\bar{p}p \rightarrow$ jet + X
$\sqrt{s}$ = 630 GeV
$d^2\sigma / dp_T d\eta|_{\eta=0}$ (nb/(GeV/c))
UA2 data
set 1 with $Q = p_T/2$
p_T (GeV/c)
10^2
10
1
10^{-1}
10^{-2}
10^{-3}
10^{-4}
0
50
100
150

Figure 2

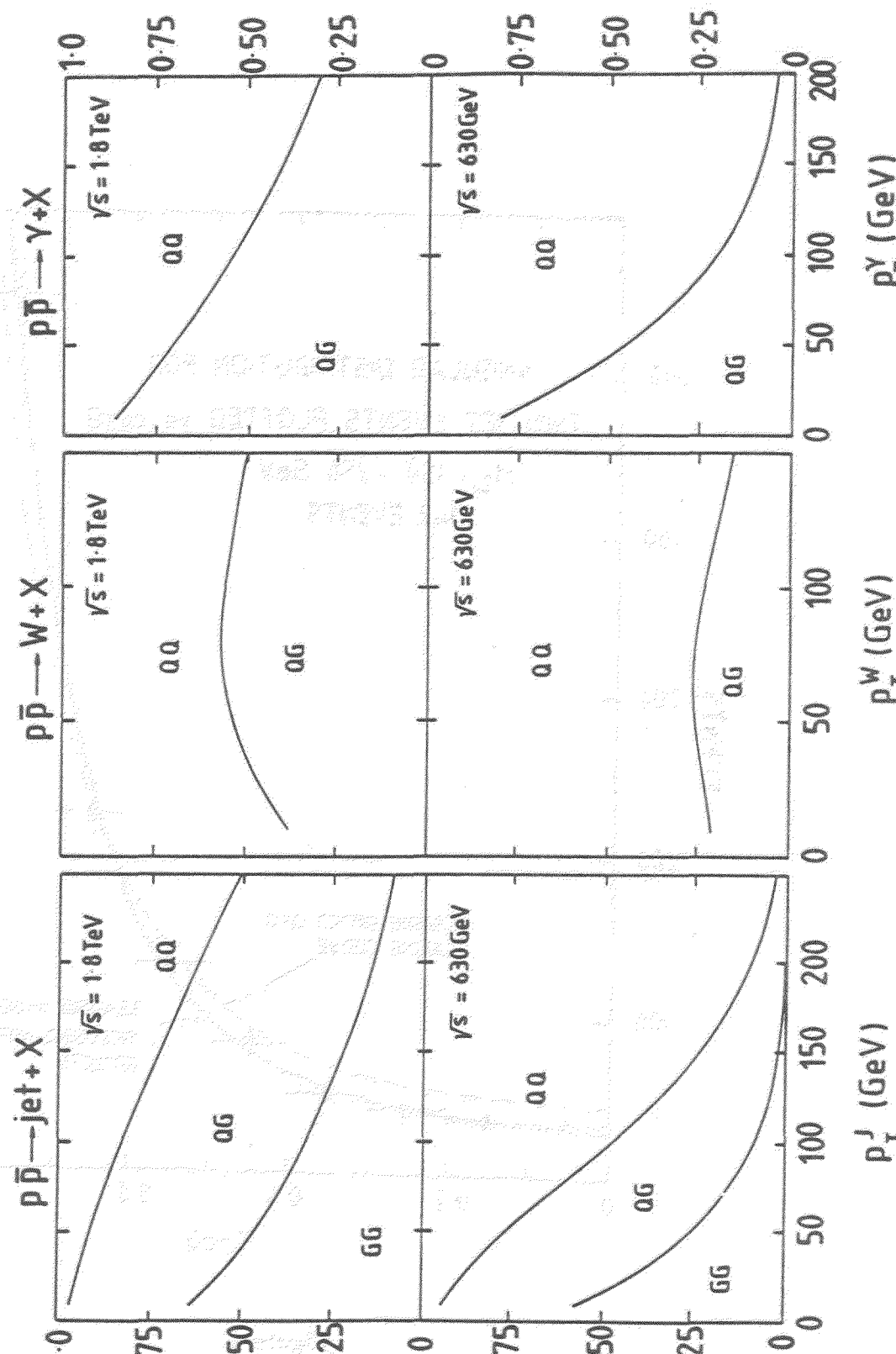
p p̄ — jet + X
p p̄ — W + X
p p̄ — γ + X
√s = 1·8 TeV
√s = 630 GeV
qq
qG
GG
1·0
0·75
0·50
0·25
0
50
100
150
200
p_T^J (GeV)
p_T^W (GeV)
p_T^γ (GeV)

Figure 3

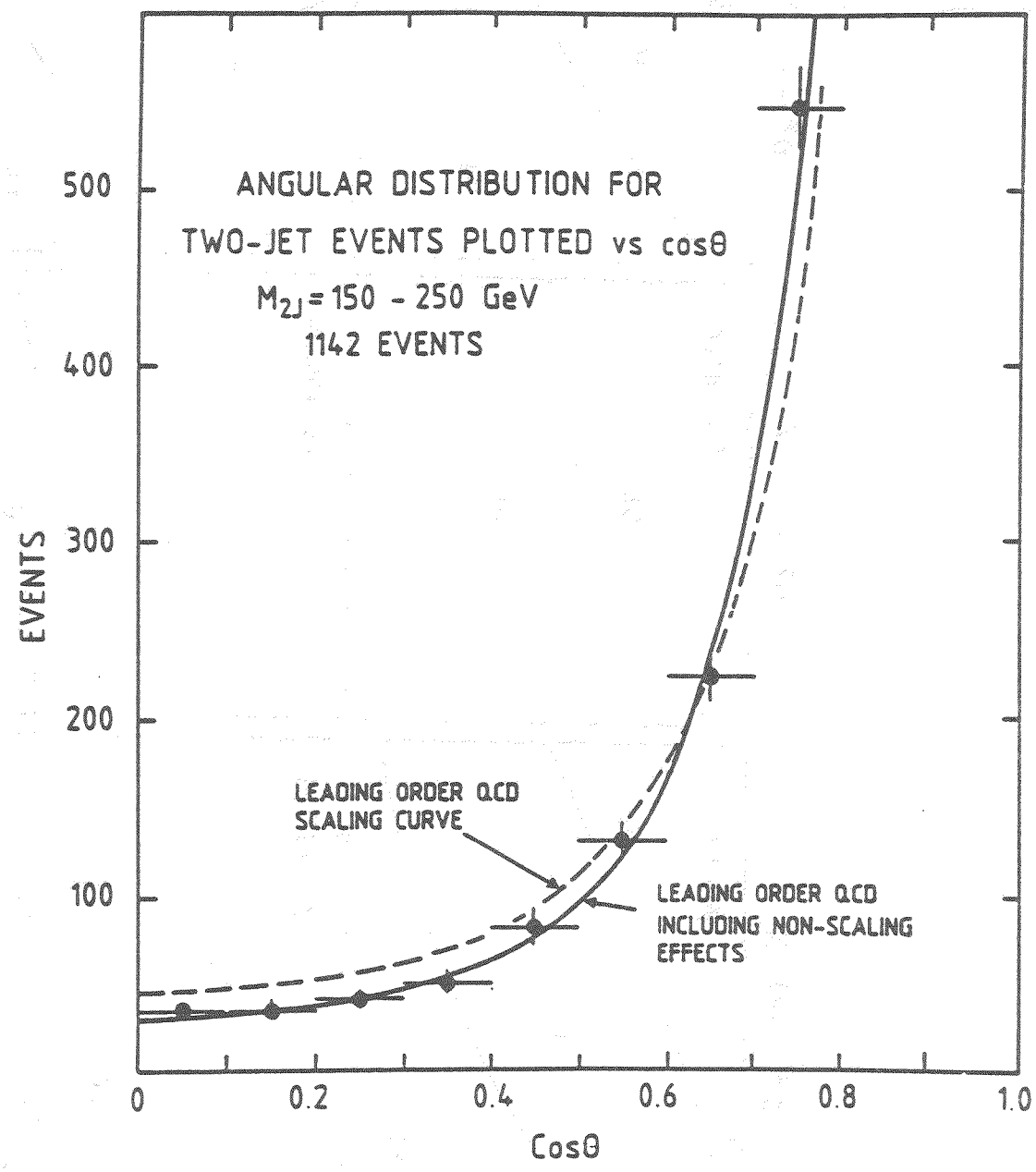
ANGULAR DISTRIBUTION FOR
TWO-JET EVENTS PLOTTED vs cosθ
M_{2J} = 150 - 250 GeV
1142 EVENTS
LEADING ORDER QCD
SCALING CURVE
LEADING ORDER QCD
INCLUDING NON-SCALING
EFFECTS
EVENTS
Cosθ
500
400
300
200
100
0
0.2
0.4
0.6
0.8
1.0

Figure 4

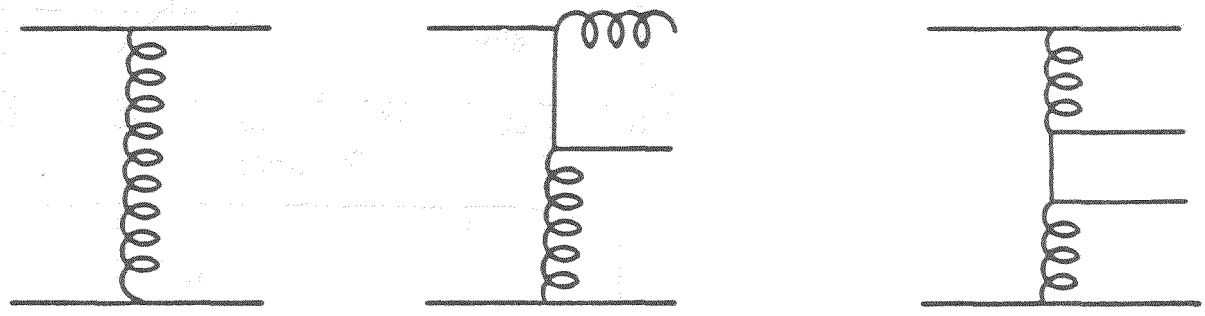

Figure 5

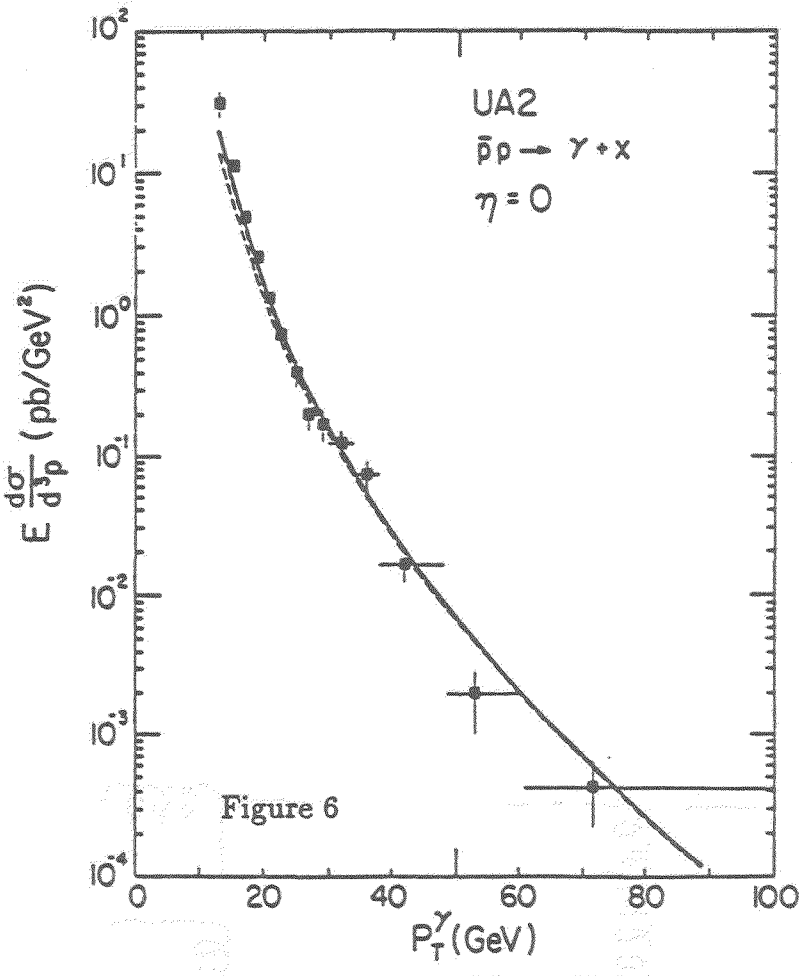

Figure 6

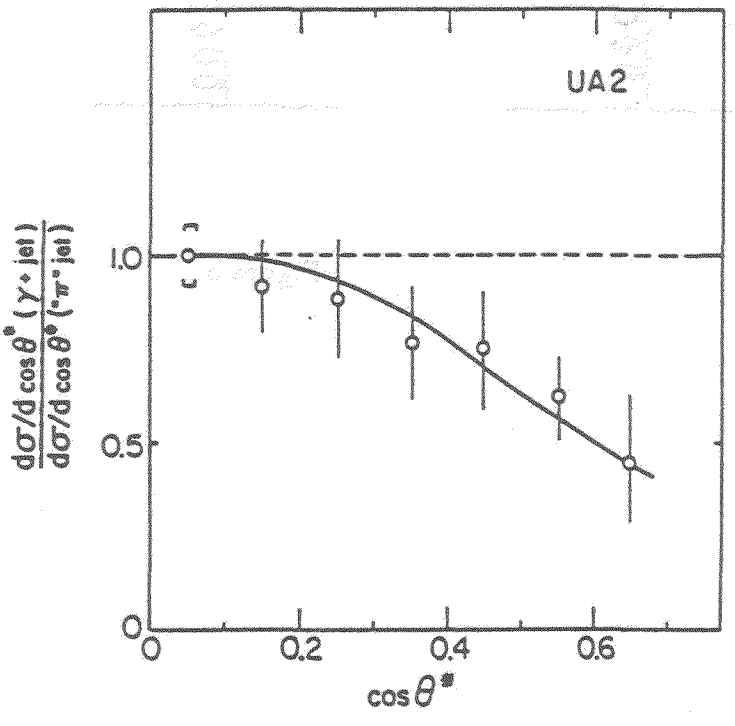

Figure 7

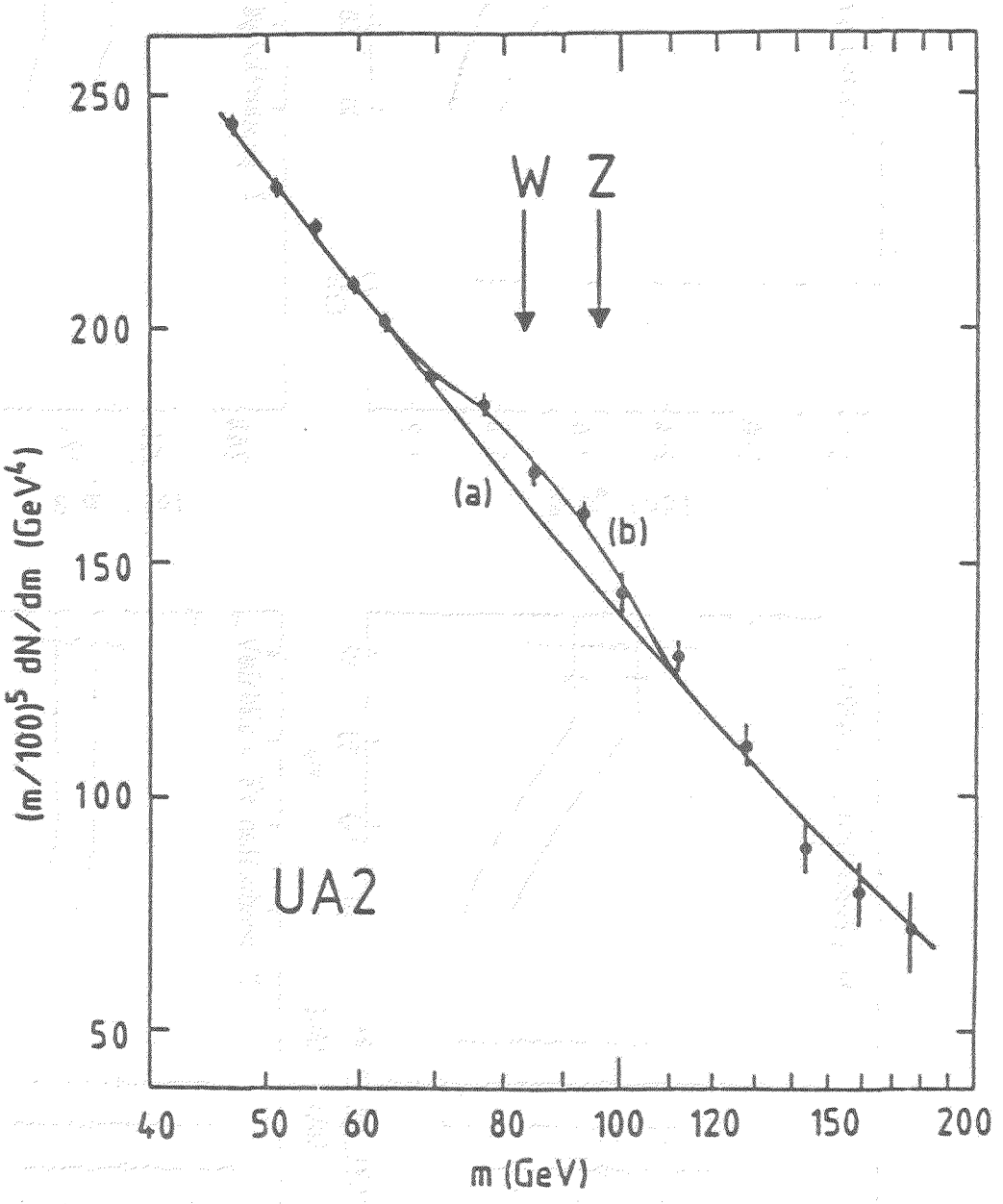
250
200
150
100
50
W
Z
(a)
(b)
UA2
(m/100)⁵ dN/dm (GeV⁴)
40
50
60
80
100
120
150
200
m (GeV)

Figure 8

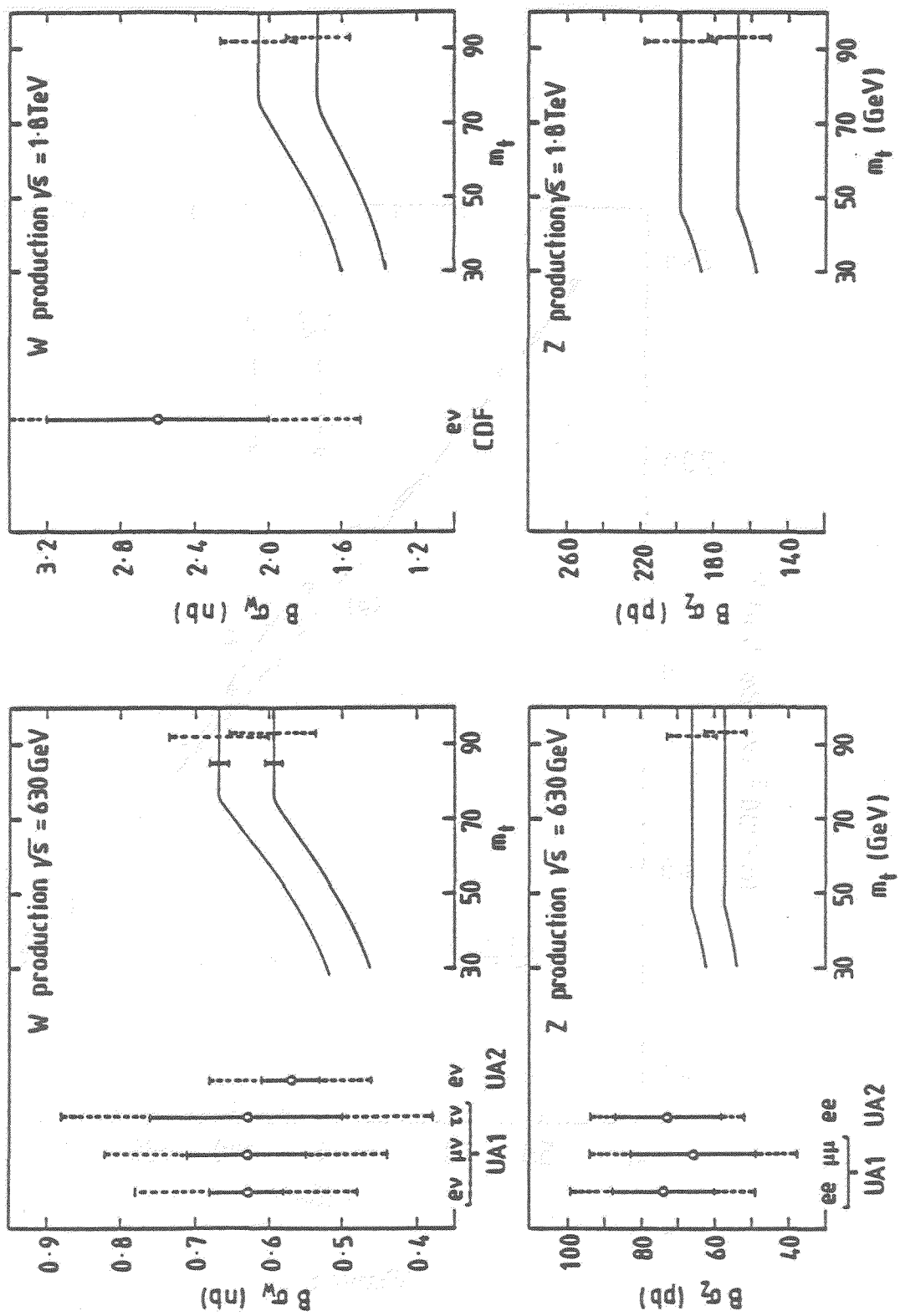
W production √s = 1.8 TeV
B σW (nb)
3·2
2·8
2·4
2·0
1·6
1·2
eν
CDF
Z production √s = 1.8 TeV
B σZ (pb)
260
220
180
140
W production √s = 630 GeV
0·9
0·8
0·7
0·6
0·5
0·4
eν μν τν
UA1
eν
UA2
Z production √s = 630 GeV
100
80
60
40
ee μμ
UA1
ee
UA2
30
50
70
90
mt
mt (GeV)

Figure 9

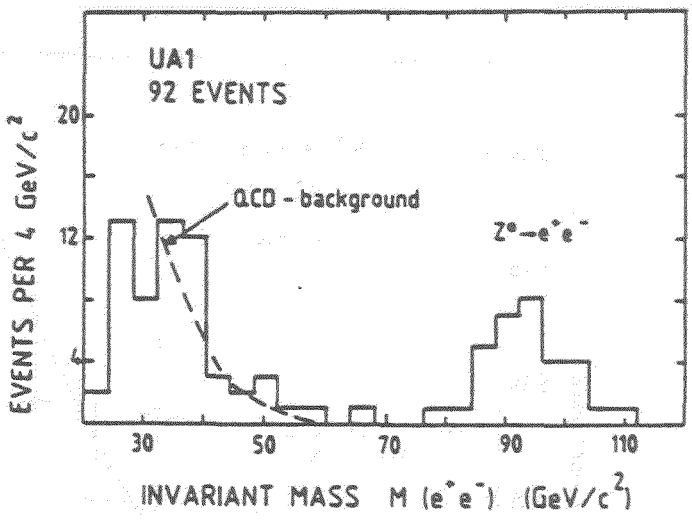

Figure 10

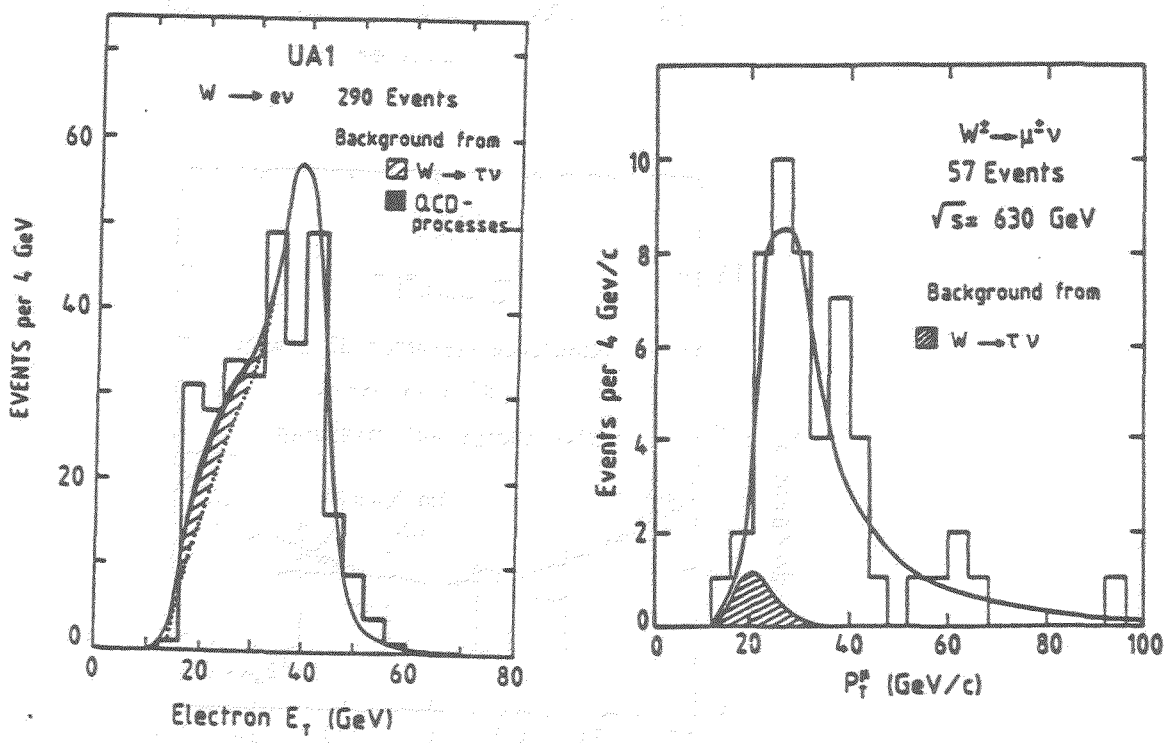

Figure 11

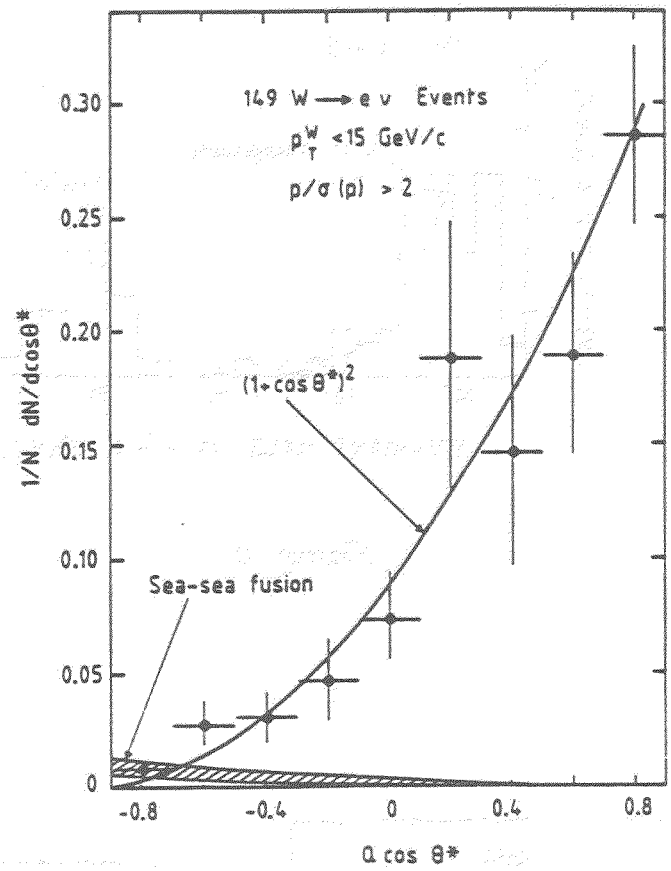
149 W → e ν Events
p_T^W <15 GeV/c
p/σ (p) > 2
$(1+\cos\theta^*)^2$
Sea-sea fusion
1/N dN/dcosθ*
0.30
0.25
0.20
0.15
0.10
0.05
0
-0.8
-0.4
0
0.4
0.8
α cos θ*

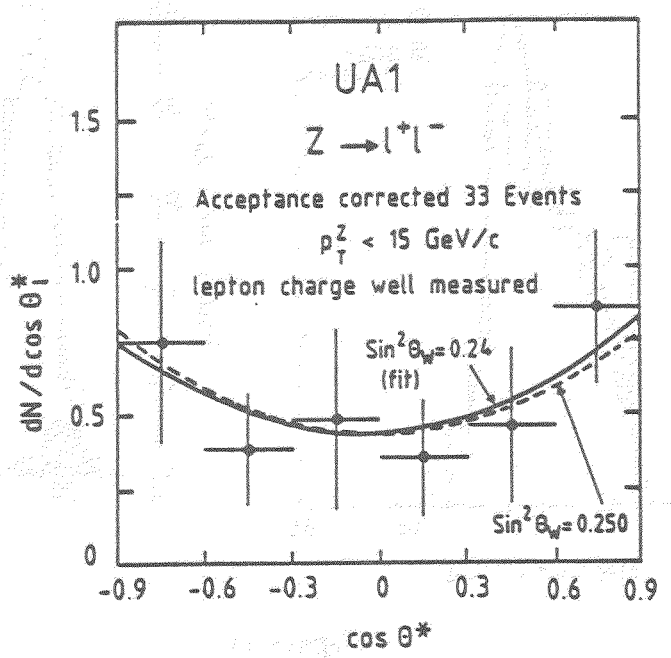
UA1
Z → l⁺l⁻
Acceptance corrected 33 Events
p_T^Z < 15 GeV/c
lepton charge well measured
$\sin^2\theta_W = 0.24$
(fit)
$\sin^2\theta_W = 0.250$
dN/d cos θ*l
1.5
1.0
0.5
0
-0.9
-0.6
-0.3
0
0.3
0.6
0.9
cos θ*

Figure 12

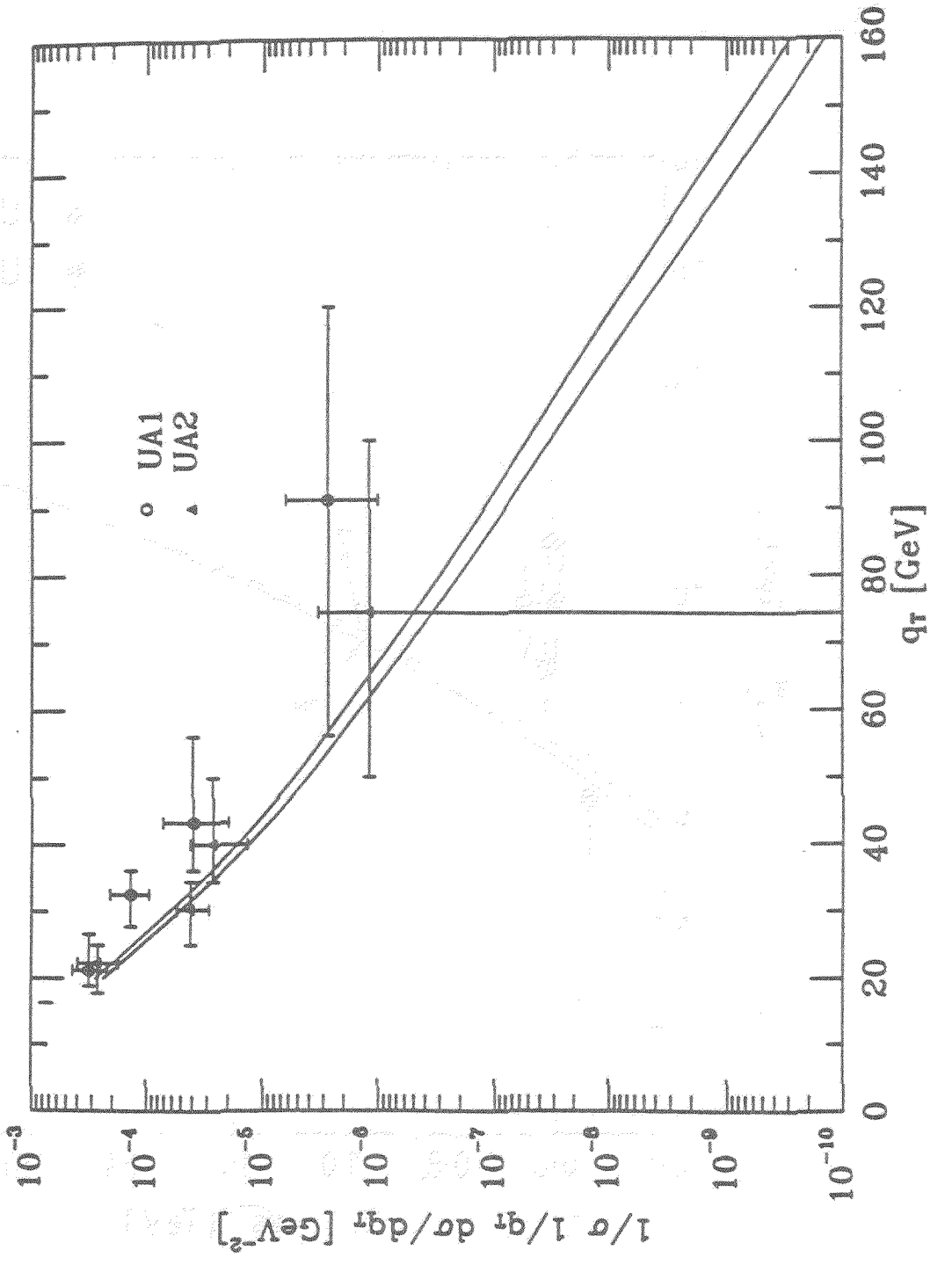
UA1
UA2
$1/\sigma\ 1/q_T\ d\sigma/dq_T$ [GeV^{-2}]
q_T [GeV]
10^{-3}
10^{-4}
10^{-5}
10^{-6}
10^{-7}
10^{-8}
10^{-9}
10^{-10}
0
20
40
60
80
100
120
140
160

Figure 13

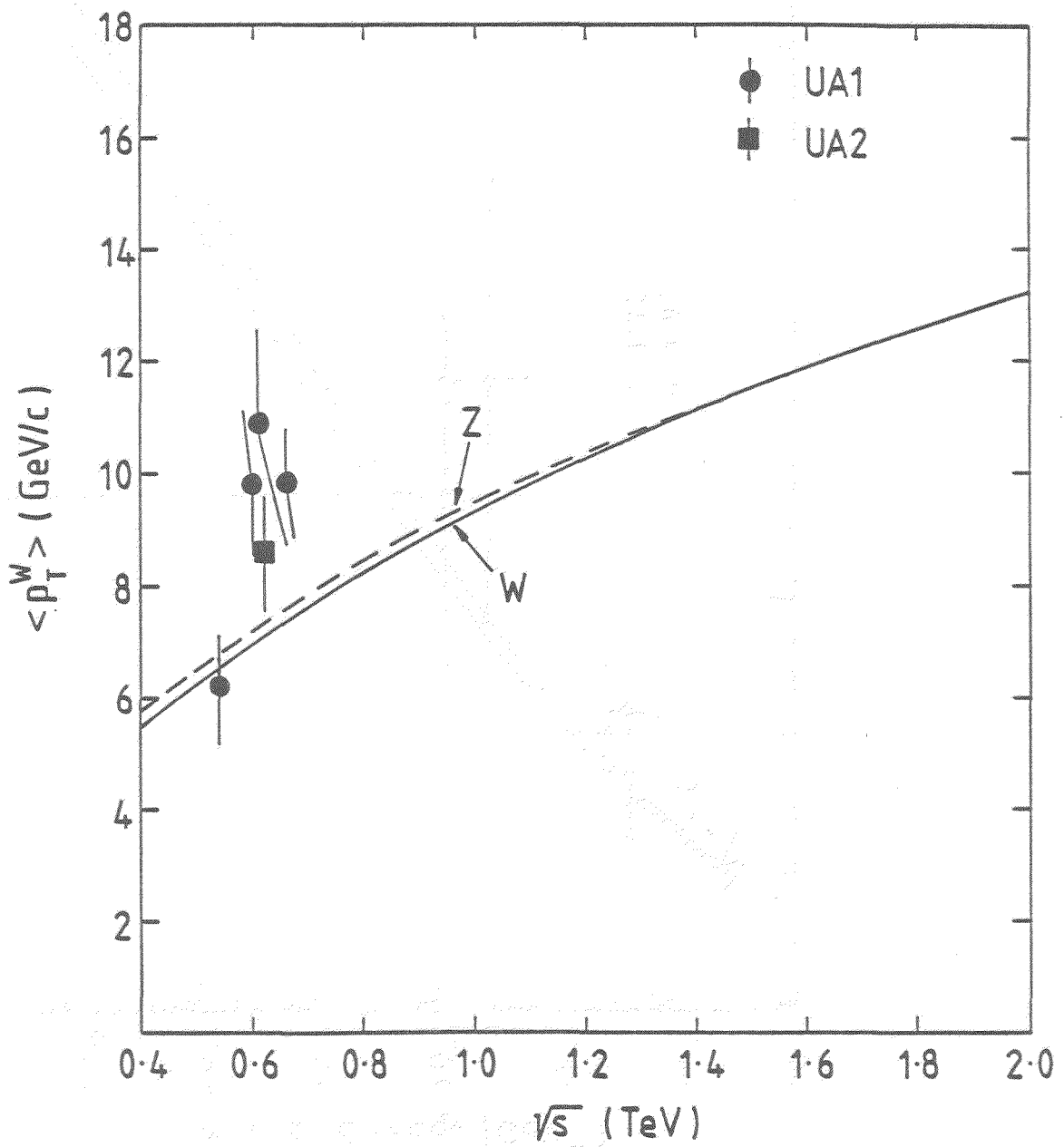
UA1
UA2
Z
W
$\langle p_T^W \rangle$ (GeV/c)
$\sqrt{s}$ (TeV)
18
16
14
12
10
8
6
4
2
0·4
0·6
0·8
1·0
1·2
1·4
1·6
1·8
2·0

Figure 14

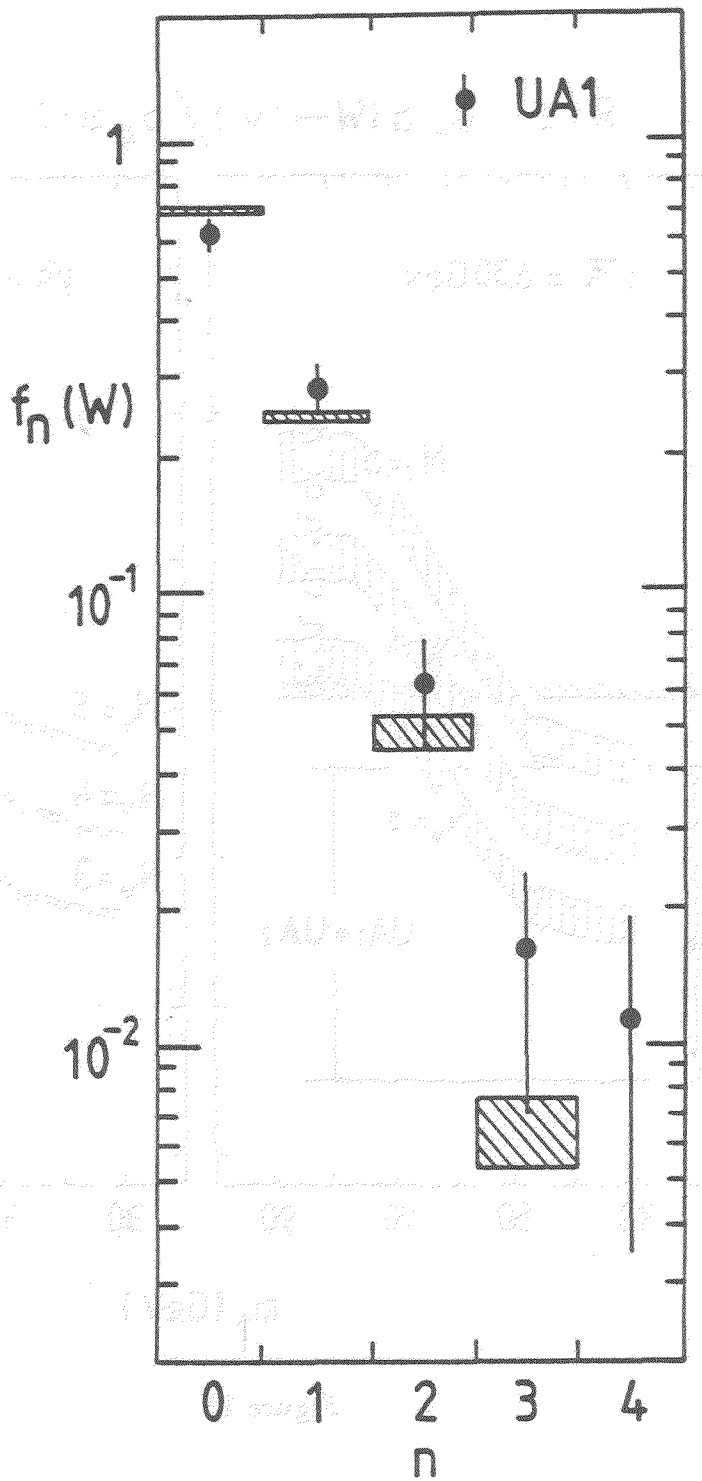

Figure 15

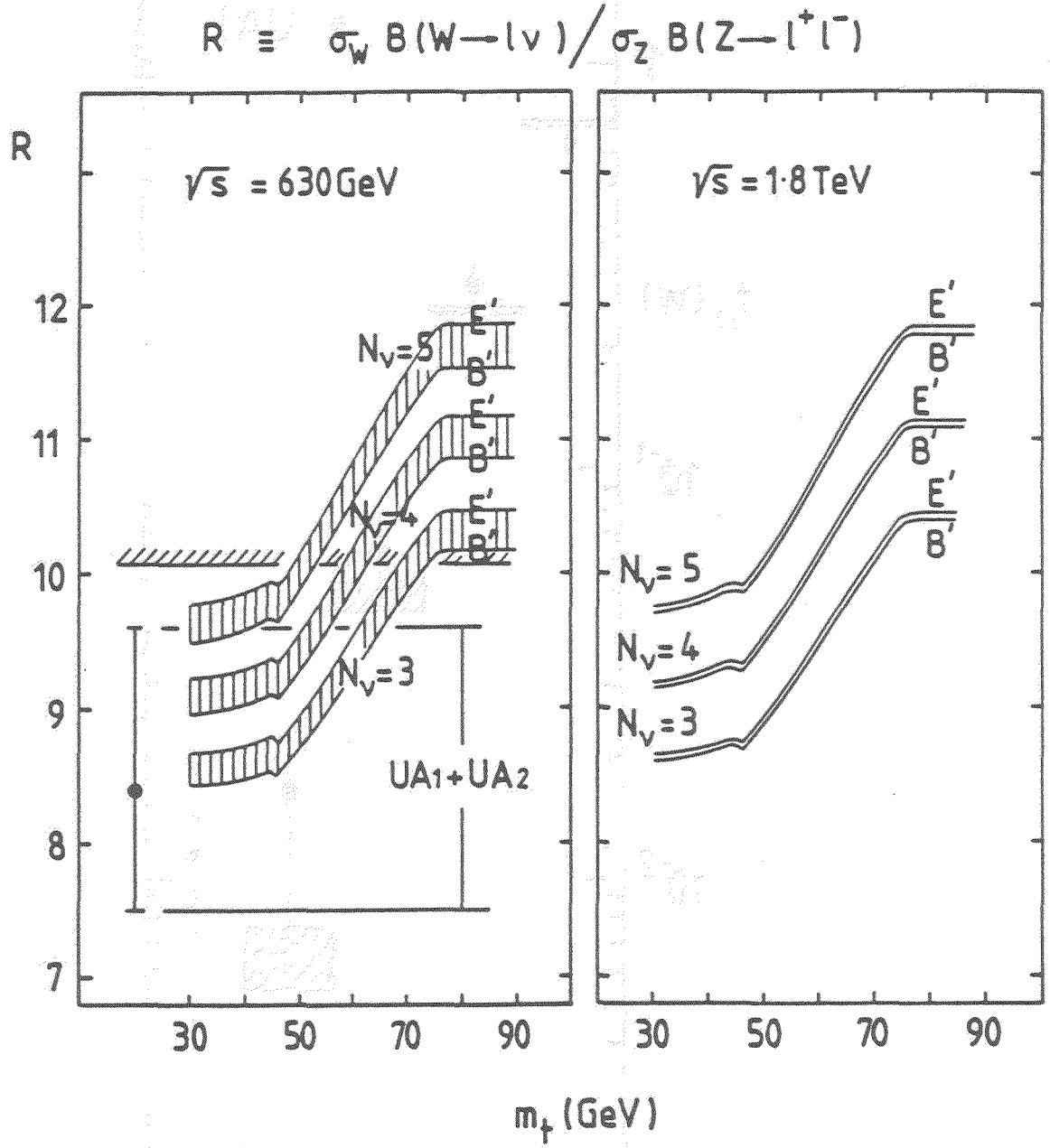
R ≡ σ_W B(W→lν) / σ_Z B(Z→l⁺l⁻)
R
√s = 630 GeV
√s = 1·8 TeV
12
11
10
9
8
7
N_ν = 5
N_ν = 4
N_ν = 3
E'
B'
UA1 + UA2
30
50
70
90
m_t (GeV)

Figure 16

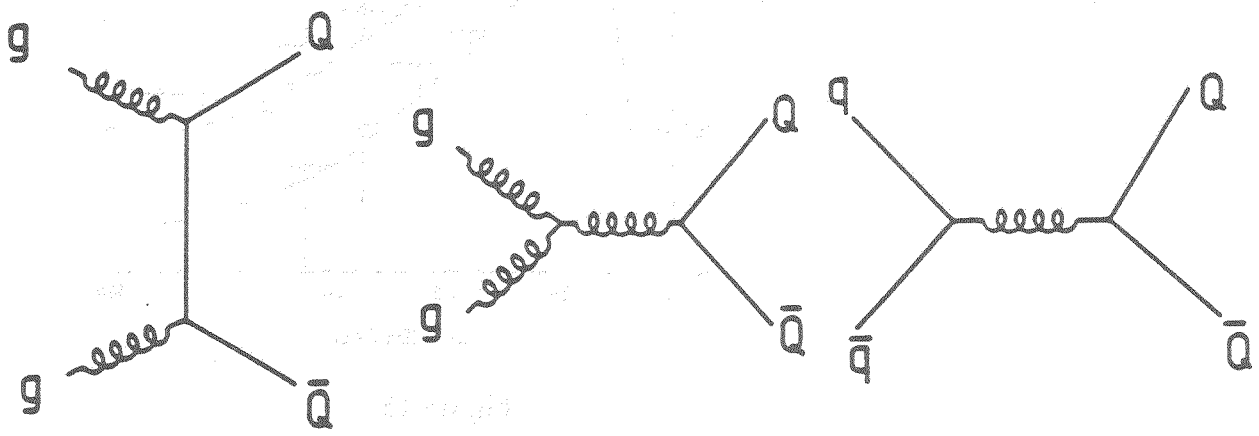

Figure 17

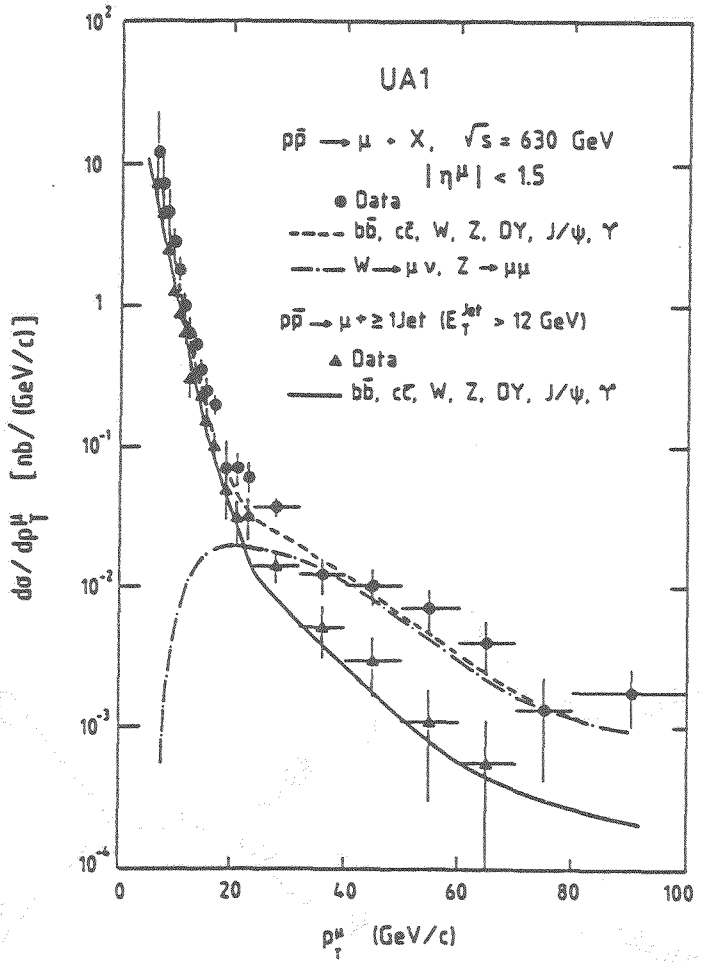

Figure 18

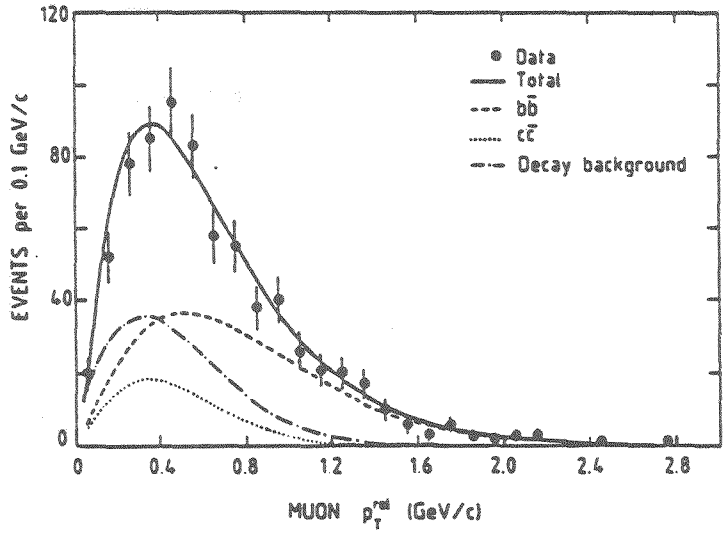

Figure 19

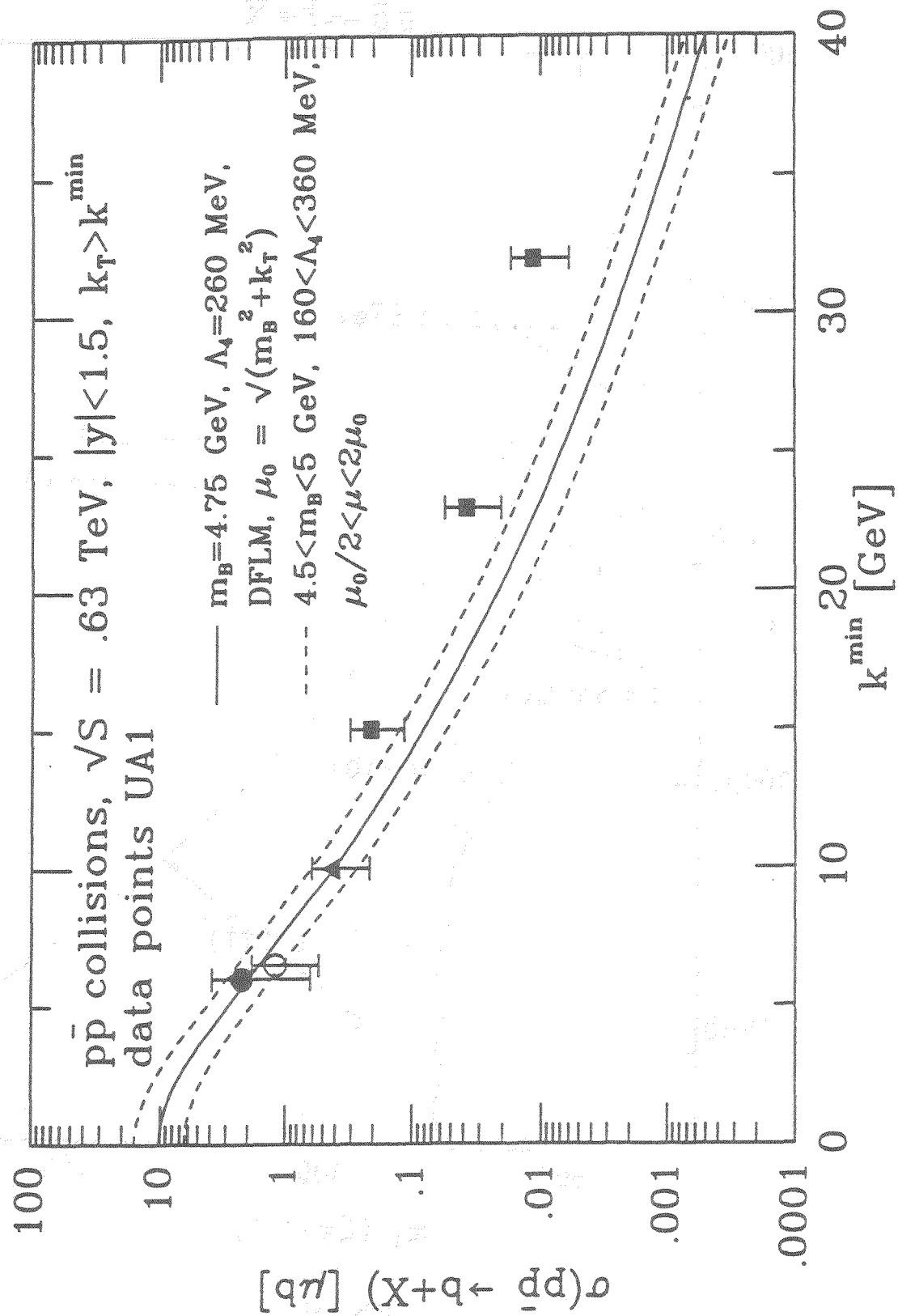
$\bar{p}p$ collisions, $\sqrt{S}$ = .63 TeV, |y|<1.5, $k_T > k^{min}$
data points UA1
m_B=4.75 GeV, Λ_4=260 MeV,
DFLM, $\mu_0 = \sqrt{(m_B^2 + k_T^2)}$
4.5<m_B<5 GeV, 160<Λ_4<360 MeV,
$\mu_0/2 < \mu < 2\mu_0$
$\sigma(p\bar{p} \to b+X)$ [μb]
k^{min} [GeV]
100
10
1
.1
.01
.001
.0001
0
10
20
30
40

Figure 20

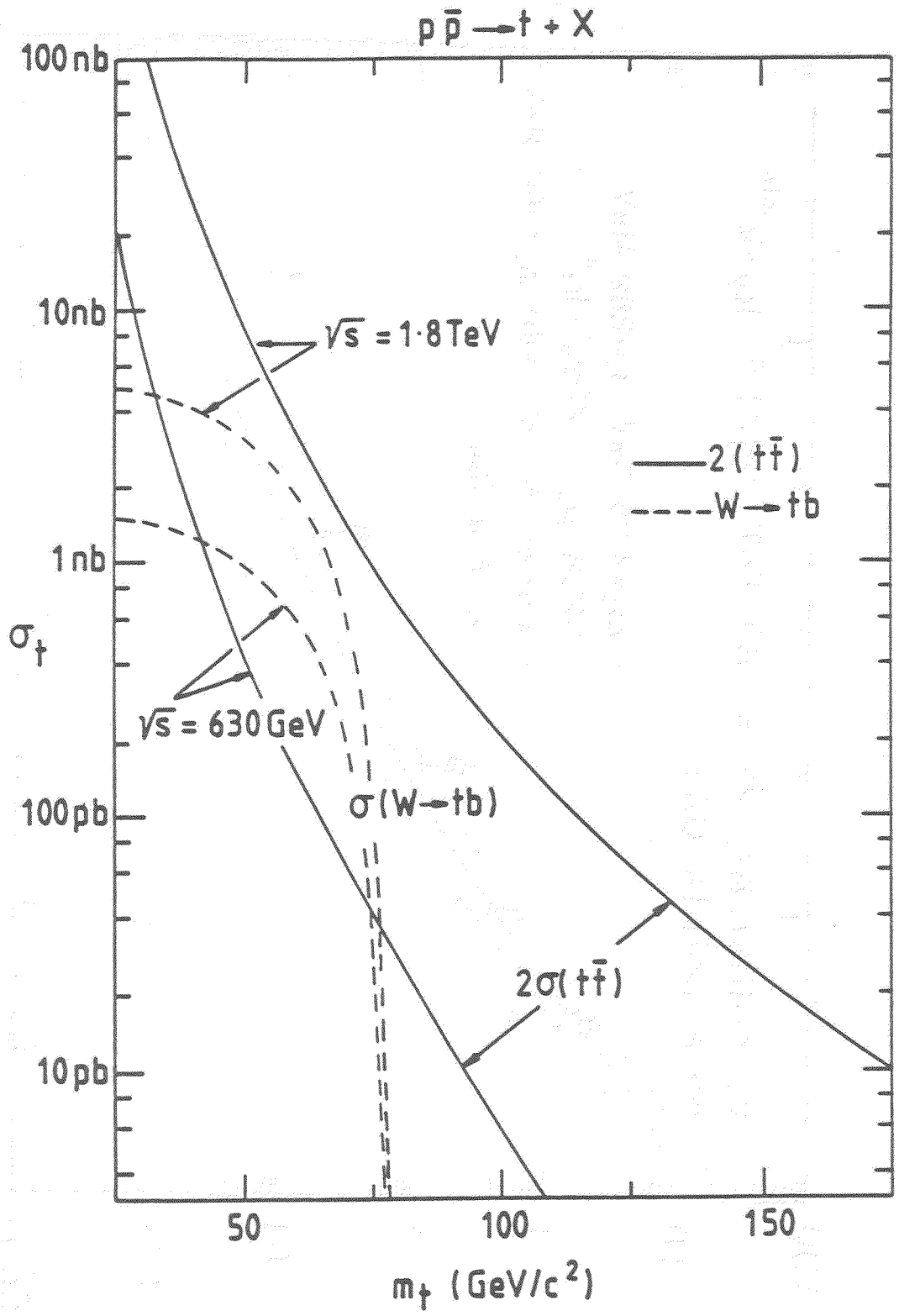
p p̄ → t + X
100 nb
10nb
1nb
100pb
10pb
σt
√s = 1·8 TeV
√s = 630 GeV
2 (tt̄)
W → tb
σ(W → tb)
2σ(tt̄)
50
100
150
mt (GeV/c²)

Figure 21

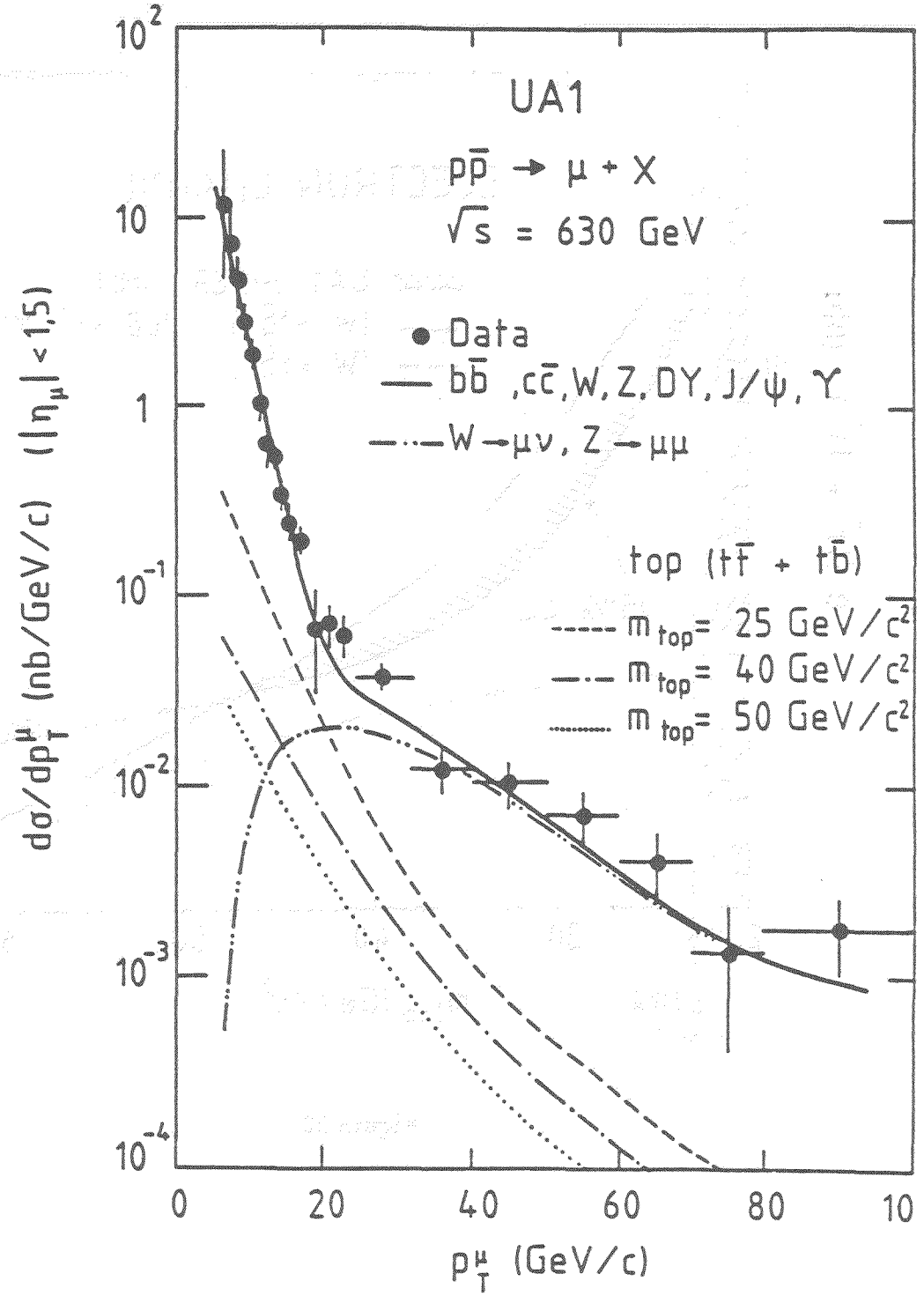
UA1
$p\bar{p} \rightarrow \mu + X$
$\sqrt{s}$ = 630 GeV
Data
$b\bar{b}$, $c\bar{c}$, W, Z, DY, J/ψ, ϒ
W → μν, Z → μμ
top ($t\bar{t}$ + $t\bar{b}$)
m_{top} = 25 GeV/c^2
m_{top} = 40 GeV/c^2
m_{top} = 50 GeV/c^2
$d\sigma/dp_T^\mu$ (nb/GeV/c) ($|\eta_\mu| < 1,5$)
p_T^μ (GeV/c)
10^2
10
1
10^{-1}
10^{-2}
10^{-3}
10^{-4}
0
20
40
60
80
10

Figure 22

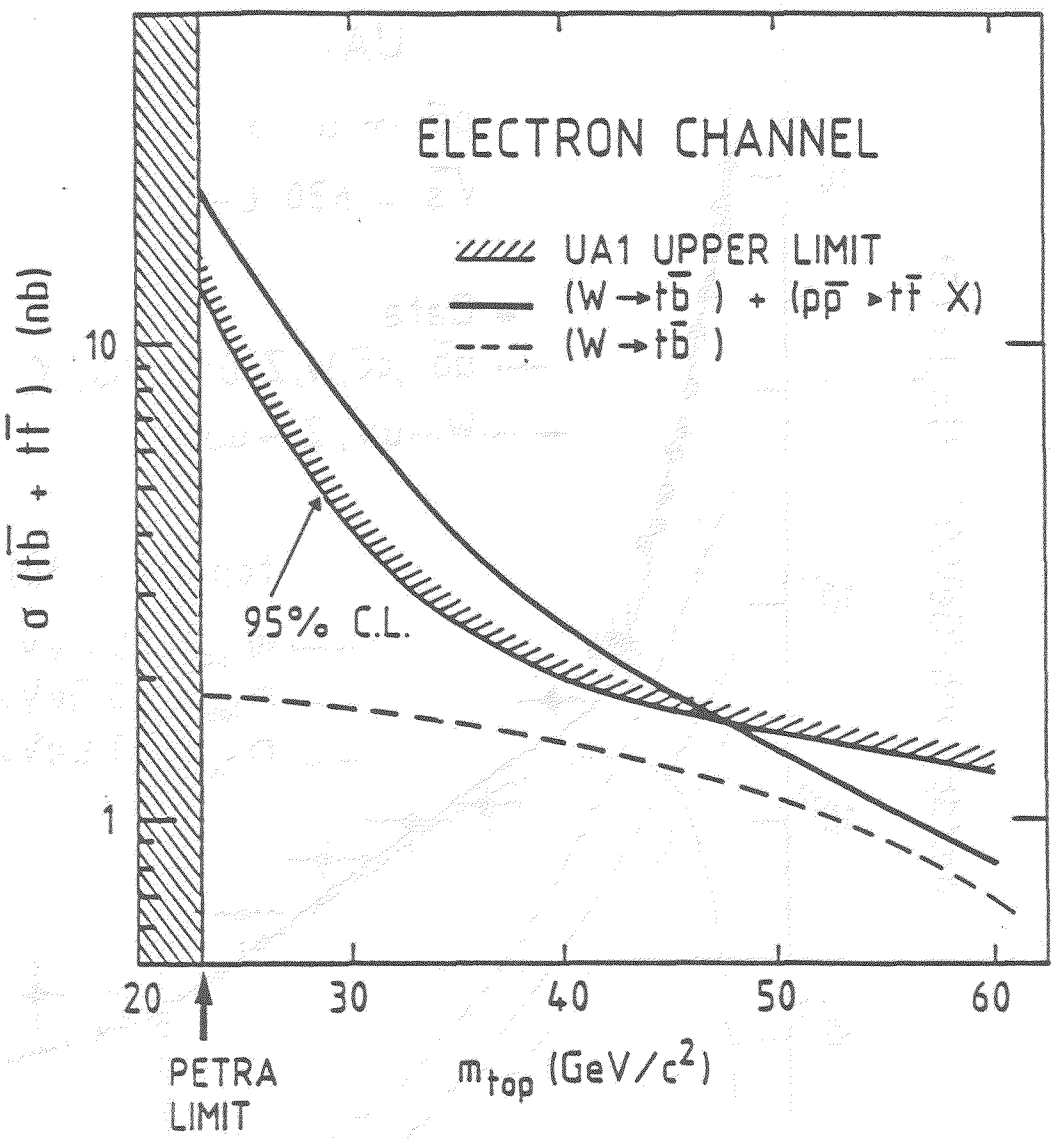
ELECTRON CHANNEL
UA1 UPPER LIMIT
(W → tb̄) + (pp̄ → tt̄ X)
(W → tb̄)
95% C.L.
σ (tb̄ + tt̄) (nb)
10
1
20
30
40
50
60
PETRA LIMIT
m_top (GeV/c²)

Figure 23

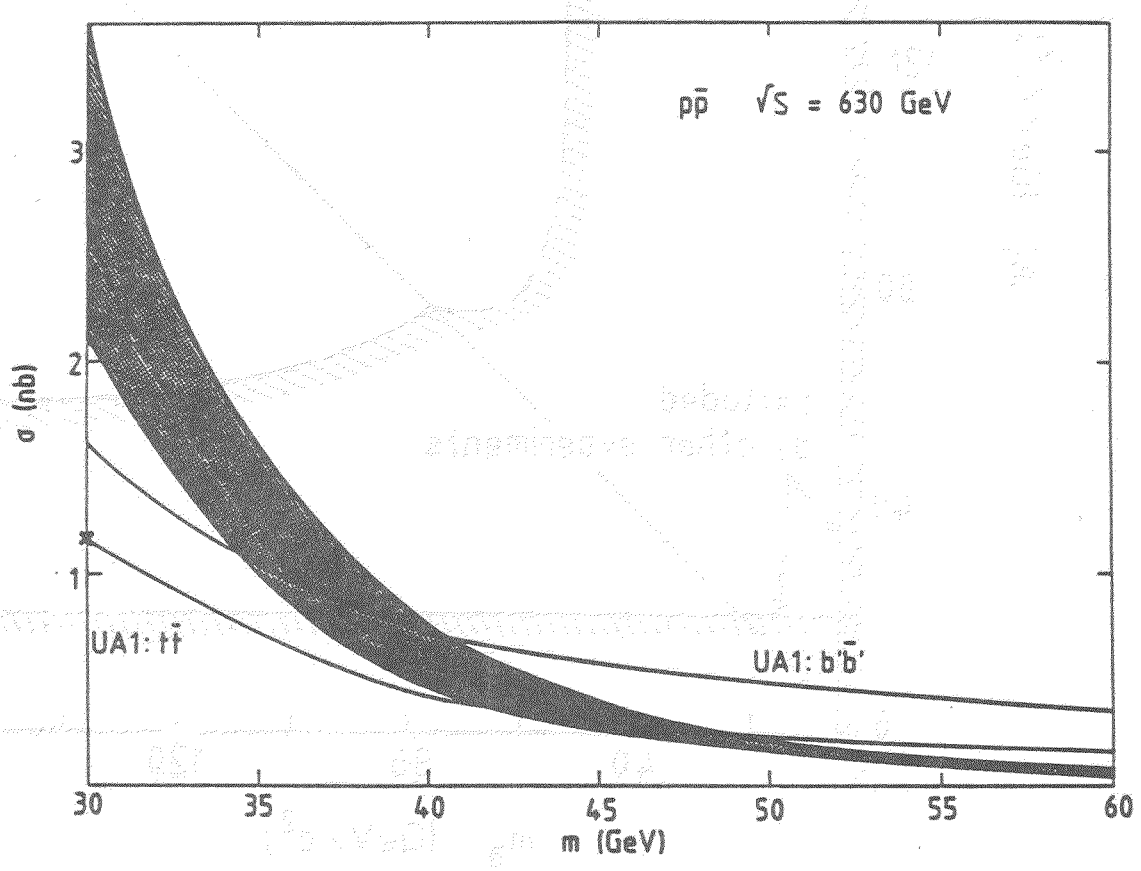

Figure 24

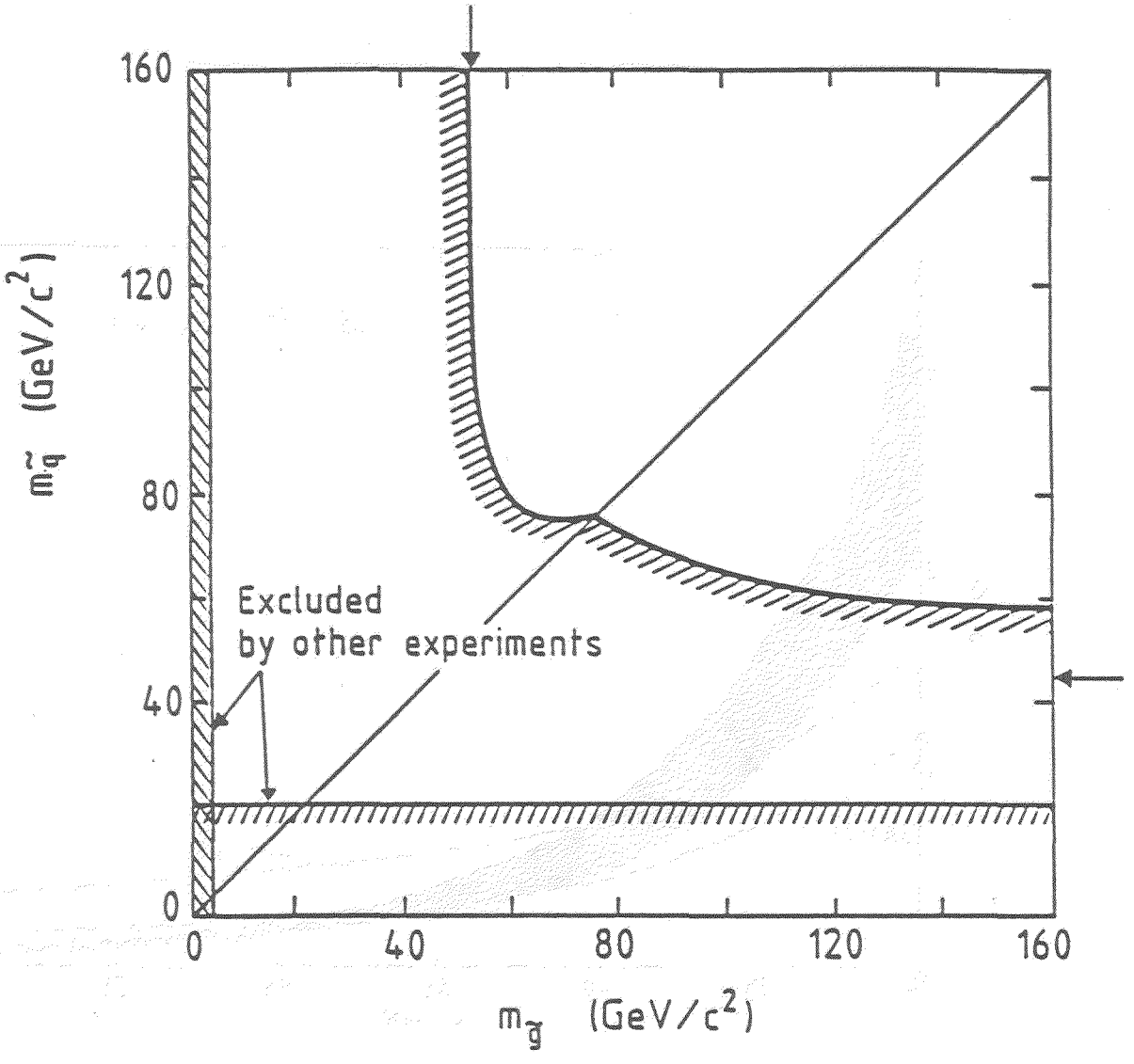
160
120
80
40
0
0
40
80
120
160
$m_{\tilde{q}}$ (GeV/c^2)
$m_{\tilde{g}}$ (GeV/c^2)
Excluded
by other experiments

Figure 25

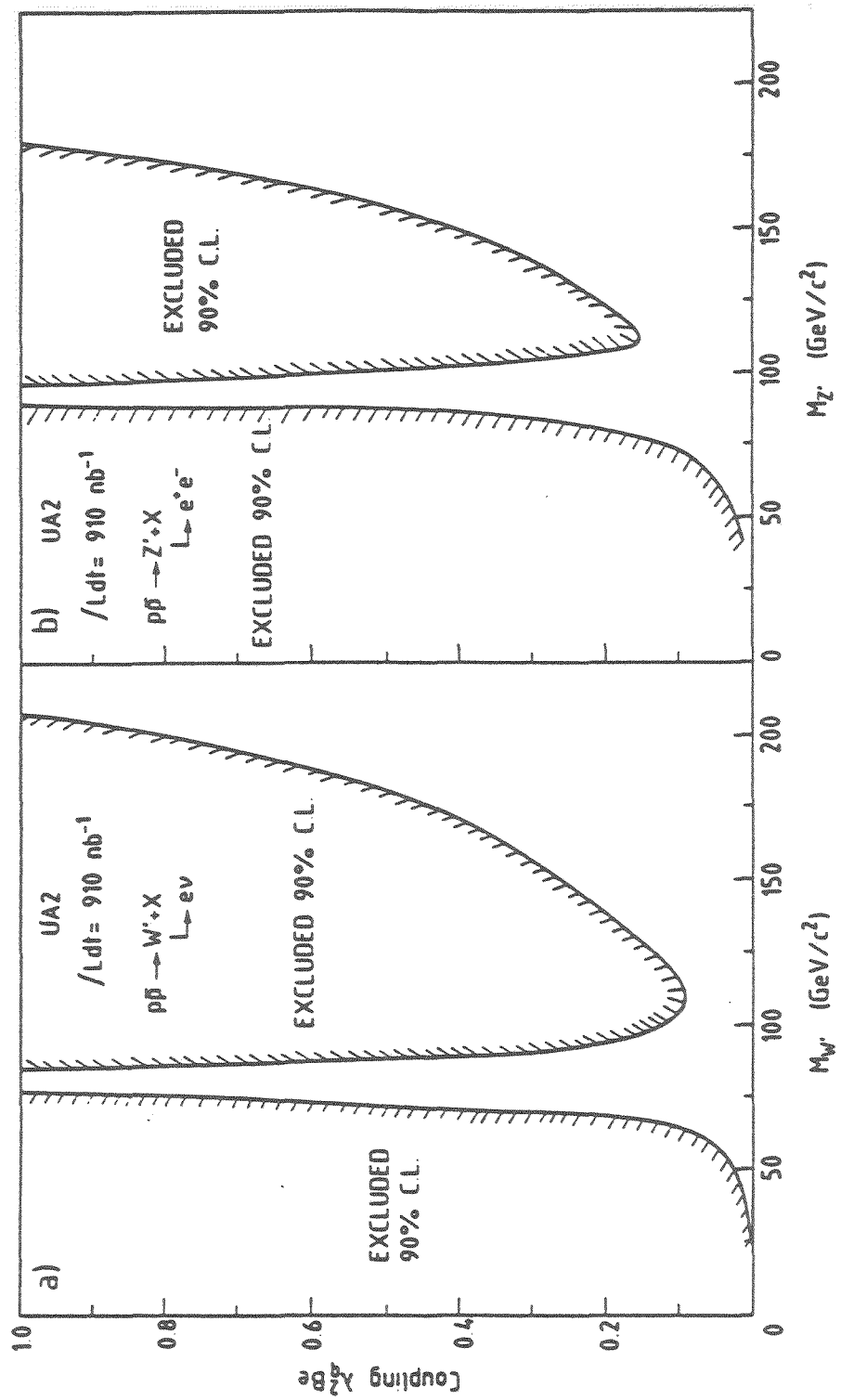
a)
UA2
/Ldt= 910 nb⁻¹
pp̄ → W'+X
L→ eν
EXCLUDED 90% C.L.
EXCLUDED
90% C.L.
b) UA2
/Ldt= 910 nb⁻¹
pp̄ → Z'+X
L→ e⁺e⁻
EXCLUDED 90% C.L.
EXCLUDED
90% C.L.
Coupling $\lambda_q^2 B_e$
$M_{W'}$ (GeV/c²)
$M_{Z'}$ (GeV/c²)
0
0.2
0.4
0.6
0.8
1.0
50
100
150
200

Figure 26

TEVATRON COLLIDER PHYSICS

by

E. Eichten

Fermi National Accelerator Laboratory
Batavia, Illinois 60510

Tevatron Collider Physics at High Luminosity

E. Eichten

$p\bar{p}$ $\sqrt{s} = 1.8 \rightarrow 2.0$ TeV $\int \mathcal{L}\, dt \geq 100\ pb^{-1}$

Goal - study physics in the few hundred GeV range

detailed study of b physics

4/5/89

Physics Opportunities - 1990's

Standard Model

- top
- Electroweak physics
- bottom physics
- Higgs

New Physics Reach

- 4th generation
- New Z° or Wt
- Supersymmetry

Foothills of the TeV Range

- Technicolor dynamics
- Compositeness

• Top

Present bounds:

$m_t < 60$ unlikely (assuming conventional decays) — CDF, UA2

Signatures $t\bar{t}$

$\mu^{\pm} e^{\mp} + X$ — clean 2% mode

$\underbrace{e^{\pm} + \nu}_{W^{\pm}} + X$ → two or more jets — 15% mode

Discovery limits: ($\mu^{\pm} e^{\mp}$ channel(s))

$5\ pb^{-1}$ $\quad \varepsilon_t \sim .15\ (\mu^{\pm} e^{\mp}) \rightarrow 2{,}000$ events

$m_t \approx 80$

$100\ pb^{-1}$ $\quad \varepsilon_t \sim .30\ (\mu^{\pm} e^{\mp}) \rightarrow 1000$ events

$m_t \approx 150$

Present theoretical upper bound

$m_t \lesssim 190$ GeV

Top production

[K. Ellis]

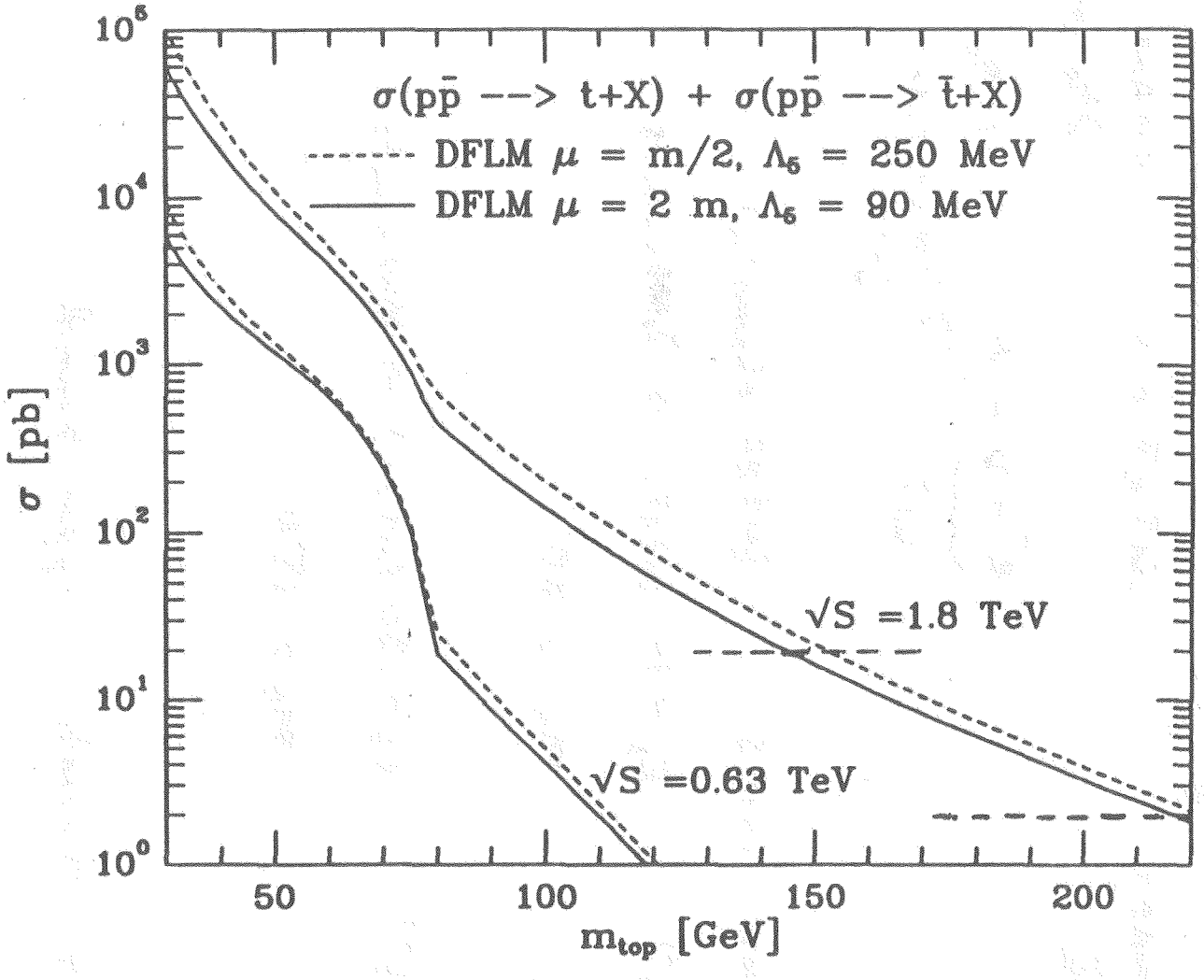

1000 $t\bar{t}$ pairs
$\int dt\, \mathcal{L} = 100\ pb^{-1}$

100 $t\bar{t}$ pairs
$\int dt\, \mathcal{L} = 100\ pb^{-1}$

Figure 8: The inclusive cross section for the production of a top quark as a function of the mass m.

W (Z^0) + jets: Mangano + Parke

2 jets: cuts

Jet: $|\eta| < 2.0$ $\Delta R > 0.7$

$p_T^J > 22$ GeV

W: charged lepton $p_T > 20$ GeV $|\eta| < 1.0$

missing " $p_T^\nu > 20$ GeV

Z: one charged lepton $p_T > 20$ GeV $|\eta| < 1.0$

other (~ unbiased) $p_T > 0.5$ GeV $|\eta| < 4.0$

Structure Functions EHLQ I

$$Q^2 = M_{JJ}^2$$

Polarization of $W^- \to e^- \nu$ decay taking into account

$W^{\pm}$ $e^{\pm}\nu + JJ$ Mangano + Panke

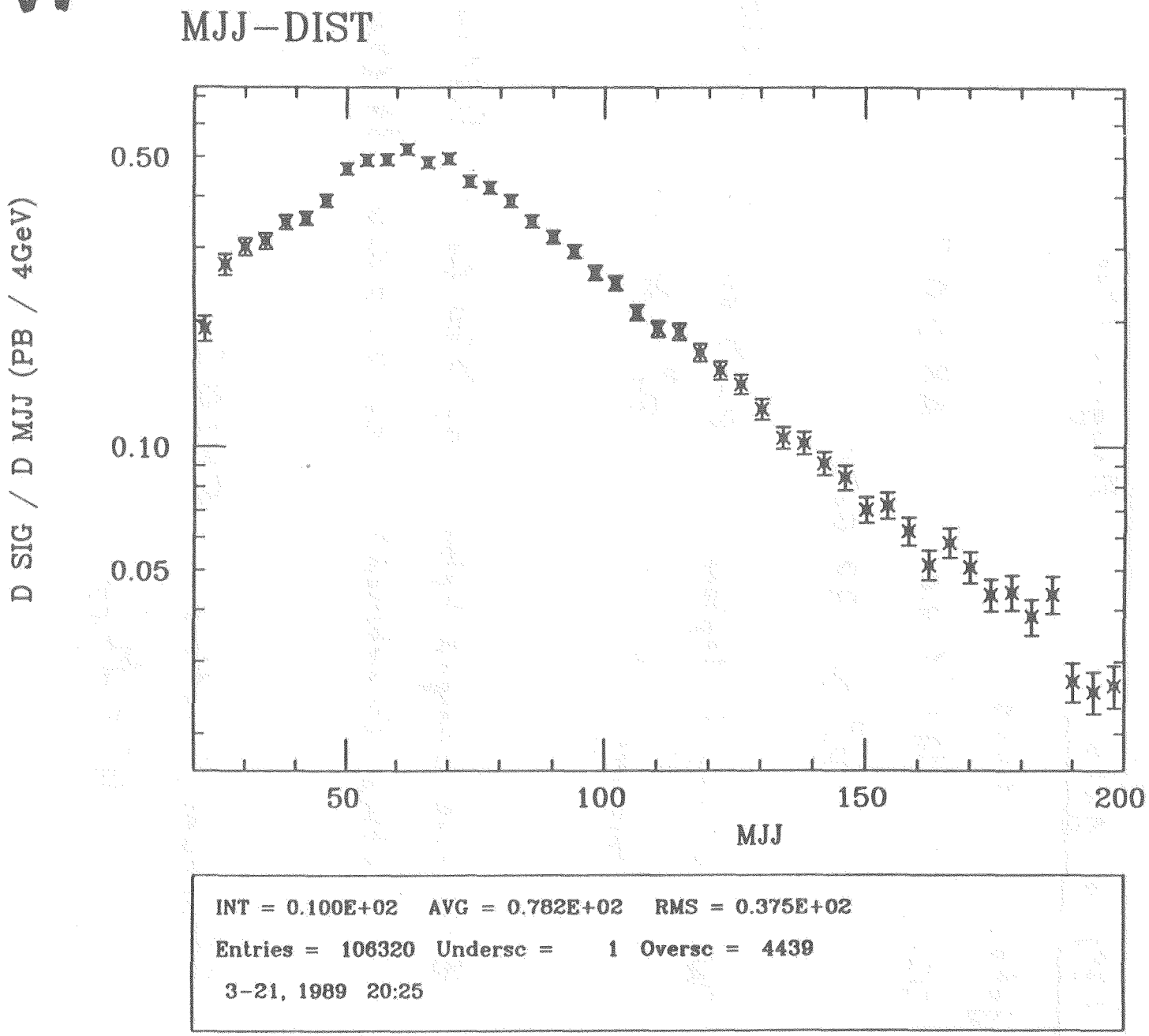

Z $e^+e^- \to JJ$ Mangano + Panke

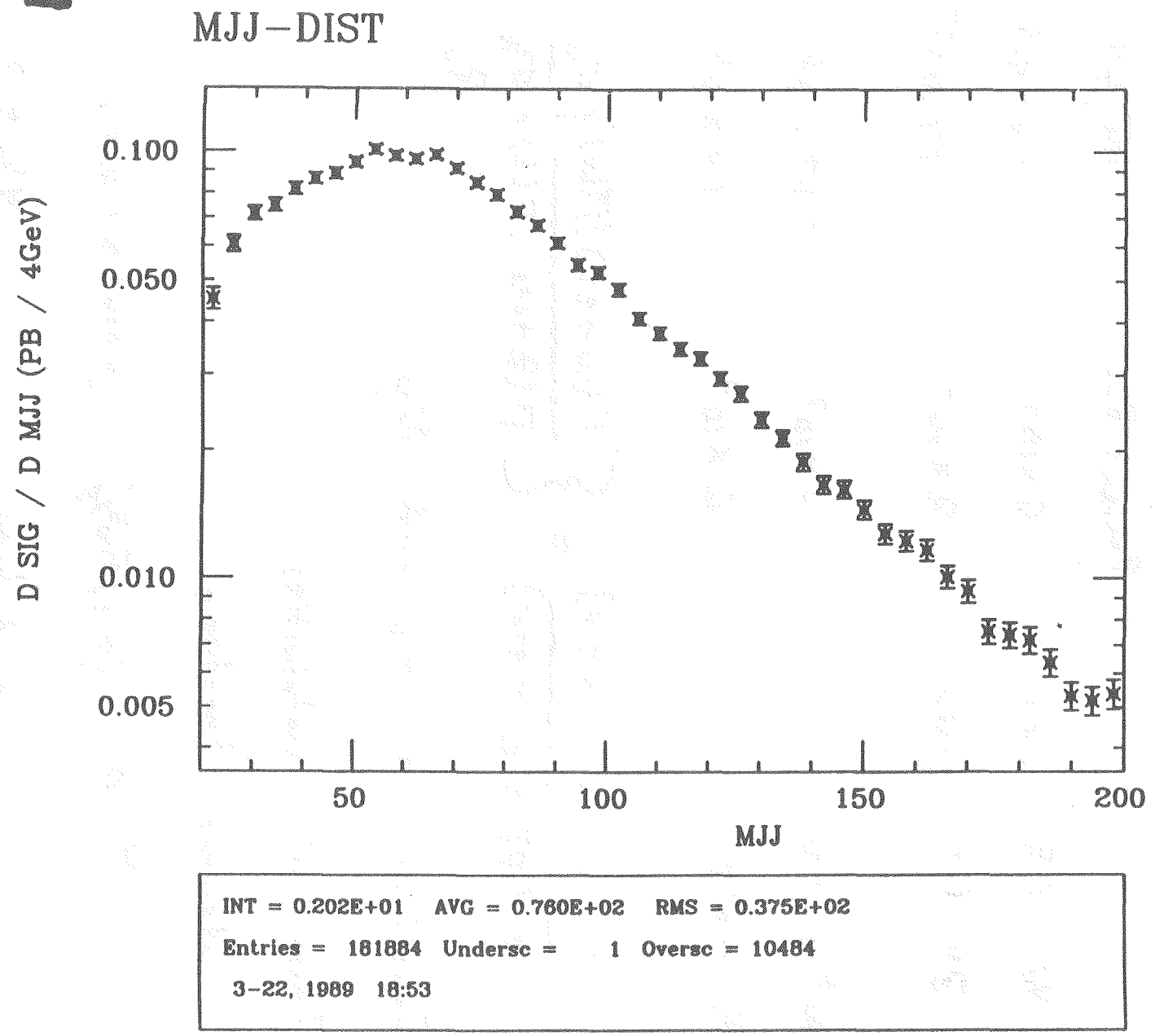

• Single Electroweak Boson Production

	Present Run	$100\ pb^{-1}$
$W^{\pm}$ (81 GeV)	6×10^4	1.2×10^6
Z^0 (92 GeV)	2×10^4	4.4×10^5
$W^+ \to e^+ \nu$	7×10^3	1.3×10^5
$Z^0 \to e^+ e^-$	6×10^2	1.2×10^4

$$R \equiv \frac{\sigma(p\bar{p} \to W \to e\nu)}{\sigma(p\bar{p} \to Z \to e^+e^-)} = \left\{ \frac{\Gamma(W \to e\nu)/\Gamma(W)}{\Gamma(Z \to e^+e^-)/\Gamma(Z)} \right\} \frac{\sigma_W}{\sigma_Z}$$

R_σ

Sensitive to m_t and N_ν

Theoretical uncertainties

Structure Functions

- $\partial u/\partial v \,|_{x \simeq \sqrt{m_W^2/s}}$ $\quad (0.016 < x < 0.12)$
- charm contributions $\quad 4\% \pm ?$

[Martin, Roberts, Stirling]

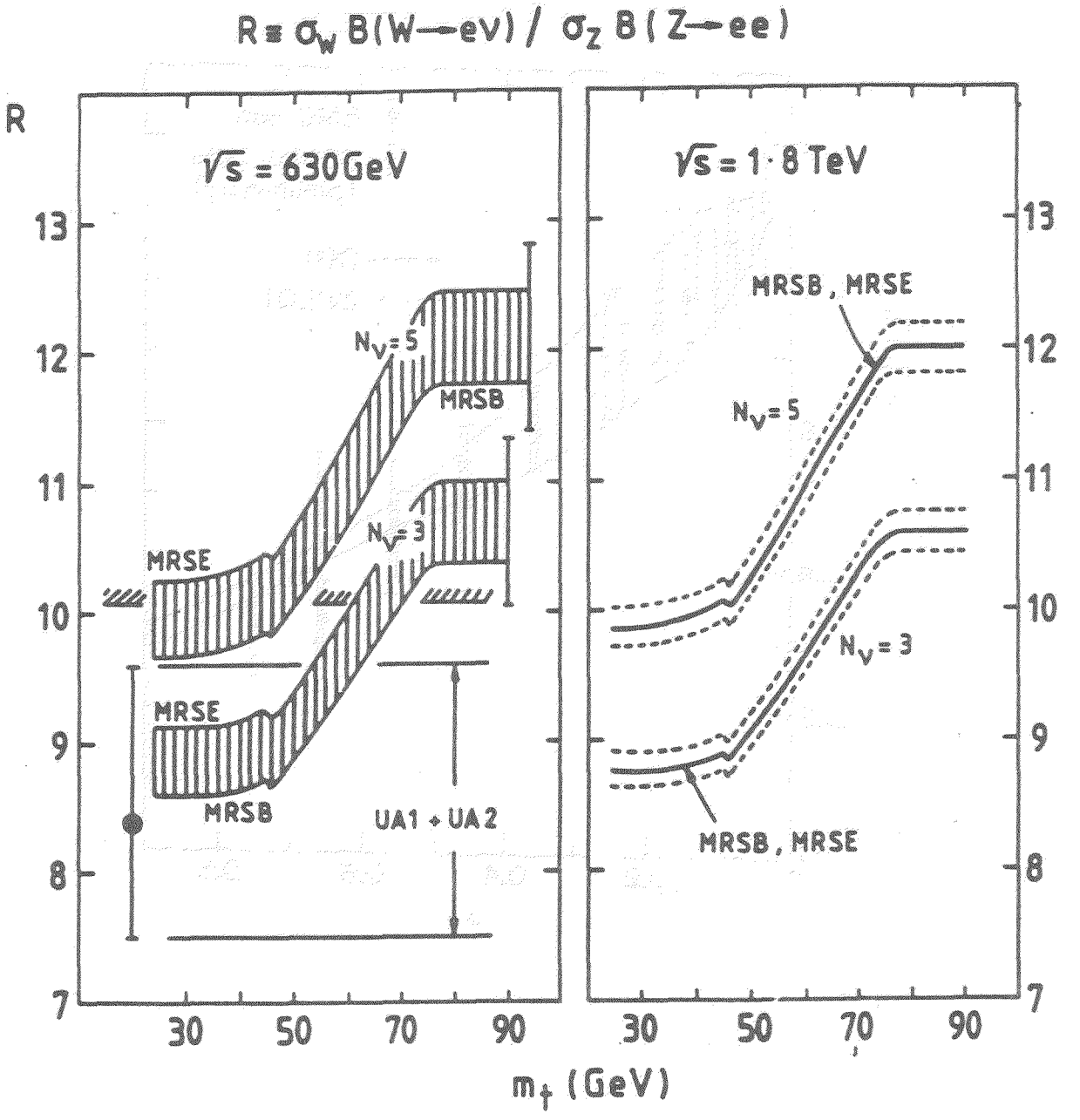

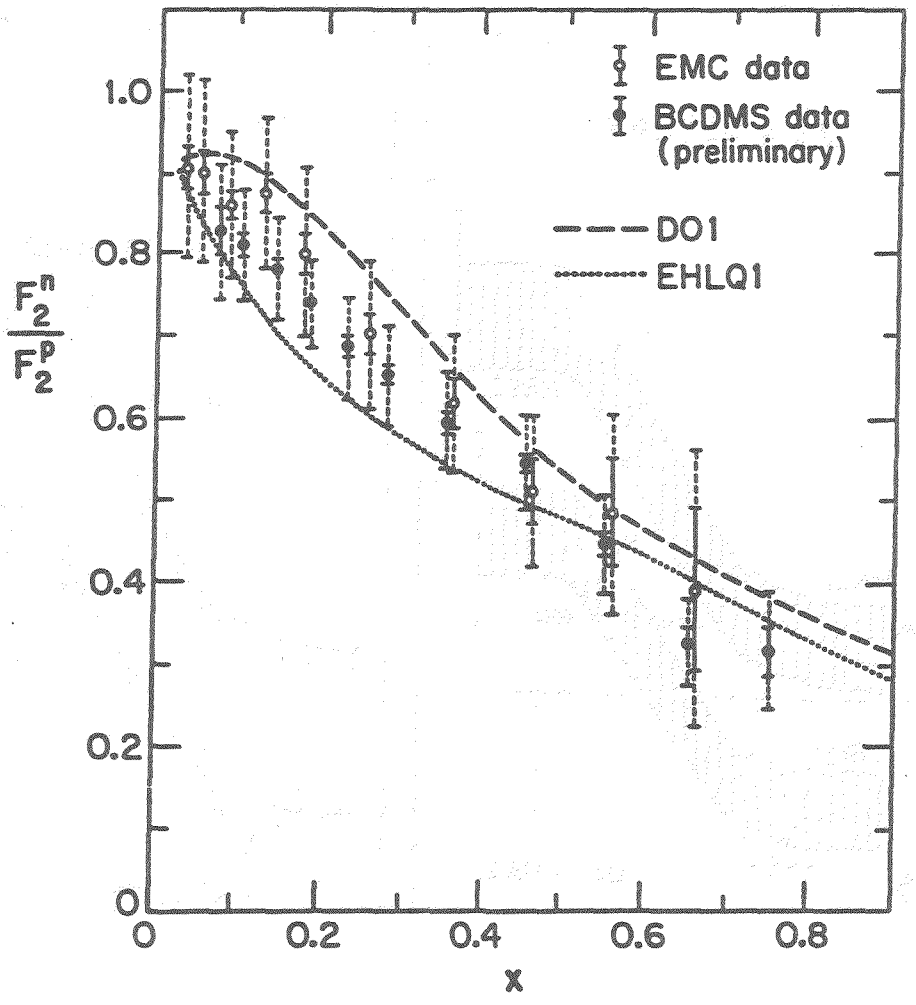
EMC data
BCDMS data
(preliminary)
DO1
EHLQ1
$\frac{F_2^n}{F_2^p}$
1.0
0.8
0.6
0.4
0.2
0
0
0.2
0.4
0.6
0.8
x

Improvements

- Measure asymmetry [Berger et. al.]

$$A(y) = \frac{\sigma(y) - \sigma(-y)}{\sigma(y) + \sigma(-y)}$$

$$\sigma(y) \equiv \frac{d\sigma}{dy}(p\bar{p} \to W^+ X)$$

- Measure the charm content of the proton more accurately

What is present uncertainty?

Can one measure

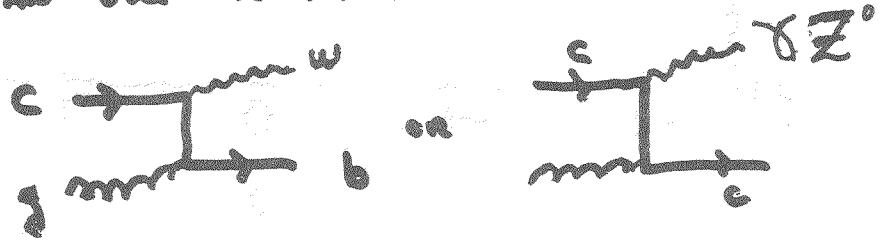

Reasonable goal: $\Delta R_c / R_c \leq 1\%$ at Tevatron energies

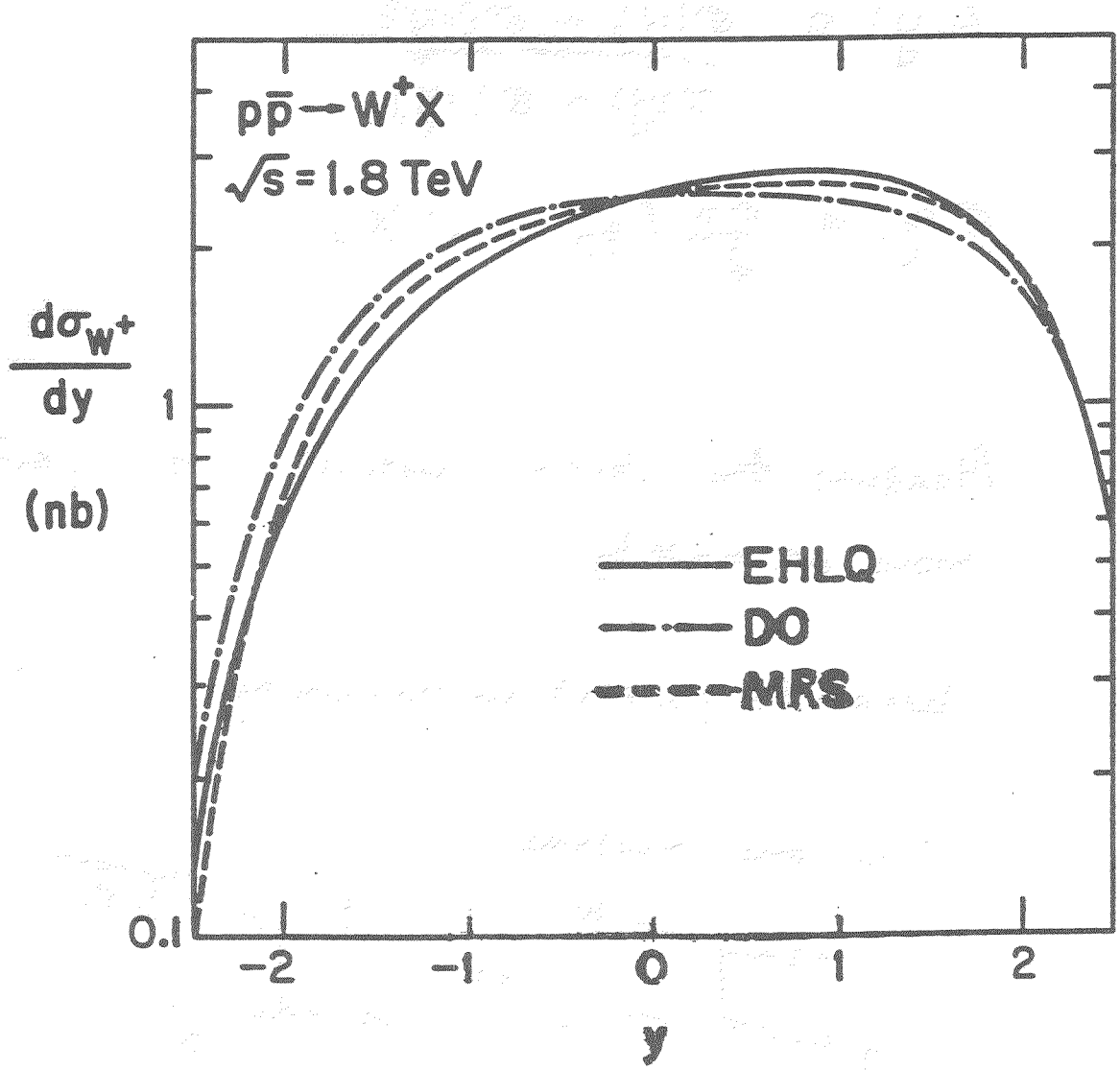
$p\bar{p} \to W^+X$
$\sqrt{s} = 1.8$ TeV
$\frac{d\sigma_{W^+}}{dy}$ (nb)
1
0.1
EHLQ
DO
MRS
−2
−1
0
1
2
y

Even if SLC / LEP measure N_ν first still useful.

- $t \to H^+ + b$

Charged Higgs in non-minimal models

Natural (a) Minimal supersymmetric models

(b) Technicolor models

$m_t < m_W \Rightarrow$ principal decay mode difficult to see top by usual methods.

$m_t > m_W$ coupling $\underbrace{\frac{g}{2\sqrt{2}\, m_W}}_{1/2v} m_t (1+\gamma_5) A$ ← order 1

$$\frac{\Gamma(t \to H^+ + b)}{\Gamma(t \to W^+ + b)} = \frac{p_{H^+}}{p_{W^+}} \frac{m_t^2 (m_t^2 - m_{H^+}^2)\ |A|^2}{(m_t^2 + 2m_W^2)\,(m_t^2 - m_W^2)}$$

generally important

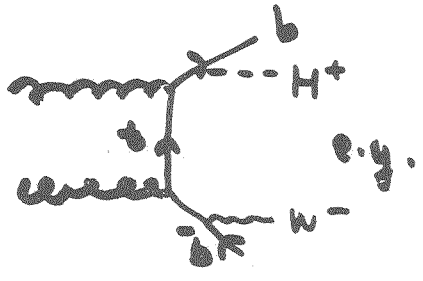

- Second important measurement for single EW boson production

$$\sin^2\theta_W \equiv 1 - M_W^2/M_Z^2$$

$$= \frac{1}{2}\left\{1 - \left[1 - \frac{1}{1-\Delta R}\left[\frac{74.562\ \text{GeV}}{M_Z}\right]^2\right]^{1/2}\right\}$$

Marciano + Sirlin PR D22, 2695 (1980).

m_t (GeV)	ΔR	$\sin^2\theta_W$
45	0.0713 ± 0.0013	0.230 ± 0.0007
90	0.0606	0.226
120	0.0512	0.223
150	0.0417	0.219
180	0.0300	0.216
210	0.0173	0.212

$M_Z = (92.0 \pm 0.1)$ GeV

LEP

$m_H = 100$ GeV

	ΔR
10	-0.0045
1000	+0.0090

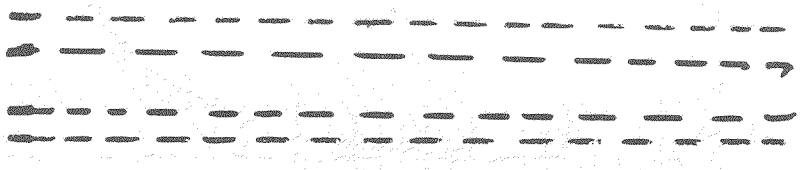

total error
mw/m2
± 1%
± .5%

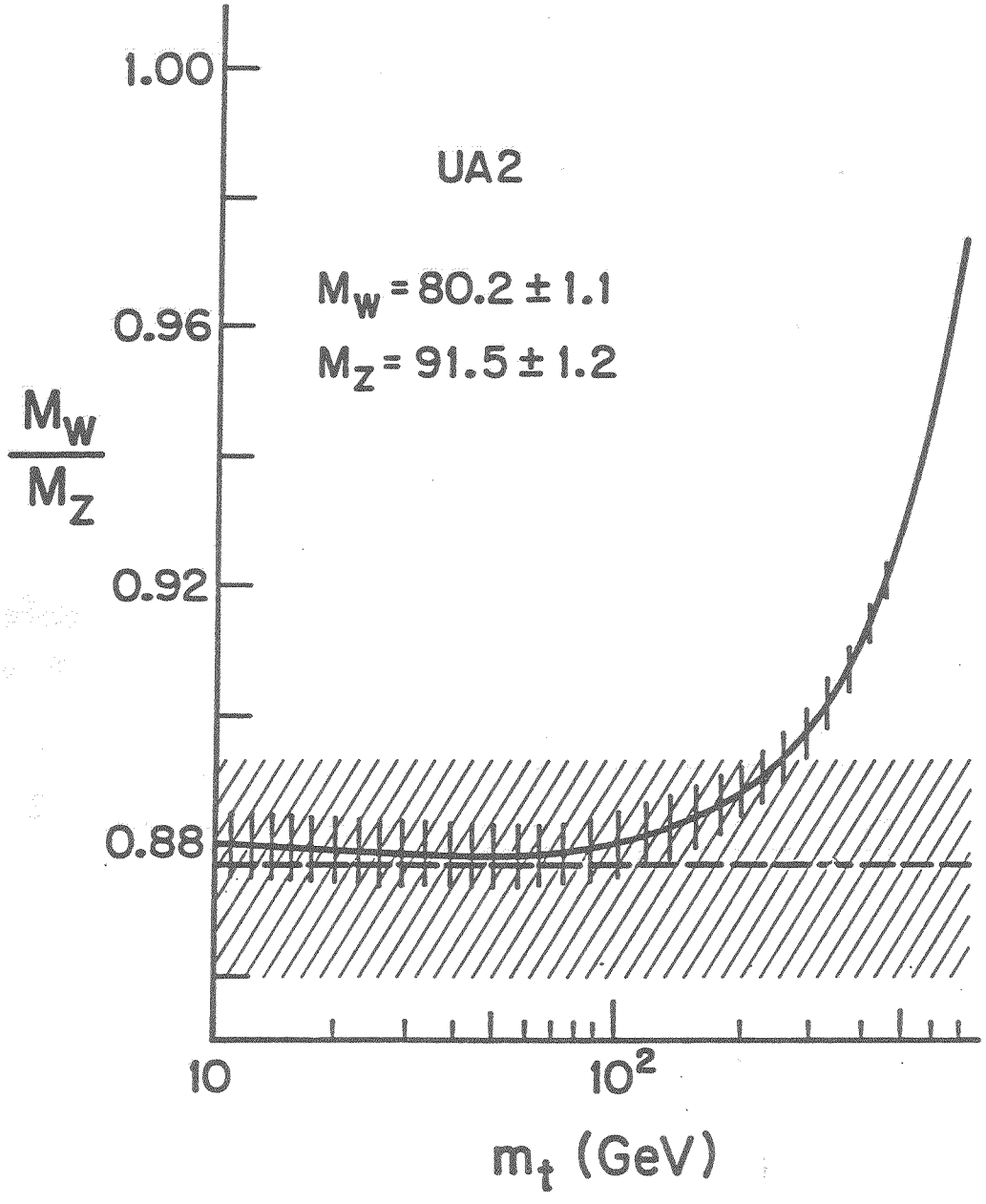

Fig. 1. Relation between M_W/M_Z and m_t from Eq. (2) for $M_Z = 91.5$ GeV (solid line). The errors reflect the measurement errors on M_Z. The dashed line is the UA2 result for M_W/M_Z and is compatible with the predicted value for $m_t \lesssim 300$ GeV.

Dependence on m_{Higgs}

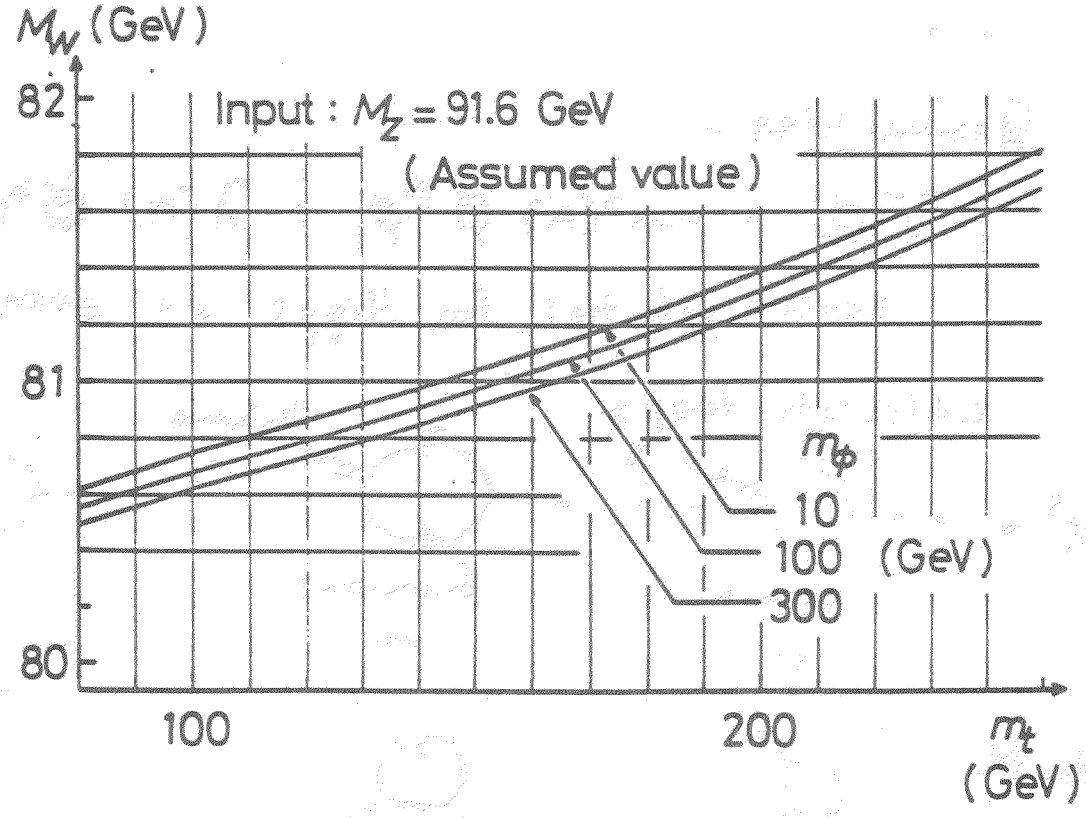

Fig. 2. An illustration of the m_ϕ dependence of the M_W–m_t plot for an assumed value M_Z = 91.6 GeV.

· Theoretical Speculations about Heavy Top

many theoretical ideas

$m_t \approx 70$ GeV		Veltman	Act. Physics Pol. B12, 437 (81)
$m_t \approx 100$ GeV	$m_H \approx 2m_t$	Nambu	EFI 89-08

...

General idea -

$$V(\phi) = -\mu^2(M)\,\phi^*\phi + \lambda(M)\,(\phi^*\phi)^2$$

scalar potential for Higgs at energy scale M

Calculate loops

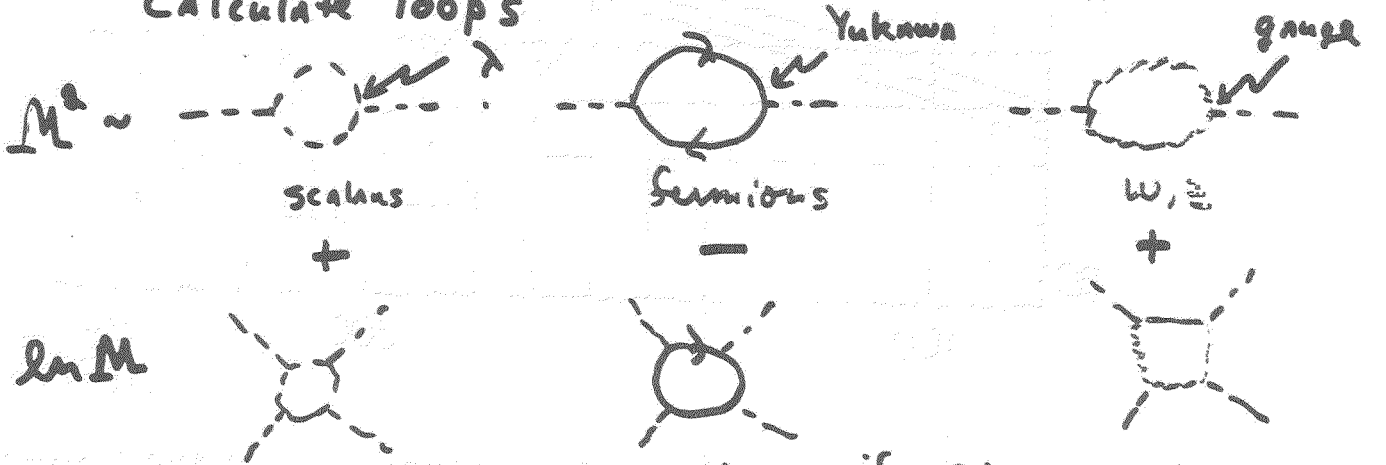

bad - would like to cancel: if as: M increases $\lambda(M)$ changes sign

then: the potential becomes unstable

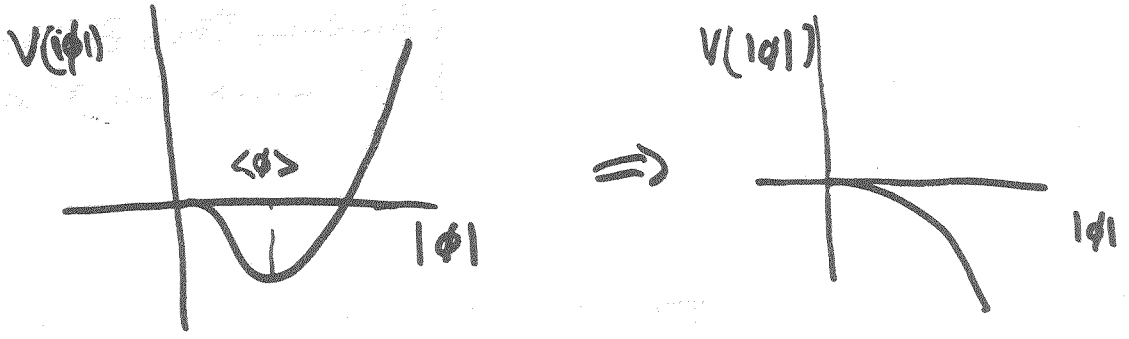

$$\lambda(M) = \lambda(v) + B \ln(M/v) \qquad v = 126\ \text{GeV}$$

EW $\langle\phi\rangle$

$$v^4 B \approx (2m_W^4 + m_Z^4) - 4\sum_f m_f^4 + m_H^4$$

$B < 0$ is A unstable potential at some scale $M > v$.

Careful analysis - Lindner, Sher, Zaglauer
Fermilab-Pub 88/206T

$\Rightarrow$ lower bound on Higgs mass for $m_t > 86$ GeV. (Fig)

[Lindner, Shen, Zaglauer
Fermilab-Pub 88/207T]

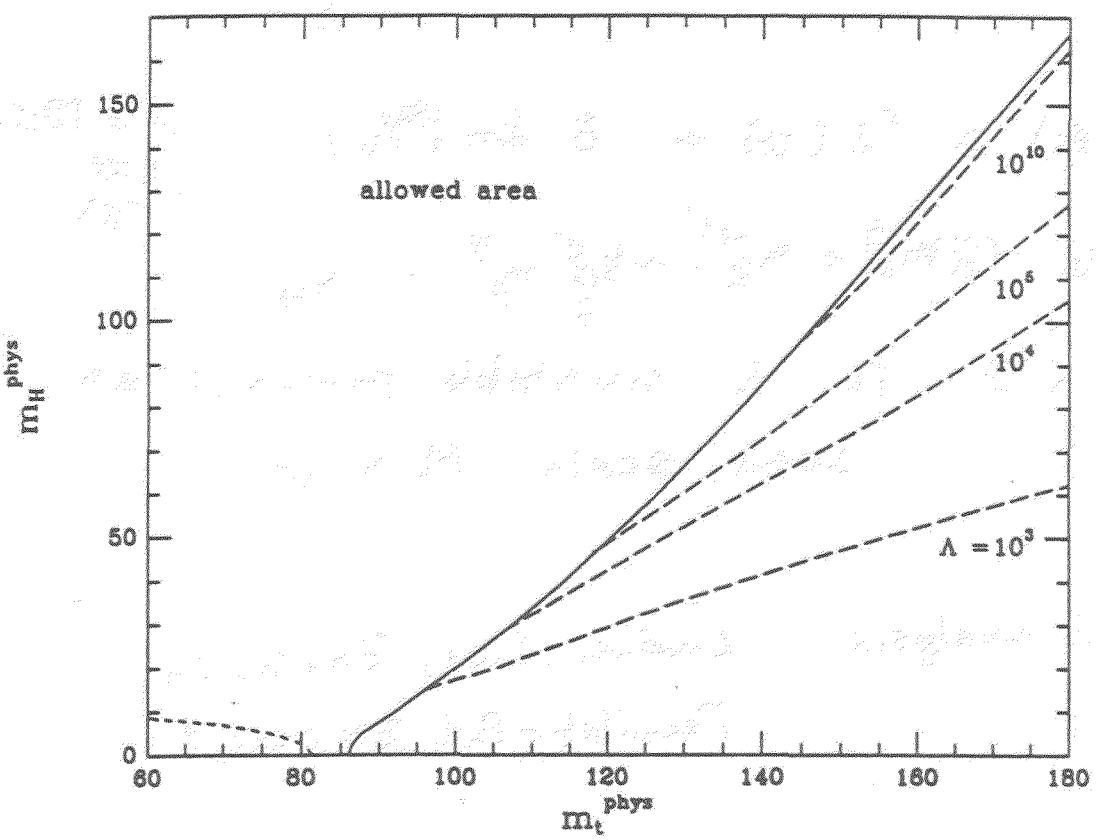

Fig. 1: The vacuum stability bounds at the two loop level with one loop boundary conditions for different cutoffs. The solid line is for $\Lambda = 10^{15}$ GeV and the dashed lines represent lower cutoffs. Systematic uncertainties are smaller than 1 GeV. The dominant uncertainty is the current knowledge of α_s (see text). The lower bound for smaller top quark masses (the "Linde-Weinberg" bound; see ref. 8) is also shown as a dotted line.

• Bottom

To study b physics need large rates

- mixing $\frac{\sigma(\mu^+\mu^+) + \sigma(\mu^-\mu^-)}{2\,\sigma(\mu^+\mu^-)}$
- Rare decays $B_d \to \psi K_{short}$ $B \to K_{short} e^+e^-$
- CP violation

Benchmark - CESR has achieved $\mathcal{L} = 10^{33}\ cm^{-2} sec^{-1}$ at $\Upsilon(5S)$

before 1995 $10^6\ b\bar{b}$/yr

after upgrade $10^7\ b\bar{b}$/yr

B_s, Λ_b - Z^0 decays, fixed target

For hadron colliders to be competitive in the long run need

$$\gtrsim 10^8\ b\bar{b}\ /\text{year}$$

Production rates in $p\bar{p}$ collider

- Large $O(\alpha_s^3)$ contributions
- Sensitive to gluon structure functions at small x

$100\ pb^{-1}$ $\sqrt{s} = 2\,TeV$ $p\bar{p}$ $\Rightarrow$ $\sim 10^{10}\ b\bar{b}$/run

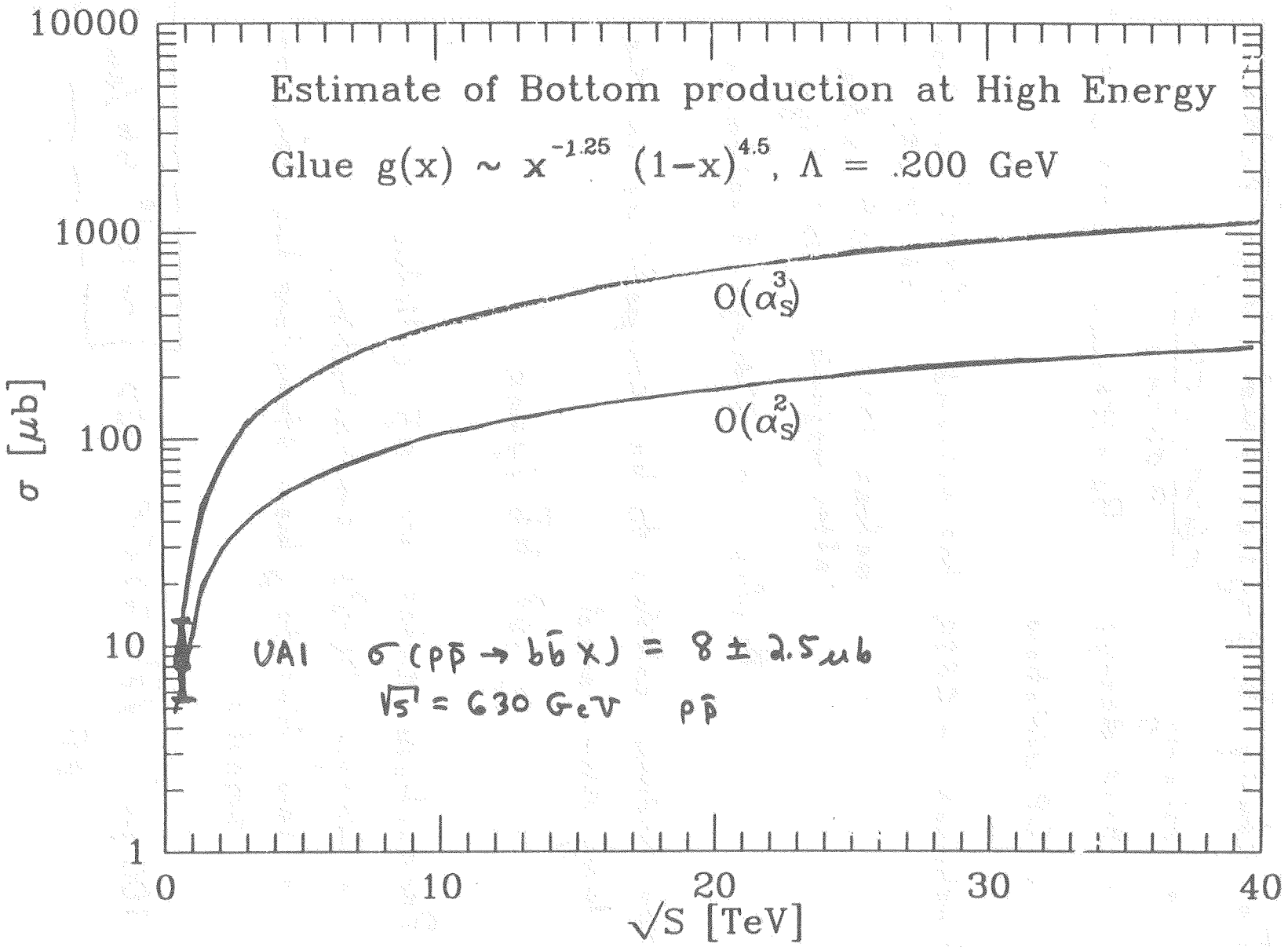
Estimate of Bottom production at High Energy
Glue g(x) ~ x^-1.25 (1-x)^4.5, Λ = .200 GeV
O(α_s^3)
O(α_s^2)
UA1 σ(pp̄ → bb̄X) = 8 ± 2.5 μb
√S = 630 GeV pp̄
σ [μb]
√S [TeV]
10000
1000
100
10
1
0
10
20
30
40

[K. Ellis]

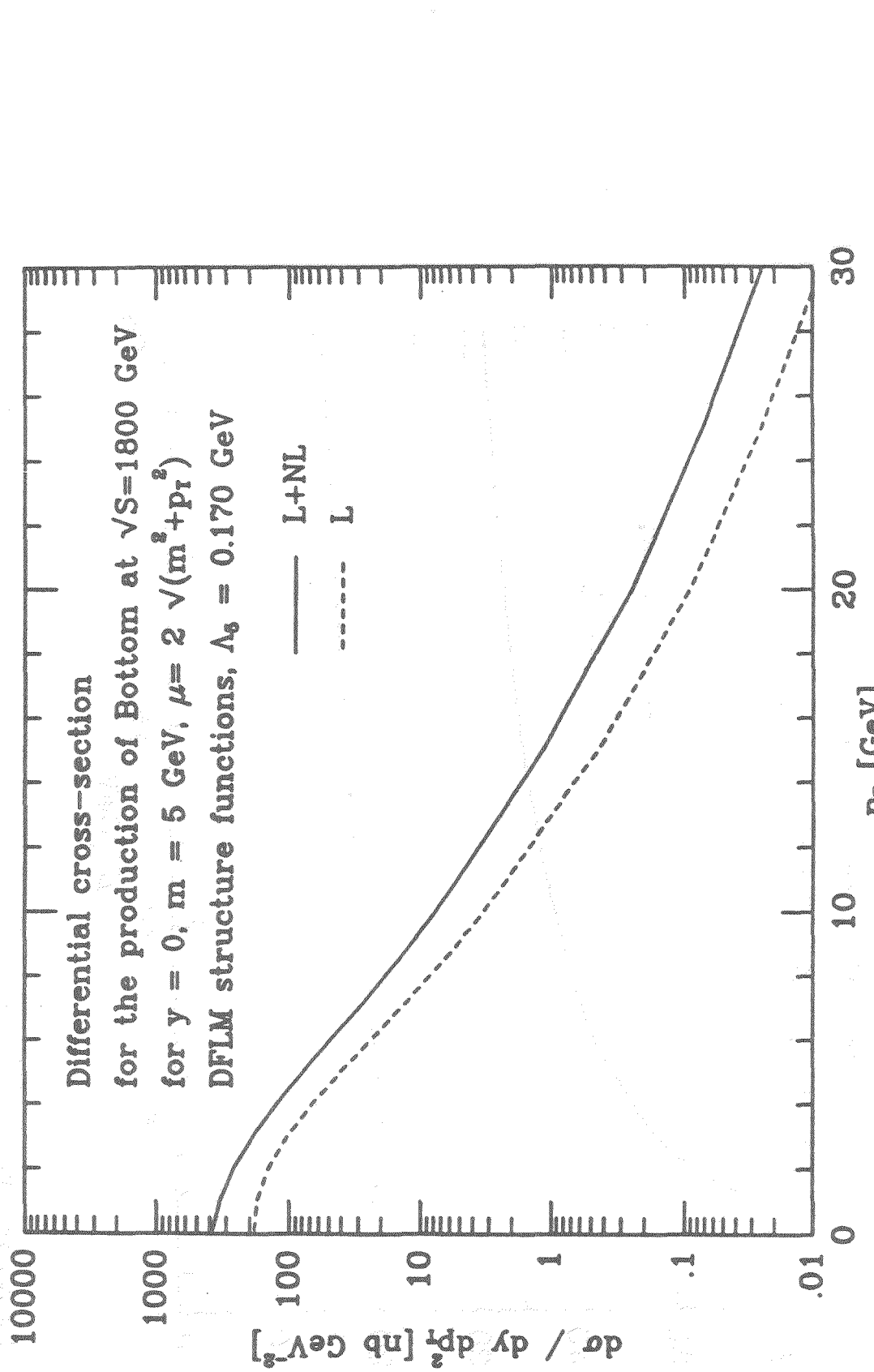

Figure 11: Leading and non-leading contributions to bottom quark production.

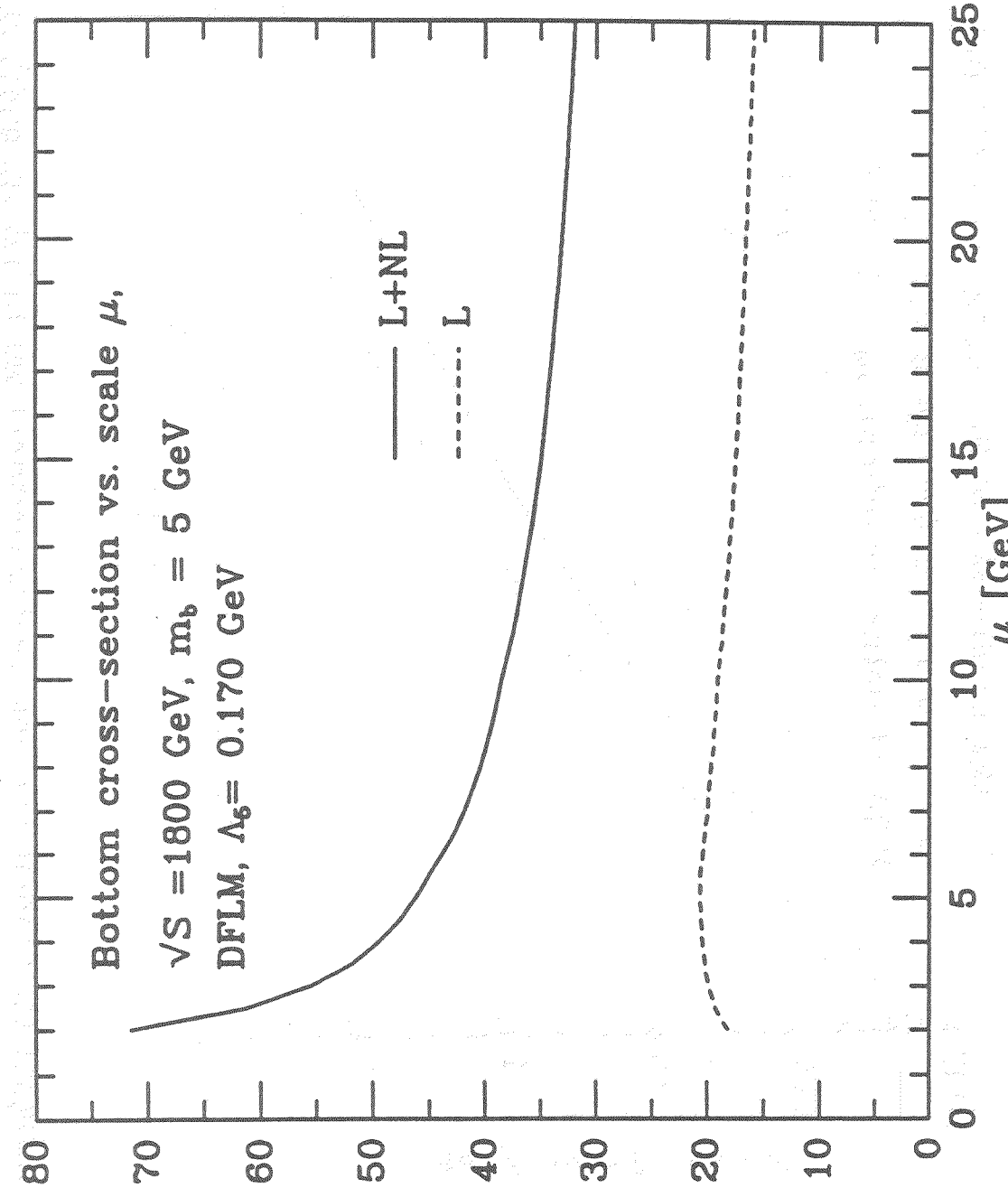

Figure 10: The total bottom quark cross section vs. μ at $\sqrt{S} = 1.8$ TeV.

Initial goals

- Map out production dynamics of $b\bar{b}$ production
- Identify reconstructable final states for B_d and B_s mesons
- Look for secondary vertices: $b \to c \to s$
- Study mixing in same/opposite sign dimuons. Impact parameter dependence of ratio might be studied with good vertex detector.
- Rare decays

TeV $\Rightarrow$ SSC

10× RATE~6

20× Luminosity

• Electroweak Gauge Boson Pairs

Pair production rates:

	Present num	$\sqrt{s} = 2.0$ TeV, 100 pb^{-1}
W^+W^-	32	750
$W^\pm Z^0$	8	180
$Z^0 Z^0$	4	90
$W^\pm \gamma$ ($E_T^\gamma > 10$ GeV)	75	1640

Events / num

NO leptonic decays – QCD backgrounds

one leptonic decay – $W(Z) + 2J$

two leptonic decays – $W^+W^- \to e^+\mu^- + X$

~ 15 events produced

(Compare $t\bar{t}$ at $m_{top} \sim 150$ GeV

$W^\pm\gamma$ looks ok – can bound anomalous magnetic moment of $W^\pm$

Might look for large resonances in $W^\pm W^-$ or $W^\pm Z^0$ channels.

W^+W^- pair production

$|y| < 1$

$\sqrt{s} = 1.8$ TeV

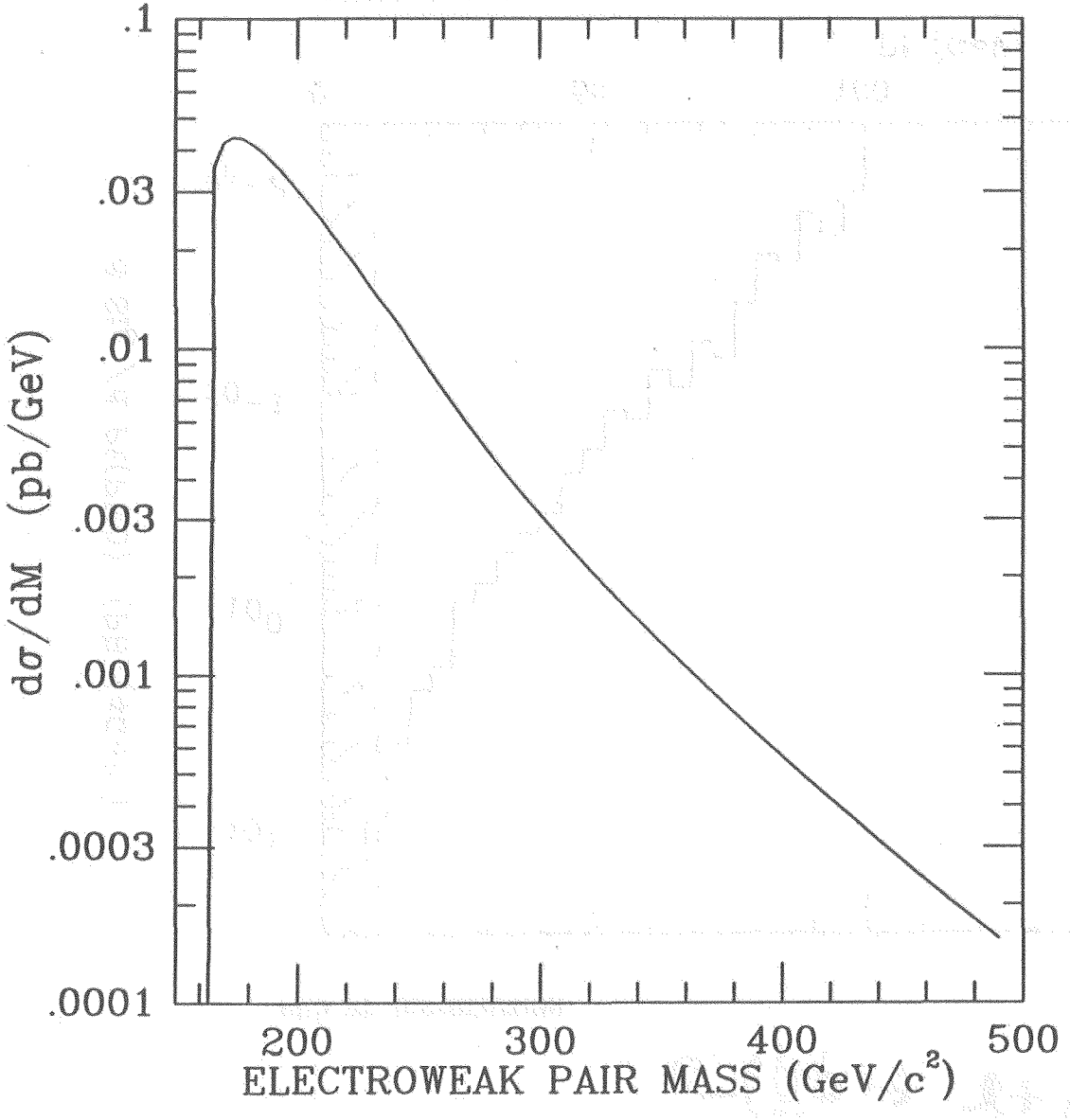

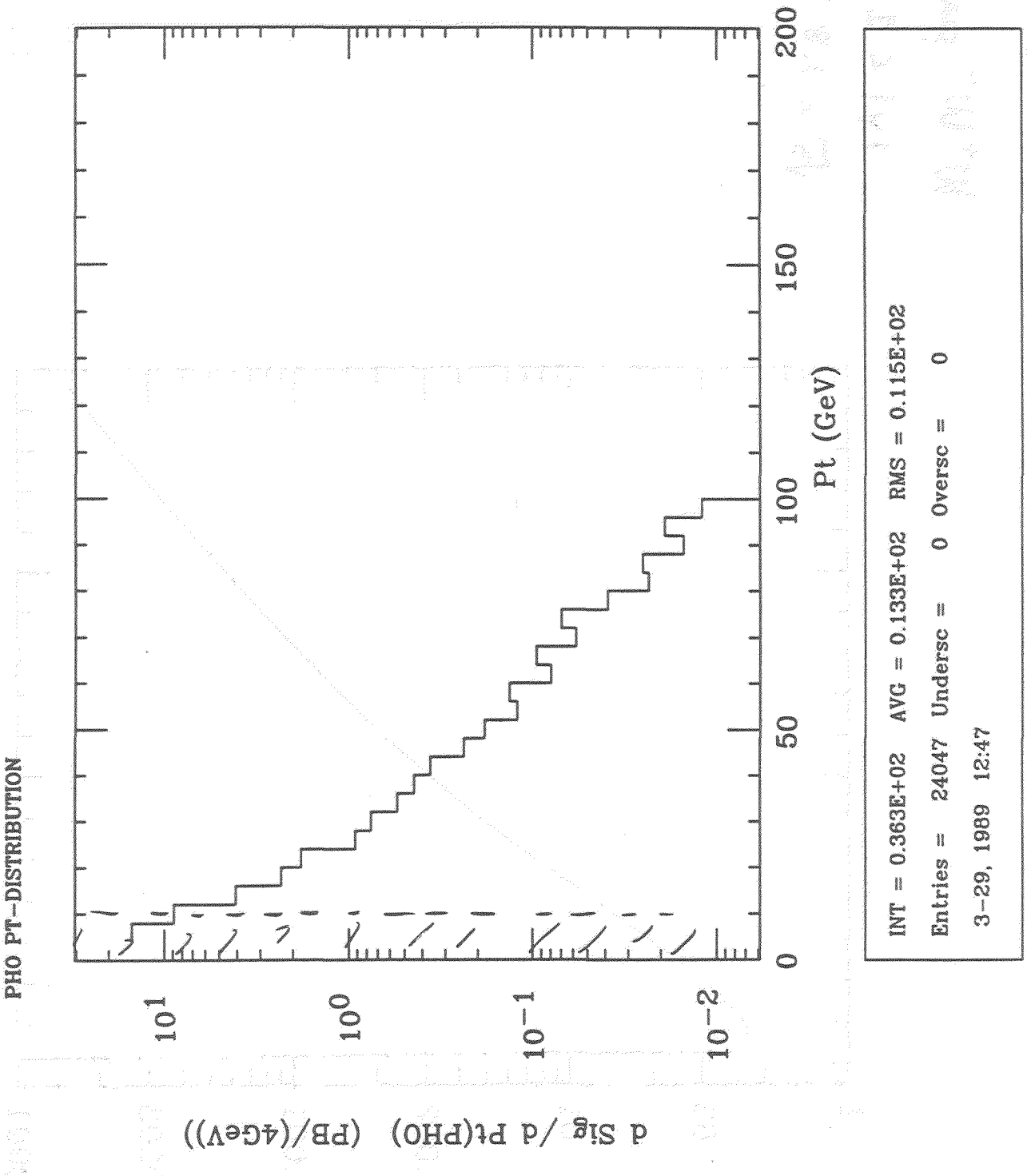
σ(p̄p → γ± W±+X)
PH0 PT-DISTRIBUTION
d Sig /d Pt(PH0) (PB/(4GeV))
Pt (GeV)
INT = 0.363E+02 AVG = 0.133E+02 RMS = 0.115E+02
Entries = 24047 Undersc = 0 Oversc = 0
3-29, 1989 12:47

$W^+ \to$	$c\bar{s}$	34%
	$e^+\nu$	11%
	$\mu^+\nu$	11%
	$\tau^+\nu$	11%

$W^+ \to c\bar{s}, e^+\nu, \mu^+\nu$ 56%

$Z^0 \to$	$b\bar{b}$	15.4%
	$c\bar{c}$	12.0%
	e^+e^-	3.4%
	$\mu^+\mu^-$	"
	$\tau^+\tau^-$	"

$Z^0 \to b\bar{b}, c\bar{c}, e^+e^-, \mu^+\mu^-$ 34%

$m_t \geq m_W$

$\sin^2\theta_W = .23$ $\frac{\alpha_s}{\pi} = 0.04$

Enhanced ability to study electroweak physic if (b, c) can be detected with reasonable efficiency.

New Physics

- 4th generation

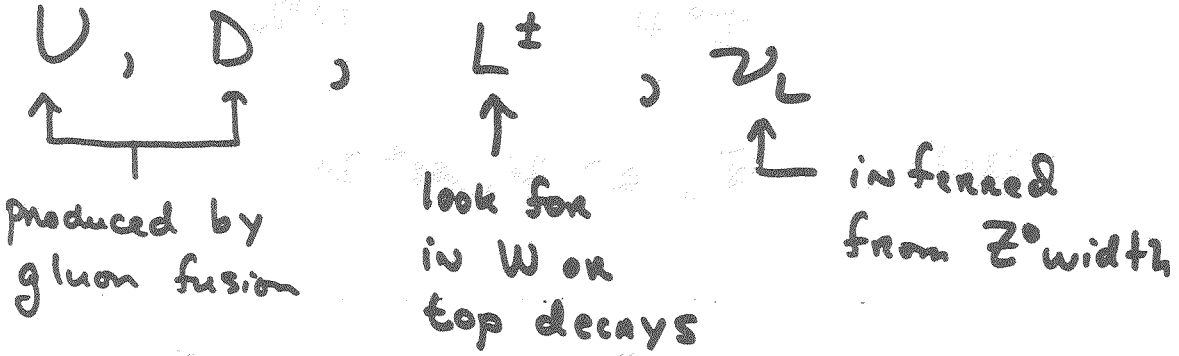

- Extending the Gauge Group

  Z'^0 or $W'^{\pm}$

  Similar couplings to usual Z^0 or $W^{\pm}$

  $\Rightarrow$ discovery limit $\approx$ 730 GeV

  $100\ pb^{-1}$ (100 produced events)

- Supersymmetry

  $\tilde{g}$ or $\tilde{q}$

$1\ pb^{-1}$	120 GeV
$100\ pb^{-1}$	210 GeV
$\int dt\, \mathcal{L}$	$m_{\tilde{g}}$ or $m_{\tilde{q}}$ discovery limit

New generation - QUARK

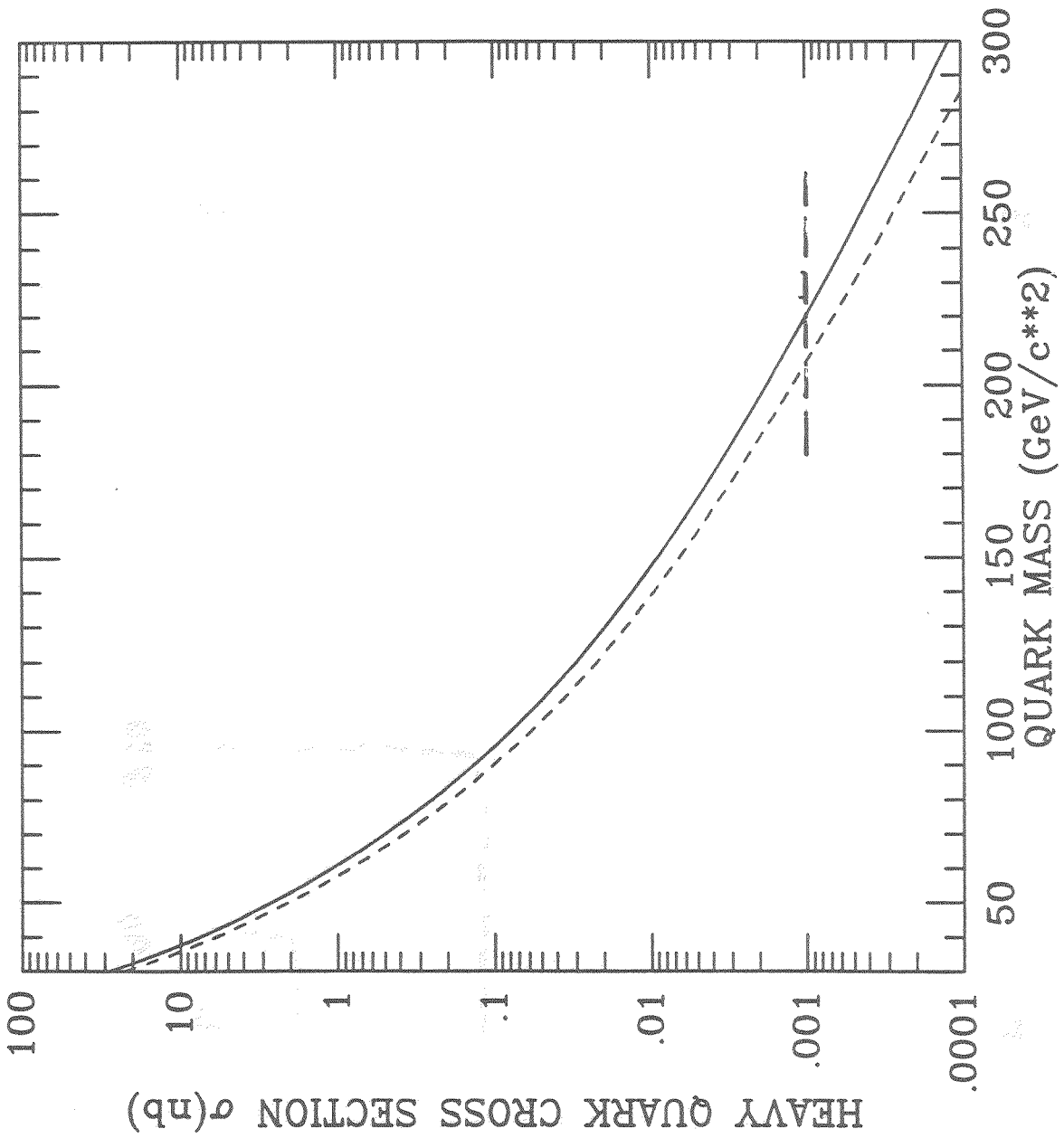

100 pF
250
90

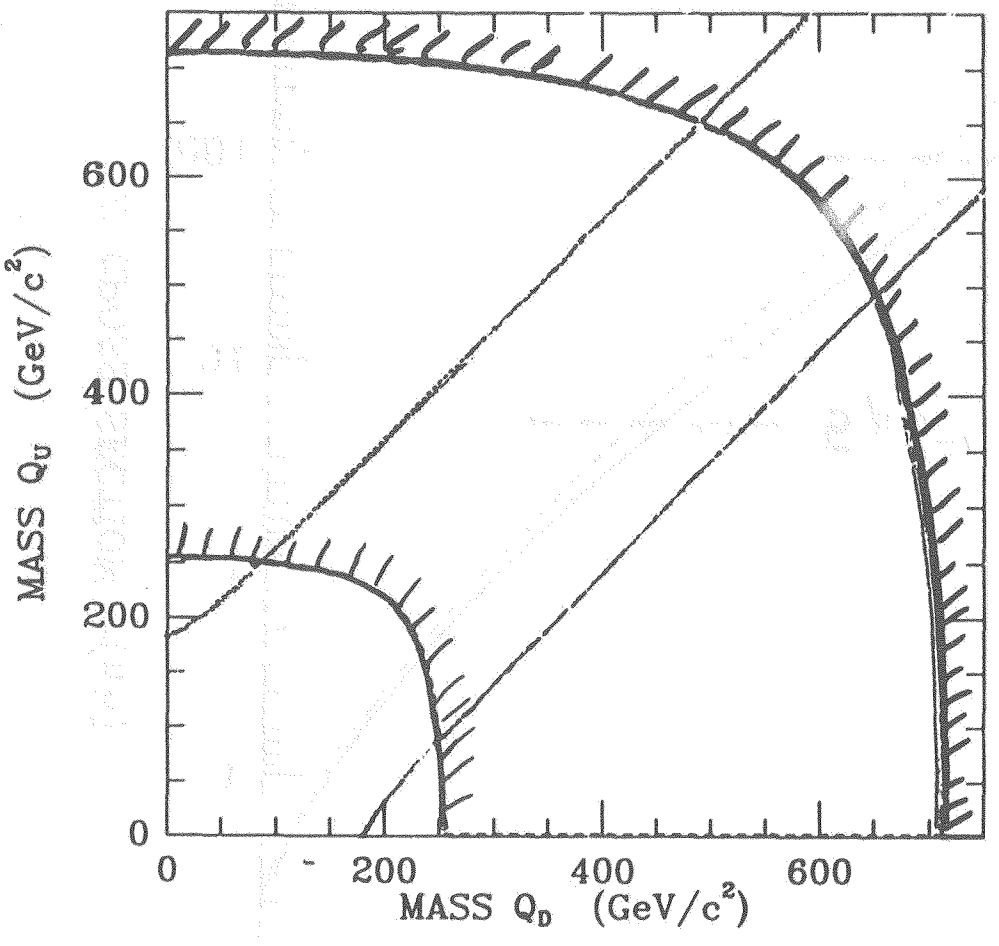

— perturbative unitarity bound

— bound from 18-11

— RG analysis [Assuming a desert to the GUTS scale]

New Z^0 production

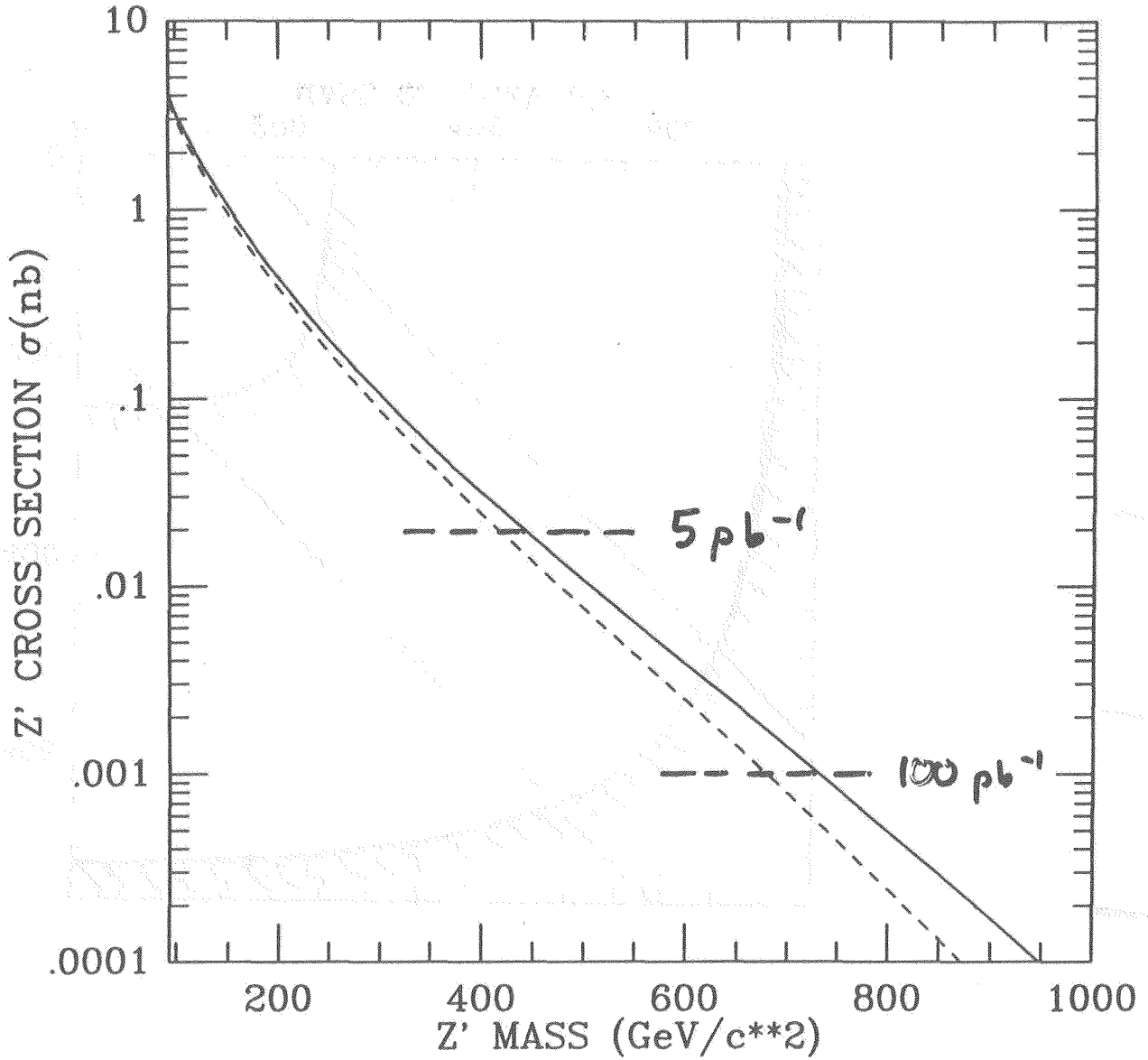

$\sqrt{s}$ = 1.8 - - -

2.0 ———

pp

100 produced events

Gluino Production

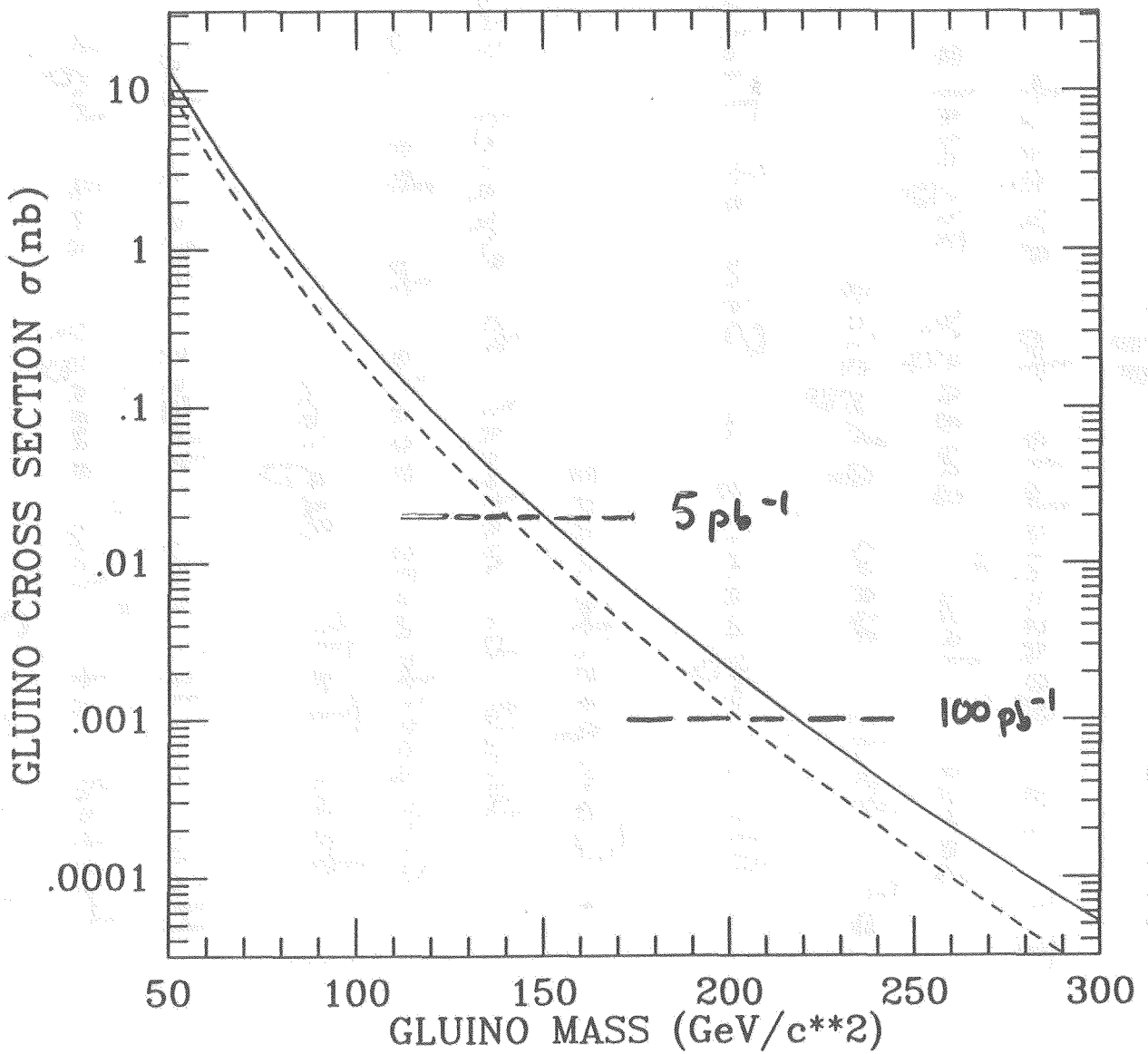

$\sqrt{s}$ = 1.8 - - -

2.0 ———

$p\bar{p}$

100 events produced

Foothills of the TeV Range

If there is a new strong dynamics at the TeV scale which replaces the standard Higgs

It is reasonable to expect some "low" energy signals of this new physics

- New dynamics - Son of Technicolor

- Compositeness

  Would be natural to expect the compositeness scale to be in the few TeV Region

How well can these ideas be tested at "low" energy and high luminosity?

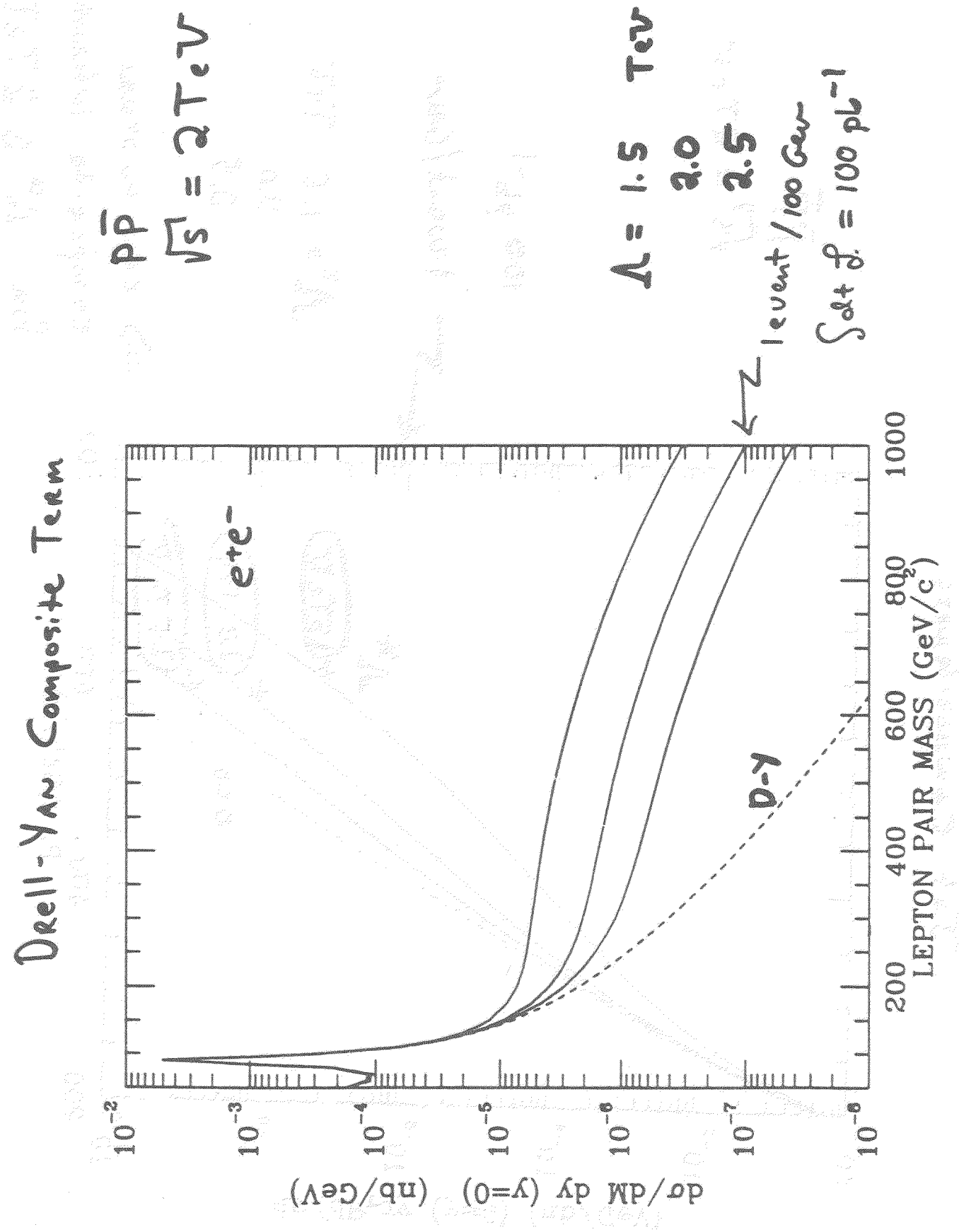
Drell-Yan Composite Term
$p\bar{p}$ $\sqrt{s}$ = 2 TeV
Λ = 1.5 TeV
2.0
2.5
1 event / 100 GeV
$\int$ dt = 100 pb^{-1}
e$^+$e$^-$
D-Y
$d\sigma/dM\,dy$ (y=0) (nb/GeV)
LEPTON PAIR MASS (GeV/c^2)
200
400
600
800
1000
10^{-2}
10^{-3}
10^{-4}
10^{-5}
10^{-6}
10^{-7}
10^{-8}

Jet Compositeness

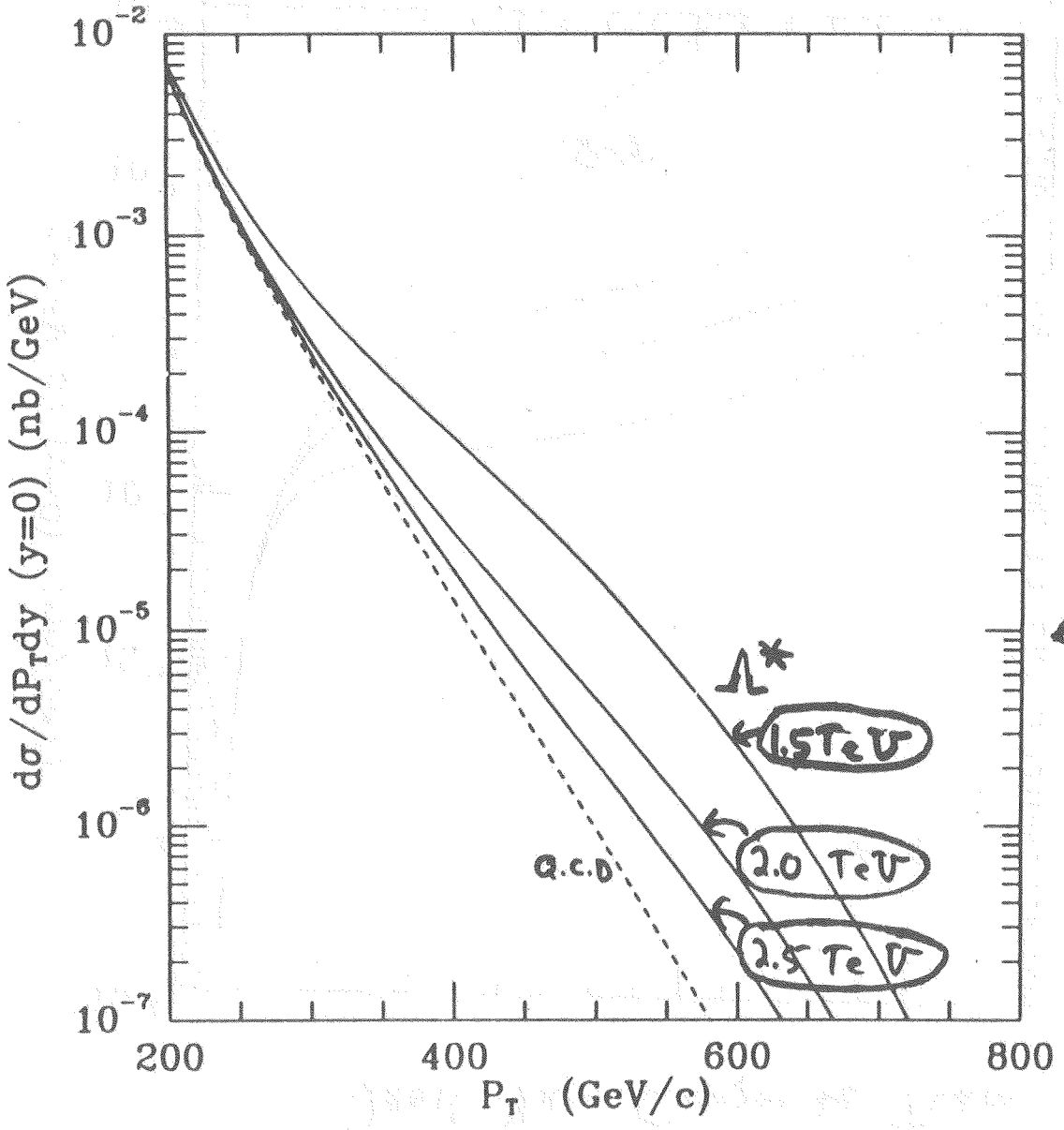

$p\bar{p}$

$\sqrt{s} = 2\,TeV$

$100\ pb^{-1}$

← 1 event/GeV

$\Lambda^* =$ 1.5 TeV
2.0
2.5

⇒ can measure composite interaction for $\Lambda^* \lesssim 2\,TeV$

Two Scale Technicolor

(K. LANE + E.E.)

Fermilab-Pub-89/33-T

n_1 doublets	T_1	R_1	d_1
n_2 doublets	T_2	R_2	d_2
	Technifermions	Representation dimension	

will chose R_1 – fundamental representation
$d_1 = N$

R_2 = higher dimensional representation
(e.g. 日 , $d_2 = \frac{N(N-1)}{2}$)

Two scales

Λ_1 – characteristic χSB scale for R_1
Λ_2 – " " " " R_2

defined by

$$\alpha_{TC}(\Lambda_i) = \alpha_{Ci} \equiv \frac{\pi}{3C_2(R_i)}$$

$\Lambda_1 < \Lambda_2$

n_1, n_2 chosen so that $\alpha(p) \approx \alpha_{C2}$ $\Lambda_2 < p < \Lambda_{ETC}$

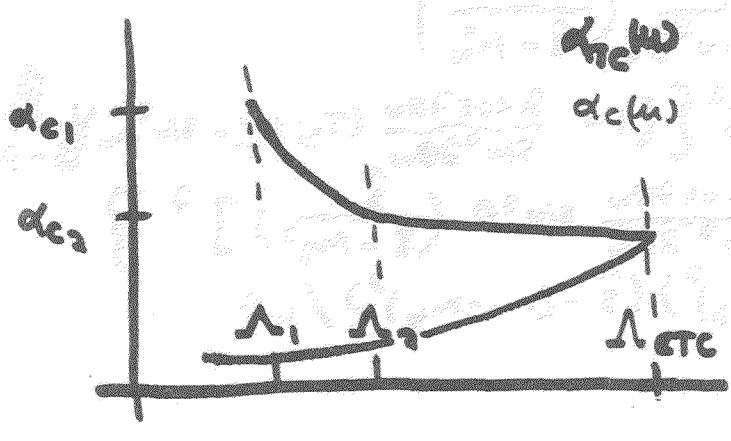

examples

$N = 5$ $n_2 = 2$ 日
$n_1 \leq 7$ 1

Technirho Production and Decay

ρ_1 1^{--} $T\bar{T}$, TT state

$(3,1)$ under $SU(2)_{EW} \otimes SU(N_f)$

↑ global flavor symmetries

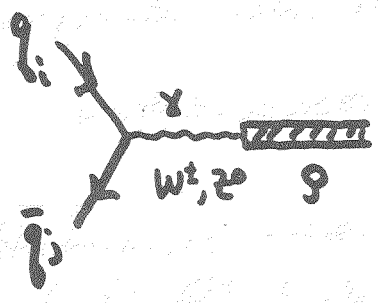

production

decay $\rho_1 \to \pi_a \pi_b$ / $\pi_a W_L$ / $W_L W_L$ (if kinematics allows)

(1) $\pi_1(\underline{3},\underline{1})\ \pi_1(\underline{3},\underline{1})$
(2) $\pi_1(\underline{3},\underline{N_f^2-1})\ \pi_1(\underline{3},\underline{n_f^2-1})$
(3) $\pi_1(3,1)\ W_L$
(4) $W_L W_L$

$W_L \equiv W_L^\pm$ or Z_L^0

$$\frac{d\hat{\sigma}}{d\cos\theta}(q_i\bar{q}_j \to \rho_1^{\pm,0} \to \pi_a \pi_b) = \frac{\pi \alpha_{EW}^2}{3\hat{s}} \frac{M_{\rho_1}^2}{(\hat{s}-M_{\rho_1}^2)^2 + \hat{s}\Gamma_{\rho_1}^2(\hat{s})} B_{ij}^{\pm,0} C_{ab} \frac{k^3}{\hat{s}^{3/2}} \sin^2\theta$$

C_{ab} - weight for each of four types of final states

$$B_{ij}^{\pm}(\hat{s}) = \frac{|K_{ij}|^2}{4\sin^4\theta_W}\left(\frac{\hat{s}}{\hat{s}-M_W^2}\right)^2$$

$$B_{ij}^{0}(\hat{s}) = \delta_{ij} Q_i^2 \left\{\left[1 + \frac{2\cos 2\theta_W}{\sin^2 2\theta_W}(T_{3i}/Q_i - \sin^2\theta_W)\left(\frac{\hat{s}}{\hat{s}-M_Z^2}\right)\right]^2 + \left[1 - \frac{2\cos 2\theta_W}{\sin^2 2\theta_W}\sin^2\theta\left(\frac{\hat{s}}{\hat{s}-M_Z^2}\right)\right]^2\right\}$$

$$k^2 = (\hat{s} - (M_a+M_b)^2)(\hat{s} - (M_a-M_b)^2)/4\hat{s}$$

Total Cross Section

$p\bar{p} \to \rho_1 \to W^+ + X$
$Z^0 + X$

$\sqrt{s} = 1.8$ TeV

$m_{\rho_1} = 250$ GeV

$|y| \leq 1.5$

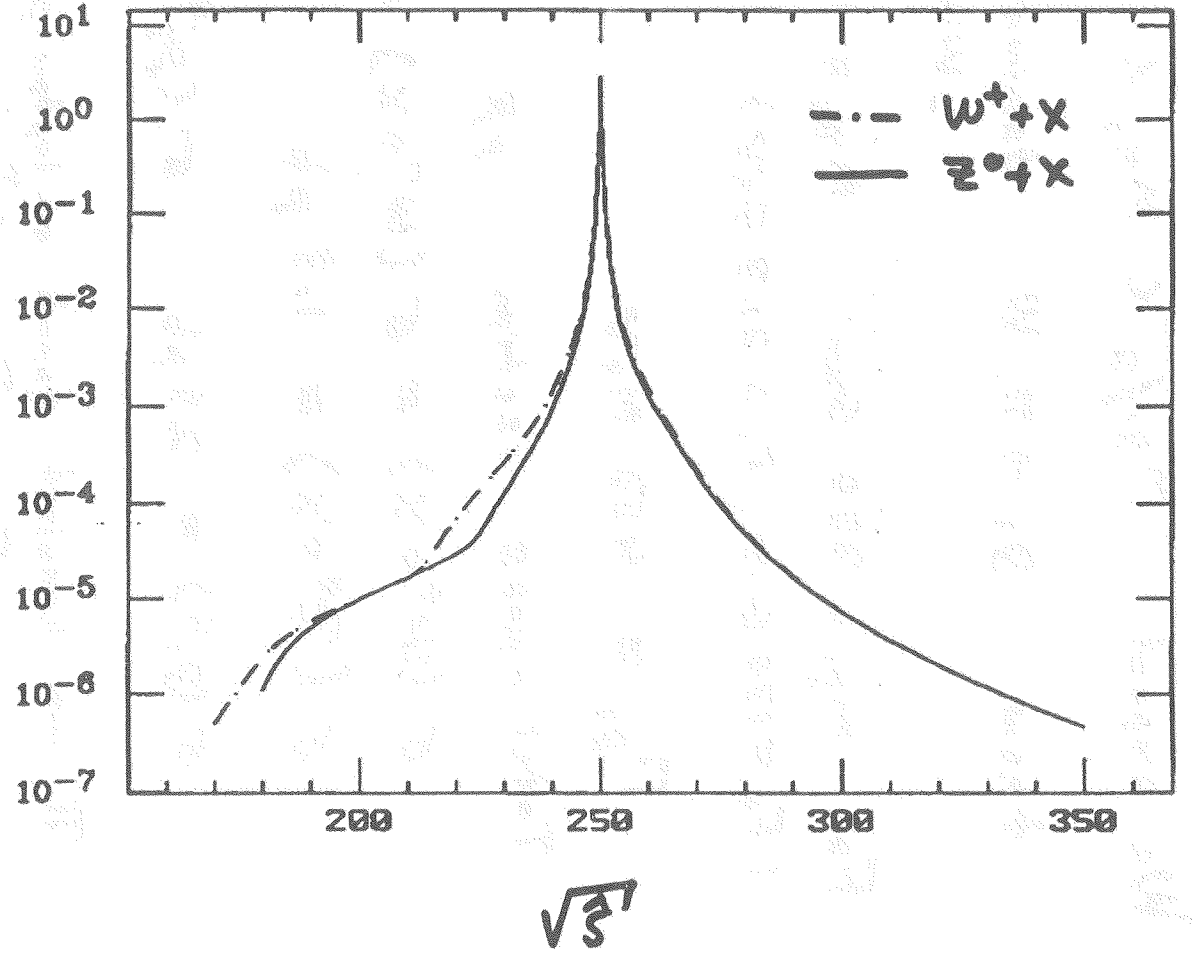

$\rho_T^+ \to W^+ + \pi_T^0$
$\hookrightarrow$
jj

$$\Gamma_{g,t\,o}(\hat{s}) = \frac{g^2}{6\pi} \sum_{ab} C_{ab}\, k_{ab}^3 / \hat{s}$$

$$g^2 = 3\, g_{\rho\pi\pi}^2 / N_{TC} \qquad (g_{\rho\pi\pi}^2/4\pi = 2.97)$$

We expect $M_{g_1}/2 < M_{\pi_1} < M_{g_1} - M_W$

then $g_1 \to \pi_1 W$ dominates
($WW \sim 10\text{-}15\%$)

For $m_{g_1} = 250$ GeV $M_{\pi_1} = 130$ GeV
($F_\pi = 170$ GeV, $F_1 = 21.7$ GeV)

$\Gamma_{g_1} \approx 450$ MeV

Total cross section $p\bar{p}$ $\sqrt{s} = 1.8$ TeV

$\sigma(W^+ + X) = \sigma(W^- + X) = 2.2$ pb

$\sigma(Z^0 + X) = 1.8$ pb

$\sigma(g_1^\pm) = 2.3$ pb $\quad \sigma(g_1^0) = 1.5$ pb

$\pi_1 \to$ heaviest quark or lepton pairs
$t\bar{t}$ $t\bar{b}$ $b\bar{b}$

Backgrounds from standard electroweak and QCD processes should be small

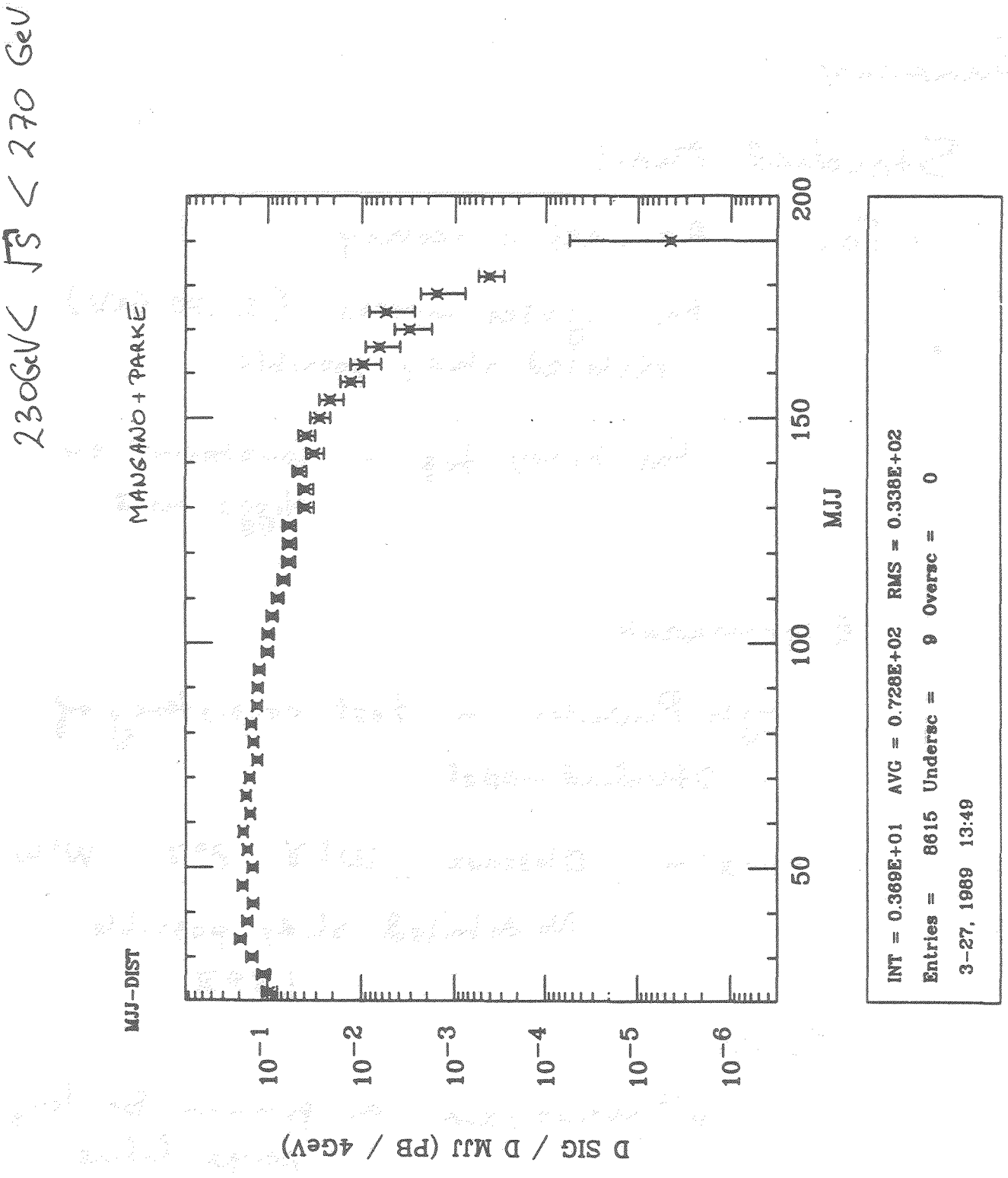
230GeV < √s < 270 GeV
MANGANO + PARKE
MJJ-DIST
D SIG / D MJJ (PB / 4GeV)
MJJ
INT = 0.369E+01 AVG = 0.728E+02 RMS = 0.338E+02
Entries = 8615 Undersc = 0 Oversc = 0
3-27, 1989 13:49

Summary

Standard Model

- Top – Assured discovery

  For lighter masses ($\lesssim 120$ GeV) detailed study possible

  For heavy top – constraint on Higgs mass

- Electroweak

  Single Production – test consistency of Standard model

  Pairs – Observe $W^{\pm}\gamma$ $Z^0\gamma$ W^+W^-

  No detailed study possible LEP II

- Bottom

  10^{10} events / Run $\Rightarrow$ potential for long range future

  For Now: B_d, B_u Low. energy e^+e^-
  $B_s, \Lambda_b \ldots$ Z^0, Fixed target

New Physics

- 4th generation – likely to discover the new quarks ($m_q \lesssim 250$ GeV)
- New Z^0 or $W^\pm$ – discovery limit 720 GeV
- Supersymmetry – discovery limit for squark or gluino 210 GeV

Foothills of the TeV Range

- Composite quarks and leptons

  Quark substructure ~ 2.3 TeV
  Drell-Yan Contact Term ~ 2.7 TeV

- Models with new dynamics

  Walking Technicolor
  May have W^+W^-, $W^\pm Z^0$ channel resonances in 250 - 350 GeV range.
  Would be observable.

Particle Identification at SSC

Frank E. Paige

Physics Department
Brookhaven National Laboratory
Upton, NY 11973

ABSTRACT

Lepton identification is crucial for a wide range of signatures at the SSC. Identification of $\pi/K/p$ seems only marginally useful except for reconstructing low-mass states, e.g. for studying B decays.

1. Introduction

Identification of individual particles has traditionally been important for extracting signals and reducing backgrounds. For the masses of interest at SSC, however, the branching ratio into any particular set of particles is negligible. Instead, any new particle will decay into the quanta of standard model, namely quarks and gluons, leptons, prompt photons, and $W^{\pm}$ and Z^0. These are what one wants to detect. All the available information indicates that $\pi/K/p$ identification is only marginally useful in separating different types of jets.

Of course if one is interested in using the SSC to study large numbers of low-mass particles such as B mesons, then particle identification of the traditional sort is crucial.

For high mass physics particle identification might still be useful for reconstructing particular low-mass states forming part of the signature. CDF has recently reported observation of a signal for $D^0 \to K^-\pi^+$ in events containing a lepton plus jets, indicating that such events come mainly from b decays, as anticipated. Presumably the background would be reduced if the K^- and π^+ were identified. For high Q^2 the c and b multiplicities become of order one or greater, so the advantage of identifying c and b states is reduced. Also, the fraction of c and b decays which might possibly be reconstructed is small, so the efficiency is limited. Hence this technique is unlikely to be very useful, but still it deserves more study than it has received.

While hadron identification is not very useful, leptons are among the quanta of the standard model, and identification of them is crucial for SSC physics. The rest of this paper discusses two signatures involving leptons: top quarks and gluinos.

2. Heavy Quarks

The production cross section for a heavy quark Q of mass m can be calculated using the QCD-improved parton model. That is, the hadron-hadron cross section is given by

$$\sigma = \sum_{i,j} \int dx_1 dx_2 \, f_i\left(x_1, \mu^2\right) f_j\left(x_2, \mu^2\right) \hat{\sigma}_{i,j} \tag{2.1}$$

where $f_i\left(x, \mu^2\right)$ is the probability for finding parton i in the incoming hadron with momentum fraction x and $\hat{\sigma}_{i,j}$ is the cross section for making heavy quarks from the partons i, j. To $\mathcal{O}\left(\alpha_s^2\right)$ there are just two processes,

$$g + g \to Q + \bar{Q}, \tag{2.2a}$$
$$q + \bar{q} \to Q + \bar{Q}, \tag{2.2b}$$

and $\hat{\sigma}$ is found by computing these processes in ordinary perturbation theory treating the quarks and gluons as real, on-shell particles. For example, the cross section for Eq. (2.2a) is given by

$$\begin{aligned} \frac{d\sigma}{dt} = \frac{\pi \alpha_s}{\hat{s}^2} \left(\frac{2 c_F d_F}{d_A^2}\right) \left(c_F - c_A \frac{\hat{t}' \hat{u}'}{\hat{s}^2}\right) \\ \times \left[\frac{\hat{t}'}{\hat{u}'} + \frac{\hat{u}'}{\hat{t}'} + \frac{4 m^2 \hat{s}}{\hat{t}' \hat{u}'} \left(1 - \frac{m^2 \hat{s}}{\hat{t}' \hat{u}'}\right)\right] \\ \hat{t}' = \hat{t} - m^2, \qquad \hat{u}' = \hat{u} - m^2 \end{aligned} \tag{2.3}$$

where c_F and d_F are the quadratic Casimir and the dimension of the color representation F of the quark.

To $\mathcal{O}\left(\alpha_s^3\right)$ one must calculate both the one-loop corrections to the processes in Eq. (2.2) and the new tree processes

$$g + g \to Q + \bar{Q} + g \tag{2.4a}$$
$$g + \overset{(-)}{q} \to Q + \bar{Q} + \overset{(-)}{q} \tag{2.4b}$$
$$q + \bar{q} \to Q + \bar{Q} + g \tag{2.4c}$$

In addition to the usual ultraviolet divergences, the individual higher-order Feynman graphs contain singularities associated with the massless nature of the external gluons and light quarks. These are of two types: infrared singularities, which come from the vanishing of a gluon momentum k, and collinear singularities, which come from the vanishing of the angle between a non-zero $\vec{k}$ and an external line. The infrared singularities cancel between real and virtual processes for inclusive cross sections. The collinear singularities do not cancel, but the singular parts factorize in cross sections. For a singularity from $i \to jk$ with $\vec{p}_i$, $\vec{p}_j$, and $\vec{p}_k$ all collinear

$$\sigma_{n+1}\left(p_j, p_k, \ldots\right) = \sigma_n\left(p_i, \ldots\right) \otimes \frac{\alpha_s}{2\pi p_i^2} P_{i \to jk}(z) \tag{2.5}$$

where $1/p_i^2$ is the singularity and $P(z)$ is an Altarelli-Parisi[8] function of the momentum fraction z carried by p_j or p_k. This factorization implies that the collinear singularities are universal, so the parton distributions in Eq. (2.1) can be consistently defined to contain them. The sum of these terms is given by the Altarelli-Parisi equations and generates the QCD evolution of the parton distributions and of jet fragmentation. Once the singularities are extracted, the remaining terms give a finite, $\mathcal{O}(\alpha_s^3)$ contribution to $\hat{\sigma}$.

The full $\mathcal{O}(\alpha_s^3)$ calculation for heavy quark production has now been carried out by Nason, Dawson, and Ellis[9,10]. This calculation is extremely complicated, primarily because of the necessity of separating out all of the infrared and collinear singularities explicitly. The numerical result, however, is very simple: the top cross section is about equal to a constant $K \sim 1.5$ times lowest order cross section, both for the one-particle inclusive cross section and for the total cross section. Of course a K-factor does not describe the event structure for the processes in Eq. (2.4).

2.1 Event Simulation

Perturbative QCD allows one to calculate inclusive cross sections for hard-scattering processes such as heavy quark production systematically. But to analyse signatures and backgrounds it is often necessary to describe not just inclusive distributions but complete events. Monte Carlo generators produce an approximation perturbative QCD in a form directly applicable for experimental analysis. Generally such generators involve three steps:

1. Generate a primary hard scattering according to an appropriate QCD cross section.
2. Use the branching approximation to generate higher order parton configurations in a way which incorporates leading-log QCD effects.
3. Convert these partons into hadrons and add beam jets from the spectator partons using some model.

The branching approximation is the link between the Monte Carlo approach and the perturbative calculations. The object is to include all of the collinear singularities in Eq. (2.5) systematically. This is possible because the factorization holds for cross sections, so the factorized pieces can be treated as probabilities in a classical, rather than a quantum mechanical, process. Furthermore, the logarithm associated with each factor comes from an integral $\int dp_i^2/p_i^2$ over a large range of p_i^2, which is possible only if $p_j^2, p_k^2 \ll p_i^2$. But this means that each radiation can be treated as independent of previous ones. Hence the leading-log singularities of QCD field theory can all be reproduced by a classical Markov branching suitable as the basis for a Monte Carlo program.

The strict leading-log approximation is not enough to make a useful event generator because all the partons are collinear. In practice the singular, factorized pieces of the the cross section are used with exact kinematics for off-shell partons; the kinematics for $i \to jk$ are generated using the actual masses and a suitable generalization of the momentum fraction z, for example

$$z = \frac{E_j + |p_j|}{E_i + |p_i|} \tag{2.6}$$

This gives noncollinear jets. By construction at the edges of phase space where the jets are collinear the cross section is correct, so the correct leading logarithms are generated. Elsewhere, the cross section involves an extrapolation of the singular term in a somewhat

arbitrary way, but typically one finds agreement with multijet QCD cross sections to within a factor of two or so. A very similar approach can be used for branching in the initial state, starting at the hard scattering and working backwards towards[11] small Q^2 partons in the incoming hadron.

Some variant of the branching approximation is used in most of the standard hadron-hadron event generators, including COJETS[12], HERWIG[13], ISAJET[14], and PYTHIA[15].

The UA1 Collaboration[16] has extracted the b cross section from measurements of $\mu^{\pm}$ and $\mu^+\mu^-$ distributions. The branching approximation as implemented in ISAJET provides surprisingly good agreement with this data and with the calculation of Nason, Dawson, and Ellis[10]. In ISAJET there are three mechanisms for heavy quark production (plus the analogous ones involving light quarks):

$$g + g \to b + \bar{b} \tag{2.7a}$$

$$g + b \to g + b \tag{2.7b}$$

$$g + g \to g + g \to b + \bar{b} \tag{2.7c}$$

For $p_T \gg m$ these processes are physically distinct: Eq. (2.7a) produces the b and $\bar{b}$ back-to-back, Eq. (2.7b) produces the b at high p_T and the $\bar{b}$ at much smaller p_T, and Eq. (2.7c) produces a $b\bar{b}$ pair at high p_T balanced by a gluon jet. In this region the processes are clearly incoherent and must be added to generate all the mass singularities; Eq. (2.7c) actually dominates by a small amount. For $p_T \sim m$ the processes are not distinguishable. There is no a priori reason to think that they should be added or that the mass singularities should give a good approximation to the cross section in this region. Nevertheless, the UA1 collaboration found that adding the three contributions agreed remarkably well with the $\mathcal{O}(\alpha_s^3)$ calculation and with the data.[16]

It would be interesting to know how well the branching approximation works for other quark masses. Unfortunately, generation of the events for Eq. (2.7c) is nontrivial: one must generate $gg \to gg$ and then select the small fraction of the events containing $b\bar{b}$. Hence the calculation has not been done. Even if the good agreement is an accident, however, it does suggest that ISAJET describes $b\bar{b}$ production well enough to use it for estimating backgrounds for top signatures.

2.2 Top at Tevatron

An analysis of signatures and backgrounds for top quarks at $\sqrt{s} = 1800\,\text{GeV}$ is being undertaken[17] using ISAJET both to learn what signatures are promising and to try to understand how well the Monte Carlo simulates QCD in the relevant regions of phase space. So far only preliminary results for $m = 60\,\text{GeV}$ have been obtained. In the CDF analysis[4] the lepton identification appears to be quite clean, so it is assumed that only real, prompt lepton backgrounds need be considered.

As explained in the previous section, the background from gluons splitting into heavy quarks requires special treatment in the Monte Carlo. Hence, the QCD background is divided into a sample *guds* in which the primary jets are gluons and light quarks and a another sample *bc* corresponding to direct $gg \to b\bar{b}$ or $gg \to c\bar{c}$ production. The signal and background samples were generated with ISAJET 6.21 and are listed in Table 2.1. In this table "hard p_T" refers to the range of p_T for the primary hard scattering; the events are distributed among a number of bins in this range to produce reasonably uniform statistics.

Table 2.1: Signal and background samples for top analysis at Tevatron.

Sample	Hard p_T (GeV)	Lepton p_T (GeV)	Events
t	10–100	—	2000
bc	20–180	—	24000
$guds$	30–180	> 8	30000
W	0	$\ell\nu$	5000

The number of events represents the Monte Carlo statistics, not the number produced per year. In the *guds* sample, all the events contain a heavy quark which decays into a lepton with $p_T > 8\,\text{GeV}$. The W sample is generated from the standard Drell-Yan process, and only $e\nu$ and $\mu\nu$ decays are The $W \to t\bar{b}$ signal has been ignored since it is small for most masses at $\sqrt{s} = 1800\,\text{GeV}$.

All events were passed through QFL[18], a program which simulates CDF calorimetry including the nonlinear response of the calorimeter for low-p_T jets. However, the uncertainty in that response has not been taken into account. Jets were found using the QFL cluster algorithm and merged in a region

$$R = \sqrt{(\Delta y)^2 + (\Delta\phi)^2} < 0.7 \tag{2.8}$$

Single Lepton: The QCD backgrounds for purely hadronic decays of $t\bar{t}$ are overwhelming. One semileptonic decay of a $t\bar{t}$ is more promising, giving a hard isolated lepton plus multiple jets. The important backgrounds are higher order QCD corrections to W production and QCD production of b and c quarks. Since the c and b total cross sections are very large but is concentrated at $p_T \sim m$, it is essential to make some cut to select high-p_T events. The variable chosen to do this is

$$\Sigma = \sum_i |p_{T,i}| \tag{2.9}$$

where the sum runs over all jets and leptons in the event. After cutting on this and other variables, the distribution of surviving events is rather flat the hard p_T variable in Table 2.1.

A first set of cuts which eliminates most of the background but leave enough of it to see a distribution is:

- At least one lepton with $p_{T,\text{lepton}} > 12\,\text{GeV}$;
- Lepton isolation, with the extra energy $E_T < 4\,\text{GeV}$ in a cone $\Delta R = .4$ around it;
- At least two jets, where the jets are found by the QFL algorithm;
- $p_{T,\text{jet}} > 16\,\text{GeV}$ for the highest p_T jet;
- $\Sigma > 40\,\text{GeV}$.

The result is a signal/background of $\mathcal{O}(1)$, as can be seen from Fig. 2.1a.

While the statistics on the QCD background in Fig. 2.1a are not very good, it appears to fall faster than the signal, so it is probably fair to raise the cuts. Also, the transverse

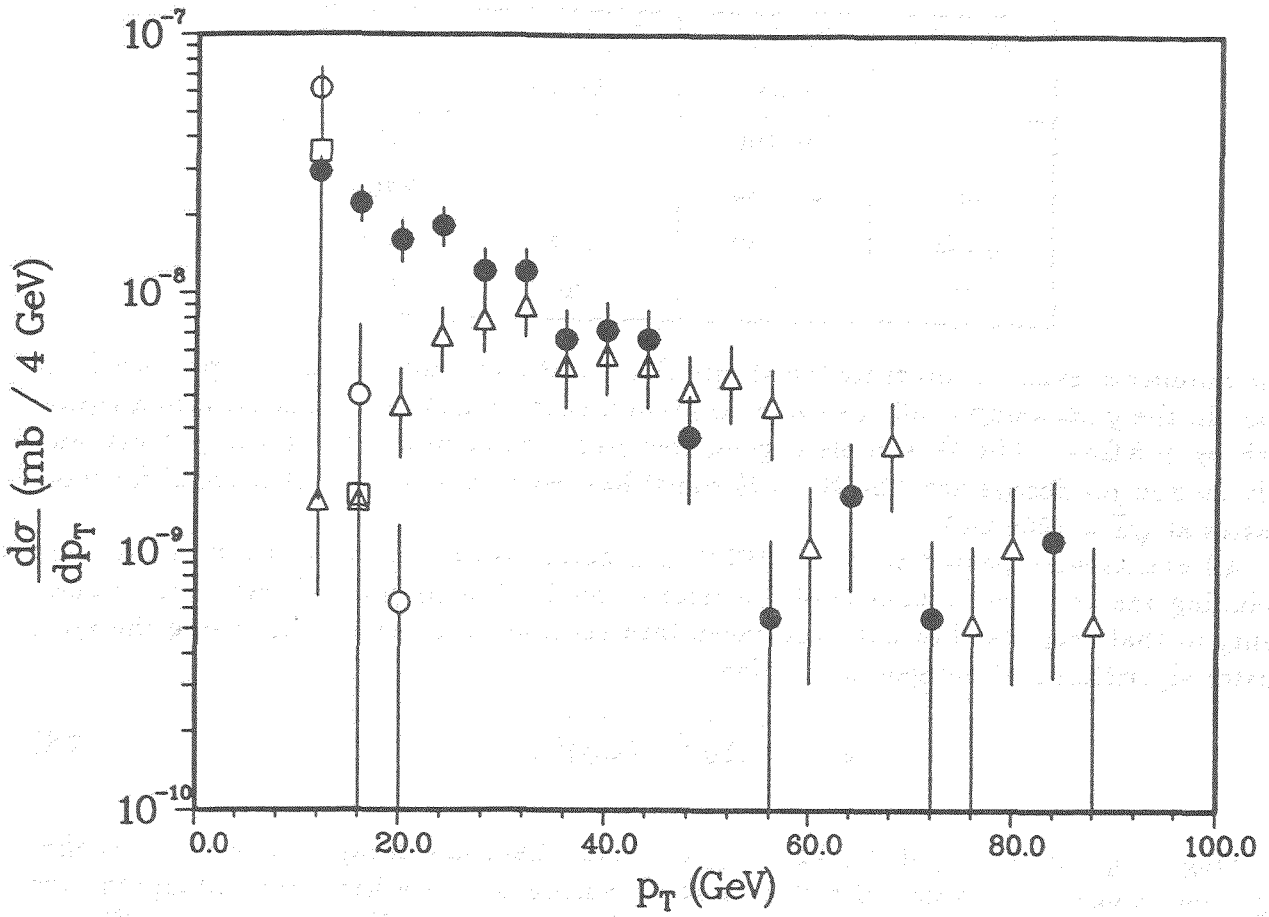

Figure 2.1a: p_T distribution of the isolated lepton with the first set of cuts for $m = 60\,\text{GeV}$ and $\sqrt{s} = 1800\,\text{GeV}$. Solid circles: t; open circles: *guds*; open squares: *bc*; triangles: W.

mass formed from the lepton and the missing p_T should peak around m_W for the W background but be concentrated at lower values a top quark with $m = 60\,\text{GeV}$. This leads to a refined set of cuts:

- Raise the lepton threshold to $p_{T,\text{lepton}} > 15\,\text{GeV}$;
- Require a transverse mass $M_T < 60\,\text{GeV}$ using the lepton momentum and $p_{T,\text{miss}}$ calculated from QFL with $|\eta| < 2.5$;
- Require both jets satisfy $p_{T,\text{jet}} > 10\,\text{GeV}$.

The lepton isolation, jet multiplicity, and Σ cuts are unchanged. The distribution of $p_{T,\text{lepton}}$ for these refined cuts is shown in Fig. 2.1b. Again the number of events refers to the Monte Carlo statistics, not to the number of events per year. The signal/background ratio is quite good, as can be seen in Table 2.2, but the acceptance is only 4.8%. Even though the uncertainty in the description of jets and of the detector is not included, there appears to be a reasonable chance of extracting a single lepton signal in this mass range.

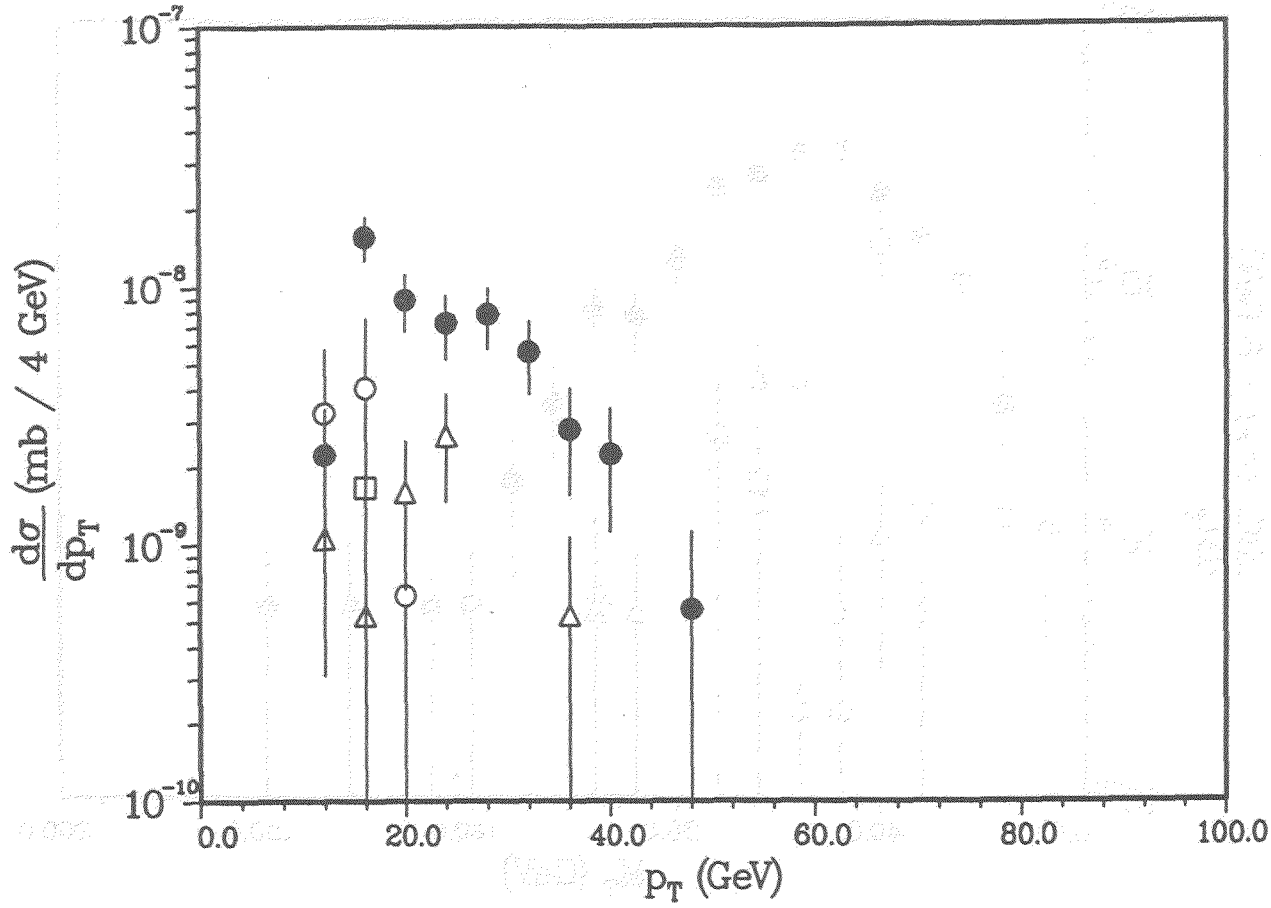

Figure 2.1b: p_T distribution of the isolated lepton with the first set of cuts for $m = 60\,\text{GeV}$ and $\sqrt{s} = 1800\,\text{GeV}$. See Fig. 2.1a for symbols.

Table 2.2: Cross sections after cuts and Monte Carlo statistics for single lepton top signal, $m = 60\,\text{GeV}$.

Sample	σ (pb)	Events
t	52.8	95
$guds$	7.9	7
bc	6.6	1
W	6.3	12

Studies with a parton Monte Carlo show that a good estimate of the quark mass is the transverse mass $M_{\ell\nu j}$ formed from the lepton, the missing p_T, and any jet in the event; an event with n jets contributes n times to the distribution:

$$M_{\ell\nu j} = M_T\,(p_\ell, p_\nu, p_j) \tag{2.10}$$

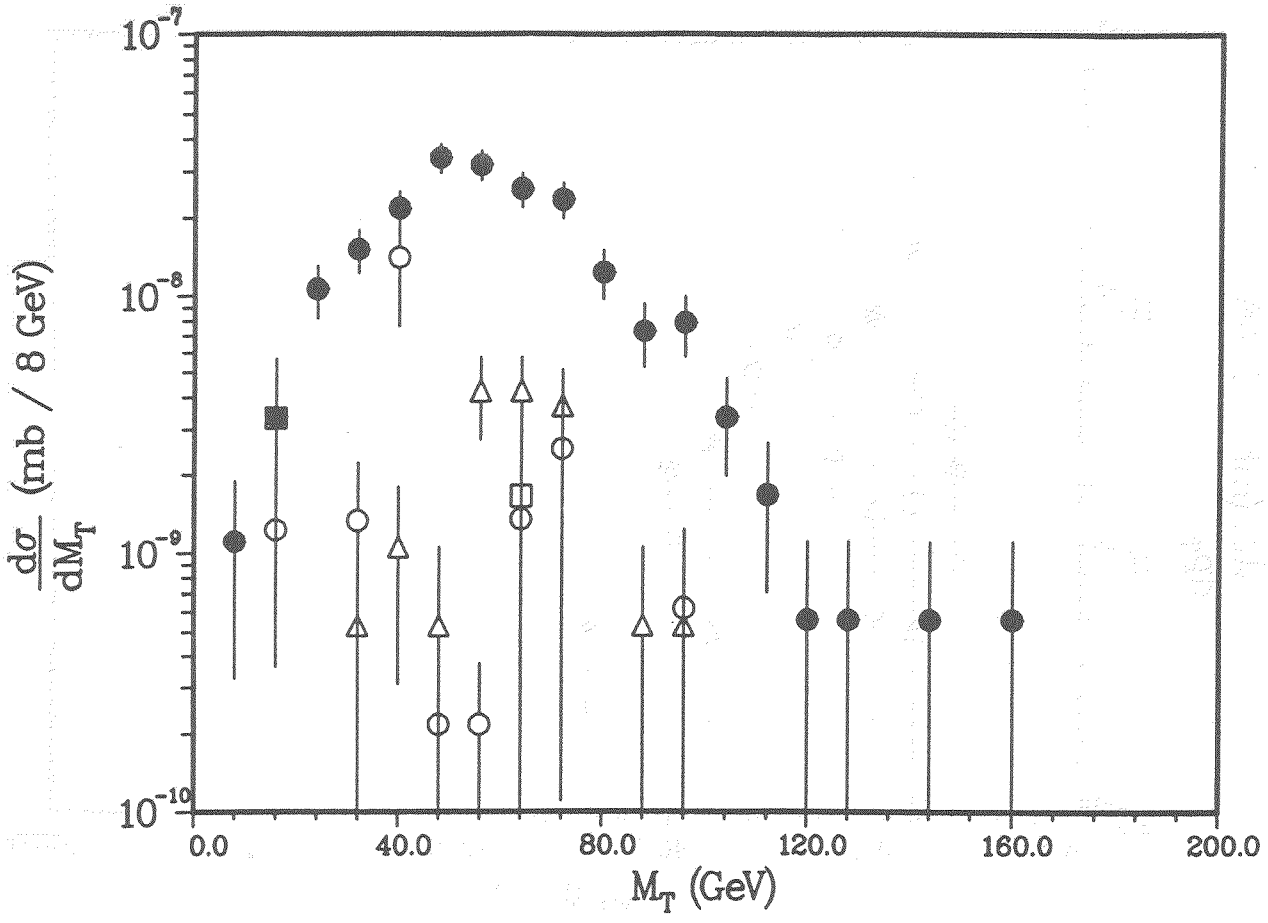

Figure 2.2: Transverse mass $M_{\ell\nu j}$ for $m = 60\,\text{GeV}$ and $\sqrt{s} = 1800\,\text{GeV}$. See Fig. 2.1 for symbols.

The distribution, shown in Fig. 2.2, is broad but $\langle M_{\ell\nu j}\rangle = 61\,\text{GeV}$.

It must be emphasised that this analysis does not take into account either the uncertainties in the simulation either of the physics or of the detector.

Two leptons: The single lepton signal relies on the calculation of the $W + n$ jets cross section. For the two lepton signal, the leading background comes from W^+W^-, which is much smaller than the signal. Hence the cuts to select the signal can be less restrictive. In particular, cuts on the associated jets are no longer required:

- $p_{T,\,\text{lepton 1}} > 12\,\text{GeV}$.
- $p_{T,\,\text{lepton 2}} > 6\,\text{GeV}$.
- $E_T < 4\,\text{GeV}$ in $\Delta R = .4$ around leptons.
- $\Sigma > 40\,\text{GeV}$.

These cuts produce a 2.9% acceptance for the $t\bar{t}$ cross section:

$$\sigma = 32\,\text{pb} \tag{2.11}$$

Table 2.3: Cross sections after cuts and Monte Carlo statistics for two lepton top signal, $m = 60\,\text{GeV}$.

Process	$\sigma(1\ell)$ (pb)	Events	$\sigma(2\ell)$ (pb)
t			32
$guds$	74	40	< 4.3
bc	37	3	$\ll 37$
W	781	1480	< 1.2

The W^+W^- background is negligible. Within the statistics, no events survive the cuts from any of the other background samples. The following table lists for each process the cross section passing the cuts for the first lepton, the Monte Carlo statistics, and the resulting upper limits on the cross section for a second isolated lepton are listed in Table 2.2. The statistical upper limits are all small except for the bc sample, for which the single lepton background — based on three events — is comparable to the two lepton signal.

This whole analysis assumes that the decay mode $t \to b\ell\nu$ dominates. If $m < m_W$ and if there is a charged Higgs boson or other charged scalar lighter than the t, then the two-body decay $t \to bH^+$ dominates over the three-body decay. A charged Higgs is not particularly unlikely; in particular, it is necessary in supersymmetry models, which are perhaps the most reasonable framework for any elementary Higgs. The decay modes of a charged Higgs are somewhat model dependent, but it is plausible to assume that $c\bar{s}$ and $\tau\nu$ dominate with a 3:1 ratio from the color factor. It is therefore important to look for such decays.

2.3 Heavy Quarks at SSC

The CDF and UA2 Collaborations have recently reported results which indicate that the top is unlikely to be lighter than 60 GeV. This suggests considering seriously the possiblity that it is so heavy that top physics is the province of the SSC.

The analysis described in the previous section has been extended[19] to the SSC for a top mass chosen to be 140 GeV. The top quark and the W background were generated using ISAJET 6.21. The QCD backgrounds have not yet been examined, but from the analysis in the previous section at $\sqrt{s} = 2\,\text{TeV}$ it is plausible that the W background is dominant.

All events were analyzed with the QFL calorimeter simulation program using the following parameters:

$$\left(\frac{\Delta E}{E}\right)_{\text{e.m.}} = \frac{0.15}{\sqrt{E}}$$

$$\left(\frac{\Delta E}{E}\right)_{\text{had.}} = \frac{0.50}{\sqrt{E}}$$

$$|\eta| \leq 6$$

$$\Delta\eta \approx \Delta\phi \approx 0.04$$

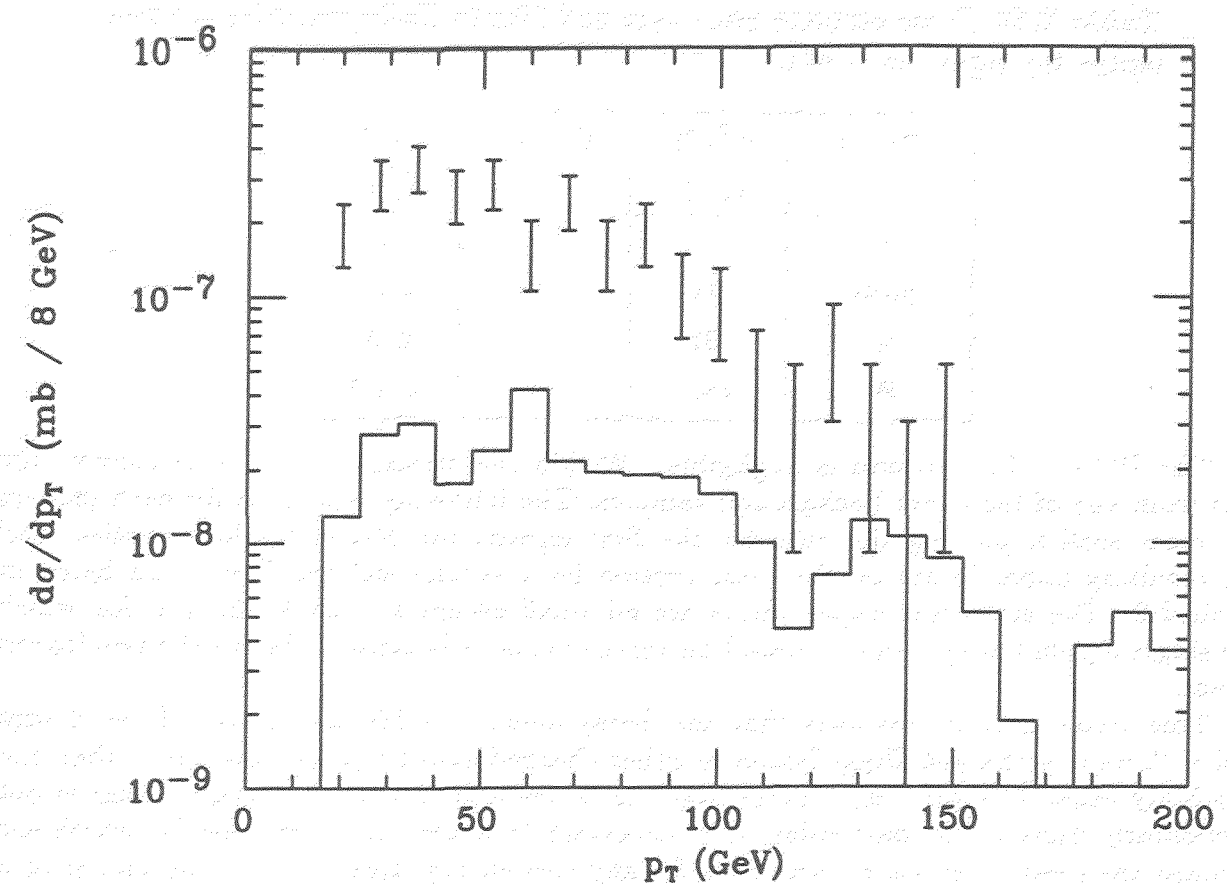

Figure 2.3: p_T distribution of the isolated lepton in the single lepton top signal for $m = 140\,\text{GeV}$ and $\sqrt{s} = 40\,\text{TeV}$. The histogram is the W background.

Jets were found with the QFL cluster algorithm, which is based on the CDF algorithm, with $\Delta R = 0.7$ and a minimum jet energy of 15 GeV.

Single lepton: The analysis follows closely the previous one. To separate the top from the background the following cuts were made:

- At least one lepton with $p_{T,\ell} > 20\,\text{GeV}$.
- Lepton isolation, with the extra energy $E_T < 4\,\text{GeV}$ in a cone $\Delta R < 0.4$ around the lepton.
- At least 3 jets, with $p_{T,1} > 25\,\text{GeV}$, $p_{T,2} > 20\,\text{GeV}$, and $p_{T,3} > 15\,\text{GeV}$.
- $\Sigma = \sum p_{T,i} > 80\,\text{GeV}$, where the sum runs over all jets and leptons in the event.

These cuts give

$$\sigma(t\bar{t}) = 2.5\,\text{nb}$$
$$\sigma(W) = 0.32\,\text{nb}$$

The p_T distribution of the isolated lepton for the signal and background are shown in Fig. 2.3.

The top mass can again be estimated using Eq. (2.10), the transverse mass formed from the lepton, the missing p_T measured by the calorimeter with $|\eta| < 6$, and any jet.

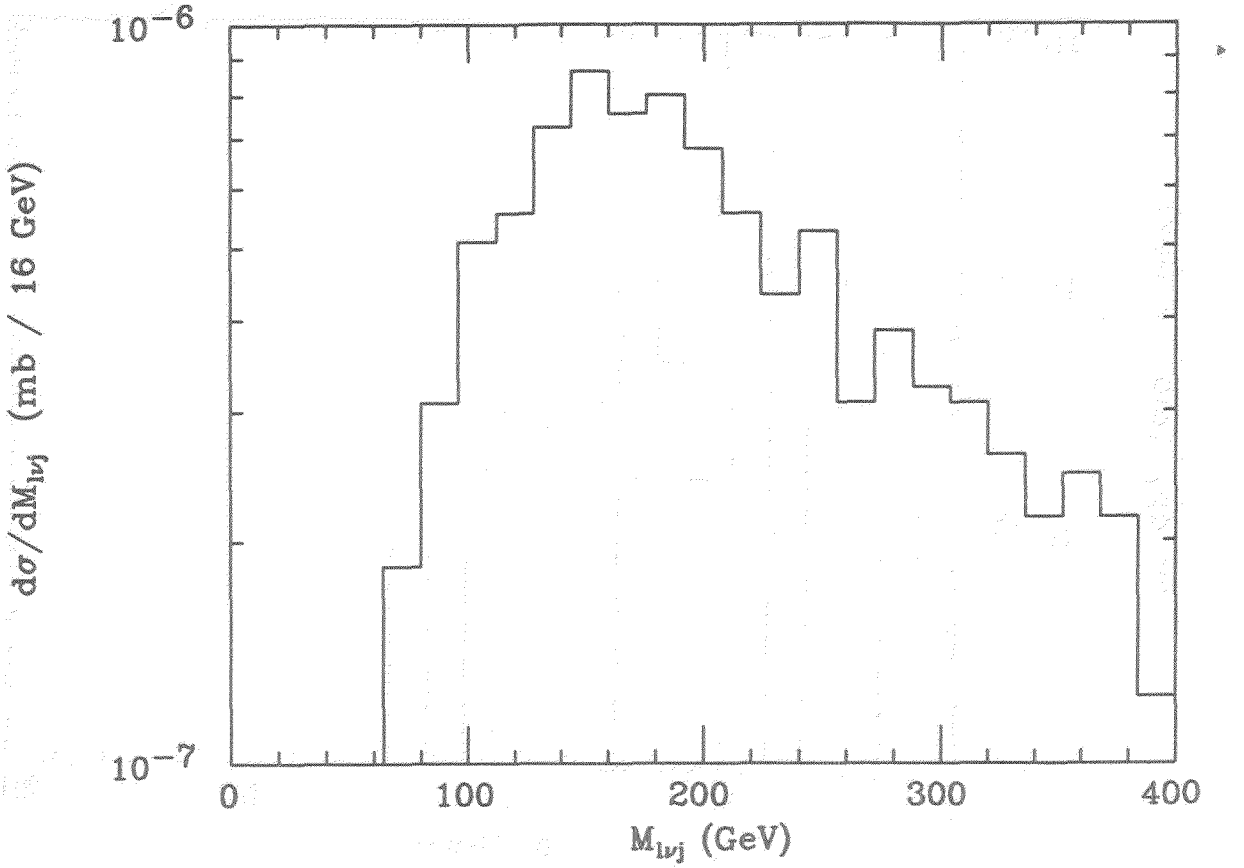

Figure 2.4: Distribution of transverse masses formed from the lepton, the missing p_T, and any jet for $m = 140\,\text{GeV}$ and $\sqrt{s} = 40\,\text{TeV}$.

(The η coverage actually needed for the measurement was not studied.) The distribution, Fig. 2.4, is quite broad, but a peak is seen near the quark mass.

The isolation cut $E_T < 4\,\text{GeV}$ in a cone $\Delta R < 0.4$ has not taken into account event pileup. A crude estimate is that each minimum bias event will deposit 0.4 GeV in this region. Hence integrating over ten interactions would cause a significant problem for our cut. Obviously the top signal can be observed at low luminosity, but this estimate illustrates the importance of pileup for lepton isolation cuts in cases where high luminosity is essential. It would be desirable to study whether the isolation cut can be made with only charged tracks, for which the timing would be better, but this has not been done.

The good signal to background ratio found in this analysis is probably due to the fact that the top signal is produced by gg fusion and so increases rapidly as $m/\sqrt{s}$ decreases. One should also remember that the analysis is implicitly assuming that both the character of the signal and the background events and the response of the detector to them is perfectly understood.

Two leptons: The two-lepton signal has also been briefly examined, requiring that the leptons be isolated as before and have $p_T > 20\,\text{GeV}$ and $p_T > 10\,\text{GeV}$ and that $\Sigma > 80\,\text{GeV}$.

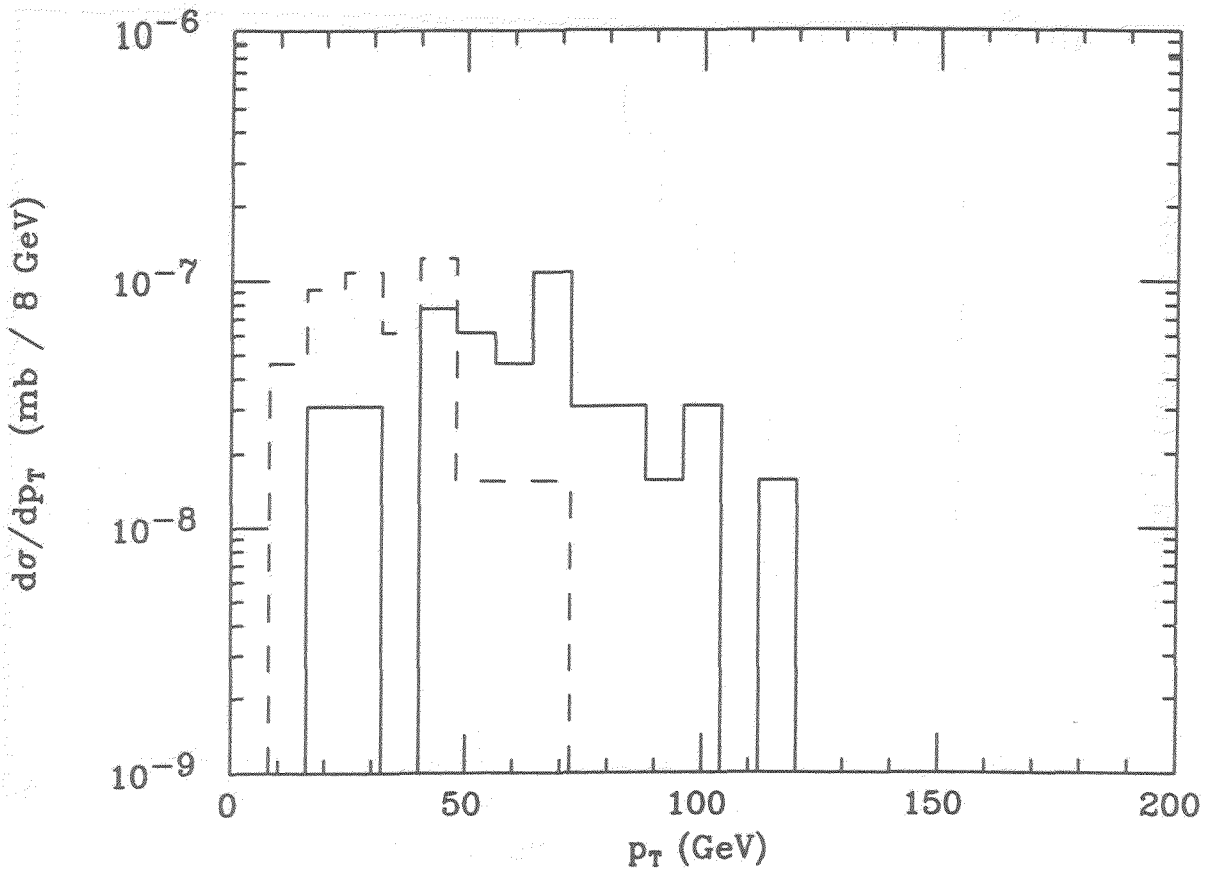

Figure 2.5: p_T distribution for the two highest p_T leptons in the two lepton top signal for $m = 140\,\text{GeV}$ and $\sqrt{s} = 40\,\text{TeV}$.

With these cuts the signal is

$$\sigma(t\bar{t}) = 0.47\,\text{nb}$$

The p_T distribution of the two highest p_T lepton is shown in Fig. 2.5 There is no background from single W production within the Monte Carlo statistics. The cross section for W events which pass just the cuts for the first lepton and for Σ is 5.3 nb, and there are 1070 such events in our sample. Thus an upper limit of 2.3 dilepton events in this sample corresponds to a cross section of 11.4 pb. From calculations for $\sqrt{s} = 1.8\,\text{TeV}$ it appears that the QCD background from $b\bar{b}$ and $c\bar{c}$ pairs is small, although this has not been checked. Any background from Z or Drell-Yan can be avoided by using only $e^{\pm}\mu^{\mp}$ events with a loss of a factor of two in rate and the WW cross section is negligible. Thus the two-lepton signal appears to be very clean.

The SSC would be sensitive to new heavy quarks with masses up to 1 TeV or more[20]. Full Monte Carlo studies of the signals and backgrounds for such quarks have not been done. There have been several parton-level studies[21,22]. Since the production cross sections are large, these have concentrated on multi-lepton signatures as representing the best

discovery channel. It appears to be possible to find such quarks if they exist, but more detailed studies are obviously needed before SSC detectors are designed.

3. Supersymmetry

Supersymmetry is an attractive possible extension of the Standard Model because it provides an elegant and natural mechanism for keeping Higgs bosons light even in the presence of additional heavy mass scales. The best experimental limits on the masses of gluinos ($\tilde{g}$) and squarks ($\tilde{q}$) come from the UA1 Collaboration[23] at the S$\bar{p}$pS and the from CDF Collaboration[24] at the Tevatron. Based on studies of events with jets and substantial $E_T^{\rm miss}$, they find

$$\begin{aligned} M_{\tilde{g}} &> 53\text{GeV}, \quad M_{\tilde{q}} > 45\text{GeV} \qquad \text{(UA1)} \\ M_{\tilde{g}} &> 73\text{GeV}, \quad M_{\tilde{q}} > 74\text{GeV} \qquad \text{(CDF)} \end{aligned} \tag{3.1}$$

These experimental analyses and most previous Monte Carlo studies have concentrated on the simplest possible decay modes, namely $\tilde{g} \to \tilde{\gamma} q\bar{q}$ if the gluino is lighter than the squark, or $\tilde{q} \to \tilde{\gamma} q$ if the squark is lighter than the gluino. The photino $\tilde{\gamma}$ has a neutrino-like cross section and escapes from the detector, so the signature is $E_T^{\rm miss}$ plus multiple jets. These simple modes are usually dominant for masses up to $60 - 70$GeV, but other modes become important for the heavier masses of interest at the SSC. The reason is that any supersymmetric extension of the Standard Model contains not just a single photino but at least four neutral color singlet fermions $\tilde{\chi}_i^0$ and two charged ones $\tilde{\chi}_i^+$. If the gluino mass is heavy, then decays into some or all of these are possible, so the branching ratio for a direct decay into any one is small. Heavier $\tilde{\chi}$ particles eventually decay into the lightest supersymmetric particle (LSP) $\tilde{\chi}_1^0$, which like a photino escapes from the detector. The cascade decays reduce the $E_T^{\rm miss}$, but they also introduce many interesting new signatures.

While many possible signatures exist, missing energy is still the most characteristic signature of supersymmetry. An analysis of the $E_T^{\rm miss}$ signature and backgrounds for heavy gluinos at the SSC has been made[25] including all the possible decay modes. Only gluino pair production and decay has been considered, since it is gluino decays which are most affected by the existence of the new modes. The main result of the analysis is that even with the more complicated decays predicted by the minimal supersymmetric model, the $E_T^{\rm miss}$ signature remains observable.

3.1 Minimal Supersymmetric Model

To give masses to up and down quarks in the minimal supersymmetric model,[26] it is necessary to introduce two Higgs doublets, resulting in three neutral and one charged pair of Higgs bosons after symmetry breaking. The supersymmetric partners of the Higgs bosons mix with the $\tilde{\gamma}$ and $\tilde{Z}$ to make four states $\tilde{\chi}_i^0$, $i = 1,2,3,4$, known collectively as neutralinos and numbered in increasing order of mass. Similarly the supersymmetric partner of the charged Higgs boson mixes with the $\tilde{W}$ to make two chargino states $\tilde{\chi}_i^+$, $i = 1,2$. Assuming that R parity is conserved, all supersymmetric particles are produced in pairs. Each supersymmetric particle decays into lighter ones, and the cascade continues

until the LSP ($\tilde{\chi}_1^0$) is reached. The LSP is absolutely stable and escapes from any collider detector.

In the minimal model all of the masses and mixings of the charginos and neutralinos are determined in terms of four parameters. One of these can be eliminated by assuming that the gaugino masses are degenerate at the grand unification or Planck scale. The remaining three parameters can be taken to be the gluino mass $M_{\tilde{g}}$, a supersymmetric Higgs mass μ, and a ratio $\tan\beta = v_2/v_1$ of Higgs vacuum expectation values. If supersymmetry is related to the electroweak scale, both $M_{\tilde{g}}$ and μ should be less than about 1 TeV; $\tan\beta$ should be of order one. Given these parameters, all branching ratios can be calculated. The resulting branching ratio for $\tilde{g} \to \tilde{\chi}_1^0 q\bar{q}$ is large for light gluinos but is less than about 20% for gluino masses above 300 GeV. Even if the details are not correct, this minimal model presumably provides a representative example.

3.2 Heavy Gluinos

To simulate the signatures it is necessary to choose specific parameters. The values of μ and $\tan\beta$ are not very crucial because the branching ratio of the gluino to the LSP depends only weakly on them, although other branching ratios vary somewhat more. A detailed analysis has been done[25] for

$$M = 750\text{GeV}, \quad \mu = +150\text{GeV}, \quad \tan\beta = 1.5. \tag{3.2}$$

The squarks are taken to be degenerate with $M_{\tilde{q}} = 2M_{\tilde{g}}$. If the squarks are heavier than the gluino, then the precise values of their masses are not very important.

The signatures for these events were simulated using ISAJET 6.21.[14] For $\sqrt{s} = 40\text{TeV}$ the total $pp \to \tilde{g}\tilde{g}X$ cross section is

$$\sigma_{\tilde{g}\tilde{g}} \simeq 70\,\text{pb} \tag{3.3}$$

All the decay modes were included in the simulation, and the resulting E_T^{miss} distribution was calculated. Many of these decay modes can also produce $W^{\pm}$'s, Z^0's, jets, and leptons, leading to many additional signatures, but these have not yet been studied.

The Standard Model background to events involving jets, leptons, and E_T^{miss} comes from the QCD production and semileptonic decay of heavy quarks $Q = c$, b, and t and from the production of $W^{\pm}$ and Z^0 at large p_T. ISAJET was used to simulate all of these backgrounds. The largest background for gluinos is the production of heavy quark pairs at high transverse momentum from higher-order processes like

$$g + g \to Q + \bar{Q} + g \tag{3.4}$$

Such higher-order processes are not directly included in ISAJET, since they are already produced by the QCD evolution, which approximates all higher-order QCD cross sections by a classical Markov branching process. To generate Eq. (3.4), therefore, it is necessary first to generate a primary hard scattering $gg \to gg$ and then to select events with the branching $g \to \bar{Q}Q$.

To analyze E_T^{miss} for the simulated events, a highly idealized calorimeter with uniform segmentation $\Delta\eta = \Delta\phi = 0.05$ for $|\eta| < 6$ and Gaussian energy resolutions

$$\left(\frac{\Delta E}{E}\right)_{\text{e.m.}} = \frac{0.15}{\sqrt{E}} \qquad \left(\frac{\Delta E}{E}\right)_{\text{had.}} = \frac{0.70}{\sqrt{E}}. \tag{3.5}$$

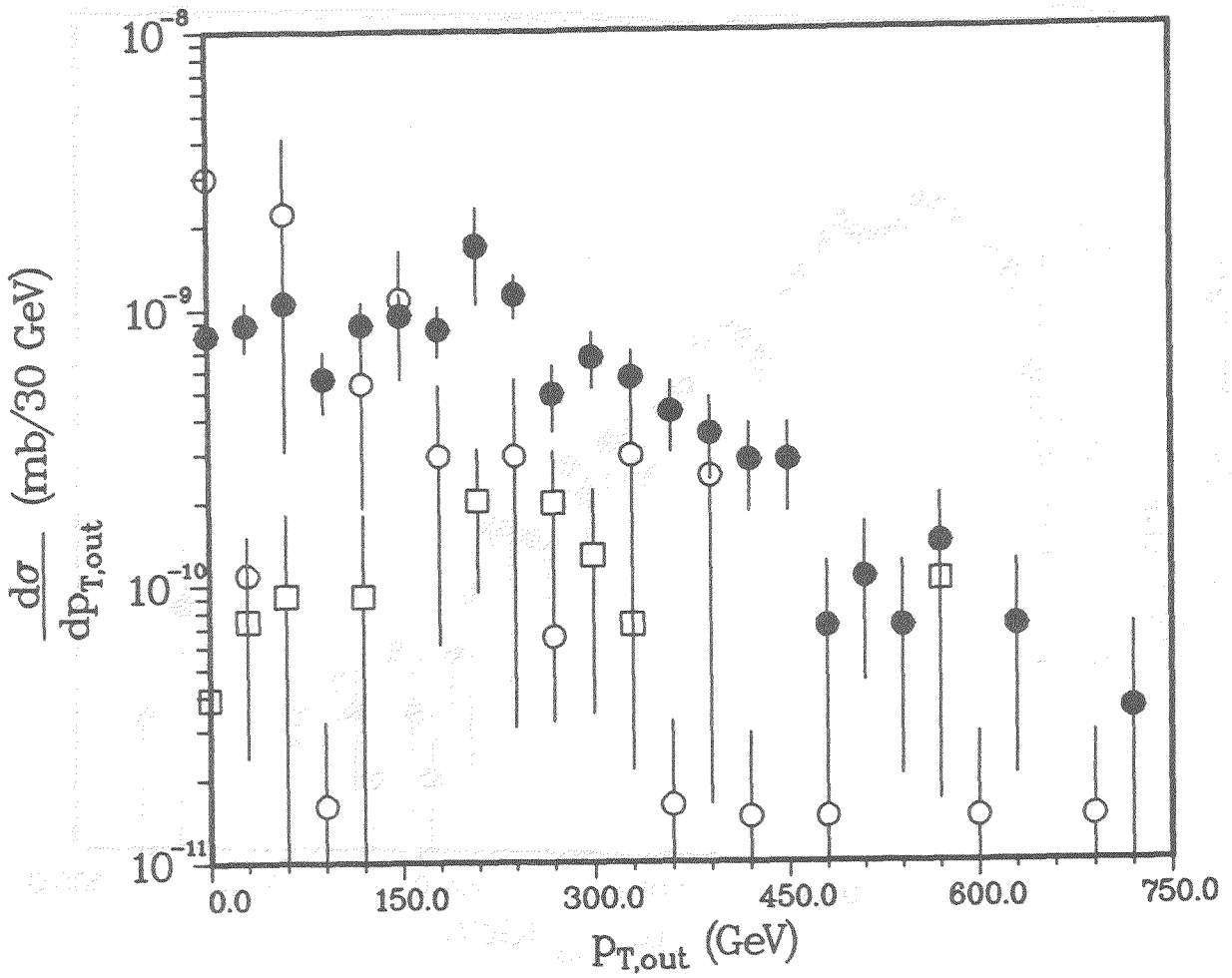

Figure 3.1: p_T^{out} distribution after cuts for gluinos with $M_{\tilde{g}} = 750\,\text{GeV}$ at the SSC.

was used. Jets with $p_T > 50\text{GeV}$ were found using a simplified version of the UA1 jet algorithm with a clustering radius $\Delta R = 0.7$. The effects of a more realistic calorimeter have not been studied.

To select the $M = 750\text{GeV}$ gluino signal from the QCD and electroweak backgrounds the following set of cuts were imposed:

- The highest jet has $p_T > 300\text{GeV}$;
- The missing transverse energy is $E_T^{\text{miss}} > 200\text{GeV}$;
- The sphericity S calculated in the transverse plane is $S > 0.2$;
- The number of jets with $p_T > 50\text{GeV}$ is $n_{\text{jet}} \geq 4$.

After these cuts the missing transverse momentum p_T^{out} out of the plane defined by the beam and the highest p_T jet was plotted. The resulting distribution is shown in Fig. 3.1. Making a further cut at $p_T^{\text{out}} > 300\text{GeV}$ gives the following cross sections:

$$\sigma_{\text{signal}} = 2.4\,\text{pb}$$
$$\sigma_{QCD} = 0.62\,\text{pb}$$

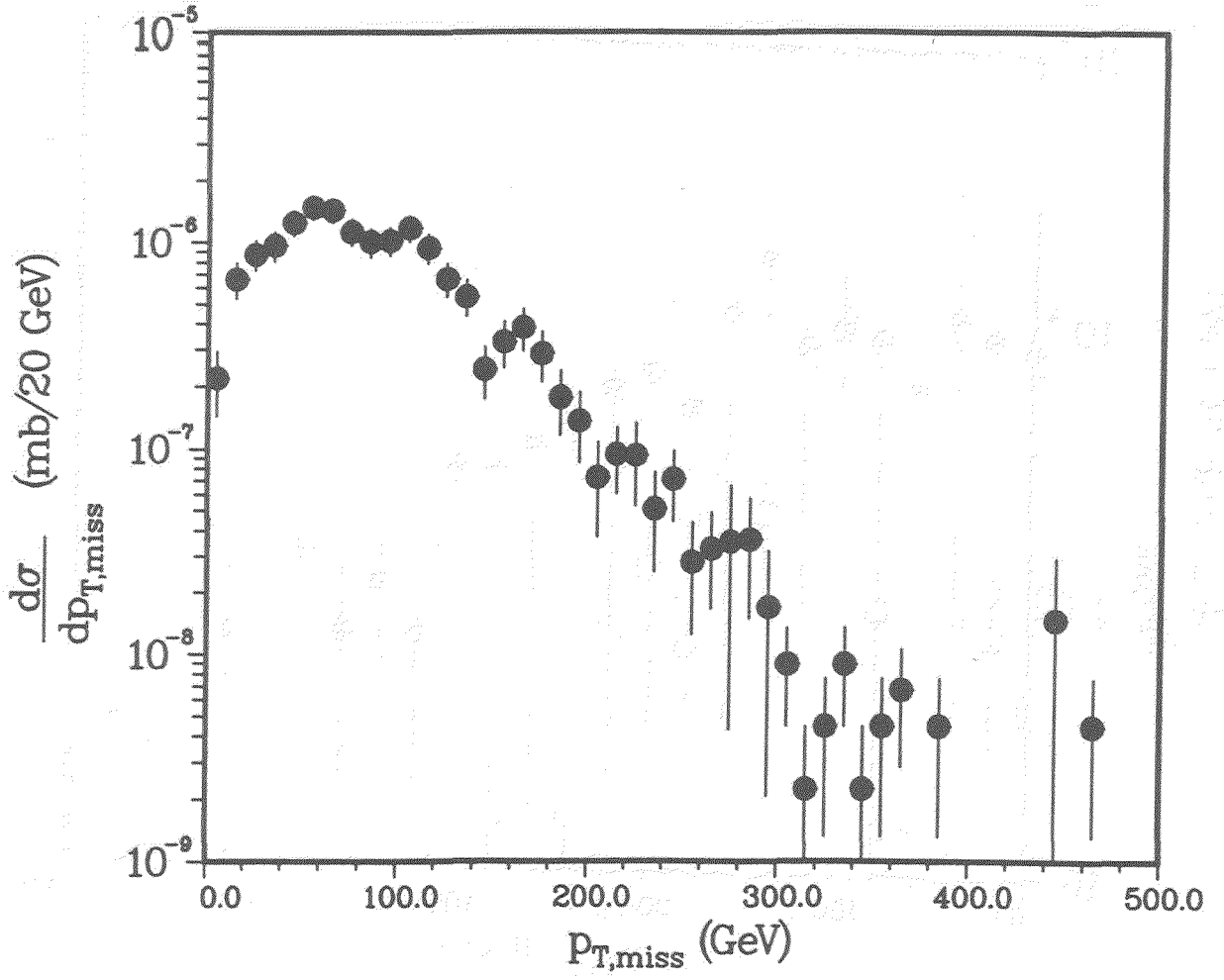

Figure 3.2: $E_T^{\rm miss}$ distribution after cuts for gluinos with $M_{\tilde{g}} = 220\,\text{GeV}$ at the SSC.

$$\sigma_{W^\pm,\, Z^0} = 0.25\,\text{pb} \tag{3.6}$$

The signal has been substantially reduced from Eq. (3.3), but it still represents 24000 events for the nominal luminosity $10^4 pb^{-1}$. The signal/background ratio seems quite adequate provided that realistic detector effects do not degrade the resolution too much. Presumably the shape of the $p_T^{\rm out}$ distribution could be used to determine the mass, but this has not been investigated.

3.3 Light Gluinos

The most serious constraint for hermeticity comes from light gluinos, since the scale for $E_T^{\rm miss}$ is smaller. The parameters

$$M = 220\text{GeV}, \quad \mu = +400\text{GeV}, \quad \tan\beta = 1.5 \tag{3.7}$$

were chosen as representative of a gluino which might be both difficult to observe at the Tevatron because of rate and difficult to observe at the SSC because of the small $E_T^{\rm miss}$

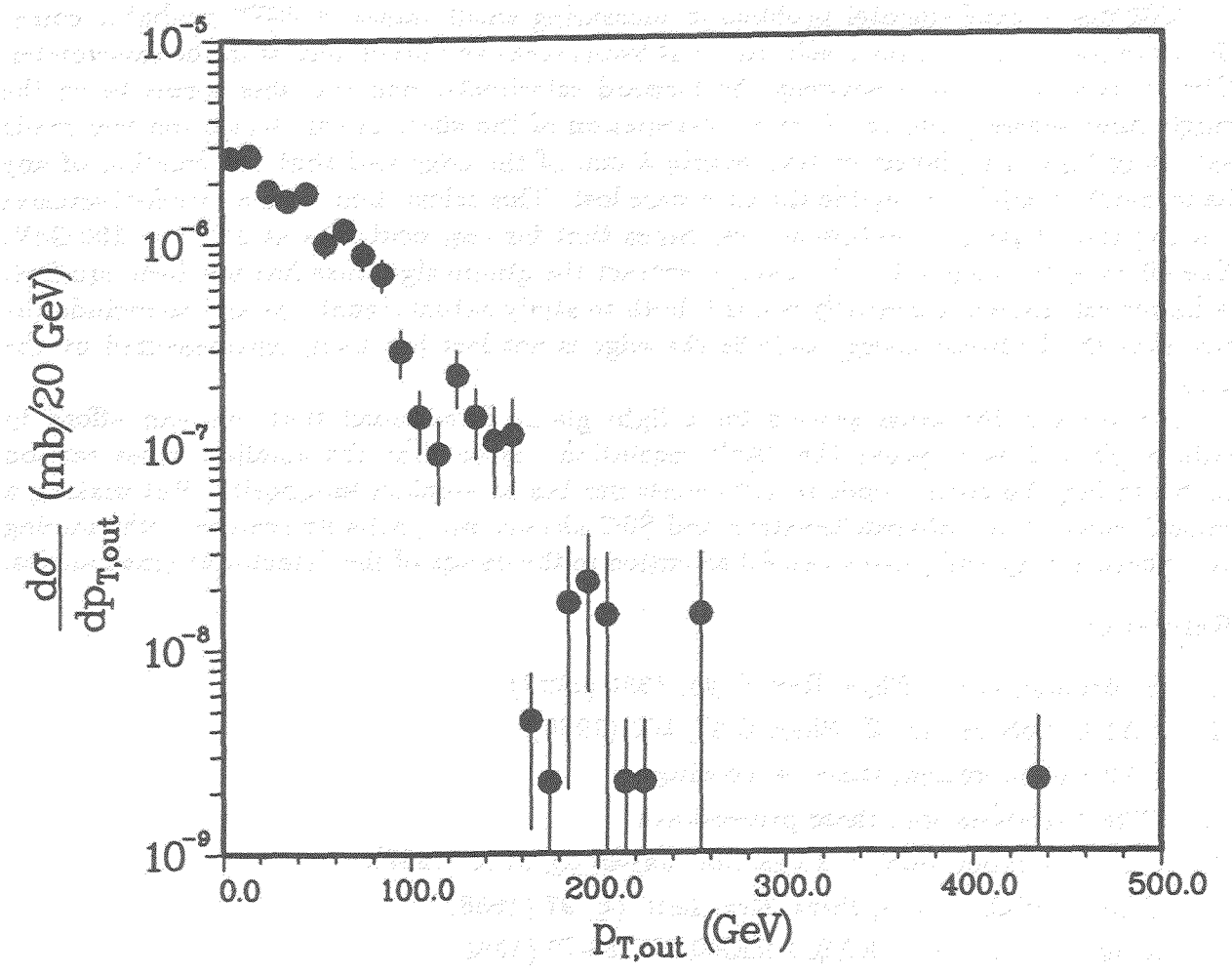

Figure 3.3: p_T^{out} **distribution after cuts for gluinos with** $M_{\tilde{g}} = 220\,\text{GeV}$ **at the SSC.**

scale. The backgrounds for this case have not been studied, but the signal including all branching ratios has been investigated for a perfect detector. While the mean missing transverse energy is small,

$$\langle E_T^{\text{miss}} \rangle = 71\,\text{GeV}, \tag{3.8}$$

the E_T^{miss} distribution extends to very large values, as can be seen in Fig. 3.2

Although the backgrounds for this case have not been calculated, experience suggests that cuts on p_T^{out} as well as E_T^{miss} are essential to separate signal and background. While large values of E_T^{miss} are possible, the values of p_T^{out} are limited by the gluino mass except for the effects of higher order QCD corrections, which do not strongly differ between signal and background. The result, shown in Fig. 3.3, is a distribution sharply cut off at a value comparable to the gluino mass (except for one anomalous Monte Carlo event). Extracting this signal cleanly would require an E_T^{miss} resolution significantly smaller than the mean value.

The major experimental problem in measuring small values of $E_T^{\rm miss}$ probably comes not from Gaussian detector resolutions but from cracks and other defects in the calorimeter. The transition at $\eta \approx 3$ between the forward calorimeter and the plug seems to be the single most severe problem. A crude calculation of the effect of this transition was made assuming that any photon hitting within 5 cm. of the edge and that the fraction of any hadronic shower falling outside the edge were lost. This calculation gives a rate for inclusive missing transverse momentum several times that for real neutrinos at $E_T^{\rm miss} = 100\,{\rm GeV}$. The effect of the edge after the cuts to extract the gluino signature has not been studied. A better calculation is urgently needed, both to study actual signatures and to include the fact that the hadronic energy outside the edge is not lost but badly mismeasured by the plug.

Fortunately, the cross section for a light gluino is so small that one can afford to reduce $\sqrt{s}$ and so improve the $E_T^{\rm miss}$ resolution. Note that the smallest cross section shown in Fig. 3.3 corresponds to 10^4 events per bin at nominal luminosity. But making a smooth connection between Tevatron and SSC physics will probably require both running at reduced energy and paying careful attention to the design of the detector at small angles.

References

1. U. Amaldi, et al., *Phys. Rev. D* 36, 1385 (1987).
2. UA1 Collaboration, *Z. Phys. C* 37, 505 (1988).
3. UA2 Collaboration, these proceedings.
4. CDF Collaboration, these proceedings.
5. Venus Collaboration, *J. Phys. Soc. Japan* 56, 3763 (1987).
6. Topaz Collaboration, *Phys. Rev. Lett.* 60, 97 (1988).
7. Amy Collaboration, KEK-PREPRINT-88-76 (1988).
8. G. Altarelli and G. Parisi, *Nucl. Phys. B* 126, 298 (1977).
9. P. Nason, S.D. Dawson, and R.K. Ellis, *Nucl. Phys. B* 303, 607 (1988).
10. P. Nason, S.D. Dawson, and R.K. Ellis, BNL-42398 (1989).
11. T. Sjostrand, *Phys. Lett. B* 157, 321 (1985).
12. R. Odorico, *Comp. Phys. Comm.* 32, 139 (1984).
13. G. Marchesini and B.R. Webber, CAVENDISH-HEP-88/7 (1988).
14. F.E. Paige and S.D. Protopopescu, *1986 Summer Study on Physics of the SSC* (Snowmass, 1986), p. 320.
15. H.-U. Bengtsson and T. Sjostrand, *Comp. Phys. Comm.* 46, 43 (1987).
16. UA1 Collaboration, *Phys. Lett. B* 197, 281 (1987).
17. E. Berger, D. Keubel, F.E. Paige, M. Pundurs, and C.P Yuan, in preparation.
18. C. Newman-Holmes and J. Freeman, FERMILAB-CONF-87/231 (1987).
19. M. Barnett, F.E. Paige, and E.M. Wang, in preparation.
20. E. Eichten, I. Hinchliffe, K. Lane, and C. Quigg, *Rev. Mod. Phys.* 56, 579 (1984).
21. H. Baer, V. Barger, H. Goldberg, and V. Ohnemus, *Phys. Rev. D* 38, 3467 (1988).
22. S. Dawson and S. Godfrey, *Phys. Rev. D* 39, 221 (1989).

23. C. Albajar et al., Phys. Lett. B198, 261 (1987).
24. J. Freeman and F. Abe, et al., Proc. of 7th International Conference on $\bar{p}p$ Collisions, Fermilab, June, 1988 (preliminary).
25. R.M. Barnett, et al., BNL-42650, to appear in *Proc. of the 1988 Snowmass Summer Study*.
26. See H.E. Haber and G.L. Kane, Phys. Rep. 117, 75 (1985) and references therein.

II. Ring Imaging Cerenkov Counters

PARTICLE IDENTIFICATION AT HADRON COLLIDERS.

THOMAS YPSILANTIS, COLLEGE DE FRANCE, PARIS.

1.Particle Identification Limits.

The particle ID capability of a Ring Imaging CHerenkov (RICH) detector may be obtained from the basic Cherenkov relation $n\beta\cos\theta=1$ which may be rewritten as

$$U\equiv\sin^2\theta=[(\gamma/\gamma_t)^2-1]/(\gamma\beta)^2=\gamma_t^{-2}-(m/pn)^2 \qquad (1)$$

where γ is the Lorentz factor of the radiating particle, p its momentum, m its mass, n the refractive index and $\gamma_t=n/(n^2-1)^{1/2}$ the γ threshold of the radiator. The number of standard deviations n_σ to discriminate mass m_2 from m_1 is then

$$n_\sigma=(U_2-U_1)\sqrt{N}/\sigma_U=[(m_2^2-m_1^2)/p^2n^2]\sqrt{N}/\sigma_U \qquad (2)$$

where σ_U is the r.m.s. error in the measure of U and N is the number of photoelectrons of the ring image. The number of photons dN_{ph} per unit energy interval dE for a radiator of length L is given by the Franck-Tamm relation

$$dN_{ph}/dE=(137\hbar c)L\sin^2\theta \qquad (3)$$

which may be integrated over ΔE the energy bandwidth of the detector to give (for an approximately constant Cherenkov angle)

$$N=N_0L\sin^2\theta \qquad (4)$$

with the detector response parameter

$$N_0=(137\hbar c)\int QTR\,dE=(370\,eV^{-1}cm^{-1})\Delta E\,\bar{\varepsilon} \qquad (5)$$

where $\bar{\varepsilon}$ is the energy average of the detector efficiencies (Q=quantum, T=transmission, R=reflection). Substituting Eq.4 into Eq.2 and noting that $\sigma_U=(2\sin\theta\cos\theta)\sigma_\theta=(2\sin\theta/n\beta)\sigma_\theta$ to obtain the momentum for particle ID

$$p=[(m_2^2-m_1^2)/2n_\sigma k_c]^{1/2} \qquad (6)$$

where the characteristic RICH detector constant is

$$k_c = n\sigma_\theta/\beta(N_0 L)^{1/2} \qquad (7)$$

and σ_θ is the total angular error per detected photon.

To get optimal particle ID requires that k_c be minimum and since N_0 and σ_θ are proportional to ΔE (see Eq.'s 5,10,11 and 13) then Eq.7 shows that k_c is proportional to $\sqrt{\Delta E}$. This implies that the detector should have minimal bandwidth but with sufficient photoelectrons N for pattern recognition. Increasing N by increasing the detector bandwidth ΔE is counterproductive and should be avoided. Radiators with the lowest chromatic dispersion should be used unless space point measurement errors dominate σ_θ.

The momentum resolution σ_p of a RICH detector is, after the particle mass has been identified, given by the relation

$$\sigma_p = k_c p^3/m^2 \qquad (8)$$

which for heavy particles (K,P) may be more precise than the magnetic deflection measurement. The two determinations are, in any case, independant and should be considered together.

1.1 Irreducible Errors.

The geometry of a RICH gas radiator is shown in Fig.1. The measurements necessary to define the Cherenkov angle θ are the photon detection point (x,y,z), the photon emission point (x_e,z_e) and the particle direction (θ_p,φ_p). The photon emission point along the particle path in the gas radiator is z_e while the particle impact parameter relative to the mirror center of curvature is x_e. Six of these variables $(x,y,z,x_e,\theta_p,\varphi_p)$ can, in principle, be infinitely well measured. The photon emission point however has an irreducible error

$$\sigma_{z_e} = L/\sqrt{12} \qquad (9)$$

which cannot be improved without reducing the radiator length. Similarly the photon energy error is

$$\sigma_E = \Delta E/\sqrt{12} \quad \text{for a square response} \qquad (10)$$

$$\sigma_E = \Delta E/\sqrt{24} \quad \text{for a triangular response} \qquad (11)$$

always for a base width ΔE. This error cannot be reduced without decreasing the detector bandwidth ΔE. The corresponding errors in the Cherenkov angle θ are

$$\sigma_\theta(z_e)= (\partial\theta/\partial z_e)\sigma_{z_e} \qquad (12)$$

and

$$\sigma_\theta(E)=(\partial\theta/\partial n)(dn/dE)\sigma_E \qquad (13)$$

These two errors are therefore irreducible and determine the limits of resolution. The chromatic contribution to the total angular error σ_θ is considered in the next section while the emission point error will be considered in section 3 after the mathematical treatment of the ring image.

2.Chromatic Errors.

The first factor of Eq.13 is given, for a mirror focused image (see Fig.1), by the derivative of the Cherenkov relation $n\beta\cos\theta=1$ hence

$$\partial\theta/\partial n=1/(n*\tan\theta)=(\gamma_t-1/\gamma_t)/[1-(\gamma_t/\gamma)^2]^{1/2} \qquad (14)$$

For a proximity focused image Eq.14 is multiplied by an additional factor $(n\beta)^2/(1-\tan\theta_p\tan\theta\cos\varphi)$ due to refraction of the Cherenkov cone as it exits the radiator medium [1]. The chromatic error $\sigma_\theta(E)$ depends, in this case, on the azimuthal angle φ.

The second factor dn/dE is the dispersion of the radiator medium which may be evaluated from the Lorentz-Lorenz equation

$$(n^2-1)/(n^2+2)=cf(E) \qquad (15)$$

with the density dependant constant $c=(4\pi/3)r_B N_A \rho/M=.3738 cm^3\ \rho/M$, r_B is the Bohr radius, N_A is Avagadro's number, ρ/M the molar density of the radiator medium=P/RT for an ideal gas. The energy dependence of the molar refractivity f(E) is usually fit to a Sellmeir two-pole form

$$f(E)=F_1/(E_1^2-E^2)+F_2/(E_2^2-E^2) \qquad (16)$$

The derivative of Eq.15 gives directly the dispersion

$$dn/dE=[(n^2+2)^2 cdf/dE]/6n \qquad (17)$$

with n from Eq.15, c from the density and

$$df/dE=2E[F_1/(E_1^2-E^2)^2+F_2/(E_2^2-E^2)^2] \qquad 18)$$

the derivative of Eq.16.

The indices of some common gases (He,Ne,Ar,Kr,Xe,H_2,N_2,O_2) have been measured [2] in the visible and UV and fit to Eq.16 to obtain the Sellmeir coefficients (E_1,E_2,F_1,F_2) listed in Table 1.

We have measured the refractive indices of some liquid fluorinated alkanes (CF_4,C_2F_6,C_4F_{10},C_5F_{12},C_6F_{14}) with the setup shown in Fig.2 [3]. It consists of a UV monochromator, a D_2 arc lamp with a MgF_2 window, a fused quartz windowed wedge cell with a quartz lens and slit mounted on a rotating arm. The lens focuses the parallel beam of refracted light onto the slit plane and when the arm is rotated parallel to the beam the image passes through the slit and is detected by the glass window photomultiplier (covered with p-terphenyl for UV sensitivity). The refraction angle determines the refractive index through the relation

$$n=\sin(\theta_W+\theta_D)/\sin\theta_W \qquad (19)$$

where θ_W is the wedge angle and θ_D the difference of the deflection angles with the wedge cell full and empty. The results are shown in Fig.3 for the cryogenic liquids (CF_4 and C_2F_6) and the room temperature liquids (C_5F_{12} and C_6F_{14}) over the measurement interval 5 to 7eV (177 to 248nm). It can be seen that the refractive indices are very low (1.22 to 1.275) and that the dispersion is small. Because of the limited range of the data a linear fit of the form

$$n=a+bE \qquad (20)$$

sufficed. The fits are shown as the full lines in Fig.3 and the fit coefficients are tabulated in Table 2 along with ρ the liquid density and M the molecular weight. From the fit n(E) the molar refractivity f(E) may be calculated from Eq.15 and df/dE from Eq.17 since dn/dE=b for this liquid state.

The dispersion dn/dE for the gaseous state may then be evaluated through Eq.'s 15&17 given f(E) and df/dE (as determined above) and $c=.3738cm^3 P/RT$ where P is the pressure T the temperature T of the gas radiator in question.

Solid transparent materials are also of interest as windows as well as Cherenkov radiators for low momentum particles. The Sellmeir coefficients of Eq.16 are listed in Table 3 for CaF_2, NaF and fused quartz. The first two are single crystals with good transmission to about 10eV whereas fused quartz is amorphous (hence cheaper) with transmission to

about 8eV. In the case of CaF_2 and fused quartz the fit was to $f(E)=n^2-1$ while for NaF [4] the fit was to $f(E)=(n^2-1)/(n^2+2)$. The constant c has been absorbed into f(E) since the density of these solids is constant.

With the data of Tables 1 and 2 and Eq.'s 15 to 20 the chromatic errors $\sigma_\theta(E)$ have been calculated for a TMAE based detector (Isobutane +Methane amplifying gas, triangular response between 6.1 to7.1eV) coupled to various gas radiators (1bar,40°C).In Table 4 is listed the radiator gas, γ_t, $\sigma_\theta(E)$ and $\sigma_\theta(E)/\theta$ for $\beta=1$ particles ($\gamma=\infty$ in Eq.14). The last quantity is the fractional error in the Cherenkov angle which is constant with changes in density. Also listed in Table 4 is the radiator length L to get N=9 for a detector with a specific response $N_0=65cm^{-1}$(corresponding to $\varepsilon=.35$ hence TR=.7 and Q=.5 at the maximum of the triangular response). The RICH constant k_c (Eq.7), due only to the chromatic error and for the listed length L, is also given with the momentum $p_{K\pi}(3\sigma)$ to obtain $n_\sigma=3$ (Eq.6). The obvious inferences from Table 4 are:

1)While He and Ne give excellent upper limits for Kπ ID (880,620GeV/c) they must be exceedingly long (21,11m) hence are useful only for limited solid angle spectrometers.

2)That Ar, Kr, Xe and N_2 are not very good radiators relative to the fluorinated alkanes.

3)That CF_4 is the best medium (equal to high density He or Ne) and C_5F_{12} has the lowest threshold. A combined CF_4(1.4m),C_5F_{12}(0.4m) radiator with a quartz separator plate and a single mirror and detector could attain Kπ ID from 2.4 to 240GeV/c.

A proximity focused liquid C_6F_{14} (1cm) RICH can cover the low momentum region between 0.17 and 6GeV/c with a lever arm of 0.2m thus allowing complete coverage up to 240GeV/c in 2.0m total distance.

3. Gas Radiator with Mirror Focusing.

3.1 Reconstruction of the Cherenkov Angle.

The geometry of a gas radiator, mirror and a schematic detector is shown in Fig.1. The Z axis is chosen to be normal to the presumed flat detector plane window with its origin at C, the mirror center of curvature. Spherical windows will also be treated. The particle direction is defined by the polar angle θ_p relative to the Z axis and φ_p is the azimuthal angle defined by the projection of the direction vector on the XY plane relative to the X axis. It is assumed, that for each particle considered, a rotation

about the Z axis has been made so that the particle lies in the XZ plane (i.e. $\varphi_p=0$) as in Fig.1. The particle does not usually pass through C but has an impact parameter x_e relative to C. The PQR coordinate system is defined by a rotation of the ZXY system about the Y axis by the angle θ_p. In this system the photon emission is from the point $(z_e,x_e,0)$ and the particle direction is parallel to the P axis with constant Q coordinate (x_e). The unit vectors of the PQR system $(\vec{a}_p,\vec{b}_p,\vec{c}_p)$ are related to the unit vectors of the ZXY system $(\vec{k},\vec{i},\vec{j})$ by a rotation about the Y axis e.g.

$$\begin{aligned}\vec{a}_p&=\cos\theta_p\vec{k}+\sin\theta_p\vec{i}\\ \vec{b}_p&=-\sin\theta_p\vec{k}+\cos\theta_p\vec{i}\\ \vec{c}_p&=\vec{j}\end{aligned} \qquad (21)$$

The radius vector of the emission point $\vec{r}_e$ is used to define a unit vector

$$\begin{aligned}\vec{n}_e&=\vec{r}_e/r_e\\ \vec{r}_e&=z_e\vec{a}_p+x_e\vec{b}_p=u_e\vec{k}+v_e\vec{i}\end{aligned} \qquad (22)$$

with $u_e=z_e\cos\theta_p-x_e\sin\theta_p$ and $v_e=x_e\cos\theta_p+z_e\sin\theta_p$ the components of $\vec{r}_e$ in the ZXY system.The photon direction $\vec{a}$ is a second unit vector. It is defined relative to the particle direction in the PQR system as

$$\vec{a}=\cos\theta\,\vec{a}_p+\sin\theta\cos\varphi\,\vec{b}_p+\sin\theta\sin\varphi\,\vec{c}_p \qquad (23)$$

by θ the Cherenkov polar angle w.r.t. the P axis and φ the azimuthal angle w.r.t. the Q axis (i.e. $\varphi=0$ or π when photon emission is in the PQ plane). The photon detection point radius vector $\vec{r}$ allows the definition of a third unit vector

$$\begin{aligned}\vec{n}&=\vec{r}/r\\ \vec{r}&=z\,\vec{k}+x\,\vec{i}+y\,\vec{j}=u\vec{a}_p+v\vec{b}_p+w\vec{c}_p\end{aligned} \qquad (24)$$

with $u=z\cos\theta_p+x\sin\theta_p$, $v=x\cos\theta_p-z\sin\theta_p$ and $w=y$ the components of $\vec{r}$ in the PQR system. These three unit vectors $(\vec{n}_e,\vec{a},\vec{n})$ are sufficient to specify the optics of the problem.

The photon is emitted in a plane defined by the vectors $\vec{n}_e$ and $\vec{a}$ which also contains C hence this plane intercepts the spherical mirror and any spherical windows in concentric circles about C. The normals to these circles, at the photon intersection point, are also in this plane hence reflection or refraction from these surfaces leaves the photon in this plane. This is expressed by the equation for the detection point unit vector

$$\vec{n}=\mu\vec{n}_e+\nu\vec{a} \qquad (25)$$

where μ and ν are coefficients to be determined. Consider the three possible scalar products

$$\begin{aligned}
&\vec{n}\cdot\vec{n}_e=\cos\Omega=(zz_e+xx_e)\cos\theta_p/rr_e+(xz_e-zx_e)\sin\theta_p/rr_e \qquad (26)\\
&\vec{n}_e\cdot\vec{a}=\cos\Omega_e=(z_e\cos\theta+x_e\sin\theta\cos\varphi)/r_e\\
&\vec{a}\cdot\vec{n}=\cos\Omega'=[(z\cos\theta+x\sin\theta\cos\varphi)\cos\theta_p+(x\cos\theta-z\sin\theta\cos\varphi)\sin\theta_p\\
&\qquad\qquad +(y\sin\theta\sin\varphi)]/r
\end{aligned}$$

which are defined in terms of the angles (Ω_e,Ω) shown in Fig.1. The third angle $\Omega'=\Omega_e-\Omega$ because, from Eq.25, the three vectors form a closed triangle which relates the three angles. The angles (Ω_e,Ω) are the generalization of the emission and detection angles for non-zero impact parameter. Of the three relations of Eq.26 only Ω can be determined from the measured detection point (z,x,y), emission point (z_e,x_e) and particle direction (θ_p). To reconstruct the emission angle θ it is necessary to solve for the emission direction $\vec{a}$ from Eq.25 which requires (μ,ν) to be known. These can be found by taking the scalar product of Eq.25 with the each of the three unit vectors $\vec{n},\vec{a},\vec{n}_e$ to obtain the relations

$$\begin{aligned}
&\mu^2+\nu^2+2\mu\nu\cos\Omega_e \qquad (27)\\
&\cos\Omega'=\mu\cos\Omega_e+\nu\\
&\cos\Omega=\mu+\nu\cos\Omega_e
\end{aligned}$$

Solving for (μ,ν) from the last two equations gives

$$\begin{aligned}
&\mu=\sin\Omega'/\sin\Omega_e=\sin(\Omega_e-\Omega)/\sin\Omega_e \qquad (28)\\
&\nu=\sin\Omega/\sin\Omega_e
\end{aligned}$$

which satisfy also the first equation if $\Omega'=\Omega_e-\Omega$. Note that from the geometry of Fig.1 and the law of sines $r_m\sin\theta_m=r_e\sin\Omega_e=r\sin\Lambda$, $\Omega_a=\Omega_e-\theta_m$, $\Omega_b=\Lambda-\theta_m$ and $\Omega=\Omega_a+\Omega_b=\Omega_e+\Lambda-2\theta_m$ hence

$$\Omega=\Omega_e+\sin^{-1}(r_e\sin\Omega_e/r)-2\sin^{-1}(r_e\sin\Omega_e/r_m) \qquad (29)$$

where r_m is the mirror radius. This equation is exact for infinitely thin windows (no refraction). Since r_e, r_m, r and Ω are known Eq.29 can be

inverted to solve for Ω_e hence from Eq.'s 25 and 28 the photon polar and azimuthal angles at emission are

$$\begin{aligned}\cos\theta &= (u/r - \mu z_e/r_e)/v \\ &= (\sin\Omega_e/\sin\Omega)(z\cos\theta_p + x\sin\theta_p)/r - (\sin\Omega'/\sin\Omega)z_e/r_e \\ \tan\varphi &= (y/r)/(v/r - \mu x_e/r_e) \\ &= y/[(x\cos\theta_p - z\sin\theta_p) - r x_e \sin\Omega'/r_e\sin\Omega_e]\end{aligned} \qquad (30)$$

These equations reconstruct the Cherenkov angles from the measured variables (z,x,y,x_e,θ_p) and the presumed photon emission point (z_e) at the middle of the radiator. If the exact emission point were known and the measurements were exact then the reconstructed angles would be also exact with, for example, optical aberrations removed leaving only the intrinsic chromatic aberrations.

For a finite thickness spherical window (inner radius r_1, outer radius r_2, index n_w) it suffices to reduce Ω by a small amount Ω_w where

$$\begin{aligned}\Omega_w = &\sin^{-1}(r_e\sin\Omega_e/r_1) - \sin^{-1}(r_e\sin\Omega_e/r_2) \\ &-\sin^{-1}(r_e\sin\Omega_e/r_1 n_w) + \sin^{-1}(r_e\sin\Omega_e/r_2 n_w)\end{aligned} \qquad (31)$$

and replace Eq.29 by

$$\Omega = \Omega_e + \sin^{-1}(r_e\sin\Omega_e/r) - 2\sin^{-1}(r_e\sin\Omega_e/r_m) - \Omega_w \qquad (32)$$

and proceed as before to calculate (θ,φ) from Eq.'s30.

A finite thickness flat window will refract the incident photon and cause a parallel displacement s in the window plane

$$s = t * \tan\theta_r[1 - \cos\theta_r/(n_w^2 - \sin^2\theta_r)^{1/2}] \qquad (33)$$

where t is the window thickness and θ_r is the angle between the window normal $(-\vec{k})$ and the reflected photon direction. Assuming in zero'th order that the window has zero thickness (t=0) the Cherenkov angles (θ,φ) are calculated as before and used to obtain the incident angle θ_r. The photon direction $\vec{a}_r$ after mirror reflection is

$$\begin{aligned}&\vec{a}_r = \vec{a} - 2\cos\theta_m \vec{n}_m = \varepsilon\vec{a} - \lambda\vec{n}_e \\ &\varepsilon = \lambda\cos\Omega_e - \cos 2\theta_m \text{ and } \lambda = 2r_e\cos\theta_m/r_m\end{aligned} \qquad (34)$$

The components of $\vec{a}_r$ can be used with the zero'th order values of (θ,φ) to give the angles of incidence (θ_r,ϕ_r) via the relations

$$\vec{a}_r \cdot (-\vec{k}) = \cos\theta_r = \lambda u_e/r_e - \varepsilon(\cos\theta\cos\theta_p - \sin\theta\cos\varphi\sin\theta_p) \qquad (35)$$

$$\vec{a_r}\cdot\vec{i}=\sin\theta_r\cos\varphi_r=\varepsilon(\cos\theta\sin\theta_p+\sin\theta\cos\varphi\cos\theta_p)-\lambda v_e/r_e$$
$$\vec{a_r}\cdot\vec{j}=\sin\theta_r\sin\varphi_r=\varepsilon\sin\theta\sin\varphi$$

hence from Eq.33 the displacement s can be evaluated. The detected point (z,x,y) may then be corrected to (z',x',y') so as to remove the window refraction (i.e. the parallel displacement) via the equations

$$\begin{aligned} z' &= z \\ x' &= x+s*\cos\varphi_r \\ y' &= y+s*\sin\varphi_r \end{aligned} \qquad (36)$$

where s is from Eq.33 and (θ_r,φ_r) from Eq.35. This calculation should be iterated several times until the angles (θ_r,φ_r) become stable and the correction definitive. With this procedure Eq.30 allows reconstruction of the Cherenkov angles at emission even with a flat detector window.

3.2 Generation of the Image.

The points of the ring image may now be easily obtained using the formulation of the previous section. Given the particle direction (θ_p,φ_p) and the impact parameter x_e, the photon energy E and the photon emission point z_e then Eq.25 gives directly the detection point unit vector $\vec{n}$. To be useful the distance r must be found and refraction by a finite thickness window included. Several other effects must also be included so as to give a realistic simulation i.e. chromatic aberrations and multiple scattering. In addition, the number of emitted Cherenkov photons must be calculated which with reflection, transmission and quantum efficiency losses will allow the number of points of the image to be estimated.

3.2.1 Photon Emission Point (z_e).

The photon emission point (z_e) must be chosen randomly between a top limit $z_{et}=(r_m^2-x_e^2)^{1/2}$ fixed by the mirror and a bottom limit defined by the entry point of the particle into the radiating medium. This will be given by $z_{eb}=(r_2^2-x_e^2)^{1/2}$ if the gas volume is limited by a spherical entry window of inner radius r_1 and outer radius r_2 or by $z_{eb}=(z_2+x_e\sin\theta_p)/\cos\theta_p$ if the gas volume is defined by a flat window from z_1 to z_2. The full path length between entry point and mirror is $D=z_{et}-z_{eb}$. The path length before radiating is $PL=D*rd_1$ (where rd_1 is a random number) and the emission point coordinate $z_e=z_{eb}+PL$.

3.2.2 Number of Cherenkov Photons.

The number of photons which should be generated for a given ring image is obtained by integrating Eq.3 between(bottom and top) energy limits E_b and $E_t=E_b+\Delta E$ using Eq.'s 15 and 16 for the n(E) dependance. The result is

$$N_{ph}=(370eV^{-1}cm^{-1})(D/\beta^2)[W(E_t)-W(E_b)-\Delta E/\gamma^2] \quad (37)$$

with D the full path length in the radiator as given above and

$$W(E)=(3cE_0/4t)[X(E,E_+)-X(E,E_-)] \quad (38)$$

and

$$X(E,E_\pm)=(\xi_\pm-1/\xi_\pm)\ln[(E_\pm+E)/(E_\pm-E)] \quad (39)$$

where, as before, $c=.3738cm^3\rho/M$ and with the following definitions from the parameters of Eq.16: $F=F_1+F_2$, $E_0^2=(F_1E_2^2+F_2E_1^2)/F$, $e=(E_1^2+E_2^2)/F$, $g=E_1^2E_2^2/F$, $h=E_0^2/F$, $m=e+2c$, $s=g+2c$, $t=(0.25m^2-hs)^{1/2}$, $\xi_\pm=[(0.5m\pm t)/h]^{1/2}$ and $E_\pm=E_0\xi_\pm$. For solid radiators (Table 4), where the Lorentz-Lorenz fit function was $n^2-1=f(E)$, Eq.'s 37-39 hold if the factor 3c in Eq.38 is replaced by unity and the quantity 2c, in the definition of m and s, is also replaced by unity. A Poisson distribution with average N_{ph} should then be generated to obtain the correct integer number of photons.

3.2.2 Photon Energy and Chromatic Aberrations.

The photon energy is chosen between the minimum E_b and the maximum $E_t=E_b+\Delta E$ so as to satisfy the distribution of Eq.3. This distribution is dependant on photon energy because $\sin^2\theta=1-(\beta n)^{-2}$ and $n=n(E)$ via Eq.s 15 and 16. The photon energy is chosen as $E=E_b+rd_2*\Delta E$ (where rd_2 is a random number) and a probability $P(E)=\sin^2\theta(E)/\sin^2\theta(E_t)$ is defined. A new random number rd_3 is then chosen and if $rd_3\leq P(E)$ the photon energy is accepted, otherwise a new photon energy is chosen and the process repeated until the condition is satisfied. Once the energy is known the Cherenkov angle $\theta=\cos^{-1}[1/\beta n(E)]$ is directly calculated and the azimuthal angle φ is chosen randomly between 0 and 2π.

3.2.3 Multiple Scattering before Radiating.

Without multiple scattering the emitted photon direction has polar and azimuthal angles (θ,φ) as defined in the preceeding section relative to the particle direction $\vec{a}_p$(see Eq.23). Multiple scattering of the particle by the radiator medium up to the emission point z_e changes the particle direction slightly. This change can be equally well attributed to slightly changed emission angles (θ',ϕ').The relations between these angles are

$$\begin{aligned}\cos\theta'&=\cos\theta\cos\psi-\sigma\sin\theta\sin\psi \quad (40)\\ \sin\theta'\cos\varphi'&=\sin\theta\cos\varphi+\tau\cos\eta\\ \sin\theta'\sin\varphi'&=\sin\theta\sin\varphi+\tau\sin\eta\end{aligned}$$

where (ψ,η) are the (polar,azimuthal) multiple scattering angles,$\sigma=\cos(\phi-\eta)$ and $\tau=\cos\theta\sin\psi-\sigma\sin\theta(1-\cos\psi)$. The space angle ψ is given by the formula

$$\psi=\psi_0*(-PL*\ln rd_4)^{1/2} \qquad (41)$$

where $\psi_0=.0212GeV/pc\beta\sqrt{X_0}$ and X_0 is the radiation length of the radiator medium. The factor $(-\ln rd_4)^{1/2}$ has been inserted to obtain the correct exponential space angle distribution. The end result of this section is to replace the Cherenkov angles (θ,φ) by the slightly altered pair (θ',φ') which are relabeled (θ,φ).

3.2.4 Photon Conversion Point (z,x,y)

3.2.4.1 Spherical Window.

For a finite thickness spherical window (outer radius r_2,inner radius r_1, index n_w). Knowing $(z_e, x_e, \theta, \varphi)$ allows Ω_e to be calculated via Eq.26 and hence $\Omega_1=\Omega(r=r_1)$ via Eq.'s 31,32. The point (z_1,x_1,y_1) at which the photon enters the detector is from Eq.25

$$\vec{r}_1=r_1\vec{n}_1=r_1(\mu_1\vec{n}_e+\nu_1\vec{a}) \qquad (42)$$

with $\mu_1=\sin(\Omega_e-\Omega_1)/\sin\Omega_e$, $\nu_1=\sin\Omega_1/\sin\Omega_e$ and the ZXY components of n_e and a from Eq.'s 21-23. The conversion point in the detector is obtained by calculating, as above, the detection unit vector on a referance spherical surface (say five absorption lengths λ_{ph} inside the inner window) hence $r_0=r_1-5\lambda_{ph}$. The direction of the photon $\vec{a}_r'$ inside the detector is then obtained from the obvious vector equation

$$q_{01}\vec{a}_r'=r_0\vec{n}_0-r_1\vec{n}_1=d_{01}\vec{n}_e+h_{01}\vec{a} \qquad (43)$$

where from Eq.25 $d_{01}=r_0\mu_0-r_1\nu_1$, $h_{01}=r_0\nu_0-r_1\nu_1$ and q_{01} determined by the requirement that $\vec{a}_r'$ be a unit vector hence

$$q_{01}=(d_{01}^2+h_{01}^2+2d_{01}h_{01}\cos\Omega_e)^{1/2} \qquad (44)$$

The conversion point is then directly given by

$$\vec{r}=\vec{r}_1+q_d\vec{a}_r' \qquad (45)$$

with $q_d=\lambda_{ph}(-\ln rd_5)^{1/2}$ such that the photon absorption is exponential with mean free path λ_{ph}.

The incidence angle of the photon onto the spherical surface $r=r_2$ is θ_{r2} where from the geometry of Fig.1

$$\theta_{r2}=\sin^{-1}(r_e\sin\Omega_e/r_2) \qquad (46)$$

hence the refraction angle into the window is from Snells law

$$\theta_{w2}=\sin^{-1}(n_r\sin\theta_{r2}/n_w)=\sin^{-1}(r_e\sin\Omega_e/r_2n_w) \qquad (47)$$

where the index of the radiator n_r is taken as unity in this context. It is now possible to calculate the reflectivity R_2 from this surface from the Fresnel equation for p-polarized light i.e.

$$R_2=[(\cos\theta_{w2}-n_w\cos\theta_{r2})/(\cos\theta_{w2}+n_w\cos\theta_{r2})]^2 \qquad (48)$$

To obtain the reflectivity R_1 from the $r=r_1$ surface the photon direction $\vec{a}_w$ inside the window is obtained, as above, from the known unit vectors $\vec{n}_1$ and $\vec{n}_2$ as

$$\vec{a}_w=(\vec{n}_1-\vec{n}_2)/q_{12}=(d_{12}\vec{n}_e+h_{12}\vec{a})/q_{12} \qquad (49)$$

where d_{12},h_{12} and q_{12} are defined as in Eq.'s 43,44. The angle of incidence onto this surface is obviously $\theta_{w1}=\cos^{-1}(-\vec{n}_1\cdot\vec{a}_w)$ and the refracted angle $\theta_{r1}=\sin^{-1}(n_w\sin\theta_{w1}/n_r)$ hence the reflectivity

$$R_1=[(n_w\cos\theta_{r1}-\cos\theta_{w1})/(n_w\cos\theta_{r1}+\cos\theta_{w1})]^2 \qquad (50)$$

Given the mirror reflectivity R, the window reflectivities R_1,R_2 , the bulk window transmittivity T and the quantum conversion efficiency Q the image generation program can then give a realistic estimate of the number N of photoelectrons of the image.

3.2.4.2 Flat Window.

For a flat window between $z=z_1$ to z_2 the photon entry point is given by the vector equations $\vec{r}_2=r_m+q_r\vec{a}_r$ and $\vec{r}_m=r_e+q\vec{a}$ (where $\vec{a}_r$ is from Eq.34 and $q=r_m\cos\theta_m-r_e\cos\Omega_e$ from the geometry of Fig.1) hence the z component gives

$$q_r=(z_2-r_en_{ez}-qa_z)/(\varepsilon a_z-\lambda n_{ez}) \qquad (51)$$

where the ZXY components of n_e and a are (from Eq.'s 21-23) $n_{ez}=u_e/r_e$, $n_{ex}=v_{e/}r_e$, $a_z=\cos\theta\cos\theta_p-\sin\theta\cos\phi\sin\theta_p$, $a_x=\cos\theta\sin\theta_p+\sin\theta\cos\phi\cos\theta_p$ and $a_y=\sin\theta\sin\phi$. The entry point may then be explicitly written as

$$x_2=n_{ex}(r_e-\lambda q_r)+a_x(q+\varepsilon q_r) \qquad (52)$$
$$y_2=a_y(q+\varepsilon q_r).$$

The incidence photon direction a_r (Eq.34) defines angles (θ_r,φ_r) w.r.t. the window normal $(-\vec{k})$ e.g.

$$\cos\theta_r = \vec{a}_r\cdot(-\vec{k}) = \lambda n_{ez} - \varepsilon a_z \qquad (53)$$
$$\sin\theta_r\cos\varphi_r = \vec{a}_r\cdot\vec{i} = \varepsilon a_x - \lambda n_{ex}$$
$$\sin\theta_r\sin\varphi_r = \vec{a}_r\cdot\vec{j} = \varepsilon a_y$$

and the refracted ray in the window satisfies the equation $n_w\vec{a}_w = n_r\vec{a}_r - K\vec{k}$. The three component equations require $n_w\sin\theta_w = \sin\theta_r$, $\varphi_w = \varphi_r$ and $K = n_w\cos\theta_w - \cos\theta_r = (n_w^2 - \sin^2\theta_r)^{1/2} - \cos\theta_r$. The exit point is then $\vec{r}_1 = \vec{r}_2 + q_w\vec{a}_w$ where $q_w = (z_2 - z_1)/\cos\theta_w$ and the conversion point in the detector $\vec{r} = \vec{r}_1 + q_d\vec{a}_r$ hence

$$z = z_1 - q_d\cos\theta_r \qquad (54)$$
$$x = x_1 - q_d\sin\theta_r\cos\varphi_r = x_2 - (q_d + q_w/n_w)\sin\theta_r\cos\varphi_r$$
$$y = y_1 - q_d\sin\theta_r\sin\varphi_r = y_2 - (q_d + q_w/n_w)\sin\theta_r\sin\varphi_r$$

where $q_d = \lambda_{ph}(-\ln rd_5)^{1/2}$ is the photon path length in the detector as given in the preceeding section. The reflection at the $z=z_2$ surface is from Fresnels equation

$$R_2 = [(\cos\theta_w - n_w\cos\theta_r)/(\cos\theta_w + n_w\cos\theta_r)]^2 \qquad (55)$$

and at the $z=z_1$ surface $R_1 = R_2$.

3.3 Measurement Errors.

The dependance of the reconstructed Cherenkov angle on the measured variables $v_i = (z_e, x_e, z, x, y, \theta_p)$ may now be simply expressed by the partial derivatives of the first of Eq.'s 30 i.e.

$$\sin\theta\,\partial\theta/\partial v_i = A\,\partial\Omega_e/\partial v_i + B\,\partial\Omega/\partial v_i + M_i \qquad (56)$$
$$M_i = (\sin\Omega'/\sin\Omega)\partial(z_e/r_e)/\partial v_i - (\sin\Omega_e/\sin\Omega)\partial(u/r)/\partial v_i$$
$$A = (z_e\cos\Omega'/r_e - u\cos\Omega_e/r)/\sin\Omega$$
$$B = (\sin\Omega_e/\sin^2\Omega)(u\cos\Omega/r - z_e/r_e)$$
$$u = z\cos\theta_p + x\sin\theta_p,\quad v = x\cos\theta_p - z\sin\theta_p$$

The derivatives of Ω are obtained from the first of Eq.'s 26 as

$$L_i = \partial\Omega/\partial v_i = (\partial\ln(rr_e)/\partial v_i)/\tan\Omega - [\partial(uz_e + vx_e)/\partial v_i]/rr_e\sin\Omega \qquad (57)$$

and the derivatives of Ω_e ($\partial\Omega_e/\partial v_i = N_i$) are, from Eq.29, related to those of Ω ($\partial\Omega/\partial v_i = L_i$) by the relation

$$N_i = (L_i + K_i)/(1 + Jr_e\cos\Omega_e) \qquad (58)$$
$$K_i = (r_e\sin\Omega_e/r^2\cos\Lambda)\partial r/\partial v_i - J\sin\Omega_e\partial r_e/\partial v_i$$
$$J = 1/r\cos\Lambda - 2/r_m\cos\theta_m \text{ with } r_e\sin\Omega_e = r\sin\Lambda = r_m\sin\theta_m$$

hence Eq.56 becomes

$$\sin\theta\partial\theta/\partial v_i = EK_i + FL_i + M_i \qquad (59)$$

$E=A/(1+Jr_e\cos\Omega_e)$ and $F=B+E$.

Explicit forms for the coefficients K_i, L_i, M_i are summarized in Table 5.

3.3.1 Emission Point Error (z_e).

We consider the errors for the most sensitive part of the combined radiator system (described in Section 2) consisting of 1400mm of CF_4 gas with a r_m=3600mm mirror, a flat quartz seperator plate at z_{eb}=2200mm and the detector near the focal plane at r=1800mm. The emission point error $\sigma_\theta(z_e)$ is shown in Fig.5 versus the azimuthal Cherenkov angle ϕ for detection radii at r=1794,1800,1810mm and for impact parameter between 0 and 80mm. As may be noted from the figure this error is ϕ dependant however, for the range of radii r and impacts x_e considered, it is smaller than the chromatic error $\sigma_\theta(E)$=60μr (see Table 4). The two extreme radii (1794 and 1810) are chosen because they give a ϕ averaged error of about half the chromatic error. To achieve this error level will require that the photon conversion point be kept within ±8mm of the best focal surface at r=1802mm. This also defines the maximum radius $r_d=(1810^2-1794^2)$=225mm of a flat detector plane assuming that the photon absorption length λ_{ph}<<8mm. A spherical windowed detector whose inner radius $r_1=(1802mm+\lambda_{ph})$ would have no such size limitation as concerns emission point errors. This error is independant of θ_p since Eq.59 is rotationally invariant for the variable $v_i=z_e$.

The corresponding errors for the C_5F_{12} (γ_t=17) part of the combined radiator consisting of 400mm of C_5F_{12} gas between the quartz seperator plate at z_{et}=2200mm and the detector near the r=1800mm focal plane of the same r_m=3600mm mirror. The ϕ averaged emission point error is less than half the chromatic error of 166μr for a detection radius 1765<r<1835mm which is easily satisfied by a detector designed for CF_4.

3.3.2 Conversion Depth Error $\sigma_\theta(z)$

The derivative $\partial\theta/\partial z$ (Eq.59) is independant of r but depends on the particle direction θ_p. The ϕ averaged derivative (for the CF_4 radiator example) is found to be linear in both θ_p and x_e with the specific values $\partial\theta/\partial z=-.11+3.5\theta_p+.193x_e$ (θ_p in radians, x_e in mm and $\partial\theta/\partial z$ in μr/mm). For θ_p=.3 and for a depth measurement error $\sigma_z=\lambda_{ph}$=0.5mm this error ranges between 47 and 54μr for x_e between 0 and 80mm. This is an indication of its magnitude however the actual error $\sigma_\theta(z)=(\partial\theta/\partial z)\sigma_z$ is ϕ dependant as shown in Fig.6 for θ_p=0 and .2 and for x_e between 0 and 80mm. Even though this error is not sensitive to the focal position it must be measured

accurately ($\sigma_z \cong 0.5$mm) so as to not become the dominant error source. This will require a short photon conversion length or a high accuracy drift time measurement of the photon conversion depth.

3.3.3 Impact Parameter Error $\sigma_\theta(x_e)$

This derivative $\partial\theta/\partial x_e$ (Eq.59) is independant of θ_p but does depend on r,ϕ and x_e however its magnitude is very small. The ϕ averaged derivative $\partial\theta/\partial x_e < 2\mu r/mm$ (for the CF_4 radiator example) for $1794<r<1810$ and $0<x_e<80$mm hence a modest measurement of the impact parameter suffices i.e. $\sigma_{xe}=5$mm.

3.3.4 Pixel Position Errors $\sigma_\theta(x)$, $\sigma_\theta(y)$

This is one of the dominant non-chromatic errors. At $x_e=\theta_p=0$ the z_e averaged derivatives reduce to $\partial\theta/\partial x=\cos\theta\cos\phi/r$ and $\partial\theta/\partial y=\cos\theta\sin\phi/r$ which, when combined in quadrature, has a value of 555μr/mm (for the CF_4 radiator example). In order that this error not dominate it will be necessary to achieve pixel resolutions $\sigma_x=\sigma_y=100\mu$m. A pad detector with $1\,mm^2$ pads can attain this resolution by measuring the center of gravity (analog or digital?) of the induced pad signal.

3.3.5 Particle Direction Error $\sigma_\theta(\theta_p)$

The relavant derivative $\partial\theta/\partial\theta_p$ is very closely equal to $\cos\phi$ for radii r near the focal plane ($\pm$50mm) and independant of θ_p and x_e. A minimization of the total error σ_θ by varying θ_p does in fact serve to measure θ_p with error $\sigma_{\theta_p}=\sigma_\theta/(\partial\theta/\partial\theta_p)$.

3.3.6 Total Measurement Error $\sigma_\theta(m)$

This is the error sum, in quadrature, from the measurements of z_e,x_e,z,x and y (Sections 3.3.1 to 3.3.4). It is shown in Fig.7 (for the CF_4 radiator example) for θ_p=0,.2,.3 and for x_e between 0 and 80mm at detection radius r=1800 (very similar curves apply at 1794 and 1810mm).

In calculating these curves measurement errors of $\sigma_{z_e}=1400/\sqrt{12}=404$mm, $\sigma_{x_e}=.29$mm, $\sigma_z=.6$mm, $\sigma_x=\sigma_y=1\,mm*cg/\sqrt{12}$ have been assumed (cg=1/3 from digital? or analog center of gravity). This error is evidently ϕ dependant as is the total error σ_θ which is the sum, in quadrature, of $\sigma_\theta(m)$ and the chromatic error $\sigma_\theta(E)=60\mu$r. The total error in this case is minimum (86μr) near $\phi=90^\circ$ and maximum (110μr) at $\phi=0,180^\circ$. The reconstructed Cherenkov angle (Eq.30) should be weighted by $1/\sigma_\theta^2$ to obtain the best resolution and the sharpest peaks for pattern recognition (identification of the photoelectrons belonging to a given ring image). The degradation of the total error from the chromatic limit of 60μr to a ϕ averaged value of 85μr entails a 42% increase of the Cherenkov constant k_c

(Table 4) and a 19% decrease of the π/K momentum separation limit to 205Gev/c (Eq.6, $n_\sigma=3$).

4. Summary and Acknowledgements.

Limits for the particle detection capability of ring imaging Cherenkov detectors and an error analysis are presented. An analytical method for generating and reconstructing ring images is given which removes certain aberrations and optimizes pattern recognition. New unpublished measurements of refractive indices of low chromatic dispersion fluorocarbons, useful as RICH radiators, are included.

I wish to acknowledge and thank my colleague Jacques Séguinot for his collaboration in all phases of our common research. The work reported here is part of the LAA project.

TABLE 1

Sellmeir Fits to Molar Refractivity $f(E)=F_1/(E_1^2-E^2)+F_1/(E_2^2-E^2)$

MOLECULE	E_1(eV)	E_2(eV)	F_1(eV^2)	F_2(eV^2)
He	23.389	40.412	451.53	788.71
Ne	17.419	45.501	278.09	3625.9
Ar	13.084	24.217	791.68	3794.0
Kr	11.500	19.790	851.67	4034.7
Xe	8.885	25.358	813.16	10961.
H_2	12.884	20.250	638.90	653.34
N_2	13.414	23.215	921.28	3569.6
O_2	13.936	16.872	1505.6	810.94

TABLE 2

Liquid Refractive Index $n=a+bE$

MOLECULE	a	b(eV^{-1})	ρ(g/cm^3)	M(g/mole)	B.P.(K)
CF_4	1.2039	.00475	1.603	88	146
C_2F_6	1.1956	.00746	1.608	138	195
C_4F_{10}	1.2037	.01025	1.594	238	265
C_5F_{12}	1.2109	.00785	1.63	288	303
C_6F_{14}	1.2177	.00928	1.68	338	329

TABLE 3

Sellmeir Fits to Refractivity $f(E)=F_1/(E_1^2-E^2)+F_2/(E_2^2-E^2)$

SOLID	f(E)	E_1(eV)	E_2(eV)	F_1(eV^2)	F_2(eV^2)
CaF_2	n^2-1	12.350	24.667	71.855	345.36
Fused Quartz	n^2-1	10.666	18.125	46.411	228.71
NaF	$(n^2-1)/(n^2+2)$	10.435	18.275	2.5764	57.788

TABLE 4

Chromatic Errors for Gas Radiators (1 bar,40°C) and a TMAE Detector (6.1 to 7.1eV triangular response, N=65cm^{-1},N=9 photoelectrons).

		(μr)		(m)		(Gev/c)
GAS	γ_t	$\sigma_\theta(E)$	$\sigma_\theta(E)/\theta$	L(N=9)	k_c*10^8	$p_{K\pi}(n_\sigma=3)$
He	124	18	.00224	21.3	4.84	877
Ne	90	26	.00236	11.2	9.60	622
Ar	42	151	.00627	2.4	120.	176
Kr	33	274	.00900	1.5	277.	116
Xe	24	941	.02220	0.8	1307.	53
N_2	41	153	.00618	2.3	124.	173
CF_4	32	60	.00194	1.4	62.5	244
C_2F_6	25	115	.00291	.87	153.	156
C_5F_{12}	17	166	.00284	. 40	325.	107

TABLE 5

The Coefficients K_i, L_i, M_i Needed to Evaluate Eq.29: $\sin\theta\partial\theta/\partial v_i = EK_i + FL_i + M_i$

v_i	K_i	L_i	M_i
z_e	$-Jz_e\sin\Omega_e/r_e$	$(z_e\cos\Omega/r_e - u/r)/r_e\sin\Omega$	$x_e^2\sin\Omega'/r_e^3\sin\Omega$
x_e	$-Jx_e\sin\Omega_e/r_e$	$(x_e\cos\Omega/r_e - v/r)/r_e\sin\Omega$	$-x_e z_e\sin\Omega'/r_e^3\sin\Omega$
z	$zr_e\sin\Omega_e/r^3\cos\Lambda$	$(z\cos\Omega/r - u_e/r_e)/r\sin\Omega$	$(uz - z_p r^2)\sin\Omega_e/r^3\sin\Omega$
x	$xr_e\sin\Omega_e/r^3\cos\Lambda$	$(x\cos\Omega/r - v_e/r_e)/r\sin\Omega$	$(ux - x_p r^2)\sin\Omega_e/r^3\sin\Omega$
y	$yr_e\sin\Omega_e/r^3\cos\Lambda$	$y\cos\Omega/r^2\sin\Omega$	$uy\sin\Omega_e/r^3\sin\Omega$
θ_p	0	$(ux_e - vz_e)/rr_e\sin\Omega$	$-v\sin\Omega_e/r\sin\Omega$

with $z_p=\cos\theta_p$, $x_p=\sin\theta_p$, $u=zz_p+xx_p$, $v=xz_p-zx_p$, $u_e=z_ez_p-x_ex_p$, $v_e=x_ez_p+z_ex_p$, $J=1/r\cos\Lambda-2/r_m\cos\theta_m$, $r_e\sin\Omega_e=r\sin\Lambda=r_m\sin\theta_m$, $A=(z_e\cos\Omega'/r_e-u\cos\Omega_e/r)/\sin\Omega$ $B=(u\cos\Omega/r-z_e/r_e)\sin\Omega_e/\sin^2\Omega$, $E=A/(1+Jr_e\cos\Omega_e)$, $F=B+E$.

REFERANCES

[1] R.Arnold et. al. Nucl. Instr. and Methods A270 (1988) 289.
[2] Langhoff and Karplus. Jour. Opt. Soc. Amer. 59 (1969) 863.
[3] J.Seguinot and T.Ypsilantis. Nucl. Instr. and Methods to be published.
[4] M.Hempstead, J.Chaveau, G.Comby, J.Seguinot and T.Ypsilantis. Nucl. Instr. and Methods to be published.

FIGURE CAPTIONS

Fig.1. Geometry of Gas Radiator with Mirror.Photon Emission from the point $(z_e,x_e,0)$ of the PQR coordinate system. Photon Detection at the point (z,x,y) of the ZXY system.

Fig.2. Experimental Setup for the Liquid Refractive Index Measurements

Fig.3. Measured Refractive Indices (points) of some Fluorinated Alkanes and the fits to n=a+bE (solid lines).

Fig.4. Particle I.D Limits for Three Radiators: 1cm liquid C_6F_{14} with proximity focusing and 0.2m lever arm; 40cm of C_5F_{12} gas with mirror focusing (f=1.8m); 140 cm of CF_4 gas with mirror focusing (f=1.8m). The thin lines show the region where particle ID is by threshold and the thicker lines the region where particle ID is by the size of the ring image. The top limit corresponds to $n_\sigma=3$.

Fig.5. Emission point error $\sigma_\theta(z_e)$ versus the azimuthal Cherenkov angle ϕ for detection radii r of 1794,1800,1810mm and impact parameter x_e between o and 80mm. Other fixed parameters are $r_m=3600mm$, $z_{eb}=2200mm$, $z_{et}=(r_m^2-x_e^2)^{1/2}$ with a CF_4 gas radiator (1 bar, 40 C, $\gamma_t=31$).

Fig.6. Conversion depth error $\sigma_\theta(z)$ versus the azimuthal Cherenkov angle ϕ for particle directions $\theta_p=0$ and 0.2 and impact parameter x_e between 0 and 80mm. Other fixed parameters are as in Fig.5.

Fig.7. Total non-chromatic error $\sigma_\theta(m)$ due to measurement errors of the photon emission point (z_e,x_e) and detection point (z,x,y) versus azimuthal Cherenkov angle ϕ for r=1800mm, θ_p between 0 and .3 and x_e between 0 and 80mm. Other fixed parameters are as in Fig.5. The measurement errors are given in the text of Section 3.3.6.

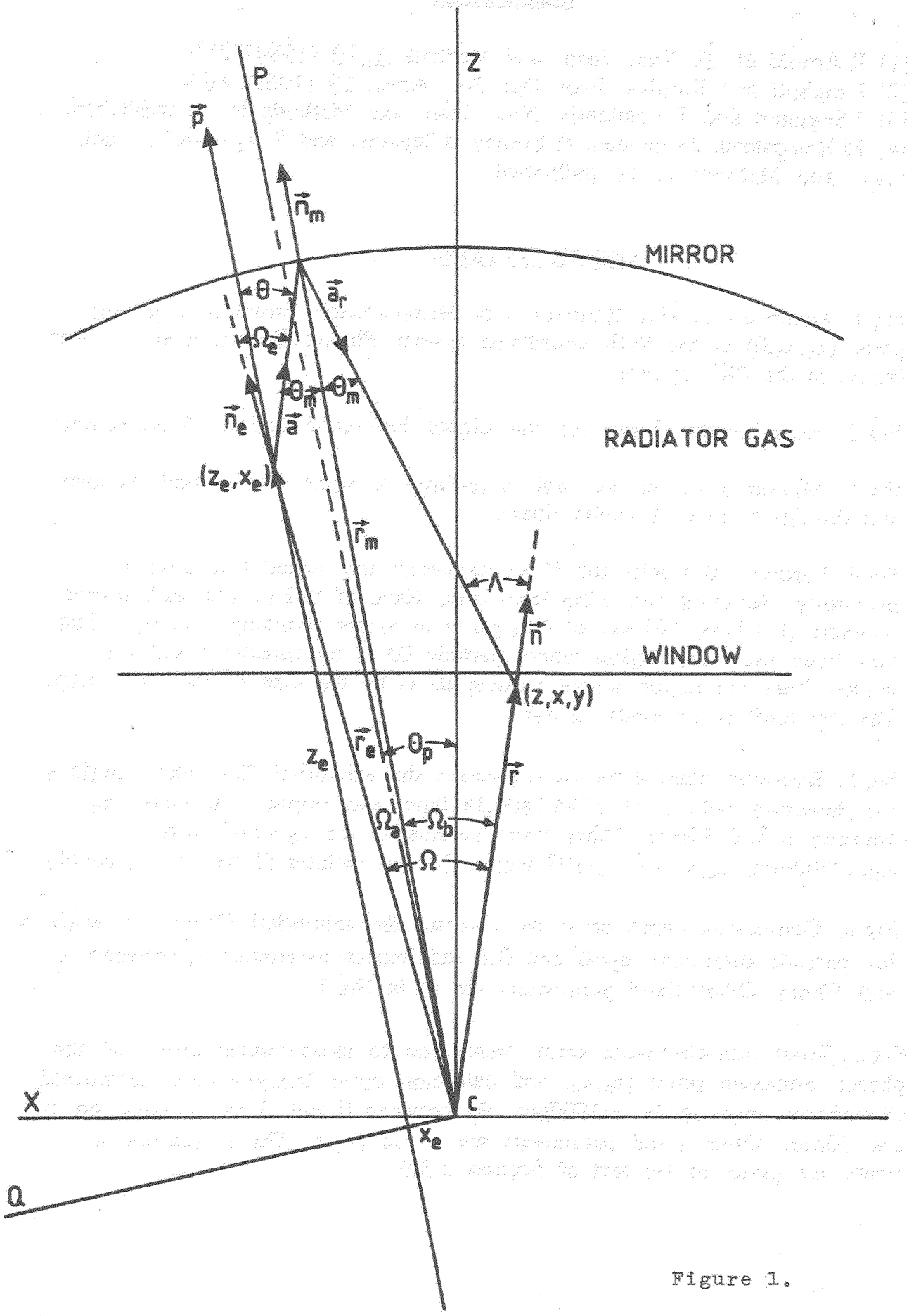
P
Z
$\vec{p}$
$\vec{n}_m$
MIRROR
θ
$\vec{a}_r$
Ω_e
θ_m
θ_m
$\vec{n}_e$
$\vec{a}$
RADIATOR GAS
(z_e, x_e)
$\vec{r}_m$
Λ
$\vec{n}$
WINDOW
(z,x,y)
z_e
$\vec{r}_e$
θ_p
$\vec{r}$
Ω_e
Ω_b
Ω
X
C
x_e
Q

Figure 1.

Figure 2.

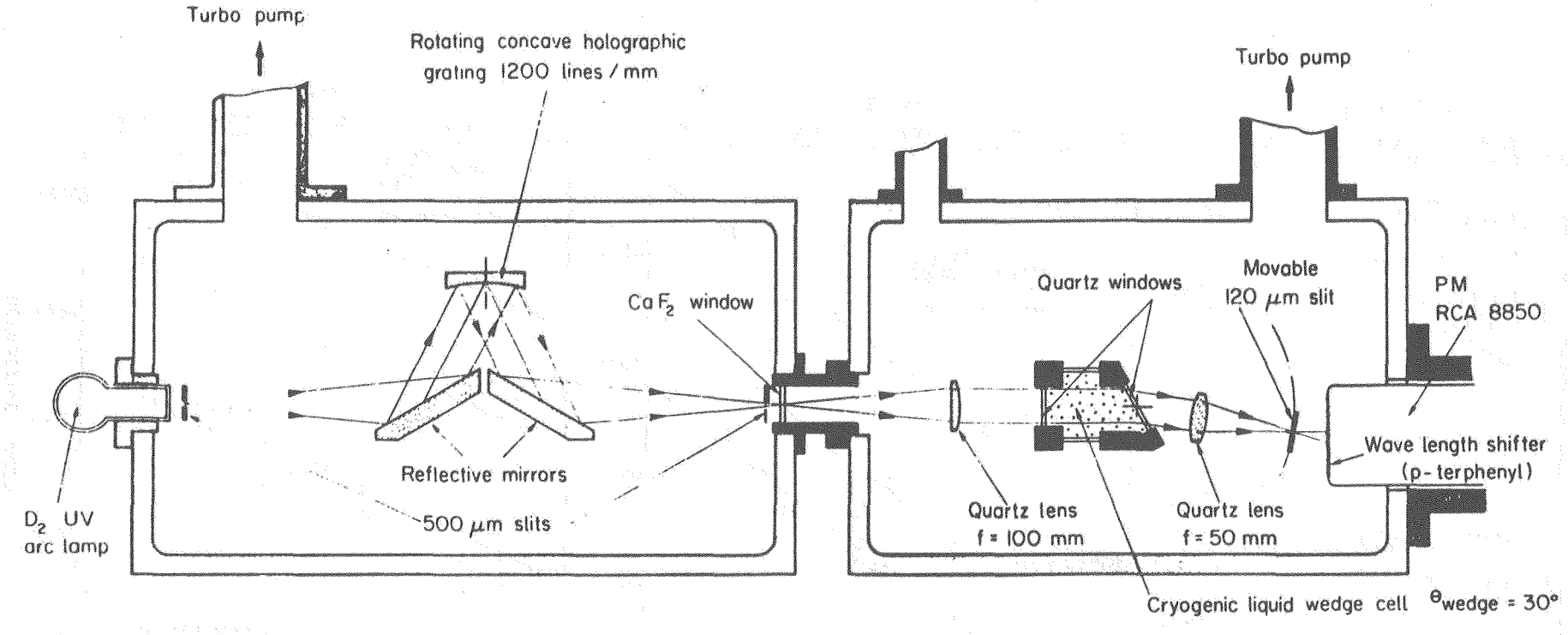

MONOCHROMATOR

(resolution 4 nm / mm)

REFRACTOMETER

$$n = \frac{\sin(\theta_w + \theta_d)}{\sin \theta_w}$$

θ_d = deflection angle (cell full - cell empty)

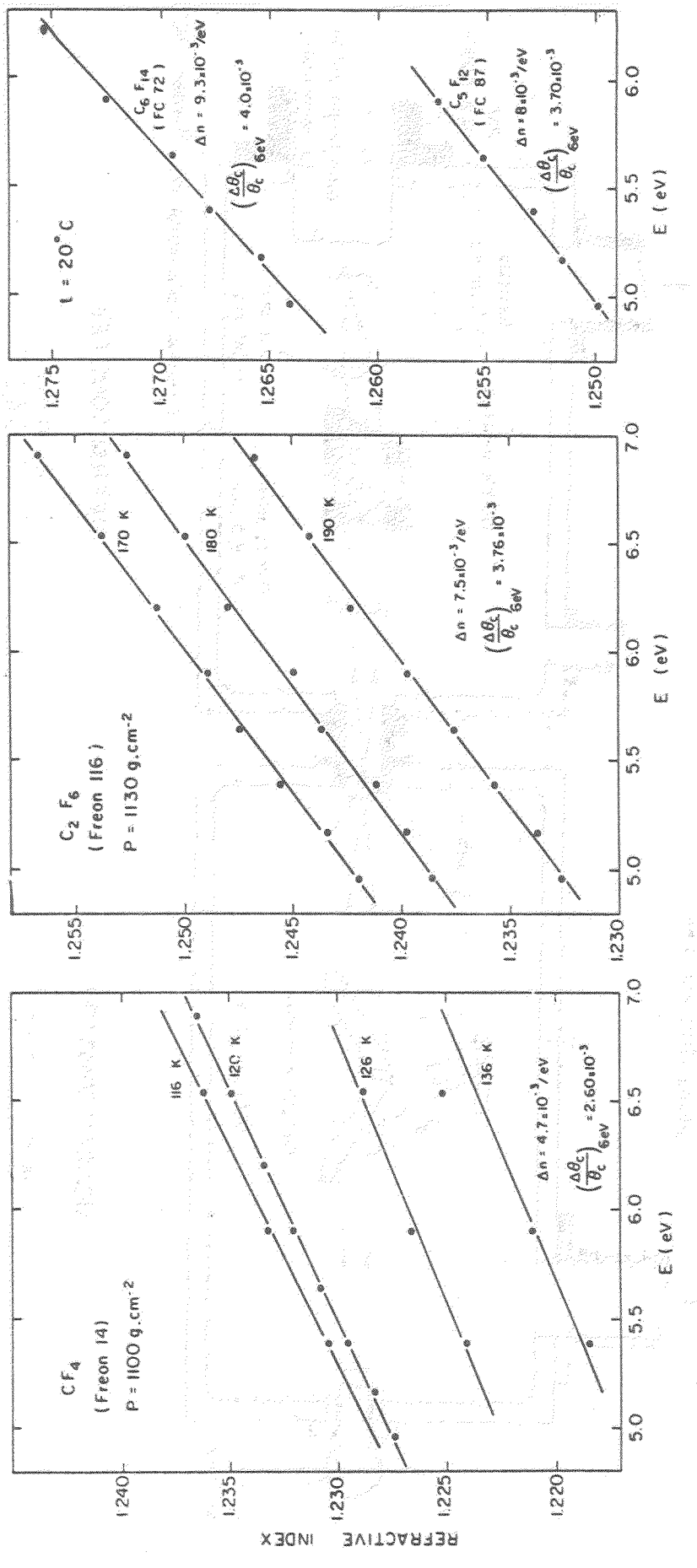
REFRACTIVE INDEX
E (eV)
CF4
(Freon 14)
P = 1100 g.cm-2
116 K
120 K
126 K
136 K
Δn = 4.7×10-3/eV
(Δθc/θc)6eV = 2.60×10-3
C2 F6
(Freon 116)
P = 1130 g.cm-2
170 K
180 K
190 K
Δn = 7.5×10-3/eV
(Δθc/θc)6eV = 3.76×10-3
t = 20°C
C6 F14
(FC 72)
Δn = 9.3×10-3/eV
(Δθc/θc)6eV = 4.0×10-3
C5 F12
(FC 87)
Δn = 8×10-3/eV
(Δθc/θc)6eV = 3.70×10-3

Figure 3.

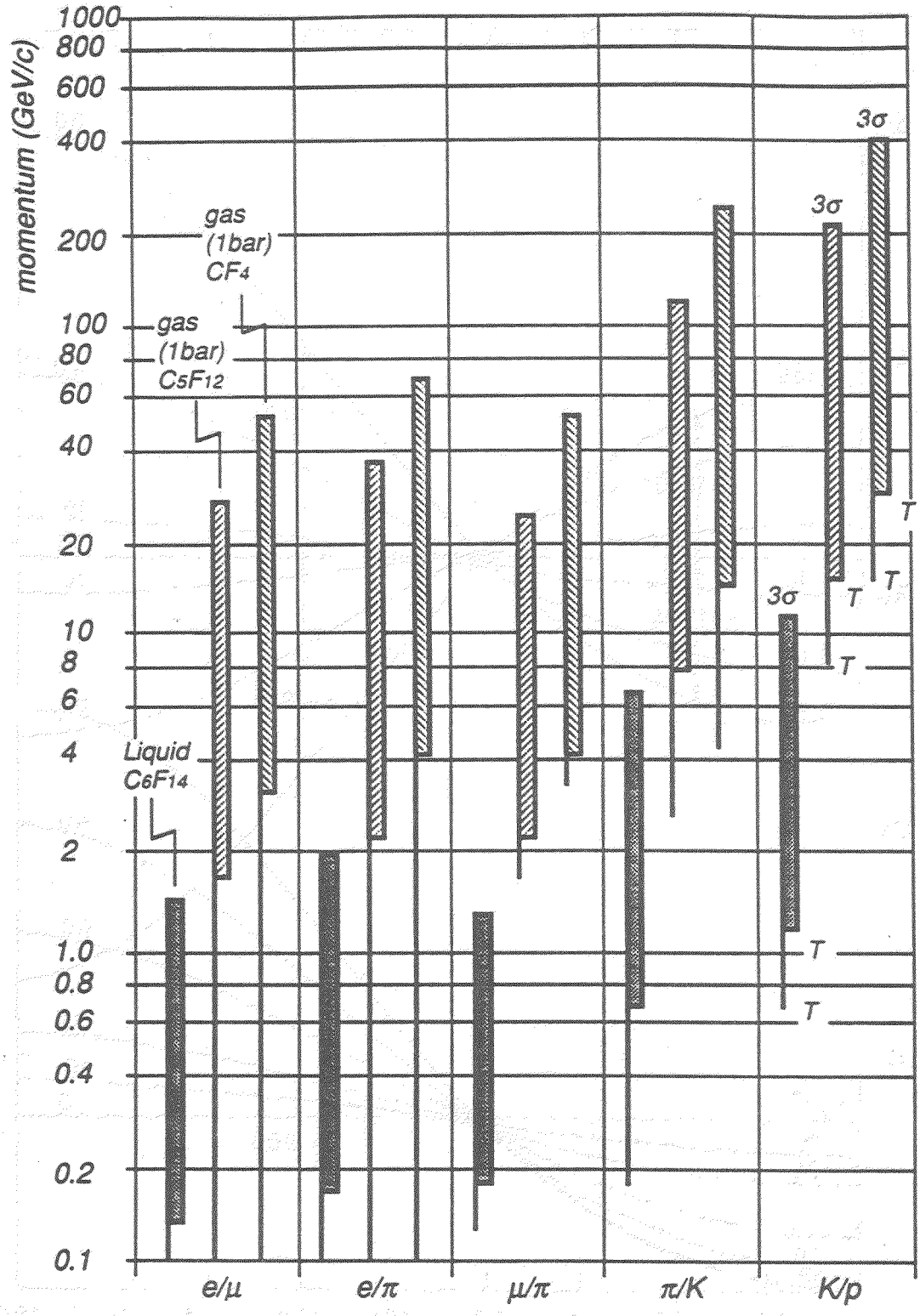
momentum (GeV/c)
1000
800
600
400
200
100
80
60
40
20
10
8
6
4
2
1.0
0.8
0.6
0.4
0.2
0.1
gas (1bar) CF4
gas (1bar) C5F12
Liquid C6F14
3σ
3σ
3σ
T
T
T
T
T
T
e/μ
e/π
μ/π
π/K
K/p

Figure 4.

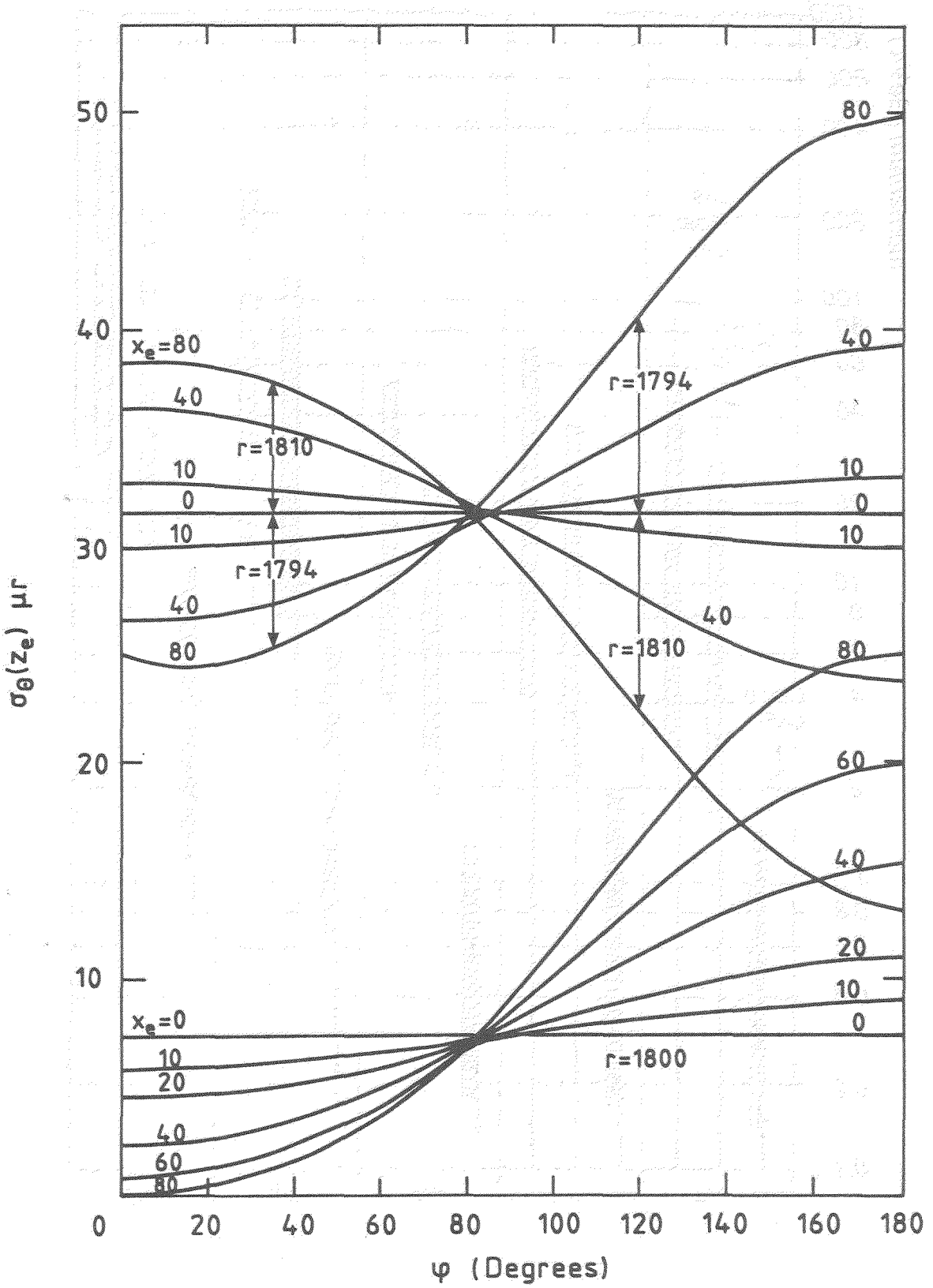
50
40
30
20
10
0
20
40
60
80
100
120
140
160
180
φ (Degrees)
σθ(ze) μr
xe=80
40
10
0
10
40
80
r=1810
r=1794
80
40
10
0
10
40
80
r=1794
r=1810
60
40
20
10
0
r=1800
xe=0
10
20
40
60
80

Figure 5.

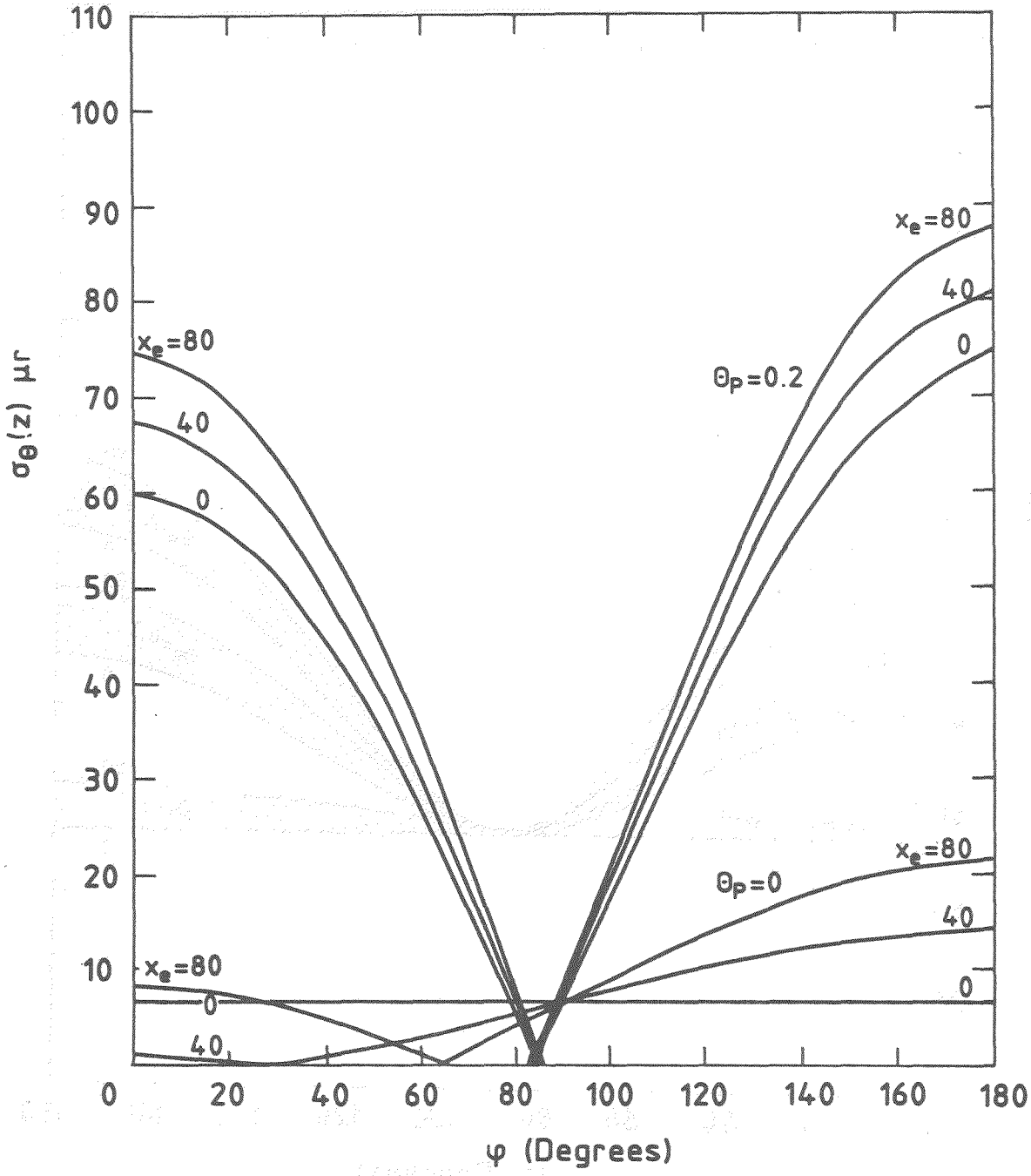
110
100
90
80
70
60
50
40
30
20
10
0
20
40
60
80
100
120
140
160
180
σθ(z) μr
φ (Degrees)
xe=80
40
0
Θp=0.2
xe=80
40
0
Θp=0
xe=80
40
0
xe=80
0
40

Figure 6.

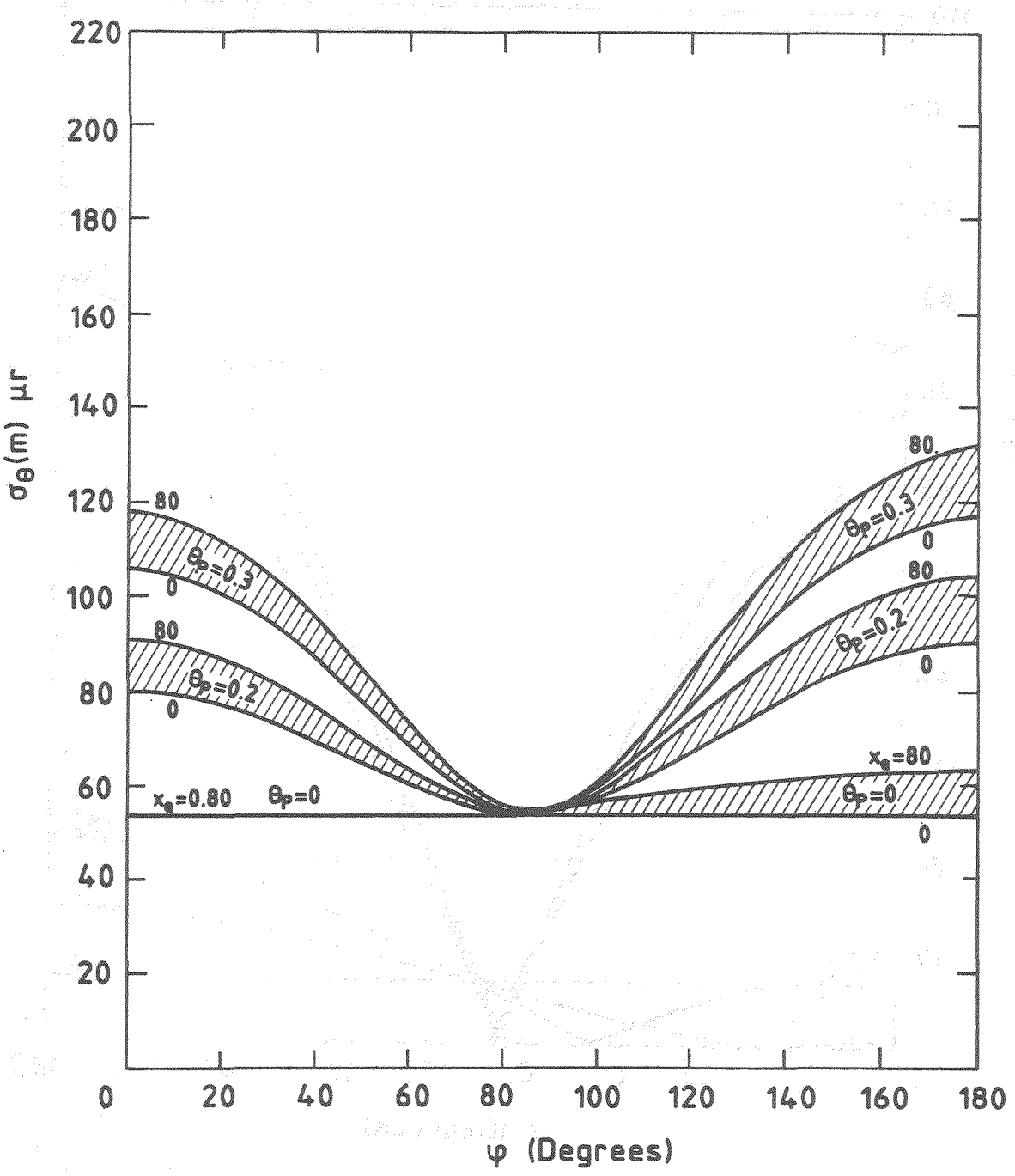
220
200
180
160
140
120
100
80
60
40
20
0
20
40
60
80
100
120
140
160
180
σθ(m) μr
φ (Degrees)
80
θp=0.3
0
80
θp=0.2
0
xe=0.80
θp=0
80
θp=0.3
0
80
θp=0.2
0
xe=80
θp=0
0

Figure 7.

A REVIEW OF 4π ČERENKOV RING IMAGING DETECTORS‡

DAVID W. G. S. LEITH

Stanford Linear Accelerator Center
Stanford University, Stanford, California 94309

ABSTRACT

The design choices for 4π ring imaging Čerenkov counters—both those of principle and those of practice—are reviewed. The progress in construction and the performance of the devices being built for DELPHI and SLD are discussed.

‡ Work supported by Department of Energy contract DE–AC03–76SF00515.

Introduction

This talk is *not* about particle identification in experiments at high-luminosity hadron colliders, as the title of this symposium suggests. Instead, the purpose of this talk is to review the status of the two full-coverage, ring imaging detectors currently being built—the RICH system[1] in the DELPHI experiment at LEP and the CRID system[2] in the SLD experiment at SLAC. We will recount the experiences and the design choices made in these two experiments, and summarize how well the devices being built actually do perform.

Figure 1 shows the layout of the SLD experiment. It is representative of all the high energy e^+e^- experiments in that it consists of nested subsystems, each of which contributes independent information on the events under study. Figure 1 is a schematic quadrant view showing each of the subsystems and indicating the projective tower structure of the calorimeter, both in the Liquid Argon and in the Warm Iron segments.

The principle of both the DELPHI and SLD ring imaging detectors is summarized in Figs. 2(a) and 2(b). There are two radiators—1 cm of a liquid and 45 cms of a gas—to give maximum coverage of the momentum range under study in Z^0 decay. Light from the thin liquid radiator falls on the front face of a long drift detector box, while light from the gas radiator is optically focused onto the back face of the same particle detector box. The image of the liquid radiator light (for normally incident particles) forms a 17 cm radius circle of ≈ 1.5 cm width, and has about 25 photoelectrons distributed around the circumference. The gas radiator light is focused to a 3 cm radius ring of about 2 mm thickness and with about 12 photoelectrons. The Čerenkov light is detected in the long drift boxes via photoionization of a minority component ($\approx 0.1\%$) of the drift gas, called TMAE, or tetrakis-(Dimethylamino)-ethylene. The photoelectron drifts under the influence of a uniform electric field, to a multiwire proportional chamber. The coordinates of the point of origin of the photoelectron are measured from the drift time, the wire address, and by the charge division on each end of the MWPC anode wire to determine the position of the avalanche along the length of the wire. These three coordinates are measured with an accuracy of $\approx \pm 1$ mm, resulting in a determination of the Čerenkov angle to $\approx 1\%$. This allows particle identification e/π, π/K, and K/π as shown in Fig. 3. The potential utility of such hadron identification is shown in Fig. 4, where heavy quark tagging in Z^0 decays is demonstrated, applying first the vertex detector information, then the particle identification, and finally both together.[3] Clean and efficient heavy quark tagging can be clearly achieved with the help of the ring imaging detectors. Finally, Fig. 5 shows experimental data on the π, K separation achieved using the SLD prototype Čerenkov counter in an 11 GeV/c test beam at SLAC.[4] Impressive π, K separation is observed.

An example of the mechanical realization of these detectors is sketched in Fig. 6. There are three separate vessels—the Barrel unit, and two End Caps—which close the solid angle coverage. For the Barrel, the components (the mirror ladders, the drift box and detectors, and the liquid radiator trays) are inserted through 10 sector openings at each end. A G–10 central plane serves as both the center mechanical support for each of the components and as a distributor of 60 kV high voltage to each of the drift boxes.

So much for a brief overview of the 4π ring imaging counters. Let us now consider first the problem of principle and then the problems of practice that one faces when designing such a device. We will then review how well these new devices are really performing.

Problems of Principle

When designing a Čerenkov Ring Imaging Detector, one has to face several basic design choices. I list the individual items, and then go on to discuss them topic by topic:

- Radiator
- Photocathode
- Optics scheme
- Electron detector design and third coordinate readout
- Photon feedback protection.

Radiator

The choice of radiator is driven by the requirement that it be transparent to light of the wavelength of interest and that the index of refraction be appropriate for the momentum range under study. The threshold velocity for Čerenkov radiation is given as $\gamma_{th} = 1/\sqrt{1-(1/n^2)}$, where n is the index of refraction. Table I, shows the radiators chosen by four experiments employing ring imaging technology, including the two experiments under review in this paper. The performance, in terms of particle identification, of the two radiators has already been spelled out in Fig. 3. The variation of Čerenkov angle for each radiator, for e, π, K, and p is shown in Fig. 7, as a function of particle momentum. One can quickly see that if an angular resolution of 1–2 mrad can be achieved, excellent particle identification may be achieved over a broad momentum region.

Photocathode

In recent years, only two photocathodes have been widely used, although there is an interesting effort in "designer-molecular chemistry" underway to develop alternative materials.[5] The photocathode is a carrier gas with a minority mixture

of a photoionizing agent—either triethylamine (TEA) or tetrakis dimethylamine ethylene (TMAE). The properties of these photocathode materials are summarized in Table II.

For large-area systems, TEA is not favored, as it requires expensive CaF windows and requires very clean gas in the radiator volume to avoid the loss of Čerenkov photons at the wavelength one wishes to detect. TMAE is more forgiving, both in the cost of window material and in the required cleanliness (or removal of oxygen and water vapor) of the gas radiator system. The disadvantages of TMAE are its low vapor pressure (which results in a long Čerenkov photon absorption length) and the high electronegativity of the chemical reaction products.[6]

Optics

The choice of the optics for a ring imaging system, as described in Fig. 2(a) above, is driven by the requirement to keep the contribution to the measurement error due to the focusing system small when compared to other errors. The various sources of error are well described in Tom Ypsilantis' 1980 talk on Čerenkov Ring Imaging for LEP experiments[7] and in Tord Ekelof's 1984 SLAC Summer School lectures.[8]

The two experiments choose different solutions to this problem. DELPHI uses larger area mirrors and has developed a new fabrication technique which uses no grinding and polishing, and preserves the virgin surface of the float glass blanks used to form the mirrors. To keep the errors due to optical distortion acceptable, they slump parabolic mirrors. They have successfully produced all of their mirrors, with the help of Bofors Co., and have achieved excellent UV reflectivity and surface flatness.[9] The average reflectance of all the DELPHI mirrors is greater than 85% for the wavelength range (1650—2000)Å.

For SLD, the optics design employs two ladders of five (27 × 30) cm mirrors, reflecting the light back to each drift box. With this size mirror, SLD can comfortably use spherical mirrors. The mirrors for the Barrel counter have all been produced by Lancaster Corp. and coated by Acton Co. They are 6 mm thick float glass pieces which are rapidly slumped in a mold in a gas oven, annealed and then ground and polished to the required surface finish. The blanks are then checked for dimensions, radius of curvature, local flatness and optical distortion; those passing, were sent to Acton Co. for a good UV reflectance coating. Figure 8(a) is the data from a detailed surface profile measurement of these mirrors, showing 26 Å rms features on the mirror surface; Fig. 8(b) displays the reflectance as a function of wavelength for the first 100 mirrors produced.

Electron Detector

The choice of design for the electron detector for a Čerenkov Ring Imaging counter has to accommodate several requirements. The detector scheme is schematically shown in Fig. 9, where the Čerenkov photon is seen entering the photocathode region and photoionizing the TMAE gas. The long absorption length in TMAE results in a parallax error which must be removed by measuring the depth at which the electron was produced (*i.e.,* the third coordinate). So the drift time and wire address come fairly straightforwardly, but the technique used to measure this third coordinate is something of a challenge.

Figure 10 shows the electron detection mechanism—the formation of a Townsend avalanche near the surface of the anode wire of the MWPC. The formation of the avalanche leaves the gas in an excited state, and a substantial fraction of this time the return to the ground state is achieved by photon emission. The very high efficiency TMAE photocathode provides the engine for a strong positive feedback situation which must be controlled in an effective detector design.

The solution chosen by the DELPHI experiment is shown in Fig. 11. The anodes are 20 μm tungsten wires strung on a pitch of 2.6 mm. The third coordinate is read out by cathode strips, as shown in the figure. To achieve good efficiency for the cathode readout, close coupling of the anode is necessary, resulting in 0.5 mm anode-to-cathode spacing. The cathode strips are 5.4 mm wide and 42 mm long, covering 16 anode wires. The large signal developed by the energy loss from the passage of a charged particle represents a challenge for this method in that the large signal is capacitatively coupled to neighboring anodes unless clever precautions are taken. A resolution of 2 mm in this coordinate measurement has been achieved by the DELPHI group.[10] The protection against photon feedback is achieved by the blinds erected between wires, as displayed in Fig. 11. They are 1 cm high alumina blinds with field defining wires placed along the wall to shape the electric field guiding the electrons onto the MWPC anode. This structure interdicts wire-to-wire paths, and limits the opening angle back into the drift volume to $\approx 14°$.

The SLD solution is shown in Fig. 12. The third coordinate is interpreted by a charge division measurement on the MWPC anodes. To achieve the required resolution, very resistive wires must be used. The SLD chamber is strung with 7 μm diameter carbon monofilaments, with a linear resistance of about 40 $K\Omega$ for the 10 cm length. The anodes are strung on a 3.2 mm pitch. A resolution of $\pm$ 0.7 mm is achieved in reading out the position of the avalanche along the length of the wire.[11] The photon feedback is tamed by machining U-shaped troughs in the cathode, giving wire-to-wire shielding. The backstreaming opening angle is limited to $\approx 5°$ by a series of copper sheets, each at graded potential to properly control the electric drift field, and etched with 1 mm slots of metal removed in front of

each anode. The observed photon feedback is shown in Fig. 13 as a function of the chamber voltage or, equivalently, of the gas gain.[12] A feedback level of $\approx 1\%$ is observed for normal operating conditions of the CRID.

Results of the charge division are shown in Fig. 14, from an average gas gain of 2×10^5. The resolution in determining the position of this avalanche along the 7 μm carbon wire is shown in Fig. 15 and indicates a measurement of $\sim 0.8\%$ of the wire length, or $\sim \pm 0.7$ mm.

Both detector solutions—that from DELPHI and from SLD—have been shown to perform satisfactorily and with the required accuracy to result in excellent particle identification over the momentum range to be examined in Z^0 decays.

Table III summarizes the various choices of principle made by these two experiments.

Problems of Practice

Moving from issues of principle to choices of practice, I list a number of areas of concern that require attention when designing and commissioning a ring imaging detector. They are:

- choice of the drift gas for long drift box
- cleanliness of the gases *
- choice of construction materials
- operating temperature
- implementation of the electrostatics *
- choice of the H.V. operating point *
- gating *
- wire aging in TMAE environment *
- calibration/monitoring of drift box/detectors. *

I will not have time to discuss all of these points, but will make some comments on each of the starred items.

Gas Cleanliness

The radiators have to be kept clean, with low contamination of oxygen and water vapor, to reduce the absorptive losses of UV photons. The drift gas also has to be kept free of oxygen and water vapor in order to minimize the electron capture losses of the precious photoelectrons as they drift of the order of 1 m in the long drift boxes (see Sec. I). In addition, we found that the commercially available TMAE comes with substantial contamination of highly electronegative

components. In Fig. 16, we show gas chromatograph plots of regular, commercial TMAE and carefully washed TMAE, indicating the removal of much of the contamination.[6]

Electrostatics

The photocathodes in both of these experiments are TMAE–gas filled, quartz windowed boxes, with uniform electric fields along the box axis, guiding the drifting photoelectrons towards the MWPC detector. The method of producing the electric field in the two experiments is rather different.

For DELPHI, the boxes are made from quartz on all four sides, glued together to form a gas-tight structure. The field cage is made with metal strips evaporated onto the quartz. This has the very real advantage of having the dialectric surface in intimate contact with the conductors defining the drift field. It has the nuisance that it is difficult to make the electrical connections to the evaporated stripes.

For SLD, the boxes are made with G-10 printed circuit board sides and quartz windows, top and bottom. A photograph of the inner core of an SLD drift box during assembly is shown in Fig. 17. The sides in these boxes are double-walled, with a purge gas flowing in the side volume to reduce the risk of the very electronegative freon gas radiator leaking into the drift volume. The field cage is formed using etched arrays stretched on tooling fixtures and glued to both sides (inner and outer) of each quartz window of the box. The etched arrays are fabricated by etching away most of the metal from a 100 μm sheet, 150 $\times$ 50 cm of BeCu. What remains are 70 μm wires every 3 mm, with solder tabs at each end and a wide ribbon around the border for handling and for mounting on the tooling fixtures. This fabrication method creates highly reproducible wire frames which can be very precisely placed with respect to tooling heads in the border frames. Reproducibility from window to window and from inside to outside on a given window is $\pm$20 μm over 130 cm. These are reasonably easily assembled on the windows; semiautomatic soldering techniques provide the electrical connection. The disadvantage in this construction is that the etched-array wire is not in intimate contact with the quartz and may allow polarization of the dielectric under certain conditions. So far in our prototype tests, we have not observed such effects.

Gating

The principle of Čerenkov photon detection was described in the Introduction and in Fig. 2. The uniform electric drift field, which guides the photoelectrons along the length of the long drift boxes and towards the multiwire proportional detector, is terminated on a grid of 100 μm tungsten wire strung on a pitch of 3.2 mm for the SLD device. The drifting electrons then experience a transfer field which sweeps it onwards into the etched array stack and focuses it down onto the

anode wire, where it avalanches to a swarm of $\sim 10^5$ electrons. For the DELPHI detector, the drift field is similarly terminated.

The nominal electron drift path and the corresponding drift path of the returning positive ions are shown as the left-hand diagrams in Fig. 18.

To protect the MWPC from premature aging and to avoid the buildup of charge on the walls of the long drift box, both the SLD and DELPHI experiments employ a gating circuit which switches +350 V and −350 V relative to the nominal voltage on alternate wires of this grid of 100 μm wires (see Fig. 18). When the gate is closed (i.e., when the ±350 V is applied), no electrons drifting from the long drift box may enter the detector and no positive ions may escape from the detector; see the right-hand drawing in Fig. 18.

A typical operation in the SLD will be to open the gate with each e^+e^- crossing of the SLC (a 120 Hz operation) and close it again after about 40 μs. In this case, only electrons associated with events at the e^+e^- crossing will be detected, and the gate may be inhibited during poor operating conditions of the machine. The positive ions from the Townsend avalanche that caused the detection of a photoelectron will have only moved a few mm through the etched array stack before the gate closes, and so will never enter the drift box volume.

Wire Aging

The addition of TMAE to regular drift chamber gas mixtures appears to drastically reduce chamber lifetimes.[13] We have measured such behavior for several different gas mixtures, flow rates, and for different size anode wires. When a chamber that shows such a loss in gain is opened and the anode surface exposed to air, droplets form on the anode; see Fig. 19. The deposit on the anode may be effectively cleaned by washing the chamber in ethanol. Normal operation is observed when the chamber is again put into service. For the SLD device, we have made serendipitous use of the resistive anodes! A d.c. current of $\sim$ 10 m.a. applied for about 15 minutes raises the surface temperature of the anodes to $> 400°$C and "self cleans" the chamber by burning off the residue. In Fig. 20, a series of "deaths" of an SLD electron detector is shown, with subsequent "rebirth" after the required 15 minute "cooking."

This should be an effective maintenance method for controlling the gain losses due to TMAE dissociation products depositing on the anodes.

Performance

Having discussed how these two experiments have been designed and put together, we should now ask how well they actually perform.

Figure 21 shows the angular resolution from both the liquid radiator and the gas radiator, as measured in the CERN tests of the DELPHI RICH prototype. Examples of single events showing π, K separation at 11 GeV/c and e, π separation at 4 GeV/c are shown in Fig. 22 for the SLD CRID prototype. The measured Čerenkov ring radius for 11 GeV/c, π's and K's for the SLD prototype was shown in Fig. 5 above. The pion ring radius is measured to an accuracy of ± 0.8 mm, corresponding to the result of measuring ~ 12 photoelectrons on the Čerenkov circle, each one measured with an accuracy of ~ 2.1 mm. Very clean π, K separation is observed.

Table III summarizes the results for the prototype program of both SLD and DELPHI. Both experiments have achieved good N_0, observing ~ 12 photoelectrons on the gas ring and ~ 25 photoelectrons for the liquid radiator. The spatial accuracy for reconstructing the point of origin of the photoelectron allows measurement of the gas Čerenkov angle to $\pm$ (1–2)%, and for the liquid Čerenkov angle to $\sim \pm$ 0.5%. Such performance allows π, K, ρ separation over most of the momentum range of Z^0 decays. The SLD CRID experiment has demonstrated that it can resolve neighboring photoelectron hits (with the second pulse only 10% in amplitude of the first) within 3–4 mm.

Status of the Experiments

Delphi

- ▷ The LEP machine is planned to turn on in July 1989.
- ▷ The RICH subsystem is now being installed in DELPHI.
- ▷ At least part of the RICH will be operational at the turn-on of DELPHI.

SLD

- ○ The SLC is running now, and we are hoping for the first Z^0's now.*
- ○ The SLD experiment is coming together well. The magnet has been ready for over a year, and the muon system and tail-catcher calorimeter are ready. The Liquid Argon Calorimeter is being installed now and should be ready for cool-down by this Fall. The Central Tracker is finished stringing and should be ready for installation in the Fall. The Čerenkov counter vessel will be installed in SLD this Summer, and part [30–50%] of the components will be inserted by this Fall. The SLD will then prepare for a cosmic ray shakedown test in January–April 1990.

* The first Z^0 from SLC was observed by Mark II on April 14, 1989—seven days after this talk.

- The remainder of the CRID components will be installed in SLD following the cosmic ray test run, in Spring 1990.
- SLD should move into the beamline in SLC during the summer of 1990. It is expected that the removal of Mark II, the installation of the new SLC Final Focus, and the roll-in of the SLD experiment will take about three months.

Conclusion

The two 4π Čerenkov ring imaging detectors are coming together quite rapidly and successfully. They promise to do their jobs well in a physics environment where they clearly have a lot to offer.

References

1. Delphi Proposal, LEPC 83–3 and LEPC 84–16.
2. SLD Design Report, SLAC–Report–273 (1984).
3. W. Atwood, private communication. Also discussed in D. Leith "Advances in Experimental Methods for Colliding Beam Physics," Nucl. Inst. Meth. A265, 120 (1988).
4. V. Ashford et al., published in Proc. XXIII Int. Conf. on High Energy Physics, Berkeley, CA, July 16–23, 1986 p. 1470.
5. T. Ypsilantis and J. Sequinot, this Symposium.
6. R. T. Rewick et al., Anal. Chem. 60, 2095 (1988), SLAC–PUB–4115.
7. T. Ypsilantis, invited talk at the Int. Conf. on Experiments at LEP, Physica Scripta, Vol. 1, 370 (1981).
8. T. Ekelof, Proceedings of the 1984 SLAC Summer Institute, SLAC–Report–281, 244 (1985).
9. Baillon et al., Nucl. Instr. Meth. A277, 338 (1989), and Nucl. Instr. Meth. A276, 492 (1989).
10. R. Arnold et al., Nucl. Instr. Meth. A270, 255 (1988).
11. D. Aston et al., presented at the Int. Wire Chamber Conference, Vienna, February 13–17, 1989; SLAC–PUB–4875.
12. P. Coyle et al., internal CRID No. 58, "Photon Feedback Measurements in the Barrel CRID Detectors," (1989).
13. J. Va'vra, IEEE Trans. Nucl. Sci. NS–34, 1987; SLAC–PUB–4116 (1986).

Figure Captions

Fig. 1. A schematic quadrant view of the SLD detector at SLAC.

Fig. 2. Demonstration of the principle of the DELPHI and SLD Čerenkov Ring Imaging Detectors. (a) shows the arrangement of the two radiators and the photon detector; (b) shows the details of the long drift photoelectron detector.

Fig. 3. The particle identification performance expected for the Čerenkov Ring imaging Detector in DELPHI and SLD.

Fig. 4. The evolution of the charm signal in $K\pi\pi$ from Z^0 decays, from a Monte Carlo study by W. Atwood. The precision CCD vertex and the CRID system are used first separately and then together to isolate, with fair efficiency, a very clean D peak.

Fig. 5. Experimental data from test beam studies on the π K separation achieved by the SLD CRID prototype at 11 GeV/c.

Fig. 6. Schematic diagram of the mechanical layout of the SLD CRID.

Fig. 7. Estimated particle separation as a function of momentum with (a) the gas radiator and with (b) the liquid radiator. Indicated are 1σ separation bands expected at the SLD, based on the prototype results.

Fig. 8. (a) Surface flatness measurements of the mirror blanks from Lancaster Co. They typically have 20–30 Å feature size. (b) The measured reflectance of the first 100 mirror blanks coated by Acton Co. for the SLD–CRID.

Fig. 9. Schematic diagram of the parallax error introduced by the Čerenkov photon attenuation length in the drift gas.

Fig. 10. Diagrammatic representation of photon feedback. First the Čerenkov photon is absorbed by a TMAE molecule in the drift gas and frees a photoelectron. The electron drifts under the action of a guide field to the high electric field region around an anode wire and experience a Townsend avalanche. The gas around the avalanche region is in an excited state and part of the time de-excites by emission of an optical photon. Such photons are quickly absorbed in the high quantum efficiency photocathode gas, thus giving use to a positive feedback mechanism. For successful operation of a Čerenkov Ring Imaging Detector this phenomena must be tamed.

Fig. 11. A schematic of the DELPHI electron detector showing the blinds between anode wires which control the photon feedback.

Fig. 12. A schematic of the SLD electron detector showing the teched arrays and U-shaped cathode which control the photon feedback.

Fig. 13. The measured photon feedback in the SLD electron detector as a function of chamber voltage.

Fig. 14. The measured charge division resolution in the SLD electron detector.

Fig. 15. The position resolution as a function of distance along the anode wire for the SLD detector.

Fig. 16. Gas chromatograph traces for (a) commercial TMAE, and (b) TMAE washed and passed through a sieve.

Fig. 17. A photograph of the core of an SLD drift box during assembly.

Fig. 18. Trajectories for electrons and positrons near the electron detector in the SLD for open and closed gate voltage settings.

Fig. 19. Photograph of the deposit on an anode wire after aging and opening to the atmosphere.

Fig. 20. Data on the aging cycle of an SLD electron detector with TMAE being repeatedly aged by exposure to radiation and "cleaned" by locally heating the anode.

Fig. 21. Comparison of the measured and calculated Čerenkov angular resolution for both liquid and gas radiators in the DELPHI RICH prototype.

Fig. 22. Single event display from the SLD CRID prototype; (a) and (b) are 11 GeV/c π^+ and K^+, respectively, while (c) and (d) are 4 GeV/c π^- and e^-, respectively.

Table I

Radiator Choices for Four Čerenkov Ring Imaging Detectors.

Radiator	n	γ_{th}	Pion Threshold (GeV/c)	Number of photoelectrons from L_{cms} of Radiator	Experiment Goals
Helium	1.000038	116	16	(TEA) 6 from 1500 cms	E-605 π, K, p (50-200) GeV/c
Nitrogen	1.00032	40	5.5	(TMAE) 28 from 500 cms	RAL-Omega π, K, p (20-150) GeV/c
C_5F_{12}	1.0017	17	2.4	(TMAE) 12 from 45 cms	SLD/DELPHI Z^0 decays
C_6F_{14}	1.2176	1.5	0.2	(TMAE) 24 from 1 cm	e, π, K, p (1/2-40) GeV/c

Table II

Comparison of TEA and TMAE Photocathodes

	TEA	TMAE
Absorption Length for Čerenkov Light	1 mm	(15-40) mm depending on temp.
High Edge of Wavelength Window	around 1500 Å	around 1950 Å
Requirement in O_2, H_2O	$\leq$ 200 ppb	$\leq$ 20 ppm
Window Material	CaF	Quartz

Table III

Choices of "Principle" for the Ring Imaging Detector

COMPONENT	SLD	DELPHI
Radiator	$\left\{\begin{array}{c}1\text{ cm }C_6F_{14}\\45\text{ cm }C_5F_{12}\end{array}\right\}$	
Photocathode	$\left\{\text{TMAE at }28°\text{C}\right\}$	
Optics	Spherical, Ground and Polished Mirrors	Parabolic, Slumped Glass
	Proximity Focusing for Liquid	Same
Electron Detector	MWPC with Resistive Anode	MWPC
	Charge Division for Third Coordinate	Cathode Strips
	Forward and Side Blinding ($\theta \sim 6°$)	Side Blinds ($\theta \sim 14°$)

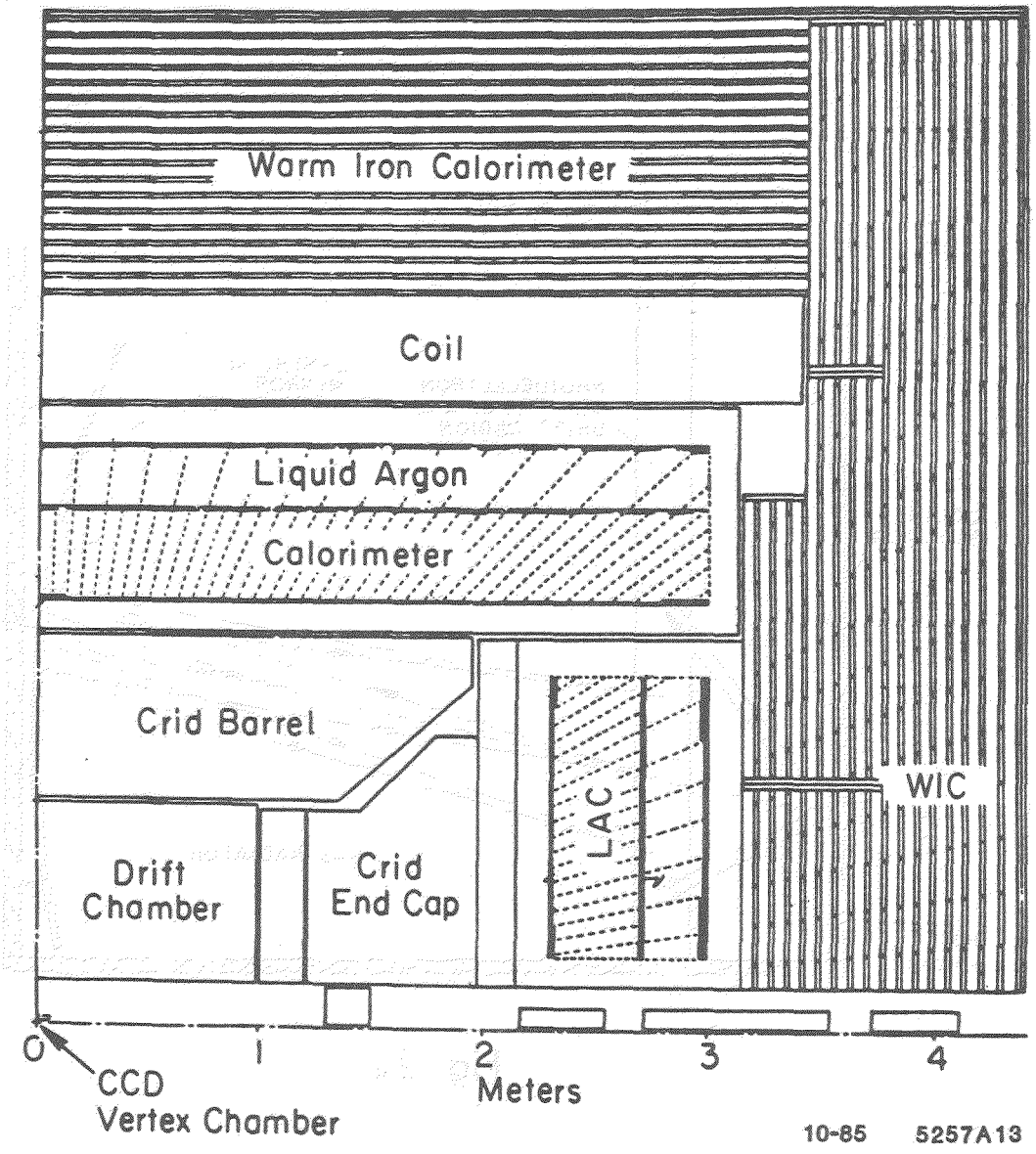
Warm Iron Calorimeter
Coil
Liquid Argon
Calorimeter
Crid Barrel
Drift Chamber
Crid End Cap
LAC
WIC
0
1
2
3
4
Meters
CCD
Vertex Chamber
10-85
5257A13

Fig. 1

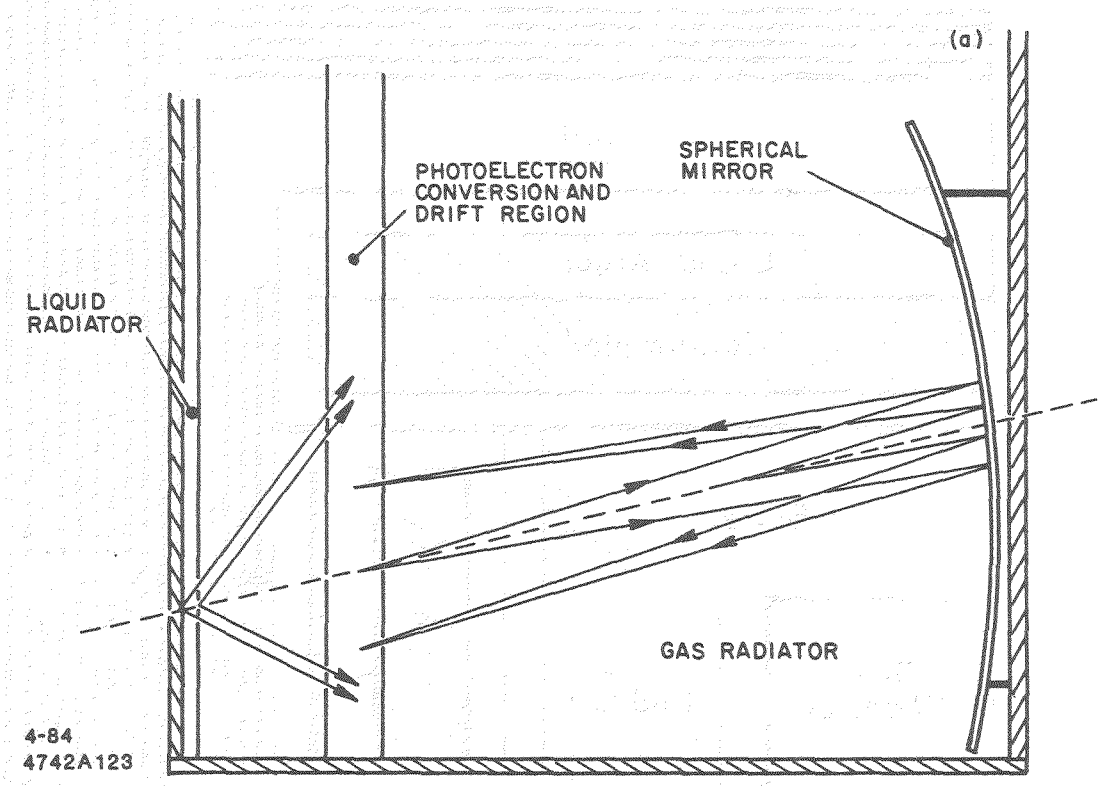
(a)
PHOTOELECTRON
CONVERSION AND
DRIFT REGION
SPHERICAL
MIRROR
LIQUID
RADIATOR
GAS RADIATOR
4-84
4742A123

Fig. 2a

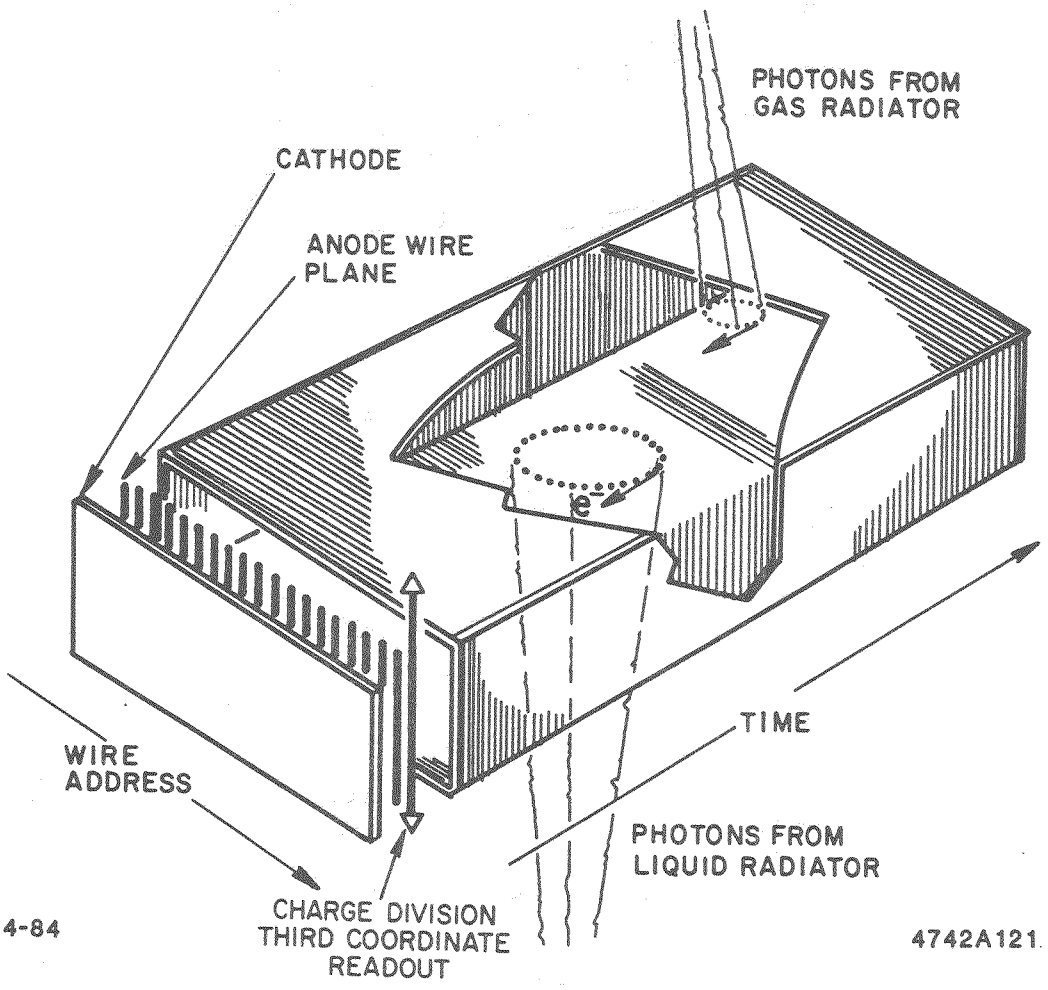
PHOTONS FROM
GAS RADIATOR
CATHODE
ANODE WIRE
PLANE
e⁻
TIME
WIRE
ADDRESS
PHOTONS FROM
LIQUID RADIATOR
CHARGE DIVISION
THIRD COORDINATE
READOUT
4-84
4742A121

Fig. 2b

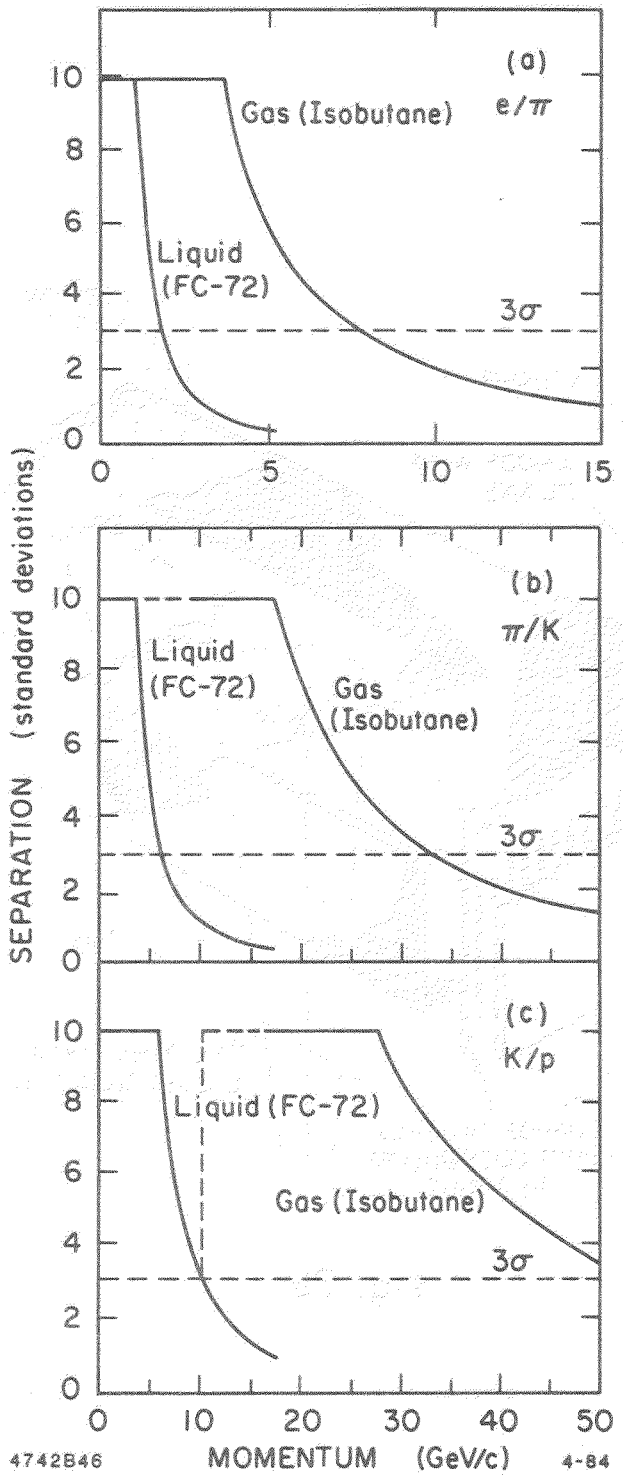
(a)
e/π
Gas (Isobutane)
Liquid
(FC-72)
3σ
(b)
π/K
Liquid
(FC-72)
Gas
(Isobutane)
3σ
(c)
K/p
Liquid (FC-72)
Gas (Isobutane)
3σ
SEPARATION (standard deviations)
MOMENTUM (GeV/c)
4742B46
4-84

Fig. 3

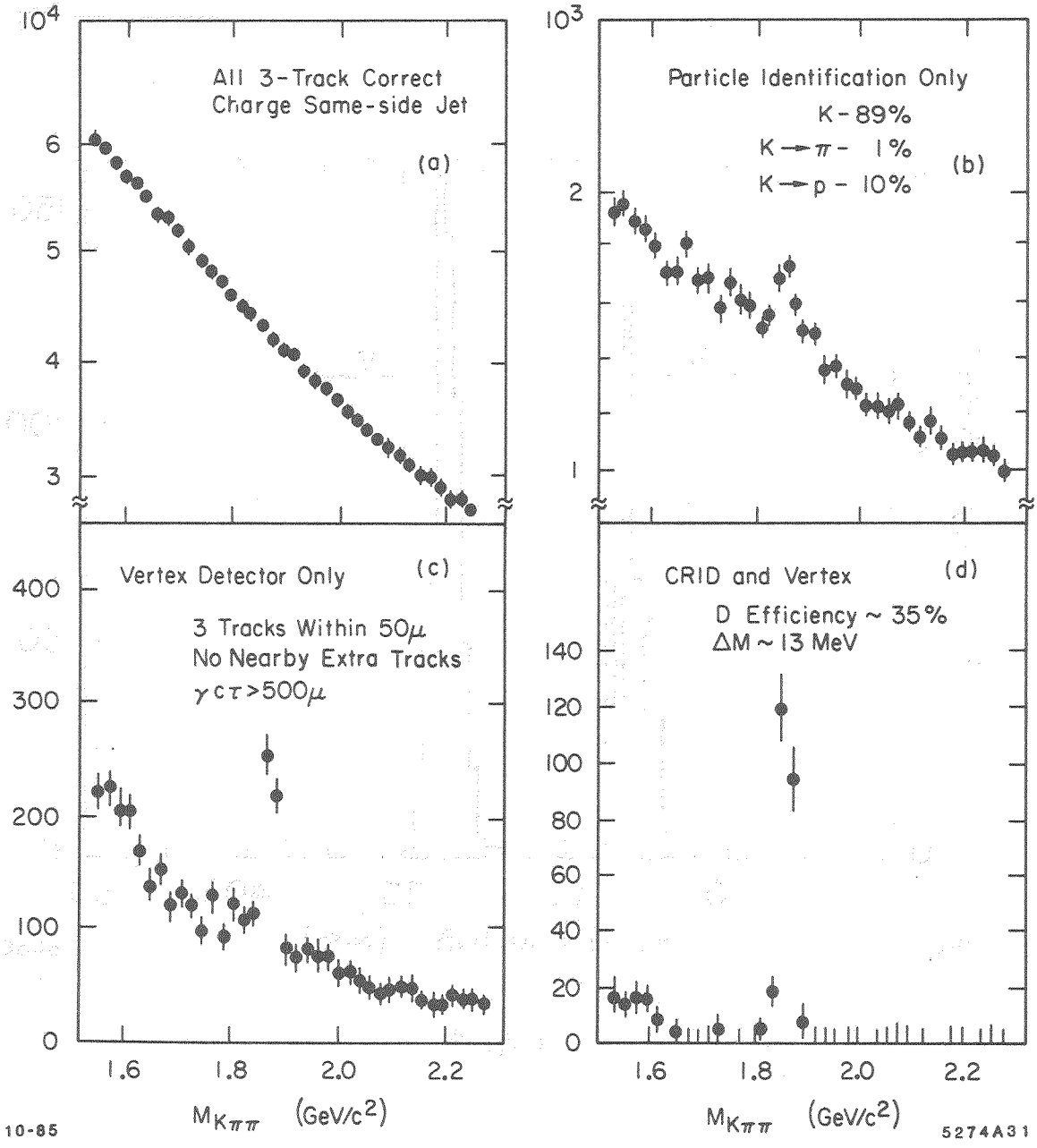
All 3-Track Correct
Charge Same-side Jet
(a)
Particle Identification Only
K - 89%
K → π - 1%
K → p - 10%
(b)
Vertex Detector Only
(c)
3 Tracks Within 50μ
No Nearby Extra Tracks
γcτ > 500μ
CRID and Vertex
(d)
D Efficiency ~ 35%
ΔM ~ 13 MeV
$M_{K\pi\pi}$ (GeV/c²)
10-85
5274A31

Fig. 4

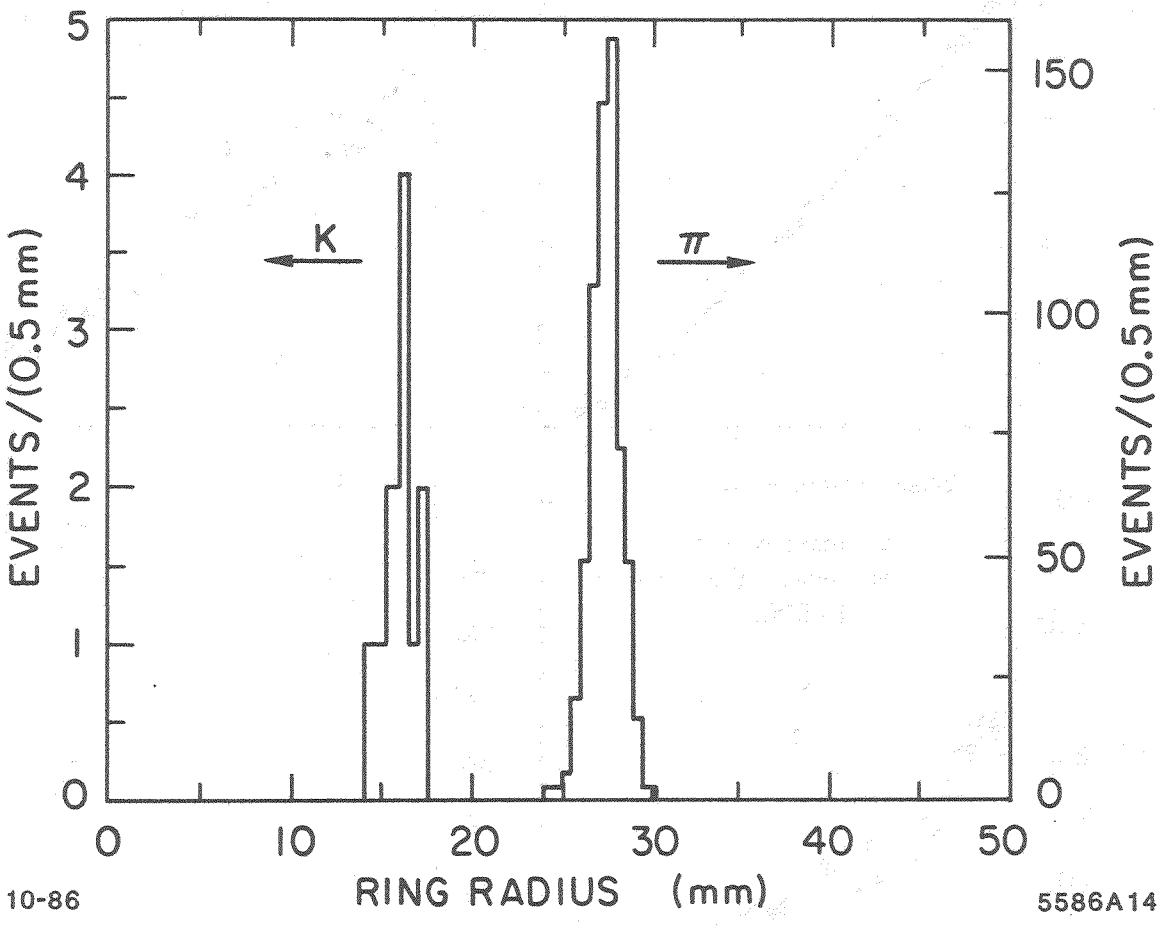
EVENTS/(0.5 mm)
5
4
3
2
1
0
K
π
150
100
50
0
EVENTS/(0.5 mm)
0
10
20
30
40
50
RING RADIUS (mm)
10-86
5586A14

Fig. 5

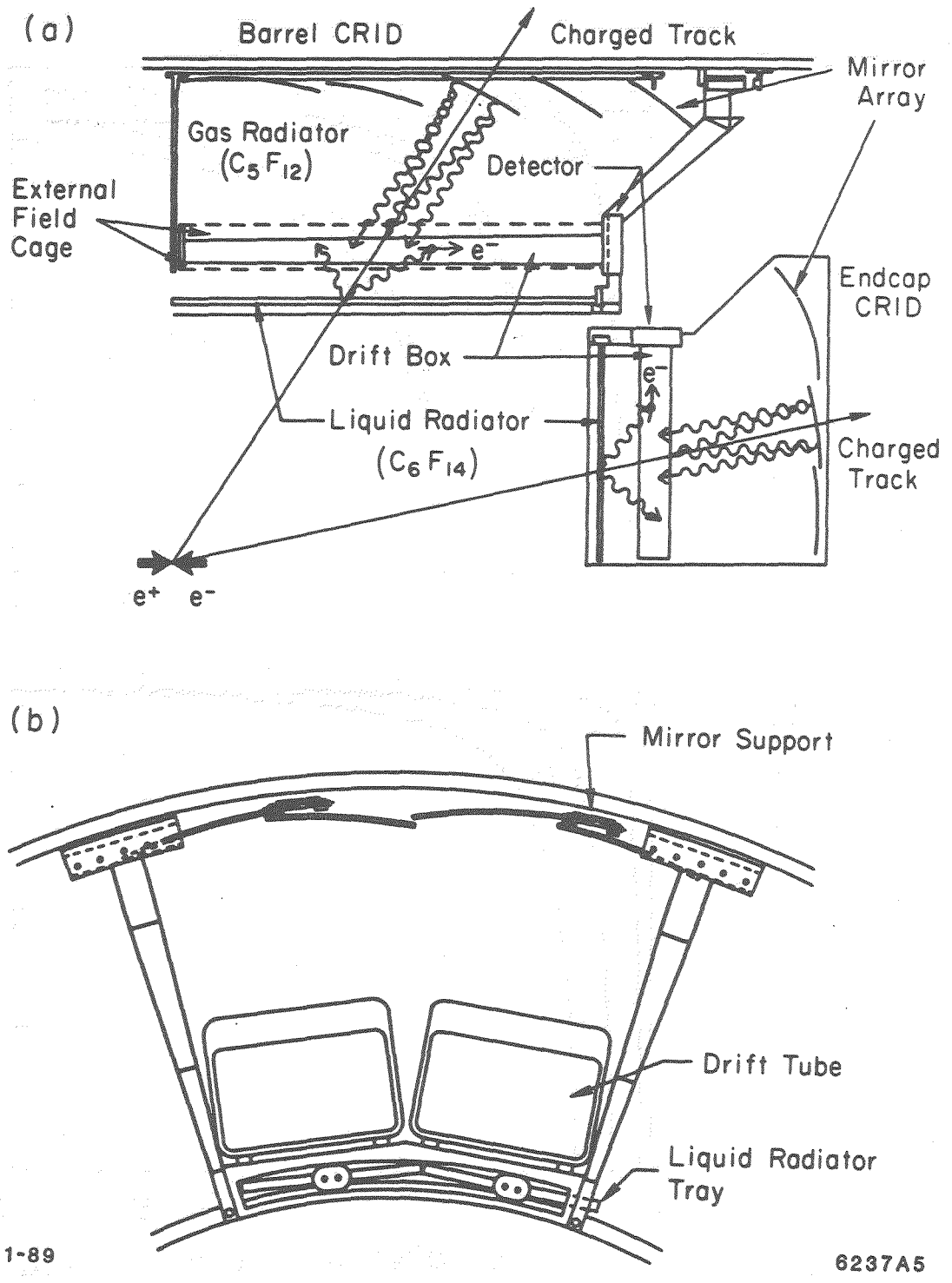
(a)
Barrel CRID
Charged Track
Mirror Array
Gas Radiator (C_5F_{12})
Detector
External Field Cage
e^-
Endcap CRID
Drift Box
e^-
Liquid Radiator (C_6F_{14})
Charged Track
e^+ e^-
(b)
Mirror Support
Drift Tube
Liquid Radiator Tray
1-89
6237A5

Fig. 6

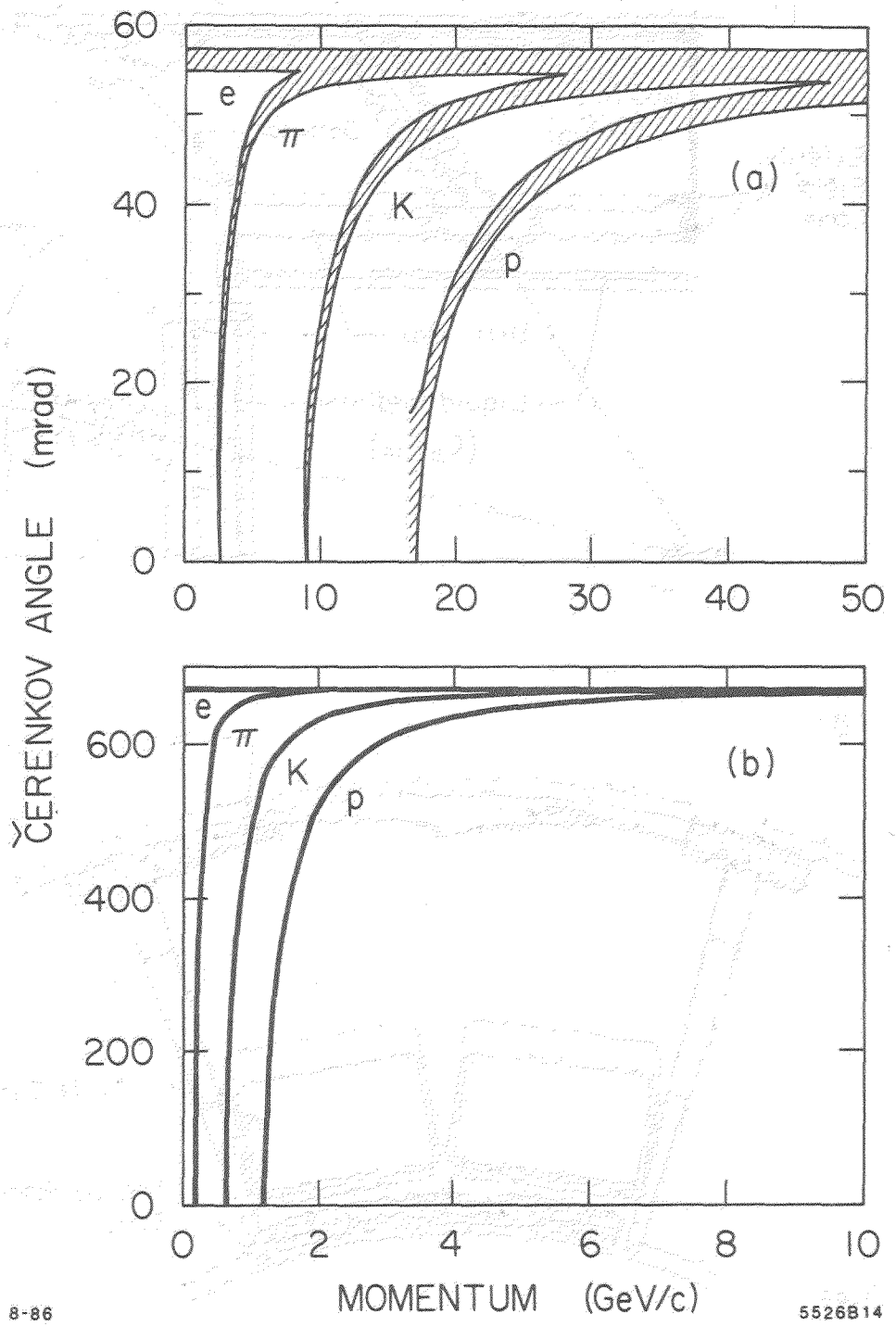
60
40
20
0
e
π
K
p
(a)
0
10
20
30
40
50
ČERENKOV ANGLE (mrad)
600
400
200
0
e
π
K
p
(b)
0
2
4
6
8
10
MOMENTUM (GeV/c)
8-86
5526B14

Fig. 7

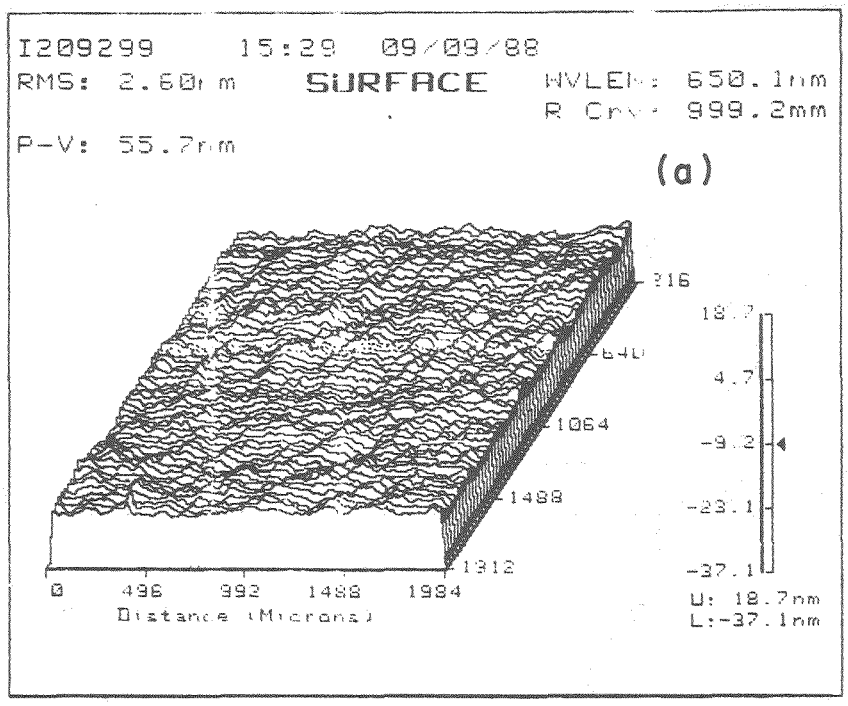
I209299 15:29 09/09/88
RMS: 2.60nm
SURFACE
P-V: 55.7nm
(a)
0
496
992
1488
1984
Distance (Microns)
18.7
4.7
-9.2
-23.1
-37.1
U: 18.7nm
L:-37.1nm

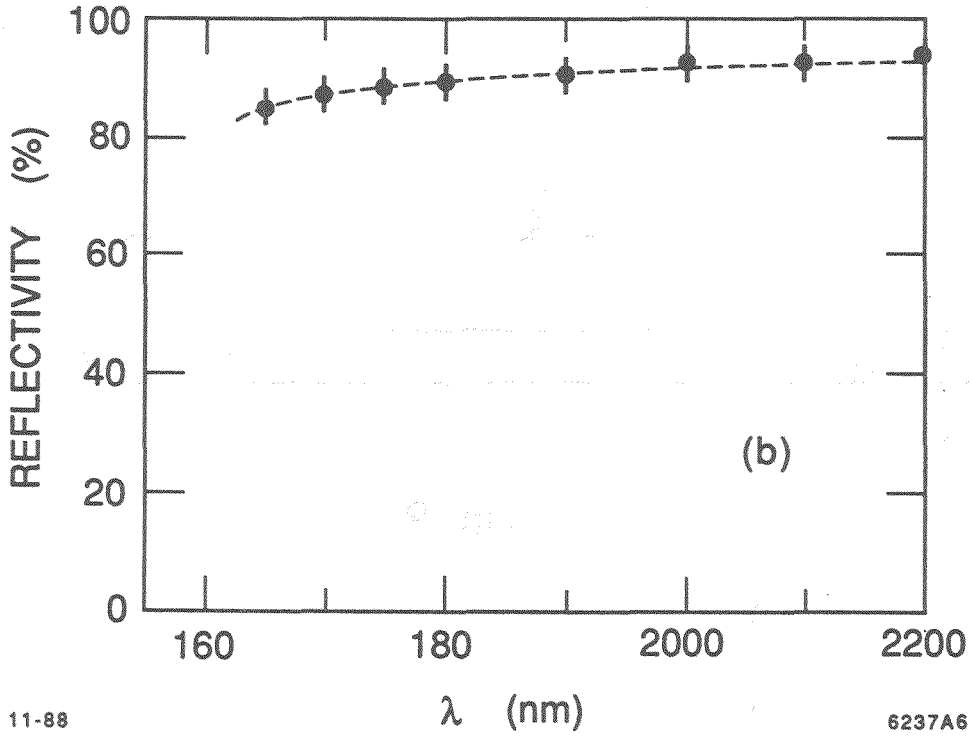
REFLECTIVITY (%)
100
80
60
40
20
0
160
180
2000
2200
λ (nm)
(b)
11-88
6237A6

Fig. 8

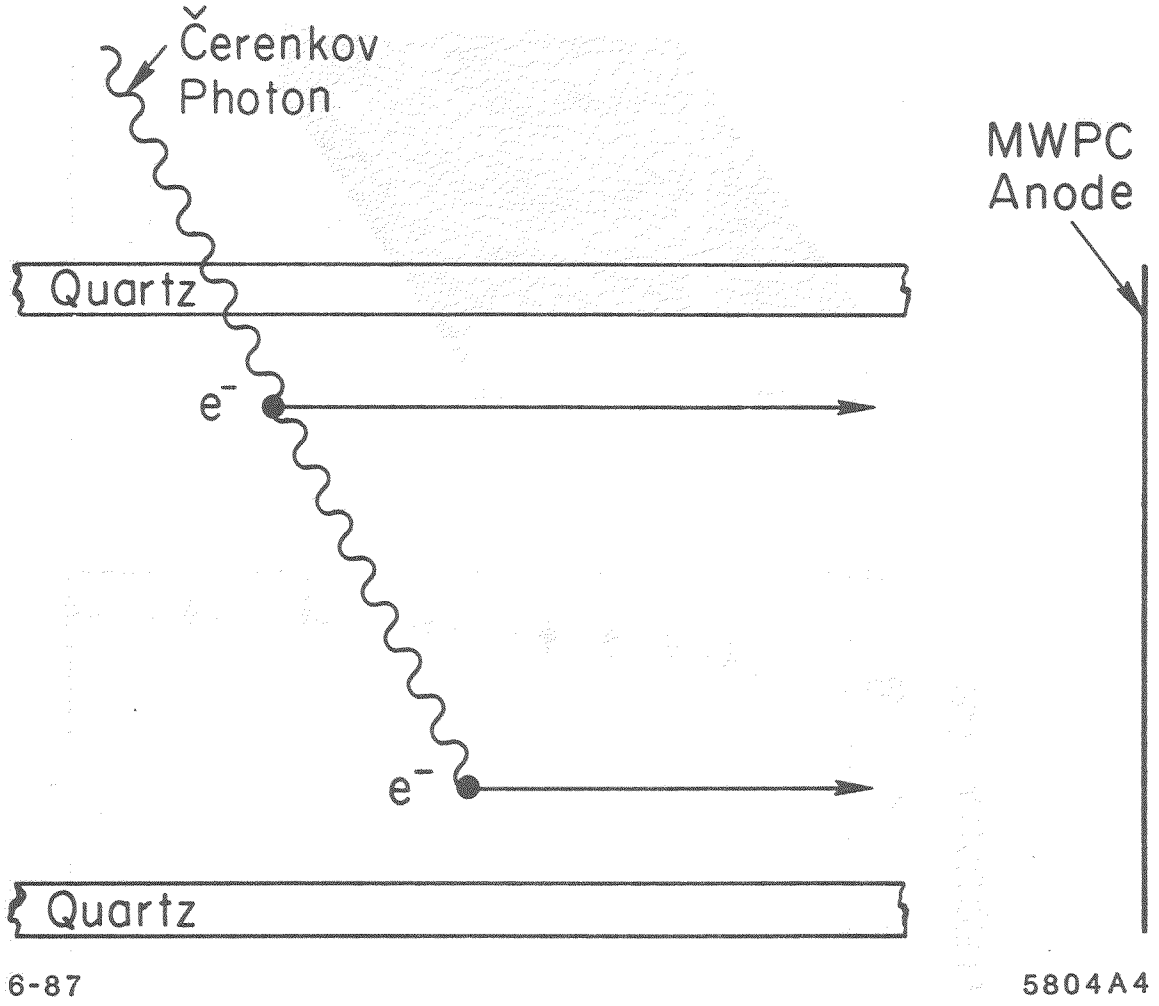

Fig. 9

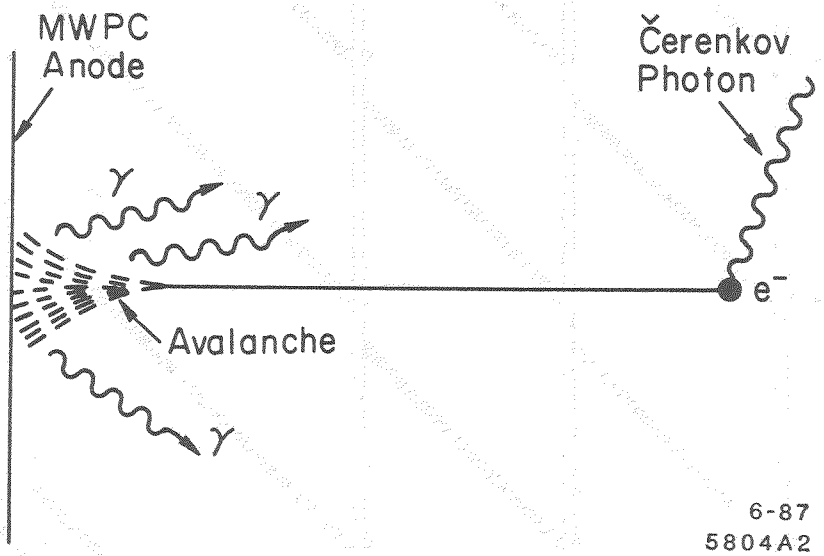

Fig. 10

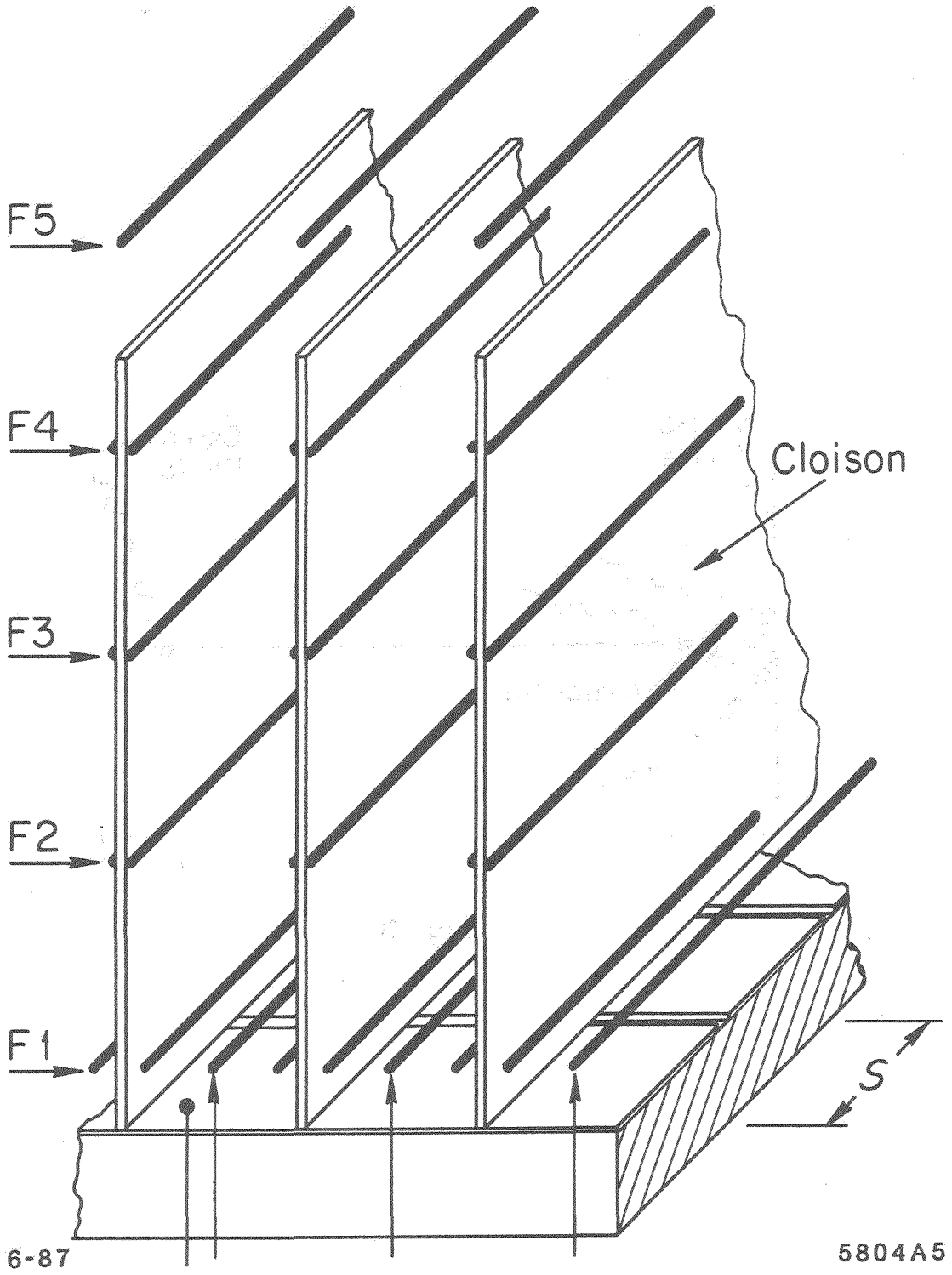

Fig. 11

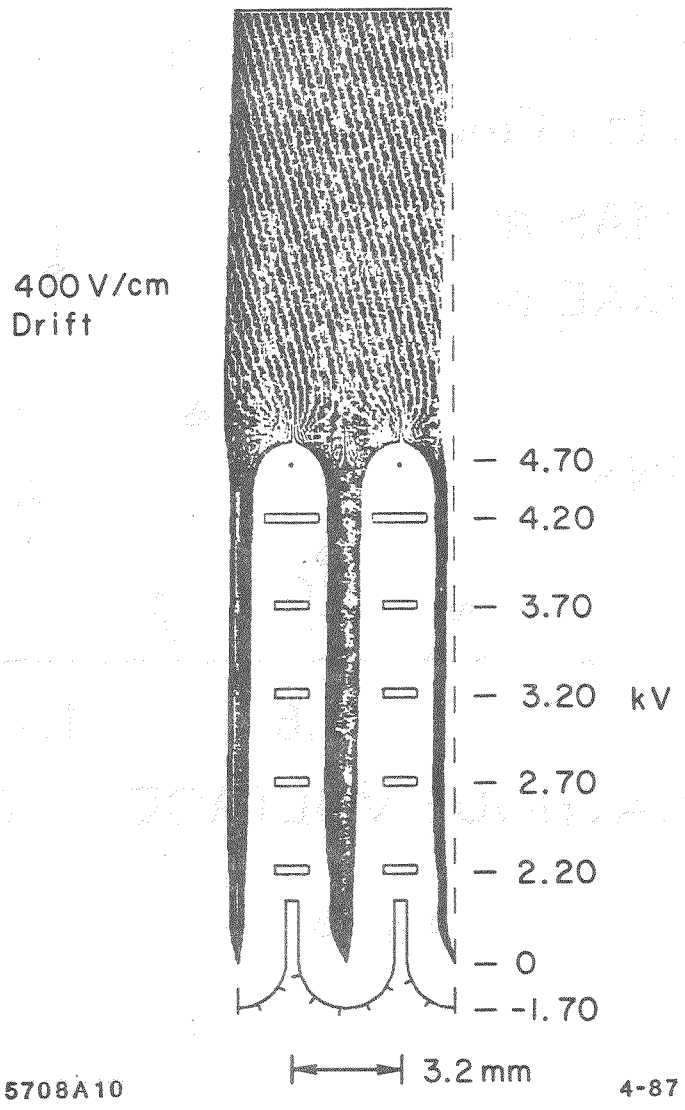

Fig. 12

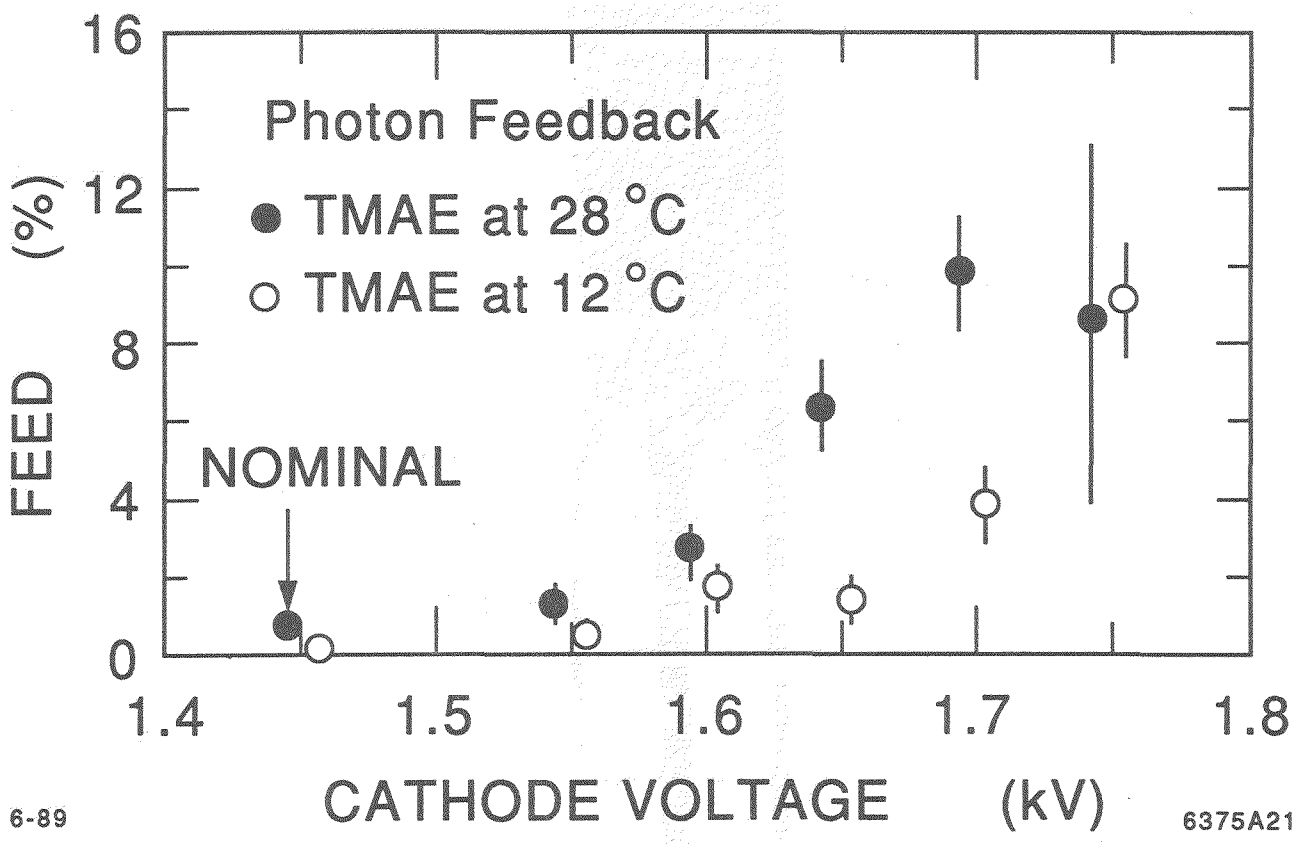
Photon Feedback
TMAE at 28 °C
TMAE at 12 °C
NOMINAL
FEED (%)
16
12
8
4
0
1.4
1.5
1.6
1.7
1.8
CATHODE VOLTAGE (kV)
6-89
6375A21

Fig. 13

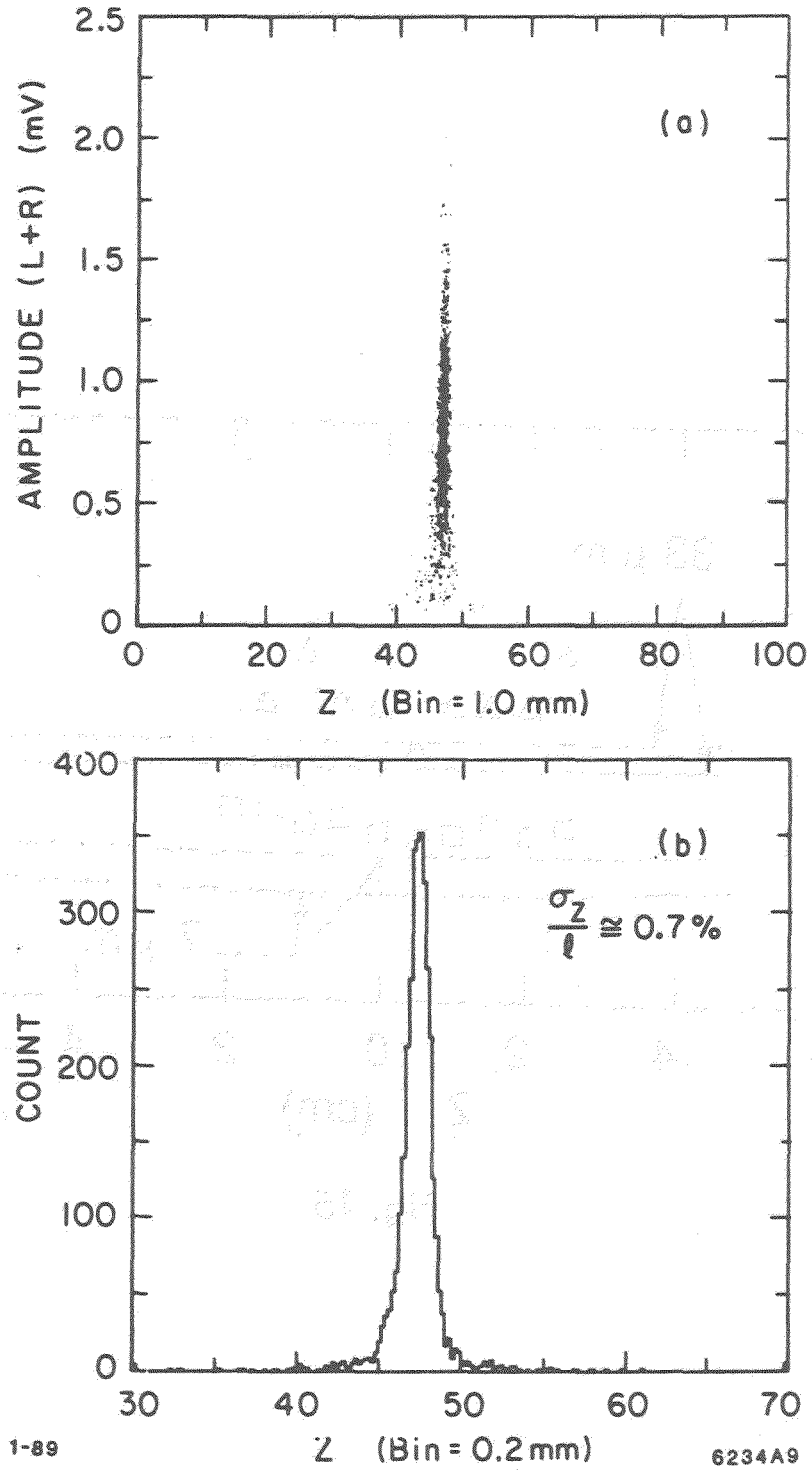
2.5
2.0
1.5
1.0
0.5
0
AMPLITUDE (L+R) (mV)
(a)
0
20
40
60
80
100
Z (Bin = 1.0 mm)
400
300
200
100
0
COUNT
(b)
$\frac{\sigma_Z}{\ell} \cong 0.7\%$
30
40
50
60
70
Z (Bin = 0.2 mm)
1-89
6234A9

Fig. 14

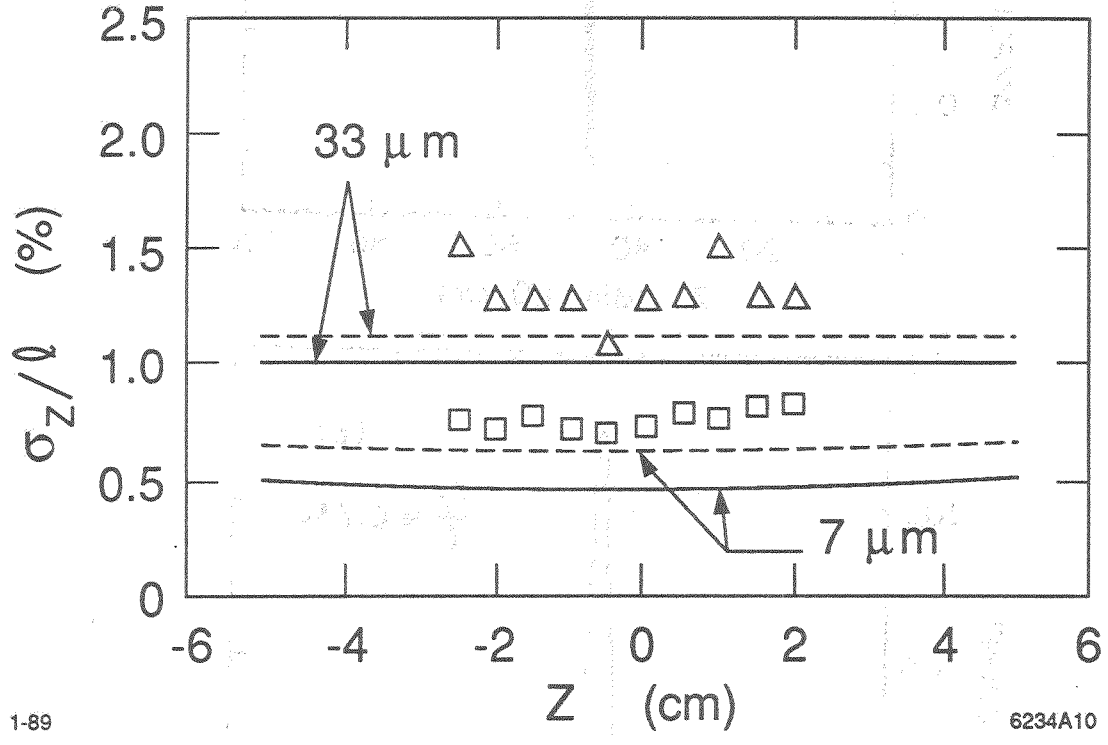

Fig. 15

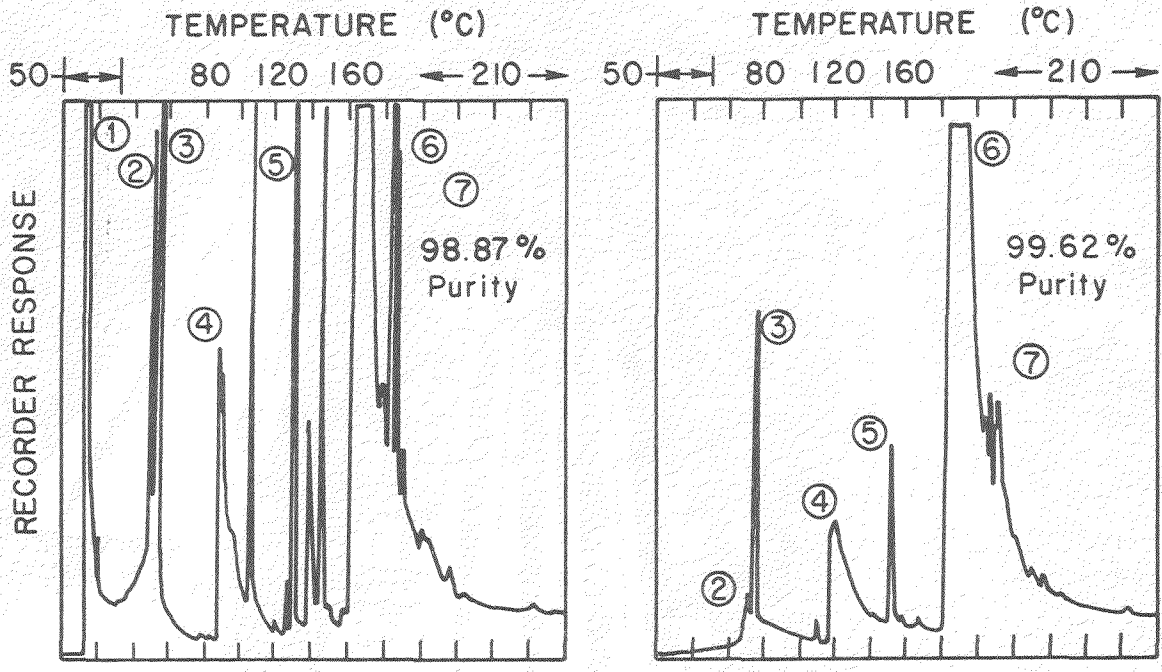

(a) As Received from RSA Corp

(b) Washed with Water and Passed through a Molecular Sieve

Symbol Identification

Symbol	Name	Formula	MW
DMA	Dimethylamine	$(CH_3)_2NH$	45
TMH	Tetramethylhydrazine	$(CH_3)_2-N-N(CH_3)_2$	88
BMAM	Bis(dimethylamino)methane	$[(CH_3)_2N]_2-CH_2$	102
DMF	Dimethylformamide	$H(C=O)-N(CH_3)_2$	73
TMU	Tetramethylurea	$[(CH_3)_2N]_2-C=O$	116
TMAE	Tetrakis(dimethylamino)ethylene	$C_2[(CH_3)_2N]_4$	200
TMO	Tetramethyloxamide	$[(CH_3)_2N]_2-(C=O)_2$	144

6-87

5804A28

Fig. 16

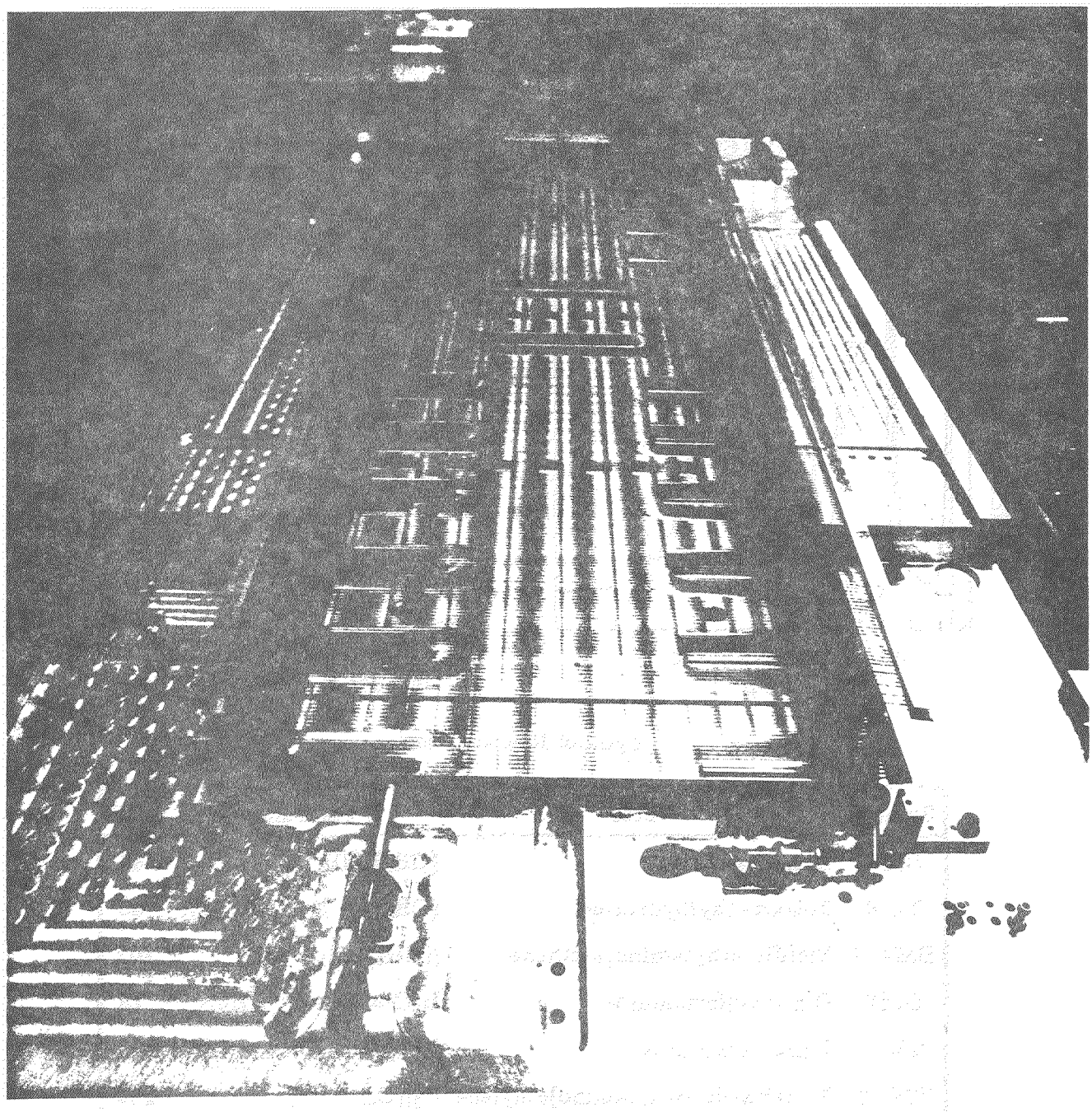

Fig. 17

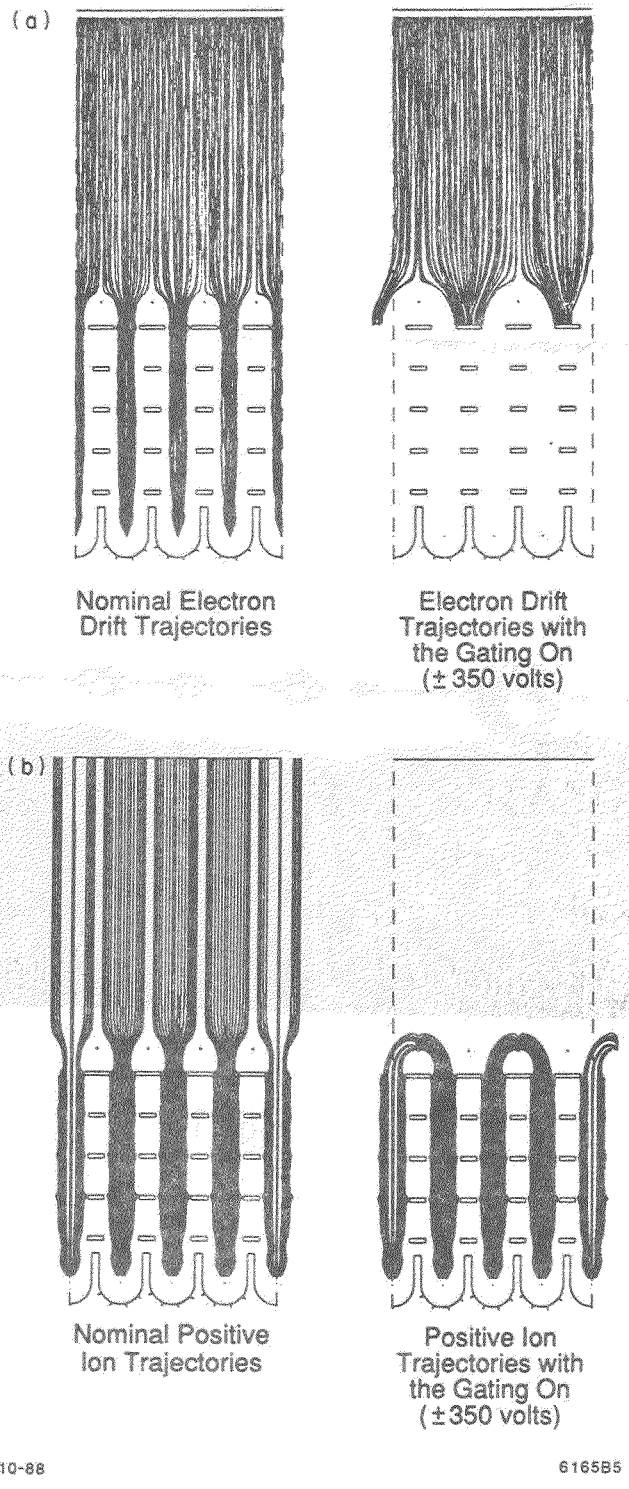
(a)
Nominal Electron Drift Trajectories
Electron Drift Trajectories with the Gating On (±350 volts)
(b)
Nominal Positive Ion Trajectories
Positive Ion Trajectories with the Gating On (±350 volts)
10-88
6165B5

Fig. 18

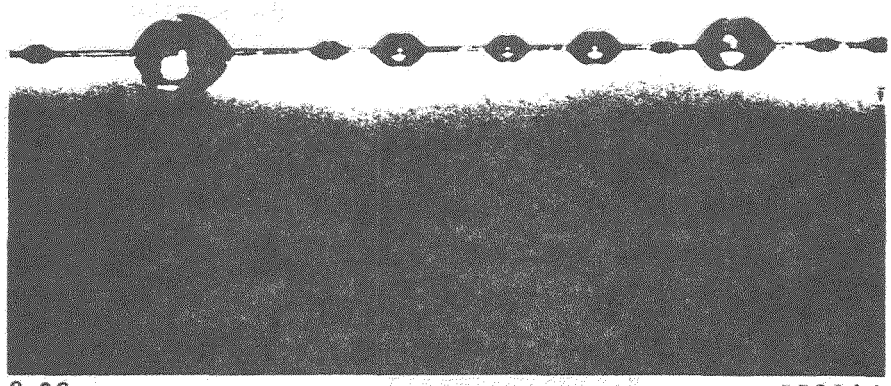

9-86 5563A1

Fig. 19

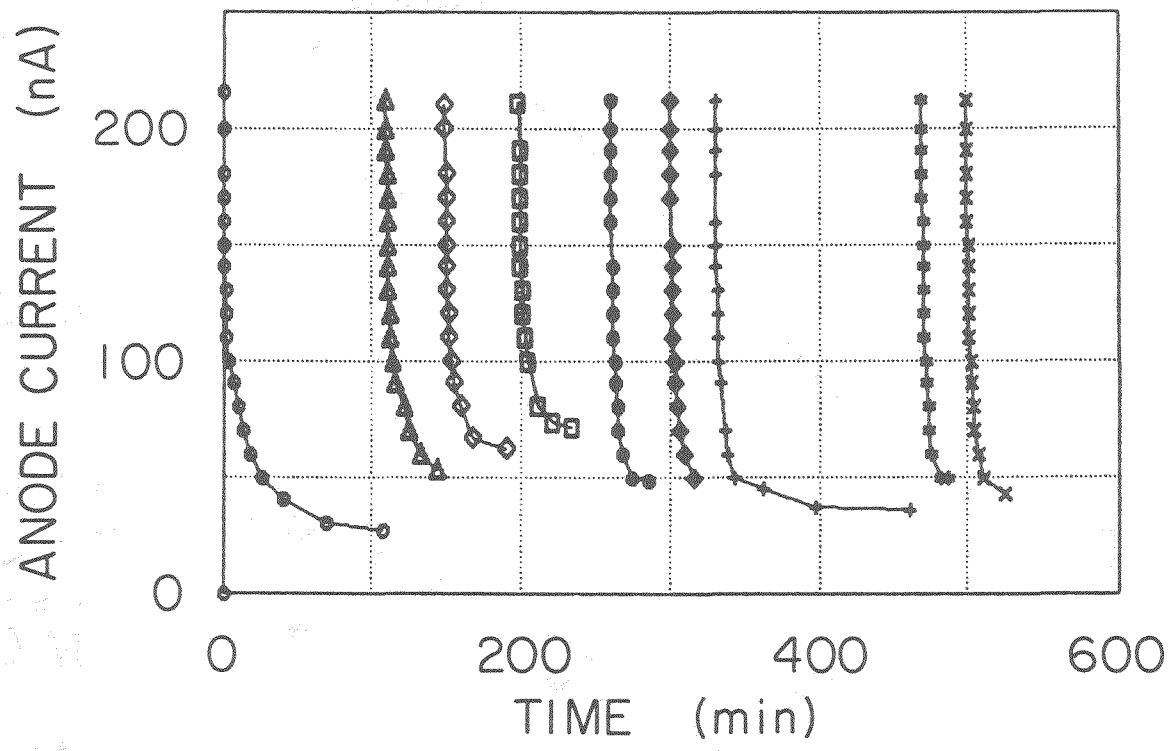
ANODE CURRENT (nA)
200
100
0
0
200
400
600
TIME (min)
6-87
5804A6
(arbitrary offsets between measurement)

Fig. 20

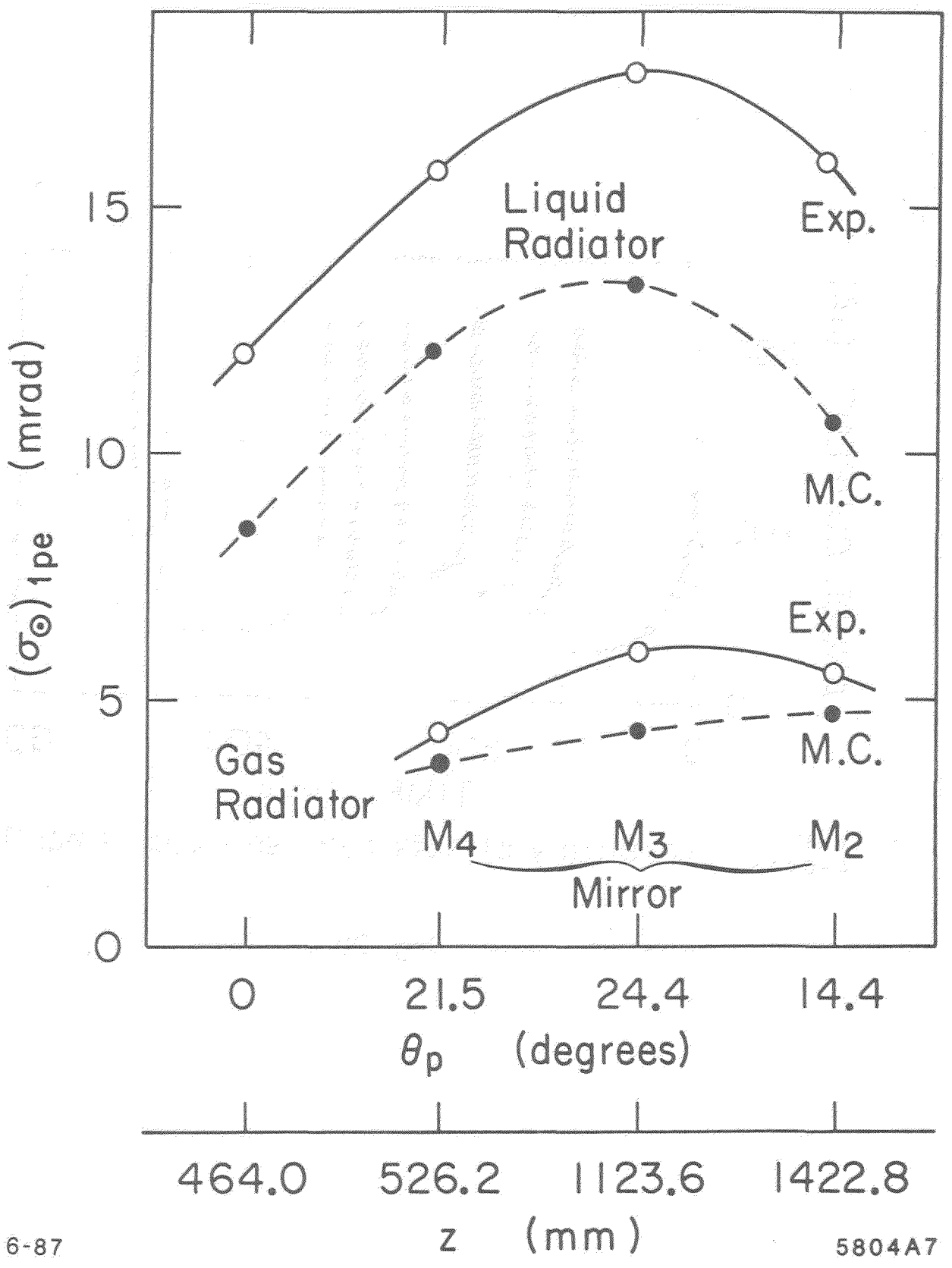
15
10
5
0
$(\sigma_\odot)_{1pe}$ (mrad)
Liquid Radiator
Exp.
M.C.
Exp.
M.C.
Gas Radiator
M_4
M_3
M_2
Mirror
0
21.5
24.4
14.4
θ_p (degrees)
464.0
526.2
1123.6
1422.8
z (mm)
6-87
5804A7

Fig. 21

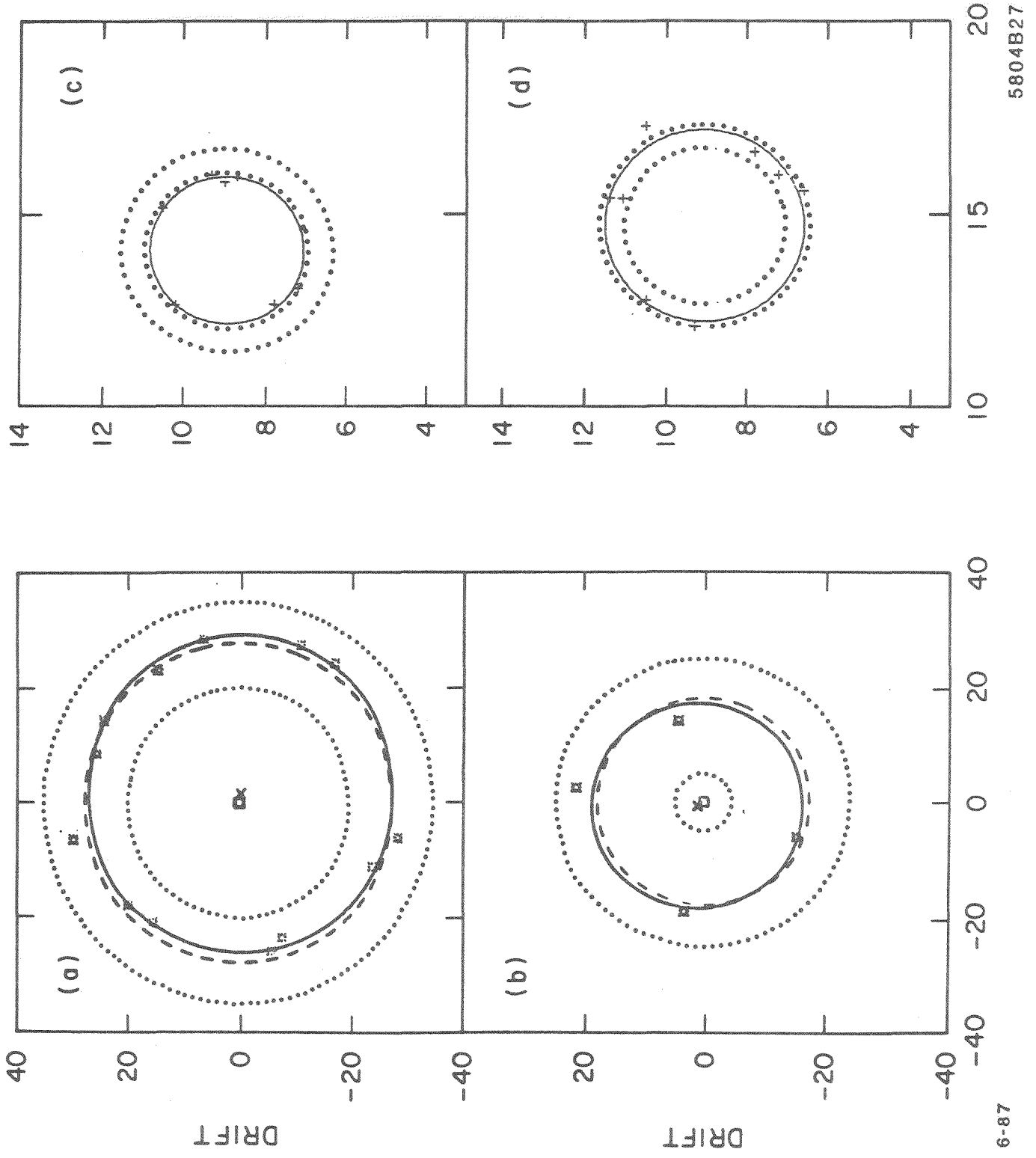

Fig. 22

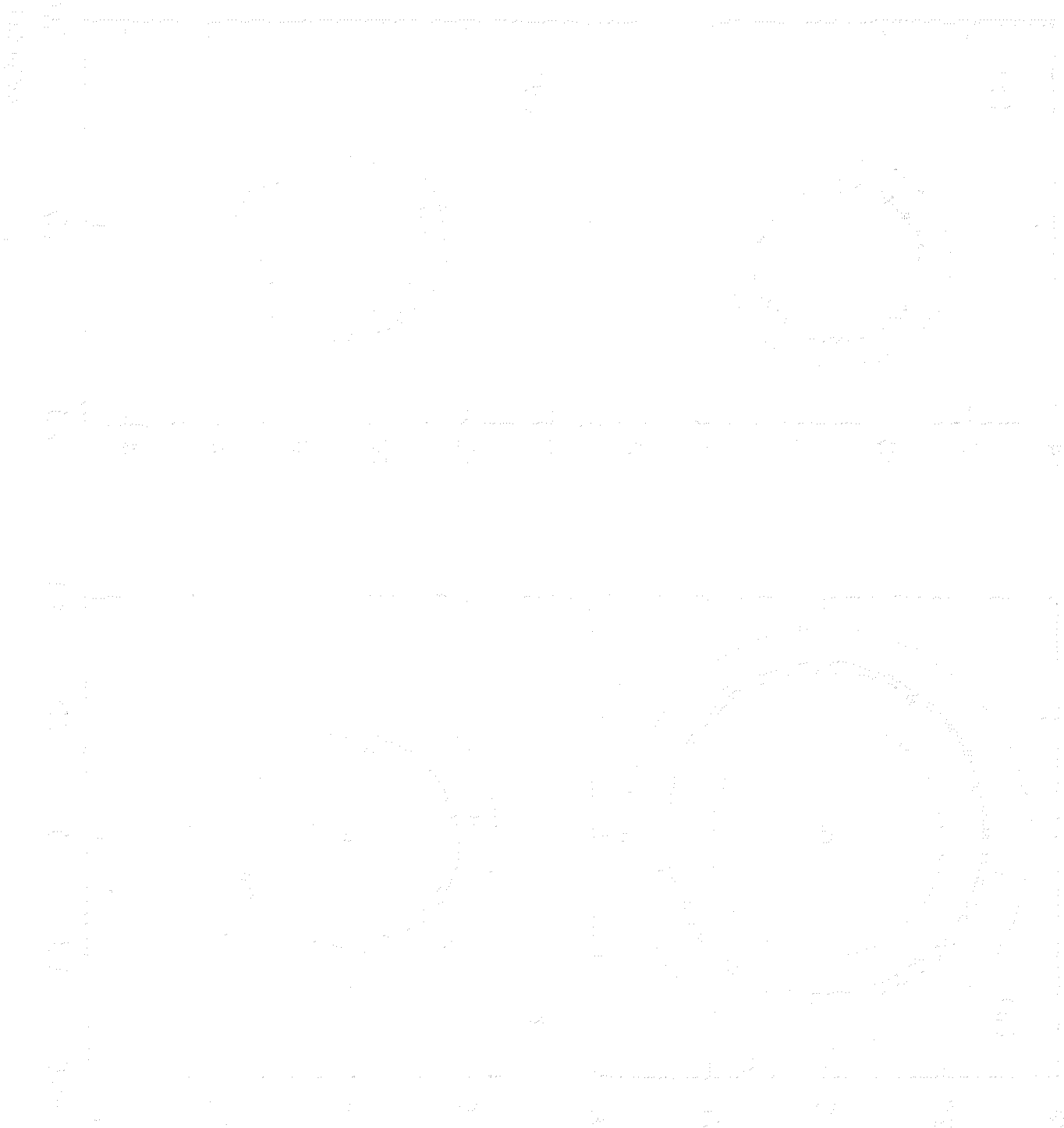

A PREAMPLIFIED DRIFT CHAMBER AS A PHOTON DETECTOR FOR HIGH-INTENSITY, HIGH-MULTIPLICITY RICH COUNTERS

G. Charpak
CERN, Geneva, Switzerland
and
N. Solomey
University of Geneva, Switzerland

Abstract

In the field of particle identification by Cherenkov ring imaging, there are two possible approaches to coping with characteristics of future colliders, such as high collision rates and high multiplicities. One of these methods is to develop detectors with a high spatial granularity by using arrays of small square pads. However, with this technique one must contemplate having millions or tens of millions of electronics channels. In this article we will show that orders of magnitude in the simplicity of the readout system can be obtained by combining a multistep avalanche chamber with a linear drift chamber; this technique is subsequently compared with that of high-density pad readout. We review the basic detector design and the performance of the multistep avalanche chamber with a linear drift-chamber readout, and describe how such a detector can be modified for use in a solenoidal magnetic field.

1. Introduction

A new gaseous detector, which combines a multistep avalanche chamber with a linear drift chamber, is proposed as the basis for a fast Ring-Imaging Cherenkov (RICH) counter in a collider experiment. Previous articles[1,2] have described the function and performance of this detector. This article reviews its basic principles and points out how it can be used as a vacuum ultraviolet (VUV) photon detector for use in a RICH at high-luminosity hadron colliders, where high multiplicities are expected. In an attempt to point out the possible advantages of our proposed scheme, a comparison is made between such a detector and the alternatively proposed method of using a high density of cathode pads in a multiwire proportional chamber (MWPC). We conclude with a discussion of how to make the detector function in a solenoidal magnetic field.

2. Detector design

The detector is constructed by combining a gated multistep avalanche chamber with a classical linear drift-chamber readout. The name 'Preamplified Drift-Chamber (PDC), is sometimes used for the sake of brevity, and because it suitably describes the operation of the detector. The amplification in the drift chamber alone would be insufficient to detect the ionization from the charged particles traversing

the detector out of time with the gate, so the intention was to have a slow drift-chamber readout of a gated 100 ns time slice. Hence the name originates from the fact that the drift chamber needs some additional amplification of the signal before the particles can be detected, and full amplification only occurs for events that are selected by the gating.

A high electric field between two parallel electrodes causes gaseous amplification by accelerating the electrons to an energy that is sufficient to further ionize the gas, thus building up a Townsend avalanche[3]. The multistep chamber is a method of combining two amplification regions that are separated by a transfer space. The original multistep chamber was a parallel-plate avalanche chamber (PPAC) coupled to a MWPC[4–6]. This work showed that is was possible to transfer the amplified swarm of electrons, in a proportional mode, to successive multiplying gaps, thus permitting gating at an intermediate stage and larger final gains.

The detector structure is shown schematically in Fig. 1. The VUV photons enter the detector gas volume from the left through a quartz window where they ionize the photosensitive gas, tetrakis(dimethylamine)ethylene (TMAE). The thickness of the conversion gap and the concentration of the TMAE determine the efficiency of photon detection. A fast-RICH needs to have a fast collection time, which in turn requires a thin conversion gap so that the electrons can all be collected within a short time-slice. All RICH detectors also require a high single-photon detection efficiency, and the aim is to have one or possibly two absorption lengths for the thickness of the conversion gap (66% or 88% detection efficiency). This requires a high TMAE concentration, which can only be achieved by heating the TMAE to high temperatures. To prevent condensation of the TMAE onto the walls of the detector, the chamber had to be heated to 10 °C higher than the TMAE temperature. When determining the thickness of the conversion gap it is necessary to take into account the drift velocity of the planned gas mixture as a function of the electric field, and the interaction length of the photosensitive gas. During the testing of our prototype we used a TMAE temperature of 42 °C with a 6 mm conversion gap. This represents one absorption length and a charge collection time of 150 ns. Future detectors, if properly designed, could conceive of using 80 °C for the TMAE temperature to achieve 15 ns charge collection time per interaction length.

The electrodes are composed of stainless-steel meshes made of 50 μm diameter wires with 0.5 mm pitch. The voltages on the electrodes are such that the electrons produced in the conversion gap are moved to the right (Fig. 1), where they enter a 3 mm amplification gap and are amplified in the high electric field. Gains of 1000 to 10,000 can easily be reached. The electrons then drift to the end of the amplification gap, where they can either be collected on the wire grid or transferred out. The percentage of electrons transferred out of the amplification region depends on the percentage of field lines leaving this region and entering the transfer gap; this is simply the ratio of the electric field in the transfer gap to that in the amplification gap[7]. Transfer efficiencies of 10% are reasonable, making an effective gain of 100 to 1000 for the amplification gap. The electric-field calculation for the transference out of the amplification gap is shown in Fig. 2. In the centre of the transfer gap there is a wire grid that gates the events of interest. A gas drift-delay in the 15 mm transfer distance to this grid allows time (1.5 μs) for an experiment to generate a trigger and open the gate for these events only. The transfer distance after the gate is also 15 mm, but it could be much smaller. The electric-field calculations for the gating electrode are shown in Fig. 3 for the two cases, gate open and gate closed. In this second transfer gap, the background signal originates from the ionization deposited by the charged particles that cross the gap but are not associated with the event of interest. If this second transfer gap is 2 mm, the background signal will be reduced. Then the gated signal from the conversion gap and the unwanted ionization from

the particles that are out of time with the event will enter a second amplification gap of 3 mm, identical to the first one. The purpose of the multistep chamber is not to amplify single photoelectrons sufficiently to detect them — it is only to amplify them above the level of the background ionization; the final detection is done with the anode wire of the drift chamber. Background ionization can also be reduced when the correct gas mixture is used. Because the photosensitive gas, TMAE, provides the single photoelectron, the carrier gas could be a low-ionization gas such as helium with the proper amount of quencher added.

After the signal is amplified in the second amplification gap it enters the transition region, where the electrons from the multistep chamber are transferred into the drift chamber (see Fig. 4) in such a way that the timing information can be used to determine the coordinate perpendicular to the anode wire. It is also important that the timing information be linear in order to make data collection and analysis easier.

The construction of the 10 mm thick drift chamber was standard: field-wire electrodes every 2 mm; 100 mm drift distance in both directions, to 50 μm anode wires. These wires were surrounded by ground electrodes on three sides and open to the drift chamber on the fourth. Behind the anode wires, an array of cathode strips, with 2.5 mm pitch, determined the coordinate of the signal along the anode wires. In this prototype, the anode wires were 200 mm long. For simplicity it was necessary to have the cathode strips at ground potential, which meant that all the multistep electrodes had to be at negative high voltage. Correct selection of the electric field in the transition region and in the drift chamber made it possible to transfer uniformly from the multistep chamber to the drift chamber; electric-field calculations were essential for making this selection. Also, such calculations showed that the drift-chamber electrodes had to have an electric field across the drift-chamber gap in order to help turn the lines of force; otherwise, many force lines from long drift distances would not terminate on the anode wire. There are also additional losses of the electrons in the transition region, because not all the electric field lines enter the drift chamber. The transparency is estimated to be 5%. A more detailed description of this type of detector is given elsewhere[1,2].

3. Detector performance

The detector was operated in the laboratory using single photoelectrons and with a gas mixture of helium (95%) + ethane (5%) bubbling through liquid TMAE at 42 °C. The detector was operated in an insulated hot box kept at 50 °C. The necessary operational voltages are listed in Table 1. Ultraviolet photons were produced by a deuterium spark-lamp, which provided a trigger when the lamp pulsed. The VUV photons were emitted over a 25 ns period and were collimated to the single photoelectrons by using a 30 cm tube with 200 μm diameter holes at both ends. Single photoelectron signals were used to determine the drift-time to drift-distance relation shown in Fig. 5. The Start signal for a timing measurement was the deuterium spark-lamp pulse; the Stop came from the cathode-strip signal. Figure 6 shows the timing measurements for a special collimating tube with two holes, 3 mm apart. Two peaks are visible, which indicates that the position resolution is better than the hole separation, and that it is comparable to the position resolution of 2.4 mm FWHM obtained by other methods. A more detailed description can be found in Ref. 2. This accuracy was obtained, despite the absorption depth of 6 mm in the conversion of VUV photons, because the electron drift velocity was much larger in the conversion gap than in the drift chamber.

Table 1

Voltages used for operation; symbols refer to those of Fig. 1.
Gate-plane voltage was for the condition of gate-open;
the gate-closed condition had ± 100 V on alternating wires.

Electrode	He (95%) + ethane (5%) with 42 °C TMAE
D	−5600
P1	−5000
P2	−3700
G	−3200
P3	−2700
P4	−1500
Drift chain	−1000 to 0
Offset across drift chamber added on entrance electrodes to DC	+10
Anode	+900

A multistep avalanche chamber is ideal for the detection of single photons in a high-rate environment. The transfer space between the amplification regions permits high final gains, of about 10^6, without the photon feedback and wire-ageing problems that plague many single-step VUV photon detectors. The gating of the intermediate swarm of electrons serves several important purposes, which should be considered:

i) It determines the resolution time, which can be as short as 10 ns but which has to be adjusted for the charge-collection time across the conversion gap.

ii) It eliminates the feedback of positive ions moving out from the second amplification gap, whilst the large transfer space stops the photon feedback by not permitting the full amplification needed to detect these single feedback photons.

iii) A delay of the order of one or several microseconds is available for the selection of only the events of interest.

These features combine to form a powerful detecting tool, well suited to the needs of a RICH detector in a high-interaction-rate environment. Maybe the most important feature of these characteristics concerns the ageing. Because the acceptance rate of the detector is selected by gating, not all the events will experience full amplification. This is an important advantage in high-intensity-radiation environments. The process of amplification between two parallel meshes does not take place on the wires but is in the high electric field region between the meshes themselves. Because of this, and the fact that the amplification of an individual PPAC gap is low, it is suspected that the ageing of the parallel-plate amplification part of the detector is not caused by high radiation doses. The anode wire in the drift chamber does collect a large amount of charge for events that are fully amplified; however, this

is at a substantially lower rate than the one to which the detector is subjected. For instance, with the gas mixture tested by us, i.e. helium (95%) + ethane (5%) bubbling through hot TMAE, the ionization of minimum-ionizing particles is about 10 ion pairs per centimetre. In our proposed detector, with a total length of 2 mm after the gating, this would give rise to about two electrons, which should be compared with the 1000 electrons that can be extracted from the first amplification gap initiated by the conversion of a single photoelectron. Because the gating is done by pulsing alternating wires at about 100 V, the noise induced in the detector electronics is paralysed for some time, and a drift delay of 1 μs is necessary after the gating. Some additional electrons originate from this drift-delay gap, but they are not subjected to the full amplification; however, because of ageing, they must be considered when calculating the total charge accumulated on the anode wire of the drift chamber. As the total number of anode sense wires is small, the detector could be constructed in such a way as to permit their periodic replacement without any great difficulty. The pulsing of the gating does present a serious problem for gaseous detectors that operate at low gas gain and need sensitive electronics, such as in the Time Projection Chamber, although here the problem is far less serious because the electronics used on the cathode strips can be simple current amplifiers that are less sensitive, and because the anode wires and cathode strips can be shielded from the pulsing of the gate plane.

Although the position resolution for charged-particle tracking with the PDC has not yet been measured, it is expected to be better than that of single photons because the depth of the conversion error for ionizing charged particles will not exist. Before such a detector could be realized for use in an actual collider experiment, it would be necessary to measure the drift-time to drift-distance relation in a magnetic field and to determine the magnetic deflection angle accurately. Also, the question of PPAC ageing should be confronted, and in this respect we should determine if the perceived advantage really exists.

4. Comparison with an alternative technique

Many other authors[8–10] have suggested that MWPCs be used with an array of small cathode pads to achieve the high granularity needed for large multiplicities. The proposed cathode-pad size varies, but it can be as small as 2 mm × 2 mm (Ref. 9). The detector would be either simple MWPCs[8,9], or multistep chambers with the second step being a MWPC[9,10]. All the proposed methods involve using large numbers of cathode pads requiring massive cabling and electronics. Another requirement for the cathode-pad chambers is that the amplification wires be extremely close to the pads, so as to reduce the spatial dimensions of the induced pulses. Although the technique of using a simple MWPC with a large number of cathode pads has, at first glance, the appearance of simplicity, this may be deceiving if one does not pay close attention to the supporting equipment that is needed in order to realize the idea.

Imagine using a 1 m gaseous RICH with the detector plane at a radius of 1 m from the collision axis and covering the $\pm 45°$ barrel region; this represents a 12 m^2 surface area to be covered by the photon detector. If such an area were to be covered with 2.5 mm × 2.5 mm cathode pads, it would need 2 million pads with their supporting electronics. On the other hand, if a PDC is used to cover such an area, with a 20 cm drift distance and 2.5 mm cathode strips, this would require only 25 thousand electronics channels. Although the electronics for the drift chamber would be slightly more expensive, the arrangement could still be kept quite simple by using flashing discriminator electronics, which do not require any flash-ADCs. The only electronics that have to sit on the drift-chamber cathode strips are the preamplifiers, and these must be constructed out of special silicon so as to permit long-term operation in the expected radiation environment. All the supporting electronics for the cathode-strip

preamplifiers could be located far away in the counting room and would not have to be constructed from radiation-hard silicon. However, the electronics for the cathode-pad readout, whilst slightly less expensive, would still have to be radiation-hard. Also, they must be controlled in order to facilitate the readout, possibly using shift registers or multiplexers to store the data in a pipeline until it is decided whether a particular event should be saved. With the drift-chamber readout, the gas drift-delay provides the pipelining of the individually spaced events until a decision is made to gate a given one. The drift-chamber readout performs the task of multiplexing by using the gas drift-delay, thus greatly reducing the number of channels needed. The high-density cathode-pad readout construction has the definite advantage of being less thick, as it occupies only 10 mm, compared with the 80 mm needed for a PDC construction. However, with the former technique, the amount of space required for the cabling and electronics could still be quite significant, and would probably put additional material in the path of the particle flux. This would be avoided with the drift-chamber technique. Also, the necessary high-voltage system for the PDC readout is high, requiring 12 high-voltage power supplies, gating electronics, and a divider chain; but this is a small price to pay, when we consider the savings in the electronics.

5. Operation in a magnetic field

During the 1989 Vienna Wire Chamber Conference, where the initial paper on the PDC was presented, we were approached by many people who were curious to know if such a detector could operate in high magnetic fields, for example the fields being considered for the SSC or the LHC. Since then, we have considered this question, and we now know how to construct a chamber that would give optimum performance in a solenoidal magnetic field. We discuss here the effects of magnetic fields that would alter the paths of the electrons, and give a brief description of the detector.

In the absence of a magnetic field, the electrons are influenced only by the electric fields that move along the electric-field lines. When a magnetic field is added, there is an additional force exerted on the electrons, which is in the direction of the vector cross-product ($B \times E$) and is proportional to the initial velocity of the electron. There are two cases to consider. First, the multistep chamber with two PPACs placed in a solenoidal magnetic field in such a way that the electric field lines point radially towards the centre of the solenoid and the magnetic field lines are parallel to the axis of the solenoidal magnet's cylinder. In this case, E and B are perpendicular to each other, and the cross-product ($B \times E$) causes the electrons to move at an angle to the electric field. In high-velocity gases, for example in mixtures containing argon, this angle is large. However, since the main gas considered here is helium, the drift velocities are low, thus the magnetic field creates proportionally smaller deflection angles. Because there is no way to compensate for this angle, the multistep part of the detector should be designed to take advantage of if, and should therefore be built at a slight tilt. The exact deflection angles in magnetic fields, with our gas mixture, are not known, but extrapolation of the data of other known gases with low drift velocities implies that in a 1.5 T magnetic field the angle should be less than 4°.

The second case—that of a drift chamber in a magnetic field—is well known[11], and this additional magnetic force can be corrected for by adding a small electric field across the drift-chamber gap to balance the force due to the magnetic field. Preliminary calculations of the effects of combined electric and magnetic fields for a low-drift-velocity gas are shown in Fig. 7a, and a sketch of how an array of PDCs could fit together to form the photon detector for a gaseous RICH is shown in Fig. 7b. Because the electron drift paths do not enter the PDC perpendicularly, as happens in the first case described above, the transfer efficiency into the PDC seems to be higher. We have done some

calculations of electric fields at this angle and find that the field lines enter the drift chamber more readily when it is slightly tilted; thus we conclude that the magnetic field will improve the performance of the detector.

6. Conclusions

We have combined the advantages of the avalanche chamber with those of a drift chamber and have shown that it is possible to design electrode configurations that permit electrons from the second amplification gap to be extracted and drifted at nearly right angles, over a distance up to 10 cm into a linear drift chamber[2]. With a drift length of 10 cm, the data readout time is 14 μs; this allows 80 kHz readout rates. With a thin conversion gap and using extremely hot TMAE (80 °C), collection times of 15 ns could be reached in the near future. This would give interaction rates of 33 MHz, which are close to the design goal of the SSC. The position resolution with 40 °C TMAE and a 6 mm conversion gap has been shown to be 2.4 mm FWHM; with higher temperatures the absorption length can be lowered to 0.6 mm and the position resolution should improve. The considerable reduction in the number of electronics channels would allow a more sophisticated processing to be envisaged: for instance, the delay and storage of the data by electronic means, so that extremely slow trigger-generating devices have sufficient time to produce a secondary trigger; or the preliminary analysis of the PDC data itself, to generate a secondary trigger. Although the method described here is unconventional, we take great pride in stressing it as an alternative to high-density cathode-pad-readout techniques. The considerable reduction in the number of channels would result in a great saving in cost, which should not be overlooked when we consider that other components of a detector at the SSC will also have staggering numbers of channels to read out.

References

[1] N. Solomey et al., Nucl. Instrum. Methods **A271** (1988) 423–31.

[2] N. Solomey et al., Univ. Geneva preprint UGVA-DPNC 1989/2–132, presented at the Wire Chamber Conference, Vienna, 1989.

[3] J. Townsend, 'Electricity in gases' (Univ. Press, Oxford, 1914).

[4] G. Charpak et al., CERN 78–05 (1978).

[5] G. Charpak and F. Sauli, Phys. Lett. **78B** (1978) 523.

[6] A. Breskin et al., Nucl. Instrum. Methods **161** (1979) 19–34.

[7] A. Breskin et al., Nucl. Instrum. Methods **178** (1980) 11.

[8] P. Fischer et al., IEEE Trans. Nucl. Sci. NS–35 (1988) 432.

[9] J. Séguinot, 'LHC/SSC Fast RICH', these proceedings.

[10] S. Dhawan, 'Pad readout techniques', these proceedings.

[11] G. Charpak et al., Nucl. Instrum. Methods **108** (1973) 413–26.

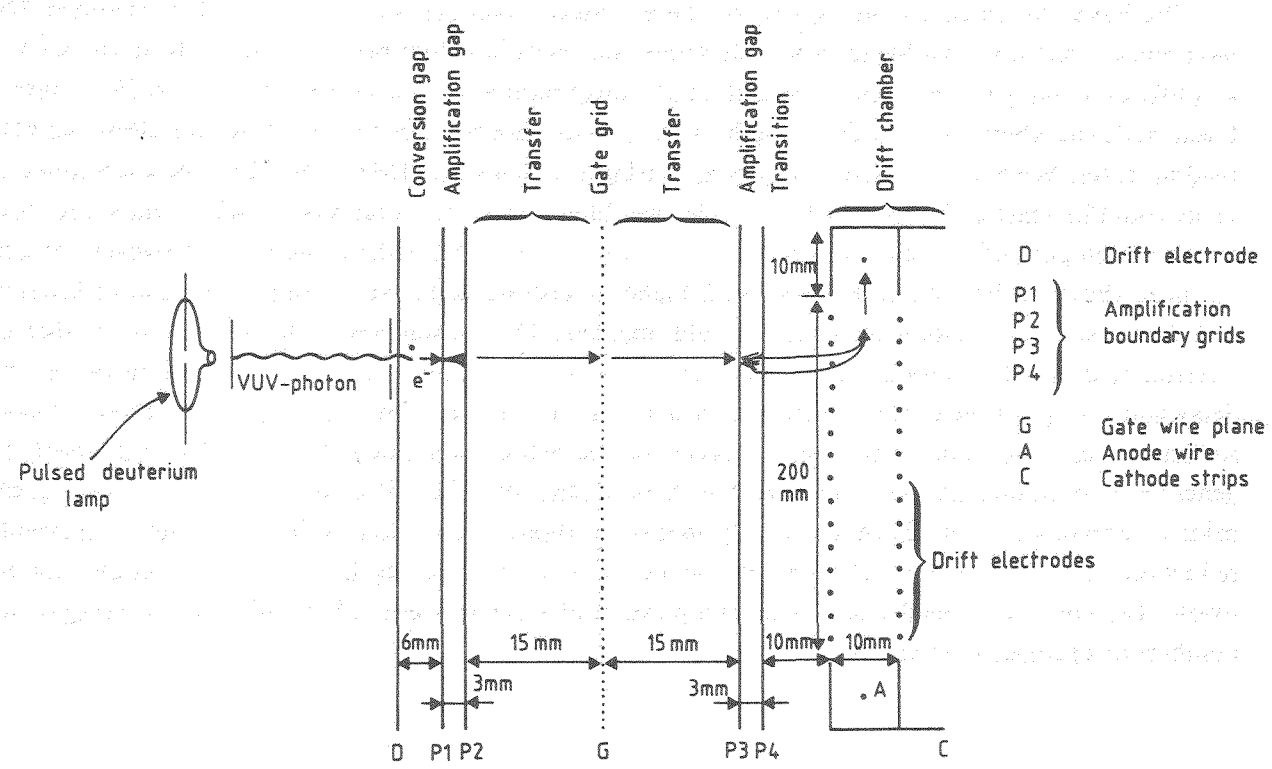

Fig. 1 Detector design showing the mesh planes (solid lines), the gating grid (dotted line), and the drift-chamber readout.

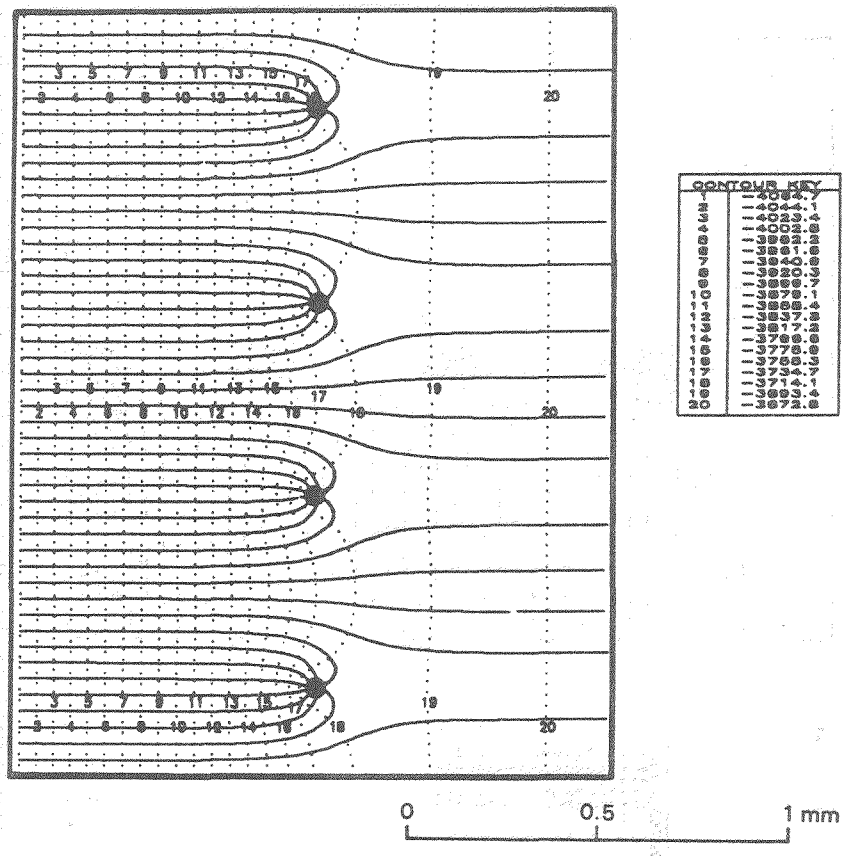

Fig. 2 Three-dimensional calculations of the electric field for a mesh-plane structure. The transfer region is shown here, with the parallel-plate amplification on the left and the transfer gap on the right. Only the wires perpendicular to the plane of the page are shown (small solid circles). The equipotential lines are dotted and the electric field lines are solid. The values of the equipotential lines are shown in the right-hand part of the figure.

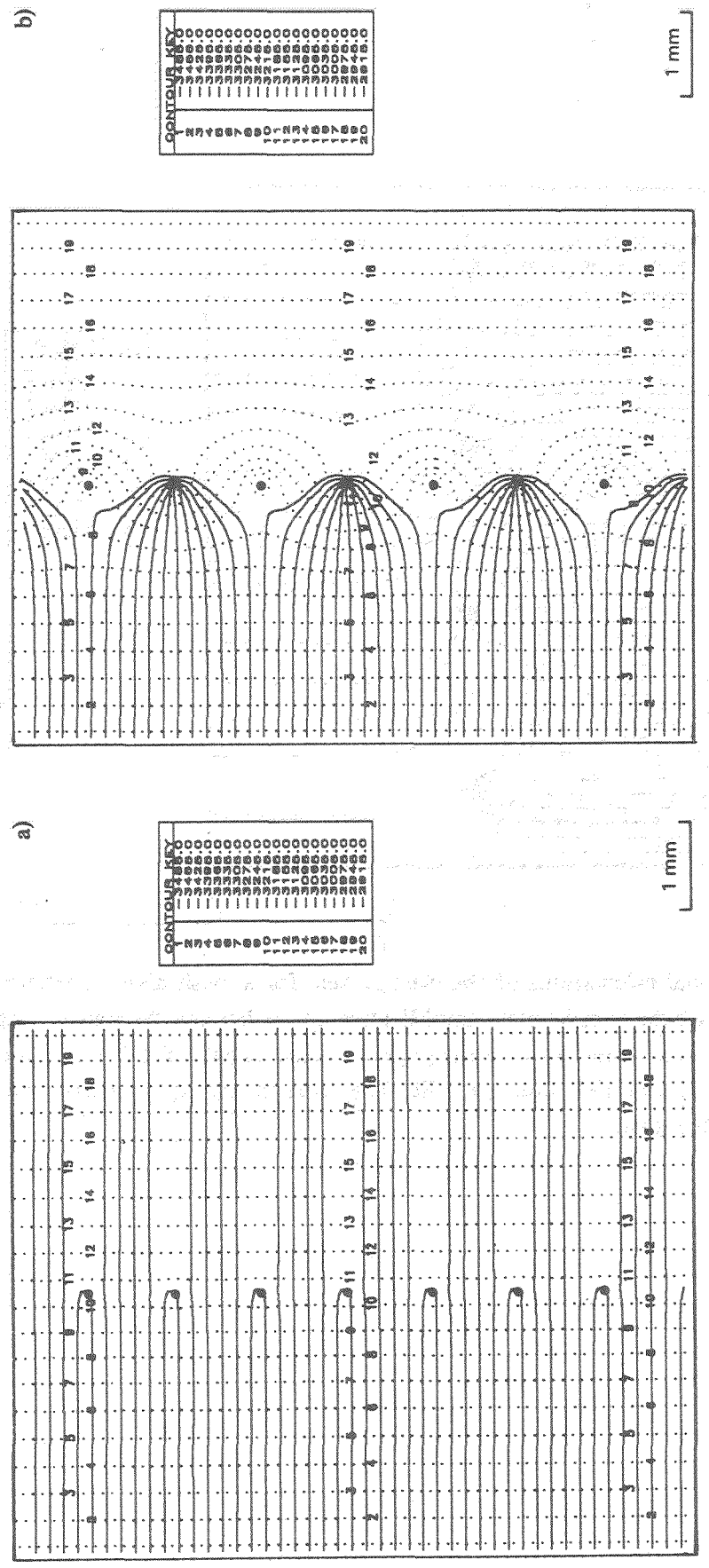

Fig. 3 Two-dimensional calculations of the electric field for the gate-wire plane structure. The wire spacing is 1 mm, and the wire diameter used in the calculations was 100 μm. Figure 3a shows the gate open; Fig. 3b shows the gate closed using 200 V potential difference.

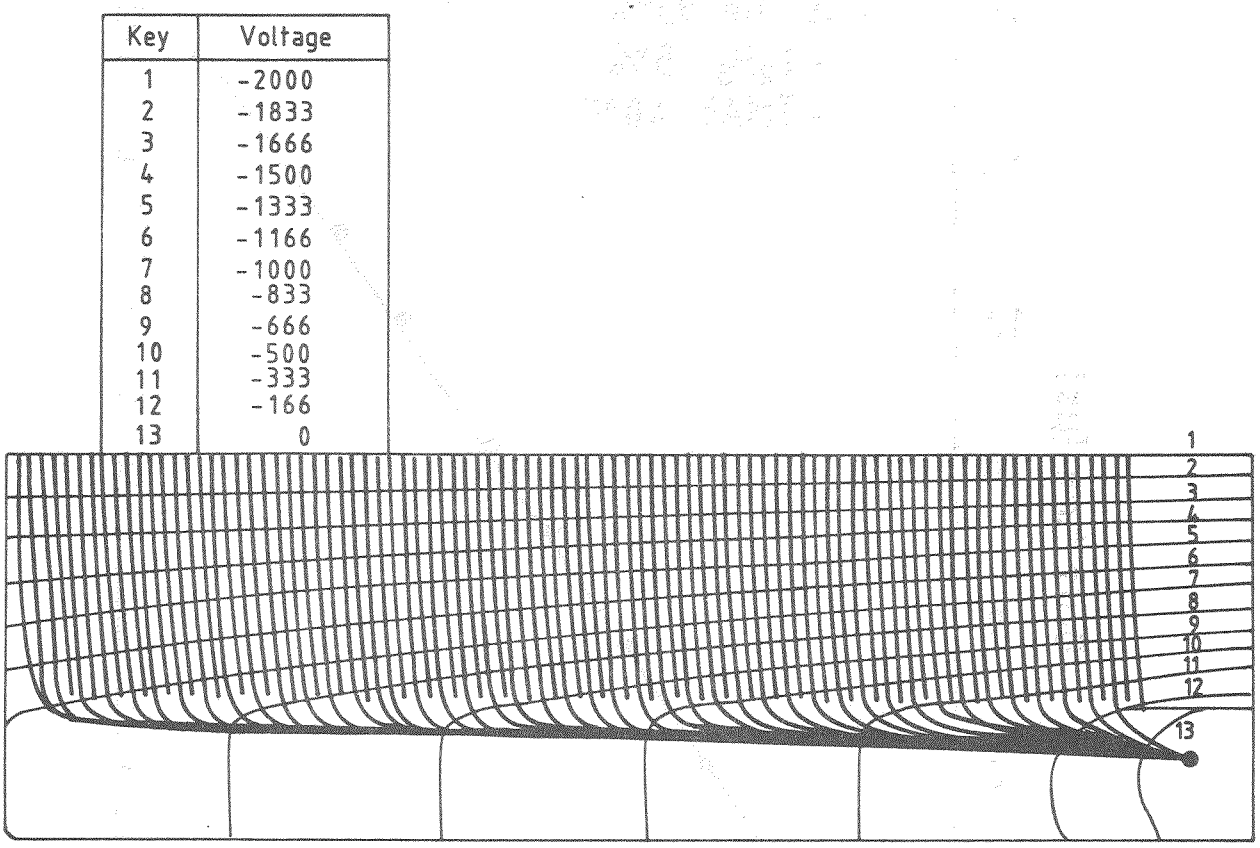

Fig. 4 Electric field calculations for the transition region from the multistep chamber into the drift chamber. The dark lines are the force lines, and the lighter are the lines of equipotentials. The values of the equipotentials are given in the key. The drift chamber has an offset voltage across the electrodes with + 10 V more on the top one.

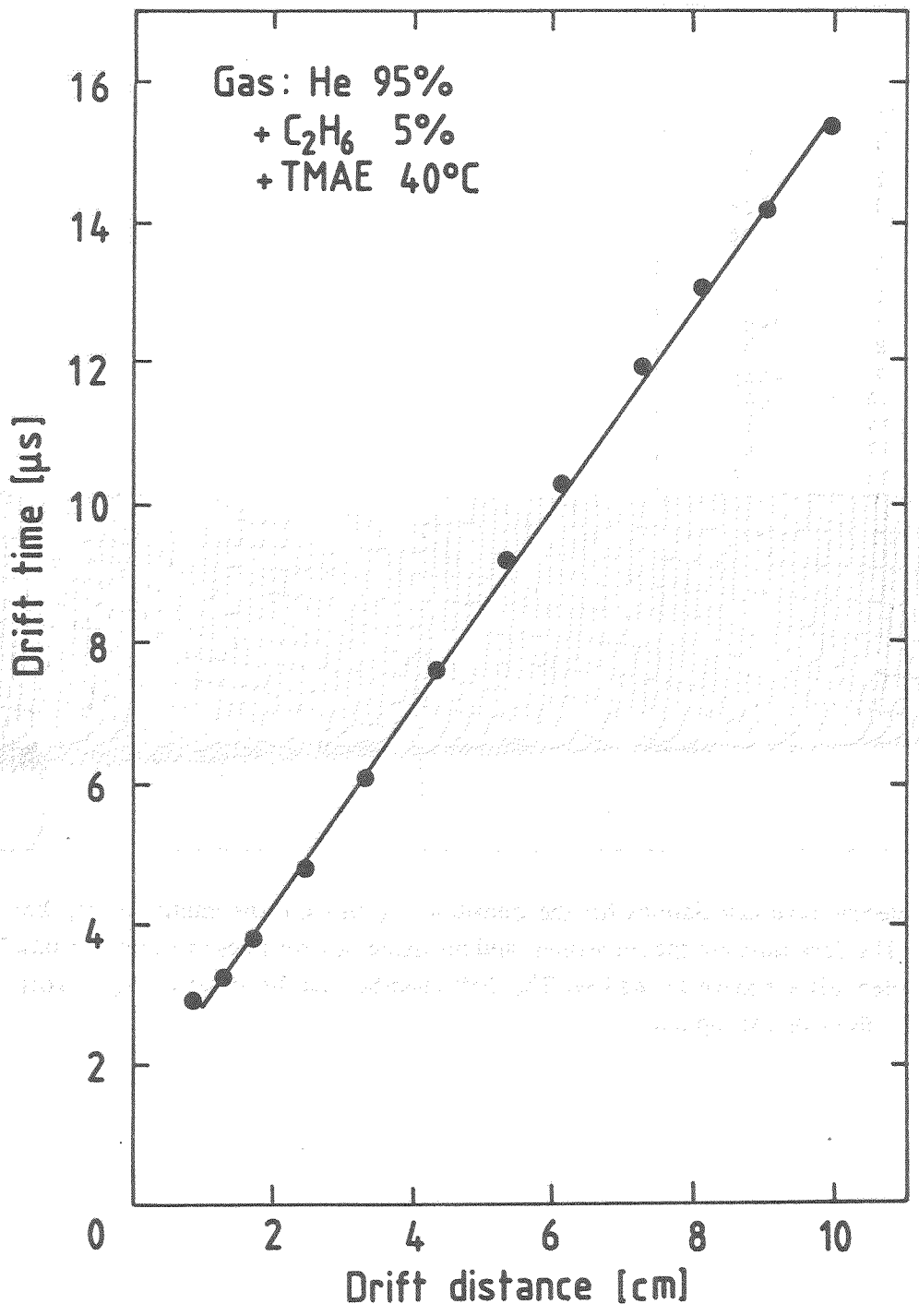

Fig. 5 Drift-time to drift-distance relation for single photoelectrons in a gas mixture of He (95%) + ethane (5%) bubbling through TMAE at 42 °C.

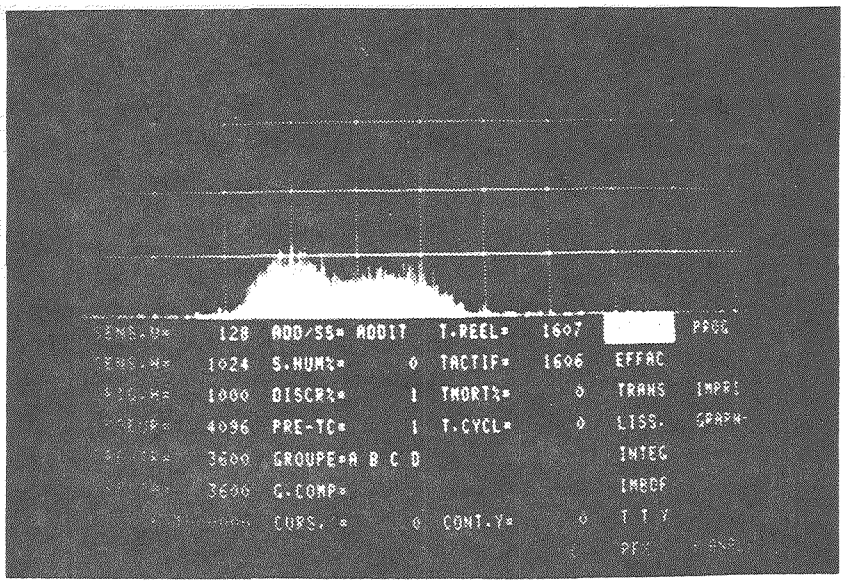

Fig. 6 Single-photoelectron timing distribution using a collimator with two 200 μm diameter holes, 3 mm apart. It can be seen that the position resolution is quite good and is comparable to the 2.4 mm FWHM position resolution found previously (Ref. 2).

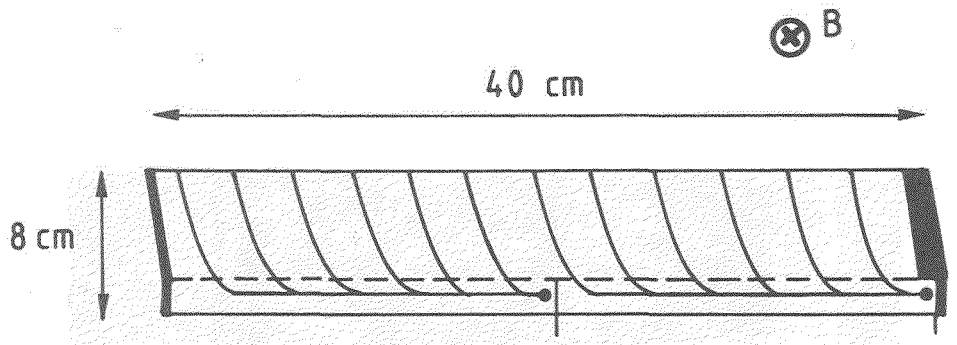

a) Possible chamber construction for use in a high magnetic field. The slight tilt is caused by the deflection of the electron drift paths in a magnetic field, and a compensating electric field is added across the drift chamber.

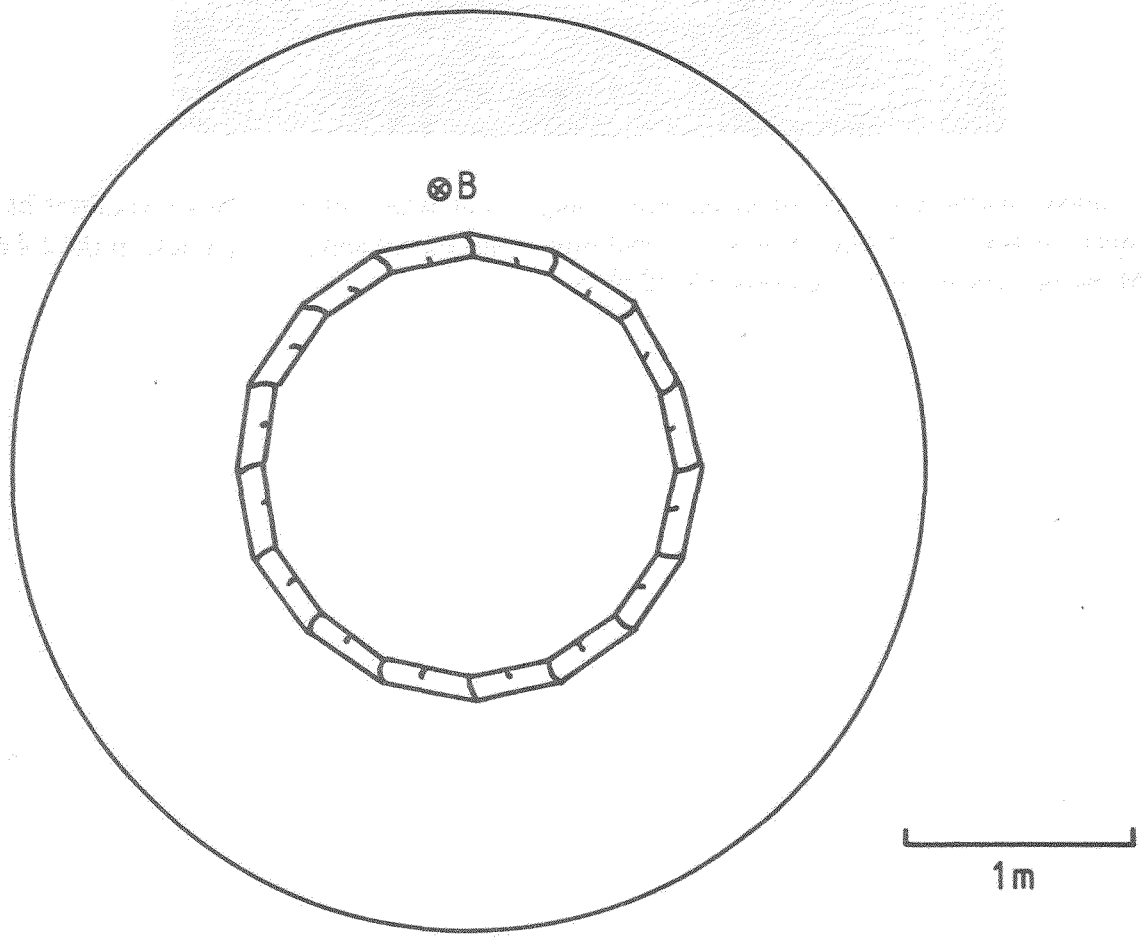

b) A 1 m gaseous RICH surrounding the collision region of a collider with the preamplified drift chambers from (a).

Fig. 7

A FAST RICH COUNTER FOR THE LHC/SSC

by

J. Seguinot

College de France

(A late arriving addendum containing Seguinot's comments to his transparencies can be found in section VIII beginning on page 671.)

J. SEGUINOT

FAST RICH DETECTORS FOR LHC / SSC / ELOISATRON

COLLABORATION

C.d.F (Paris) : J. Séguinot, T. Ypsilantis

C.R.N (Strasbourg) : R. Arnold, J.L. Guyonnet, E. Christophel

R.A.L (Rutherford) microelectronic group : J. Alsford, M. Bramhall, M. French

Support : IN^2P^3 (Fr.) - LAA project (CERN)

OUTLINE :

1.- THE FAST RICH TECHNIQUE :

i) the requirements (time dispersion - data acquisition rate - importance of a RICH det^r at LHC/SSC)

ii) the possible choices :

- Photosensitive organic agents (new lab. measur^{ts})
- Photodetectors : results of tests (det. effic. - cluster size - résolution ...)

2.- THE BMF RICH DETECTOR

Example of a fast RICH (4.10^5 elect. channels)

3.- VLSI SILICON CHIP DEVELOP^T AT RAL for fast readout of a pad RICH detector.

FAST PHOTONDETECTORS

-

1.- **SPATIAL RESOLUTION**

i)- for reconstructing the photoel. conversion point

⇓

According to T.V :

- least dispersive gaseous radiator (He, CF_4 ...)
- mirror focal length : 4 m

⇓

reconstruction error ≥ chromatic error

for, 2×2 mm^2 measur.t pixels

ii) reconstruction ambiguity (multi-hit capability for large multiplicity ev.ts)

2.- **MERIT FACTOR N_0** :

Photosensitive organic agent dependant .

3.- **TIME DISPERSION Δt**

for collecting p.e

interaction rate (LHC / SSC) $\geq 10^8$ sec^{-1}

⇓

$\Delta t < 10$ ns

to avoid overlapping of ev.ts from successive beam crossings

4.- **DATA ACQUISITION RATE** :

up to 10^4 ev.ts sec^{-1}

A difficult but exciting challenge

LHC / SSC :

interaction rate $\gtrsim 10^8$ sec^{-1}

⇓

Photon collection time dispersion < 10 ns

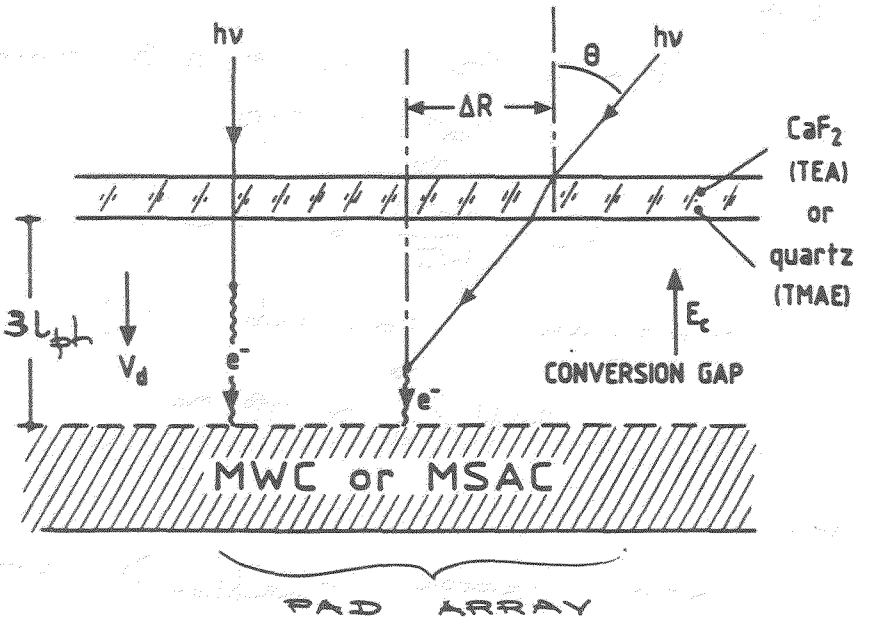

$3\,l_{ph}$ (ph. absorpt. length) ⇒ 95% absorption

⇓

$3\,l_{ph}/v_d$ = Total dispersion time

v_d = el. drift velocity

PHOTOSENSITIVES MOLECULES

TMAE , TEA , TMA

in various carrier gas

(CH_4, C_2H_6, iC_4H_{10} ...)

$\sigma \leq 10$ ns

⇓

$l_{ph} = 1$ mm – TEA or TMAE in CH_4

0.6 mm – TMAE in $CH_4 + C_2H_6$
or $CH_4 + iC_4H_{10}$

TEA :

$t = 20°C \Rightarrow p \cong 50$ torr

$\sigma_a \cong 10$ Mb

⇓

$$l_{ph} = \frac{kT}{p\sigma} \cong 0.6 \text{ mm}$$

$(k = 1.036 \text{ mm} \cdot \text{torr} \cdot \text{Mb} \cdot °K^{-1})$

⇓

$3\, l_{ph}/v_d \simeq 18$ ns

TMAE

one needs $t_{bubbler} > 100°C$

⇓

construction problems ?

TMA

gaseous at room t°

$\sigma \cong 3$ Mb

$l_{ph} = 1$ mm ⇒ $p = 100$ torr

detectors work .

TEA Q.E. measts :

- chemical actinometry : Salomon et al. (Journal of chem. Physics 62 (75)) ⇒ $(Q.E)_{8.4\,eV} = (.47)$
- Ionis. chamber – monoch. { Goehlich et al. (Rev. Sc. Inst 58 (87) ⇒ $(QE)_{max} = (.43$; Holroyd et al. (NIM - A261 (87) ⇒ $= (.33)$

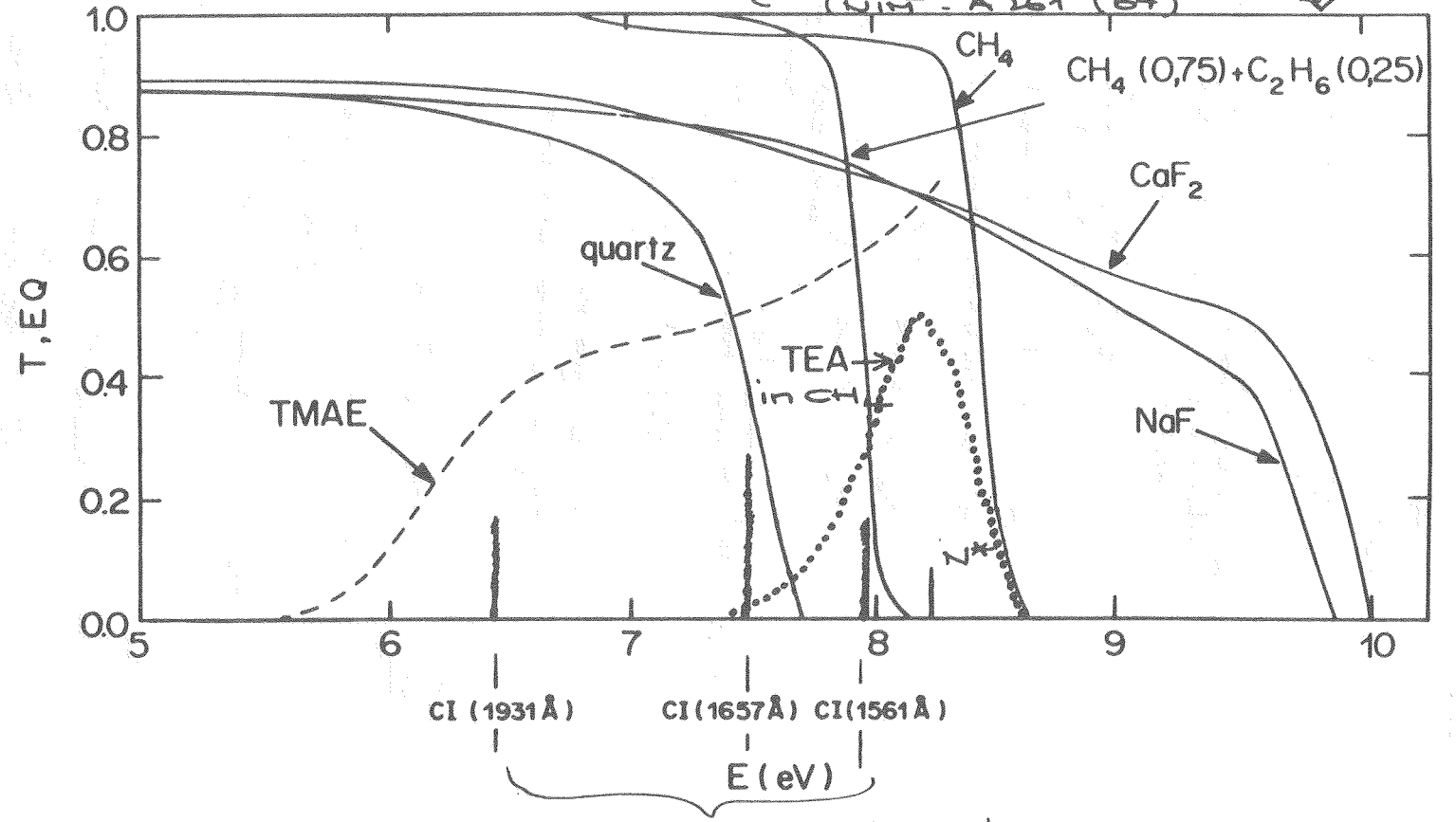

Atomic C excitation lines

Relative intensities : 3 : 5 : 3

ELECTRONIC TIME SLEWING

DETECTOR + PA

⇓

Signal :

$$S(t) = \int_0^t i(t-\tau) \cdot v(\tau) \cdot d\tau$$

$i(t)$ ⇒ develop^t of the induced charge by a pe on a wire

$$i(t) = Q_0 \cdot \frac{C_0}{4\pi\varepsilon_0} \cdot \frac{1}{t+t_0}$$

Q_0 = total induced charge

C_0 = capacitance/unit length of wire

ε_0 = 8.85 pf/m

$t_0 \simeq 1$ ns (gas and detect^r geometry dependant)

$v(t)$ ⇒ (impulse time response of the PA

$$v(t) = K \cdot \frac{t}{\tau_0} \cdot e^{-t/\tau_0}$$

K ≃ gain

τ_0 = time constant

Ex. $\tau_0 = 5$ ns

$S(t)$ max ⇒ $t_{max} \simeq 10$ ns

$(Q/Q_0 \simeq .25)$

For a furry (exponential) distribution of Q_0

⇓

t_{max} = max. time dispersion

$$\sigma = 10/\sqrt{12} \simeq 3 \text{ ns}$$

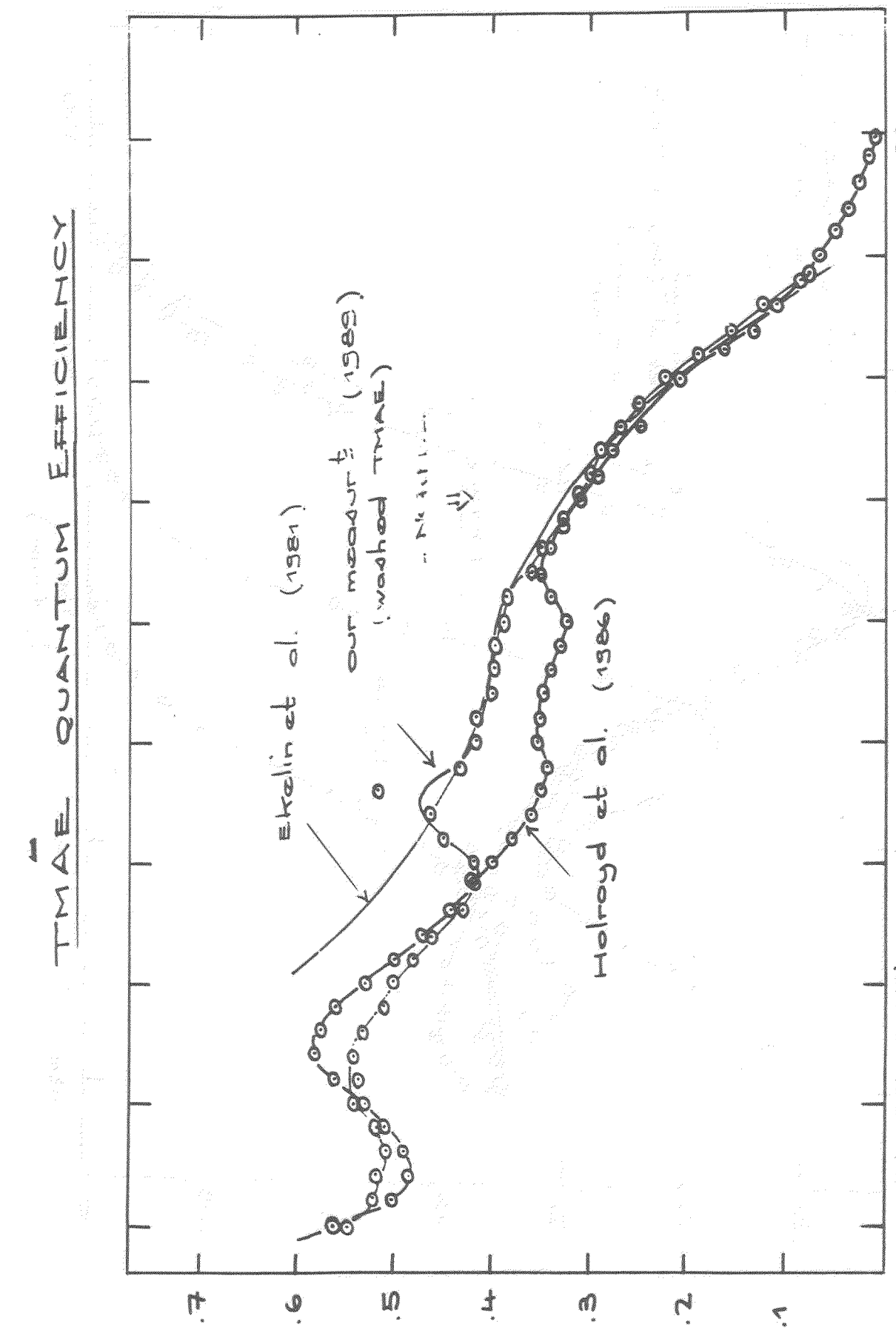
TMAE QUANTUM EFFICIENCY
Ekelin et al. (1981)
our measurement (1989)
(washed TMAE)
Holroyd et al. (1986)
0.
0.1
0.2
0.3
0.4
0.5
0.6
130
140
150
160
170
180
190
200
210
220
λ (nm)

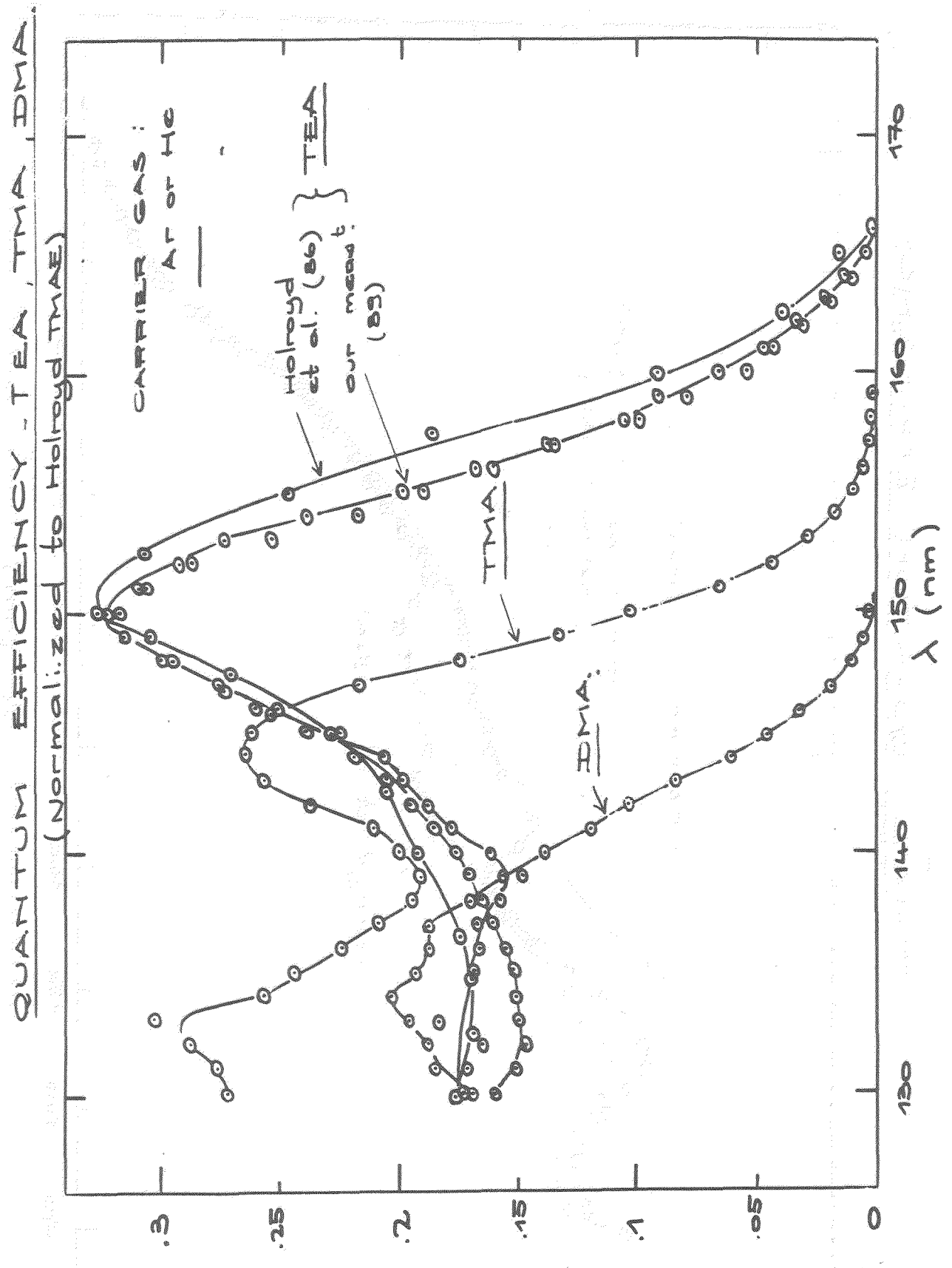
QUANTUM EFFICIENCY - TEA, TMA, ADMA
(Normalized to Holroyd TMAE)
CARRIER GAS:
Ar or He
Holroyd et al. (86) } TEA
our meas. (85)
TMA
ADMA
.3
.25
.2
.15
.1
.05
0
130
140
150
160
170
λ (nm)

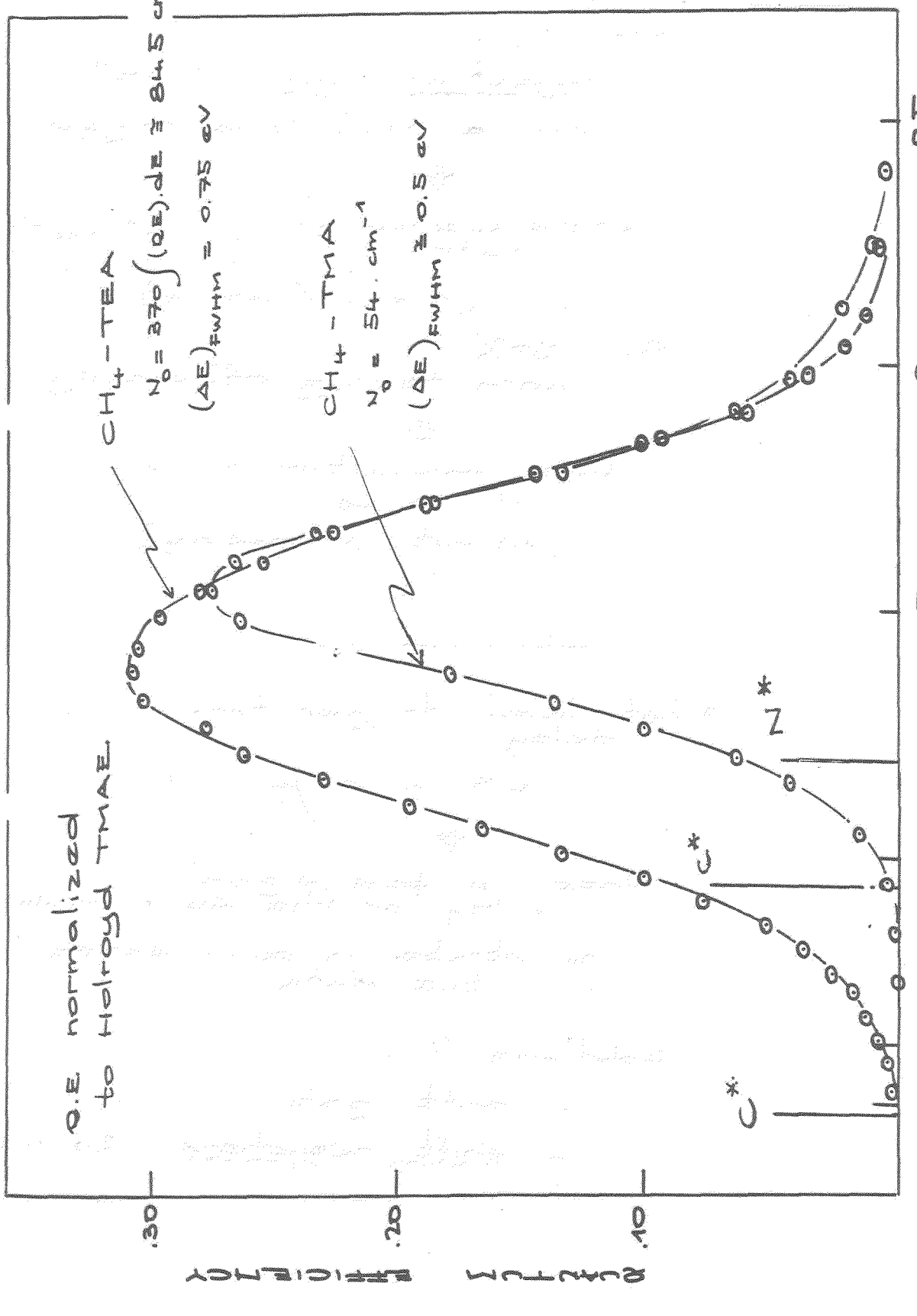
QUANTUM EFFICIENCY
.30
.20
.10
9.5
9
8.5
8
7.5
Eph (eV)
Q.E normalized to Holroyd TMAE
CH_4 - TEA
$N_0 = 370 \int (QE).dE \cong 8445\ cm^{-1}$
$(\Delta E)_{FWHM} = 0.75\ eV$
CH_4 - TMA
$N_0 = 54\ cm^{-1}$
$(\Delta E)_{FWHM} \cong 0.5\ eV$
Z*
J*
J*

DATA ACQUISITION RATE

Assuming,

rejection factor $\cong 10^4$

from a first level trigger

⇩

Data acquisition rate $\Rightarrow 10^4$ sec^{-1}

(1 evt. / 100 μs)

for 90% data taking efficiency

⇩

Data acquisition time of 10 μs (without processing)

?

First level trigger time delay :

0.5 ~ 1 μs ?

⇩

Need a pad signal delay of the same order to strobe in coincidence the data

Solutions ? :

- drift gap
- shift registers (50 MHz)

FAST RICH DETECTOR FOR LHC / SSC

—

4π spherical geometry
(T.Y - UCLA workshop)

⇩

$r_{det} \approx 2\ m$

⇩

$S = 50\ m^2$

with pixels $2 \times 2\ mm^2$

⇩

~ 12.5 Million elect channels

implanted on the back side of the detectors

⇩

dedicated :

ANALOGUE & DIGITAL VLSI chips

for, Amplification, discrimination local buffering and readout

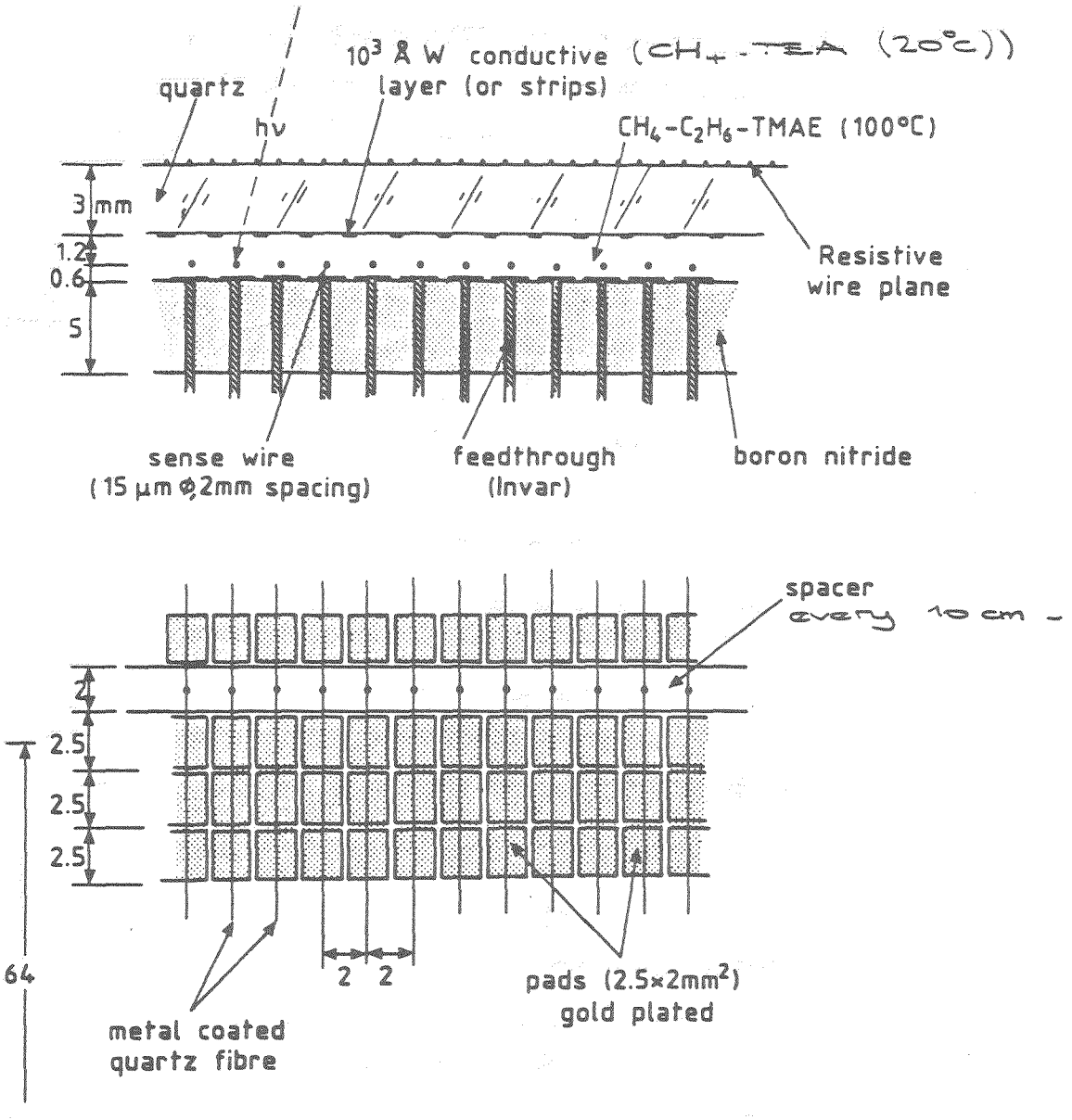

Fig. 6 MWPC photoelectron hot detector

PHOTOELECTRON HOT DETECTOR

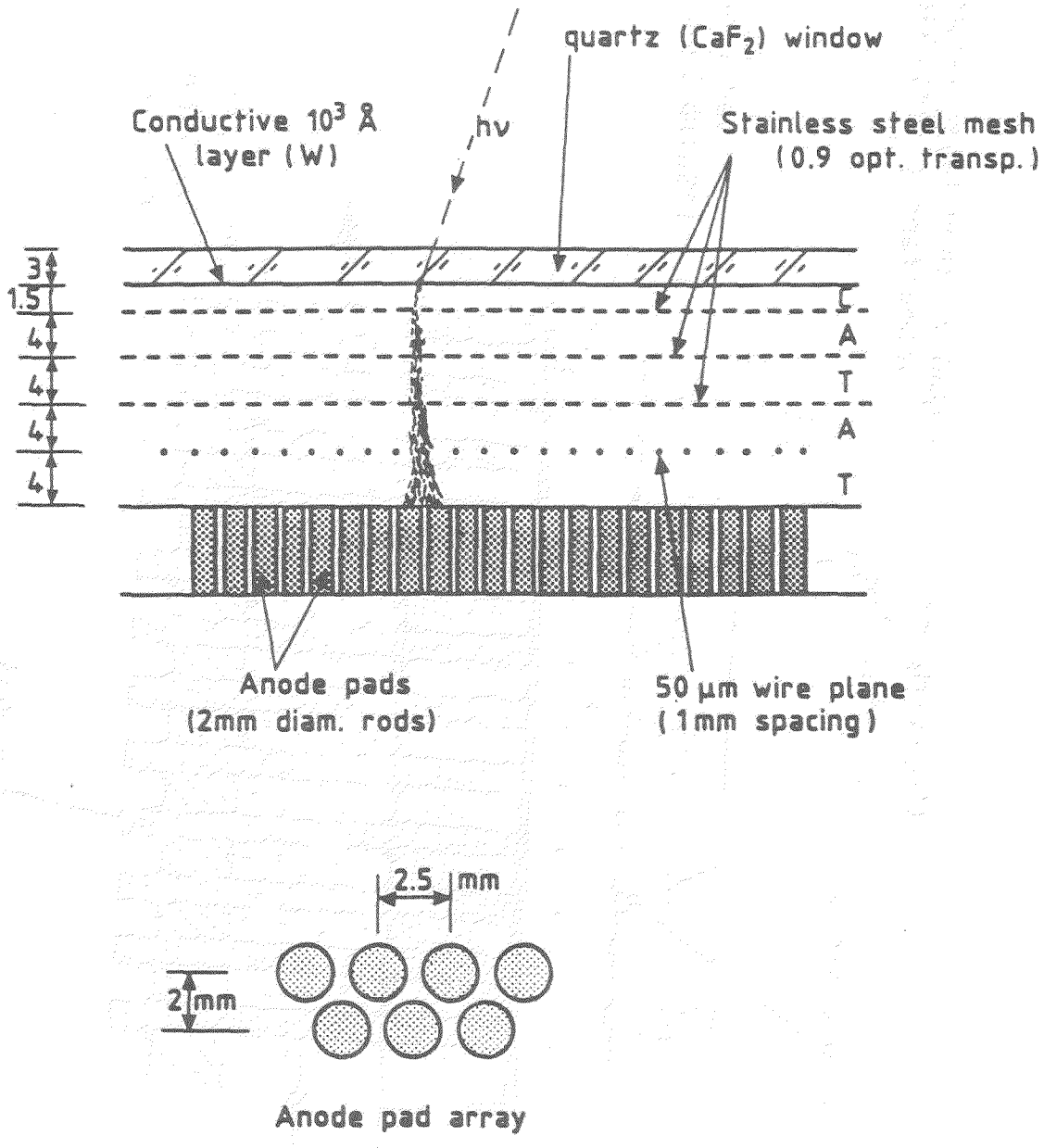

Fig. 5 MSAC photoelectron detector

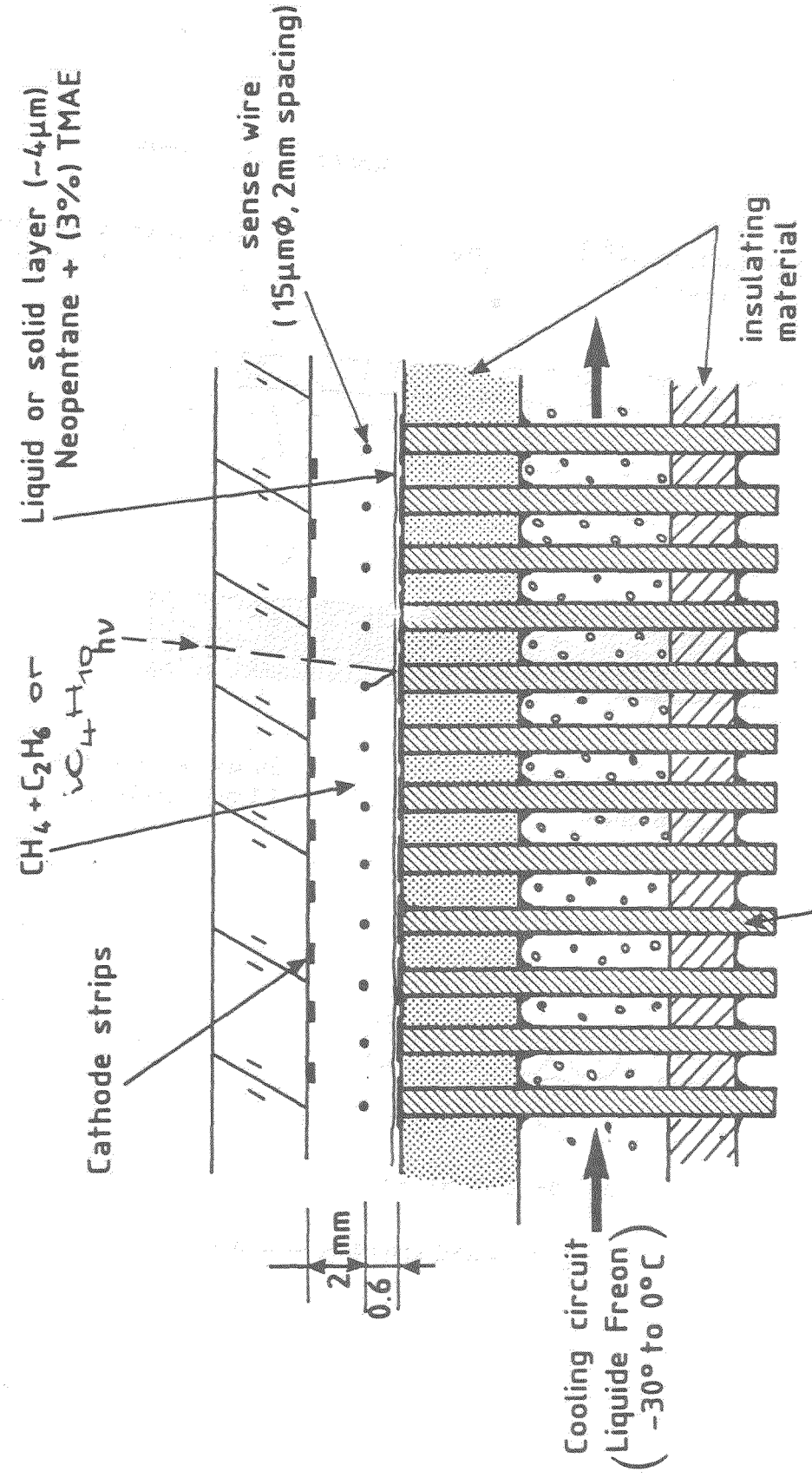

Fig. 4 Photodetector with liquid or solid photocathode

FAST RICH GROUP
(C.d.F – CRN Strasbourg – PSI)

I.– PHOTON DETECTOR
(Prototype)

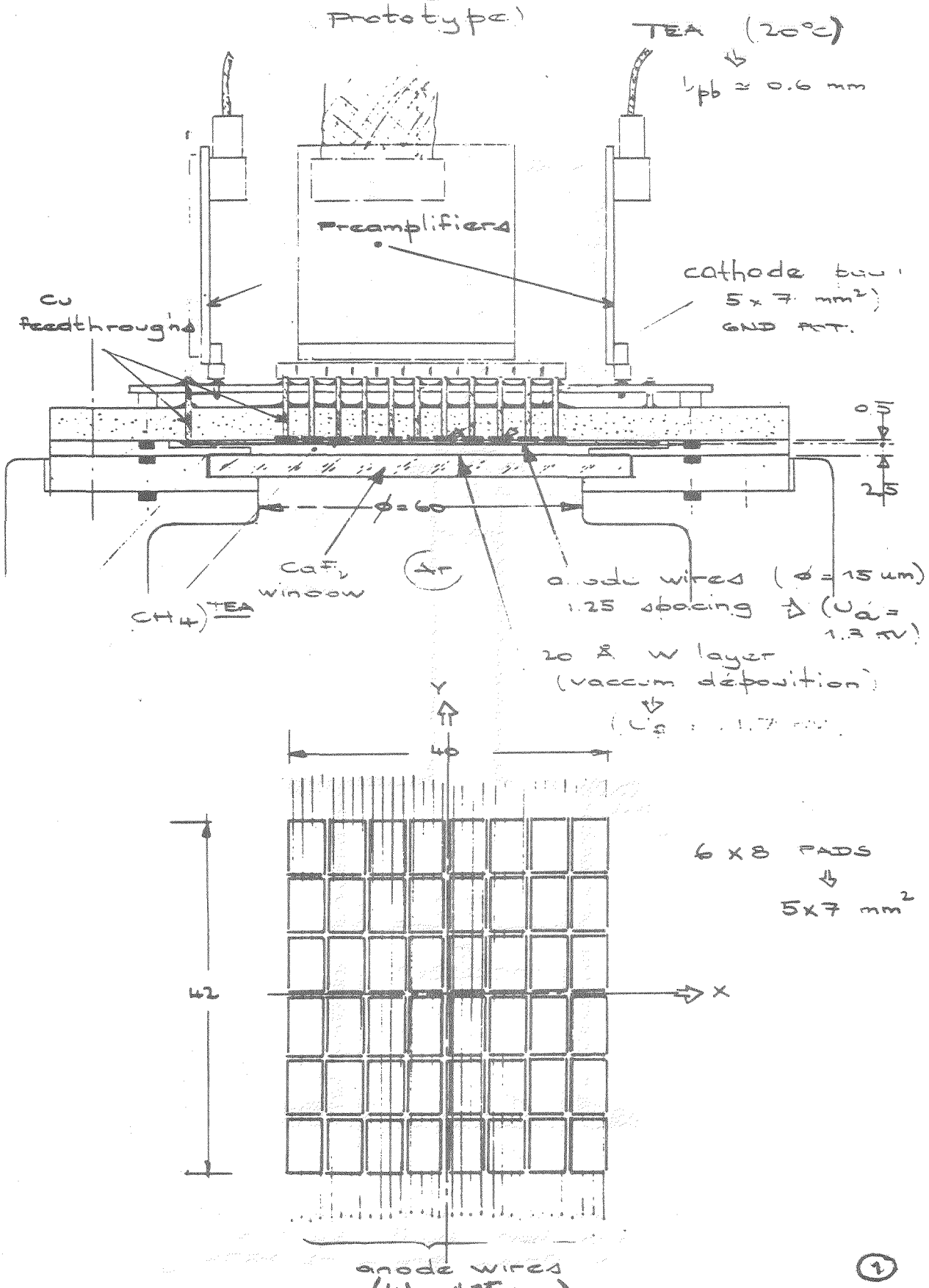

TEST BUNCH

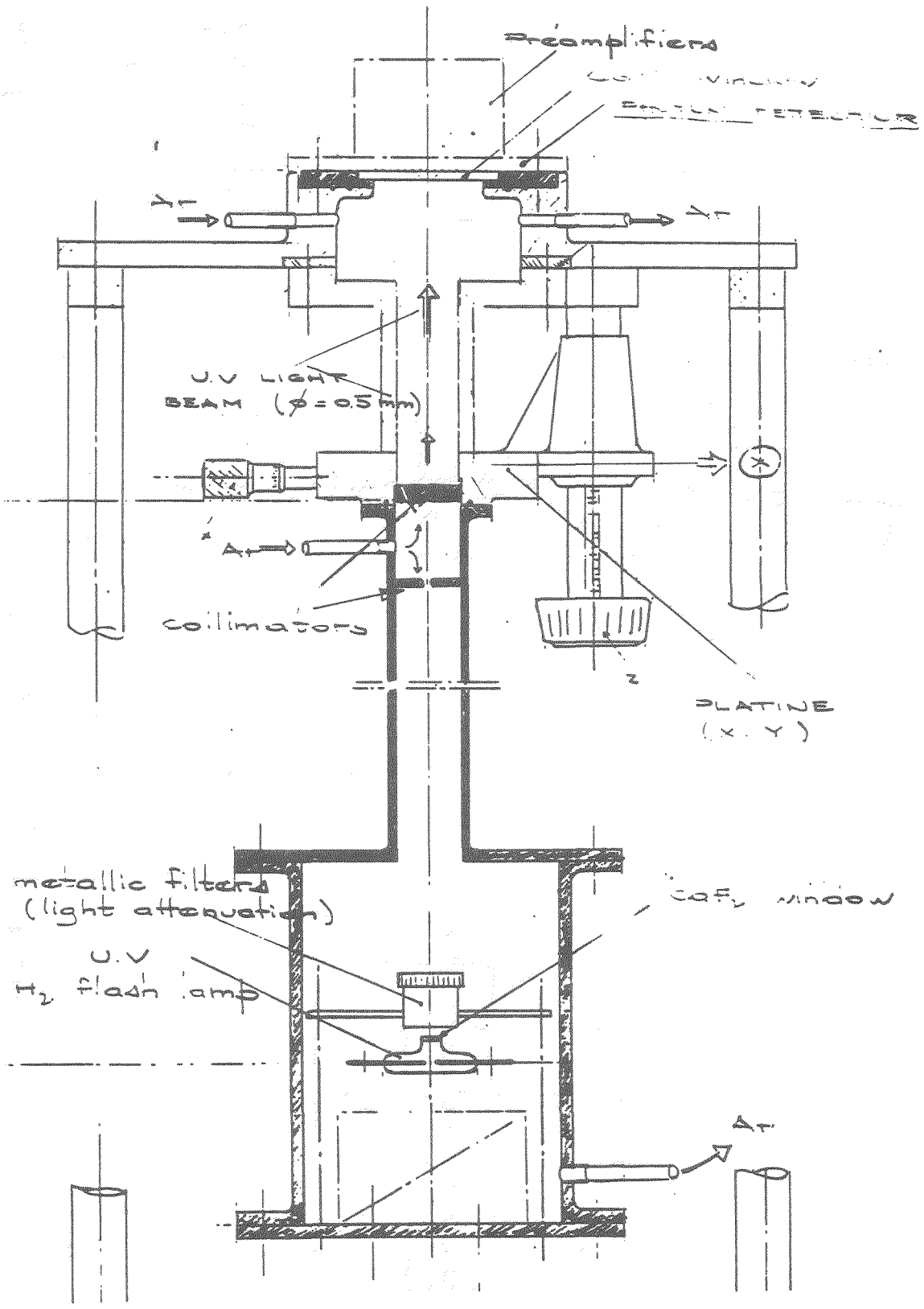

[Photon detector and test bunch have been built by the M. Price group at CERN]

(2)

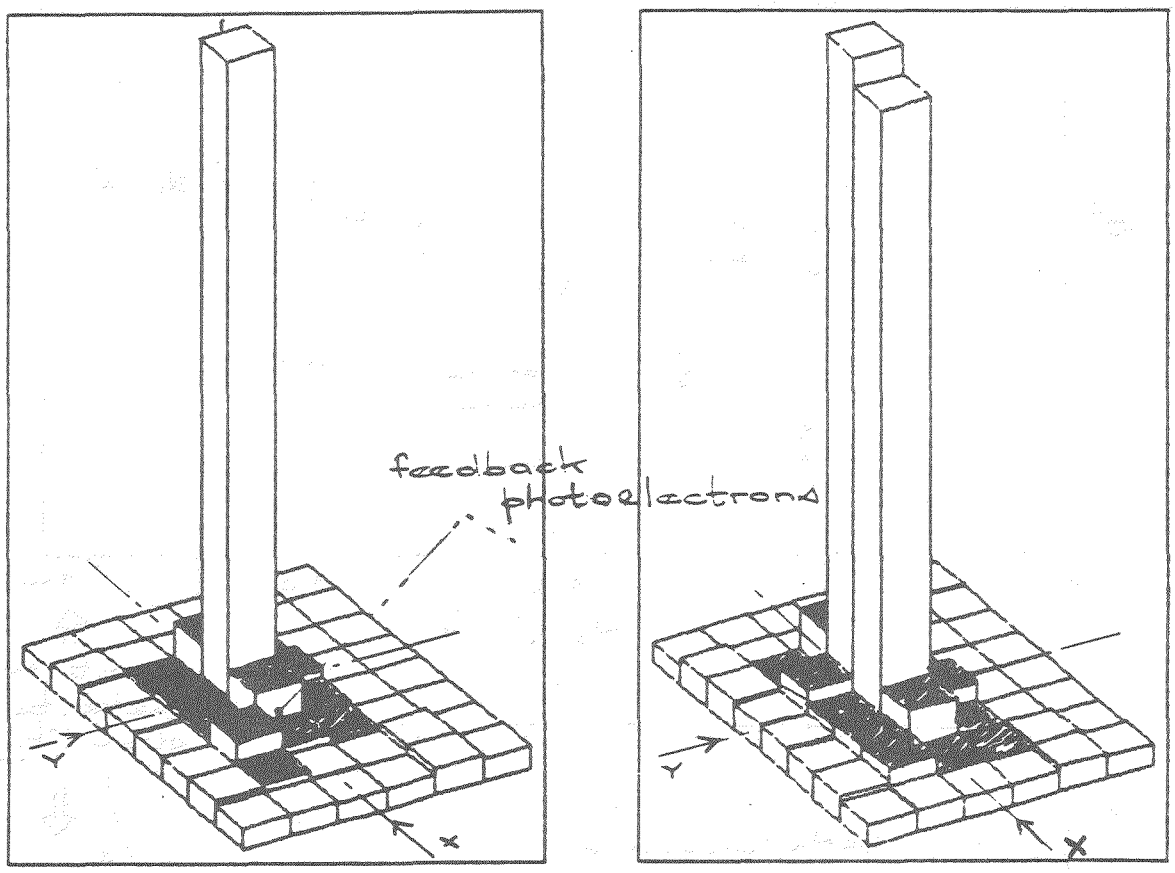

HITS / PADS (LEGO)

HITS / PADS (LEGO)

Light spot

⇧

CENTRE
PAD

⇧

BETWEEN
2 ADJ. PADS

< m pad/cluster > :

⇩

1.18

⇩

1.55

(3)

CH_4 + TEA (20°C) ⇒ l_{ph} = 0.6 mm

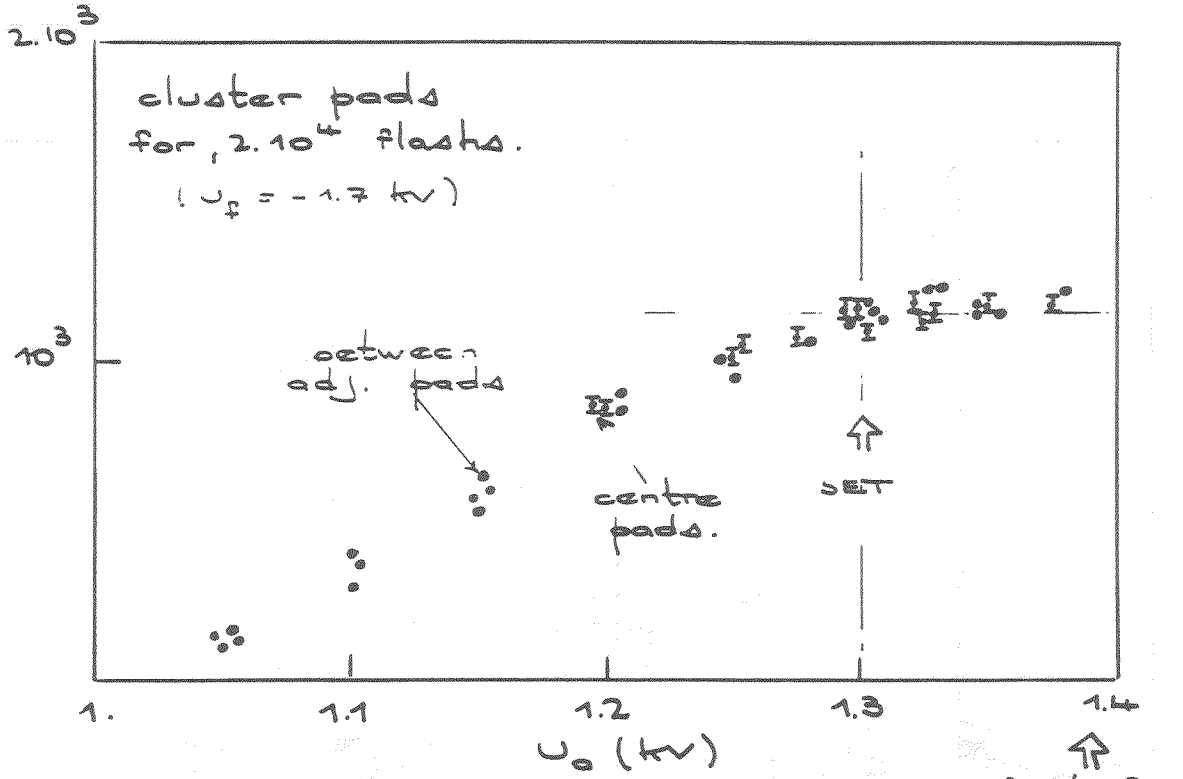

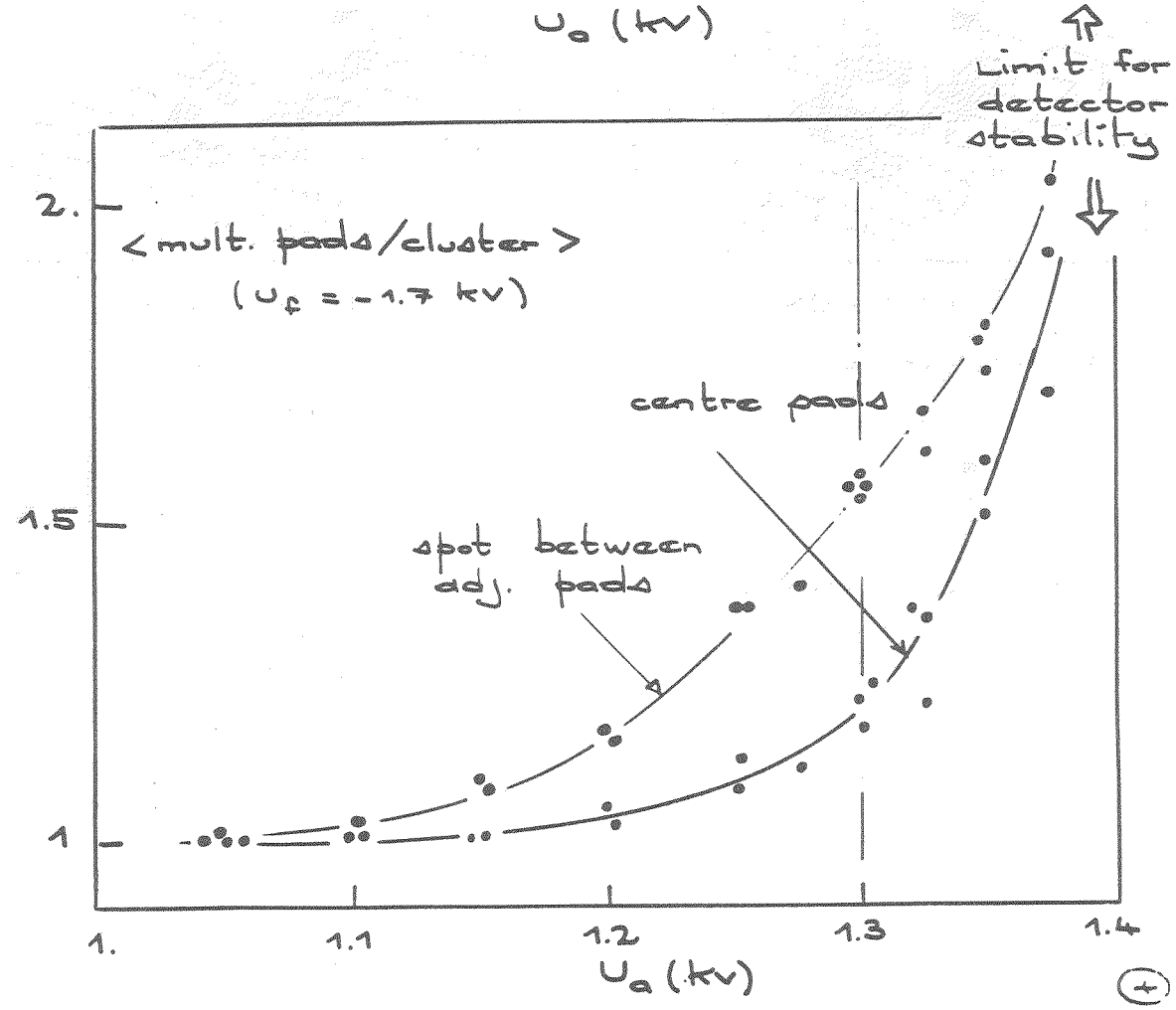

Relative cathode pad detection efficiency

$$\varepsilon_c = \frac{\text{nb. cluster pads}}{\text{nb. clust. anode wires}}$$

TEA (20°C) – $U_f = -1.7$ kV

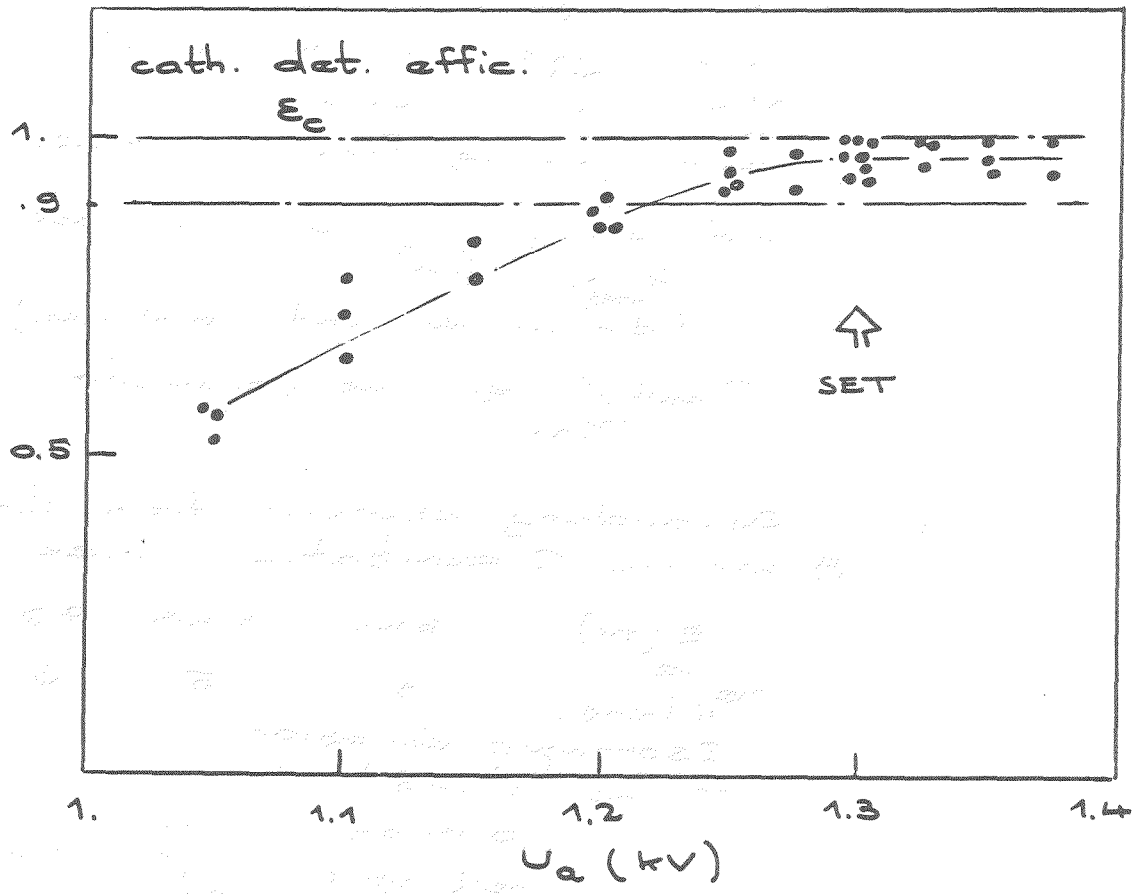

$\varepsilon_c > 0.93$

ε_c (proposal) = 0.80

MONTE-CARLO DETECTOR SIMULATION

Takes into account :

1.– Spot size, photoabsorption, photoionization

2– Electrostatic configuration for collecting p.e on the wires –

3 – Charge distribution in the aval.
⇩
Polya type for $G > 5.10^4$
Furry – below
mean gain ⇒ free parameter

4 – Induced charge dist. on pads :
$q_{cath} e^{-r^2/2d^2}$
(d = anode - cath. distance)
$q_{cath.}/q_{an.}$ ⇒ free parameter

5.– Secondary photons from the 3 atomic C excitation lines :

E (eV)	6.42	7.48	7.94
rel. ve intens.	3	5	3

Isotropic emission
Total intensity :
0,0408 pf/fC av. charge
(test calibration) Photo RICH DELPHI
– screening effect of the wire
– photoel. effect on surfaces
⇩
iterations until process stops –

6.– Pre-amplifier response

7.– Threshold of the discriminator = 9.10^3 el.

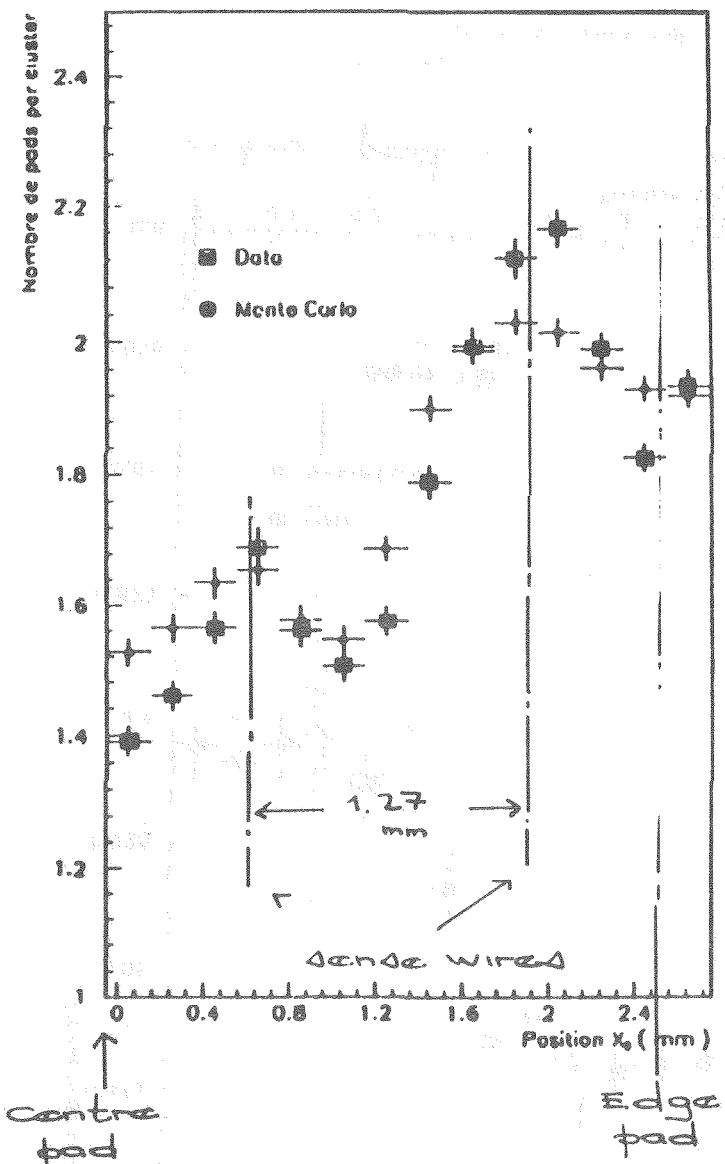

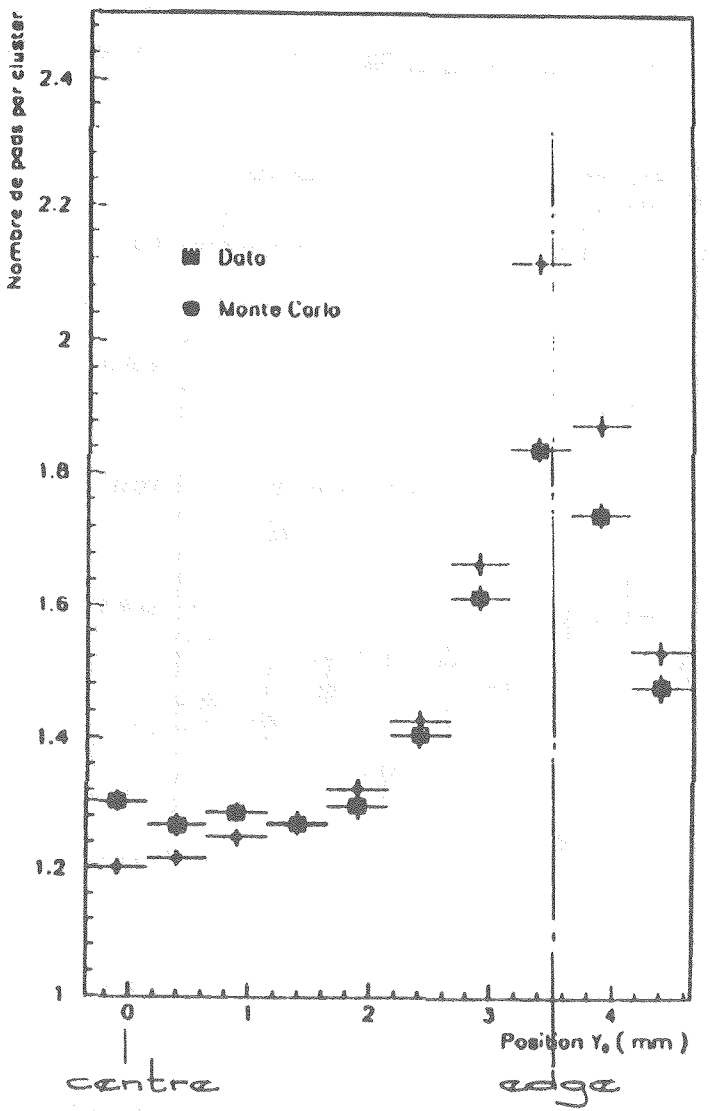

CLUSTER SIZE vs X (left) and Y (right)

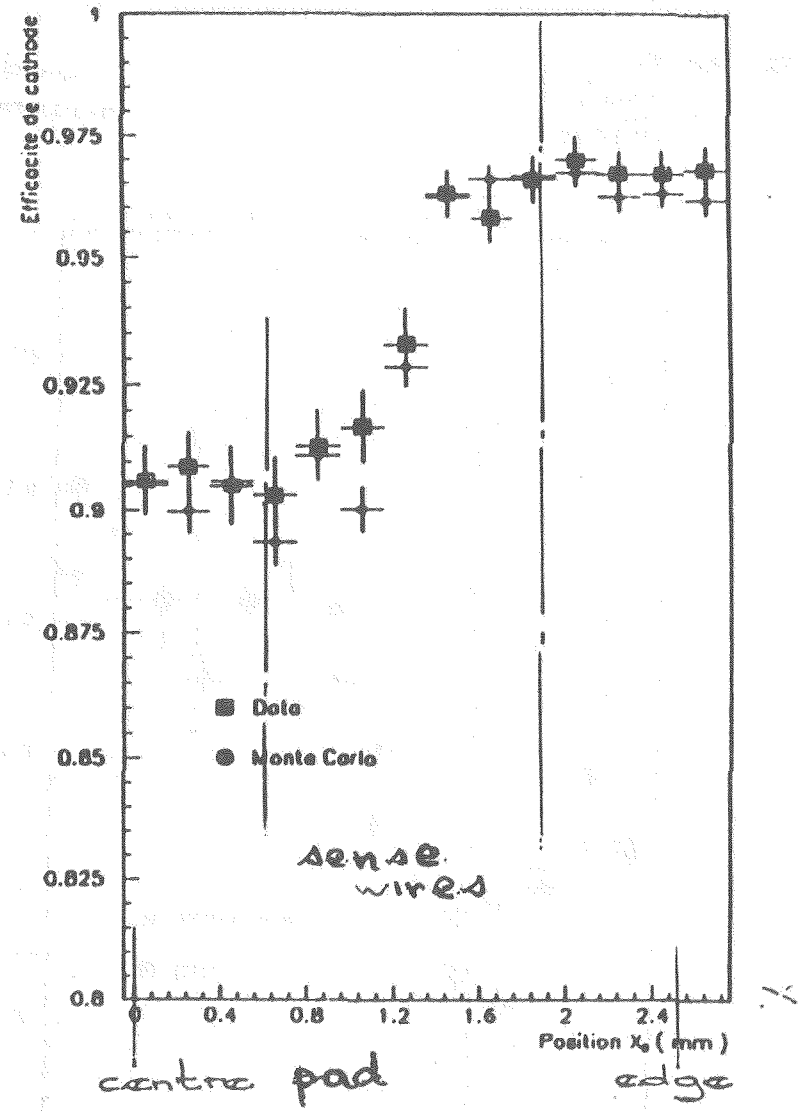

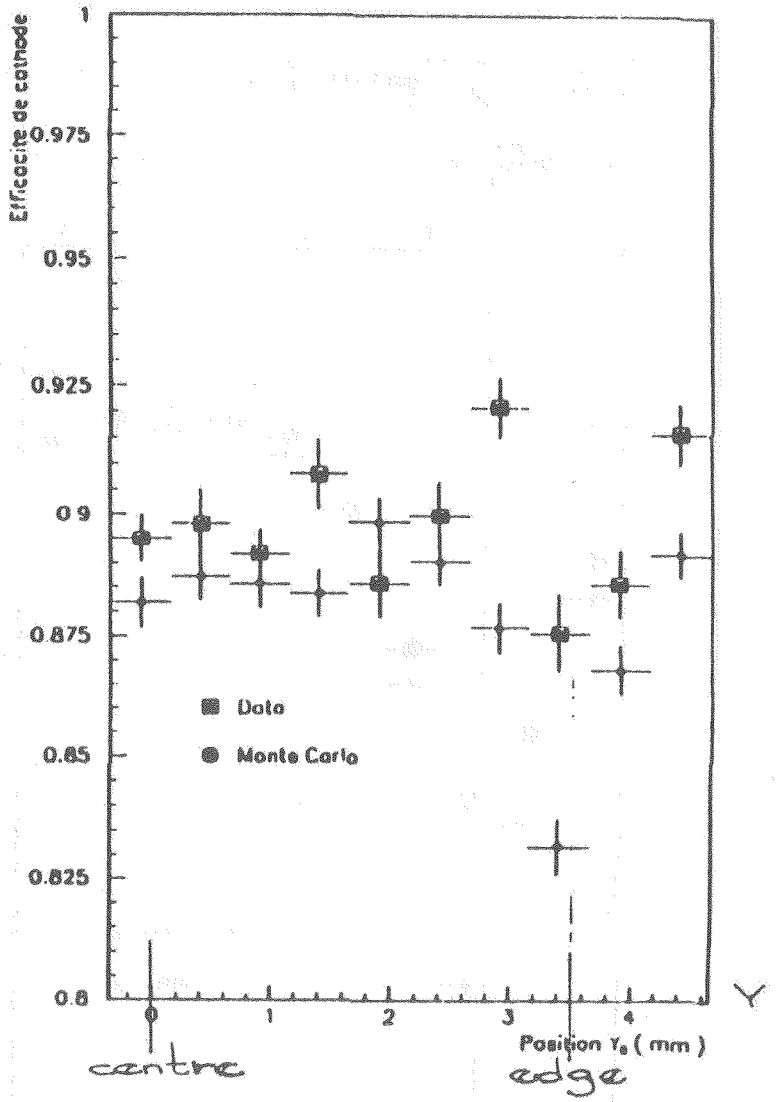

CATHODE PAD DETECTION EFFICIENCY
vs X and Y -

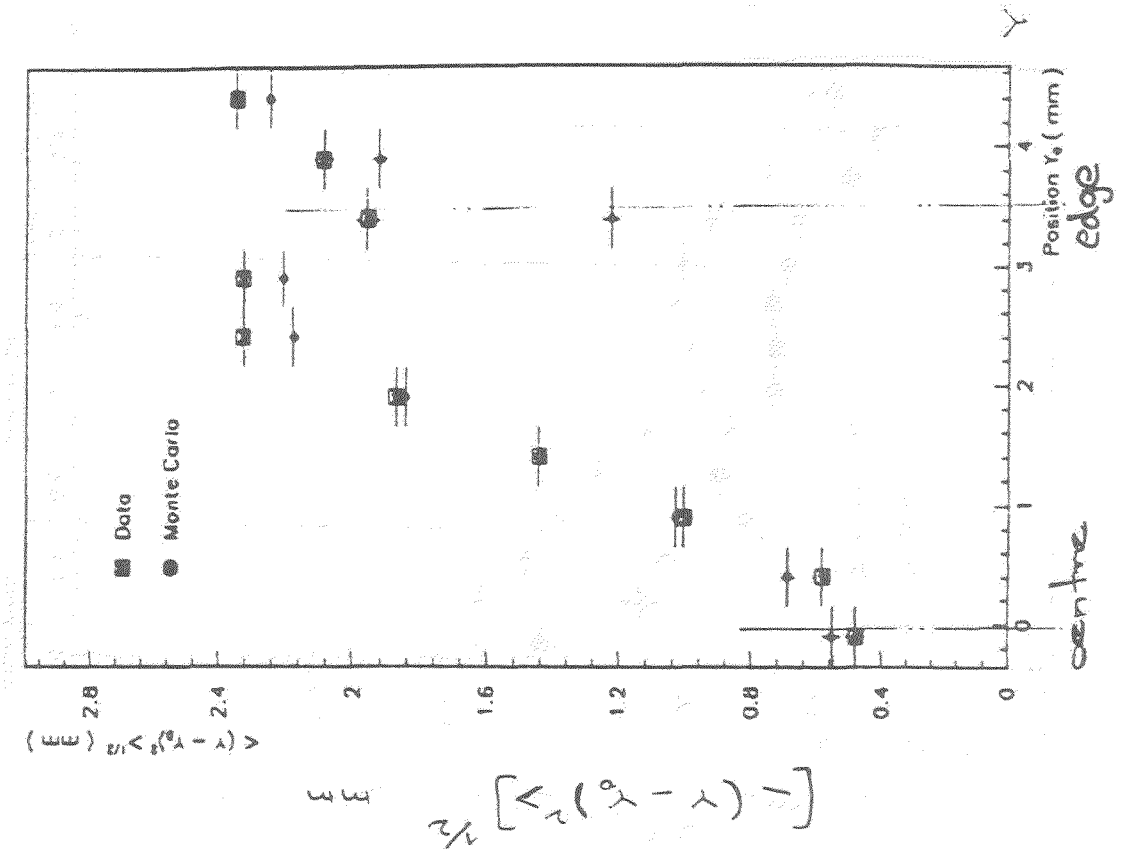

$\langle (Y - Y_0)^2 \rangle^{1/2}$ (mm)

$\left[\langle (Y - Y_0)^2 \rangle \right]^{1/2}$ mm

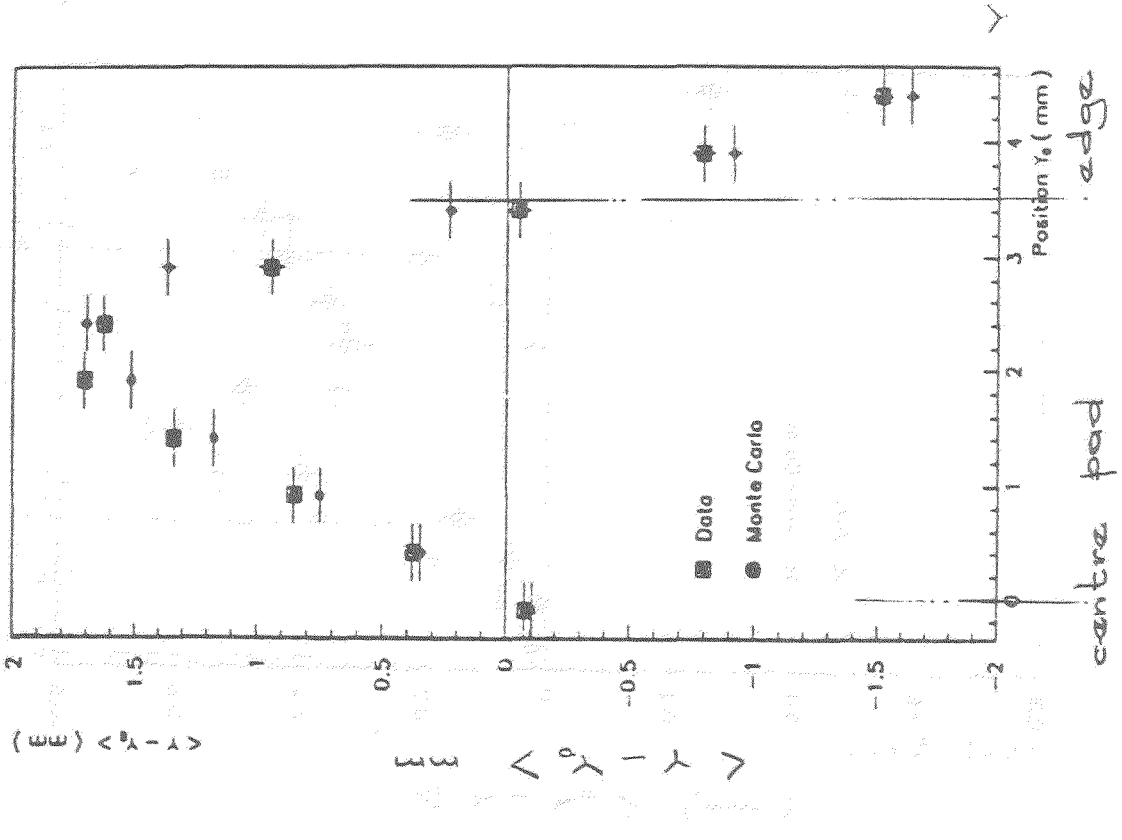

$\langle Y - Y_0 \rangle$ (mm)

$\langle Y - Y_0 \rangle$ mm

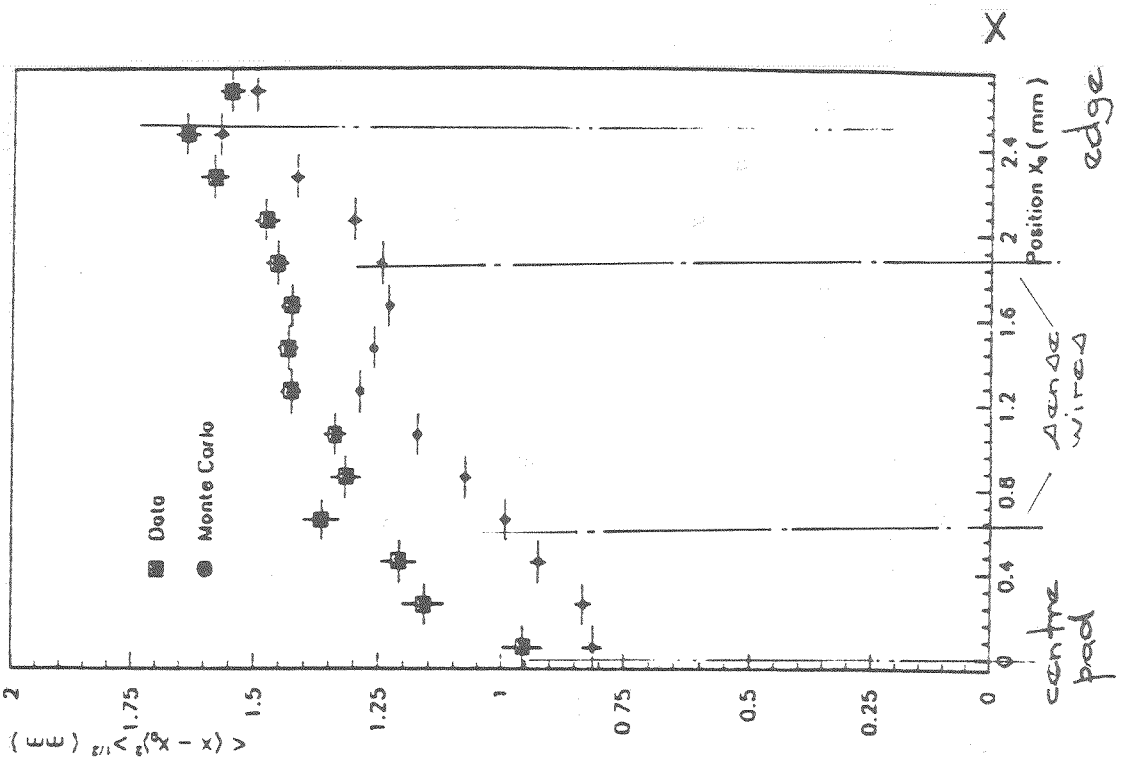

$\langle (x - x_0)^2 \rangle^{1/2}$ (mm)

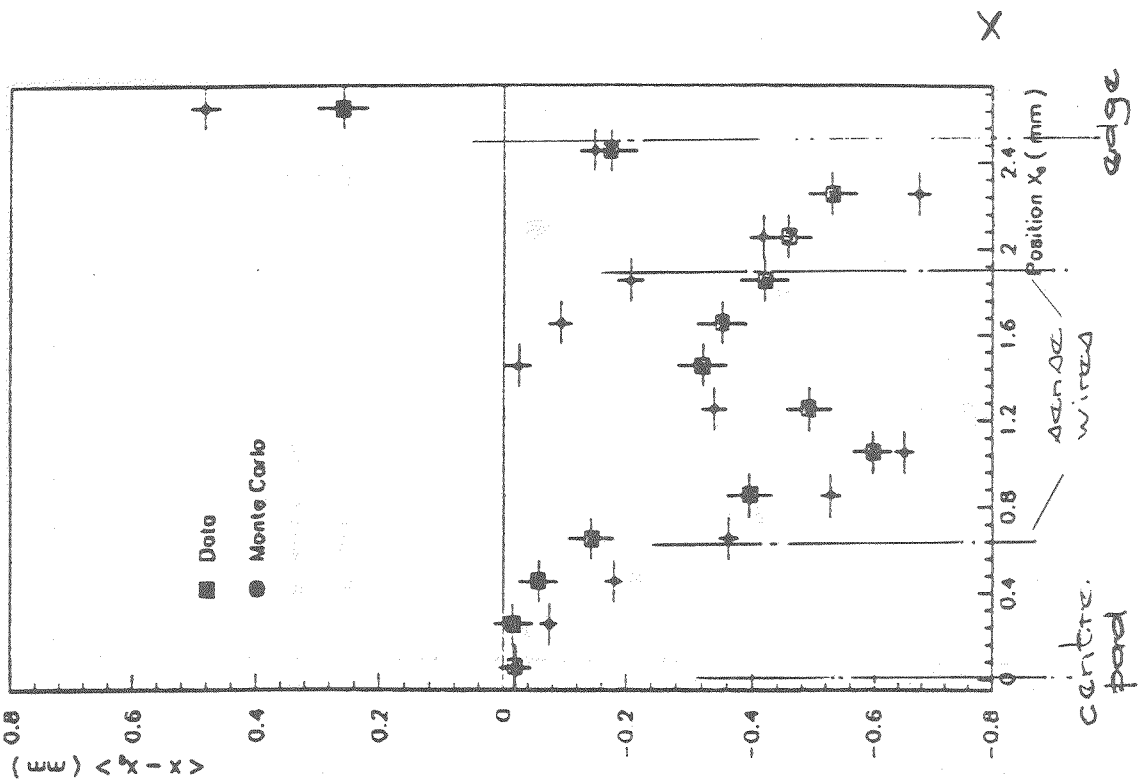

$\langle x - x_0 \rangle$ (mm)

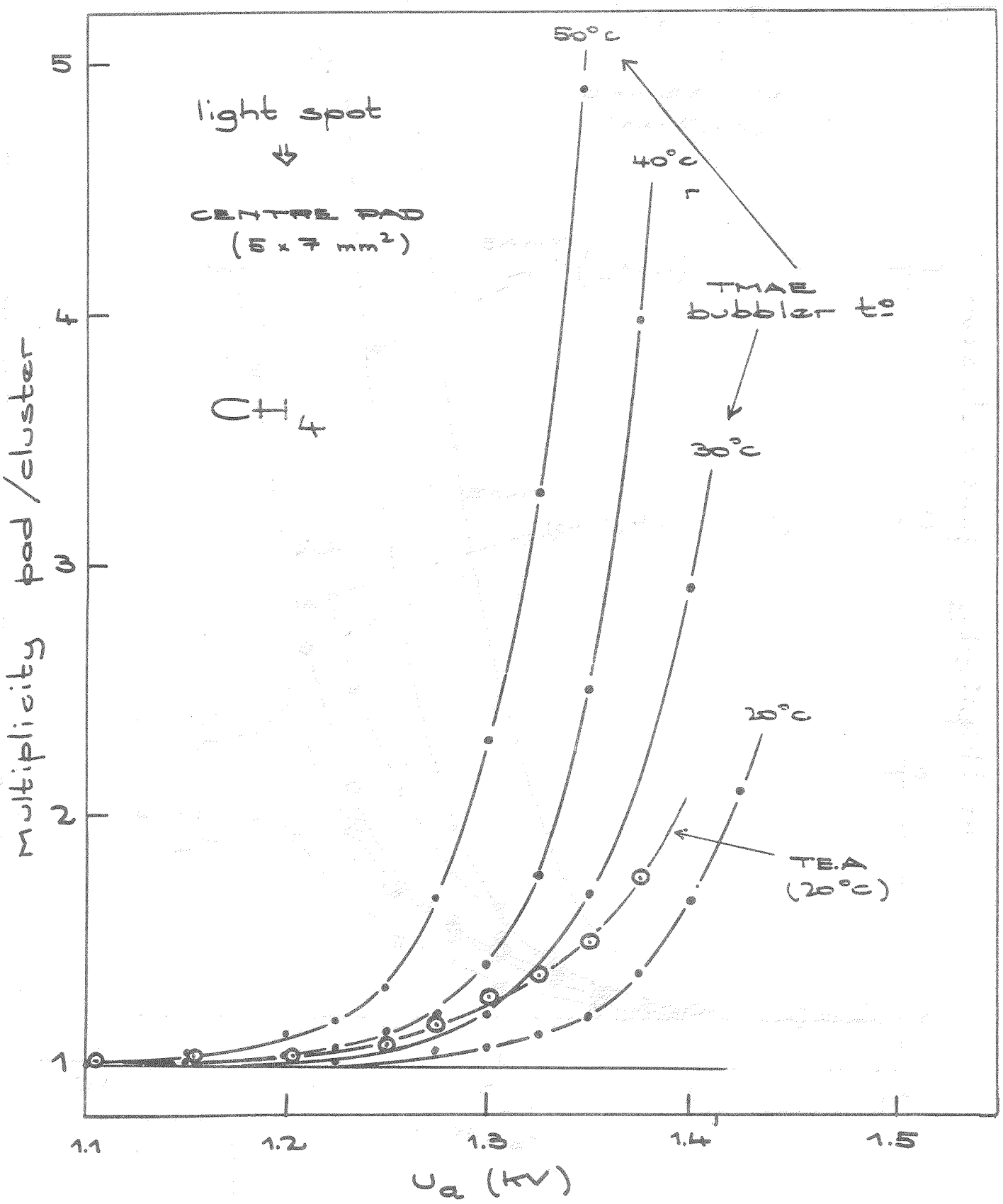
light spot
CENTRE PAD
(5 x 7 mm²)
CH4
50°C
40°C
TMAE
bubbler to
30°C
20°C
TEA
(20°C)
Multiplicity pad/cluster
1
2
3
4
5
1.1
1.2
1.3
1.4
1.5
Ua (kV)

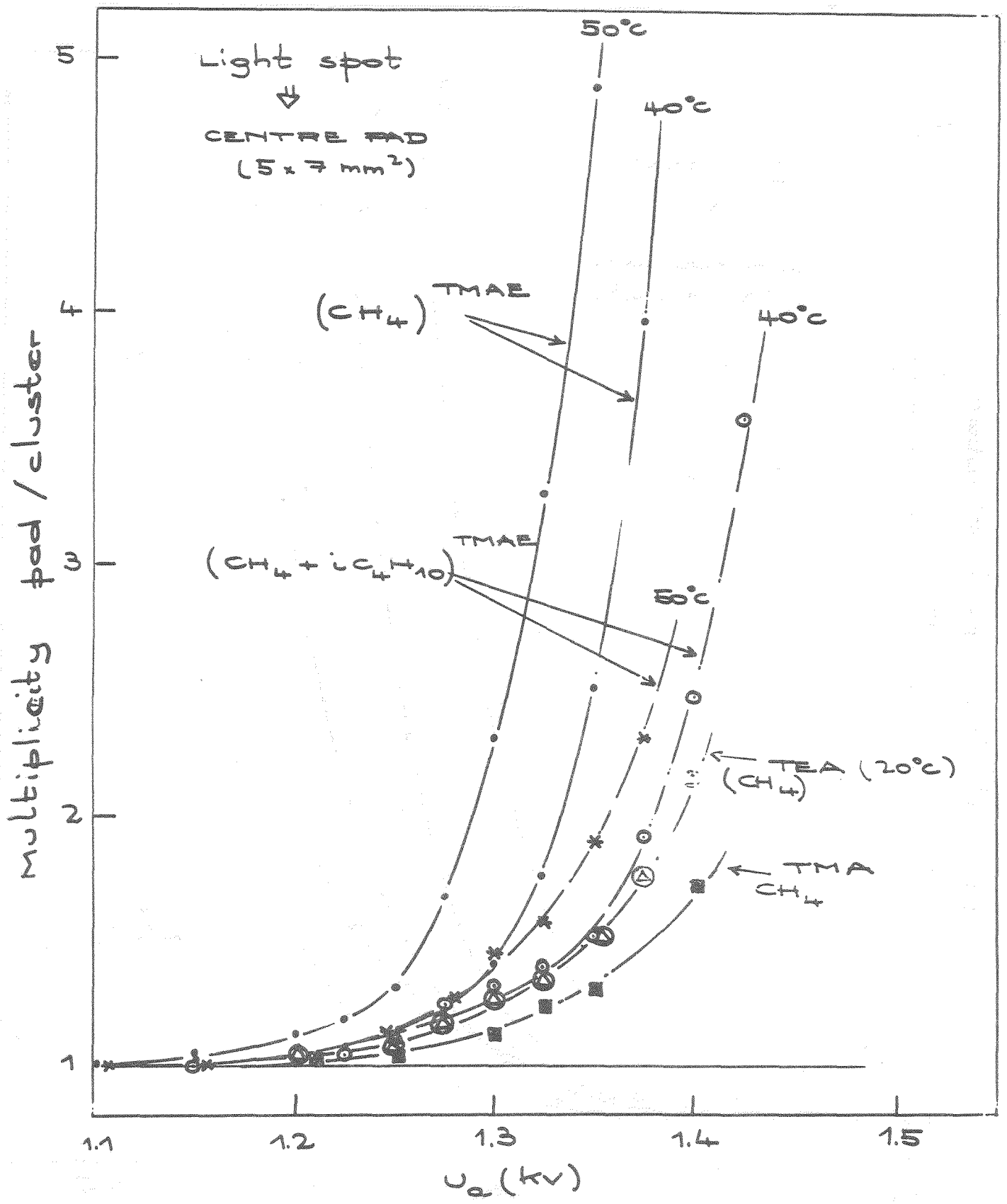
Light spot
⇩
CENTRE PAD
(5 × 7 mm²)
50°C
40°C
(CH4) TMAE
40°C
(CH4 + iC4H10) TMAE
50°C
TEA (20°C)
(CH4)
TMA
CH4
Multiplicity pad / cluster
1
2
3
4
5
1.1
1.2
1.3
1.4
1.5
Ua (kV)

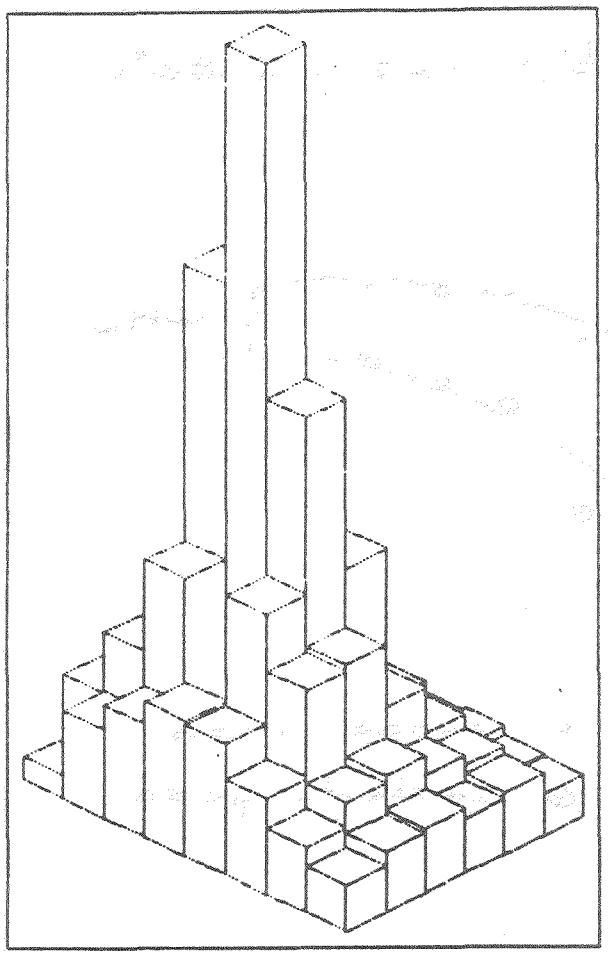

HITS · PADE (LEGO)

⇧

CH_4 - TMAE (50°C)

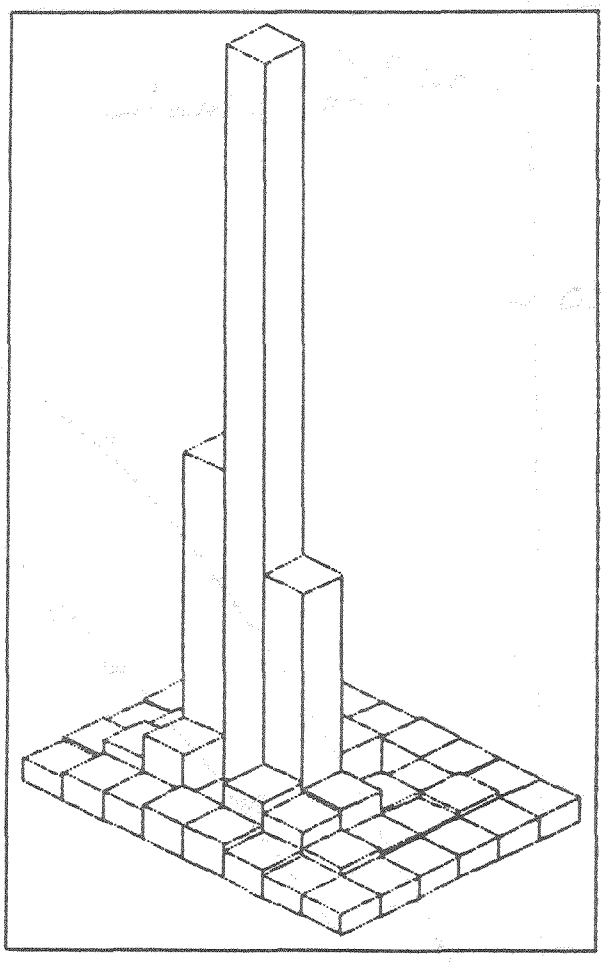

⇧

$(CH_4 + iC_4H_{10})$ - TMAE (50°C)

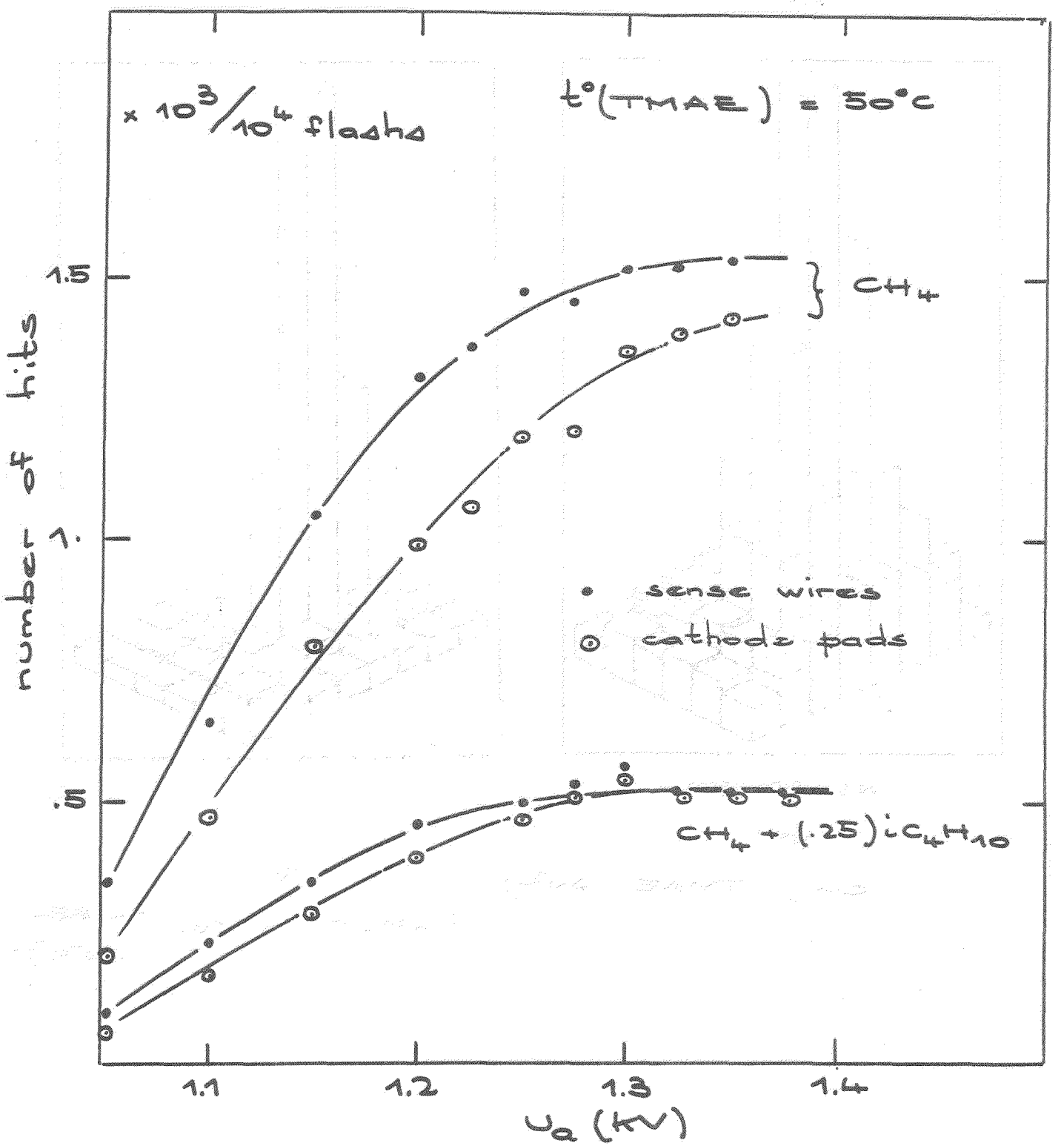
× 10³/10⁴ flashes
t°(TMAE) = 50°C
number of hits
1.5
1.
.5
} CH₄
sense wires
cathode pads
CH₄ + (.25) iC₄H₁₀
1.1
1.2
1.3
1.4
Ua (kV)

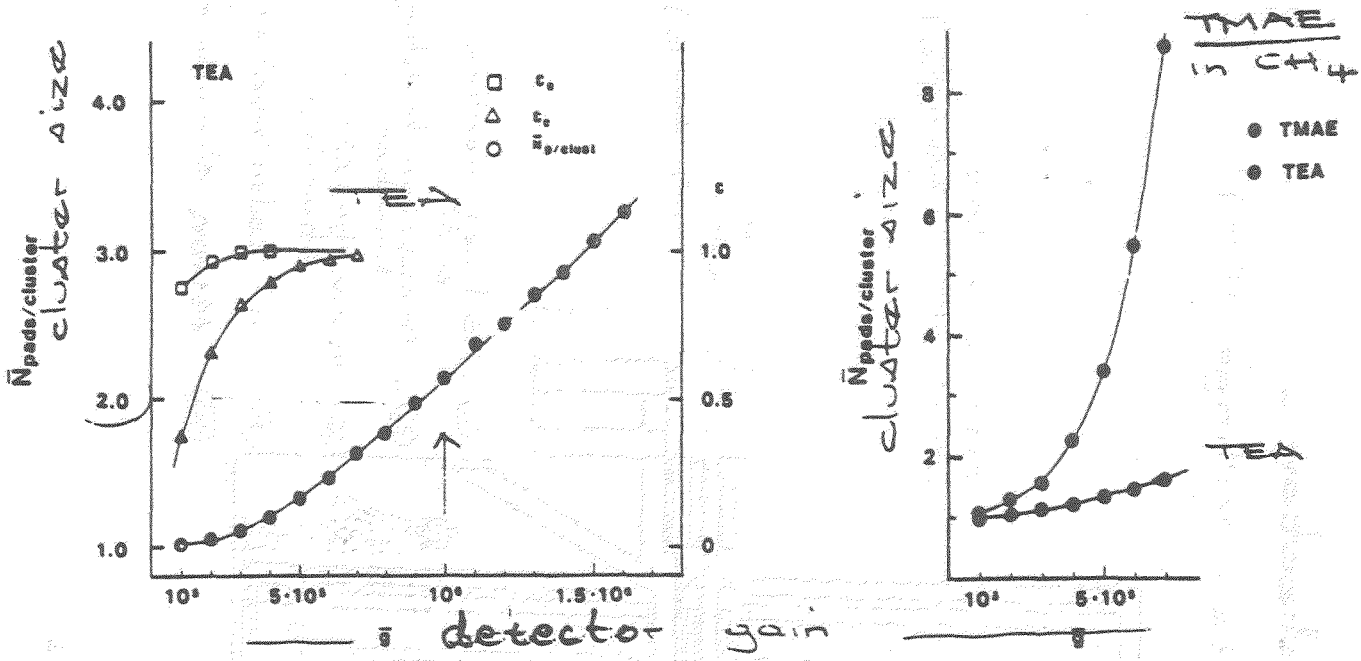

. The cluster size of the pad signals (number of hit pads per cluster) as functions of the average detector gain when using TEA or TMAE. The detection efficiency on the anode wires ε_a and cathode pads ε_c are also shown.

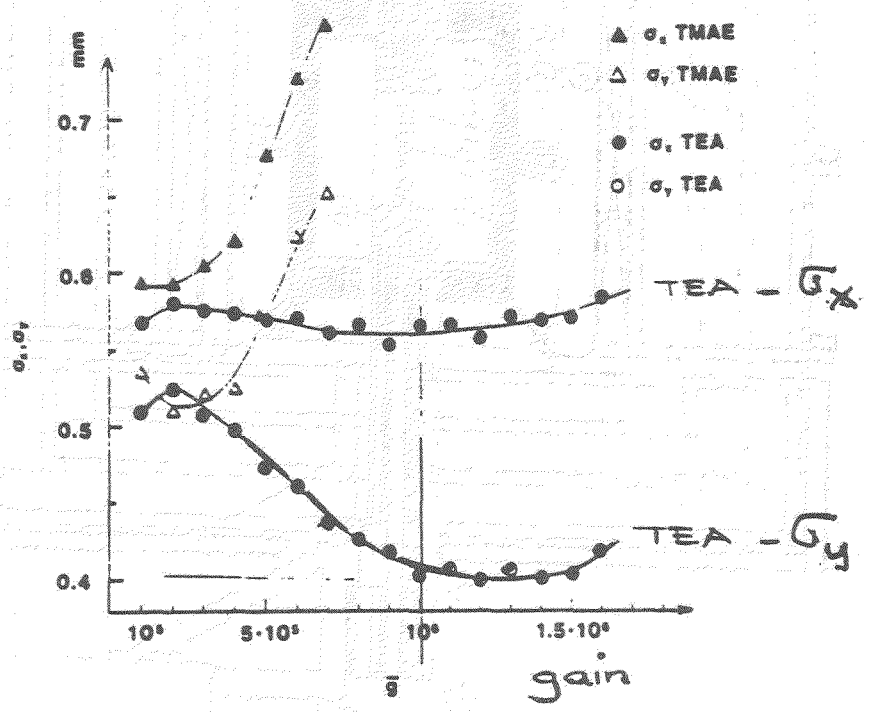

The resolutions σ_x and σ_y (y along the wire direction) as functions of the detector gain $\bar{g}$ when using TEA or TMAE.

- B Meson Factory detector -

(Paul Scherer Institute - Villingen (CH))

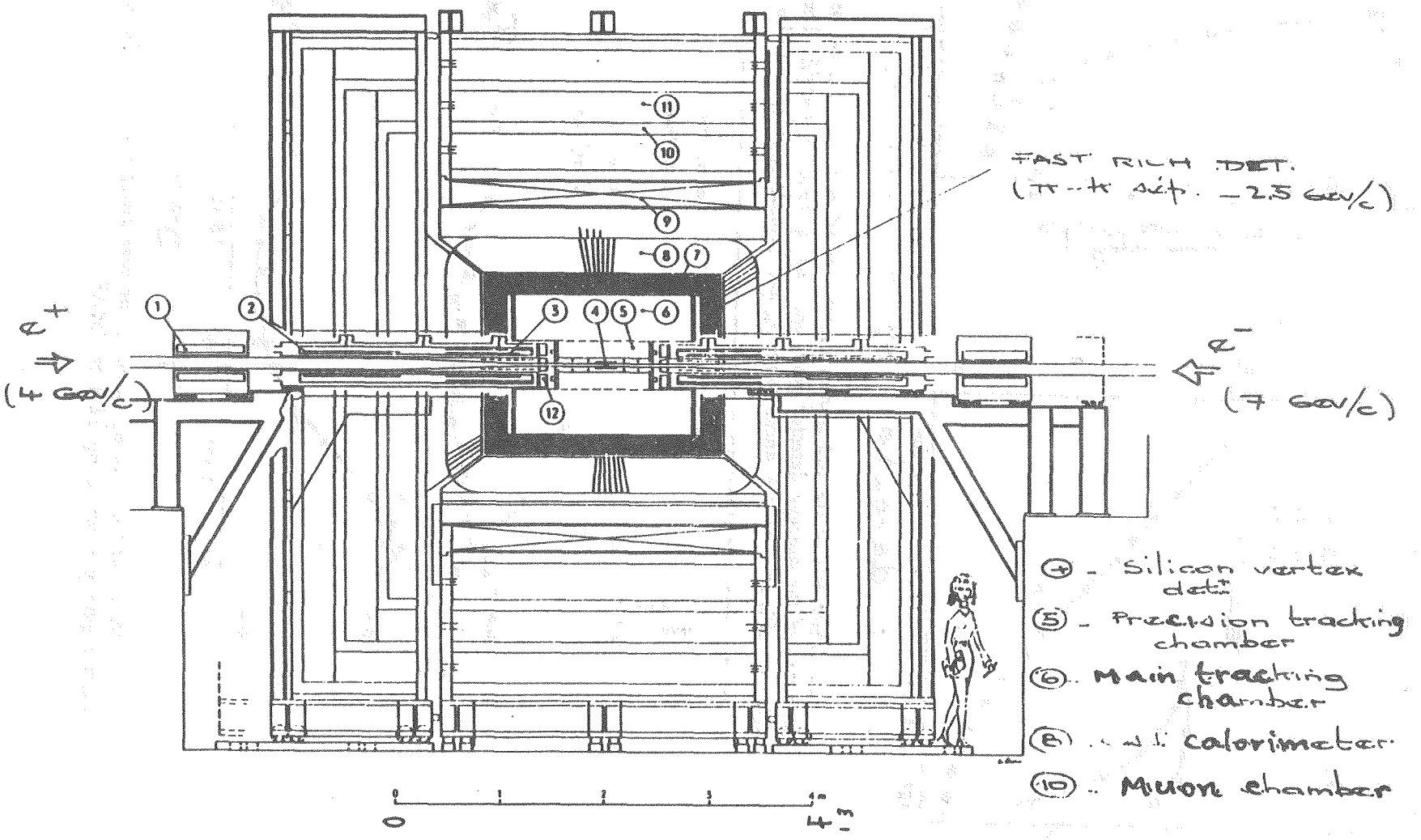

④ - Silicon vertex det.

⑤ - Precision tracking chamber

⑥ - Main tracking chamber

⑨ - e.m. calorimeter

⑩ - Muon chamber

collaboration France - Germany - Swiss

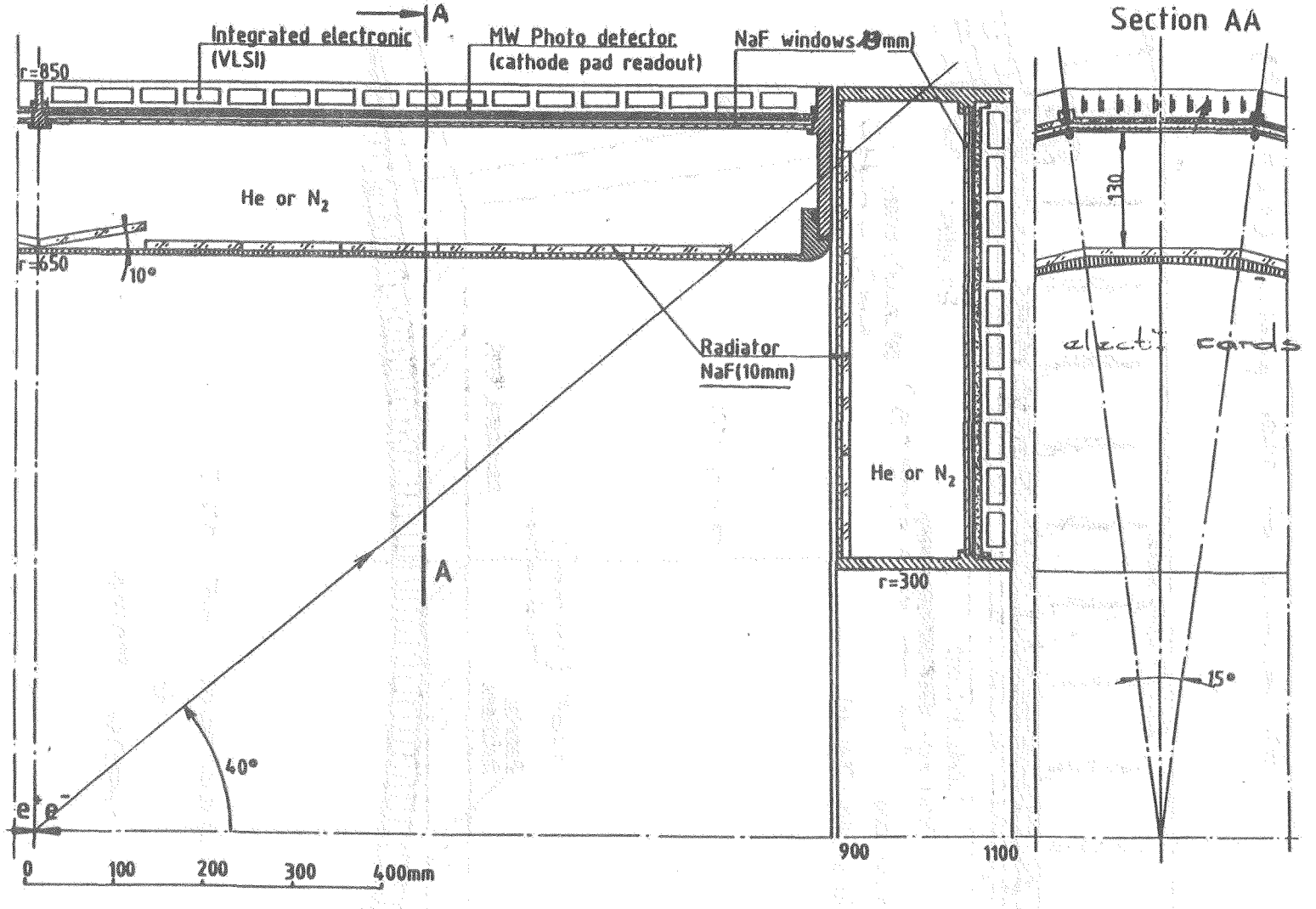

COLLABORATION :

C.R.N Strasbourg { R. ARNOLD, J.L. GUYONNET, E. CHRISTOPHEL

C.d.F Paris { J. SEGUINOT, J. TOCQUEVILLE, T. YPSILANTIS

P.S.I - (Switz.) - J. EGGERT & K. GABATHULER

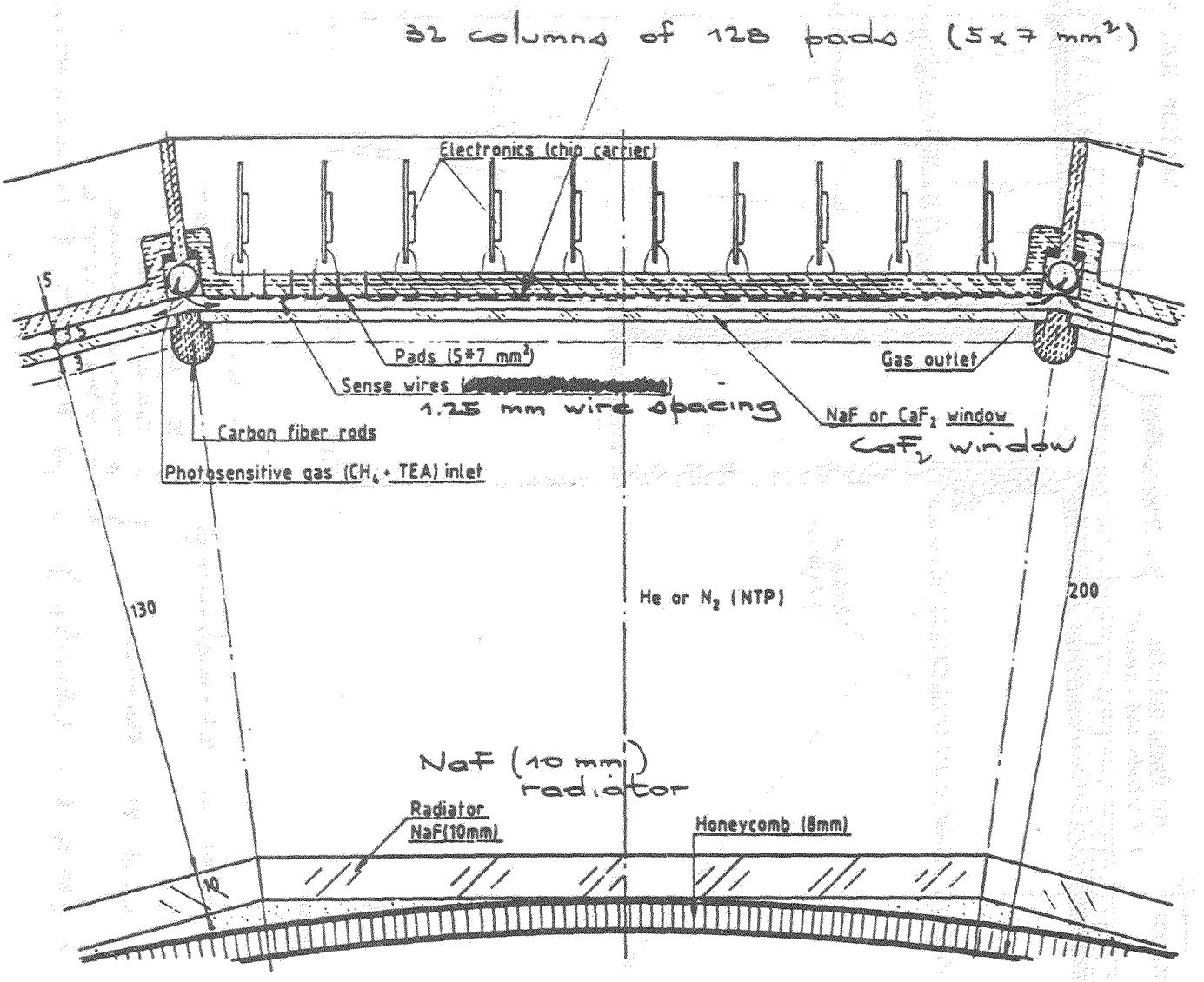

SECTOR OF 12°

⇩

4096 PADS

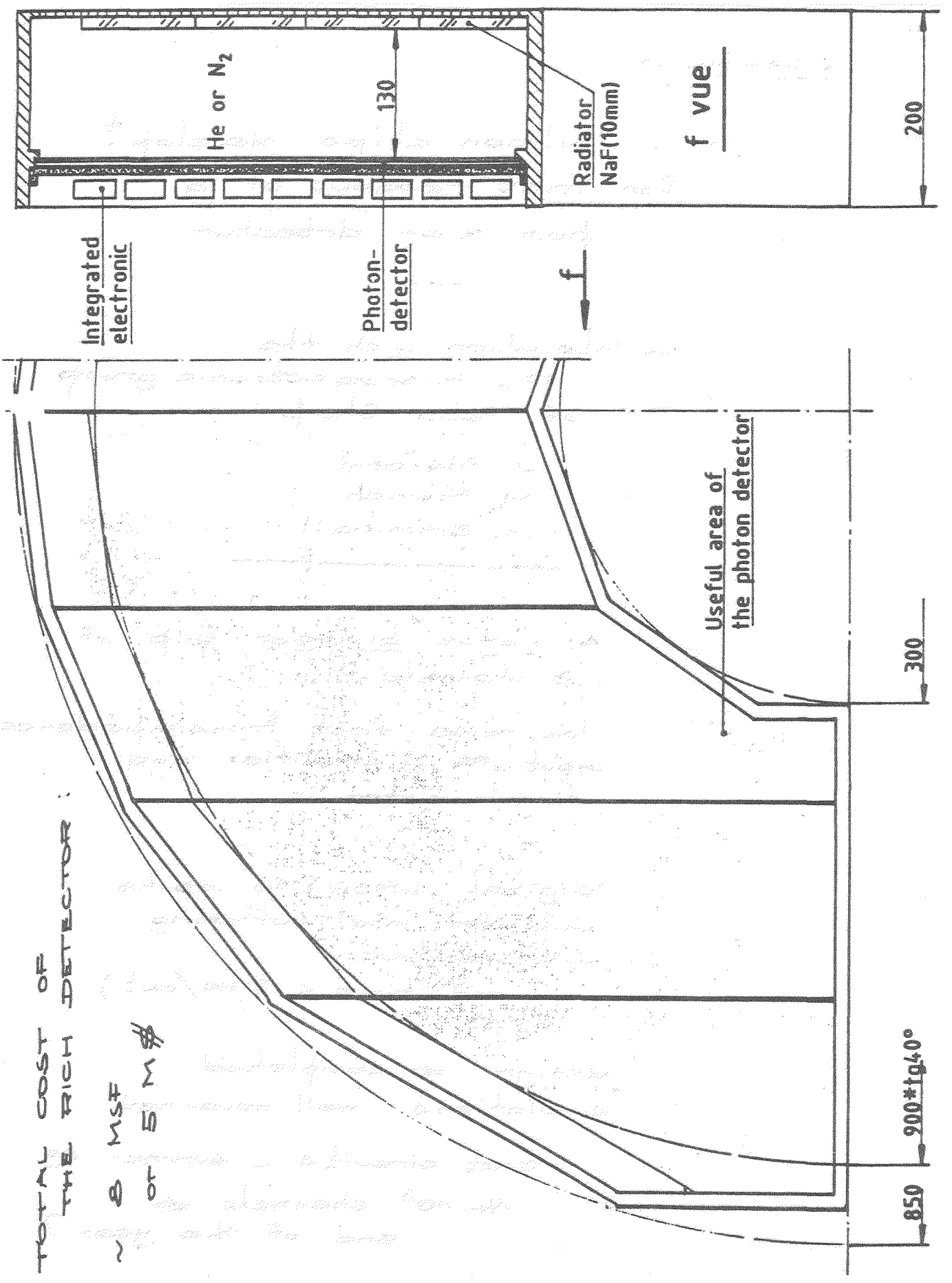
He or N_2
130
Radiator
NaF(10mm)
f vue
200
Integrated
electronic
Photon-
detector
f
Useful area of
the photon detector
300
900*tg40°
850
TOTAL COST OF
THE RICH DETECTOR :
~ 8 MSF
or 5 M$

J. SEGUINOT

VLSI silicon chips developt for fast readout of a pad RICH detector

---

Collaboration with the RAL microelectronic group of Peter Sharp :

J. Alsford
M. French
M. Bramhall

- Analogue bi-polar chip of 8 channels :

  low noise fast transimpédance input PA - amplifier and discriminator.

- Digital cmos 16 inputs chip for local buffering and readout -
  (acq. time < 5 μs/evt)

design ⇒ completed
simulations well advanced

test circuits – summer 89

$14 \cdot 10^3$ channels ⇒ end of the year ?

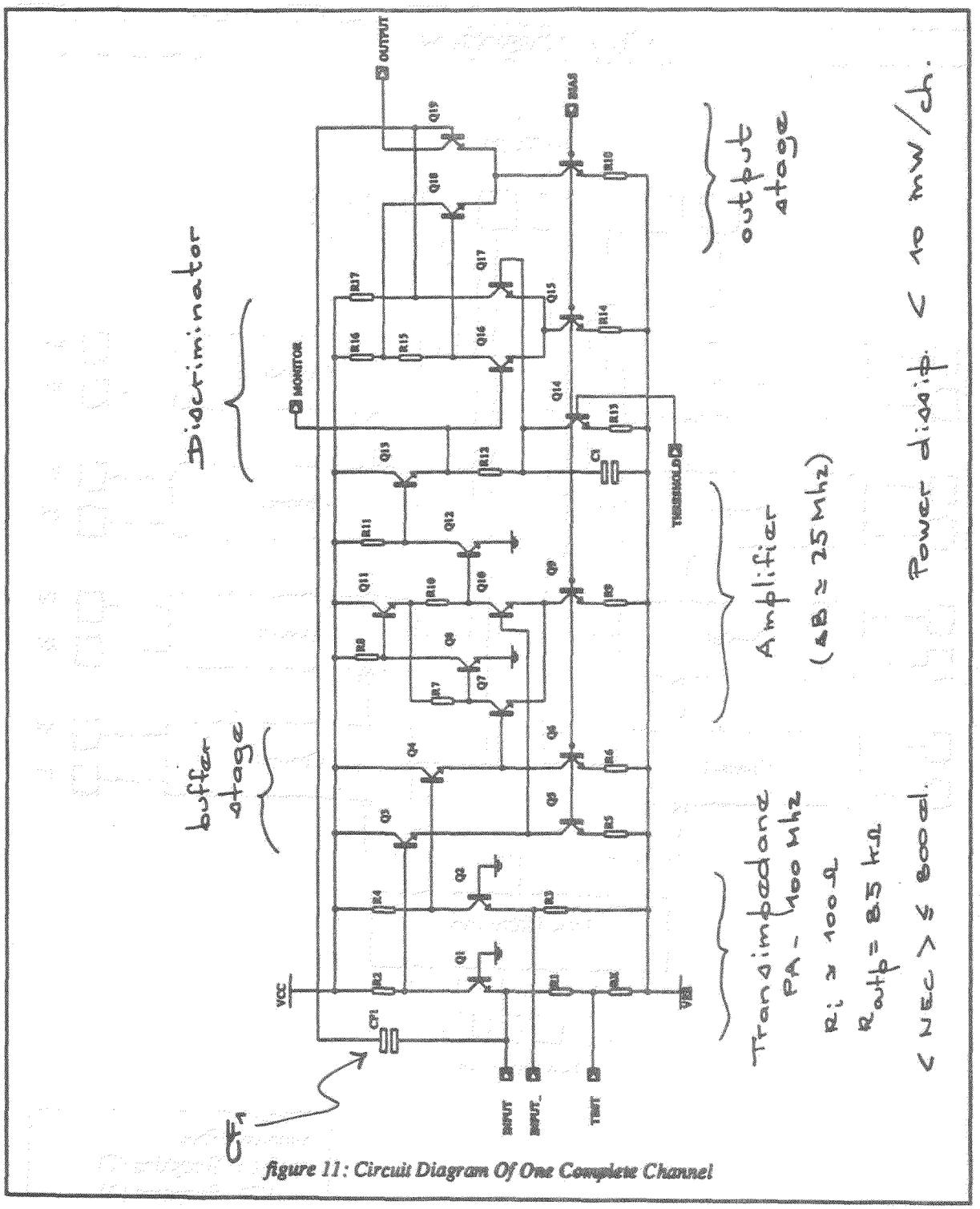

figure 11: Circuit Diagram Of One Complete Channel

Chip Overview

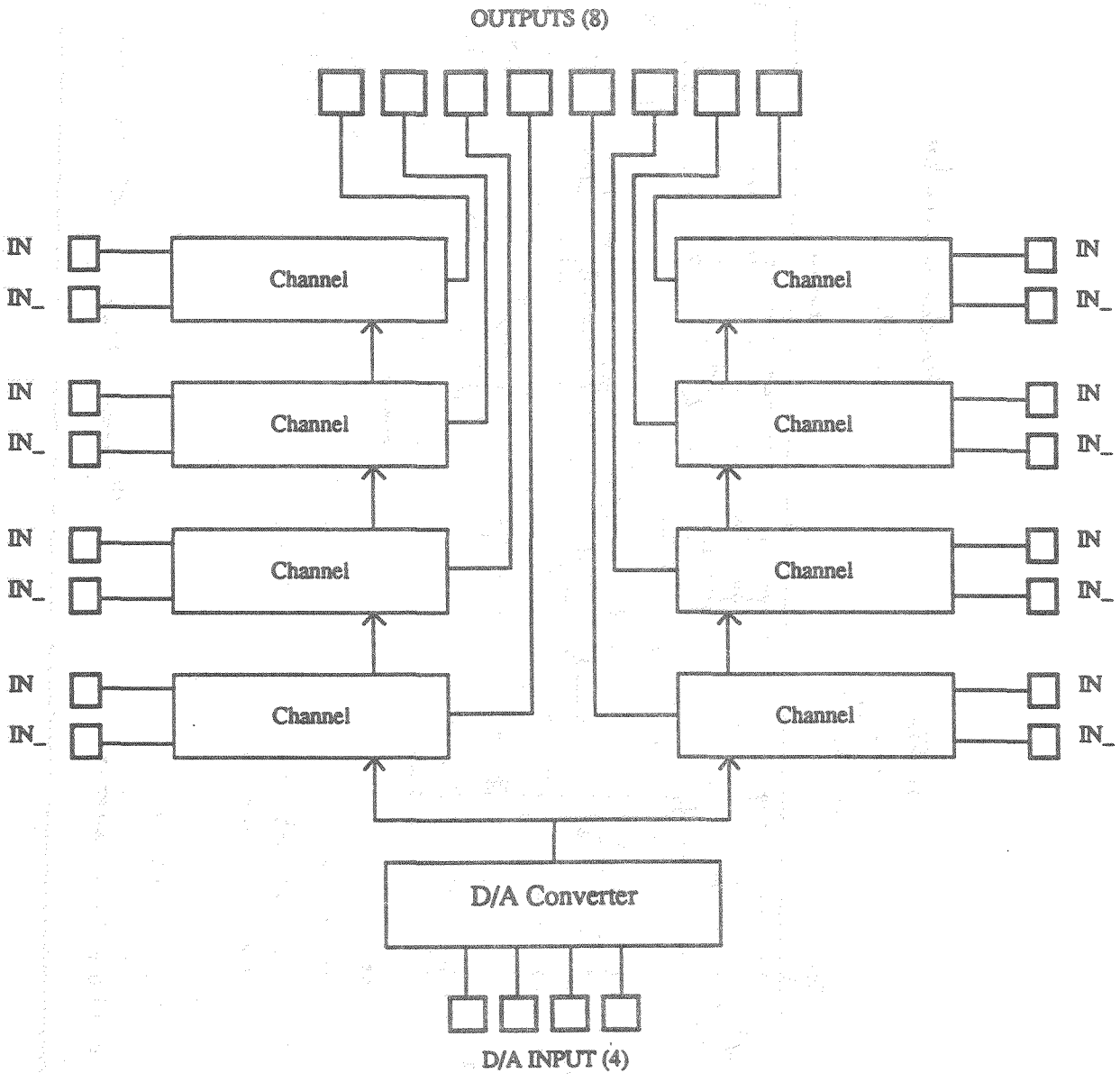

Not Shown:
- Bias Circuitry

Additional Pins:
- VCC Supplies (2)
- VEE Supplies (2)
- GROUNDS (4)
- Monitor Output (1)
- Test Input (1)

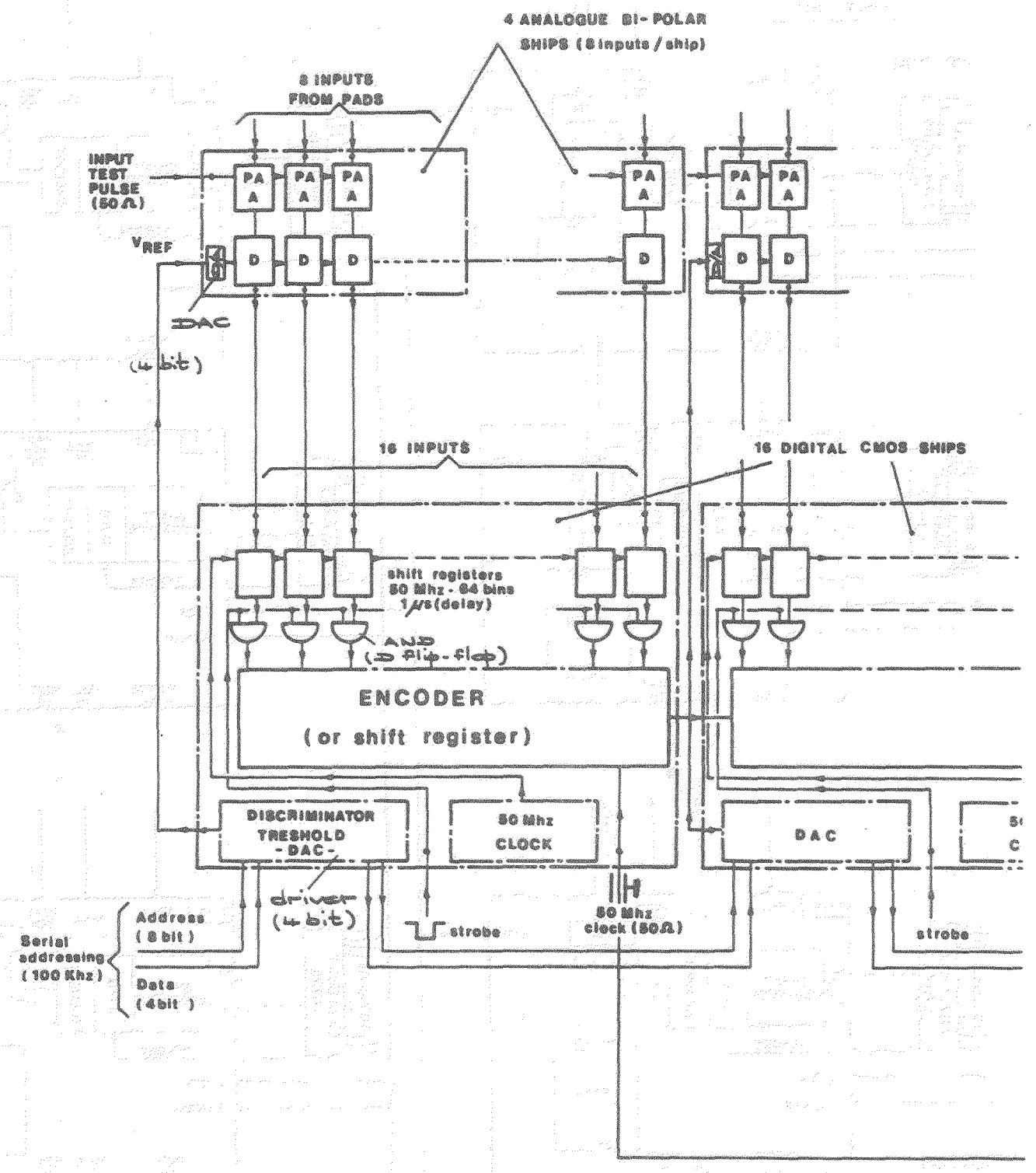
4 ANALOGUE BI-POLAR SHIPS (8 inputs / ship)
8 INPUTS FROM PADS
INPUT TEST PULSE (50Ω)
PA A
D
V_{REF}
DAC
(4 bit)
16 INPUTS
16 DIGITAL CMOS SHIPS
shift registers 50 Mhz - 64 bins 1μs(delay)
AND (D flip-flop)
ENCODER
(or shift register)
DISCRIMINATOR TRESHOLD -DAC-
50 Mhz CLOCK
DAC
driver (4 bit)
strobe
50 Mhz clock (50Ω)
Address (8 bit)
Serial addressing (100 Khz)
Data (4 bit)

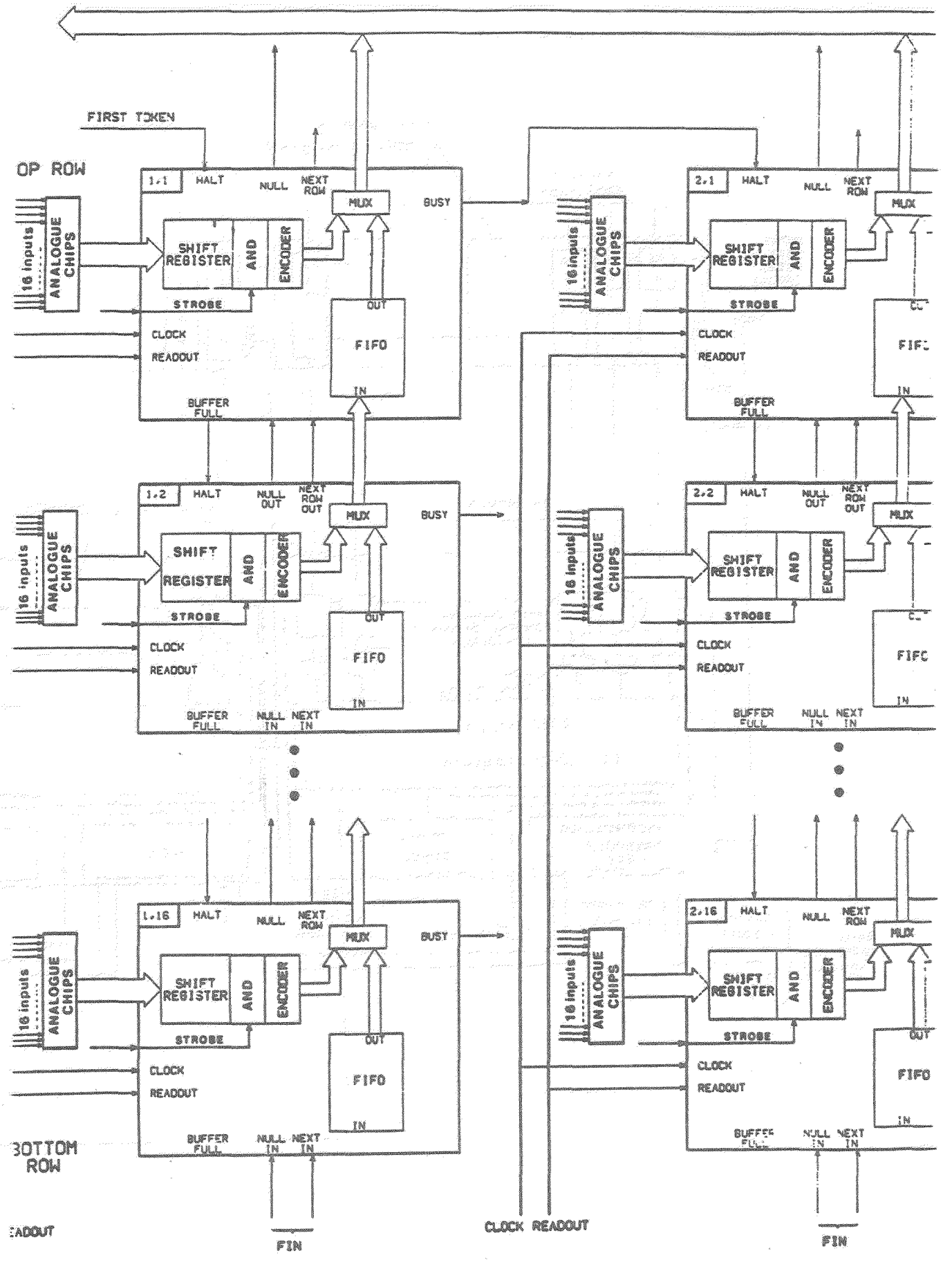
FIRST TOKEN
OP ROW
1,1
HALT
NULL
NEXT ROW
MUX
BUSY
16 inputs
ANALOGUE CHIPS
SHIFT REGISTER
AND
ENCODER
STROBE
CLOCK
READOUT
OUT
FIFO
IN
BUFFER FULL
2,1
1,2
NULL OUT
NEXT ROW OUT
2,2
NULL IN
NEXT IN
1,16
2,16
BOTTOM ROW
FIN
CLOCK READOUT

ELECTRONICS
(Analogue and Digital)

COST ESTIMATE
(DEVELOPMENT and PRODUCTION)

DEVELOPMENT :

240 KSF / CHIP
for 1 iteration
(addit^{l} iteration : 50 KSF)

TOTAL DEVELOP^{T} : min. 500 KSF
(or 320 k$)

PRODUCTION

10^3 chips / wafer
(8.10^3 anal. channels)
⇩
12 KSF
or ~ 1.5 SF / channel

Anal. + Digital ⇒ ~ 3 SF / chan.
or ~ 2$ / ch.

FAST, LOW-PRESSURE UV-PHOTON DETECTORS FOR ČERENKOV RING IMAGING

A. Breskin
Department of Nuclear Physics
The Weizmann Institute of Science
Rehovot, Israel.

Abstract

Photosensitive multistep avalanche detectors, operating at low gas pressures (40-100 Torr) can efficiently localize UV-photons. The application to Čerenkov Ring Imaging is discussed and some electronic and optical readout schemes are described. Fast UV-detectors, operating with CH_4 and "hot" TMAE are good candidates for RICH devices in experiments at future colliders. We report on some preliminary results of this operating mode and discuss possible UV-detector schemes.

1. Introduction

Since the pioneering work of Seguinot and Ypsilantis on the use of photosensitive gaseous detectors to image UV-photon Čerenkov rings[1], there has been quite intensive development in this field. Several groups have proposed various techniques to localize single UV-photons, a task which is quite difficult in the presence of high background originating mostly from charged particles and gamma radiation. Particles crossing the UV-detectors create a considerable amount of charges, as compared to single UV-induced photoelectrons, a fact which seriously limits the detector gain. Many of the technological problems, related to the physics of the detectors themselves or to the construction of large area devices, often of complex geometrical shapes, have been solved in various elegant ways. The handling of the rather aggressive TMAE [Tetrakis (dimethylamine) ethylene] photosensitive vapours has been mastered and considerable information on materials[2-5] suitable for operation with TMAE and on aging[6], is available. Secondary photon avalanches are limited by sophisticated "photon traps" located at the vicinity of the sensing elements in long-drift TPC-like devices[7]. Such traps are not necessary in multistep avalanche UV-detectors[8,9].

Most present experiments using Ring Imaging Čerenkov (RICH) detectors are equipped with the TPC-like UV-photon localization devices. However such devices are far too slow to satisfy particle identification in future colliders. The reader's attention should be pointed towards the following specific advantages of multistep avalanche detectors, which may fulfill this task, even at the 60MHz SSC beam crossing rates:

- A short UV-photon conversion region - reduced dead time and electron diffusion.
- A two-stage amplification mechanism enables high detection efficiency (high gain).
- A transfer region between the two stages acts simultaneously as a "secondary photon trap" and as an incorporated delay for trigger purposes.
- A gate element in front of the second stage enables the amplification and the recording of well selected events in the presence of high particle intensities.

UV-detectors of this kind have been successfully employed at the E605 experiment at FNAL[10]. Over the last few years we have developed multistep avalanche detectors operated at low gas pressures[11]. Low-pressure UV-photon detectors based on this technique[12,13] have some interesting properties. In addition to the lower gas density, the low-pressure operation is characterized by increased electron diffusion. Despite the considerably lower operation potentials, which result in reduced electrostatic problems, higher reduced electric fields (E/p) enable to reach large amplification factors ($> 10^7$). The high gains also result from the reduced charge density in these operating conditions. As compared to normal operating conditions low-pressure UV-photon detectors based on this technique have therefore the following additional considerable advantages;

- higher detection efficiency.
- reduced sensitivity to ionizing particles (dE/dx) and gamma-background.
- the carrier gas (usually hydrocarbon) has a higher transparency to UV-photons resulting in an increased N_o.
- reduced aging (due to the low charge density in the avalanche and the parallel grid amplification mode).
- high rate capability due to a fast (1-5μs) positive ion collection.

The localization accuracy is dictated by primary photoelectron diffusion within the conversion gap. It is typically of the order of 0.2-1 mm rms.

We have studied in detail UV-photon RICH detectors based on this technique, equipped with various electronic and optical readout systems. Details are given elsewhere[14-16].

In the present article I would like to summarize some beam test results with low pressure multistep UV-detectors equipped with various readout schemes. I will briefly describe a double-RICH electron-pair spectrometer, based on this technique, designed in collaboration with the University of Heidelberg for the search for Quark Gluon Plasma in relavitistic heavy ion collisions at the CERN-SPS[17]. I will present some recent data on the operation of low-pressure multistep detectors with CH_4-TMAE, at high TMAE concentrations, and discuss the technological problems related to this high temperature operation mode. Fast UV-detectors based on this technique are under study. Their possible application to future colliders will be discussed.

2. The low-pressure multistep UV-detector

The multistep detection structures we have developed and beam tested[18] are shown on fig. 1.

Photons impinging through an appropriate UV-window photo-ionize the TMAE molecules in the conversion region. The photoelectrons drift towards the preamplification stage. The width L of this conversion gap is dictated by the absorption length λ of UV-photons in the photosensitive gas (usually $L \geq 3\lambda$). λ depends on the vapour pressure (temperature) of the photosensitive vapour. For example, λ=0.6 and 10 mm for T=80°C and 35°C respectively, in TMAE[13]. L determines the intrinsic localization resolution of the UV-detector, which mostly depends on the diffusion of single photoelectrons across the conversion gap. L also determines the dead-time of the detector,

or its rate capability, a crucial parameter in fast cycle future colliders.

In the parallel grid preamplification stage a first multiplication of the order of 10^4-10^5, occurs. A fraction of the electron swarm is transmitted to the second amplification stage, usually through a gate element. The field across the parallel grid gate element is normally backward-biased. The electrons can be transmitted to the second amplification stage by pulsing the gate electrodes to restore the electric field[8]. The second amplification stage provides the full detector gain only during the gate opening period. This also inhibits the amplification of delayed secondary photoelectrons and therefore limits the number of secondary parasitic avalanches.

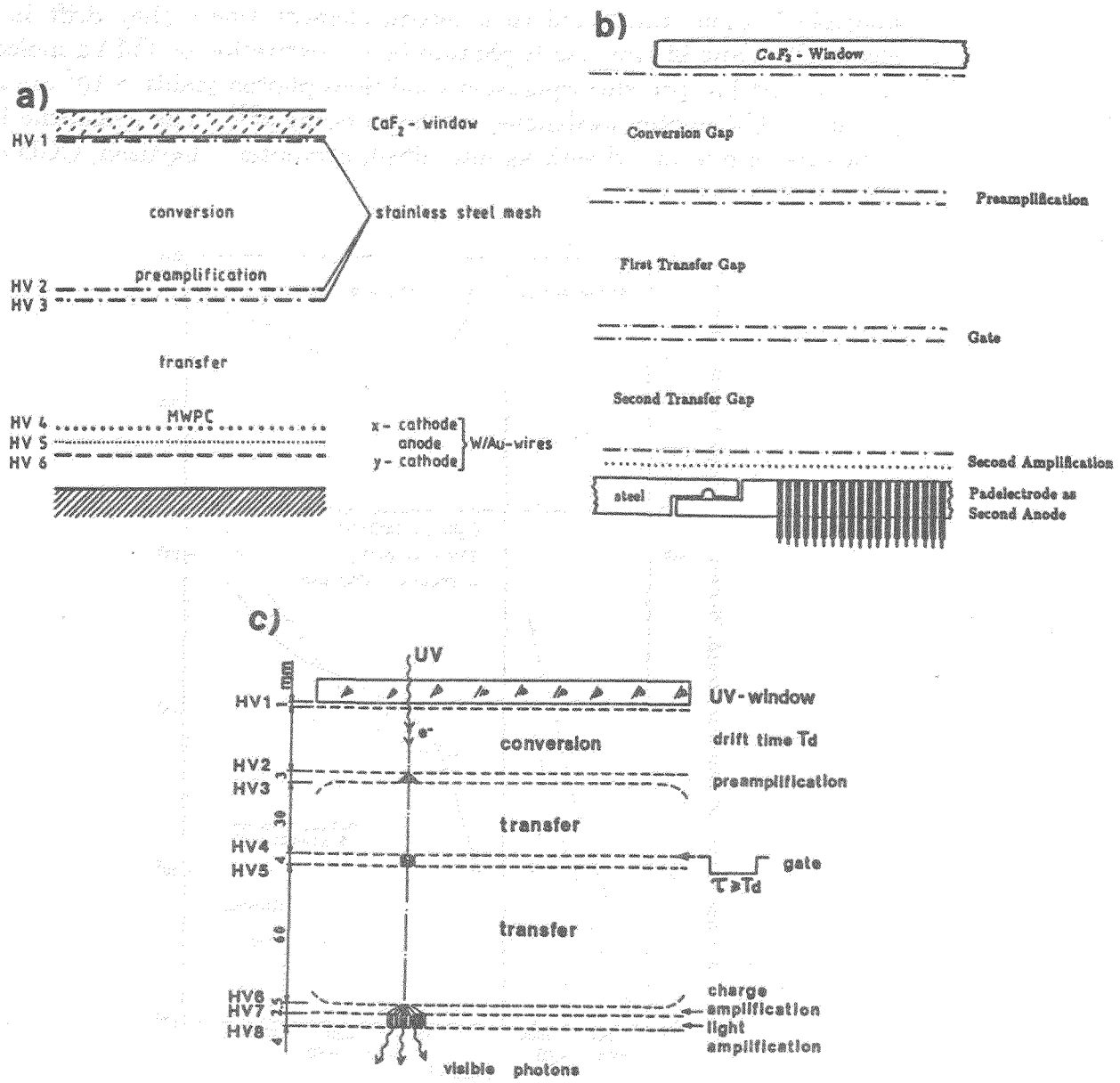

Fig.1. Schematic diagrams of the UV-photon detectors:
a) FADC wire readout; b) Pad readout; c) Optical readout.

The second amplification element can be of various types:

- a multiwire or a parallel-grid structure with cathode and anode wires running at various angles and read out with FADCs[14]. The FADCs ensure a high detection efficiency of multiple simultaneous electrons photoproduced at various conversion depths. (fig. 1a).
- a parallel gap structure with a pad anode or a system with a parallel grid element and a further transfer of the avalanche electrons to the pad electrode (fig. 1b). Pad signals can be amplified, daisy-chained and multiplexed to ADCs[15] or read out individually when rapidity is concerned[19].
- an optical readout: a two-stage parallel grid structure where electrons are first multiplied, then transferred to a second element where they drift in a high electric field and induce visible photons by the excitation of TMAE molecules[16] (fig. 1c). At low-pressure operation conditions photon yields $> 10^7$ are reached per single UV-photon avalanche, as shown on fig.2[20]. The avalanche induced light spots are recorded with an intensified, computer - digitized, CCD camera.

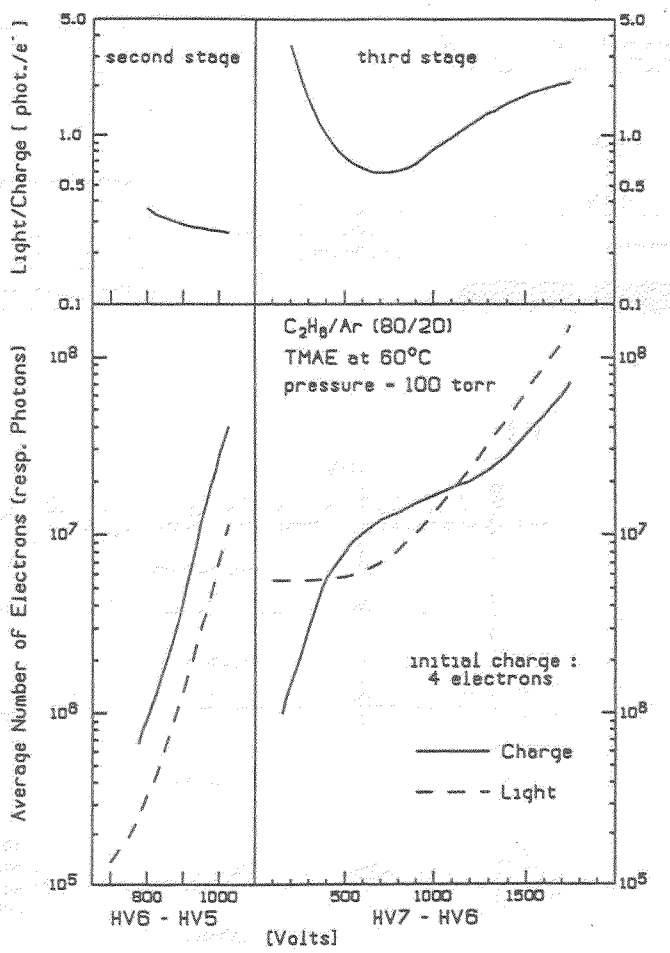

Fig.2. Electron and photon amplification curves and light-to-charge yields in a 2-stage and a 3-stage avalanche chamber. C_2H_6/Ar (80/20) and TMAE (60°C). Operation pressure : 100 Torr.

All three readout methods have been investigated with 3-5 GeV/c electrons, on a 200×200 mm^2 UV-photon detector coupled to a CH_4 radiator. A detailed comparison is given elsewhere[18]. Best results in terms of efficiency were obtained with the Pad and Optical readout schemes. A major reason is the incorporated gate, which allowed a stable operation at the high experimental gamma-background. Single Čerenkov rings, recorded in both methods, are shown in fig. 3. The rings are practically free of secondary photon avalanches, as expected in this gated double stage operation mode. The single photon detection efficiency is close to 100% in both cases, as deduced from the number of photons recorded,our data on gas and window transmission[16] the quantum efficiency of TMAE[21], and the present physical constraints of our experimental set-up.

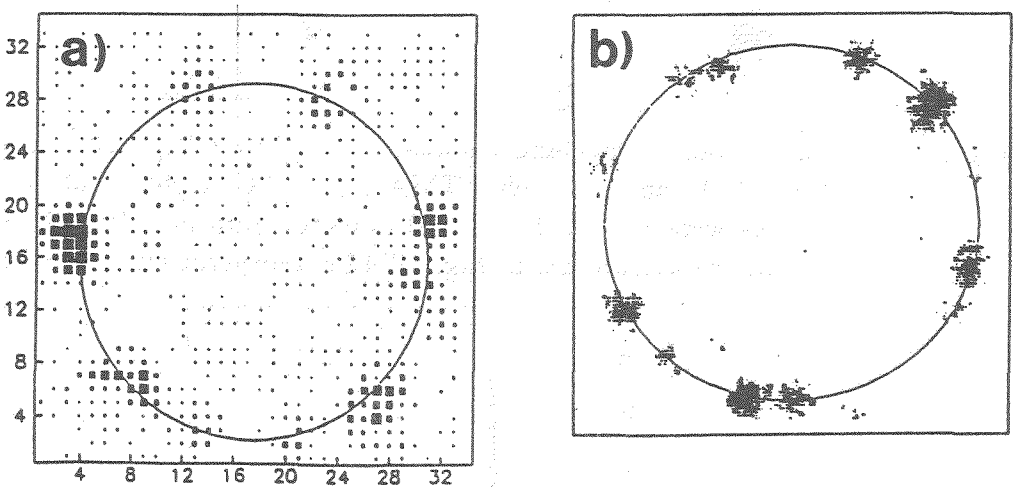

Fig.3. Examples of typical Čerenkov rings (each spot is an image of a single UV-photon avalanche). a) Pad readout, R=33 mm. b) Optical readout, R=52 mm.

The detectors were operated with gas mixtures of C_2H_6, Ar and TMAE. The TMAE was kept at 34°C and the operation pressure was 40 Torr. The localization resolution was measured and was found to conform to the diffusion of the photoelectrons in the 30 mm conversion gap and to the chromatic dispersion in the radiator gas. Ring radii were measured to an accuracy of about 2 mm rms. The avalanche spot size, depends on electron diffusion during the multiple avalanche and transfer processes and on the mean free path of secondary UV-photons emitted during avalanche formation. It was experimentally demonstrated that spot sizes of avalanches recorded optically and electronically are of the same order[22] for equal operation conditions. In fig. 4 are shown avalanche spots optically recorded at a pressure of 100 Torr of C_2H_6/Ar (80/20) and TMAE at 40°C and 60°C with a CCD camera. It can be noted that at the higher TMAE concentration (60°C, 5 Torr) the spot size is smaller and there is no secondary photon background like the one visible at 40°C (1 Torr). This is due to the efficient re-absorbtion of secondary photons in the nearest vicinity of the avalanche. The charge gain is the same in both cases, and is of the order of $5 \cdot 10^7$. The spot size with TMAE at 60°C has an rms value of the order of 1 mm. More details can be found in Ref.13.

The localization resolution of single photoelectrons was measured at high TMAE temperature with an optical detector having a 7.4 mm conversion gap. In Fig. 5 are shown the one- and two-dimensional distributions of the computed centers of gravity of about 1200 events corresponding to two, 100μm diameter pinholes irradiated with UV-photons. The localization resolution is of the order of 720μm (FWHM)as expected from electron diffusion considerations[13].

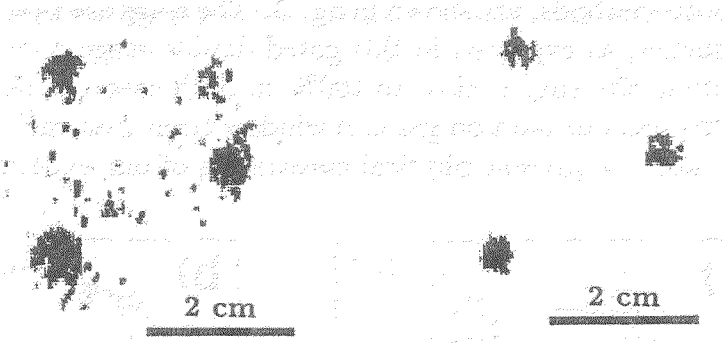

Fig.4. Single-electron avalanche spots, induced by UV-photons and recorded with the CCD camera. Left: TMAE at 40°C; right: TMAE at 60°C. Both figures were recorded at equal detector gain of $\sim 10^7$. The suppression of secondary avalanches at high TMAE temperature is evident.

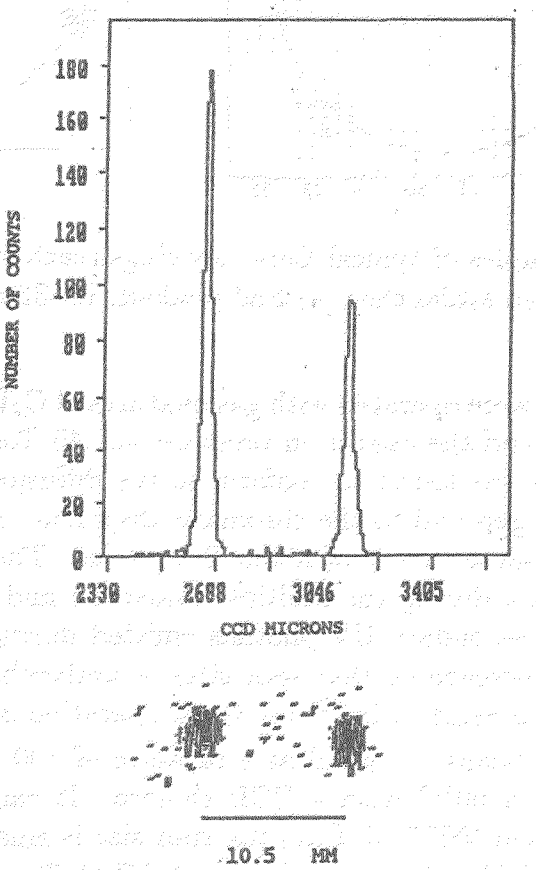

Fig.5. One and two-dimensional distributions of the center-of-gravity of 1232 avalanche light spots, in a 3-stage optical detector, induced by collimated single UV-photons. The distance between the two peaks is 10.5 mm, the FWHM is 720μm. C_2H_6/Ar (80/20) and TMAE (60°C), p=100 Torr.

3. Present application

Low-pressure multistep UV-photon detectors have been designed for a large electron pair spectrometer. The spectrometer shown in fig. 6 is in the process of being built by the Heidelberg/Weizmann CERES collaboration, for the study of e^+e^- pairs produced in relativistic heavy ion collisions at the CERN-SPS[17]. It is based on a very particular "hadron blind tracking" using the Čerenkov Ring-Imaging technique. It consists of two RICH detectors, having a full azimuthal coverage, with gas radiators. One detector is situated before, the other one after a short double-solenoid magnet. The Čerenkov thresholds are sufficiently high so that essentially only electrons create rings (with a saturated radius). The UV-detectors are placed at backward angles with respect to the target so as to reduce particle background. The electron momentum is obtained from the change in its direction, by measuring the ring centers in both UV-RICH detectors.

The large UV-photon detector, of a diameter close to 2.5 m, is electronically read out by about 50,000 pads. The pads, 7.62×7.62 mm^2, are multiplexed into 13 ADCs via 400 preamplifier modules having 128 channels each[23]. It is designed to operate at a pressure of 40 Torr with TMAE at 40°C. The small inner detector, about 0.9 m in diameter, will operate at 100 Torr and with TMAE at 60°C. It will be equipped with an optical imaging system shown in fig. 7. The image, recorded by a large aperture lens, is intensified by a 40 mm gatable double MCP image intensifier. It is reduced, further intensified and split into four small CCDs (144×208 pixles) in order to reduce the readout time.

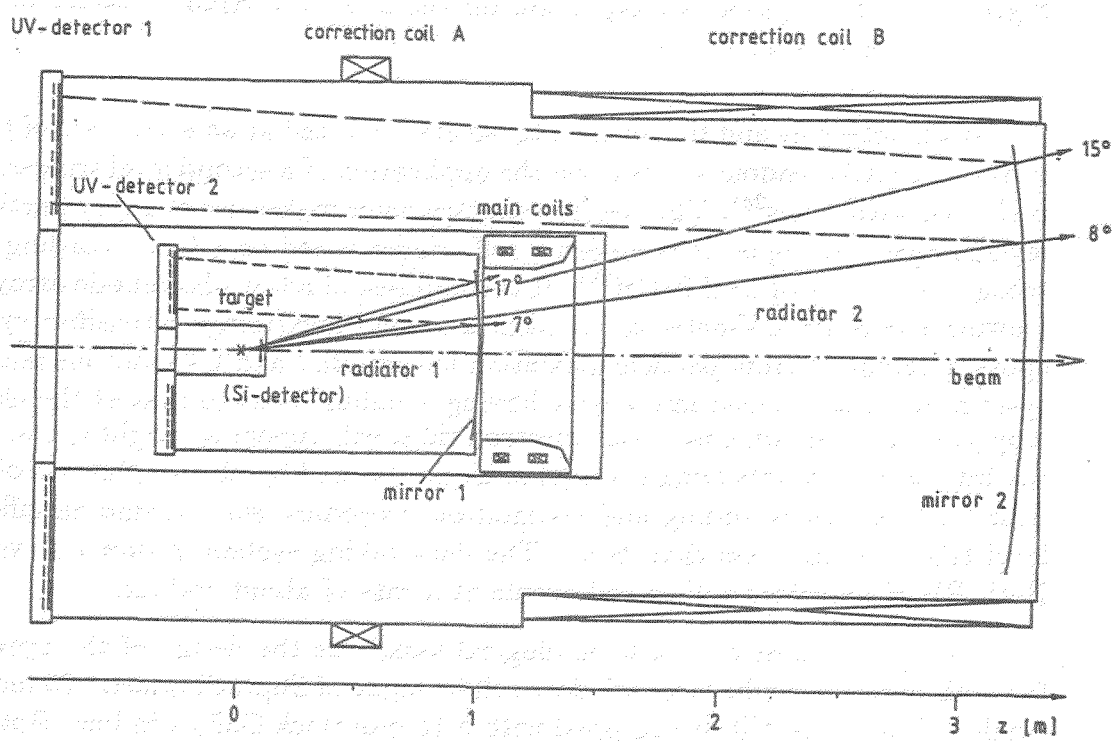

Fig.6. A schematic view of the double RICH, hadron blind, electron pair spectrometer of CERES.

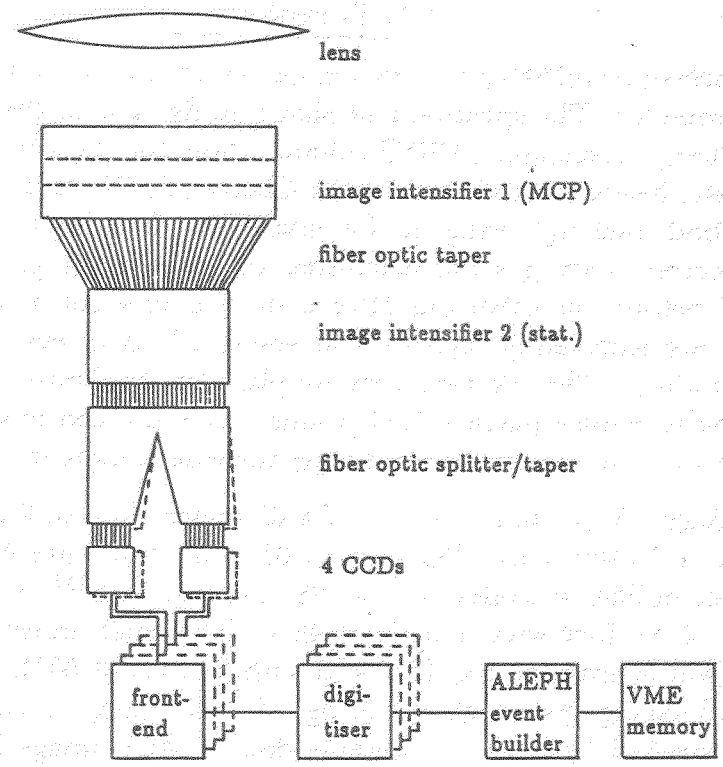

Fig.7. The optical readout chain for the inner UV-RICH detector of the electron pair spectrometer.

Both detectors and the image intensifiers are gated at an event rate of the order of 10 KHz. The CCD readout starts upon the application of a second level trigger, otherwise it is cleared within $1\mu s$[24]. The electron spectrometer makes use of a very particular second level trigger technique. It is indeed a self-trigger based on a fast recording and pattern recognition of the optical RICH[25]. It is composed of a fast photodiode array (128×128), viewing the inner UV-detector through a second lens/image intensifier system. Light spots, originating from particle ionization background and UV-photons recorded by the system, are transformed into circles having a radius equal to that of the electron rings. Applying a threshold, only "real" electron rings will appear as bright spots, representing the intersection points (ring centers) of circles formed by all UV-photons of these rings. This fast pattern recording and recognition procedure will provide an efficient second level trigger within less than $50\mu s$. The data taking system is slow but very selective. Both RICH detectors will record events at a rate of about 160 Hz.

One of the most crucial technological tasks was the design of the optical windows for both detectors. The large window will be made of Suprasil-quartz, 25 mm thick. The small UV-detector will be equipped with a 15 mm thick CaF_2 window. Both segmented windows will support a pressure difference of 1 atmosphere.

The spectrometer is planned to be operational in spring 1990.

4. Some comparison between TMAE and TEA

Several options have been proposed so far by various groups, for fast UV-photon detectors. Most authors have chosen single or multistep[19,26] wire chambers with pad-anode readout. It is proposed that the "cold" (TEA) detectors or "hot" (TMAE) detectors will operate at normal gas pressures. As already discussed above, the length of the conversion element (photoelectron drift-time) determines the dead-time of the detector. As compared to the short UV-photon mean-free-path in TEA at room temperature ($\sim 600\mu$m),liquid TMAE temperature has to be raised above 70°C in order to reduce the photon mean-free-path to values below 1 mm[13].

We have been successfully operating "hot" TMAE detectors over the last two years[20]. This "hot" operation mode induces some technological constraints, which can be solved, as will be discussed in the last section.

Despite the somewhat more complex operation with "hot" TMAE, one should take into account its considerably greater quantum efficiency and compatibility with cheaper quartz UV-windows and standard carrier gases (hydrocarbons). An example of the transmission of some gases and windows and the quantum efficiency of TEA and TMAE are shown in fig.8. The transmission data of thick Suprasil quartz windows were recently measured on samples provided by Heraeus[27]. The gas transmission at low pressures was recently measured in our laboratory; examples are shown in fig.9. There are two sets of data on the quantum efficiency of TEA and TMAE[21,28]. There is a considerable discrepancy between them and we await new results for these two gases. Some clarification on this matter is provided by J. Seguinot in these proceedings[19]

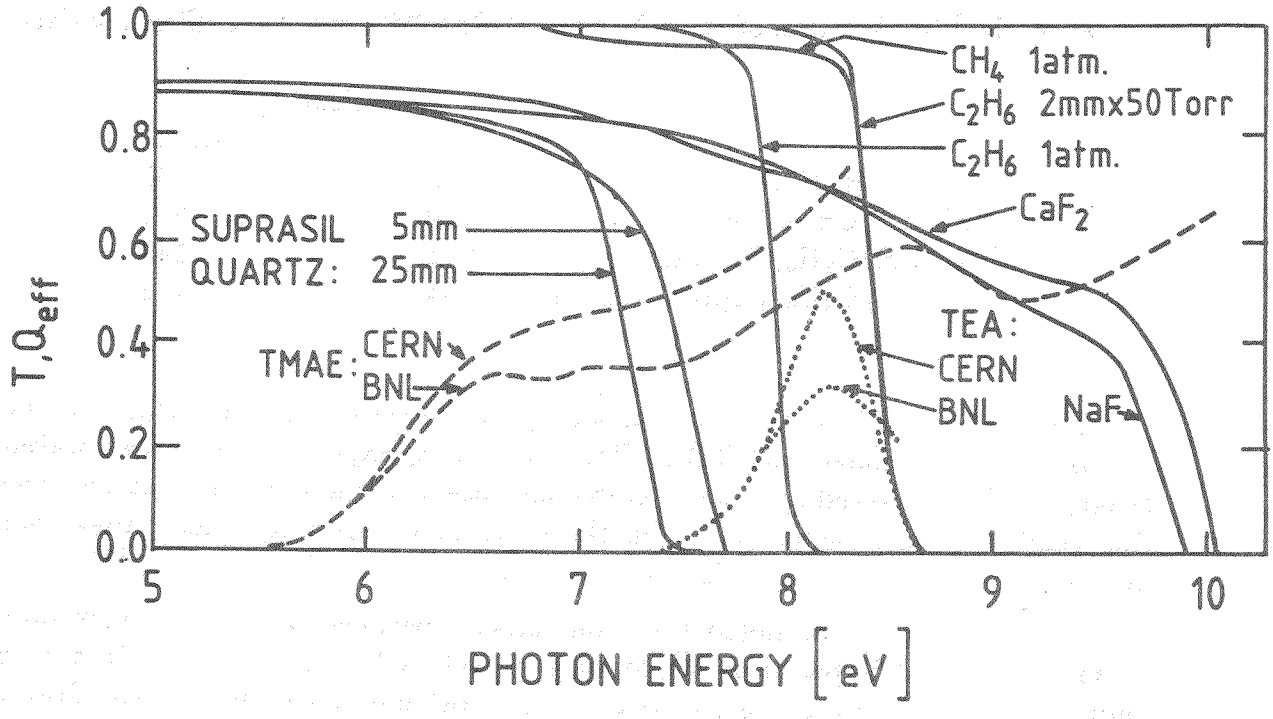

Fig.8. Gas and window transmission curves and the quantum efficiency of TEA and TMAE, as function of the UV-photon energy.

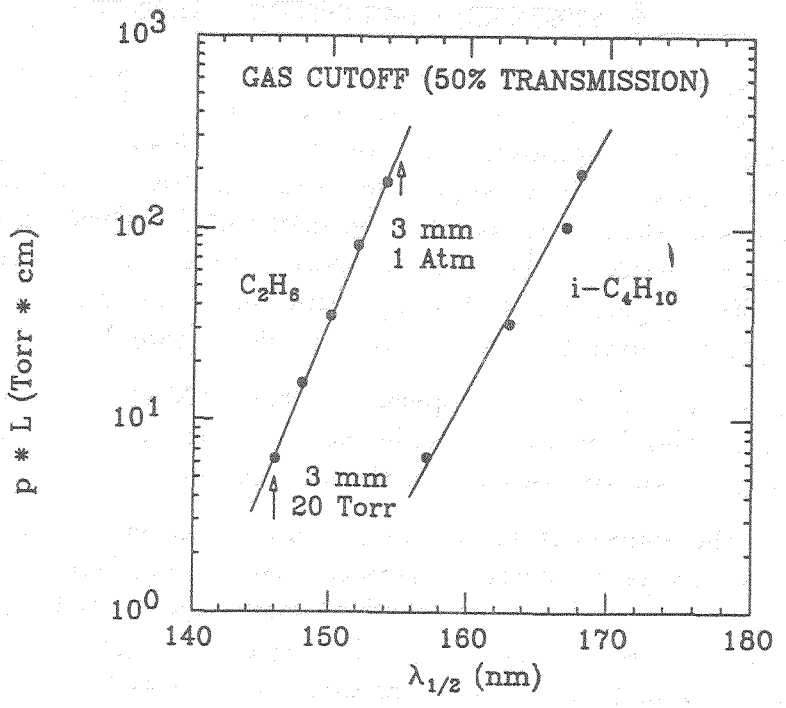

Fig.9. Gas cutoff at 50% transmission, for C_2H_6 and i-C_4H_{10}, as a function of the density factor $p \times L$ (pressure $\times$ gap length).

On the basis of the data shown in fig. 8 the following theoretical quality factors can be reached (as function of the BNL[21] and CERN[27] quantum efficiency data):

	$N_o[\mathrm{cm}^{-1}]$	
	BNL	CERN
$TEA/CH_4/CaF_2$	40	65
$TMAE/CH_4/CaF_2$	219	275
$TMAE/C_2H_6$/Suprasil (5 mm)	115	140
$TMAE/C_2H_6$/Suprasil (25 mm)	94	112

These numbers have to be multiplied by the detector efficiency which, in the best case is ϵ=0.8. Compared with TEA, TMAE sensitivity expands over a broad wavelength range, which is reflected by a considerable increase in the number of photoelectrons per ring (higher quality factor N_o). On the other hand the ring quality may somehow deteriorate due to chromatic dispersion over the increased spectral range[29].

It should be further noted that comparisons between photon-feedback processes in TEA and TMAE, based on single stage detectors[19], are irrelevant in the case of multistep detectors, for the simple reason that most secondary photons are absorbed in the transfer gap between the two amplification stages.

5. A fast "hot" CH_4/TMAE UV-detector

Most of our work on UV-photon detectors was done with C_2H_6/Ar/TMAE mixtures. From fig. 8 we can see that a gas thickness of 2 mm of C_2H_6 at 50 Torr is as UV-transparent as CH_4 at atmospheric pressure. However, the maximum drift velocity of electrons in C_2H_6/TMAE mixtures is of about 5.5 cm/μs[13], which corresponds to a total drift time in a 2 mm gap of the order of 36 ns. The drift-time in CH_4 is about twice as short as in C_2H_6. However, it was recognized that high gas amplification factors in CH_4 cause serious feedback problems even in multistep amplification structures[30]. A typical example of the photon feedback mechanism is shown in fig. 10a. The multistep detector is operated with single UV-photons at 100 Torr with a mixture of CH_4/TMAE (30°C). The detector gain is of $2 \cdot 10^7$ and the transfer gap length is of 30 mm. An increase of TMAE concentration reduces this effect dramatically. We have operated the detector under the same conditions but with CH_4/TMAE at 60°C[31]. The mean-free-path of UV-photons is 2 mm, as compared to about 15 mm at 30°C. Pulses recorded under these conditions, at the same detector gain, show no feedback effect (fig. 10b).

We have studied the charge and light gain of the 3-stage detector designed for optical imaging, with CH_4/TMAE (60°C). The results shown in fig.11 are very similar to those obtained with C_2H_6/TMAE (60°C) (fig.2). Charge gains as high as $5 \cdot 10^7$ can be reached without photon feedback.

We have measured the drift velocity under these conditions by recording the time spectrum of UV-photon absorbed in the conversion gap. It is of 9.2 cm/μs, almost as high as in pure CH_4 (at E/p$\cong$ 1V/cm·Torr) (fig.12). We have measured the transverse and longitudinal electron diffusion parameters in pure CH_4 (fig.13). The method is described elsewhere[13]. The minimum value of the transverse diffusion is larger than in pure C_2H_6 only by a factor of 20%. It should be noted here that the transverse diffusion in C_2H_6/TMAE is about 25% lower than in pure C_2H_6[13], and we expect the same trend in CH_4/TMAE.

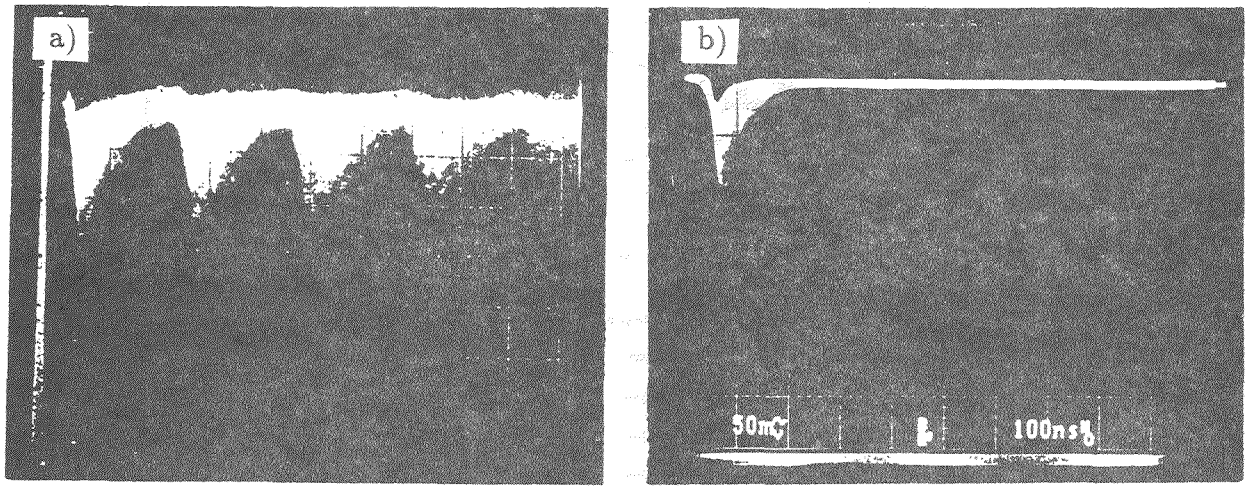

Fig.10. Current pulses in a 2-stage avalanche detector operating with single UV-photons at a pressure of 100 Torr. The charge gain is $2 \cdot 10^7$.
a) CH_4 + TMAE at 30°C, a very strong secondary avalanche effect.
b) CH_4 + TMAE at 60°C, no secondary avalanches.

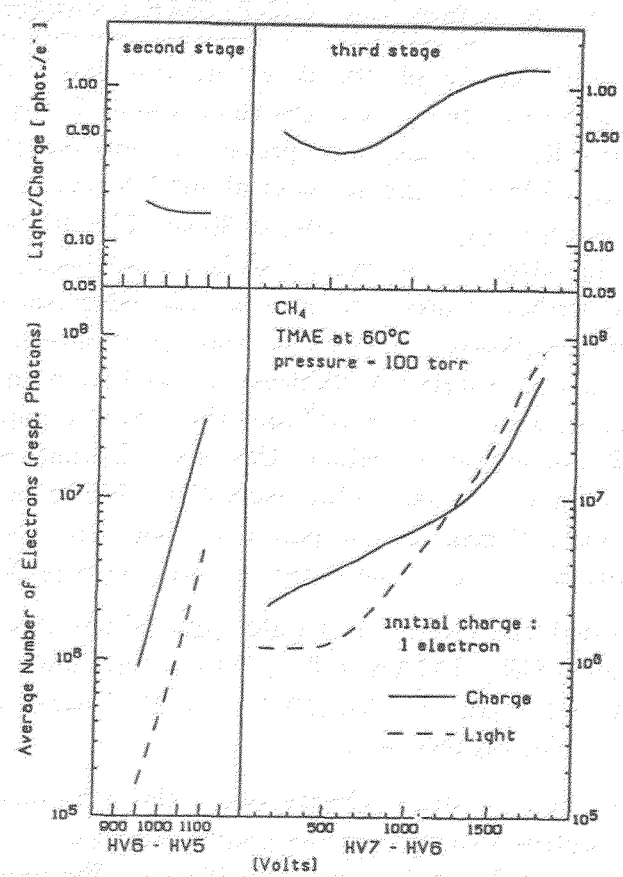

Fig.11. Electron and photon amplification curves and light-to-charge yields, in a 2-stage and a 3-stage avalanche chamber. CH_4/TMAE (60°C), p=100 Torr. The maximum gain and the light-to-charge yields are comparable to that of C_2H_6/Ar/TMAE (fig.2).

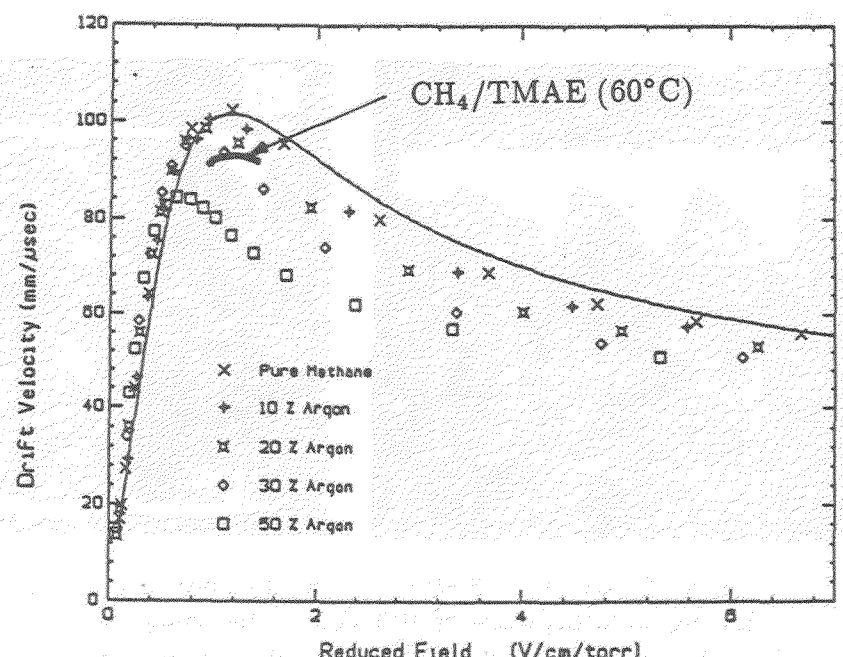

Fig.12. Electron drift velocities as a function of the reduced electric field (E/p), in CH_4, CH_4/Ar and CH_4/TMAE mixtures. (The solid line is computed).

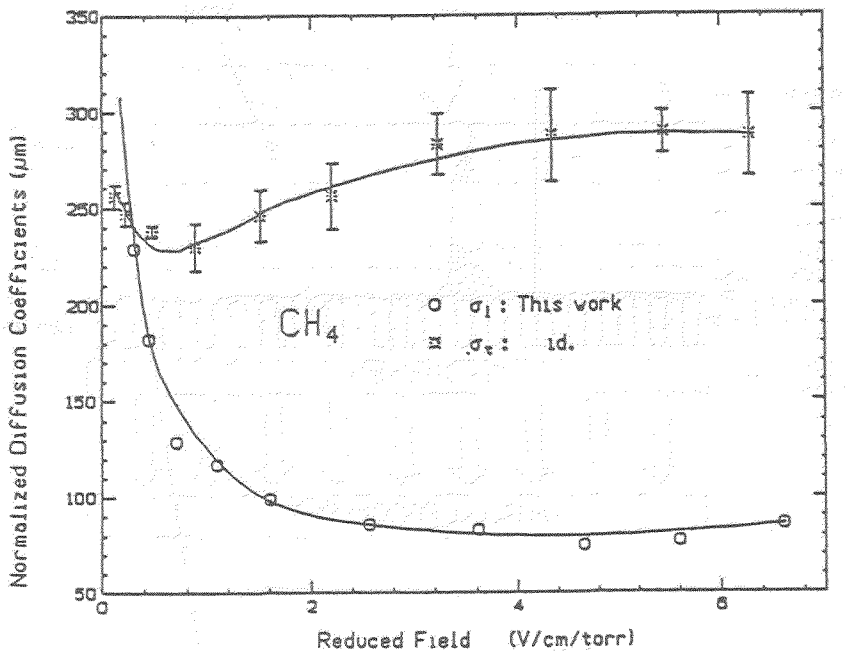

Fig.13. Transverse and longitudinal electron diffusion parameters in CH_4, normalized to 1 atm. and 1 cm drift (σ_0). (The solid lines are computer fits).

A possible fast UV-detector scheme is shown in fig.14. Photoelectrons are created along a narrow conversion gap. They are preamplified and transferred through a gate to a second parallel grid amplification stage. All electrodes are made of stainless steel mesh. There is no need for amplification wires, which makes the detector very rugged. The mesh transparency is 81% (50μm wires, 500μm space), except for the window mesh which should be more transparent. The length of the transfer gap, in front of the gate electrode, has to be chosen according to the delay required by the first level trigger circuit. For reasons explained in the introduction, we propose to operate the detector at a pressure of 50-100 Torr.

The localization can be done by a pad-electrode. We propose to use the following method, shown in fig.14. The anode of the second amplification stage is a resistive layer deposited on a thin (0.2-0.4 mm) G-10 or Kapton foil. The foil is glued to the pad electrode. The reason for the proposed scheme is to keep both the window and the pad-electrode, at ground potential. This simplifies the mechanical construction and the readout circuit of the pads. The resistive anode is at positive voltage. Compact readout electronics, based on VLSI technology, is needed. An example is given in ref.19. The pad size is chosen according to the application, the readout speed and the requested resolution. We have recently studied the geometrical distribution of current signals induced on pads covered with a G-10 foil and a resistive layer ($\approx 2M\Omega$/square). It has a FWHM of the order of 3.5 mm[32].

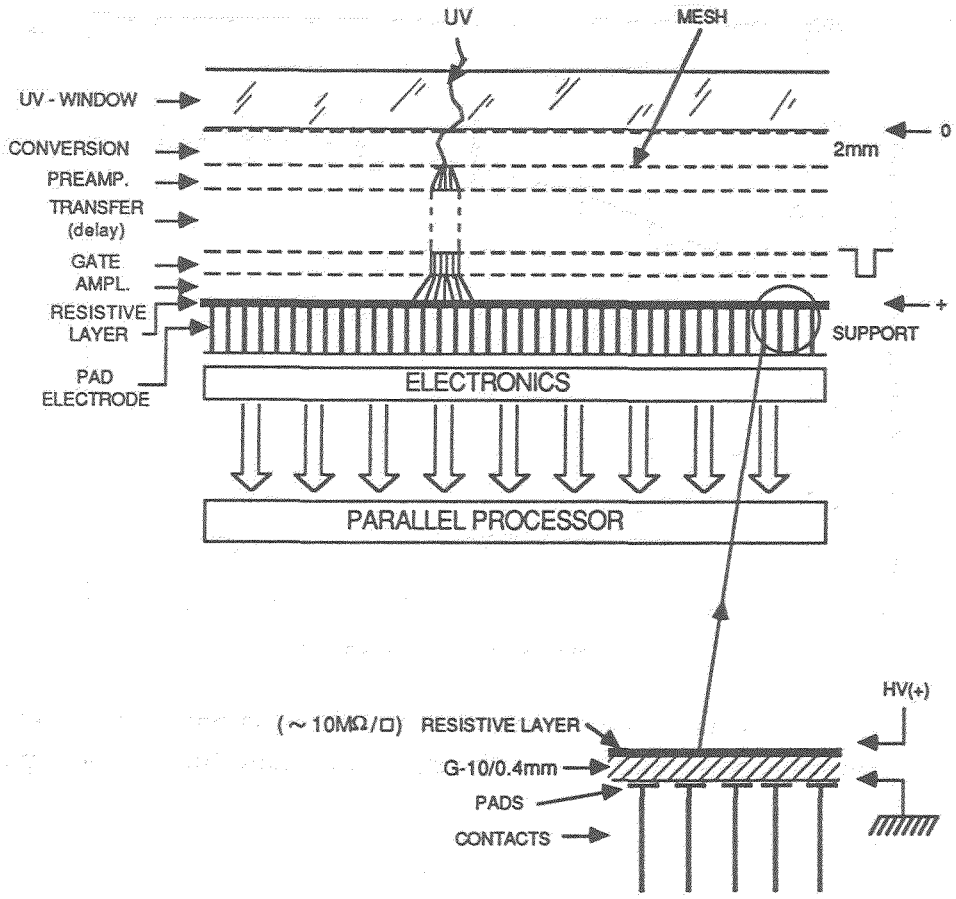

Fig.14. A proposed scheme for a fast UV-photon detector, based on the low-pressure multistep avalanche chamber technique. Photoelectrons are preamplified and transferred via a gate element to a second, parallel grid, amplification element. The signals are recorded on a pad-electrode.

An alternative readout method can be an optical recording of the light emitted by the avalanches. One could think of "optical pads", replacing the electrical pads shown in fig.14. In such a scheme the anode of the second amplification stage consists of a semitransparent fibre-optic plate. The fibres are directly coupled to fast photodiode arrays and are read out by similar electronics to that of the electrical pads. The optical recording of $10^5 - 10^7$ photons/avalanche may offer a better signal-to-noise as compared to the electrical readout. In addition, the photon emission process is much faster than the buildup of electrical signals, which also reflects the rather slow movement of positive ions away from the anode. Therefore, an optical solution may result in a better time resolution, a crucial parameter in the present application.

The length of the conversion gap is chosen according to the requested time resolution. As already discussed, the choice of this gap will dictate the TMAE temperature i.e., a gap of 2 mm of CH_4/TMAE will imply a temperature of about 80°C[13] and will result in a total drift time of 21 ns. In cases where one could afford "losing" photons,

the conversion gap could be reduced to values of $L < 3\lambda$. As an example, at 80°C ($\lambda \cong 0.6$ mm), a gap of 1.3 mm or 0.65 mm will provide respective efficiencies of 87% and 63% and total drift times of 14 ns and 7 ns. However, for technical reasons it is not recommended to reduce the gap below a value of 1 mm.

In practice, a detector operating with CH_4/TMAE/CaF_2 can reach a quality factor (N_o) of the order of 220 cm^{-1} (taking into account an efficiency of 0.8). The following table summarizes the performance (time resolution, number of photoelectrons) of two possible RICH systems, the UV-detectors operate with TMAE at 80°C.

		Conversion Length L=2 mm (3λ)		Conversion Length L=1.3 mm (2λ)	
radiator	γ_{th}	Δt[ns]	n[p.e.]	Δt[ns]	n[p.e.]
NaF, 1cm	1.45	21	105	14	96
He/CF_4, 4m	50	21	35	14	32

6. Technological hints

The low-pressure mode of operation on one hand and the high detector temperature, dictated by the TMAE concentration, on the other hand, require some precautions. The detector vessel has to be vacuum-tight, which is indeed strongly recommended even when operating TMAE-filled detectors at atmospheric pressure. We have found for example, that the spontaneous electron emission of our prototype detectors strongly depends on their tightness, which may indicate that it depends on TMAE oxidation. Our detectors are currently pumped down to a vacuum of $10^{-4} - 10^{-5}$ Torr, prior to the introduction of TMAE and before any opening. This enables long-term stable operation and prevents deposits of TMAE oxidation products.

The construction materials have to be carefully selected so as to avoid outgassing and deterioration of mechanical and electrical properties[2,3]. For example G-10 epoxy laminate and Epon 826/Versamid 140 epoxy-glue were found to be TMAE resistant at normal temperatures[4,5]. We have found no deterioration of these materials also at a temperature range of 60-80°C.

Particular care should be taken to match thermal expansion coefficients of the construction materials, such as UV-windows, mechanical supports, wire mesh and electrode frames. We have gained much experience in this field in designing our large area low-pressure UV-detectors and CaF_2 and quartz windows for the electron-pair spectrometer of the future CERES experiment (see Section 3). The windows were designed to simultaneously support high temperature and a pressure difference of 1 atm. The window support-frames materials are Invar and Aluminium for quartz and CaF_2 respectively.

Though considerable experience has been gained in the last few years, the high temperature operation mode certainly requires more investigation. We are presently studying the effects of outgassing of materials on electron and UV-photon mean-free-path in gases, high rate operation in the presence of intense background, fast optical readout possibilities and other topics related to the application of this technique for experiments at future colliders.

References

1. J. Seguinot and T. Ypsilantis, Nucl. Instrum. Meth. **142** (1977) 377.
2. D. Aston et al., IEEE Trans. Nucl. Sci. **NS-36** (1989) 276.
3. P. Carolan and D. Evans, The sue of TMAE as a photo-ionizing gas additive and its effects on various materials used for dynamic seals. Rutherford Appleton Lab., unpublished report (1983).
4. R.T. Rewick et al., Anal. Chem. **60** (1988) 2095.
5. M. Cavalli-Sforza, CRID Int. Note No. 15 (1986).
6. J. Vavra, Nucl. Instrum. Meth. **A252** (1986) 547.
7. See for example R. Arnold et al., Nucl Instrum. Meth. **A252** (1986) 188.
8. See for example, A. Breskin, G. Charpak, S. Majewski, G. Melchart, G. Peterson and F. Sauli, Nucl. Instrum. Meth. **161** (1979) 19.
9. G. Charpak and F. Sauli, Nucl. Instrum. Meth. **225** (1984) 627.
10. R. Bouclier et al., Nucl. Instrum. Meth. **205** (1983) 403.
11. A. Breskin and R. Chechik, IEEE Trans. Nucl. Sci. **NS-32** (1985) 504.
12. S. Majewski, D.F. Anderson, C. Constanta-Fanourakis, B. Kross and G. Fanourakis, Nucl. Instrum. Meth. **A264** (1988) 235.
13. R. Chechik and A. Breskin, Nucl. Instrum. Meth. **A264** (1988) 251.
14. A. Drees et al., Nucl. Instrum. Meth. **A273** (1988) 793.
15. P. Fischer et al., IEEE Trans. Nucl. Sci. **NS-35** (1988) 432.
16. A. Breskin et al., Nucl. Instrum. Meth. **273** (1988) 798.
17. U. Fashingbauer et al., CERN/SPSC/P237/88-25.
18. A. Breskin et al., IEEE Trans. Nucl. Sci. **NS-35** (1988) 404.
19. J. Seguinot, These proceedings.
20. A. Breskin, R. Chechik and D. Sauvage, A 3-stage gated UV-photon gaseous detector with optical imaging. Preprint WIS-89/9/March-PH. Submitted to Nucl. Instrum. Meth.
21. R.A. Holroyd et al. paer 6408 submitted to the XXIII Int. Conf. on High Energy Physics, Berkely (July 1986).
22. A. Schön, Diplomarbeit, Physikalisches Institut der Univ. Heidelberg, (1988).
23. G. Lutz et al., Nucl. Instrum. Meth. **A263** (1988) 16.
24. S. Reynaud, CERN/EF/Instr. **86-1** (1986).
25. R. Männer and J. Glass, Proposal for a RICH trigger, Univ. of Heidelberg, internal CERES note No. 31, Nov. 1988.
26. E. Chesi et al., CERN/EF 89-xx.
27. H. Ries, Univ. of Heidelberg, private communication.
28. B. Lund Jensen et al., in preparation.

29. T. Ypsilantis, these proceedings.
30. A. Breskin, G. Charpak and S. Majewski, Nucl. Instrum. Meth. **220** (1984) 349.
31. A. Breskin and R. Chechik, in preparation.
32. A. Breskin, R. Chechik, G. Malamud and S. Majewski, in preparation.

A NaF Ring Imaging Cherenkov Counter

Tom Francke*
Manne Siegbahn Institute of Physics
Stockholm, Sweden

Martin Suffert*
Centre de Recherches Nucléaires
Strasbourg, France

ABSTRACT

The performance of NaF as a Cherenkov medium has been studied using photosensitive multiwire proportional chambers at low pressure. Tests with cosmic rays at normal incidence gives 60 photoelectrons/event, and tests in beam with β=0.82 negative pions show good determination of the Cherenkov ring. A 5 cm thick NaF-RICH using pad readout and operating at atmospheric pressure has been constructed, and is now being tested. Preliminary results give 4 photoelectrons/event when using TEA and methane, and 15 photoelectrons/event when using TMAE and ethane. Simulations indicate good π/K-separation up to 2.5 GeV/c.

*Visitor at CERN

Presented by Tom Francke at the
Symposium on Particle Identification at High Luminosity Hadron Colliders
Fermi National Accelerator Laboratory, Batavia, Illinois, USA
April 5-7, 1989.

1. Introduction

Fastness is essential for particle identifying detectors since they are often used in triggers and compactness desired to reduce the volume and hence the cost of outer-laying detectors, e.g. an expensive electromagnetic calorimeter. The fastness require the detector to be based on quick physical processes as well as using fast electronics for the readout. If it is to be used at high rates, the local dead-time has to be short, and the number of channels has to be kept at a minimum to reduce the readout-time. To be compact, scintillators, radiators etc. has to be as thin as possible and possible driftspaces has to be minimized.

Particle identification can be achieved using various techniques such as measurements of Cherenkov radiation, time of flight, dE/dx and so on, each one having their specific momentum window and application. In most applications only various measurements of Cherenkov radiation is efficient, since time of flight needs quite large distances and dE/dx measurements are only efficient for low energy particles. Cherenkov detectors are normally based on two different techniques. Traditionally they are used as threshold counters where particles with a velocity larger than a specific value gives light in a radiator, and the others do not. The threshold velocity depending on the index of refraction of the material used as a radiator. In late years Ring Image Cherenkov (RICH) counters are becoming more and more useful, where the opening angle of the Cherenkov cone is used to determine the velocity of the particle. If the spread in momentum is not too large, threshold techniques works well, but for multiparticle identification or separation, either a sandwich of various Cherenkov media has to be used or, preferably, RICH-counters, especially if the momentum spread is large.

RICH-counters are efficient and dynamic, and they can be made very compact and fast. They require no PM-tubes and are hence not strongly affected by magnetic fields, which makes them very useful for particle identification in modern and future high energy experiments. RICH-counters of today use liquids or gases as radiators, which has the disadvantage that they need some kind of UV-transparent vessel to contain them. So the idea came up in our group to try to use a solid radiator and to see how well such a detector could perform.

In the following sections properties of solid radiator candidates will be presented, concentrating on NaF which seems to be the most promising material. It will be shown how well such a detector can separate particles and the latest experimental results will be presented together with simulations.

2. Solid radiators

Up to now conventional Cherenkovs and RICH-counters use gases or liquids as radiators which have the major drawback that they need some kind of UV-transparent vessel to contain them. These vessels are expensive and give unwanted background in the form of Cherenkov light produced in the walls. A solid radiator, on the other hand, is it's own container and no extra space is needed for the walls. In this way either the detector could be made more compact or the radiator could be made thicker, which would increase the efficiency of the detector.

Such a radiator should have low index of refraction to allow as large fraction as possible of light to refract out of the radiator, and not to be trapped inside by total reflection. It should have good UV-transmission since most of the Cherenkov photons are produced in the far UV-region, and it should be chemical resistant, not to be affected by the surrounding.

The index of refraction as a function of wavelength for various crystals is shown in figure 1 [1]. Those, which are the most interesting ones are CaF_2, LiF and NaF, because of their low index of refraction and since they are commercially available as monocrystals with

high purity. CaF_2 and LiF are transparent down to ~110 nm while NaF has a cutoff around 130 nm. All three of them are very chemical resistant though NaF is slightly hygroscopic.

The low index of refraction and the good UV-transmission of NaF makes it the most promising candidate for a Cherenkov radiator in a solid radiator RICH-counter, and will be presented in more detail in below. CaF_2 has also been tested by Piuz et al. [2] with good results, but no light refracts out of the crystal for ß=1, normal incidence particles as expected from the high index of refraction.

3. Properties of NaF

NaF has the lowest index of refraction of all known solids (except aerogels), and is commercially available as monocrystals of 1-2 dm^2 area. Figure 2 shows the index of refraction and transmission of NaF as a function of wavelength in the far UV-region. The index of refraction is measured down to 180 nm [3] and extrapolated using a dispersion equation. Recent measurements down to 145 nm by Ypsilantis et al. [4] agree very well with this extrapolation (to an accuracy of < 1%). The index of refraction stays below $\sqrt{2}$ for wavelengths down to at least 170 nm, which is the value where Cherenkov light can refract out for ß=1, normal incidence particles.

Various measurements of the transmission differs in the steepness of the cutoff at short wavelengths, but they all confirm that the cutoff is around 130 nm [4][5][6]. The reflection losses are very small as a consequence of the low index of refraction, and stays below 2.5% (2 surfaces) down to 140 nm [5], making it nearly impossible to see the crystal when mounted.

NaF is very chemical resistant though it is slightly hygroscopic and should not be exposed too long to humidity and handled with care. It is not affected by TMAE or TEA, nor by hydrocarbon gases. Damaged crystals can be recovered either by pumping on them or by repolishing.

No measurements have been performed on the radiation hardness of NaF, but there is no obvious reason why it should not be as radiation hard as similar crystals such as BaF_2 and CaF_2 which are very radiation hard. A possible radiation damage would mainly affect the transmission properties increasing the cutoff-wavelength. The radiation length of NaF is of the order of 9 cm, so γ-rays barely interact with 10 mm of NaF (~10% of a radiation length).

If NaF is to be used as a radiator for Cherenkov light it should not scintillate, since that would completely drown the Cherenkov light. In Stockholm, Moszynski and Lindblad looked for scintillation light from NaF by mounting a small sample onto a photomultiplier tube (PM-tube) equipped with a quartz window and irradiated it with 1.2 MeV gamma rays from a ^{60}Co source [7].

The time spectrum of the light emission of NaF is shown in figure 3, in comparison with the light emission from quartz and BaF_2. The time-scale is reversed, with time increasing from the right to the left, and the three intensities are multiplied by 1, 10, and 100 respectively to clearly separate them. The peak is due to Cherenkov light from Compton-scattered electrons. One clearly sees the fast component of BaF_2 with a measured time-constant of 750 ns, but there is no difference, within errors, between NaF and quartz. When expanding the time-scale, the slow component of BaF_2 is clearly seen, but no difference between quartz and NaF can be observed.

From these measurements an upper limit of scintillation light output of NaF was set to be less than 10^{-6} of that of NaI(Tl). This is down to the cutoff of quartz (~160 nm).

4. Photosensitive compound

The Cherenkov photons produced in the solid radiator are converted into photoelectrons by a photosensitive compound. These photoelectrons are then drifted towards a multiwire proportional chamber (MWPC) where they are amplified and read out.

The two photosensitive materials most frequently used are the complex organic ring molecules of tetrakis(dimethylamine)ethylene (TMAE) and trimethylamine (TEA), used in gaseous form. The quantum efficiency of these two are shown in figure 2 [8] as a function of wavelength together with the index of refraction and transmission of NaF.

4.1 TMAE.

TMAE has the advantage of having high quantum efficiency and is sensitive from 220 nm and down. It has on the other hand a long absorption length, due to the low vapour pressure, why it needs to be heated to typically 50°C or more, and it is difficult to work with since it is immediately destroyed by oxygen, which requires very gas-tight systems.

4.2 TEA.

TEA is easy to work with. It is not destroyed by oxygen why it can be handled in air and it has a very short absorption length. The main disadvantage is that it has low quantum efficiency and is only sensitive below 170 nm, which requires the use of very transparent amplification gases, e.g. methane.

Since TEA is only sensitive from 170 nm and down, where the index of refraction of NaF is very close to or larger than $\sqrt{2}$, such a detector would not detect $\beta=1$ particles at normal incidence where it is necessary to use TMAE. This has been confirmed experimentally.

5. Number of photoelectrons from 10 mm of NaF

To see how well NaF would perform as a solid radiator, an approximate upper limit on the number of photoelectrons produced was measured using the set-up shown in figure 4. A 10 mm thick NaF-crystal with a diameter of 120 mm was irradiated with cosmic rays in the range between $\beta=0.97$ to $\beta=1$. 10 cm of lead was used to select only high momentum particles, and three scintillators in coincidence defined the trigger with an acceptance angle of 32 msterad at 0° and 18 msterad at 25°.

The cosmic particles (mostly muons) enters the detector from above and Cherenkov photons are emitted when they traverses the NaF radiator. These Cherenkov photons refracts out of the crystal and are converted into photoelectrons by TMAE at 30°C. The conversion gap is 38 mm which corresponds to 3.2 conversion lengths, i.e. 96% of the Cherenkov light is converted by the TMAE.

These photoelectrons are drifted towards a low pressure MWPC with good single photoelectron resolution. The MWPC consists of an anode wire plane between two cathode planes with an anode-to-cathode gap spacing of 3 mm. The anode is composed of 12 μm diameter gold-plated tungsten wires with 1 mm spacing in between them. The cathode wires are perpendicular to the anode wires, and are made of 50 μm diameter gold-plated tungsten, spaced 1 mm apart. The chamber is saturated with TMAE vapour before filling with ethane up to 4 hPa.

Only the anode plane is read out, where all wires are grouped together and the charge is converted by a 142PC Ortec pre-amplifier. The output pulse is later shaped and amplified again 20 times by a 571 Ortec amplifier with 1 μs shaping time, and fed into a multichannel analyzer. The trigger signal opens a 3 μs gate for the shaped signal to allow for some time jitter.

Figure 5 shows the anode sum spectra for 0° and 25° incidence angle and full photon absorption. For 0° this corresponds to ~60 photoelectrons and for 25° it corresponds to ~80 photoelectrons, so there is a large number of photoelectrons to work with which encourage further investigations of the performance of a NaF RICH-counter.

6. Experimental set-up

The NaF-RICH project to develop a compact and fast solid radiator RICH-counter was originally dedicated for the CP-LEAR experiment at CERN (PS 195). There the detector is to be used mainly for π/K-separation up to 2 GeV/c, and it has to be fast and extremely compact. Fast since there will be $2 \cdot 10^6$ pp annihilations/second and the counter is to be used for particle identification in the trigger.

Since there are only 4 cm at the disposal of the detector, it has to be extremely compact. The idea came up in our group to use the NaF crystal both as a radiator and as a window and to use a flat UV-mirror to reflect the Cherenkov photons back through the crystal.

The set-up of the prototype is shown in figure 6. Cherenkov photons are emitted when a charged particle traverses the 10 mm thick, 120 mm diameter NaF radiator. These photons refracts out of the crystal and are reflected back by a UV-mirror, back through the crystal, this time acting as a window, into the conversion gap. The UV-mirror is made of evaporated aluminium, coated with MgF_2, and has 80% reflectivity[1] down to 140 nm.

In a first prototype, TMAE was chosen as photocathode to get as many photoelectrons as possible. The photoelectrons are detected by a low pressure MWPC with good single photoelectron resolution. Since ethane had proven earlier to work well as amplification gas and since it has good UV-transmission it was chosen in this set-up as well. Low pressure operation (6 hPa) was chosen to minimize the ionization from the primary particle. But, as will be shown later, the ionization is still of the order of 1-2 electrons/event.

The MWPC is 15x15 cm^2 with 1 mm distance between wires and 5 wires are connected to form a strip (32 strips/plane). It consists of an anode plane between tho cathode planes with an anode-to-cathode distance of 3 mm, and the three planes are tilted by ±60°. The anode wires are composed of 12 μm gold-plated tungsten and the cathode wires are made of 50 μm gold-plated tungsten. Each strip is equipped with a low-noise, charge-sensitive pre-amplifier, a shaper and an ADC, and all three planes are read out giving three projections of the Cherenkov ring.

The driftspace between the NaF and the UV-mirror is variable as well as the conversion gap, and some extra meshes were installed to try to minimize the ionization background.

7. Experimental results and simulations

The solid radiator RICH-prototype has been tested for nearly one year at the CERN SC with 200 MeV/c negative pions and electrons. Figure 7 shows ~1000 superimposed events for 200 MeV/c π^-, corresponding to β=0.82, at a NaF-mirror distance of 15 mm. One clearly sees the two horns of the projection of the Cherenkov ring in the anode projection as well as in the two cathode projections. The peak in the middle of each projection is due to ionization from the primary particle, which gives 1-2 electrons/event. The ring is quite broad due to the long absorption length of TMAE at 21°C (~2.1 cm) [9], but can be made sharper by heating the detector.

---

[1] The mirror is easily destroyed by silicon oil, so oil from the primary pump has to be prevented from entering the system.

With this set-up about 15 photoelectrons were produced per event, but since only the projections of the ring was read out, ambiguities arose when trying to reconstruct the original hit positions. To be able to reconstruct these hits the conversion gap had to be reduced to 6 mm corresponding to ~25% conversion giving 4-5 photoelectrons/event. Using a simple reconstruction algorithm the hitpattern shown was reconstructed from the three projections of each event. One clearly sees the Cherenkov ring with a diameter of ~8 cm and the ionization of the primary particle in the middle. The hits between the ionization area and the Cherenkov ring are due to imperfections in the trigger and scattering in the walls of the vacuum chamber. Some events also originates from parasitic reflections in the crystal, i.e. Cherenkov light that is partially reflected in the upper surface of the crystal and not by the UV-mirror. These photons gives a second ring inside the main ring, and the effect is large near the total reflection angle, i.e. at short wavelengths and for particles close to $\beta=1$.

These results agree very well with simulations, as shown in figure 8. Here 200 events of 200 MeV/c negative pions ($\beta=0.82$) has been simulated and superimposed, using the same set-up as in the experimental results shown in figure 7. One clearly sees the horns from the projection of the ring as well as the parasitic ring inside. As the Cherenkov angle approaches the total reflection angle the coefficient of partial reflection increases rapidly as shown in figure 9. This is another reason why the index of refraction of the solid radiator has to be as low as possible. In these simulations the contribution from the ionization of the primary particle has not been included, to show the parasitic ring.

8. Particle separation

With the NaF-RICH detector there are mainly two ways of separating particles. The natural way is by the radius of the Cherenkov ring but also the number of photoelectrons produced per event provides useful information. Below, the analysis will concentrate on separation between kaons and pions since this was the original goal of the development project.

8.1 π/K-separation

Figure 10.a shows the radius of the ring as a function of momentum for pions and kaons for a NaF-mirror distance of 5 mm. Even with quite poor resolution in the determination of the radius of the ring (Δr~0.5 cm) it is possible to clearly separate particles up to relatively large momentum. The number of photoelectrons produced per event as a function of momentum is shown in figure 10.b for pions and kaons using TMAE and full absorption. Even though the spread is quite large it improves the particle separation efficiency by combining this information with the information from the radius of the ring.

Below 520 MeV/c the detector works as a threshold counter where pions do give light and kaons do not, making it possible to separate them just by looking for signal or no signal. To be able to separate the ring from a pion from the ionization of the primary particle the momentum has to be larger than 160 MeV/c.

Combining the information from the radius of the ring with the number of photoelectrons produced per event it is possible to separate pions from kaons even far above the threshold for Cherenkov light. The efficiencies calculated below are from simulations, but using the resolution in the determination of the radius of the ring and the spread in the number of photoelectrons produced per event that has been obtained experimentally.

Figure 11.a shows the identification efficiencies for an incoming pion using the algorithm described above. The probability of missidentifying the pion as a kaon is less than 0.5% up to 2.5 GeV/c, which is an important number since there is normally an enormous pion background from which one wants to dig out the kaons without missidentifying a pion as a kaon. The identification efficiency is nearly 100% up to 700 MeV/c and drops to 80% at

2.5 GeV/c. The remaining 20% are events which has to be rejected since the particle is not identified.

In figure 11.b the identification efficiencies for an incoming kaon are shown. The probability of missidentifying the kaon as a pion is less than 0.5% up to 1.4 GeV/c and then increases to 35% at 2.5 GeV/c. The identification efficiency is close to 100% up to 1.4 GeV/c and then drops to 30% at 2.5 GeV/c.

This means that up to 1.4 GeV/c nearly all kaons will be truly identified with an accuracy of less than 0.5%, and with a probability of missidentifying a pion as a kaon of less than 0.5%. Up to 2.5 GeV/c the probability of missidentifying a pion as a kaon is still less than 0.5% but the total identification efficiency of the counter drops, increasing the number of unidentified events.

9. Pad readout

Using a MWPC for the detection of the photoelectrons one can only obtain the projections of the ring and if the number of photoelectrons per event is large (>5 phe/event) ambiguities arise when trying to reconstruct the actual hit-position of the photoelectron. A rough estimation of the diameter of the ring can be obtained from the distance between the two horns of the projection, but this requires the number of photoelectrons per event to be large.

A two-dimensional readout without ambiguities can be obtained by replacing the lower cathode plane with a pad plane. Such a prototype has been built in collaboration with Piuz et al. and tests has just started at the CERN PS. It uses the same basic idea as shown in figure 5 but the lower cathode plane is replaced by a pad plane using 6x6 mm^2 or 8x8 mm^2 pads (see figure 12). The anode is made of 20 μm diameter gold-plated tungsten wires and the upper cathode is a stainless steel mesh with 81% transmission as the mesh below the NaF-radiator. The anode-to-cathode distance is fixed to 2 mm, but the anode-to-pad distance can be regulated to be either 2 mm or 1.5 mm to try to increase the induced signal on the pads and to reduce the spread of each hit.

In a first step, TEA and methane was used at atmospheric pressure using a 3 mm conversion gap to have full absorption. Very preliminary results gives ~4 photoelectrons per event for 1.25 GeV/c protons which corresponds to β=0.80. This agrees well with the expected number due to the low quantum efficiency of TEA and the small overlap between the cutoff of NaF and the wavelength from which TEA starts to be sensitive.

Both the anode wires and the pads are read out. The anode wires are connected to current-sensitive pre-amplifiers and the shaped signal of each wire is read out. The signals from the pads are amplified and multiplexed by Amplex chips before being readout by DRAMS developed by Chesi and Martinengo [10] at CERN.

In this way the outer dimensions can be made less than 4 cm including covers, support, UV-mirror, driftspace, NaF-radiator, conversion gap, MWPC, pad-plane and electronics, representing about 10% of a radiation length. Fast, primary information is available from the anode wires and the pads provide a more detailed information at a later stage when they are read out.

10. Conclusion

Solid radiators open a new field for the development of RICH-counters, and it has now been verified experimentally that the technique works. Since no expensive, UV-transparent vessels are needed to contain the radiator, the detector can be made more compact and easier to manufacture. NaF has proven to be the most promising candidate for such a radiator since it

is the only solid with an index of refraction smaller than $\sqrt{2}$ in the far UV-region, where photosensitive compounds with high quantum efficiency, like TMAE, are sensitive.

If the crystal is used both as radiator and as window, having a UV-mirror to reflect the Cherenkov light back through the crystal, the detector can be made extremely compact (< 4 cm) and representing less than 20% of a radiation length. TMAE is used to get as many photoelectrons as possible and to detect Cherenkov light that refracts out of the crystal even for $\beta=1$ particles at normal incidence. Pad readout is needed to get good precision in the determination of the ring diameter, but fast, primary information is available from the projection of the ring by reading out the anode wires as well. Such a detector, operating at atmospheric pressure, has been constructed and is now being tested with promising results. Using a 10 mm thick radiator of NaF, the set-up described above gives ~15 photoelectrons/event when using TMAE and ~4 photoelectrons/event when using TEA.

References

[1] E.H. Melvin, Phys. Rev. Vol. 37 (1932) 1230.

[2] J. Piuz et al., proceedings of 1989 Wirechamber Conference, Vienna, February 1989, to appear in Nucl. Instr. and Meth.

[3] A. Smakula, U.S. Dept. of Commerce, Office of Technical Document 111052. page 88-89, Oct. 1952.

[4] M. Hempstead, J. Chauveau, G. Comby, J. Séguinot and T. Ypsilantis, Nucl. Instr. and Meth., in preparation.

[5] Measurements by A. Braem and T. Francke, CERN, August 1988.

[6] Progress report on B-physics project at KEK, February 4, 1989.

[7] M. Moszynski and Th. Lindblad, Nucl. Instr. and Meth., **A246** (1988) 388.

[8] R.A. Holroyd, J.M. Preses, C.L. Woody and R.A. Johnson, Nucl. Instr. and Meth. **A261** (1987) 440.

[9] D.F. Anderson, Physics Letter **118B** (1982) 230.

[10] E. Chesi, P. Martinengo, PS 202 Internal Note, CERN, September 11, 1988.

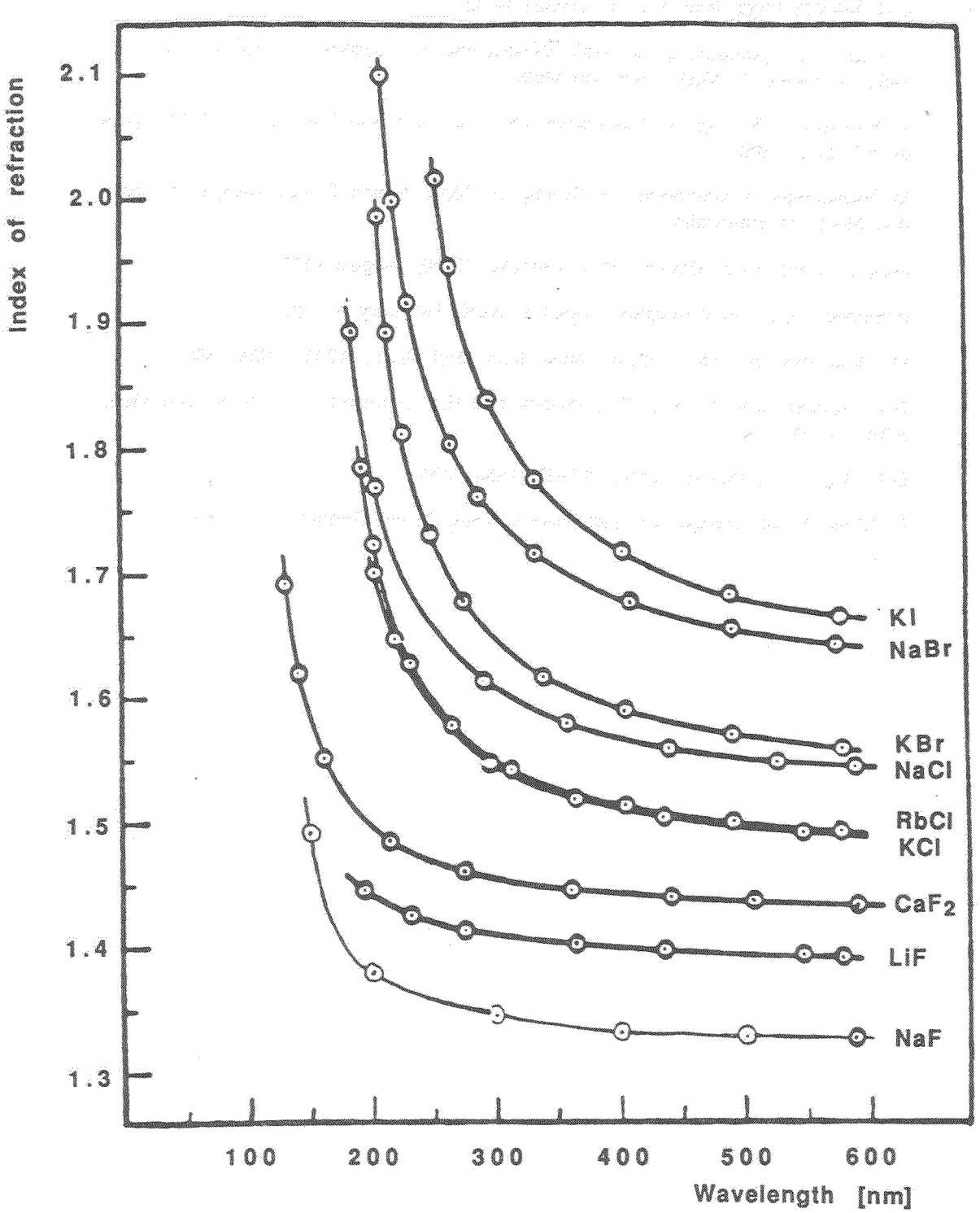

Figure 1. Index of refraction as a function of wavelength for various crystals [1]. The fluorides are given most consideration, since they have the lowest index of refraction of all solids known today.

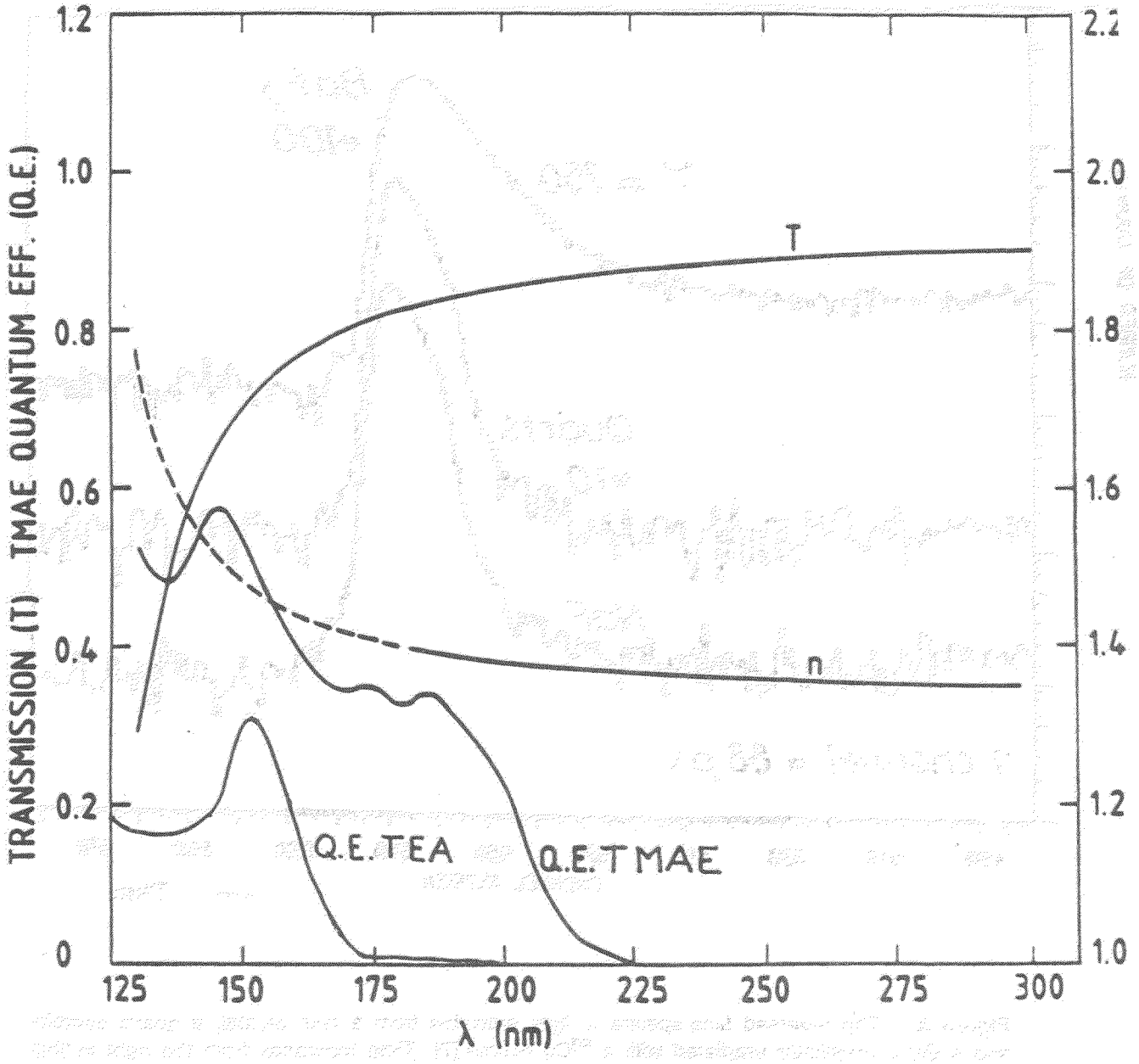

Figure 2. Index of refraction and transmission of NaF as a function of wavelength in the far UV-region. The index of refraction is measured down to 180 nm [3], and extrapolated using a dispersion equation. It agrees very well with recent measurements down to 145 nm [4].Quantum efficiency of TMAE and TEA as a function of wavelength [8] are added to show the overlap with the transmission of NaF.

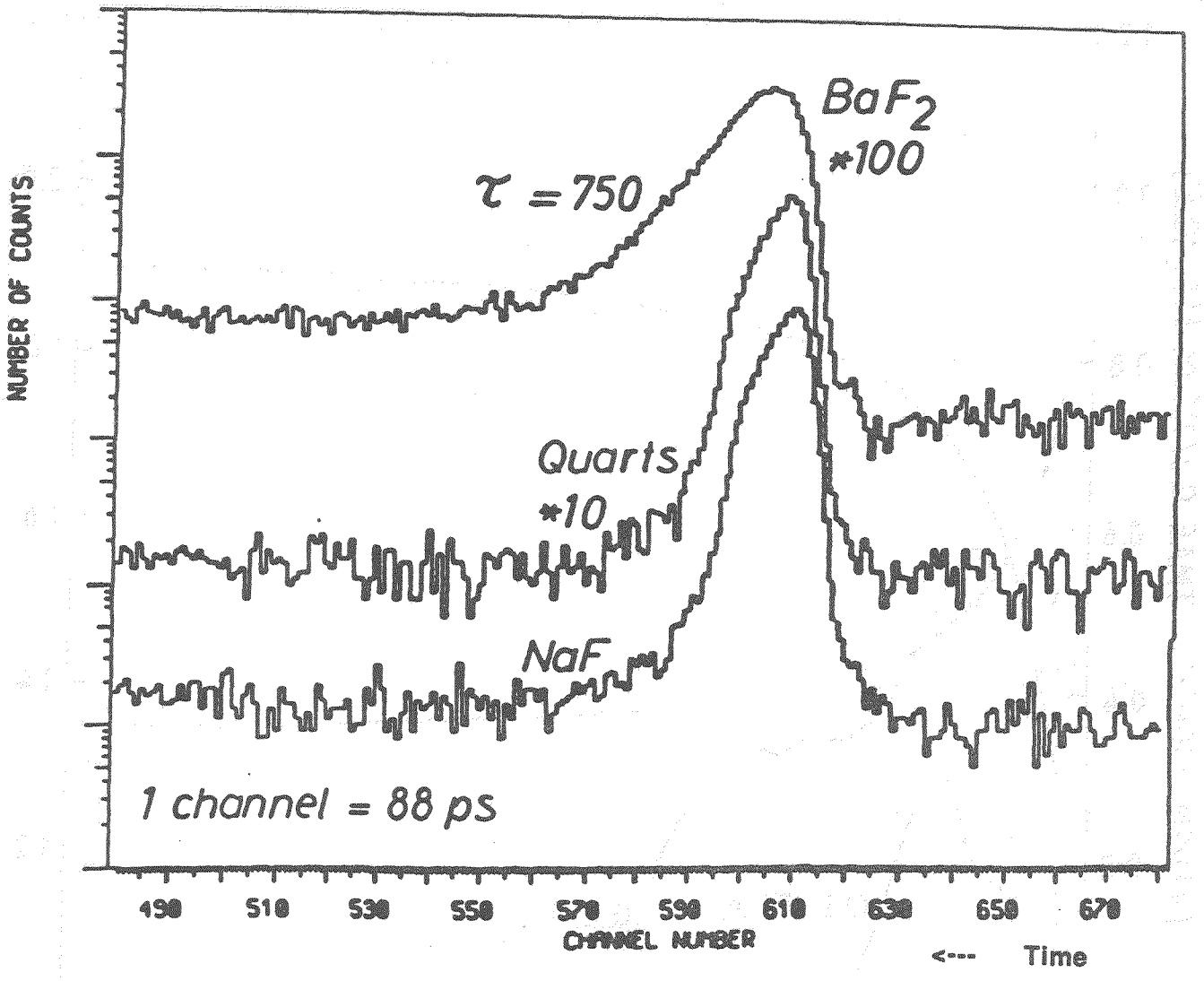

Figure 3. The reversed time-spectra of light emission from a NaF crystal, a quartz sample and a BaF_2 scintillator irradiated with a ^{60}Co source [7]. Time increases from the right to the left.

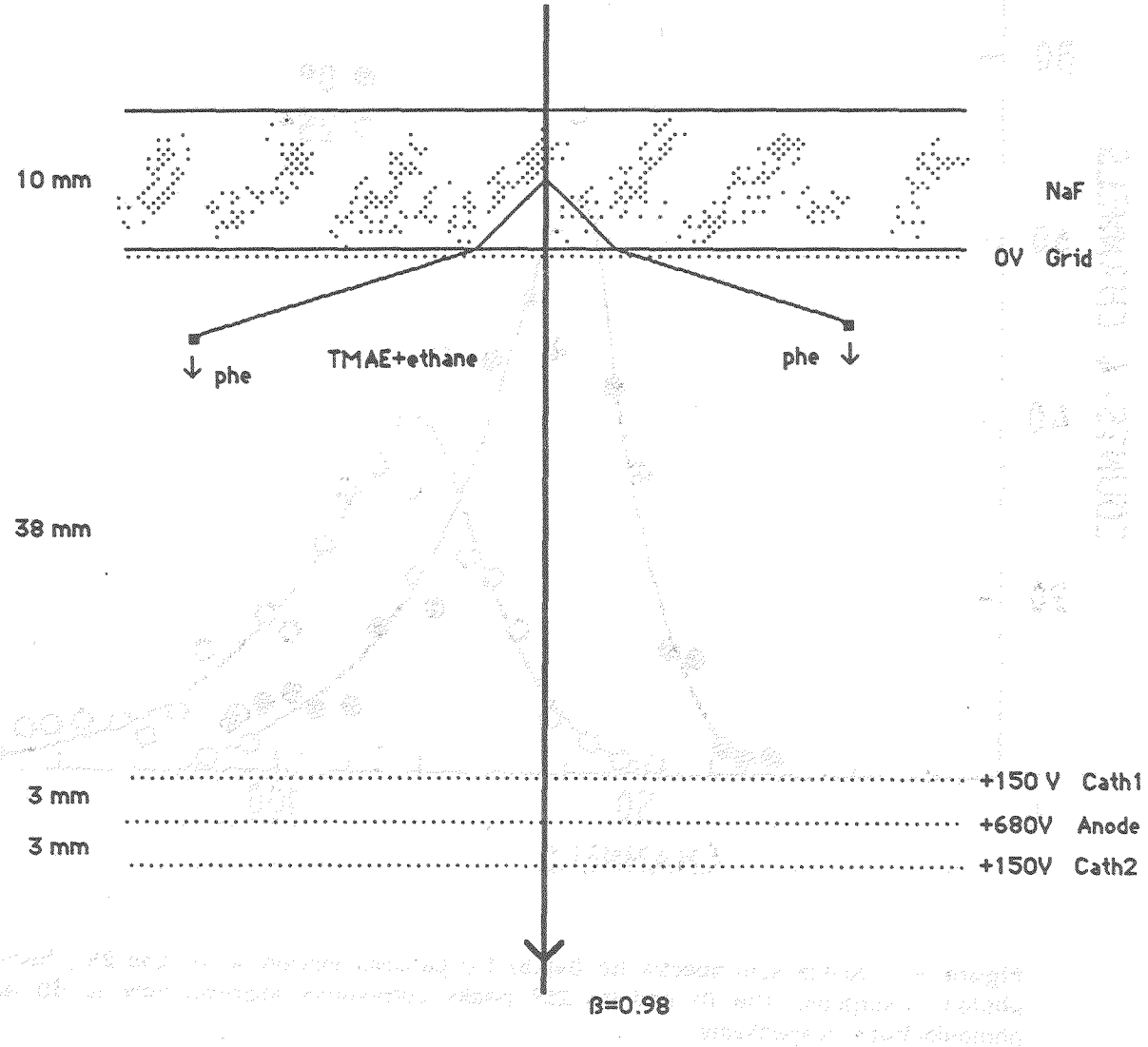

Figure 4. Test set-up for measurements of Cherenkov light emission from NaF using cosmic rays. The ethane pressure is 4 hPa, and the Cherenkov photons are fully absorbed by TMAE in the conversion gap.

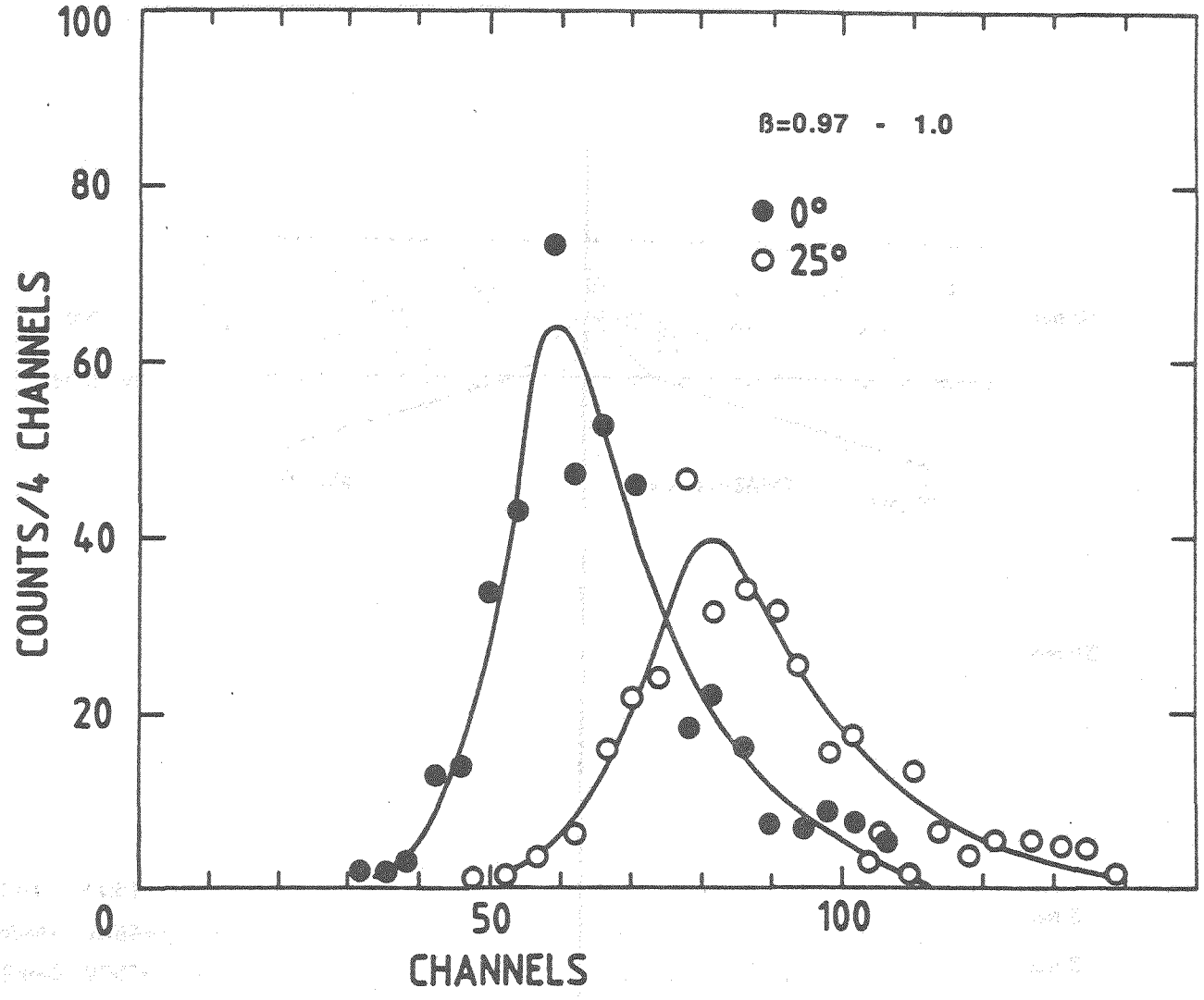

Figure 5. Anode sum spectra for ß=0.97-1.0 particles incident at 0° and 25°, having full photon absorption. The 0° and the 25° peaks correspond approximately to 60 and 80 photoelectrons respectively.

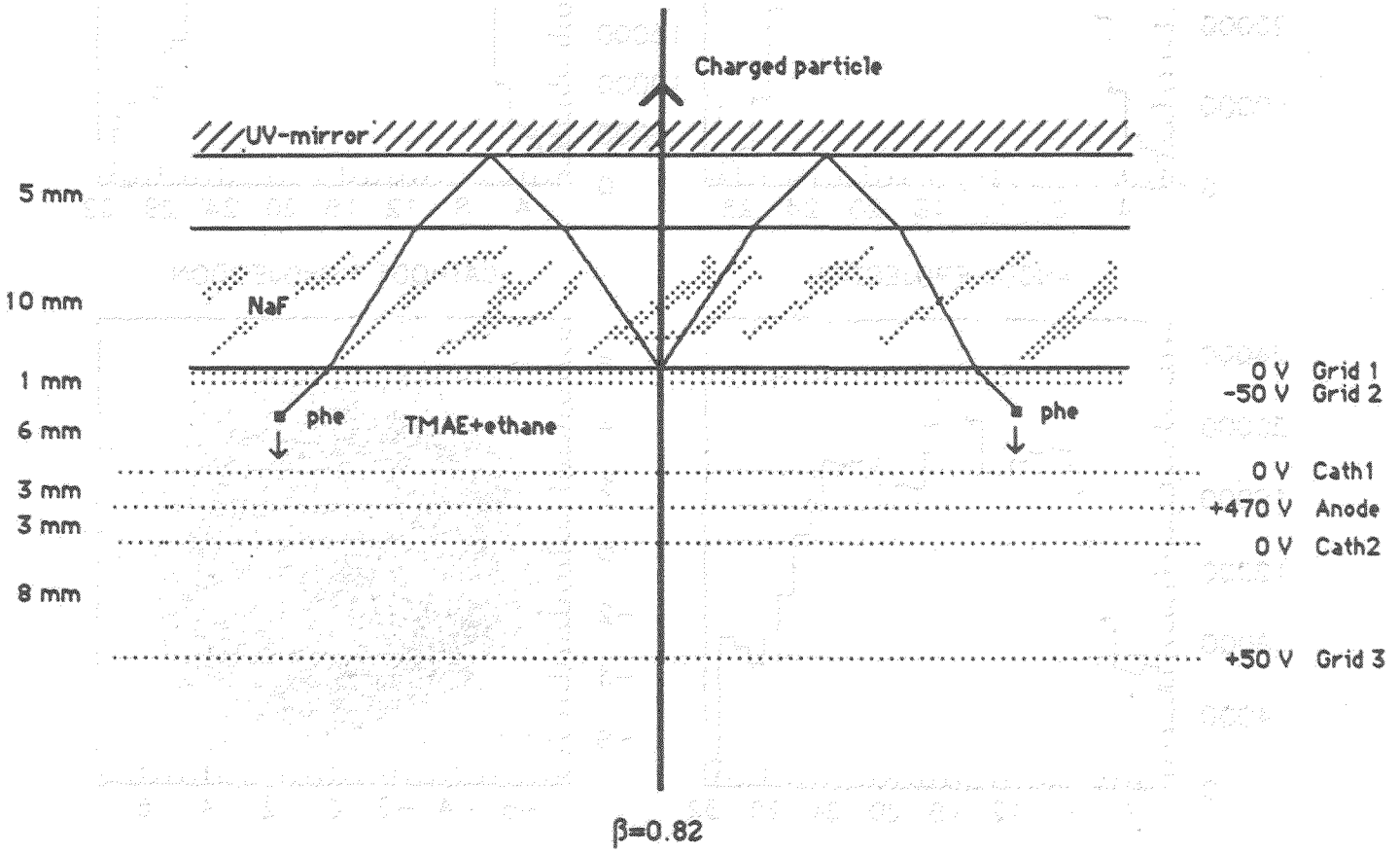

Figure 6. Principle of construction of the NaF-RICH detector. The driftspace and the conversion gap are variable and the ethane pressure is 6 hPa.

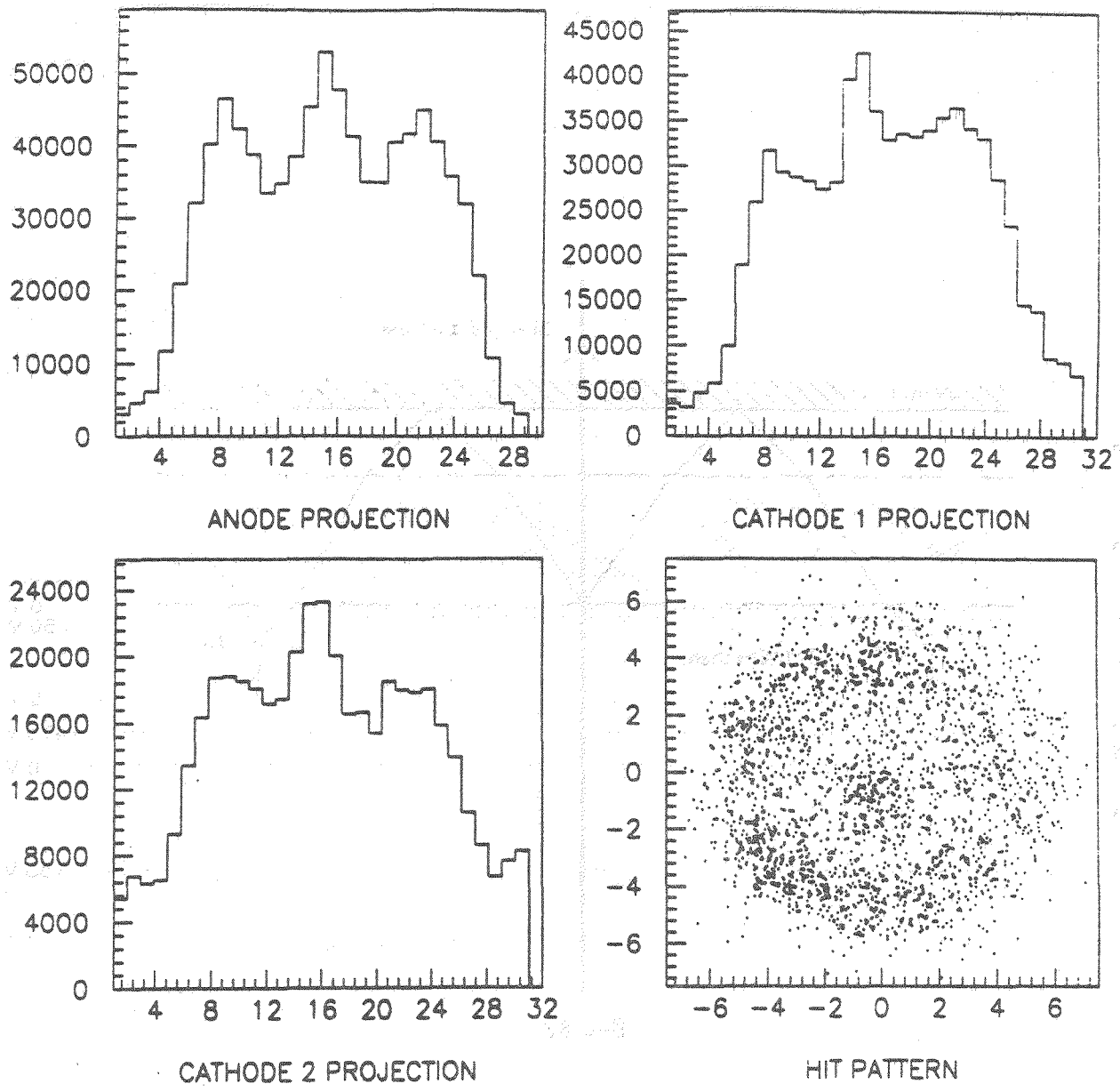

Figure 7. ~1000 superimposed events for 200 MeV/c negative pions (ß=0.82) and a NaF to-mirror distance of 15 mm. The conversion gap is reduced to 6 mm (25% conversion) to reduce ambiguities in the reconstruction of the hitpattern. The central peak is due to ionization by the primary particle.

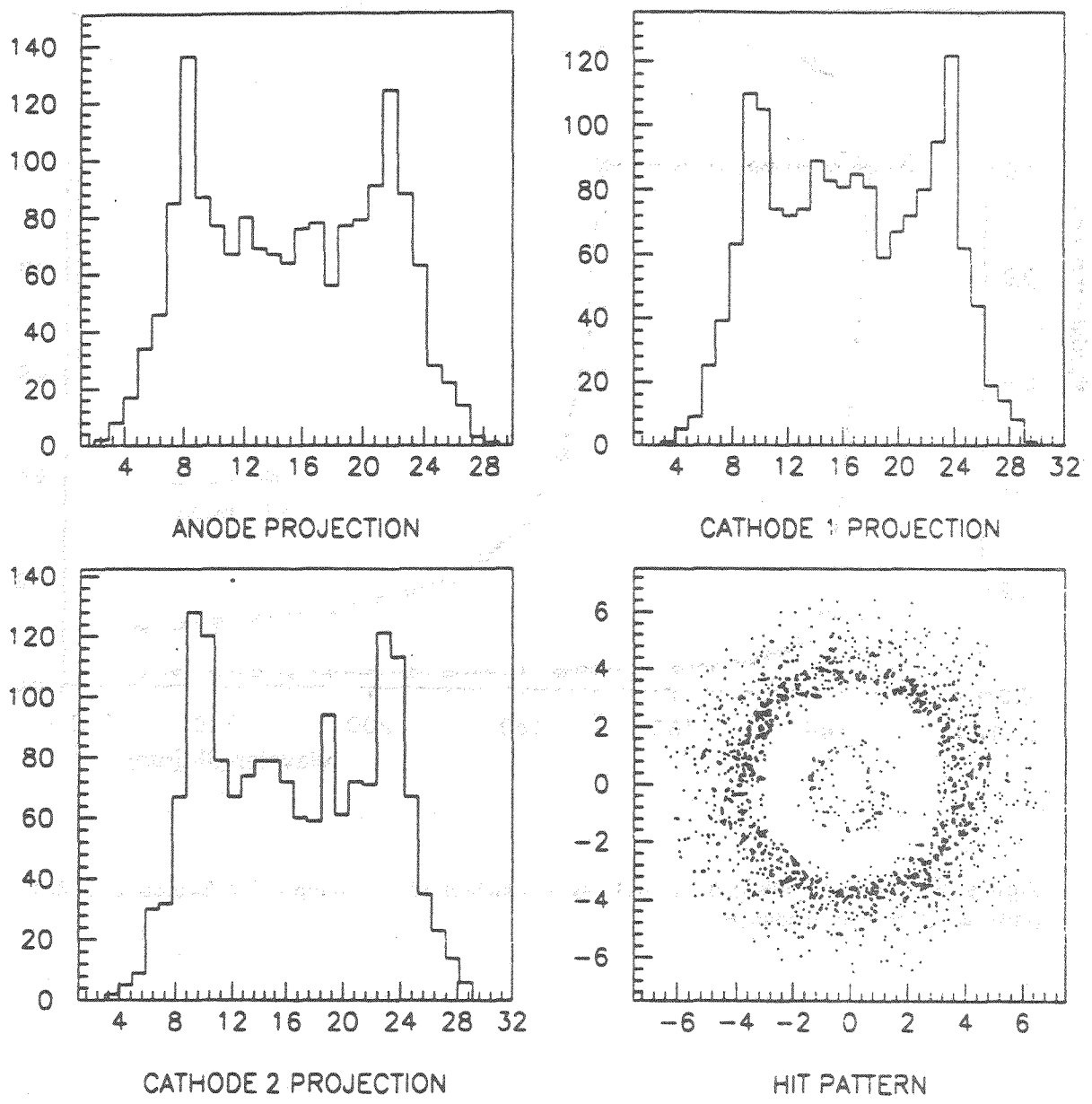

Figure 8. 200 simulated and superimposed events of ß=0.82 particles. The second, inner ring from partial reflection in the crystal is clearly seen inside the main ring.

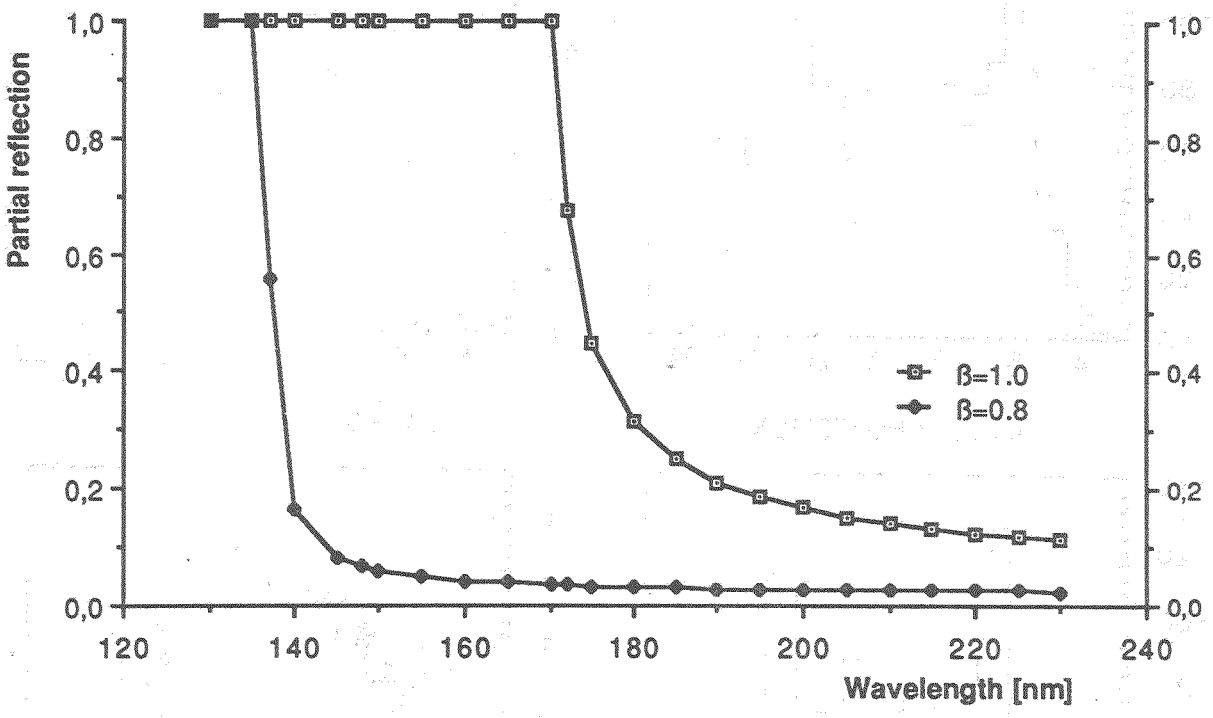

Figure 9. Partial reflection of NaF as a function of wavelength for ß=0.80 and ß=1.0 particles at normal incidence.

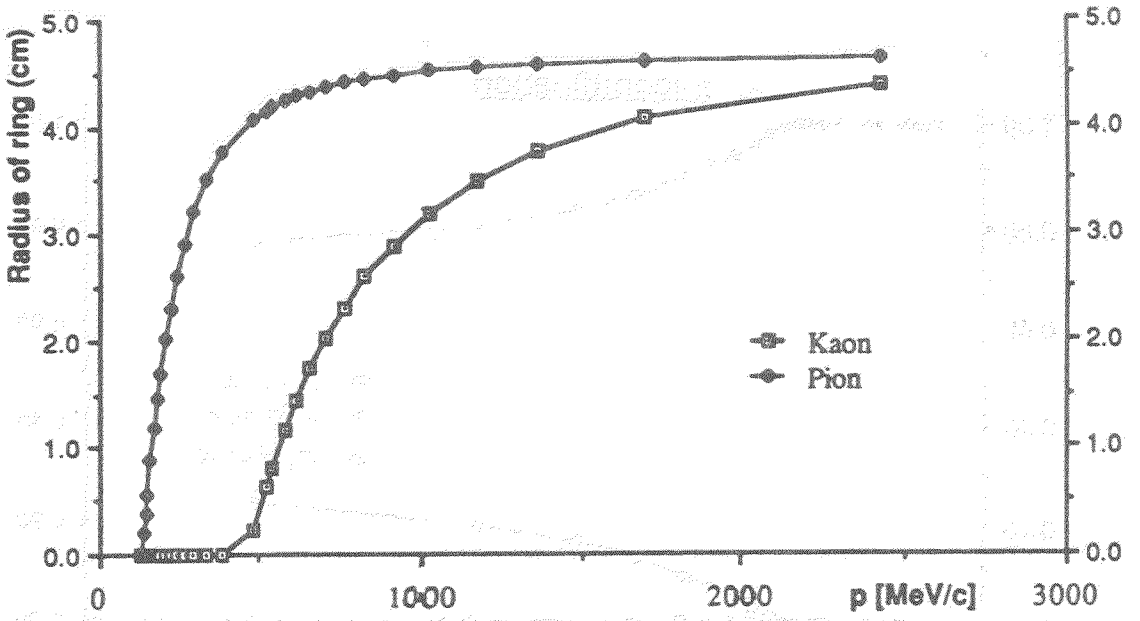

Figure 10.a. Radius of the Cherenkov ring as a function of momentum for pions and kaons. NaF-to-mirror distance is 5 mm.

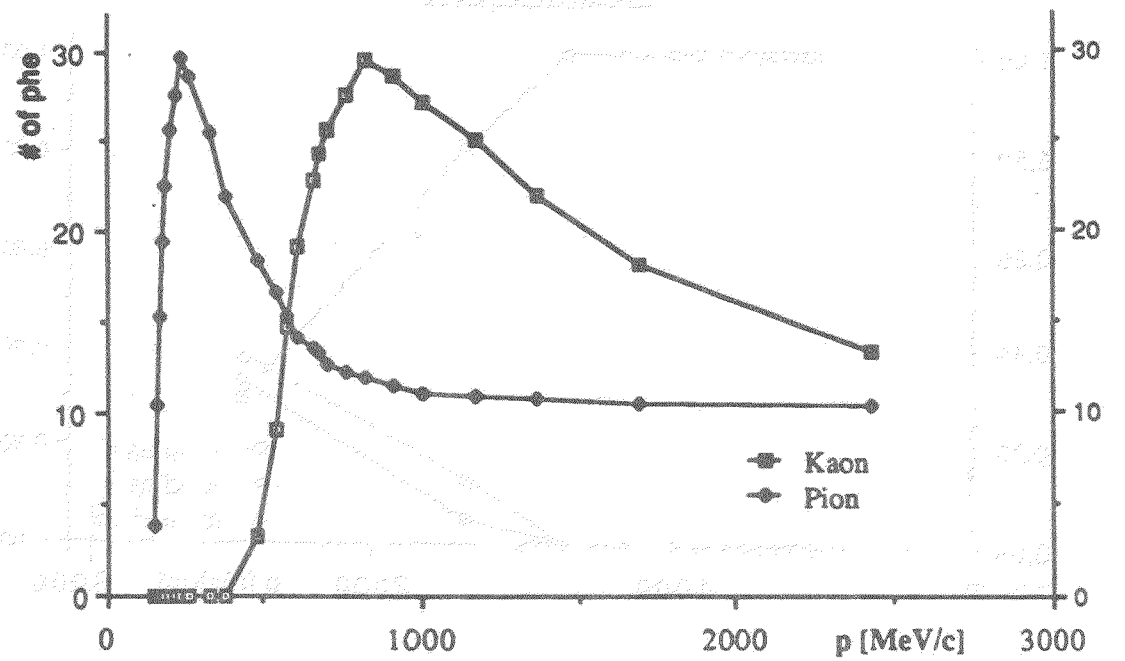

Figure 10.b. Number of photoelectrons produced/event as a function of momentum for pions and kaons, using TMAE and full photon absorption.

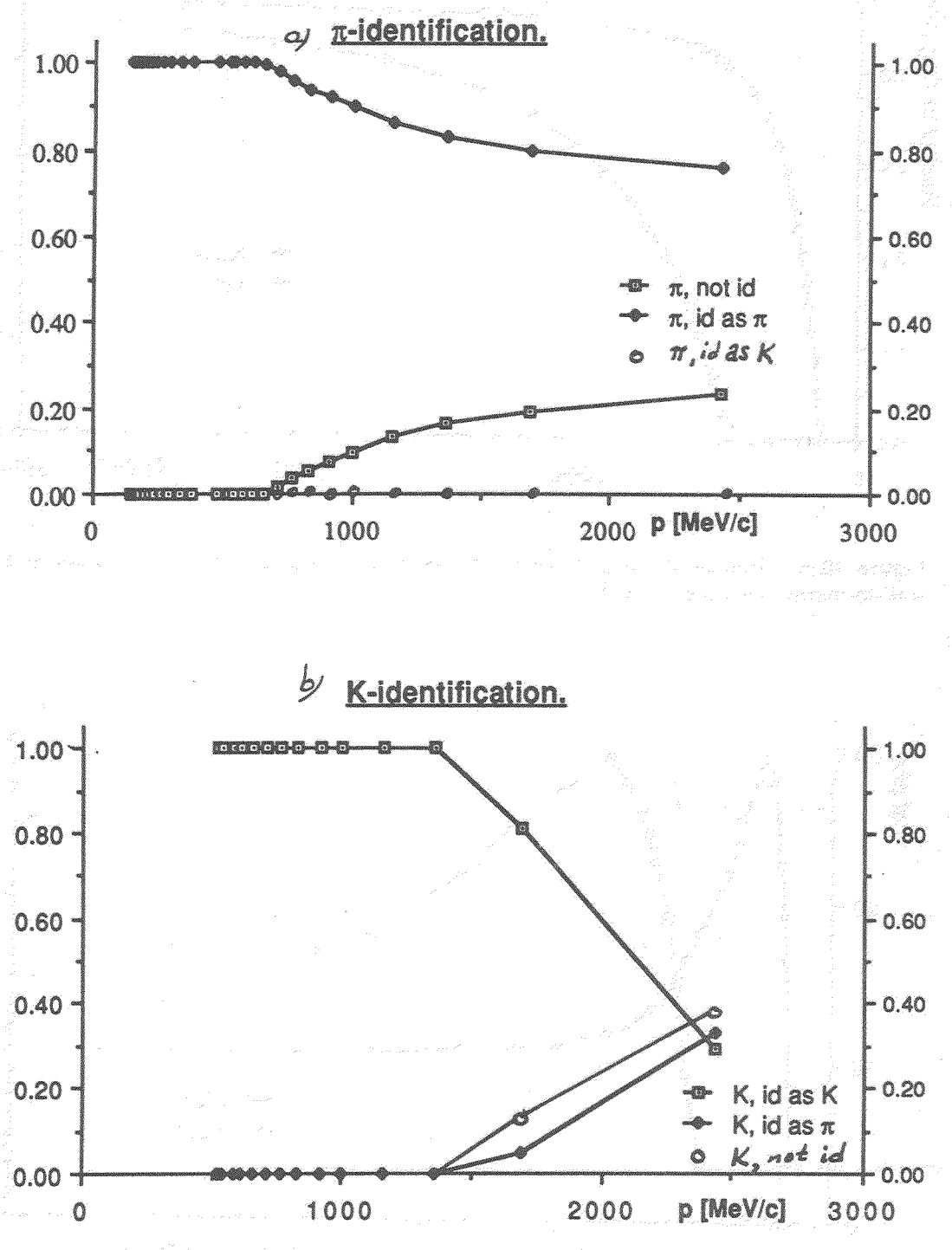

Figure 11. π/K-separation efficiencies using the combined information of ring radius and number of photoelectrons produced. Identification efficiencies of an incoming pion (a) and kaon (b).

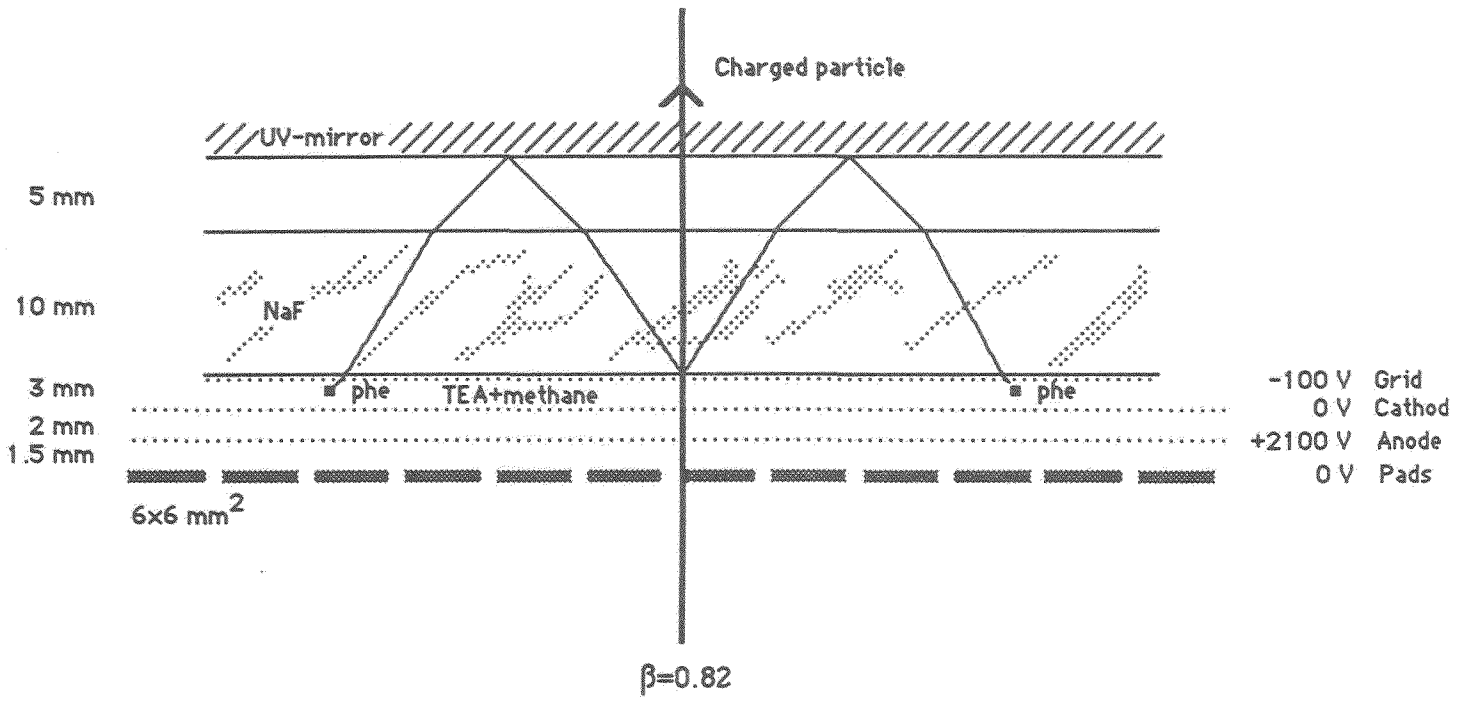

Figure 12. Principle of construction of the NaF-RICH detector using pad readout, and operated at atmospheric pressure using TMAE/ethane or TEA/methane. The NaF-to-mirror distance is variable.

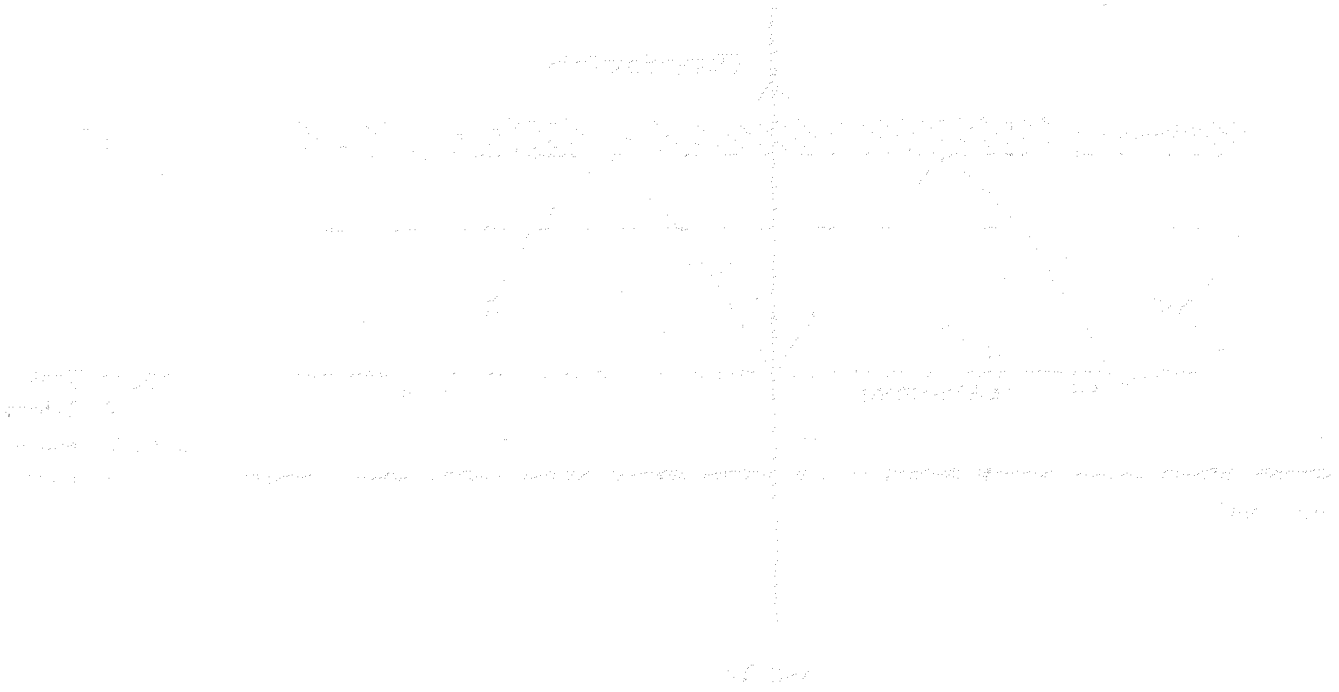

NEW SCINTILLATORS FOR PHOTOSENSITIVE GASEOUS DETECTORS

G. Charpak, V. Peskov and D. Scigocki

CERN, Geneva, Switzerland

and

J. Valbis

Inst. Solid-State Physics, Latvian State University, Riga, USSR

Abstract

A new family of scintillators are presented. Their properties are similar to those of barium fluoride, and the spectrum of the scintillation emission is between 140 and 300 nm. Our latest efficiency measurements of ethyl ferrocene and triethylamine liquid or caesium iodide solid photocathodes, in parallel-plate avalanche chambers (PPACs) at high electric field, are also presented. We discuss the revolutionary consequences of the combination of the new scintillators with PPACs with semitransparent photocathodes deposited on the crystals, such as high speed, high resistance to radiation damage, compacity, high gamma efficiency, and applications to tracking devices with scintillation optical fibres.

1. Introduction

The proposal to couple a dense inorganic scintillator, barium fluoride (BaF_2), with a low-pressure multiwire proportional chamber (MWPC) filled with a photosensitive vapour such as tetrakis-(dimethylamino)ethylene (TMAE) or liquid TMAE photocathode, in order to detect its light emission, came from Anderson et al. [1–3]; they named the device the solid scintillation proportional counter (SSPC). The properties of BaF_2 are: a high density (4.9 g/cm^3); a short radiation length (2.05 cm); a very fast ultraviolet scintillation component with a decay time of 600 ps [4]; a photon yield that is independent of temperature [5, 6]; and a resistance to radiation damage up to 10^5 Gy [7, 8]. Adding these advantages to those of a low-pressure chamber — resulting in a very fast collection time and good time resolution [9], a high rate capability, and a very low sensitivity to direct ionization — made the SSPC working with TMAE vapour a very attractive device for many applications, such as nuclear medicine [10, 11] and electromagnetic calorimetry [12]. But nobody succeeded in using liquid TMAE photocathodes in an SSPC, because of its low efficiency [13].

Until recently BaF_2 was the only known scintillator to possess adequate properties; on the other hand, the only photosensitive compound that had been used with MWPCs to detect the fast component emitted by BaF_2 was TMAE.

The discovery of a new vapour, ethyl ferrocene (EF), photosensitive to the BaF_2 fast emission, broke the monopole of TMAE vapour in SSPCs [14]. Also a new type of organic photocathodes, much more efficient in the VUV region than liquid TMAE, was investigated by Peskov et al. [13]; some of these could be used to detect the BaF_2 fast scintillation in an SSPC [13, 15]. A new concept of SSPC was

then developed successfully: it consists of BaF_2 crystals coupled with a parallel-plate avalanche chamber (PPAC) working at room temperature and with a gas mixture at atmospheric pressure [16]. This type of detectors permits us to keep most properties of the traditional SSPC, with high-temperature, low-pressure wire chambers filled with TMAE vapour, eliminating its main disadvantages (see Section 3).

The other way to improve the SSPC would be to find new scintillators that would have properties similar to those of BaF_2, but a shorter emission wavelength, in the range where the known photosensitive vapours and photocathodes achieve higher efficiencies. The discovery of a scintillation peaked at 173 nm, with a decay time of $\sim$ 6.3 ns, in lanthanum fluoride (LaF_3) crystals doped with Nd^{3+} allows its use in an SSPC filled with TMAE vapour [17]. The light yield is very small and the detection efficiency was not higher than that obtained with the BaF_2 device. The main advantages of LaF_3 over BaF_2 are its higher density (5.94 g/cm^3) and its shorter radiation length ($X_0 \simeq 1.7$ cm).

On the other hand, the mechanism by which BaF_2 emits light with a fast component (which gave it its unique properties) was not understood. Studies made by Jansons et al. [18] have now allowed them to explain this fast scintillation process. Based on this research, a new family of inorganic scintillators was discovered [18, 19]. Their properties are similar to those of BaF_2, but they emit light in a wavelength region between 140 nm and 300 nm.

In this paper we detail the characteristics of these scintillators, and discuss the implications of their use in SSPCs for a wide range of applications. In particular, we show the revolutionary consequences of the association of this new type of scintillators with a PPAC at room temperature and at atmospheric pressure, using semitransparent photocathodes as readout.

2. The new scintillators

Recently Valbis and his group investigated the luminescent properties of heavy alkali and alkaline-earth metals such as BaF_2, CsCl (caesium chloride), RbF (rubidium fluoride), etc. [18], of KF (potassium fluoride), $KMgF_3$ (potassium magnesium fluoride), $KCaF_3$ (potassium calcium fluoride), and solid solutions of KF + RbF [19]. In these crystals the energy separation between the valence band, involving mainly the halogen electronic states, and the upper cation core band is smaller than the band gap. After excitation generating holes in the core band, radiative electronic transitions from the valence band to the core band take place, giving rise to a specific emission which these authors proposed to call cross-luminescence (CRL).

The spectra and decay kinetics of CRL were studied under excitation by a 7 keV electron beam, with current density $\approx$ 100 μA/cm^2 in the pulsed regime. The experimental set-up, based on a Seya–Namioka-type vacuum monochromator with a concave diffraction grating (1200 grooves/mm) was used as described in Ref. [20]. The spectra were measured in a photon-counting regime, using a FEU-106-type photomultiplier tube with a magnesium fluoride (MgF_2) entrance window. The decay kinetics were studied using the correlated photon-counting method under excitation by 100 ns long electron pulses having a decay time of 2 ns, which was also the limit of the minimum measurable CRL decay times.

The fluoride crystals were grown by the Bridgman method, in graphite crucibles, in fluorizing or inert atmosphere. The chlorides and bromides were grown in fused silica crucibles, in air. For CRL measurements, small samples (about 1 $\times$ 1 $\times$ 0.5 mm^3) were fixed to the cryostat's cold-finger using indium metal.

In these studies, the fast emission spectrum of BaF_2 (see Fig. 1 [18]) was explained as coming from the radiative electronic transitions between the F-2p valence band and the Ba^{2+}-5p core band. Since the ionization threshold of the Cs^+-5p core bands of caesium halides is lower than that of other alkali

halides' core bands, the CRL was anticipated in the region of relatively low photon energy. Figure 2 (from Ref. [18]) presents the spectra of the fast component of the emission of two Cs halides, CsCl and CsBr (caesium bromide). It was expected [18] that, with RbF, the whole CRL spectrum would also correspond to the transparency region of the crystal; consequently, the CRL intensity would be comparable to that in CsCl and CsF (caesium fluoride). The results confirmed these expectations (see Fig. 3 from Ref. [18]).

In order to illustrate the fact that the emission wavelength of these scintillators can be controlled, we show in Fig. 4 (from Ref. [19]) the different emission spectra of KF when the Rb^+ concentration is changed. Such wavelength shifts could be used, for instance, to obtain a better overlap of the emission spectrum with the transparency region. The CRL spectra of $KMgF_3$ and $KCaF_3$ (see Fig. 5, from Ref. [19]) exhibit two main maxima, of nearly equal intensity. The total CRL intensity is comparable to that of BaF_2; it remains constant (within 10%) in the temperature range between 80 K and 400 K. The CRL spectrum lies entirely within the transparency region. As all the scintillators described in this paper, $KMgF_3$ and $KCaF_3$ have an emission decay time (< 2 ns) comparable to that of the BaF_2 fast emission. In addition, their resistance to radiation damage [21] was also estimated to be comparable to that of BaF_2.

All these properties, combined with an emission wavelength between 140 and 300 nm, made these two scintillators an interesting alternative to BaF_2, their main disadvantages being their lower density (~ 3 g/cm^3) and long radiation length ($X_0 \approx 7$–8 cm). However, these scintillators are not unique, and others are being developed by the same group; belonging to the same family, they have the same general characteristics, but their atomic number and density are higher.

Recently, Valbis and his group studied BaF_2 crystals doped with a large proportion of hydrogen (up to one atom of H for one atom of Ba). Their preliminary measurements showed that these crystals kept the other properties the same as those of the pure BaF_2.

3. Application to SSPCs

3.1 Wire chambers filled with photosensitive vapours

All the scintillators quoted in the first section emit light in the wavelength region below 300 nm. Some of them, such as $KMgF_3$ and $KCaF_3$, have properties similar to those of BaF_2 and, in addition, have a maximum light emission between 150 and 180 nm. In this region the common photosensitive vapours used in SSPCs, such as TMAE, have achieved very high efficiencies (between 35 and 60% for TMAE, see Fig. 6); other photosensitive vapours, such as triethylamine (TEA), nitrogen monoxide (NO), toluene, ..., are sensitive to this scintillation (see Fig. 6). Some of them, e.g. TEA, have a rather high vapour pressure at room temperature and do not interact with air, simplifying their manipulation. It was thus attractive to use TEA to detect the emission of these new scintillators in SSPCs. This was done by Buzulutzkov et al. [21], who coupled a $KMgF_3$ crystal with a wire chamber filled with a gas mixture of methane (CH_4) + 7.5% TEA at one atmosphere. They measured an efficiency of $\sim$ 4–5 photoelectrons per MeV of energy deposited in the crystal. The sensitivity is half that obtained with TMAE and BaF_2, but a major improvement is the possibility to work at room temperature, whereas the temperature needed to achieve a high enough pressure, and thus efficiency, is 40 °C with TMAE and 80 °C with EF. However, even with TEA vapour, it is still necessary to work at low pressure in order to exploit the good timing properties and insensitivity to direct ionization of traditional SSPCs. Furthermore, the BaF_2 fast emission was recently detected also with a layer of TEA adsorbed on a BaF_2 crystal in an SSPC [22], making it less interesting to use the new scintillators with TEA. It seems more

attractive to use them with TMAE vapour: the efficiency would then be higher, by factors of at least 5 to 10, than with TEA (see Fig. 6). This high sensitivity would not only greatly improve the results obtained with BaF_2 in electromagnetic calorimetry [12] and in positron emission tomography (PET) [10, 11], but it would also open a new range of applications in astrophysics, industrial imaging, nuclear medicine imaging, and so on.

3.2 Parallel-plate amplification counters (PPACs) with liquid or solid semitransparent photocathodes

The main physical limitations of the traditional SSPC, made with BaF_2 and a low-pressure wire chamber filled with TMAE, are set, on the one hand by the fast ageing effect due to polymerization observed with TMAE in a wire chamber [23], and on the other hand by the small spectral overlap between the BaF_2 fast scintillation and the TMAE quantum efficiency (see Fig. 7), which had allowed only a small part of the BaF_2 fast emission to be detected. The practical disadvantages of this detector are that it has to be operated at low pressure in order to keep the properties of this traditional type of SSPCs, and also that TMAE vapour is very reactive to air and corrosive for many materials. Besides, in order to increase the vapour pressure of TMAE in the chamber, and hence the efficiency, it is necessary to work at high temperature. The discovery of the new photosensitive vapour, ethyl ferrocene (EF) [14], interesting since it does not interact with air, did not allow us to increase the efficiency with respect to TMAE vapour, and did not solve the problem of high temperature. The solution may come from the work of Peskov et al. [13], who observed that there is an increase of up to 3 orders of magnitude of the quantum efficiency of metallic photocathodes when they are covered by liquid or solid layers of organic compounds (see Fig. 8). The shift in ionization potential, which is smaller when these organic compounds are in the liquid or solid phase than in the gaseous one [13], allows some of these compounds to be used, in an SSPC, to detect the BaF_2 fast scintillation. Semitransparent photocathodes of liquid EF, adsorbed or condensed on a BaF_2 crystal, were tested in an SSPC containing a mixture of He + CH_4 at atmospheric pressure and room temperature with good results [15]. Semitransparent photocathodes deposited directly on the surface of the scintillator crystal serve as the photosensitive element in the SSPC; this makes it possible to eliminate the gap that is needed to convert the VUV light emission in the photosentitive vapour. The low-pressure chamber can then be replaced by a PPAC working at atmospheric pressure and room temperature, directly coupled with the crystal, and keeping similar properties.

A prototype, made of a BaF_2 crystal covered by an EF (condensed or adsorbed) layer as the photocathode, coupled to a PPAC of 4 mm thickness and filled, at atmospheric pressure, with a gas mixture of helium and 100 Torr of tetramethyl silane (TMS), worked successfully at room temperature [16]. The properties of this new type of readout for SSPCs are: compacity (3–4 mm thickness), very fast collection time ($\leqslant$ 10 ns) and very good time resolution ($\leqslant$ 1 ns), negligible sensitivity to direct ionization at atmospheric pressure (with helium) and to a magnetic field [24], high gain (single-photoelectron detection), high rate capability [24] (no space-charge effect), and we did not observe any ageing effect due to polymerization. Nevertheless, the efficiency obtained with this new device is no higher than the traditional one, with a low-pressure wire chamber and TMAE vapour.

In order to improve this new SSPC, it would be attractive to find photocathodes that detect the BaF_2 fast scintillation more efficiently. A promising result was obtained with a solid photocathode, made with a new compound [16] called CPIHMB (for cyclopentadienyl–iron–hexamethyl–benzene) (see Fig. 9). It belongs to a large new family of organometallic compounds, discovered by Astruc [25]. They

have good chemical stability, associated with very low ionization potential (some of them between 4.2 and 4.8 eV in the gaseous phase). A programme of measurements of the quantum efficiencies of these new promising compounds, in the gaseous and in the liquid or solid phases, is being developed.

The most revolutionary improvement for the SSPC concept is the coupling of the new scintillators, covered with semitransparent photocathodes, in the liquid or the solid phases, with PPACs working at room temperature and atmospheric pressure. The advantage of this type of counter, developed originally with BaF_2, was explained above. Moreover, our calculations show that it is very inefficient, for photon collection, to detect the scintillation light with photosensitive vapours in SSPCs, because all these crystals have a high index of refraction ($n = 1.56$ for BaF_2 and $n \simeq 1.5$ for $KMgF_3$): by internal reflection, only a small part of all the photons produced by the scintillation escape out of one face of the crystal. This phenomenon is also well known when the BaF_2 is coupled to a photomultiplier (PM)—the light yield then increases by a factor of at least 2, if a good optical contact is obtained by applying an optical grease between the surface of the crystal and the PM window. In the case of liquid or solid semitransparent photocathodes, which are of course in direct contact with the surface of the crystal, the light yield increases significantly, since the difference of refraction index is smaller: typically $n = 1.3$ for liquid photocathodes. We estimate that the light yield would increase by a factor of 2.5 to 5 (depending on the transparency of the crystal).

These organic photocathodes achieve rather good efficiencies already in regions of relatively high wavelengths, e.g. ~ 2–7% at 235 nm (see Fig. 8). This efficiency can increase strongly in regions of shorter wavelengths; see, for example, Fig. 10, where the increase of the efficiency of an EF liquid photocathode is of at least one order of magnitude when the wavelength drops from 235 to 200 nm. In the wavelength region of maximum emission of the new scintillators (for $KMgF_3$ and $KCaF_3$ between 150 and 180 nm), the quantum efficiencies of our photocathodes would be much higher, and could probably achieve values equivalent to what can be obtained with a photomultiplier. Moreover, it was observed by Holroyd et al. [26] that the number of photoelectrons extracted from the liquid photocathode into the gaseous phase increases with the intensity of the applied electric fields. This effect was verified by our measurements in SSPCs. For example the increase of efficiency measured between 1 kV/cm and 5 kV/cm is shown in Fig. 8 for a photocathode made of methane + neopentane (NP) + TMAE, cooled at $T < -20$ °C; Fig. 10 shows this increase between 1 kV/cm and 7.5 kV/cm for an EF-liquid photocathode. As a consequence, in a PPAC, in which the applied electric fields are higher than ~ 10 kV/cm, the use of the liquid photocathodes optimizes the quantum efficiency of the SSPC. Even if the sensitivity is generally rather lower, it is more attractive, from the point of view of practicability (e.g. manipulation) and of stability, in SSPCs, to use solid photocathodes at room temperature than liquid ones. A good candidate would be pure tetramethyl-p-phenylenediamine (TMPD), in which a relatively high efficiency was achieved at 200 nm [13]; another could be caesium iodide (CsI), with a quantum efficiency of ~ 10% in the wavelength emission region of the new scintillators (see Fig. 6). We estimate that a CsI photocathode should achieve an efficiency equivalent to or higher than that obtained with TEA in an SSPC with $KMgF_3$.

In addition, it is estimated that PPACs are much less sensitive to the ageing effect due to polymerization observed in the majority of proportional wire counters; this is because the local charge density is much lower in a PPAC than around wires. Moreover, in order to avoid photon feedback on the photocathode and to reach a high gain in the PPAC, it is necessary to use a good quencher in the gas mixture, tetramethyl silane (TMS) for example. Next, the quenchers we introduce should have very good ageing properties; the best known so far candidate is dimethyl ether (DME). No ageing effect was

observed in proportional wire chambers filled with pure DME up to 1.2 C per centimetre of wire [27].

We expect that the association of the new scintillators, covered with CsI semitransparent photocathodes, with a PPAC filled with helium and DME, could achieve properties and results equivalent to those obtained with BaF_2 associated with a low-pressure wire chamber filled with TMAE. In addition, there would be no ageing effect in the counter, the radiation resistance would be equivalent to that of BaF_2, and the compacity would be better: $\sim$ 3 mm as against 1 cm.

4. Discussion

An electromagnetic calorimeter made with PPACs as described above, estimated to be very resistant to radiation damage, to have a time resolution of < 1 ns and a signal collection time of < 10 ns, with an energy resolution of $\sim 4\%/\sqrt{E(\text{GeV})}$ or better, would be very well adapted to the needs of experiments in high-luminosity accelerators, such as the SSC and the LHC. In many other applications, positron emission tomography (PET) for instance, this type of SSPC would be a great improvement, since it could cover large surfaces at a low price, with a good position resolution. If electromagnetic calorimetry is important in high-energy-physics experiments, another aspect, as essential, of the experiments planned for the high-luminosity accelerators is hadronic calorimetry. In fact, homogeneity would make it necessary to use the same technique in electromagnetic and hadronic calorimetry.

Ideally, these new detectors should possess all the following qualities:

- high speed,
- high resistance to radiation damage,
- ability to realize compensation phenomena, in order to achieve a good energy resolution,
- technical ease of building,
- compacity.

Classical sampling calorimeters made of uranium or lead and organic scintillators [28, 29], or those based on the new approach developed by Wigmans [30], with lead and scintillating fibres, are fast enough and can achieve compensation, but their radiation resistance is not high enough in the hot region of the SSC or LHC, whereas those made of uranium with a warm liquid such as TMP [30] are good on radiation resistance but not fast enough. Also, they are technically difficult to realize. To make a hadronic sampling calorimeter, it would be of advantage to use SSPCs made of a PPAC and photocathodes with inorganic scintillators, such as BaF_2 or the other ones presented in this paper, sampled with uranium or lead. Such a calorimeter would have all the qualities required above, except for the compensation, since the inorganic scintillators do not contain the hydrogen which is necessary to achieve it.

The BaF_2 crystals doped with a large proportion of hydrogen may be of interest for the purpose. Then a fine-sampling hadronic calorimeter, using uranium or lead and this 'new' crystal coupled to PPACs with semitransparent photocathodes as readout, should combine the speed and technical practicability of the uranium (or lead)/organic scintillator detectors with the good resistance to radiation damage of the uranium/warm liquid detectors. In addition, this compact calorimeter would also probably achieve compensation.

A recent step forward in the manufacturing of BaF_2 optical fibres*) opens considerable prospects for the solution of an important problem in detector physics. While scintillating fibres present attractive

*) D. Winn (Fairfield University), private communication.

features for many problems in particle physics, they suffer from a major defect when they are compared to gaseous detectors, namely the difficulty to delay the information for a time long enough for the selection and gating of the events of interest to be made.

The solution that has been found for the manufacturing of BaF_2 fibres can be extended to a vast variety of scintillators. It consists in depositing the substance on a quarz fibre, by chemical vapour deposition (CVD). The author*) advocates that BaF_2 films of 1 to 100 μm can be deposited on quartz fibres of diameter 10 μm to 500 μm. This opens the way for devices where the light coming from a bundle of such fibres is converted into electrons in a gaseous photosensitive device; there the photoelectrons are amplified, delayed, gated and multiplied again in a multistep device, with the emission of light induced by the adequate addition of a vapour such as TEA or TMAE and the detection of the image pattern in a CCD. With some of the new scintillators, the photosensitive device could consist of the thin transparent photocathodes discussed previously, with efficiencies of the order of 10%. Since a single photoelectron can easily be imaged with the multistep chamber, this may lead to the efficient detection of the energy deposited in the fibres, although the yield of light is smaller for these scintillators than in the plastic scintillation fibres investigated up to now for particle tracking or calorimetry. It is an alternative approach to a solution imagined by Sauli**), where visible light is transformed into VUV by accelerating electrons, in vacuum, between a photocathode sensitive to visible light and a thin layer of BaF_2.

5. Conclusion

The perfect overlap between the emission spectra of the new scintillators and the quantum efficiencies of the photosensitives elements used in gaseous detectors would strongly improve the SSPC concept. In particular, an SSPC made of these scintillators covered with solid or liquid photocathodes, coupled with a PPAC working at room temperature and at one atmosphere, would reach a sensitivity that would be practically equivalent to that of a PM ($\geq$ 10%), keeping the properties of proportional gaseous detectors, i.e. compacity, possibility to cover large surfaces, negligible sensitivity to magnetic fields, low noise, ... In addition, this detector would be very fast (time resolution $\leq$ 1 ns and collection time of the signal $\leq$ 10 ns), with a high rate capability and a very high resistance to radiation damage.

All these characteristics should allow substantial improvements in many fields of application, at low energies (PET, for example) as well as high energies (electromagnetic and hadronic calorimetry, for instance).

We expect that a new field of applications would also be opened with the scintillating fibres made of BaF_2 and probably of the new scintillators, coupled with photosensitive gaseous detectors as readout.

This work was carried out in the framework of the LAA Project.

*) D. Winn (Fairfield University), private communication.

**) F. Sauli, Proposal for the development of an optic-electronic image delay tube, Proposal for LAA project, CERN, 6 June 1988.

References

[1] D.F. Anderson, Phys. Lett. **18** (1982) 230.

[2] D.F. Anderson, R. Bouclier, G. Charpak and S. Majewski, Nucl. Instrum. Methods **217** (1983) 217.

[3] D.F. Anderson, G. Charpak, Ch. von Gagern and S. Majewski, Nucl. Instrum. Methods **225** (1984) 8.

[4] M. Laval, M. Moszynski, R. Allemand, E. Cormorèche, P. Guinet, R. Odru and J. Vacher, Nucl. Instrum. Methods **206** (1983) 169.

[5] P. Schotanus, C.W. van Eijk, R.W. Hollander and J. Pijpelink, Nucl. Instrum. Methods **A238** (1985) 564.

[6] M. Suffert and G. Charpak, CERN EP Internal Report 86-03 (1986).

[7] S. Majewski and D. Anderson, Nucl. Instrum. Methods **A241** (1985) 76.

[8] A.J. Caffrey et al., IEEE Trans. Nucl. Sci. **NS-33** (1986) 230.

[9] A. Breskin, Nucl. Instrum. Methods **196** (1982) 11.

[10] P. Miné et al., IEEE Trans. Nucl. Sci. **NS-34** (1987) 458.

[11] P. Miné et al., Nucl. Instrum. Methods **A269** (1988) 385.

[12] R. Bouclier et al., Nucl. Instrum. Methods **A267** (1988) 69.

[13] V. Peskov et al., Nucl. Instrum. Methods **A269** (1988) 149.

[14] G. Charpak, V. Peskov, F. Sauli and D. Scigocki, CERN-EP Internal report 88-02 (1988).

[15] G. Charpak, V. Peskov, F. Sauli and D. Scigocki, preprint CERN-EP/88-166 (1988), submitted to Nucl. Instrum. Methods.

[16] V. Peskov, G. Charpak, F. Sauli and D. Scigocki, Organometallic photocathodes for parallel-plate and wire chambers, presented at the Wire Chamber Conference, Vienna, 1989.

[17] P. Schotanus, C.W. van Eijk and R.W. Hollander, Nucl. Instrum. Methods **A272** (1988) 913.

[18] J.L. Jansons, V.J. Krumins, Z.A. Rachko and J.A. Valbis, Phys. Stat. Sol. (b) **144** (1987) 835.

[19] J.L. Jansons, V.J. Krumins, Z.A. Rachko and J.A. Valbis, Solid State Commun. **67** (No. 2) (1988) 183.

[20] J.L. Jansons and Z.A. Rachko, Phys. Stat. Sol. (a) **53** (1979) 121.

[21] A.F. Buzulutzkov et al., Serpukhov preprint IHEP-88-167 (1988).

[22] G. Charpak, V. Peskov and D. Scigocki, Group internal report.

[23] C.L. Woody, IEEE Trans. Nucl. Sci **NS-35** (1988) 493.

[24] F. Sauli, Proc. Meeting on the Future of Intermediate and High Energy Physics in Switzerland, Les Rasses, 1985 (SIN, Villingen, 1985), p. 167.

[25] D. Astruc, Accounts Chem. Res. **19** (12) (1986) 377.

[26] R.A. Holroyd, S. Erhenson and J.M. Preses, J. Phys. Chem. **89** (1985) 4244.

[27] M. Jibaly et al., The ageing of wire chambers filled with dimethylether, paper presented at the Wire Chamber Conference, Vienna, 1989.

[28] T. Åkesson et al., Nucl. Instrum. Methods **A262** (1987) 243.

[29] E. Bernardi et al., Nucl. Instrum. Methods **A262** (1987) 229.

[30] R.M. Wigmans, The Spaghetti calorimeter project at CERN, Paper presented at the Workshop on Future Directions in Detector R & D for Experiments at pp Colliders, Snowmass, 1988.

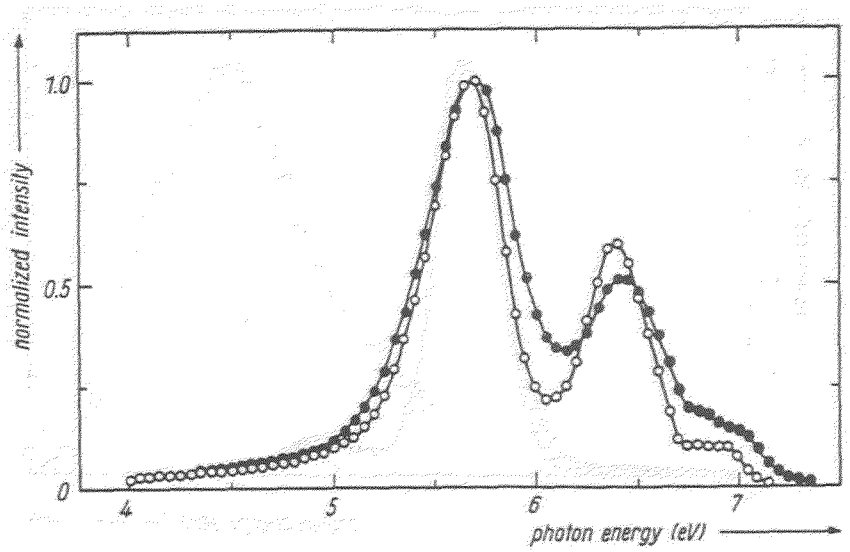

Fig. 1 Luminescence emission spectra normalized to equal maximum intensity of BaF_2 at 80 K (○) and 300 K (•).

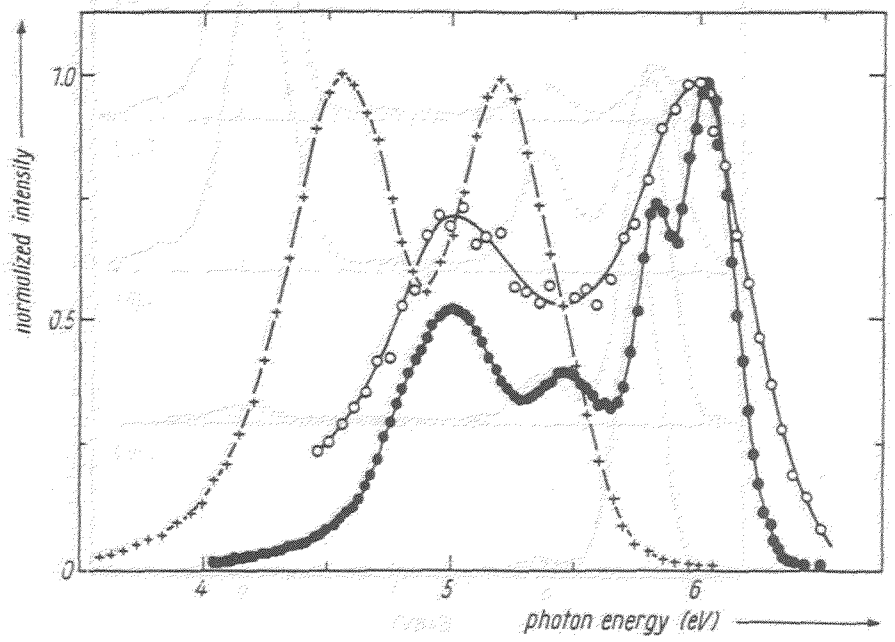

Luminescence emission spectra normalized to equal maximum intensity of CsCl at 300 K (+) r at 300 K (○) and 80 K (•).

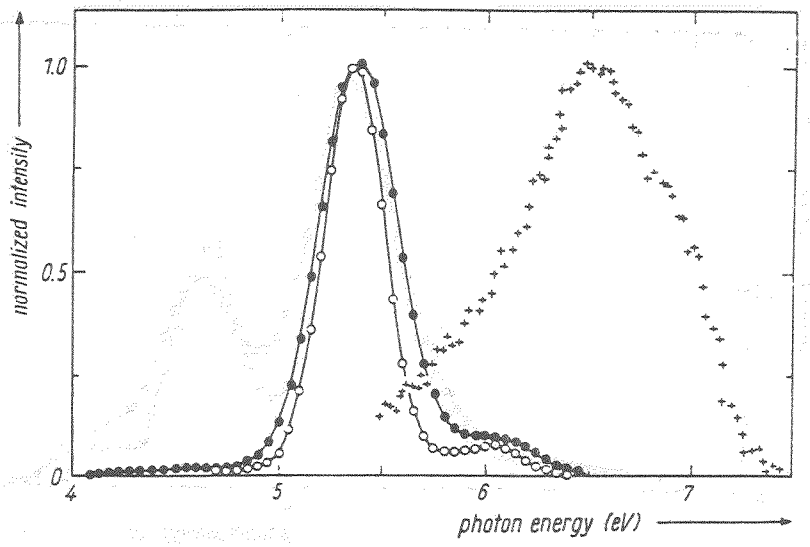

Fig. 3 Luminescence emission spectra normalized to equal maximum intensity of RbF at 80 K (○) and 300 K (•) and RbCl at 300 K (+).

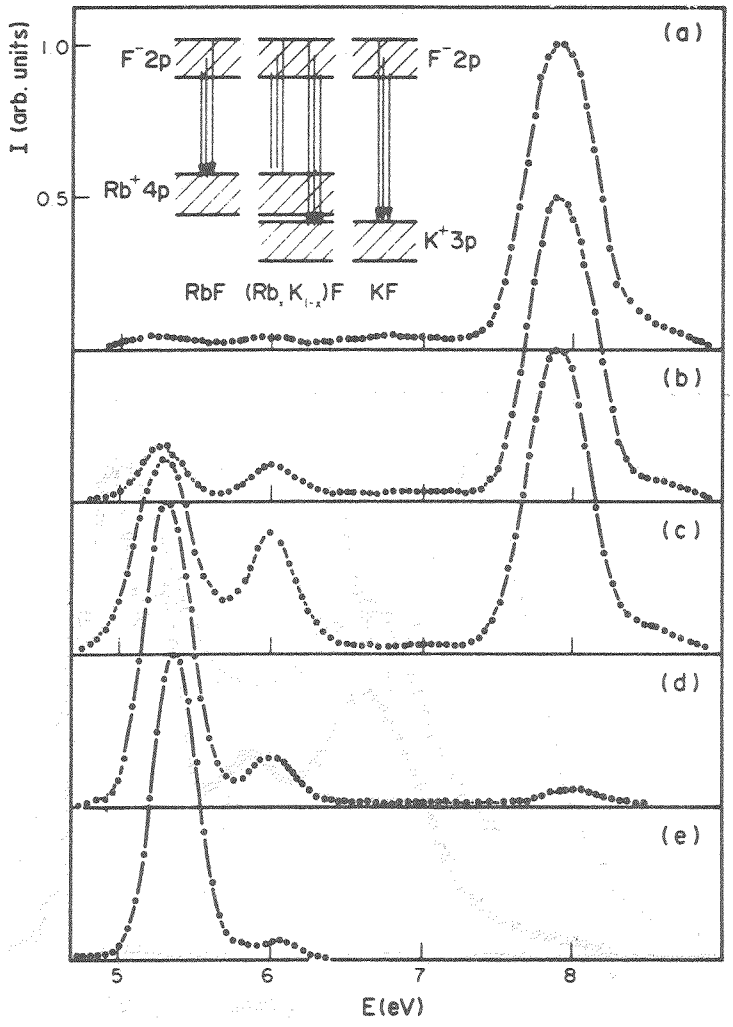

Fig. 4 Luminescence emission spectra of $K_{1-x}Rb_xF$ solid solutions, with varying x = 0 (a); 0.001 (b); 0.01 (c); 0.1 (d); 1 (e).

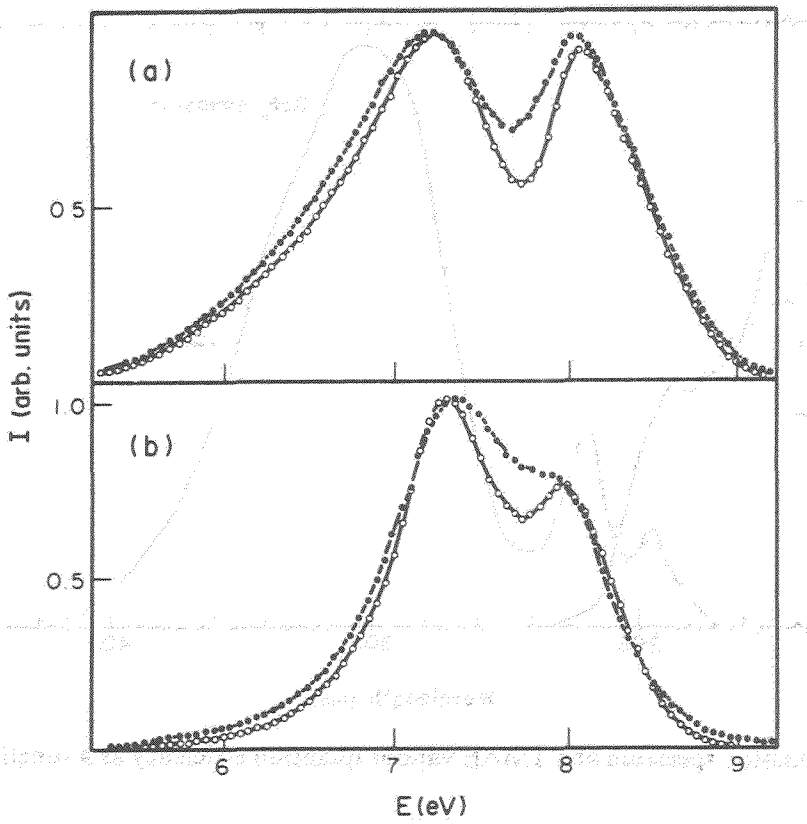

Fig. 5 Luminescence emission spectra of $KMgF_3$ (a) and $KCaF_3$ (b) at 80 K (○) and 300 K (•).

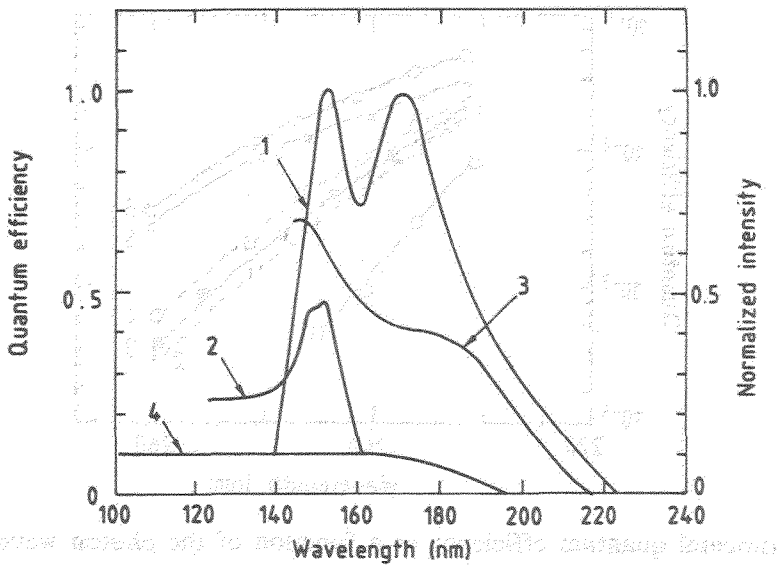

Fig. 6 Emission spectrum of $KMgF_3$ and quantum efficiencies of TEA and TMAE vapours and of CsI solid photocathodes as a function of photon wavelength λ. (1) $KMgF_3$ emission spectrum; (2) TEA vapour quantum efficiency; (3) TMAE vapour quantum efficiency; (4) CsI solid photocathode quantum efficiency.

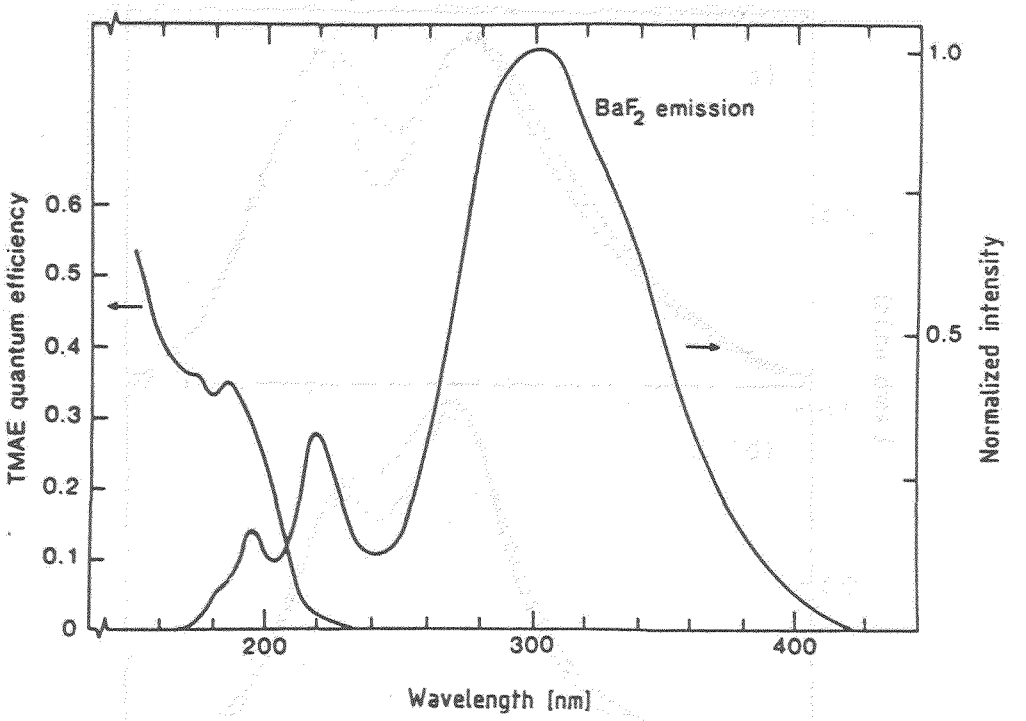

Fig. 7 BaF_2 emission spectrum and TMAE vapour quantum efficiency as a function of wavelength

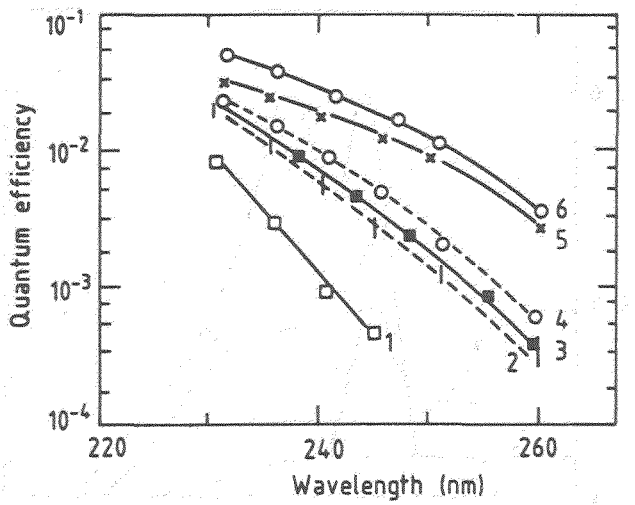

Fig. 8 The experimental quantum efficiency as a function of the photon wavelength λ for various liquid and solid photocathodes at a pressure of 1 bar, unless otherwise noted, and electric field E = 1 kV/cm; (1) methane + TMAE, T_{cath} = 0 °C; (2) methane + TMP + TMAE, T_{cath} = −15 °C; (3) methane + neopentane (NP) + TMAE, T_{cath} = 0 °C; (4) methane + TMS + TMAE, p = 1.5 bar, T_{cath} = −5 °C; (5) methane + NP + TMAE, T_{cath} < −20 °C; (6) same as (4) with electric field E = 5 kV/cm.

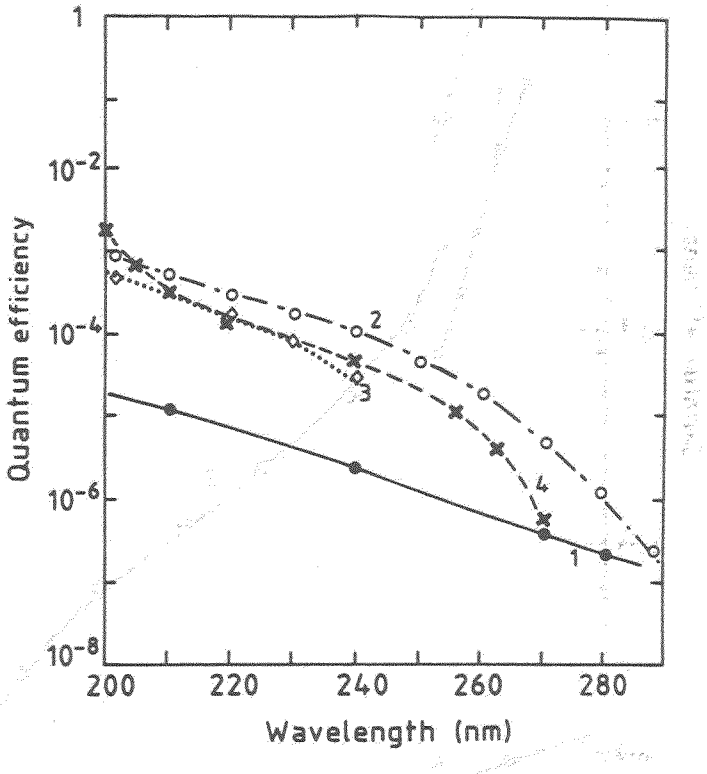

Fig. 9 Quantum efficiency as a function of wavelength for different photocathodes. (1) Clean Cu; (2) Cu + condensed CPIHMB; (3) Cu + condensed CPIHMB + TMS; (4) Cu + condensed EF.

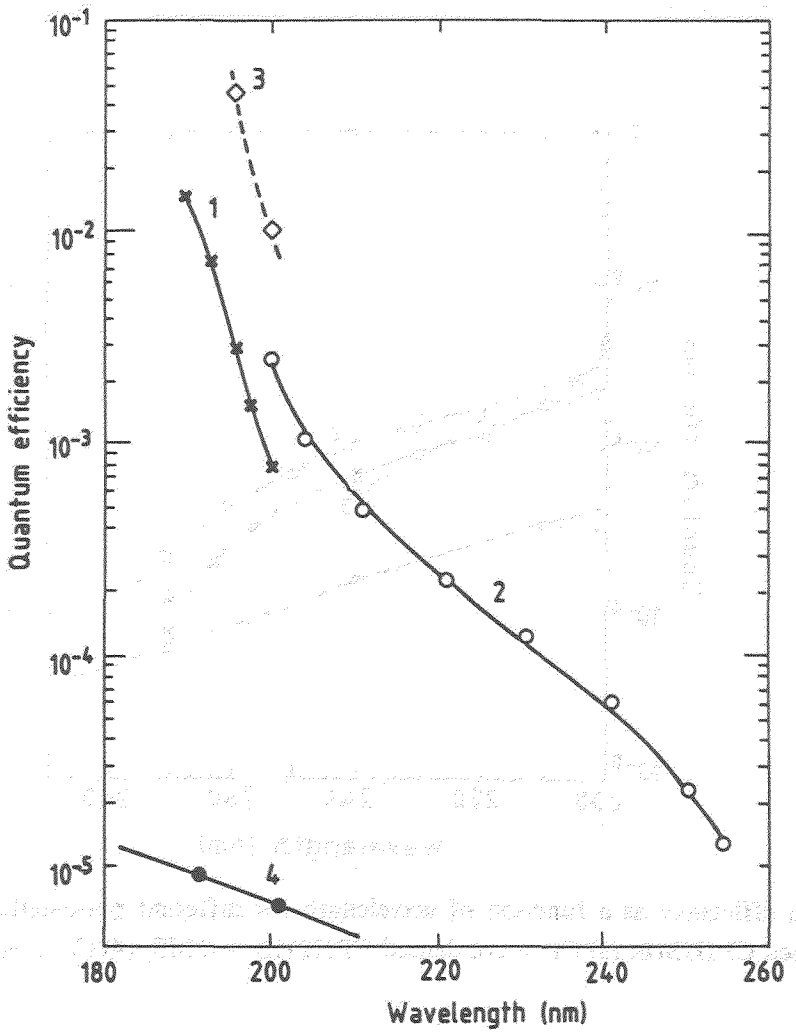

Fig. 10 Quantum efficiencies measured with a single-wire counter: (1) EF at T = 40 °C and a gap L = 15 mm; (2) thin layer of EF condensed on a copper cathode in an electric field E = 1 kV/cm; (3) same as (2), with E = 7.5 kV/cm; (4) clean copper cathode.

III. Transition Radiation Devices

FERMILAB-Conf-89/170-E
WISC-EX-89-305

A High Rate Transition Radiation Detector for Particle Identification in a Hadron Beam*

Talk given by M. Sheaff at the Symposium on Particle Identification at High Luminosity Hadron Colliders Fermilab April 5-7, 1989

D. Errede and M. Sheaff
Physics Department
University of Wisconsin
Madison, Wisconsin, 53706

H. Fenker, L. Lueking, and P. Mantsch
Fermilab
Batavia, Illinois, 60510

Abstract

A Transition Radiation Detector (TRD) was built for the purpose of tagging beam particles in a high rate (~2 MHz) 250 GeV/c hadron beam during data taking for Experiment 769 at Fermilab. The availability of a good "tool kit", including a Monte Carlo program which could reliably predict the detector performance, made it possible to design and build the TRD in approximately one year. Pion or proton samples, each with a small contamination due to the other, could be selected with high efficiency by making cuts on the number of planes of the TRD registering hits for each incident beam particle. The detector is expected to work well to separate kaons from pions in the 500 GeV/c negative beam for E791.

Introduction

A Transition Radiation Detector was built to separate pions from kaons or protons in the incident 250 GeV/c charged hadron beam for E769 at Fermilab. This is the first reported use of a TRD for beam particle identification in a running experiment[1], although several authors have demonstrated the ability to separate pions from the heavier hadrons in test beams at similar energies using prototype TRD's[2,3,4,5].

The Physics objectives of E769 are to measure the dependence of open charm hadroproduction on the atomic number of the target material, the kinematic variables x_F and p_t of the produced charm particle, and the flavor of the incident beam particle. A Differential Isochronous Self-Focusing Cerenkov Counter (DISC)[6] that had been used successfully to identify beam particle type for previous experiments at Fermilab in this energy regime was refurbished for use in E769, and it was decided to set it at a pressure to give a positive tag for kaons. While this single tagging element would have sufficed to identify pions and kaons in the negative beam which was 91% pions, 7% kaons, and 2% anti-protons, two tagging detectors were required for particle identification in the positive beam, which was 59% pions, 35% protons, and 6% kaons. The decision to build a TRD as the second tagging

detector was motivated by several factors, among them the fact that a future run at higher energies was anticipated for which the DISC, with a limiting resolution of $\Delta\beta \geq 4 \times 10^{-7}$, would no longer be capable of separating pions from kaons. The response of the TRD, by contrast, grows with energy since the number of TR photons produced by an incident beam particle depends on its Lorentz factor, γ. There is a saturation effect which keeps this response from growing indefinitely. The energy at which this occurs depends on the materials chosen for the radiator foils and inter-foil gaps and the relative thickness of the foils and gaps. Since these parameters are rather tightly constrained by the available materials and available space, this detector can be regarded as typical of practical TRD's. The response expected for the E769 TRD is displayed in Figure 1, which shows the average number of photons produced in the radiators and detected in the xenon-filled proportional chambers as a function of energy for pions, kaons, and protons as predicted by the Monte Carlo program[7] which will be discussed further in what follows. Saturation is not included in the program calculations and thus it has been put in by hand according to the formulae in Reference 8. Also, all numbers have been multiplied by the measured efficiency of 83% for the detection of x-rays at TR energies in the chambers when the electronics threshold was set to 4 keV. This efficiency was determined by exposing a prototype chamber to x-ray sources. Figure 2, which shows the events from a typical E769 positive beam data run plotted along two axes, one of which is the number of DISC photomultiplier tubes (of 8 total) that fired, and the other of which is the number of TRD planes (of 48 total) that registered a hit above the 4 keV threshold, demonstrates the power of the two detectors used together to separate the particles by species. During the course of data taking, several calibration runs were taken for the TRD with the DISC pressure set to tag pions or protons rather than kaons as for the normal data tapes.

Since the decision to build a TRD for E769 was made only about one year in advance of data taking, the time available for design and construction was short. Fortunately, there was a good "tool kit" with which to work. This included the Monte Carlo program[7], which had been written by University of Maryland personnel to predict the performance of a prototype TRD they had built and operated in a test beam. Since there was no a priori reason to believe the results of the program, it was tested by using it to simulate the TRD that had been built at the Leningrad Nuclear Physics Institute for E715 at Fermilab[9]. This TRD had operated successfully to identify electrons with high efficiency and with a large rejection factor for pions at energies ranging from 5-80 GeV. The Monte Carlo predictions were found to be in good agreement with the measured performance of the E715 detector. Also available in the "tool kit" was the design for a multiwire proportional chamber (MWPC) with 1 mm. wire spacing and $\sim$ 3mm. anode-cathode distance, which was suited for use at the expected high rates ($\sim$2 MHz) because of the relatively short drift distances. A chamber with these design parameters had been built as a prototype for the beamline MWPC's used throughout Fermilab[10] and it was quickly reassembled for use in the source tests. Despite its small size, the maximum drift time in this chamber was measured during the run to be approximately 120 ns, since xenon is a relatively slow gas. Also, chamber electronics could be built with a minimum of new design effort by making modifications to existing designs for CDF tracking chamber amplifier cards[11,12]. Since time

was short it was not possible to expose prototype chambers and readout electronics to a test beam with the appropriate γ, of order 1800, which corresponds to an electron beam of about 1 GeV. Thus an x-ray source which outputs the k_α lines of various elements[13] was the last crucial item in the "tool kit". Since these x-rays bracketed the expected TR spectrum, it was possible to predict the detector response to TR photons under different conditions by performing tests on prototype chambers with this source varying the gas fill and the high voltage settings. The only elements of the system that could not be tested before the run were the radiators, which required actual beam particles in order to produce photons. But, these could easily be replaced should it be found that the TRD performance was below that expected based on the Monte Carlo results. (The radiators were, in fact, modified once during the run for reasons that will be explained below.)

Description of the Detector

Since details of the Monte Carlo simulations and of the source testing that led to the final choice of design and operating parameters for the detector have been published elsewhere[1], only a brief description of the detector and associated electronics will be presented here. Figure 3 depicts one of the 24 modules of the TRD in plan view oriented such that the incident hadron beam entered from the left side of the figure. The 200-foil radiators were built by stacking 12.7 μm polypropylene foils alternately with 180 μm nylon net to maintain the gaps, which were flushed with helium. This was done to reduce the total amount of material in the beam. Also, helium has a lower plasma frequency than air which makes it a better gap material. Since the nylon net was found during the early part of the data taking run to attentuate the TR photons by approximately 50%, the radiators were removed and unstacked. They were restacked and replaced after cutting out the area of the nets traversed by the beam. Two MWPC planes with 1 mm wire spacing and 3.175 mm anode-cathode separation were placed following each radiator stack to detect the TR photons produced. The active area of these chambers was 7.62 cm square. The wires were .4 mil gold-plated tungsten and the cathodes .5 mil mylar with 140 $\AA$ aluminum on both sides. The active volume was filled with xenon, which has a short attentuation length for TR photons, bubbled through methylal at 0^o C, which results in a mixture that is approximately 90% Xe. The xenon and helium volumes were separated by a 3.175 mm volume filled with nitrogen to prevent helium from leaking into the chamber and changing the gain. Care was taken to maintain the nitrogen and xenon volumes at the same pressure so that the cathodes would be flat and thus the gain would be uniform across the plane. The entire set of 24 radiator-chamber assemblies was 111 inches long, and the total amount of material presented to the beam by the TRD was 8.3% of an interaction length and 16.9% of a radiation length.

Figure 4 is a cartoon of the most important elements in the chamber electronics and readout system. The 64 wires in each plane were wire-or'd in groups of four into a common base, low-noise preamplifier designed by Radeka[11] for use in high-rate chambers. The signals then traveled on short coaxial cables to amplifier-shaper-discriminator (ASD) cards. These contained a pole-zero filter which shaped the pulses so that the signal resulting from capture of an Fe_{55} x-ray was ~26 ns wide. Following the filter was an amplifier

with adjustable gain, which was tuned to impose system-wide uniformity. The amplified signals were input to fast LeCroy discriminators (MVL407) set to a threshold of 4 keV as determined in the source tests. These ASD cards were close copies of some that had been designed for use in CDF[12] where multiple hit capability in drift chamber cells was the goal. Here, the short integration times made it possible to use the method of cluster counting, which had been shown to give better discrimination among particle types than selection on the total integrated charge collected in each chamber plane[14]. All discriminator outputs from a single plane were input to a LeCroy 4564, which performed a logical OR of the 16 signals. The resulting plane-by-plane hit signals were input to a LeCroy 4448 latch gated by an event trigger, and the plane hit patterns were read out as part of the event data. Thus only one cluster could be registered per plane per event, but since the cluster probabilities were small, $\sim$.45 for the upstream plane and $\sim$.20 for the downstream plane of the pair, there was little loss in the TRD resolution from this choice of readout.

Detector Performance

Figure 5 shows the distribution in the number of TRD planes registering hits per event for events where the incident beam particle was not tagged by the DISC as a kaon in a typical positive beam data run, SQ1123. The proton peak averages to 3.2 planes/event and the pion peak to 14.5. Figure 6 shows the plane count distributions for DISC tagged samples where the events in a) are the tagged kaons from SQ1123, and in b) and c) are the tagged protons and pions, respectively, from TRD calibration tapes taken at approximately the same time in the data taking run. Although triggers which were within 120 ns (the TRD latch gate width, which was set to accommodate the maximum drift time in the chambers) of another were hardware suppressed, some events with two tracks going through the TRD were still recorded. These have almost all been eliminated from the distributions by making a cut on events with more than 9 (clustered) hits in the 8 planes of beam MWPC which were downstream of the TRD. However, there are still events with high plane counts remaining in the DISC tagged proton distribution. This high plane count tail appears to have the same shape as the two-track background derived from the same tape. Events with such high plane counts are well outside the range allowed by binomial statistics according to a Monte Carlo study in which the average plane count for each of the planes was input and plane hit counts were generated using these probabilities. These anomalous events constitute the only background to pions when a high enough plane count cut is imposed with the result that there is an approximately constant background of order 2% for all choices of the plane count cut above 10. Table I shows the efficiency for selection of either pions or protons and the background for each due to the other as a function of plane count cut as determined by making plane count cuts on the distributions shown in Figure 6 b) and c). The relative fraction of each in the positive beam is used in calculating the contaminations.

Table I

TRD Performance

Pions

# of TRD Planes That Fired	Pion Efficiency	Proton Contamination
≥ 8	.946	3.0%
≥ 10	.868	2.0%
≥ 12	.733	1.9%

Protons

# of TRD Planes That Fired	Proton Efficiency	Pion Contamination
≤ 6	.865	3.5%
≤ 7	.924	5.7%
≤ 8	.951	9.7%

A fit to the plane count distribution for the events not tagged by the DISC as kaons shown in Figure 5 was made using a trial distribution generated by adding together the pion and proton distributions shown in Figure 6 b) and c) in the appropriate ratios. Since the event trigger selection included the requirement that there be an interaction in the target, and since protons have a 50% larger inelastic cross section at 250 GeV/c than pions or kaons, the proton fraction in the beam has been multiplied by a factor of 3/2 relative to the other species and the three components renormalized to total 1. A small admixture of kaons (60% of the kaons but only 3% of the total in the summed distribution) has been included in the trial distribution, since approximately 60% of the kaons were outside the tightly collimated beam direction for which the DISC has good efficiency. Also added in is an assumed 2% residual two-track background modeled by using the plane count distribution for events with more than 9 clustered MWPC hits from SQ1123. The trial distribution has been normalized to the same total number of events as the data and is displayed as the dotted line in Figure 5. The resulting fit for this data tape was quite good, yielding chisquare of 43 over the 34 bins which contained data.

Expected Performance at Higher Energy

The results discussed above were obtained toward the latter part of the data taking period after it was discovered that the high beam rates coupled with high gain operation of the chambers had damaged the cathodes by removing the aluminum surfaces, which were only 140 $\AA$ thick, over the beam area. Since the chambers were larger in active area than the beam, the array was simply raised by one inch, after which the TRD behaved as it had before the damage was incurred. The gains, however, were reduced to prevent this from happening again. Thus the performance of the detector is somewhat below the Monte Carlo predictions for these data. However, as shown in Figure 7, the data and Monte Carlo were in good agreement when the gains were tuned to the settings expected by the Monte Carlo. Figure 7 compares the hit probability per event for data and Monte Carlo for each plane in the TRD. The two upper curves are the pion data (solid line) and pion Monte Carlo (dashed line). The lower solid line is the response to protons, i.e., to minimum ionizing particles in the absence of TR. While the Monte Carlo systematically overpredicts the response of the more upstream planes and underpredicts the response of the more downstream planes to TR, the agreement for each module as a whole is good. The average number of planes registering a hit per pion event for these data is 18.8 compared to the prediction of 20.0.

Figure 8 shows the predictions of the same Monte Carlo program for operation of the TRD in the 500 GeV/c negative beam for E791. The beam has been assumed to be 98% pions and 2% kaons, which is the expected ratio at this energy[15]. Figure 8 b) displays the low plane count region of Figure 8 a) with a change of scale to demonstrate that the kaons can be well separated from the pions. The cathodes for the chambers are being rebuilt in preparation for E791 using aluminized mylar that has ten times the thickness of aluminum as on the originals ($\sim$ 1400$\AA$) to enable operation for a longer period without a significant loss of performance. Also, analog output circuits, which were used to monitor the response to on-board Fe_{55} sources to establish gain uniformity from one chamber to the next for the duration of the running period, were sampling edge wires of the chamber and therefore were not sensitive to the beam damage. These will be re-routed to sample wires which are in the beam area for E791 so that any degradation in performance will be evident immediately.

*Work supported under NSF PHY-86-15287 and DOE
DE-AC02-76-ER00881-Task D and DE-AC02-76-CHO-3000.

References

[1] D. Errede et al., "Design and Performance Characteristics of the E769 Beamline Transition Radiation Detector", presented by M. Sheaff at the 1988 IEEE Nuclear Science Symposium, Orlando, Florida, Nov. 9-11, 1988, IEEE Transactions on Nuclear Science **36**, 106 (February 1989). A more detailed report, to be submitted to NIM, is in preparation.

[2] C. Fabjan et al., "Practical Prototype of a Cluster-Counting Transition Radiation Detector", NIM 185 (1981) 119.

[3] M. Atac et al., "An Unconventional Transition Radiation Detector", NIM 145 (1977) 251.

[4] C. Camps et al., "Transition Radiation from Electrons at Low Gamma Values", NIM 131 (1975) 411.

[5] H. Haggerty, "A Beamline Transition Radiation Detector for MW", Fermilab - TM - 1201.

[6] M. Benot et al., "Cerenkov Counters for Particle Identification at High Energies", NIM 105, (1972) 431.

[7] H. Stroebele et al., "A Transition Radiation System for Identification of Pions in a 200–400 GeV Beam", submitted to NIM (1982).

[8] X. Artru et al., "Practical theory of the multilayered transition radiation detector", Phys. Rev. D12 (1975) 1289. See p. 1297 for a discussion of saturation.

[9] A. Denisov et al.,"Performance of the E715 Transition Radiation Detector", Fermilab - CONF - 84/134 - E.

[10] H. Fenker, "A Standard Beam PWC for Fermilab", Fermilab - TM - 1179.

[11] J. Fischer et al., "Proportional Chambers for Very High Counting Rates Based on Gas Mixtures of CF_4 with Hydrocarbons", NIM A238 (1985) 249.

[12] R.J. Yarema et al., "A Surface Mount Amplifier-Shaper-Discriminator and Preamplifier for the Fermilab CDF Tracking Chambers", IEEE Transactions on Nuclear Science, Vol. 33, No. 1, February 1986.

[13] See the data sheet on product code AMC2084, Amersham Laboratories, White Lion Road Amersham, Buckinghamshire, England, HP7 9ll.

[14] T. Ludlam et al.,"Particle Identification by Electron Cluster Detection of Transition Radiation Photons", NIM 180 (1981) 413.

[15] R. Rubinstein, "Fermilab Research Program 1988 Workbook", May 1988, Figure 18, p. 25, gives relative fluxes for negatives at 500 GeV/c as measured in the MW beamline at FErmilab.

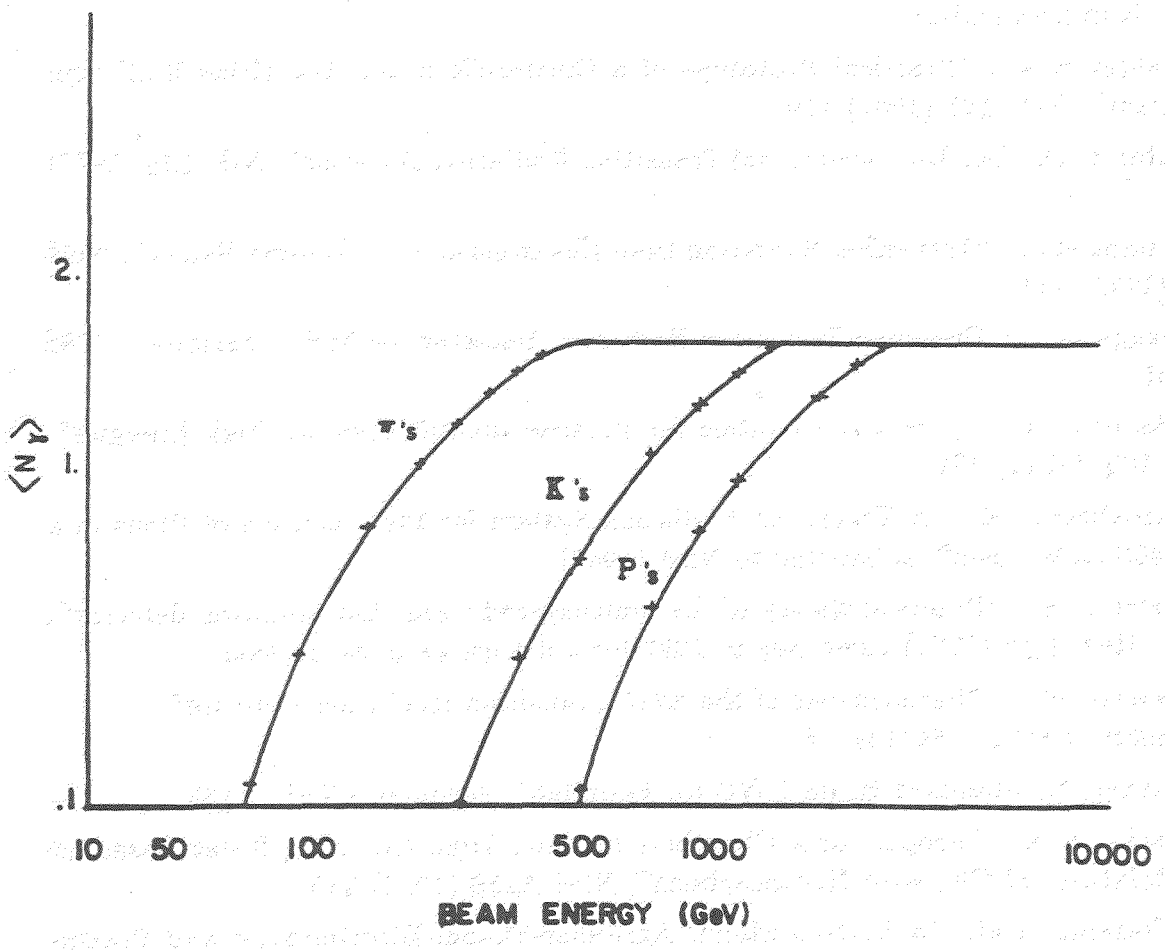

Fig 1. Average number of TR photons detected per module of the TRD for π's, K's, and p's as a function of beam energy. The efficiency factor of .83 measured in the source tests is included. γ_{sat} has been calculated using the formulae in Reference 8.

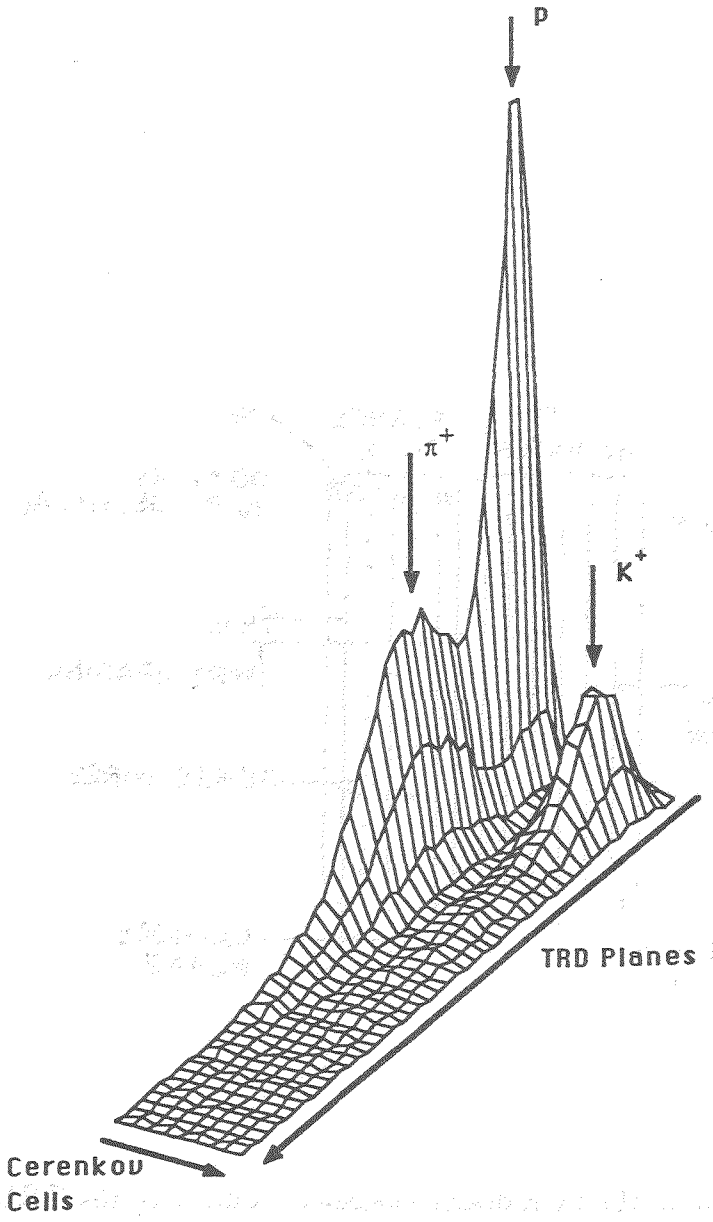

Fig 2. Distribution of events from a typical E769 positive beam data tape plotted along two axes, one of which is the number of TRD planes that fired and the other of which is the number of DISC photomultiplier tubes that fired.

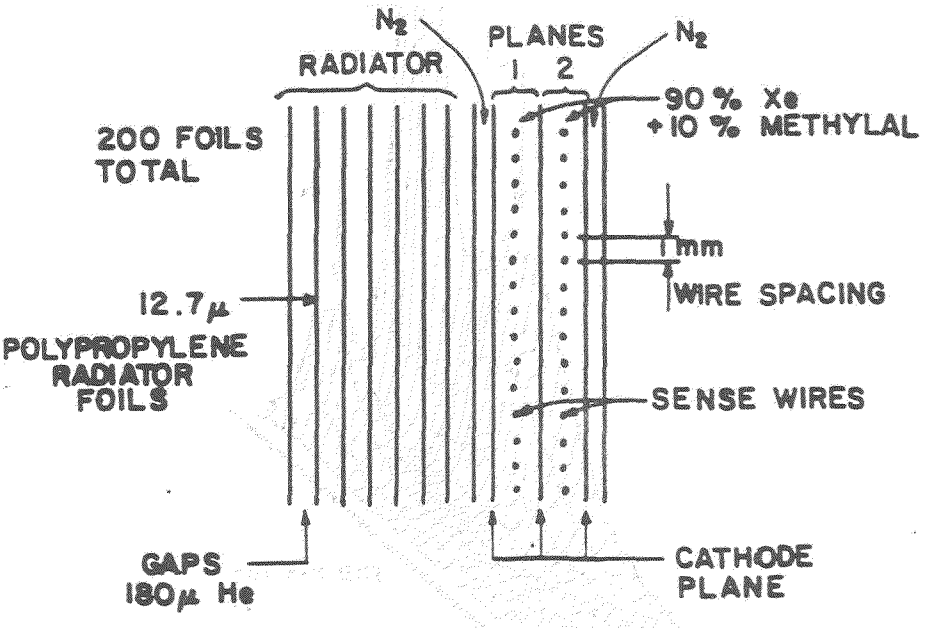

Fig 3. Schematic of one of the 24 radiator-chamber modules of the TRD.

TRD ELECTRONICS

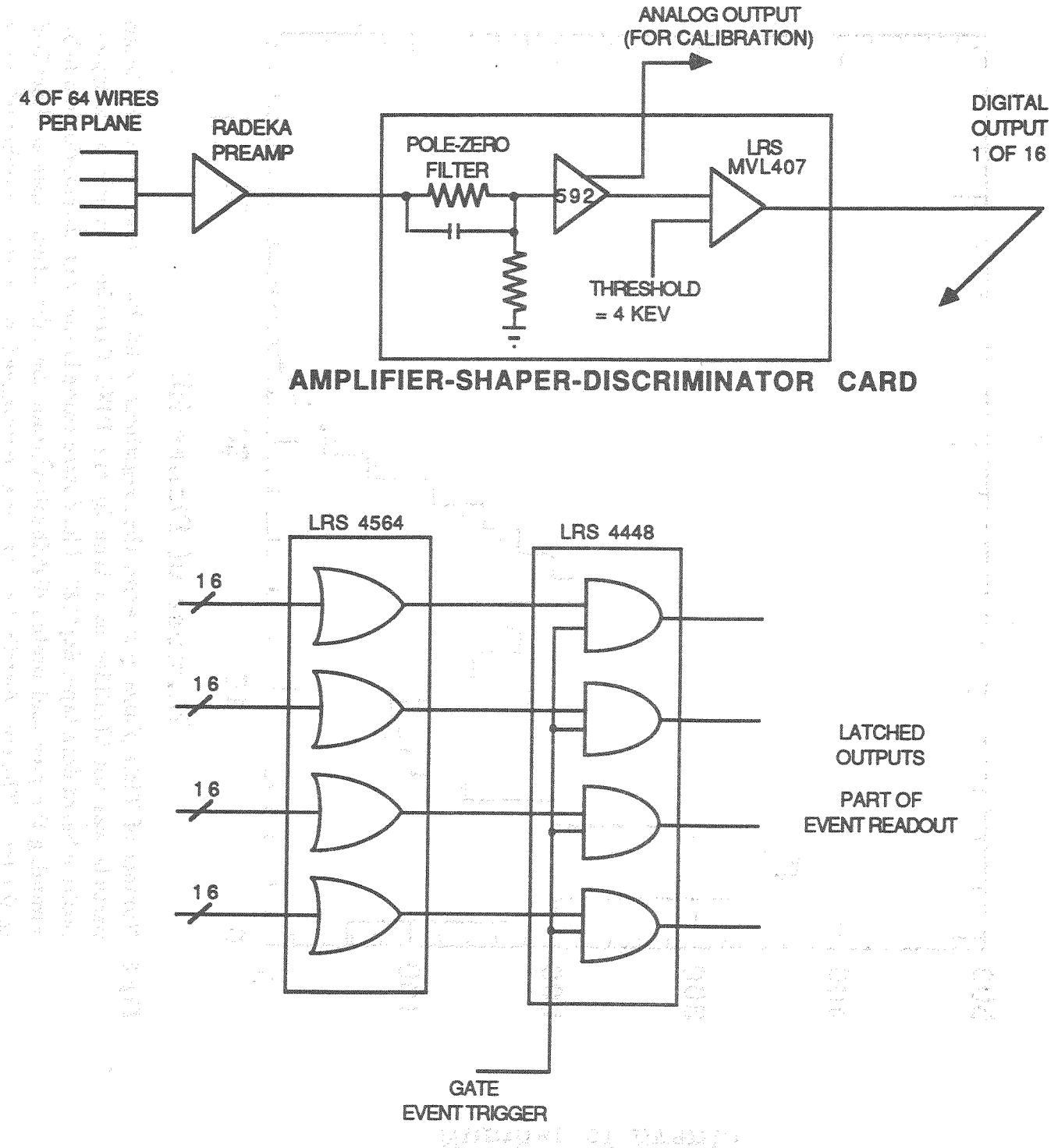

Fig 4. TRD front end electronics and read out system.

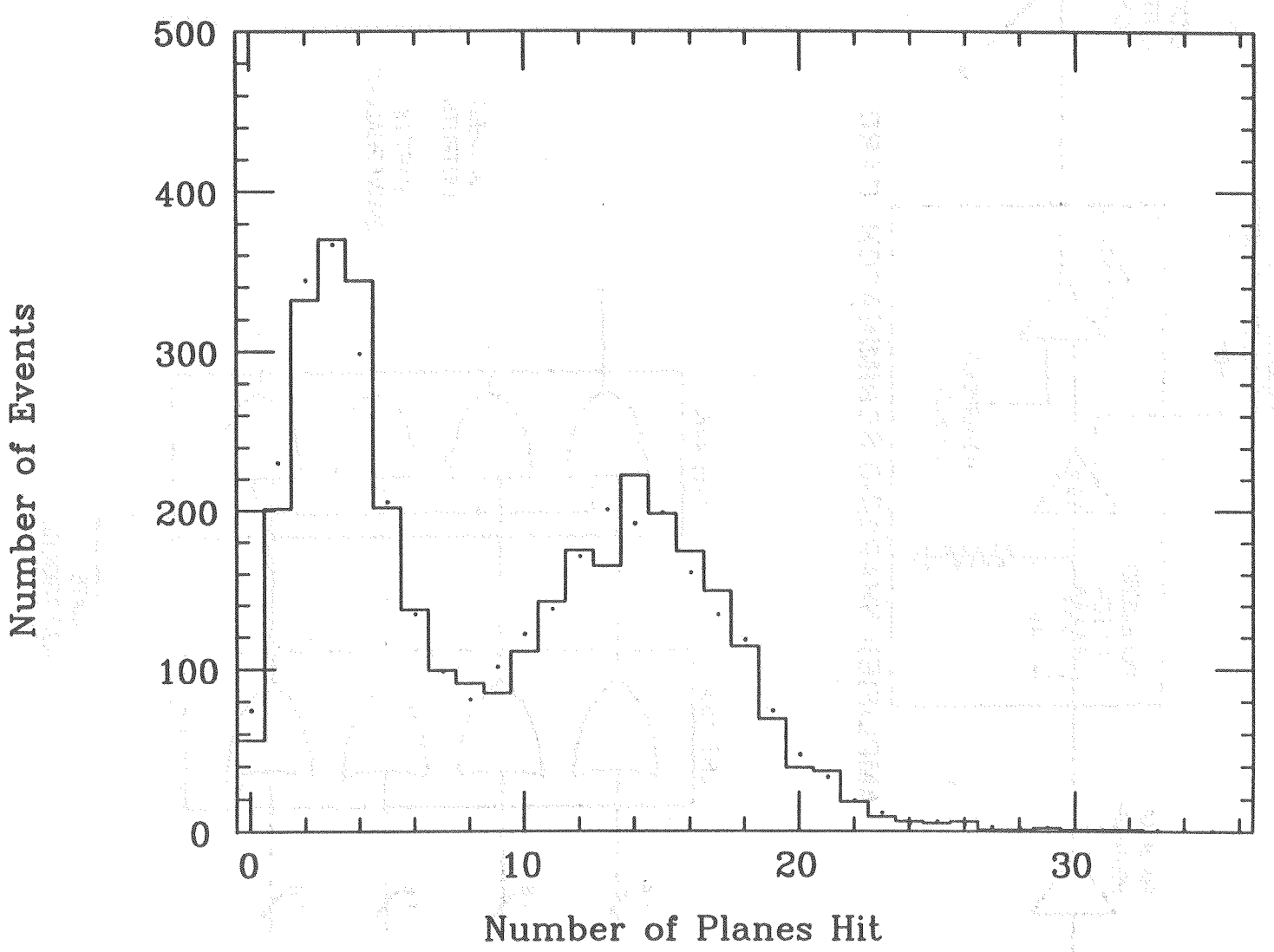

Fig 5. Number of TRD planes per event that registered a hit for events where the beam particle was not identified as a kaon by the DISC Cerenkov counter on a typical positive beam data tape, SQ1123. The dotted curve is the trial distribution made by summing the pion and proton distributions from the calibration tapes as described in the text. The trial distribution has been normalized to the same number of events as the data.

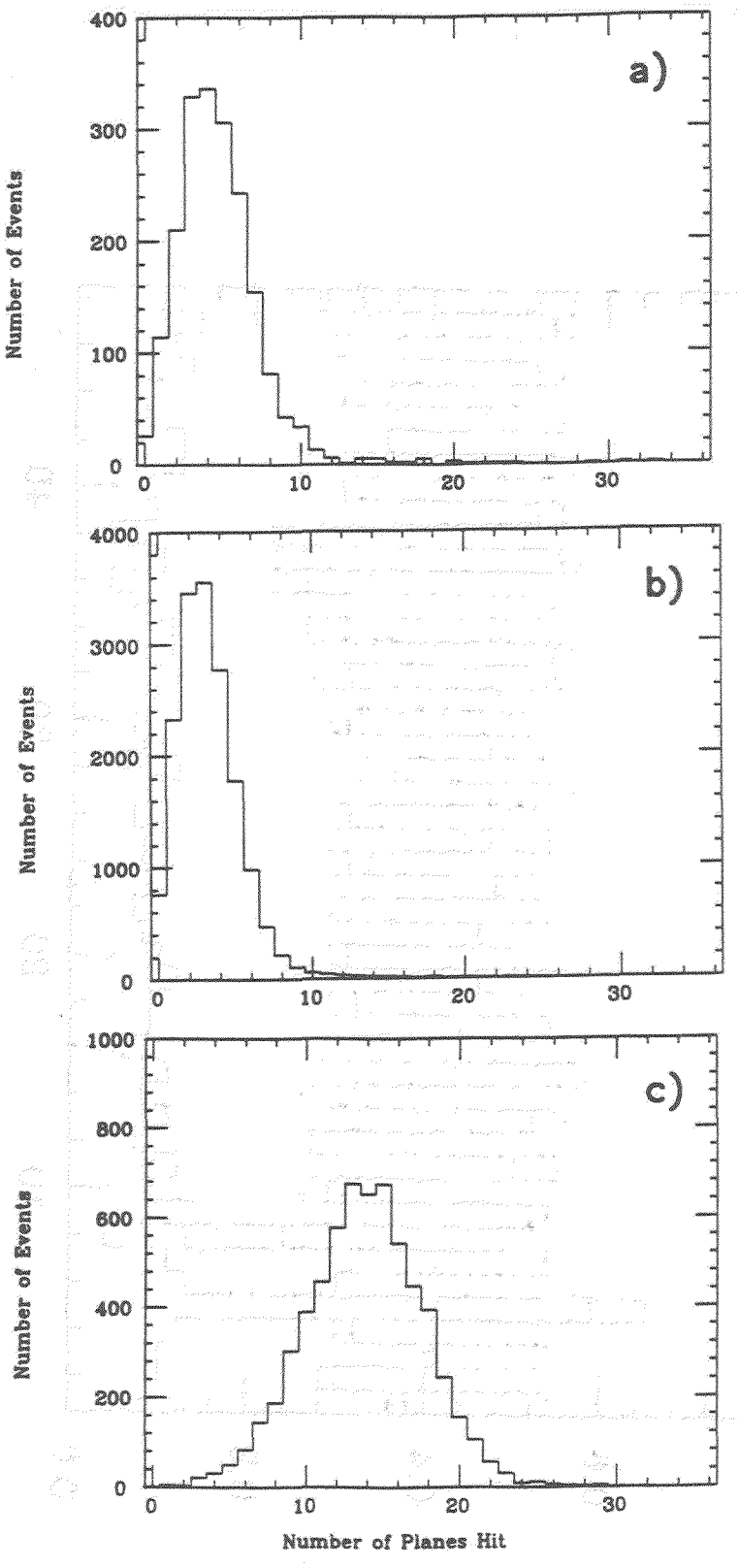

Fig 6. Number of TRD planes per event that registered hits for samples of DISC tagged events. The events shown in a) are the kaons from SQ1123. The events shown in b) and c) are the protons and pions, respectively, from calibration runs taken at about the same time in the data taking run.

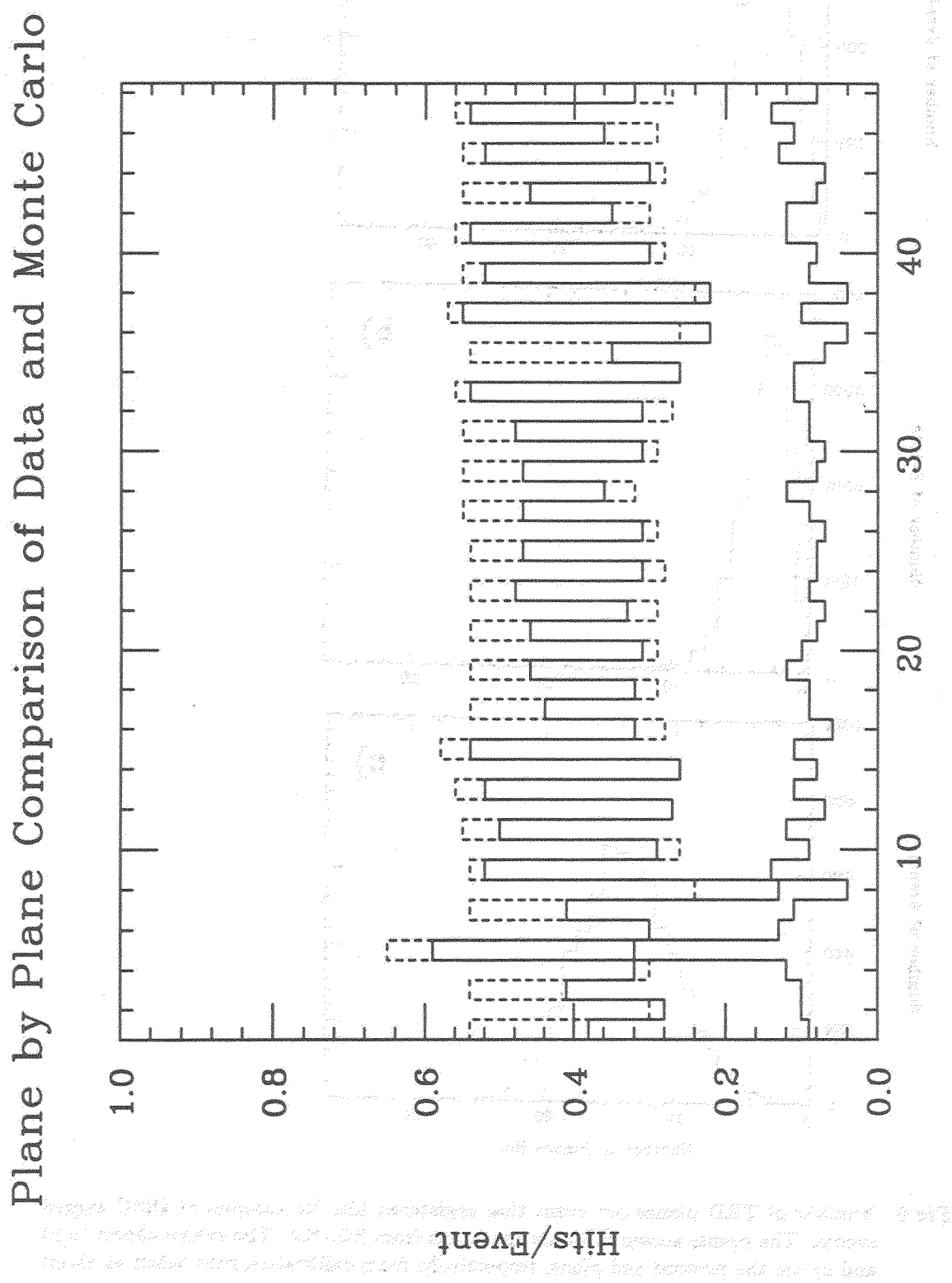

Fig 7. Hit probability per plane of the TRD per event for protons (lower solid line) and pions (upper solid line). The Monte Carlo prediction for the pion hit probability per plane per event is shown as the dashed line.

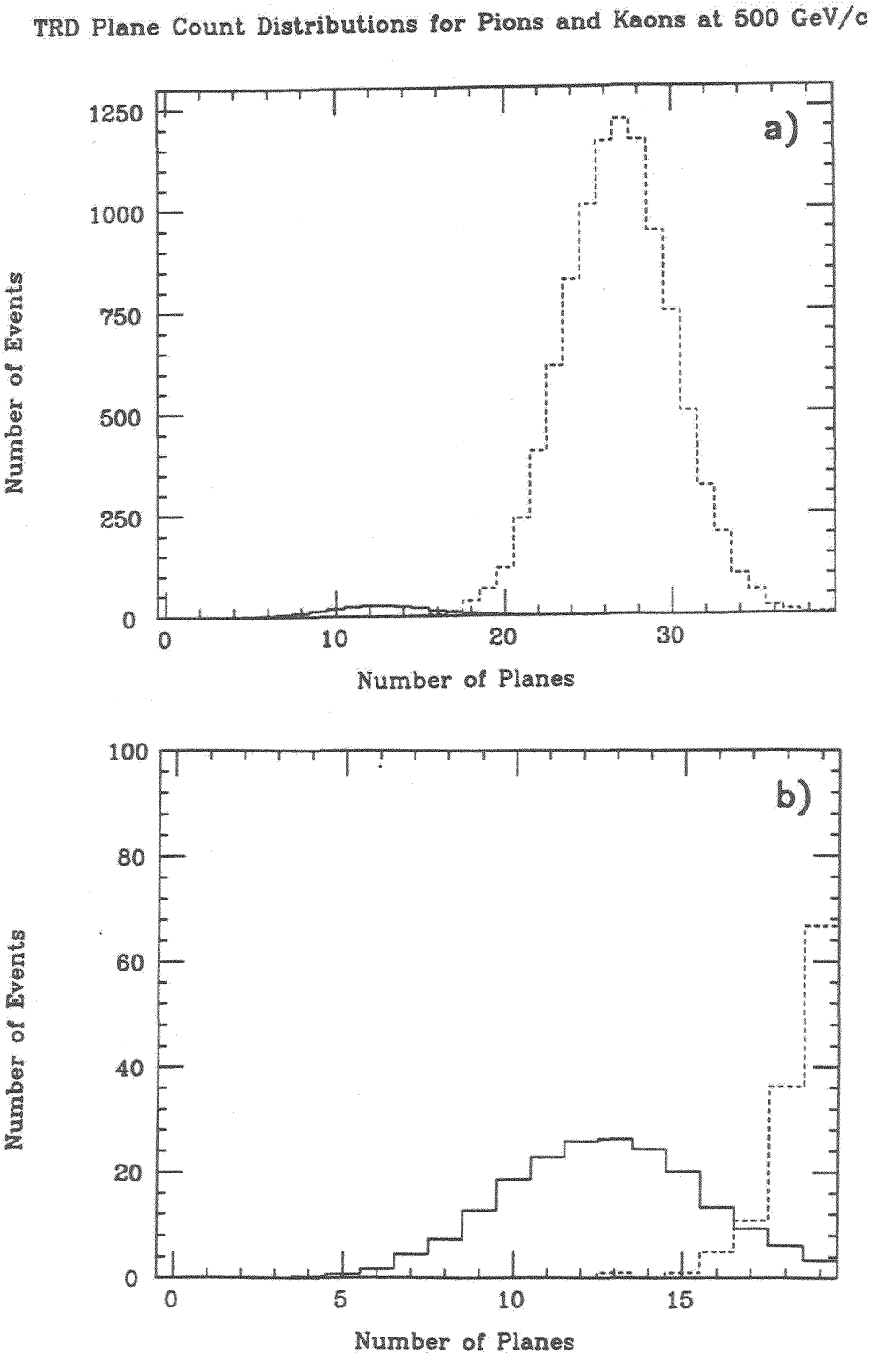

Fig 8. TRD plane count distributions for pions (dashed line) and kaons (solid line) as predicted by the Monte Carlo program for a 500 GeV/c beam incident. The kaons have been assumed to be 2% of the beam. b) is a detail of the low plane count portion of a) with a different scale to show in more detail the separation expected for the two species.

The NA31 Transition Radiation Detector

Talk given at the Symposium on Particle Identification
at High Luminosity Hadron Colliders
Fermilab April 5-7 1989

Giles Barr
CERN, 1211 Geneva 23, Switzerland

Abstract

The NA31 collaboration have recently added a transition radiation detector to their experiment. The detector includes a number of novel features which are described.

Introduction

The NA31 collaboration[1] at CERN have recently upgraded their detector by the addition of a transition radiation detector. Although the detector and readout are unsuited to the very high rate environment which will be encountered at the SSC, the detector incorporates a number of modern design features which work successfully and could be used in the design of an SSC detector.

The primary purpose of the NA31 experiment[2] is to measure the parameter that quantifies direct CP violation in the neutral kaon system, ϵ'/ϵ. To do this, the experiment measures the double ratio

$$R = \frac{\Gamma(K_L \mapsto \pi^\circ\pi^\circ)/\Gamma(K_L \mapsto \pi^+\pi^-)}{\Gamma(K_S \mapsto \pi^\circ\pi^\circ)/\Gamma(K_S \mapsto \pi^+\pi^-)}.$$

During the analysis of the data taken in 1986, it was realised that one of the important contributions to the systematic error was the subtraction of the background ($K_L \mapsto \pi e\nu$, $\pi\mu\nu$ and $\pi^+\pi^-\pi^\circ$) in the $K_L \mapsto \pi^+\pi^-$ mode. A transition radiation detector has been added for the 1988 and 1989 runs in order to improve the electron/pion identification of the experiment. The design criteria for the TRD were as follows.

1. Large area ($\approx 5\text{m}^2$).
2. Depth 1 m maximum.
3. 4 wirechambers preceeded by 4 sets of radiators
4. Maximum separation of π and e at around 50 GeV.
4. Mylar wirechamber cathodes to minimise the amount of matter in the experiment.
5. Chambers at atmospheric pressure so that the pressure on either side of the mylar foils is the same.
6. Long term gain stability because the cuts which are made in the K_L beam are also made in the K_S beam to eliminate the effect of the acceptance of the cut on R.

The overall layout of the detector is shown in figure 1. The detector is described in detail elsewhere[3-6].

The Gas in the Radiators and Chambers

In order to minimise spatial gain variations in the chambers it is important to equalize the gas pressures on either side of the mylar foils. A 10μbar difference causes a 100 μm shift in the foil position which will change the gas gain of the wires by 2.5%. Since the chamber is mounted vertically, the hydrostatic pressure difference from the top to the bottom is also important. If there is a one amu difference in molecular weights between the gasses on either side of the cathode, the differential pressure will change by 10μbar from top to bottom of the chamber. In order to eliminate this, we use a heavy radiator gas, CO_2, and a mixture of xenon, helium and the light quencher methane in the chambers. The fraction of methane (15%) keeps the total drift time in the 2.5cm chamber gap below 2μs. The remaining components of approximately 30% xenon and 55% helium are tuned so that the mixture has the same density as CO_2.

We use a recirculating gas system to purify the chamber gas. A microprocessor is used to regulate the differential pressure at the centre of the chambers to within 1 μbar by adjusting the flow control valve to the chambers every 50 seconds. Since the helium diffuses out of the system faster than the other gasses, we find it necessary to inject about 20 l/day of helium into the recirculating mixture to maintain zero differential pressure at the top and the bottom of the chambers. This is also done under control of the microprocessor.

The Gas Gain Regulation System

The detector incorporates a gas gain stabilization system (fig 2) which monitors the gains of the chambers and maintains them constant. Four cadmium-109 sources are installed on each chamber. A MicroVAX computer is used to accumulate pulse height distributions (fig 3) from each source. The peak position of the source is kept constant by adjusting the chamber high voltage. This corrects for gain variations caused by pressure, temperature and gas composition changes. A voltage change occurs when a total of $N_{ch} = 10^5$ trigger have been collected on each chamber which takes approximately 7 minutes. The RMS gain variation σ_g for different values of N_{ch} is shown in figure 4. The gain variation is less than 0.2% for a wide range of values of N_{ch}. For large values of N_{ch}, slow fluctuations in the system dominate σ_g, while for small N_{ch}, statistics dominate. The data for the source regulation are taken outside of the SPS burst. We have verified that the gain does not change during the burst[3].

Data concerning the behaviour of the chambers are shown in figure 5 for a period of about 3 days. Figure 5(a) shows the amount of gas in the storage tank. Gas is transferred between the tank and the chambers to regulate the chamber pressure. The tank pressure also reflects the daily additions of helium. The density of chamber gas is measured by monitoring the difference in pressure at the top and bottom of the chambers (figure 5(b)). Figure 5(c) shows the high voltage applied to one of the chambers over the same period of time and figure 5(d) shows the gas gain at one of the source positions. The discontinuities correspond to the daily inlet of helium.

Electron–Pion Separation

As part of the routine calibration of the experiment during the summer running period of 1988, the detector was exposed to beams of pions, electrons and muons. The TRD signals associated with each charged track are reconstructed by first searching for independent clusters in each of the TRD chambers and selecting the closest cluster to the trajectory of the track as measured by the drift chambers. Figure 6 shows the response of one chamber of the TRD to the electron and pion beams.

The four pulses on each track are combined by calculating the mean of the three lowest pulse heights. Omission of the highest pulse height reduces the possibility that a pion is misidentified as an electron when there is delta ray production. The responses of the trimmed mean for the muon, electron and pion beams are shown in figure 7. The electron rejection as a function of pion loss is calculated from this data (figure 8). For example a 2% pion loss in the analysis removes all but 11% of the electron sample. The use of a maximum likelihood method of combining the four chamber signals gives a slightly better electron-pion separation[5]. The muon and pion distributions in figure 7 are similar except at high pulse height where the pion tail is due to pion interactions in the radiators.

Comments on the Applicability of these Techniques to Future Detectors.

Our experience with the $Xe/He/CH_4$ mixture has been very good. The drawback to the technique is that the depth of the chamber must be increased to contain enough xenon for x-ray absorption which increases the charge collection time.

It is worth considering whether it would have been better to purge the chambers with fresh gas rather than to invest in a complicated gas regulation system. The answer to this depends on how expensive the xenon is and how long the experiment must run for. An advantage of our system is that the gas mixture remains stable long term which is very important in our experiment. A disadvantage of the recirculating system is that over time N_2 builds up in the system (it is not removed by the purification). This is not a severe problem for us but it does dilute the amount of Xe and changes the absorption probability of the transition radiation.

The sources are used to regulate the gas gain of the chamber, which is slightly different from the chamber response to the passage of pions and electrons through the TRD. The regulation does not take account of the variation of the amount of charge deposited from ionisation loss and x-ray absorption due to density variations. It would have been better to run the chambers at fixed absolute pressure. Such a design was not possible, because of incompatibility with existing parts of the experiment.

References

[1] The NA31 collaboration is
CERN: G. Barr, D. Coward, D. Cundy, N. Doble, L. Gatignon, V. Gibson, P. Grafström, R. Hagelberg, G. Kesseler, J. van der Lans, H. Nelson, H. Wahl, EDINBURGH: R. Black, D. Candlin, J. Muir, K. Peach, MAINZ: H. Blümer, R. Heinz, K. Kleinknecht, P. Mayer, B. Panzer, B. Renk, H. Rohrer, ORSAY: E. Augé, D. Fournier, P. Heusse, L. Iconomidou-Fayard, I. Harrus, H. Sander, A. Schaffer, PISA: L. Bertanza, A. Bigi, P. Calafiura, M. Calvetti, R. Carosi, R. Casali, C. Cerri, G. Gargani, I. Mannelli, A. Nappi, G. Pierazzini, SIEGEN: H. Burkhardt, C. Becker, M. Holder, A. Kreutz, R. Ossa, G. Quast, M. Rost, W. Weihs, R. Werthenbach, G. Zech.

[2] H. Burkhardt et. al. Nucl. Instrum. Methods **A268** (1988) 116.

[3] G. D. Barr et. al. IEEE Trans. Nucl. Sci. **36** (1989) 66.

[4] In preparation for Nucl. Instrum. Methods

[5] A. Kreutz, Diploma Thesis, University of Siegen, FRG. (1989)

[6] I. Harrus, These de Docteur en Sciences Physiques, Université de Paris Sud, Centre d'Orsay. LAL 89-13.

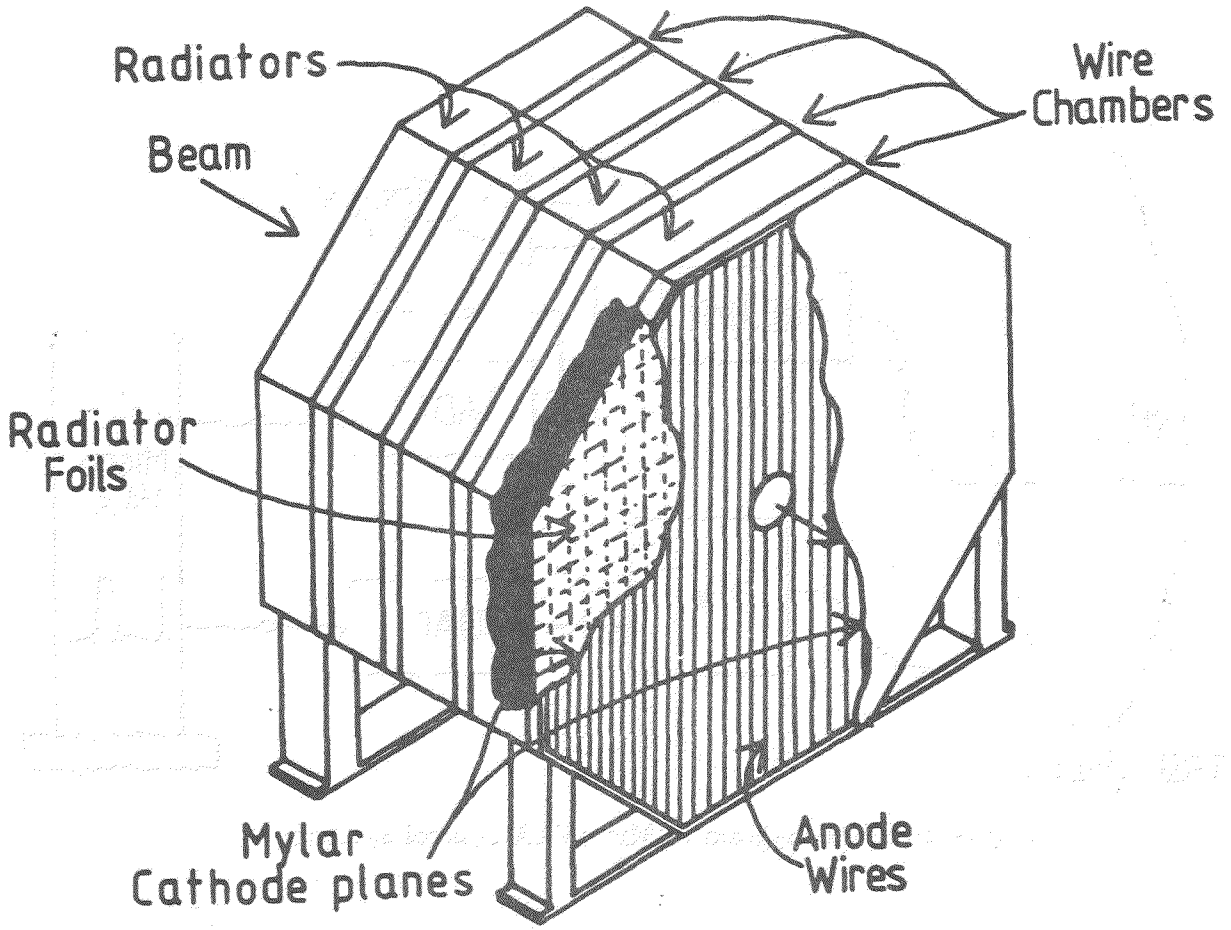

Figure 1: Detail of the TRD radiator and wire chamber construction.

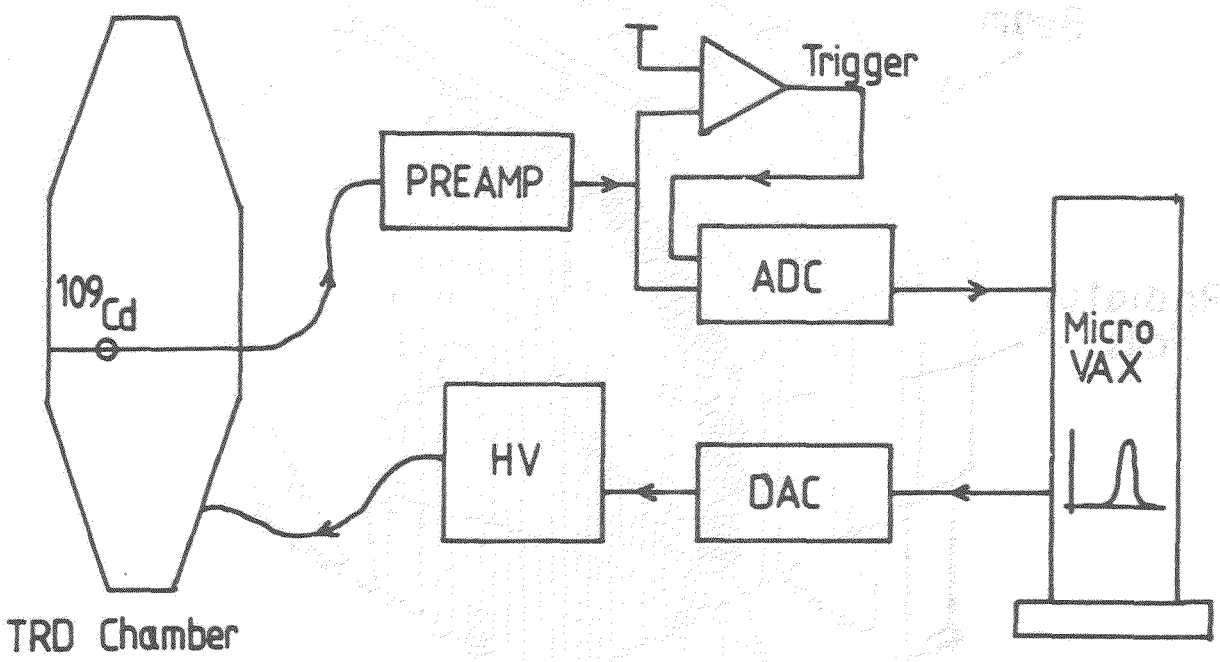

Figure 2: Block diagram of MicroVAX control system.

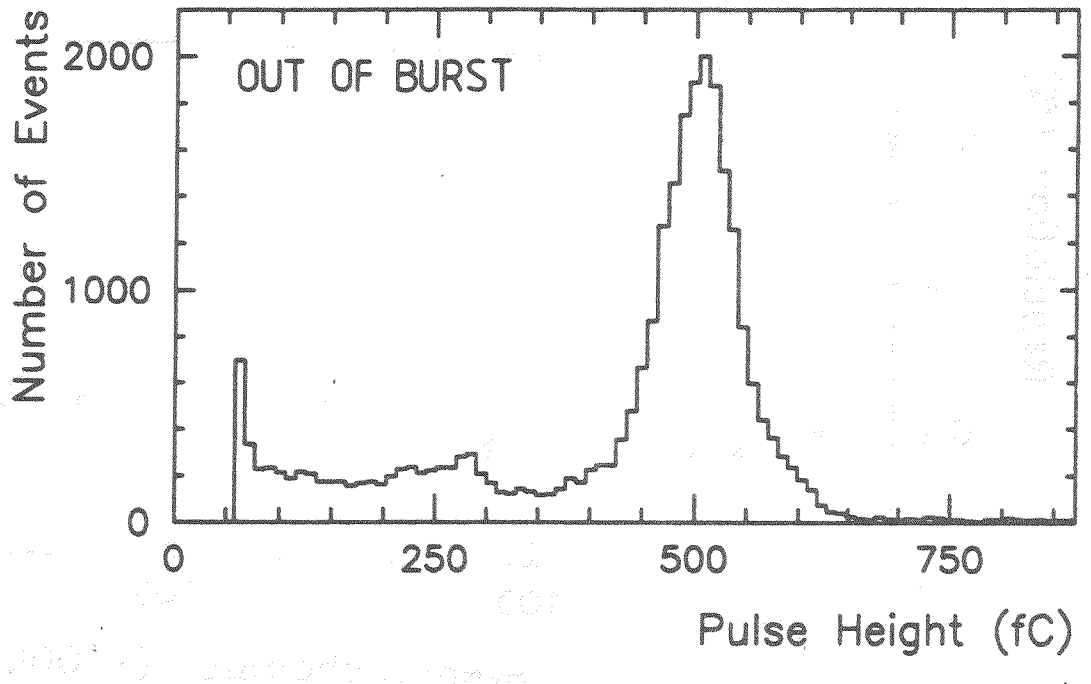

Figure 3: Monitor channel pulse height distribution, out of burst, showing the peak from the ^{109}Cd source.

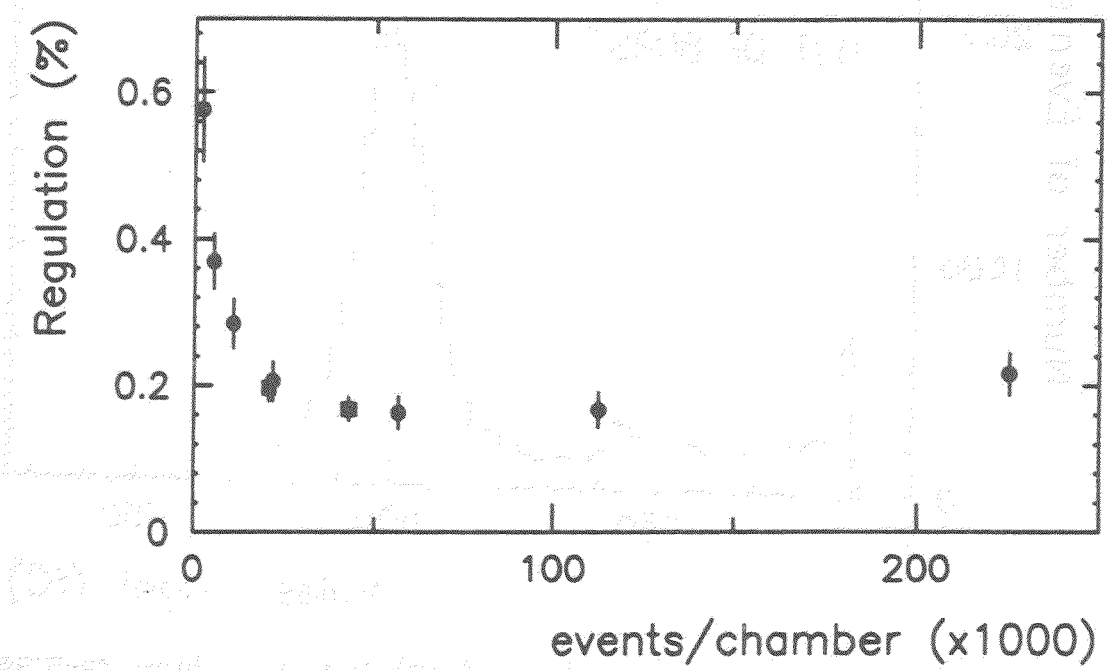

Figure 4: RMS gain variation as a function of number of events used to determine correction.

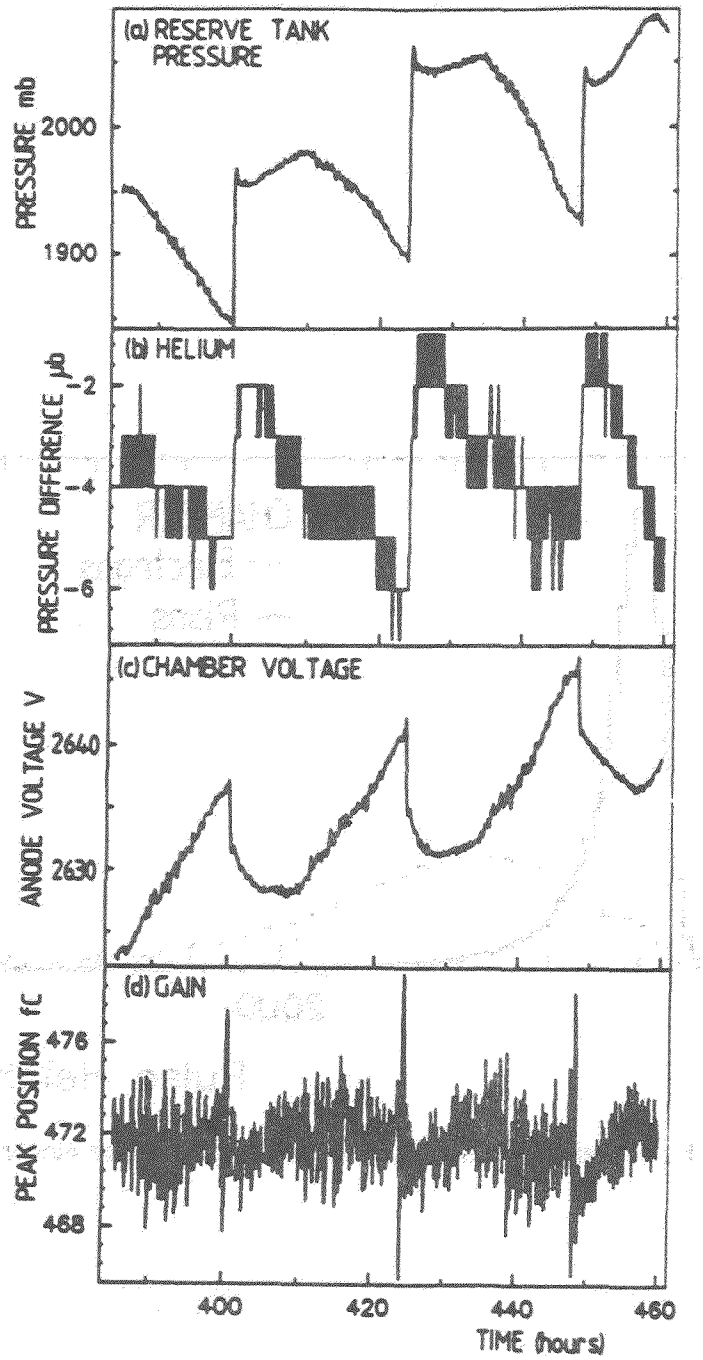

Figure 5: System variation over 3 days. (a) gas in high pressure vessel; (b) gas density, indicated by pressure differential from top to bottom or chamber; (c) High Voltage on cathode; and (d) Gain of one source.

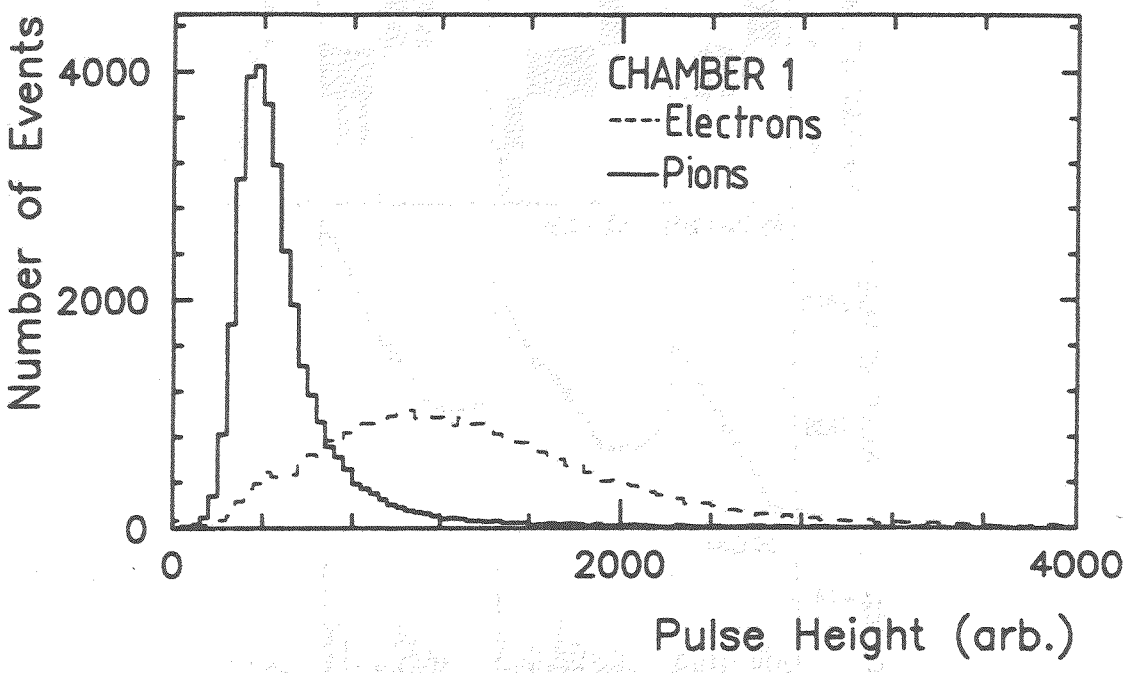

Figure 6: Pulse height distribution of one chamber for electrons and pions.

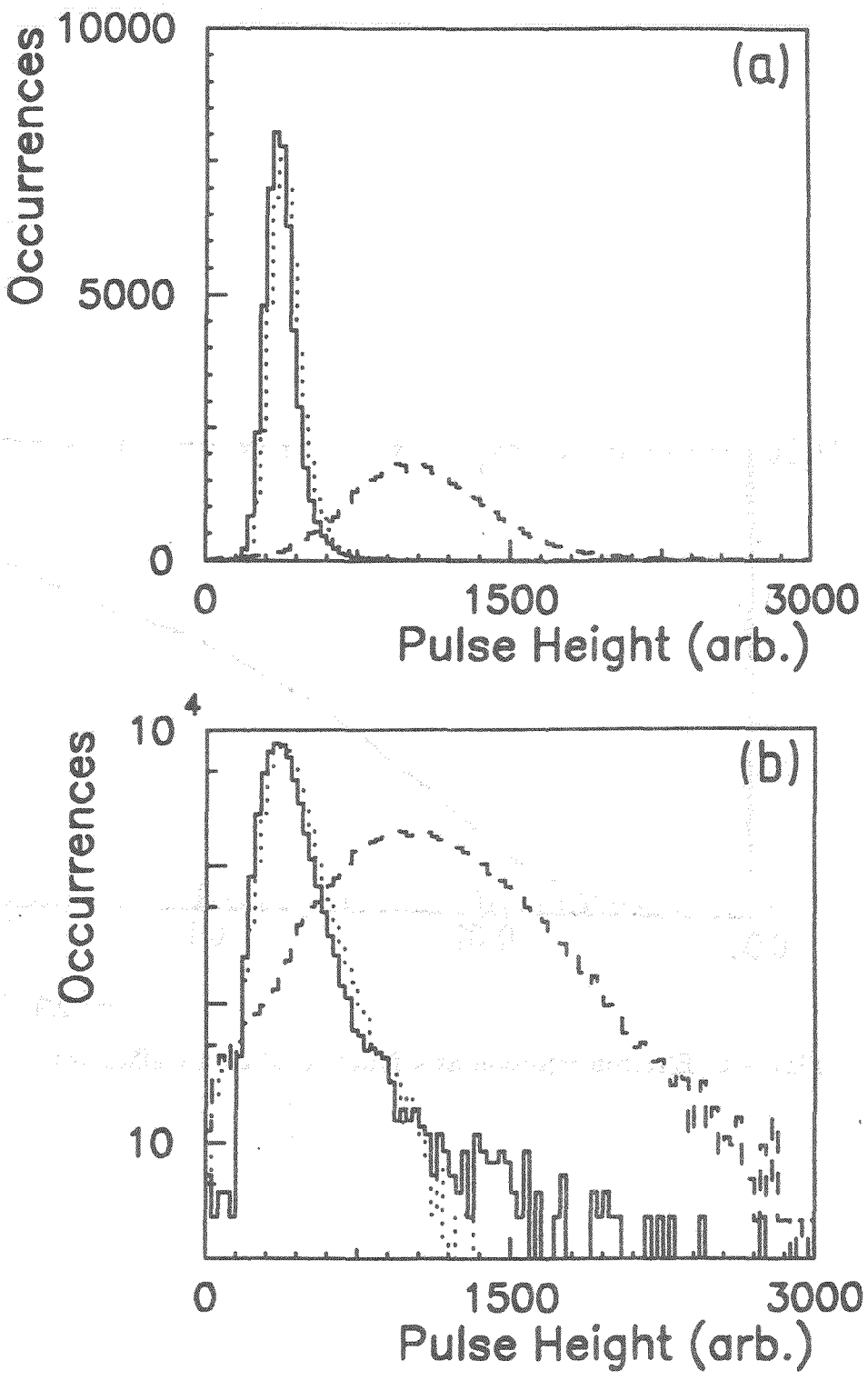

Figure 7: Distribution of mean of lowest 3 pulse heights. Solid-Pions; Dashed-Electrons; Dotted-Muons. (a) linear and (b) logarithmic scales.

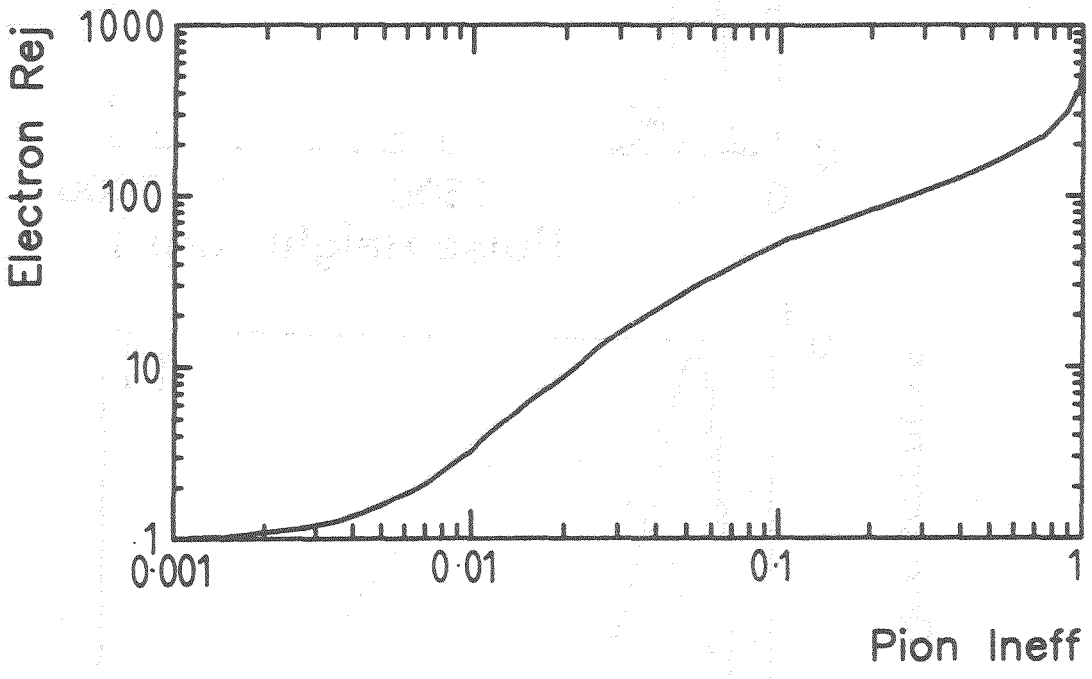

Figure 8: Electron rejection as a function of pion inefficiency.

THE HELIOS TRD

Talk presented by M. Clemen
University of Pittsburgh
Pittsburgh, Pennsylvania

(Representing the HELIOS Collaboration at the
Symposium on Particle Identification at High Luminosity Hadron Colliders)
April 5-7, 1989

This is a description of the Transition Radiation Detector (TRD) built for, and used in, the electron trigger in the HELIOS experiment at CERN. Transparency 1 shows those involved in the construction of the TRD.

The HELIOS Electron Spectrometer is designed to measure the electron/positron signal produced directly in p-Be interactions, at 450 GeV beam energy. HELIOS is a fixed-target experiment. The detector layout is shown in Transparency 3. The TRD lies about 3m downstream of the target, covering the center 100 mrad. cone, with a hole for the beam. The electron trigger incorporates a fast lookup table, extrapolating tracks directly from the interaction point in the target, through the TRD, to a shower in a highly segmented Uranium Liquid Argon Calorimeter (ULAC). The active components of the trigger are a 400 channel silicon pad detector, with two levels of discrimination to suppress target photon conversions, a TRD with X/Y tracking capability, and the ULAC. The TRD provides the online pion rejection, and the ULAC electro-magnetic section provides the shower energy measurement.

Transition radiation occurs when a relativistic charged particle crosses an interface between two media with differing dielectric constants. The total intensity of photons radiated at each interface is proportional to the relativistic quantity gamma $= 1/\sqrt{1-(v/c)^2}$. Transparency 6 shows the normalized intensity of transition quanta as a function of the quanta frequency. (Note the variable "ν" here is the quanta frequency normalized to the particle γ, and to the plasma frequency of the material transversed). Typically, the range of $\nu = 0.1$ to $\nu = 1.0$ covers the region of x-rays in the few KeV range, up to 10's of KeV. TRD detectors are generally built to measure the quanta in this range, and so are sensitive to about 1/2 of the total TR energy.

Real TRD's can take advantage of a coherent behaviour between multiple interfaces. In Transparency 7 one sees that the differential intensity, by TR quanta frequency and by quanta angle from the particle track, for many, equally spaced planes of material, is simply that for a single plane of material, times this coherence factor. The formulae shown do not include self absorption in the radiator foils. This coherence factor is a function of the material thickness and the material spacing, both normalized to a characteristic "formation length" for transition radiation. This "formation length" is primarily a function of the plasma frequency of the material, the TR photon frequency, and the the incident particle γ; the "formation length" is typically 10's of microns. A good radiator material then gives a reasonable probability for TR production, with low absorption. By a judicious choice of transition material, thickness and spacing, one can achieve a significant amount of transition radiation, for particle γ's of a few thousand.

The mechanical construction of the TRD is as shown in Transparency 4. The device is approximately 0.9 x 0.9 x 0.7 m^3, and weighs about 1/2 of a metric ton. It sits on a granite

table, for stability, and is divided into 8 planes of radiator and Proportional Wire Chamber. The PWC's have wires in each of the X and Y directions, for the capability of track finding.

The HELIOS TRD uses Polypropylene foils, $(CH_2)_n$, which gives a formation length, for the transition quanta of interest, of about 20 μm. The radiators are divided into two groups of foils. One group has 150 foils of PP, 20 μm thick, with a 250 μm spacing, and the other group has 100 foils, 30 μm thick, with a 170 μm spacing. The first group is optimized for the softer x-rays detected, and the second group for the harder x-rays. Since a major loss of TR x-rays is caused by absorption in the radiator foils themselves, and since the lower frequency x-rays have a larger absorption cross-section, the thicker foils are placed upstream of the thinner foils in each radiator set. There are eight planes of radiators. The total thickness of the radiators is 11% of a radiation length of PP.

The PWC's used in the HELIOS TRD contain 95% Xe, 5% iso-butane. Each set of 250 radiator foils sits in front of a PWC. The "drift space" of the PWC is 10 mm of the gas mixture, making about one characteristic absorption length of Xe for the TR quanta produced in the radiator. A photo-electron is produced, which travels about 100 μm before it is stopped. A trail of ionization is left along its path as it looses energy in the gas in the ionization electrons then drift in the "drift space" towards the wire cathodes leading into the avalanche region. The cathodes separating the drift and gain regions of the PWC's are formed with wires strung up-and-down, in the vertical, so that they sample the X coordinate. The "cluster" of ionization from the electrons drifts towards the cathodes, passing them into the avalanche region. Here, the higher field gradient causes an avalanche toward the anode wires. The anode wires are strung back-and-forth, sampling the vertical, Y, coordinate. The gas gain is about 2×10^4.

The charge from the avalanche is collected directly on the anode wires, and goes to a preamp and a modified time-pickoff. This pulse of charge induces a pulse on the spatially adjacent cathode wires. The characteristic spatial distribution of cathode wires with an induced pulse is about 3 times the anode wire spacing. Hence the cathode wires are hard-wired together into cathode strips. The characteristic pulseheight of the induced pulse on the cathode strip is about 1/3 that on the anode wire. The charge induced on each cathode strip then is pre-amplified, and goes to its own time pickoff. These time pickoffs were used at the ISR. In HELIOS they have been modified to discriminate the incoming pulse so that the outgoing result is a 20 nsec pulse. The deadtime of the pickoffs is about 40 nsec. The deadtime to count one cluster is limited by the size of the cluster when it reaches the cathode strips (diffusing to a spatial size of about 1 mm), and by the deadtime of the avalanche region during charge collection at the anode wire.

The time distribution of clusters counted in electron triggers, is shown in Transparency 11. One sees an initial peak, constituting about 10% of the total clusters. This initial peak is due to the passage of minimum ionizing particles through the avalanche region of the detector. Ionization deposited in this region will occasionally result in a cluster counted. The dominance of the peak is a result of the large number of pions present. The total drift time for the ionization electrons resulting from capture of TR x-rays from a single electron crossing the detector is about 700 nsec. At this point the gate to the scalers counting the pulses is closed, preventing more from being counted.

After the initial minimum ionizing peak in the number of clusters counted, the time distribution reaches a plateau that slowly falls. These, then, are the TR clusters drifting in. The slow fall in the plateau is from the diffusion of the clusters. This loss of clusters to diffusion gives an efficiency loss for TR quanta detection. There is a bias against detecting those quanta that are absorbed early in the drift space. One method to avoid this efficiency loss is to lower, as a function of drift time, the pickoff thresholds. For this reason the "Intelligent Threshold Generator" (ITG) was built. The threshold on the pickoffs, after the interaction, with the ITG, is shown in Graph 2, on Transparency 11. The threshold drops from

a constant value, after the initial minimum ionizing "clusters," and then falls linearly until the end of the scaler gate. The resulting distribution of clusters counted, as a function of time, is shown in the 3rd graph in Transparency 11.

In the high multiplicities of real data taking conditions, HELIOS experienced a much lower pion rejection than expected in the TRD. The electron-trigger background consists of mis-identified pions, and of electrons from trivial sources. Pions can give a trigger, both from "clusters" that are counted due to ionization in the avalanche zone itself, and from the β rays, or knock-on atomic electrons that the pions can cause in the drift region. For the large mis-identified pion background, in use of the ITG is a disadvantage, in that it allows ionzation "clusters" from pions to be counted.

The ITG in HELIOS was used in the 1986/1987 data taking, but has been removed. Several other steps were taken to improve the pion rejection, and the reliability of the TRD operation. A hole was made in the center of the radiator material, for the beam. The scaler gate has been moved, as in Transparency 12, to exclude the initial peak in the cluster spectra. This avoids counting the minimum ionization "clusters." In this configuration it is believed that the best rejection for a given efficiency is achieved. The difference between the initial and current TRD rejection can be seen, in the level of contamination in the electrons, identified offline.

The TRD cluster-counting scalers are interfaced to an elaborate trigger involving lookup tables between the ULAC, the silicon pad array, and the TRD. A schematic for the scalers is shown in Transparency 13. The anode wires (cathode strips) in each plane are made to be projective from the target. Those that are aligned this way each go to a scaler card, with 8 inputs for the 8 TRD planes. These signals are multiplexed to test inputs, and then each go to 4 bit scalers. The number of clusters counted per anode wire (cathode strip) per plane is not expected to be more than 2 for each passing electron. The results of the scalers are added, to provide an addition for all 8 projective planes, called a channel sum. To insure that clusters shared between two anode wires (cathode strips) are fully counted in the trigger, a "long addition sum" is formed. The channel sum from the adjacent channel is added to the channel sum initially recorder for the current channel, to form the long addition sum. The long addition is compared to a programmable threshold, typically 6 or 7, and the result is a single bit on or off, signaling the presence of an electron along that projective channel in the TRD.

The electron correlation trigger begins with showers found in the ULAC. The ULAC is divided into 2 x 2 cm towers, and overlapping energy sums of about 6 towers each form what is called a superpad sum. The superpad sums are discriminated, and those over threshold poll the TRD scalers. If there is a spatially corresponding TRD anode wire and cathode strip signaling an electron, then a FIRST LEVEL electron trigger is said to be satisfied. This process is diagrammed in Transparency 14.

A much longer process is performed in the SECOND LEVEL electron trigger. For each superpad over threshold, the silicon pad is polled for a single minimum ionizing particle in a spatially corresponding silicon pad, near the target. If such a hit is found, a closer correlation is defined between the silicon pad hit, and the ULAC, at the TRD. The smaller number of anode wires and cathode strips are polled for an electron signal. If such a signal exists in both the X and Y coordinate, a SECOND LEVEL trigger is said to be satisfied.

The timing for the electron trigger process is shown in Transparency 15, which shows that the TRD drift time figures prominently in the FIRST LEVEL electron trigger. The average beam crossing rate is 1MHz, and, with an interaction pretrigger, the FIRST LEVEL electron decision is ready in about 2 usec.

The TRD hadron rejection has been measured from the 1988 electron triggered data. The method is outlined in Transparency 16. There are two drift chambers, situated one in front,

and one in back, of the TRD. A track is found in the drift chambers pointing back to the ULAC. If there is an isolated ULAC shower that is greater than 5 GeV, and is within 6 mm of that extrapolated point at the ULAC, according to the cuts in the transparency, then the track is called an electron. If there is no electromagnetic shower within 4 cm of the extrapolated point, at the ULAC, then the track is called a pion. The TRD response was measured with this data set.

The total number of TR clusters counted in a channel sum (a channel sum being the sum of the clusters counted in 8 planes of anode wires or cathode strips that form a projective channel) are shown in Transparency 17. The top two graphs are the responses of the TRD anodes and cathodes to the "pions," the bottom two to the "electrons." One can see that the "electrons" show some pion contamination, due to the finite ULAC rejection, and possibly due also to track overlap. The pion response curves were scaled accordingly, and subtracted from the electron response curves. The result is shown in the top two graphs of Transparency 18. By making a suitable cluster cut, one can find the electron efficiency from these top graphs, and the pion efficiency from the top graphs on Transparency 17. The result is plotted in the graph on the bottom of Transparency 18. Also shown is the result for individual electron and pion beams, both at 45 GeV.

The typical rejection factor for pions in a real electron triggered event is about 50:1. The HELIOS collaboration has found that the rejection of the TRD has suffered greatly just from the high multiplicity environment in p-Be collisions at 450 GeV beam energy. The HELIOS TRD is not capable of X/Y correlated tracking, and the hodoscope ambiguity from mis-identified pions, and real secondary electrons, becomes prohibitive.

In summary, a working TRD has demonstrated pion rejection of 50:1 in moderate primary multiplicity events (approximately 12 charged particles) in the HELIOS experiment at the CERN SPS. This device is capable of X/Y tracking, in an online trigger mode. The pion rejection has been found to be comparable to other TRD's. In retrospect, the use of a pad readout rather than a X/Y strip geometry would greatly enhance the practical TRD rejection, as the background becomes prohibitive at high multiplicities.

B. Dolgoshein
C.W. Fabjan
I. Gavrilenko
A. Kalinovsky
A. Kantserov
S. Maybarov
S. Muraviev
P. Nevski
A. Shmeleva
S. Smirnov
A. Sumarokov
V. Tchernyatin
V. Tikhomirov
W. Willis

High
Energy
Lepton
Ion
O
Spectrometer

Transition
Radiation
Detector

reported by Mark Clemen

HELIOS TRD

Ø. HELIOS

I. Transition Radiation

II. TRD Apparatus

III. Electron Trigger

IV. Results

HELIOS ELECTRON SPECTROMETER

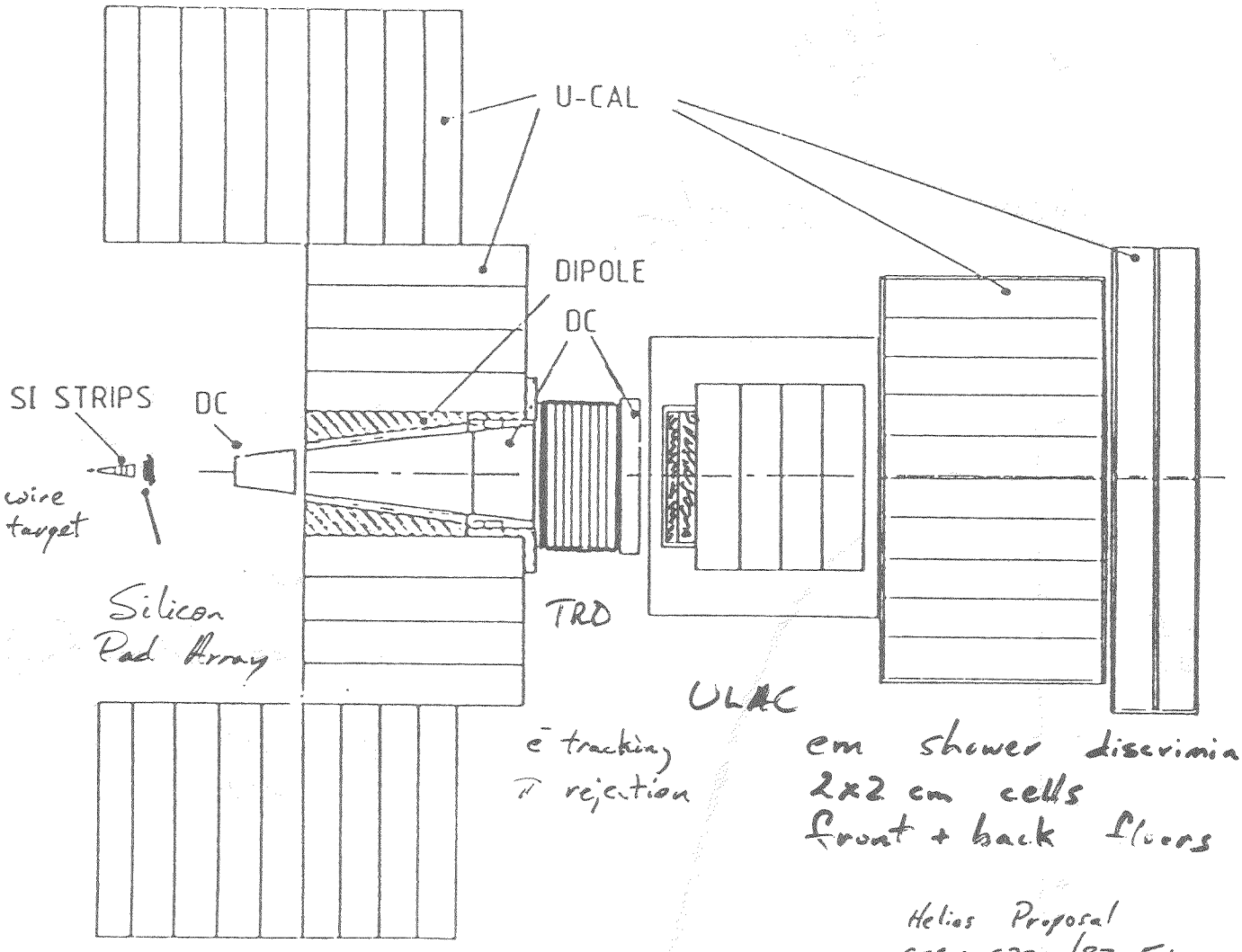

e⁻ tracking
↑ rejection

em shower discrimination
2×2 cm cells
front + back floors

Helios Proposal
CERN-SPSC/83-51
Updated

γ - Conversion Suppression

Transition Radiation

Single Interface

$$\frac{dI}{d\nu} = \frac{\alpha\hbar\gamma\omega_p}{\pi}\left[(1+2\nu^2)\ln\left(1+\frac{1}{\nu^2}\right)-2\right]$$

$$I = \frac{\alpha\hbar\gamma\omega_p}{3}$$

$$N(\nu) = \frac{2\alpha}{\pi}\left[\ln\left(\frac{1}{\nu\sqrt{2}}\right)-\frac{1}{2}\right]$$

$\gamma >> 1$

$\varepsilon(\omega) \approx 1-\left(\frac{\omega_p}{\omega}\right)^2$

$\alpha = \frac{1}{137}$

$\omega_p = 2\pi \times$ (plasma freq.)

$\nu = \frac{\omega}{\gamma\omega_p}$

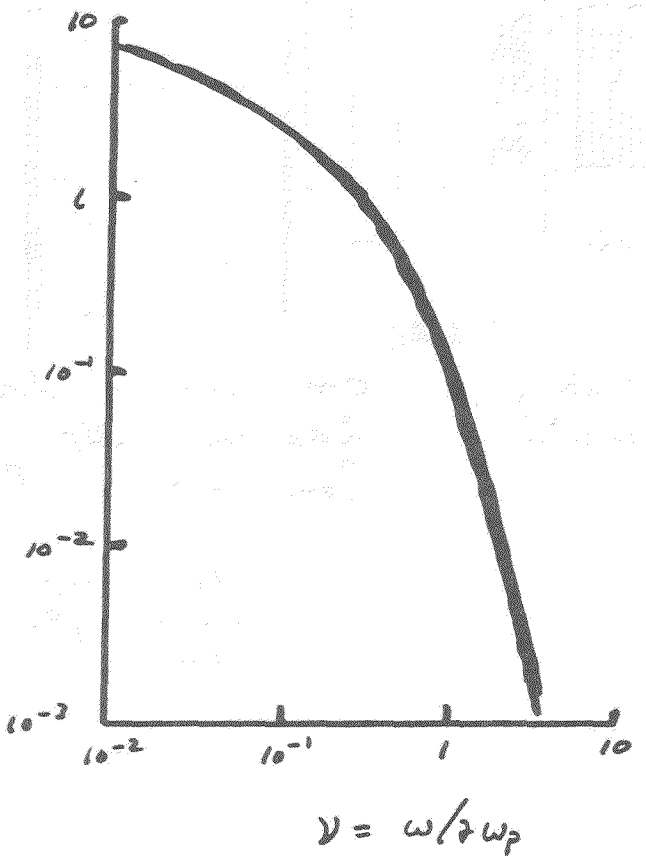

(J. D. Jackson)

G. M. Garibyan

Artru, et al.

- Stack of N foils -

$$\frac{dI}{d\nu\, d\eta} \approx \left[\text{Single Interface}\right] \times \mathcal{L}$$

$$\mathcal{L} = 4\sin^2\left(\frac{\Delta}{2}\right) \frac{\sin^2\left[N\left(\Theta + \Psi\right)\right]}{\sin^2\left(\Theta + \Psi\right)}$$

$$\Theta = \frac{a}{D} \times f(\nu, \eta) \propto \frac{\text{thickness}}{\text{form. l.}}$$

$$\Psi = \frac{b}{D} \times g(\nu, \eta) \propto \frac{\text{spacing}}{\text{form. l.}}$$

$\nu = \frac{\omega}{\gamma\omega_p}$

$\eta = (\gamma\theta)^2$

a = thickness of radiators

b = spacing " "

D = formation length : $d(\nu) = d(1) = \frac{\gamma c}{\omega_p}$

J.D. Jackson

X. Artru, et al.

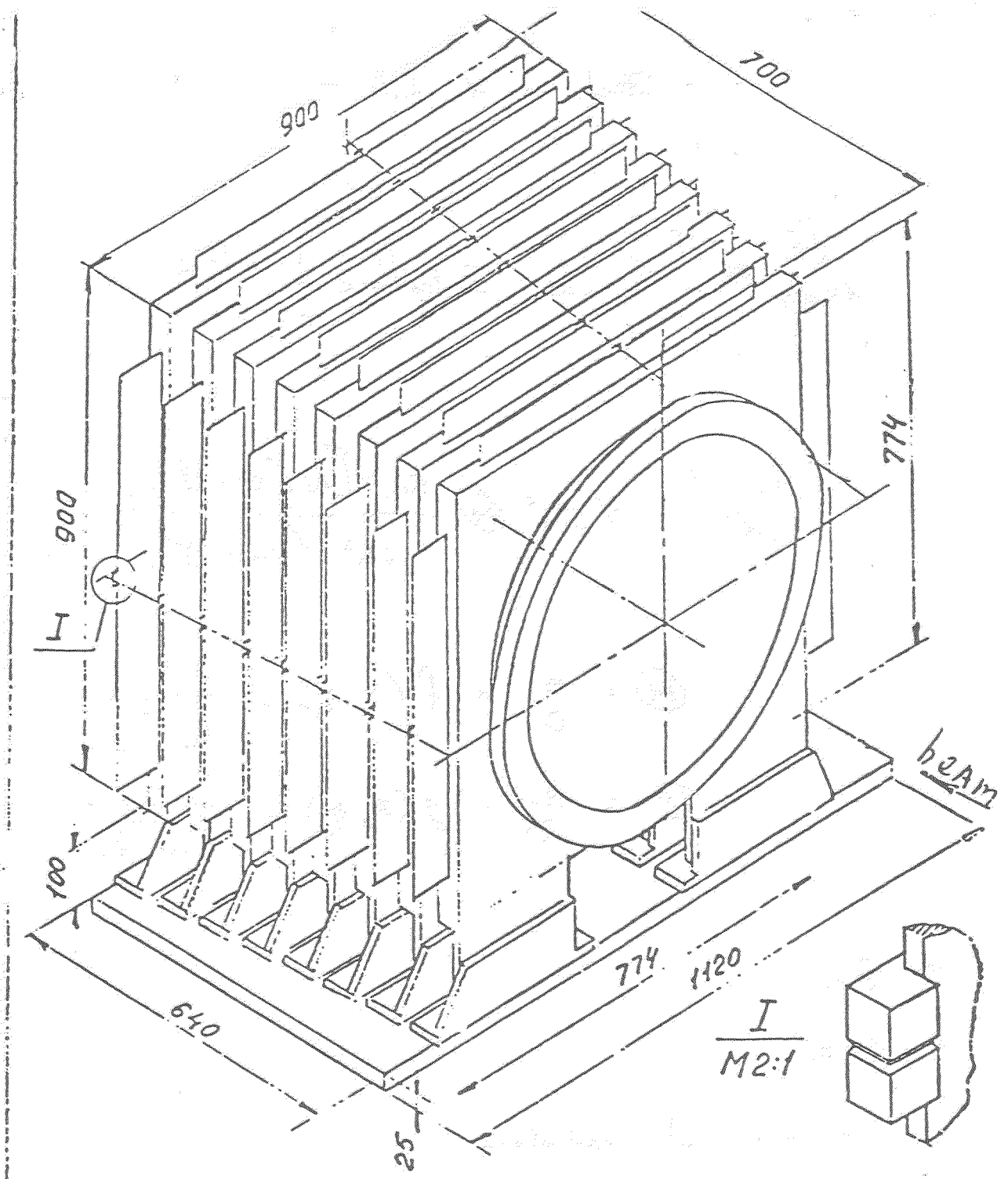

I
M2:1

				ИФК7 61 0000 000		
Изм	Лист	№ докум	Подпись	Дата		
Разработ				TRD	Лит.	Масса / Масштаб
Провер.						1:10
Т. Контр.					Лист	Листов 1
Н. Контр.					МИФИ к.7	
Утв.						

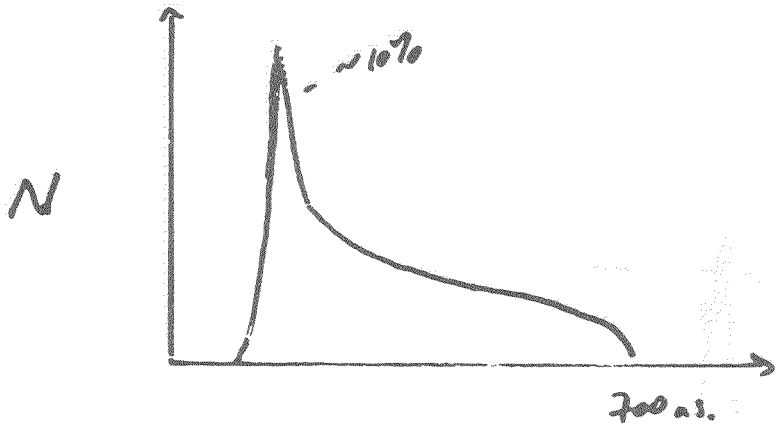

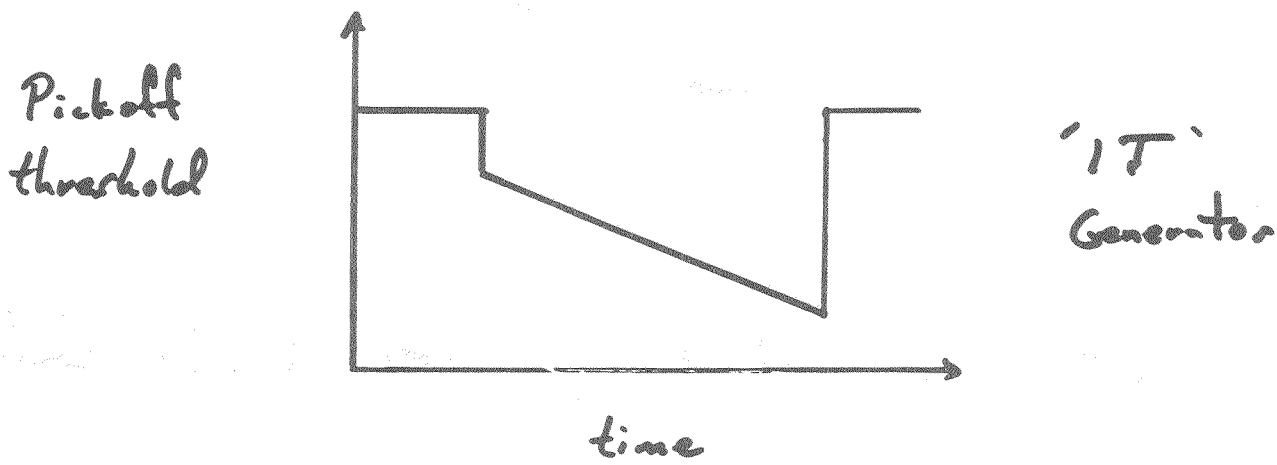

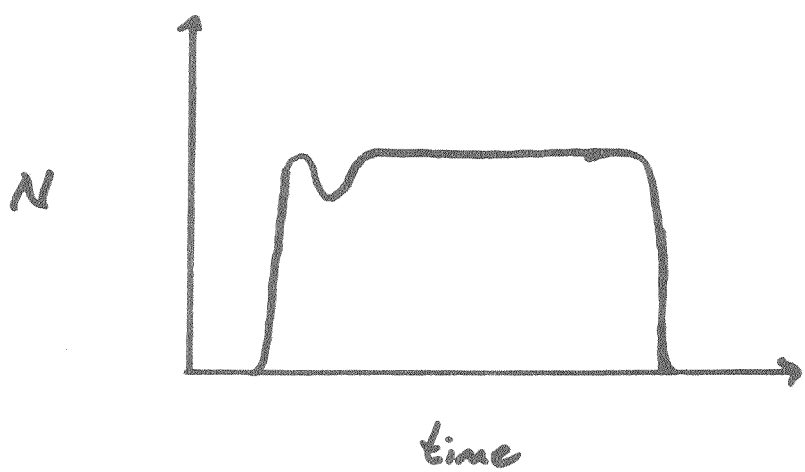

Effect of Intelligent Threshold Generator

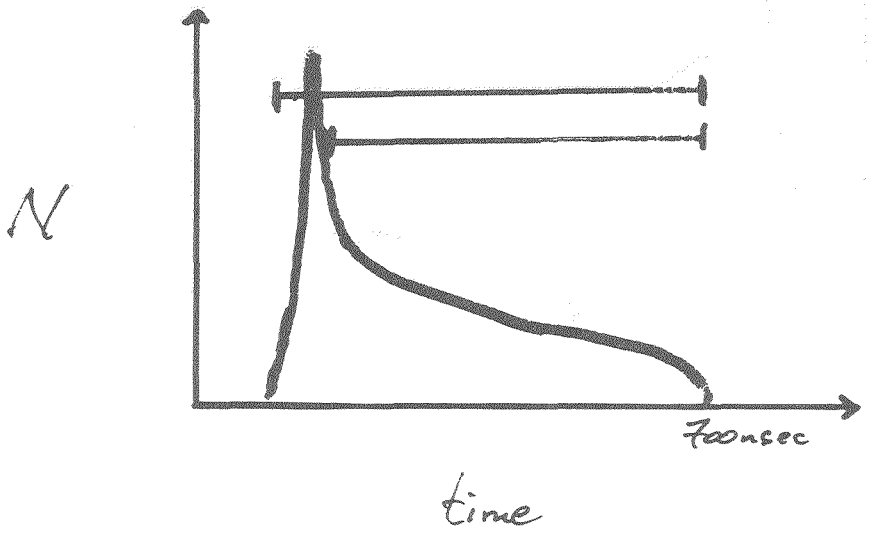

Effect of Shortening TRD Scaler Gate

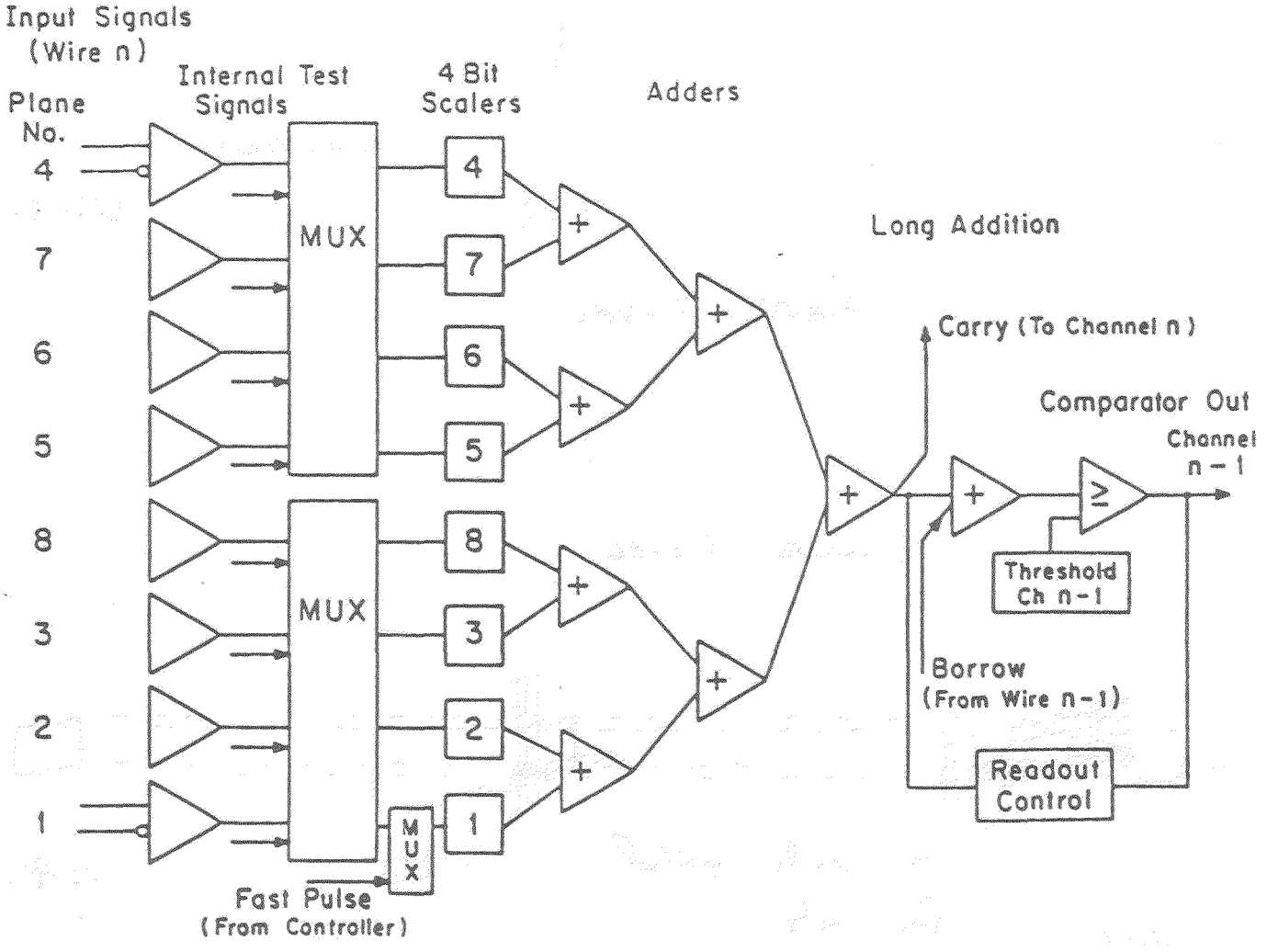
Input Signals
(Wire n)
Plane No.
Internal Test Signals
4 Bit Scalers
Adders
Long Addition
4
7
6
5
8
3
2
1
MUX
MUX
MUX
+
Carry (To Channel n)
Comparator Out
Channel n-1
≥
Threshold Ch n-1
Borrow
(From Wire n-1)
Readout Control
Fast Pulse
(From Controller)

Electron Trigger

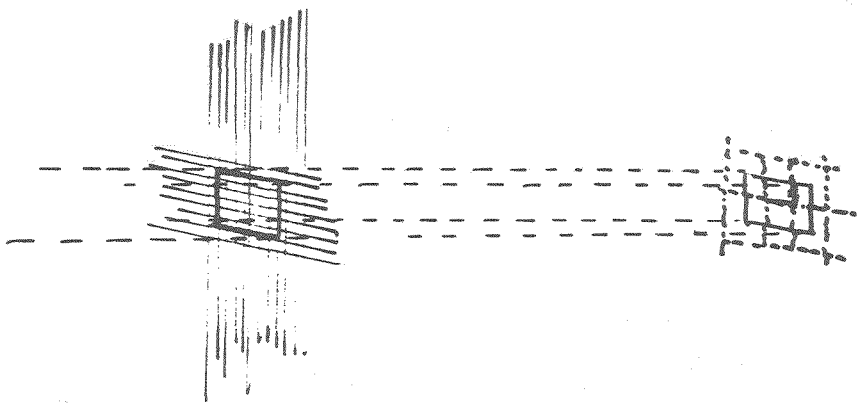

FIRST LEVEL

SECOND LEVEL

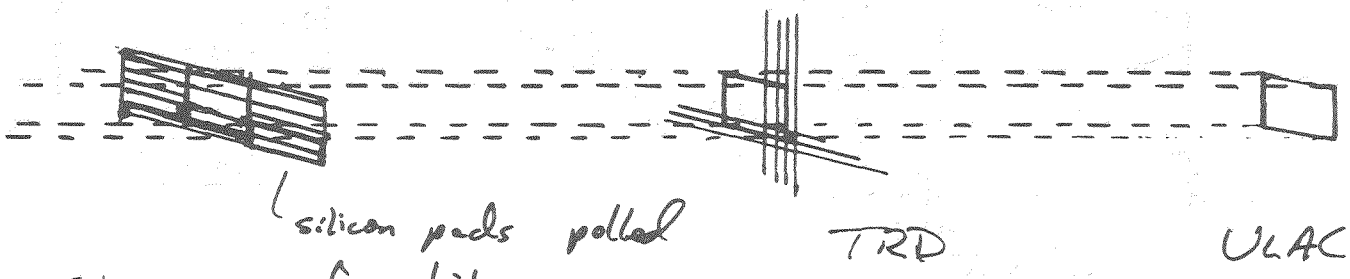

Silicon Pad Array

charged particle deposits ionisation charge on pad.

require ≥1 .AND. (.NOT.≥2)

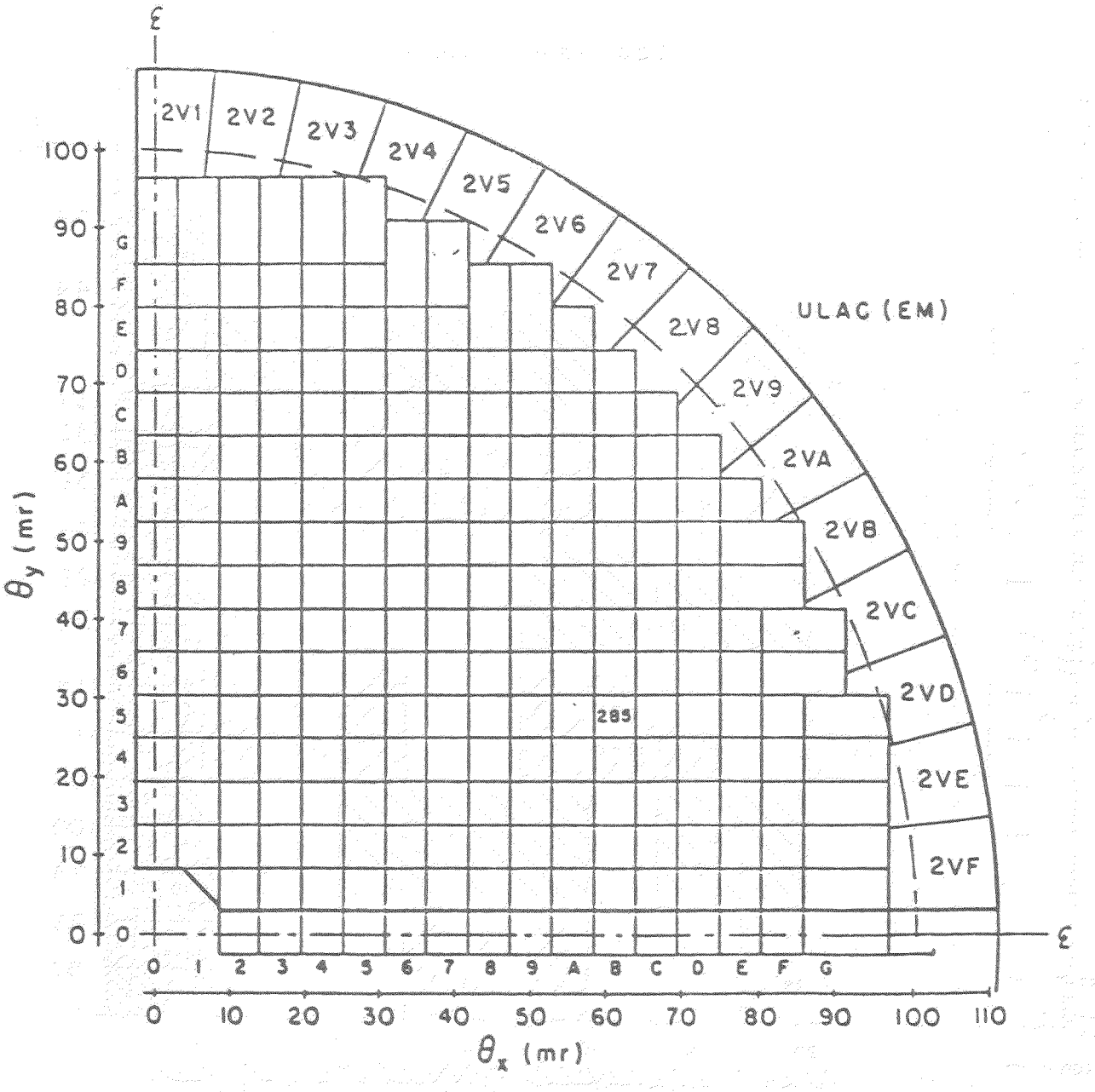
ℰ
2V1
2V2
2V3
2V4
2V5
2V6
2V7
2V8
2V9
2VA
2VB
2VC
2VD
2VE
2VF
ULAC (EM)
285
100
90
80
70
60
50
40
30
20
10
0
G
F
E
D
C
B
A
9
8
7
6
5
4
3
2
1
0
θ_y (mr)
0 1 2 3 4 5 6 7 8 9 A B C D E F G
0 10 20 30 40 50 60 70 80 90 100 110
θ_x (mr)
ℰ

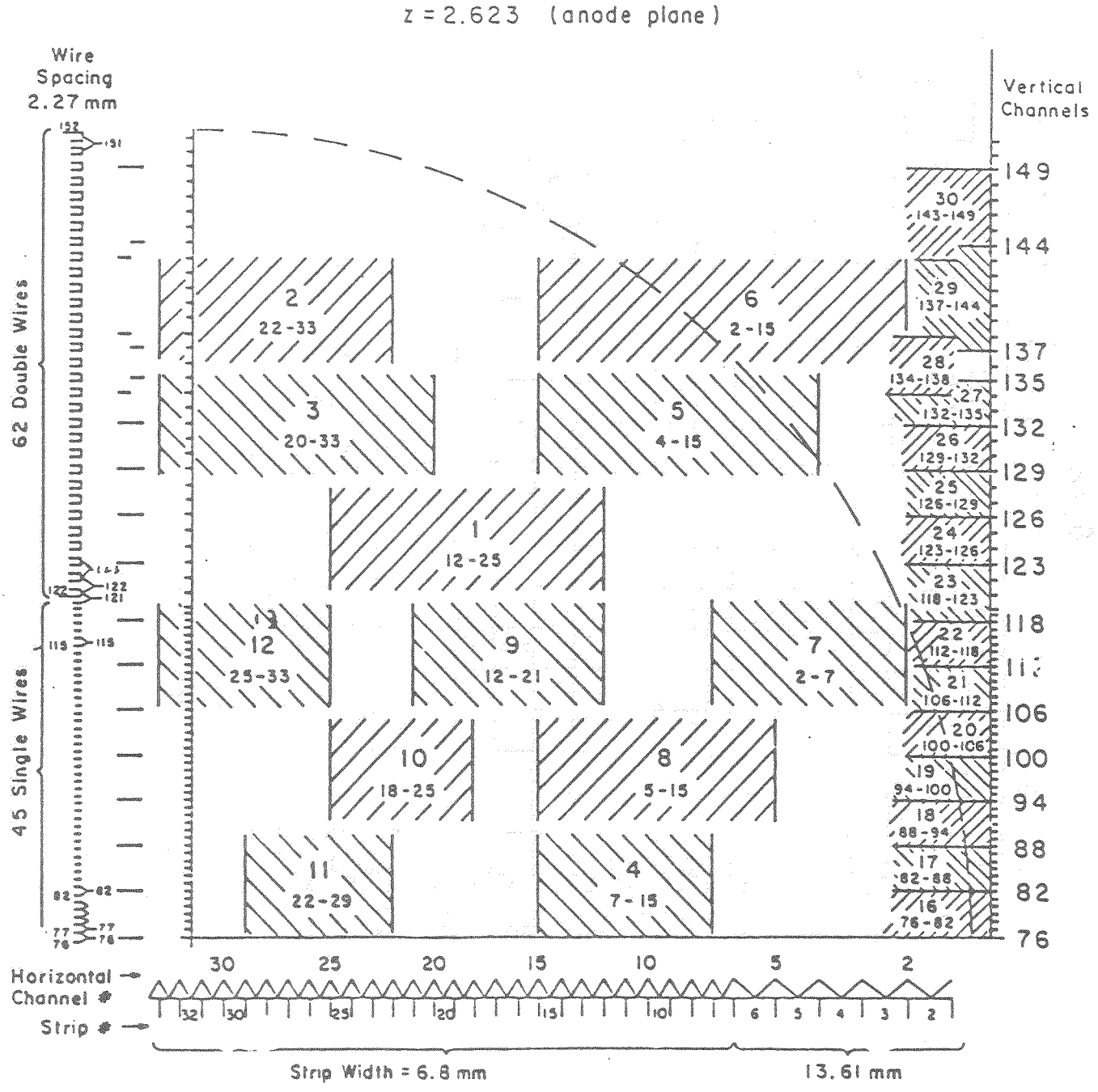
z = 2.623 (anode plane)
Wire Spacing 2.27 mm
62 Double Wires
45 Single Wires
Vertical Channels
Horizontal Channel #
Strip #
Strip Width = 6.8 mm
13.61 mm
1 12-25
2 22-33
3 20-33
4 7-15
5 4-15
6 2-15
7 2-7
8 5-15
9 12-21
10 18-25
11 22-29
12 25-33
16 76-82
17 82-88
18 88-94
19 94-100
20 100-106
21 106-112
22 112-118
23 118-123
24 123-126
25 126-129
26 129-132
27 132-135
28 134-138
29 137-144
30 143-149

TRD Logic Timing

(Beam Crossing Rate: 1 MHz)

	Δt	t
TOA at detector	--	8 ns
Preamplifier	10	18
3 m cable	15	33
Time Pickoff	20	53
29 m cable	150	203
TRD drift time	700	903
TRD OR Circuits	110	1013
Cables	20	1033
Enable ANDs	60	1093
Analog Multiplicity		1285
Controller Strobe		1325
1st Level Digital Electron Multiplicity Strobe		1835

1988 TRD Rejection

Drift Chamber → (ULAC EM) Pointing:

Electron

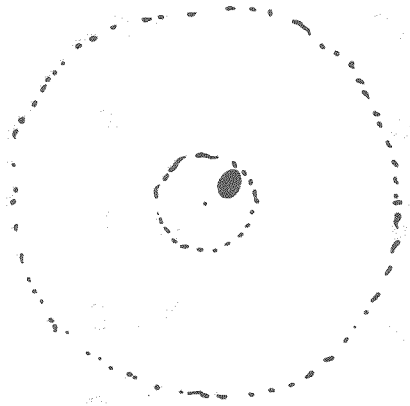

Pion

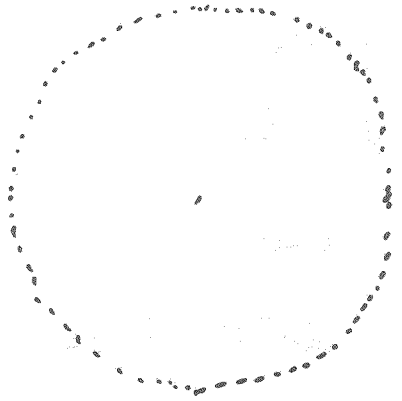

$R_{DC-ULAC} < 6$ mm / 1.5m

No Second Shower within 4 cm

No Shower Within 4cm

$E_{SH} > 5$ GeV

$E_1 / E_{SH} \geq 0.2$

$R_1 \leq 1.6$ cm

$R_2 \leq 1.9$ cm

V. Tikhomirov

TRD clusters for DC-ULAC

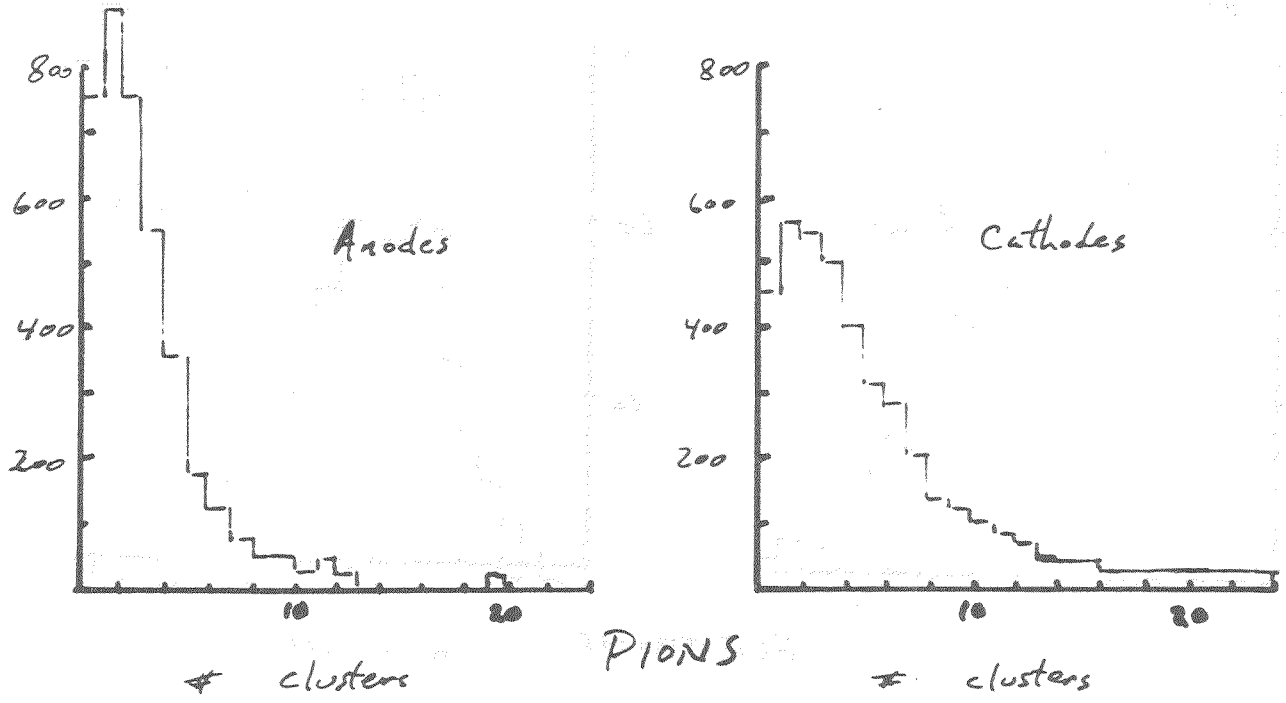

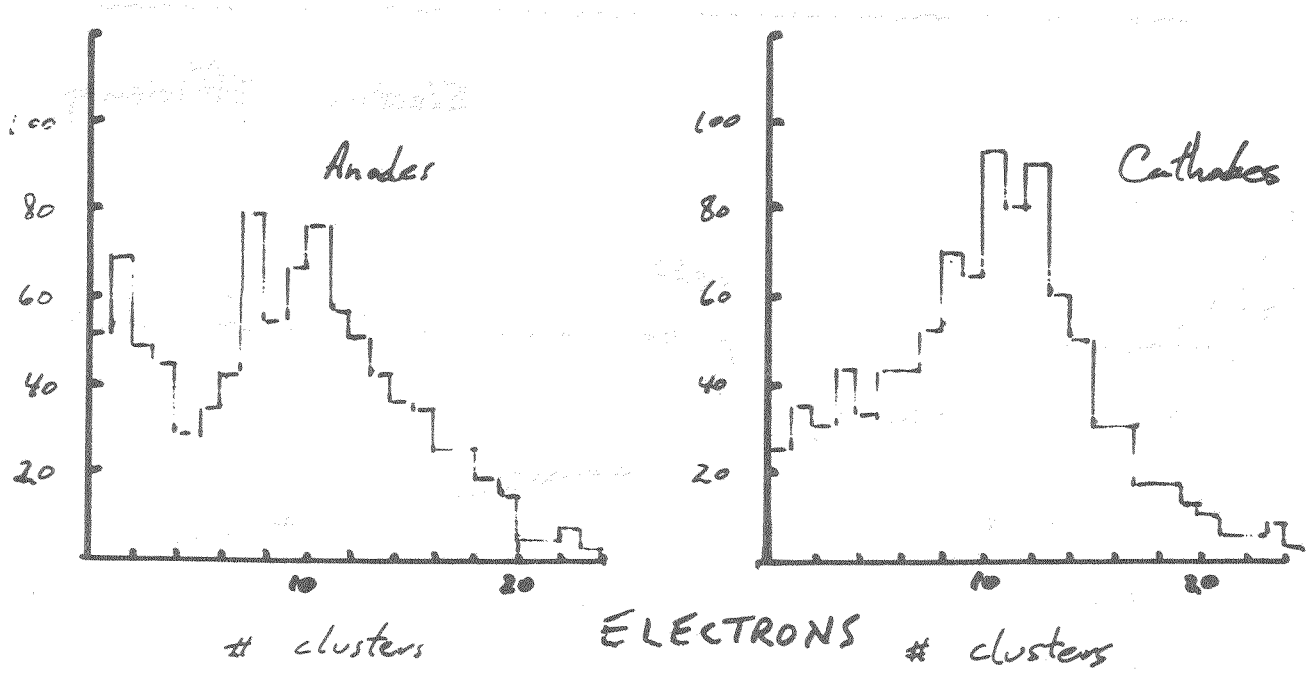

ow contamination: ULAC rejection

accidental coincidences

TRD Clusters - Subtracted

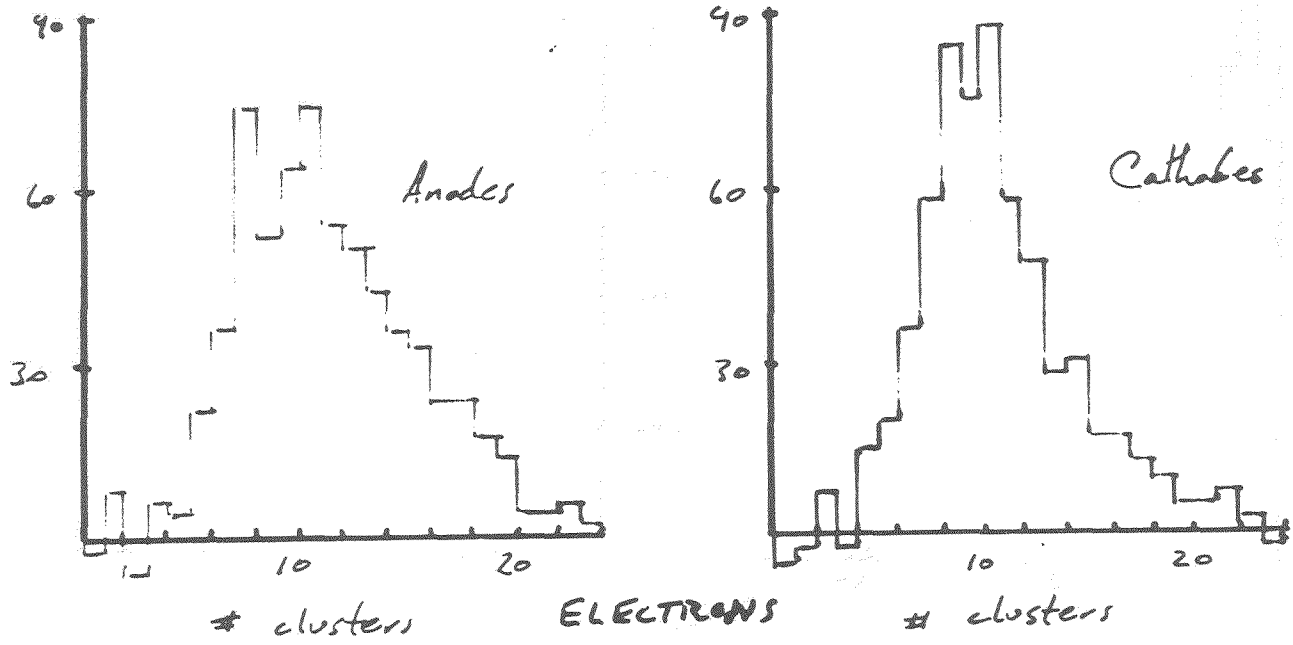

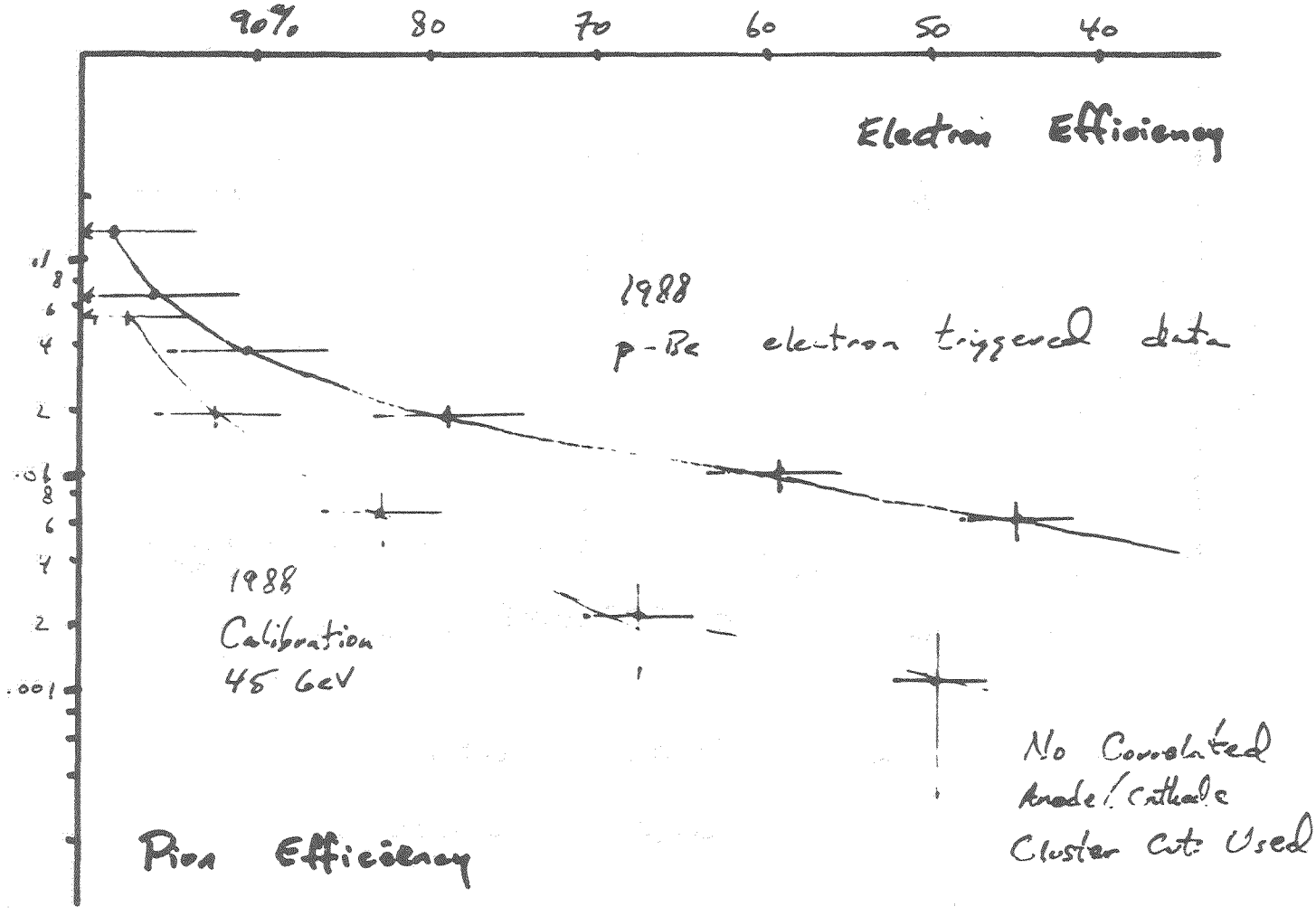

TRANSITION RADIATION DETECTORS

FOR HADRON COLLIDERS

R. Ansari , B. Merkel

Laboratoire de l'Accélérateur Linéaire, Bât. 200, 91405 Orsay, France

Abstract : Electron identification by the detection of transition radiation is described, with an emphasis on electron identification at Collider experiments UA2 at CERN Sp$\bar{p}$S and D$\emptyset$ at FNAL. Present experience gained at Sp$\bar{p}$S and extension to next generation Colliders will be presented.

I. INTRODUCTION : LEPTON IDENTIFICATION

Lepton identification is an essential feature for event selection among a larger sample of events dominated by large cross section phenomena. Hard parton - parton scattering processes have been shown to play the dominant contribution to the relevant high P_t event rate on collider experiments [1,2]. They give rise to final state with large transverse momentum gluons and quarks, intermediate bosons , or to the production of new states whose decay involve leptons, gluons and quark. Quarks and gluons then fragment to ordinary hadrons, and they are observed as jets of hadrons, mostly charged and neutral pions. At next generation colliders with an order of magnitude increase in the total centre of mass energy, soft gluons radiation give rise to multijets events[3], the event complexity is much worse, the inclusive jet cross section is much higher[4,5]. Jets are expected to be a predominant feature of the interesting events. Such a pattern implies a very powerful selection for the extraction of the large amount of physics issues. Any new high mass object will decay mainly into the highest mass quark available, also all high mass quarks have a sizeable semileptonic decay branching ratio.

Leptons from quark decay are observed as pairs $e\nu$, $\mu\nu$, $\tau\nu$. Electron identification is made by an isolated track and the observation of an electromagnetic shower in the calorimeter cells selected around the track impact. Muon identification is made by the identification of a penetrating track. τ lepton identification can be relevant with high momentum τ, the 3 body decay giving rise to overlapping tracks in the tracking detector. ν identification is made by the missing energy momentum since ν will escape the calorimeter, this implies a good resolution on the P_t measurement by the calorimeter together with a calorimeter hermeticity as good as possible. Electron decays or τ lepton decays are very difficult to isolate inside jets ; on the contrary μ decays can be identified within jets[6] .

Electron identification by the combined use of a calorimeter and a Transition Radiation Detector (TRD) has already been used by many experimental apparatus. Furthermore the rejection factors obtained in the TRD and in the electromagnetic calorimeter are multiplicative. For example using a very large sample of Ξ^- semi-leptonic decays, it has been shown[7] that considered separately the electromagnetic shower information and the TRD provided pion rejection factors of 1000 : 1 and 48 : 1 respectively ; and that they give a value of 45000 : 1 for the combined pion rejection factor.

But on collider experiments the event complexity is increased and the pion rejection factor cannot be defined in the same way as in a low multiplicity environment or in test beam data analysis. Background particles come mainly from jets, so that the electron selection has to reject other types of background than isolated hadrons. Actually jets from parton fragmentation lead to a copious production of π^0, η^0, which then decay. Misidentified leptons contributing to the background events are due to π^0 (η^0) decay, γ conversions, and overlap between a charged pion and a γ within the calorimeter cell granularity. It has been shown that the P_t spectra of the background faking electron has the same slope as the inclusive jet cross section.

Transition radiation emission by a charged particle along its path in the radiator is a sizeable effect for particles having a Lorentz factor of the order of 10^3 - 10^4. Thus energetic electrons or positrons traversing a radiator will give rise to transition radiation emission, on the contrary transition radiation emission by hadrons of the same momentum have a much lower probability. The charged track + $\pi^0(\gamma)$ overlap background involving an accompanying charged hadron is the typical example of the background which will be reduced by a TRD.

II. DESIGN

X-rays are emitted when a charged particle traverses the interface between two different medias. Such interfaces are obtained by stacking thin foils inside a gas container. The total radiated energy being proportional to the particle Lorentz factor $\gamma = E/M$, electrons radiate transition radiation X-rays along their path in the radiator whereas hadrons produce much less (see for example[8]). X-ray absorption in the gas of the detector is the signature of transition radiation emission in the radiator by the passage of a charged particle. It gives rise to local charge clusters, which are superimposed with the ionization loss along the charged track. Identification of X-ray absorption in the detector can be made either by measuring the total deposited charge along the track, or by the observation of local charge clusters. Signal processing by Flash ADC's offers the opportunity to measure the direct current as a function of the arrival time on the anode wire or the cathode strip. The subsequent analysis can be done using several algorithms : total integrated charge, charge inside clusters, cluster counting, and likelihood methods.

Monte-Carlo simulations of transition radiation help to optimize the detector geometry, by generating X-ray emission according to well established theoretical description[8]. X-ray detection in a multiwire proportional chamber filled with xenon is also simulated. The simulations allow to

get an optimized geometry of the radiator by maximizing the X-ray yield at the exit of the radiator as a function of the foil spacing, the number of foils.

In collider experiments the radial thickness available for the insertion of a TRD is very critical as far as the rejection factor is concerned[9]. Within the space available for the TRD the number of sets should be optimized, a set is an assembly of a radiator and an X-ray detector. In the case of the UA2 detector 2 sets are adequate for a radial thickness of 210 mm and the design rejection factor is 10 at 90% electron efficiency. In the case of the DØ detector, the space available is 315 mm 2 sets are adequate if the radiators are built with lithium foils, whereas 3 sets give the most effective TRD if the radiators are built with polypropylene foils ; the design rejection factor is 50 at 90% electron efficiency with polypropylene foils.

II.1 THE UA2 TRD

Results obtained with a prototype in a test beam have already been published[10]. The TRD is now built and under use in the UA2 experiment, a cross section view is shown on Figure 1.

The radiators are cylindrical with an inner radius of 170mm and 276mm respectively and a thickness of 77mm. Polypropylene foils 20μ thick are used as radiator media, the foil spacing of 200μ is obtained by etching. The radiators are installed in containers, under permanent helium flow, the thickness of the exit window is critical as far as X-ray attenuation is concerned, a mylar foil (25μ thick) from which the cathode of the detector (a kapton foil 25μ thick) is separated by a 3mm gap in which a permanent CO_2 flow is maintained (see Fig. 1).

One of the two identical detectors used is sketched on the expanded view in figure 1 : a 15mm drift space is defined by the entrance window and a grid ; the amplification space is 8mm thick between the grid and the exit cathode. The entrance window is a kapton foil 25μ thick with graphite on the interior side for cathode voltage setting. The exit cathode is equipped with strips inclined at 35° with respect to the anode wires. The gas used is a Xenon (95%) methane (5%) mixture with a permanent closed circulation across the chambers and purifiers. The Xenon concentration is monitored with small test chambers. Due to its recirculation across the wire chambers the gas is progressively polluted by small air leaks from outside the chambers or the CO_2 from the entrance window. The oxygen, the water vapour and the CO_2 are removed by purifiers and specific absorbents, but the nitrogen contamination increases with time. To stabilize this contamination we have installed a small permanent gas outlet (1.5 l/h) in such a fraction that the nitrogen outlet compensates the nitrogen inlet and its concentration is stable at 4%.

A low noise amplifier is used to detect the wire signal, the amplified signal is fed by a 85 meter long cable to a zero pole filter to correct for the signal distortions introduced by the wire chamber and the cable. The resulting pulse shape is gaussian with a FWHM of 40 ns, which is then digitized by a 100 Mhz Flash ADC, for the two chambers there are 752 channels in total. A similar amplification chain is used on the strips with a FWHM of 160 ns, and the signals are digitized by 15 Mhz Flash ADC (1216 channels in total).

Figure 2 is a typical current versus time plot given by the 100 Mhz Flash ADC from the signal associated to an electron (positron) track from the decay of a W boson $W \rightarrow e\bar{\nu}$.

II.2 THE DØ TRD

Results obtained with the test bench have already been published[11]. The TRD is now built and ready to be inserted inside the DØ experiment at FNAL. Test beam results are also available with the full set up[12].

The final set-up is designed as a three coaxial units 305 mm thick. Each unit consists of a carbon fibre radiator vessel containing a 65 mm thick polypropylene foils radiator, a low mass window made of two thin mylar foils separated by 2mm, a gas filled chamber as detector 23mm thick, and an 11 mm lightweight outer shell.

The radiators are made[11] of 400 polypropylene foils 18μ thick, the technique chosen to obtain the foil spacing of 150μ is to emboss the foil. The exit window is critical as far as X-ray attenuation is concerned, it is made with a mylar foil (23μ thick) from which the cathode of the detector (a mylar foil 23μ thick) is separated by 2mm space under N_2 flow, to avoid pollution of the chamber. The sphericity and stability of the mylar windows is determined by the N_2 relative pressure.

The detectors used are sketched in figure 3 : a 15mm radial drift space separated by a grid from an amplification zone 8mm thick between the grid and the exit cathode. The exit cathode is equipped with helicoidal strips, 256 per chamber. The gas used is a Xenon methane mixture with a permanent circulation across the chambers and purifiers, a Xenon CO_2 mixture have been rejected because test beam data reflected a large effect of electron attachment ; also a Xenon isobutane mixture have been rejected.

All three drift chambers have 256 readout channels with projective geometry, 256 strips on each chamber for a total of 1536 readout channels. A fast preamplifier is mounted on the detector, a

shaper which includes several filters and 3 pole-zero cancelation circuits is located near the detector, digitization is performed in the counting room by 100 Mhz Flash ADC 's developed by FNAL.

III. TEST BEAM RESULTS

The evaluation of the electron efficiency ε_e of a full TRD set-up and its corresponding rejection ability η_h is initially done by the Monte-Carlo simulation. The Landau description of the energy loss distribution of hadrons and electrons is very difficult in the gas of a chamber. Values of ε_e η_h closer to reality are obtained from test beam data.

III.1 Total integrated charge

Typical distributions of the total charge are shown on figure 4 from the DØ test data analysis on a 5 GeV/c beam. There is a clear difference between the hadron data 4(a) which exhibit the well known Landau shape of ionization loss, and the electron data 4(b) which show the contribution of the X-rays detected in the chamber gas, added to the electron ionization loss which is also higher in the ratio of the relativistic rise.

The curve drawn on figure 4(a) and 4(b) across the data histogram are the result of the Monte-Carlo simulation[13]. Description of the total energy loss in the detector could not be done by the Landau theory, the energy transfer spectrum is used to simulate the δ-rays contribution. A very detailed description of the chamber response was necessary to get a good agreement with data. Finally the ADC channel gain is normalized to deposited energy clusters using data taken with radioactive sources (^{54} Mn).

Similar results have been published by UA2, together with a likelihood method based on the total charge measured in each detector set.

III.2 Cluster counting

A cluster algorithm identifies local bumps in the time distribution of the anode wire current or cathode strips current as given by the sequential data from the flash ADC, they are interpreted as charge clusters. Xrays associated to transition radiation emission by electrons are detected in the chamber gas giving rise to charge clusters. Figure 5 shows the experimental energy spectrum of the

detected clusters with 5 GeV/c electrons as obtained by the DØ test beam analysis, the results of the Monte-Carlo calculations are also shown (see ref 13 for more details). Low energy Xrays from transition radiation give rise to low energy clusters, the density of detected Xrays per unit path length in the chamber decreases exponentially. As expected higher density occurs immediately behind the entrance window and the slope of the detection distribution is steeper at lower Xray energy.

Cluster energy detection probability and energy allows to built a likelihood method for electron selection [10-11].

III.3 Efficiency and rejection

In the absence of magnetic field, the Xray spot is superimposed to the particle energy loss in the chamber. A selection of particles based on a very loose criteria will have the same efficiency on electrons and hadrons i.e. as good as the gas chamber efficiency, nearly 100 %. The number of charge clusters and their energy, or the total deposited charge is higher for electrons than for hadrons, so that by increasing the selection cut, the efficiency for hadrons decreases more rapidly than for electrons. The TRD detector quality is measured by the correlation between the electron efficiency ε_e and the hadron rejection η_h .

Several events taken on test beam with one detector set are combined to simulate a full detector assembly consisting of two or three sets, values of ε_e and η_h can thus be extrapolated. Several likelihood methods have been compared in UA2 and in DØ. At high electron efficiency (more than 90%), the hadron rejection obtained with one set only is the same for total charge algorithm or cluster energy versus position algorithm, but the latter selection gives higher hadron rejection for electron efficiency smaller than 80%. A likelihood algorithm which combines the total charge of the two sets for UA2[10] give similar results as a likelihood on the full information on cluster energy versus position for electron efficiency higher than 70%, the latter algorithm give a better rejection at low electron efficiency (smaller than 60%). Combining three sets for a simulation of the DØ full set up, the likelihood on the total charge was found to be the most powerful [11].

UA2 and DØ results are drawn on figure 6, in both analysis the most efficient algorithm is taken to estimate of the pion rejection as a function of the electron inefficiency. The DØ results are obtained with the full DØ detector, the three sets were read out and combined. Results thus obtained give a pion rejection[12] better than the previously published simulation based on single set test bench[11]. As expected the rejection ability increases with the total TRD thickness, this

feature explains the rejection increase between the two test beam results. The pion most probable energy loss is also higher with 40 GeV/c beam (UA2 test data) than with 5 GeV/c beam (DØ test data) ; this also contributes to the observed difference between the rejection ability measured.

IV. COLLIDER DATA

From test beam data to collider data the event configuration is characterized by a wider range of hadron momenta, with a contribution of momenta smaller than the momentum at which the particle energy loss in the gas chamber is minimum ($\gamma\beta = 4$), the energy loss increases rapidly with decreasing momenta. Furthermore the charge detected on the wires and the strips of the chambers is to be associated with the candidate electron(positron) track avoiding charge pile-up due to the event complexity .

Data from collider runs are available with the UA2 TRD with an integrated luminosity of 2.4 pb^{-1}. The TRD is used mainly to reject events with a fake electron identified in the calorimeter with an associated charged track. Overlap between a low energy charged pion and a neutral π^0 (or photon) within the electromagnetic calorimeter space resolution is the source of such background events.

Due to the limited space resolution of the TRD itself and the tracking devices, such overlap events with a converted photon ($\gamma \rightarrow e^+e^-$) where the two tracks are not resolved cannot be rejected using the TRD.

In the case of UA2 detector, two Si-pad layers, located before the TRD provide dE/dx measurement. This information can be used to reject γ-conversions occurring before the Si-layers. Close overlap of charge pion, and a π^0 (or photon) converted after the Si layers cannot be easily rejected. Such events have been observed in UA2.

IV.1 Data samples selection

For a good description of the UA2 TRD results on collider data we have selected four class of events using the other tracking devices available and the calorimeter . Around the Be beam pipe is located the inner layer of Silicon pads, a Jet Vertex Detector, the outer layer of Silicon pads, the

TRD and a Scintillating Fibre Detector as outer tracking device, immediately followed by the preshower. A more detailed description of UA2 can be found elsewhere[14].

An electron(positron) candidate is selected by a track and a preshower in front of the calorimeter cluster satisfying a penetration cut, a good track preshower match, a shower quality factor given the impact point of the track. Both Silicon layers give a good measurement of the particle dE/dx with good 1 m.i.p. to 2 m.i.p. separation :

- Clean sample of $W \rightarrow e\bar{\nu}$ decays : all cuts and Si pulse height < 1.6 m.i.p.
- Early conversions : all cuts and Si pulse height > 1.6 m.i.p.
- Hadrons : no cuts on calorimeter, ask for absence of preshower signal within a cone around the track
- Charged track + $\pi^0(\gamma)$ overlaps : same as $W \rightarrow e\bar{\nu}$ decays, ask for a bad track preshower match.

IV.2 Single set results

A comparison between test beam data and the selected sample of W events is given in Figure 7. The total integrated charge distribution obtained with 40 GeV/c test beam is shown on 7(a) for electrons and 7(b) for pions.

On collider data, high charged track multiplicity events, associated with projective geometry detector make precise charge measurement in TRD difficult. In order to enhance charge determination, and track/charge association, we have used cathode strip information, in addition to wire information.

Using track angle and impact point reconstructed by tracking devices (JVD, Si pads, SFD) in each TRD chamber, charge deposition pattern in the nearest wires, is compared. With the one on strips, the associated wire, or wires (up to two wires can be associated to a single track) are selected.

Also, using the track information, the charge distribution from strips is evaluated, minimizing the pile up effect, due to projective geometry and limited space resolution.

At the last step, the most reliable charge, either from wires, or strips is chosen. Given the finer time and space resolution on wires, wire charges are selected primarily, but in 30-35 % of the cases, strip charge are used, when the two conditions are satisfied :

- strip charge estimation is lower than the wire charge,
- this is confirmed by the ratio of observed strip charges/wire charge projected on strips.

The charges from two TRD detectors, determined as described above are associated to the track, and are used for electron identification. The rejection/efficiency results presented below are based on total TRD charge cut, although a likelihood algorithm using total charges from the two sets, or the full charge versus time information can be used.

The results of this algorithm are shown on figure 7(c) for the electron (positron) track in $W \rightarrow e\bar{\nu}$ decays : 395 electrons(positrons) and 7(d) for isolated hadrons in the same W events sample (3492 selected tracks). The abscissa has been chosen for convenience of the comparison between test beam and collider data. Electron data nicely reproduce test beam results the hadron data on the contrary give a lower peak position together with a wider tail. Hadrons present in a jet from parton fragmentation or in the underlying event, have a wide momentum spread ; in the absence of a magnetic field in UA2 a momentum selection cannot be made. For a comparison between test beam hadrons and collider hadrons it is necessary to scale the dE/dx distribution as measured on test beam ; the variation with $\gamma\beta$ of the particle dE/dx in Xenon is taken from Sternheimer's formula[15] relative abundance of particle momenta is taken from the charged particle inclusive invariant cross section published by UA1[16]. The resulting dE/dx distribution is shown in figure 7(e), agreement with collider data (Fig 7(d)) is better ; the tail is mostly accounted for by low energy pions, a low momentum cut-off is set at 100 MeV in the simulation. Nevertheless, charge pile-up due to event complexity may still contribute to the tail.

A direct comparison between hadrons on collider data and test beam data is not very significant, the same is true for the rejection at a given electron efficiency. The momentum spread spanned could have been reduced with a direct measurement of the momentum in a magnetic field.

IV.3 Full TRD results

The total integrated charge is associated to each reconstructed track, for each detector set. As explained in previous section, care is taken to overcome as much as possible charge pile-up from multitracks. Non homogeneous azimuth acceptance of both detectors lead us to use an algorithm based on the smallest deposited charge observed in a set, if not zero.

The results of this algorithm are shown on figure 8(a) for the electron (positron) track in $W \rightarrow e\bar{\nu}$ decays : 468 electrons(positrons) and 8(b) for selected tracks associated with early

conversions, i.e. conversions occurring before the TRD. The charge distribution is wide but the ratio of the mean value of 8(b) by that of 8(a) is very close to a factor 2, as expected for photon conversions.

The results of this algorithm are shown on figure 9(a) for isolated hadrons in the same W events sample (1669 selected tracks) and 9(b) for selected tracks associated with charged track + $\pi^0(\gamma)$ overlaps (213 selected tracks). Charged track + $\pi^0(\gamma)$ overlap background is foreseen to give the same pulse height distribution as hadrons, nevertheless the tail is wider. For comparison with test beam we can choose a cut with efficiency 90% on electron(positron) tracks, this cut gives a rejection factor $\eta_h = 1.7 \pm .1$ for the selected sample of charged track + $\pi^0(\gamma)$ overlap 9(b). Rejection factor increases to $\eta_h = 3.9 \pm 1$ for the hadrons distribution shown in 9(a). With a selection cut such that the electron efficiency $\varepsilon_e = 80\%$ the rejection factor increases to $\eta_h = 11 \pm 1.3$ for the hadrons distribution shown in 9(a) to be compared to a design value $\eta_{pion} = 26$.

Looking at the remaining sample of background events, a new class was discovered. Identification of single hadron tracks is made with the silicon pulse height signal, when a photon conversion occurs in the TRD radiator itself, both leptons then radiate transition radiation X-rays and give rise to a track seen by the outer tracking. This leads to a background if the tracks are not resolved in space.

V. TRD AT NEXT GENERATION COLLIDER

In any detector, the lepton selection ability will have to attain the best achievable rejection at a reasonable efficiency. The most significant sources of background are induced by jets produced in hard collisions, the two jets rate is very high, the multijet rates are also significant. Lepton selection inside jets seems to be hopeless for electron identification, given the overwhelming contribution from π^0 (η^0) decays. The μ identification is a more promising source of events interpretation for lepton inside jets.

Electron or positron selection is to be restricted to isolated tracks ; under these conditions the TRD rejection ability is useful. As already pointed out the P_t spectra of the background faking electrons observed in UA2 has the same slope as the inclusive jet cross section. The absolute rate vs P_t of the background events is decreasing with increasing the electron P_t. A search for leptons from a new W'(Z') boson decay in the 1000 GeV mass range can be performed at low level of background ; this is not the case for example in the case of a search for new 4^{th} family heavy

quarks with masses in the 500 GeV range. Monte-Carlo simulations (see for example ref 17) show that isolated leptons with P_t from 20 GeV to 100 GeV have to be selected, background level is higher by about 3 order of magnitude. In this momentum range, insertion of an extra rejection factor given by a TRD is sensible. In other words insertion of a TRD expands to lower electron(positron) P_t the discovery limit of the experimental set-up.

Magnetic field availability will be essential at LHC or SSC, mostly for the identification of the lepton electric charge, for a separation of soft and hard tracks in order to reconstruct primary and secondary vertices. Magnetic determination of particle momentum is also very useful for particle selection : electron/hadron separation can be given by comparing the energy measured by calorimetry to the momentum, rejection factor of the order of 10 to 15. Adding a TRD will just multiply the rejection factors, Xrays are emitted in the radiator, they have to be detected in a gas chamber, if the detector is located just behind the radiator the Xray spot extend between the extrapolation of the track at the radiator entrance and the track position at the exit ; with a typical radiator thickness of 10 cm, the spot extension is as low as 60μ for a 50 GeV/c P_t lepton and a 2T magnetic field.

Experimentally the detectors will have to cope with extreme conditions, luminosities of the order of $10^{33}cm^{-2}sec^{-1}$, a separation between crossings of 15 to 20 ns. The basic effect of TRD is the emission of soft X-rays, and detection in a gas detector. It is known that the collection time in a proportional chamber is limited by the drift velocity of the electrons. It has been proposed to use multidrift tubes to improve the performances of central tracking detectors ; a similar approach has been studied for the detection of transition radiation X-rays .

VI. CONCLUSION

We have shown that it is possible to use TRD on hadron colliders experiments. Signal associated with electron from W or Z decays is in very good agreement with electron test beam data. Transition Radiation Detector simulation can reproduce very well test beam data and extrapolate to real collider data. Rejection to hadron cannot be compared without ambiguity due to the specific selection procedure to be used on real data.There is still room for a Transition Radiation Detector at next generation collider, the main benefit is an extension of the experiment's sensitivity to lower electron (positron) P_t.

REFERENCES

[1] G.Wolf , Proceedings of the 21st International Conference on High Energy Physics, Paris (1982) C3-529.

[2] UA2 Collaboration J.P. Repellin et al., Proceedings of the 21st International Conference on High Energy Physics, Paris (1982) C3-571.

[3] Z. Kunszt, Proceedings of the workshop on physics at future accelerators CERN 87-07 E. Eichten et al., Rev. of Mod. Phys. 56 (1984) 578.

[4] The LHC Jet Study Group ECFA-CERN Workshop (Lausanne) 1984.

[5] I. Hinchliffe, Experiments, Detectors and experimental Areas for the SSC Berkeley (1987).

[6] F. Palmonari, Proceedings of the workshop on physics at future accelerators CERN 87-07.

[7] M. Bourquin et al., WA2 Collaboration, NIM 204 (1983) 311.

[8] X. Artru et al., Phys. Rev. D12 (1975) 1289.

[9] B. Dolgoshein et al., NIM A252 (1986) 137.

[10] R. Ansari et al., NIM A263(1987) 51.

[11] J.F. Detoeuf et al., NIM A265 (1988) 157.

[12] A. Zylberstein, Proceedings of the 7th Topical Workshop on Proton Antiproton Collider Physics, Fermilab (1988) 492.

[13] Y. Ducros et al., NIM A277 (1989) 401.

[14] C.N. Booth, 6th Topical Workshop on $p\bar{p}$ Physics Aachen (1986).

[15] Sternheimer et al., Phys. Rev. B3(1971) 3681

[16] UA1 Collaboration G.Ciapetti, 5th Topical Workshop on $p\bar{p}$ Physics, Saint Vincent (1985).

[17] S. Dawson et al., Experiments, Detectors and experimental Areas for the SSC Berkeley (1987).

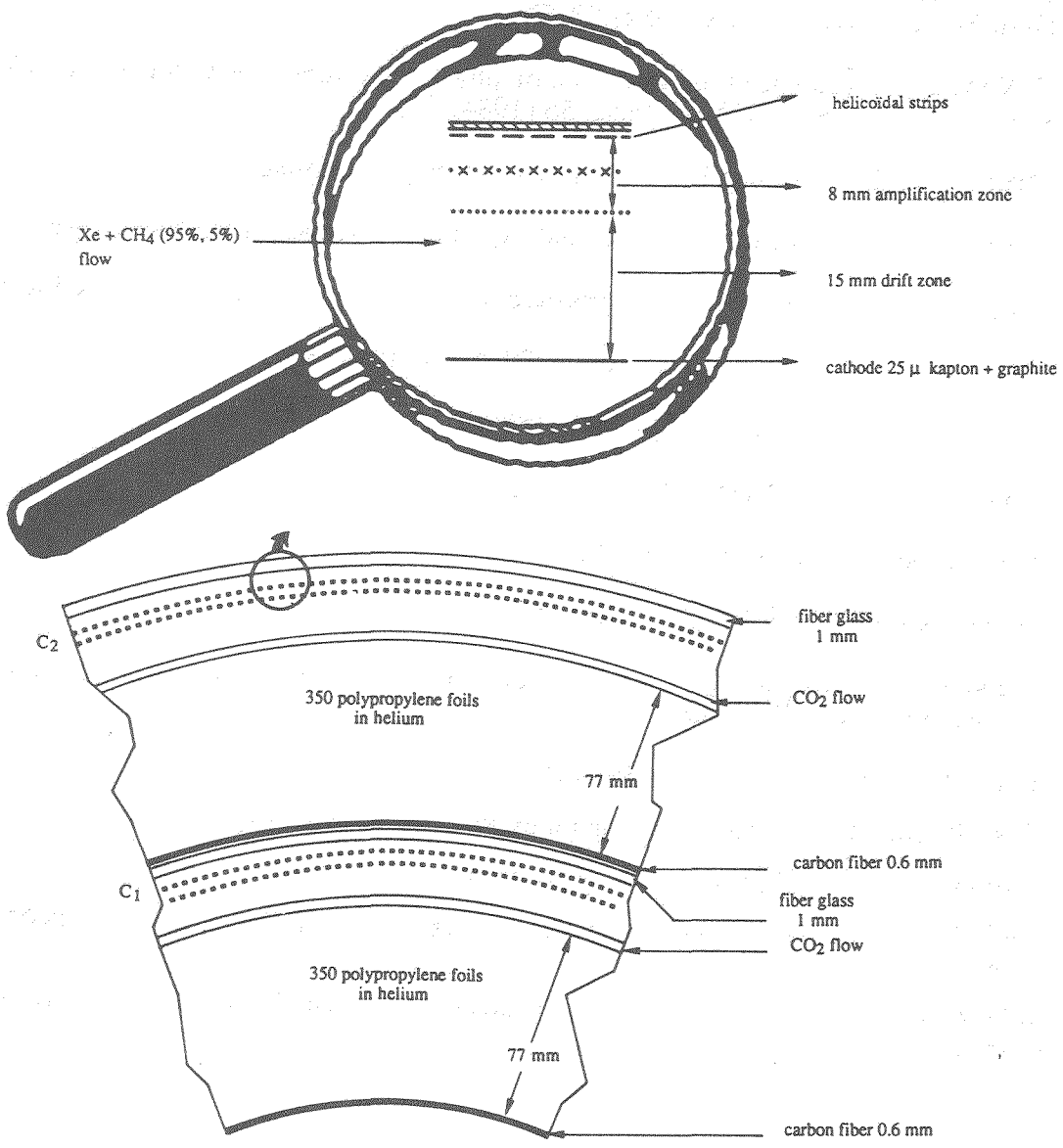

Figure 1 : The UA2 TRD : the radiators are inside container with permanent helium flow ; the detectors, an asymmetric drift chamber filled with a Xenon methane mixture (95%,5%).

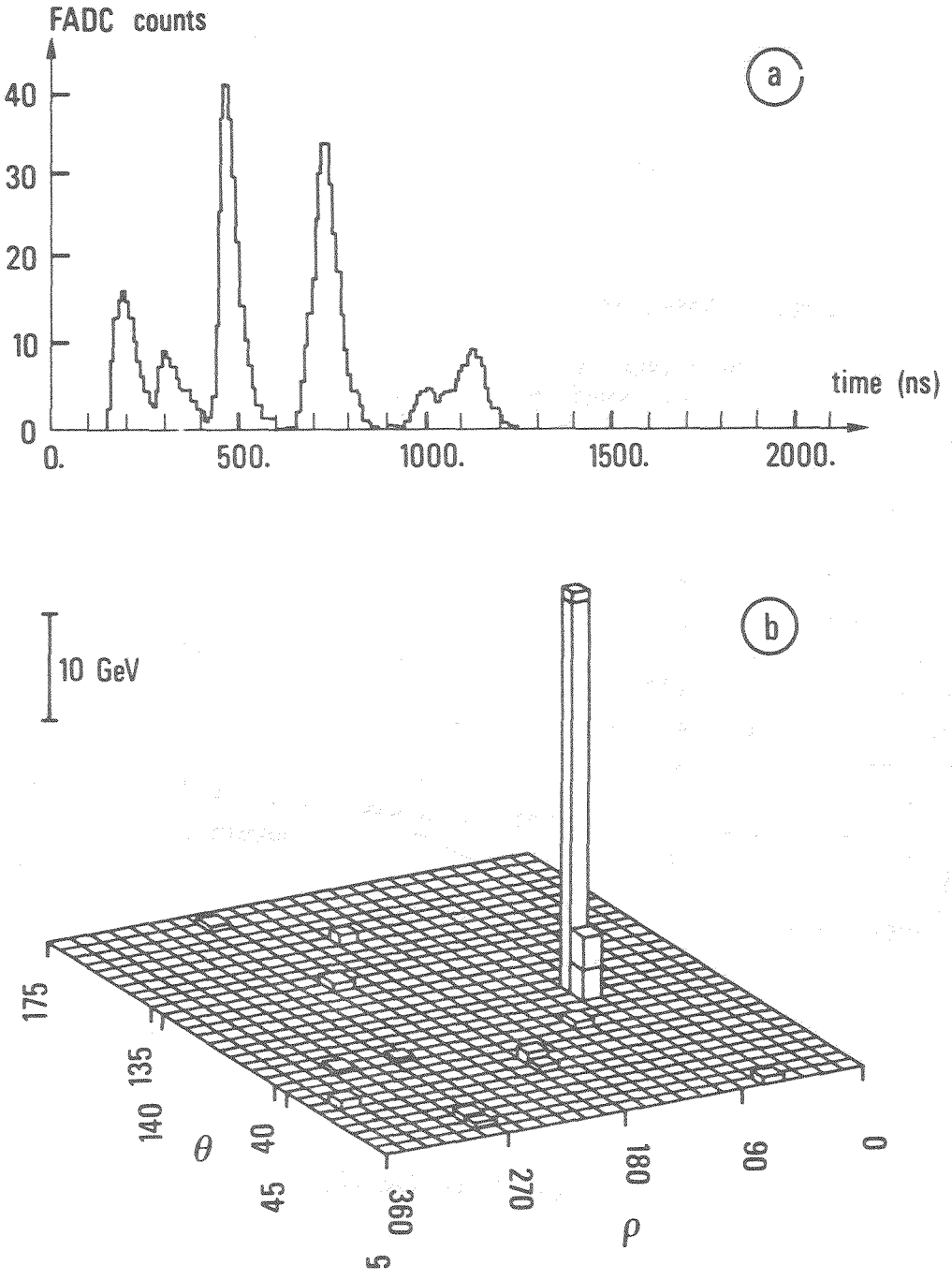

Figure 2 : Example of a signal digitized by the 100 Mhz Flash ADC, the event is identified as an electron from W decay ; the top of the figure shows the pattern of transverse energy detected by the UA2 calorimeter cells in this event.

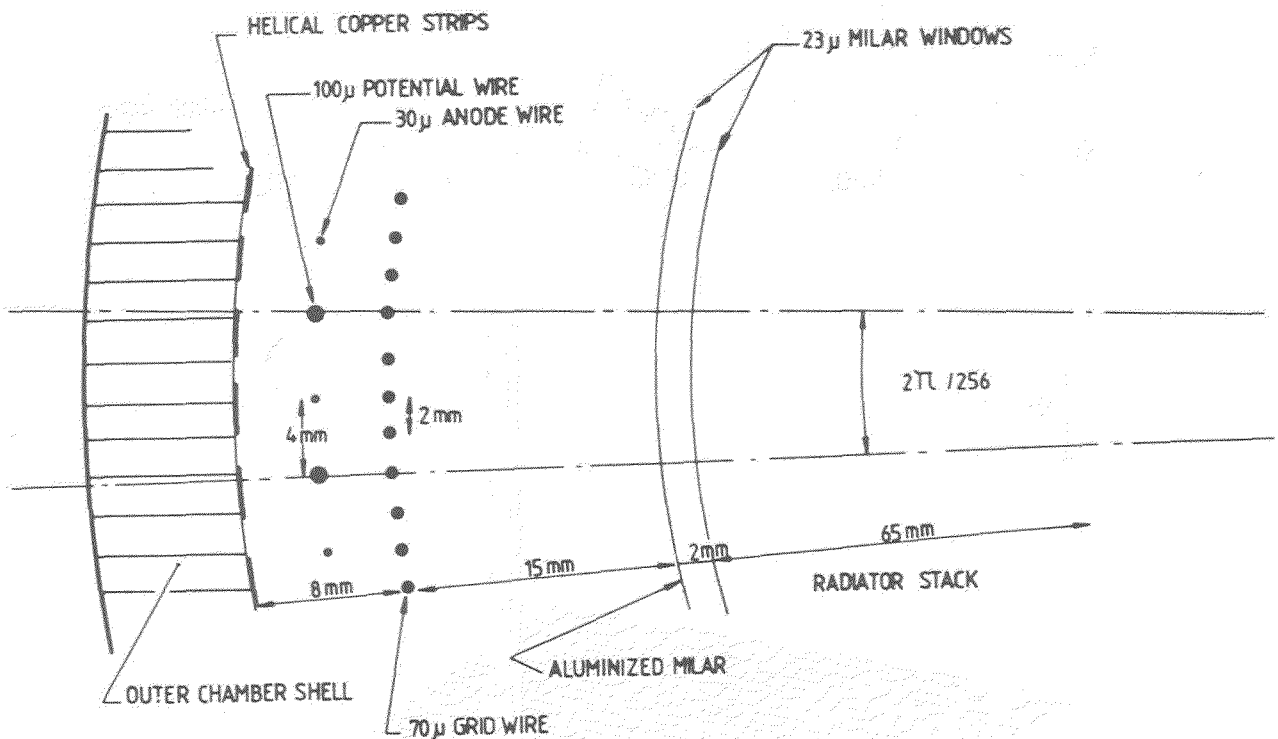

Figure 3 : The DØ TRD.

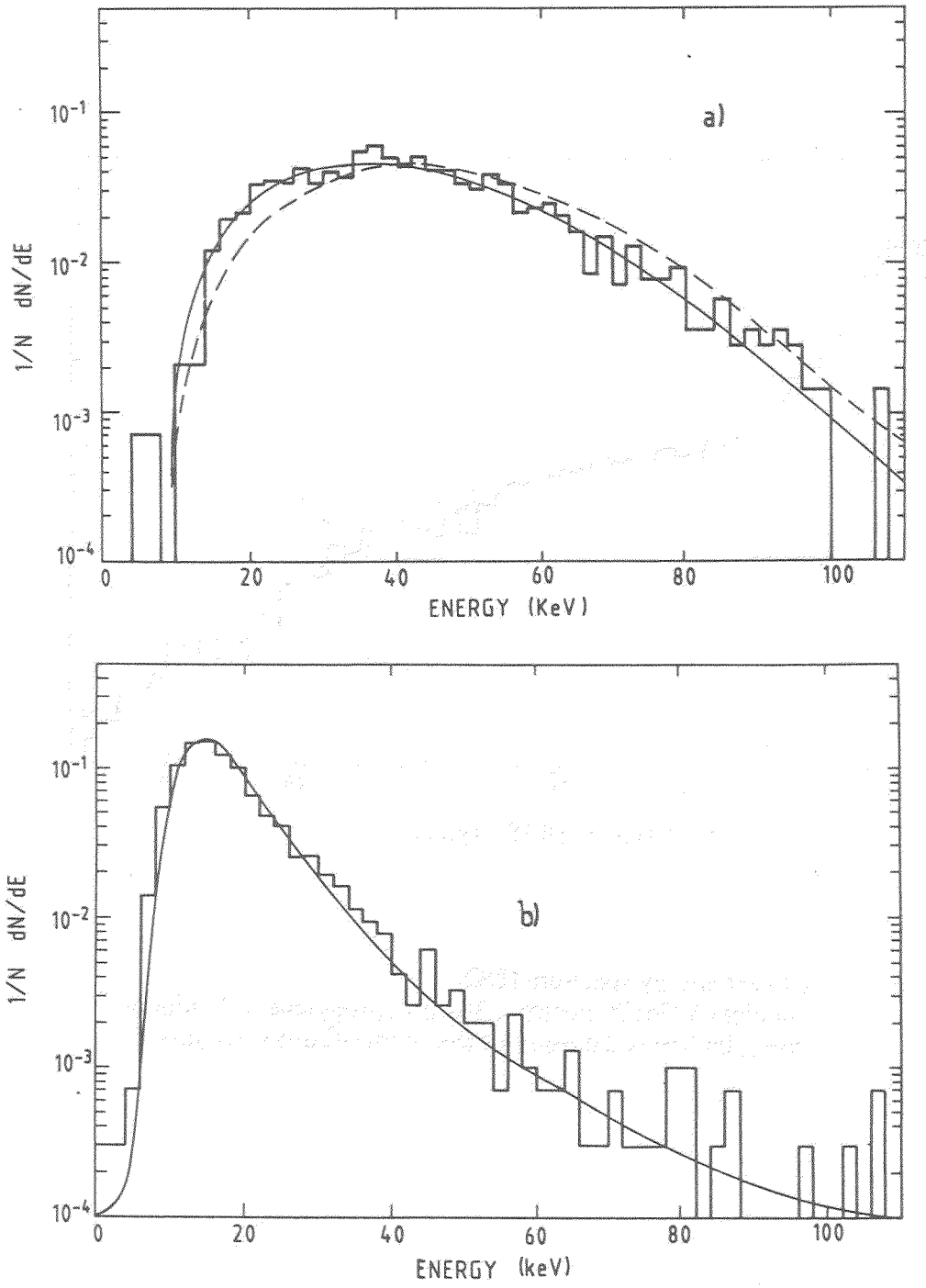

Figure 4 : The total integrated charge distributions (DØ) :
(a) incident 5 GeV/c pion, the solid line is the result of the Monte-Carlo simulation
(b) incident 5 GeV/c electron, 382 polypropylene foil radiator,
the solid line is the result of the Monte-Carlo simulation.

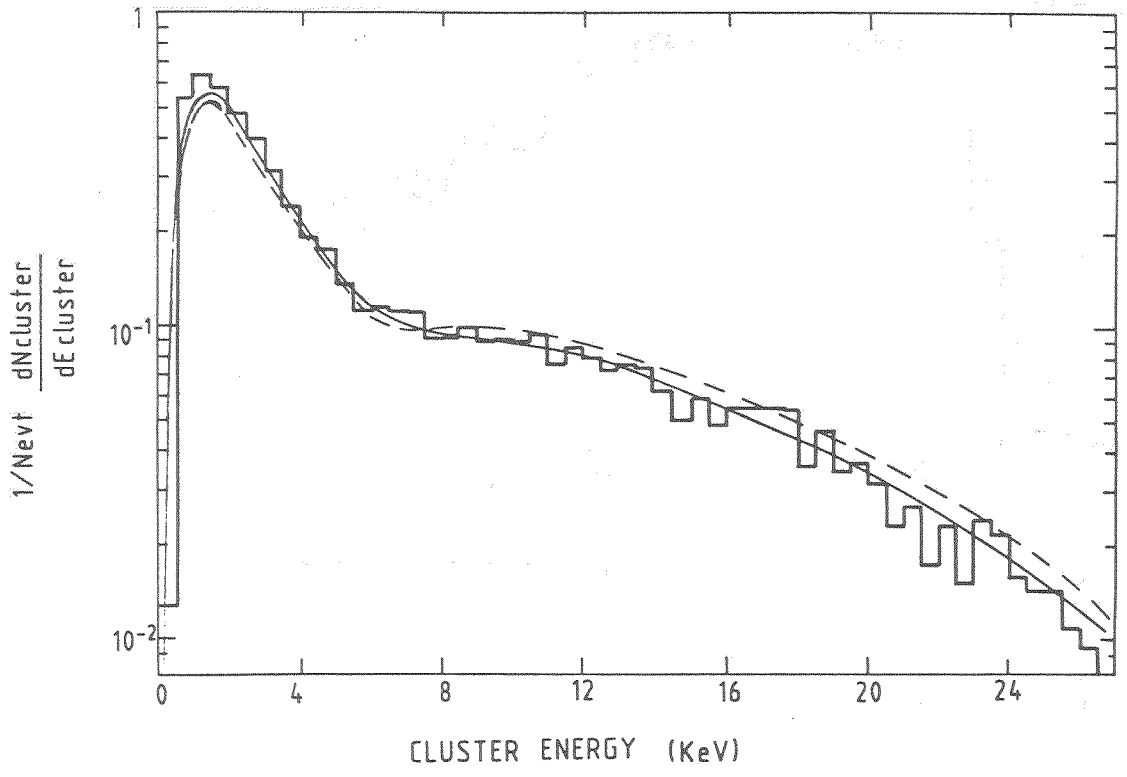

Figure 5 : Cluster energy spectrum (DØ) :
incident 5 GeV/c electron, 382 polypropylene foil radiator,
the solid line is the result of the Monte-Carlo simulation .

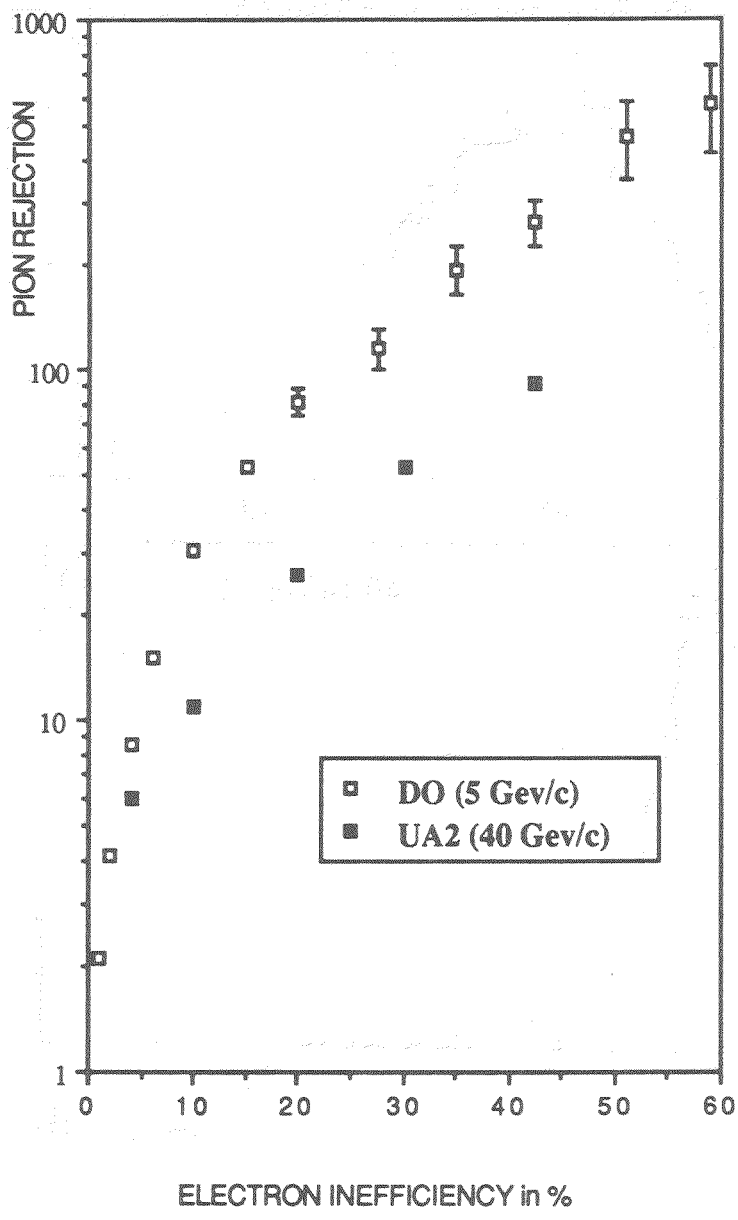

Figure 6 : Pion rejection as a function of the electron efficiency : upper points are the results from DØ at 5 GeV/c beam with 3 sets over a thickness of 305 mm ; lower points are the results from UA2 at 40 GeV/c beam with 2 sets over a thickness of 210 mm.

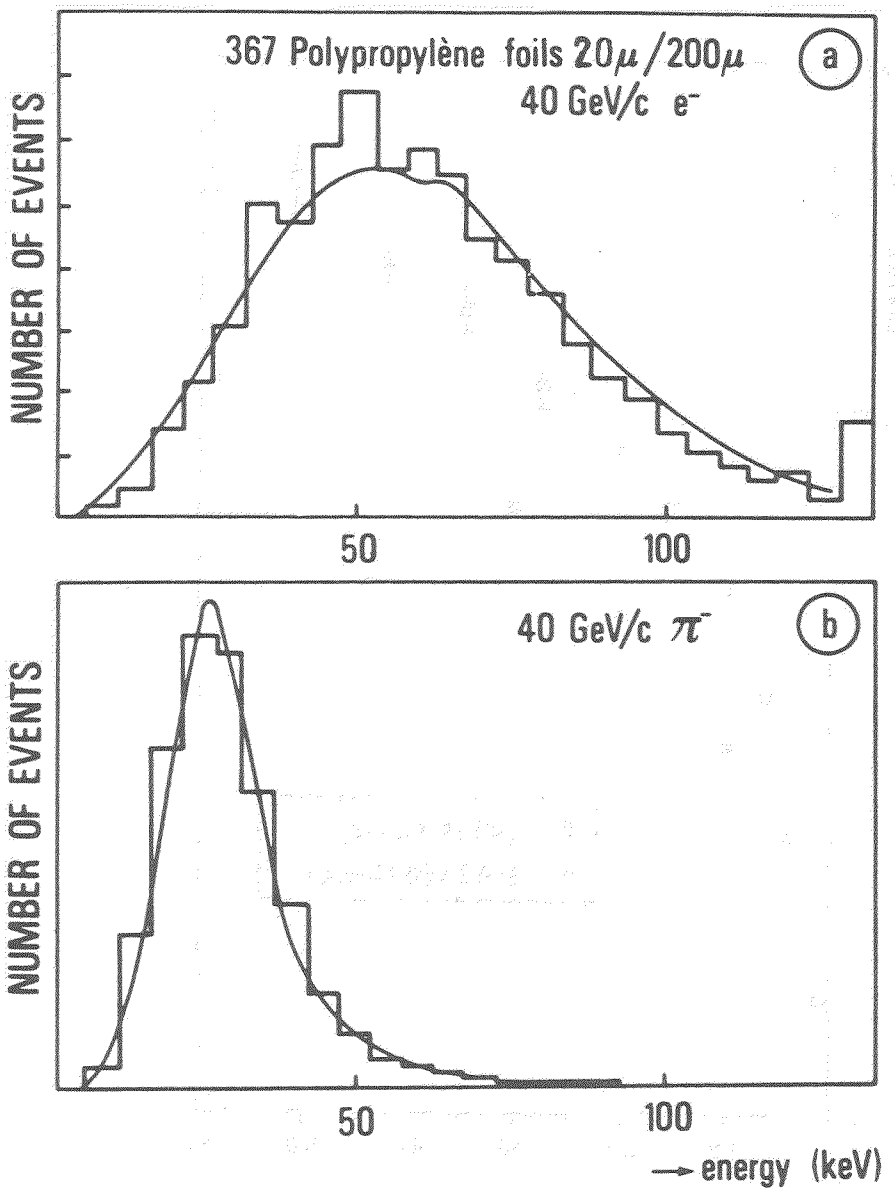

Figure 7 : Measured total integrated charge with one set (UA2) :
(a) test beam data with 40 GeV/c electrons
(b) test beam data with 40 GeV/c pions

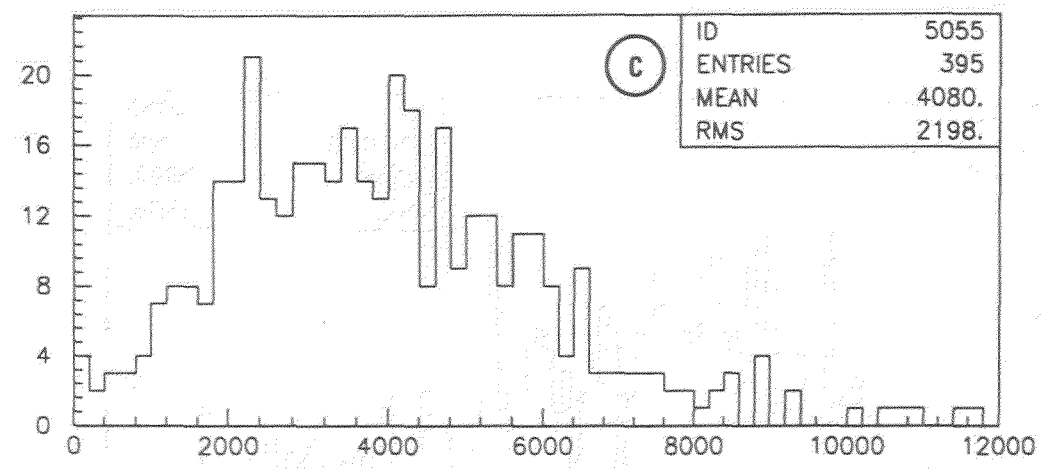

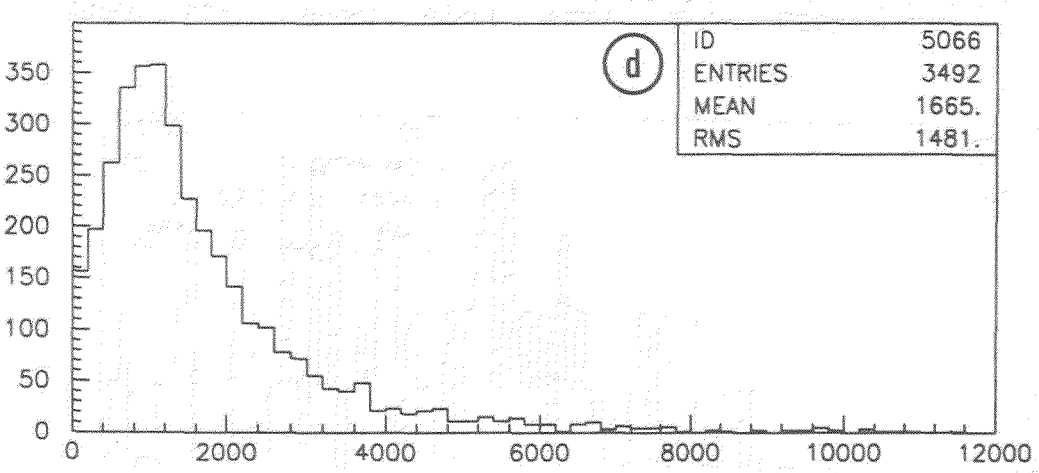

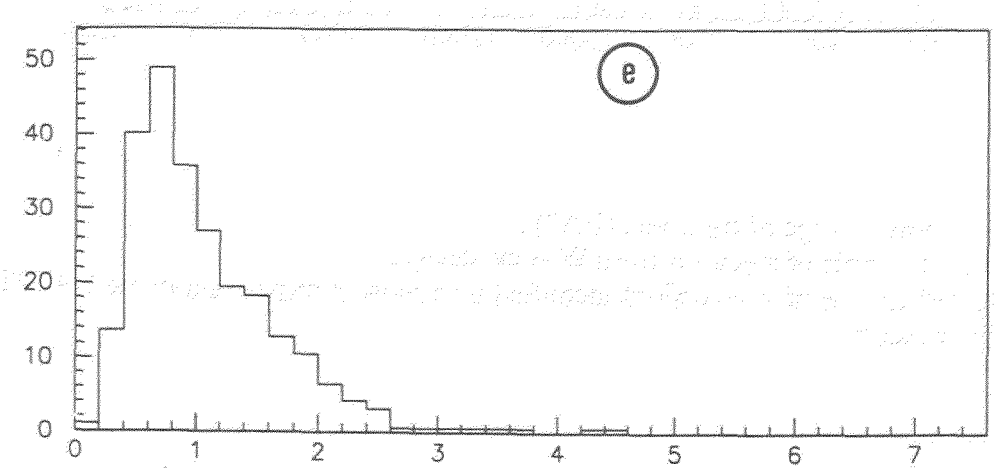

(c) selected sample of electrons from $W \rightarrow e\bar{\nu}$ decays
(d) selected sample of isolated hadrons from $W \rightarrow e\bar{\nu}$ events
(e) Monte-Carlo extrapolation of the energy loss distribution from test beam pion data to the realistic collider data.

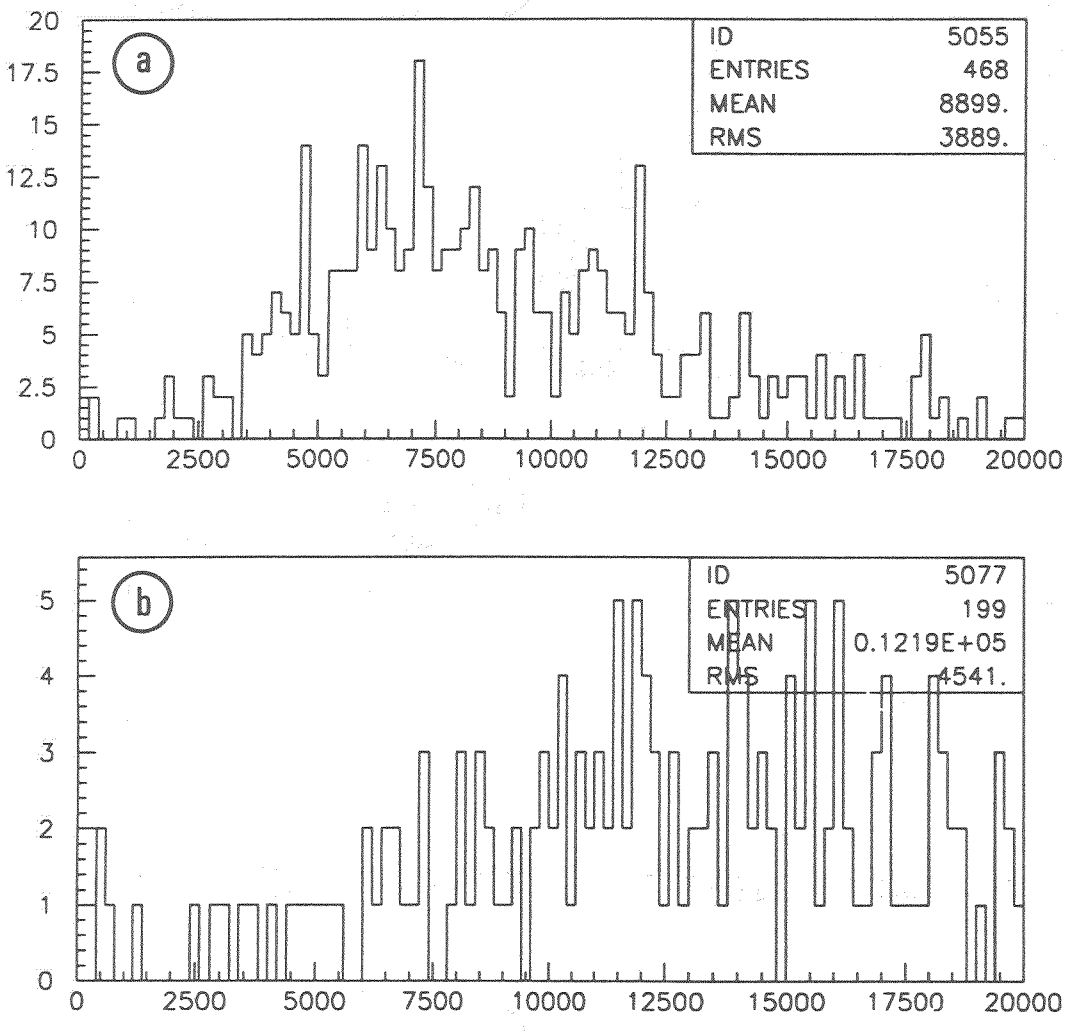

Figure 8 : Combined total charge of the 2 sets (UA2) :
(a) selected sample of electrons from $W \rightarrow e\bar{\nu}$ decays
(b) selected sample of conversions identified by a pulse 2 mip height in the UA2 Silicon pads detector.

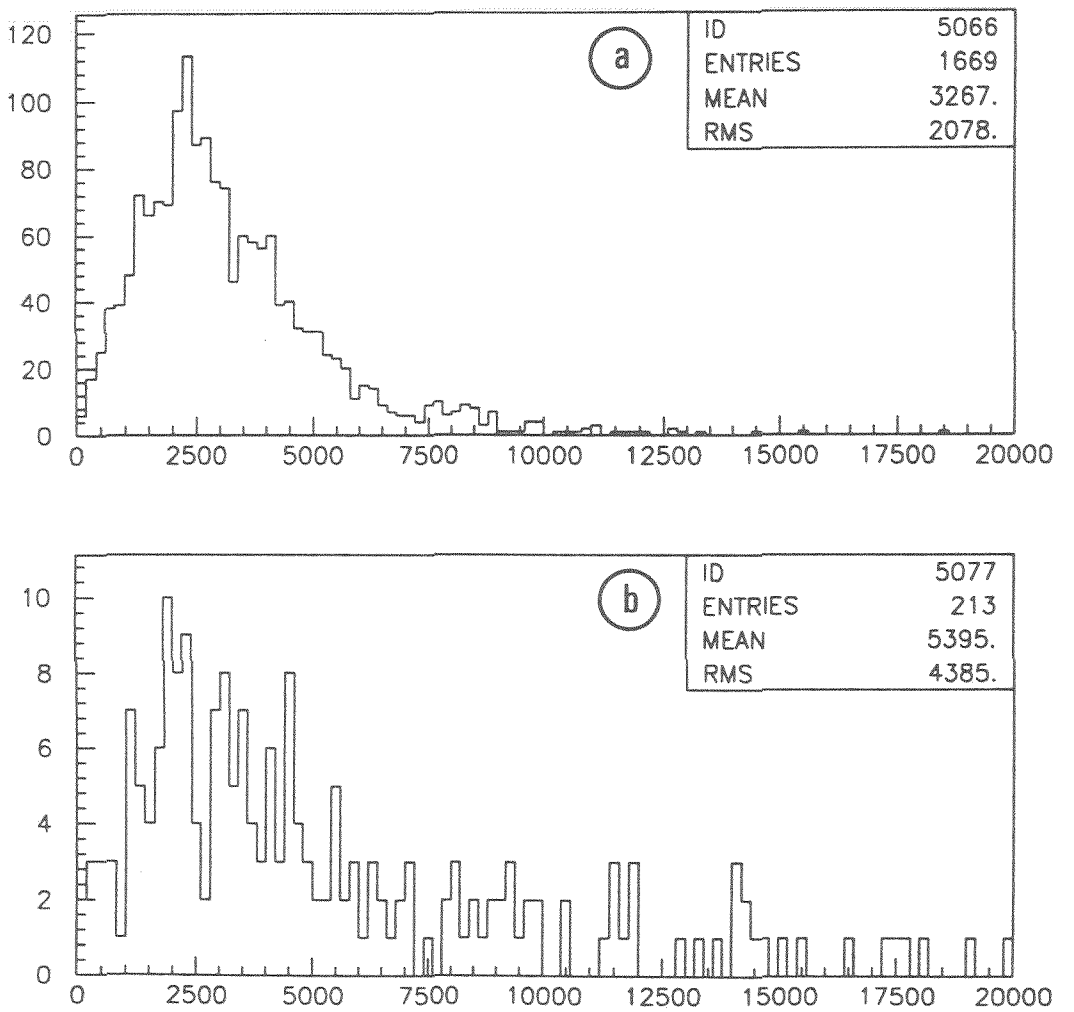

Figure 9 : Combined total charge of the 2 sets (UA2) :
(a) selected sample of isolated hadrons from $W \rightarrow e\bar{\nu}$ events
(b) selected sample of charged track + $\pi^0(\gamma)$ overlaps identified by a 1 mip pulse height in the UA2 Silicon pads detector.

A TRD FOR VENUS AT TRISTAN

Itsuo Nakano*
Institute of Physics, University of Tsukuba,
Tsukuba City, Ibaraki 305, Japan

The VENUS detector at TRISTAN has an upgrade program in response to high luminosity project which starts in summer 1990. A TRD reported here forms a link in the chain of the program. The design of VENUS TRD system, and its R&D results, and expected performance are presented.

Introduction

The VENUS detector has been operating since the first collision of TRISTAN in November 1986. Although many physics results are already published, the performance of the VENUS detector has to be upgraded in order to go into further study of detailed and precise physics with high luminosity. For instance, the present electron identification in barrel part is achieved by an E/p method that is a ratio of particle energy to its momentum. The energy E and the momentum p are measured by lead glass counters (LG) and a central drift chamber (CDC), respectively. Their resolutions are

$$\Delta E/E = 5.4/\sqrt{E} + 2.8 \quad (\%) \quad (E \text{ in GeV}),$$

and

$$\Delta p/p = \sqrt{(0.8 p_t)^2 + (1.2)^2} \quad (\%) \quad (p_t \text{ in GeV/c}).$$

Monte Carlo simulation with LG shows that the E/p method gives an S/N ratio of ~1 for $p > 1$ GeV/c tracks in hadronic events. We would like to gain a factor of 5-10 in the S/N ratio by installing a TRD[1], which results in sufficient performance.

Since the VENUS detector already has a reserved space between CDC and outer drift tubes for the upgrade, the shape of the TRD is cylindrical and the size is 127 cm of inner radius, 155.7 cm of outer radius, and 296 cm in length. This size is large compared to existing and planned TRDs such as UA2[2], D0[3], and ZEUS[4]. This caused mechanical and stability difficulties and cost problem to be overcome at the initial stage of the design.

In this paper, we would like to report description of the TRD system which consists of radiator, X-ray chamber, readout

electronics, and gain stabilization system. Expected performance from R&D and a Monte Carlo calculation is also reported.

Description of the VENUS TRD

Structural features

We have had a series of beam tests in order to design the TRD. Since the total shape and size of the TRD had been given, we performed a beam test to determine the number of layers. We got pion contamination of 12 % and 7 % at 90 % of electron efficiency for 3 and 4 layers, respectively. Therefore we took 4 layers. We also divided the cylindrical shape into eight segments for construction simplicity.

Figure 1 shows a perspective and a part of end view of the TRD. Holes were prepared at the edge of each segment to insert RI sources to control gas gain. The frame was made of aluminum plate to reduce the construction cost. The thickness of the TRD is 0.18 radiation lengths in all. A beam test and a Monte Carlo calculation say that degradation of energy resolution of LG is negligible.

Structure of radiator part of one layer is shown in fig. 2. The window is made of 3 mm thick rohacell-31 and glued to aluminized-Mylar which is a negative field plane of X-ray chamber. This structure is different from balloon structure of other groups like UA2[2], D0[3] and ZEUS[4] as shown in fig. 3. The reasons other groups use the balloon structure are that the window can be thin, that it avoids bulging of X-ray and radiator chambers by flowing nitrogen gas between them, and that it keeps He gas from leaking into X-ray chamber. But this structure will be difficult to support a large TRD like ours. Therefore we took rohacell-31 as a window to get rigidity, stability, and easiness to assemble at the sacrifice of transmission probability. But the loss against pion contamination due to this turned out to be ~1 %.

If the TRD had temperature gradient, it would cause position dependence of gain. Therefore, we will do plumbing of water cooling pipe to cool down and keep a constant temperature for TRD together with preamplifiers as shown in fig. 4.

Radiator

Advantages of polypropylene fibers over lithium foils as a radiator have been described elsewhere[5]. We tested two types of polypropylene fibers. One is irregularly compressed to the densities

between 0.05 and 0.15 g/cm^3. The other one is combed, compressed to the same densities as the first ones, and woven. The first one gave slightly better e/π separation at the density of 0.15 g/cm^3 . But the separation power was the same at the density of 0.12 g/cm^3 . However, the second one is mechanically more stable and easier to assemble. Therefore we chose the second one of 18 μm diameter fiber. The thickness of the radiator is 45 mm as shown in fig. 2.

X-ray detector

The X-ray detector is longitudinal drift chambers as shown in fig. 2. The thickness of the chambers is 20.0 mm and the drift space is 12.6 mm. The anode wires and field wires have a diameter of 30 μm and 100 μm, respectively. The gold-plated tungsten anode wires are strung by a tension of 100 g and fed by a high voltage of +1.74 kV. The gold-plated Cu-Be field wires are strung by a tension of 300 g. The wire spacing between anode wires are from 12.5 to 13.2 mm depending on the layer.

The gas used is a mixture of xenon (90%) and methane (10%). A permanent gas recirculation and purifier system maintains the oxygen and water contamination down to less than 1 ppm[6] and –76°C of dew point, respectively.

Readout electronics

In early stage of R&D, we studied a cluster counting method but it gave us essentially the same e/π separation power as a total charge integration method[5),7)]. Therefore we chose the total charge integration type readout system and we have developed a low noise JFET charge sensitive preamplifier shown if fig. 5. This charge sensitive preamplifier is implemented as a form of single-in-line hybrid circuit. The measured equivalent noise charge (ENC) is 375~400 (rms) at a shaping time constant of 0.2 μsec with no load. 16 channels of the hybrid preamplifiers are installed on an each preamplifier card with a calibration signal receiver circuit and H.V. decoupling capacitors. The preamplifier cards will be mounted and be kept to be a constant temperature by a water cooling system shown in fig. 4 as mentioned previously. The output signals of the preamplifiers are fed into a TKO[8)] module which contains 32 channels of receiver-shaper amplifiers, gated integrators, and then a successive approximation type ADC. The shaping amplifier and the gated integrator are also developed as shown in fig. 6.

Gain control system

Temperature of TRD gas can be kept constant by cooling water as described previously. However, pressure in chamber is relative to atmospheric pressure. Gas gain of X-ray detector varies depending on the atmospheric pressure as $\Delta G/G \sim -7\Delta p/p$. According to our study, the gain variation $\Delta G/G$ should be less than 10 % to keep pion contamination 6-7 % at 90 % of electron efficiency. If the $\Delta G/G$ goes up to 20 (30) %, the pion contamination increases up to 9 (15) % unless the gain change is corrected. Atmospheric pressure can change by 20 mbar every week or so, and that corresponds to 14 % gain variation. Therefore, we need some method to keep the gain variation less than 10 %.

There are two possible methods to maintain pion rejection power less than 7 % against the variation. Both methods monitor gas gain of a reference wire which is irradiated by an RI source such as ^{55}Fe. First method is to correct it later at an analysis stage and the second one is to change high voltage periodically so that the gas gain is constant.

We chose the second method and we have tested a gain control system with a monitor and a test chambers exposing an RI source ^{55}Fe. High voltage was changed to control the gain by measuring pulse heights of the monitor chamber. The results are shown in fig. 7. We could keep the gain variation within a few percent. We will plug an RI source at the edge of each segment and control the gain by monitoring the edge wires and changing the high voltage.

Incidentally, we would like to discuss on nitrogen problem. Generally speaking, it is very difficult to remove nitrogen in a gas recirculation system. We estimated that we would get a few percent nitrogen contamination per year through permeation and leak via aluminized-Mylar window. Nitrogen contamination has two effects. The first effect is to change the drift velocity of electron in the gas. The second effect is to attenuate a pulse height about 5 % per 1% nitrogen contamination into a mixture of xenon (90 %) and methane (10 %). We confirmed with a beam test that if the gain change is corrected, the e/π separation powers for 300 ppm and 6 % nitrogen contamination are the same for the mixture of xenon (90 %) and methane (10 %). Therefore, the gain control system is expected to take care of these effects.

Performance

Figure 8 shows TRD performance of a test chamber with a test beam. The horizontal coordinate is a total length of the detector as a parameter to compare our data with others[2),3),9)]. We concluded that our optimization parameters, that is, radiator material, chamber thickness, window material, the number of layers and so on, are reasonably good. This result promises that the TRD gives us a factor of 18 gain of S/N ratio at an electron efficiency of 90 % for a single charged particle.

In real VENUS detector, there would be bremsstrahlung because of existence of materials inside of TRD such as beam pipe, inner chamber, and CDC. In addition, there would be overlapping of particles in hadronic events. Therefore, we could not expect a factor of 18 gain in S/N ratio in hadronic events. We estimated the gain of S/N ratio in hadronic events in VENUS detector by a Monte Carlo calculation. Hadronic events at $\sqrt{s}$ = 55 GeV were generated and tracks with momentum greater than 1 GeV/c were analyzed. The results are shown in fig. 9. Dotted histogram is an E/p distribution with only LG counters. If we add TRD information, pion background will be reduced as shown in solid histogram. That gives us a factor of 5 gain of S/N ratio with 90 % of electron efficiency.

Conclusion

We would like to conclude this report as the followings.

(1) A very large (~3 m in diameter, ~3 m in length, and 29 cm in thickness) cylindrical VENUS TRD is under construction and almost completed.

(2) The VENUS TRD will be operated with a radiator of polypropylene fibers (18 μm in diameter and density of 0.12 g/cm^3), a gas of xenon (90 %) and methane (10 %) mixture, and an identification method of total charge integration.

(3) With the TRD, the pion rejection power in hadronic events (single charged track) is expected to improve a factor of ~5 (~18) with an electron efficiency of 90 %. The TRD is expected to be useful to do good physics with VENUS detector.

(4) The gain control system is expected to keep the gain variation within a few percent.

Acknowledgement

It is a pleasure to thank the member of the organizing committee for the invitation to participate in this Symposium. Thanks are due to my colleagues in the VENUS collaboration for fruitful discussions. Thanks are also due to Prof. K. Takahashi, Prof. S. Iwata, and Prof. K. Kondo for their continuous support and encouragement.

References

* Representing the VENUS TRD group.
Y. Fukushima, T. Kohriki, S. Nakamura, K. Ogawa, M. Sakuda, Y. Watase
KEK, National Laboratory for High Energy Physics, Tsukuba, Ibaraki 305, Japan.
Y. Chiba, T. Ohsugi, N. Terunuma
Department of Physics, Hiroshima University, Hiroshima 730, Japan.
T. Kanda, Y. Suzuki, A. Tsukamoto, H. Yamamoto
Department of Physics, Osaka University, Toyonaka, Osaka 560, Japan.
and I. Nakano
Institute of Physics, University of Tsukuba, Tsukuba City, Ibaraki 305, Japan.

1) Y. Suzuki et al., "The Proposal of the Transition Radiation Detector for the VENUS Experiment", VENUS Note 208, March, 1988, (unpublished).
2) R. Ansari et al., Nucl. Instr. and Meth. A263 (1988) 51.
3) J. Detoeuf et al., Nucl. Instr. and Meth. A265 (1988) 157.
4) ZEUS Collaboration, "The ZEUS Detector Status Report 1987", PRC 87-02 (1987).
5) Y. Watase et al., Nucl. Instr. and Meth. A248 (1986) 379.
6) Y. Chiba et al., Nucl. Instr. and Meth. A269 (1988) 171.
7) B. Dolgoshein, Nucl. Instr. and Meth. A252 (1986) 137.
8) KEK Data Acquisition Development Working Group, "TKO specification", KEK Report 85-10 (1985).
9) R. D. Appuhn et al., Nucl. Instr. and Meth. A263 (1988) 309.

Figure Captions

Fig. 1. A perspective and a part of end view of the VENUS TRD.

Fig. 2. Schematic configuration of a radiator, a window, and an X-ray detector.
Fig. 3. Comparison of rigid window with balloon structure.
Fig. 4. A schematic diagram of end plate part of VENUS TRD. Preamplifier cards and water cooling pipe are installed on this end plate and are shielded by aluminum plate.
Fig. 5. A circuit diagram of a low noise JFET charge sensitive preamplifier.
Fig. 6. A circuit diagram of shaper amplifier and gated integrator.
Fig. 7. Gain variation (a) without feedback and (b) with feedback.
Fig. 8. Pion contamination of VENUS TRD at 90 % of electron efficiency together with those of UA2, D0, and ZEUS.
Fig. 9. E/p distribution for Monte Carlo hadronic events at $\sqrt{s}$ = 55 GeV with LG only (dotted histogram) and LG + TRD-cut (solid histogram). Only charged tracks with momentum greater than 1 GeV/c are analyzed.

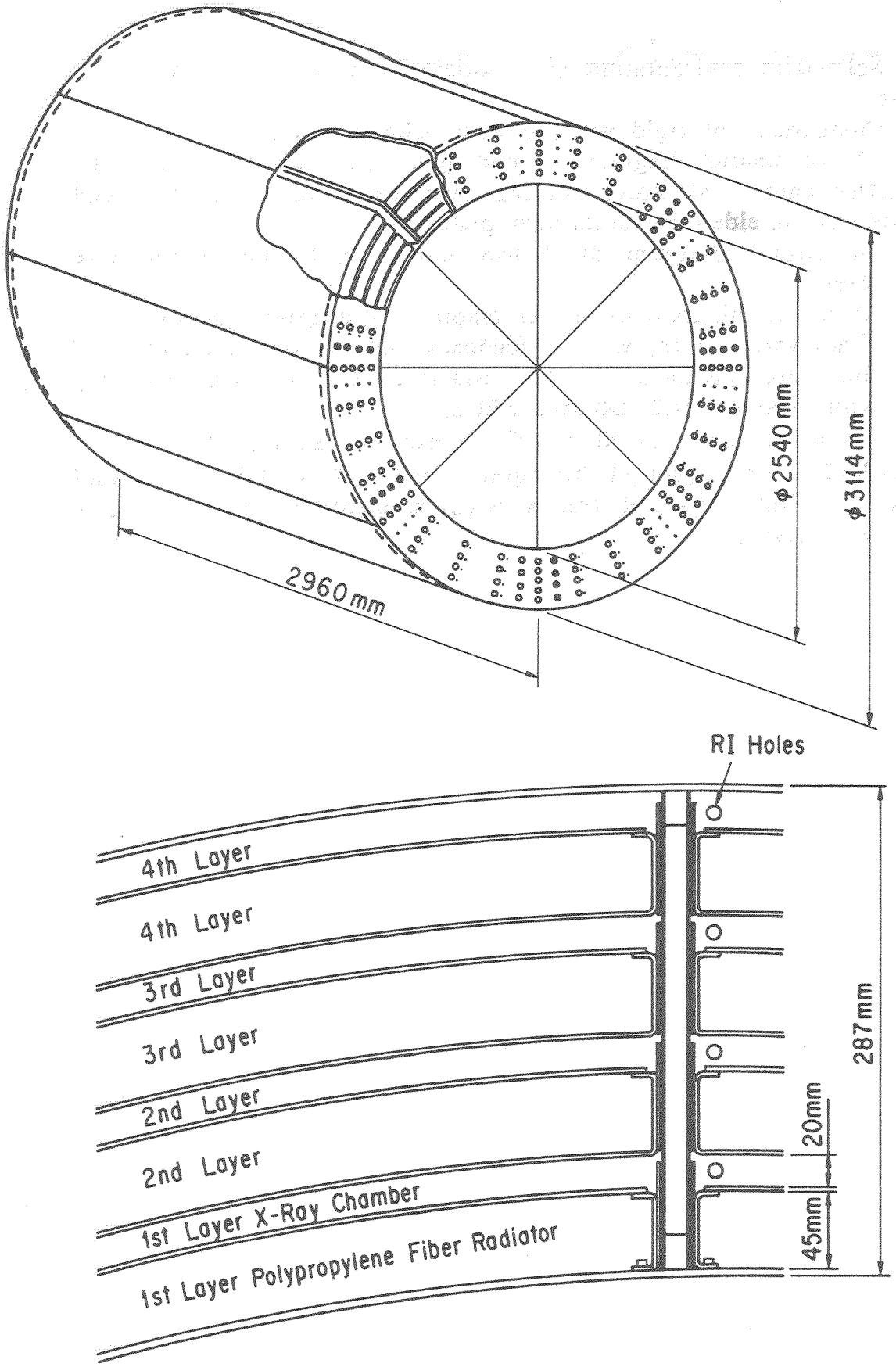

Fig. 1. A perspective and a part of end view of the VENUS TRD.

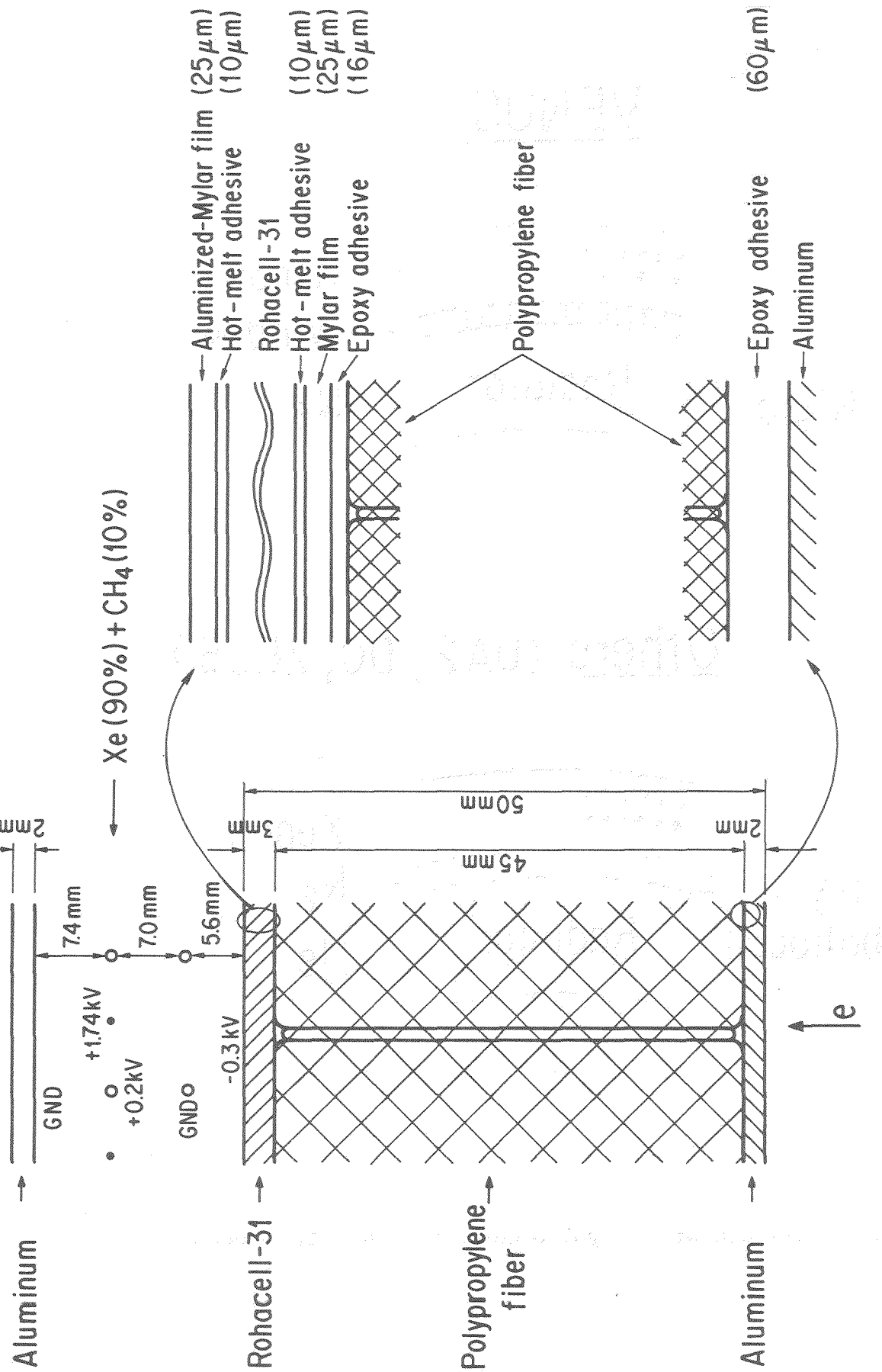

Fig. 2. Schematic configuration of a radiator, a window, and an X-ray detector.

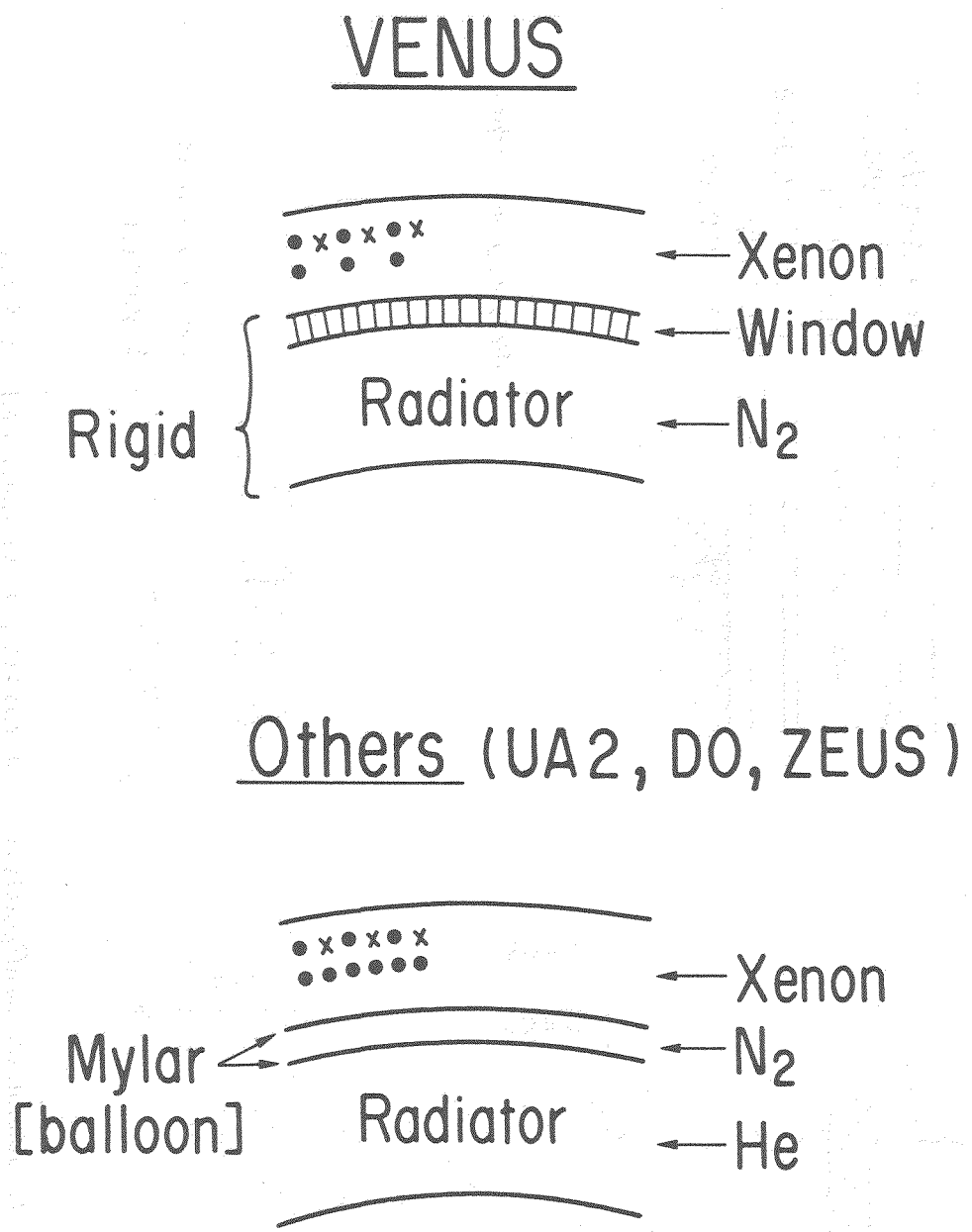

Fig. 3. Comparison of rigid window with balloon structure.

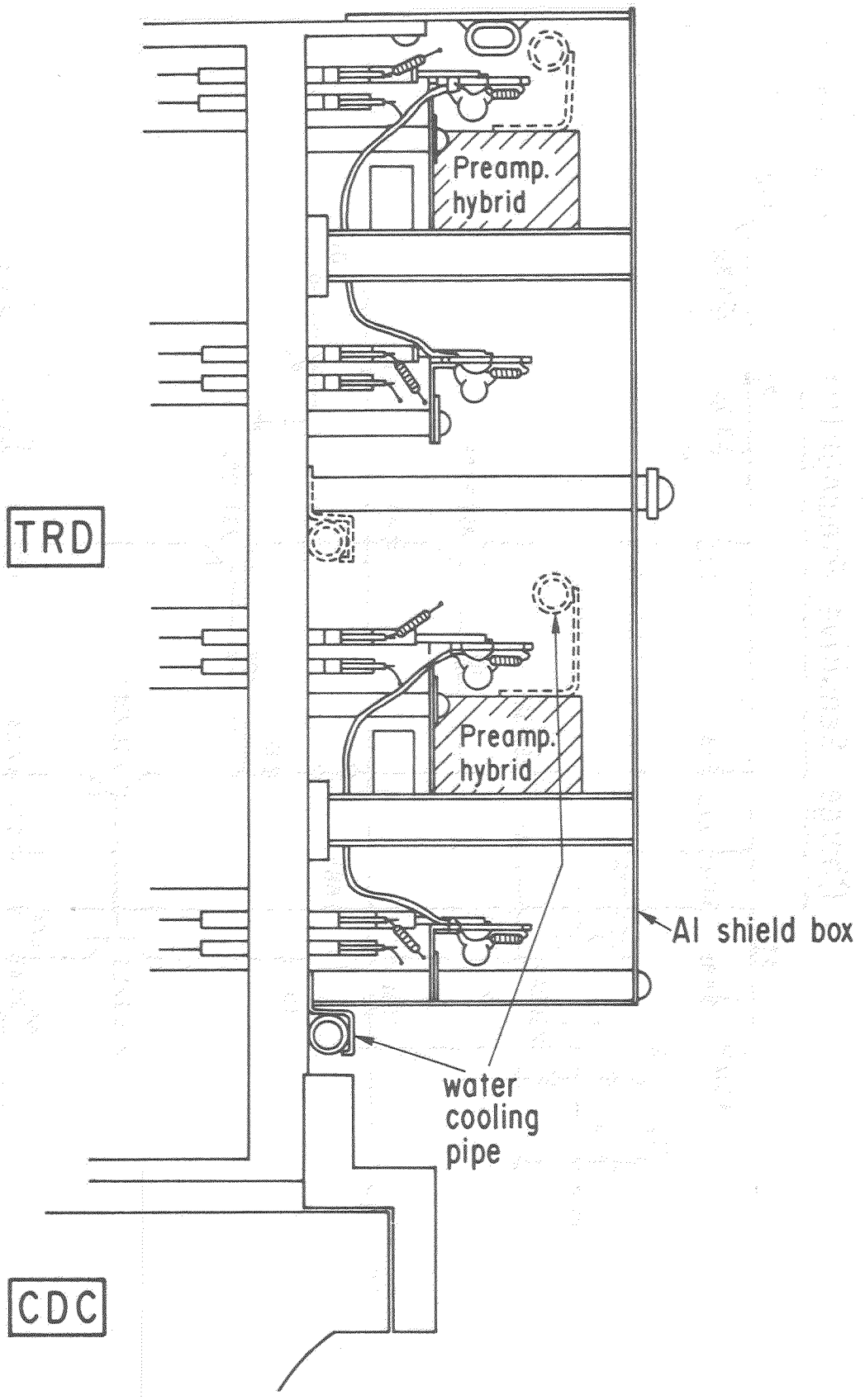

Fig. 4. A schematic diagram of end plate part of VENUS TRD. Preamplifier cards and water cooling pipe are installed on this end plate and are shielded by aluminum plate.

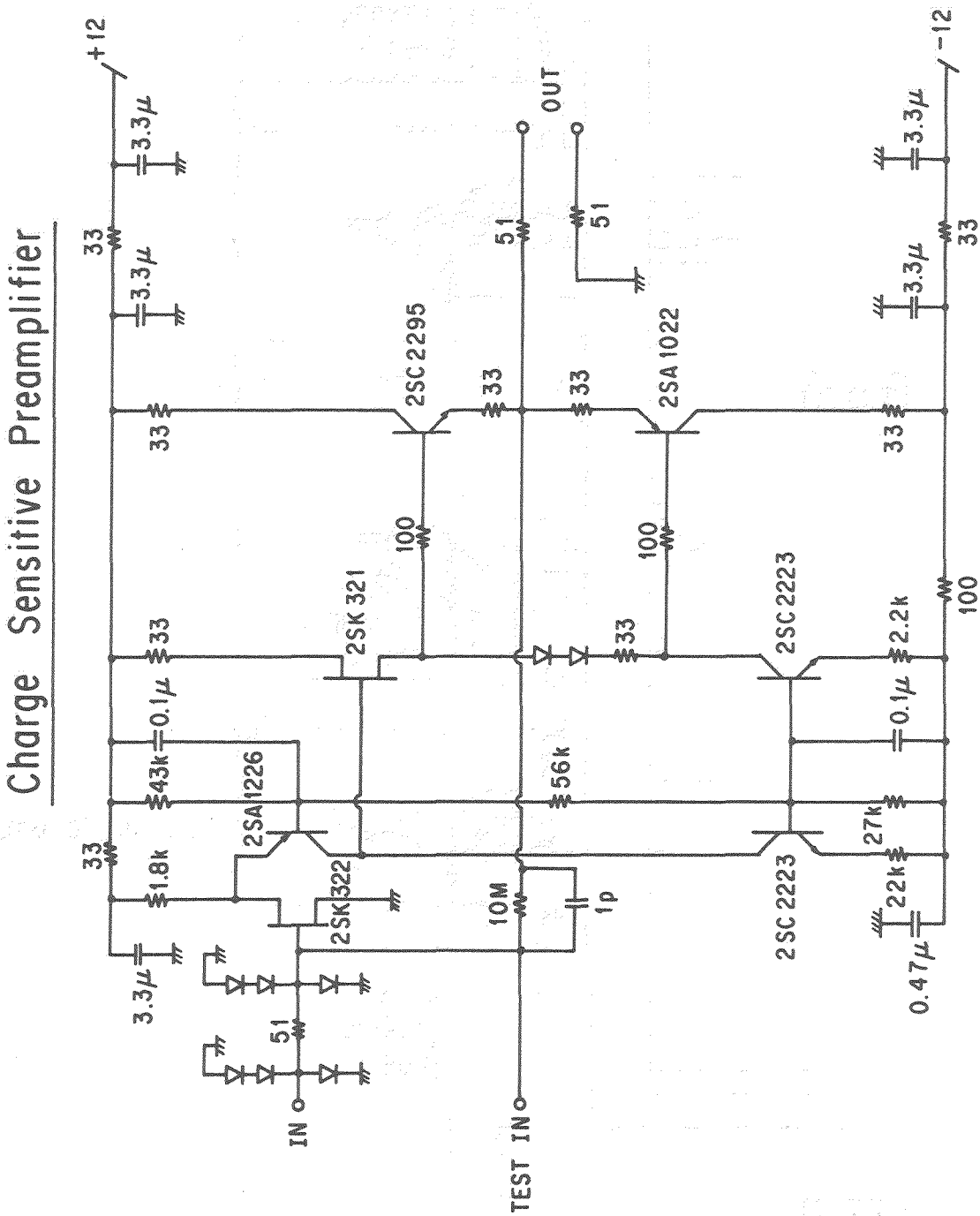

Fig. 5. A circuit diagram of a low noise JFET charge sensitive preamplifier.

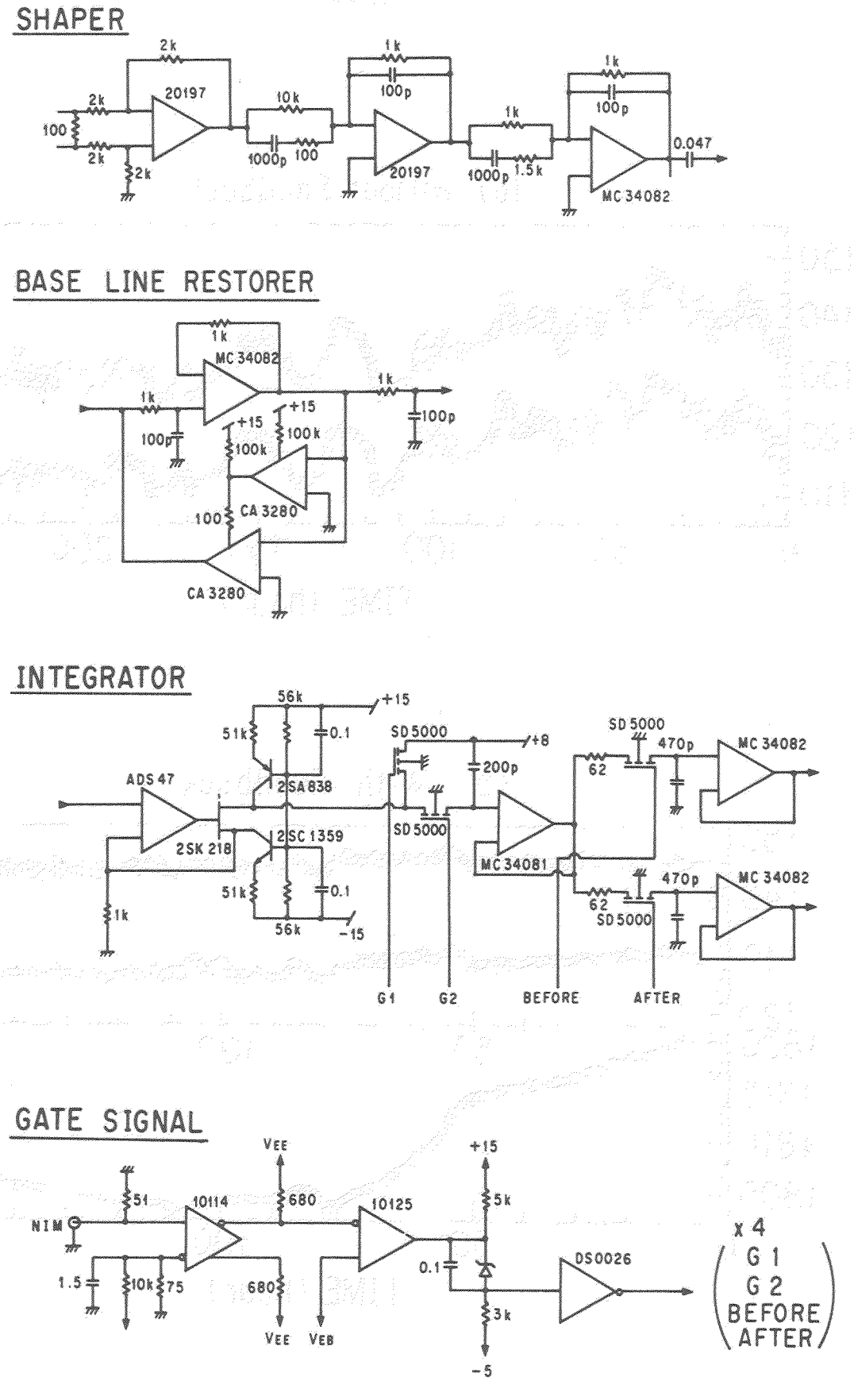

Fig. 6. A circuit diagram of shaper amplifier and gated integrator.

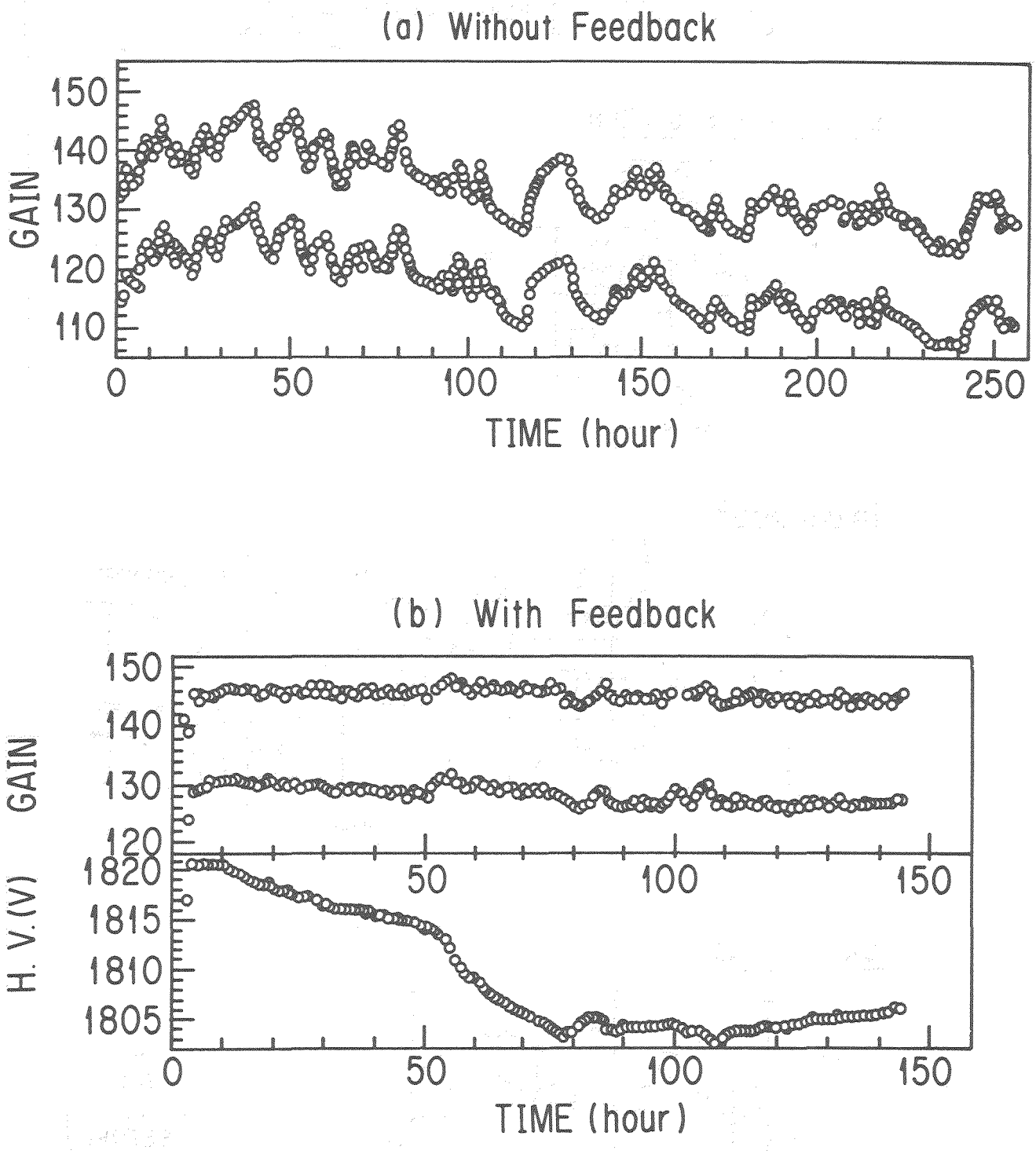

Fig. 7. Gain variation (a) without feedback and (b) with feedback.

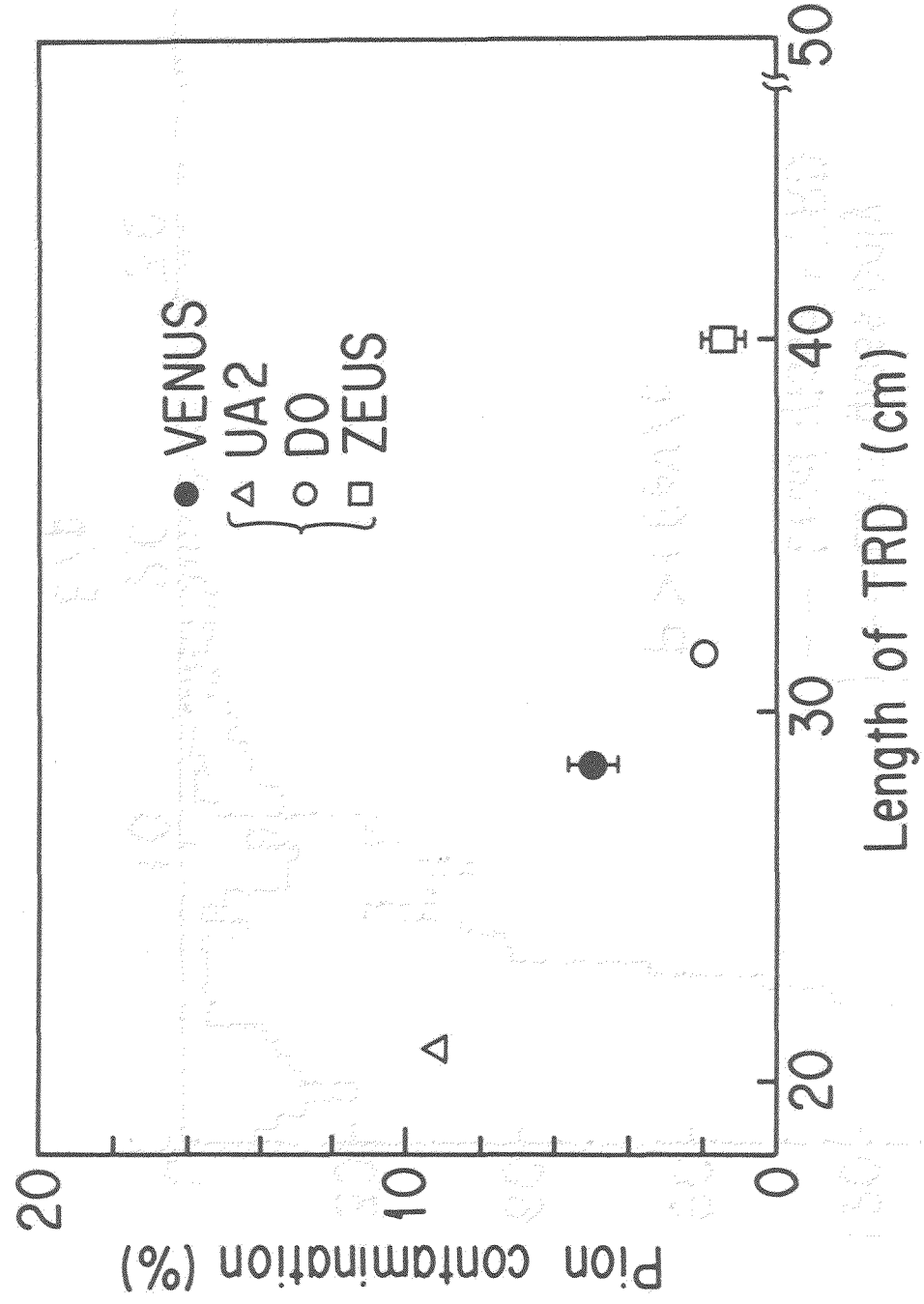

Fig. 8. Pion contamination of VENUS TRD at 90 % of electron efficiency together with those of UA2, D0, and ZEUS.

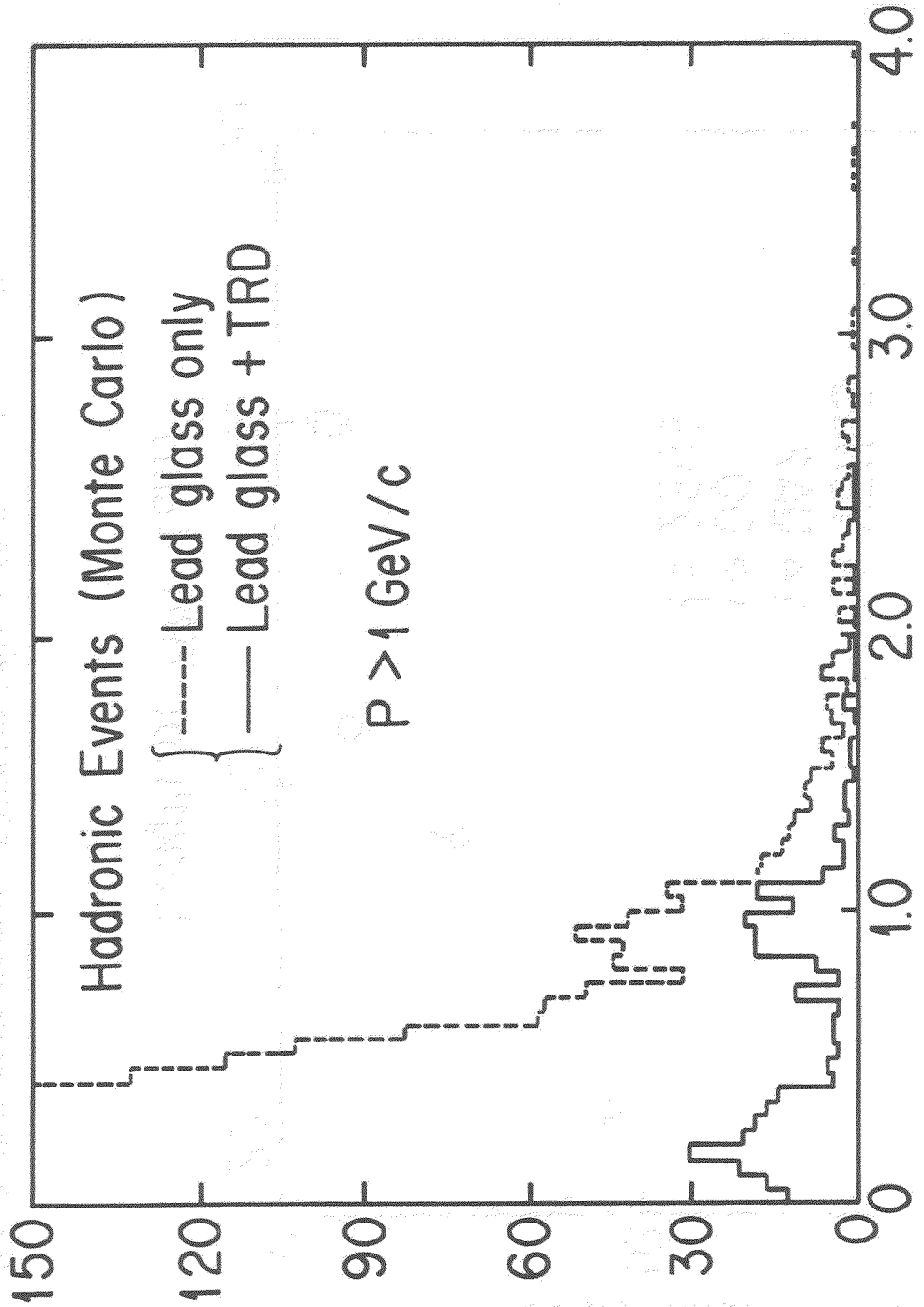

Fig. 9. E/p distribution for Monte Carlo hadronic events at $\sqrt{s}$ = 55 GeV with LG only (dotted histogram) and LG + TRD-cut (solid histogram). Only charged tracks with momentum greater than 1 GeV/c are analyzed.

A TRANSITION RADIATION DETECTOR AND TRACKER FOR THE SSC.

J. Shank, J. Beatty, T. Coan, A. Marin, S. Whitaker, R.J. Wilson, B. Zhou
Boston University
Boston, Massachusetts

Abstract.

A preliminary study of the feasibility of a combined tracker/transition radiation detector for the SSC is discussed. A design using 32 transition radiation detector modules, each containing a radiator and two layers of 4 mm diameter straw chambers, is modeled with a Monte Carlo program. Additional tracking is provided by 8 inner layers of straws and 4 outer layers. The model indicates this design can provide a pion rejection on the order of 10^{-3} for isolated particles, and tracking performance is adequate. Straw chamber occupancy and lifetime have been examined. Further optimization is required to get these to acceptable levels.

Introduction

It has become a commonplace that most of the interesting physics to be studied at the SSC is most accessible through study of leptonic channels. The massive particles that should occur at or before the TeV scale of electroweak symmetry breaking are expected to have significant branching fractions for channels including high energy electrons or muons. These may be direct decay products, as in the case of a massive $Z' \rightarrow e^+e^-$, or they may arise from decays of W and Z bosons produced in the primary decay, as in the "golden" decays $H \rightarrow ZZ \rightarrow e^+e^-e^+e^-$. Efficient lepton identification over large solid angle and down to low momenta will enhance acceptance for these multileptonic decays.

The event rate for leptonic decays is down from hadronic decay modes because of small branching fractions, but this is amply compensated by the lower background. For example, a 1 TeV Z' is expected to decay to e^+e^- with a branching fraction of $\approx 10^{-2}$. The background to this signal is the Drell-Yan continuum; this is lower by a factor of 10^6 than the QCD two-jet continuum background to hadronic decays of the Z'. Thus the signal-to-noise ratio will be four orders of magnitude higher for the leptonic decay mode. Of course, in order to achieve this dramatic enhancement of S/N, it will be crucial that hadrons have a very low probability to satisfy the lepton identification criteria.

Our work has been directed at the development of a combined tracking system and transition radiation detector(TRD). The goal has been to achieve adequate charged par-

ticle tracking and to provide, via generation and detection of transition radiation x-rays, electron identification power to supplement the principal electron selection by calorimetric signatures. Although the question of what constitutes adequate charged particle tracking is addressed briefly later, the focus of our work so far has been on the development of a "straw design" for a TRD that would meet the electron identification requirements of an SSC detector. To this end, we have selected a first-order design and carried through a study of its performance for single particles. The present design is far from optimized, and we have yet to study the performance in a realistic multi-track environment; work in these areas is in progress.

The Detector.

The starting point for the design studied here is the "Non-Magnetic Detector" described in the Berkeley 1987 meeting[1]. This design emphasized hermetic calorimetry and no or low magnetic field. It also included a transition radiation detector/tracker using straw wire chambers. Figure 1 shows the detail of a possible design for a transition radiation detector/tracker which we have chosen to model here. It consists of three main sections: an inner group of axial straws for r-θ tracking, 32 transition radiation (TR) modules, and an outer group of axial straws. The inner tracking section consists of 8 layers of 4mm diameter straws, close packed. The outer tracking section has 4 layers of close packed 4mm diameter straws.

The transition radiation modules form a hexagonal cylinder about the beam line. Each module consists of a one centimeter thick radiator followed by two layers of straws. The straws run in the r-θ plane; they constitute the x-ray detector and also provide r-z tracking. The radiators are modeled as a stack of polypropylene foils separated by helium filled gaps. Our present design has 50 20μm thick foils with 180μm gaps, but we have considered several alternatives. Table 1 shows the material inventory for several design variations. The straws are assumed to be made of mylar and polycarbonate with 30μm thick walls. The design has not been optimized and we are in the process of considering various thickness foils (or fibers) and gaps.

This design has a total of 24k tracking straws in the axial direction and 166k in the TR modules assuming a coverage of $|y| < 1.5$. This number would approximately double to cover rapidity of $|y| < 3$.

Transition Radiation X-ray Production.

The production of transition radiation has been extensively studied[2]. Briefly, x-rays

Table 1. Material in Transition Radiation Detector.		
Material	Radiation Lengths	
8+64+4 Straws + wire	0.030	
Xe in 64 straws	0.013	
32 TR Radiators:		
(a) 100 20μm foils CH_2, 80 μm gap	0.133	
(b) 50 20μm foils CH_2, 180 μm gap		0.067
Total	0.18 (a)	0.11 (b)

are coherently produced when a relativistic charged particle crosses the interface between two media. The yield of x-rays is of order α (1/137) for a single interface so practical devices use multiple interfaces. This requires the radiator material be of low Z so x-rays produced in early layers make it through the last layer. Materials that have been used include lithium foils and polypropylene (CH_2) foils and fibers. The number of x-ray photons produced is proportional to the Lorentz factor, γ, initially, but saturates typically a factor of ten higher than the threshold value. The x-ray production depends on the incident particle only through γ, so a pion with energy,

$$E_\pi = \frac{M_\pi E_e}{M_e}$$

will produce x-rays the same as an electron of energy E_e.

Figure 2 shows the x-ray production as a function of γ for some of the radiators we are considering, including (a) and (b) from table 1. In trying to choose an optimum radiator, we want one that has the steep increase in x-ray yield as high as possible so electrons in the interesting energy range produce x-rays and pions do not. We also want to reduce the total thickness of the radiator material, which, as seen from table 1, is the major contributor to material in the detector. It is interesting to note the difference between (a) and (b) in figure 2. The saturation level for (b) is almost as high as (a), but (b) has half the amount of material. Radiator (b) also has a slightly higher γ threshold. We have only just begun this optimization process, but for the remainder of this paper we will use (b): 50 foils, 20 μm thick, with a 180 μm thick gap.

Figure 3 shows the x-ray spectrum for radiator configuration (b). The peak of the distribution is at 7.5 keV and the average about 10 keV. The angular distribution of the X-rays is a complicated function. Figure 4 shows this dependence for an incident 50 GeV

electron. The x-ray energy was taken to be 7.5 keV, the peak of this x-ray spectrum. The yield oscillates rapidly as a function of $(\gamma\theta)$ with the major contribution coming from $\gamma\theta = 93$, or $\theta = 1$ mr, with a significant secondary peak at $\theta = 1.6$ mr.

X-ray Detection.

In order to detect the x-rays a high Z gas is required, typically xenon. There are trade-offs to be balanced in choosing a gas; mainly between good x-ray detection and high speed. This will be discussed below in the section on occupancy and lifetime. For the transition radiation simulation here, we have used a mix of 60% Xe, 40% CH_4 which for the x-ray spectrum produced gives a probability of 45% that an x-ray will interact in the gas of either of the two straws immediately following the radiator. Approximately 20% of the x-rays are absorbed in the subsequent radiator, and the remaining 35% mostly interact in the third and fourth layers.

We are presently assuming an energy threshold method would be used for tracking and x-ray identification. If the energy deposited in the straw is above E_t, it is considered an x-ray hit. A track is flagged as an electron if the number of straws (of the 64 traversed by the track) that have energy deposition greater than E_t is greater than or equal to N_t. The thresholds, E_t and N_t, would be chosen for optimum electron selection and could be dependent on the energy measurement from the calorimeter. The energy threshold used for tracking would be less than the typical dE/dx. This allows the use of "two bit" electronics: a low threshold bit flags a tracking hit, and a high threshold hit flags an x-ray.

The TRD Monte Carlo Program.

A single track Monte Carlo program was run to study the pion rejection ability of this system. Each radiator was taken to consist of 50 foils of polypropylene (CH_2) 20μm thick with 180 μm wide helium gaps. The algorithm used in the program is:

- Assume an incident particle (electron or pion) with a given energy.
- Generate an x-ray spectrum, taking x-ray absorption of the radiator material into account.
- Propagate the incident track and all generated x-rays through all 32 TR modules. For each of the 64 straws hit, calculate the energy deposited in the straw. This includes dE/dx, delta rays, and the sum of all x-ray energy deposited. The x-ray interaction was modeled assuming secondary fluorescent x-rays, produced according to the known fluorescence yields for the Xenon K and L shells, escape from the straw.

- Apply the threshold criteria mentioned above to get the electron efficiency: the probability that the number of straws with $E > E_t$ is $\geq N_t$. For pions this same probability is the chance that the pion is mistakenly flagged as an electron.

Figure 5 shows the electron efficiency calculated for 50 GeV incident electrons. There is a "wall" along the low energy side which is the result of dE/dx energy loss. Almost all straws are hit when the energy threshold is less than the typical dE/dx of about 1.5 keV. The slice of figure 5 taken at $N_t = 1$ is mostly due to the long high energy tail of the dE/dx distribution: a point is added to this slice if any one of the 64 dE/dx samples is above the threshold energy, E_t. Transition radiation x-rays also contribute to this slice. The interesting region in the plot is the region just beyond the dE/dx wall and at $N_t \approx 10 - 15$ where the efficiency is greater than 90%. This region is filled in mainly due to transition radiation x-rays.

Figure 6 shows the same plot for a run with the incident particle a 50 GeV pion. This corresponds to a γ of about 350, which is below the steep rise in x-ray yield shown in figure 2. The same dE/dx wall is seen as for electrons since the dE/dx loss is about the same for electrons and pions at 50 GeV. The region above E_t =5 keV and near N_t =10 to 15, where the electron efficiency is high, is very sparsely populated by pions.

This performance at 50 GeV is maintained down to several GeV, since this is still above the electron x-ray production saturation level (see figure 2) and the average dE/dx changes very little over this range.

TRD Performance.

The conclusion from figures 5 and 6 is that this system can yield a pion rejection ratio of the order 10^{-3} with an electron efficiency of greater than 90%. Realized systems[3] have not achieved this high a rejection; typical performance is several times 10^{-2}. These systems have not had as many TR modules as this one but it is clear that this Monte Carlo simulation yields an optimistic pion rejection. Only single tracks at a time were modeled, not entire events. We need to treat backgrounds and occupancy more realistically, perhaps by incorporating this simulation into a package such as GEANT[4].

Tracking

The question of what will constitute adequate tracking for an SSC detector is very complex, involving detailed analyses of feasibility, actual utility of tracking information for TeV-scale physics analysis, and compromises in detector size and complexity. Tracking

is most often considered in the context of a magnetic field, which enhances the power of a tracking system but which may also complicate the structural engineering and require compromises in calorimeter hermeticity and performance. A tracking system could serve a variety of functions, including:

- Determination of charged particle topology and multiplicity
- Point-back to the beam line for multiple event tagging
- track extrapolation to the calorimeter, with matching to shower centroids
- photon identification by the absence of tracks
- identification of secondary vertices.

With a magnetic field, a tracking system could also:

- measure the momentum of charged particles
- determine the sign of the particle's electric charge
- improve secondary vertex finding by rejecting low momentum tracks
- provide electron identification through a comparison of momentum from tracking and energy from calorimetry.

It has also been asserted that a magnetic field could curl up low momentum particles and so reduce the occupancy in the detectors farther from the beam line — the silver lining to the dark cloud of high occupancy due to looping low-momentum particles.

The focus of our work so far has been on the TRD performance of this system. In principle, TRD capability could be added to most tracking systems, at the cost of increased multiple scattering in the radiator and slower drift times in the gas (see below). Since many other groups are studying tracking issues in detail, we have limited our efforts to a simplified analysis of the capabilities of the present design. The estimated tracking performance is displayed in Table 2.

Table 2
Tracking Performance.

Track Momentum	Point Back to beam	Extrapolate to Calorimeter
50 GeV	0.6mm along beam. 1.5mm transverse.	0.5mm along beam. 1.4mm transverse.
1 GeV	1.5mm along beam. 20.0mm transverse.	1.4mm along beam. 3.7mm transverse

Point-back to the interaction region has millimeter resolution along the beam line,

entirely adequate for the resolution of multiple events that will be distributed with a σ of 5 cm. Resolution in the transverse direction is millimeters at high momenta and a few centimeters at low momenta, indicating a need for more axial straws if this performance is deemed important. The tracks can be extrapolated to the calorimeter with millimeter resolution, small compared to the shower centroid resolution that might be achieved with typical 5cm × 5cm calorimeter segmentation.

We have also looked at the momentum measurement capability of the system if there were a magnetic field. The present design has too few axial straws to give any reasonable performance. Making half the straws axial and providing a 5 kG axial magnetic field, the resolution is roughly

$$\frac{\Delta P_\perp}{P_\perp} = \frac{P_\perp}{10\mathrm{GeV}},$$

saturating at roughly 15% around 1 GeV/c P_t due to multiple scattering. This provides a rough momentum measurement for typical charged particles, which have transverse momentum about one GeV. Higher resolution would require more axial straws, and probably drift time measurement; a higher magnetic field would extend the performance to higher momenta. As noted above, the utility of precision tracking in an SSC detector remains a point of discussion.

Straw Occupancy and Lifetime.

Two major concerns of running wire chambers in the SSC environment are the average occupancy and the lifetime of the chambers. Hits to central wire chambers in an SSC detector will be dominated by the contributions from real event-associated charged particles; effects from albedo neutrons and photons are expected to be negligible in comparison[5].

The occupancy of a straw will be determined by the frequency of charged particle traversals of the straw and by the duration of the response to a traversal. Taking the density of charged particles per event to be $dn/d\eta = 8$, assuming 1.4 events per crossing, 16 ns between crossings, and using the geometric acceptance of a typical TRD straw, we find the occupancy of a typical straw to be $\approx 1.4\% \times \tau/16\mathrm{ns}$, where τ is the maximum drift time in the straw.

We have attempted to calculate the drift velocity versus electric field for some candidate gases[6]. The results are shown in figure 7. Drift velocities tend to be low in xenon mixes, and admixture of helium to reduce dE/dx produces very low velocities. Part (b) of this figure displays the interesting result of the calculations that the drift velocity is nearly proportional to 1/E for high fields in these noble gas mixes. We have found data

to check the calculations only for the low field region $E \leq 2.5$ kV/cm. The assumptions of our program are probably invalid for electric fields much in excess of 10 kV/cm, which includes perhaps 25% of the radial extent in these small-diameter straws. We expect that the drift velocity would decrease from its peak value as the electric field increases, but perhaps not so far as our program indicates.

If we now use the calculated dependence of drift velocity on electric field, and assume an operating voltage of 1800 volts for a 50μm wire, we find a maximum drift time of 110 ns for 60% xenon and 40% methane. If we use just the peak value of the drift velocity, approximately 4.5 cm/μsec, the maximum drift time is about 50 ns. The actual drift time is probably bracketed by these estimates. It is clearly important to measure experimentally the gain and the drift velocity at high fields in candidate gas mixtures.

The occupancies corresponding to this range of drift times are approximately 5–10%, with the inner axial straws running somewhat hotter. This is on the margins of comfort, and probably establishes the need for increasing the inner radius of the TRD/tracker – and in fact most discussions now posit an inner radius closer to 50 cm than to the 20 cm we have assumed. The occupancy is highly correlated layer-to-layer, since it is dominantly caused by charged particles that emanate from the interaction region. It remains to be determined if this is a mitigating or a detrimental feature.

The lifetime of a typical wire chamber is directly related to the total charge per unit length of wire that has been generated in avalanches. Using the same parameters as above, and estimating 50 electrons per traversal and a gas gain of 10^5, we find that the typical average current from a wire is 20 nanoamps/cm. This corresponds to a total charge of one coulomb per cm after 5 years of operation of 10^7 seconds per year – a daunting level considering .1 to 1 coulomb/cm is the typical lethal dose range! This is another reason to favor increasing the inner radius of the straw system.

Summary.

Our simple Monte Carlo simulation indicates that the desired TRD performance, namely, pion rejection of order 10^{-3}, can be achieved with a straw system. At least minimal tracking can be achieved with the same system. Much more work needs to be done to determine an optimum configuration. We need to optimize the number of TRD modules and the radiator thickness in each module. The straw gas mixture needs to be optimized, balancing the two trade-offs of good x-ray detection and fast drift time to reduce occupancy. We are continuing Monte Carlo studies in order to perform these

optimizations and obtain realistic performance.

References.

1. T. Akesson *et al.*, in *Experiments, Detectors, and Experimental Areas for the Supercolider.*, R. Donaldson and M.G.D. Gilchriese, ed., Berkeley, 1987, p.472.
2. See for example: M.L. Cherry *et al.*, Physical Review D, **D10**, 3594, (1974); X. Artu *et al.*, Physical Review D, **D12**, 1289, (1975); G.M. Garibian *et al.*, Nuclear Instruments and Methods, **125**, 133, (1975).
3. B. Dolgoshein, Nuclear Instruments and Methods, **A252**, 137, (1986).
4. R. Brun *et al.*, GEANT3, CERN DD/EE/84-1, 1987.
5. Radiation Effects at the SSC, section 2.1, SSC-SR-1035 (1986).
6. We have used a program originally written by P. A. Coyle. See P. A. Coyle *et. al.*, SLAC-PUB-4403, November, 1987.

SSC Transition Radiation Detector

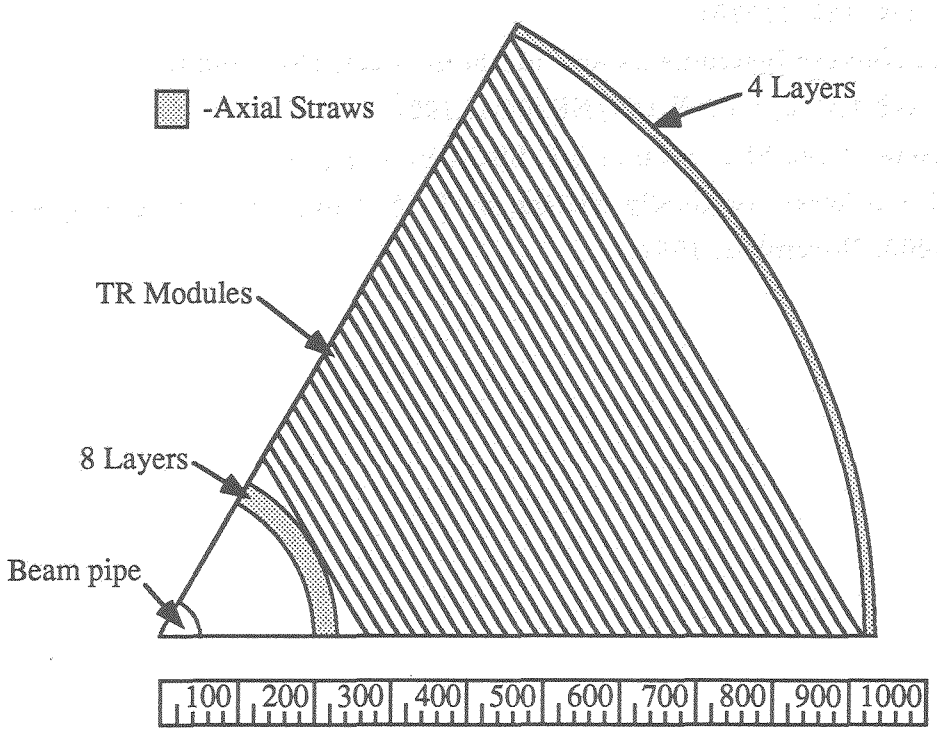

Each TR Module: (32 modules)

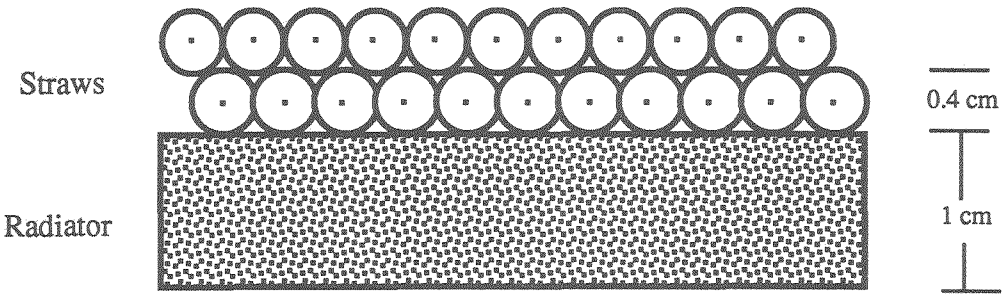

Straws are in the r-θ plane.

Figure 1.

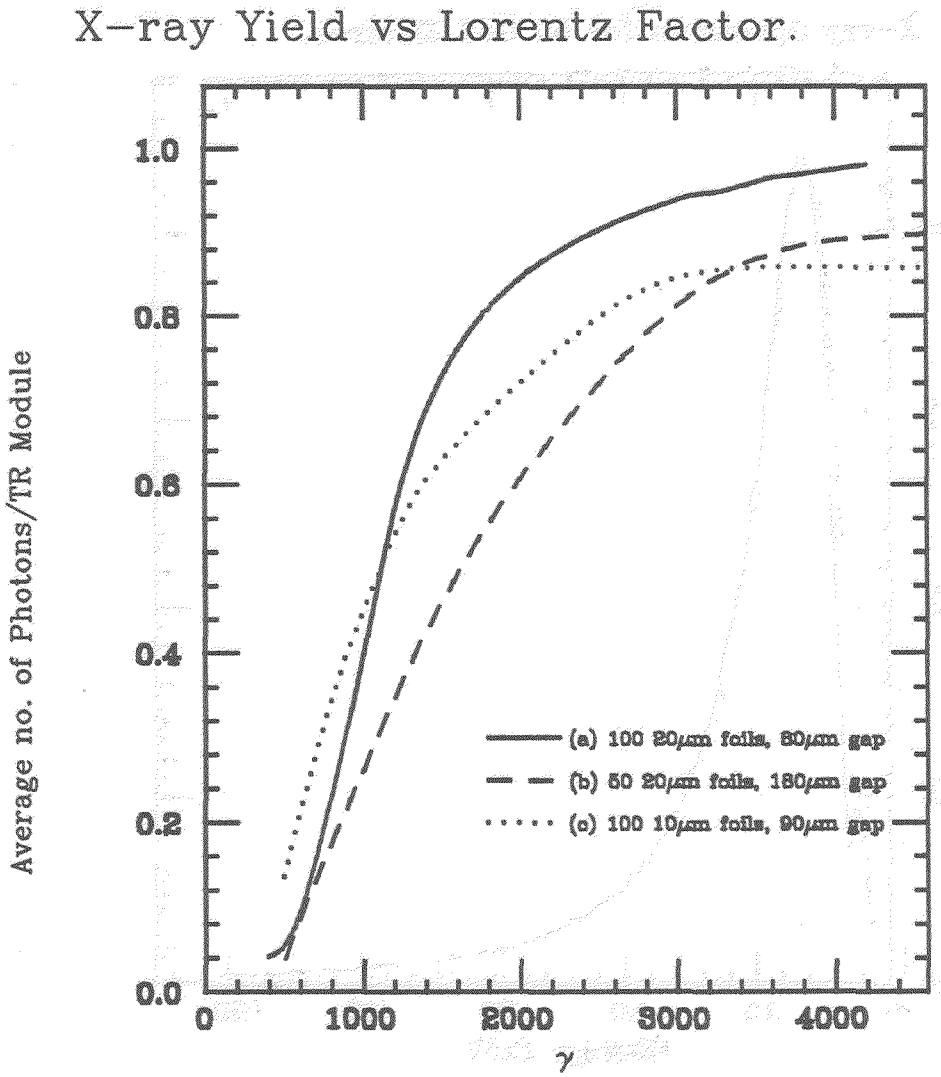
X-ray Yield vs Lorentz Factor.
Average no. of Photons/TR Module
1.0
0.8
0.6
0.4
0.2
0.0
0
1000
2000
3000
4000
γ
(a) 100 20μm foils, 80μm gap
(b) 50 20μm foils, 180μm gap
(c) 100 10μm foils, 90μm gap

Figure 2.

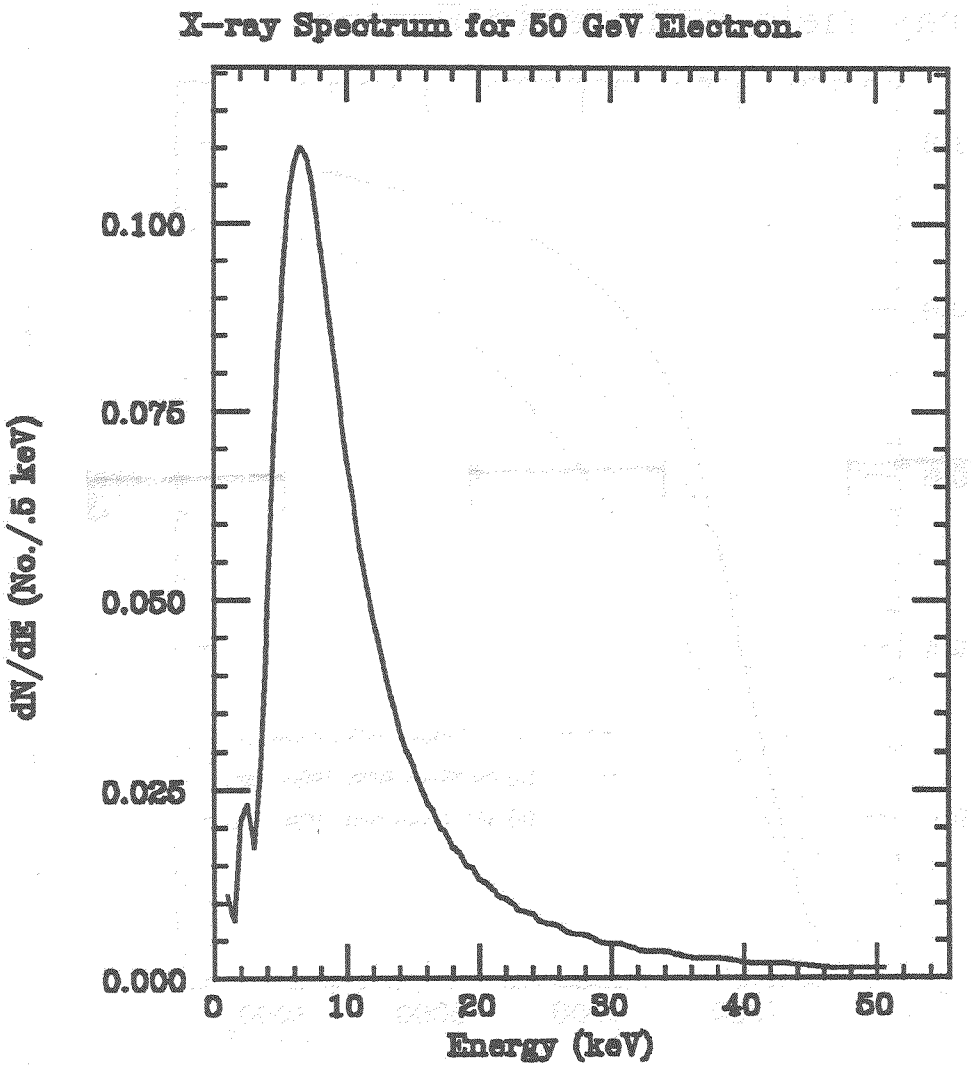
X-ray Spectrum for 50 GeV Electron.
0.100
0.075
0.050
0.025
0.000
dN/dE (No./.5 keV)
0
10
20
30
40
50
Energy (keV)

Figure 3.

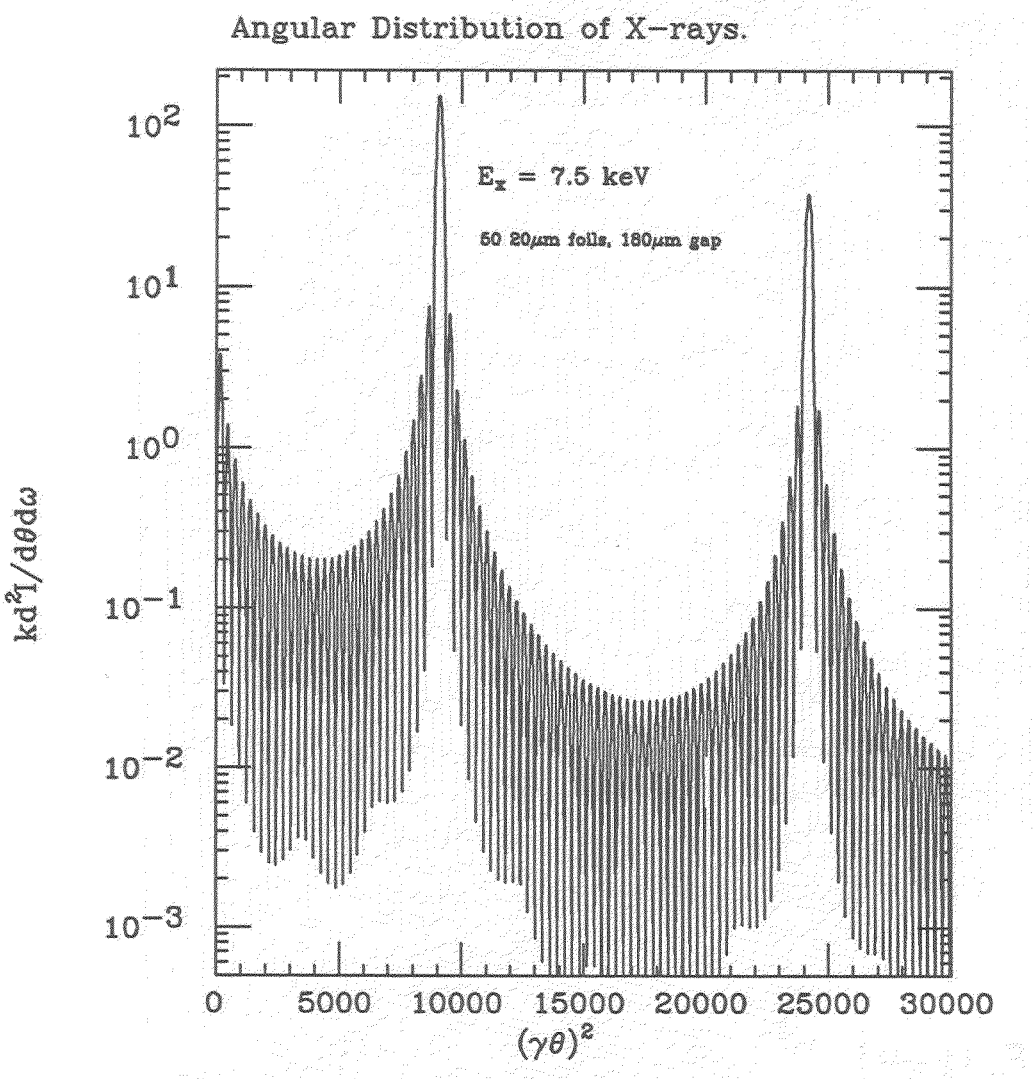
Angular Distribution of X-rays.
E_x = 7.5 keV
50 20μm foils, 180μm gap
10^2
10^1
10^0
10^{-1}
10^{-2}
10^{-3}
$kd^2I/d\theta d\omega$
0
5000
10000
15000
20000
25000
30000
$(\gamma\theta)^2$

Figure 4.

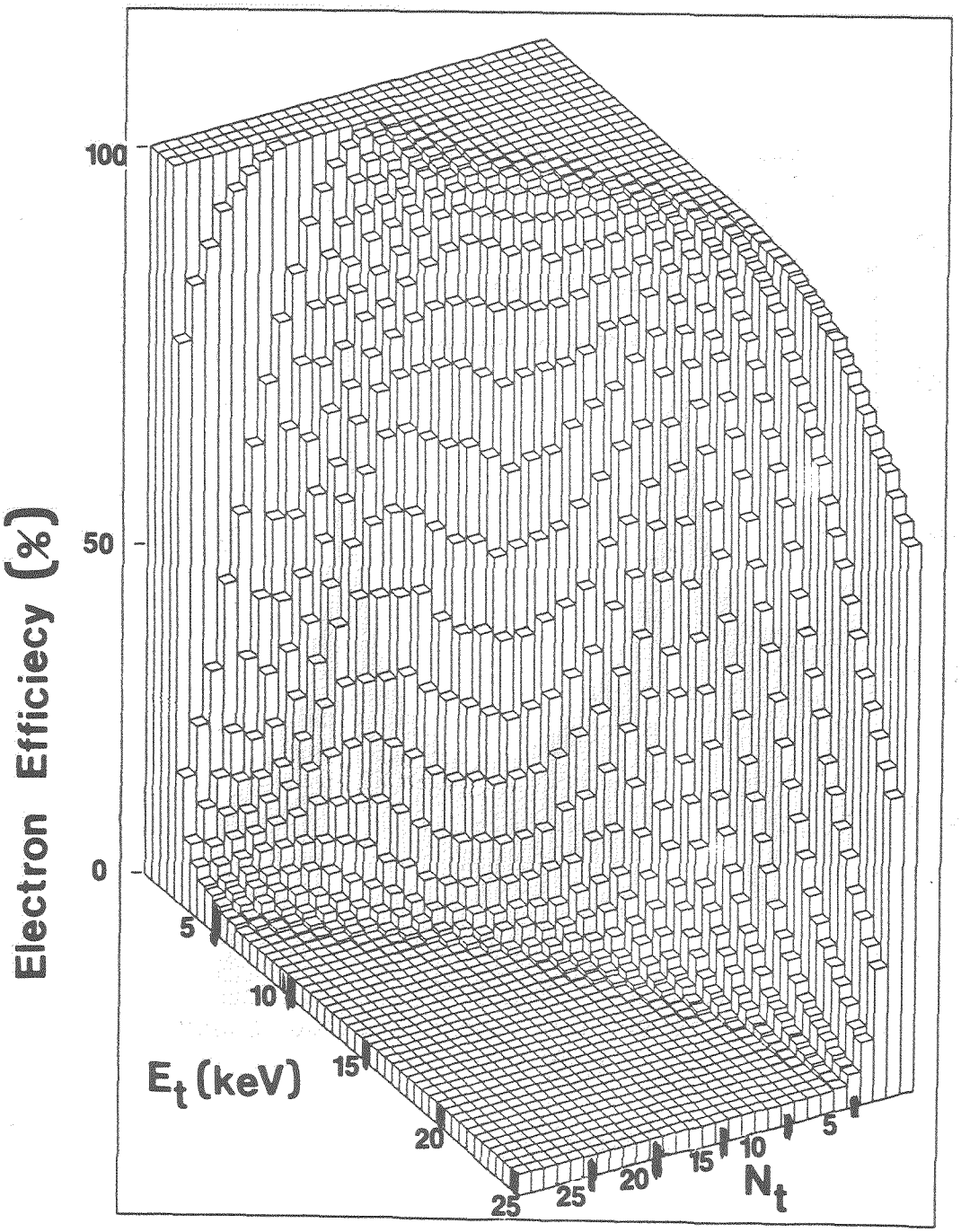

Figure 5. Electron identification efficiency.

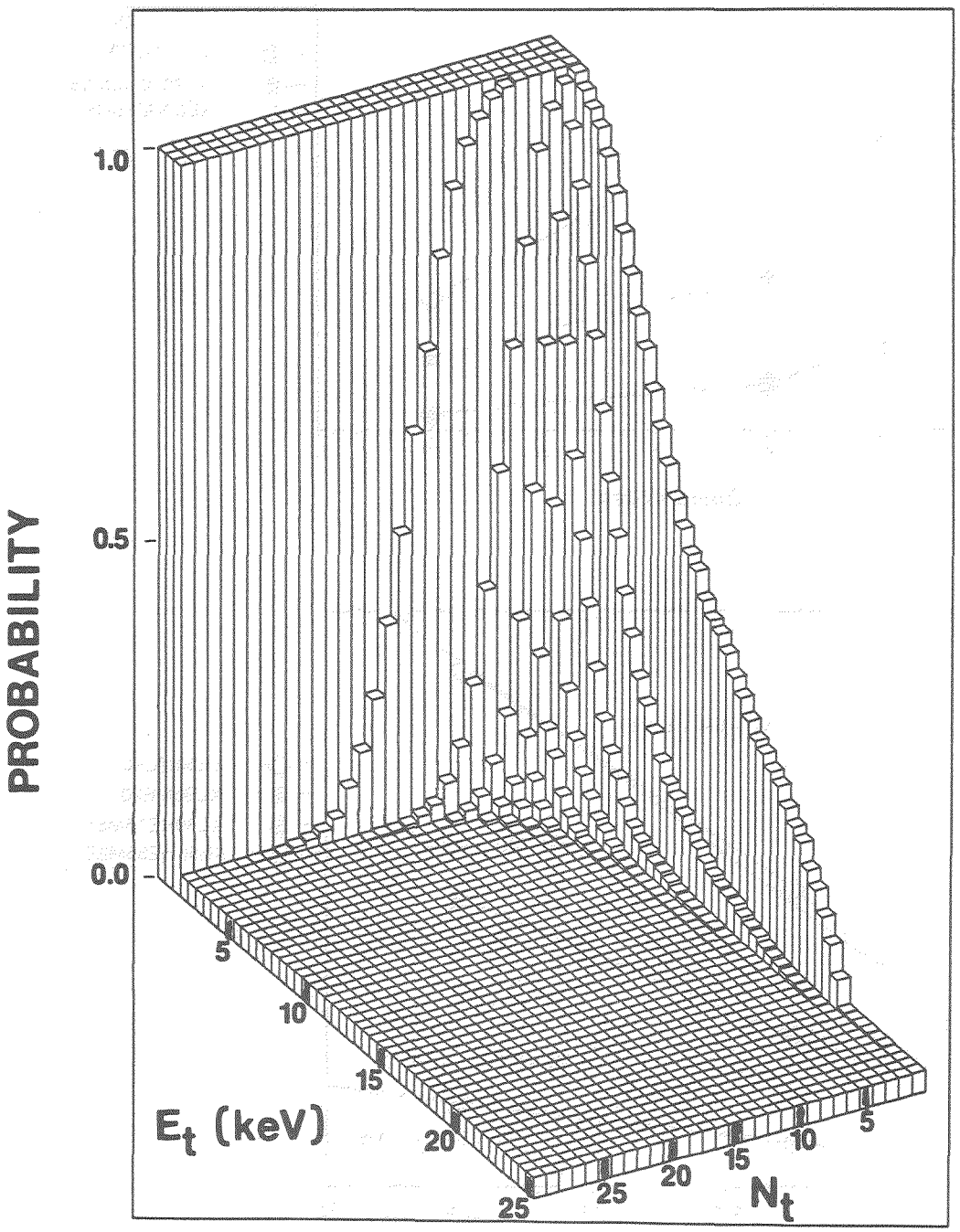

Figure 6. Pion Mis-identification. The height is the probability that a 50 GeV pion passes the electron selection criteria.

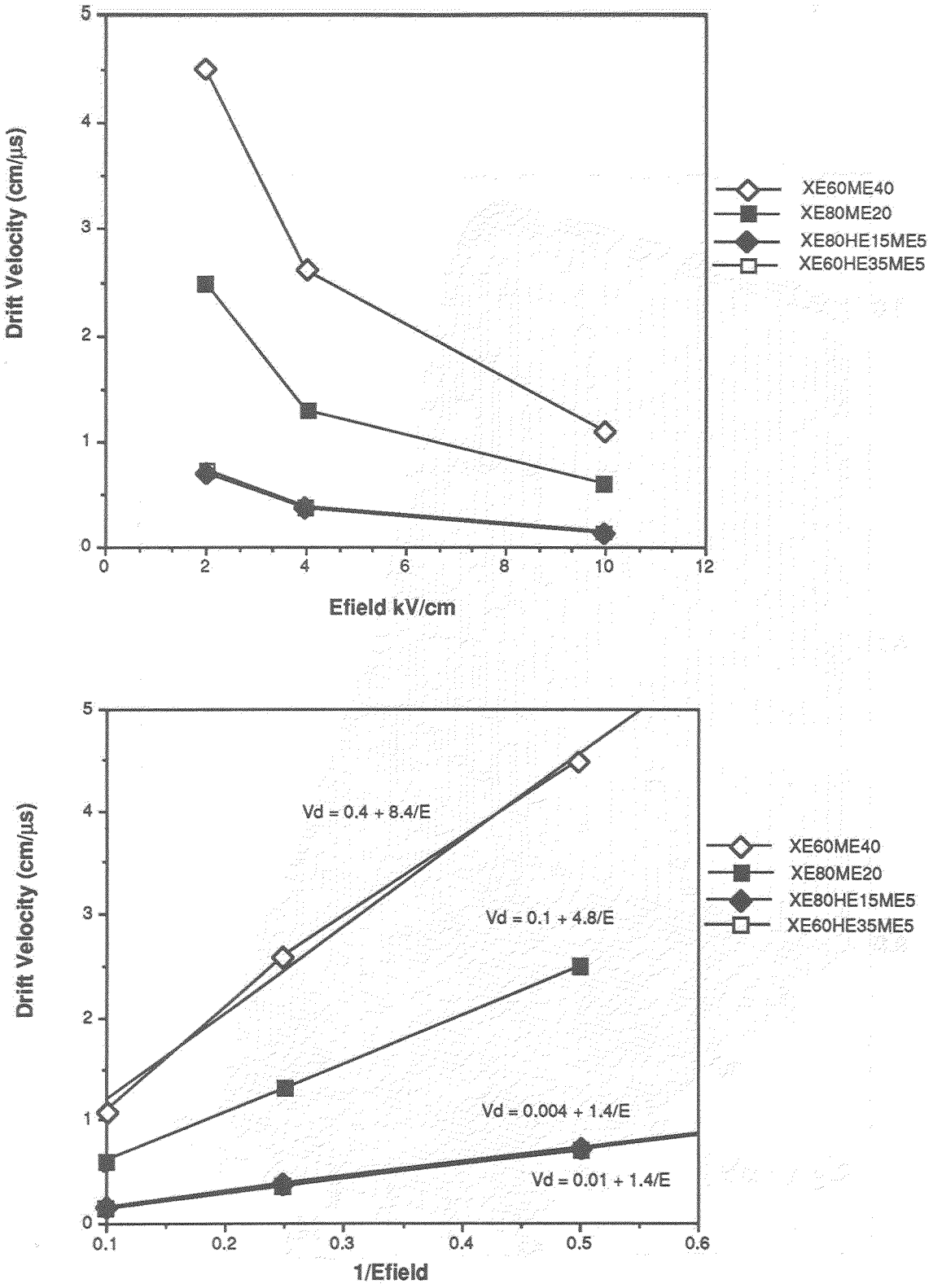

Figure 7. Drift Velocity vs Electric Field (Candidate TRD Gases)

TRANSITION RADIATION DETECTORS IN HYPERON EXPERIMENTS AT FERMILAB

V. T. Grachev, A. G. Krivshich, V. A. Schegelsky,
N. N. Smirnov, N. K. Terentyev and A. A. Vorobyov
Leningrad Nuclear Physics Institute
Leningrad, USSR

P. S. Cooper, J. Lach
Fermi National Accelerator Laboratory
Batavia, Illinois, 60510

M. Foucher
Yale University
New Haven, Connecticut, 06511

Talk by N. K. Terentyev at the Symposium on Particle Identification at High Luminosity Hadron Colliders, Fermi National Accelerator Laboratory, Batavia, Illinois, April 5-7, 1989.

Introduction

An intensive program to study the hyperon rare decays is now in progress in the Fermilab Proton Center polarized charged hyperon beam. In these experiments the challenge is to identify the particles which are the products of rare hyperon decays. For this purpose transition radiation detectors (TRD) have been designed and studied at the Leningrad Nuclear Physics Institute (LNPI).

At the beginning of this talk we discuss the TRD which was used in the Fermilab E715, **High Precision Measurement of Polarized Σ^- Beta Decay**[1]. Here the goal was to identify electrons from the semileptonic decay, $\Sigma^- \rightarrow n\, e^-\, \overline{\upsilon}$, and to reject the pions from the 10^3 times more copious decay $\Sigma^- \rightarrow n\, \pi^-$.

The next part of paper is devoted to new applications of TRD as a precision position detector for high energy photons. These photons are first converted into electromagnetic showers. It is the forward high energy charged component of these showers that is detected by the TRD detector. This detector will be installed in the Fermilab E761, **An Electroweak Enigma: Hyperon Radiative Decays**[2], scheduled to run in 1990 fixed target run. The performance characteristics of one module of this gamma detector as measured in the electron beam at the Institute of High Energy Physics (IHEP) at Serpukhov will be presented.

As a continuation of the Fermilab hyperon program, an experiment to study the production and decays of the charm strange baryons[3] will be performed in the 1990's. The technical problem here is the identification of 600 GeV/c Σ^- in a hyperon beam flux of 2×10^6 particles/sec. Some details of the TRD prototype made at the LNPI as well as Monte Carlo separation curves for the proposed design are also presented in this talk.

The E715 TRD: High precision measurement of polarized Σ^- beta decay

In E715 the transition radiation detector was used to identify e^- from the reaction, $\Sigma^- \rightarrow n\, e^-\, \overline{\upsilon}$, in the presence of the pions from the 1000 times more frequent $\Sigma^- \rightarrow n\, \pi^-$ decay. The decay asymmetries and the form factors were measured in this experiment. To measure the decay asymmetries with precision and to suppress significantly the background caused by pions it was necessary to provide a TRD electron efficiency $\varepsilon_e > 99\%$ and a pion rejection factor $R_\pi = \varepsilon_e / \varepsilon_\pi > 10^3$. These parameters were the most crucial in the TRD calculation and design.

The TRD consisted of 12 identical modules (one module is shown in fig. 1), each containing a radiator followed by a multiwire proportional chamber (MWPC). The sensitive area of the TRD was $1.0 \times 0.6\ m^2$. These detectors occupied a total length in the beam of 4.2 m. The total amount of TRD material in the beam was 0.1 radiation lengths (L_r) and 0.06 interaction lengths (L_i). The radiator module consisted of 220 sheets of 17 μm thick polypropylene separated by 1.0 mm air gaps. The MWPC contained 512 25 μm diameter gold plated tungsten anode wires (2 mm spacing) placed symmetrically between two aluminized mylar cathodes. Each 8 anode wires were ORed together into one channel giving a total of 768 channels for all 12 modules of the TRD. The distance between anode and each cathode was 8 mm. The active gas was a mixture of 70 % Xe and 30% CH_4 flowed through all of the 12 chambers in series at a rate of 100 cm^3/min. This low flow rate meant that no gas recovery system was needed. At the operating voltage of 4.6 kV the electron drift time was 330 nsec over the 8 mm gap.

To keep good gas purity and uniform gas gain everywhere in proportional chamber volume, we flowed CO_2 in the special

"compensating" gas volumes (fig. 1). These volumes were at a slightly higher pressure to compensate for the bulging of the Xe volume. Note that this is a significant effect since Xe is 4.6 times the density of air. This measure allowed us to keep the deviations in the gas gain everywhere in the chambers to <15%.

The "cluster counting" technique[4] was used to identify electrons traversing the TRD. The signal from each channel was input to a fast preamplifier-discriminator circuit. This special hybrid circuit was designed at LNPI and fabricated one channel per hybrid and mounted 16 channel per card[5]. The output produced a standard logic signal when the level of input amplitude was more than 7.1 keV. This means a threshold 6.5 keV for photons if we take into account the ionization pedestal from the incident particle. The dead time of the preamplifier-discriminator was <50 nsec, so during the time of drift (330 nsec) it was possible to count several pulses corresponding the ionization "clusters". For each chamber the signals from the preamplifiers were ORed and counted by a fast scaler. The information from all 12 scalers was summed in a special fast processor[6] which provided a fast trigger signal if the sum of clusters exceeded a preset value.

The performance characteristics of the TRD were measured in the Fermilab hyperon beam during the E715 run . The results as well as more detailed description of the TRD have been published[7,8]. Fig. 2 from reference 8 shows the measured average number of transition radiation photons detected per module of the E715 TRD as a function of the Lorentz factor of e^- and π^-. One can also observe the good agreement of data with Monte Carlo calculations done in the reference 8 and based on the formulae from Garibian[9].

In the "cluster counting" method the total number of clusters, N_{Cl}, measured for all modules is used as a criteria to select electrons. The distribution of the number of clusters is Poisson. In

E715 we have used additional available information-the number of "active" chambers N_a (where at least one cluster was detected), which obeys the binomial distribution. The combination of these two criteria allowed us to increase the pion rejection R_π by a factor of 5-6 with the same electron efficiency[8] (Fig. 3). Figure 3 represents the results of the offline analysis of the data from the electron beam with momentum 9-55 GeV/c and data with pions from $\Sigma^- \rightarrow n\,\pi^-$ decay with energy 9-95 GeV/c. We used a multiplicity criteria to select events with only single particles thus avoiding interactions in the detector material. With the requirements $N_{Cl} \geq 12$ and $N_a \geq 7$, we measured[8] an efficiency ε_e =97.7% with $R_\pi = 1.8 \times 10^3$.

An electron trigger for beta decay in E715 consisted of the same TRD cuts $N_{Cl} \geq 12$ and $N_a \geq 7$. This trigger has provided online R_π=40 which was sufficient. The decreased rejection in this sample was due to pion interactions in the TRD. In E715 the TRD was combined with a lead glass calorimeter providing offline suppression of $\Sigma^- \rightarrow n\,\pi^-$ decays by a factor 50000 while maintaining 94 % efficiency for the electron (Fig. 4).

The TRD as a precision spatial gamma detector.

Our experience with the E715 TRD has demonstrated that the TRD is a detector whose response is calculable and whose range of applicability can be extended. In E761 we plan to use a TRD as a precision spatial high energy gamma detector.

When a high energy photon showers in a converter with a thickness of about 1 - 2 radiation lengths, most of the high energy electrons produced in the electromagnetic shower follow closely the initial photon direction. Since the transition radiation yield has a threshold behavior with the Lorentz factor of particle (fig. 2), the TRD placed downstream the converter will be mainly sensitive to the most

energetic charged component of the electromagnetic shower and will be relatively insensitive to the low energy component.

A Monte Carlo simulation of the electromagnetic showers and of the TRD response confirmed this conclusion. In Fig. 5a we plot the number of electrons produced with photon energies between 10 - 150 GeV after one radiation length of lead. In Fig. 5b we plot the number of detected ionization clusters per TRD chamber as a function of incident photon energy. To show the enhanced response for the high energy charge shower component we plot separately the response due to produced electrons with energy less than 2.5 GeV and greater than 2.5 GeV .

We now make use of the fact that transition radiation photons have a sharp peak in the forward direction with respect to the electron trajectory given by an angle, $\theta=m_e/E_e$. By measuring the positions of the transition radiation photons produced in the TRD radiator, we infer the position of the high energy charged component of the shower and hence the position of the incident high energy gamma.

One module of this TRD used as a high energy gamma detector was tested in a 25 GeV e^- beam at Serpukhov. The configuration of the experiment is shown in Fig. 6. A beam with an intensity of about 10^4 particles/sec. containing mainly π^- and 2-3% electrons was used. The electrons were selected at the trigger level by the coincidence of Čerenkov and scintillation counters. The offline analysis utilized a selection based on lead glass gave a hadron background at the level less than 0.5%.

Two proportional chambers PC1 and PC2 each containing x and y planes with cathode delay readout were placed before the TRD. They measured the incident e^- trajectory which was projected onto the TRD with an accuracy $\sigma=0.5$ mm. Multiplicity defining scintillation counters S_4-S_6 allowed us to select, offline, events with showers in

the Pb converter. Different thicknesses of the Pb (L_r = 5.6 mm) converter placed 0.5m upstream of TRD proportional chamber were used (2, 4, 6.9 and 8.5mm.

To measure the number and x position of ionization clusters we have used one module of the E715 TRD, but now each wire (wire spacing 2 mm) of proportional chamber of TRD was instrumented. The readout electronics built in LNPI and based on the ring buffer memory (the depth 16 slices) for each channel allowed us to record with step 40 nsec the history of each ionization cluster during its drift time. A data acquisition system[10] was used to write data on the tape and perform online analysis.

The position of shower was measured by the TRD as the mean of hits in TRD with weights proportional to number of ionization clusters recorded from hit wires. The difference between the measured TRD position and the intercept of the incident trajectory projected from the proportional chambers PC1 and PC2 is presented in Fig. 7 for set of Pb converter thicknesses of 4, 6.9, 8.5 mm and without converter. To describe the experimental data we used our previous data on E715 TRD response and the EGS4 code[11] for simulation of showers. The results are in reasonable agreement with these predictions in terms of FWHM.

The high energy gamma coordinate TRD for E761 is shown in Fig. 8 and consists of two identical modules with Fe converter of 1.5 L_r thickness in each module. The converter material (steel) was chosen for practical reasons; it is much easier to provide the same thickness everywhere in the converter. With increasing the converter thickness the number of high energy electrons in the shower decreases and the shower becomes wider. The Monte Carlo study shows that it is enough to use two modules to have relatively high efficiency for conversion (90%) and to keep good coordinate resolution (FWHM $\approx$ 2 mm) at the same time. The conventional PWCs are included into gamma detector with the goal to compare PWC and TRD as coordinate detectors.

We will use this gamma detector in E761 to measure the coordinates of photons from the radiative decays $\Sigma^+ \to p\gamma$ and $\Xi^- \to \Sigma^-\gamma$. For initial hyperons energies of 350 GeV the energy of the gamma is up to 130 GeV in the first decay and up to 60 GeV in the second. An energy will be measured by a lead glass array placed downstream of the TRD.

The E781 beam TRD at Fermilab.

The physics goals of E781 include a systematic survey of charm baryon production and decay mechanisms, a search for new charmed baryon and exotic states and a study of charm and beauty production in high flux of 2×10^6 particles /sec. 600 GeV hyperon beam at the Proton Center hyperon facility. The content of the negative beam produced at p_t=1.25 GeV/c by 800 GeV/c incident protons is about 50 % Σ^- and 50 % π^- 10m downstream of the hyperon production target. Beam tagging by a TRD system should provide very clean Σ^- selection. Other hyperons as well as K^- are a negligible fraction of the beam.

The design of the beam TRD for E781 is now in progress at LNPI. The TRD will consisted of 20 identical modules with a polypropylene radiator and a multiwire proportional chamber in each module. The sensitive area of the TRD is 2×2 cm^2. The 200 foils of radiator with thickness of each 17 μm are separated by 500 μm air spaces. To achieve the high rate capability of the TRD each MWPC includes 3 anode planes with anode-cathode distances of 2 mm which will provide a drift time of about 80 nsec with a gas mixture of Xe + 30 % CH_4. The anode wire spacing is 1 mm and all wires in each plane will be ORed.

In fig. 9 a Monte Carlo beam TRD response to 600 GeV beam with equal numbers of Σ^- and π^- is presented as a number of events versus the number of "active planes" (where at least one cluster was detected). The test of several modules of beam TRD is scheduled to be

during the run of E761 in 1990 fixed target at Fermilab.

Conclusions.

A multi-module transition radiation detector with large area 1.0 × 0.6 m^2, uniform gas gain, good stability, high pion rejection $R_\pi > 10^3$ and electron efficiency $\varepsilon_e > 99\%$ was built at LNPI and successfully used in E715 at Fermilab. A good agreement of data with Monte Carlo calculations based on the theoretical expectations of transition radiation yield was observed.

A novel application of a TRD combined with a gamma converter is planned to measure the coordinate of high energy photon with accuracy ≈ 2 mm (FWHM) in E761. One module of this gamma detector was tested in the electron beam at Serpukhov. The results were described by using the response of the E715 TRD and EGS4 code for simulation of electromagnetic showers.

We plan to construct a high rate beam TRD with multiwire proportional chambers consisting of 3 anode planes each and providing drift times of ≈ 80 nsec. According to our calculations this should be able to identify the Σ^- in the 600 GeV hyperon beam in E781.

Acknowledgements.

We wish to thank our colleagues at LNPI and Fermilab for their assistance. Also we would like to acknowledge the important help of Yu. D. Prokoshkin, A. M. Zaitsev, V. V. Lapin and S. I. Bityukov at IHEP(Serpukhov) who have made the test of gamma detector at Serpukhov not only possible but successful.

References.

1. S. Y. Hsueh et al., Phys.Rev. D38 (1988) 2056.
   S. Y. Hsueh et al., Phys.Rev.Lett. 54 (1985) 2399.

2. Fermilab-LNPI(Leningrad)-ITEP(Moscow)-IHEP(Beijing)-University of Iowa-University of Sao Paulo-Yale University-CBPF(Rio de Janeiro). "An electroweak Enigma: Hyperon Radiative Decays"-Proposal E761, Fermilab.

3. Carnegie-Mellon University-Fermilab-LNPI(Leningrad)-ITEP (Moscow)-IHEP(Beijing)-University of Iowa-University of Sao Paulo -CBPF(Rio de Janeiro). "A proposal to construct SELEX-Segmented Large-X Baryon Spectrometer"-Proposal E781, Fermilab.

4. T. Ludlam et al., NIM 180 (1981) 413.
   C. W. Fabjan et al., NIM 185 (1981) 119.

5. V. Belenky, N. Bondar et al., LNPI preprint-1049,Leningrad,1985 (in Russian).

6. A. Kaschuk et al., LNPI preprint-1089, Leningrad, 1985(in Russian).

7. A. Denisov et al., Fermilab-Conf-84/134-E and published in the Proceedings of the Annual Meeting of the Division of Particles and Fields of the American Physical Society, Santa Fe, New Mexico, Oct. 31 - Nov. 3, 1984, AIP Conference Proceedings.

8. V. Andreev et al., LNPI preprint-1186, Leningrad, 1986 (in Russian).

9. G. Garibian et al., NIM 125 (1975) 133.

10. S. Bityukov et al. IHEP preprint 87-74, Serpukhov, 1987 (in Russian).

11. W. R. Nelso et al., The EGS4 Code System, SLAC-265 (December 1985).

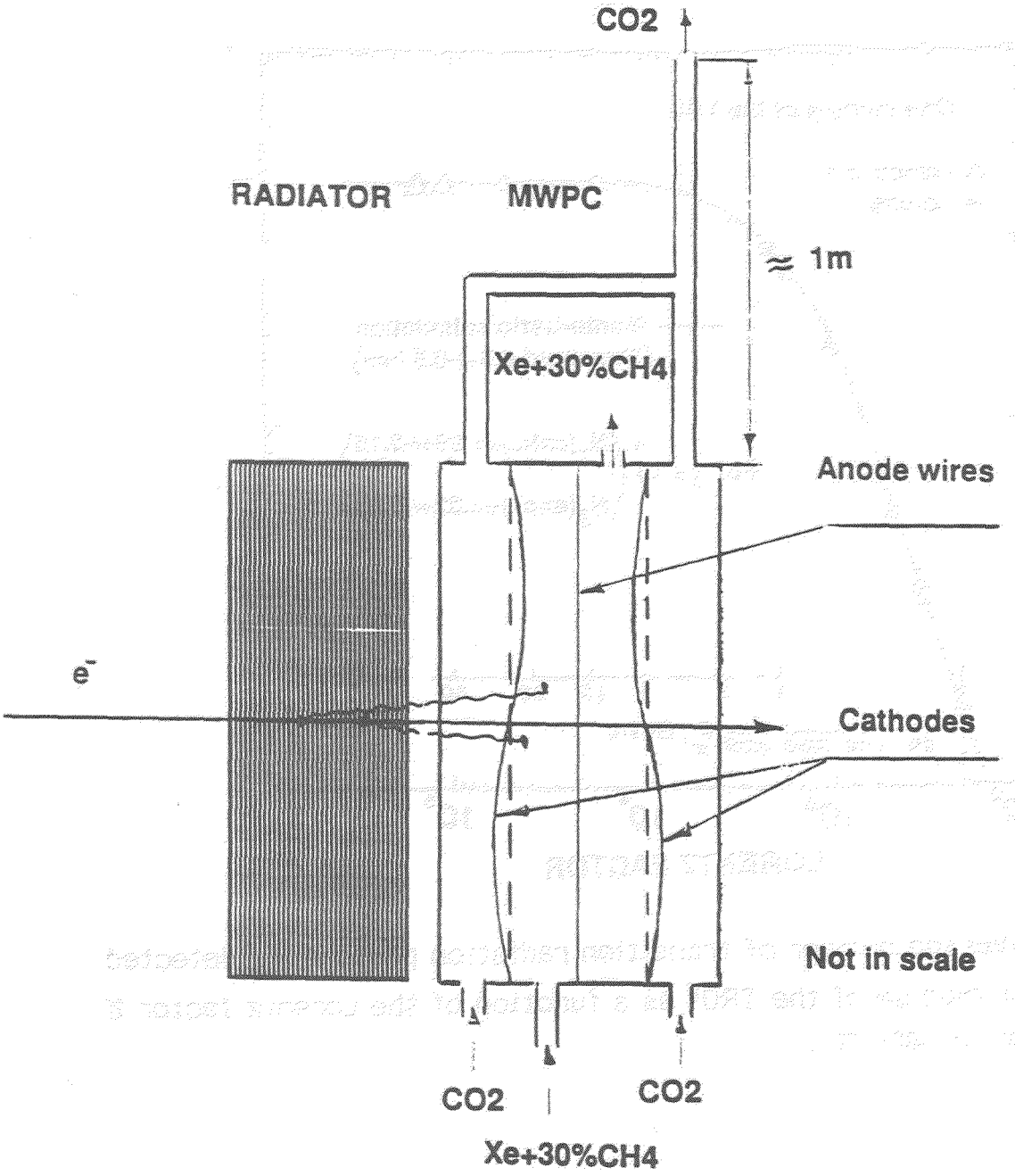

Fig. 1. Schematic cross section of one module of the E715 TRD.

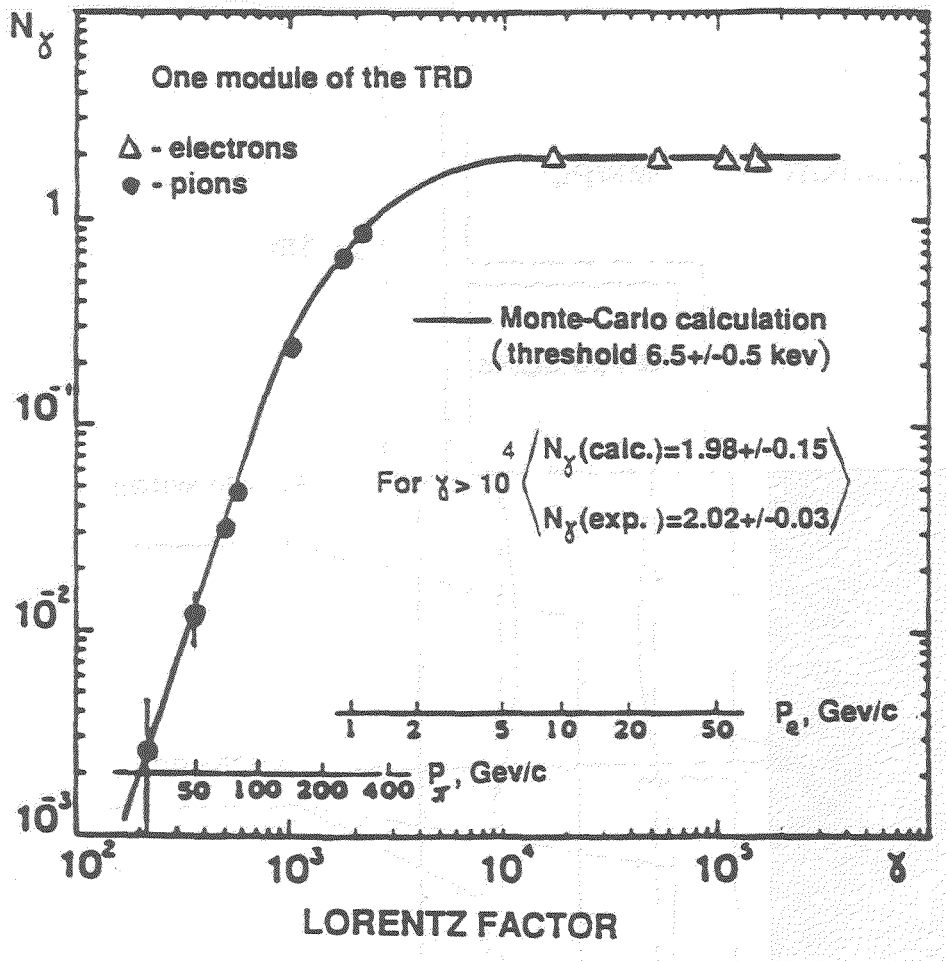

Fig. 2. Average number of transition radiation photons N_γ detected per module of the TRD[8] as a function of the Lorentz factor γ for e^- and π^-.

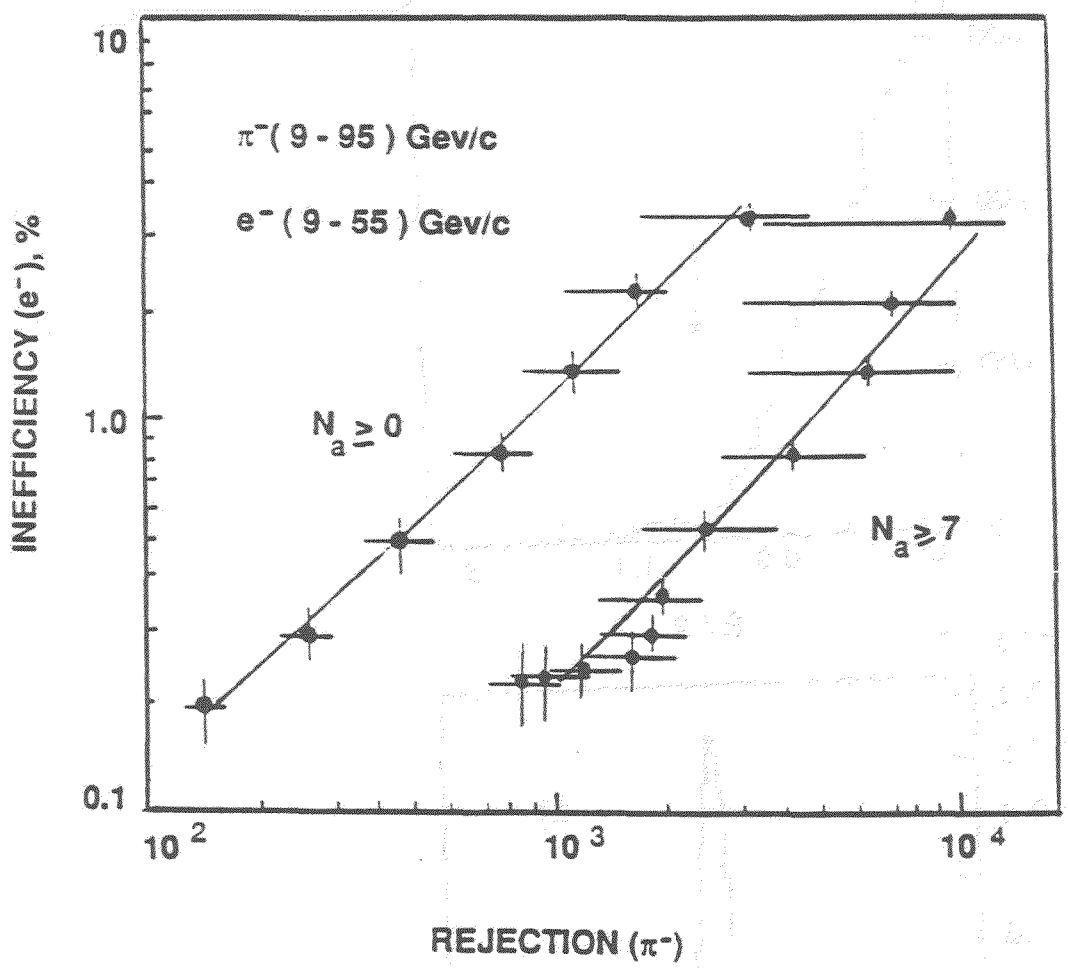

Fig. 3. Electron inefficiency vs pion rejection power without and with the criteria of the number N_a of "active" chambers in the TRD. The points correspond to different cuts on the number of detected ionization clusters N_{Cl}. The lines are given to guide the eye.

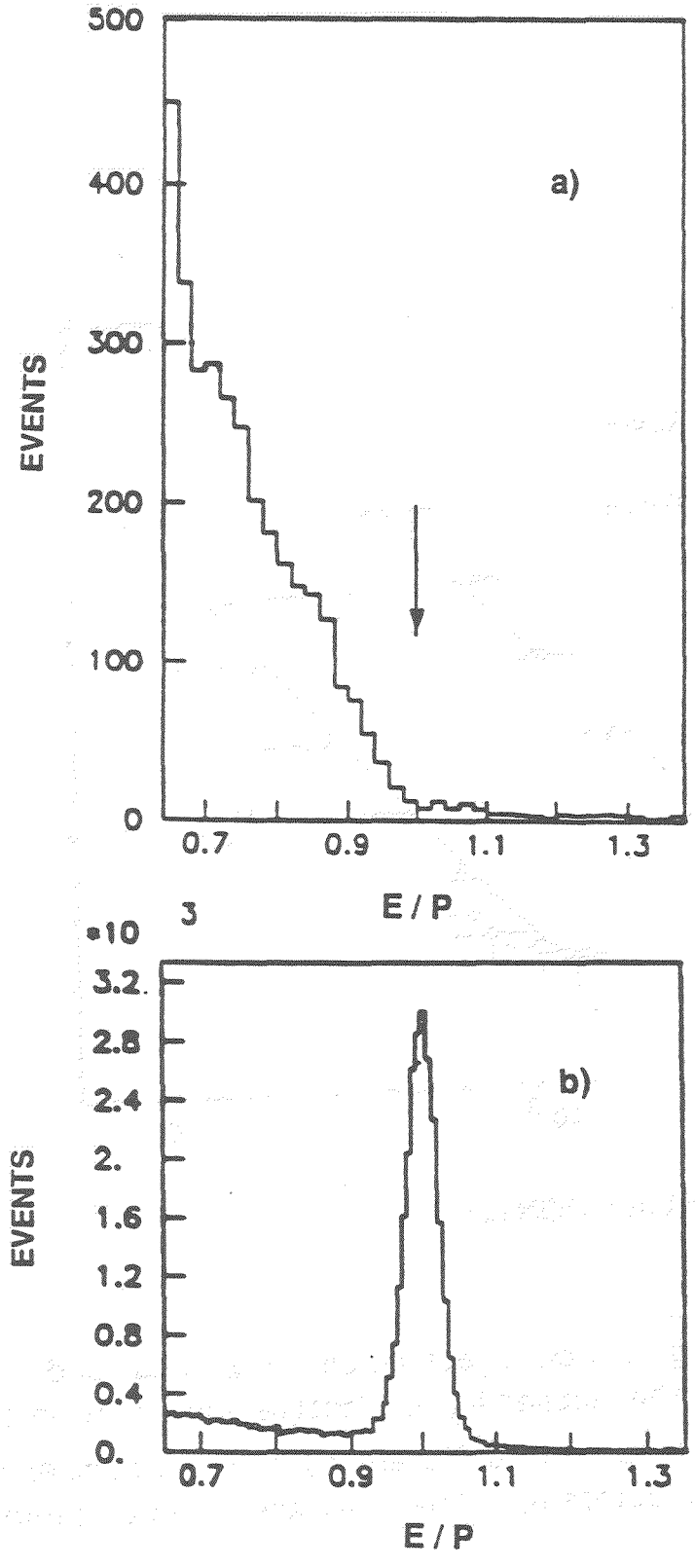

Fig. 4. Plot of E/P (energy measured by lead glass calorimeter divided by the momentum of the particle) for Σ^- decay events
a) a subsample without TRD requirements and
b) with TRD offline cut.

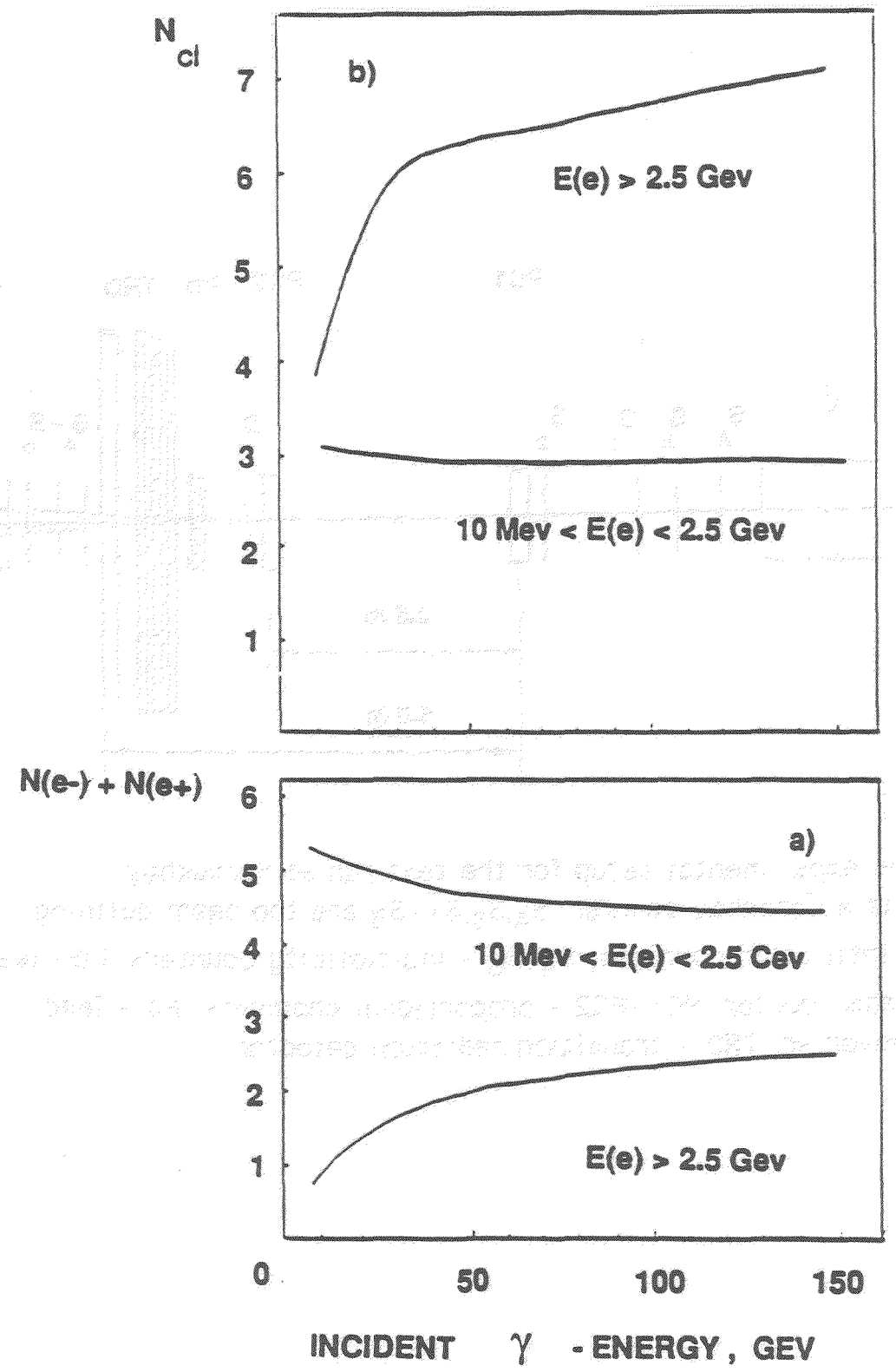

Fig. 5. a) The number of electrons and positrons $N(e^-)+N(e^+)$ in the shower.
b) the number of detected ionization clusters N_{cl} per TRD chamber as a function of incident photon energy between 10-150 GeV.

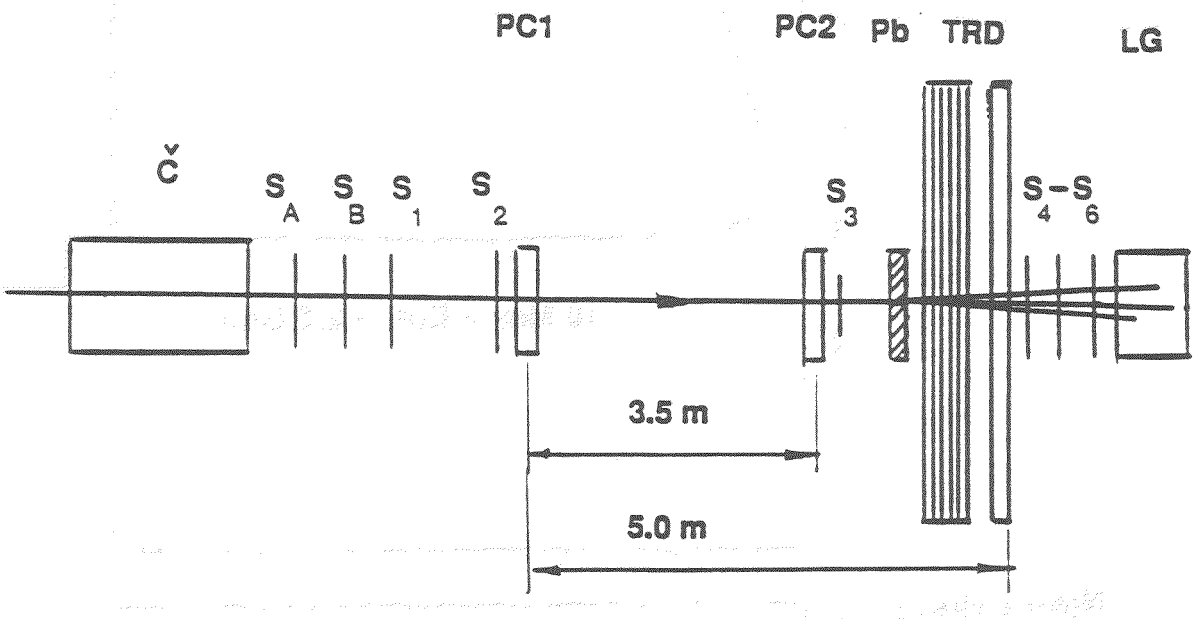

Fig. 6. The experimental setup for the test run at Serpukhov. $\hat{C}$ is a Čerenkov counter, S_A,S_B,S_1-S_3 are the beam defining scintillation counters, S_4-S_6 - multiplicity counters, LG- lead glass counter, PC1-PC2 - proportional chambers, Pb - lead converter, TRD - transition radiation detector.

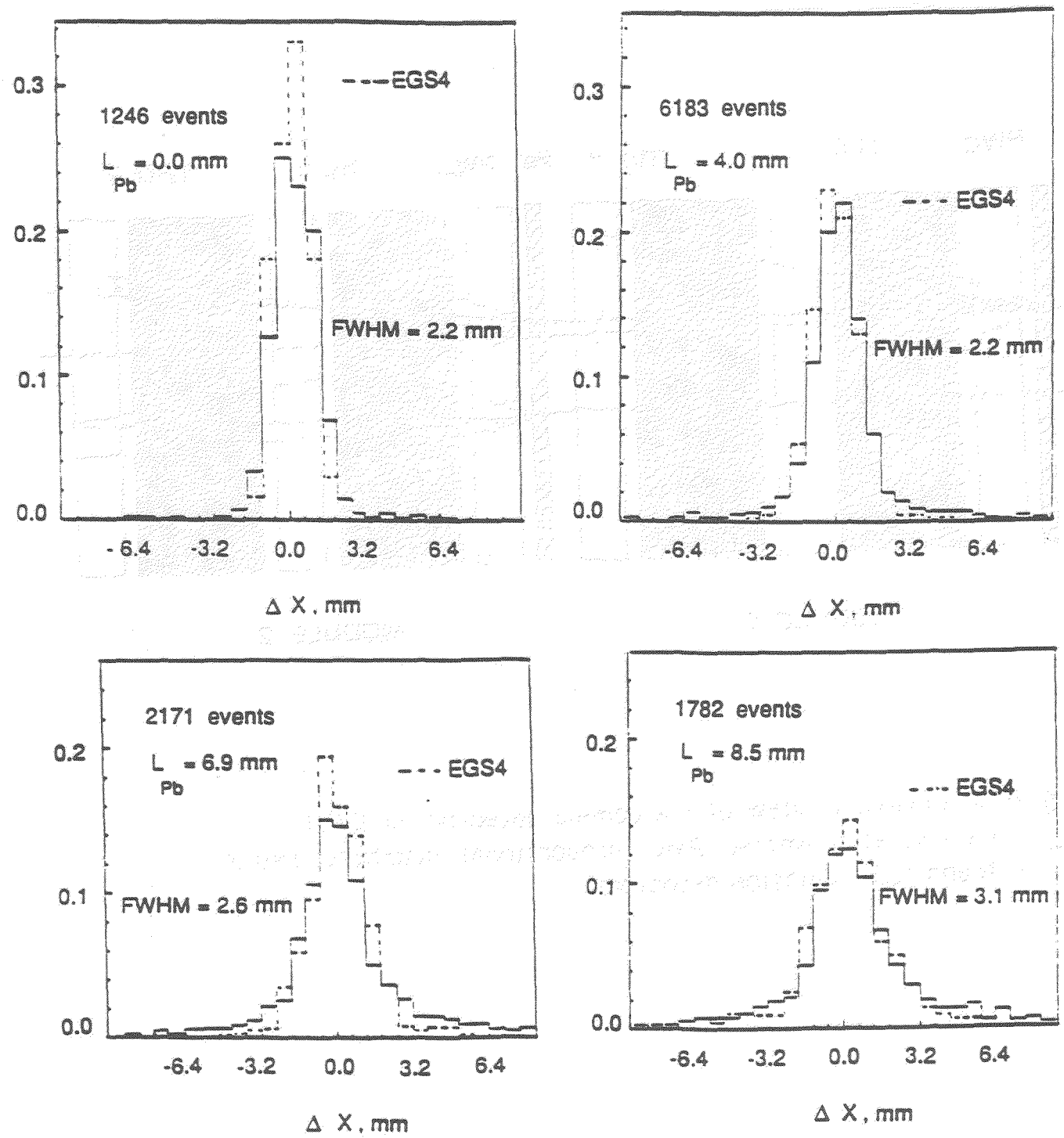

Fig. 7. Spatial resolution curves of the gamma detector for 25 GeV incident electrons and different thicknesses of converter.

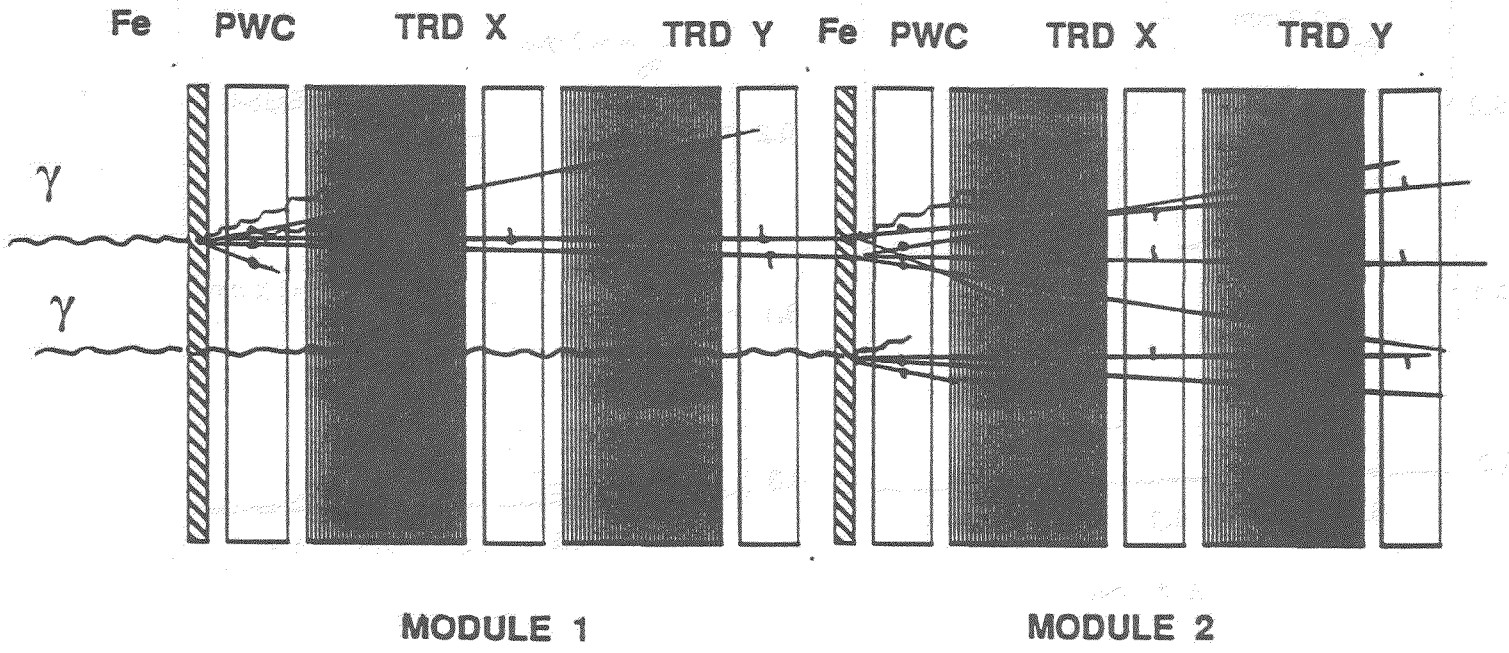

Fig. 8. A schematic view of the gamma detector for E761.
Fe - steel converter, PWC- proportional chambers, TRD X,Y-
transition radiation detectors.

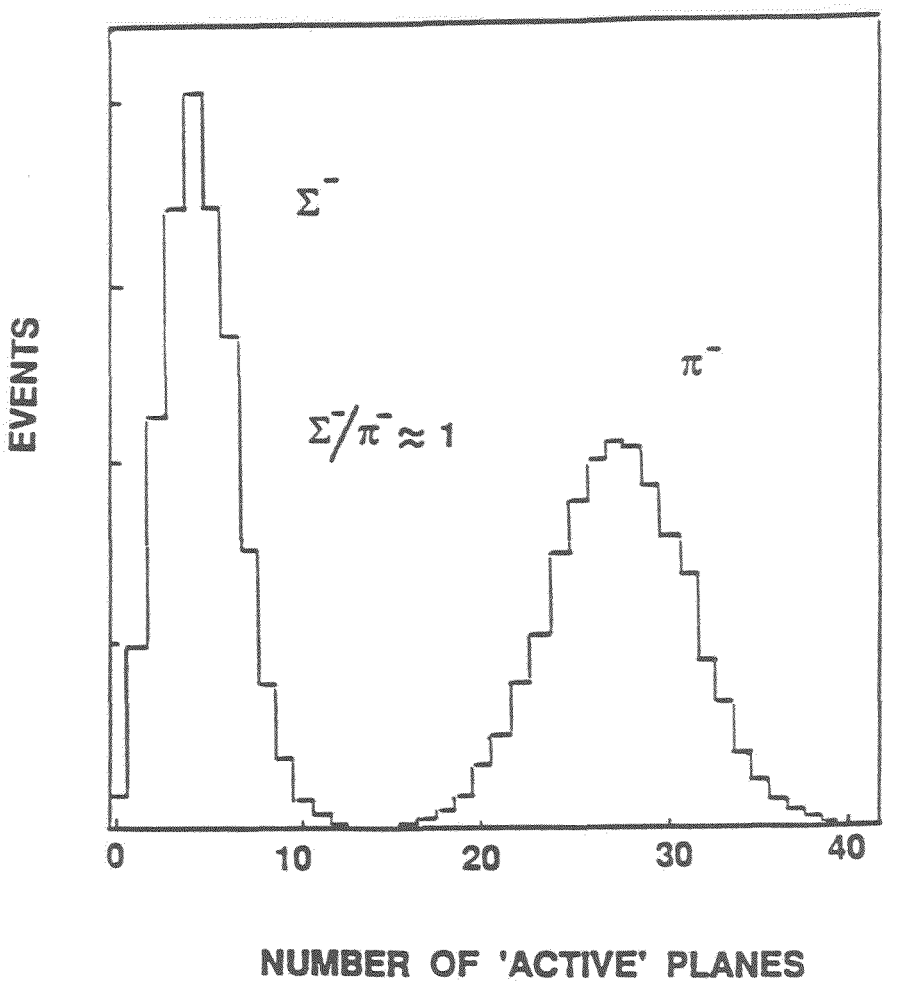

Fig. 9. A Monte Carlo calculation of the E781 TRD response to 600 GeV/c beam (50% of Σ^-, 50% of π^-). The distribution in number of "active" planes is plotted.

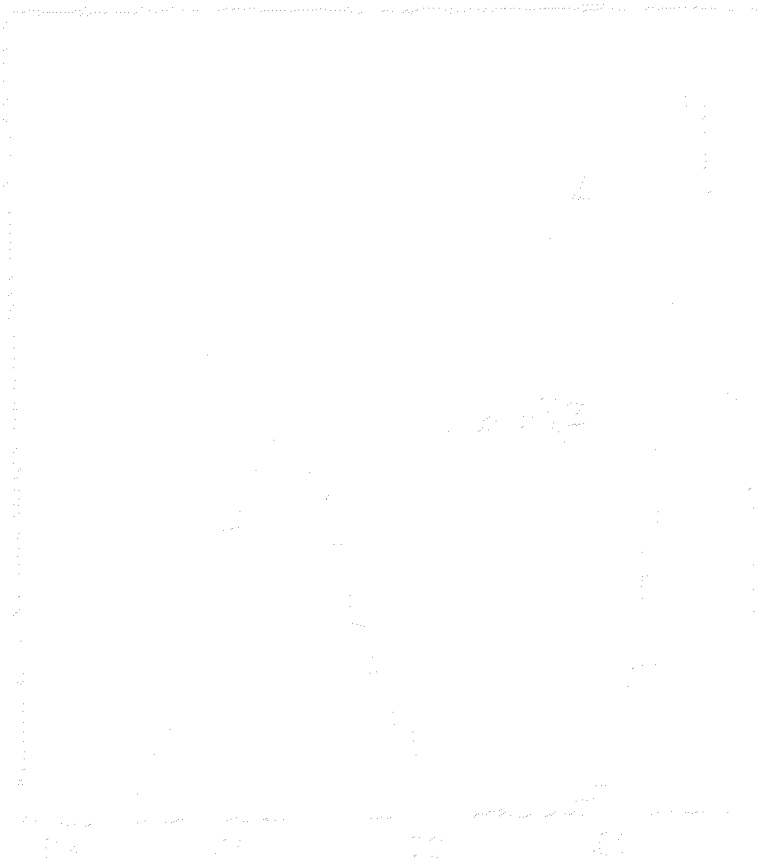

IV. Synchrotron Radiation Detectors

USE OF SYNCHROTRON RADIATION FOR ELECTRON IDENTIFICATION

by

Robert Handler
University of Wisconsin
Madison, WI. U.S.A.

This paper will be divided into three general parts:

A. A general review of the theory of synchrotron radiation (SR).

B. A description of the performance of a Xenon filled mutli-wire proportional chamber as a SR X-ray detector in a neutral beam experiment at Fermilab.[1]

C. Some speculation on how an SR detector could be used at colliders for electron identification.

A. Properties of Synchrotron Radiation

a) Angular distribution

A charged particle of mass m and momentum P moving in a magnetic field will emit radiation in a forward cone of angular width on the order of m/P. For a highly relativistic electron this angle is very small and the radiation can be considered to be emitted parallel to P for the purposes of this talk.

Thus for a particle bending in a magnet and then striking a chamber at point P (as shown in Fig. 1), the SR photons will intersect the chamber along the line PQ, where Q is the projection of the incoming trajectory.

b) Total energy radiated

I, the total energy radiated per unit length, by a particle of mass m, charge e and velocity v in a magnetic field H is[2]

$$I = (2e^4H^2v^2)/\left[3m^2c^6(1 - v^2/c^2)\right] \qquad \text{(cgs units)}$$

where c is the velocity of light.

The same formula can be written in units more familiar to high energy physicists

$$I(\text{keV/meter}) = (2\alpha\hbar c^3B^2P^2)/(3m^4)$$

where $\alpha = 1/137$, $\hbar$ is in units of keV-sec, c in meters/sec, B is the field strength in Tesla and P and m are in electron volts.

For an electron

$$I = 1.27B^2P^2$$

For B = 1.6 Tesla the following table shows I for various values of P (GeV)

Table 1.

P	I	
5	81.3	keV/meter
10	325	keV/meter
25	2.03	MeV/meter
50	8.1	MeV/meter
75	18.3	MeV/meter
100	32.5	MeV/meter
100	0.006	eV/meter for π

I have written for 100 GeV the amount of energy a charged pion would radiate. Since I varies inversely as m^4, it is very small. Thus an electron in a magnetic field radiates considerable energy, and this radiation should be detectable, whereas a charged pion radiates only a negligible amount.

c) Spectral distribution of SR photons

I, the energy per meter radiated into the n^{th} harmonic of the rotation frequency $W = c^2B/P$ is given by[2]

$$I_n = \left[(-2\ \alpha\hbar c^3B^2\sqrt{u}\ )/(\sqrt{\pi}\ mP)\right]\left[\phi(u) + (u/2)\int_u^\infty \phi(v)dv\right]$$

where $\phi(u)$ is the Airy function defined by the integral

$$\phi(u) = (1/\sqrt{\pi}\ )\int_0^\infty \cos(t^3/3 + ut)dt$$

ϕ is a bounded solution to the equation

$$d^2\phi/du^2 - u\phi = 0.$$

$u = n^{2/3}/\gamma^2$ with $\gamma = E/m$ where E is the particles energy.

The energy of the n^{th} harmonic is $\epsilon = n\,\hbar\omega$. In an interval $\Delta\epsilon$ there are $\Delta\epsilon/\hbar\omega$ harmonics, so that the total energy radiated into this interval $\Delta\epsilon$ is given by

$$I(\epsilon)\Delta\epsilon = (I_n \Delta\epsilon)/(\hbar\omega)$$

thus

$$I(\epsilon) = \left[(-2\alpha cB\sqrt{u}\,)/(\sqrt{\pi}\,m)\right]\left[\phi(u) + (u/2)\int_u^\infty \phi(v)dv\right].$$

In practice the various harmonics are very close together and the spectrum can be considered continuous with a spectral intensity given by $I(\epsilon)$. Fig. 2 shows $I(\epsilon)$ for three different electron energies in the region 0 to 100 keV.

While Table 1 shows more energy is radiated as the electron energy increases, it can be seen that the energy radiated into the region 4 keV to 20 keV, where X-rays can be easily detected with a proportional counter, decreases with E for $E > 10$ GeV.

The number of photons emitted per meter at an energy ϵ into an interval $\Delta\epsilon$ can be defined by the equation

$$N(\epsilon)\Delta\epsilon = \left[I(\epsilon)/\epsilon\,\right]\Delta\epsilon.$$

The total number of photons all colors emitted per meter is given by the integral

$$N = \int_0^\infty N(\epsilon)d\epsilon = (5\alpha cB/2\sqrt{3}m).$$

For an electron in a field of 1.6 Tesla N is very nearly 10, so that $N = 10(B/1.6)$ in a field B. In a magnet of total length L, the number of photons radiated is

$$NL = (2.5\alpha/\sqrt{3}m)cBL = (2.5\alpha/\sqrt{3}m)P_T = 20.6\ P_T \quad (GeV)$$

where p_T is the transverse momentum of the magnet. Knowing $N(\epsilon)$ and N one can write a Monte Carlo program to simulate the emission of Synchrotron radiation by an electron.

B. Detection of SR X-Rays

a) Design of the Xenon filled chamber

In this Section the use of synchrotron radiation for electron identification in a neutral beam experiment at Fermilab will be described. The experiment was E-361, whose purpose was to study Lambda beta decay. A magnet M with a 24" by 8" aperture and a p_T of 0.95 GeV was used both to momentum analyze the decay products of the beam Lambda and to produce the field necessary to cause electrons to radiate.

Figure 3 shows the number of photons expected at various energies in the X-ray range for 10, 25, and 100 GeV electrons. In order to detect these X-rays a multi-wire proportional chamber (MWPC) was placed just downstream of M. At X-ray energies photons are absorbed in matter chiefly by the Photo Electric effect. When the absorption occurs in the gas of the MWPC the photo electron is detected along with a possible Auger electron.

Figure 4 shows the mean free path for X-rays in Argon and Xenon in the range of 3 to 100 keV X-ray energy. For a given depth of detector you are always better off with Xenon. For a 2 cm deep chamber, such as was used in E-361, Argon would be useful below about 6 keV.

The chamber used as the SR detector (see Fig. 5) consisted of two planes of sense wires strung parallel to the field of M with wire to wire spacing of 2 mm. The two planes were separated by 1 cm. The chamber was filled with a mixture of 90% Xenon and 10% methylal gas at one atmosphere. Figure 6 shows the range of a photo electron in this gas. In the region of X-ray energies where absorption of the SR is likely this range is only a couple a millimeters or less, so that a single X-ray would be detected in only one plane, whereas a charged particle going through the chamber would be seen in both planes. Thus the X-ray signature was a hit in either of the sense planes (but not both). An electronic device which could read out the chamber and recognize this signature in 16 microseconds was built.

When the single X-ray hit was only 1 wire away from the electron track in either plane the hit was taken to belong to the electron track (about 5% of charged particles will register on two adjacent wires). This results in an inefficiency that becomes quite important at high electron energies.

In order to maximize the efficiency of the SR detector it is necessary to minimize the absorption of X-rays before the detector. Thus, the region between the pole pieces of M was filled with He gas. The He bag extended right up to the Xenon filled chamber, and the He pressure was kept higher than the Xenon presure to keep the 1 mil mylar window of the chamber pressed tightly against the cathode wires (Fig. 7).

Figure 8 shows the number of X-rays radiated by the electron while in the field of M, according to the theory given in the last Section, at various energies. Also shown are the number which would be absorbed in the 2 cm deep Xenon chamber. Below 3 keV most of the X-rays are absorbed in the He gas or the mylar window before reaching the chamber. Above 16 keV most pass through the chamber without being detected.

b) Electron efficiency

During the course of the Lamda beta decay experiment the performance of the SR detector was monitored by observing its sensitivity to electron-positron pairs made by gamma rays in the neutral beam. Figure 9 shows a histogram of the multiplicity of X-ray hits for 8 and 28 GeV electrons. Shown in dots are the X-ray mutliplicities which would be expected from Poison statistics if the average number of X-rays were 3.1 (8 GeV electron) and 1.65 (28 GeV electron).

The top curve in Fig. 10 shows the number of detected X-rays expected from theory as a function of electron energy for a Xenon filled chamber. The bottom shows the same function for the same chamber if Argon had been used. The middle (dashed) curve shows the number expected for Xenon amended by the inefficiency in detecting X-rays too near the electron track. The number actually observed at 8 and 28 GeV are shown for comparison.

Given the average number of X-rays one can calculate the efficiency of the SR chamber in identifying electrons (detecting at least one SR X-ray). Figure 11 shows this efficiency as calculated (solid curve) and measured (dots). The overall efficiency averaged 88% in the range 8 to 32 GeV electron energy.

c) Pion rejection

Figure 12 shows the pion rejection of the Xenon chamber for various energies, measured by observing the response of the Xenon chamber to Lamda goes to proton plus π^- decays. The average value was about 50 in the range 8 to 28 GeV. It was felt that if there had been some unambiguous information on the vertical coordinate of the X-ray hit (which is constrained to be the same as that of the electron), the pion rejection would have been much higher. One way to obtain this information is through charge division.

C. Possible Use of SR in Electron Identification at Colliders

In the Collider Detector at Fermilab there is an array of axial drift wires imbedded in a solenoidal magnetic field surrounding the beam at the point of collision. This is known as the central tracking chamber (CTC). The path length radially through this chamber is about 125 cm and the field about 1.5 Tesla. The top curve in Fig. 13 shows the number of X-rays of energy 3 keV or more expected to be detected on a sense wire of the CTC for electrons at various energies. The lower curve in Fig. 13 shows the number of photons which are 2 mm or more away from the radiating electron when they are absorbed. Thus, in all probability, these X-rays would be collected on the same drift wire as the track of the parent electron. The wires corresponding to the X-ray hits would have pulse height twice as big or higher that the average minimum ionizing electron signals and would be out of time (either early or late) by the order of 10 nanoseconds. Perhaps this signal is visable and useful on data that have already been written to tape.

At higher electron energies or perhaps higher values of the central magnetic field the average SR photon is in the gamma ray rather than X-ray region of energy. Thus at the SSC it would be feasible to put a gamma-ray detector of only a small number of radiation lengths in front of any calorimetry which would be reached by a particle after passing through the central magnetic field. It would be far easier to detect the many SR photons radiated by this electron than the electron itself.

References

1. Nuclear Instruments and Methods, A247, 412 (1986).

2. The Classical Theory of Fields, (second edition), L.D. Landau & E.M. Lifshitz, 226-230.

Figure Captions

Fig. 1. Spatial distribution of SR photons.

Fig. 2. Energy radiated into 4 keV bins by electrons for 10, 25, and 100 GeV.

Fig. 3. Number of photons radiated by electrons in a magnet with $p_T = 0.95$ GeV.

Fig. 4. Mean free path of X-rays in Argon and Xenon.

Fig. 5. A typical sense plane pattern from an electron with two detected X-ray photons. The allowed X-ray detection region corresponding to the electron trajectory is shown.

Fig. 6. Range of an electron in Xenon.

Fig. 7. Sketch of He gas system.

Fig. 8. Total number of X-ray photons radiated and detected for a 25 GeV electron.

Fig. 9. Multiplicities of X-ray hits for 8 and 28 GeV electrons. The dots represent a fit with a Poison distribution for photon number = 3.1 (8 GeV) and 1.65 (28 GeV).

Fig. 10. Number of X-rays expected to be seen in SR detector for Xenon and Argon. The dotted curve represents the calculation for Xenon modified by pattern recognition inefficiency. The two experimental results are shown for comparison.

Fig. 11. Calculated electron efficiency (curve) an experimental results (dots).

Fig. 12. Pion rejection of SR chamber.

Fig. 13. Number of X-rays detected for an electron moving radially in the field of the superconducting solenoid through the central tracking chamber (CTC) at Fermilab (top curve). Corresponding electron efficiencies are indicated. The bottom curve is the same with the constraint that the X-ray hit has to be at least 2 mm from the electron track.

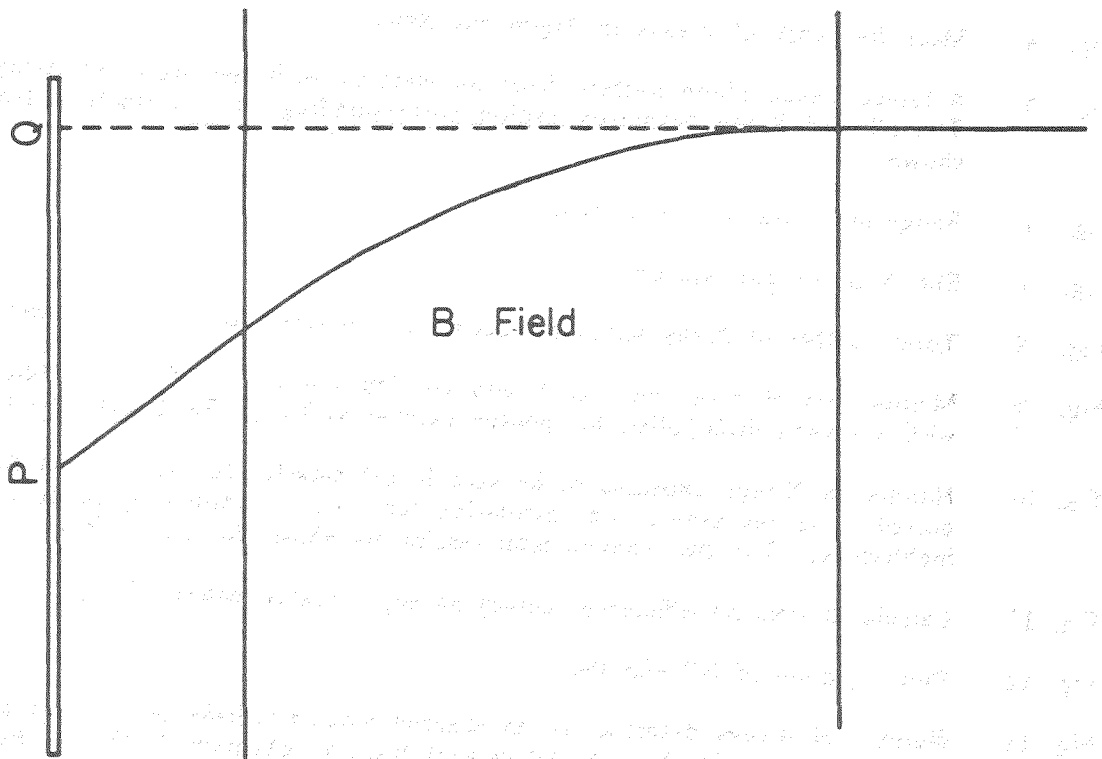
Q
B Field
P

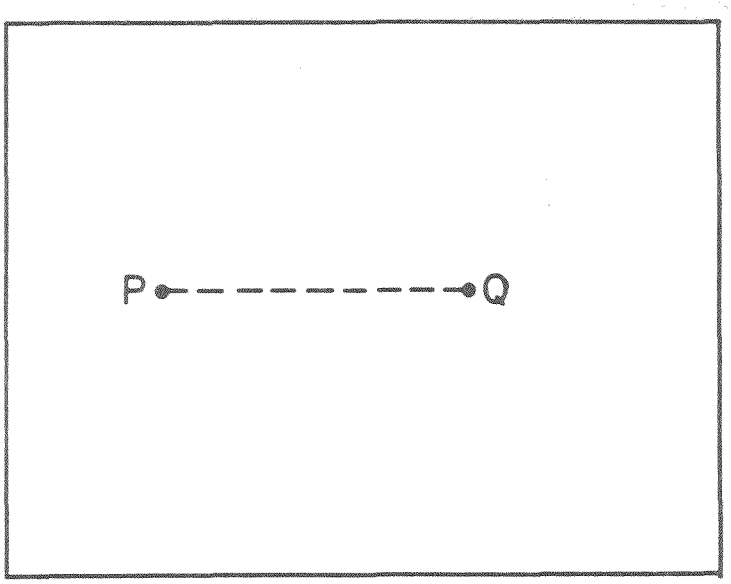
P
Q

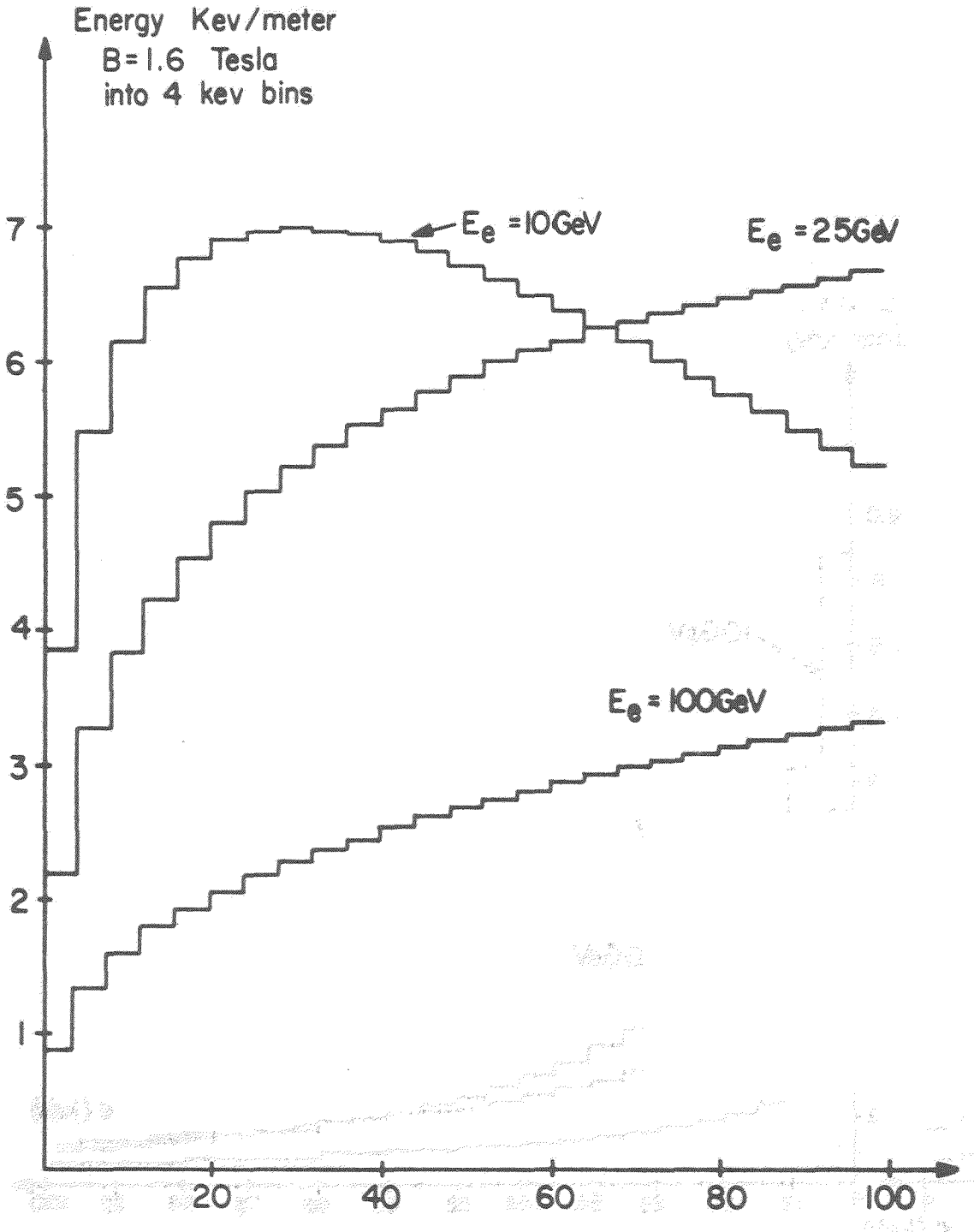
Energy Kev/meter
B=1.6 Tesla
into 4 kev bins
E_e =10GeV
E_e =25GeV
E_e =100GeV
7
6
5
4
3
2
1
20
40
60
80
100

Number of Photons
radiated in magnet M
P_T = .95GeV

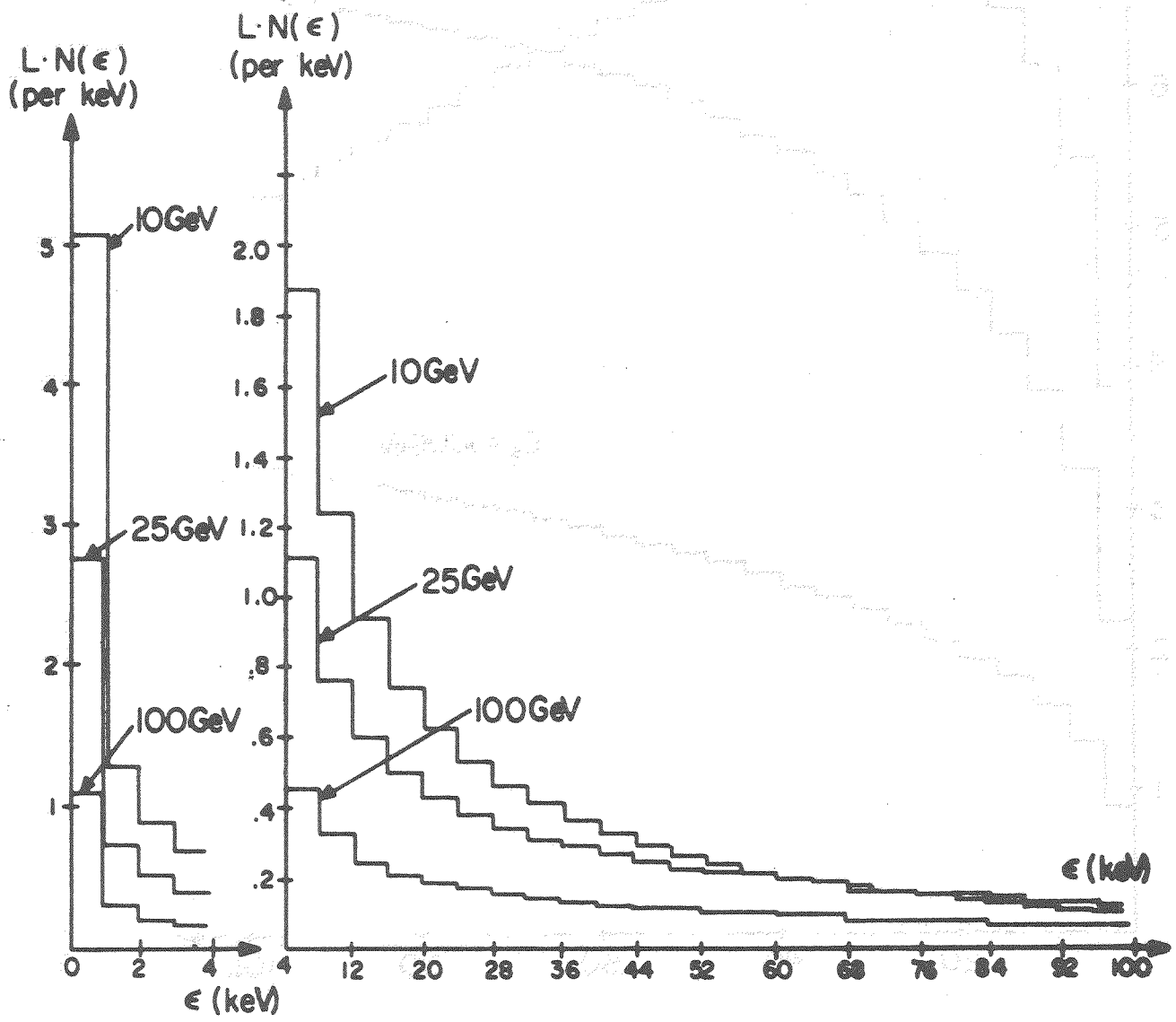

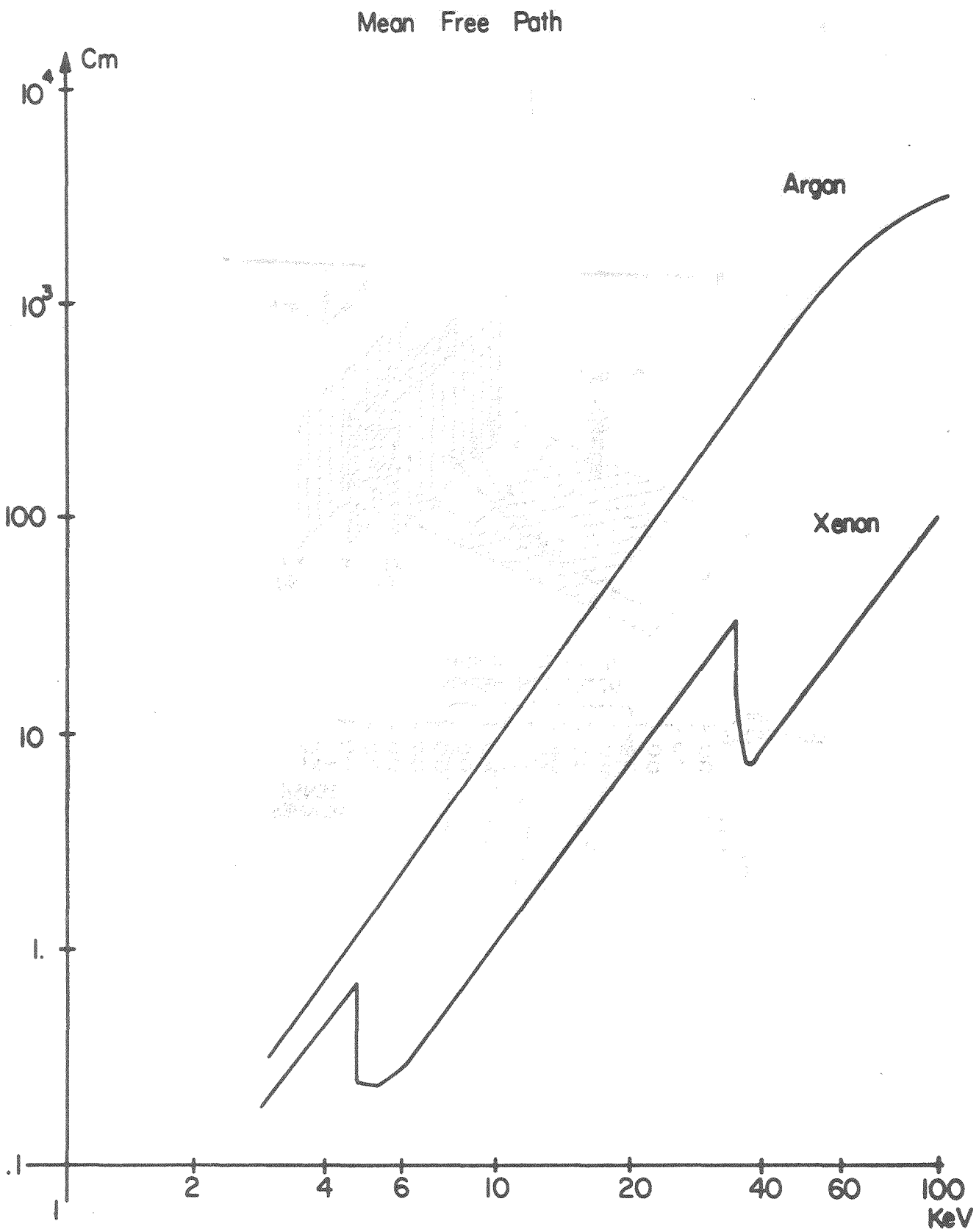
Mean Free Path
Cm
10^4
10^3
100
10
1.
.1
Argon
Xenon
1
2
4
6
10
20
40
60
100
KeV

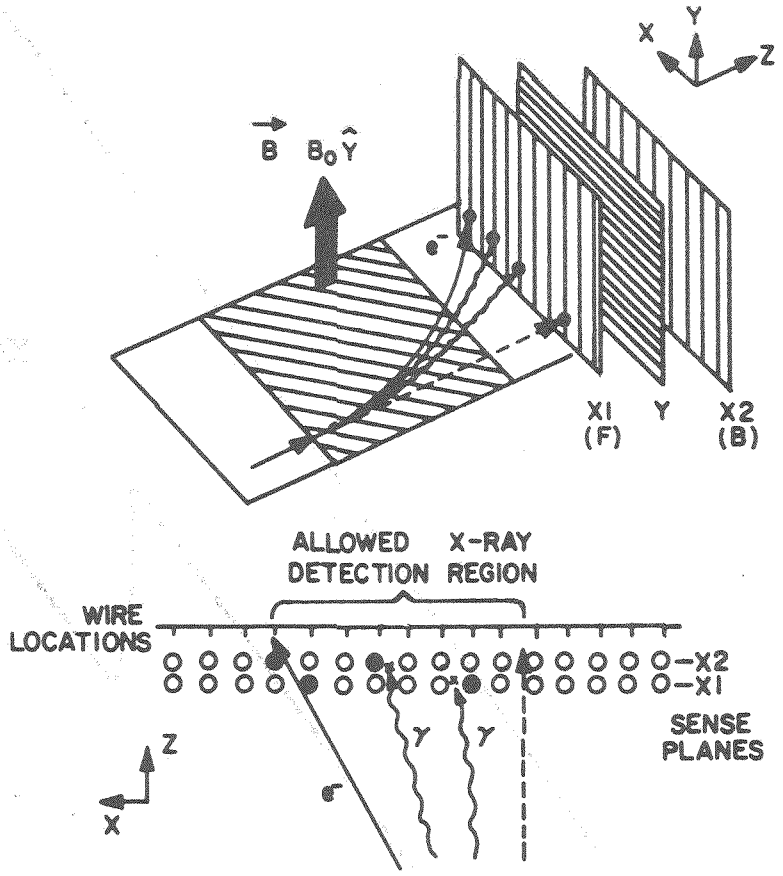
X
Y
Z
B
$B_0\hat{Y}$
e⁻
X1
(F)
Y
X2
(B)
ALLOWED X-RAY
DETECTION REGION
WIRE
LOCATIONS
O—X2
O—X1
SENSE
PLANES
γ
γ
Z
X
e⁻

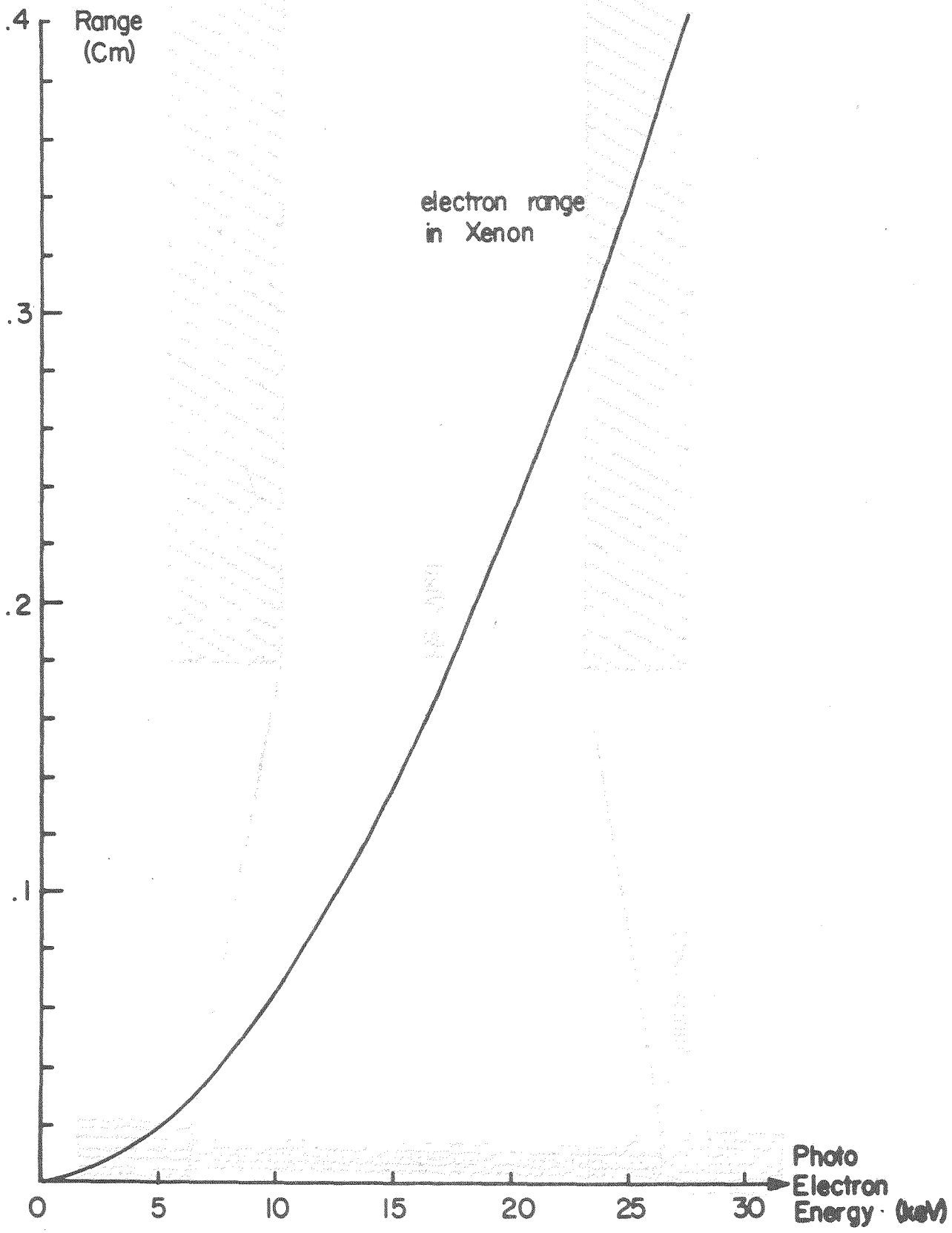
.4
Range
(Cm)
electron range
in Xenon
.3
.2
.1
0
5
10
15
20
25
30
Photo
Electron
Energy (keV)

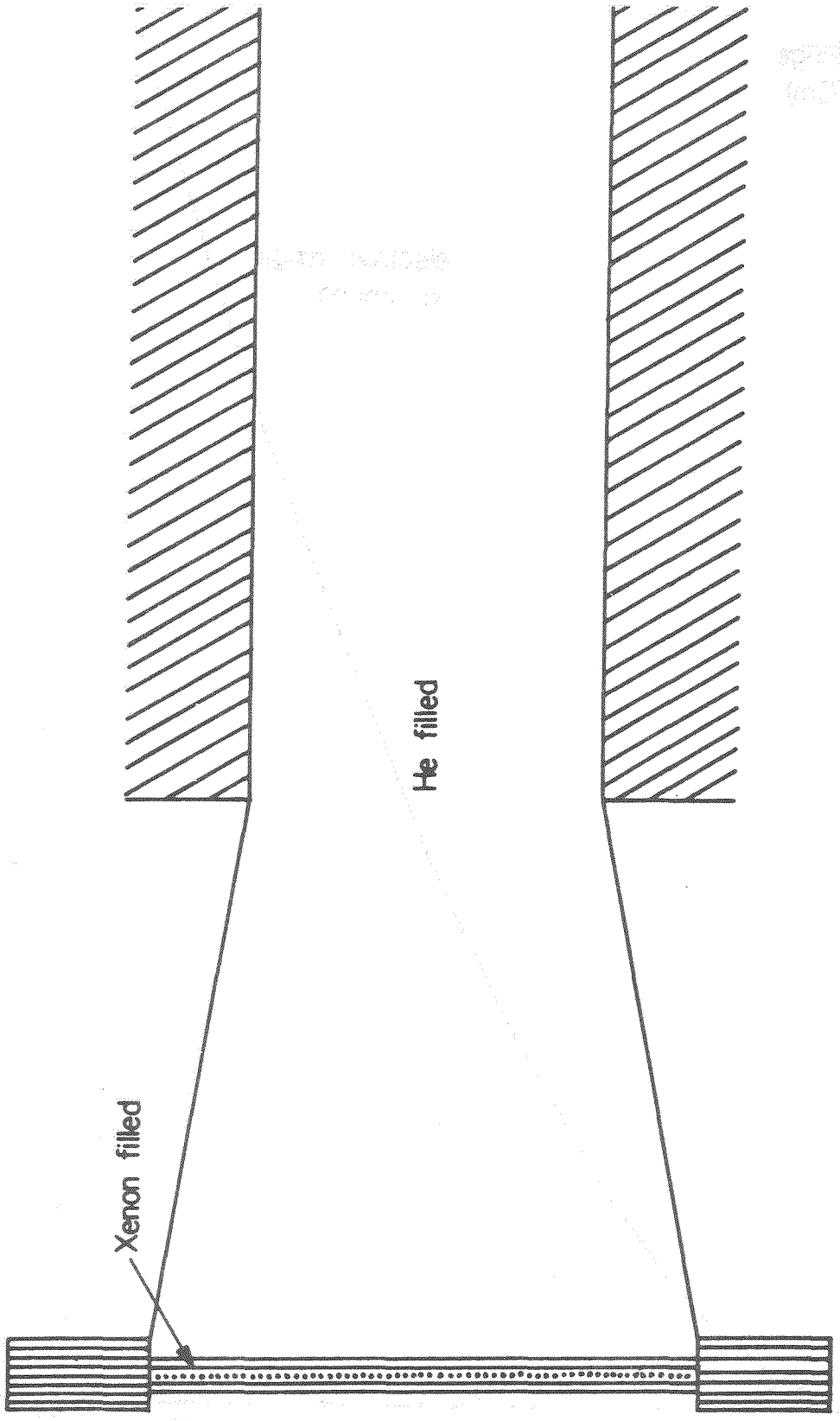
He filled
Xenon filled

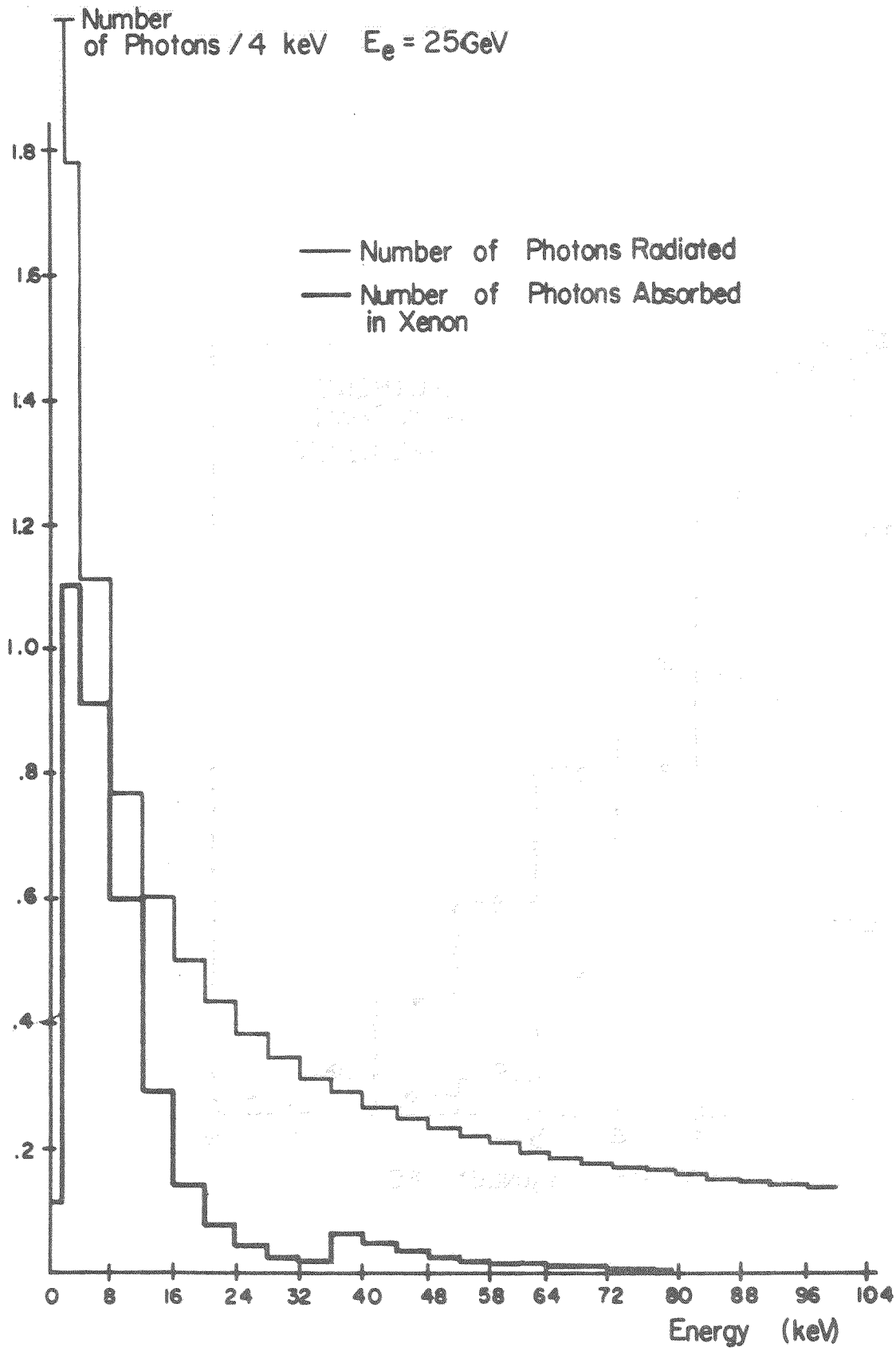
Number
of Photons / 4 keV
E_e = 25GeV
Number of Photons Radiated
Number of Photons Absorbed in Xenon
1.8
1.6
1.4
1.2
1.0
.8
.6
.4
.2
0
8
16
24
32
40
48
58
64
72
80
88
96
104
Energy (keV)

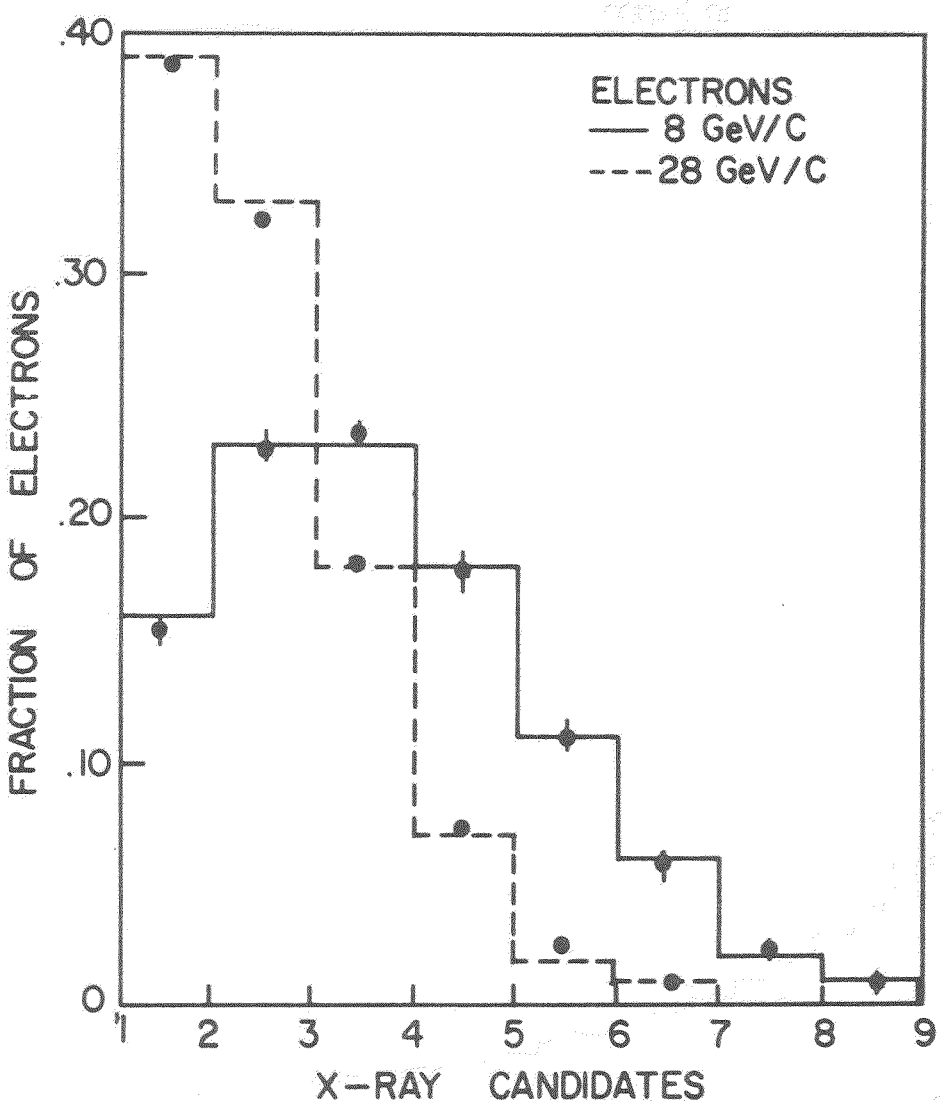
ELECTRONS
— 8 GeV/C
---28 GeV/C
FRACTION OF ELECTRONS
.40
.30
.20
.10
0
1
2
3
4
5
6
7
8
9
X-RAY CANDIDATES

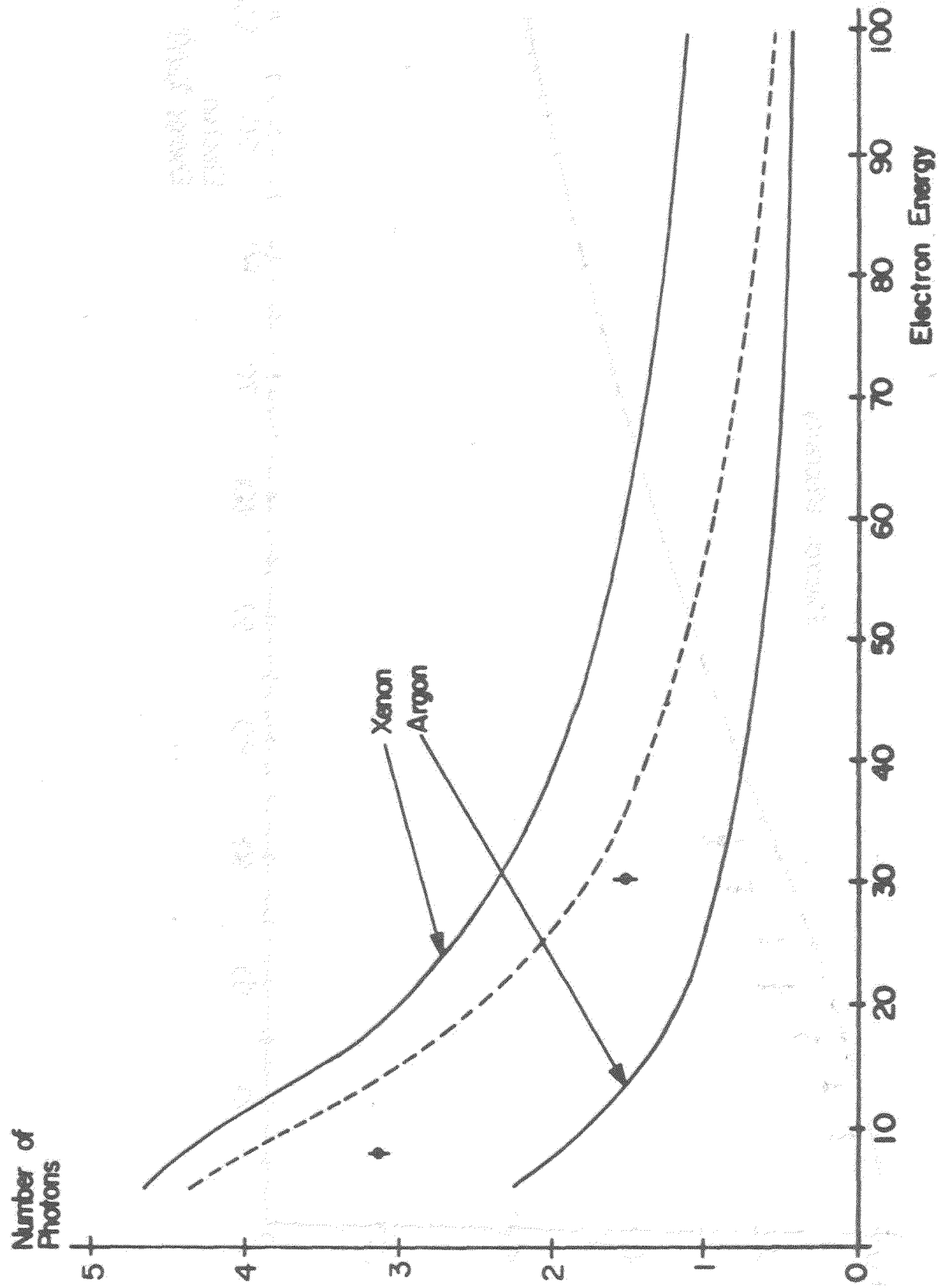
Number of Photons
0
1
2
3
4
5
10
20
30
40
50
60
70
80
90
100
Electron Energy
Xenon
Argon

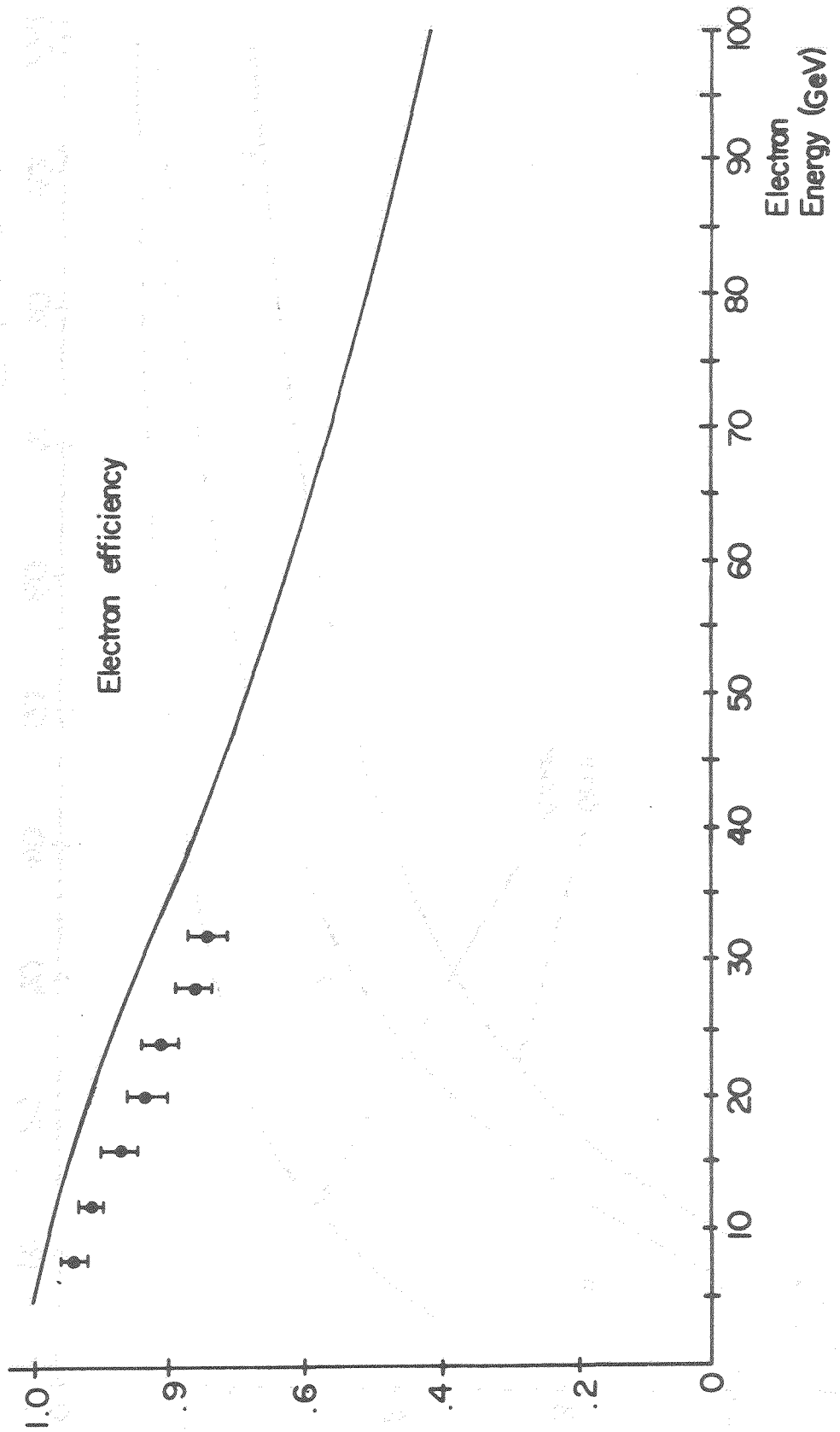
Electron efficiency
1.0
.9
.6
.4
.2
0
10
20
30
40
50
60
70
80
90
100
Electron
Energy (GeV)

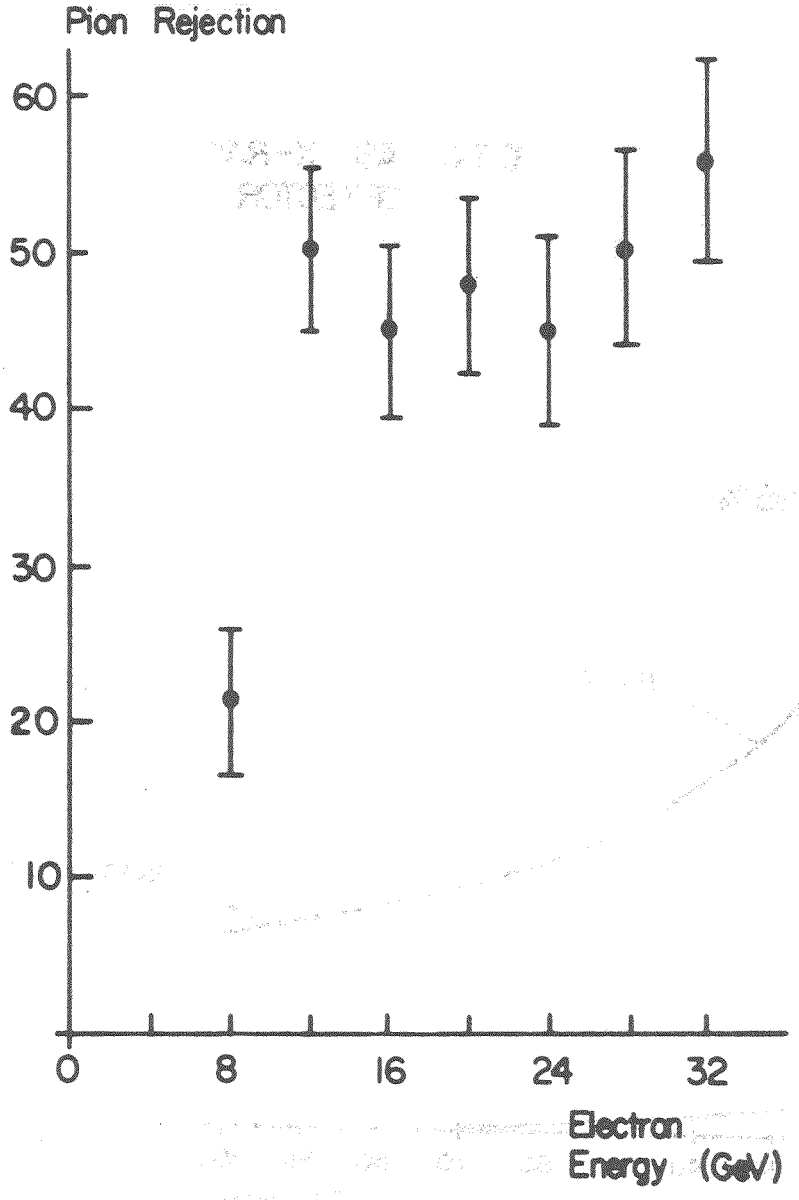
Pion Rejection
60
50
40
30
20
10
0
8
16
24
32
Electron
Energy (GeV)

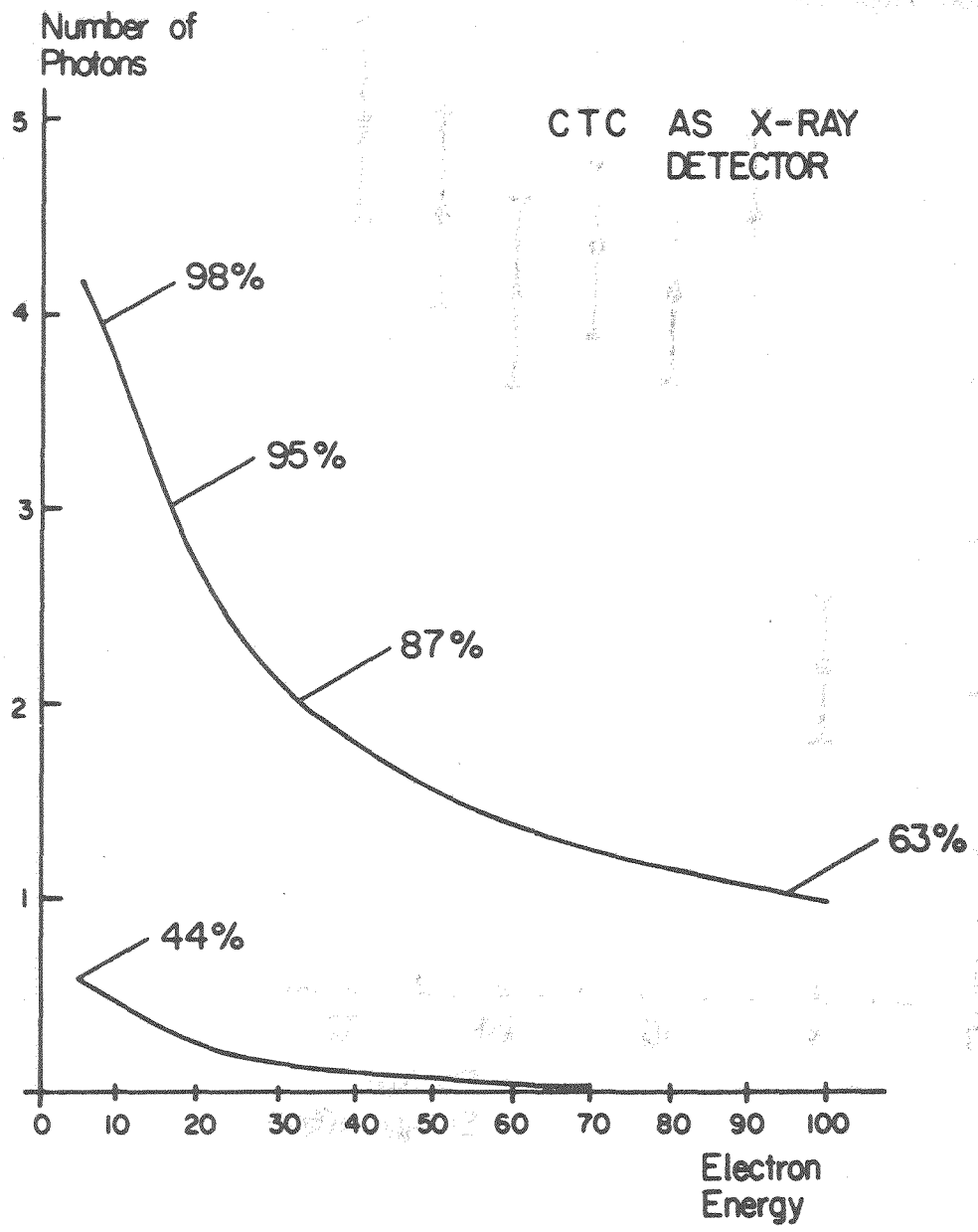
Number of Photons
CTC AS X-RAY DETECTOR
98%
95%
87%
63%
44%
5
4
3
2
1
0
10
20
30
40
50
60
70
80
90
100
Electron Energy

A PRESHOWER DETECTOR FOR TAGGING ELECTRONS WITH SYNCHROTRON RADIATION

P. Melese R. Rusack
Rockefeller University, New York, U.S.A.

P. Cushman
Yale University, Connecticut, U.S.A.

Abstract

The use of synchrotron radiation to identify electrons with an energy above 25 GeV is discussed. With the advent of the SSC and the availability of solenoid magnetic fields of 5 T or greater[1], the energy of the synchrotron radiation photons becomes high enough that they can be detected by observing pair production in a lead/scintillating fiber detector. A Monte Carlo simulation of such a detector, using the GEANT 3.12 program, has been developed. From these calculations it appears that a clear signal for identifying electrons is present and that a fast trigger with a good rejection of electron background (γ's from π^0's, with over-lapping charged particles) can be designed for the SSC. A prototype detector is presently under construction and will be tested at Fermilab in 1990.

Introduction

Synchrotron radiation (SR) has been used in high-energy physics experiments to tag electrons for several years now.[2-4] The most recent example is the AMY detector[4], in which electrons produce SR while bending in the 3 T magnetic field. These experiments use xenon filled chambers to detect the SR photons which are emitted with energies in the X-ray region. We are investigating the possibility of identifying electrons with the much higher energy SR that will be emitted in a high magnetic field detector at the SSC.

In a high field solenoid experiment, such as the one discussed by the Compact Solenoid Group at the Berkeley SSC workshop in 1987[5], a preconverter directly in front of the calorimeter can be used to detect the SR photons. Our prototype detector is designed to test this method of electron identification.

Synchrotron Radiation

The physics of synchrotron radiation is discussed in several review articles and text books on electricity and magnetism.[6,7] The radiation can be characterized by the total emitted energy I and the critical energy $\hbar\omega_c$. For electrons

$$I = 1.27\ E^2B^2L\ [\text{KeV}] \quad (1)$$

and

$$\hbar\omega_c = 1.33\ E^2B\ [\text{KeV}] \quad (2)$$

where E is in GeV, B is in Tesla and L is expressed in meters.

The photon number density can be written as

$$\frac{dN}{d\omega} = \frac{1}{\omega}\frac{dI}{d\omega} = 2\sqrt{3}\ \frac{e^2}{c}\ \frac{\gamma}{\omega_c}\ \int_{2\omega/\omega_c}^{\infty} K_{5/3}(x)\ dx$$

or

$$\frac{dN}{d\omega} = 2\sqrt{3}\ \frac{e^2}{c}\ \frac{\gamma}{\omega_c}\ \int_0^{\infty} \frac{\cosh\frac{5t}{3}}{\cosh t}\ \exp\left(-\frac{2\omega}{\omega_c}\cosh(t)\right) dt. \quad [3]$$

The integral in equation 3 can be calculated numerically.[8] Figure 1 shows the function $dN/d\omega$ plotted against energy for a 200 GeV electron traversing a 5 T magnetic field. The shape of this plot scales with ω/ω_c. There is a cut-off at the lower end of the energy scale due to the fact that although the distribution goes to infinity as $\omega \to 0$, the radiated energy goes to zero, so this part of the spectrum can be safely ignored.

Values for I and $\hbar\omega_c$ are shown in Table 1 for electron energies between 25 and 200 GeV for an electron traversing a 1 meter, 5 T magnet. From the table it can been seen that a 200 GeV electron radiates 1.27 GeV in SR photons which, if detected and separated from the main bulk of the electron shower, could provide a very clear signal to identify electrons.

The SR is emitted tangentially to, and in the same plane as the electron orbit. Thus it is deposited in a narrow strip in the bend plane of the magnet, outside of the electron's orbit. The length of the strip is proportional to the bend of the electron, varying inversely with energy. An electron traversing a 5 T, 1 m magnet produces a strip 3.75 mm long at 200 GeV and 15 mm at 50 GeV. The maximum electron energy accessible by this method is defined by the limit where the SR can no longer be distinguished from the bulk of the electromagnetic shower. Our Monte-Carlo studies show that for the first 2 radiation lengths this limit is around 1.4 mm away from the shower maximum, for 200 GeV electrons, and decreases slowly with increasing energy.

The electron energy is bounded on the low end by poor detection efficiency since at low energies, the SR photons have a relatively long mean free path and the produced electrons have a relatively short range. The mean-free path of a photon goes through a maximum at 3 MeV, where it is 22 mm of lead, then decreases to a value of 10 mm at 100 MeV. On the other hand, the range for 5 MeV produced electrons is only 3 mm in lead. Thus as the energy of the primary electron, and its associated SR, decreases it becomes more difficult to identify electrons using their SR signal.

The Prototype Detector

The prototype detector we are building is shown in Fig. 2. It consists of 8 layers of lead and scintillating fibers. Each layer consists of a 1.25 mm lead sheet and 6 scintillating fiber ribbons. We will use 0.5 x 0.5 mm square fibers arranged in ribbons 10 cm or 200 fibers wide. The fibers will either be the conventional polystyrene PBD-POPOP, or polystyrene and PMP, depending on the results of tests currently underway at Bicron.

The six fiber ribbons in each layer are arranged in pairs. Each pair provides one of three stereo views set at -15^0, 0^0 and $+15^0$ (the stereo views within each layer are not illustrated in Fig. 2). The fibers of one layer are all brought to an end-plate to which an image intensifier is connected. At the end-plate the fibers are all held with a spacing of 150 μ between fibers. This is achieved by building a 26 mm wide U shaped block with 150 μ spacers set every 650 μ. They are fixed at only one end forming a comb-like arrangement. Forty fibers are laid across the U, one fiber per spacer. Once this is done, another 150 μ spacer is laid across the top of the fibers abutting the vertical spacers and the process is repeated 30 times. The top of the U is then closed and the fibers are all glued in place. Finally the end of the resulting fiber and epoxy block is cut, machined flat and polished.

The detector is read out by two image intensifier tubes (IIT), each of which reads out four layers of fibers. The IIT's, fabricated by the DEP company in Holland, consist of two stages of light amplification. The first stage is the same as the 80/18 tube used by the UA2 group[9]; it demagnifies the image by a factor of 4.7. The second stage of the IIT is a proximity focussed dual micro-channel plate. The amplified light output of the IIT is transmitted to four CCD's with fiber optic light guides such that each CCD receives amplified light from one of the four end-plates, corresponding to one fiber layer, connected to the front of the IIT chain. The CCD's and the electronic readout are exactly the same as the ones used by UA2.[10]

Monte-Carlo Results

As part of the design process we have used the GEANT 3.12[11] program to simulate our detector response in SSC conditions. We have assumed a 1 m radius, 5 T magnet in all our simulations. The questions we want to answer are:

1) What is the minimum energy at which one can expect to be sensitive to the SR photons?

2) What is the signal to noise of the SR at different longitudinal positions along the shower?

3) Can the SR deposited in a pre-converter be used for π^0 rejection in a fast electron trigger?

In the next two sections we discuss results obtained with the detector simulation.

Electron Identification

The SR deposits energy in a narrow strip in the plane of the electron's orbit. Thus, if a cut perpendicular to the plane is made a distance Δx away from the center of the electron shower, as shown in Fig. 3, and the energy deposited between lines B and C is projected onto C, then the SR should appear as a peak where the bend plane intercepts C. Figures 4 and 5 show the signal for both the SR and for the background from the electromagnetic shower. For the 50 GeV electrons (Fig. 4) the Δx cut was 1.55 mm, while it was 1.4 mm for the 200 GeV electrons (Fig. 5). Each plot was generated using 100 Monte Carlo events.

For both energies there is, for the first radiation length, a very clear signal over the background. For the 50 GeV electrons, there is approximately 1.8 MeV deposited in the scintillator, while for the 200 GeV electrons, at the same depth, 10 MeV is deposited. This corresponds to averages of 56 and 400 SR-generated photoelectrons for 50 GeV and 200 GeV incident electrons respectively. Beyond the first radiation length the SR signal continues to grow, but the background from the electron shower development starts to become significant. For 25 GeV incident electrons, the mean number of photoelectrons produced in the first radiation length is 13. For the fibers and the photocathode we are using in our prototype, this seems to be about the lowest energy at which this method will work.

Triggering

An important quality of any 4π SSC detector will be its ability to select electrons at the trigger level. It is unlikely that the SR signal discussed in the previous section could be used at the trigger level due to the requirement of reconstructing the event. However the signal produced could be used in a much simpler way to generate an electron enrichment in times on the order of 100 nsec.

The major background to the electron signal comes from π^0's where the decay photons overlap with minimum ionizing particles. The early shower development for γ's and electrons is different. The photons from the π^0 need to convert before they can be detected, whereas the electrons start depositing energy as soon as they enter the detector. In view of this, it is then reasonable to ask if this difference in the shower development can be used to select electrons at the trigger level. The presence of high energy SR enhances this difference, producing additional low energy photons which deposit a significant amount of energy in the early part of the shower. This is especially true for 200 GeV electrons where, as can be seen in Fig. 6b, the total energy deposited by the SR is greater than the <u>total</u> energy deposited by the electron up until 1 radiation length. Figure 7b indicates that even with the overly-pessimistic assumption of Gaussian fluctuations, there is a clear separation between π^0 and electron plus SR after 1 R.L. for 200 GeV incident particles. For 50 GeV electrons the effect is much less significant (Fig. 7a).

Such a trigger could be implemented in a SSC detector by reading out the the fibers, on the ends not connected to an IIT, with a phototube. The output of the phototube would then be compared with a threshold level that is scaled by the total energy deposited in the electromagnetic calorimeter which follows the preconverter.

A Preconverter at the SSC

In this paper we have concentrated on how a pre-converter can be used to identify the SR from electrons offline, and possibly separate π^0's from electrons at the trigger level. A pre-converter in a 4π SSC detector would provide other useful information about the event. The UA2 experiment has installed a similar detector in their apparatus to separate electrons from π^0's with overlapping charged particles, and has done so successfully without the presence of a magnetic field. In addition to the electron identification, a pre-converter will also provide a precision measurement of the location of the start of an electromagnetic shower, thus helping to resolve isolated γ's.

There are still technical problems to be solved before a scintillating fiber pre-converter can be used in this way at the SSC. The most obvious limitation is the slow read out times for the CCD, which is greater than 1 msec. Others include the radiation resistance of the fibers and the light output of thin fibers. It is hoped that current research into these problems will provide solutions which will enable such a detector at the SSC to be feasible.

References

[1] "A Very High Field Magnet". S. Terada et al. KEK preprint 88-68.

[2] "Transition and Synchrotron Radiation Produced by Electrons and Particle Discrimination". B. Merkel et al. NIM 138 (1976) 625.

[3] "Electron Identification Using a Synchrotron Radiation Detector". J.S. Dworkin et al. NIM A265 (1988) 141.

[4] "Electron Identification Using Synchrotron Radiation". H. Harada et al. NIM A265 (1988) 141.

[5] "Report of the Compact Detector Subgroup". J. Kirkby et al. Proc. of the Workshop on Experiments, Detectors and Experimental Areas for the Super Collider, Berkeley, 1987.

[6] Classical Electrodynamics. J.D. Jackson (Wiley, New York, 1975).

[7] The Classical Theory of Fields. L.D. Landau and E.M. Lifshitz (Pergamon Press, Oxford, 1975).

[8] Dr. B. Handler and Dr. T. Sanda private communications.

[9] "Performance of a Scintillating Fiber Detector in the UA2 Upgrade". R.E. Ansorge et al. NIM A265 (1988) 33.

[10] "A Fastbus Digitizer for the UA2 Scintillating Fiber Detector". S.G. Katvars et al. NIM A276 (1989) 482.

[11] CERN DD/EE/84-1. R. Brun et al.

Electron Energy [GeV]	25	50	100	150	200	250
I [MeV]	19.8	79.4	317	714	1270	1984
$\hbar\omega_c$ [MeV]	4.16	16.6	66.5	150	266	415

Table 1. Synchrotron Parameters for $B = 5$ T and $L = 1$ m.

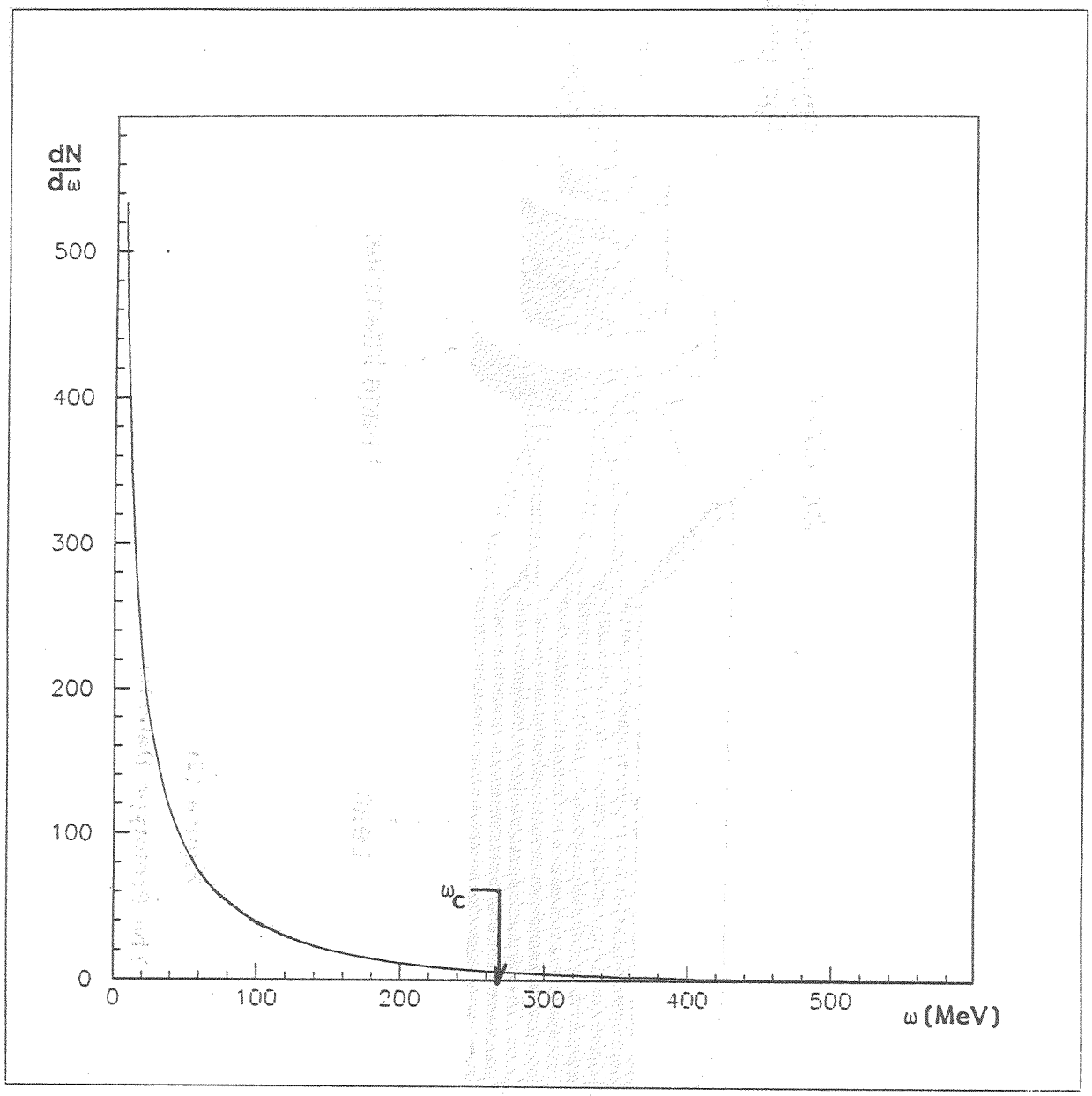

Figure (1)
$\frac{dN}{d\omega}$ for the synchrotron radiation
of a 200 GeV electron
traversing a 5T magnet.

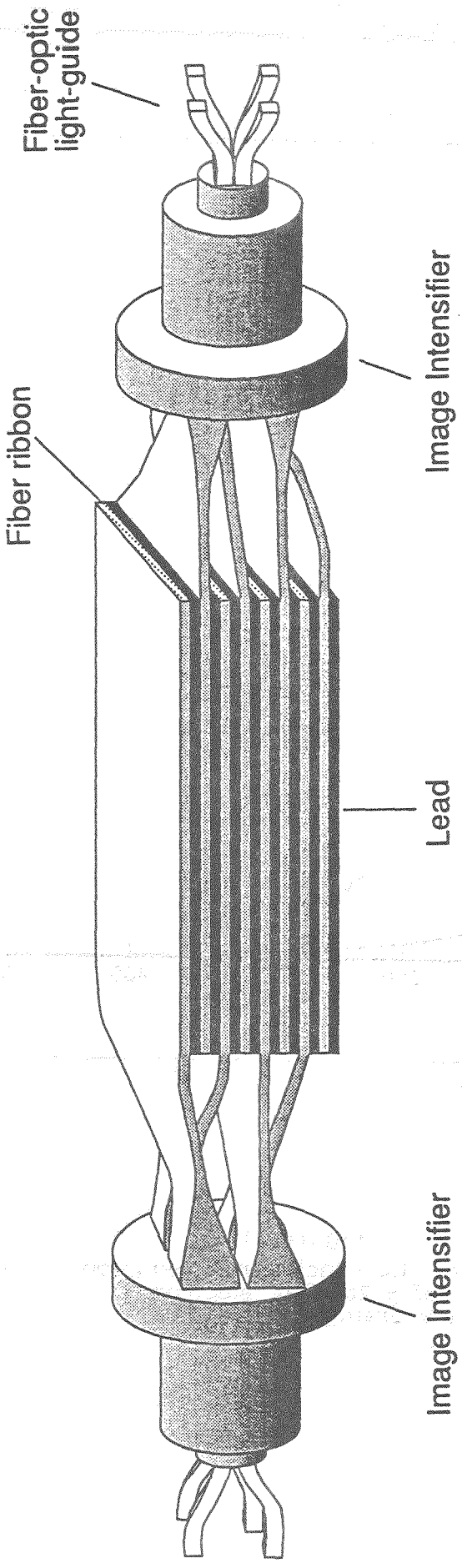

Figure (2)

The Prototype Detector

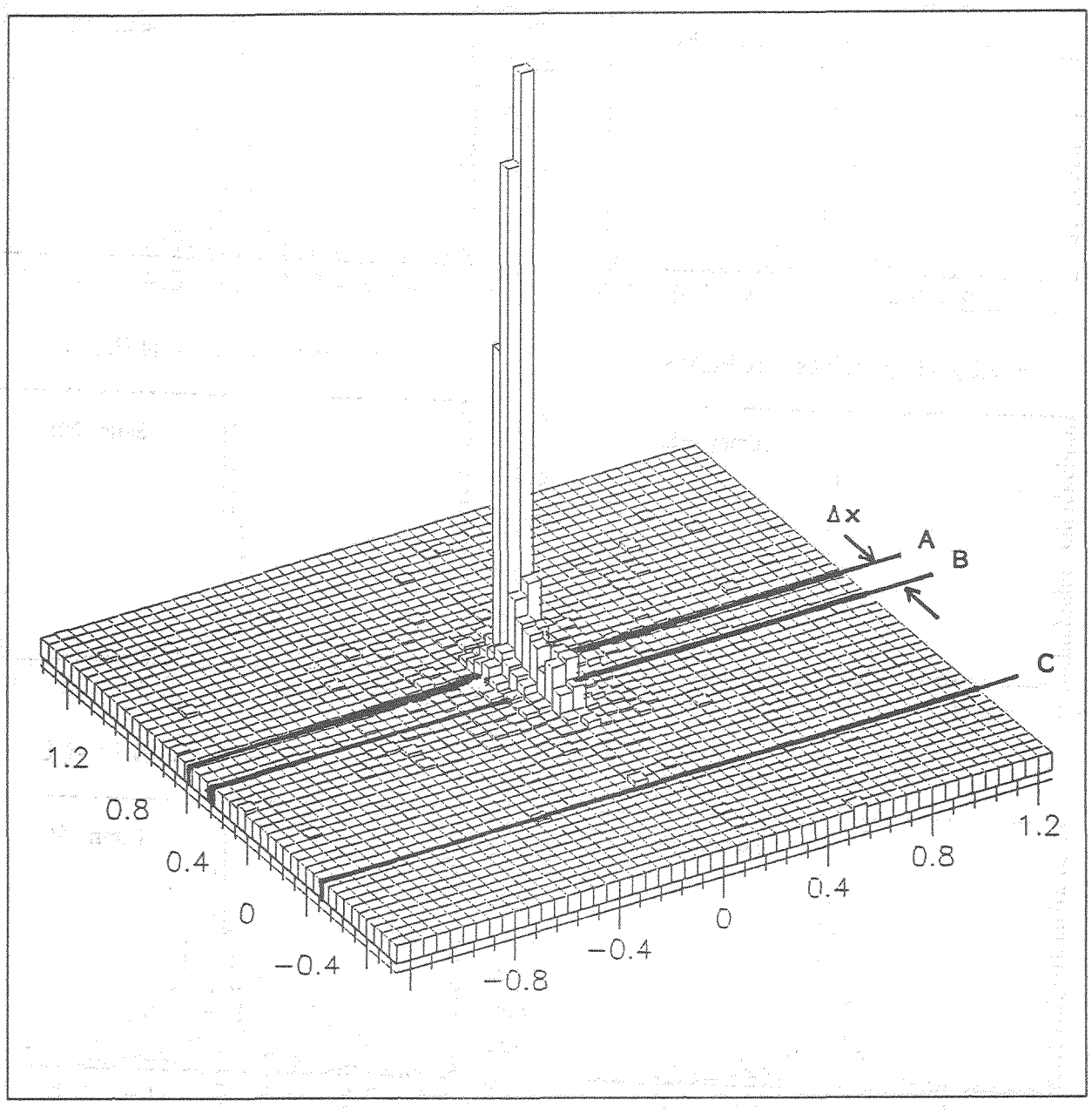

Figure (3)
Energy deposited by a 200 GeV electron and its associated synchrotron radiation in less than 1 radiation length of lead.

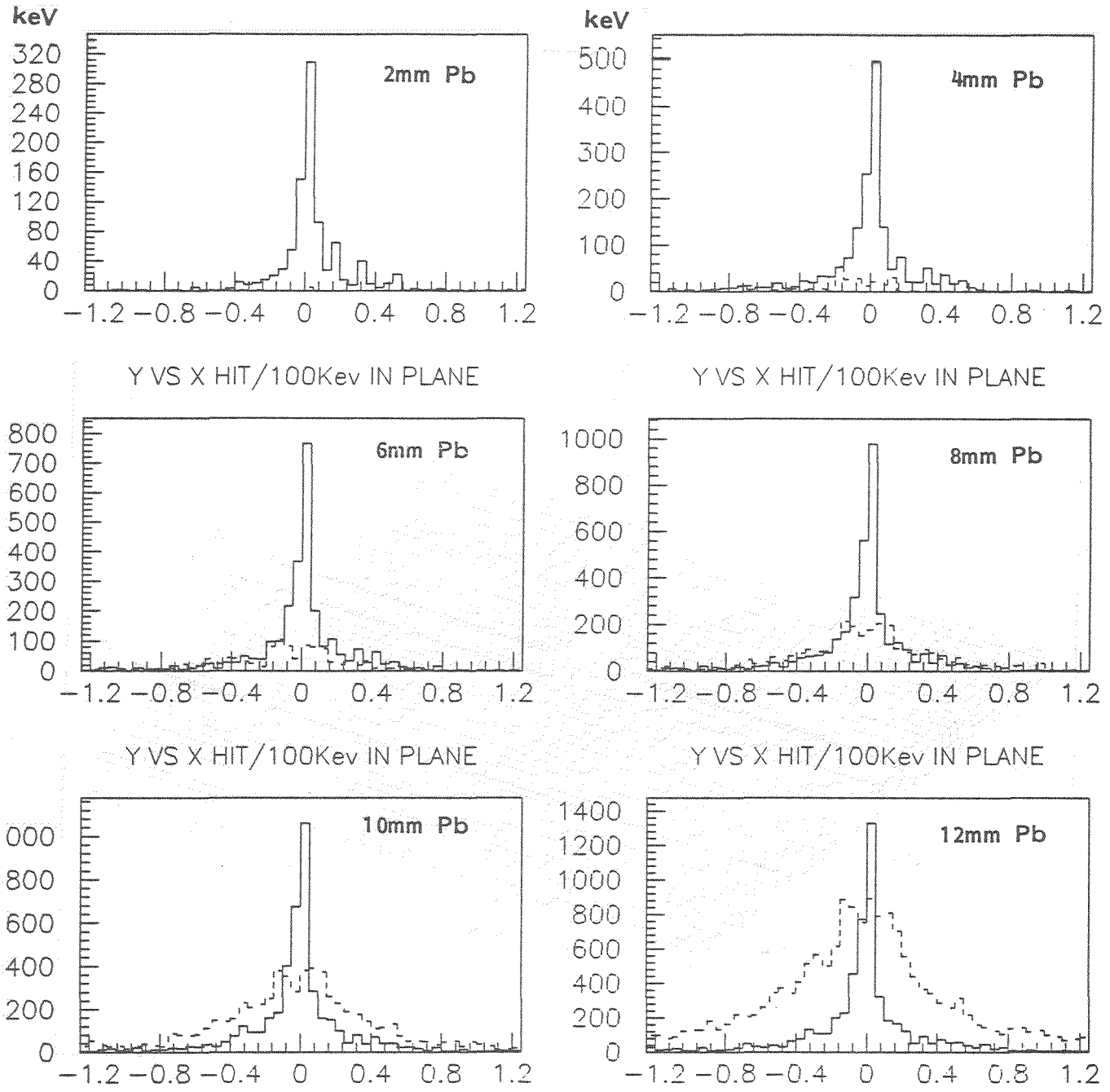

Figure (4)

The cumulative synchrotron radiation signal after cuts described in the text for a 50 GeV electron traversing a 5T 1 meter magnetic field for increasing depths inside the detector. The solid line is the signal and the dashed line is the background from the electron signal.

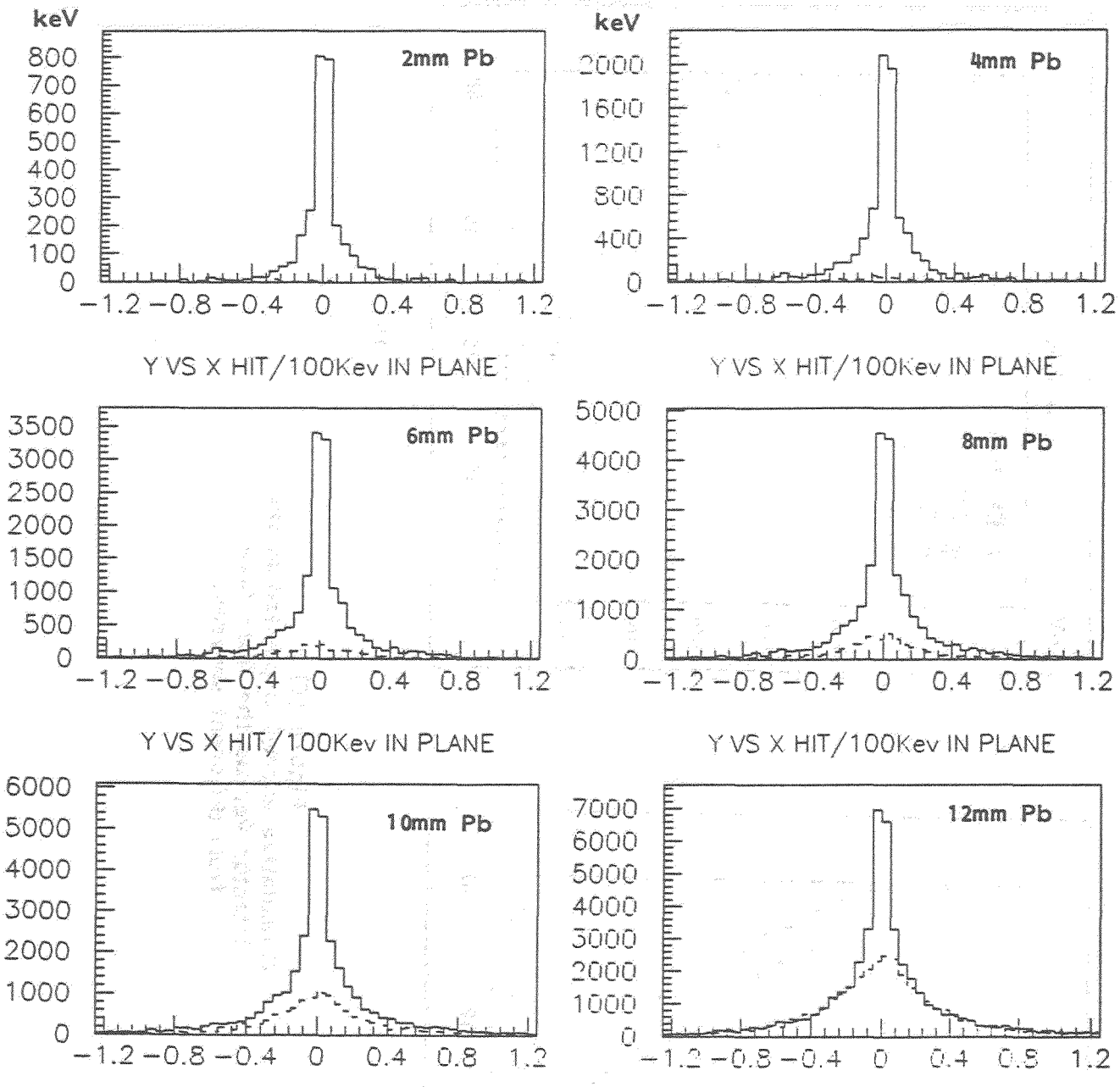

Figure (5)

The cumulative synchrotron radiation signal after cuts described in the text for a 200 GeV electron traversing a 5T 1 meter magnetic field for increasing depths inside the detector. The solid line is the signal and the dashed line is the background from the electron signal.

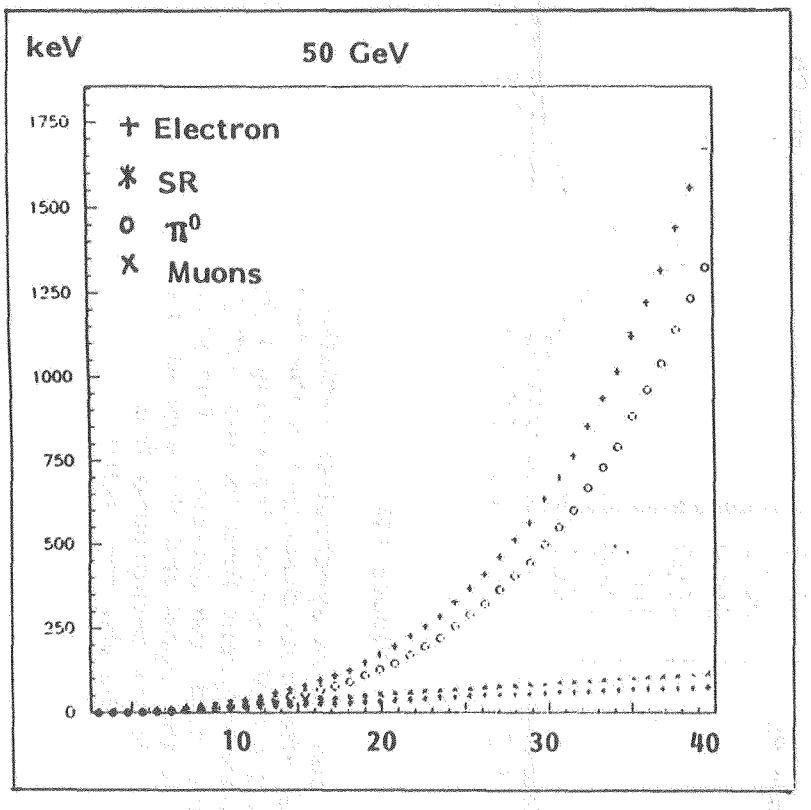

(a)

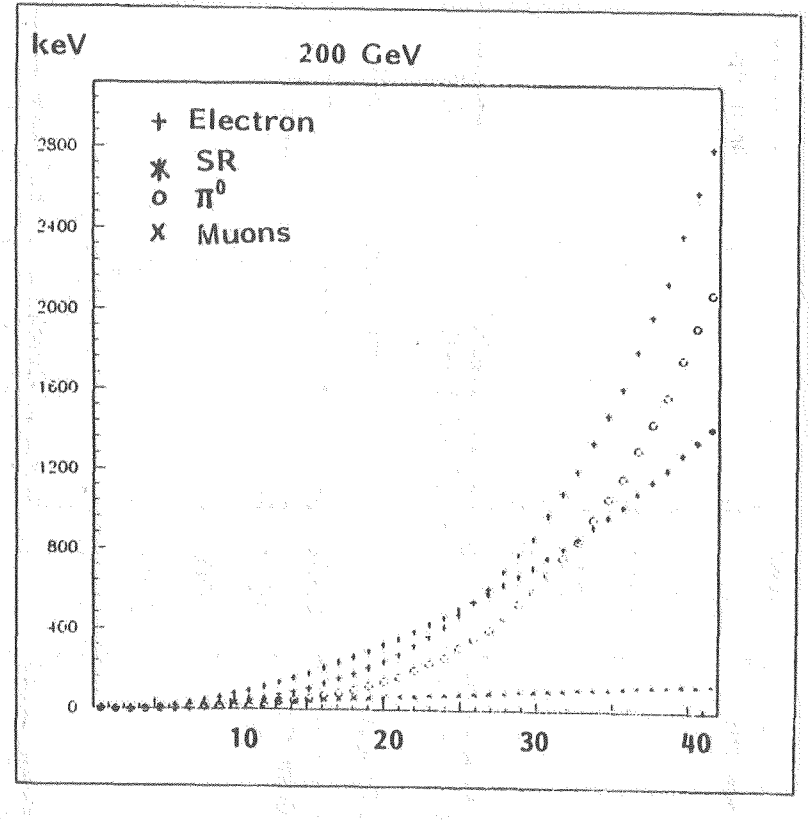

(b)

Figure (6)
Cumulative energy deposited in the detector versus the fiber layers from different sources.

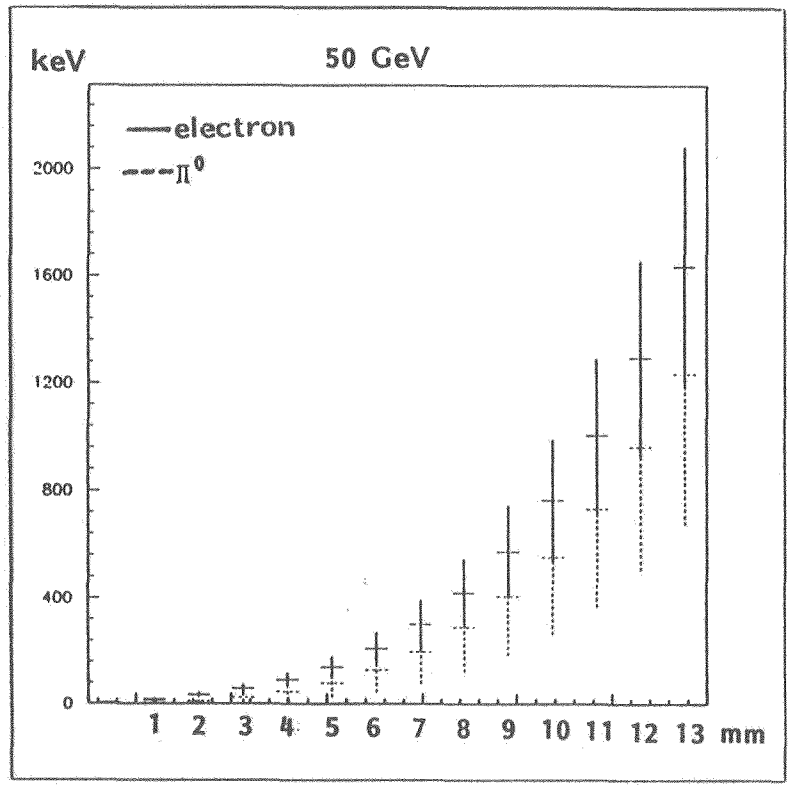

(a)

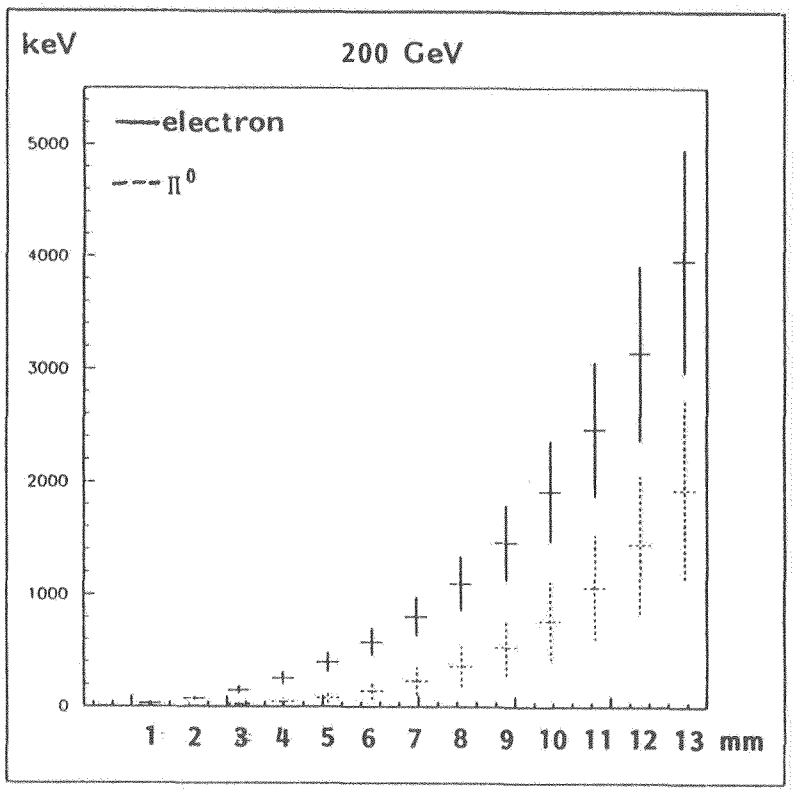

(b)

Figure (7)

Cumulative energy deposited in the fibers versus depth in lead.

V. Time-of-Flight and dE/dX Techniques

REVIEW OF TIME OF FLIGHT TECHNIQUES

Suzanne E. Willis
Northern Illinois University
DeKalb, Illinois

Summary

Time of flight systems are most useful for identifying low-β particles; in a collider experiment, they will probably only be used in the central region. This, however, introduces difficulties associated with geometry and operating in a magnetic field.

The best existing systems operating in a collider environment have a resolution of around 100 ps, limiting particle identification to particles of a few GeV/c momentum at a 2 m distance. It may be possible to push the scintillator - photomultiplier tube technique to 50 ps; further improvements will require new techniques.

We will begin by discussing the traditional time of flight technique, using photomultiplier tubes and scintillator, its limitations, and give examples of how it has been implemented in a collider environment. Variations on this technique which hold promise for improved resolution will then be discussed, and we will conclude by describing a proposal for an SSC time of flight detector using a totally different technique.

Basic Method

Time of flight (TOF) techniques have been used both in fixed-target and in collider experiments to identify low-momentum particles[1]. The time of arrival of charged particles at a point well separated from the production point is measured; this allows calculation of the velocity and, combined with the momentum of the particle (which is measured separately), calculation of the mass as well. If the particle travels a distance L, the time it takes to do so is given by $t = \frac{L}{\beta c}$ and the fractional error on the time by $\frac{\delta t}{t} = \frac{\delta \beta}{\beta}$. The mass can then be calculated using $m = \frac{p}{\gamma \beta}$, giving a fractional error on the mass of $\frac{\delta m}{m} = \gamma^2 \frac{\delta \beta}{\beta}$. Only low-momentum particles will have velocities sufficiently different from the velocity of light; the momentum limit will depend on the mass of the particle, the distance from the production point to the measurement point, and on the intrinsic resolution of the system.

Conventional TOF

A conventional TOF system consists of two banks of scintillators, one near the production point which measures a start time (in a collider experiment, these may be replaced by forward-backward counters along the beam, which use $\beta=1$ particles to define a start time[2]) and one as far away as possible, to measure the flight time. Ideally, each scintillator has a photomultiplier tube on each end; this gives two independent measurements of the stop time, reducing the measurement error by a factor of $\sqrt{2}$. The distant set of counters must be finely segmented enough so that not more than one particle per event, on the average, hits a single counter.

The measured flight time must be corrected for several effects to yield the actual flight time of the particle:

Counter-to-counter variations in electronics, cable lengths, and so on (t zeroes)

Travel time of the light to the ends of the scintillator from the point where the particle passes through - this point must therefore be measured separately (presumably by the same tracking detectors

used for the momentum measurement).

Pulse-height slewing - this occurs because the time at which a fixed-threshold discriminator fires will depend on the pulse height of the incoming signal, assuming the rise time is constant. The best results are obtained not by using a rise-time compensated discriminator, but by using a fixed-threshold discriminator and correcting the time based on the pulse height[1], which must therefore also be measured.

For a long (at least 1 m) scintillator which is not too thick, the time resolution is given by[3]

$$\sigma_t = \sqrt{\left(\frac{1}{2.35}\right)^2 \frac{\left(\tau^2_{scint} + \left(\frac{1}{2}\frac{n(n-1)}{c}L\right)^2 + \tau^2_{pm}\right)}{N_e} + \sigma^2_{walk}}$$

where τ_{scint} is the decay time of the scintillator, n is the index of refraction, L is the distance from the hit position to the photomultiplier tube (this term results from the difference in path lengths through the scintillator between a photon coming straight out and one traveling at the internal reflection angle), τ_{pm} is the time jitter of the photomultiplier tube, σ_{walk} is the electronic time resolution, including the pulse height correction, and N_e is the number of photoelectrons produced. Putting in optimistic values (τ_{scint} = 2.0 ns, n = 1.6, L = 1 m, τ_{pm} = 0.5 ns, σ_{walk} = 75 ps, N_e = 300) gives σ_t=100 ps as an estimate of the best achievable resolution. Making the scintillator thicker increases N_e but introduces another factor due to travel time of the particle through the scintillator[4] (in 100 ps, a β=1 particle travels 3 cm). Figure 1, from a Monte Carlo calculation described in Ref. 4, illustrates the improvement which is possible if thick counters are segmented in depth.

In a collider experiment, the central magnetic field makes it necessary to have very long light guides, so that L may be several meters; space considerations may also force the light guides to be nonideal in shape, further reducing the number of photoelectrons. In this case, the best achievable resolution may be several hundred picoseconds.

Two recently published experiments illustrate the type of results which may be obtained in a collider environment. The first is a prototype for the CLEO II detector[5]. The scintillators were 2.8 m long, 10 cm wide, and 5 cm

thick, with 1.3 m long light guides on each end. In a test setup, a resolution of 110 ps per counter (combining the times from both photomultiplier tubes) was achieved, comparing very favorably with the calculation above. In the CLEO II setup, illustrated in Figure 2, these counters will cover the central region. The long light guides are necessary to remove the photomultiplier tubes from the magnetic field.

The second experiment is in the CO colliding beam area at Fermilab[2], and is illustrated in Figure 3. The setup is more like that of a fixed-target experiment than of a collider experiment, except that the start time is measured by scintillators located upstream and downstream along the beam pipe. They have two sizes of scintillator in the transverse direction, TOF 1 which are 305 cm long, 15 cm wide, and 5 cm thick; and TOF 2 which are 150 cm long, 10 cm wide, and 5 cm thick. Both sets of counters have approximately the same resolution, 100 ps per counter (combining both photomultiplier tubes) when using reconstructed tracks. When using a laser for calibration, they measure resolutions as good as 60 to 75 ps per photomultiplier tube. They are still working on understanding their calibrations, in order to improve their resolution further.

New Developments

The above discussion of conventional TOF systems gives the successes and limitations of the technique as currently implemented. Further improvements are possible, but it seems that significant improvements will only come with a different technique, either a variation on current methods or a totally different method. Three variations on the scintillator - photomultiplier tube technique will be discussed, followed by a variation on another technique - narrow-gap spark chambers.

Microchannel Plate Photomultiplier Tubes

The use of microchannel plate photomultiplier tubes for time of flight was also investigated by Giles et al. and is discussed in Ref. 5. Microchannel plates have a very low intrinsic time jitter, but the photomultiplier tubes are very small, typically 18 mm in diameter, making the number of photoelectrons quite low. Also, the photocathode efficiency is about half that of conventional photomultiplier tubes, further reducing the number of electrons. This has the effect of worsening the time

resolution of the system, and negates the advantages of using these fast tubes.

Photomultiplier Tubes which will Operate in a Magnetic Field

These were also studied in Ref. 5 for use in CLEO II. The results quoted above are for the central TOF counters; because of geometry, the endcap TOF counters have a 90° bend in their light pipes, resulting in a low number of photoelectrons and a resolution no better than about 450 ps. The photomultiplier tubes studied were Hamamatsu R2490; the gain drops by about a factor of 100-300 in a 15 kG axial magnetic field. Counters with these tubes and no light guide were measured to have a resolution of 200 ps, a significant improvement.

Scintillating Fibers

Kuhlen and collaborators (Ref. 4) have been investigating the use of scintillating fibers for timing, for use in an SSC detector. Their system is illustrated in Figure 4. The advantages of fibers are that the cladding reduces the critical angle, therefore reducing the travel time spread; they may be easily segmented in depth to correct for travel time through the scintillator; and the cladding reduces reflection losses. Also, these workers are investigating the use of faster scintillator and faster photomultiplier tubes. Their goal is to build a system with 50 ps resolution.

Narrow Gap Spark Chambers

Planar narrow-gap spark chambers have been known for some time to have very good time resolution[6] (the best published resolution is 24 ps[7]), but are difficult to handle. They require large electric fields, resulting in forces which can be difficult to handle, and high-pressure gas (about 10 atmospheres), necessitating the use of a pressure vessel. Finally, segmentation is poor.

Bowcock and collaborators at Harvard[8] propose to investigate the use of such chambers in a cylindrical geometry. The gap would still be 0.1 to 1.0 mm, the diameter a few millimeters, and the length a meter or so. The advantages of this geometry are that electrostatic forces will not be a problem (the inner and outer tubes will need to be stabilized, but the forces

will cancel); the tubes can be stacked, and allow for fine segmentation; and no pressure vessel will be needed (the outer cathode will be made of stainless steel; the inner anode will be some sort of glass). They have not yet constructed a prototype, but expect to be able to achieve 50 ps resolution easily, and possibly as good as 10 ps (although this will require improved electronics as well).

The following table shows π/K and K/p separation at the 2 σ level for counters of various resolutions located at a distance of 2 m from the production point:

Resolution, σ_t	π/K	K/p
450 ps	0.8 GeV/c	1.3 GeV/c
200 ps	1.3 GeV/c	2.2 GeV/c
110 ps	1.8 GeV/c	3.3 GeV/c
50 ps	2.7 GeV/c	4.7 GeV/c
10 ps	6.4 GeV/c	10.5 GeV/c

In order to determine the resolution needed in a particular experimental setup, detailed Monte Carlo studies of physically interesting events need to be done. However, it is generally true that particles close to 90° will be low momentum, and, at least at the Fermilab collider, very few particles of $p > 10$ GeV/c are emitted close to 90°.

References

1. W. B. Atwood, Proc. 1980 SLAC Summer Institute, p. 287.

2. S. Banerjee et al., NIM **A269** (1988), p. 121.

3. P. C. Chi and W. Z. Hong, NIM **A252** (1986), p. 67.

4. Michael Kuhlen, CALT-68-1547, presented at the International Industrial Symposium on the Super Collider, New Orleans, Feb. 1989.

5. Giles et al., NIM **A252** (1986), p. 41.

6. J. Keuffel, Rev. Sci. Instr. **20** (1949), p. 202; F. Belli and C. Franzinetti, Nuovo Cimento **10** (1953), p. 1461.

7. G. V. Fedotovich, Yu. N. Pestov, and K. N. Putilin, in Proc. Int. Conf. on Instrumentation for Colliding Beam Physics, SLAC - Report 250 (1982).

8. T. Bowcock et al., Development of Detectors with Unique Time-of-Flight Capability, unpublished.

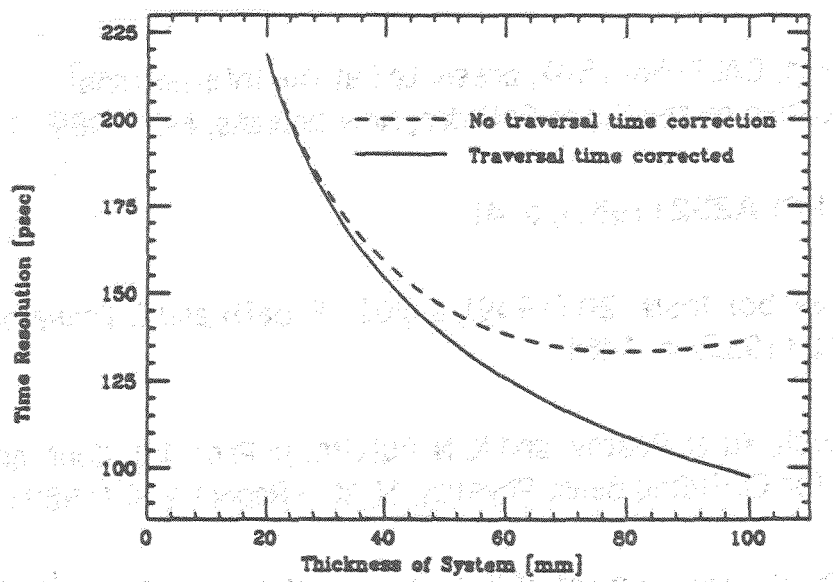

Figure 1
Monte Carlo simulation of time-of-flight resolution, showing effect of correcting for thickness of scintillator.
From Ref. 4

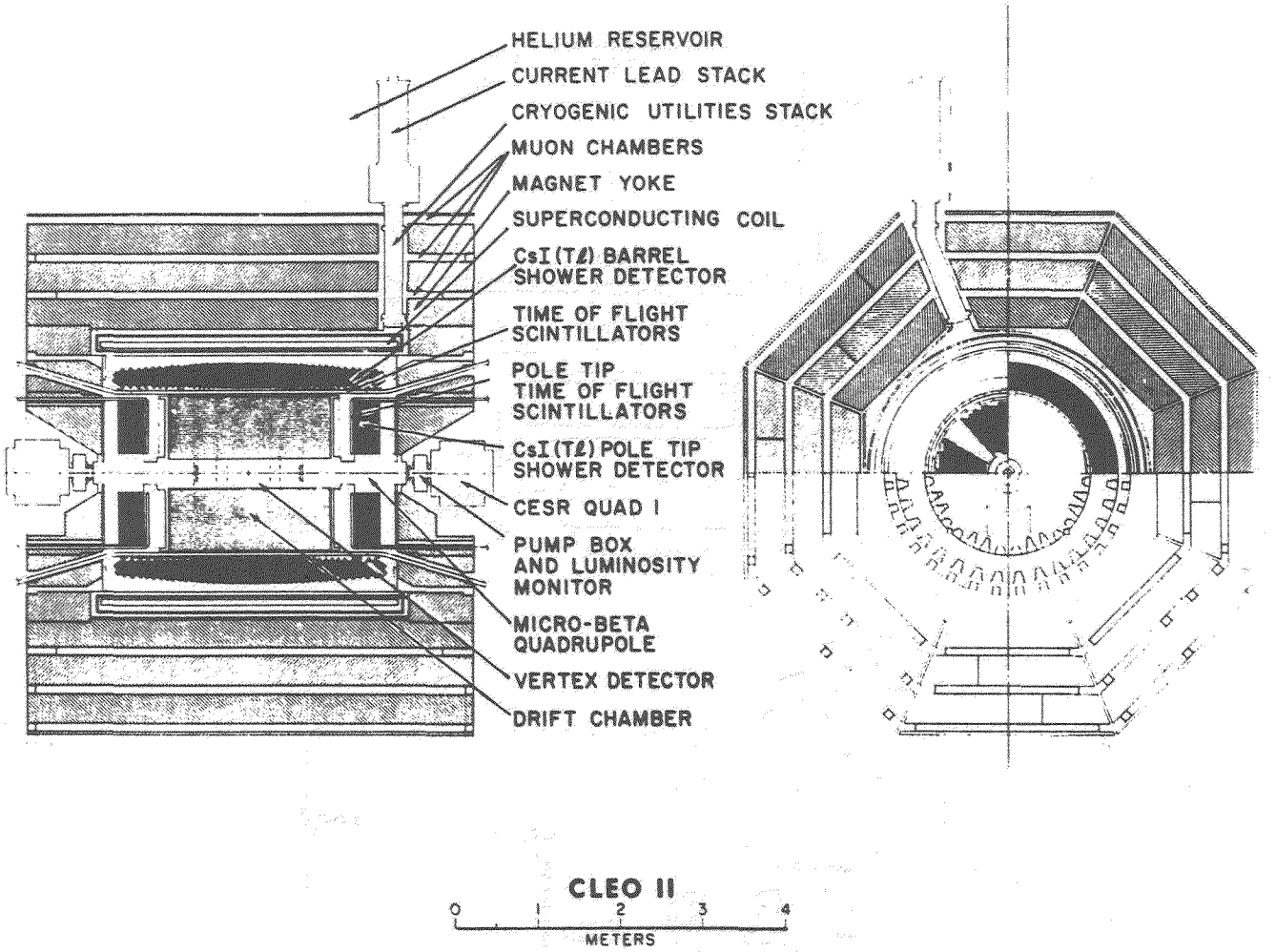

Figure 2
The CLEO II detector
From Ref. 5

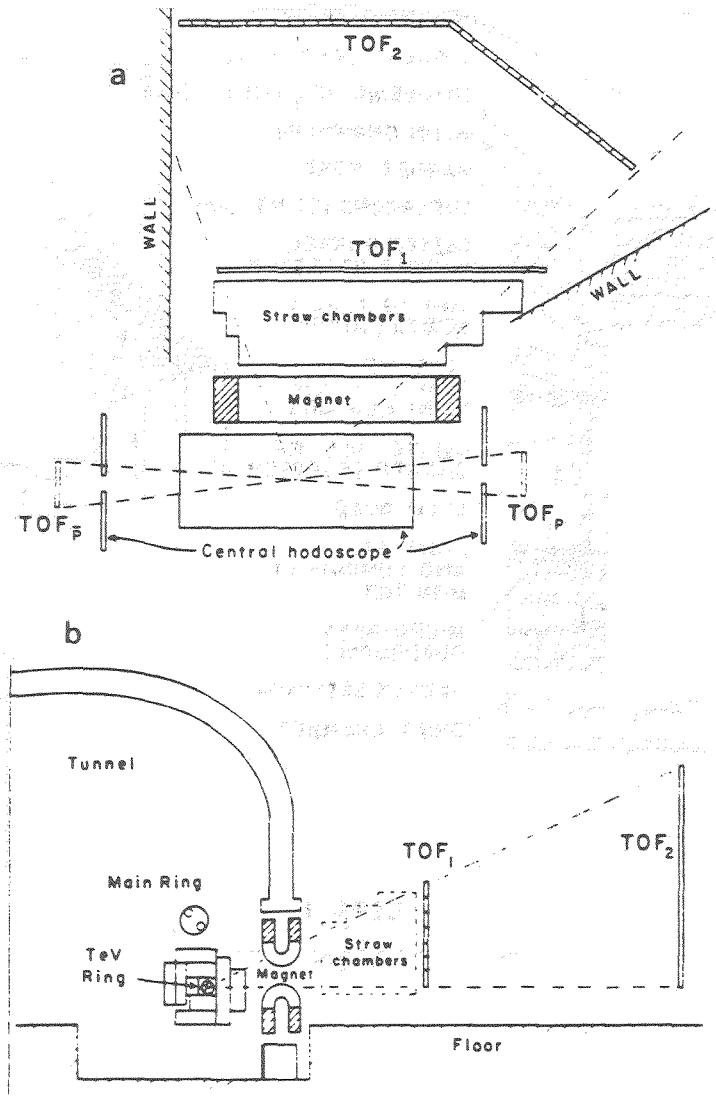

Experimental setup of time-of-flight hodoscopes: (a) top view, and (b) side view.

Figure 3
Fermilab E735, at the CO collider region
From Ref. 6

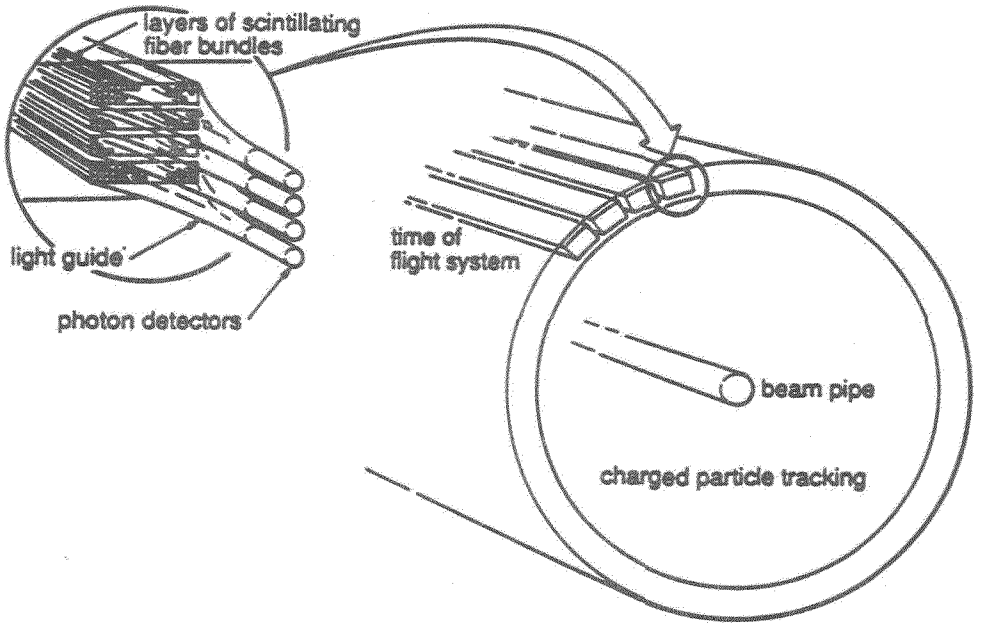

Schematic view of a TOF system for a SSC detector

Figure 4
A time-of-flight system using scintillating fibers.
From Ref. 4

REVIEW OF DE/DX FOR PARTICLE IDENTIFICATION

Gerald R. Lynch
Lawrence Berkeley Laboratory
University of California, Berkeley, California

Momentum Dependence of Energy Loss

The energy loss (dE/dx) of a particle passing through a gas is a function of the gas properties and the velocity of the particle. A curve of the most probable energy loss versus momentum has the same shape for every particle. We subdivide this curve into the following regions:

1. The $1/\beta^2$ region at low velocity.
2. The minimum ionizing region, that includes the region of η between 3 and 6.
3. The relativistic rise. In this region the energy loss increases approximately linearly with lnP.
4. The plateau region at large velocity.

The relativistic rise gets larger as the pressure gets lower and the Z of the gas gets larger. Particle identification with dE/dx is done by measuring both the energy loss of a particle and its momentum. The momentum dependence of dE/dx is shown in figure 2.

Frequency Distribution of Energy Loss

The frequency distribution of energy loss has a long tail at high energy, but is nearly Gaussian below the peak, as is shown in figure 1.

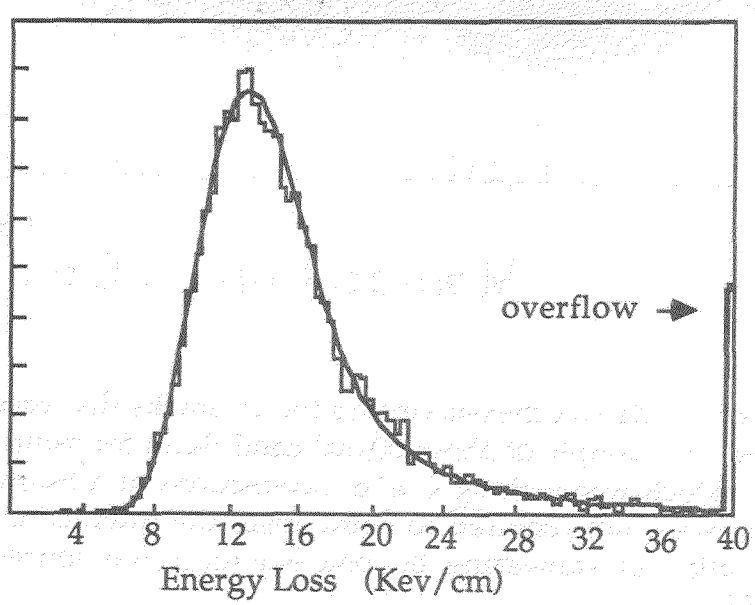

Figure 1. A measured dE/dx distribution for 4 Gev/c muons in the PEP TPC. The average path length per sample was 4.2 mm.

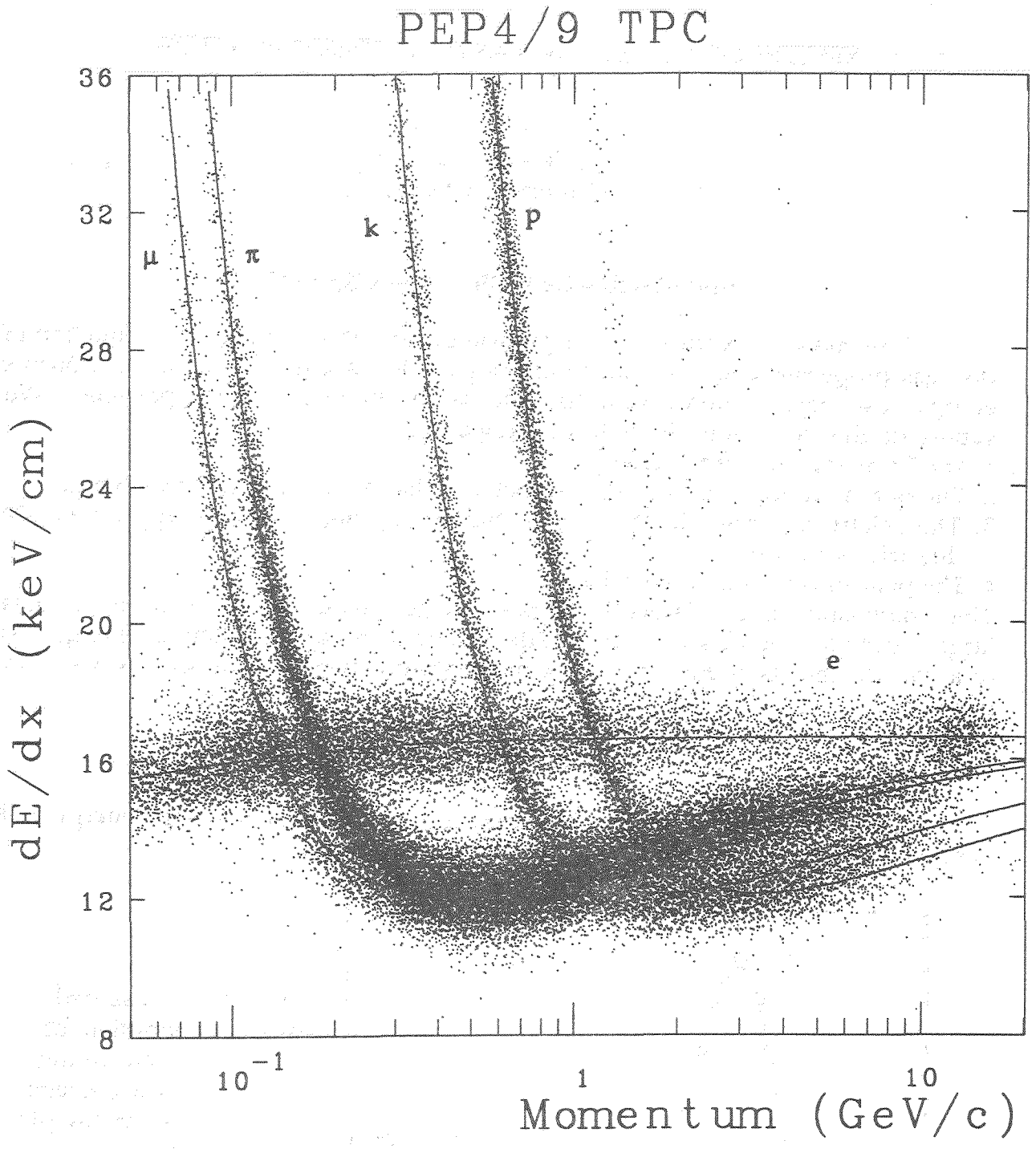

Figure 2. A scatter plot of the dE/dx measurements for all tracks that read out at least 80 of the 183 wires in a sample of about 50,000 candidates for multi-hadron events in the PEP TPC, which was looking at e^+e^- interactions at a beam energy of 14.5 GeV. The tracks were not required to come from the interaction region. A significant contamination of showering Bhabha events is the source of the electrons above 10 GeV/c.

The Gaussian lower part of this distribution is formed from the many low energy excitations of the electrons in the outer shell. Most collisions are of this type. The long tail comes from the knock-on electrons (δ-rays) that have a $1/E^2$ distribution at energies above the atomic levels.

The Statistics of Energy Loss

This energy loss distribution defies the statistical intuition that many of us have. It behaves more like a Landau distribution than is does like a Gaussian distribution. To illustrate the difference, suppose we take take the mean of two sets of measurements from a Gaussian distribution, the second having four times as many measurements as the first. Then we do the same thing with measurements from a Landau distribution. We all know what to expect for the distribution of such means from the Gaussian distribution. The distribution of both means will have the same peak position and the width of the distribution of the one with four times as many measurements will be reduced by a factor of two. When we do the same thing with measurements from a Landau distribution, the mode (most probable value) will be different for these two cases, but the width of the distribution will be the same! The most probable value increases with the log of the number of measurements in the average.

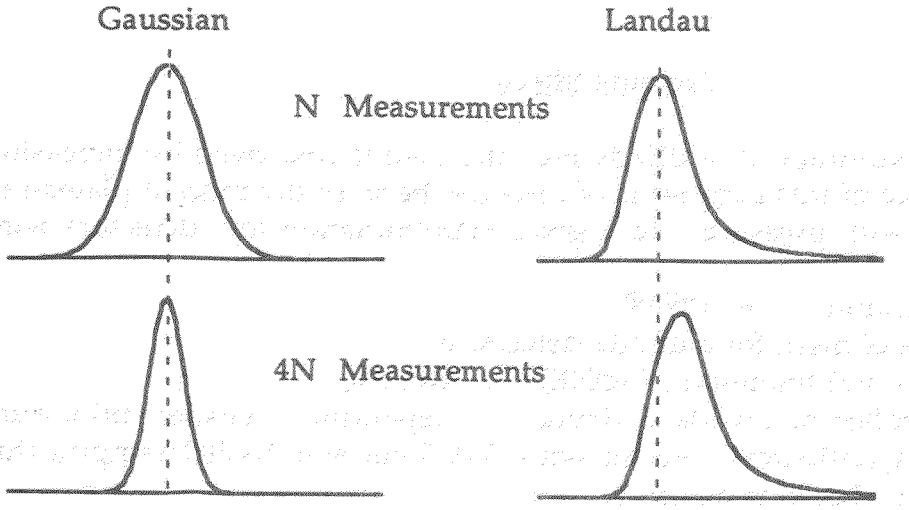

Figure 3. Illustration of the different statistical behaviors of Gaussian and Landau distributions.

Thus, to the extent that the energy loss distribution is a Landau distribution, the measurement of energy loss in a thick sample is no more accurate than the energy loss in a thin sample, as long as only one measurement is made. To get more accuracy it is necessary to divide the sample into many independent measurements. The procedure that is used in all experiments is to calculate a "truncated mean", which is a mean of the first p per cent of the data. The accuracy is not very sensitive to the value of p. In practice values in the range of 40 to 80% have been used for p. The dE/dx measurements from the PEP TPC shown in this note used a 65% truncated mean, which is close to the most probable value.

Resolution

Many different gasses have been tested for dE/dx detectors. Most recent detectors have used an Argon-CH_4 mixture with 10 to 20% CH_4. The resolution that such detectors have achieved can be summarized fairly well by the following formula[1]

$$\frac{\sigma(dE/dx)}{dE/dx} = 0.47\ (P\,D)^{-0.32}\ (N)^{-0.43}$$

where P is the Pressure in atmospheres, D is the sample size in cm, and N is the number of samples. This is an empirical formula, not a theoretical one and the coeficient of 0.47 is approximate. It works fairly well for most existing detectors. I expect it to work well as long as N>>1, D>the transverse diffusion, and P*D>>0.04cm (which means that the number of samples is much larger than the number of drift electrons). The preceding formula can be written as

$$\frac{\sigma(dE/dx)}{dE/dx} = 0.47\ (P\,L)^{-0.32}\ (N)^{-0.11}$$

These formulas say that:
1. If we double P L and keep N fixed, we improve the resolution by 25%.
2. If we keep P L fixed and double N, we improve the resolution by 8%.

Thus increasing path length helps much more than increasing the number of wires.

Pressure Effects

Although the accuracy of a dE/dx measurement is improved by increasing the gas pressure, most of this increase is of little use because the ratio of plateau to minimum decreases with pressure. To a good approximation for detectors with Argon,

$$\text{Plateau / Minimum} = 1.61\ P^{-0.08}.$$

One reasonable figure of merit for a dE/dx detector is

$$FM = [\ \text{Ln}(\text{Plateau}/\text{Minimum})\ ] / [\sigma(dE/dx) / dE/dx],$$

which gives the number of standard deviations separation between minimum and plateau. For a hypothetical detector with D=0.5 cm and N=200 samples this gives the relationship shown in figure 3.

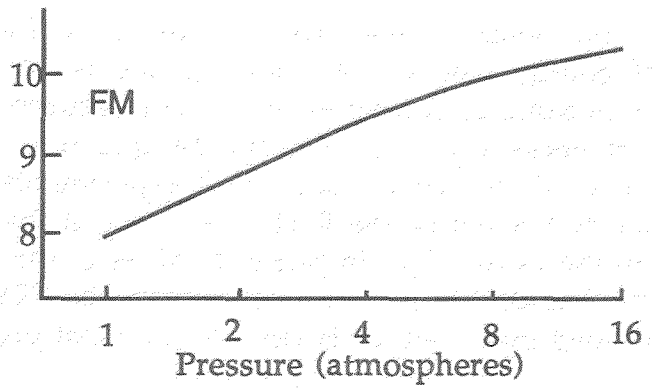

Figure 4. Figure of merit (or π/e Separation at 500 Mev/c) as a function of Pressure for D=0.5 cm and N=200.

Pressure and Gas Mix

Although this figure of merit is a useful one, it does not describe everything. In particular it overestimates the value of high pressure at at high momenta. Lehraus[2] has found that for 15 Gev/c tracks in a detector with Argon-CH_4 that has 64 samples of 4 cm the π/e separation is three standard deviations, almost independent of pressure in the range from 0.5 to 5 atmospheres. Therefore, if one wants to build a dE/dx detector that works well at high momentum, the pressure that it operates at is not a very important consideration.

However, the gas that one uses is an important consideration. For the above configuration at 15 GeV/c and one atmosphere, the e/π separation is (again using the data of Lehraus)

≈1	for Hydrocarbons
2.5	for Neon/C_2H_6
3.0	for Argon/Ch_4
4.6	for Krypton
4.8	for Xenon

So, in this case, going from Argon to Krypton improves the resolution by as much as making a detector with Argon in it 2.5 times as long with 2.5 times as many cells.

dE/dx Detectors at e^+e^- Colliders

Many of the detectors at e^+e^- colliding beam facilities measure dE/dx. Here is a tabulation of the properties of e^+e^- detectors that are set up.

Collider	Detector	N	D (cm)	L (cm)	P (atm)	Plateau	Res %	FM
SLC	MARKII	72	0.83	60	1.0	1.60	7.2	7
CESR	CLEO	51	1.4	90	1.0	1.57	6.5	7
TRISTAN	TOPAZ	175	0.4	70	3.5	1.42	4.6	8
LEP	DELPHI	192	0.4	78	1.0	1.61	5.5	9
PEP	PEP TPC	183	0.4	73	8.5	1.36	3.4	9
LEP	ALEPH	340	0.4	136	1.0	1.61	5.1	9
LEP	OPAL	120	1.3	160	4.0	1.43	3.4	11

Most of these reported resolutions are in agreement with the formula that was presented earlier. The exceptions are DELPHI and CLEO, which report resolutions somewhat better than the formula. In this table D=Sample size, L=Length, P=Pressure, Plateau=Ratio of plateau to minimum , Res=Resolution, and FM=Figure of merit or standard deviations between minimum and plateau.

As can be seen from the preceeding table, the e^+e^- detector with the best figure of merit is OPAL. Figure 5 shows how well the OPAL prototype did in distinguishing 6 Gev/c particles[3].

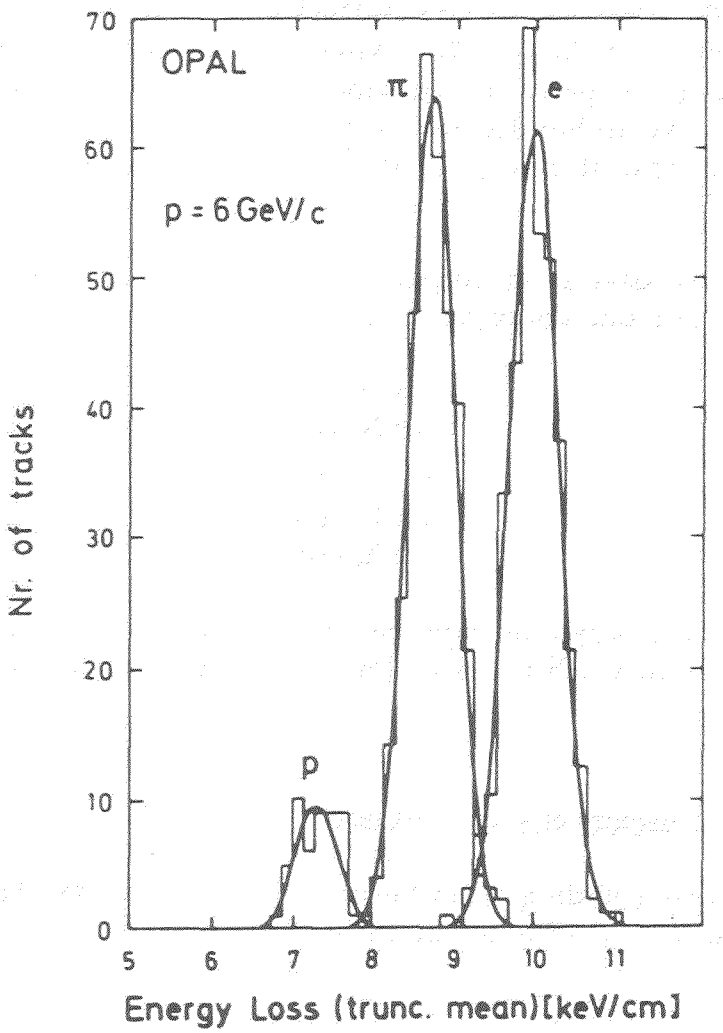

Figure 5. Measured truncated mean of protons, pions and electrons at 6 Gev/c with the OPAL jet chamber.

Adjusting the predictions to the data

What we measure is not really dE/dx. We measure the result of a process that includes:

1. Energy loss,
2. Production of primary and then secondary electrons,
3. Drift, diffusion, and capture of these electrons,
4. The avalanche at the sense wire,
5. Pulse shaping in the electronics, and
6. Various software corrections.

We cannot expect to be able to predict this process exactly. Instead we try to make a good estimate and then adjust it to fit the actual measurements, as illustrated in figure 6.

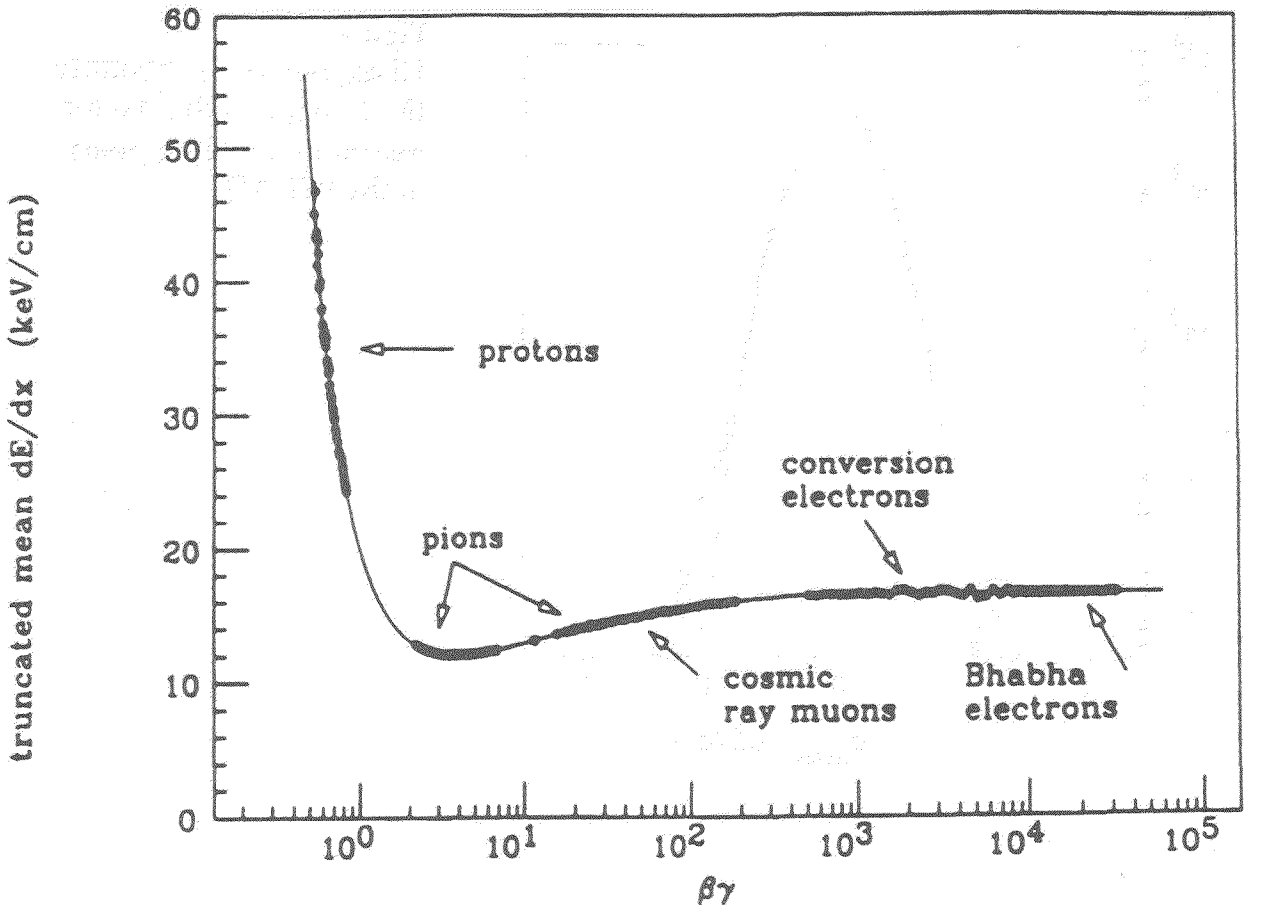

Figure 6. The data points are the truncated means from several track samples in the PEP TPC as a function of $\gamma\beta$. The curve is the parameterization of the dE/dx model, linearly adjusted to fit the data[4].

Some Strengths of dE/dx

One important asset of dE/dx measurements is that they can be combined with the position measurements that are made in a drift chamber. Energy loss and momentum can be measured in the same detector. The advantages of this are:

1. The space devoted to dE/dx is "free". There is no need to allocate valuable space to a special particle ID device.
2. The track matching problem is nearly eliminated. The association of the tracking information and the particle ID information is relatively straight forward.

DE/dx measurements can be quite clean. Figure 7 has measurements of the truncated mean for minimum ionizing pions in multi-hadron events in the PEP TPC[4]. The quantity R is the ratio of measured to predicted values of the truncated mean. We see that these truncated mean measurements are very nearly Gaussian.

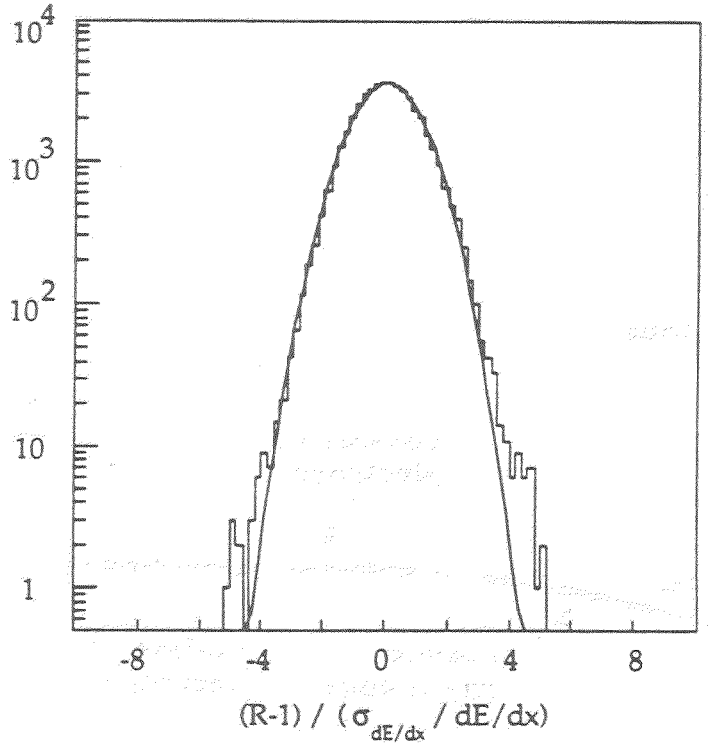

Figure 7.
Histogram of the quantity $(R-1)/(\sigma_{dE/dx}/dE/dx)$ for minimum ionizing pions in the PEP TPC.

Another way of showing how clean dE/dx data can be is to look at the data in the $1/\beta^2$ region as shown in figure 8 and treat the detector as a mass spectrometer. Such an exercise is especially clean when one uses only tracks that have a dE/dx greater than twice plateau, which eliminates most overlaping tracks. These mass plots are shown in figures 9a and 9b. One sees that a deuteron peak and even a triton peak stand out above the background. (None of these tracks can be antideuterons or antitritons coming from the interaction region.)

Weaknesses of dE/dx

One weakness of the dE/dx method is that there are "cross-over" regions in which identification from dE/dx is ambiguous. This effect is seen in figure 10, which shows measurements of particle fractions in multi-hadron events at PEP[4]. On this plot one can see the gaps that correspond to the πk, πp, and kp cross-over regions. Another obvious weakness of the dE/dx technique is that one loses separation power at high momentum.

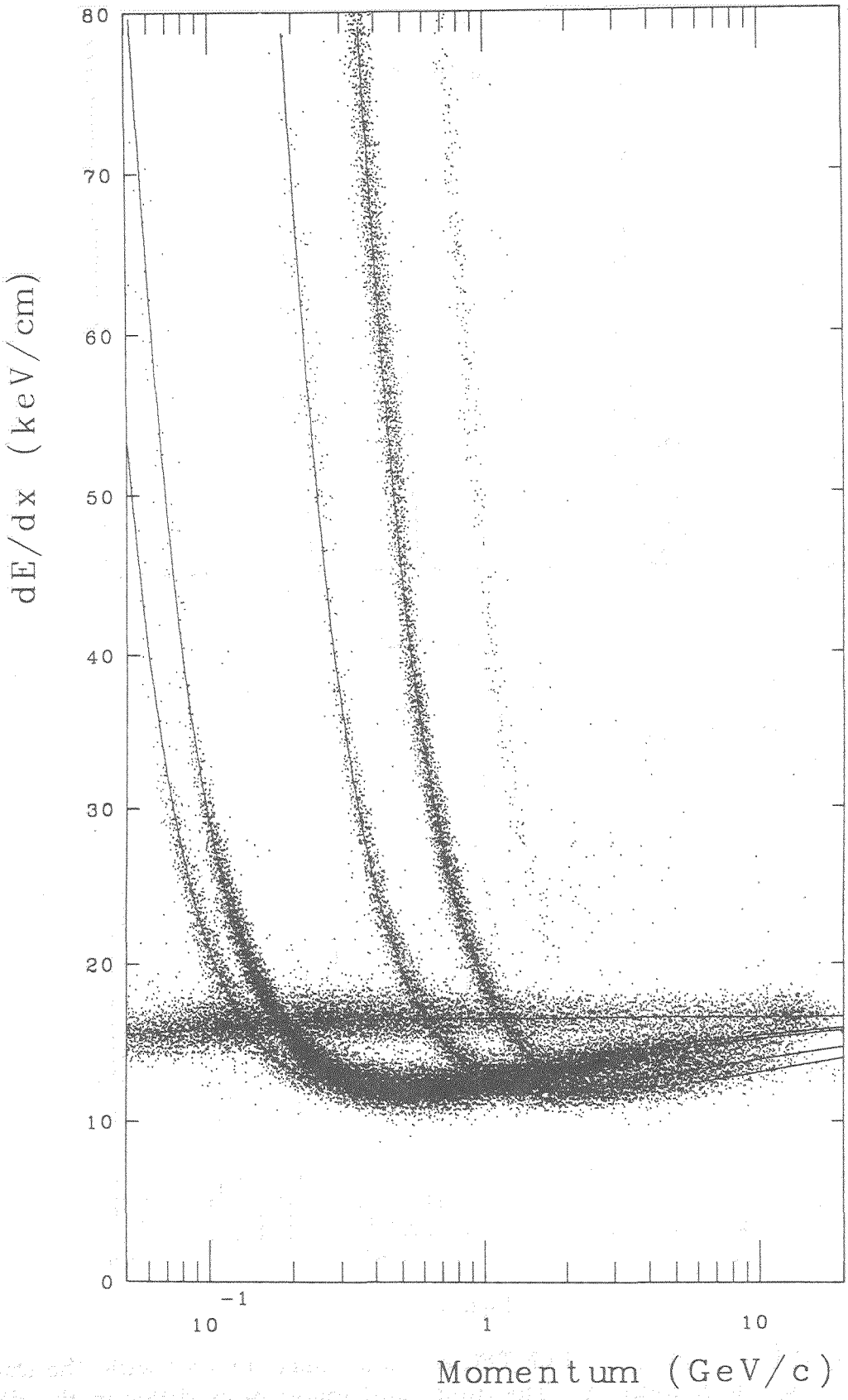

Figure 8. This has the same data as figure 2, plotted over a larger dE/dx range.

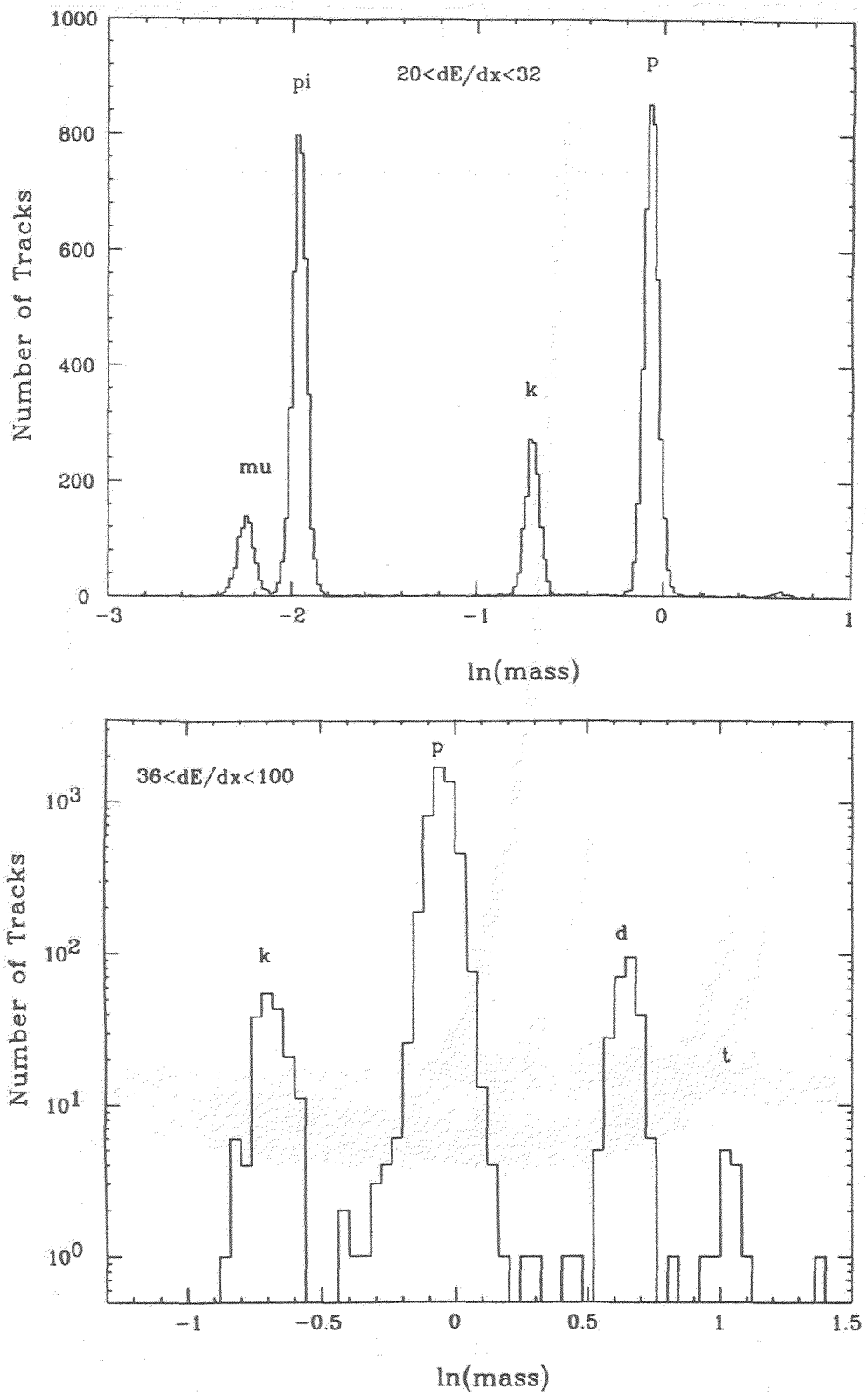

Figure 9. Result of treating the PEP TPC as a mass spectrometer with the tracks in the $1/\beta^2$ region of figure 8. The upper and lower plots differ in the dE/dx region that is used for the spectrum.

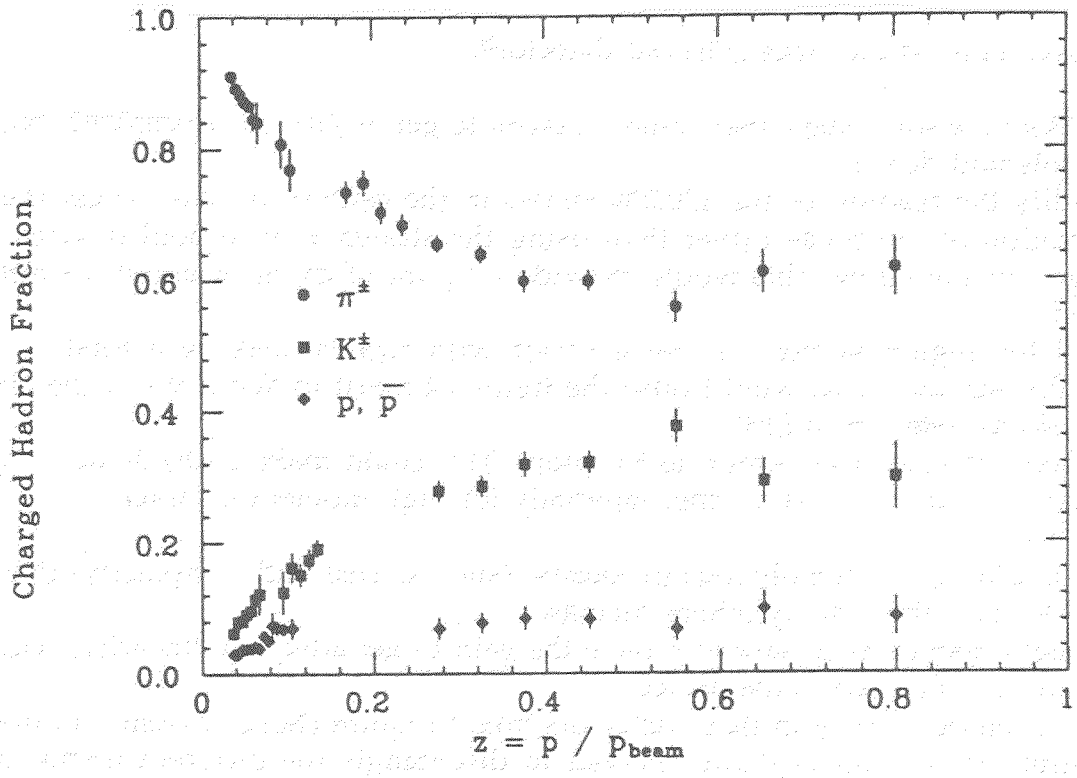

Figure 10. The charged hadron fractions in e^+e^- annihilation events at an energy of 29 GeV as a function of $z=p_{hadron}/p_{beam}$

dE/dx Improvements

It is still possible to get better resolution from dE/dx detectors in various ways. One way to get better resolution would be to count individual clusters rather than using the truncated mean. At this conference I became aware of a paper by Breskin et al.[5] that describes a method that allowed them to count clusters in a low pressure gas. They project that they could build a detector that would get 2.8% resolution with three meters of isobutane at 0.06 atmospheres. This performance is significantly better than what has been obtained with detectors at one atmosphere using the truncated mean method.

Does dE/dx have a role at the SSC?

There are probably better methods than dE/dx to get particle identification in a SSC detector, but let's consider dE/dx anyway on the grounds that particle ID information is always useful and it can be obtained from some detectors as a byproduct of tracking information. For the SSC we want to do well for high energy particles. Therefore, we probably do not want to go to high pressure and do want to use a gas with high Z. A detector with Krypton or Xenon is called for. Rather than making a completely new proposal, let's try to add dE/dx to one of the existing proposals. The proposed large P_t detector that has momentum measurements and a large enough central detector to do worthwhile dE/dx

measurements is the large solenoid detector[6].

Here are some steps that could be taken to get dE/dx measurements with the large solenoid detector.

1. Modify the readout of the 120,000 straws in the central detector to get the time evolution of the pulse rather than using the straws as threshold devices. With Argon in the straws this would provide a figure of merit of about 6 - not very good.
2. Fill the region of the central detector with straws, making a total of about 300,000 straws. This would raise the figure of merit to about 9 - in the class of the dE/dx detectors at LEP.
3. Change the gas from Argon to Krypton. This could make a dE/dx detector that is better than any existing one, especially for high momentum tracks.

In addition to the obvious problems (such as cost and complexity) that such a detector has, there many others such as:

1. It might also be necessary to reduce the gain to get adequate linearity, requiring preamps to be close to the detector.
2. The high occupancy in these detectors might require charge division to measure z, sophisticated pulse shape analysis to disentangle the different tracks, or kill the whole idea.

References

1. Parameterizations of this type was advanced by A.H. Walenta, Nucl. Instr. and Meth. 161 (1979) 435, and by W.W.M. Allison and J.H.Cobb, Ann. Rev. Nucl. Part. Sci. 30 (1980) 253.
2. I. Lehraus, Nucl. Instr. and Meth. 217(1983) 43.
3. H. Breuker, et al., Nucl. Instr. and Meth. A260 (1987) 329.
4. H. Aihara et al., Phys. Rev. Lett. 61 (1988) 1263., and G.D. Cowan, Inclusive $\pi^{\pm}$, $K^{\pm}$, p , $\bar{p}$ Production in e^+e^- Annihilation at $s=\sqrt{29}$ GeV, LBL-24715 (1988)
5. A.Breskin et al, IEEE Trans. Nucl. Sci. 36 (1989) 326.
6. Workshop on Experiments, Detectors and Experimental Areas for the Supercollider, July 1987, pp.340-387.

VI. Fast Readout Techniques

EFFORTS ON FRONTEND ELECTRONICS IN KEK*

HIROKAZU IKEDA

National Laboratory for High Energy Physics
1-1 Oho, Tsukuba, Ibaraki-ken, 305 Japan

ABSTRACT

Developments of new generation of frontend electronics around KEK are described. Silicon strip read out VLSI, readout of multi-anode PMT, and frontend system of Super KKMIOKANDE are topics discussed about. They are based on advanced technologies of integrated circuits.

* Contribution to Symposium on Particle Identification at High Luminosity Hadron Collider, April 5-7, 1989, Fermi National Accelerator Laboratory

1. INTRODUCTION

Developments of new generation of frontend electronics are under way based on advanced integrated circuit technology. These developments are applied for high luminosity hadron collider, SSC, and/or electron positron collider for B-factory. The spin-off technology has given impacts on the design of underground experiments and/or balloon born experiments.

The recent frontend electronics has been characterized by:

1. Application specific integrated circuit, ASIC
2. High density integration
3. Low power
4. Advanced performance
5. Wide frequency bandwidth
6. Radiation hardness when applied for the SSC experiment

This paper deals with three topics of development on the frontend electronics around KEK:

1. 64 channel amplifier VLSI for silicon strip readout
2. Readout of Multi-anode PMT
3. Frontend circuit for Super-KAMIOKANDE[1]

Another important development in KEK, that is skipped here to describe, is a time interval measurement VLSI, TMC. The design of the TMC is based on the NTT's sub-micron CMOS technology, which is presented in Toronto Workshop[2].

2. VLSI FOR SILICON STRIP READOUT[3]

2.1. Monolithic Process

The process technology used for the amplifier is a bipolar super self-aligned technology (SST)[4] developed by LSI Laboratories, NTT, Atsugi, Japan. Typical parameters of the SST transistors used in this design are listed in Table 1. The SST process can handle sub-micron structures of bipolar transistors; achieving a high current gain and a very high cutoff frequency. The SSTs have been applied for a GHz-Band optical transmission system[5] and high speed flash A to D converters[6], showing its high performance. The side product of the SST process is its radiation hardness; an integrated circuit based on the SST process still works regularly after an exposure of 1 Mrads of ^{60}Co[7]. The h_{FE} degradation of the SST integrated circuit is expected to be moderate on behalf of its high f_T and high initial h_{FE}. The actual exposure by reactor neutron showed a reasonable radiation hardness[8]

2.2. TEG* FABRICATION

In order to examine the scheme, a TEG version of the amplifier was designed and fabricated at the research fabrication line of NTT LSI Laboratories. The results were presented in 1988 NSS symposium[9]. Two kinds of current sensitive amplifiers were fabricated: one had a feed back resistor of 25 KΩ and another had 75 KΩ. The filter amplifiers had a shaping time constant of 2.5 ns, 5 ns, 10 ns or 20 ns. Preamplifiers and filter amplifiers were combined into 4 types of TEG chips. Each chip occupies 2*2 mm^2 area on a silicon wafer. They were evaluated in terms of an equivalent input noise. The noise level achieved was 1000 electrons of input equivalent charge with shaping time of 10 ~ 20 nsec and input capacitance of 5 ~ 10 pF.

---

* Test Element Group

2.3. CIRCUIT CONFIGURATION FOR NEW CHIPS

Based on the TEG chip design, a 64 channel amplifier VLSI was designed to be used in practice. The features of the new chip are summarized in Table 2. Figure 1 shows an analog chain of the new VLSI. The analog chain is subdivided into 3 parts, preamplifier, filter amplifier and comparator; they are described in sequence. The power consumption of the analog chain is about 3.5 mW/ch plus additional dissipation of the subsidiary circuits.

Preamplifier The schematic of the preamplifier is shown in Figure 2. The input stage of the current sensitive preamplifier is a common emitter npn transistor whose quiescent current is 100~200 μA. The operation condition is adjusted by power supply voltage. Several transistors are tried to fit there with $r_{bb'} = 29 \sim 116\ \Omega$ for production. The collector signal is fed into a cascode transistor to be followed by emitter followers. The feedback resister R_F is $20K\Omega$ with small capacitor $C_F = 0.05$ pF in parallel; that is to improve circuit stability in the high frequency region. The f_T of the transistors are 2.5 GHz for input transistor, and 10 GHz typically for other transistors.

Shaper In order to suppress the noise level in a tolerable range, we need a low pass filter that determines a noise frequency band width. The filter amplifier designed here is a second order low pass filter that satisfies a critical damping condition. The filter amplifier has a transfer function

$$\frac{1.}{(1. + S * T_M)^2} \tag{2.1}$$

in Laplace transform, where S is a frequency variable and T_M is a measurement time of the shaping function. The impulse response is

$$(\frac{t}{T_M}) * exp(\frac{-t}{T_M}) \tag{2.2}$$

The schematic of the filter amplifier is shown in Figure 3. The time constant is determined by capacitors and resistors. The capacitors are made of two aluminum

plates with a silicon dioxide in between, i.e. MIM structure. The resistors are made of poly-silicon film. The time constant (T_M) is not necessarily accurate because of the uncertainties of process conditions. A simulation study shows that the system is immune from the fluctuation of the time constant (i.e. 15 nsec $\pm$ 5 nsec).

Comparator The schematic of the comparator is shown in Figure 4. The comparator consists of a linear amplification stage and a switching stage; there is no latching function. The DC stability is maintained with a reference generator circuit which keeps same DC characteristics as those of signal channels. The threshold stability of $\pm$ 0.1 mV/°C is expected due to SPICE simulation. The output of the comparator has a logic swing of 2.3V. V_{OH} as well as V_{OL} is adjusted by V_{CC} to provide a proper logic level for the Digital Time Slice Chip, DTSC[10].

The process for fabrication is going to be completed in this month.

3. READOUT OF MULTI-ANODE PMT[11]

The readout system of multi-anode PMT is developed in conjunction with scintillation fiber detector R & D[12]. Figure 5 shows a configuration for readout of multi-anode PMT. A conventional way of readout is shown in Fig. 5 (a) which consists of delay lines and charge integrators with gate signals provided by a trigger logic. The conventional scheme is hardly applied for multi-anode PMT. We need to have a scheme to multiplex 64 channels, to eliminate delay lines, and to be persistent in a high rate environment . A new scheme, shown in Fig. 5 (b), consists of shaper amplifier, analog memory, and readout controller with A to D converter. The input signals are continuously sampled in regular timing interval to be stored in the analog memory. Once TRIGGER is issued, the analog memory terminates to sample input signals to move to readout mode. Signals arrived at the analog memory are recorded for last timing period over (sampling depth)*(sampling width) before moving to the readout phase. The analog data are scanned to be converted into digital data. Those data whose amplitudes are greater than predetermined

value are written into FIFO memory. Table 3 summarizes features of the readout system of multi-anode PMT.

3.1. CIRCUIT DESCRIPTION

Shaper Amplifier The shaper amplifier is made of bipolar linear array of Thomson SGS[13]. The linear array chip contains 8 channels of amplifier; 8 chips are used for the 64 channel multi-anode PMT. The output of the shaper amplifier has a peaking time of $\sim$ 200 nsec with a peak voltage $\sim$ 3.0 V for 64 pC of input charge, that gives a full scale signal. Figure 6 shows a schematic of the shaper amplifier. The signal from PMT is terminated by 500 Ω. The circuit is a second-order low-pass filter.

Analog Memory The output signal of the shaper amplifier is sampled with a frequency of 10 $\sim$ 20 MHz. When receiving TRIGGER, the sampling is terminated to move to readout phase. The analog memory used here is AN201[14], Analytek, California, which has 32 input channels with full scale input swing of 3.0 V. Since the sampling depth of AN201 is 4, we have used two chips for each signal input to obtain a sampling depth 8; 4 chips are used for the multi-anode PMT. The sampling frequency is supplied externally or generated in the ADC module.

Readout Controller The shaper amplifier and the analog memories are fit in a breeder box. The analog data are serially output to be fed into the readout controller module. The readout controller consists of 8b 10 MHz flash AD converter, FIFO memory, timing controller, and CAMAC interface; which is a single width CAMAC module. The DC powers for shaper amplifiers and analog memories are also supplied from the readout controller.

3.2. DEMONSTRATION

Preliminary data for cosmic ray events were acquired with combination of a scintillation fiber bundle, which is made of 1600 fibers of 1 mm in diameter[15], and this readout system. The effective area of the multi-anode PMT used was 40 mm by 40 mm; that was divided into 64 anodes of 5 mm by 5 mm[16]. The sampling frequency was 12 MHz; the sampling interval was $\sim$ 83 nsec. Figure 7 shows a track of cosmic ray penetrating through the scintillation fiber bundle. The Lego plot shows peak pulse heights for each signal channel. In the right hand side of the figure, the wave forms for the largest response in each row of the multi-anode PMT are displayed. The rise and/or fall time are consistent with design parameters. Details on performances are still under evaluation in conjunction with a gain calibration scheme.

4. FRONTEND CIRCUIT FOR SUPER-KAMIOKANDE[17]

Figure 8 shows a scheme of the frontend circuit of TAC/QAC system for Super-KAMIOKANDE. The frontend circuits consists of frontend signal splitting hybrid , discriminator, timing controller, and TAC/QAC integrated circuit. TAC is a function of Time to Amplitude Conversion, and QAC is a function of Charge to Amplitude Conversion. The distinct feature of the system is a double buffer capability for each frontend. Each channel can acquire consecutive two signals even if they have arrived in close interval, i.e. a few hundred ns.

4.1. FRONTEND HYBRID

The signals from the 20" photomultiplier[18] are fed into this frontend hybrid IC. The voltage swing for input is -200 μV to -0.5V ; in terms of peak current that is 4 μA to 10 mA. The frontend hybrid splits the input current into four ways for:

1. Summing circuit of trigger
2. QAC-1 (with inverted polarity)

3. QAC-2 (with inverted polarity)

4. Discriminator: the amplitude swing at the discriminator input for minimum input signal, 0.16 pC, is 20 mV. Response for single photo-electron is several times larger than the minimum signal specification.

Figure 9 shows a schematic of the frontend hybrid. The circuit consists of 18 npn's (2SC4245, 2400 MHz), and 14 pnp's (2SA812, 180 MHz) to be fit in a 40 p DIP package. The signals for the QAC channels are delayed by 200 nsec and passed to a current mirror circuit to meet the input signal specification of the TAC/QAC integrated circuit. The voltage gain of the discriminator channel is achieved by two stages of Rush amplifier[19] (Figure 10). Another important feature of the frontend hybrid is a rejection of low frequency components of input signal, which is mainly due to environmental electro-magnetic interference. Test pulse input is also provided at the input of the frontend hybrid for the sake of quick inspection of the analog chain. The features of the frontend hybrid are summarized in Table 4.

4.2. TIMING CONTROL

The discriminated signal is used in three ways:

1. Generate quantized current pulse for trigger; 100 μA /hit

2. Generate integration gate for QAC channel

3. Generate Start/Stop gate for TAC channel

The two TAC channels and two QAC channels are operated in independent timings. The integration gate is 400 nsec for the present design. The start/stop gate is opened at the leading edge of the discriminated signal and closed by TRIGGER signal from the trigger system. When no TRIGGER signal is received, the analog information of QACs and TACs are restored to zero. The TRIGGER TIMEOUT period is set as 1.1 μsec .

4.3. TAC/QAC Integrated Circuit

The performance of the integrated circuits was presented in 1988 Nuclear Science Symposium[20]. The integrated circuit is made of bipolar linear array master slice A600 of Fujitsu. A typical cutoff frequency of npn transistor used for the circuit is 500 MHz. In order to implement two TACs and two QACs on a chip, 89 npn transistors, 29 pnp transistors, 1 zener diodes were used together with 20 input protection diodes. Figure 11 shows a circuit configuration of TAC, QAC, and output buffer. The output buffer is designed to compensate input base current; maintaining the capacitor charge more than 0.5 msec with an accuracy of 0.1 %. Table 5 shows a summary of performance of the TAC/QAC chip.

Assembly of frontend hybrids and TAC/QAC chips is under way together with other digital circuits, readout scanners, buffer memories and timing interfaces.

5. SUMMARY

Developments on the frontend electronics around KEK are described. The integrated circuit technologies are applied for advance detectors, silicon strip detectors, scintillation fiber detector with multi-anode PMT, and others. The technology is also applied for underground experiments such as Super-KAMIOKANDE. The common features for these frontend circuits are high performance, high density, low power, and high reliability for long term operation.

ACKNOWLEDGEMENTS

I would like to acknowledge supports and encouragement of directors H. Sugawara, K. Takahashi, and S. Iwata. This work is partially supported by SSC/CDG and a Grant in Aid from Japanese Ministry of Education, Science, and Culture.

REFERENCES

1. Y. Totsuka, proceedings of the seventh Workshop on Grand Unification, April 1986, Toyama, Japan
2. Y. Arai, "Time Measurement System at the SSC", Contribution paper to the Workshop on Triggering and Data Acquisition for Experiments at the Supercollider, Toronto, Canada, Jan 16-19, 1989
3. The work is done in collaboration with N. Ujiie, Y. Watase, T. Kondo, T. Ohsugi, and Y. Akazawa.
4. S.Konaka, Y.Yamamoto, and T.Sakai,"A 30 ps Si Bipolar IC using super self-aligned process technology", Proc. of 16th conf. on solid state devices and materials, Kobe, Japan, 1984, pp.209-212
5. Y.Akazawa, N.Ishihara, T.Wakimoto, K.Kawarada and S.Konaka,"A design and packaging technique for a high-gain, giga-hertz-band single chip amplifier", IEEE Journal of Solid-state Circuits SC-21 (1986) 417-423
6. Y.Akazawa, A.Iwata, T.Wakimoto, T.Kamoto, H.Nakamura, and H.Ikawa, " A 400 Msps 8 b flash AD conversion LSI", ISSCC Dig. Tech. Paper (1987)98-99
7. M. Umehira, H. Kikuchi, S. Konaka, and S. Kato,"High-speed and Precise Monolithic Multiplier with Radiation Hardness Using Silicon Bipolar SST", Elec. Lett. 3rd July Vol.22 No.14 pp.744-746
8. H. Ikeda and N. Ujiie, preliminary result of degradation coefficient ($\Delta(h_{FE}^{-1})$) was 0.001 $\sim$ 0.002 for neutron fluence of 10^{13} neutrons/cm^2
9. H. Ikeda, N. Ujiie, and Y. Akazawa, "Monolithic Preamplifier with Bipolar SST for Silicon Strip Readout", KEK Preprint 88-71, Nov 1988, to be published in IEEE Transactions on Nucl. Sci.
10. Joel DeWitt, "The Digital Time Slice Chip", UC Santa Cruz, private communication

11. The work is done in collaboration with F. Takasaki, Y. Narita, S. Inaba, and M. Ikeda.

12. F. Takasaki, "Recent Development of Scintillating Fiber Detectors for SSC around KEK", KEK Preprint 88-120, Jan 1989, Invited talk at the Workshop on the Scintillation Fiber Development for the SSC, Fermi National Accelerator Laboratory, Nov 14-16, 1988

13. Thomson SGS, Poly-Use G, $f_T = 550$ MHz for npn

14. G.M. Haller, D.R. Freytag, J.T. Walker and S.I.Chae, "Performance Report for Stanford/SLAC Multi-channel Sample-and-Hold device, IEEE Trans. on Nucl. Sci. NS-33 (1986) 221-225

15. F. Takasaki, H. Saito, T. Fukui, T. Matsushita, and T. Suzuki, "Development of Multianode Photomultiplier Tube", Nucl. Instr. & Methods A260 (1987) 447-450

16. Hamamatsu Photonics, R3383-64

17. The work is done in collaboration with T. Tanimori, M. Mori, K. Kihara,H. Haren, and H. Kitagawa.

18. T. Hayashi et al., Proceedings of the 1981 INS International Symposium on Nuclear Radiation Detector, March 23-36, 1981, Tokyo, Japan

19. C.J. Rush, "Technique for Designing Fast Rise Transistor Pulse Amplifiers", Rev. Sci. Instr. 35 (1964) 149-155

20. T. Tanimori, H. Ikeda, M. Mori, K. Kihara, H. Kitagawa, and Y. Haren, "Design and Performance of Semi-Custom Analog IC Including Two TACs and Two Current Integrators for Super-KAMIOKANDE", KEK Preprint 88-87, Submitted to IEEE Nucl. Sci. Symposium, Orlando, Florida, Nov 1988

TABLE CAPTIONS

Table 1. Parameters for Small Geometry SST Transistor

Features	Parameters
Emitter size	0.5*5 μm^2
Current Gain	120
Cutoff frequency	$\sim$ 15 GHz for optimum operation
Base-Collector Capacitance	8.0 fF
Base-Emitter Capacitance	20. fF

Table 2. Features of 64 Channel VLSI Chip

Features	Parameters
Chip Size	6.82*4.9 mm^2
Preamplifier	R_F = 20 KΩ
Input Impedance	220 Ω (I_c= 100 μA)
	110 Ω (I_c= 200 μA)
Shaper	T_M = 15 nsec
Comparator	W/O latch
	$V_{OH} - V_{OL} = 2.3V$
Reference Voltage	± 0.1 mV /°C
Noise	1000 electrons (5 ~ 10 pF)
Power Consumption	3.5 mW

Table 3. Readout System of Multi-anode PMT

Features	Parameters
Readout channels	64
Shaper	Peaking time = 200 ns Input : 64 pC (max) Output: 3.0 V (max)
Sampling Frequency	10 MHz ~ 20 MHz
Depth of Analog Memory	8
A to D Converter	8 b, 10 MHz FADC
Conversion Frequency	~ 1 MHz

Table 4. Features of Frontend Hybrid

Features	Parameters
Input Signal	4 μA ~ 10 mA (0.16 pC ~ 400 pC) T_r = 10 ns, T_f = 50 ns
Input Impedance	50 Ω (100 KHz ~ 10 MHz) > 100Ω(< 10KHz) ~ 1 KΩ (DC)
QAC Signal Delay	200 ns
Rush Amplifier Chain	20 mV / μA
Power Requirements	± 8.0V 200 mW

Table 5. Performance of TAC/QAC IC

Features	Parameters
Linearity	0.1 % of F.S.
Full Scale	1 μsec (TAC) 400 pC (QAC)
Resolution	1 ns (TAC) 0.4 pC (QAC)
AD Converter	12 bit Conversion Time = 1.5 μsec
Gain Spread	1.0 $\sim$ 1.5 %
Time for Reset	1.0 $\sim$ 1.5 μsec
Output Holding Time	0.5 msec (0.1 %)
Holding Capacitor	100 pF
Power Requirements	$\pm$ 8.0 V and 5.0 V 200 mW
Power Supply Tolerance	$\pm$ 5 %
Temperature Range	25.0 $\pm$ 5 °C

FIGURE CAPTIONS

1) Analog Chain of New VLSI
2) Schematic of the Preamplifier
3) Schematic of the Filter Amplifier
4) Schematic of the Comparator
5) Configuration for Readout of Multi-anode PMT
6) Schematic of Shaper Amplifier for Multi-anode PMT
7) Cosmic Ray Track Measured by Scintillation Fiber with Multi-anode PMT readout
8) Scheme for Frontend of TAC/QAC System
9) Schematic Frontend Hybrid Circuit
10) Schematic of Rush Amplifier
11) Schematics of TAC, QAC, and Output Buffer

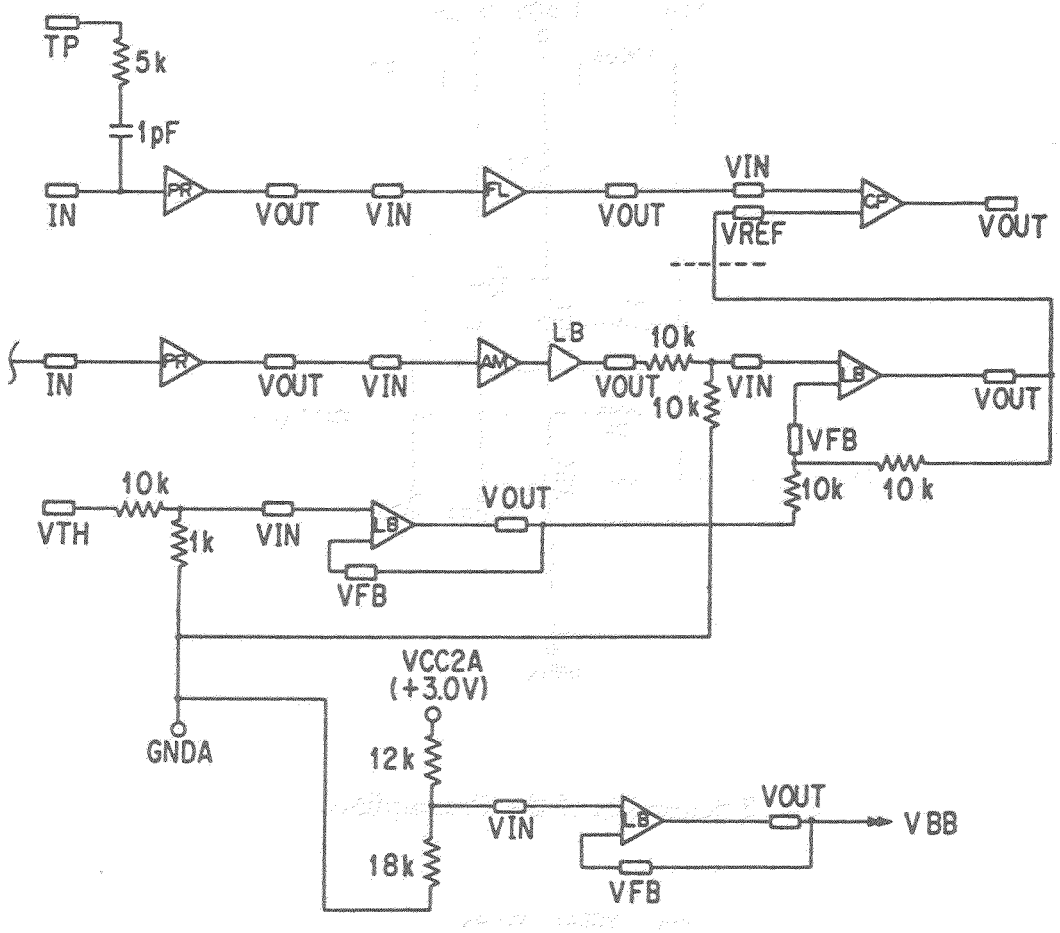

Fig 1. Analog Chain of the New VLSI

PR: preamlifier, FL: filter amplifier, CP: comparator, AM: filter amplifier with shorter shaping time (T_M = 5.0 nsec), LB: unity gain buffer, VTH: threshold input, TP: test pulse input, VREF: reference voltage for comparator, and VBB: base voltage of the cascode transistors for preamlifier and/or filter amplifer.

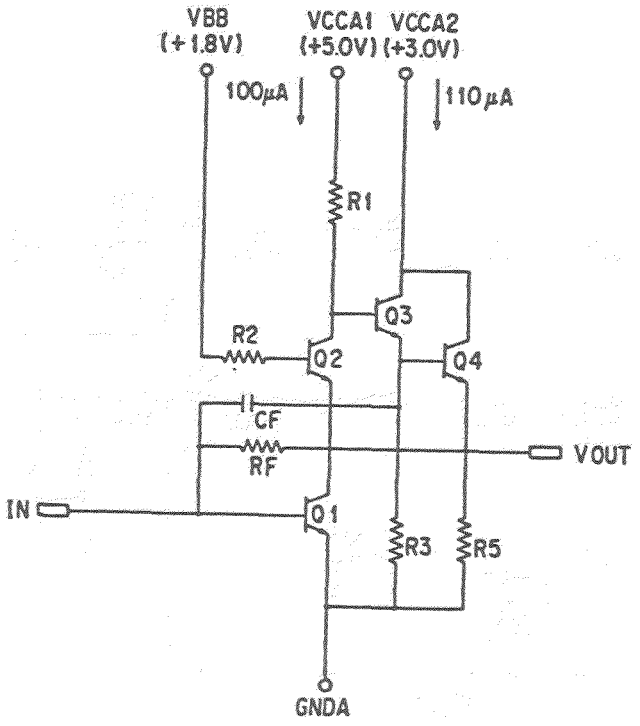

Fig. 2 Schematic of the Preamplifier

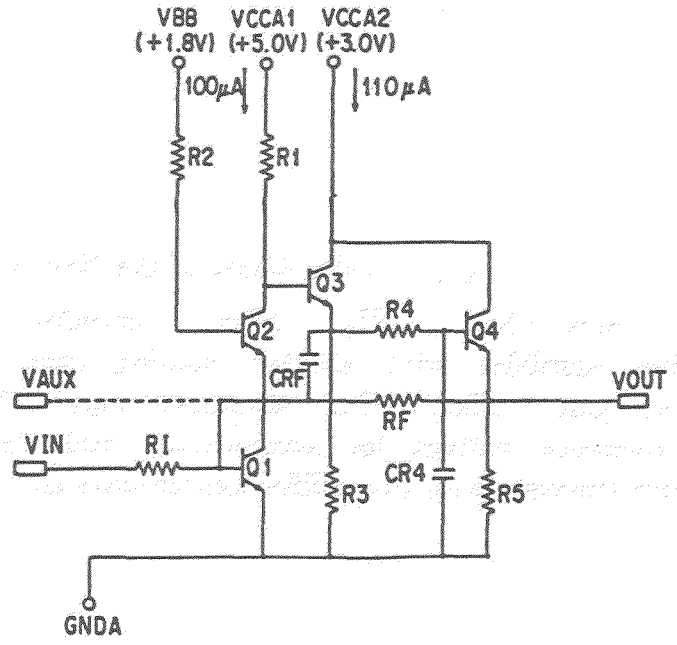

Fig. 3 Schematic of the Filter Amplifier

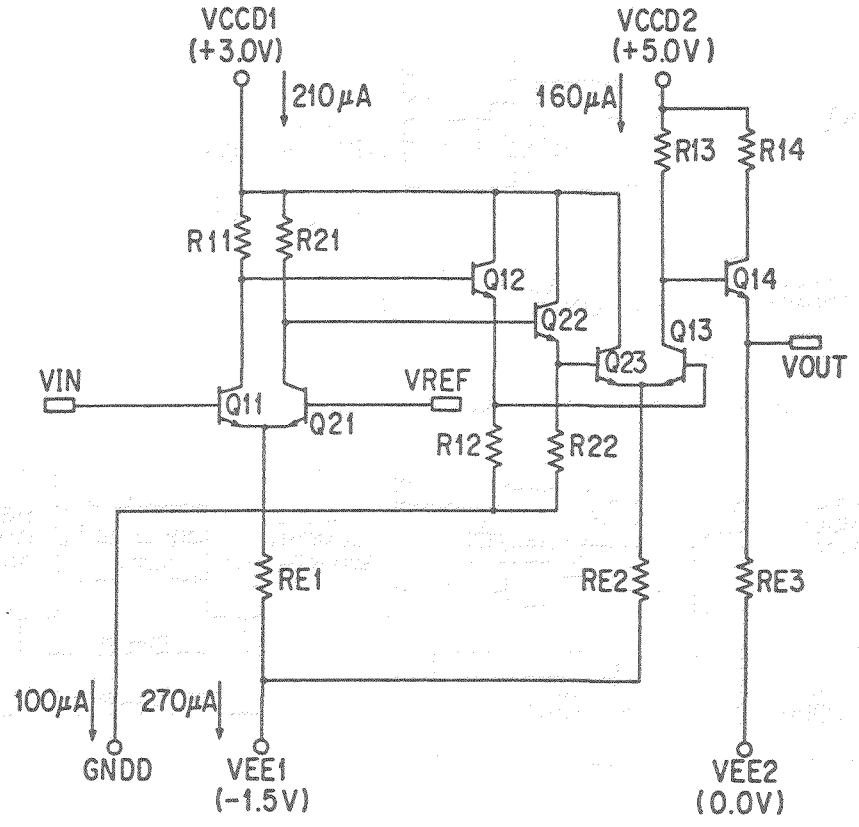

Fig 4. Schematic of the Comparator

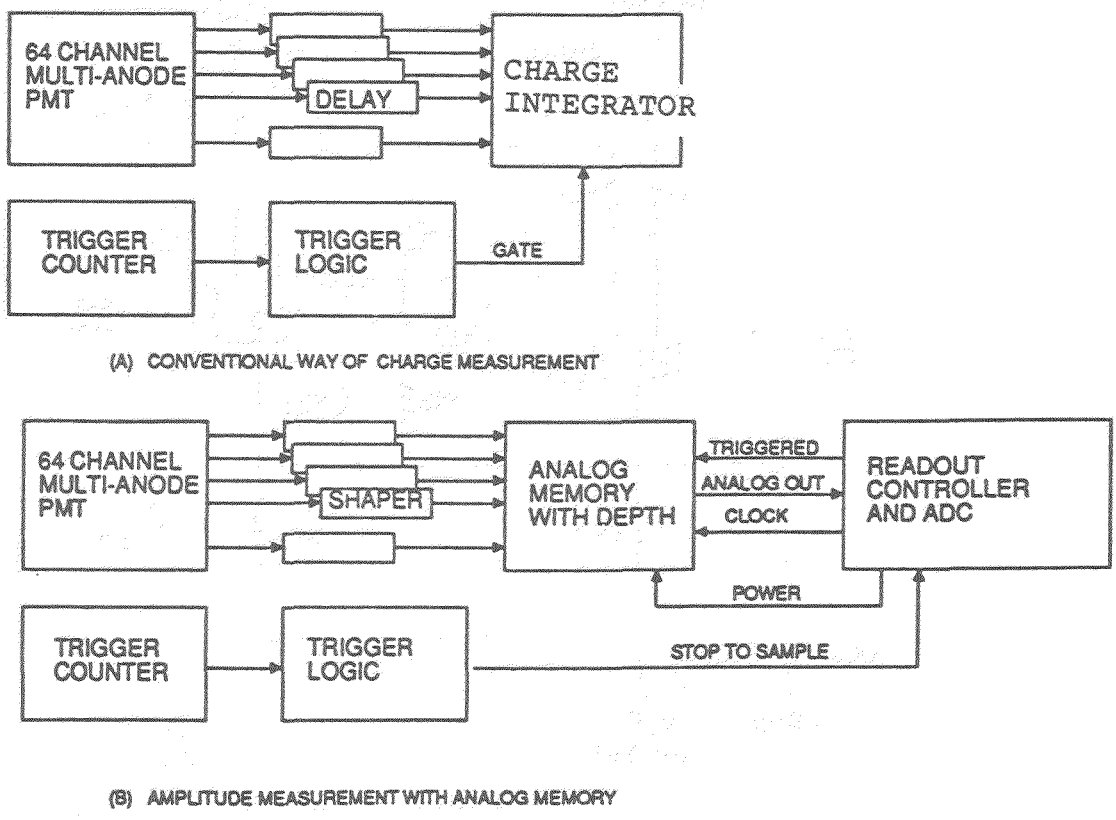

Fig. 5 Configuration for Readout of Multi-Anode PMT

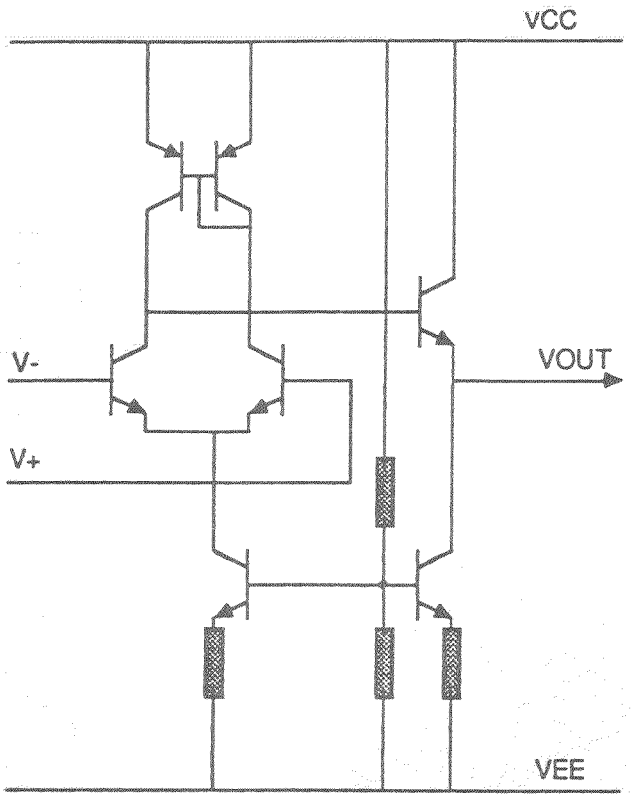

Fig. 6 (a) Amplifier Element of the Shaper Amplifier
for Multi-anode PMT

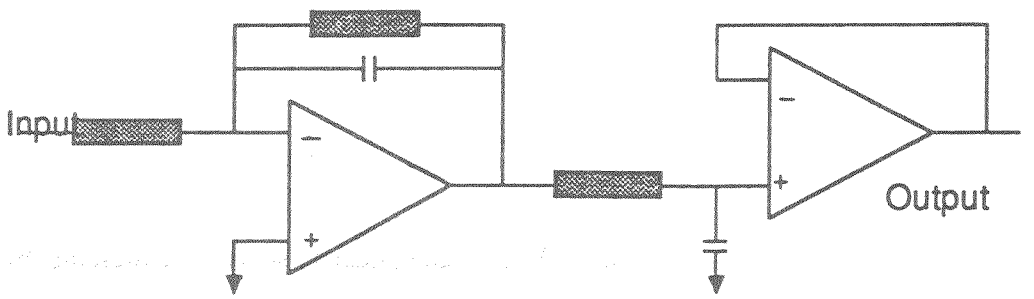

Fig. 6 (b) Schematic of the Shaper Amplifier
for Multi-anode PMT

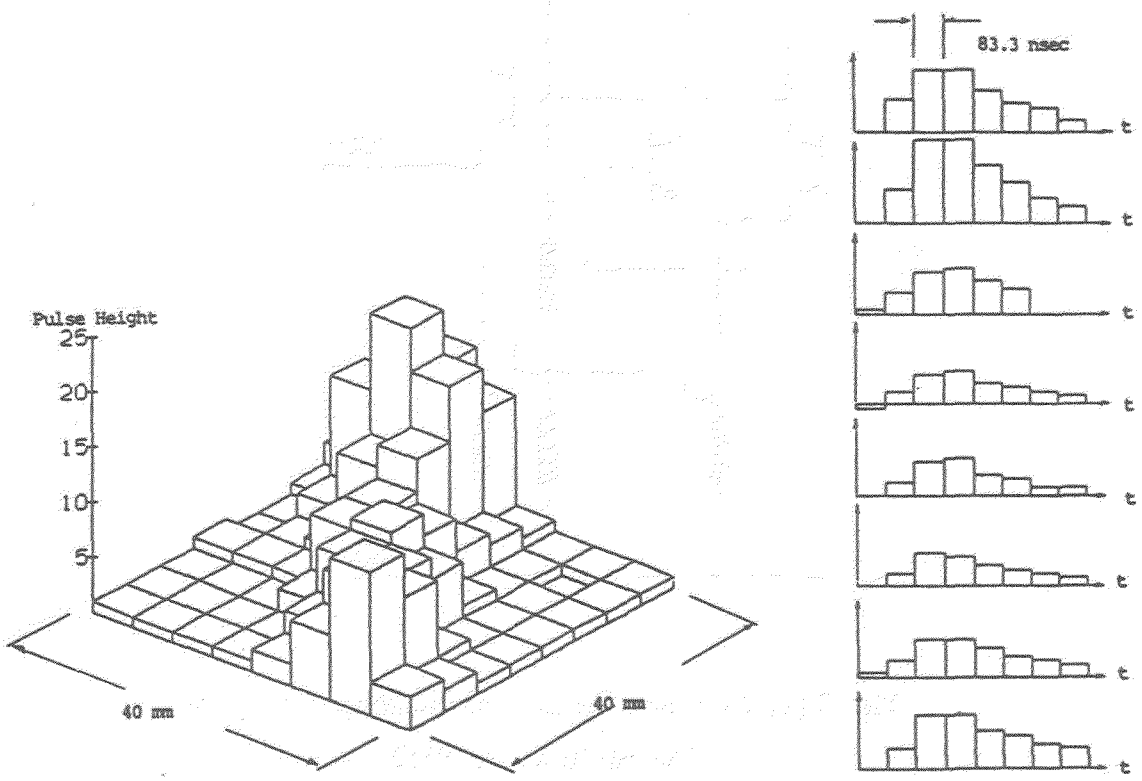

Fig. 7 Cosmic Ray Track Measured by Scintillation Fiber
with Multi-anode PMT Readout

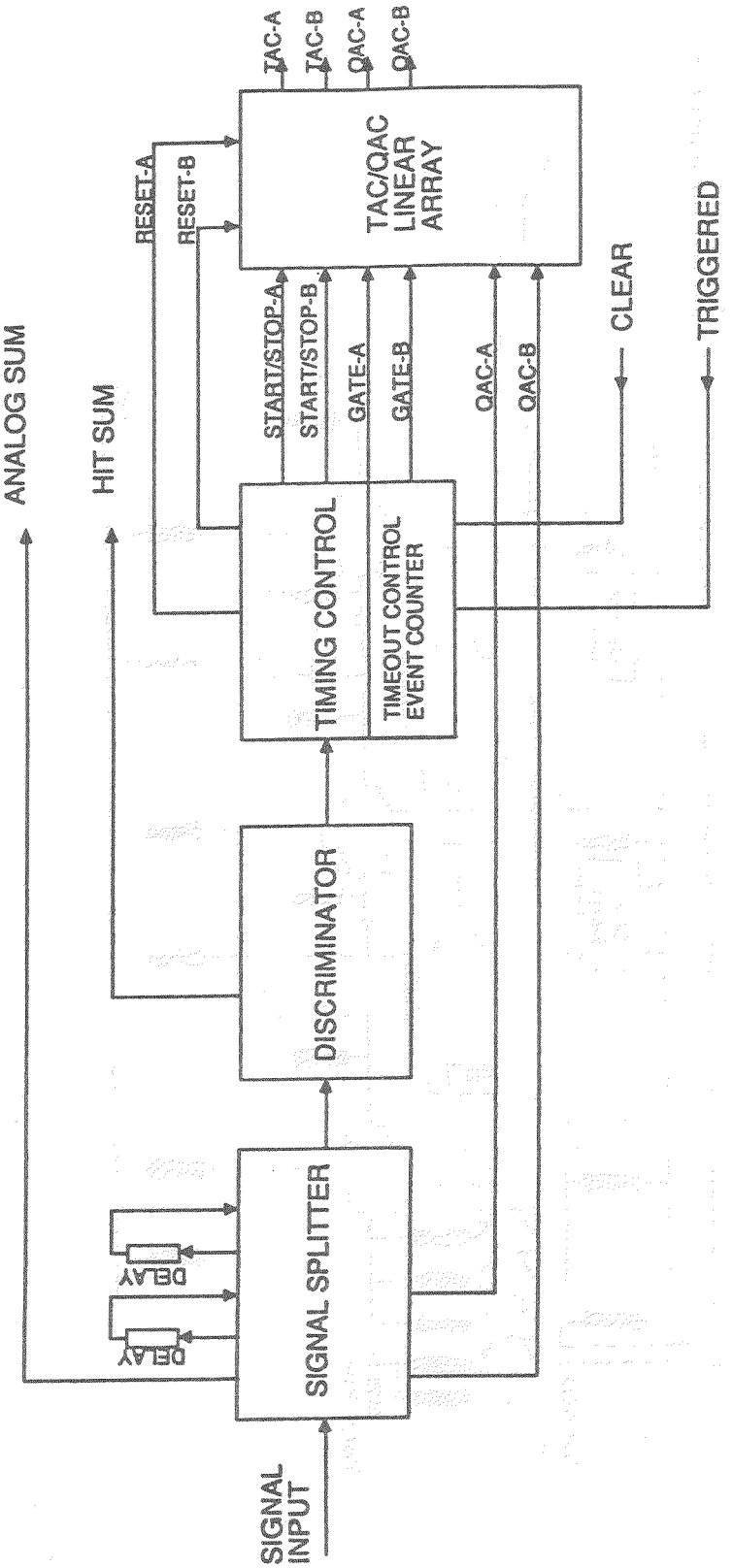

Fig. 8 Scheme for Frontend of TAC/QAC System

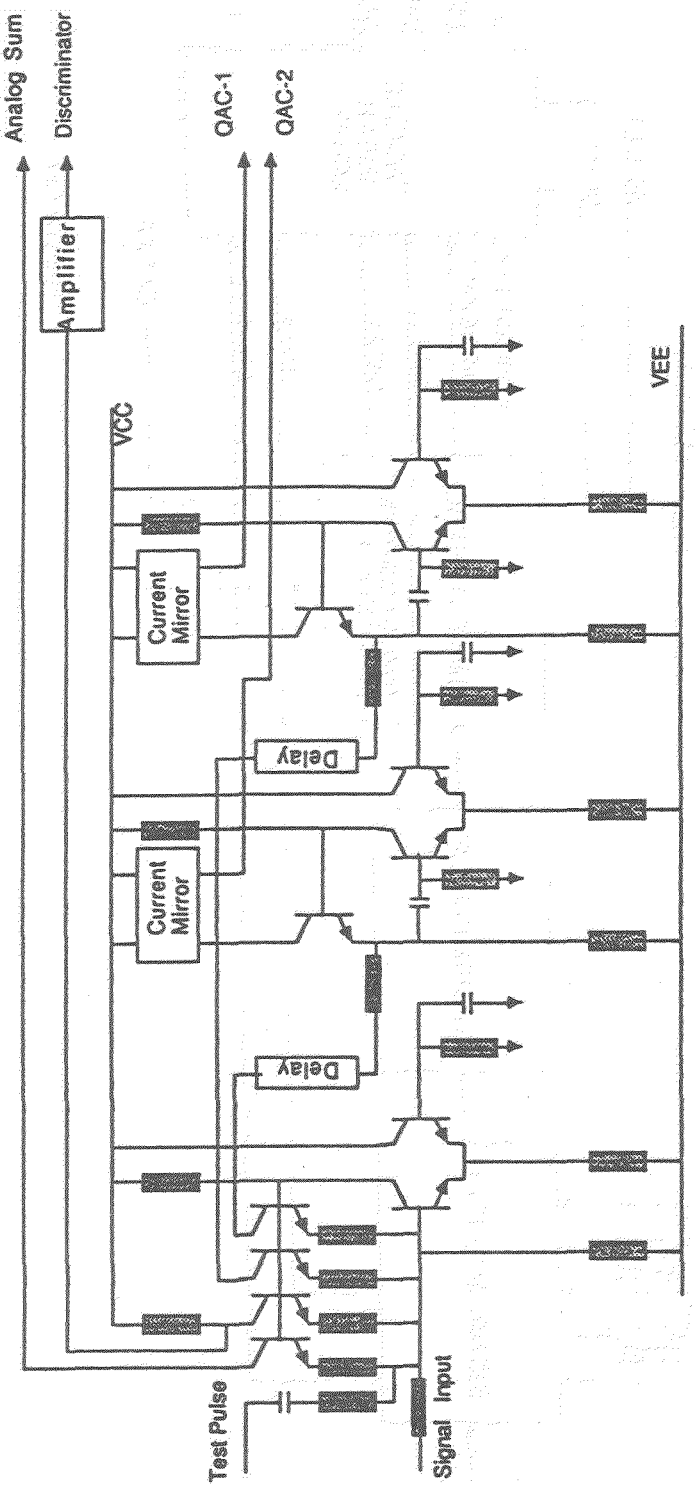

Fig. 9 Schematic of Frontend Hybrid Circuit

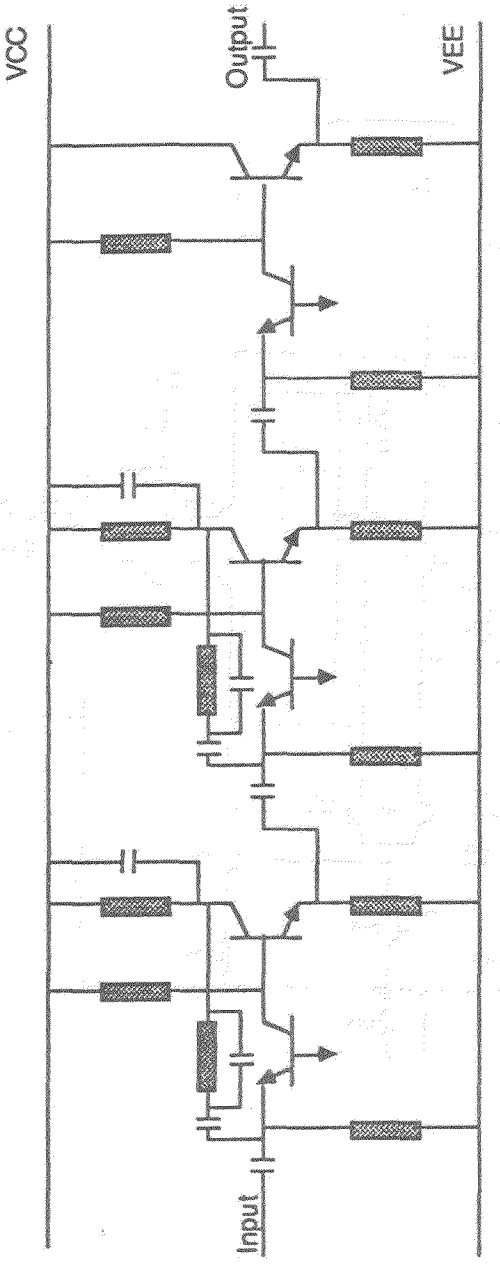

Fig. 10 Rush Amplifier

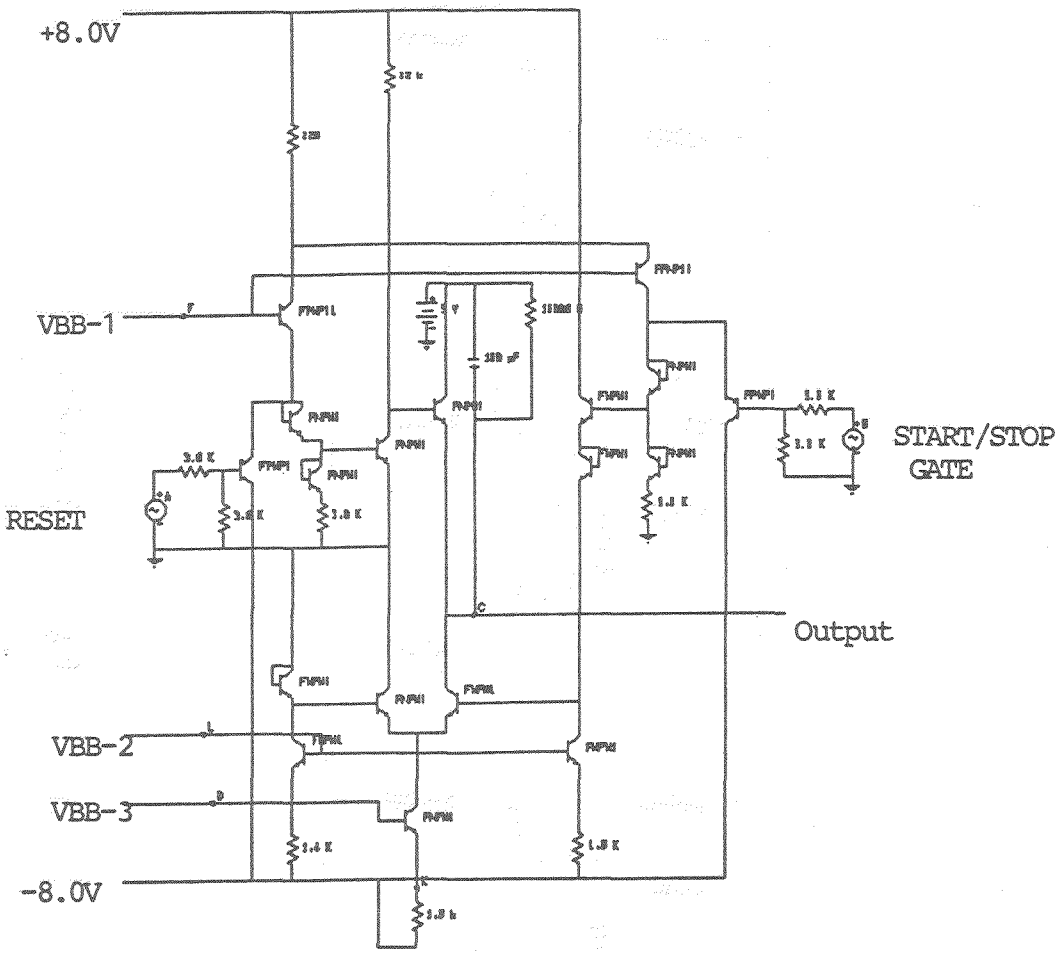

Fig. 11 (a) Schematic of TAC

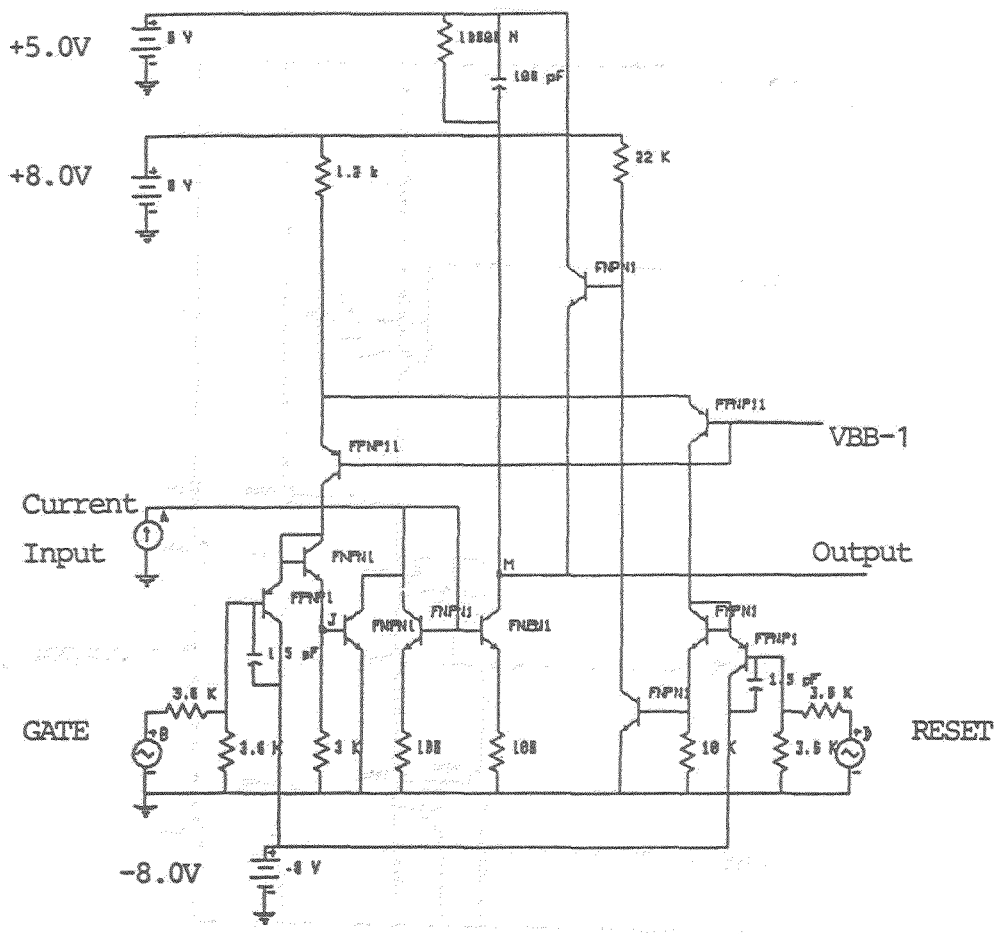

Fig. 11 (b) Schematic of QAC

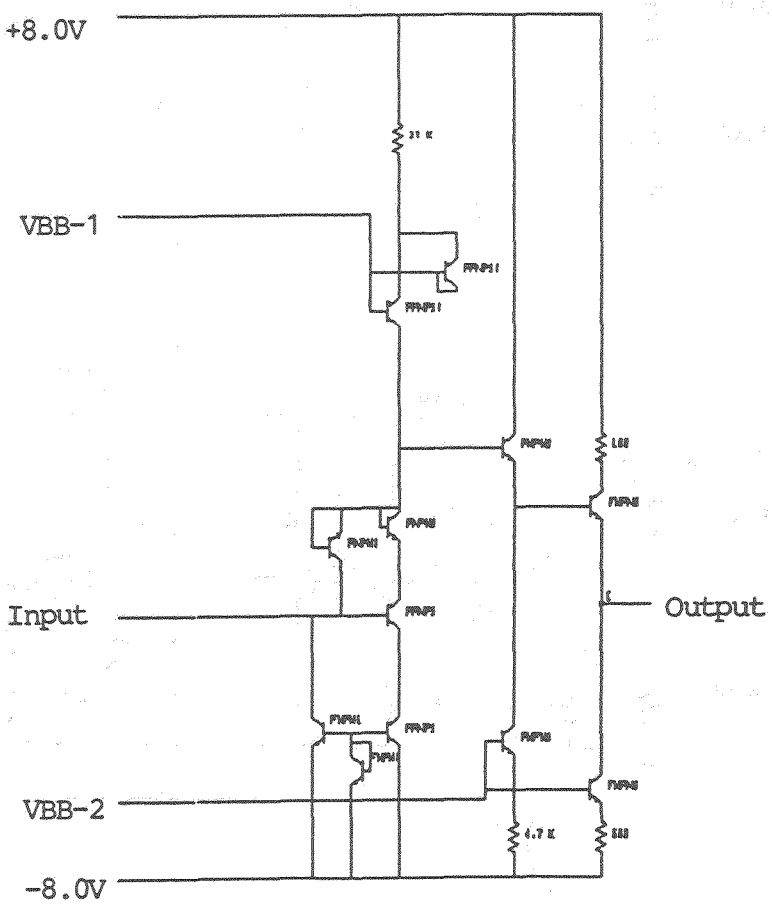

Fig. 11 (c) Schematic of Output Buffer

The SVX IC: A 128 Channel Charge Amplifier with Sparse Scan

Presented by Carl Haber*
Lawrence Berkeley Laboratory
Berkeley, California 94720
USA

ABSTRACT

The SVX IC is a 128 channel array of charge amplifiers with sparse data scan and a multiplexed serial readout. It is suitable for use with detector capacitances up about 50 pf. The function and performance of this device are described in this paper.

1. Introduction

The SVX IC is a 128 channel array of charge amplifiers with sparse data scan and a multiplexed serial readout. It has been developed at Lawrence Berkeley Laboratory by Kleinfelder and others [1] for use in the CDF Silicon microstrip vertex detector [2]. The circuit will function under certain circumstances with capacitances as large as 50 pf. In addition to its use with Silicon microstrip readout, it may be applicable to readout of other capacitive loads such as pads in imaging detectors for particle identification. In this contribution to the Fermilab Particle Identification Workshop we describe the function and performance of the SVX IC.

2. Functional Description

The SVX IC is a VLSI circuit fabricated in a CMOS process with 3 μm minimum feature size. A number of versions of this device have been prototyped and studied. Unless otherwise noted, this discussion will always refer to the final production version which is known as SVX Revision D. In Figure 1, four of the chips can be seen mounted on a readout hybrid circuit. In the SVX IC analog and digital functions are integrated onto the same chip. In Figure 2 we show a functional diagram of the SVX IC. The device contains 128 high gain charge sensitive amplifiers, each is followed by a sample and hold stage, a threshold storage stage, a comparator and latch, and digital circuitry to control a serial multiplexed readout. During operation of the device, a threshold is stored, incoming data is then compared to the threshold and a corresponding latch is set for channels

* See appendix for a list of names of individuals who participated in this work.

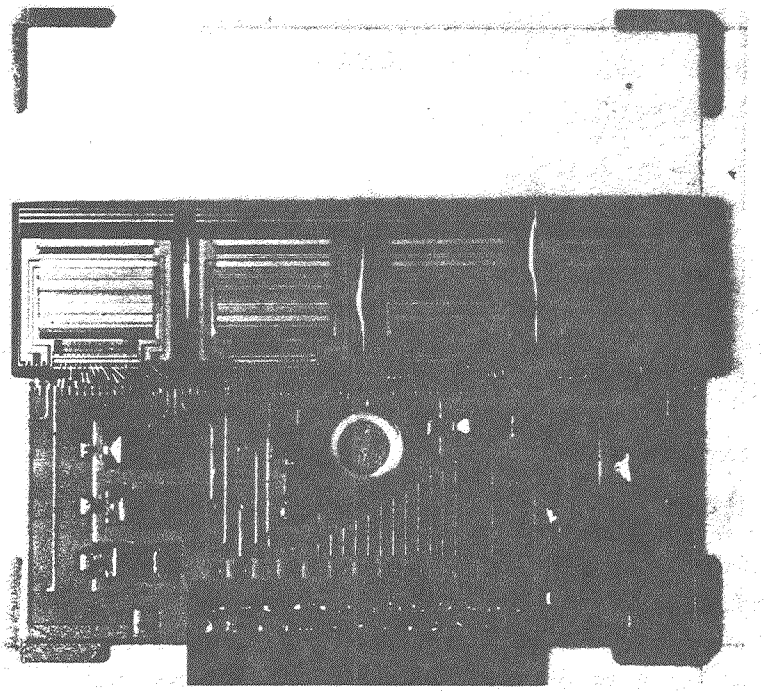

Figure 1: Four SVX IC's mounted on a readout hybrid. The chip dimensions are approximately 7 *mm* on a side.

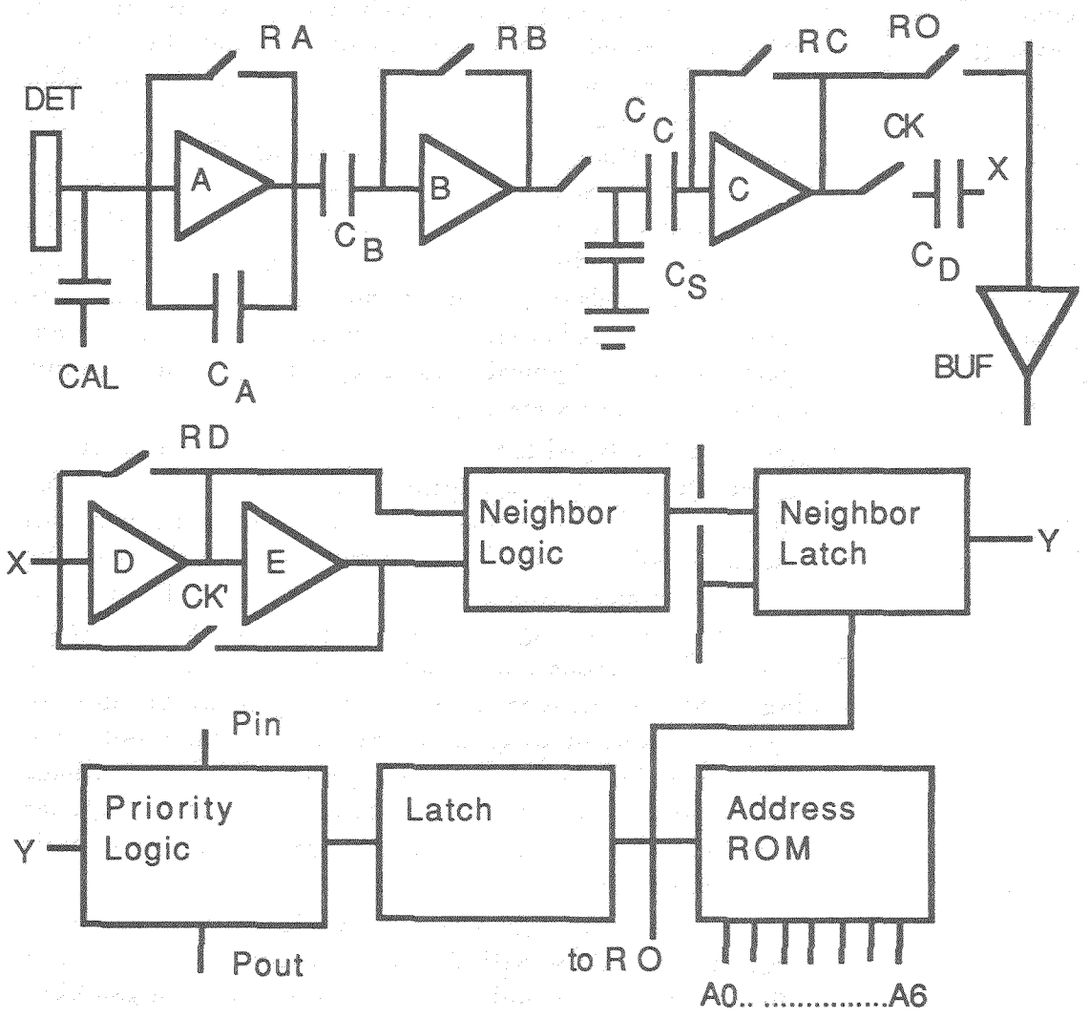

Figure 2: Functional diagram of the SVX IC circuit.

Figure 3: SVX IC timing cycles for a quadruple sample and hold followed by a full readout.

above threshold. When the chip is read out, the digital control circuitry switches sequentially only to those channels which are latched. For each latched channel, the analog voltage stored is connected to a single analog bus and the channel address is simultaneously connected to a 7 bit digital bus. With this on–chip sparsification feature the readout time of the device is dramatically decreased and is set by the occupancy rather than the total channel count. Because of this feature, the SVX IC is appropriate for use in systems with large channels counts, in a high luminosity or high multiplicity environment. A maximum of 63 SVX IC's may be daisy–chained together for readout. In addition to the sparse readout, options exist for reading out all channels or just hit channels plus their immediate neighbors. In the latter case, some shared charge, which may fall under threshold, can be picked up in a sparse readout. Typical readout speed is $1\mu s$ per channel when both analog and digital information are required.

Since the SVX IC has been developed for use with Silicon microstrips at the Fermilab Tevatron-1 collider, its front end performance has been optimized for that type electronic environment. Typical ionization from high energy particles in Silicon microstrips is about 25000 eh pairs (4 fc). Beam crossing times at the collider are every 3.5 μs. The front end performance of the SVX IC is determined by the charge integrator as well as the voltage amplifier stages indicated in Figure 2. The charge amplifier is a CMOS cascoded inverter with a 0.3 picofarad feedback capacitor. Current flowing in the cascode is set by a current mirror circuit and can be adjusted externally by a bias resistor to ground. Bench tests have indicated an open loop gain of about 2000 for the SVX IC integrator. With a feedback capacitance of 0.3 pf, the integrator has an effective capacitance of 600 pf, far in excess of typical detector capacitances of ten of picofarads. This is a basic requirement for good charge collection.

The procedure for establishing a sparsification threshold in the SVX IC is also engineered for the requirements of use with Silicon microstrip detectors. The procedure has a certain flexibility which could allow it to function with gas filled detectors also. In its design application, the SVX IC, would integrate charge during a fixed interval at the time of collider beam crossing. This time is on the order of 1 μs and is determined primarily by the amplifier response at the sample and hold point. During the integration time, leakage currents will flow from the Silicon detector into the integrator. Normally these are on the order of a few $nA/strip$ although individual "bad" strips may have currents many time larger than this. For a leakage current of 3 nA, in 1 μs a charge of 3 fc is integrated. In a threshold comparison, the threshold will be of the same order or less than the integrated leakage current. (since the charge from a minimum ionizing particle (MIP) is 4 fc). Since these leakage currents can vary from strip to strip it is necessary to include the individual strip leakages in the threshold. In order to do this the SVX IC has the ability to perform a quadruple correlated sample and hold (as distinguished from the more common double correlated sample and hold which is used widely in collider detector readout systems). The basic procedure is to integrate twice, once

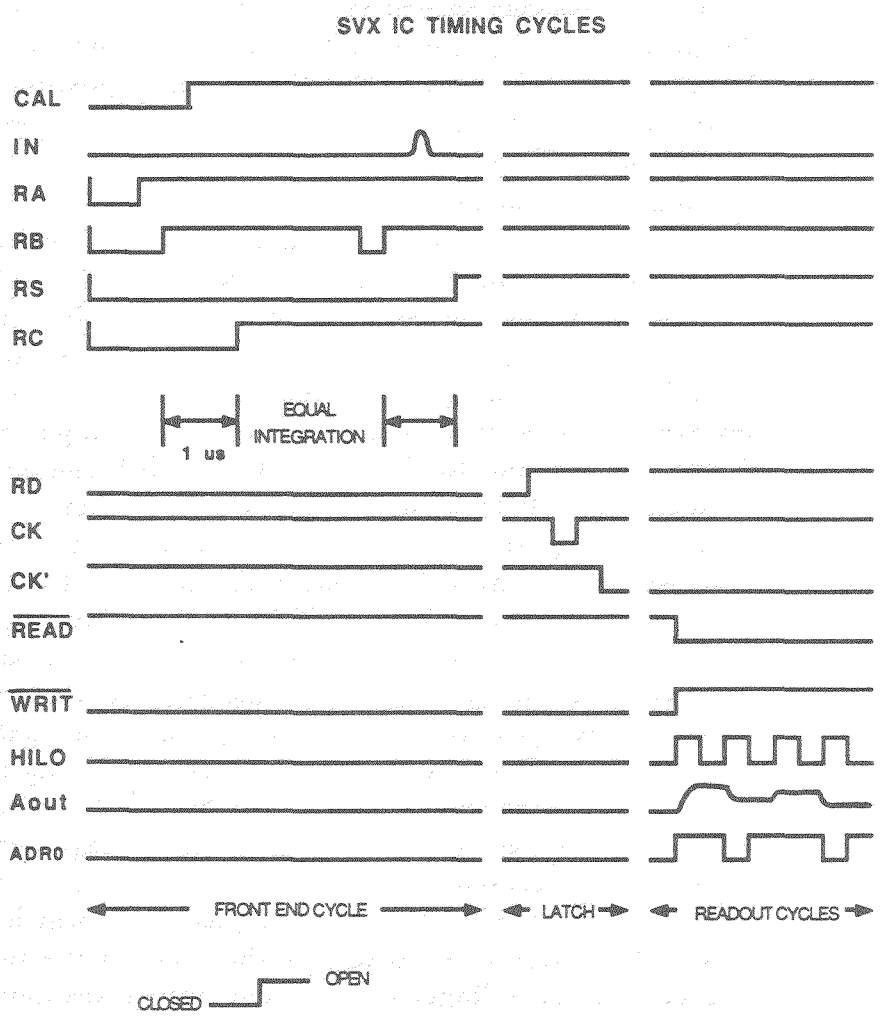

Figure 3: SVX IC timing cycles for a quadruple sample and hold followed by a full readout.

with no beam (before a crossing for example), and once with beam. During the first integration, the integrated leakage as well as an injected threshold would be stored on a threshold capacitor. During the second integration, which must be of the same duration, the integrated leakage as well as charge from a possible MIP in the detector will be stored on another sample and hold capacitor. The two stored voltages can then be compared at the input to a latch.

The procedure described above can be realized in the clocking sequence shown in Figure 3. Refer also to the functional diagram shown in Figure 2. The active element A is the CMOS charge sensitive amplifier. Elements B (Comp1), C (Comp2), D, and E are CMOS inverters. When the reset switches on the CMOS inverters are OPEN, the inputs have very large impedance. When the reset switches are CLOSED, the inputs are fixed at a voltage in the middle of the operating range of the inverter, ie. they are connected to a fixed potential. For example, consider the case of R_A OPEN, and R_B, R_S, and R_C CLOSED. Charge is being integrated by A. At the moment R_B is set OPEN a corresponding voltage (minus the DC offset on the output of A) will appear across C_S and C_C. If R_C is then opened, the voltage stored on C_C will be held fixed from that time onwards. Let the time between R_B opening and R_C opening equal τ_{INT}. If R_B is then closed again the charge stored on C_S will be cleared. Opening R_B again allows C_S to again track the input starting from zero. If R_S is then opened a time τ_{INT} [3] since the last opening of R_B, the integrated leakage current stored on C_S will equal that stored on C_C from before. The scheme is therefore to inject a threshold during the first integration period and wait for charge from a MIP in the Silicon detector to appear during the second. If the voltage across C_S exceeds the voltage across C_C then the output of element C will exceed its reset level. Elements D and E are a latch which indicate the state of the comparison to digital logic which follows after appropriate clocking. An option exist to reverse the order of the threshold and data measurements also. Held voltages can be kept until a readout of the chip is initiated after which hit channels can be multiplexed out serially at about 1 MHz. Note also that with a slighlty simpler clocking scheme a double sample and hold operation can be performed. In this case, the second reset of R_B would be omitted. This might be the type of cycle to use in a case where leakage current variations or pedestals are not a concern.

The SVX IC has been designed for use in a multi-channel system. The circuit uses an economical control protocol in order to simplify system integration and cabling. The SVX IC pin out is indicated in Table 1a. This protocol uses two sets of digital lines to determine the various modes of operation available. The first set are the CONTROL lines, HiLo (HL), not Read Enable ($\overline{RE}$) and not Write Enable ($\overline{WE}$). The second set are the DATA lines, $A0$–$A7$. Depending upon the configuration of the CONTROL lines, the DATA lines will have one of four possible uses. These are defined as follows:

1. *Write Clocks*: In this mode the states of the various reset and sample and hold switches are controlled by logic levels sent to the SVX IC.

Table 1A: SVX 1C Pin Definition

Pin	
1	Detector Guard Ring Connection
2	Analog Ground
3	Analog Ground
4	Calibrate Step 1n
5	Analog Power (+6 VDC)
6	Analog Power (+6 VDC)
7	Digital Section Ground
8	$\overline{\text{BN}}$ (Not Bottom Neighbor In/Out)
8	$\overline{\text{PO}}$ (Not Priority Out)
9	A7
10	A6
12	A5
13	A4
14	A3
15	A2
16	A1
17	A0
18	$\overline{\text{RE}}$ (Not Read Enable)
19	$\overline{\text{WE}}$ (Not Write Enable)
20	HL (HiLo)
21	$\overline{\text{PI}}$ (Not Priority In)
22	$\overline{\text{TN}}$ (Not Top Neihbor In/Out)
23	Analog Output
24	Analog Output Clocked by Priority
25	Digital Power (5–6 VDC)
26	Analog Power (6 VDC)
27	Analog Power
28	Cascode Current Bias Resistor
29	Analog Section Ground
30	Analog Section Ground
31	Detector Guard Ring Connection

Table 1B: SVX IC Control and Data Lines

HL	1	1	0	0	X	X
$\overline{\text{RE}}$	1	0	0	1	1	0
$\overline{\text{WE}}$	0	1	1	0	1	0
$\overline{\text{PI}}$	0	0	0	X	X	X
$\overline{\text{PO}}$	1	1	1	X	X	X
A0	write chip ID 0	read chip ID 0	read channel bit 0	set latch all mode	off	illegal
A1	"	"	"	latch ϕ_2 C_K	"	"
A2	"	"	"	reset comp 3 R_D	"	"
A3	"	"	"	latch ϕ_1 C_K	"	"
A4	"	"	"	reset comp 2 R_C	"	"
A5	write chip ID 5	read chip ID 5	"	reset S+H R_S	"	"
A6	pos/neg threshold mode	read threshold mode	read channel bit 6	reset comp 1 R_B	"	"
A7	set neighbor readout	read neighbor mode	latch all mode	reset integrator R_A	"	illegal
Analog out	$Z = \infty$	$Z = \infty$	channel pulse height	$Z = \infty$	$Z = \infty$	$Z = \infty$

2. *Write Chip ID*: In this mode an ID number (0–63) may be written into a register on the SVX IC.
3. *Read Chip ID*: In this mode the chip ID number may be read out of the SVX IC.
4. *Read Channel Address*: In this mode the number of the channel on the analog bus is read out of the SVX IC.

These states are listed in Table 1b. This type of protocol reduces the cabling and interconnection requirements significantly. The DATA lines are bi–directional and tri–stated and thus a number of chips can be connected to the same data bus. In a daisy–chained configuration, a priority bit transition is held by the particular chip being read or addressed at the time.

To read out the SVX IC, the CONTROL lines are configured for read and the HL line is toggled at the readout frequency. On alternate phases of this line, the Chip ID or the channel address will appear on the DATA bus. During read out, the priority bit transition resides within the particular SVX IC being read. In a sparse readout, during the read of a particular hit channel, the priority bit transition will pass to the next hit channel. Once all channels of a particular chip have been read out, the priority bit transition will be passed to the next chip on the daisy–chain. The speed of the priority trickle down is about 5 $ns/channel$.

The inputs to the charge amplifiers are protected with back to back diodes to prevent damage to the input transistors. This feature is important if the SVX IC is to be connected to gas filled detectors which may have breakdowns. No tests have however been made to see whether the SVX IC can survive such discharges. For example, there could be response time effects in a discharge situation which are important.

4. Performance

In this section some results of bench tests of the SVX IC performance will be given. These should be regarded as preliminary since the production run is in progress and some run dependant variation can be expected in integrated circuit fabrication. The results of the final characterizations will be presented later [4].

The nominal operating voltage for the analog section of the SVX IC (integrating amplifier) is 6 VDC. The nominal cascode current is 80 μA and is set with an $11 Kohm$ resistor on the bias line. The total analog power is 78 mW. The digital section can be operated between 5 and 6 VDC in which case the total digital power is between 65 and 210 mW. Some increase in speed is available with the higher digital power.

The charge gain of the SVX IC is 17 mv/fc and the dynamic range is indicated in Figure 4. The on–chip calibration capacitor is 50 ff. These results are for the clocked analog bus. The unclocked analog bus, which cannot be used in a daisy–chained system without external analog multiplexers, has more dynamic range for negative injected pulses.

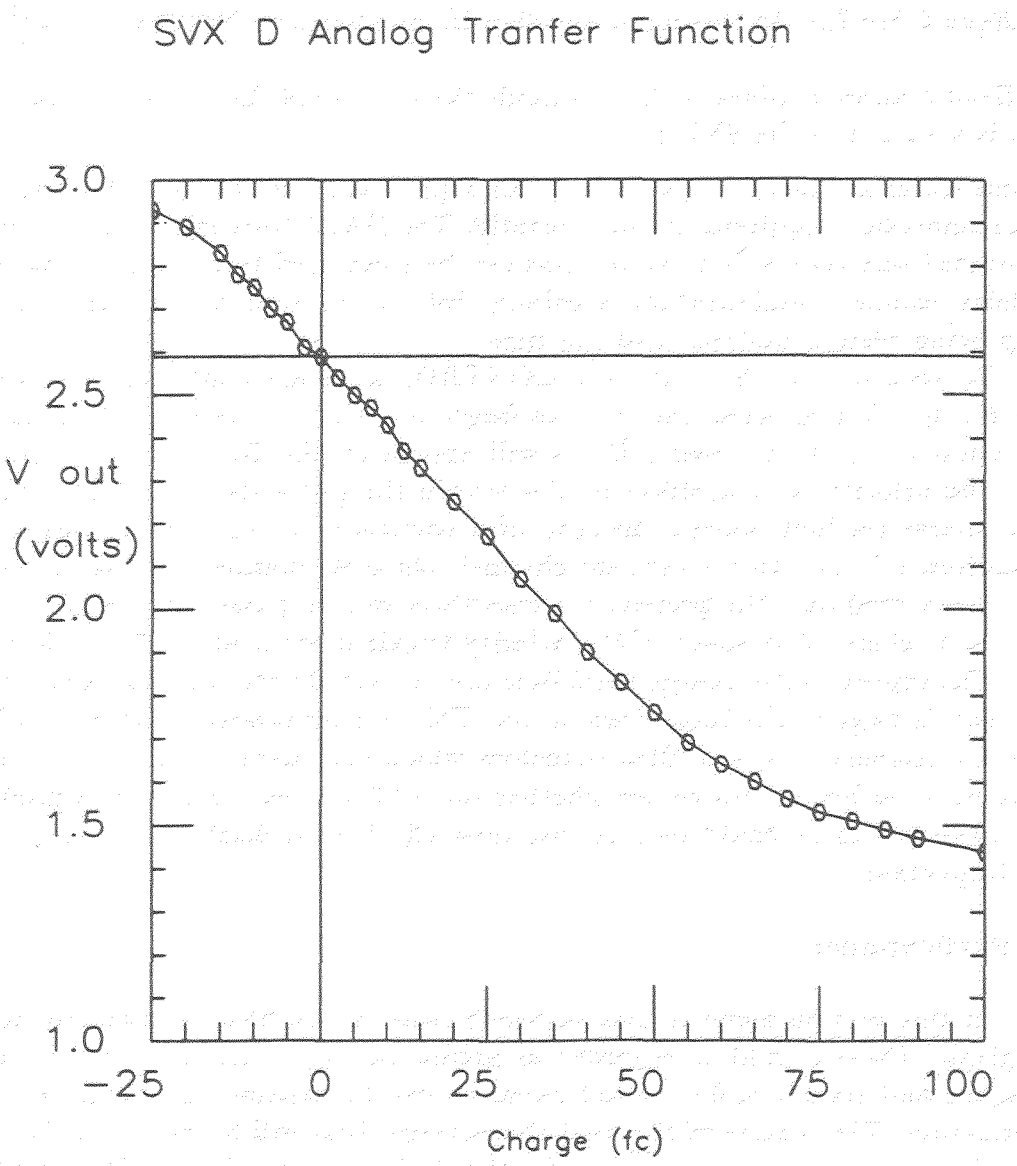

Figure 4: Analog transfer function of the SVX IC for positive and negative injected charge.

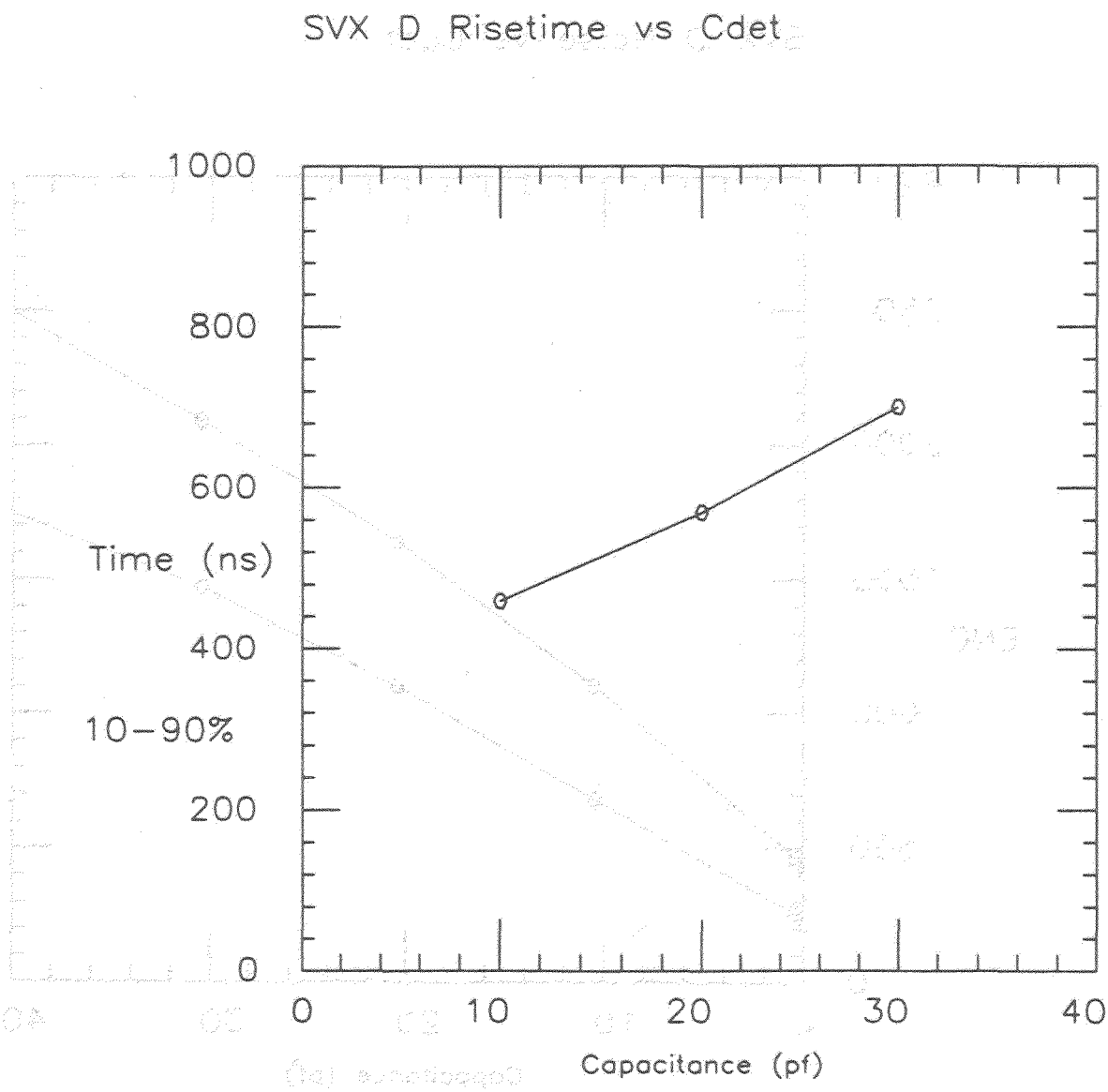

Figure 5: Risetime (10%–90%) at the sample and hold capacitors for the SVX IC.

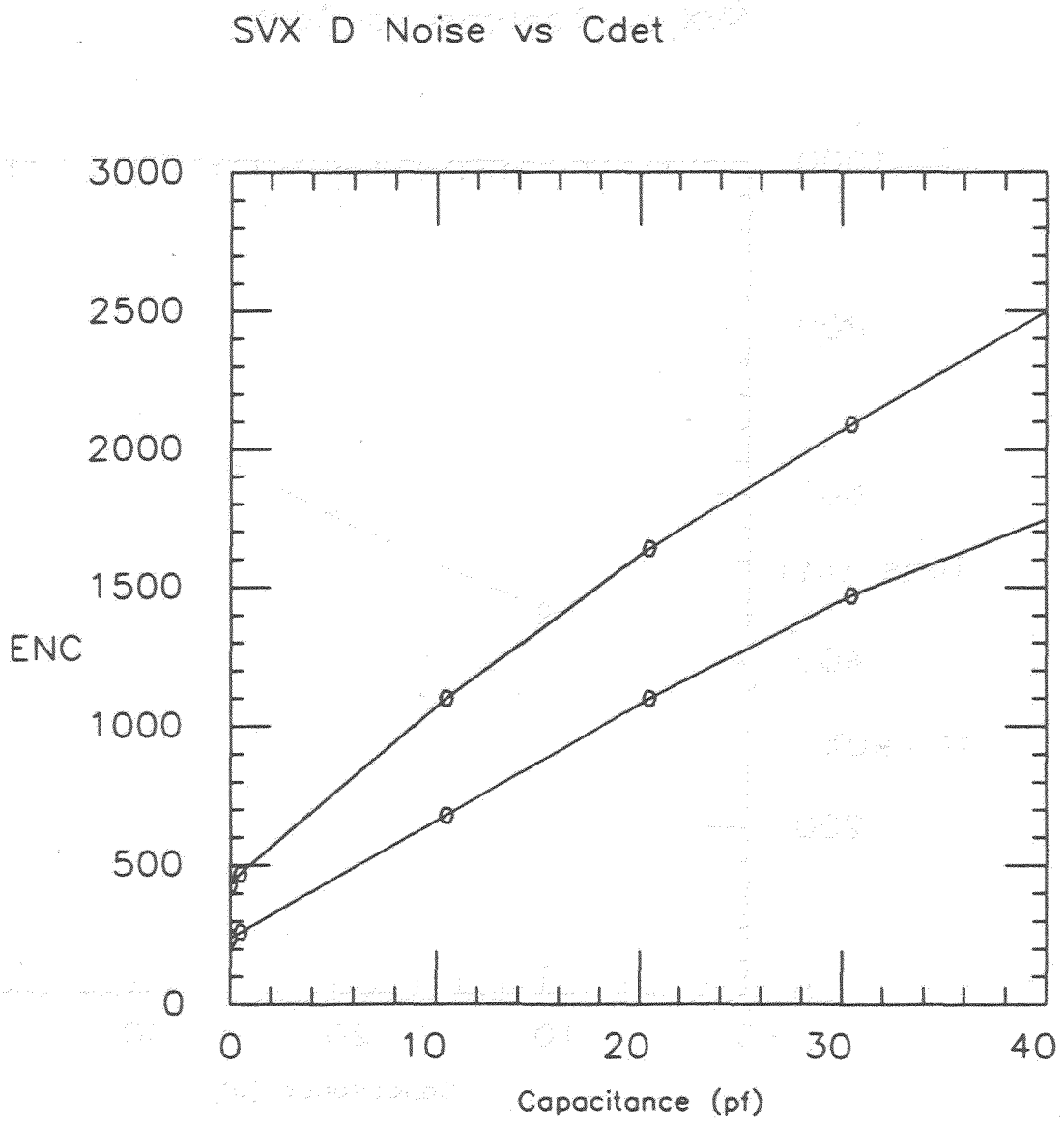

Figure 6: Input noise in electrons for the SVX IC versus detector capacitance for double and quadruple sampling.

The risetime of the integrator will vary as a function of detector capacitance. The risetime at the sample and hold capacitors will be the combination of the integrator and Comp1 risetimes but is dominated by the integrators response. These values for a digital voltage of 5 VDC are shown in Figure 5. These were measured by charge injection through an external capacitor. The response will be slightly slower when the on–chip calibration capacitor is used due to the simultaneous injection into 128 channels.

Noise measurements as a function of detector capacitance are shown in Figure 6 for a double and quadruple sample and hold. The quadruple sample and hold should have roughly 40% more noise than the double since two additional measurements of a random quantity are made.

4. Radiation Resistance

In its use as front end readout electronics in the CDF Silicon vertex detector, the SVX IC will be in a radiation environment. A number of measurements have been made on earlier versions of the SVX IC to determine its radiation resistance. Susceptibility to radiation can differ as a function of particle type (charged particles, photons, and neutrons) as well as particle energy. Radiation damage can manifest itself in a number of ways including total device failure, changes in noise and gain, and loss of dynamic range. Tests done with gamma rays from ^{60}Co have indicated a doubling of the electronic noise occurs after an exposure of 20 (45) $KRad$ with a detector capacitance of 30 (0) pf for a quadruple sample and hold. Measurements with higher energy charge particles are currently in progress [5].

4. System Integration

Because of the on–chip sparsification which occurs in the SVX IC, the potential data record from a system of these circuits is reduced considerably. In spite of this, it is probably necessary to have control and data acquisition hardware capable of handling the large amount of information which can be produced. For example, systems will often have calibration and monitoring procedures which require full readout.

As part of the development of the SVX IC a number of control and data acquisition circuits have been designed and constructed [6]. These are typical of the type of circuits needed in large multi–channel systems of chips like the SVX IC.

Appendix 1

The following individuals contributed to the work described in this paper: W. C. Carithers, R. Ely, C. Haber, F. Kirsten, S. Kleinfelder, H. Spieler, and W.

C. Wester III of Lawrence Berkeley Lab, and R. Yarema and T. Zimmermann of Fermi National Accelerator Lab.

References

1. S. Kleinfelder et al, Proc IEEE NSS Symposium, Oct. 1987.
2. C. Haber in Proc. of the 7^{th} Topical Workshop on Proton-Antiproton Collider Physics, World Scientific, Singapore, 1989, p.443
3. In its actual use, the risetime at the sample and hold capacitor will be slightly different when B is loaded by just C_S or by C_S+C_C. For this reason, a perfect cancellation of the leakage current occurs for a pair of integration times which are tuned to compensate for the small risetime differences.
4. S. Kleinfelder et al, to be published in Proc. of IEEE NSS, Oct. 1989, San Fransisco, USA.
5. R. Yarema et al, to be published in Proc. of IEEE NSS, Oct. 1989, San Fransisco, USA.
6. F. Kirsten and C. Haber, to be published in Proc. of IEEE NSS, Oct. 1989, San Fransisco, USA.

ELECTRONICS FOR TRACKING DETECTORS AT HIGH LUMINOSITIES - SSC, LHC, TEV+,...

R. Van Berg
University of Pennsylvania

1 Introduction

Experiments at future high luminosity colliders (and even at present high rate fixed target machines) present a new class of challenges for front end electronic systems. In fact the combination of detector and accelerator requirements present a very restricted space in which one can optimize the electronics design. The *front end electronics* is that part of an experiment which begins at the output conductor of an individual detector element and ends with a data carrying cable leaving the immediate experimental area. Begun at Snowmass in 1986, [1] a high rate architecture for tracking chambers has been further developed and refined under an SSC R&D program [2]. A "complete" demonstration system for track chamber readout should be available in the near future.

While the detailed requirements of particle identification detectors are somewhat different from the general tracking case, the amount of overlap is very large and I believe that it will be possible to successfully adapt many features of this "Generic" architecture (Figure 1) to a wide variety of detector types and that in any event most of the same detector and accelerator driven challenges will remain.

[1] Electronics, Triggering and Data Acquisition for the SSC, T.J. Devlin, A. Lankford, and H.H. Williams, p. 439, Proceedings of the 1986 Summer Study on the Physics of the Superconducting Supercollider, June 23-July11, 1986.

[2] A collaboration between the University of Pennsylvania, Brookhaven National Laboratory, AT&T, and The Catholic University of Leuven

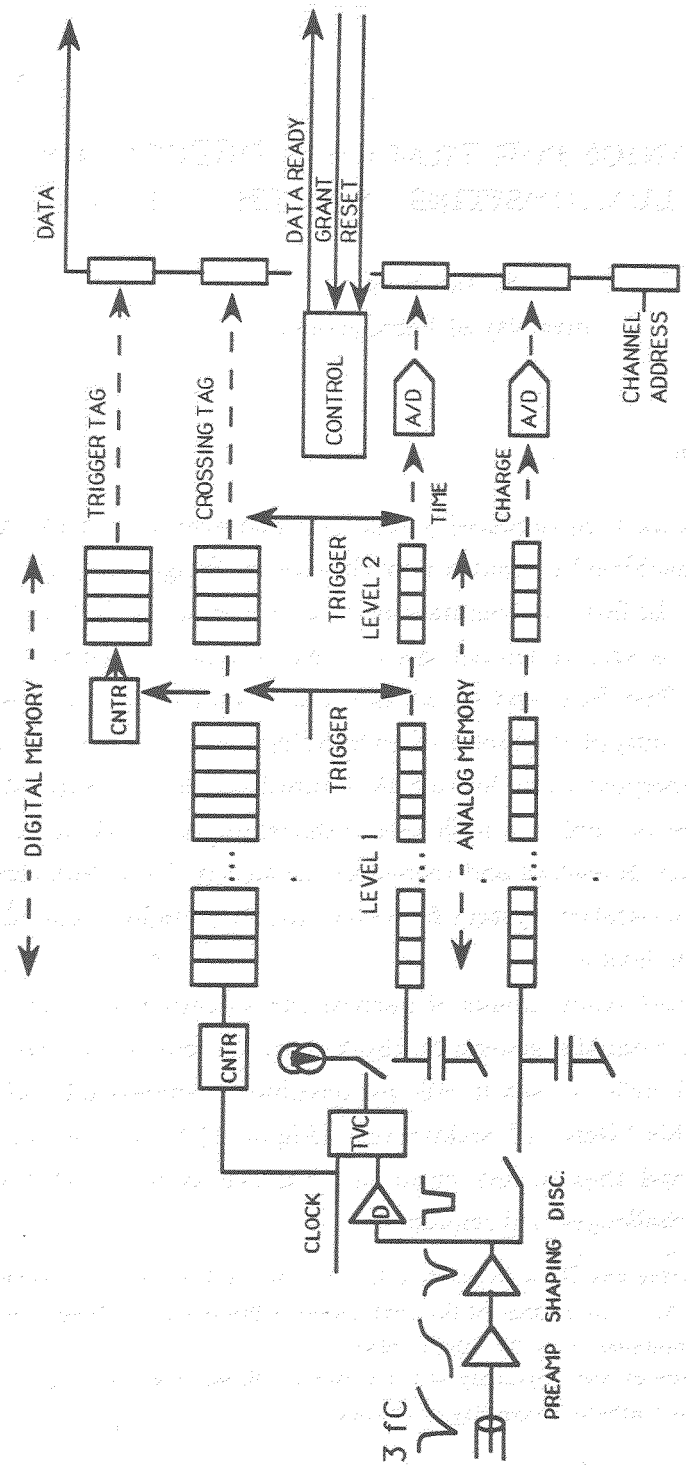

Figure 1: High Rate Tracking Electronics - Block Diagram

2 Accelerator and Detector Characteristics

From a physics point of view, the major defining characteristic of the new generation accelerators such as SSC or LHC is the greatly increased mass scale available to experiments. However, from an instrumentation view, the dominant characteristic is the very high luminosity goals which result in a potential interaction rate ($\sim 10^8 Hz$ at SSC) driven by a nearly as daunting crossing rate (60 MHz).

Proposed detectors are, of course, no less ambitious and typically [3] are many meters on a side with $\mathcal{O}$ 10^6 individual detector elements in the tracking and calorimetric sections alone. (Note that RICH and TRD detectors have the potential to greatly increase this channel count, as many contributions to this workshop have demonstrated). The driving force behind this great increase in channel count over presently operating detectors is the projected increase in multiplicity which drives up the number of tracking channels and the much greater definition and dynamic range required of both electromagnetic and hadronic calorimeters.

In addition to the large number of channels there are several other challenging characteristics of proposed detectors. First there is an increasing reliance upon missing energy for both trigger and analysis signatures, which means that there may be a much higher premium on spatial hermeticity in next generation detectors. Secondly the radiation levels within the volume of the detector will be disturbingly high both for the electronics and for the actual detector elements themselves.

Furthermore, the detectors will be so large that even sending triggering data to a common trigger point and then returning a trigger to the detector will take nearly a microsecond. Thus if one wishes to use global (but incomplete) information to accept or reject an event it will be necessary to store all data locally for at least one microsecond or transport all data on delay cables as is now common practice. As both the space and power

[3] Proceedings of the Workshop on Experiments, Detectors, and Experimental Areas for the Supercollider, July 7-17, 1987, ed. R. Donaldson, M.G.D. Gilchriese

requirements of the second "solution" are prohibitive, some local storage is required. Because one microsecond is many beam crossings, it is also useful to supress zeros so that only crossings with data present will require storage space.

3 Electronics Requirements

In addition to these architectural reqirements, there are further detailed specifications which should be met.

3.1 Noise - $\ll$ 1500 electrons

Inherent electronic noise must be kept very low either because the detector elements produce only very small signals ($\mathcal{O}$ 20,000 electrons for silicon strips or pixels) or because the inherent gain of the detector must be kept lower than present practice because of radiation damage (proportional wires) or because of the large dynamic range (calorimeters). Pickup noise is another serious problem but is intimately linked to the detailed detector design and is not a difficulty if less than the inherent electronic noise of the electronics.

3.2 Speed - $T_{measure} \sim 10nsec$

With a basic time between collisions of only 16 nsec, it is clear that there is a considerable premium on speedy measurement, but

the actual number used will depend upon a variety of factors. $T_{measure}$ as used here is the half time for a pulse to recover to baseline - the accuracy to which one can measure the position of the leading edge of such a pulse is a different quantity more closely related to T_{rise} but is also driven by similar considerations.

If the occupancy of a detector element is very low (e.g. pixel detectors) then the $T_{measure}$ can be very much longer without producing embarrassing overlap problems and T_{rise} is uninteresting. If the detector element happens to have a relatively long charge clearing time (e.g. proportional tubes with $\sim 50nsec$ drift times), then a $T_{measure} = 5$ to $10ns$ for the first cluster allows

good front edge timing. Nevertheless the proportional tube is effectively dead until all of the initial charge clusters are cleared away.

3.3 Power - $\mathcal{O}$ 10 mW/element

Power *limits* are, of course, not crisply defined, but for a 5 mm straw tube tracking detector, 10 mW per element corresponds to the same areal power density at the endplate as a fully loaded Fastbus board. While it it clearly possible to cool power densities of this order, even a factor of three greater power per channel would start to require heroic cooling technologies and incur large costs in terms of extra mass (cooling liquids) and lost hermeticity (piping or vents). For systems nearer the center of a large detector, such as vertex detectors, the power per channel must be much less, and for systems farther out on the periphery, such as calorimeters, the power budget is correspondingly increased. In no part of a detector, however, is it possible to to be profligate with power - it is expensive to bring power into a detector and even more expensive to bring it back out again.

3.4 Radiation Resistance - $\mathcal{O}$ MegaRads/year

Fortunately ionizing radiation levels drop with the square of the perpendicular distance from the beam, as 10 MRads at the beam pipe [4] is a very hostile environment for both detectors and electronics. While there is no guarantee of our ability to obtain electronics capable of withstanding megarads (especially given several examples of circuits that suffer severe damage at levels of 10's of kiloRads), there are existence proofs from several manufacturers [5] of *digital* devices operating at many 10's of MHz after dosages of 10 or even 100 MRad. In addition there are encouraging measurements of some

[4] Radiation Levels in the SSC Interaction Regions, Task Force Report,**SSC-SR-1033** ed. D.E. Groom, June 1988.

[5] Harris Semiconductor, Palm Bay, Florida; United Technologies Microelectronics Center, Colorado Springs, Colorado.

bipolar analog devices at several MRads [6] [7].

3.5 Space Utilization - $\sim mm^3$ /element

For our "typical" 5 mm diameter straw tube electronic system several mm^3 of electronics per straw could be easily accomodated in most designs. The space available for vertex detector electronics is at least an order of magnitude smaller. Calorimeter or muon detectors have, by contrast, almost infinite volumes available. However, for either the straw or vertex detector case, it is clear that the number of cables out of the detector system must be $\ll 1$ per channel. The cable limit arises from two different considerations:

1. An *hermitic* detector simply can not afford the cracks, crevices, and other openings necessary to feed out 10^5 to 10^6 cables.

2. The power required to drive a cable with an analog signal is on the order of all the power required to do all other front end electronic functions. [NOTE that digital signals require much less drive power for the case where the duty cycle is $\ll 1$.]

4 Front End Electronic Specification

Thus we arrive at a straightforward list of desired properties for our *front end electronics*. This list is based on a proportional drift straw system in a large SSC detector [8] but would vary only in details for many other tracking or particle I.D. detectors.

- Deadtimeless operation at collision rates of 10^8Hz (detector rates of up to $\sim 1 - 5 \times 10^6 Hz$)

- Local zero suppression.

---

[6] R. Yarema, T. Zimmerman, measurements of Tektronix Quickchip 2 circuits, private communication

[7] J. Dawson,measurements of AT&T LA200 devices, private communication

[8] Front end and signal processing electronics for large detectors, L. Callewaert et al., IEEE Transactions on Nuclear Science, **36**, p. 446, February 1989.

- Local storage of all data for a few microseconds (**L1** trigger time).
- Local first level event rejection via a synchronous trigger signal.
- Local storage of remaining data for some tens of microseconds.
- Local second (or further) level event rejection via an asynchronous trigger signal.
- Local digitization of any analog quantities.
- Noise, speed, power, and density specifications as in section 3.

Obviously there is a very tight coupling between the trigger system and the *front end* system. It does not seem feasible to operate tracking detectors without requiring very considerable rejection of background events *before* the bulk of the tracking data is removed from the detector as tracking is estimated [9] to comprise nearly half of the total data stream from an event. Local compression of this data into, for instance, track segments could reduce the output data load by a factor of three to five if one were willing to give up individual hit information at this early stage, but this option is probably most interesting for as a separate trigger output.

Figure 1 is a very schematic representation of a generalized electronic system. The initial analog processing stages are very detector specific, but the middle and right hand sections of the figure are dependent only indirectly on the detector parameters and are determined almost entirely by rate considerations. The noise, speed, and power specifications are, similarly, determined by the initial analog processing elements (preamplifier, shaper, discriminator) while the zero suppression, storage, event rejection, and digitization add complexity (and significant silicon area) to the system but have little effect on the other critical specifications.

[9] Preliminary Summary of Detector Element Parameters Group, E. Barsotti et al., Workshop on Triggering and Data Acquisition for the SSC, Toronto, Ontario, January 16-19, 1989.

5 System Operation

The logical operation of each of the blocks in Figure 1 will be described in this section and some examples of the present state of developments will be presented in the next section.

5.1 Analog Processing

The goal of the preamplifier and shaping stages is to accurately present an amplified version of the input signal to later stages and to do so a the lowest cost in added noise and power. The very first gain element in the preamplifier stage is the major determinant of the noise performance of the system and, because noise decreases with added current in the first stage, is also a major contributor to the overall power budget. Additional stages used for gain and shaping will add to the power costs but at a much lower rate as these stages are no longer noise limited. The shaping stage not only limits the noise bandwidth, but also serves in general to compensate for detector and preamp induced effects (tail cancellation) and thus to return the signal back to baseline in a time short enough to avoid pileup from a high average occupancy. Thus in the case of the SSC tracking electronics, we have chosen to use a nearly gaussian shaping function with a relatively short measurement time ($\sim 5ns$).

The discriminator provides the timing signal which determines the ultimate tracking accuracy. Any discriminator will exhibit some time walk caused by the finite T_{rise} of the input pulse and the differences in amplitude pulse to pulse. This walk then becomes a limiting factor in the tracking precision and any discriminator used for this purpose must have outstanding walk properties. Recovery from overloads and readiness to accept a second pulse are also important specifications but affect the rate limit rather than the precision of the detector.

In this design the discriminator performs the additional function of providing hit/nohit information to the storage logic. The on chip storage is data-driven and no operation takes place unless there has been a discrimi-

nator output.

The charge integrator indicated near the bottom of figure 1 is not present in any of the test chips which are presently being fabricated, but the addition of a charge measurement channel in parallel with the time measurement channel should not be difficult (for the case of a modest dynamic range of 7 to 9 bits).

5.2 Time measurement

The TVC is, as is indicated schematically, a simple current source that is switched into a storage capacitor. The detailed operation is such that the operating range of the TVC corresponds to 0.5 to 1.5 clock periods or 7.5 to 22.5 ns for a 15 ns clock period. Thus longer times (i.e. collision to first drifted electron time of 45 ns) must include a record of the crossing number as well as the *fine* time stored in the capacitor. This requirement is met by the clock counter in the upper left. This count (3 bits give a 120 ns range) is stored in a digital register at the same logical address as the analog storage element.

5.3 Trigger Delay Storage

Local data storage for several μsec requires a mechanism to ready new storage elements for additional hits. Thus the analog and digital time measurements must be advanced into a delay queue (as would a charge measurement if one existed) to await the level 1 trigger decision and a new storage element must be readied. The simplest structure that one might imagine would be an analog shift register (for example a CCD) coupled with a digital shift register. Unfortunately a shift register grows in length directly with the trigger delay time, 64 elements would give about a microsecond at SSC clock rates and 192 elements would be neccessary for three microseconds of delay. In addition shift registers run whether or not there is data present and a running shift register consumes power (and CCDs consume rather a lot of power). Since we already have a discriminator pulse to tell us that a hit has occurred, we can be somewhat sneakier and advance our queue only on a

hit and tag the storage element such that we can recover the data a fixed time from the initial hit.

It is still necessary to keep temporal track of one bit (the discriminator), but that can be done in a memory with a single address counter for input at N + 1 and output N clocks away at stage N - such a memory and counter scheme keeps only four flip flops going at 60 MHz rather than 64 or 192. If the output of this delay register is continuously compared with the level 1 trigger input then any coincidence can be used to advance the data from the level one queue to the level two queue, if there is no level 1 trigger when a given discriminator pulse comes out of the delay register then the storage elements can be recycled to the front of the level 1 queue. Figure 2 shows the five different states that a given storage element (capacitor) can move through.

Similarly the level 2 queue must store information for periods on the order of tens of microseconds. Clearly simple shift registers are not appropriate at this point, and in addition, the level 2 trigger will probably include iterative and branching logic so that it would not be possible to specify a fixed time to complete the level 2 decision. Thus a queue is necessary such that items are entered as level one triggers and hits occur and where items are removed (to a digitizing and readout queue) as the level 2 decisions becomes available. As long as the level 2 decisions come in the same order (are monotonic) as the level 1 triggers, then this scheme can be implemented with only two counters and a tag to indicate whether or not a given channel had data associated with a given level 1 trigger.

In the circuitry presently under fabrication, charge is not actually moved from capacitors of the level 1 queue to capacitors of the level 2 queue. In order to avoid the inherent errors and offsets associated with charge movement, we have opted to try a scheme where only an identifying tag is changed on the storage location. Thus the transfer can be done very quickly and it should not introduce any analog errors.

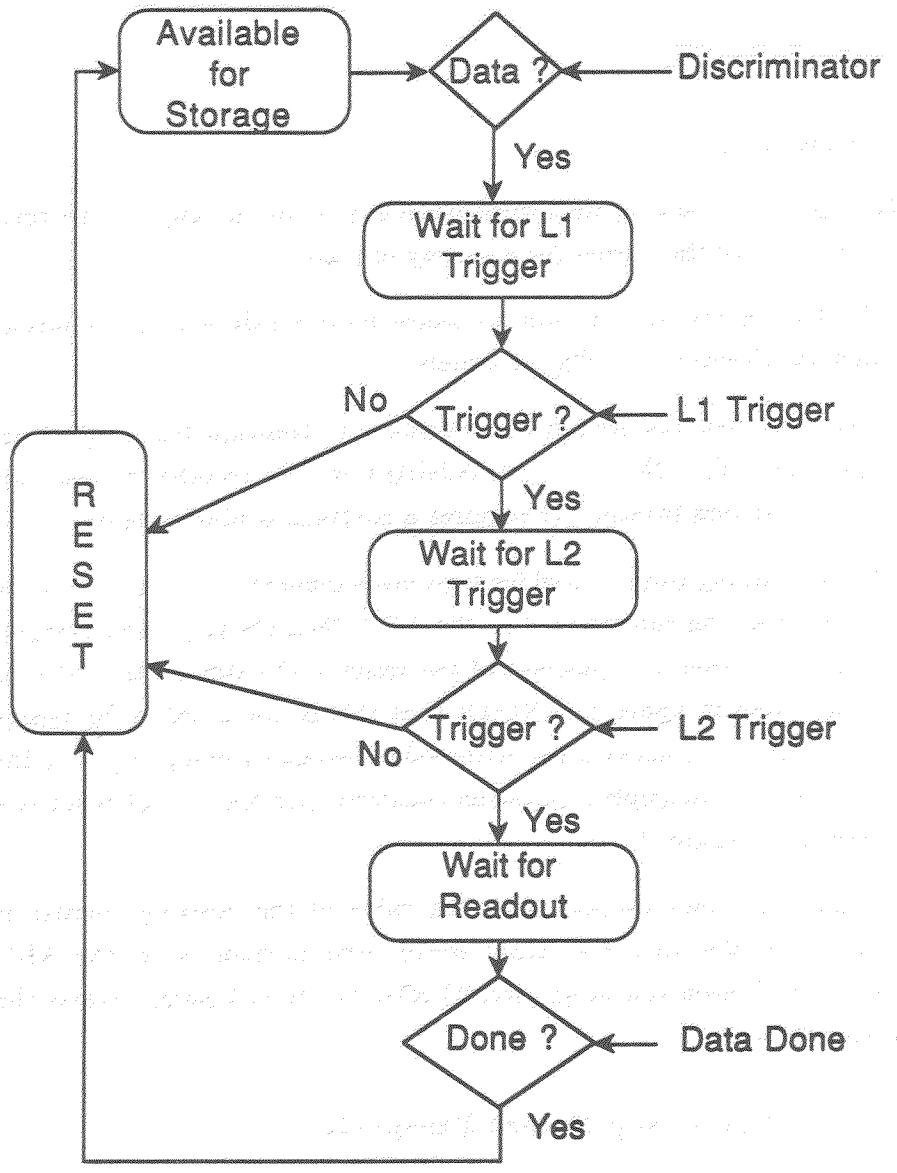

Figure 2: Storage Element State Diagram

5.4 Digitization

Digitization of the analog time measurement is done directly on the same chip that provides the queues for a variety of reasons.

- Analog signals sent off chip are much more sensitive to noise pickup and interference than digital signals.
- Analog signals require much more power to transmit than digital signals especially if the duty cycle is fairly low if for no other reason than that an analog transmitter requires a continuous bias current.
- If the charging current used for time measurement is ratioed on chip to the discharging current used in the ADC, then the time measurement is, to first order, independent of the value of the storage capacitor as is indicated in figure 3. [NOTE that this is not possible for charge measurements where the capacitor values would enter directly thus the possibility of multiple calibration constants per detector element is a very real menace.]

The digitized data coupled with the value of the crossing counter is then made available to the external world some microseconds (the ADC is a simple Wilkinson run down circuit) after the level 2 accept starts the digitization process.

6 Present Status and Future Prospects

In addition to the original CMOS TVC design [10] a high speed low noise low power bipolar preamp and three stage shaper has been designed using the AT&T LA200 linear array [11] and is now being measured. A high performance discriminator is presently under design and may be ready for fabrication soon. A second generation TVC incorporating almost all of the

[10] A fast low power time-to-voltage converter for high luminosity collider detectors, A.E. Stevens et al., IEEE Transactions on Nuclear Science, **36**, p. 517, February 1989.

[11] High Speed Bipolar Integrated Circuits for SSC Applications, F.M. Newcomer et al., to be published in Nuclear Instruments and Methods, November 1989.

Figure 3: Charge and discharge TVC cycle.

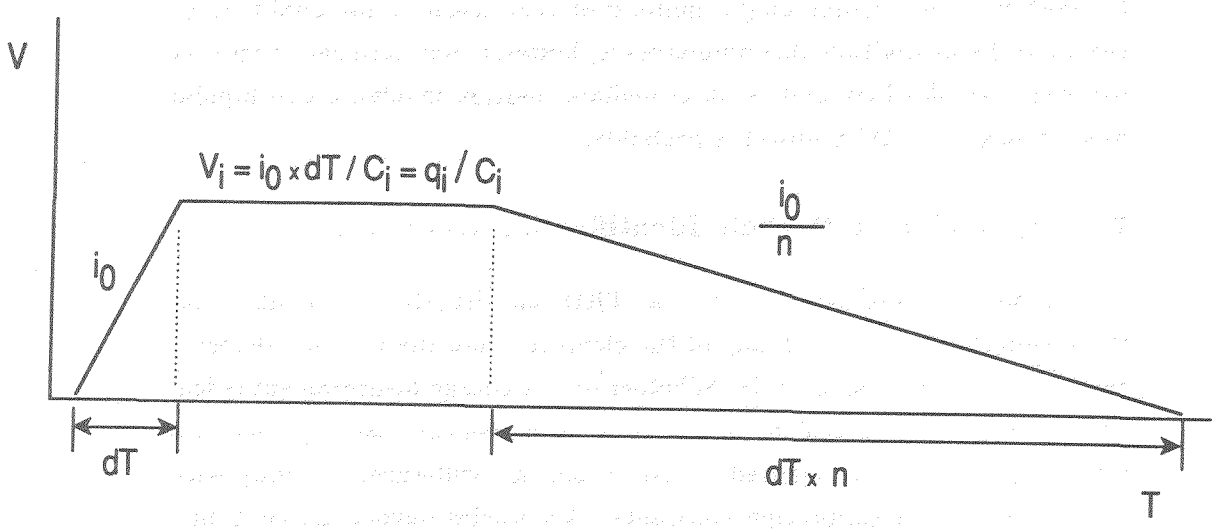

logic necessary to implement the two trigger queues and digitization queue is presently being fabricated and will be tested this Fall.

The bipolar elements promise to meet or exceed almost all of our original specifications from section 3 above. The only major shortfall is in the very important area of power where we still are about a factor of three away from our final goal. We expect to be able to close some of this gap by use of more advanced bipolar processes and test designs should be submitted late this Fall in a much higher speed process.

The TVC now being fabricated is designed to provide zero suppression, storage, trigger rejection, and on chip digitization. The trade off in this present design is not power but chip area. While this single channel device is about 3 mm square, we expect that a subsequent version will benefit both from more compact gate design and from fabrication in a somewhat finer process. It is reasonable to expect a factor of two to four compaction from these two effects which will bring the system areal density down to an acceptable value.

In a final production system, we envision a full custom bipolar chip feeding a CMOS chip a few millimetres away. Each chip would handle four to eight channels. Combining a number of very sensitive preamplifiers on the same die as multiple discriminators is, however, not necessarily an easy (or even feasible) task and an intermediate solution involving two bipolar objects and one CMOS object is probable.

7 Application to Particle Identification Detectors

For certain classes of detectors such as TRDs and RICHs it is possible that the architecture and even many of the elements from the tracking detector case will be directly applicable. Whether or not charge measurement is feasible using simple extensions of the time measurement case depends to a large degree upon the required accuracy and our willingness to cope with a large number of calibration constants. Accuracies beyond about 9 bits will probably require a dual scale approach, but that would not necessarily be difficult. The complexity and relatively large area associated with the present CMOS chip is related to the bookkeeping tasks, the storage capacitors and analog switches are neither large nor complex. The addition of a charge measurement section should not be exceptionally difficult. Conversely, if only hit/nohit information were important, the CMOS structure could be reduced to a less complex all digital device.

PAD READOUT TECHNIQUES

by

S. Dhawan

Yale University

FERMILAB E665 MUON SPECTROMETER

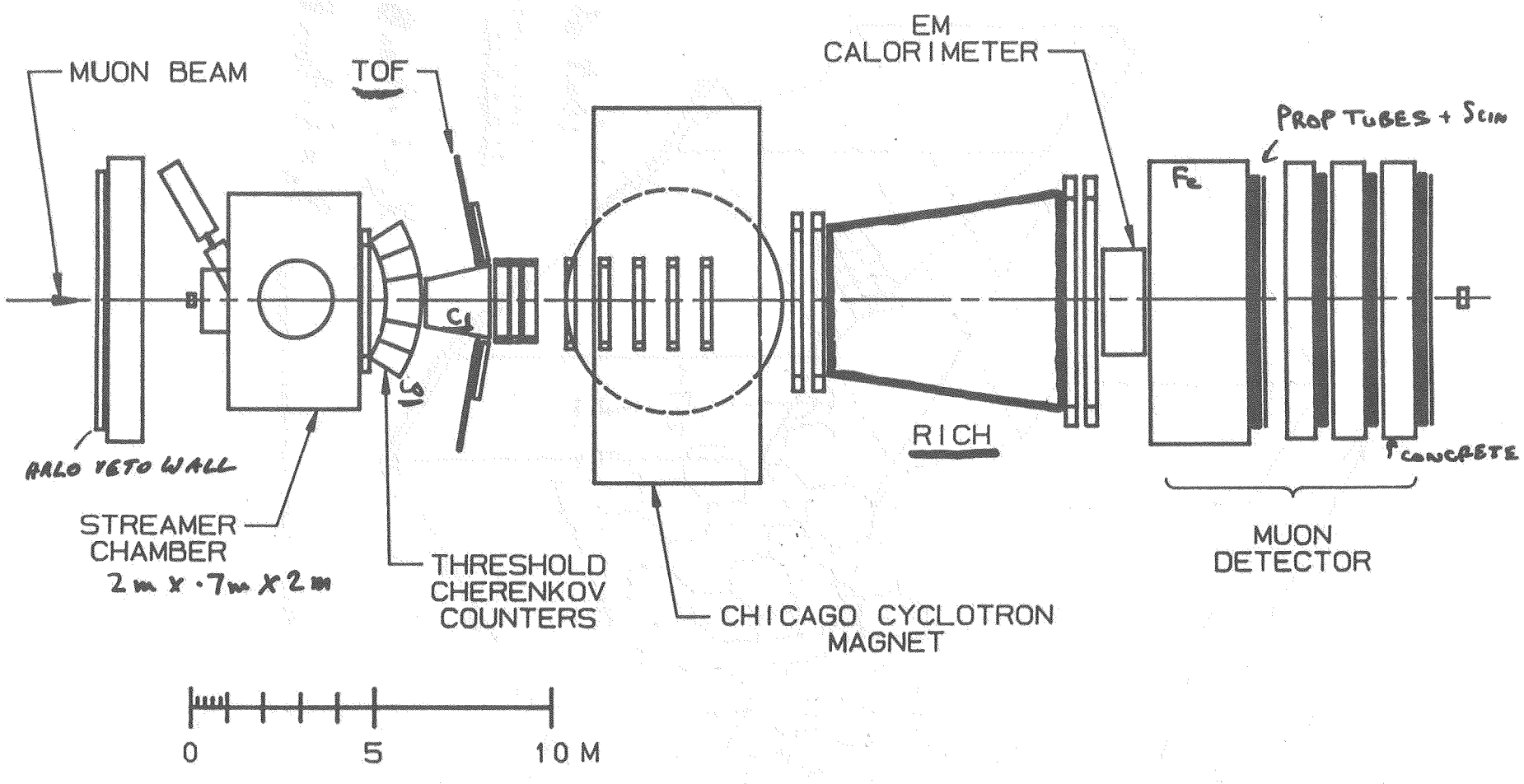

10/19 13.47.43 96115

LARGE COLLABORATION
US & EUROPE

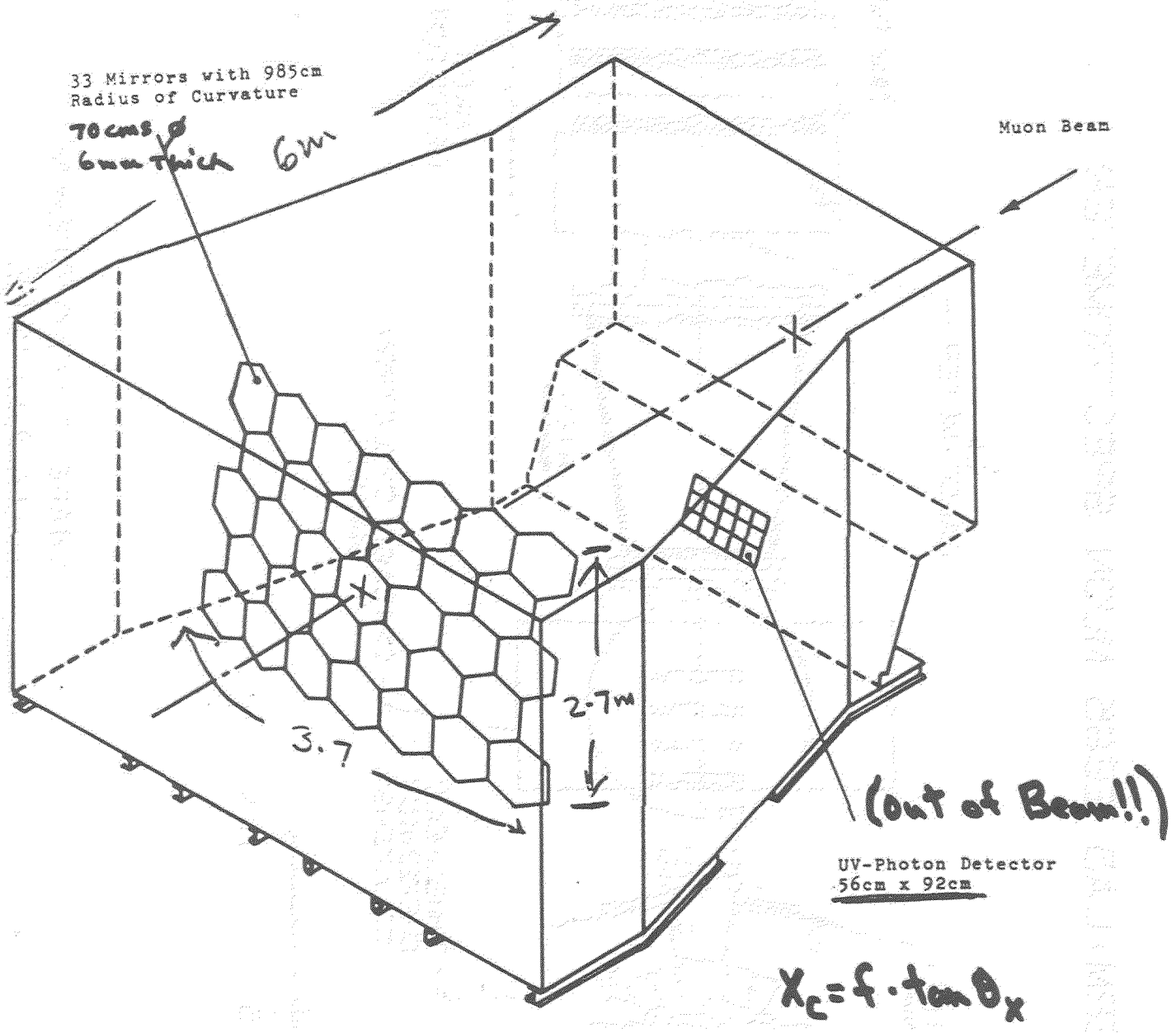

Fig. 1. E665 Ring Imaging Cherenkov Counter

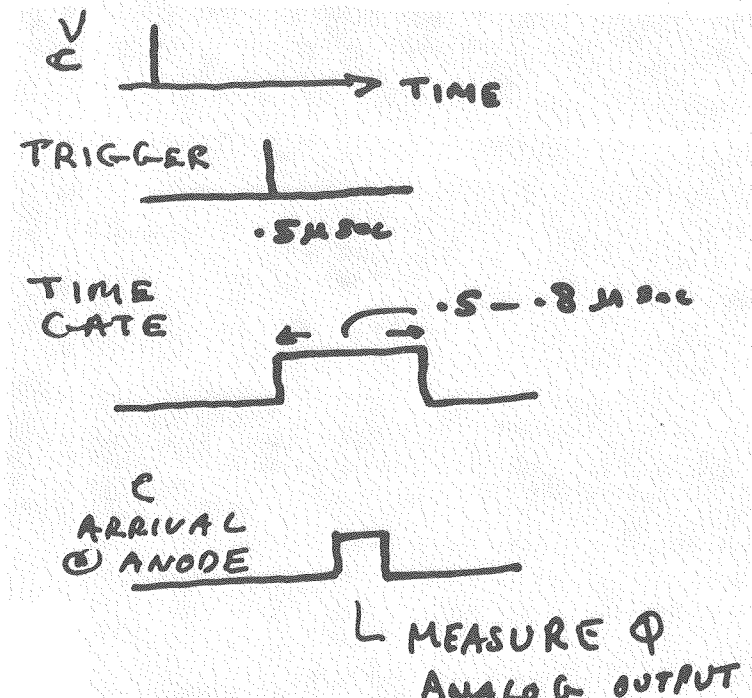

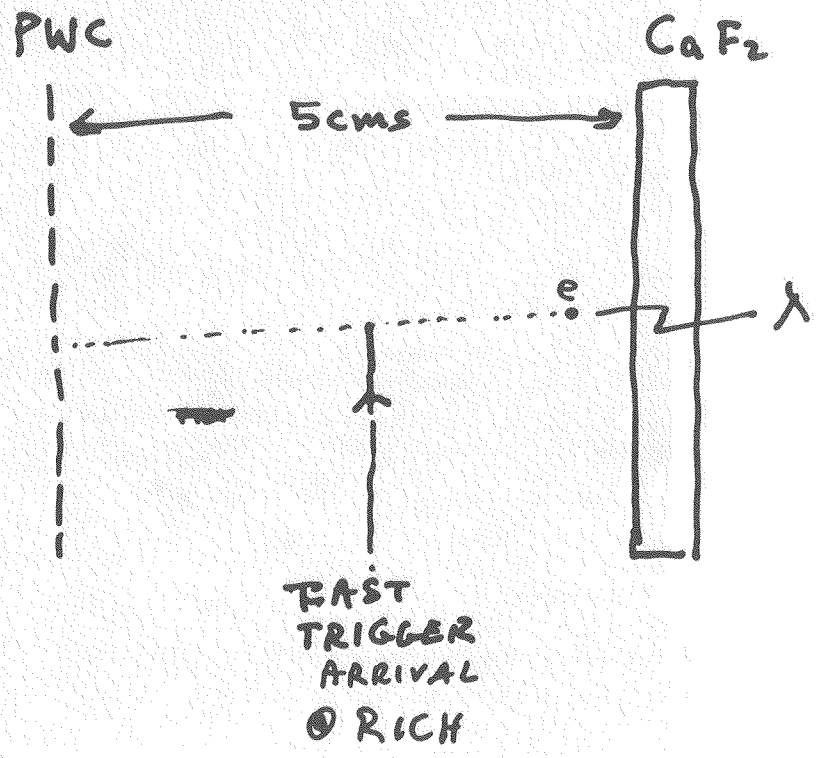

TIME DELAY IN GAS

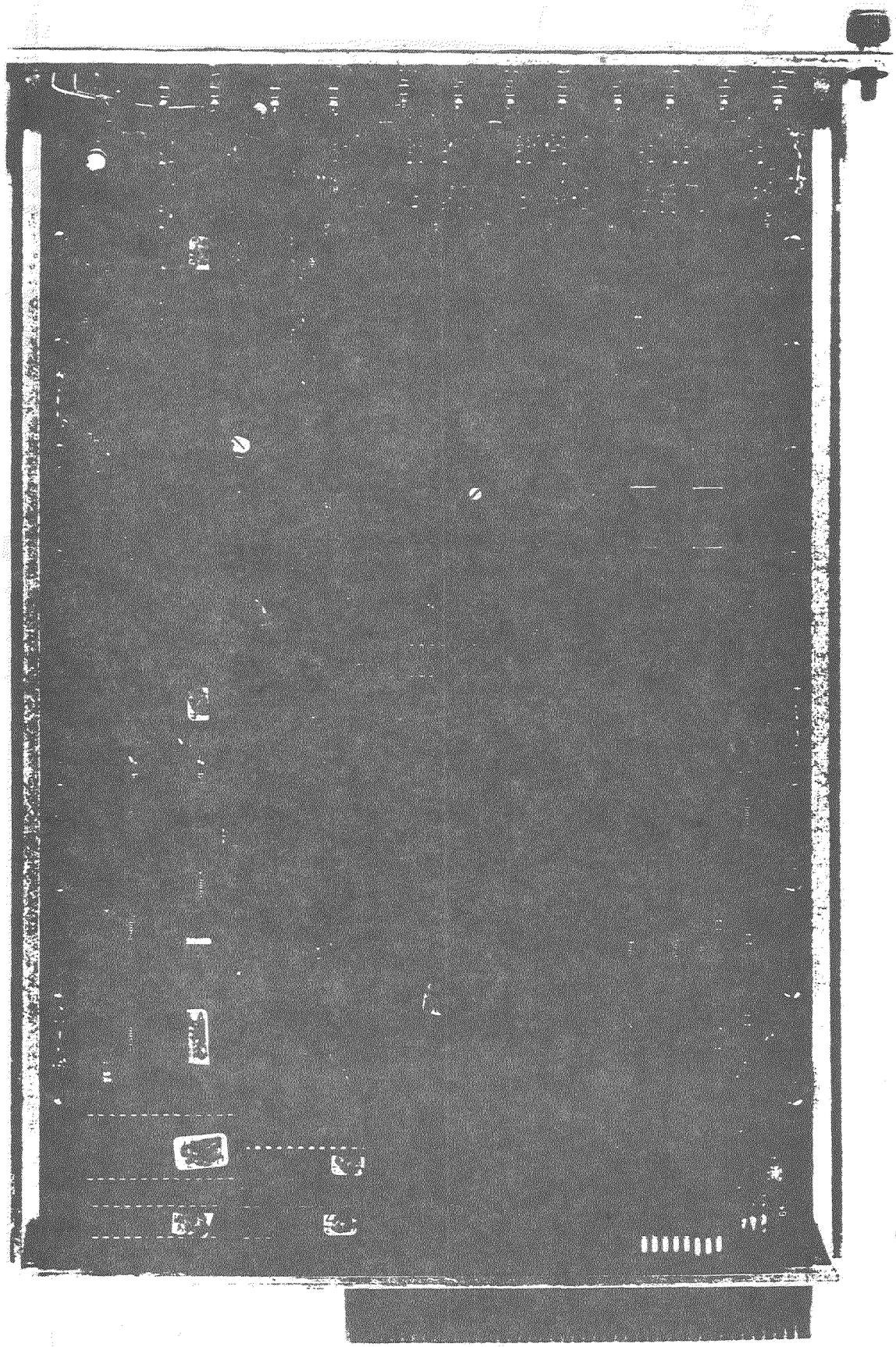

C.L.K. Logic

8 Pulses

PEDESTAL DRIFT = $\frac{1}{80}$ Ch IN 14 HOURS

Σ 1152 PADS

24 CARDS

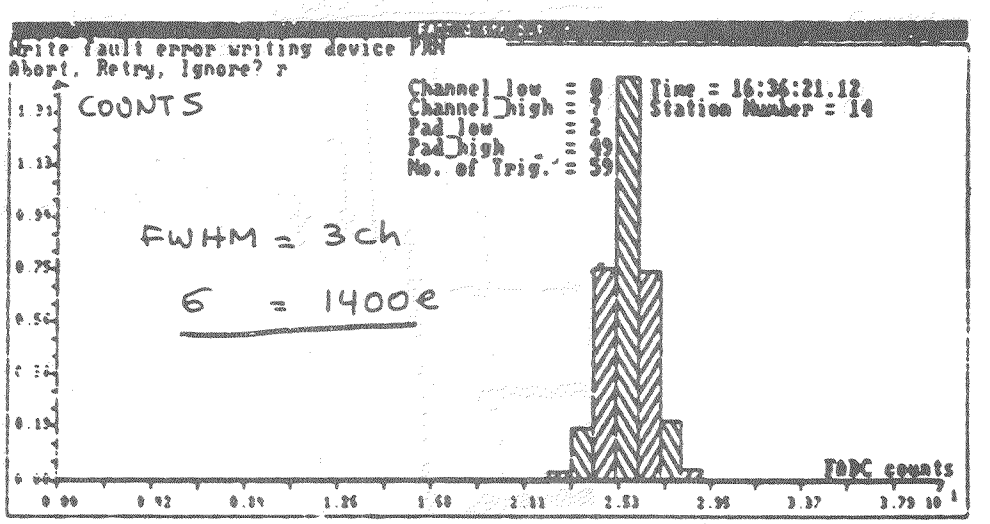

→| FW = 7ch |← PULSE HEIGHT

Σ 480 WIRES

20 CARDS

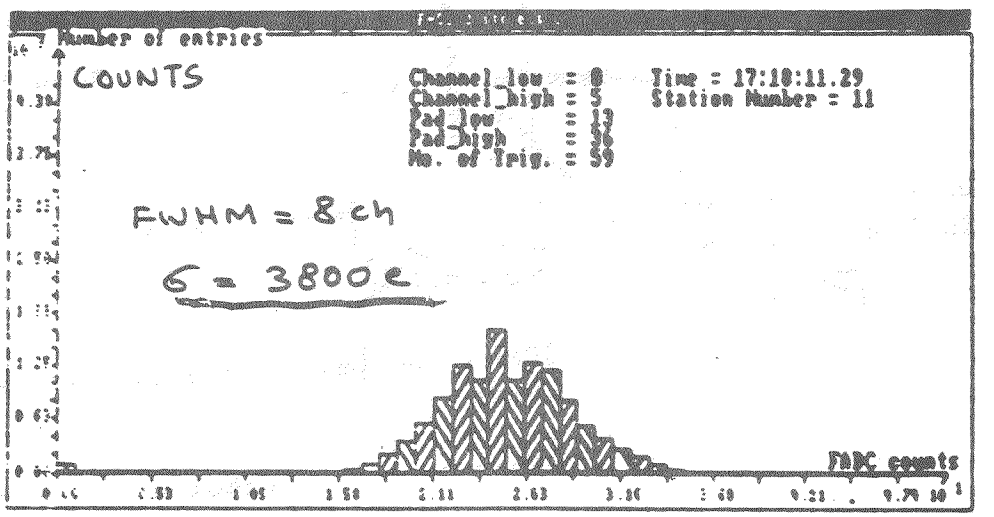

|← FW = 19 ch →| PULSE HEIGHT

1 Ch = 1100 e

= 3mV

1 fc = 6 ch

μPLEX · 18 mV/fc

NOISE WITH HV ON MWPC

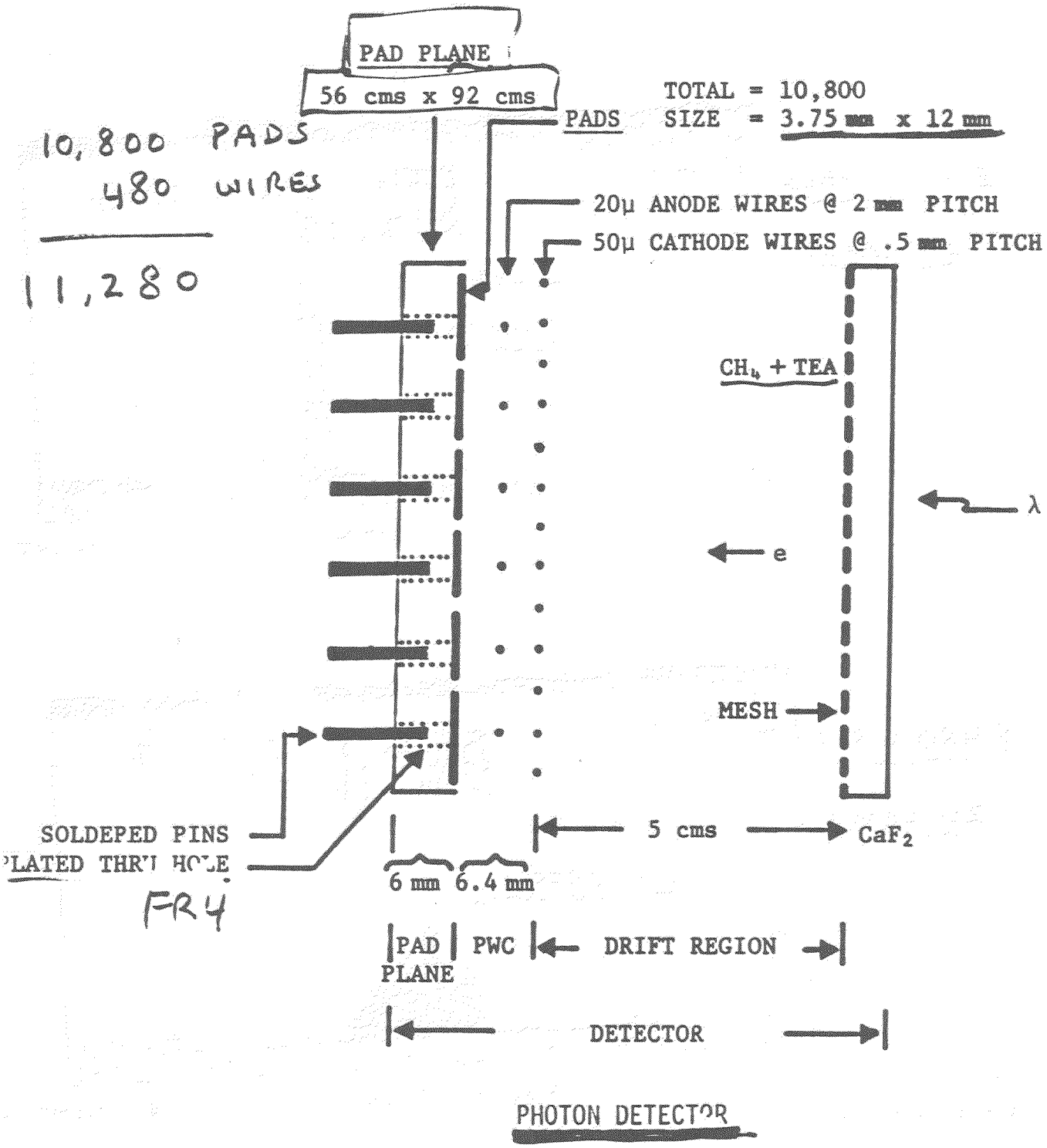
PAD PLANE
56 cms x 92 cms
PADS
TOTAL = 10,800
SIZE = 3.75 mm x 12 mm
10,800 PADS
480 WIRES
11,280
20μ ANODE WIRES @ 2 mm PITCH
50μ CATHODE WIRES @ .5 mm PITCH
CH_4 + TEA
λ
e
MESH
SOLDEPED PINS
PLATED THRU HOLE
FR4
5 cms
CaF_2
6 mm
6.4 mm
PAD PLANE
PWC
DRIFT REGION
DETECTOR
PHOTON DETECTOR

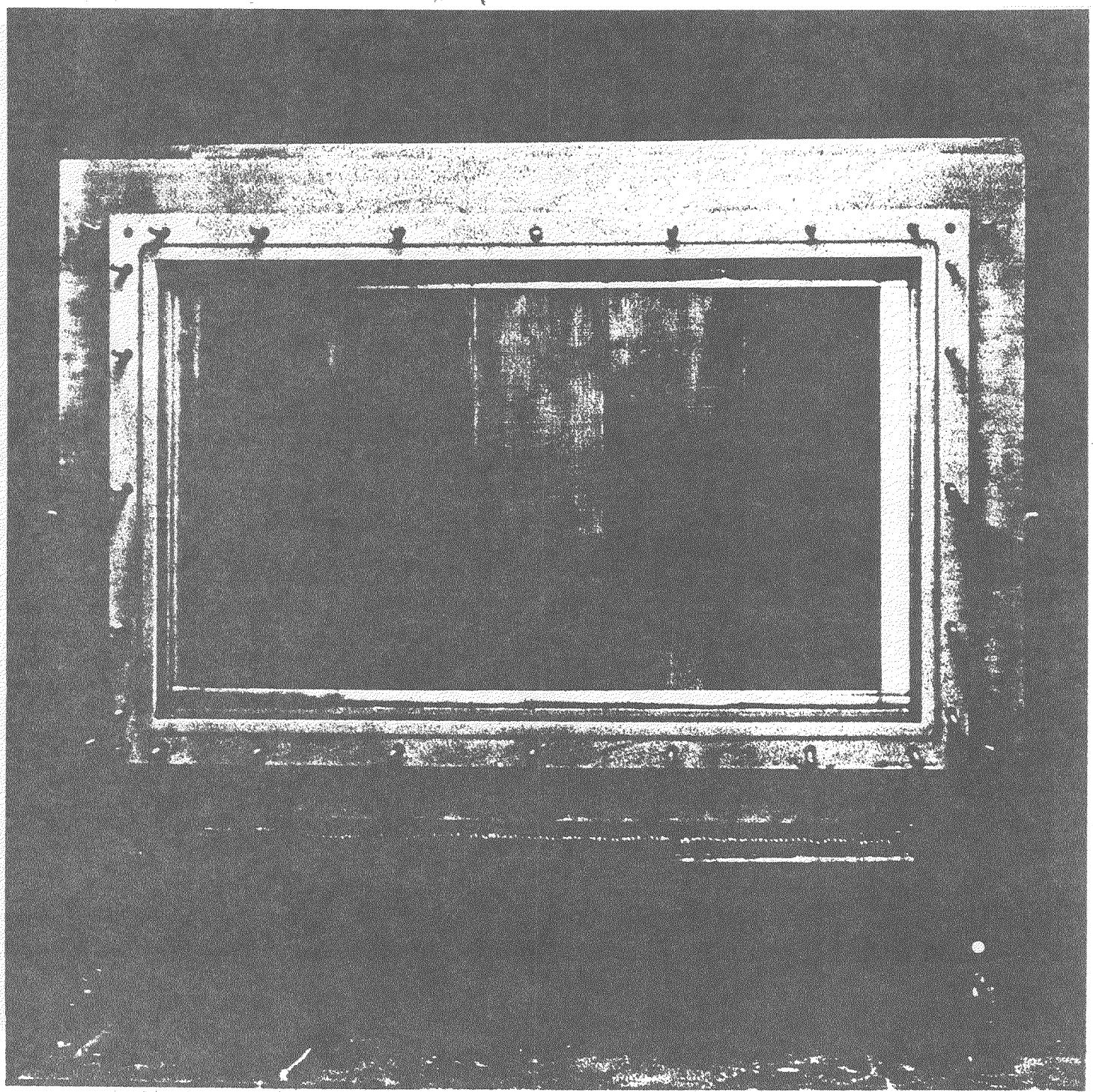

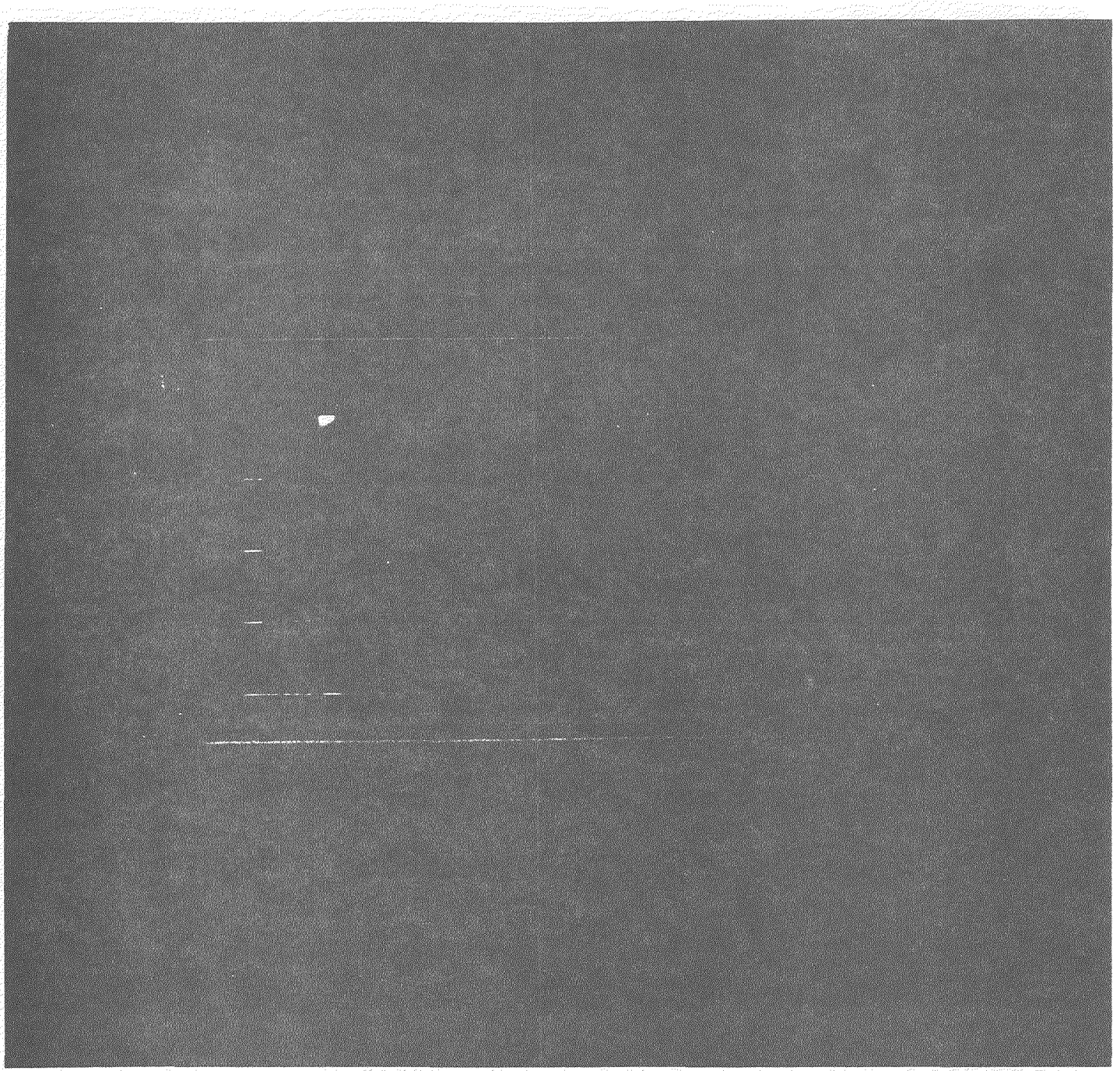

87-367-6

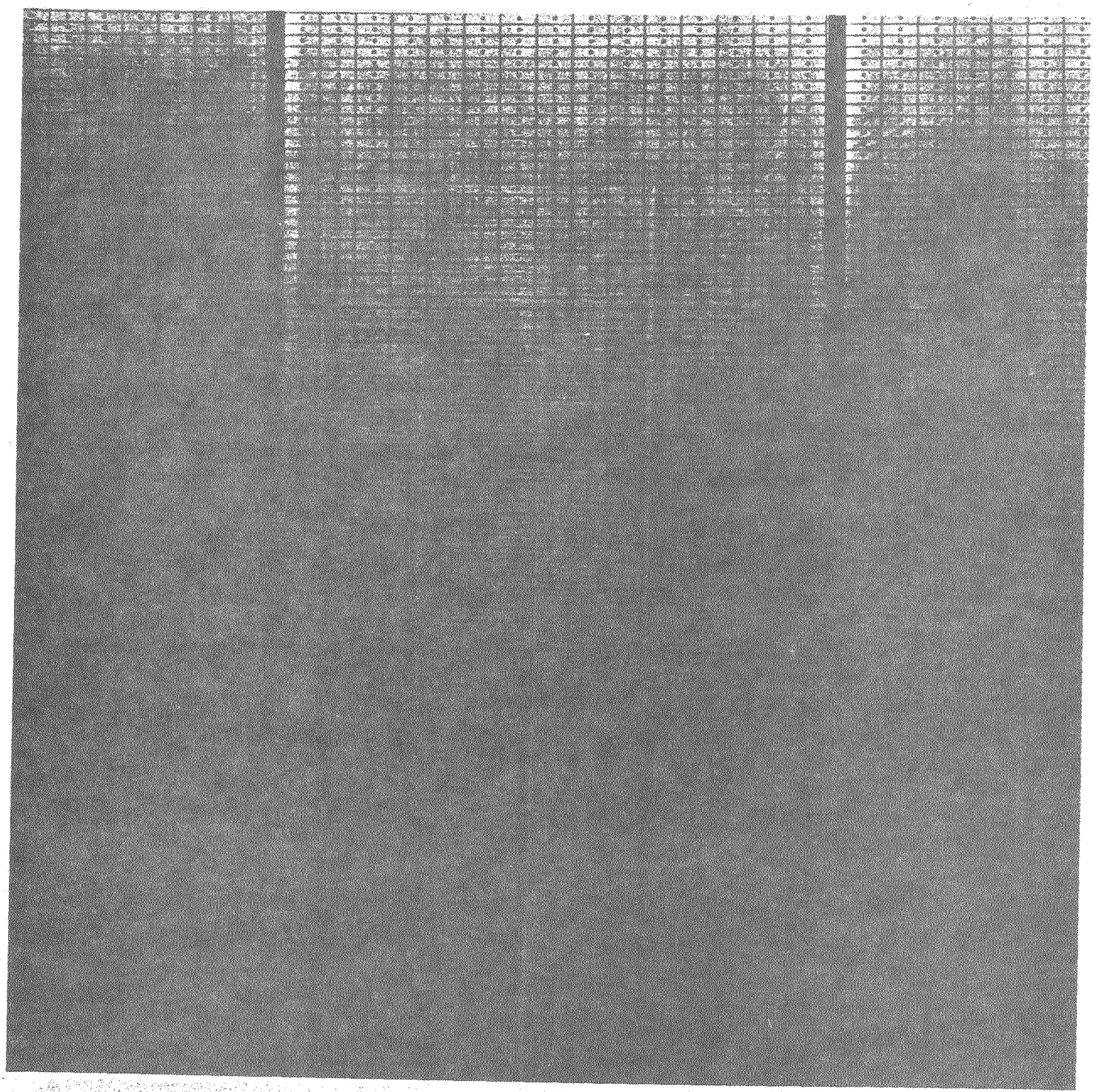

TILE 7" X 7" TOTAL 15 TILES

720 PADS / TILE

Sys Philosophy

NO CABLES!

Reduce as much as possible

Previous Saved Pwr

MOUNT ALL ELECTRONICS ON PAD PLANE

NO Preamps / Amps

NOISE < 2000 electrons

SIMPLICITY FOR USER, interconnection

Internally can be Complex

COST GOAL $14/ch

Explored Semicustom I.C's.

FIXED TARGET

CUSTOM I.C. DEVELOPED FOR SI STRIP DETECTORS

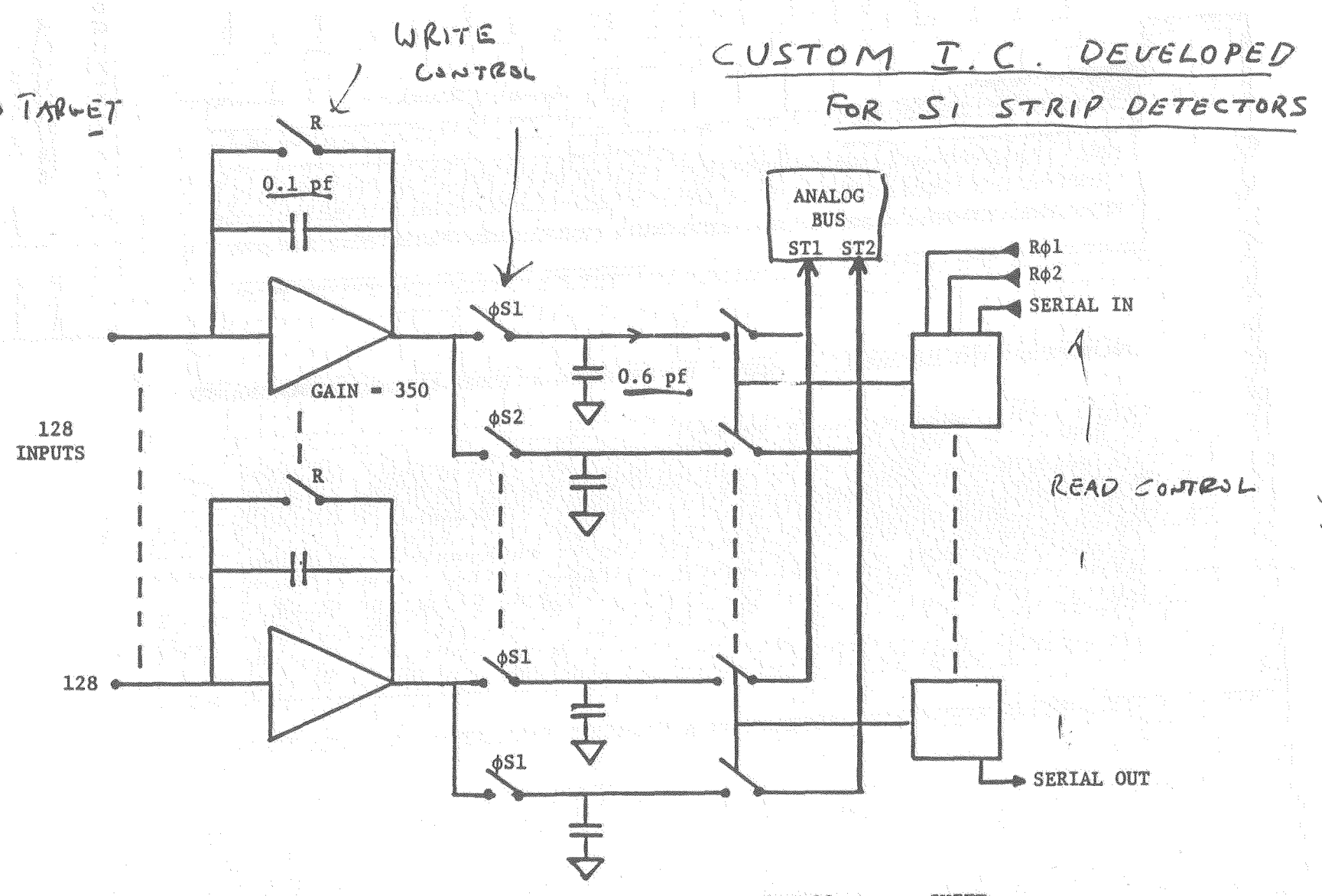

BASIC MICROPLEX CHIP

USE 48

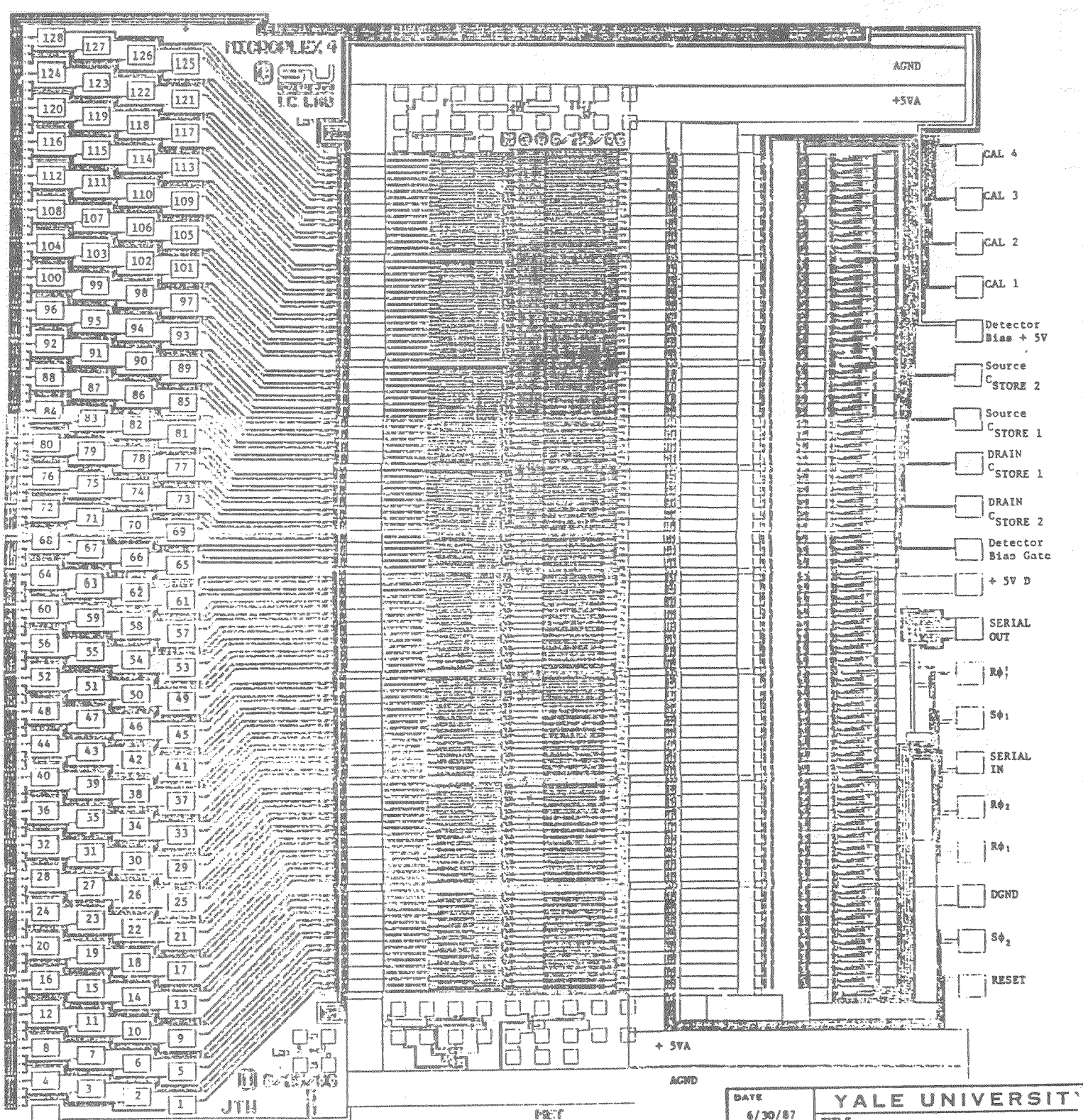

DATE 6/30/87	YALE UNIVERSITY	
PREPARED	TITLE MICROPLEX CHIP PINOUT	
CHECKED	GROUP EPI 665	DRAWING NO.

INPUTS

9V → CONTROL, POWER, OUT

1fc — 11 —

11ff

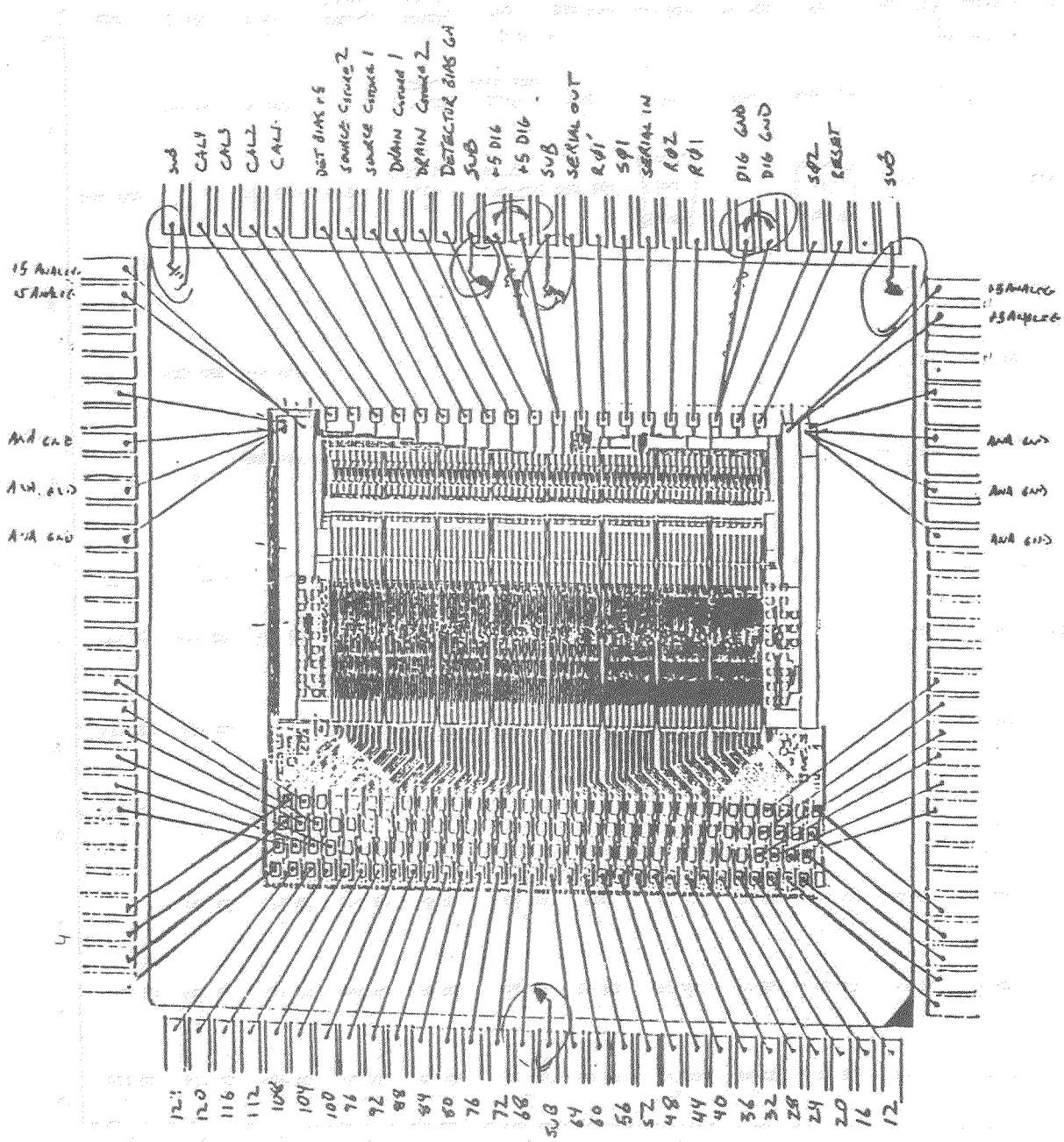

BONDING DIAGRAM

121 PGA

REV. B 2/10/87 DR

121 PIN PGA FR-4

3/5/87

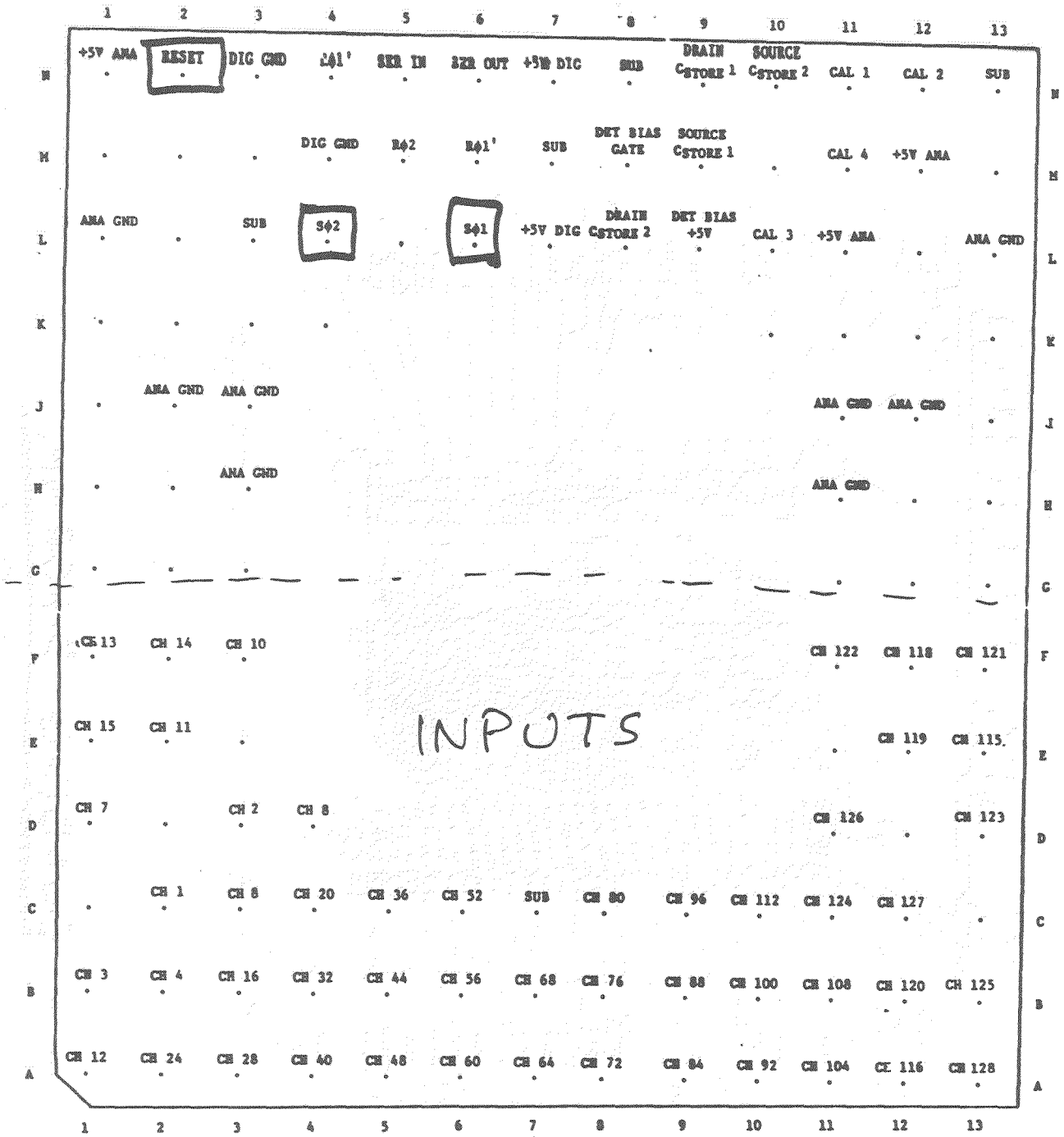

Pin Spacing = 0.1"

Rev. B: 121 pin PGA

Connector to RICH Pad

Scale 4:1
1" = 0.250"

Channel numbers are uplex channels, not pad numbers

VIEW FROM SOLDER SIDE

DATE 2/10/87	YALE UNIVERSITY	
	TITLE MICROPLEX PINOUT REV. B - 121 PIN PGA	
PREPARED		
CHECKED	GROUP EPI E665	DRAWING NO.

- WATCH HOW TRACES RUN ON PACKAGE
- 48 PIN CERAMIC NOT FUNCTIONAL

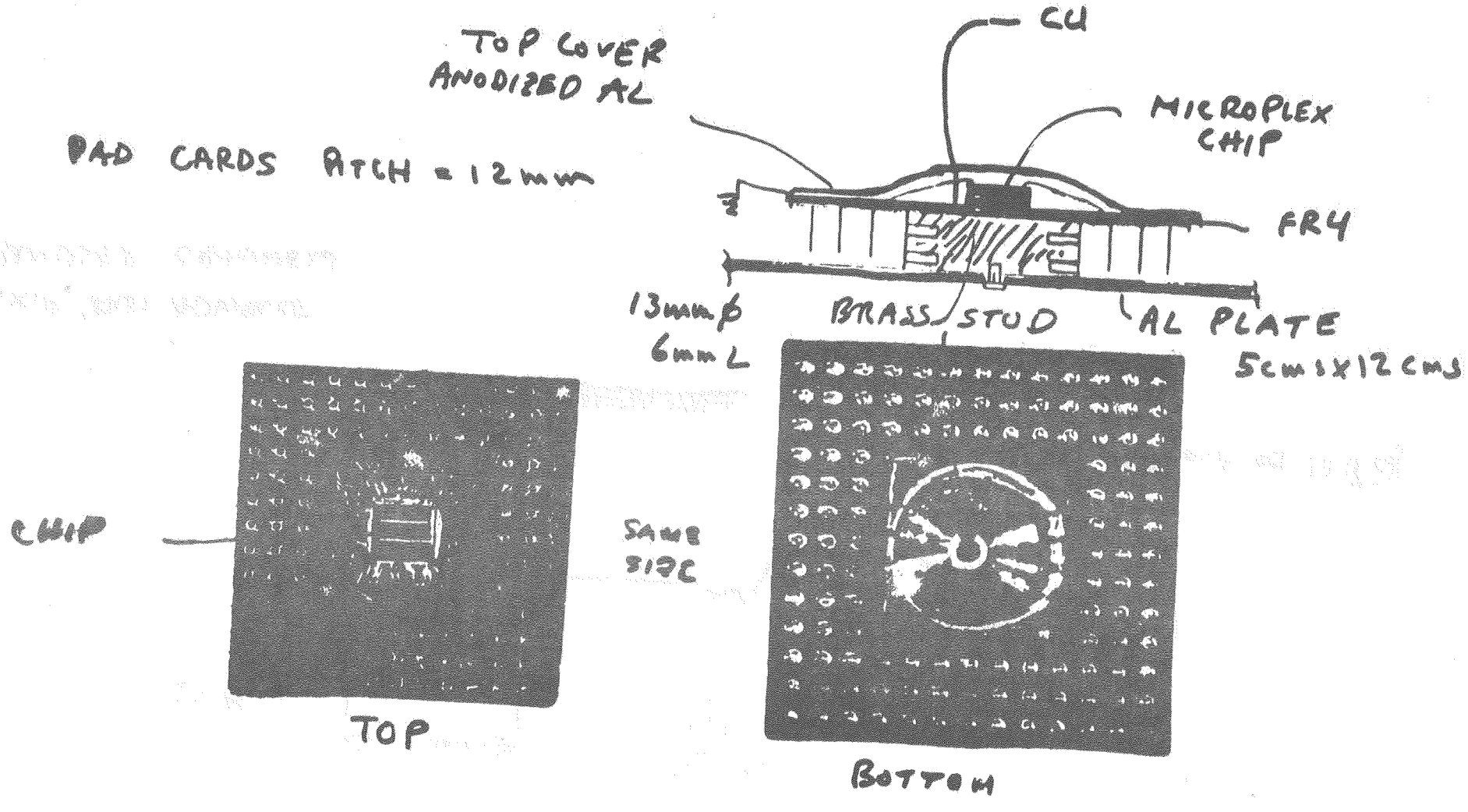

121 PIN - PIN GRID ARRAY

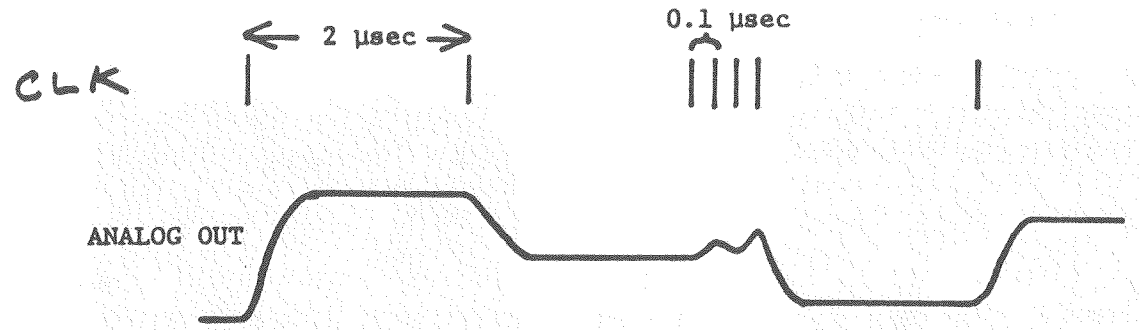

SERIAL ANALOG

USE 48 out of 128 ch

SKIP/FAST ADVANCE
UNUSED CHANNELS

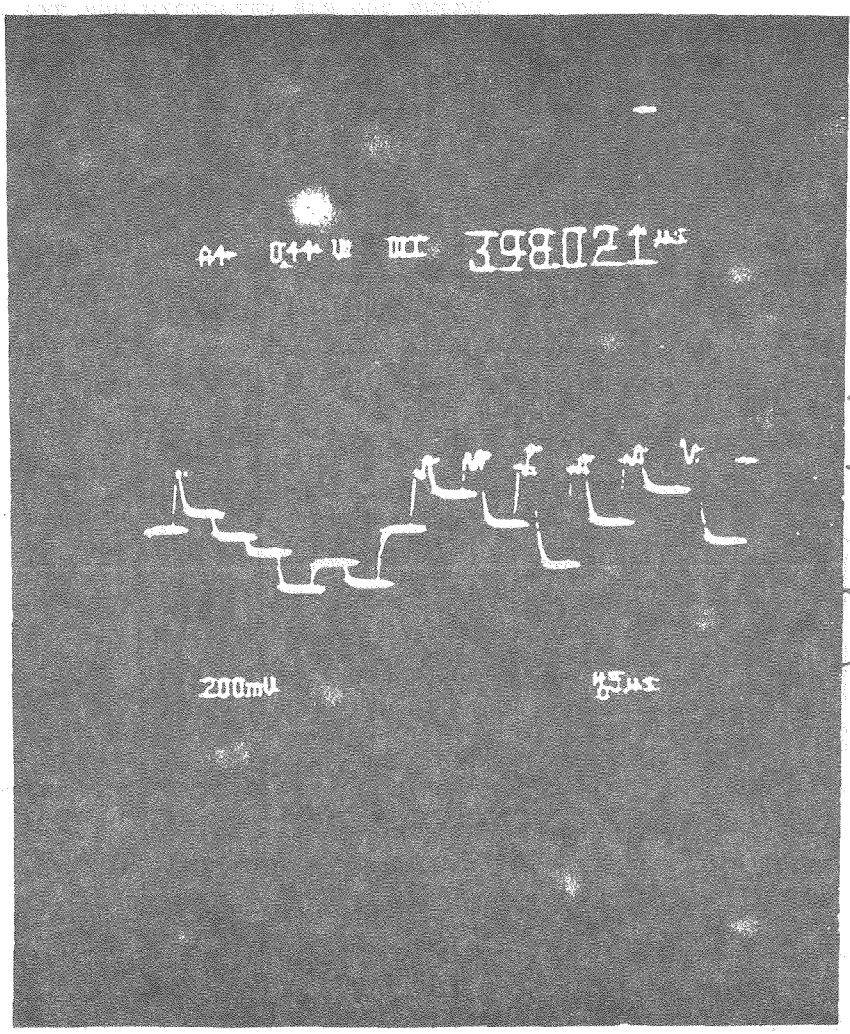

20 fc

FULL SCALE

40 fc

- Q INJECTION C
- BONDED WIRES PICK UP FROM CLOCK

PEDESTAL VARIATION

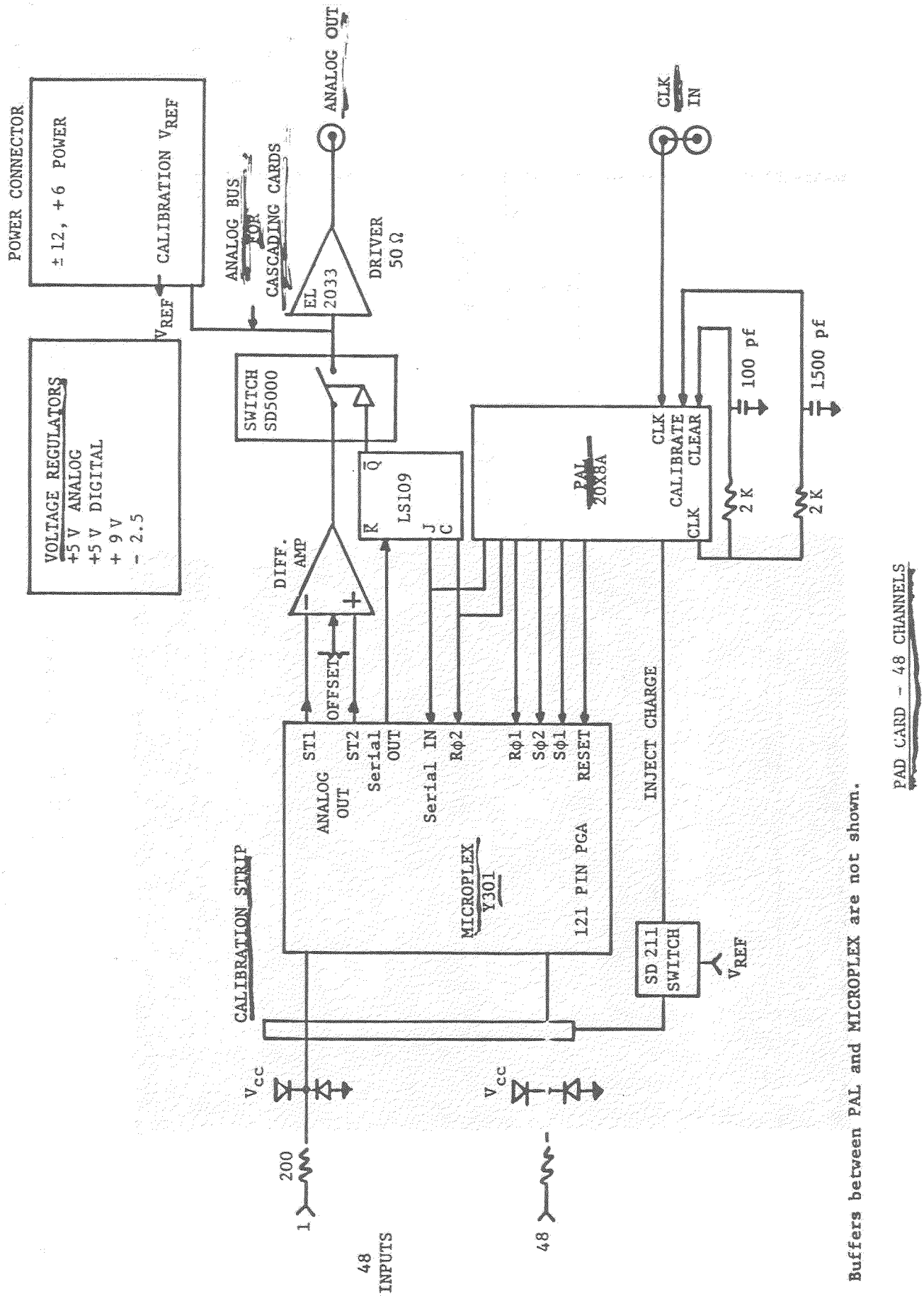

Buffers between PAL and MICROPLEX are not shown.

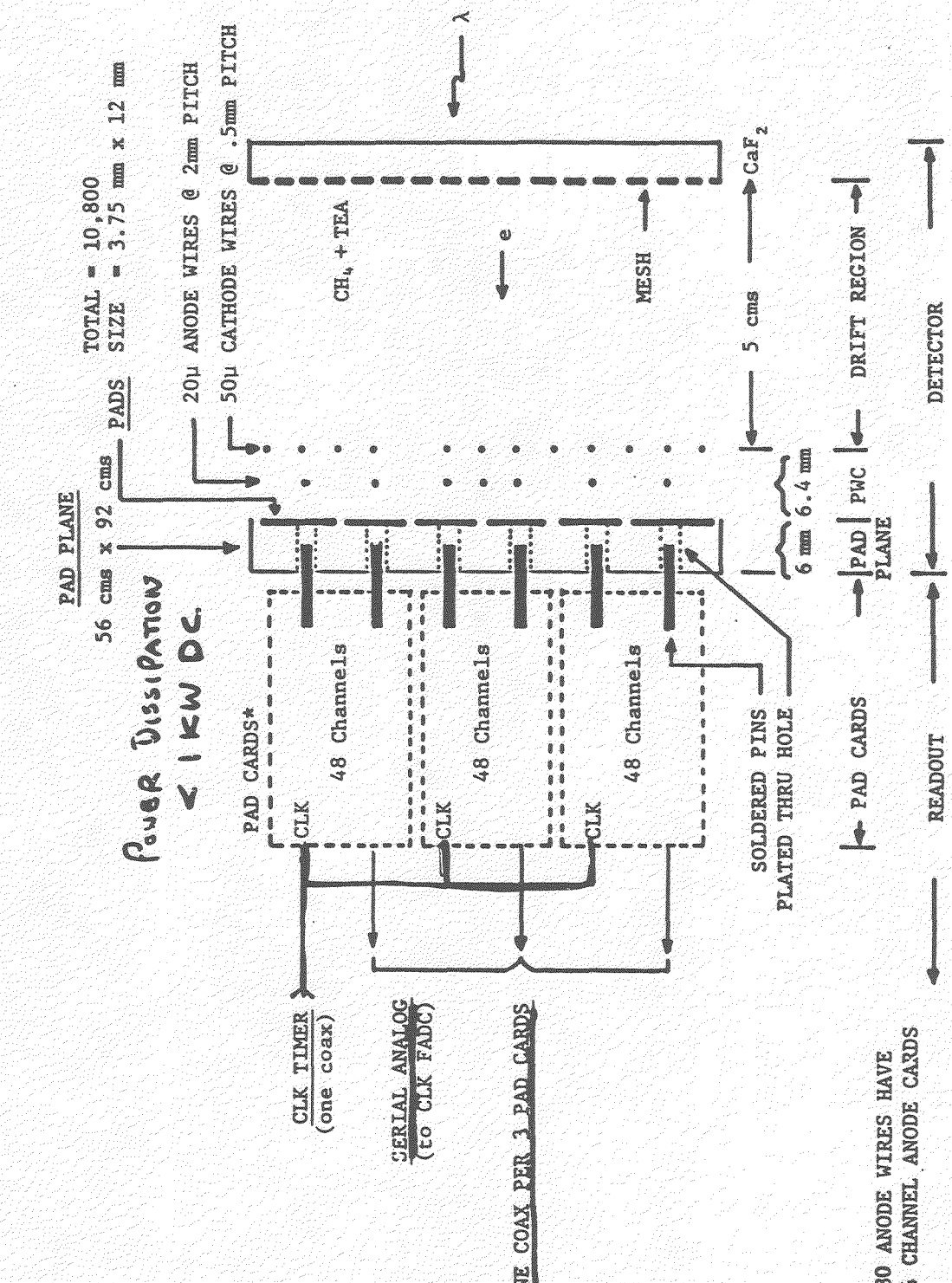

PHOTON DETECTOR AND PAD READ OUT

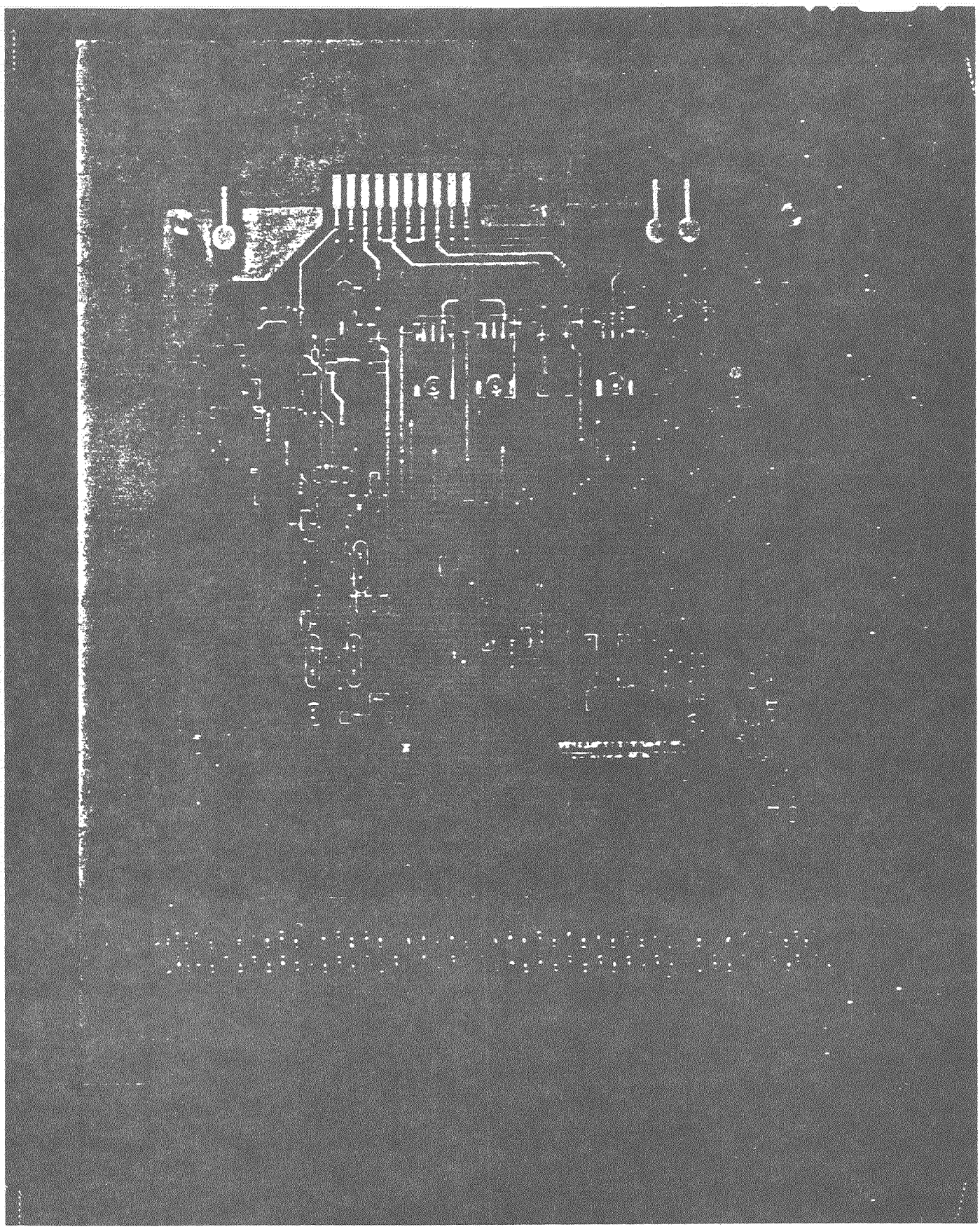

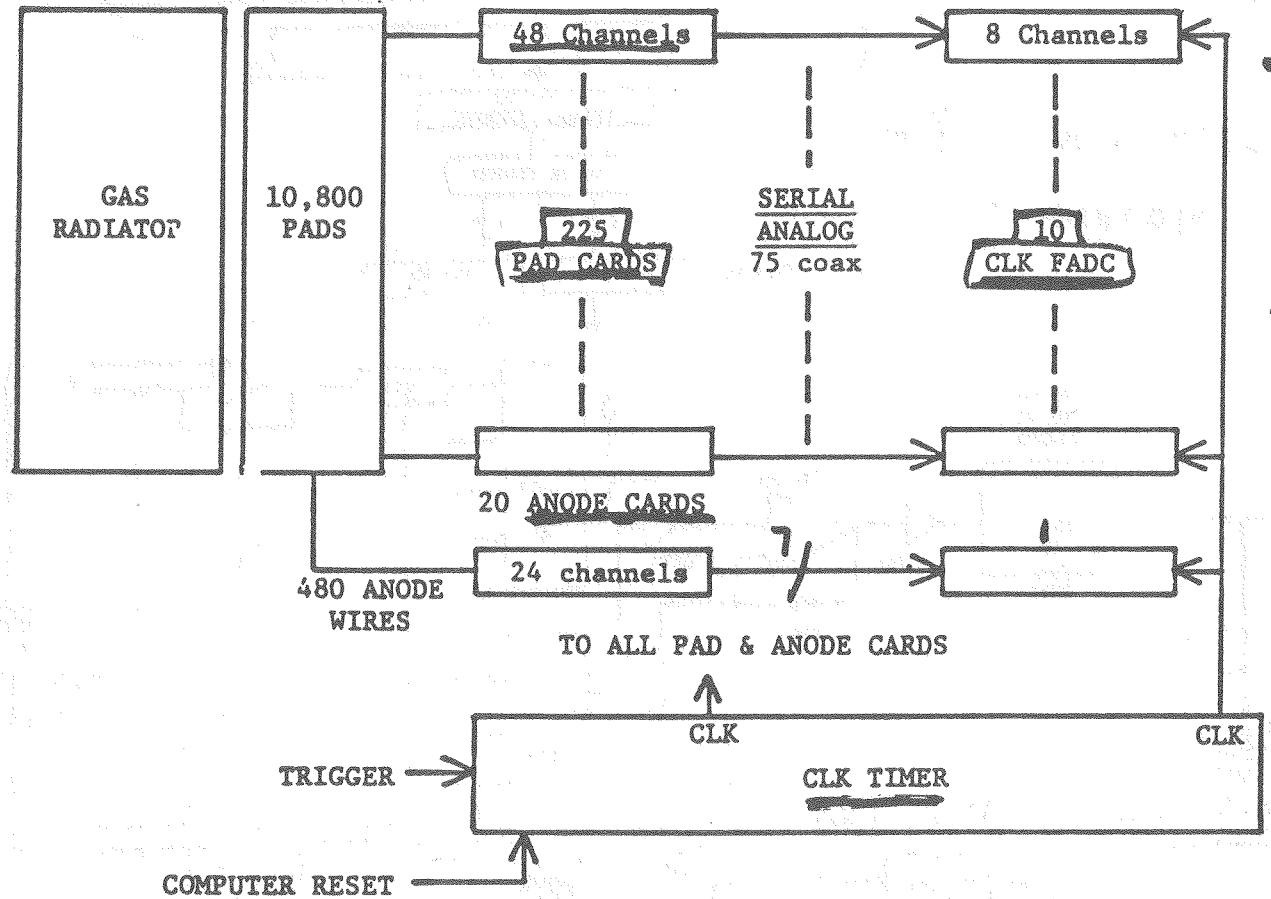

SYSTEM BLOCK DIAGRAM

SPARSE DATA SCAN

- ANALOG PED SUB FOR EACH ch
- 8 BIT FADC
  LEVEL → COUNT 25
- THRESHOLD
- HIT LIST WITH
  PULSE HEIGHT
  & PAD ADD.

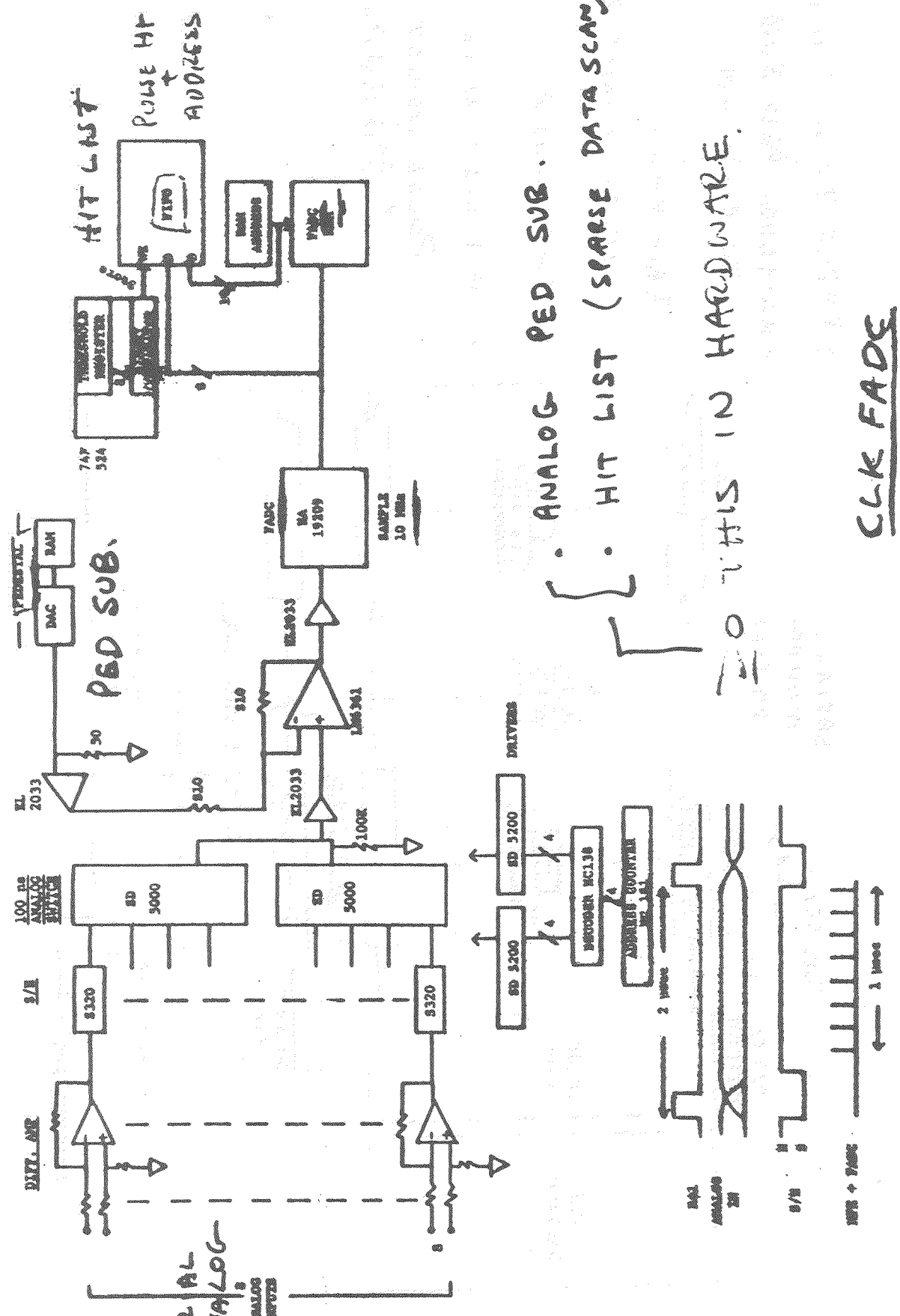
HIT LIST
PULSE HT + ADDRESS
PED SUB.
SERIAL ANALOG
. ANALOG PED SUB.
. HIT LIST (SPARSE DATA SCAN)
20 BITS IN HARDWARE.
CLK FADC

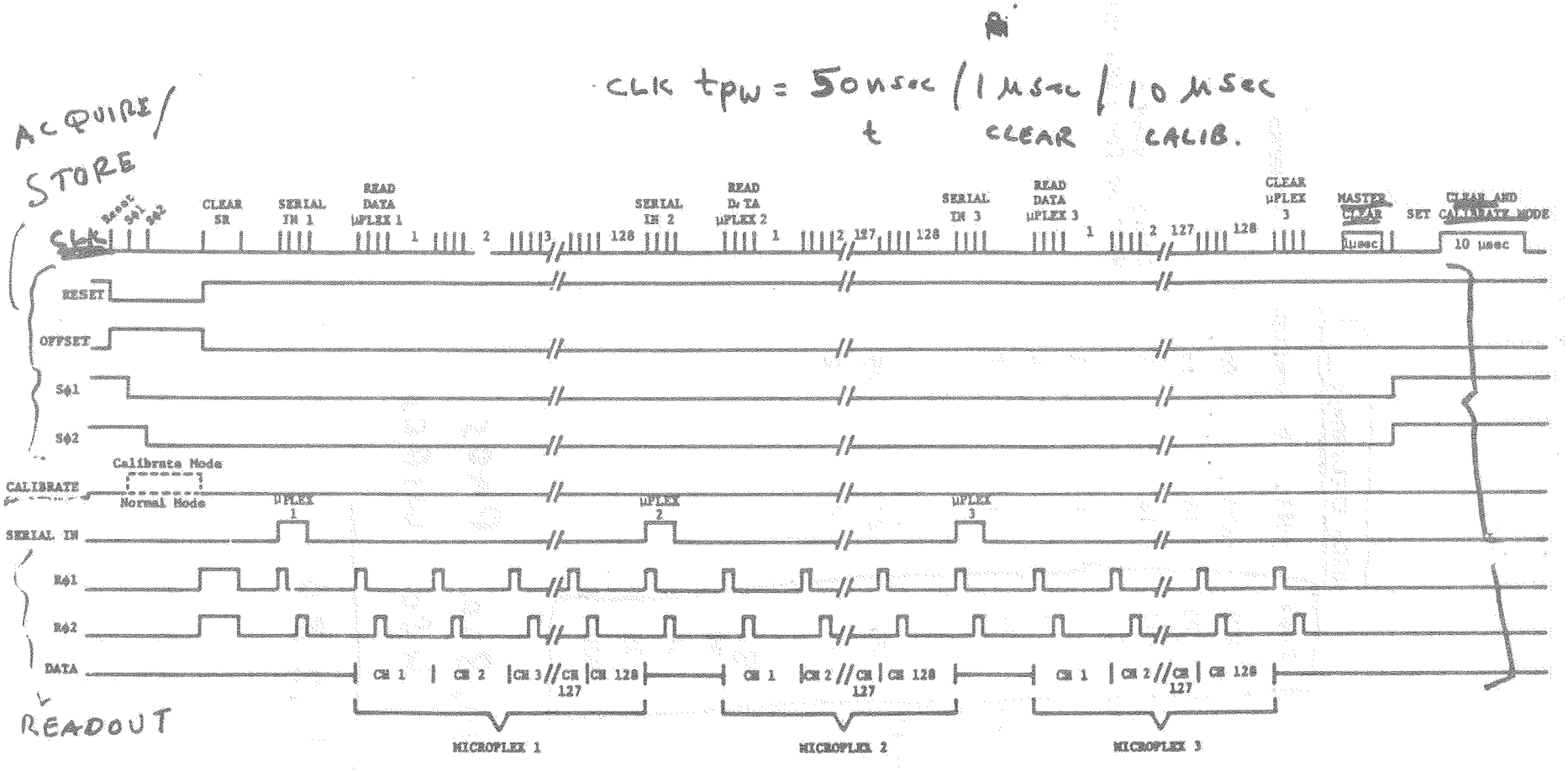
ACQUIRE/
STORE
CLK tpw = 50 nsec / 1 μsec / 10 μsec
t CLEAR CALIB.
CLK
RESET
OFFSET
SΦ1
SΦ2
CALIBRATE
SERIAL IN
RΦ1
RΦ2
DATA
CLEAR SR
SERIAL IN 1
READ DATA μPLEX 1
SERIAL IN 2
READ DATA μPLEX 2
SERIAL IN 3
READ DATA μPLEX 3
CLEAR μPLEX 3
MASTER CLEAR
1μsec
CLEAR AND SET CALIBRATE MODE
10 μsec
Calibrate Mode
Normal Mode
μPLEX 1
μPLEX 2
μPLEX 3
CH 1
CH 2
CH 3
CH 127
CH 128
MICROPLEX 1
MICROPLEX 2
MICROPLEX 3
READOUT

CLK TIMING

Sept. 11, 1987
Yale University

RICH ELECTRONICS

	Item	Need	Built	@ Fermilab	Remarks
I.	Pad cards	225	225	80	
	Anode cards	20	16	14	
	CLK FADC	11	12	8	fully tested - waiting for FIFO chips
	CLK Timer	1	4	1	
	T^2L Fanout	1	1	0	
	T^2L Line receiver	1	1	1	
II.	Power Cables (9 pins/cable)				
	Pad cards	25	27	25	
	Anode cards	2	2	2	
III.	LEMO Cables	82			
	25'	~~75~~			
	3'	75			
	15'	15			
	2"	225			

10,800 PADS
480 WIRES

11,280

PRODUCTION COST

		UNIT Cost $	Number of Channels/Unit	Cost per Channel $
A.	Microplex (48 channels)			
	Silicon	3	48	.06
	Packaging	15	"	.31
B.	Pad Card (48 channels)			
	Components	48	"	1.00
	P.C. Board	19	"	.40
	Assembly	28	"	.58
C.	CLK FADC		1,152	
	Components	601	1,152	.52
	P.C. Board	75	"	.06
	Assembly	80	"	.07
	CAMAC crate slot	150		
D.	Power			
	Cables	45	432	.10
	Power Supplies	5,902	11,280	.52
	90 Coax Cables Runs @36	2,000	"	.18
E.	CLK Timer & Misc.	1,000	"	.09

'System Cost per Channel = $ 4.00

Ratio of system Cost/Silicon Cost = 67:1

PAD PLANE COST

		Cost/PAD
PC BOARDS	5x300 = $1500	13¢
AU	x500 = 2500	22¢
	PINS	19¢
PINS, TACH TIME TO CHECK ALL HOLES SOLDER, RECHECK	= $8000	~~22~~ 53¢

TOTAL COST / PAD $1.07

STATUS

- COMPLETED OCT 87

  TOOK DATA TILL FEB 88

  NEXT RUN FALL 89

- HARSH – PRESENT RESULTS

- WOULD LIKE TO SEE RICH !

  LATER TODAY / TOMORROW

- THIS RICH IS THE LARGEST USER OF MICROPLEX CHIPS & LARGEST WORKING PAD PLANE

VII. Open Forum Contributions

Pattern Recognition and Electron Identification in a High Multiplicity Environment

R. Lipton
Carnegie Mellon University

I. Introduction. The pattern recognition problem in calorimetry has historically been secondary to other issues in experimental design. At the SSC, however, issues of shower separation will be crucial to shower energy resolution and electron identification. This is especially true in the forward direction (<100 mr). In this region the multiplicity is high and varies rapidly with angle. The presence of the beam pipe adds another complication. I will report on our experience with the liquid argon calorimeter in E653, a Fermilab fixed target experiment. In terms of geometry and particle density the detector operates in an environment much like the one expected at hadron colliders.

II. The E653 Liquid Argon Calorimeter. E653 is a hybrid emulsion experiment located in an 800 Gev/c proton beam at Fermilab. The experiment has a forward muon trigger and must be kept short to minimize decays[1], the electromagnetic calorimeter is only five meters downstream of the target (Figure 1).

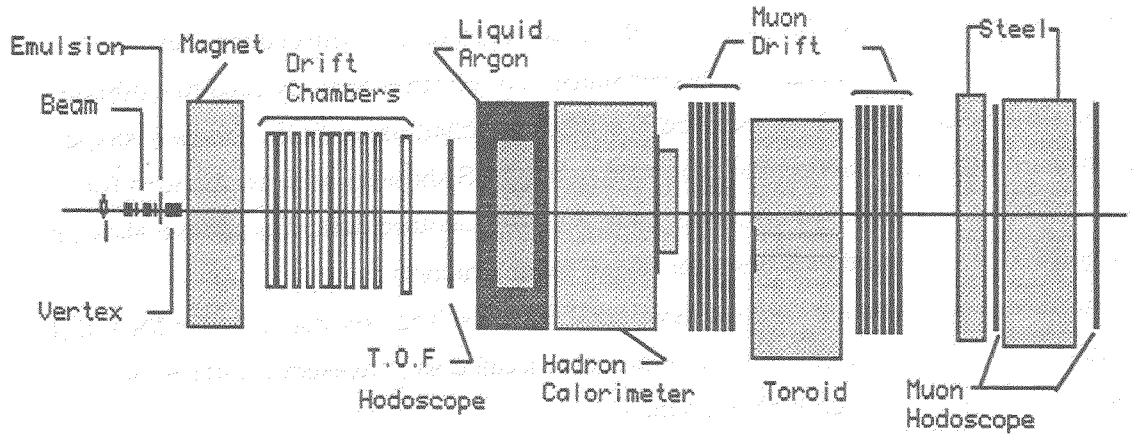

Figure 1. Plan view of the E653 Hybrid Emulsion Spectrometer.

We wished to have full acceptance for electrons and photons from charm and beauty decays so there is no beam hole in the calorimeter. The multiplicity from the proton emulsion events is substantial, 18 charged particles and a similar number of neutrals are reconstructed in each event. An average of seven showers/event are reconstructed in the central 20 cm x 20 cm of the detector.

The design of the calorimeter was driven less by the requirement for excellent energy resolution then by the need for good pattern recognition, shower separation, and position resolution. Best position resolution and shower separation is achieved by projective views with transverse separation smaller than the natural shower width. However these projective views are subject to pattern recognition ambiguities. Pads (or towers) allow unambiguous two dimensional location of a shower, but the cost of providing pads with position resolution approaching that of strips is prohibitive. Our design, shown in Figure 2, is a hybrid strip-pad system with .51 cm strips providing 6 useful transverse samples per shower and a set of pads ranging in size from 2 cm x 2 cm near the beam to 16.2 cm x 16.2 cm at the edge of the detector. We also decided to further divide the central region of the detector into .51 cm x 2 cm rectangular pads which match the segmentation of the outer region. In addition to the good position resolution and pattern recognition ability of this design the fact that one projective view strip crosses several electodes in the other views makes cross calibration possible. Electrically the readout boards (X, Y or Pad) are maintained at ground potential and the lead radiator is at negative high voltage. The boards are double sided with the Front to back connections made by soldered rivets. Sampling is (X-Pad) (Y-Pad) (X-Y) giving approximately equal charge in each view.

III. Pattern Recognition. Our LAC analysis is based on the uniformity and reproducibility of the electromagnetic shower shape. An electron beam is used to calibrate the response of the detector. The response was also modelled using EGS. Shower shape as a function of angle and energy was tabulated using EGS showers with corrections for crosstalk and other effects based on comparison with the electron data. The known shower shape (Figure 3) is then used as a basis for event reconstruction.

The algorithm is based on a technique developed for a Cal Tech photon detector for E350 at Fermilab in the 1970's [2]. Each detector element is treated as a measured point with associated errors. A chi-square is then formed:

$$\chi^2 = \sum_{x\ y\ pad} \frac{(E_i^{measured} - E_i^{predicted}(E_{shower}, x_{shower}, y_{shower}))^2}{\sigma_i^2}$$

where the predicted energy in each strip or pad is based on the energy expected from the known shower shapes. The errors include normal energy measurement errors as well as variations expected in the shower shape. An important additional source of error is associated with "excess energy", energy above that predicted by the model. This may be due to tails of nearby showers, hadronic showers, or pattern recognition errors.

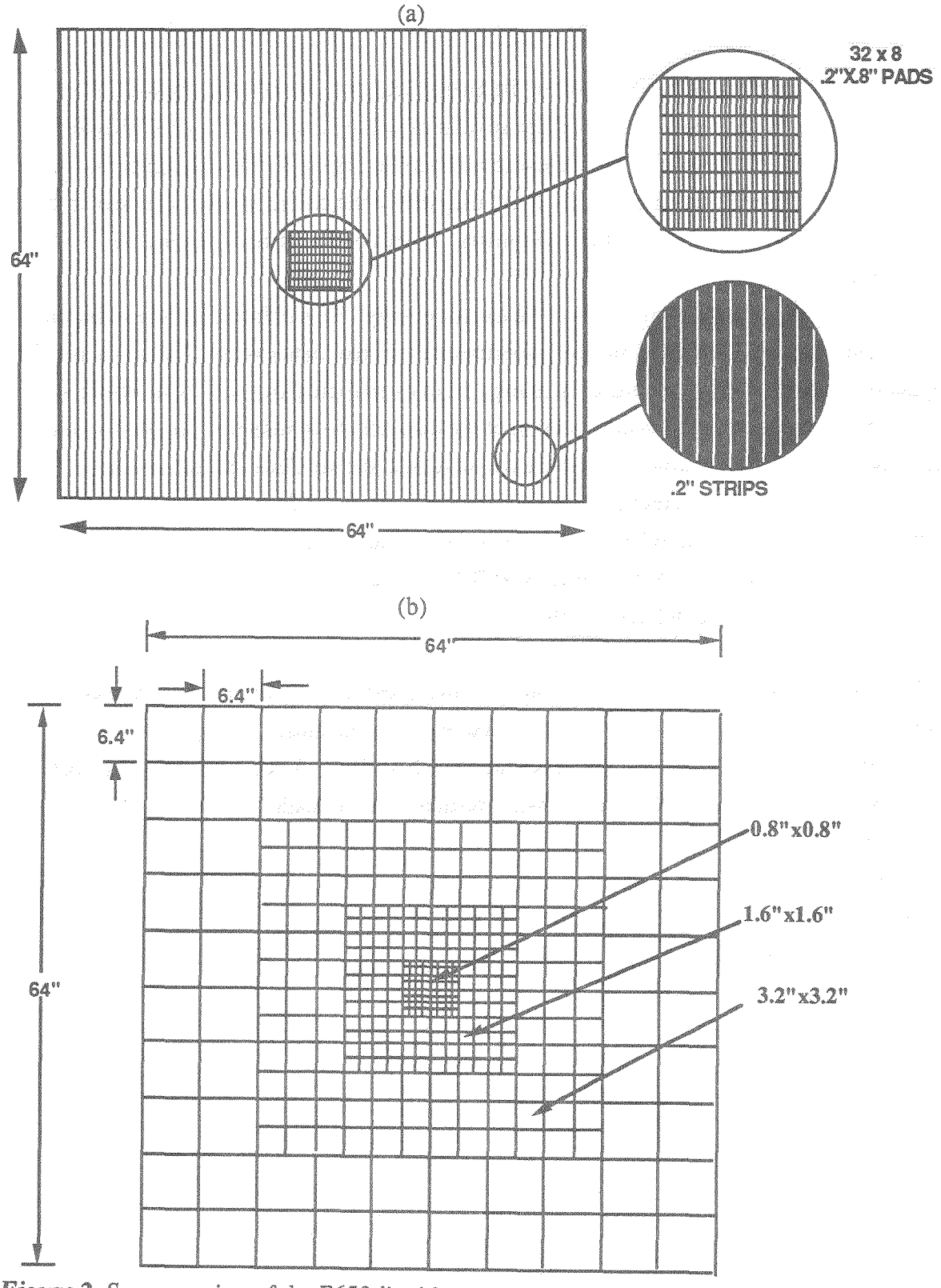

Figure 2. *Segmentation of the E653 liquid argon calorimeter readout boards.(a) Strip board showing the additional fine segmentation in the center region. (b) Pad board.*

Chi-square is minimized with respect to the energy and position of each shower. The most weight given to views with smallest amount of energy from overlapping showers. This is usually the pad view. A typical event is shown in Figure 4. Pulse heights from the projective views are displayed along the axes, the radii of the circles are proportional to pad pulse heights and are centered on the pad centers. Lines are drawn representing the reconstructed showers.

The energy error depends strongly on the excess energy. This effect is shown in Figure 5 for events with a 5 GeV EGS shower superimposed on real data events. There is a strong dependence of the energy resolution on energy from overlapping showers. This effect is especially pronounced in the middle section of the detector (6-14 radiation lengths) where the showers spread substantially and there are increased shower fluctuations. In many cases showers which have clear separation in the front section (2cm) cannot be distinguished at all in the middle. This is the dominant source of energy error overall. Energy resolution, which is approximately $15\%/\sqrt{E} + 1.2\%$ in an electron beam, is increased to $25\%/\sqrt{E}$ in emulsion events.

IV. Electron Identification. Electrons are identified by matching LAC showers with spectrometer tracks to 2 cm. Most of these electrons originate from photon conversions in the emulsion and are in the range of 1-10 Gev. A typical E/P plot for the pad view is shown in figure 6. The following further cuts are made

- E/P between .75 - 1.25
- Front/Total energy >.6
- Shower shape chisquare < 3

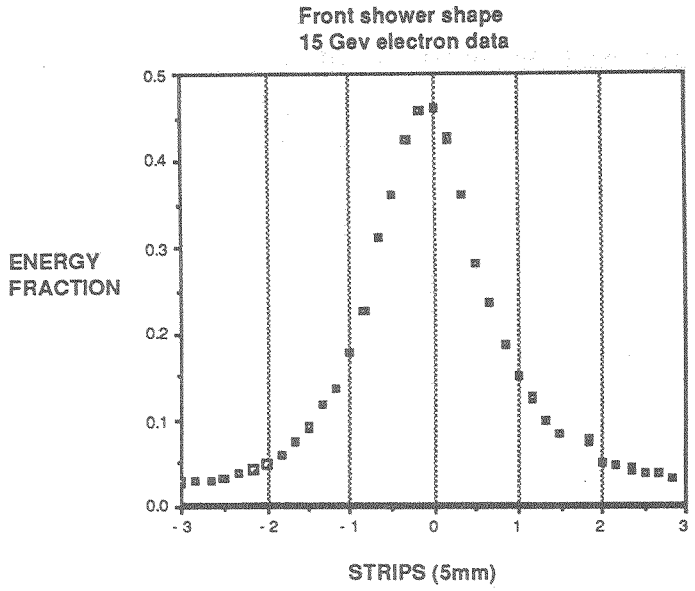

Figure 3. *Electromagnetic shower shape in the first 6 radiation lengths of the liquid argon calorimeter.*

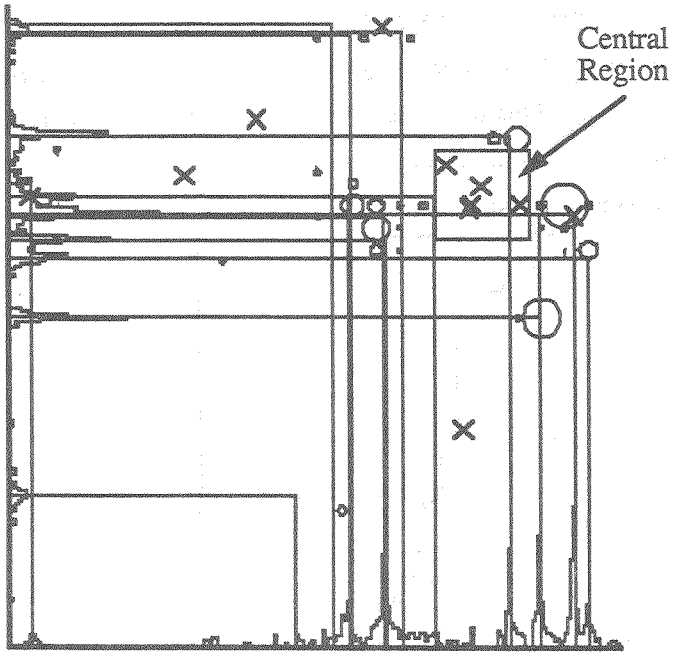

Figure 4. *A "typical event" in one quadrant of the front section of the E653 liquid argon calorimeter. The horizontal and vertical axes are the measured x and y view pulse heights. Pad view energies are represented by circles centered on the pads whose diameters are proportional to the pad pulse height. Track intercepts are shown by crosses. Lines are drawn for reconstructed showers.*

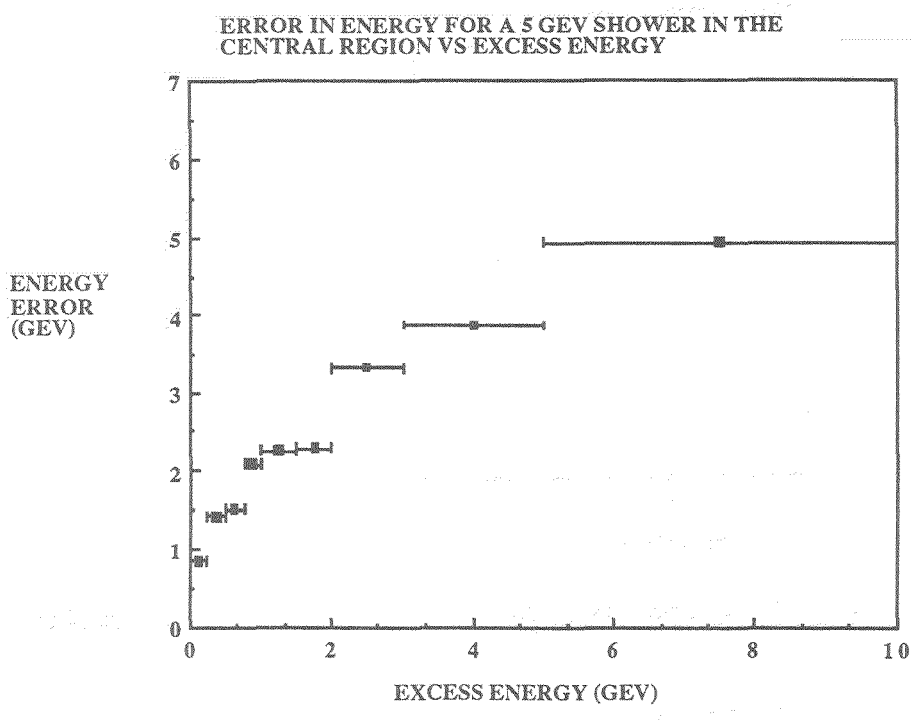

Figure 5. *The error in the distribution of reconstructed energies as a function of the background energy beneath the shower. This plot was generated by superimposing 5 GeV EGS showers on backgrounds from real emulsion data.*

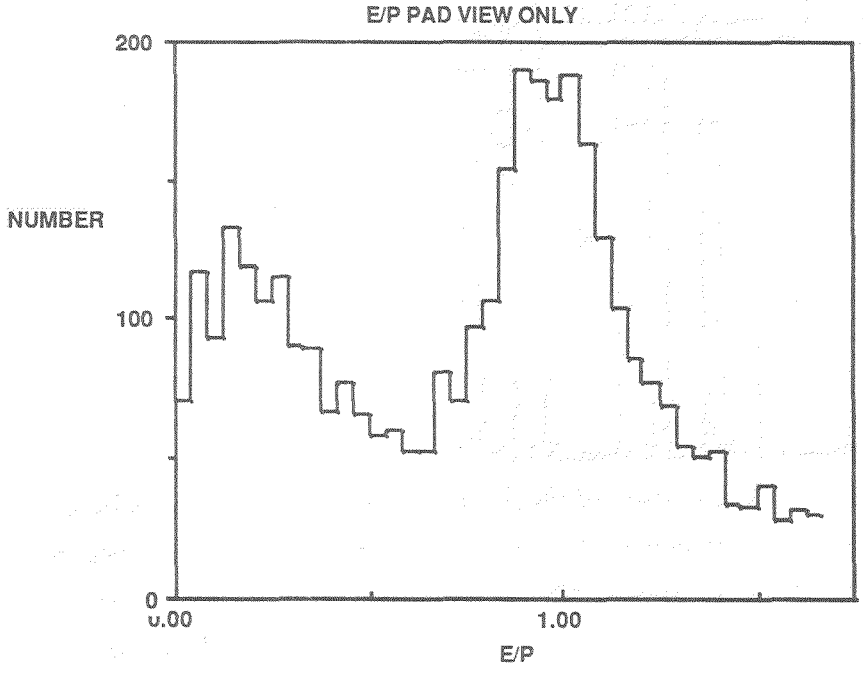

Figure 6. *E/P distribution in the pad view for electron candidates (low mass pairs) in emulsion data.*

Electron efficiency is determined using low mass pairs in the spectrometer with one identified electron. It is about 75% for tracks above 3 Gev/c. Hadron misidentification probabilities are determined using emulsion tracks tagged as originating from the primary vertex and K^0 decay products. This probability is about 1% for the same momentum range.

VII. Conclusion. Reliable electron identification in the forward direction at the SSC will depend on tracking and Cerenkov devices as well as excellent calorimetry. In addition to decisions on detector segmentation techniques to minimize shower overlap will be important. Reduction of the effects of shower tails by minimization of the radiation length of the detector is crucial. This is consistent with using narrow argon gaps to improve the time resolution of the detector. The E653 hybrid strip-pad detector provides valuable lessons about how to approach these issues.

References

[1] N. Ushida et. al.,"Hybrid emulsion Spectrometer for the Detection of Hadronically Produced Heavy Flavors", in preparation for Nuclear Instruments and Methods.

[2] G.C. Fox, R.G. Kennett, "Treat - An Analysis Program for the CEX Detector", Cal . Tech. internal report.

RESULTS FROM A TOF PARTICLE ID SYSTEM AT THE TEVATRON COLLIDER

A.P. McManus, V. Balamurali, S. Banerjee, P.D. Beery, N.N. Biswas,
V.P. Kenney, J.M. LoSecco, J. Piekarz, S.R. Stampke, Y. Zhan

Department of Physics, University of Notre Dame
Notre Dame, IN 46556

Abstract

The TOF system operating at the C0 intersection region of the Fermilab Tevatron collider is evaluated in terms of time and space resolution. The time resolution was found to have a σ of 110 to 140 psec in practice depending on the method chosen to determine the resolution. Some of the design characteristics needed for the successful operation of a TOF system at the Tevatron collider are also discussed including the method used to find the event time in a collider with an extended bunch structure.

Introduction

A time-of-flight[1] system is in operation at the C0 area of the Fermilab collider. The experimental arrangement is shown in Fig1. The detector systems in the experiment include a Central Tracking Chamber (CTC), a scintillator hodoscope surrounding the collision region, a magnetic spectrometer at polar angle $\theta = 90°$, and a time-of-flight (TOF) system. There are a total of four hodoscopes comprising the TOF system in the experiment. Two TOF arrays in the Tevatron tunnel, each surrounding the Tevatron pipe, are located upstream (TOF$\bar{p}$) and downstream (TOFp) of the proton beam, approximately 2 meters from the center of the collision region. The spectrometer TOF arrays, TOF1 and TOF2 are located behind the straw chambers at 2 and 4 meters from the Tevatron beam, respectively. The arrangement of the counters in these hodoscopes are shown in Fig2a-c.

The objective of the TOF system was to separate π, K and $p/\bar{p}$ up to momenta of about 1.7 GeV/c. The arrangement of the hodoscopes was based primarily on two considerations: (a) It is necessary to have a long flight path to separate π's and K's at a momentum of 1.7 GeV/c, but one must also have a short flight path to have sufficient probability for K survival at the lowest momentum. In the spectrometer arm, these contradictory requirements were satisfied by using two TOF arrays, one array (TOF1) as close as possible to the interaction region to provide separation at low momentum and one array as far away as possible (TOF2) to provide high momentum separation. (b) A second consideration is related to one of the specific characteristics of the Fermilab collider. Each bunch of $p/\bar{p}$ beams has a longitudinal spread of $\sim$ 40 cm (Gaussian), which introduces a spread of 2 nsec in the timing of beam-beam interactions if beam pickups were used to determine the time of interaction. The TOFp and TOF$\bar{p}$ hodoscopes were used to determine the interaction time with a resolution of at least 300 psec FWHM. These counters were placed as close as possible to the beam pipe and as far away as possible from the interaction region to measure flight times of particles produced in the beam directions (i.e. high momenta, β=1). If there is at least one hit in each array it is possible to find both the z position and the time of interaction of the event. In addition, these counters were used as part of the trigger.

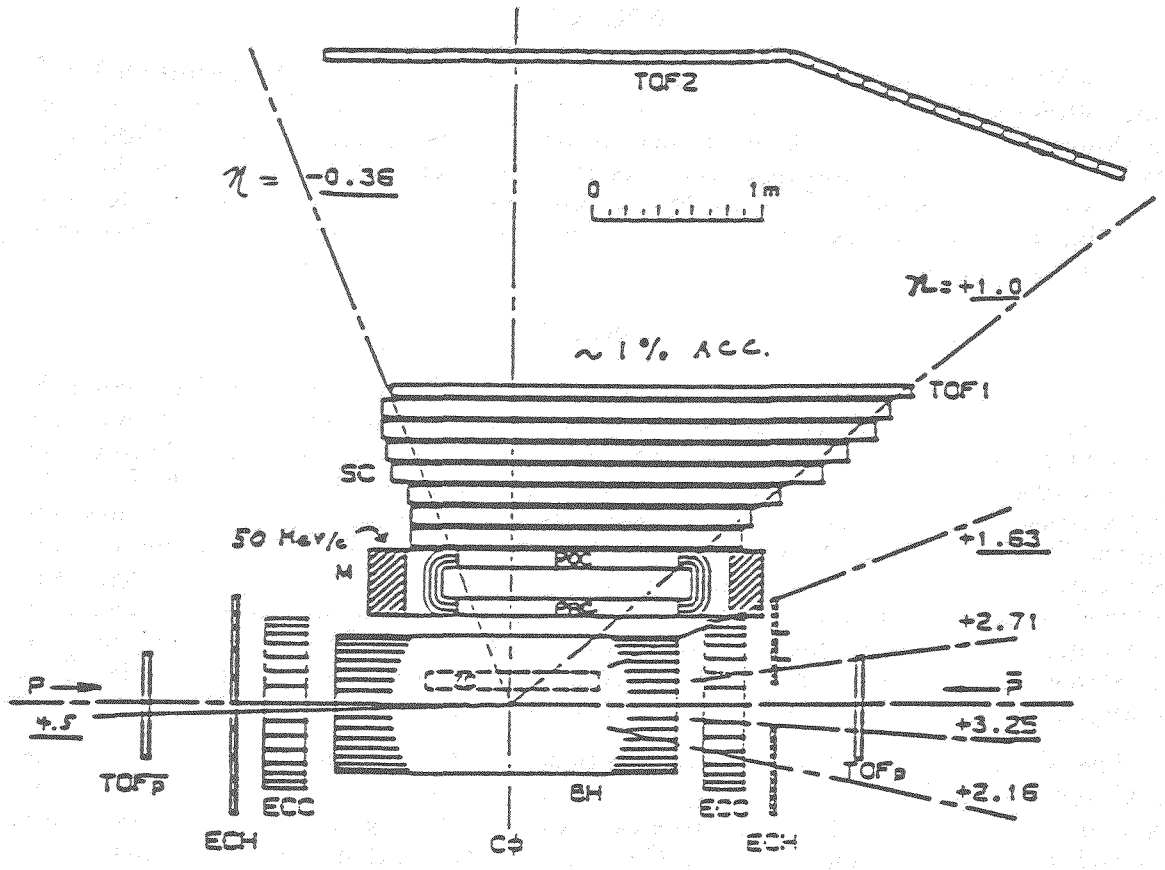

Figure 1: The major components of the E735 detector are shown. The visible components are the TOF hodoscopes, the central hodoscope comprising the barrel (BH) and endcap (ECH) hodoscopes, the endcap drift chambers (EEC), The magnet (M) with entrance (PRC) and exit (POC) drift chambers, and the straw drift chambers (SC) after the magnet.

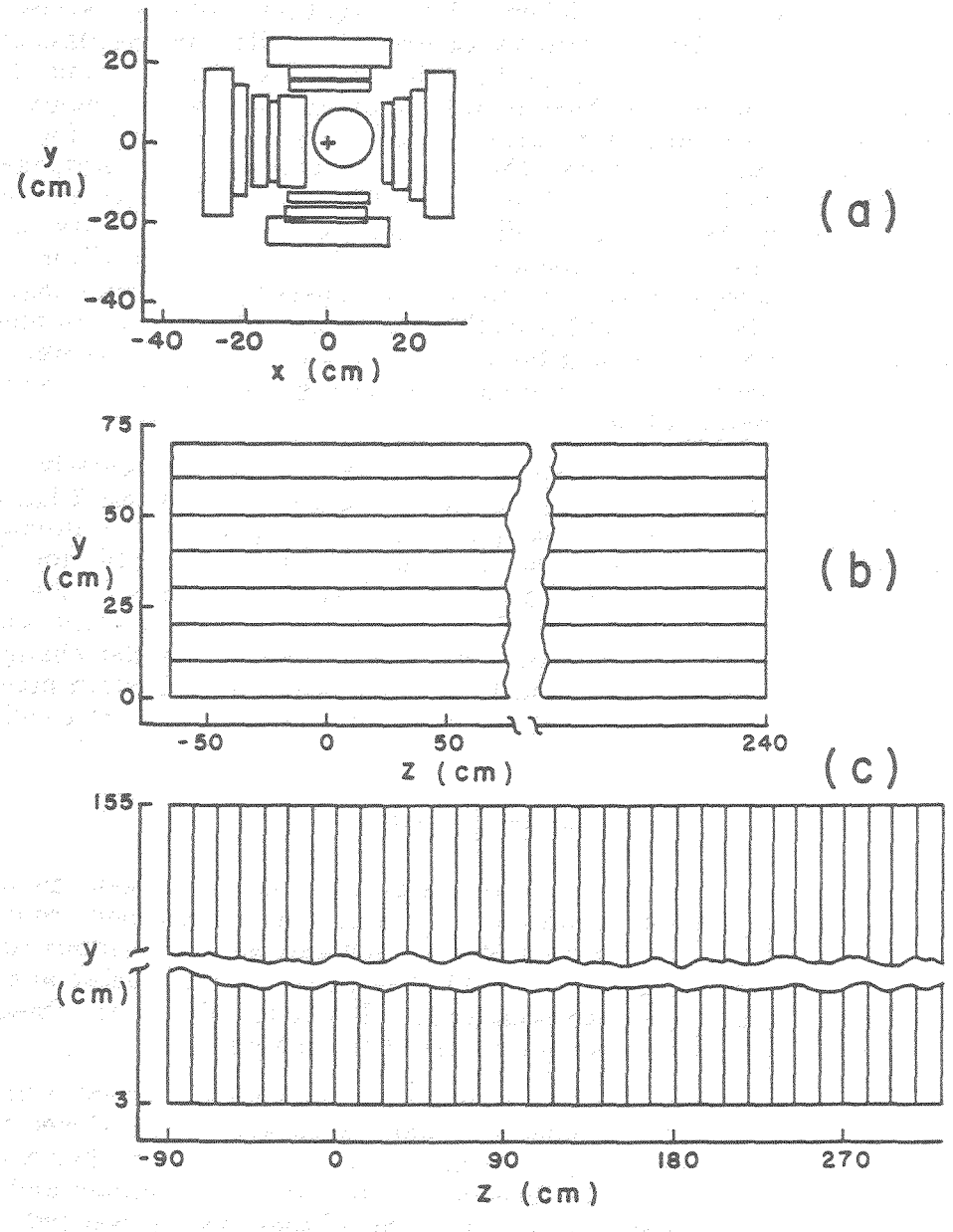

Figure 2: The arrangements of the TOF hodoscopes are shown, a) TOFp/TOF$\bar{p}$ b) TOF1 c) TOF2.

Monitoring of the TOF system

The performance of the TOF system was monitored using a LN103 nitrogen laser (Photochemicals Research Associates, Toronto, Canada) to generate light pulses in the scintillators. The laser is a UV laser with a pulse width of 300 psec, peak power of 400 kW and with a wavelength of 337 nm. With a light pulse of this wavelength, the waveshifter in the scintillator is directly excited and emits photons simulating the passage of a charged particle through the scintillator. A small fraction of the laser beam was led via an optical fiber to a P/N photodiode which generates a sharp analog pulse and is used as a monitor of laser intensity, as a gate for ADC units, and as a start for the TDC units. The remaining laser beam was propagated through five long optical fiber cables (each cable 600 microns in diameter with a polymer silica clading, 33 m long) to distribution boxes in the vicinity of the four TOF hodoscopes. From a distribution box, the beam was then diverted to the counters of the hodoscope using a bundle of small fibers (UV transmitting, 240 micron diameter, step index fiber 840R from Spectran Corp) which are a few meters long. All of the small fibers connecting the counters in a given hodoscope were cut to the same length in order to use the laser data for the alignment of all the counters in a hodoscope with a common time.

To monitor the stability of the system, laser runs were taken regularly. The quantity $T_{ave} = (T1_{ave} + T2_{ave})/2$ was determined for each counter, where $T1_{ave}$ and $T2_{ave}$ are the TDC values corrected for the pulse hight slewing of the discriminators ("time-walk") from the phototubes at the two ends of each TOF scintillator. The value of T_{ave} for all of the TOFp/TOF$\bar{p}$ counters during the course of the 1987 collider run is shown in Fig3. For most of the counters T_{ave} was constant within 100 psec over the run period. Two counters (# 4 and 5) showed a sudden change at about run #800. The practice of constantly monitoring the TOF system made it possible to correct for even large fluctuations in T_{ave} during the course of a collider run.

Calibration of the system

The TDC readings for the system corresponds nominally to a least count of 50 psec. Precise values of least counts for each unit were determined from the evaluation of TDC readings as a function of a delayed gate generator input to the TDC's. This check on the linearity of the TDC response on time delay and the determination of least count was done occasionally. It was found that the linearity of the TDC units did not change over the course of the collider runs.

The procedure for determining the time resolution and time alignment is briefly sketched here. The laser- and the collider data were taken with identical electronic and electrical conditions by switching from one trigger to the other. For a laser run, the trigger was generated by the laser beam via a P/N photodiode and was split into two signals using a linear fan-out unit. One of these signals was fed to an ADC unit to monitor the laser intensity. The typical deviation in the pulse height distribution of this signal is 15% (FWHM). The other signal, after discrimination, was used as an ADC gate and as the start for the TDC's. The dispersion and the average of the TDC readings for a a given counter were calculated from these laser runs. The dispersion in TDC readings corresponds to a measure of the counter's time resolution. The variation of the average values of TDC readings (T_{ave}) from

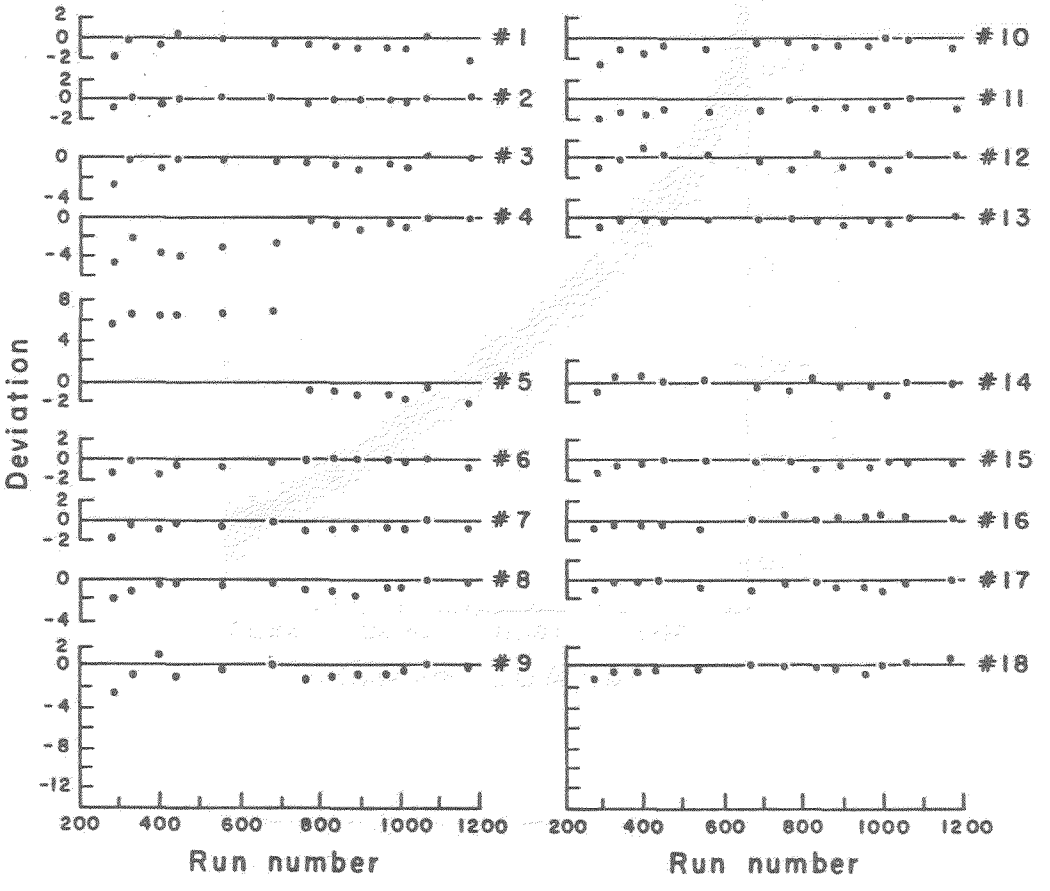

Figure 3: The deviations of the time alignments (T_{ave}) of the TOFp/TOF$\bar{p}$ counters over the course of the 1987 collider run. The vertical axis is in units of 50 psec and the horizonal axis is in run numbers and spans 5 months.

counter to counter (in a given hodoscope) is a measure of time misalignment which arises because all phototube bases and signal cable lengths are not exactly alike.

The calibration was done using several laser runs by attenuating the laser beam with combinations of UV filters to obtain TDC readings as a function of ADC response. A typical dependence of T on A is shown in Fig4a for one of the photomultipliers. This apparent time deviation with pulse height is the "time-walk" effect and the data must be corrected for this effect (see ref 1 for details).

The variation of T vs. A is shown, greatly magnified, in Fig4b after applying the "time-walk" correction for laser data from the 1987 collider run. The dispersion of the data in Fig4b is related to the intrinsic resolution of the TOF counter. Adding the dispersion of the two ends of each counter in quadrature, one finds a resolution of 130 psec (FWHM) for TOFp/TOF$\bar{p}$ counters, 120 psec for TOF1 counters and 115 psec for TOF2 counters. This implies that the intrinsic resolution of the TOFp/TOF$\bar{p}$ to TOF1 system is 80 psec (σ) and resolution of the TOFp/TOF$\bar{p}$

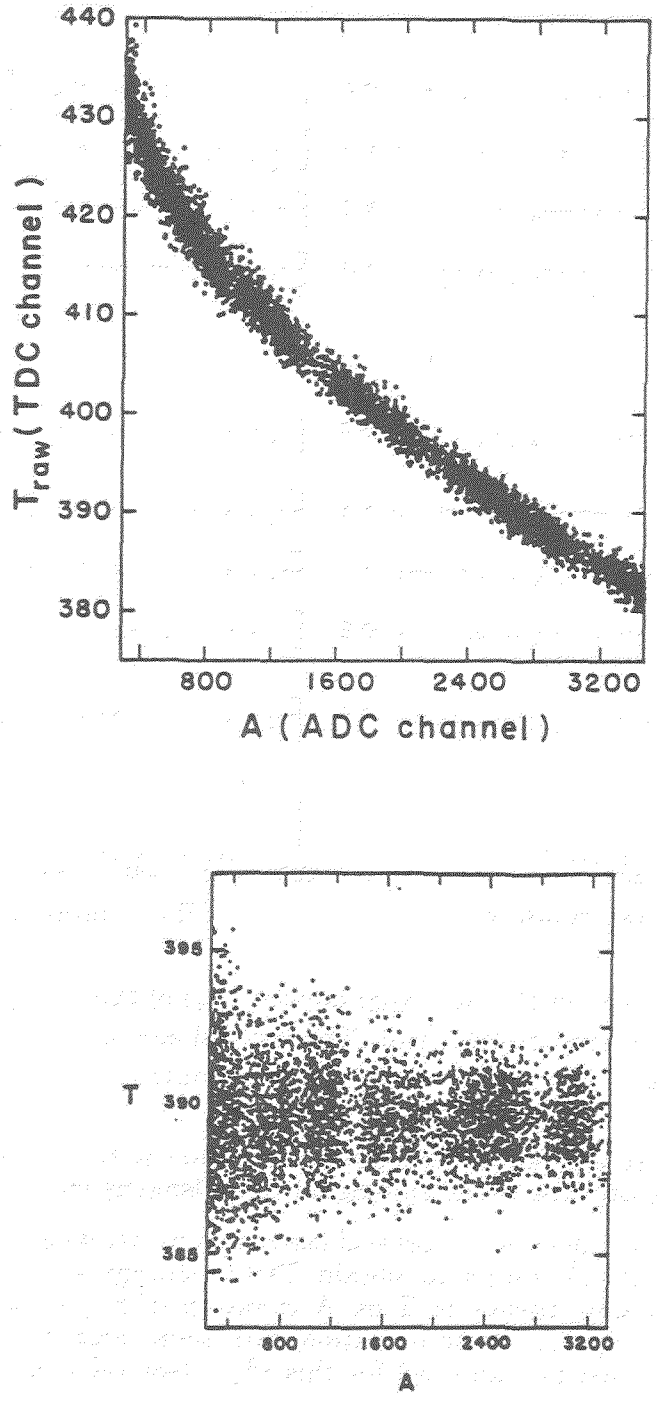

Figure 4: a) The variation of time (T_{raw}) with pulse hight (A) from laser data ("time-walk" effect). b) The variation of time with pulse hight after applying "time-walk" correction (time scale is greatly magnified).

to TOF2 system is 75 psec. For various reasons (tracks that do not go completely through the counter, multiple hits in a counter, and small misalignments in T_{ave}) the actual resolution achieved by the system is somewhat worse than the intrinsic resolution. The TOFp/TOF$\bar{p}$ system was improved by making the counters smaller and lowering the discriminator threshold for the 1988-1989 collider and the resolution of the system should be somewhat better for this later data.

Performance of the TOF system

The time resolution of the TOF system was found to have some dependence on the event multiplicity since at high multiplicities it was more likely that a TOFp/TOF$\bar{p}$ counter was hit with more than one minimum ionizing track. Multiple tracks in a TOFp/TOF$\bar{p}$ counter will skew the event time to a shorter time causing a tail on the high mass side of a particle peak. A cut was made on the ADC's of the TOFp/TOF$\bar{p}$ counters to eliminate multiple hits and slower non-minimum ionizing tracks. Several plots of Mass squared spectra from 1987 collider run data are shown in Fig5 compared to a monte-carlo simulation which includes multiplicity effects. A Global fit of the data yields a time resolution of $\sigma = 140$ psec for the TOFp/TOF$\bar{p}$ to TOF1 system and about 5 psec less for particles that hit TOF2. In the 1988-1989 collider run the resolution should be better since the the TOFp/TOF$\bar{p}$ counters have been made smaller and the probability of multiple hits is reduced.

One can also determine the hit position of the particle traversing a TOF counter, z_{tof}. In Fig6, the values of z_{tof} for the TOF1 hodoscope are compared with the corresponding hit position obtained from the tracking (z_{trk}) by plotting the difference between these values. The FWHM of spacial resolution is 3-4 cm which approximately represents $\sigma = 90$ psec for a single TOF1 counter.

The difference of the event vertex from tracking minus the event vertex from the TOFp and TOF$\bar{p}$ hodoscopes is shown in Fig7 and is a measure of the resolution of the TOFp/TOF$\bar{p}$ system. The width of the data plotted in Fig7 is 4 cm FWHM which yields a resolution of $\sigma = 110$ psec for the TOFp/TOF$\bar{p}$ system (total error of both hodoscopes).

Some physics Results

From the data collected during the 1987 collider run, results have been published[2] on the dependence of average transverse momentum $\langle P_t \rangle$ on the charged multiplicity N_c, using charged particles in the spectrometer arm without particle identification information from TOF1/TOF2. The information from TOFp/TOF$\bar{p}$ was used in this analysis to ascertain the beam-beam interaction vertex and to reduce background events. The TOFp/TOF$\bar{p}$ system was also used in the trigger to distinguish beam-beam from beam-gas events based on timing. Results on the $\Lambda/\bar{\Lambda}$ production have been published[3] using TOF1 to separate $p/\bar{p}$ from π's.

Work is in progress[4] on transverse momentum distributions of π , K, and $p/\bar{p}$ using both TOF1 and TOF2 data. Transverse momentum distributions from work in progress are shown in Fig8, where mass identified data for TOF1 as well as for TOF2 hodoscopes are plotted. The data have been corrected for geometrical, decay and trigger losses. The agreement between the two sets of data (TOF1 and TOF2), in the region of overlap, is quite good.

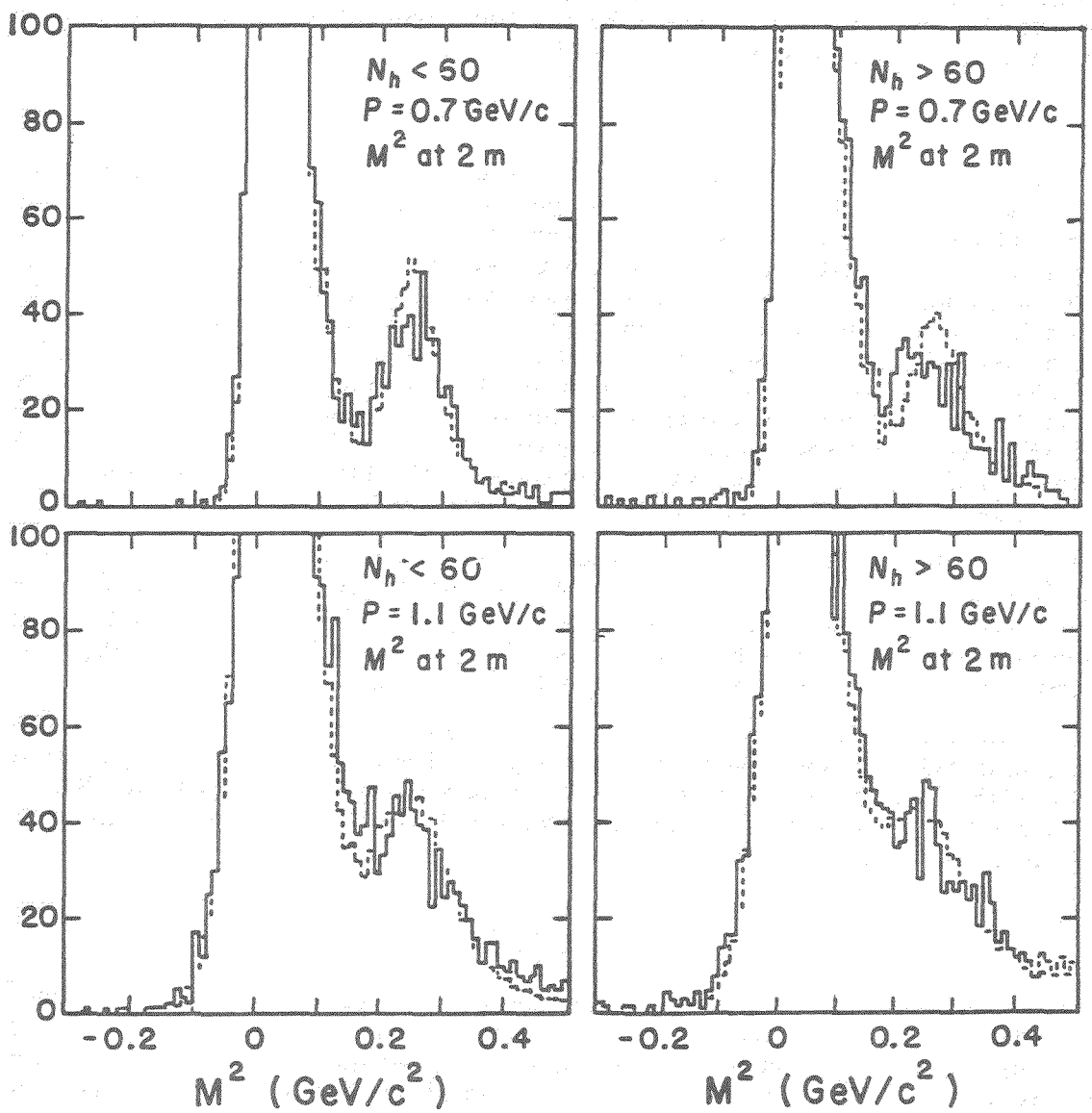

Figure 5: The M^2 spectrum for two different momentum ranges (0.65-0.75 GeV/c and 1.05-1.15 GeV/c) and two scintillator hodoscope multiplicity regions ($N_h > 60$, high and $N_h < 60$, low) from collider data (solid line) and monte-carlo (dashed line).

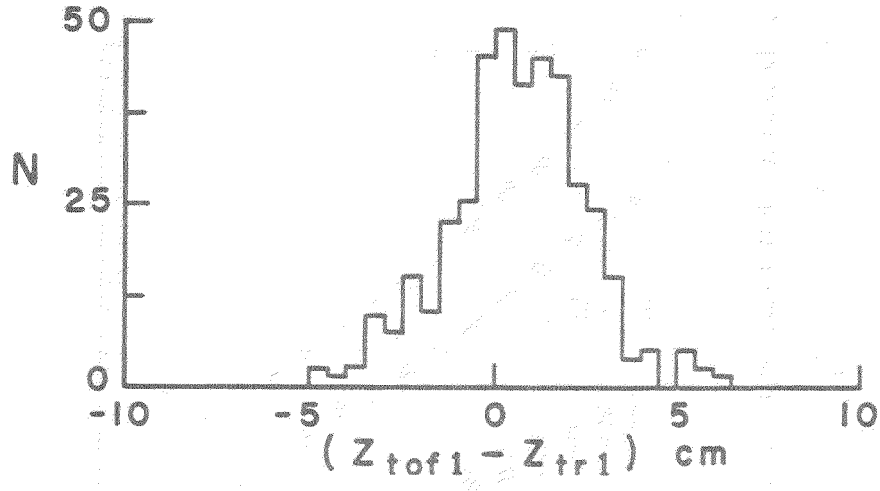

Figure 6: Difference of the z intercepts at TOF1 determined from tracking (Z_{tr1}) and from the time difference in the TOF1 counters (Z_{TOF1}).

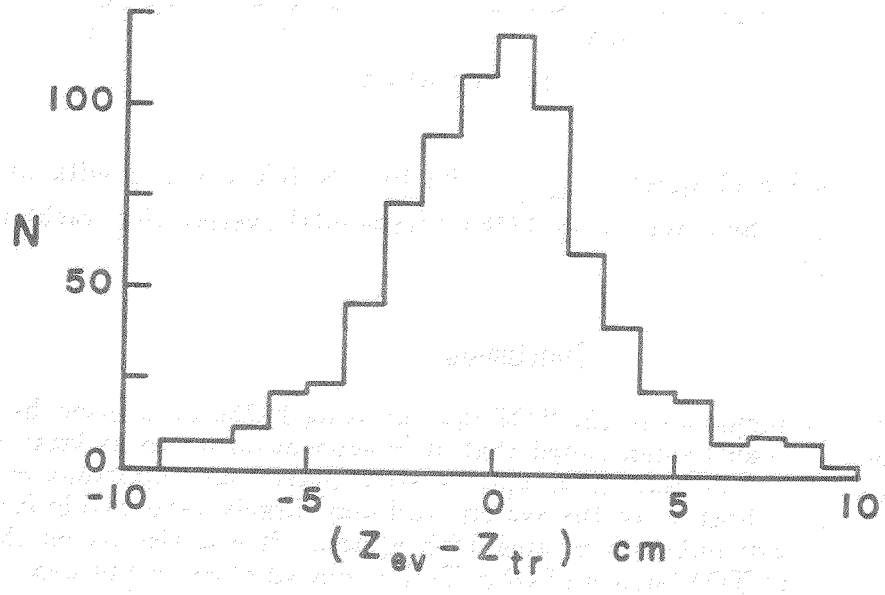

Figure 7: Difference of the event vertex determined from tracking (Z_{tr}) and determined from the TOFp/TOF$\bar{p}$ system (Z_{ev}).

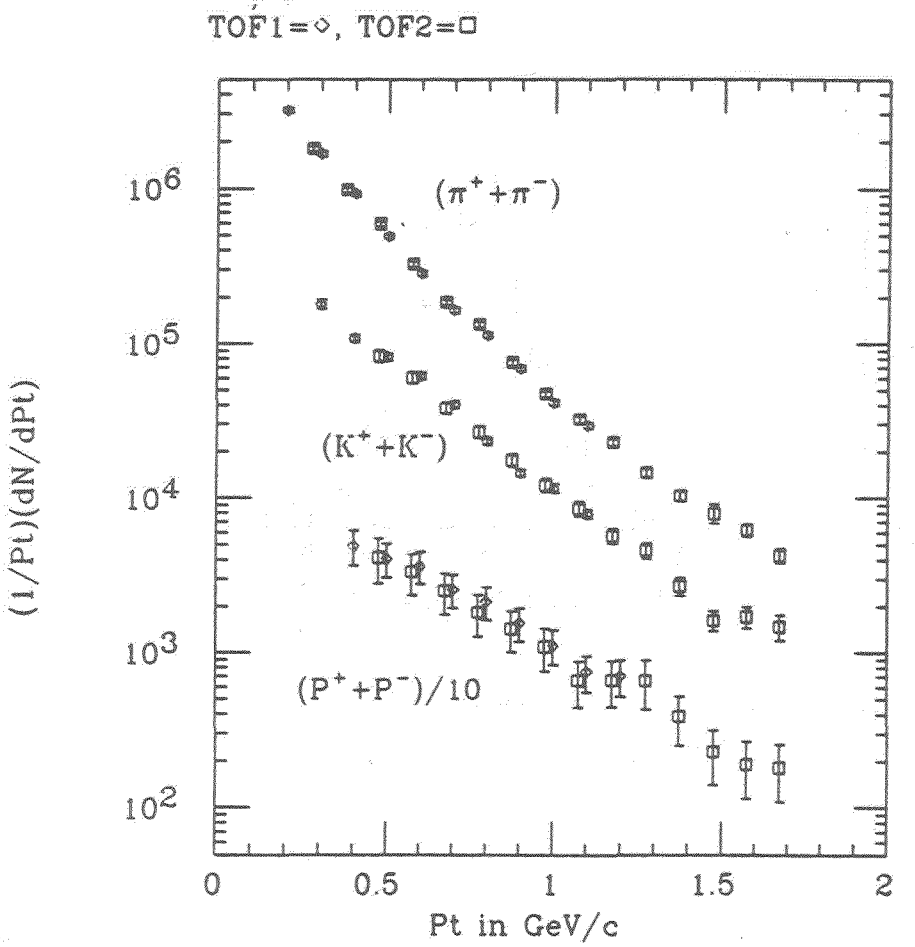

Figure 8: The inclusive P_t spectra ($\frac{dN}{dy dP_t^2} vs. P_t$) for π's K's and $p/\bar{p}$ with all acceptance corrections. The tracks from TOF1 (diamonds) overlay the tracks from TOF2 (squares) nicely.

Conclusion

Evaluating the performance of the TOF system using E-735 data from the first collider run (1987), it can be concluded that K/π separation up to at least $P_t \sim$ 1.5 GeV/c is possible. The laser-fiber optic system played an important role in the monitoring and calibration of the system and was largely responsible for the excellent time resolutions obtained by this TOF system. It was also found that a set of highly segmented TOF arrays (TOFp/TOF$\bar{p}$) placed close to the beam axis provided a good determination of the event time (σ = 110 psec) and a reasonable estimation of the event vertex.

References

1. S.Banerjee et. al., Nucl. Inst. Meth., A269 (1988) 121.

2. T.Alexopoulis et. al., Phys. Rev. Lett. 60, (1988) 1622.

3. S.Banerjee et. al., Phys. Rev. Lett., 62 (1988) 12.

4. N.N. Biswas et. al., Proc. 24^{th} Int. Conf. on High Energy Physics, eds. R. Kotthaus and J.H. Kuln, Springer-Verlag Berlin, (1989)

A Large Area Fast TRD for the 1990's.

R. Tschirhart
Princeton University

Several large area ($> 2m^2$) Transition Radiation Detector (TRD) systems[1] have delivered π/e rejection factors of $\times 100$, ($\epsilon_e = 90\%$), in the momentum range $5 < p < 100\ GeV$. The non-destructive nature of TRD particle ID systems make them complementary to calorimetric π/e rejection, and hence of particular interest in a high rate enviroment. Unfortunately, the basic design features of existing large area TRDs make them unusable in high rate enviroments where event rates approach 100 MhZ, with charged multiplicities into the hundreds.

Existing[2] large area TRDs are composed of 3 to 12 modules, where each module has a volume of radiator material followed by a wire chamber that detects the x-rays produced by electrons traversing the upstream radiator volume. The radiator volume is usually filled with a stack of several hundred thin ($15-20\ \mu m$) polypropylene films, or an equivilent mat of thin polypropylene fibers. The radiator volumes dominate the total amount of material in the TRD, which typically corresponds to 5% of a radiation length for a system that can deliver a π/e rejection of $\times 100$, (4 modules). The x-ray detecting wire chamber is $\sim$ 1.5 cm thick, with xenon as the major x-ray dectecting component of the gas mixture. Charge collection times of existing TRDs are (300 ns $-$ 2500 ns). In order for TRDs to function in a high rate enviroment, it is desireable to minimize the total amount of material, and it is *essential* to reduce the charge collection time.

The x-ray spectrum generated by a conventional radiator[3] is shown in figure 1a. Also shown in figure 1a is the spectrum that survives to the detecting xenon volume, and the corresponding spectrum that is detected by 1.5 cm of 90% xenon at 1 atm. Similarly, figure 1b shows the number of x-rays generated, arriving at the chamber, and detected by the chamber. The requirement for high x-ray detection efficiency, (which corresponds to thick chambers and long collection times), is clearly evident from the low number of x-rays that survive to the xenon volume. Also evident from figures 1a and 1b is that 75% of the photons that are generated in the radiator volume are absorbed by the radiator stack itself. These lost x-rays could be recovered if the radiator stack were finely sampled. The optimal[2] chamber thickness of a fine sampling TRD is significantly smaller than conventional chambers, allowing a shorter charge collection time. In addition, since more x-rays are detected in the radiator stack, the same π/e rejection as conventional TRDs can be acheived with less material.

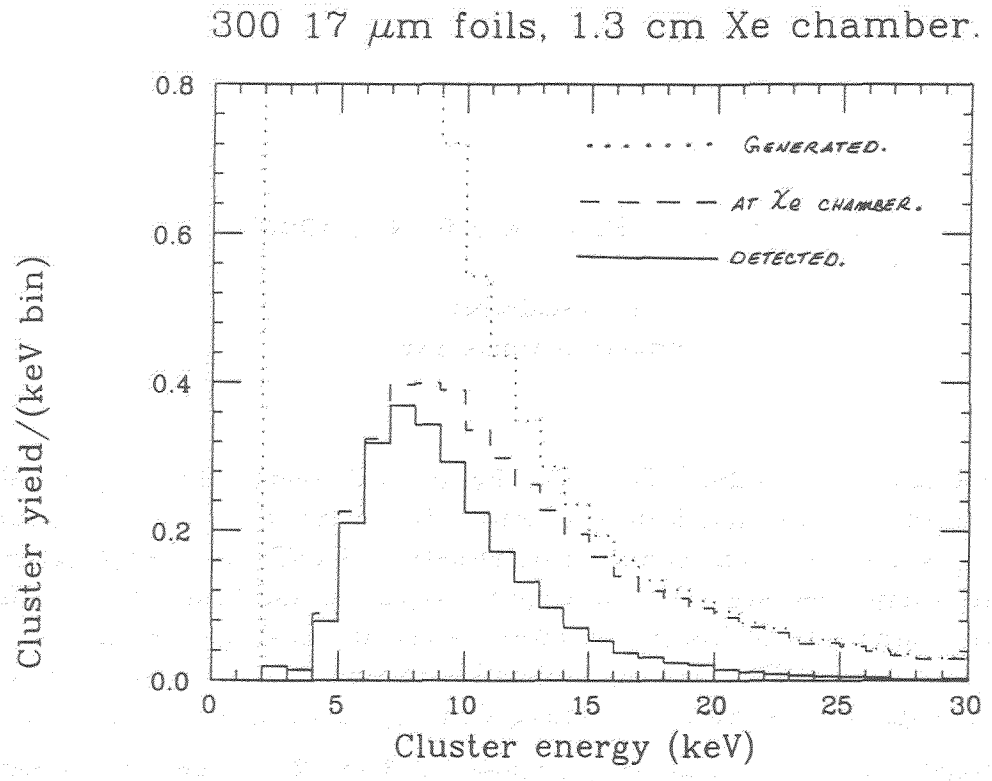

FIGURE 1a.

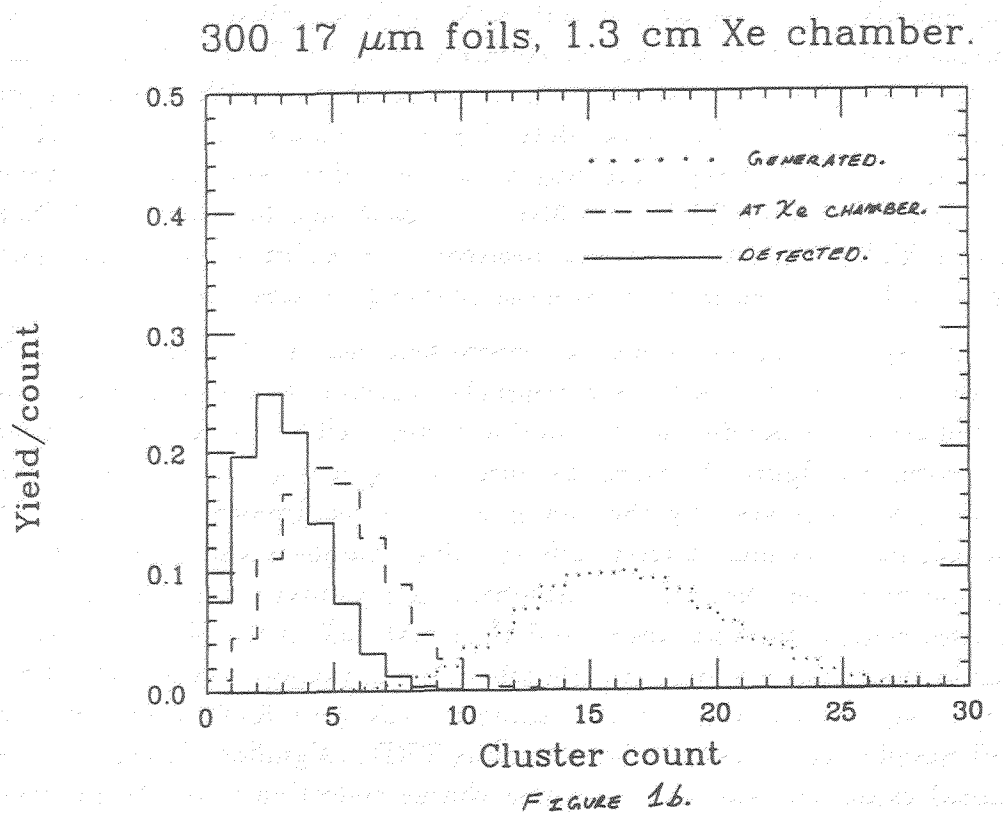

FIGURE 1b.

A fine sampling system suggested by Dolgoshein[2] would be composed of 50 modules, where each module has 20-40 polypropylene foils followed by a chamber with a 2 mm gap. Only the positions of sense wires over threshold are readout per chamber plane, with the threshold typically set at 5 keV. Hence the number of fired wires along a track is binomially distributed. This TRD has nearly the same amount of material as a conventional 4 module system, but delivers a π/e rejection that is at least $\times 10$ greater. The expected properties of this fine sampling system have been verified in tests[2] of a small prototype at Serpoukhov. Unfortunately, the mechanical and electrostatic problems associated with narrow gap chambers will prevent a straight-forward extrapolation of this design to large area.

A possible solution to the mechanical and electrostatic problems of a fine sampling TRD is illustrated in figure 2. As can be seen in the figure, the detecting chamber is constructed from a raft of thin-walled, (25 μm), aluminized conductive-polymer[4] tubes $2-4$ mm in diameter. Tubes of this type have been produced in quantity, primarily for use in vertex straw chambers. Extending the tube lengths up to and beyond 2 meters is a reasonable extension of existing tube winding technology[5]. Two immediate problems with a tube-based chamber system are nonuniform x-ray absorbtion in the tube wall as a function of track impact parameter, and varying x-ray detection efficiency as a function of impact parameter. The variation of x-ray absorbtion and path length as a function of impact parameter for one module is shown in figures 3a and 3b. A 30-module tube-based system with threshold readout has been simulated[6], and no significant dependence of π/e rejection on track impact parameter is seen.

The advantages of a tube-based fine sampling system are the following:

(1.) Charge collection times of 30 ns are attainable with 4 mm diameter tubes flowing 80/10/10% $Xe/CF_4/C_2H_2$[7].

(2.) Significantly less, ($\sim 1/2$), radiator material is required in a fine sampled system to acheive the same π/e rejection as a convential TRD system.

(3.) Relatively simple electronics (amplifier/discriminator circuts) is required, corresponding to a minimal event data record from the TRD system.

(4.) A matrix of thin-walled plastic tubes is mechanically very strong, easing the design of the surrounding support structure and recirculating gas system.

(5.) The conductive tubes mechanically and electrically isolate the sense wires from each another, reducing problems associated with broken wires and electrostatic instabilities.

(6.) Straight-forward construction.

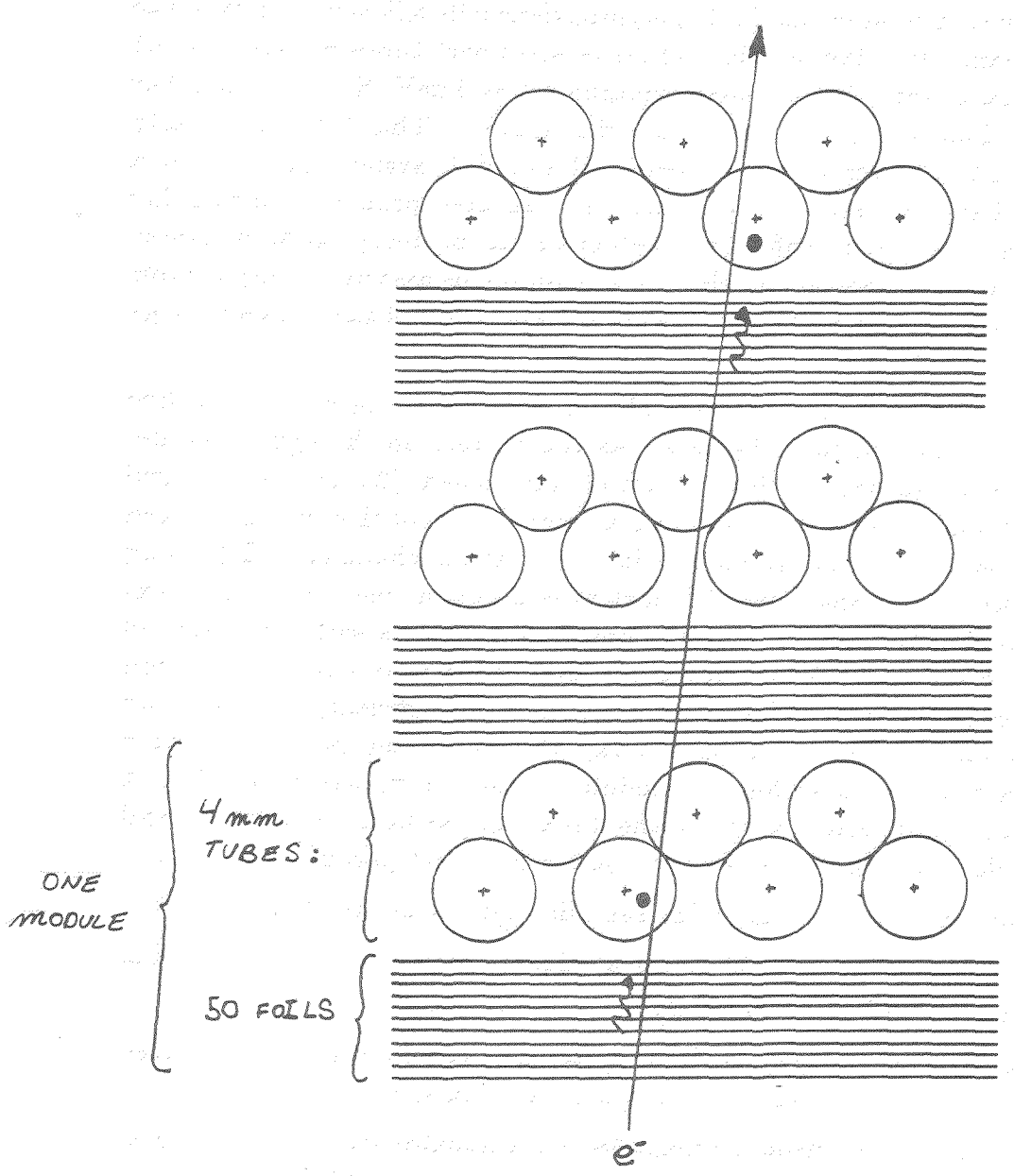

FIGURE 2.

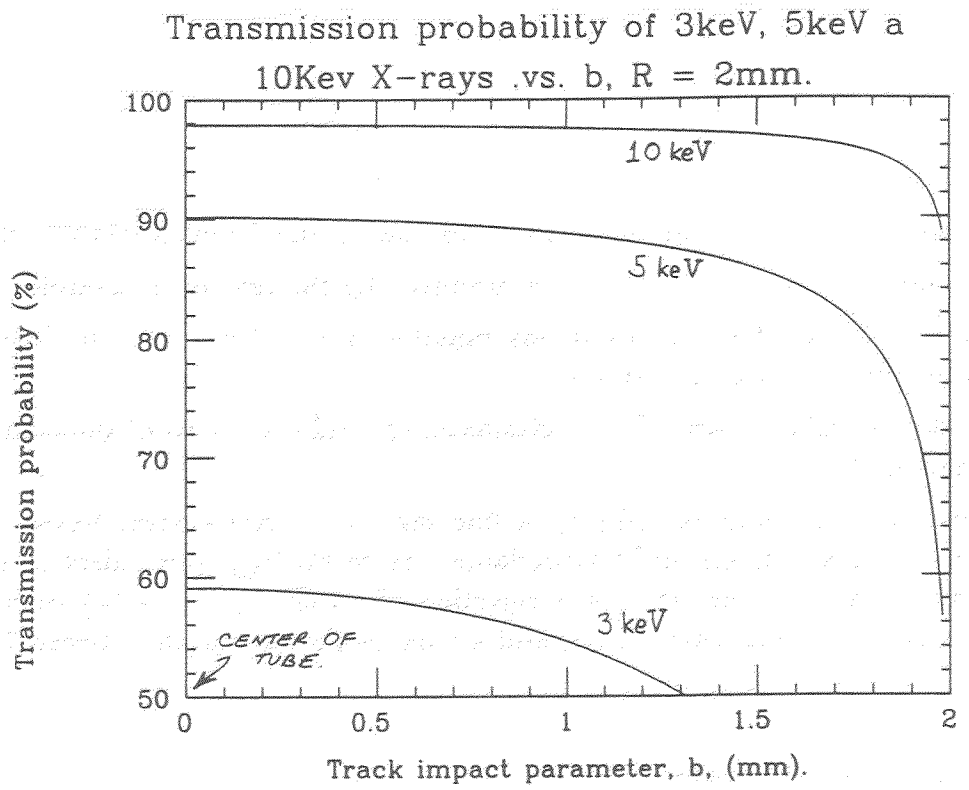

FIGURE 3a.

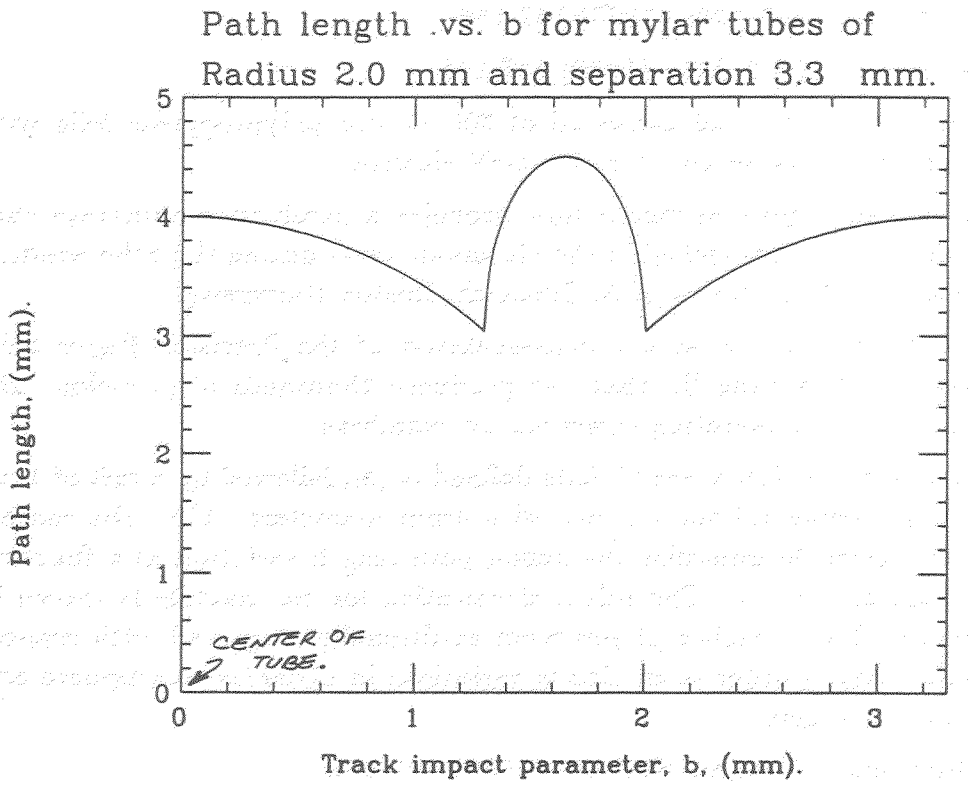

FIGURE 3b.

Problems that remain to be solved in a tube-based fine sampling system are:

(1.) Can high quality low cost tubes be produced by the tens of thousands?

(2.) How do you build a leak tight gas manifold for 10,000 - 30,000 closely packed thin-walled plastic tubes?

(3.) How do you reliably amplify, discriminate, and calibrate tens of thousands of channels?

Although the challenge of building a fine sampling TRD system based on 10,000 - 30,000 straws is certainly formidable, the technology now exists to do so. Such a system could deliver a π/e rejection of $\times 100$, ($\epsilon_e = 90\%$) with a charge collection time less than 50 ns, and a total radiation length between 2% and 3% .

References & footnotes:

[1] For example: the E715 TRD, FERMILAB-conf-84/134-E, and more recently the NA31 TRD, September 1988 IEEE proceedings, and the D0 TRD system, NIM A265 (1988) 157-166.

[2] B. Dolgoshein, NIM A252 (1986) 137-144.

[3] The radiator simulated consisted of 300 17 μm polypropylene foils with 1000 μm gaps, traversed by a 12.8 GeV electron.

[4] Carbon loaded polycarbonate film provides a conductive substrate that will bridge scratches etched in the aluminum layer during the tube winding process. See Ph.D. thesis of A. Tomasch, Boston University.

[5] Personal conversation with a representative of the Precision Paper tube company of Wheeling Il., that has produced thousands of precision drift tubes for several operating straw vertex chambers.

[6] The module simulated was 50 foils defined in [3], followed by a raft of $1mil$ thick mylar/polycarbonate tubes with $4mm$ diameters. The tube centers were staggered to minimize the xenon path length variation as a function of impact parameter. The minimal variation for one module is shown in figure 3b. The chamber planes were additionally staggered with respect to each other in order to minimize variations in mylar/polycarbonate and xenon gas traversed.

[7] L. Christophorou et, al. NIM 171 (1980) 491-495.

SSC R&D PROGRAM

by

M. Gilchriese

SSC/CDG

Detector Research and Development for the Superconducting Super Collider

- The present R&D program
- Continuation and expansion of SSC detector R&D
- Tentative plans for initiation of the SSC experimental program

Why Detector R&D for the SSC?

- Significant general technical challenge posed by increased energy and, primarily, much increased luminosity at the SSC.
- Some experiments eg. B physics clearly require significant improvements in technology to be successful
- Timescale for construction of large SSC experiments will be comparable to construction time of accelerator => do R&D as soon as possible to influence choice of detector technologies

GENERIC DETECTOR R&D HISTORY

July 86	*Ad hoc* proposal from Snowmass '86 meeting for generic SSC detector R&D plan
Oct 86	DOE person assigned to coordinate SSC detector R&D
Feb 87	International Advisory Committe formed by CDG and proposal procedures established
Oct 86 - Feb 87	DOE funds 3 projects @$150K prior to formation of procedures
April 87	Committee meets to consider 31 tasks requesting $3.7M and recommends $545K for 11 projects
April-May 87	11 projects funded by DOE as recommended
July 87	Preliminary meeting for FY88 proposals
October 87	Meeting to consider 50 tasks for FY88 requesting $8.9M and recommended 36 tasks at $3.4M. Funding of 33 tasks for FY88 at $2.25M.
November 88	Committee meets to consider 45, mostly new, FY89 proposals. Recommend 26 for approval
Present(FY89)	Continuation of most FY88 efforts at $3.4M. New tasks at $2.9M.

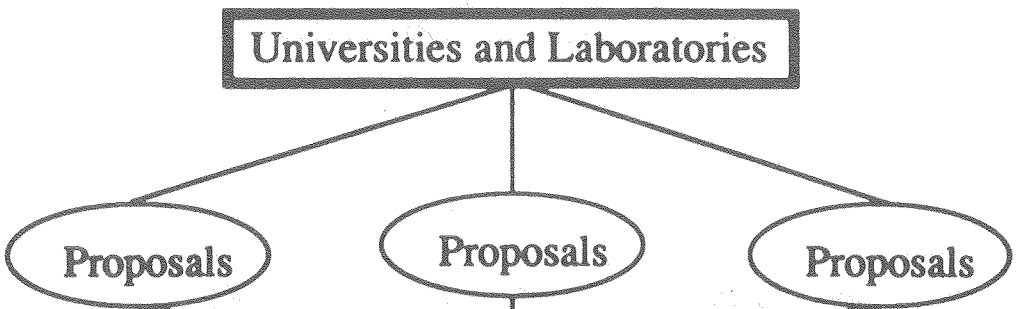

International Advisory Committee on Generic Detector R&D

Dr. D. Bryman(TRIUMF)	Dr. D. Nygren (LBL)
Dr. C. Fabjan (CERN)	Dr. L. Price (ANL)
Dr. J. Jaros (SLAC)	Dr. V. Radeka (BNL)
Dr. R. Kephart (FNAL)	Dr. P. Rancoita(INFN-Milano)
Dr. R. Klanner (DESY)	Dr. R. Ruchti (Notre Dame)
Dr. T. Kondo (KEK)	Dr. M. Shaevitz (Columbia)
Dr. S. Mori (Tsukuba)	Dr. H. H. Williams (Pennsylvania)

Who Is Involved in SSC Detector R&D?

Universities

- Boston Univ.
- CalTech
- Carnegie Mellon
- Florida
- Florida State
- Harvard
- Hawaii
- Illinois
- Indiana
- Michigan
- Mississippi
- Northeastern
- Notre Dame
- Oklahoma
- Oregon
- Pennsylvania
- Pittsburgh
- Princeton
- Rockefeller
- Stanford(CIS)
- Stony Brook
- Tennessee
- Texas A&M
- UC Berkeley(Space Sciences)
- UC Davis
- UC San Diego
- UC Santa Cruz
- UCLA
- Yale

Labs

- Argonne
- Brookhaven
- Fermilab
- LBL
- Oak Ridge
- Sandia
- SLAC

Industries†

- Martin Marietta
- Hughes Aircraft
- United Technologies Microelectronics
- Harris Semiconductor
- Bicron Corp.
- Hutchinson Technology
- Micron Semiconductor
- Rockwell

† There is also SBIR involvement

Future of Detector R&D for the SSC

- Clear need to continue and, in fact, expand substantially the R&D effort for potential SSC experiments.
- In the next year, the expectation is to have an R&D effort with two aspects - continuation of the generic R&D and start-up of a large-scale R&D devoted to major subystems of potential SSC experiments
- It is anticipated that the present generic R&D program will continue in FY90
  - Consideration for renewal of ongoing tasks will be handled according to established DOE procedures
  - The deadline for new proposals to DOE is June 5
  - Generic R&D must be of wide applicability to potential SSC experiments

Future of R&D Cont.

- In addition, it is the intent to support in FY90, subject to the availability of funds, R&D on major subsystems of SSC detectors. Examples of such subsystems include
  - calorimetry
  - tracking systems (silicon and wires)
  - electronics systems, particularly VLSI and radiation hardened circuitry
  - data acquisition and triggering systems
  - particle identification systems
  - physics and detector simulation codes
- It is anticipated that this R&D would involve multi-institutional collaborations and
- would be accomplished so as to have influence on proposals for first round experiments - see schedule later
- Proposals for this type of R&D will be made to the SSC laboratory. Deadline is Oct. 2.

More on R&D

- Proposals for major subsystem R&D will be reviewed by the detector advisory committee in Nov.
- This R&D on major subsystems is intended to meet the very clear need for energetic activities ASAP in support of design of big components of first round of SSC experiments.
- Cannot wait for proposal approval to do all of the R&D
- Get moving now to match tentative schedule for initiation of SSC experimental program

- Additional details about the R&D efforts will appear very soon within a general mailing to the community.

Tentative Schedule of Events Leading to the Initiation of the SSC Experimental Program

1989	
Spring	Form Scientific Policy Committee(SPC)
June 5	Deadline for generic detector R&D proposals to DOE
July	Meeting of detector R&D advisory committee to consider generic R&D proposals
October 2 -4	Supercollider Physics meeting and open house in Texas Announce scope of experimental program Announce general guidelines for letters of intent and precise due date Discuss SSC physics and experiments
October 2	Deadline for major detector subsystem R&D proposals to the SSC laboratory
November	Meeting of detector R&D advisory committee to consider major detector subsystem R&D proposals
1990	
January	First Program Advisory Committee(PAC) meeting Consider interaction between accelerator design and the experimental program Issue precise guidelines for letters of intent
May	Deadline for letters of intent for first round of experiments
July	PAC meeting to consider letters of intent
1991	
January	PAC meeting for mid-course review of first round of experiments
May	Deadline for proposals for first round of experiments
July	PAC meeting to consider proposals Stage I approval

Summary

- The present generic detector R&D program has been successful in starting many of the activities required to meet the challenge of doing experiments at the SSC.
- However, it is time to not only continue this broad-based R&D effort, but to also begin concerted work on R&D for big parts of SSC experiments. This is required to match the schedule for the SSC experimental program.
- Let's get moving!

CLEO II TOF COUNTERS

by

S. Alam

S.U.N.Y., Albany

CLEO II TOF SYSTEM

M. S. Alam, C. R. Sun, P. Wang, W. C. Li, M. Zoeller, & D. Chen
S. U. N. Y. A. (Endcaps)
F. Pipkin, R. Wilson, M. Procario, R. Giles
Harvard Univ. (Barrel)

I. The CLEO II Detector
II. The Barrel TOF System
III. The Convention Design of the Endcap System
  (i) Scintillator slab design
  (ii) Scintillating Fibre ..
  (iii) Microchannel Plate Multiplier design
IV The Novel Design of the Endcap System
  (i) Design Details
  (ii) R2490 description
  (iii) Magnetic Field Measurements
  (iv) TOF Resolution Measurements
V. Conclusions

Particle ID at High Luminosity Hadron Colliders
April 6 '89

CLEO II
Quadrant (Sideview)

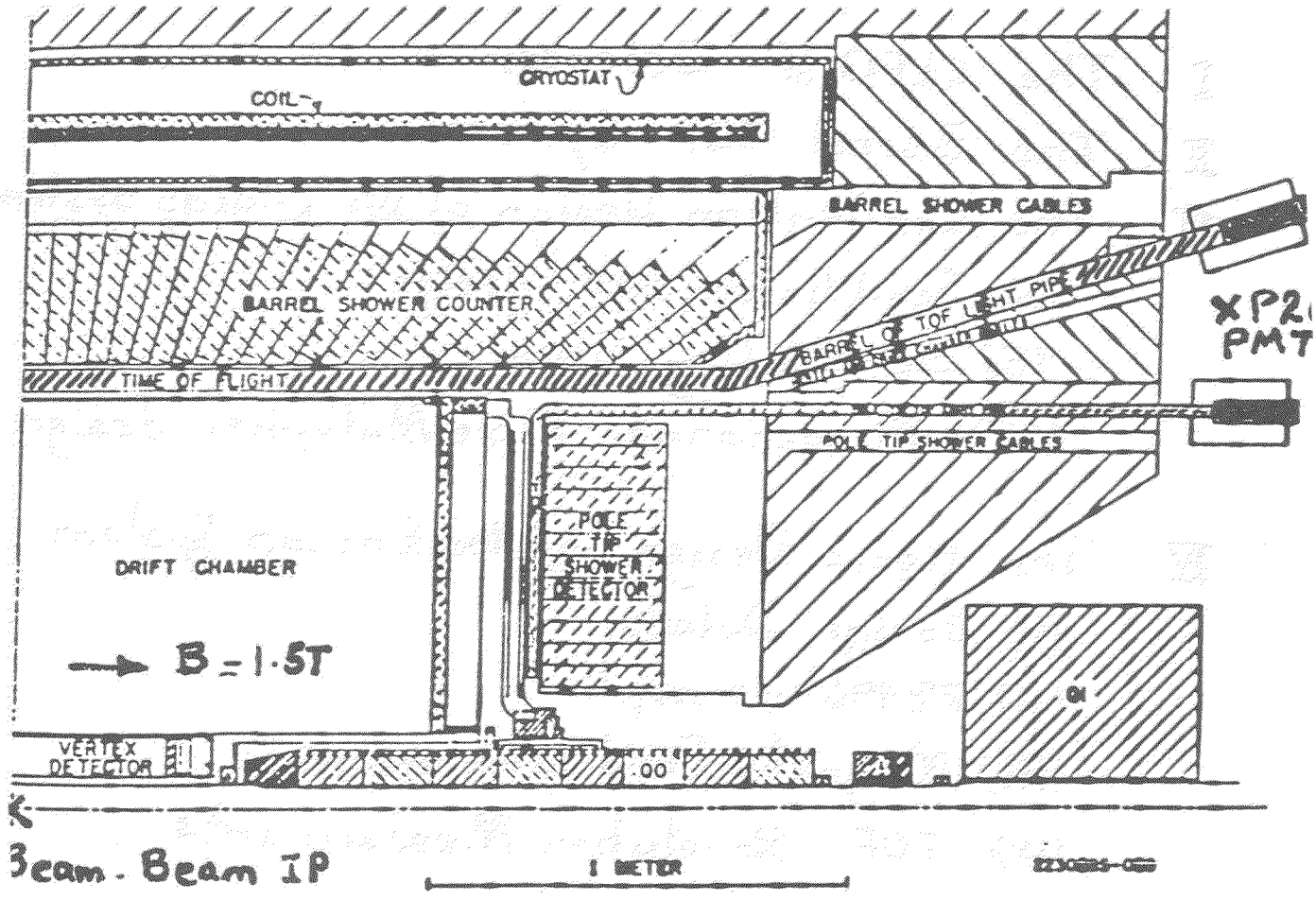

Barrel TOF ~ .80 of 4π

Endcap TOF ~ .11 " "

Barrel TOF

2030368-001

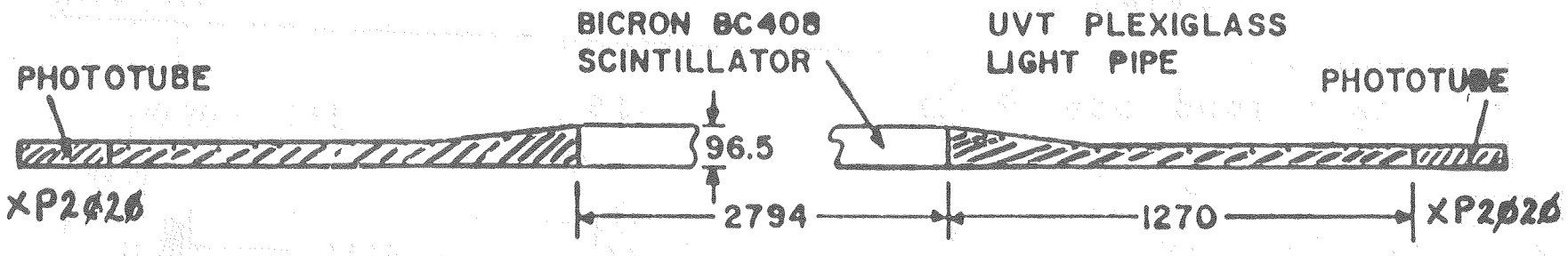

a) The Whole Counter

σ_t = 110 picoseconds

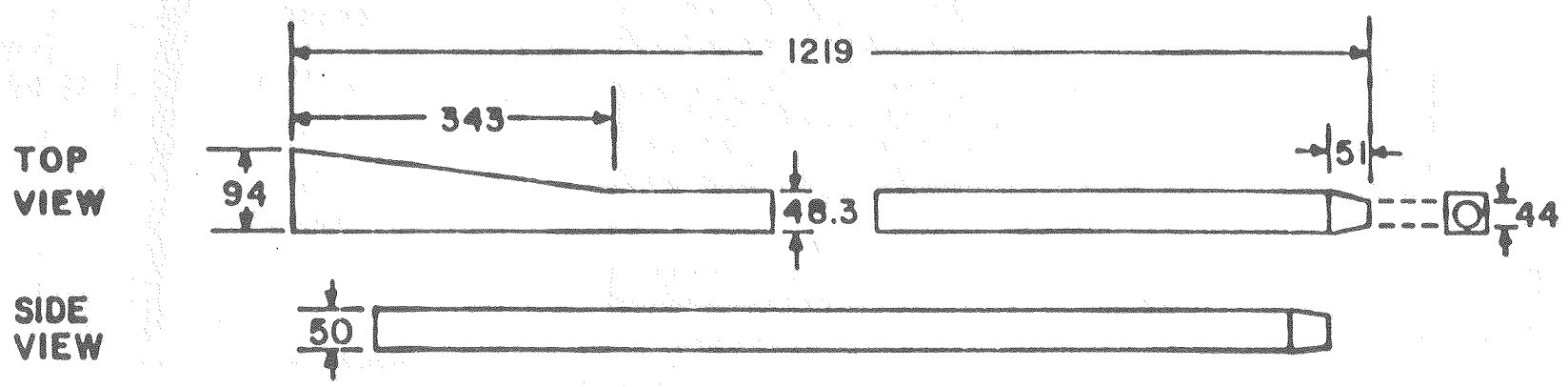

b) The Light Pipe

Fig. 2

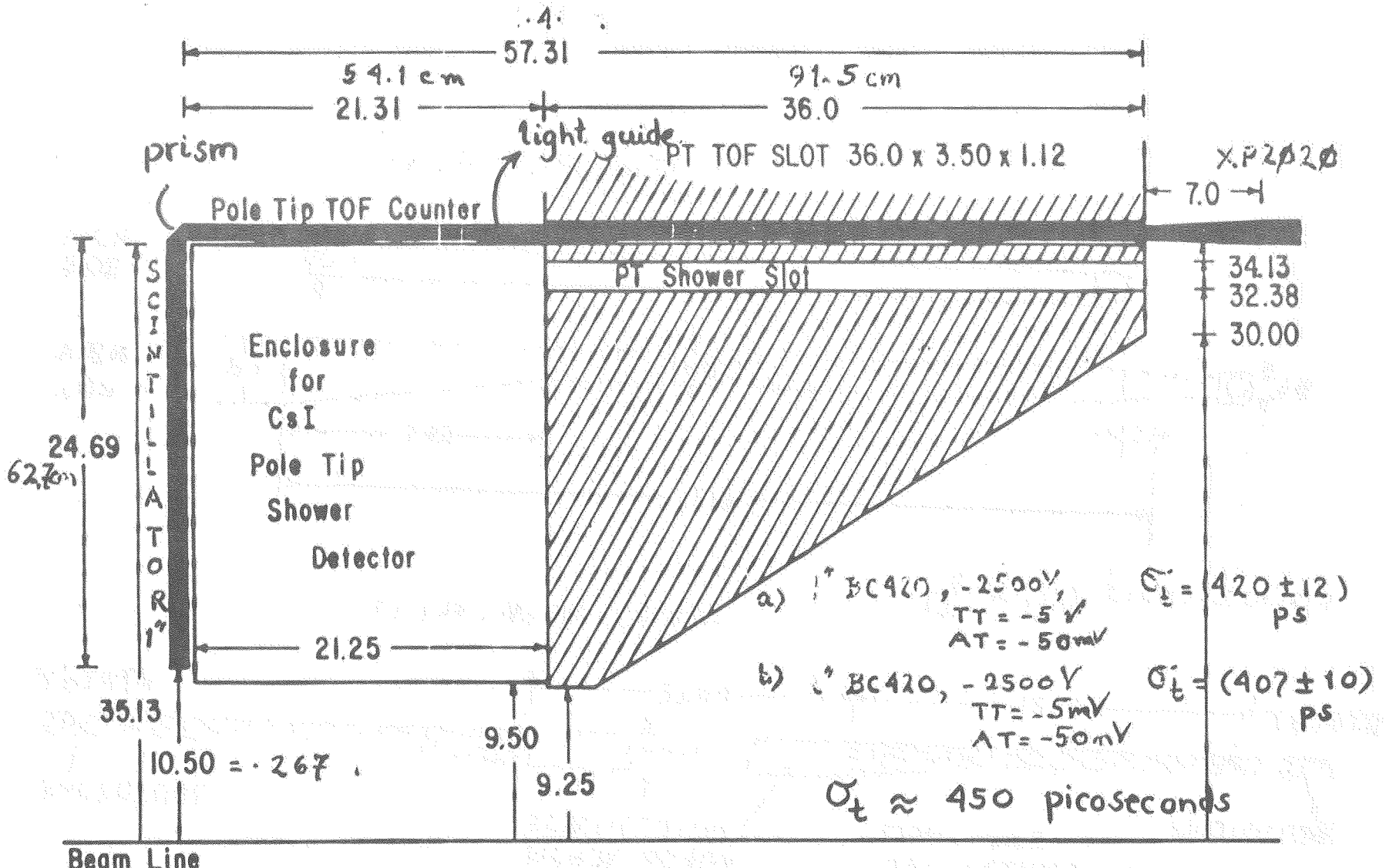

Figure 5

POLE TOF COUNTER (Side View) Scale = 1:8 Dim = Inches

optimal Design
(32 x 2) Counters

Figure 7. ECTOF Side-View Inside CLEO II

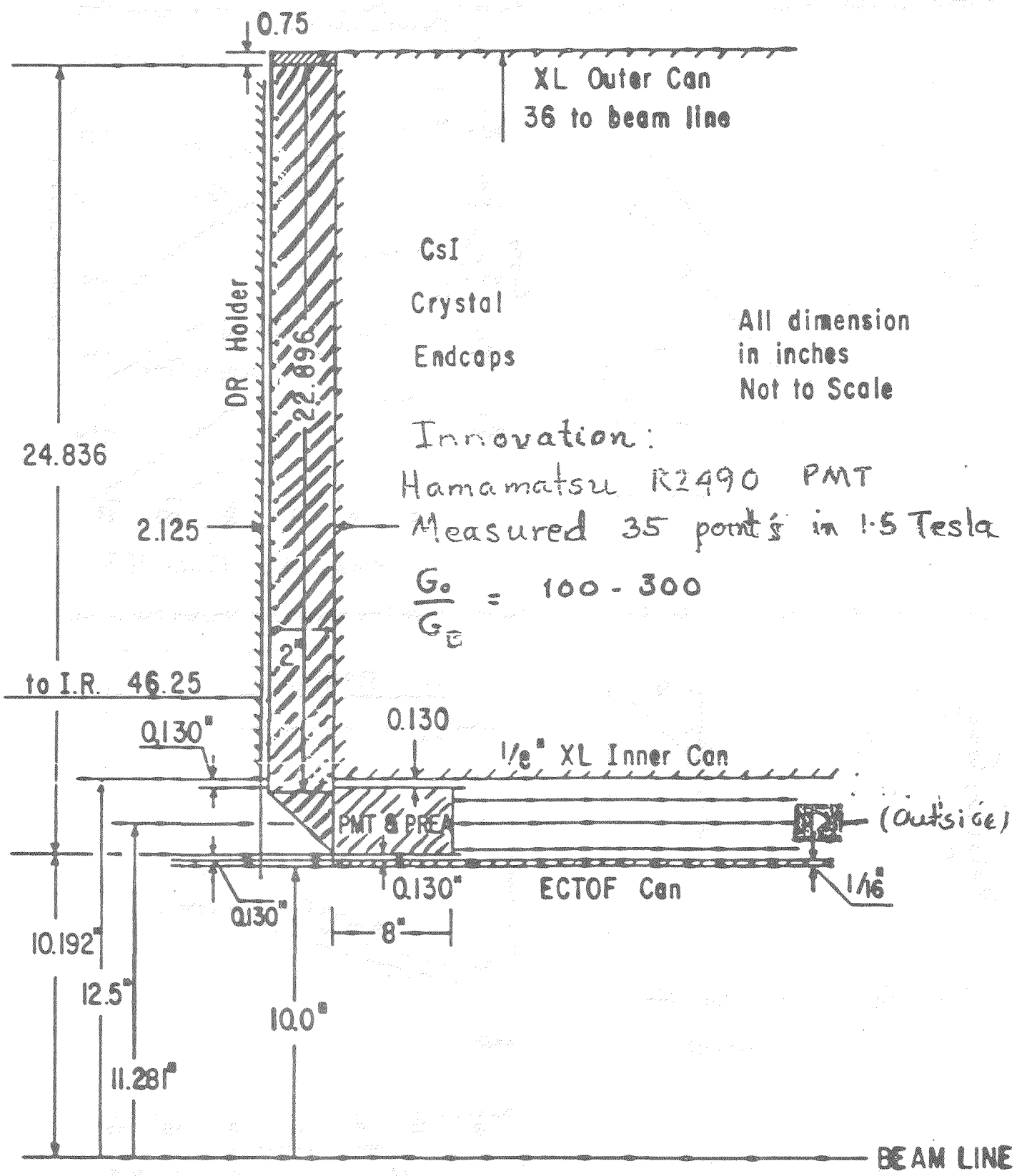

R2490 Spec Sheet (from Hamamatsu)

Figure 2: Typical Gain vs. Supply Voltage (at 0 gauss)

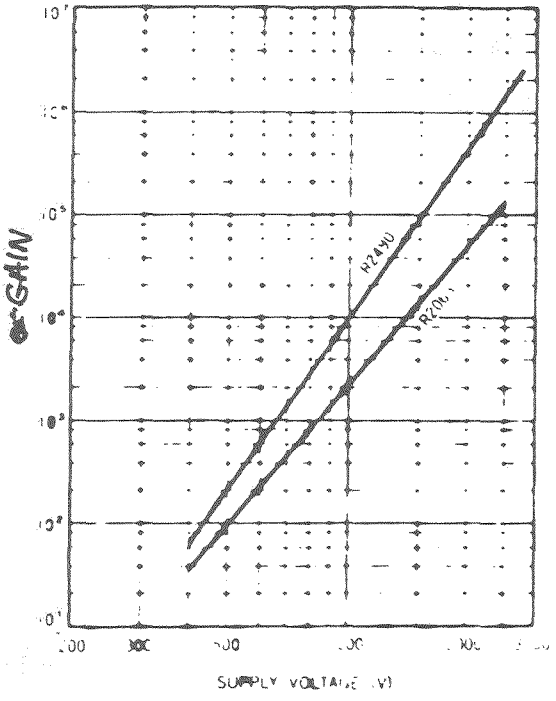

Figure 3: Typical Gain and Dark Current in Magnetic Field (Parallel to Tube Axis)

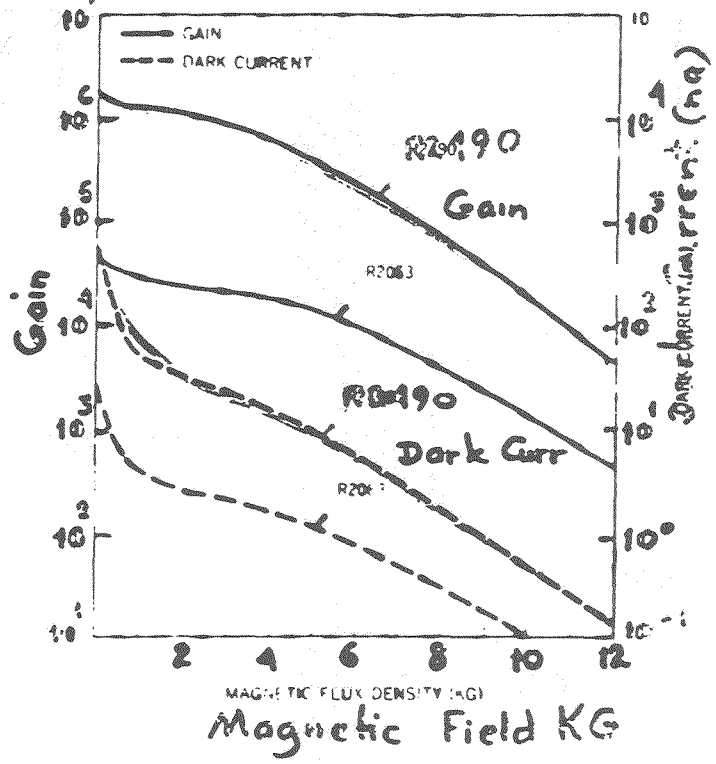

Figure 4: Typical Gain vs. Magnetic Flux Direction

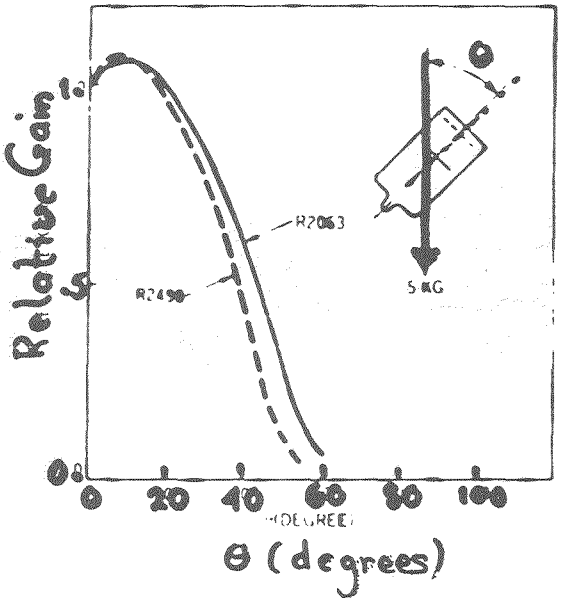

Figure 5: Typical Time Response vs. Magnetic Flux Density

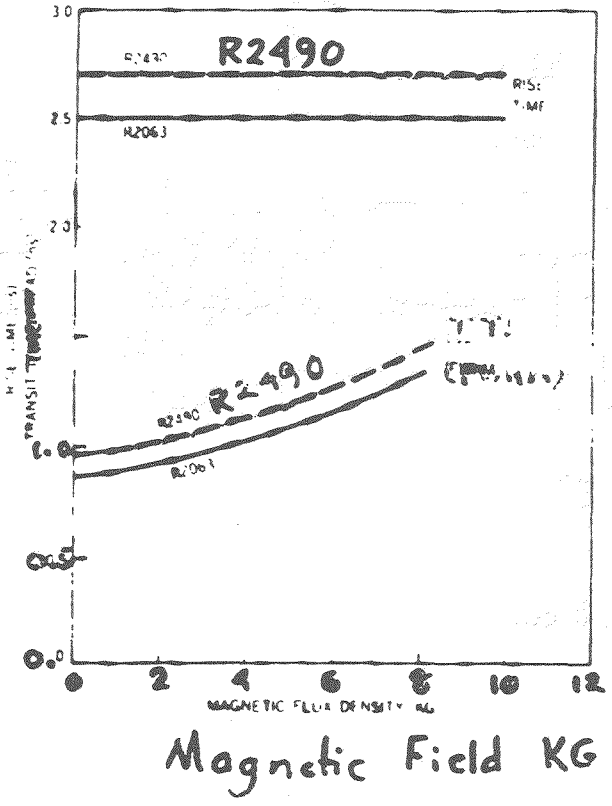

May 26, 19

1.5 T Magnetic Field Gain Loss Test

Data Acquisition System

	B = 0	B = 1.5T	B = 1.5T θ = 27°
Amp =	1234 ch	9.2 ch	8.2 ch
σ_{tof} =	(284 ± 1)ps	(292 ± 1)ps	(327 ± 10)ps
$\frac{G_0}{G_B}$ =		134	150

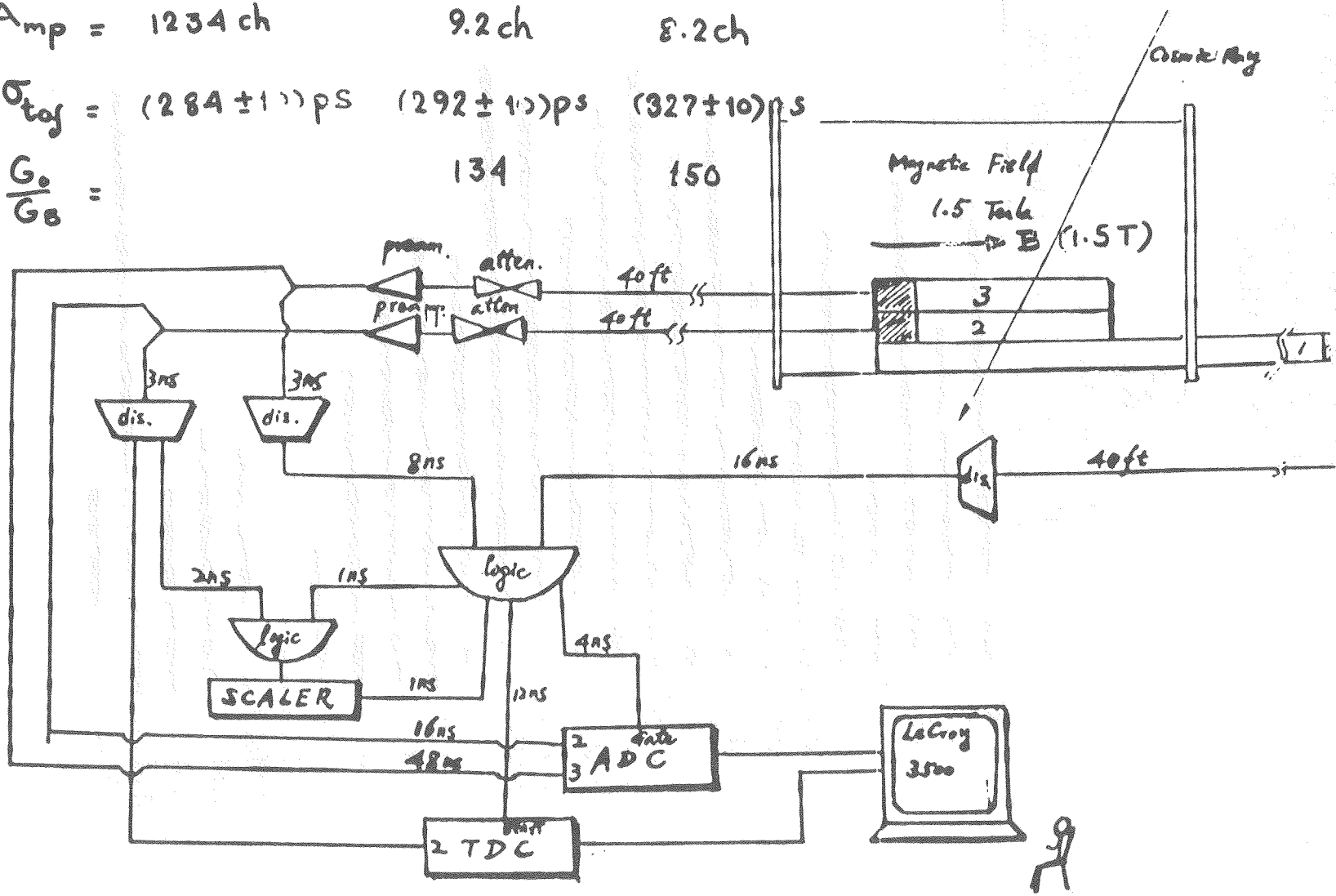

FINAL TEST FOR END CAP TOF COUNTERS

High Energy Group

SUNY at Albany

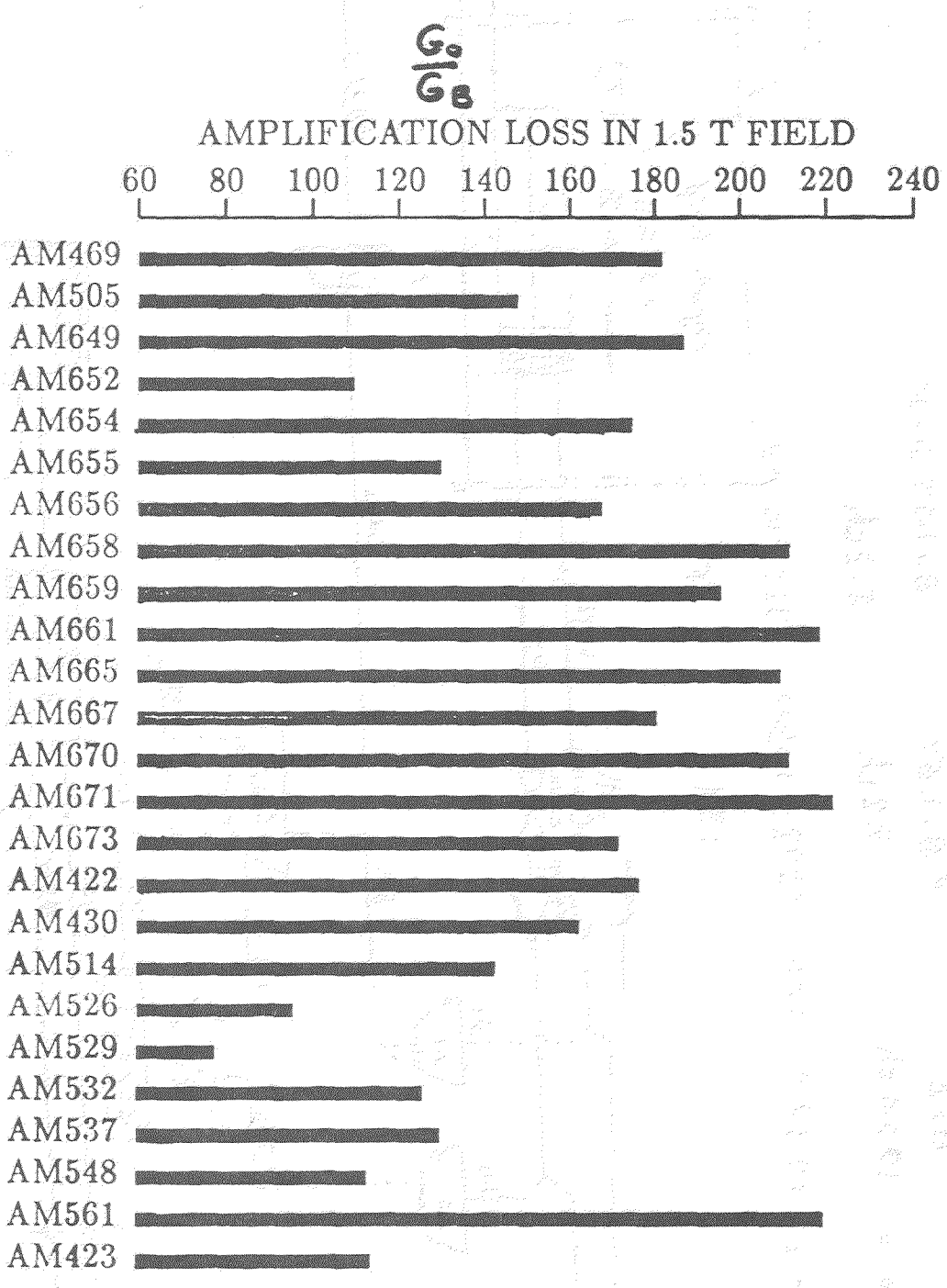

ATT. JOHN G

RE : SUNY ALBANY / R2490.

HERA Results :

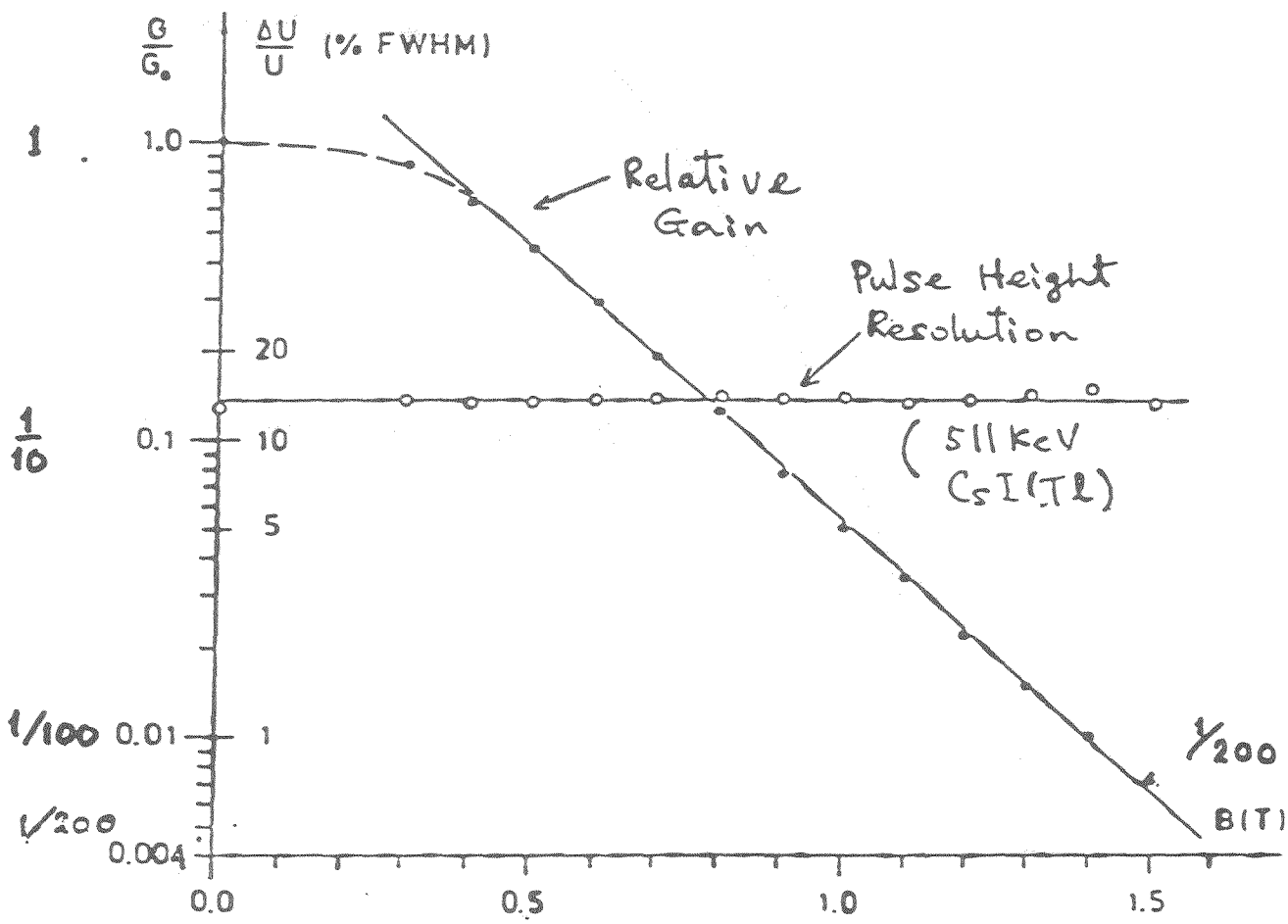

Fig. 2: Relative position G/G₀ (•) and amplitude resolution ΔU/U (o) for the 511 keV-photopeak vs. B for an axial field (source: ^{22}Na; scintillator: CsI[Tl]; photomultiplier: HAMAMATSU Type R 2490).

Reported by S. Mordhorst, H. Duhm, R. Langkau of Univ of Hamburg / H1 at HERA.

Tested with 17 x 48 x 137 cm³ Gap. Magnet.

FINAL TEST FOR END CAP TOF COUNTERS

High Energy Group
SUNY at Albany

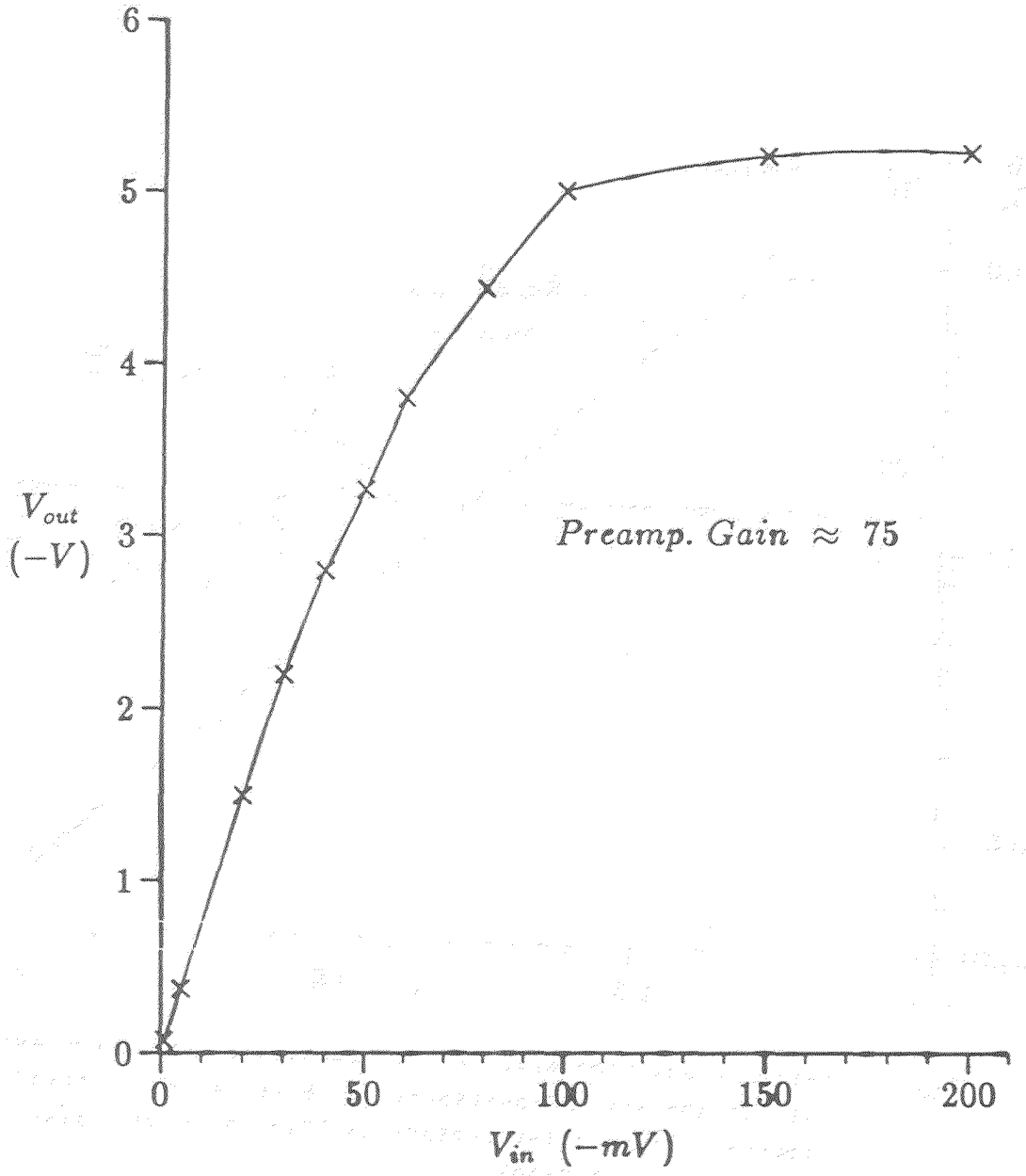

TOF Test Setup

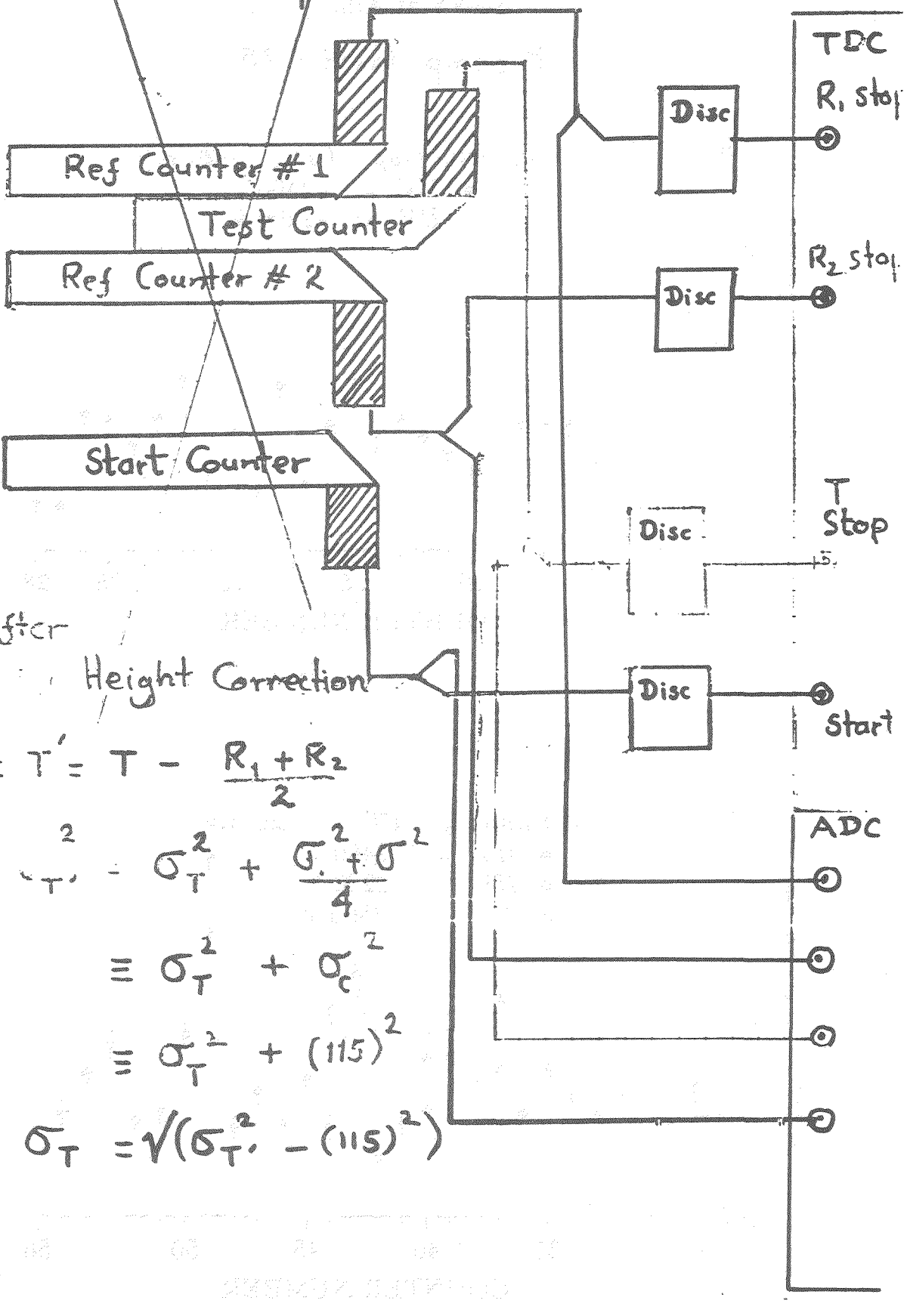

After Height Correction

plot $T' = T - \frac{R_1 + R_2}{2}$

$$\sigma_{T'}^2 = \sigma_T^2 + \frac{\sigma_{\cdot}^2 + \sigma^2}{4}$$

$$\equiv \sigma_T^2 + \sigma_c^2$$

$$\equiv \sigma_T^2 + (115)^2$$

$$\therefore \sigma_T = \sqrt{(\sigma_{T'}^2 - (115)^2)}$$

FINAL TEST FOR END CAP TOF COUNTERS

High Energy Group
SUNY at Albany

Preamp Gain = 75

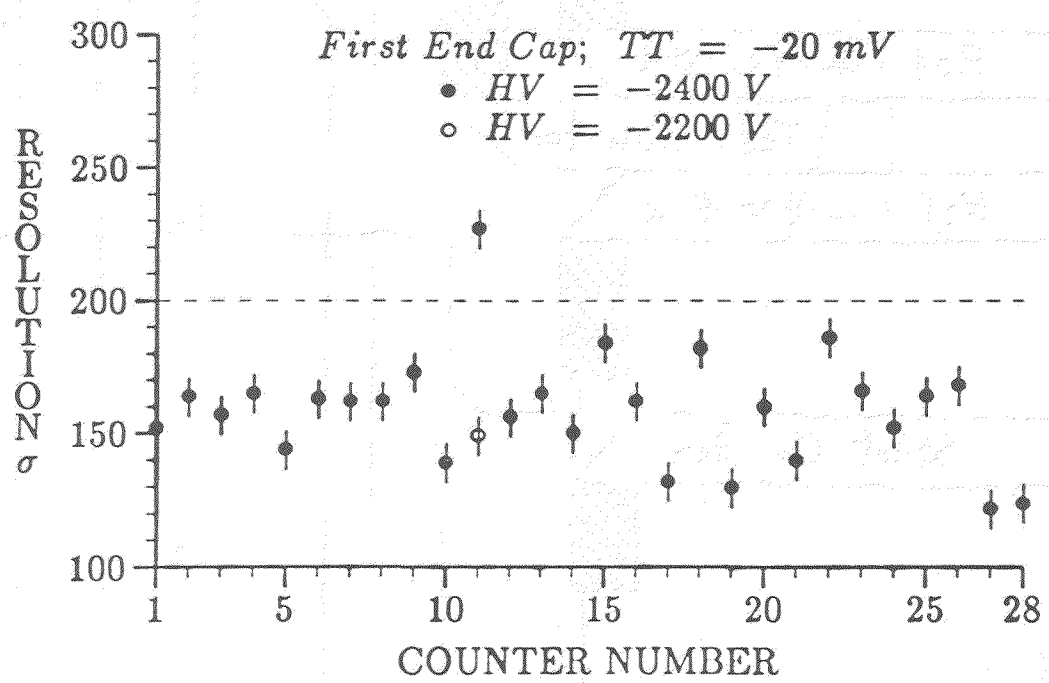

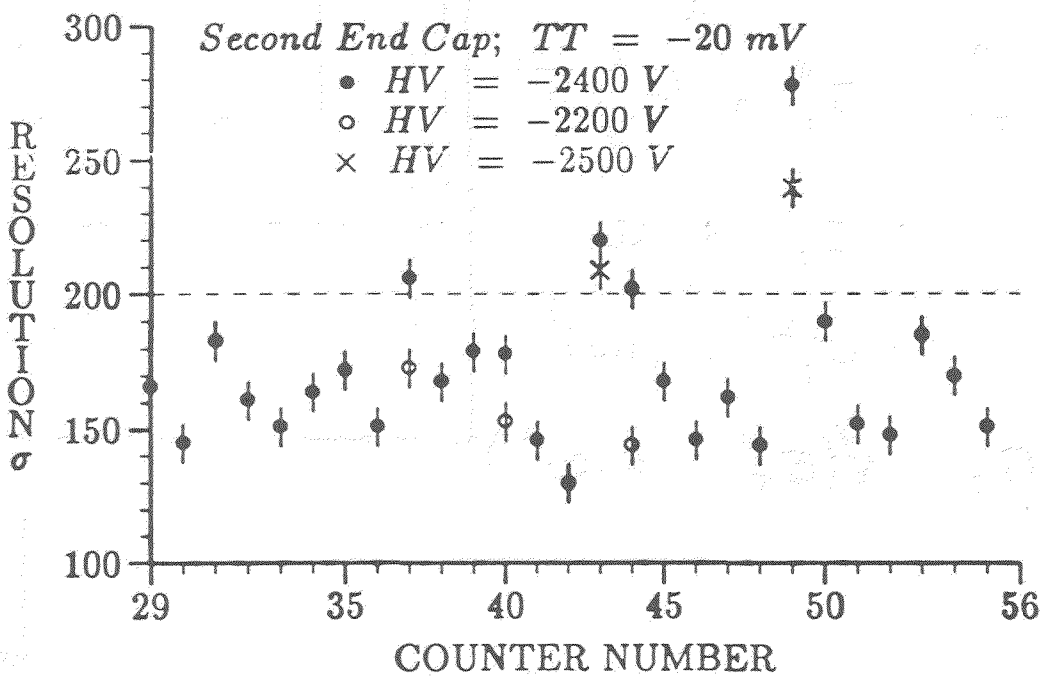

FINAL TEST FOR END CAP TOF COUNTERS

High Energy Group
SUNY at Albany

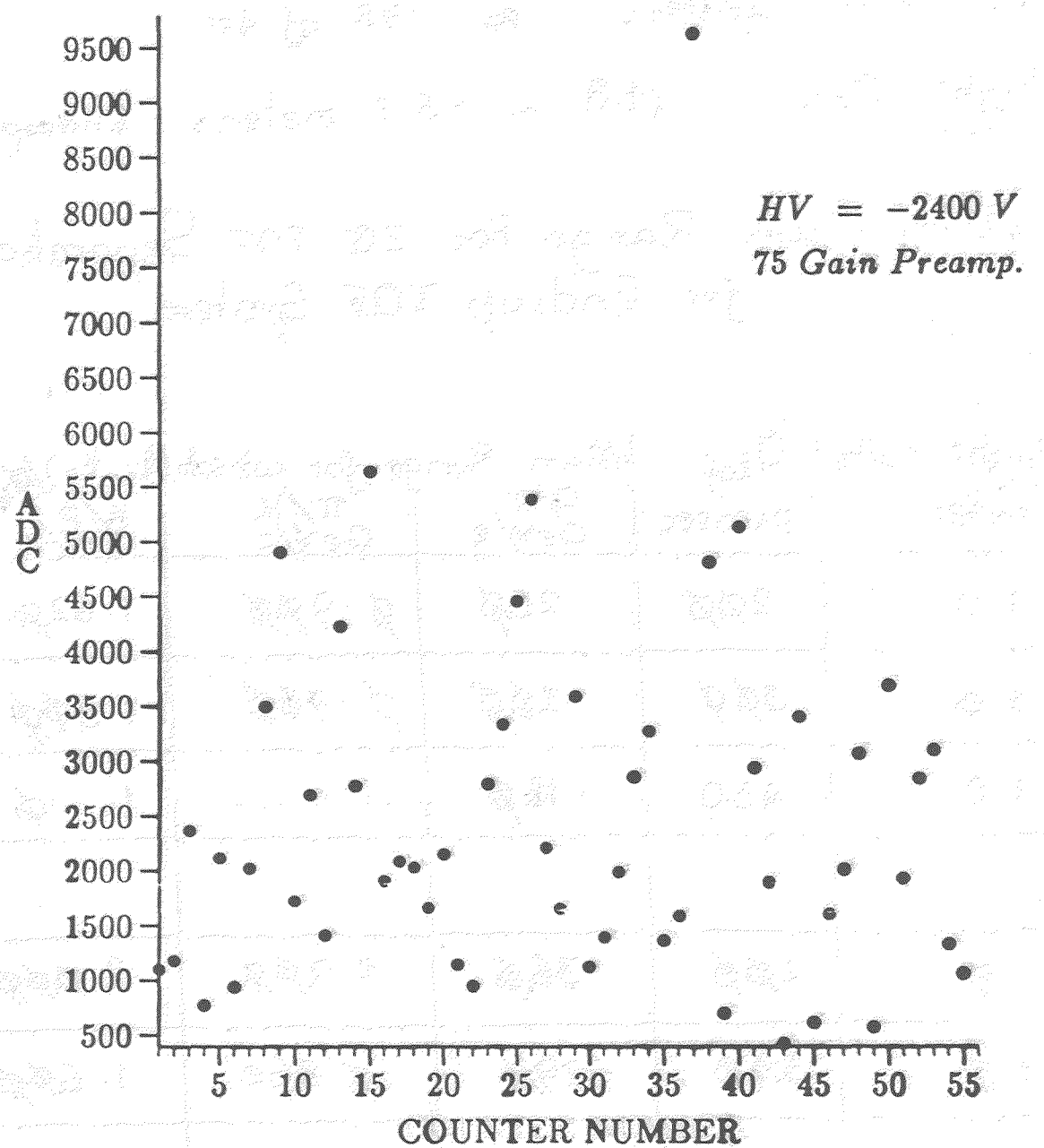

Conclusion

Barrel TOF System $\approx$ .80 of 4π $\theta = \pm 35°$

Both Endcap TOF System $\approx$ .18 of 4π $\theta = 13° - 37°$

Full TOF System $\approx$ .98 of 4π

Flight Path (1.2 ~ 1.5) meters Endcap

Momentum Range For 2σ TOF Separation for Endcap TOF System

Flight Path meter	σ_{tof} picosec	Mom. Range for which $(t_i - t_f)/\sigma_t > 2.0$ e/π GeV/c	π/K GeV/c	K/P GeV/c
1.0	200	.260	.900	1.620
1.0	300	.200	.760	1.300
1.0	450	.160	[illegible]	1.[illegible]0
1.5	200	.360	1.200	2.000
1.5	300	.290	.960	1.600
1.5	450	.220	.800	1.300

GO FOR NEW DESIGN !!!!!

The E665 RICH COUNTER

Harsh Venkataramania*
Yale University
New Haven
Connecticut

July 24, 1989

Abstract

Brief descriptions of the Fermilab E665 experiment and the E665 Ring Imaging Cerenkov (RICH) counter are given. The properties of the RICH counter have been studied using the rings made by the incoming muon beam. These rings have also been used to study the properties of the beam and to measure the refractive index of argon gas around 1500 angstroms. Rings associated with reconstructed charged tracks from interesting interactions have also been observed.

*Talk presented at the Symposium on Particle Identification at High Luminosity Hadron Colliders, April 5-7, 1989, Fermi National Accelerator Laboratory, Batavia, Illinois.

List of Figures

List of Tables

1 The E665 experiment

The primary aim of the Fermilab experiment E665, as stated in the proposal[1] is to explore properties of hadrons recoiling from deep inelastic muon collisions in hydrogen and heavy nuclei for incident muon beam energies of up to 650 GeV. To do this one has to reconstruct and identify most of the hadrons, muons, electrons and photons produced in such interactions. The information will be used to study quark and gluon jets, multiplicities and fragmentation functions, charge and baryon number of recoil hadrons and hadron production from heavy nuclei[1].

E665 is a fairly large experiment[2]. The distance between the center of the target(TARGET in Figure 1) and the downstream end (PLRF in Figure 1) of the experiment is about 36 m. In addition there is a beam spectrometer located upstream of the target which is used to tag incoming muons and to measure their kinematics. The beam spectrometer is about 55 m long.

In the experiment, the beam spectrometer in addition to tracking incoming muons provides the beam trigger, the forward spectrometer tracking chambers (PCV, PC, PCF, DC1-4, PSA, PSB in Figure 1) are used for reconstructing forward going charged tracks, the muon detector (SPM, SMS, PTM in Figure 1) is used for triggering the experiment and for identifying muons, the electromagnetic calorimeter (CAL in Figure 1) is used for detecting photons, electrons and measuring the distribution of neutral electromagnetic energy. This distribution can also be used to select interesting events.

Figure 2 shows, for a 500 GeV muon beam hitting a hydrogen target, the expected momentum distribution of charged pions, kaons, protons which are accepted by the RICH counter (RICH in Figure 1). The plots were obtained using the Lund monte carlo for leptoproduction[3,4] and a very simplified detector simulation of the E665 experiment; in the Lund monte carlo, default values for all the cuts and for most of the parameters were used. The detector simulation consisted of applying on each charged track transverse momentum kicks from both magnets (CVM and CCM in Figure 1) and imposing aperture constraints from the second magnet and the RICH counter mirrors. The scattered muon is almost always detected in the RICH counter.

2 The E665 RICH counter

The E665 RICH counter[5](Figure 3) is a focusing type of RICH counter. This means that the optics of the counter are such that if spherical aberrations are neglected then parallel rays of light image to a point. Charged particles having boosts above the threshold value for the medium used in the counter when passing through the RICH counter emit Cerenkov light. This light is directional and usually strikes one or more of the 33 RICH counter spherical

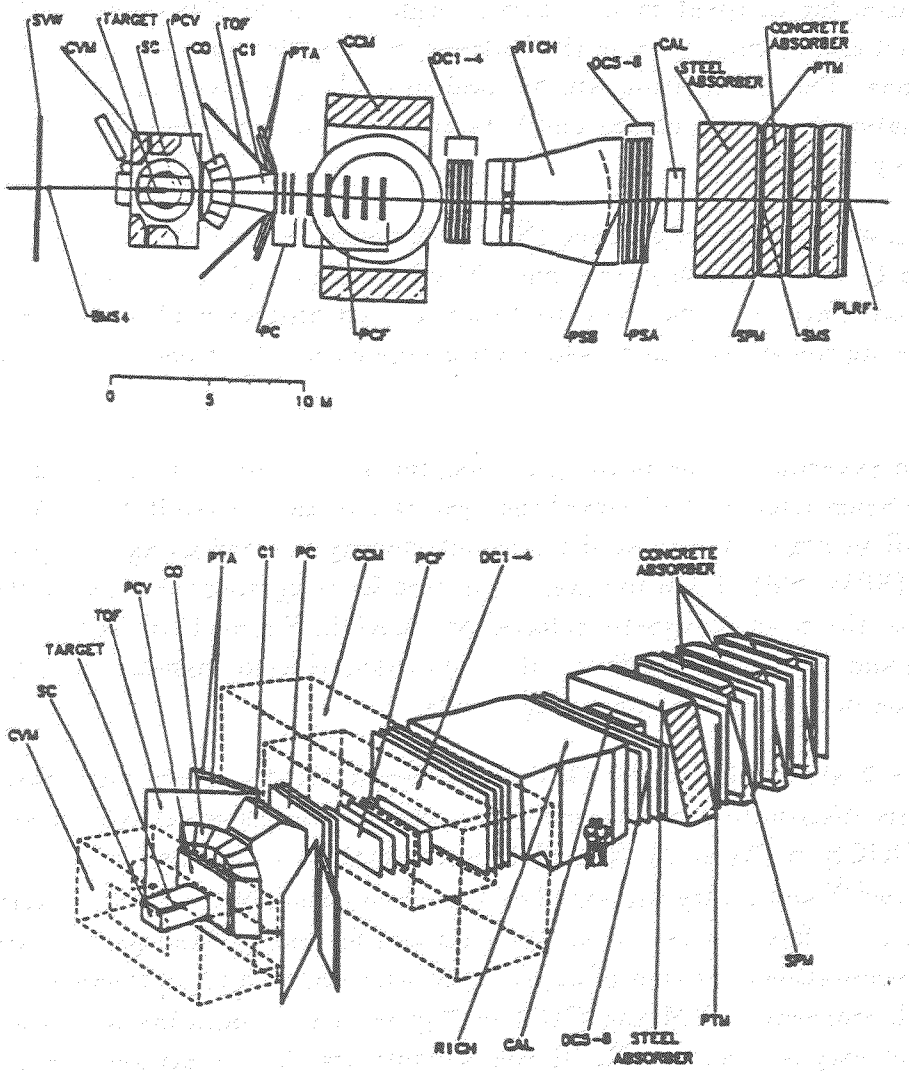

Figure 1: The E665 experiment.Plan and perspective views of the experiment are shown.

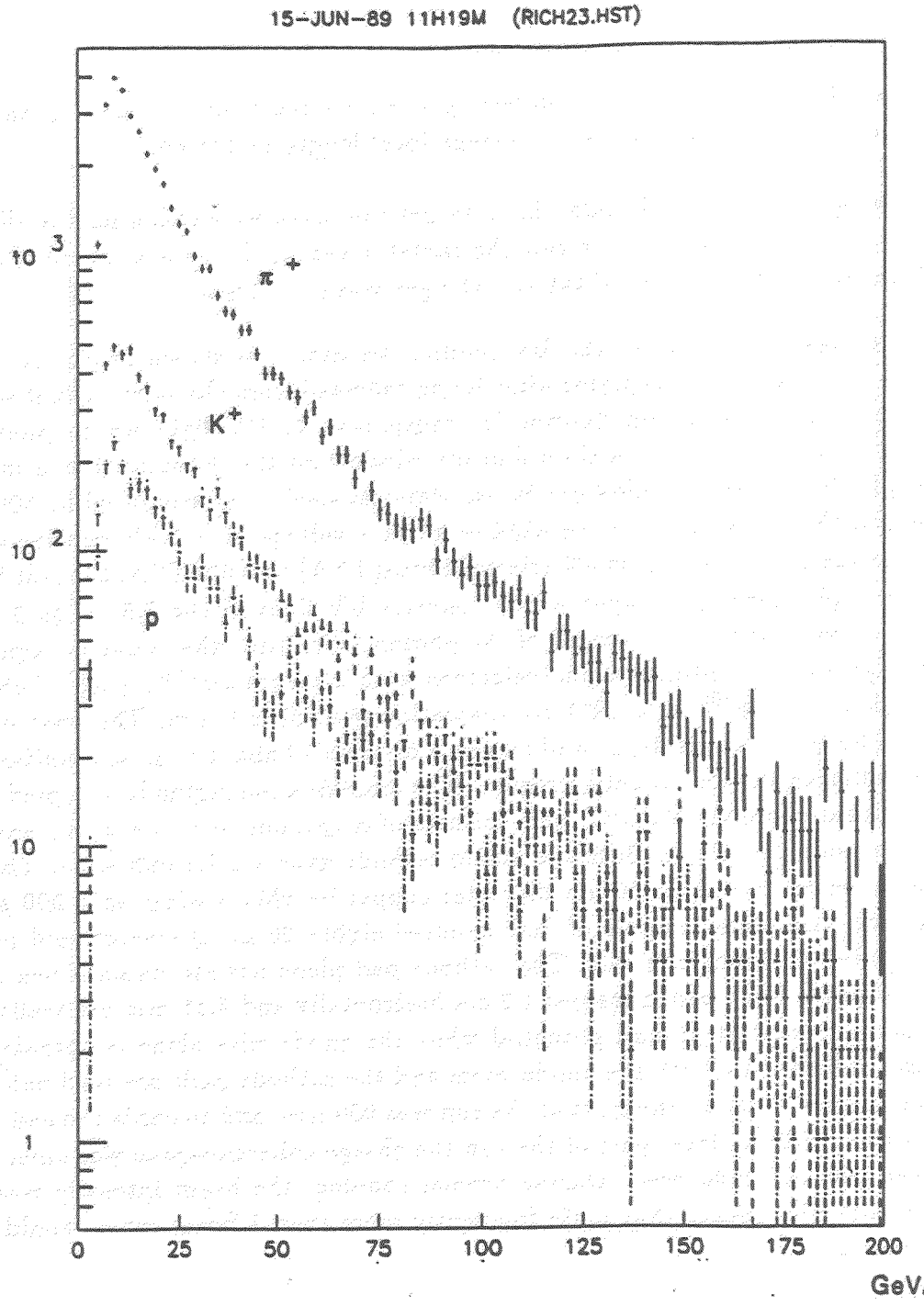

Figure 2: Expected momentum spectra of π, K and p. 60000 Lund monte carlo events were generated to produce this plot. On the horizontal axis momentum of the particle in GeV/c while on the vertical axis number of particles per 2 GeV/c bin is shown. The errors are statistical. On average $\sim$ 2.5 charged particles per event are expected to fall within the acceptance of the RICH counter mirrors.

mirrors. The detector used for detecting the reflected light is placed at the focal plane of the mirrors. The mirrors have an average focal length of 485 cm.

During the 1987-'88 Fermilab fixed target run, data were taken for two different radiator gases. For a small part of the run the radiator gas used was a mixture of 50% argon and 50% helium while for most of the run the gas was pure argon.

A schematic diagram of the UV photon detector[5] is shown in Figure 4. A Cerenkov photon produced in the radiator after being reflected from the mirrors first sees the calcium fluoride window. Calcium fluoride is transparent to UV light up to photon energies of 9.5 eV. Flush against the calcium fluoride window on the detector side is mounted a mesh electrode. The mesh is made from 50 μm stainless steel wires separated by 500 μm. Both the mesh and the brass frame of the window sit at a voltage of -1.5 kV relative to ground. The detector gas used varied from 3% triethylamine(TEA) to 0.5% TEA; the rest being methane. TEA is a photosensitive vapor which converts UV light in the 7.5 eV to 9 eV region into photoelectrons. If the wavelength of the photon falls inside the sensitive region of TEA, the photon gets converted into a photoelectron with a maximum efficiency of about 30%. The conversion distance[6] for a TEA concentration of 0.7% is 5 mm. The photoelectron then is repelled by the mesh electrode and travels a distance of about 5 cm in a uniform electric field before entering the amplification region. The amplification region is occupied by a multiwire proportional chamber(MWPC) and consists of a cathode wire plane, an anode wire plane and a cathode pad plane. Both the anode-cathode gaps are 3.2 mm wide. The cathode wire plane is constructed from 50 μm diameter copper beryllium wires on a 500 μm pitch while the anode wire plane consists of four hundred eighty 20 μm diameter gold plated tungsten wires spaced at 2 mm intervals. The cathode pad plane has etched on it ten thousand eight hundred pads. Each pad measures 1.2 cm horizontally and 3.81 mm vertically. The cathode wire plane is kept at ground potential while the anode wire plane is operated at +2.8 kV. Charges collected by both the anode wires and the cathode pads are read out[7]. The charge collection gate width at the start of the run was 950 nsec and towards the end it was reduced to 550 nsec. For the later part of the run the charge collection gate was open for drift times between 590 and 1140 nsec. During normal running, the beam intensity was typically 10^6 muons/sec. This meant that quite frequently more than 1 beam muon would fall inside the RICH counter gate.

The RICH counter is one of several particle identification detectors in experiment E665. Different detectors cover different momentum as well as angular regions. Figure 5 shows the individual as well as combined particle identification capability of the detectors in E665. The RICH counter covers the high momentum range and should provide π/K/p separation up to momenta of 100 GeV/c.

The RICH counter is a large device. Along the beam direction it is about 6m long, vertically it is 4m high and horizontally it has maximum and minimum widths of 6m and 4m respectively.

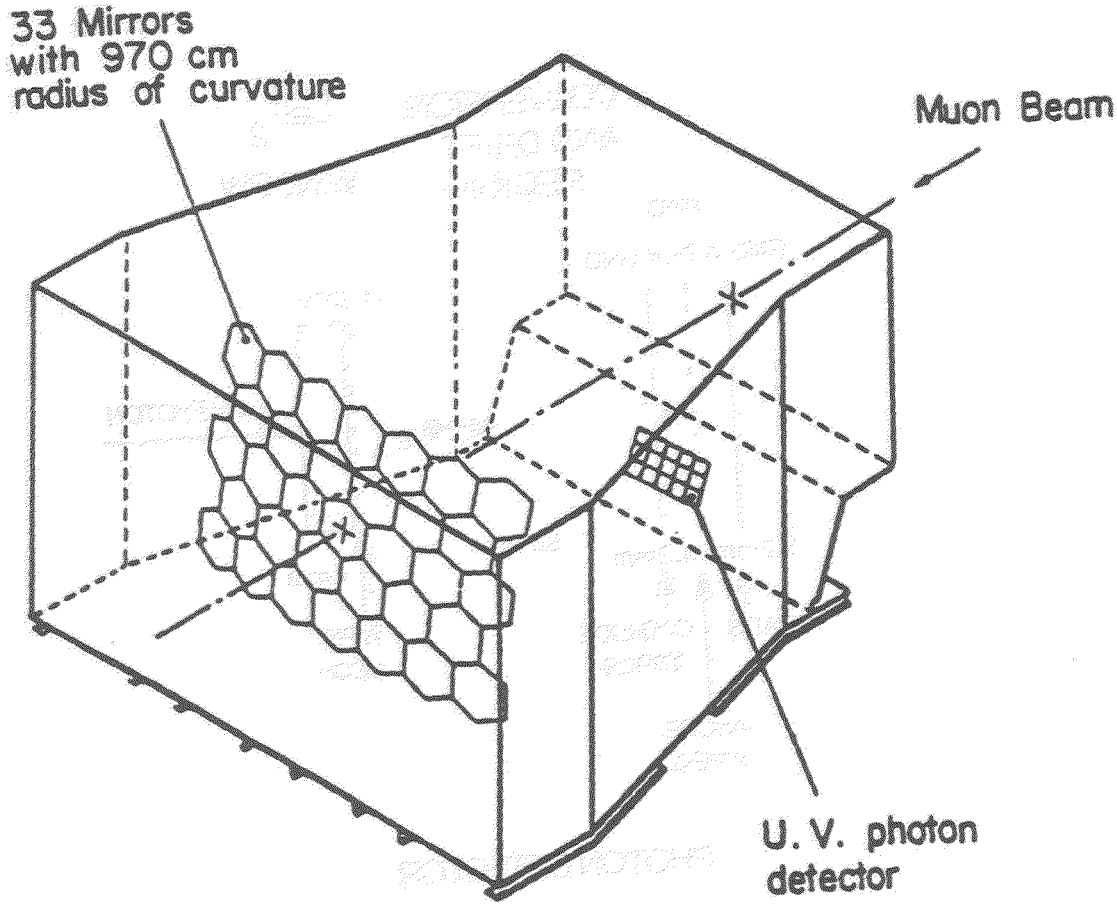

Figure 3: The E665 RICH counter

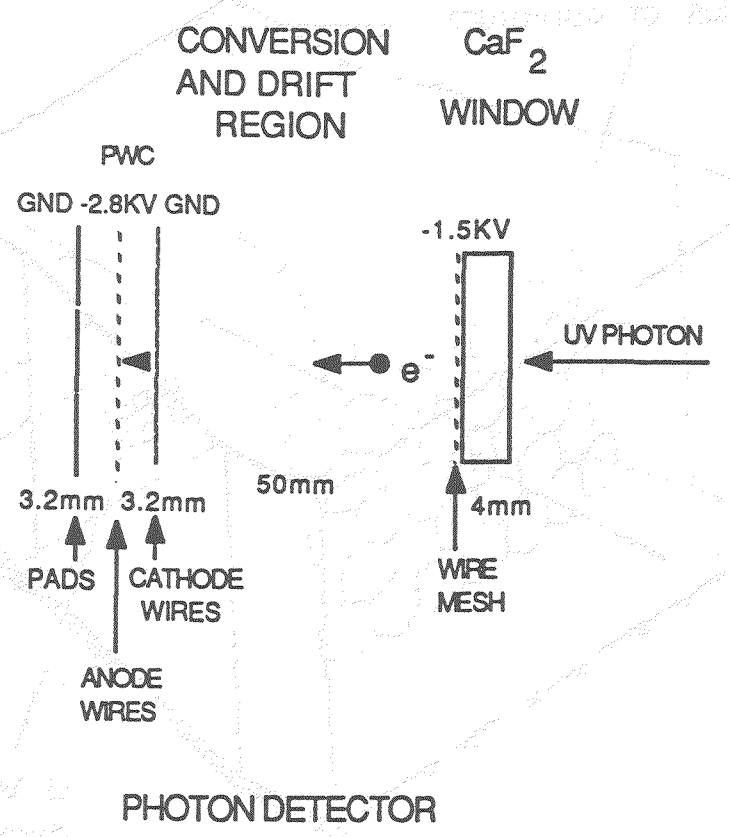

Figure 4: The detector used to detect UV photons. A schematic diagram of the detector is shown.

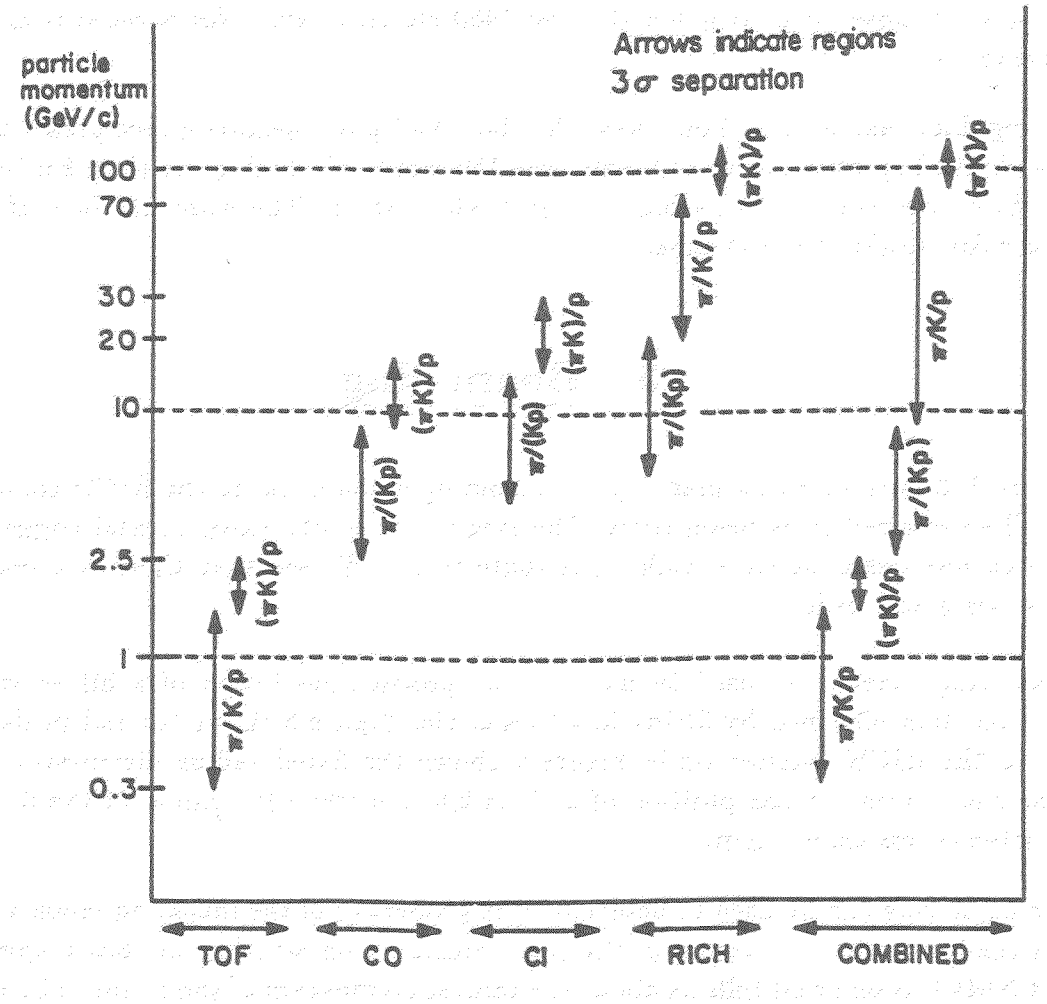

Figure 5: Particle identification in E665

Figure 6 illustrates the noise level in the RICH counter readout. The two histograms are pulse height distributions for no external input for pads and wires respectively. The plots were made by first levelling pedestals of all the electronic channels and then issuing 5 and 100 dummy triggers to the RICH counter readout for pads and for wires respectively. The r.m.s. value of noise for pads is found to be 1400 electrons while for wires it is found to be 5000 electrons.

During data taking only those channels which had pulse heights above preset thresholds were readout. Typically the word length was 150 words of which more than half were noise words. One word consists of 24 bits of useful information. The word has in it the address and the pulse height of the channel.

3 Beam ring

Figure 7 illustrates a ring made by the incoming muon beam in the RICH counter. Such rings will be referred to as beam rings. The ring is due to one experimental trigger however more than one beam particle could contribute to it. We see that there is a good match between wires and pads.

Beam rings have been used to measure the position resolution of a hit as well as the radius resolution obtained by fitting hits to a circle. Figure 8 shows the radius distribution of hits in the RICH counter while Figure 9 shows the fitted radius distribution. We see that the r.m.s. error on the position of a hit is 2.6 mm while the r.m.s. of the fitted radius distribution is less than 1 mm.

The beam ring can be used to determine the properties of the incoming muon beam. The shift in the location of the center of the ring depending on whether the beam spectrometer magnet NMRE is on or off tells us about the central momentum of the beam. The movement is illustrated in Figure 10. The vertical divergence of the beam can be estimated from the spread in the vertical coordinate of the fitted ring (Figure 11).

The number of hits produced by an ultrarelativistic particle has been measured using the beam ring. This has been done by looking at the difference in the number of hits in the RICH counter between 2-beam and 1-beam events (Figure 12). 2-beam and 1-beam events are events where the track reconstruction program in the beam spectrometer finds exactly 2 and 1 beam tracks respectively. One has to take the difference because on average the RICH counter sees more than one beam particle per trigger.

From the properties of the RICH counter one can estimate the expected number of photoelectrons for an ultrarelativistic particle. This is shown in Figure 13 assuming the value of the TEA quantum efficiency to be that given by Holroyd et al[6]. The expected number of photoelectrons is roughly factor of 2 higher than what is experimentally seen.

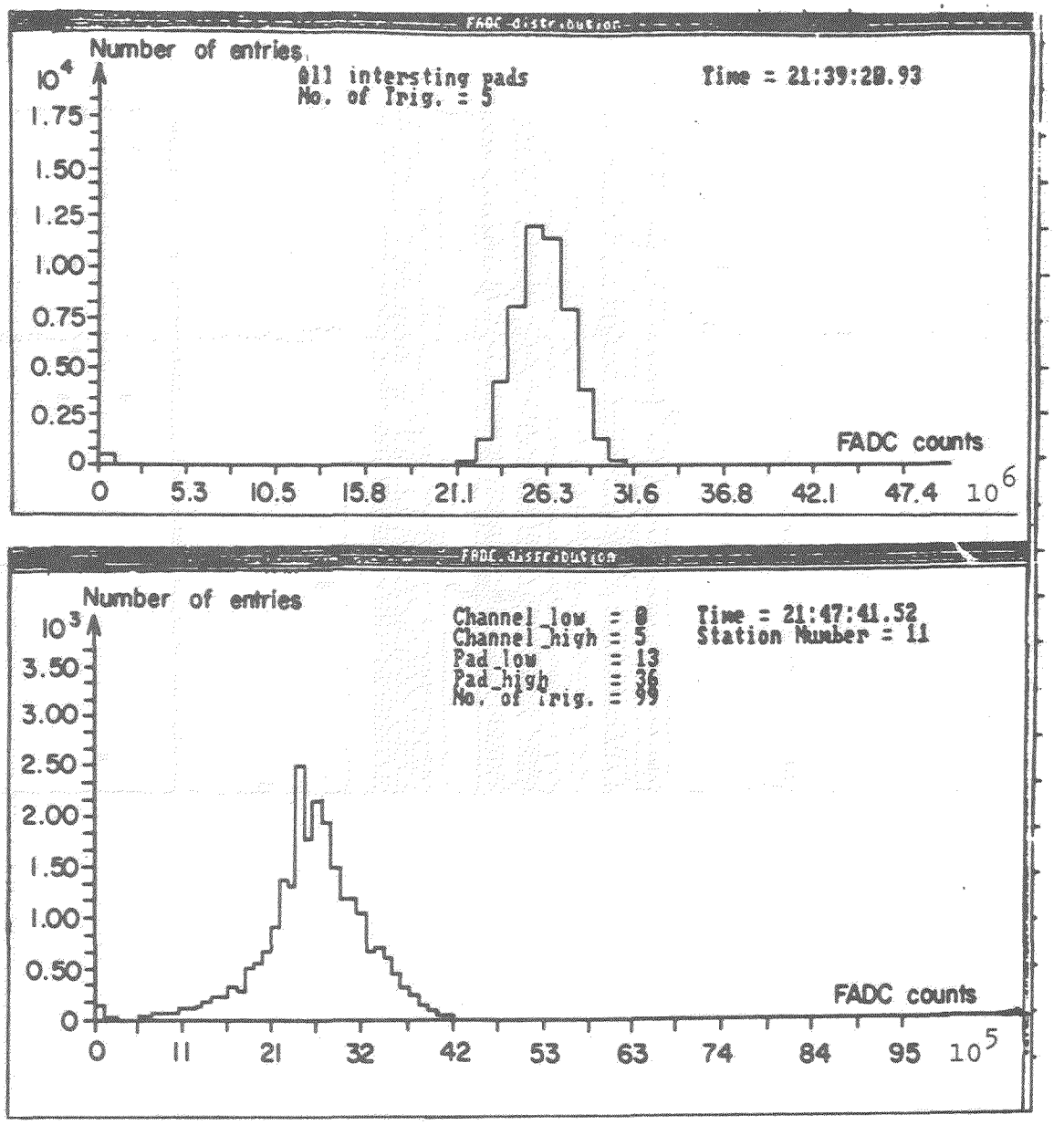

Figure 6: Noise in the RICH counter readout. The top plot is for all the pads while the bottom plot is for the anode wires. In the plots 1 bin corresponds to 1 count of the FADC (Flash ADC) and 1 count is 1/7 femtoCoulombs of charge. The location of the peak can be set to a desired value. During the run both peaks were centered at 25 counts of the FADC, the full scale of the FADC being 256 counts.

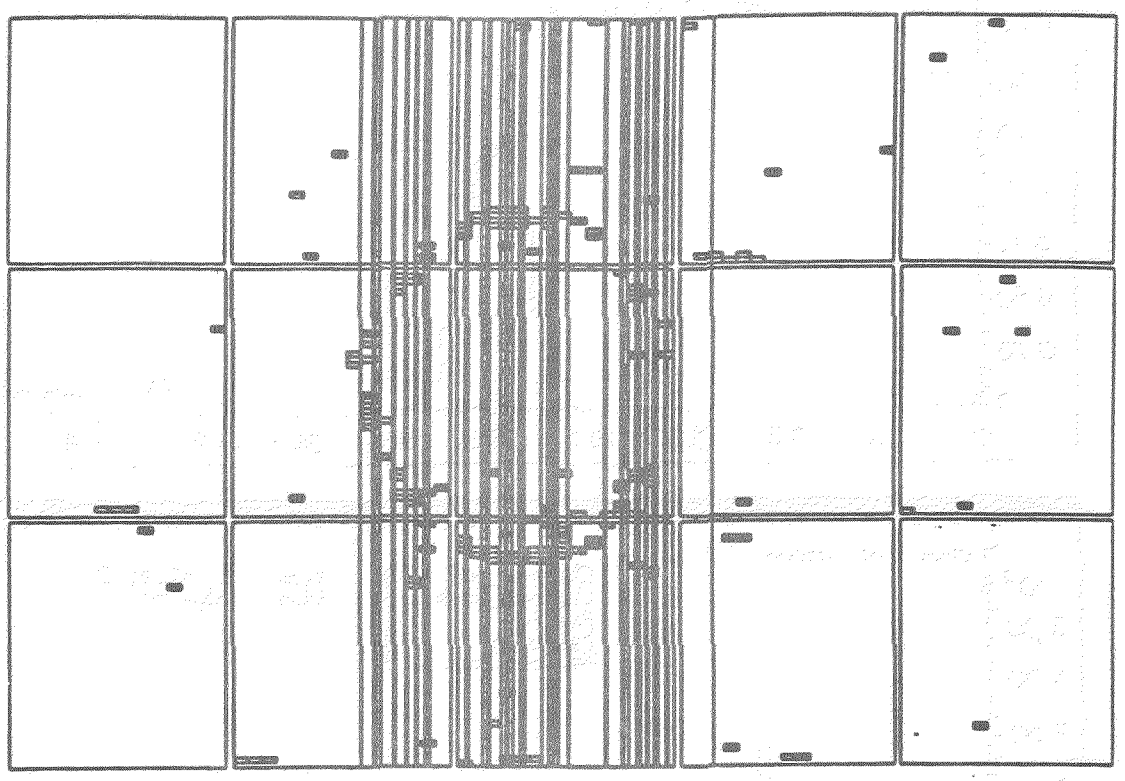

Figure 7: Beam ring seen in the RICH counter. In the figure the small rectangles are pads with signal above threshold, the vertical lines are wires with signal above threshold. The pad plane, as shown in the figure, has a tile structure to it and the tiles are arranged in 3 rows and 5 columns.

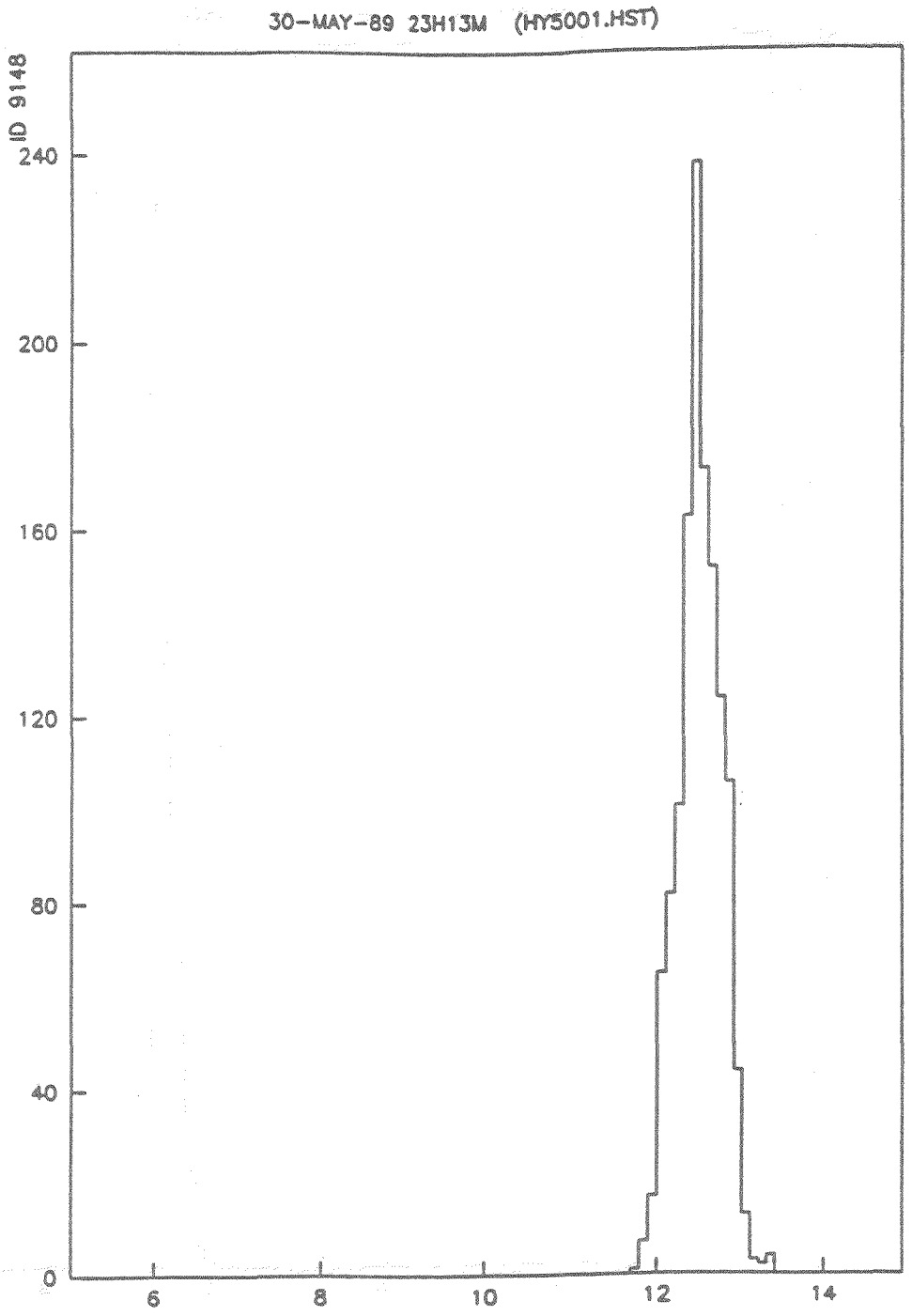

Figure 8: Position resolution of a hit in the RICH counter. The plot is a distribution of the distance in centimeters between the fitted center and all hits in the region of the beam ring. The bin size is 1mm.

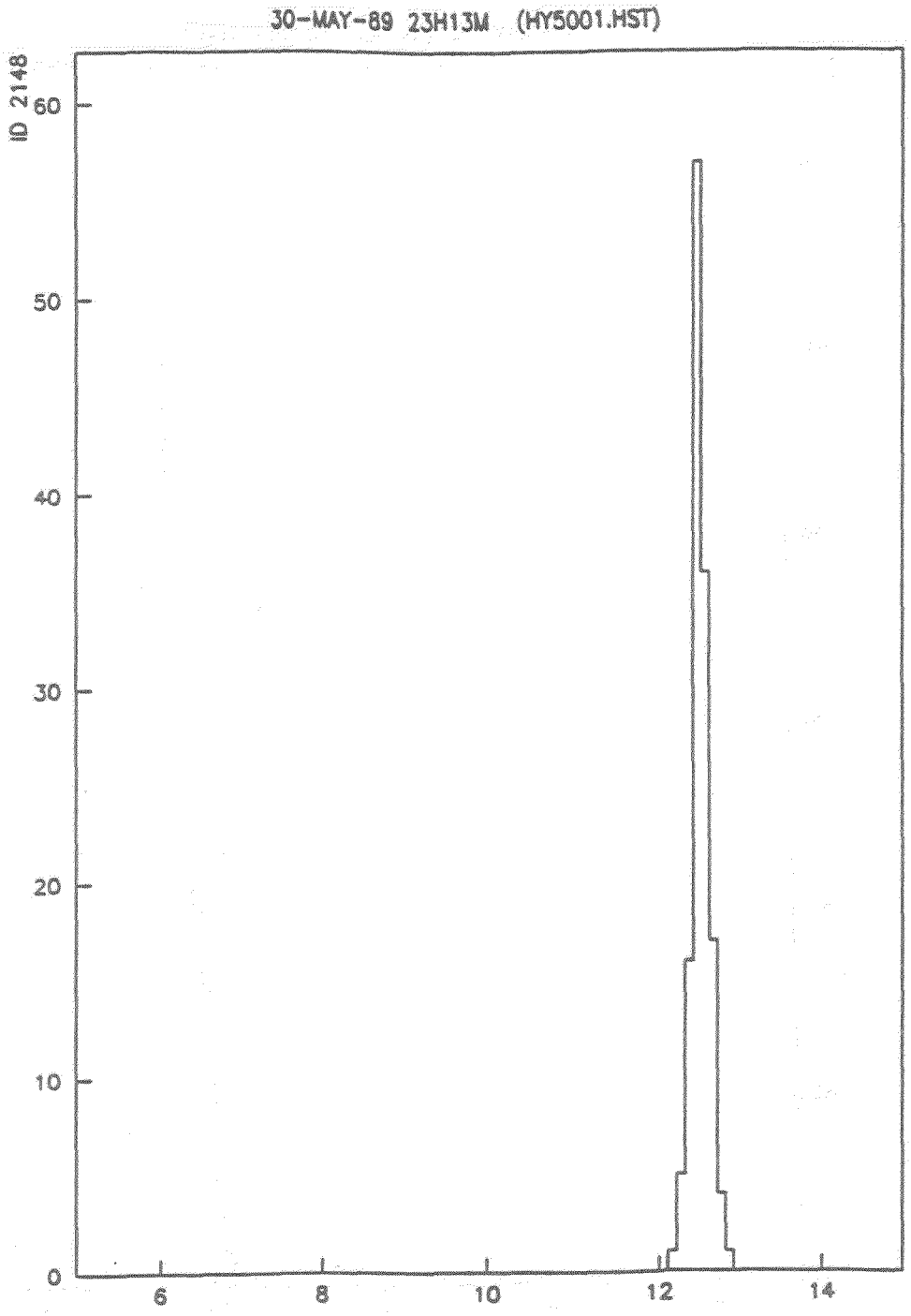

Figure 9: Fitted radius resolution of the RICH counter. The plot is a distribution of the fitted radius in centimeters of all beam rings. Each fit was required to have an error on the radius of less than 1mm. The bin size is 1mm.

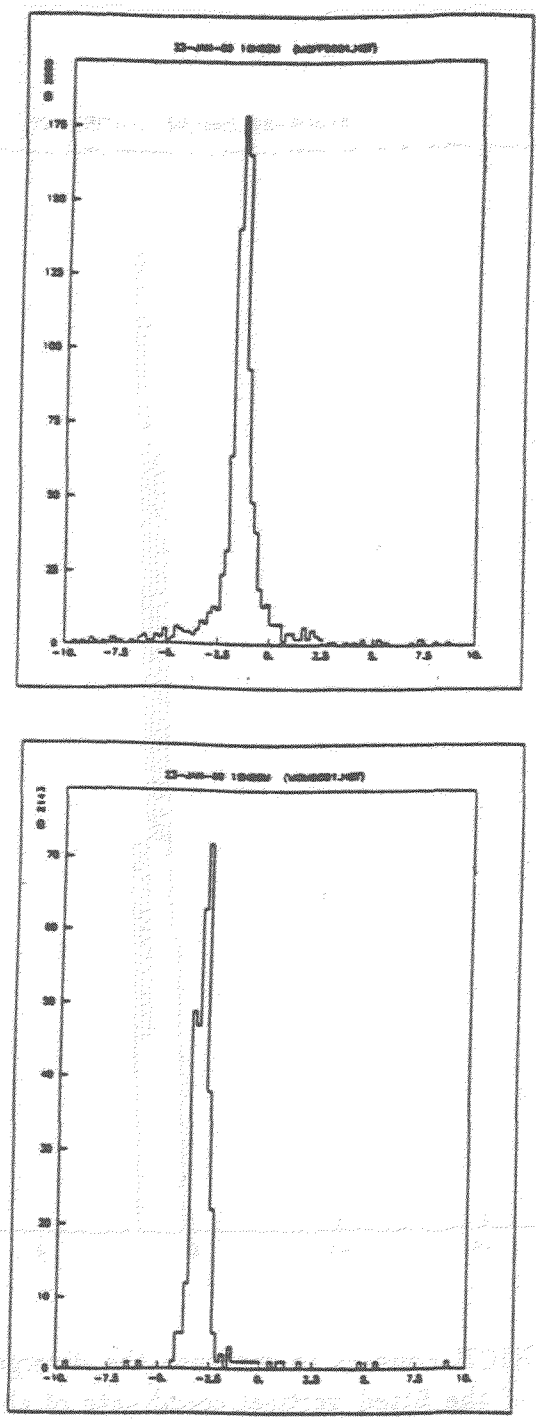

Figure 10: Using the RICH counter to measure the momentum of the beam. The plot show the distribution of the fitted horizontal coordinate of the center of the beam ring i centimeters. In the top plot the beam spectrometer magnet NMRE is off and the peak centered at -1.448 cm while in the bottom plot the magnet NMRE is on and the peak centered at -3.0999 cm. The shift in the location of the peak is inversely proportional to t momentum of the beam. The bin size is 2mm in both plots.

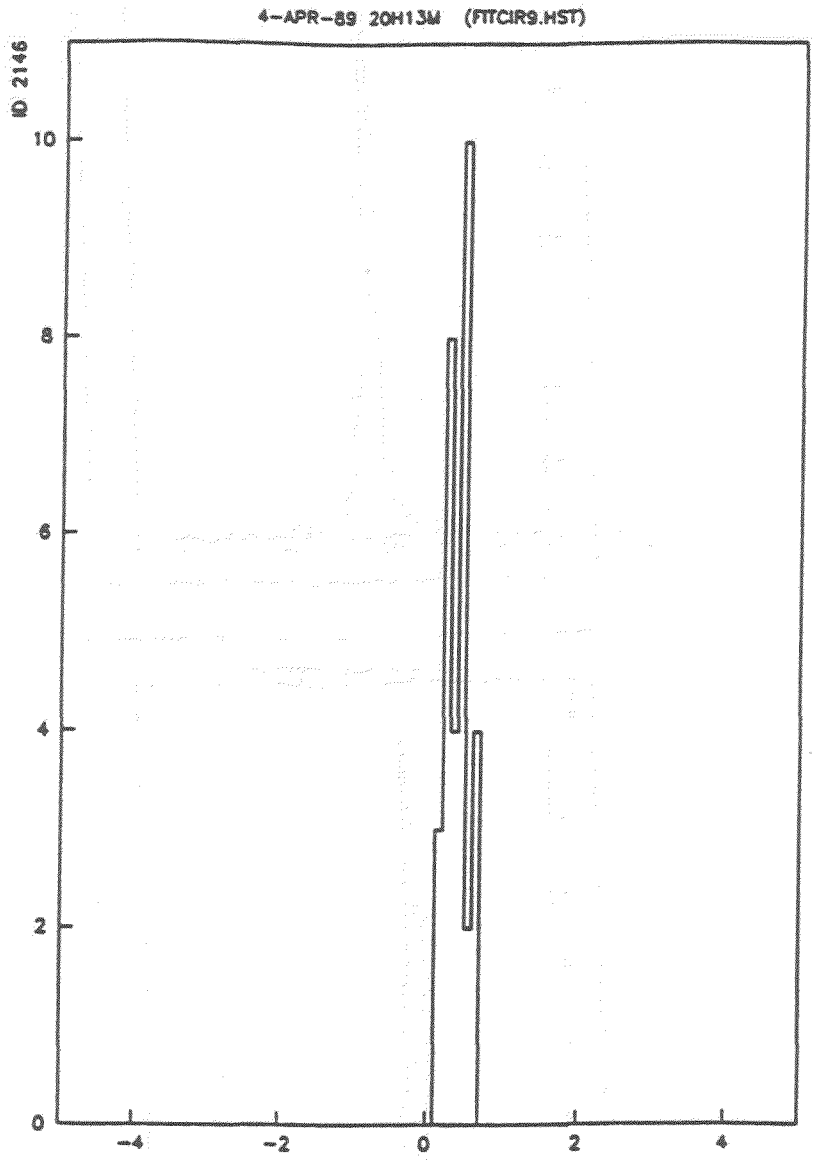

Figure 11: Using the RICH counter to measure the divergence of the beam. The plot shows the distribution of the fitted vertical coordinate of the center of the beam ring in centimeters. Each fit was required to have an error on the vertical coordinate of center of less than 1mm. The r.m.s. of the distribution is 1.5 mm which implies that the r.m.s. of the vertical divergence of the beam is less than 1.5mm/f = 309 μrad where f is the focal length of the central mirror. The measured r.m.s. of the vertical divergence of the beam from the beam spectrometer is 270 μrad. The bin size is 1mm.

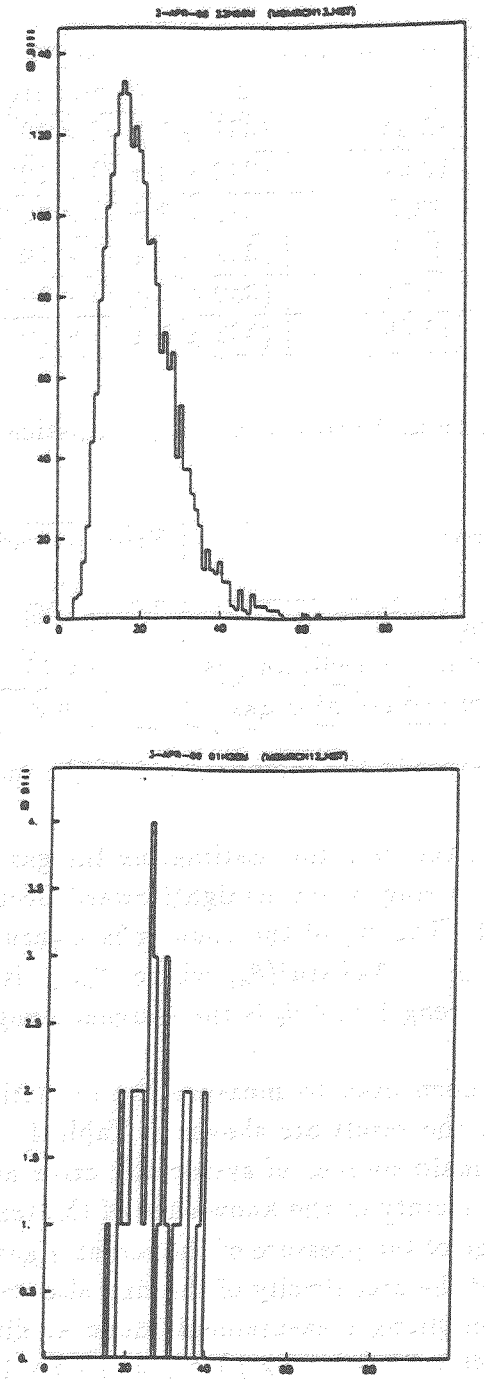

Figure 12: Number of hits per particle in the RICH counter. The top and bottom plots show the number of hits in the beam ring region for 1-beam and 2-beam events respectively. The mean of the 1-beam distribution is 20.0 ± 0.1 while the mean of the 2-beam distribution is 26.3 ± 1.

Temperature ^{0}C	Pressure mbar	Measured radius cm	$n-1$ at 20^0C, 770 mm Hg
23.5	969	12.35	$(337 \pm 3 \pm 7) \times 10^{-6}$
23.5	985	12.54	$(342 \pm 3 \pm 7) \times 10^{-6}$
23.3	1009	12.7	$(342 \pm 3 \pm 7) \times 10^{-6}$
18.9	997	12.7	$(342 \pm 3 \pm 7) \times 10^{-6}$
23.8	995	12.56	$(339 \pm 3 \pm 7) \times 10^{-6}$
23.3	984	12.45	$(338 \pm 3 \pm 7) \times 10^{-6}$

Table 1: $n-1$ of Argon gas. The first error in $n-1$ is statistical while the second error is systematic.

Source of error	Error on radius %
uncertainty in the focal length of the mirror	± 1 [8]
uncertainty in the temperature of the radiator gas	± 0.15
uncertainty in the pressure of the radiator gas	± 0.2

Table 2: Systematic error in the measurement of the radius of the ring

This could be due to low gain of the detector. Estimating the gas gain of the detector from pulse heights of hits in the beam ring is not straightforward because the readout imposes a threshold on the pulse height. The N_0 of the counter is measured to be 16.6 cm^{-1}. N_0 is given by the expression $N_{ph.el.} = N_0 L sin^2(\theta_c)$ where $N_{ph.el.}$ is the number of detected photoelectrons, L is the radiator length and θ_c is the Cerenkov angle.

The radius of the ring has been used to measure the refractive index of argon gas in the TEA region. The data and the result are shown in Table 1. The dominant errors are systematic (see Table 2). The main sources of systematic error are the uncertainty in the focal length of the mirrors, uncertainty in the knowledge of the temperature of the radiator gas, uncertainty in the knowledge of the pressure of the radiator gas. The difference between measured and expected values of the eccentricity of the ring also contributes a small amount to the error on the radius. Combining measurements done at different temperatures and pressures we obtain a value of $340 \times 10^{-6} \pm 1.2 \times 10^{-6}(stat.) \pm 7 \times 10^{-6}(sys.)$ for the value of n-1 of argon in the TEA region at 20^0C and 770 mm of Hg where n is refractive index. This is to be compared with the value of $345 \times 10^{-6} \pm 6 \times 10^{-6}$ measured by Charpak et al[9] using 5% TEA and commerical grade helium in their detector. One could expect some difference between the two measurements beacause the detector gases used are different. Different detector gases are transparent to UV light to different degrees and n-1 is known to change with the wavelength of light.

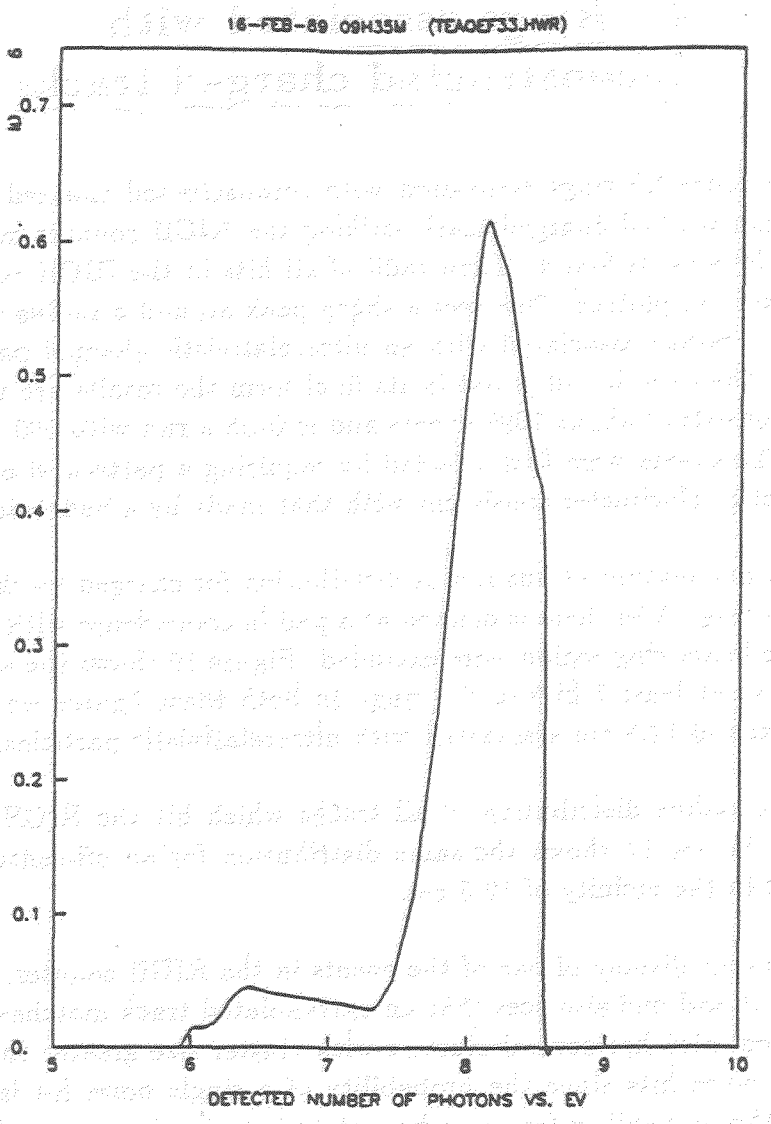

Figure 13: Expected number of photoelectrons per particle. The figure shows the expected spectrum of detected photons for an ultrarelativistc particle for a fully efficient detector. On the horizontal axis the photon energy in eV is plotted while the scale on the vertical axis is arbitrary. The area under the curve corresponds to 9.4 photons. To derive this spectrum, variation of refractive index with wavelength, reflectivity of the central mirror, absorption of photons in the radiator gas, transparency of the calcium fluoride window and the mesh electrode, quantum efficiency of TEA, absorption length of photons in the detector gas and gate width were taken into account.

4 Rings associated with reconstructed charged tracks

In Figure 14 evidence for rings associated with reconstructed charged tracks is shown. First, for every reconstructed charged track striking the RICH counter mirrors the center of the ring on the detector is found. Then radii of all hits in the RICH counter calculated relative to this center are plotted. One sees a sharp peak around a radius of 12.5 cm which is approximately the radius associated with an ultrarelativistic charged particle. Since the charged tracking in the experiment is not in its final form the results are preliminary. The data sample used consists of about 1000 events and is from a run with 500 GeV muons on a hydrogen target. The events were first selected by requiring a pattern of energy deposition in the electromagnetic calorimeter consistent with that made by a hadronic event.

Figure 15 shows momentum versus radius distribution for charged tracks with at least 4 hits in a 5 mm wide ring. A hit here is defined as a pad in coincidence with a wire. To make this plot, hits in the beam ring region were excluded. Figure 16 shows the same distribution for tracks which have at least 7 hits in the ring. In both these figures we see a horizontal band at radius of around 12.5 cm associated with ultrarelativistic particles.

In Figure 14 the radius distribution of all tracks which hit the RICH counter central mirror was shown. Figure 17 shows the same distribution for an off-central mirror. Here again we see a peak in the vicinity of 12.5 cm.

Figure 18 is an event display of one of the events in the RICH counter. One sees a ring with several hits on it and one also sees that an extrapolated track matches with the center of the ring. The event also has several clusters with cluster size greater than 1. These are very unlikely to be noise hits since the probability of a single noise hit is less than 0.5% which implies that the probability for two adjacent pads to fire is very small.

From the beam ring the pad cluster size distribution has been measured. Figure 19 illustrates the cluster size distribution where only clustering along a pad column has been considered. One sees that on average a photoelectron fires more than one pad.

5 Conclusions

In conclusion the beam ring seen in the RICH counter has been used to measure properties of the RICH counter, measure refractive index of argon in the TEA region and to study the properties of the beam. In addition rings connected with reconstructed charged tracks have been seen.

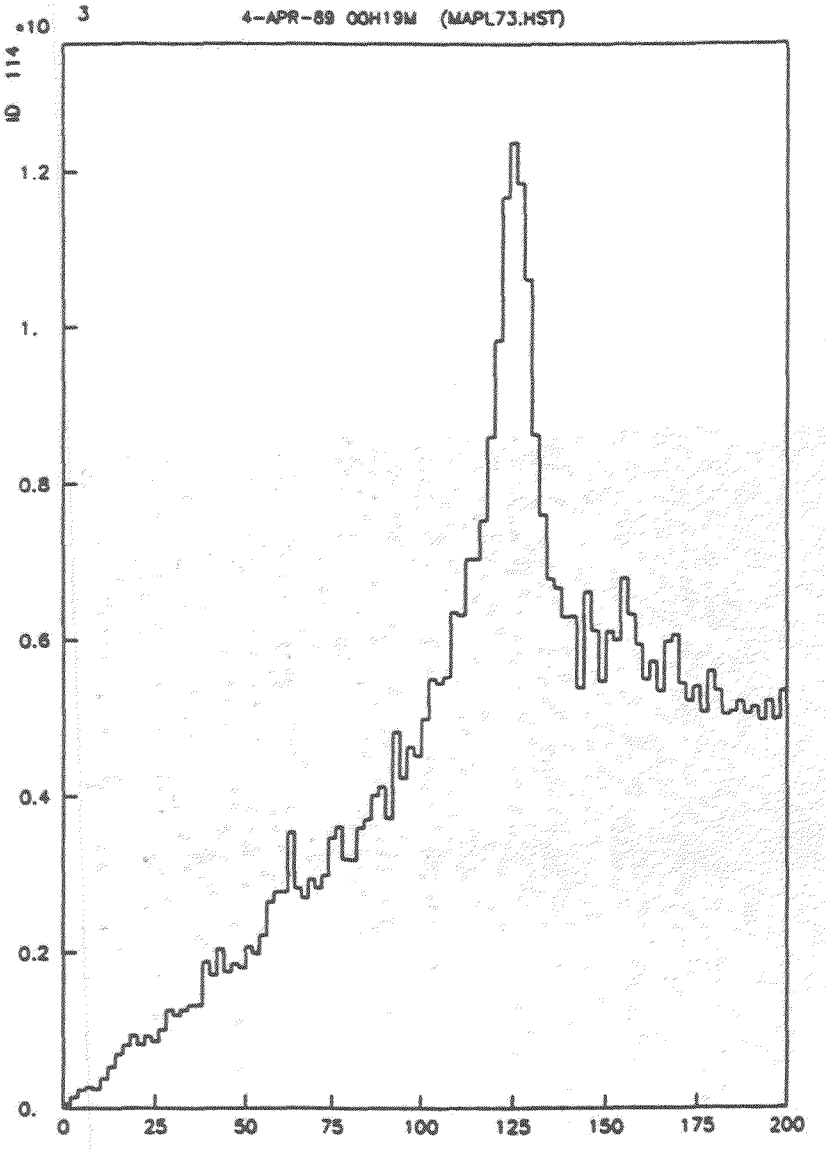

Figure 14: The radius distribution of all hits. This plot is for tracks which hit the RICH counter central mirror. The bin size is 2mm.

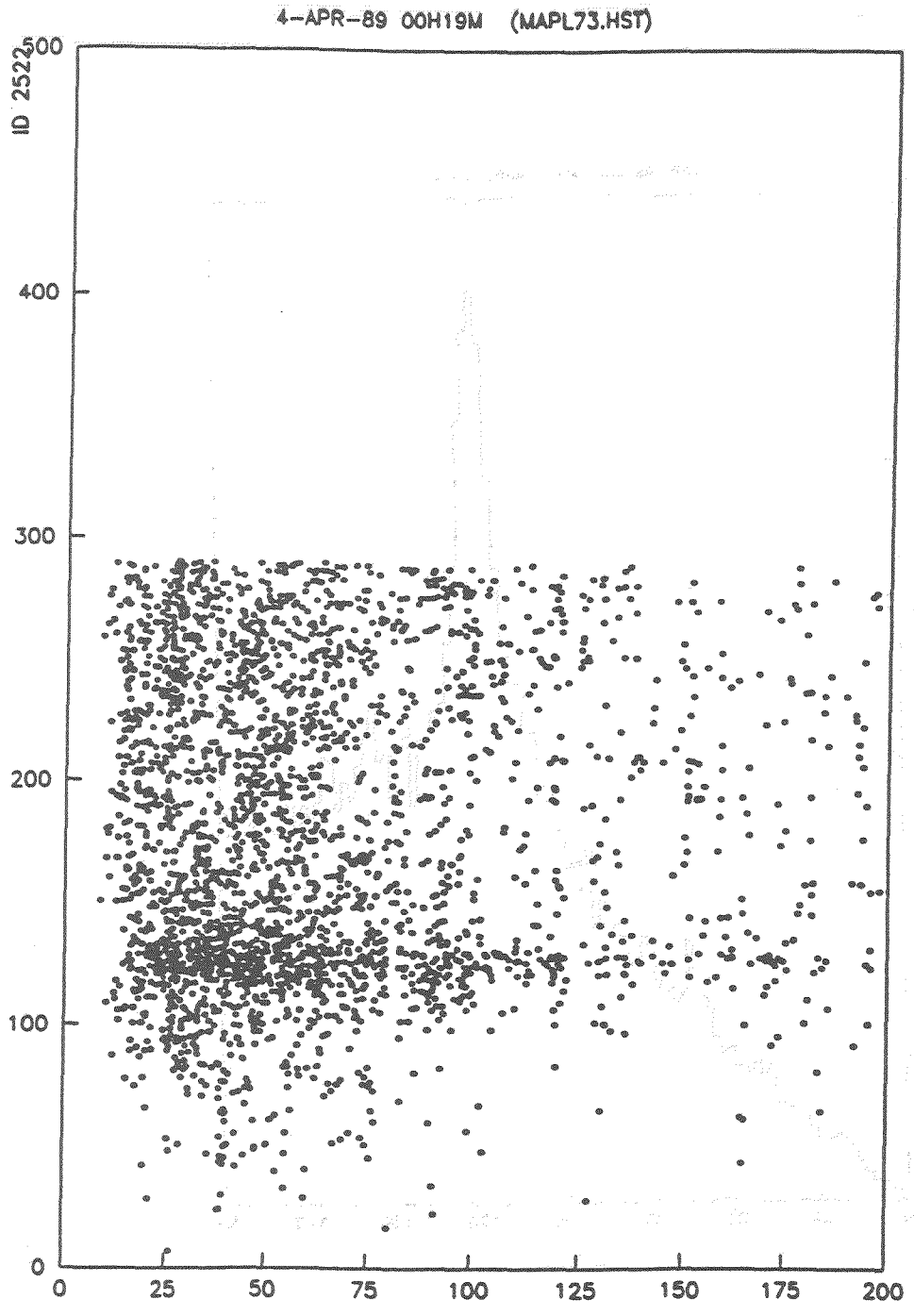

Figure 15: Momentum versus radius. For an entry to be made in the plot at least 4 hits are required in a 5mm wide ring. On the horizontal axis momentum in GeV/c while on the vertical axis radius in mm are plotted. The cutoff at 300 mm is an artifact of the program used to make the plot.

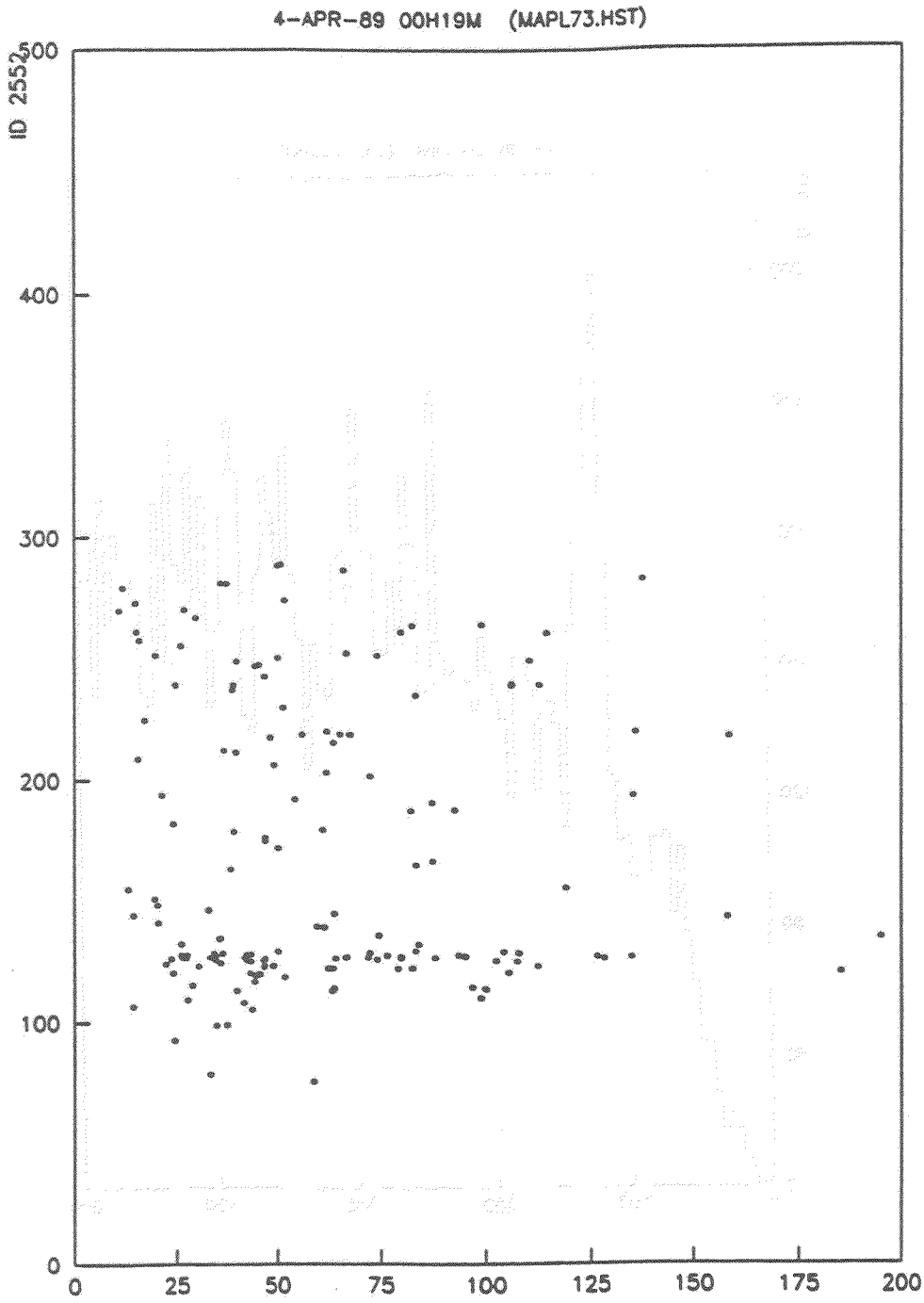

Figure 16: Momentum versus radius. For an entry to be made in the plot at least 7 hits are required in a 5 mm wide ring. On the horizontal axis momentum in GeV/c while on the vertical axis radius in mm are plotted. The cutoff at 300 mm is an artifact of the program used to make the plot.

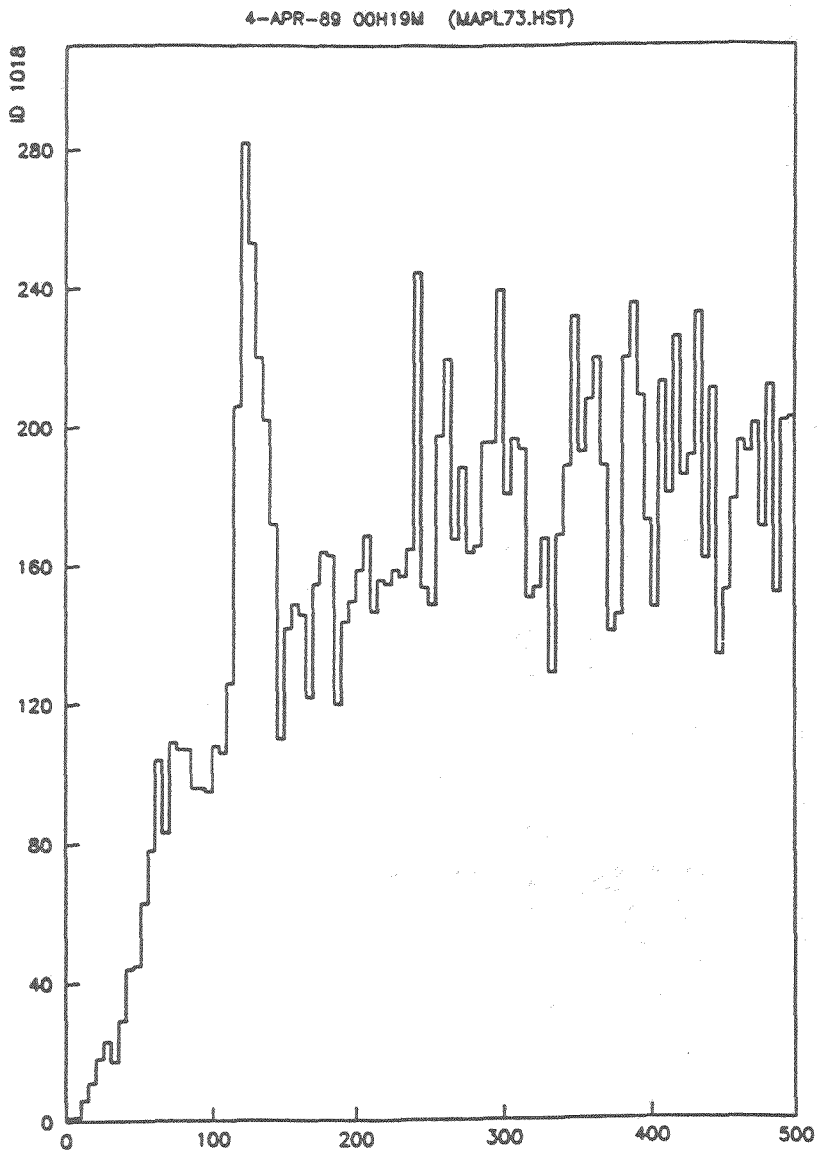

Figure 17: Radius distribution for tracks which hit Mirror no.18. The bin size is 5mm.

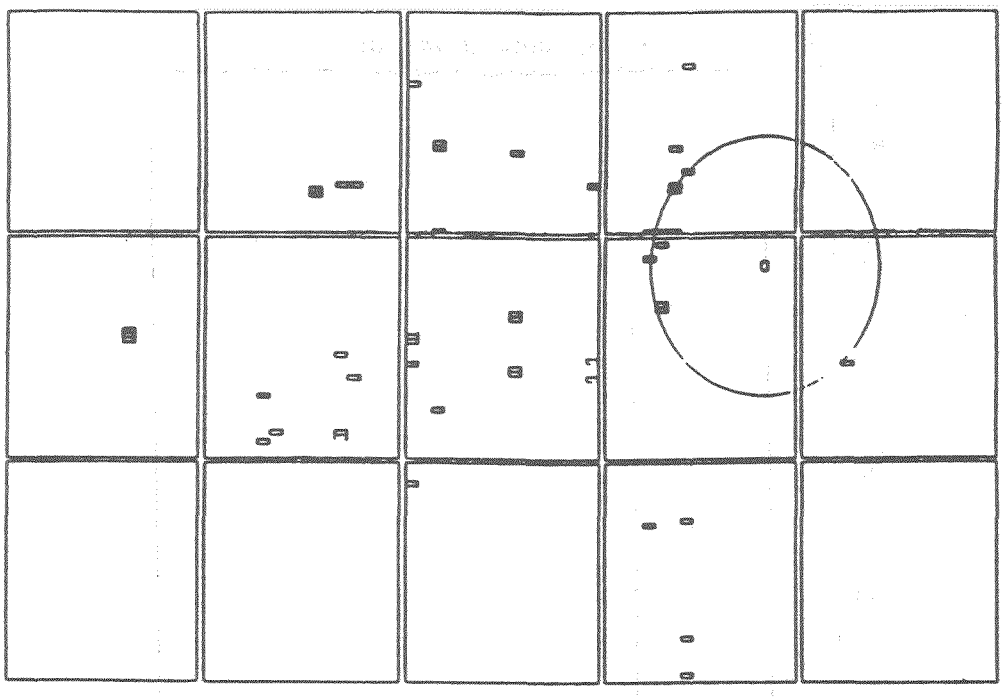

Figure 18: RICH counter event display. In the figure the small rectangles are pads with signal above threshold and in coincidence with an anode wire. The pad plane, as shown in the figure, has a tile structure to it and the tiles are arranged in 3 rows and 5 columns. The symbol 'O' shows the expected center of a ring from tracking. The circle centered around the 'O' is a 5mm wide ring with at least 6 hits in it.There are more tracks in the event but centers associated with them are not shown.

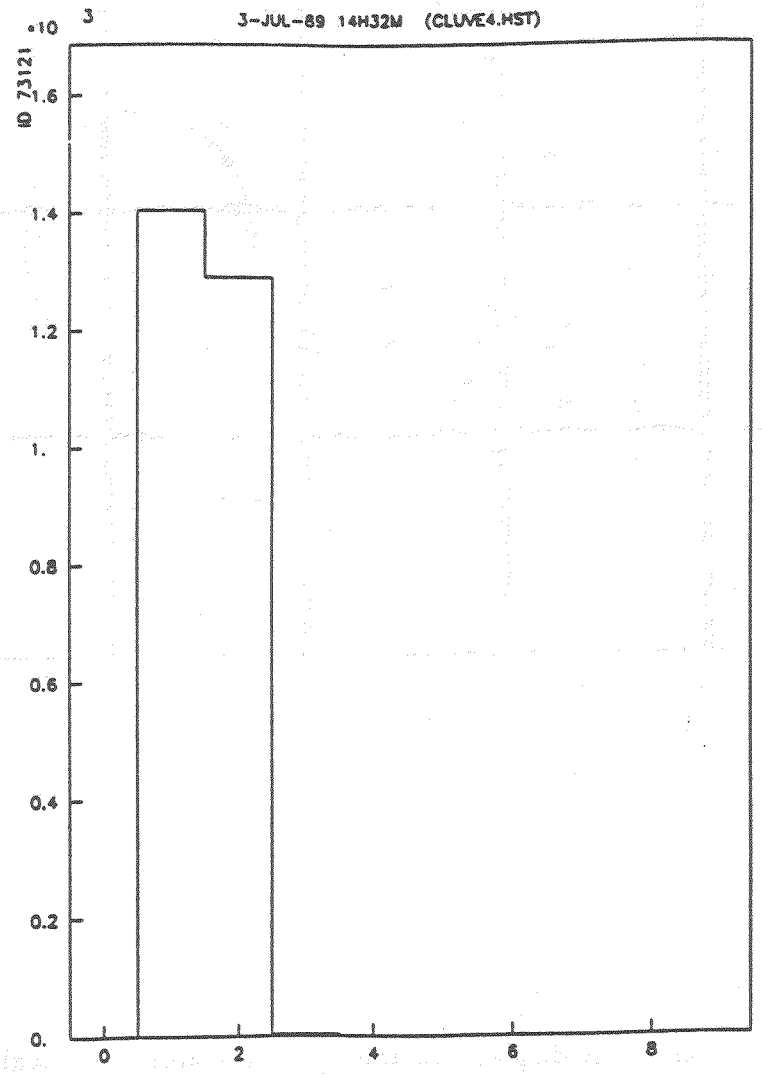

Figure 19: Pad cluster size distribution. The plot illustrates for a hit pad in the beam ring region, how many out of the two adjacent pads along a column, fire. Here, the pad cluster size is defined to be 1 + number of adjacent pads that fired.

Acknowledgements

I would like to thank D.F.Anderson, G.B.Coutrakon, S.K.Dhawan, P.F.Gorak, V.W.Hughes, H.E.Montgomery, J.G.Morfin, K.P.Schuler and members of the E665 collaboration for criticism, suggestions, encouragement and help during data taking. I would also like to thank the organizers especially J.G.Morfin for organizing a very stimulating symposium.

This work was supported by the Director, Office of Energy Research, Office of High Energy and Nuclear Physics, Division of High Energy Physics of the U.S. Department of Energy under Contract No. DE-AC02-76ER03075.

References

[1] Fermilab E665 proposal,*Muon scattering with hadron detection at the Tevatron, 1980.*

[2] E665 Collab., M.R.Adams et al.,*A spectrometer for muon scattering at the Tevatron, submitted to Nucl.Instrum.Methods*

[3] T.Sjostrand, Comp.Phys.Comm. 39(1986)347-407.

[4] G.Ingelman, *CERN program library long writeup W5035.*

[5] G.B. Coutrakon et al, IEEE Trans. Nucl. Sc. NS-35(1988)470.

[6] R.A. Holroyd et al, Nucl.Instrum.Methods A261:440, 1987.

[7] S.K. Dhawan et al, IEEE Trans. Nucl. Sc. NS-35(1988)436.

[8] R.J.Apsimon et al, *The Design of the Optical Components and Gas Control Systems of the CERN Omega Ring Imaging Cerenkov Detector, RAL-85-014, June 1985.*

[9] G.Charpak et al, Nucl.Instrum.Methods 164 (1979) 419-433.

VIII. Addendum

Fast Photo-detectors for RICH at Hadron Colliders

Jacques Seguinot, College de France, Paris.

Notes to accompany the numbered transparencies.

1. I shall report on recent laboratory quantum efficiency measurements we have performed on various photosensitive molecules and mostly on the results of extensive tests on fast photon detectors.

I shall then describe briefly the fast RICH detector we are developing for the B Meson Factory which may be built at the Paul Scherrer Institute in Switzerland by 1994 according to present planning. This project has initiated most of the tests reported and in particular the development at RAL of dedicated VLSI silicon chips for fast readout of RICH pad detectors. This topic will be discussed in the last part of the talk.

The physicists and engineers who are working on the development are listed on the first transparency.

This work is supported by IN2P3 in France and by the LAA project at CERN.

2. There are four main parameters which characterize the design of a photodetector:

1. The spatial resolution to reconstruct the photon conversion point.
2. The merit factor N_0 which determines the p.e. statistics.
3. The time dispersion in collecting photoelectrons.
4. The data acquisition rate.

T.Ypsilantis (these proceedings) has discussed the first two parameters with respect to the particle ID capability and has shown that using the least dispersive gaseous radiator with mirror focal length of 2m, measurement pixels of 1 by 1mm^2, would match the chromatic error and should provide the multihit capability for high multiplicity events.

For an interaction rate of 10^8Hz at SSC/LHC, the time dispersion for collecting p.e.'s should be less than 10ns in order to avoid overlapping events from successive beam crossings. Data acquisition rates up to 10kHz are desirable with a fast RICH detector system.

3. A small time dispersion is obtained, as shown in transparency 3, with direct coupling between the conversion volume and the p.e. detector which can be, in principle, either a MW chamber or a multi-step avalanche chamber (MSAC), the 2D projected image point being obtained by digital detection of pad signals. Analog measurement for weighted centroid determination seems difficult at the requested data acquisition rate. The total time dispersion time for 95% photon absorption is $3\lambda_{ph}/v_d$ where λ_{ph} is the photo-absorption length and v_d the electron drift velocity. The

presently available photosensitive molecules are TMAE, TEA and TMA with different combinations of carrier gases with CH_4 the dominant component because of its U.V. transparency and its good single electron counting capability.

4. To obtain a dispersion time less than 10ns requires λ_{ph} to be between .5 and 1mm depending on the photon energy bandwidth used. The partial pressure of TEA at 20 C is 50torr and its photoabsorption cross section is about 10Mb in the region of TEA response (7.5 to 9eV) giving λ_{ph}=0.6mm and hence 18ns total time dispersion. To obtain the same absorption length with TMAE would necessitate a 100 C bubbler and an even higher detector temperature to prevent condensation. This represents a non-trivial difficulty in detector construction and operation.

Tri Methyl Amine (TMA) is less well known. It is gaseous at room temperature and so is easy to use. We have measured a photoabsorption cross section of about 3Mb hence for λ_{ph}=1mm requires about 100torr of TMA. We have verified that a MW detector works at this concentration and higher.

5. Obviously, when discussing time dispersion, one must take into account the time slewing of the analog electronic chain attached to each pad. The signal from the MW detector and pre-amplifier combination is given by the convolution of the induced pad charge (generated by a p.e. on a wire) with the time response of PA. The latter, given here, corresponds to a transresistance PA with low input impedance for fast counting. The time constant t_0=1ns depends on detector geometry and gas. For a PA time constant of 5ns the output signal is maximum at 10ns at a level of 25% of the total induced charge with an exponential falloff. This corresponds to a time jitter s.d. of about 3ns which is acceptably short provided the detection efficiency is acceptable. With a MSAC the response is even faster since one collects directly the electrons created in the avalanche.

6. So far TEA and TMAE have been used for RICH photodetection however there is still some contradictions concerning the TEA quantum efficiency. The TEA q.e. , shown in this transparency with 50% maximum, was obtained by fitting the N_0 obtained in ring imaging tests (Lund-Jensen et.al. 1981, Mangeot et.al. 1983) and is in agreement with chemical actinometry (Salomon and Scala 1975). A later ionization chamber measurement with flux calibration based on the known NO photoresponse gave 43% maximum (Goehlich et.al. 1987) however measurements at a synchrotron light source gave only 33% maximum (Holroyd et.al. 1987). This latter result is the source of the confusion regarding the true maximum for TEA.

Because of the large interest in TEA for fast RICH detectors we have started laboratory measurements to cross check the TEA and TMAE response as well as to investigate new agents. These tests were performed,

with a U.V. monochromator, by measuring the photocurrent in a single wire cell operating as an ionization chamber with unit gain. Usually, calibration of the incident light flux is obtained by measuring a known organic agent. Holroyd used Benzene and cis-2-Butene while Goehlich used NO and we use TMAE.

7. The transparency shows our relative TMAE measurements, normalized at 190nm, compared to the absolute values given by Holroyd et.al. and Ekelin using ring imaging normalization (see Arnold et.al. 1988). There is good overall agreement, with the deviation between 160 to 180nm due probably to different purities.

8. This transparency shows our measurements for TEA, TMA and DMA (Di Methyl Amine) in He or Ar as carrier gas, using the Holroyd TMAE q.e. as reference for normalization. As can be seen our TEA response agrees with Holroyd's. The consistency of the two measurements is impressive. The inconsistency between the 44 to 50% maximum q.e. estimates (see Fig. 6) and these results could be resolved if the TMAE q.e. were underestimated by about 30% in the TEA response region or that our TEA is not sufficiently clean (Goehlich et.al. used a special GC (?) preparative in cleaning amines). It is difficult to believe that the TMAE ring imaging tests underestimated the response by 30% however the contradiction arises partially from other ring imaging data in which it is equally difficult to believe that the response was overestimated by 30%. Anyway, we foresee new ring imaging tests with TEA and a pad detector to resolve this contradiction.

On the same figure can be seen the TMA and DMA responses with thresholds of 7.8 and 8.2eV respectively. The maximum q.e.'s are 30% and 20% respectively relative to 32% for TEA.

9. With CH_4 as the carrier gas we obtained the responses shown for TEA and TMA. The response of DMA overlaps the methane absorption hence this combination cannot be used. Also shown are two of the C* photon feedback lines (a third is at 6.42eV) and one N* line. Only one of the C* lines can photoionize TEA, and none TMA, producing secondary feedback photoelectrons. These feedback p.e.'s determine the cluster size of the hit pads and limits the maximum gain attainable in MW photon detectors. For this reason TEA is a good agent since it is about four times less sensitive to photon feedback than TMAE in CH_4 but about equally sensitive to TMAE in a CH_4-Isobutane mixture because Isobutane absorbs the C* line at 7.48eV. In this respect TMA should be the best agent because it is barely sensitive to the N* line and because the N concentration is low. The Cherenkov constant $k_c = n\sigma_\theta(E)/\beta\sqrt{N_0 L}$ determines the particle ID capability hence in comparing TMA with TEA note that the N_0 attainable is only 2/3 as large but the energy bandwidths are in the same ratio (0.5 to 0.75eV FWHM). The constant k_c is smaller if the ratio of the chromatic dispersions dn/dE

(at 8.55 versus 8.35 eV) is not greater than the square root of the energy band width ratio (i.e. 1.22) which will occur for low dispersion gas radiators such as He ,Ne, CF_4. Even for the same Cherenkov constant TMA is attractive for stable detector operation.

DATA ACQUISITION RATE

10. Assuming a rejection factor of 10^4 for a first level trigger (from fast calorimetry and scintillators) the data rate would be reduced to 10KHz or one event per 100μs. To obtain 90% data taking efficiency will require a maximum data acquisition time of 10μs per event without processing. This is a difficult goal which, as will be shown, probably can be reached. To accommodate a first level time delay of about 1μs a similar time delay of the pad signal must be provided. This can be realized by means of a drift gap, or as we prefer, by using 50 Mhz. shift registers.

11. A simple 4π spherical geometry for a RICH detector at the LHC/SSC would, according to a proposal by Ypsilantis, have photon detectors at 2 m radius with a surface area of about 50 m^2. With a pixel size of 2 by 2 mm^2 one expects a minimum of 12.5 million electronic channels, several order of magnitude higher than the present detectors. Of course, readout electronics should be implanted on the back side of the detector in such a way a limited number of optical fiber bus-lines, for data and control, would relay the detector sectors to the main data acquisition system. The key, therefore, of the fast RICH technique is the availability of dedicated Analogue and Digital high density integrated electronics (VLSI) for fast amplification and discrimination, local buffering and readout. Later I will discuss the solutions we are developing in collaboration with the Rutherford Laboratory.

PHOTON DETECTORS WITH PAD READOUT

Several type of fast photon detectors with pad readout can be envisaged.

MW DETECTOR

12. The distance anode to cathode pad distance is small so as to increase the signal on the pads. Due to the thinness of the gas layer (2 or 3mm) the ionization produced by charged particles crossing the detector does not cause feedback photoelectron problems if TEA with CH_4 or TMAE with CH_4 and Isobutane are used hence the use of 'blinds' between wires is not necessary. Operation with TMAE at 100^0C, or even higher to avoid condensation, imposes severe mechanical constraints on the detector to limit the distortions from thermal expansion. The difficulty can be

overcome using Boron Nitride for the detector body and metalized quartz fibers for the anode wires. Electronics mounted on the back side must then be cooled to a lower temperature. The wires can also provide fast signals from charged particles, using upper level discrimination, and so participate in the first level trigger. The TEA detector is the solution we have adopted for the B-Meson Factory RICH detector and has been fully tested.

PPAC

13. Parallel Plate Avalanche Chamber photon detector (or MSAC) will be discussed by A.Breskin. He shows the photoelectron feedback background suppression obtainable with such a detector, however, it seems to me very difficult to find an acceptable solution for the construction of parallel mesh planes of large area to operate at 100^0C with TMAE. With TEA, the interest of PPAC is not evident to me, however we are preparing tests to directly compare the PPAC and MW solutions.

SOLID PHOTOCATHODES

14. An attractive solution, already mentioned by Ypsilantis and which will be discussed in detail by V.Peskov, is the use of a solid reflective photocathode of TMAE in NeoPentane(NP), for example, which is easily deposited by cryopumping. Such a photon detector is shown in this transparency. Isobutane must be used with CH_4 to reduce both feedback photoelectrons and the photon energy acceptance for chromatic aberrations. If it works as expected the advantage on the time dispersion is obvious. We plan to extensively test such cathodes in the near feature.

15. This figure shows a small prototype photon detector which we have built and tested for the BMF project. It consists of a CaF_2 window MW detector with cathode pad readout operated with CH_4 and TEA at room temperature. Moreover tests with TMAE and TMA have also been performed. The gas thickness is 3 mm (which is five photon absorption lengths in 20^0C TEA, the wire spacing 1.27 mm and the pad size is 5 by 7 mm^2 to match the expected chromatic error of a NaF radiator. The window is coated with 2nm of tungsten and the distance between the anode wires and the cathode pads is 500μm with an accuracy of 20μm. The wire spacing must be small to collect all the field lines from the window onto the wires and thus efficient photoelectron detection in the gas volume.

The preamplifier attached to each wire and pad has a 10ns time constant and the electronic threshold corresponds to an equivalent input charge of $9*10^3$ electrons.

16. The figure shows the experimental set-up. A self triggered H_2 flash lamp, located at the bottom, delivers a collimated U.V light spot of 0.5 mm diameter and about 10 ns duration. The peak of current in the discharge

provides a trigger to strobe the data via a 50ns width gate. The light intensity was reduced by means of metalic filters in such a way that the probability of having 2 or more photoelectrons in the same flash is less than few %. Moreover, the spot can be accurately moved to scan the surface of the pad array and measure the response (detection efficiency, cluster size, reconstruction accuracy) as a function of the impact position.

17. This figure shows two typical 3-dimensional scatter plots of superimposed images obtained when the light beam hits the detector at the center of a pad and between two adjacent pads. The tail around the peaks are produced by feedback photoelectrons. As can be seen, this is not a serious problem here because of the short photon absorption mean free path.

The multiplicity of pads/cluster is 1.2 and 1.6 respectively and increases up to about 3 to 4 when a charged particle crosses the detector. If several pads are hit, the digital barycenter gives improved spatial resolution.

18. This figure shows the number of clusters detected on pads and the multiplicity (pads/cluster) as a function of the anode wire voltage which varies the avalanche gain. The results are given for the light spot centered on or between pads. Above 1.4KV, the multiplicity of hit pads increases very rapidly and the detector reaches the limit for corona discharge. Above 1.3KV a plateau is observed which shows that the cathode pad efficiency is good.

19. The above observation is confirmed by measuring the cathode pad efficiency with respect to the anode wire signals as shown in this figure. The detection efficiency is better than 90%.

M.C SIMULATION

20. We have simulated the detector response with a M.C. program in order to better understand and interpret the experimental results. As a result we believe we can simulate any detector configuration as, for example, pads of 2 by 2 mm^2 as needed for LHC/SCC instead of 5 by7 mm^2. The program takes into account the following factors:

- photoabsorption and quantum efficiency of the photoionizing gas.
- electrostatics for photoelectron collection.
- charge fluctuations in the avalanche.
- spatial dependance of the induced pad charge.
- secondary photon emission from atomic C* excitation-repeated until the feed back production stops.
- screening effect of the anode wires and photoelectric surface effect.
- electronics response using an input threshold of 9000 electrons.

21. This is an example of the comparison between data and M.C. simulation. Both figures show the variation of the number of hit pads per cluster (cluster size) when scanning the pad along two perpendicular directions (x, y). The y direction is parallel to the anode wires. Note the very good agreement.

22. This shows the variation of the cathode pad detection efficiency with position (x or y) which is well reproduced by the M.C. The mean detection efficiency over the surface of a pad is better than 93%.

23. The next transparency displays the averaged values of $(y-y_0)$ and $(y-y_0)^2$ a function of the y position for x=0. The results are periodic with the pad size. Good agreement between the M.C. simulation and the data is seen.

24. Same as above however for a scan in x. The small deviations between data and M.C. reflect a difference in detection efficiency between adjacent pads. We have concluded from these tests that the behavior of a photodetector with TEA is well understood.

25. This transparency shows the cluster size variation when TMAE, instead of TEA, is used with pure CH4 in the photodetector. The multiplicity difference is due to the additional C* excitation lines, at 6.42 and 7.48 eV, which photoionize TMAE but not TEA. The rapid onset of the curves shifts to lower voltage with increased TMAE concentration. These curves show the difficulty of operating a high gain MW photon detector with TMAE at 100 C in pure CH_4.

26. If the C* excitation lines are suppressed, by using a mixture of CH4 and Isobutane, the behavior of the detector is improved, as expected, with performance approaching that obtained with TEA. With TMA, as photoionizing gas, performance is even better because is not ionized by the C* excitation lines but only by the lower concentration N* line at 8.2 eV.

27. The two scatter plots show photon feedback with TMAE, obtained without and with Isobutane, at the same detector gain. The comparison is revealing.

28. The use of Isobutane also improves the cathode pad efficiency. This is visible on this figure. One obtain nearly 100% pad efficiency instead of 92% in pure CH4. The difference on the total number of hits is due to the photoabsorption in Isobutane of a large part of U.V. spectrum of the H_2 flash lamp.

29. These figures summarize what we can expect with an array of 2 by 2 mm^2 cathode pads using the same M.C. simulation.

With TEA in CH_4 and a MW detector operated at a gain of 10^6, the cluster size increases only by a factor of two. The resolution is not gain dependent, but gets better along the wire (y), as previously observed, because the feedback photoelectrons improve the barycenter determination.

For TMAE in CH_4 and a MW detector the maximum gain attainable is too low to obtain a good pad detection efficiency.

At the present time TEA is certainly the best candidate for a fast RICH detector. A CH_4-Isobutane mixture with TMAE could be used but at high temperature ($\approx 100^0$C) in order to get a sufficiently short absorption length. This mixture is useable with a quartz window and has consequently lower chromatic dispersion.

30. Here is a drawing of the detector proposed for the B-Meson Factory project , which may be built in Switzerland by 1994. The machine can be run as a symmetric (5.4 against 5.4Gev/c) or asymmetric (7 against 3 Gev/c) electron-positron collider at 10 MHz with an interaction rate of few Hz. The time is too short to comment on the detector which has a more or less classic architecture.

The fast RICH we have proposed for this machine allows π/K and K/P separation up to 2.5 and 4.2 GeV/c respectively. Fast implies for the present design,100ns maximum gate width to strobe the data in order to avoid background contamination from synchrotron radiation, beam pipe or beam-gas interactions. This gives a detector more in conformity with what is needed for LHC or SSC.

31. This transparency shows an enlarged view of a quarter of the RICH detector barrel and end cap:

- The inner radius of 65 cm.
- The length of 1.8 m.
- Overall detector thickness of 20 cm.

The radiator is a 10mm thick NaF monocrystal. The photon detector is a MW chamber, similar to the detector previously discussed, using TEA in CH_4 and is equipped with CaF_2 window. The pad array is 5 by 7 mm^2 with 7 mm along the wire direction. Wires are stretched along the z (beam) axis and are supported every 10 cm by a spacer. The lever arm is 13 cm. Parameters have been optimized to approximately match measurement and chromatic errors. Electronics and readout are implemented on the back side of the detector, on longitudinal PC board. The total radiation length is about 20%.

32. The structure is more visible in this cross sectional view of the barrel, which is divided in azimuth into 12^0 sectors.

33. This is a partial view of the end caps. The use of detectors with pad readout allows easy construction, full coverage and the minimum radiation length. Also this technique is not sensitive to the magnetic field. The price to be paid is the number of electronic channels, for this project $4*10^5$ pads will be needed.

The total estimated cost of the project is 5.3 M$, but I have to point out that the cost of the crystals is even higher than electronics.

A prototype of three full barrel sectors, 90 cm in length with 14000 pads is under construction. Tests should start next year.

34. In collaboration with the Microelectronics group of Peter Sharp at RAL, we are developing 2 different VLSI chips for detection and readout :

-An Analogue bi-polar chip of 8 channels, consisting of a low noise fast transimpedance input preamplifier, amplifier and discriminator.

-A digital CMOS 16 input chip for local buffering and readout. The objective being a data acquisition time of less than 5 μs/event. The design of these chips is nearly completed and the simulations well advanced. The first test circuits should be produced by summer and if we are lucky, the production of the 14000 channels should start at the end of this year to equip the prototype under construction.

35. Here is the circuit diagram of a bi-polar analogue chain. The input stage is a fast differential transimpedance preamplifier with unity current gain, 100 Ω input impedance and 8.5 KΩ output impedance. The bandwidth is, as needed, about 100MHz. These two stages generate 1mV for a 1fC input charge. The noise is less than 800 electrons for 10 pF input capacitance which should allow a threshold setting of 2500 electrons, a good number for the detector operation.

The amplifier uses a differential stage with a bandwidth which has been limited to 25 MHz, for the BMF detector application, since this machine runs at 10 MHz. This limitation can be removed for use at LHC/SSC with a higher power consumption, estimated for the present design to about 10 mW/channel.

The last output stage provides a digital output current for the pulses above the threshold and incorporates a hysteresis loop so that the output is always defined. The feedback capacitor CF1 suppresses the feedback effect, from the switching of the output stage, hence improving the stability.

36. There is a common control voltage per chip to adjust the threshold, which is set by a 4 bit D/A converter integrated in the Analogue chip. This DAC is driven via the CMOS digital. Threshold will be adjustable between 1000 and 16000 electron equivalent input charge.

37. Here is the electronic architecture as foreseen for the BMF detector. The drivers of the DAC are integrated on the CMOS chip and set using a

serial low frequency address. This allows local adjustment of the thresholds in order to correct for gain dispersion or for locally noisy channels. The output signals of the discriminators are fed into shift registers, 64 buckets deep, running at 50 Mhz to delay the input pulses by 1.028 μs corresponding to the expected maximum delay time of the first level trigger

To avoid crosstalk from a clock distribution line with the input PA each chip has an integrated clock. We will have, therefore, an additional time dispersion of $20ns/\sqrt{12} = 6$ ns because of the non synchronization between clock and signals. The output pulses of the shift register are loaded in coincidence with a strobe in a D flip-flop for buffering and then readout. The strobe width is less than 100 ns for the present application.

The simplest solution, originally proposed for readout, consisted to use 50 MHz registers relaying 256 pads. Time readout less than 10 μs could in principle be obtained.

38. A more efficient solution, shown on this transparency, has been proposed by our colleagues at RAL. In this solution each digital chip of 16 inputs encodes and outputs only the hit pad. Ideally, this means that one should need 1 clock pulse per hit. The disadvantage is that it necessitates a higher number of connections between chips per sector allowing each to be uniquely identified.

A complete description of the readout process, which is a bit sophisticated, will take time. I can only point out the main features. Two elements in each chip contribute to the efficiency of the data compression:

-the priority encoder of 4 bits which give the address of any hit pad.

-the FIFO memory with seperate read and write operations.

access to the FIFO being regulated by two flags : BUFFER FULL or EMPTY.

These elements can operate simultaneously hence data can be entered into the FIFO while the encoder is outputing data. Data are transferred onto the chip immediately above it in the same column and accumulated in the FIFO. At the last data a NEXT ROW flag is associated and if a chip is empty a FULL flag is generated in order to preserve the order of the data. Counting of these flags will determine the row address at the top chip of the column.

39. Once a chip has transferred its data to the chip just above it, it then transfers the data stored in its FIFO. This process causes the data to stack up at the top of the column. At this stage in each column, operating in parallel, is stored one word per hit plus one word per empty chip. In the last phase, simultaneously at all top chips, the row address is reconstructed by counting NEXT and NULL flags.

For the BMF detector, each sector of 32 by 128 pads are readout in parallel. One expects for readout one clock pulse per hit plus a variable

number, between 0 and 32, dependant upon the position of the data within the sector. With a clock frequency of 20 Mhz and 20 hits/sector, the mean readout time should be of (20+16)*50 ns or 1.8 μs, which is very fast.

40. The total cost of the development corresponds to about 320K$ for both chips and for only one iteration. This value includes the production of about 20000 electronic channels.Then the cost of the production is of the order of 2$/ channel.

41. This transparency shows how we foresee to mount electronics on the detector. The protection circuits will be wired on the fan-in board on the back side of the detector in such a way output pins of 2 adjacent columns of pads are aligned with 3.5 mm spacing. The chips will be used with PLCC standard packaging, and we plan to produce printed circuits of 64 or 128 channels. Analogue chips will be mounted on one side and the digital chip on the opposite side with a grounded mask in between to avoid cross-talk. These cards are 30 mm high and will be mounted normal to the fan-in board and connected pin to pin with a conductive plastic layer.

IX. List of Registrants

Symposium on Particle Identification at High Luminosity Hadron Colliders

List of Registrants

Adams, Mark	*University of Chicago*
Alam, M.S.	*S.U.N.Y.*
Anderson, David F.	*Fermilab*
Atac, Muzaffer	*Fermilab*
Baker, Mark D.	*Massachusetts Institute of Technology*
Baker, Winslow F.	*Fermilab*
Banerjee, Sudeshna	*University of Notre Dame*
Barr, Giles	*CERN*
Bhat, Pushpalatha C.	*Fermilab*
Bhatti, Anwar	*University of Washington*
Binkley, Morris	*Fermilab*
Biswas, Nripen N.	*University of Notre Dame*
Borcherding, Fred	*Fermilab*
Breskin, Amos	*Weizmann Institute*
Burnstein, Ray A.	*Illinois Institute of Technology*
Carey, Tom	*Alamos National Laboratory*
Charpak, George	*CERN*
Childress, Sam	*Fermilab*
Christenson, Jim	*Fermilab*
Clark, Allan G.	*Fermilab*
Clemen, Mark	*University of Pittsburgh*
Coleman, Rick	*Fermilab*
Conrad, Janet	*Harvard University*
Cook, Victor	*University of Washington*
da Motta, Helio	*Fermilab*
Darden, Colgate	*University of South Carolina*
Darling, Chris	*Fermilab*
Denby, Bruce	*Fermilab*
Dhawan, Satish	*Yale University*
Eartly, Dave	*Fermilab*
Edwards, M.	*Rutherford Appleton Laboratory*
Finley, David A.	*Fermilab*

Foley, K.J.	*Brookhaven National Laboratory*
Francke, Tom	*Manne Sieg bahn Inst. of Physics*
Fukui, Yasuo	*Fermilab/KEK*
Fuzesy, Raymond	*Lawrence Berkeley Laboratory*
Garbincius, Peter	*Fermilab*
Gourlay, Steve	*Fermilab*
Graff, Norman	*Fermilab*
Green, Dan	*Fermilab*
Guyonnet, Jean-Louis	*C.R.N. Strasbourg*
Haber, Carl	*Lawrence Berkeley Laboratory*
Hadley, Nicolas J.	*University of Maryland*
Haggerty, Herman	*Fermilab*
Hagopian, Sharon	*Florida State*
Handler, Robert	*University of Wisconsin*
Hauser, Jay	*University of Chicago*
Hissong, John G.	*Yale University*
Hoeneisen, Bruce	*Universidad San Francisco de Quito*
Hogan, Gary E.	*Los Alamos National Laboratory*
Hojvat, Carlos	*Fermilab*
Ikeda, Hirokazu	*KEK*
Jacobs, Tom	*AT&T Bell Labs*
Jansen, Douglas	*University of Washington*
Johnson, Kurtis	*Florida State University*
Jostlein, Hans	*Fermilab*
Kadel, Richard	*Fermilab*
Karchin, Paul	*Yale University*
Kautzky, Hans	*Fermilab*
Kephart, Robert	*Fermilab*
Kross, Brian	*Fermilab*
Lach, Joseph	*Fermilab*
Lander, Richard	*University of California, Davis*
Lang, Karol	*Stanford University*
Lankford, Andrew J.	*SLAC*
Lau, Kwong	*University of Houston*
Leith, David W.G.S.	*SLAC*
Lipton, Ronald	*Carnegie Mellon University*
Lockyer, Nigel	*University of Pennsylvania*
Lopez, Angel	*University of Puerto Rico*

Ludlam, Thomas	*Brookhaven National Laboratory*
Luk, Kam-Biu	*Fermilab*
Lundin, Mark	*Fermilab*
Lynch, Gerald R.	*Lawrence Berkeley Laboratory*
Mahon, Roberto	*Universidade de Sao Paulo*
Majewski, Stan	*University of Florida*
Makoff, Greg	*University of Chicago*
McClelland, John B.	*Los Alamos National Laboratory*
McDonald, Kirk	*Princeton University*
McManus, Arthur P.	*University of Notre Dame*
Merkel, B.	*LAL*
Michael, Douglas	*Harvard University*
Mishra, Shekhar	*Los Alamos National Laboratory*
Morfin, Jorge	*Fermilab/Univ. Aut. Barcelona*
Morgan, Norman	*Purdue University*
Nakano, Itsuo	*University of Tsukuba*
Paige, Frank E.	*Brookhaven National Laboratory*
Papavassiliou, V.	*Fermilab*
Parker, Sherwood	*University of Hawaii*
Pavletta, G.	*University of Udine*
Peoples, Jr., John	*Fermilab*
Peskov, Valdimir	*CERN*
Polychronakos, Venetios A.	*Brookhaven National Laboratory*
Price, M.J.	*CERN*
Qian, Sijin	*INFN - Frascati*
Quigg, Chris	*SSC*
Ragan, Kenneth	*University of Pennsylvania*
Read, Linc	*Fermilab*
Rusack, Roger	*Rockefeller University*
Rutherfoord, John	*University of Arizona*
Sannes, Felix	*Rutgers University*
Sansoni, Andrea	*INFN - Frascati*
Seguinot, Jacques	*College de France*
Shank, Jim	*Boston University*
Sheaff, Marleigh	*University of Wisconsin*
Sheldon, Paul D.	*University of Illinois*
Shupe, Michael	*University of Arizona*
Slaughter, Jean	*Yale University*

Ludlam, Thomas	*Brookhaven National Laboratory*
Luk, Kam-Biu	*Fermilab*
Lundin, Mark	*Fermilab*
Lynch, Gerald R.	*Lawrence Berkeley Laboratory*
Mahon, Roberto	*Universidade de Sao Paulo*
Majewski, Stan	*University of Florida*
Makoff, Greg	*University of Chicago*
McClelland, John B.	*Los Alamos National Laboratory*
McDonald, Kirk	*Princeton University*
McManus, Arthur P.	*University of Notre Dame*
Merkel, B.	*LAL*
Michael, Douglas	*Harvard University*
Mishra, Shekhar	*Los Alamos National Laboratory*
Morfin, Jorge	*Fermilab/Univ. Aut. Barcelona*
Morgan, Norman	*Purdue University*
Nakano, Itsuo	*University of Tsukuba*
Paige, Frank E.	*Brookhaven National Laboratory*
Papavassiliou, V.	*Fermilab*
Parker, Sherwood	*University of Hawaii*
Pavletta, G.	*University of Udine*
Peoples, Jr., John	*Fermilab*
Peskov, Valdimir	*CERN*
Polychronakos, Venetios A.	*Brookhaven National Laboratory*
Price, M.J.	*CERN*
Qian, Sijin	*INFN - Frascati*
Quigg, Chris	*SSC*
Ragan, Kenneth	*University of Pennsylvania*
Read, Linc	*Fermilab*
Rusack, Roger	*Rockefeller University*
Rutherfoord, John	*University of Arizona*
Sannes, Felix	*Rutgers University*
Sansoni, Andrea	*INFN - Frascati*
Seguinot, Jacques	*College de France*
Shank, Jim	*Boston University*
Sheaff, Marleigh	*University of Wisconsin*
Sheldon, Paul D.	*University of Illinois*
Shupe, Michael	*University of Arizona*
Slaughter, Jean	*Yale University*

Smith, Elton	*CEBAF*
Spiegel, Leonard	*Fermilab*
Stefanski, Ray	*Fermilab*
Stirling, James W.	*University of Durham*
Stutte, Linda	*Fermilab*
Takach, Steve	*Fermilab*
Terentyev, N.	*Leningrad Nuclear Physics Institute*
Theriot, Dennis	*Fermilab*
Tollestrup, Alvin	*Fermilab*
Trendler, Robert	*Fermilab*
Tschirhart, Robert	*Princeton University*
Turkot, Frank	*Fermilab*
Van Berg, Richard	*University of Pennsylvania*
Vandijk, Jacobus	*Brookhaven National Laboratory*
Venkataramania, Harsh	*Yale University*
Videbaek, Flemming	*Argonne National Laboratory*
Volk, Jim	*Fermilab*
Wagoner, David	*Prairie View A&M University*
Wah, Yau	*University of Chicago*
Whitaker, S.	*Boston University*
Wilhelm, Mathias	*University of Freiburg*
Willis, Suzanne	*Northern Illinois University*
Winn, David R.	*Fairfield University*
Wiss, James E.	*University of Illinois*
Yamada, R.	*Fermilab*
Yamanaka, Taku	*Fermilab*
Yang, W.	*Fermilab*
Yokosawa, Akihiko	*Argonne National Laboratory*
Ypsilantis, Thomas	*College de France*
Ziock, Hans-Joachim	*Los Alamos National Laboratory*

Smith, Elton	*CEBAF*
Spiegel, Leonard	*Fermilab*
Stefanski, Ray	*Fermilab*
Stirling, James W.	*University of Durham*
Stutte, Linda	*Fermilab*
Takach, Steve	*Fermilab*
Terentyev, N.	*Leningrad Nuclear Physics Institute*
Theriot, Dennis	*Fermilab*
Tollestrup, Alvin	*Fermilab*
Trendler, Robert	*Fermilab*
Tschirhart, Robert	*Princeton University*
Turkot, Frank	*Fermilab*
Van Berg, Richard	*University of Pennsylvania*
Vandijk, Jacobus	*Brookhaven National Laboratory*
Venkataramania, Harsh	*Yale University*
Videbaek, Flemming	*Argonne National Laboratory*
Volk, Jim	*Fermilab*
Wagoner, David	*Prairie View A&M University*
Wah, Yau	*University of Chicago*
Whitaker, S.	*Boston University*
Wilhelm, Mathias	*University of Freiburg*
Willis, Suzanne	*Northern Illinois University*
Winn, David R.	*Fairfield University*
Wiss, James E.	*University of Illinois*
Yamada, R.	*Fermilab*
Yamanaka, Taku	*Fermilab*
Yang, W.	*Fermilab*
Yokosawa, Akihiko	*Argonne National Laboratory*
Ypsilantis, Thomas	*College de France*
Ziock, Hans-Joachim	*Los Alamos National Laboratory*